

VOL-I

304
1

**POST CENTENARY GOLDEN JUBILEE
OF UNIVERSITY OF CALCUTTA, INDIA**

PROCEEDINGS

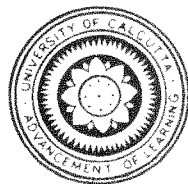
of

International Conference on Modeling and Simulation, MS'07 India

Theme: Control, Instrumentation, Embedded System Engineering and General Applications

December 3-5, 2007 Kolkata, India

Organised by



University of Calcutta, Department of Applied Physics, India

In Association with



AMSE, France

Co-organized by



The Institution of Engineering and
Technology (UK)

Technical Collaborators



IEEE (USA), Kolkata, India



IETE, Kolkata, India

CUK-H00465-1-07166014

POST CENTENARY GOLDEN JUBILEE OF UNIVERSITY OF CALCUTTA, INDIA

*Proceedings
of
International Conference
Modeling And Simulation, MS'07 INDIA*

Theme : Control, Instrumentation, Embedded System Engineering and General Applications



December 3-5, 2007 Kolkata, India

Organised by



Department of Applied Physics, University of Calcutta, India

**In association with
AMSE : International Association for Modeling and Simulation
Technique in Enterprise, France**

**Co-organiser
IET, Calcutta Branch**

**Technical colaborator
IEEE (USA), Kolkata Chapter, IETE, Kolkata Centre**

G166014

Professor Asis Kumar Banerjee
VICE-CHANCELLOR
University of Calcutta



87/1, College Street
Senate House
Kolkata-700 073
Telephone Nos. 2241-3288/0071/4984
Fax No. 91-33-2241-3288
E-mail : vc@caluniv.ac.in

November 7, 2007

FOREWORD

The University of Calcutta, established on January 24, 1857, is devoted to advancement of learning and is presently celebrating its Postcentenary Golden Jubilee. The Department of Applied Physics was established in 1925 as a Department of the University for the purpose of carrying out post graduate studies and research in Electrical Tehnology and allied Sciences. Since then it has produced a number of eminent teachers and pioneer technologists of national and international fame.

This Department organizes various types of academic activities in order to unravel new technologies before professionals and students throughout the year. The present Conference is an example. To address some critical issues in the areas of Control and Instrumentation, the Department resolved to take a venture in a broader spectrum in which they could obtain the association of AMSE, International Association for Modeling and Simulation Technique in Enterprise, France, a leading professional body engaged in dissemination of technology throughout the globe.

With the fast changing and compctitive global industrial environment, engineers in the power and process sectors are confronted with unprecedented uncertainty in efficient operation of an industry. Unification of control technologies and restructuring and deregulation of power sectors have made things more complicated. Control and instrumentation constitute the lifeline of an industry and it is the use of state-of-the-art-technology in these matters that can eradicate this uncertainty.

Professor Asis Kumar Banerjee
VICE-CHANCELLOR
University of Calcutta



87/1, College Street
Senate House
Kolkata-700 073
Telephone Nos. 2241-3288/0071/4984
Fax No. 91-33-2241-3288
E-mail : vc@caluniv.ac.in

Embedded systems technology has attempted to add to modern control and instrumentation techniques a new dimension. This technology, as a concept and in its numerous technological incarnations, is arguably one of the most influential transformations which have shaped our society in the recent past. No one can deny that it is gaining its relevance in every sphere of life. Rapid advances in computer and communication technologies have bolstered it. It is thus natural for the Department of Applied Physics to wish to explore the extent and diversity of developments in these technological arenas.

To achieve this goal the Department has, in association with AMSE: International Association for Modeling and Simulation Technique in Enterprise, France, planned to organize this Three-Day International Conference on "Modeling And Simulation" with the theme "Control, Instrumentation, Embedded System Engineering and General Applications" during 3-5 December, 2007 at Kolkata, India. The Conference will explore the deep-rooted linkages between existing and emerging concerns faced by the engineers in these and related fields. It will try to develop appropriate strategies and decision making tools and create awareness of the best practices in the fields of technology, management and general applications.

The Conference Proceedings, containing rich contributions from eminent experts in the relevant fields, aims at giving ample opportunity to the scientists, academicians, technologists and engineers to take stock of technological advancements in relevant areas, understand future trends and deliberate on other related issues of technical and social consequences.

I wish the Conference all success and I am confident that the Proceedings will be a lasting contribution to knowledge.

A. K. Banerjee
Asis Kumar Banerjee

PREFACE

With the advent of modern technologies, industries are having recourse to newer processes for efficient and zero breakdown running of a plant. On the other hand, power sector with its restructured environment has also started utilizing the advancement of technology in the different aspects of power and energy sectors. Control and instrumentation are the life lines of efficient operation of a plant or a system. Embedded systems technology combined with advanced computer and communication technologies has enriched modern control and instrumentation techniques. It is thus necessary to explore the extent and diversity of development in these technological arenas.

To discuss the rapid developments in the areas of control, instrumentation and embedded system engineering, Department of Applied Physics, University of Calcutta, India in association with AMSE, France and co-organised by IET, Calcutta Branch is going to organize an international conference on December 3-5, 2007 where speakers from all over India and abroad will present their original research works.

183 research papers, authored by eminent engineers, scientists, technologists and research workers, screened out from about 330 submissions, are included in this proceedings. Nine Invited Speeches, delivered by eminent national and international speakers, have also been included. All the papers and the invited speeches will be presented in 24 technical sessions and three plenary sessions. It should be mentioned that a number of good submissions could not be included due to space and time constraints for which the organizers apologize. The areas covered are,

- Control Theory
- Monitoring and control of power system components
- Process control and instrumentation
- Power Quality, HVDC and FACTS Technology
- Modern Protection, Instrumentation and Control
- Electro-optic Devices and Optical Communication
- Transmission and Distribution System Automation
- Application of Artificial Intelligence, Neural Network and Fuzzy Control Techniques
- Power Electronics and Drives
- Power System Dynamics, Control and Optimization
- Electric Power Market, Deregulation and restructuring
- Power System Modeling and Simulation
- Wind Power and Other Renewable Power, DG and Interconnection
- Modern Communication for Metering, Control and Protection
- Neural networks and Genetic Algorithms
- Embedded system engineering and Expert systems
- Pattern recognition and image processing
- Knowledge based decision systems
- Application for economy, finance, sociology, medicine and others
- General application of Modeling and Simulation; Case studies and Experimental results

The organizers have taken all efforts to make the proceedings error free. But still some errors might have crept in for which they apologize in anticipation. It is hoped that the readers will enjoy these volumes.

ACKNOWLEDGEMENT

Organizing Committee of MS'07 India would like to place on record its gratitude to the esteemed participants, engineers, scientists, technologists and research workers, for their valued technical contributions and participation.

Members of the international advisory committee and national organizing committee have contributed significantly in organizing the conference and also for this publication. The members of the Publication Sub-committee are grateful to the reviewers of the papers who have made tremendous efforts to maintain the time schedule and standard of the publication.

The committee also thanks the Superintendent of Calcutta University press along with his enthusiastic working force to publish these volumes within a short time.

It is a pleasure to acknowledge all supports, financial and moral, provided by the Associator, Co-organizer, Technical Collaborators, Sponsors and Advertisers without which this event could not come into reality.

The committee also puts on record the co-operations provided by the staff members of the conference secretariat, those of the Department of Applied Physics and those of the venue, different agencies and many more.

**International Conference
on
Modeling And Simulation, MS'07 INDIA**

Co-organiser

The Institution of Engineering and Technology, Kolkata Section

Technical Collaborator

Institute of Electrical & Electronics Engineers, Kolkata Section

The Institution of Electronics and Telecommunication Engineers, Kolkata Centre

SPONSORS

All India Council for Technical Education, Government of India

Department of Science and Technology, Government of India

Council of Scientific and Industrial Research, Government of India

Department of Information Technology (DIT), Government of India

Science and Technology Department, Government of West Bengal

Defence Research & Development Organisation, Government of India

University Grants Commission

Technical Education Quality Improvement Programme, TEQIP, UCT-CU

West Bengal State Electricity Distribution Company Limited, India

RTDS Technologies Inc., Canada

Usha Intercontinental (India), New Delhi, India

TATA Consultancy Services, Kolkata, India

Tech Mahindra Limited, Kolkata, India

Century Transformers Pvt. Limited, Kolkata, India

RAHUL Foundation, Kolkata, India

YOKOGAWA India Limited, India

Rockwell Automation

M. N. Dastur & Company (P) Limited, Kolkata, India

Principal Patrons
Professor Asis Kumar Banerjee,
Vice Chancellor,
University of Calcutta, India

Professor Jaime Gil Aluja
President, AMSE, Spain

Patrons
Professor Tapan Kumar Mukherjee
Pro Vice Chancellor,
University of Calcutta, India

Professor Suranjan Das
Pro Vice Chancellor,
University of Calcutta, India

Professor Christian Berger-Vachon
General Secretary, AMSE, France

International Advisory Committee
Chairman: D. K. Basu, Former Vice Chancellor, Burdwan University, India

A Ogulu, University of Kwa Zulu-Natal, South Africa
A. R. Thakur, Vice Chancellor, WBUT, India
Aladin Zayegh, Victoria University of Technology, Australia
Andrew Forsyth, The University of Manchester, UK
Andrzej Horodecki, Lublin Technical University, Poland
Asoke K Nandi, The University of Liverpool, UK
B. B. Chaudhuri, ISI, Kolkata, India
Brad Lehman, Northeastern University, Boston, USA
C. S. Jha, Professor Emeritus, IIT, Delhi, India
D. P. Kothari, IIT, New Delhi
D. Sanyal, IET, Kolkata, India
Dragutin Debeljkovic, University of Belgrade, Belgrade Serbia
Francesco Carlo Morabito, University of Reggio Calabria, Italy
Frederico Gonzalez Santoyo, University of Michoanacana, Mexico
Hamlaoui Abdessalam, University of Malaya, Kuala Lumpur
Jeno Kovaks, University of Oulu, Finland
K. Bhattacharyya, IEEE, Kolkata, India
K. C. Mukhopadhyay, IET, Kolkata, India
Li Ge, National University of Defense Technology, China
M. A. Kashem, University of Tasmania, Australia
Malcolm R Irving, Brunel University, Uxbridge, UK
N. R. Banerjee, Vice Chancellor, Bengal Engineering and Science University, India
P. Banerjee, IETE, Kolkata, India
Petr Stemberk, Czech Technical University, Czech Republic
P. N. Ghosh, Vice Chancellor, Jadavpur University, India
R. N. Lahiri, IET, Kolkata, India
Raed Abu Zitar, Philadelphia University, Jordan
S. Bhattacharyya, IIM, Kolkata, India
S. K. Sanyal, IEEE, Kolkata, India
S. N. Mishra, Sikkim, India
T. K. De, IETE, Kolkata, India

GENERAL CHAIR

A. K. Mukhopadhyay
Ex-Vice Chancellor, Tripura University, India and
Sir R. B. Ghosh Chair Professor of Department of Applied Physics,
University Of Calcutta, India

ORGANISING COMMITTEE

Chairman

G. Sarkar
Head and Labonyamoyee Das Chair Professor of Department Of Applied Physics, University Of Calcutta,
India

General Secretary

S. Sengupta, Applied Physics, University Of Calcutta, India

Joint Convenors

M. Mitra and J. N. Bera, Applied Physics, University Of Calcutta, India

Members

S. K. Bandyopadhyay, Registrar, CU, India
S. Sen, Dean, FET, CU, India
S. Sarkar, Secretary, UCSTA, CU, India
T. K. Mitra, Applied Physics, CU, India
Balaram Bhattacharyya, Applied Physics, CU, India
S. Phaujdar, Applied Physics, CU, India
S. C. Kar, Applied Physics, CU, India
R. Brahmachari, Applied Physics, CU, India
S. C. Bera, Applied Physics, CU, India
C. Dey, Applied Physics, CU, India
S. Chowdhury, Applied Physics, CU, India
R. Gupta, Applied Physics, CU, India
K. K. Mazumdar, UCT-CU, India
M. K. Sengupta, UCT-CU, India

Technical Committee

Chairman: K. K. Bandyopadhyay, Applied Physics, CU, India
Convenor: S. Chattopadhyay, Applied Physics, CU, India

Finance Committee

Chairman: S. K. Sen, Applied Physics, CU, India
Convenor: S. Phaujdar, Applied Physics, CU, India

Publication Committee

Chairman: A. Deb, Applied Physics, CU, India
Convenor: S. C. Kar, Applied Physics, CU, India

Event Management Committee

Chairman: S. K. Sen, Applied Physics, CU, India
Convenor: R. Gupta, Applied Physics, CU, India

Reception, Hospitality and Travel Management Committee

Chairman: S. Chowdhury, Applied Physics, CU, India
Convenor: C. Dey, Applied Physics, CU, India

CONTENTS

VOL I

	Page No.
<i>Foreword</i>	<i>i</i>
<i>Preface</i>	<i>iii</i>
<i>Acknowledgement</i>	<i>iv</i>
<i>Sponsors</i>	<i>v</i>
<i>Committee</i>	<i>vi</i>
Technical Session 1A: Power System Stability	
1. An Offline Simulation Method to Identify The Weakest Bus And its Voltage Stability Margin in a Multibus Power Network <i>Kabir Chakraborty, Sangita Das Biswas</i>	1
2. A Review of Analytical Techniques for Determination of Voltage Stability in a Multi-bus Power System <i>Suman Saha, Abhijit Chakroborti, C. K. Chanda, A .B. Chowdhury</i>	6
3. Bulk Power System Reliability Evaluation Using Fuzzy Logic <i>K. Thippeswamy, V. K. Keshavan</i>	11
4. Stability Investigation of Power System and Its Stabilization by a Coordinated Application of Power System Stabilizers in Multi-machine Systems <i>N. Albert Singh, F. Shamila, K. A. Muraleedharan and K. Gomathy</i>	16
5. Incorporating Static Synchronous Series Compensator in Optimal Reactive Power Allocation for Improving Voltage Stability Margins <i>P. Kanta Rao and K. Vaisakh</i>	21
6. Analysis of Voltage Control Stability Indices of Radial Distribution in Modern Power System <i>S. Sao, Sriniwasa Rao. Gorantla, M.V.Ramesh</i>	28
7. Assessment of Voltage Stability in Longitudinal Power Supply System <i>S. Halder nee Dey, A. Chakrabarti, A. De</i>	33
8. Single Cycle Mathematical Model for Harmonic Power in d-q Plane <i>Surajit Chattopadhyay, Madhuchhanda Mitra, Samarjit Sengupta</i>	38
Technical Session 1B: Process Control	
9. A Novel approach for the Design of Stabilizing PI Controllers <i>M. Siva Kumar, B. J. J Raju , A.Sarada Devi, P. Naga Manasa</i>	43
10. Improving Automation Benefits of Process Control System Using Performance Evaluation by Statistical Analysis <i>S. G. Hingmire, S. G. Karad, . D. S. Karanjkar</i>	47
11. Performance of Orifice Plates in Transient Cavitating Flow: Experimental Study <i>K. S. Sumam, S.G. Thampi, N. Sajikumar</i>	52
12. Design of H _∞ based Robust Controller for AVR System <i>V. Mukherjee, Bijoy K. Mukherjee, and S.P. Ghoshal</i>	56
13. Study of Energy Losses of a High Capacity Boiler and Design of Flue Gas Heat Recovery Unit for the Optimum Efficiency of a Thermal Power Plant <i>S. C. Bera, M. S. Bhowmick</i>	61
14. A Report on Modification of Burner Management System of a Steam Generation Unit in Naphtha and Natural Gas based Fertilizer Plant <i>S. C. Bera , M. S. Bhowmick</i>	66
15. Position Control System of a Motorized Valve in a Process Plant using PLC <i>S. Chattopadhyay, S. Pal, U. Chakraborty, S. C. Bera</i>	70
Technical Session 1C: Power Electronics Simulation	
16. Design, Analysis and Simulation of DC-to-DC Flyback Converter <i>R. A. Gupta, Rajesh Kumar, Saurabh Goyal, Parikshit Yadav</i>	75
17. Modeling of a 3-Phase Current Controlled Inverter With Observer-Feedback and Decoupling <i>Dipankrita Gangopadhyay, K.Selvaajothi, P.A.Janakiraman</i>	80

18.	Switch Mode Rectifier With Improved Power Factor & High Quality Input Waveforms <i>P. K. Gujarathi, M. V. Aware</i>	85
19.	Simulation and Design of An Active Power Filter for SCR Converter <i>Prabal Deb, Shilpi Bhattacharya, Sujit K. Biswas</i>	89
20.	SiC based Buck Boost Converter <i>Vineeta Agarwal, Neeraj Verma</i>	94
21.	Simulation of a Novel Zero Voltage Transition (ZVT) Technique Based Boost Power Factor Correction (PFC) Converter with EMI Filter <i>P. Ram Mohan, M. Vijaya Kumar, O. V. Raghava Reddy</i>	99
22.	Design and Simulation of 30 Watt Phase Modulated Converter <i>Rajesh Babu Kollipara, P. K. Chaturvedi, K. C. Pradhan</i>	104
Technical Session 1D: GA and its Application		
23.	Qualitative GA Based Identification and Control of 2DOF Inverted Pendulum <i>Altreza Rezazade, Mohsen Modarres</i>	110
24.	An Object Oriented Neural Network Model Optimized by Genetic Algorithm for Microwave FETs <i>Anil Ahlawat, Rajesh Tyagi, Sujata Pandey, Manoj Pandey</i>	115
25.	Genetic Algorithm Driven Modeling of Defect States in Poly-Thiophene (PT) and Poly-Selenophene (PS) under Zero Band-Gap Constraint <i>Rahul Sharma, S. P. Bhattacharyya</i>	119
26.	Optimum Design of Stewart Platform By Using Genetic Algorithm <i>R. Kaviani, A. Rastgo</i>	124
27.	Optimization of Surface Roughness in End Milling of Stainless Steel (SS 304) Using Genetic Algorithm <i>Anayet U Patwari, A.K.M. Nurul Amin, and Ishhtiyag M. Hossain</i>	129
28.	Genetic Algorithm Based Tabu Search Method for Solving the Unit Commitment Problem with Cooling – Banking Constraints <i>C. Christofer Asir Rajan</i>	133
29.	Automated Active Filter Design using Genetic Algorithm <i>Rupaban Subadar, Swanirbhar Majumder</i>	138
Technical Session 2A: FACTS		
30.	Dynamic Stability Analysis of Power System Using Thyristor Controlled Series Capacitor <i>P. Bera, D. Das, T. K. Basu</i>	143
31.	Simulation and Modeling of GA Optimized Distribution Static Compensator for Power Quality Improvement <i>Deepika Masand, Shailendra Jain, Gayatri Agnihotri</i>	147
32.	Improvement of Voltage Stability Margins with OPF Incorporating Static Series Synchronous Compensator <i>L. R. Srinivas, K. Vaisakh</i>	153
33.	Multi-Area Unit Commitment Using Dynamic Programming Approach and Checking of Dynamic Stability <i>Rambabu.Ch</i>	158
34.	Ratings of FACTS Devices for Power Flow Control in Power System Network <i>Subrata Majumdar, P. K. Chattopadhyay, A. K. Chakrabarty</i>	163
35.	Design of STATCOM Controller Based on State Predominant Approach <i>R. K. Pandey, Akashdeep Agrawal</i>	167
36.	Normal Form Analysis of Stressed Power System Incorporating STATCOM <i>Ramtin Hadidi Ahad Kazemi</i>	172
37.	A Homogeneous Model of SSSC in Power Network <i>R. K. Pandey, N. K. Singh</i>	177
38.	SSSC Based Power Oscillation Damping Controller <i>R. K. Pandey, N. K. Singh</i>	182

Technical Session 2B: Biomedical Signal Processing		
39.	Erythrocyte Shape Investigation and Analysis using Image Processing Technique Umalakshmi A, Rajeshwari S, Sandhya Rao, Shilpa G. S, Manjunatha M, Mallikarjuna Swamy <i>M. S, Mallikarjun S. Holi</i>	187
40.	Computer based Investigation of Hearing Disorders through Distortion Product Otoacoustic Emission Analysis <i>Jyothiraj V.P, Suresh Kumar A</i>	192
41.	Diagnosis Of Eye Diseases Using Medical Imaging. <i>Sheeba O, Suresh Kumar A.</i>	196
42.	Effect of Fractal Image Compression on Screening for Diabetic Retinopathy. <i>David. J, Suresh Kumar. A, Harsha. A</i>	201
43.	Protein Secondary Structure Prediction through Combination of Decisions from Multiple MLP classifiers <i>Piyali Chatterjee, Subhadip Basu, Mahantapas Kundu, Mita Nasipuri, Dipak Kumar Basu</i>	206
44.	Study of EEG Signals under Photic Stimulation <i>Mohandas K P, Rameshkumar P</i>	211
45.	ECG Signal Processing for Analysis of Abnormalities based on QT Interval-A Novel Approach <i>Madhuchhanda Mitra, Saurabh Pal, Swarnabhar Majumder</i>	216
46.	Rough Set Based Classification of Myocardial Infarction <i>Sucharita Mitra, M. Mitra, and B. B. Chaudhuri</i>	219
47.	Pattern Grammar and Histogram Based ECG Features Extraction <i>Sucharita Mitra, M.Mitra, and B.B. Chaudhuri</i>	224
Technical Session 2C: Modeling and Simulation		
48.	First-Principles Modeling and Simulation of the Electronic and Magnetic Properties of C_8 , Si_8 and MnC_7 , $MnSi_7$ <i>T. Benabdesselam, A. Tadjer, and B. Bouhafs</i>	229
49.	Symmetry Through Group and Linear Transformations <i>Samir Zaki Mohamed Mehrez</i>	234
50.	Mathematical Modeling for Predicating the Mechanical Properties of Plain-Weft Knitted Fabric <i>H. R. Karimi, A. A. A. Jeddi, A. Rastgoo</i>	238
51.	A Simulation Model For Partial Discharge with Stochastic Features <i>P. Das</i>	243
52.	Developed Model of Exciter Mechanism in Vibrating Screen and its Influence on the Efficiency of Grading Particle in Iron Ore Production Line <i>A. Rastgoo, H. Sohanian, A. Aram</i>	247
53.	Modulus of Highest Eigenvalue of a Polynomial <i>J. R. P. Gupta, Yogesh V. Hote, D. Roy Choudhury</i>	251
54.	Heat And Mass Transfer with Interaction Effects Analysis between an External flow and a Capillary Porous Body <i>S. Larbi, M. Malki, H. Belhaneche</i>	255
55.	Extension Classification Method and Its Application <i>Yang Chunyan</i>	260
56.	Computation of Optimum Expansion Coefficients in Generalized Block Pulse Function Domain <i>Anish Deb, Gautam Sarkar, Nabanita Nath Chowdhury</i>	265
57.	An Approach to Detect Cause of Over Current in Power System Network Using Real Time Digital Simulation <i>A. K. Dhara, S. Chowdhuri, J .N. Bera, S. C. Kar, S. Sengupta</i>	269
Technical Session 2D: Fuzzy Logic Applications		
58.	An approach for translation of Fuzzy Petri nets to Ladder Logic Diagrams <i>P.R. Venkateswaran, Jayadev Bhat, S. Meenatchisundaram</i>	273
59.	An Approach to Relate and Optimize Metal Forming Process Parameters by Fuzzy Logic <i>S.L. Mahmood, Fazilatunnessa, M. H. Banna, M. Raju Hossain</i>	277

60.	Selection of Membership Functions in the Prediction of Shoot Length of Mustard Plant at Maturity <i>Satyendra Nath Mandal, J. Pal Choudhury, Dilip De and S. K. Mukherjee</i>	282
61.	Behavior Modelling Based Fuzzy Controller for Combustion Control of Utility Boiler <i>T. R. Rangaswamy</i>	288
62.	Numerical Solution of Takagi-Sugeno Fuzzy Model Based State Equations via Block Pulse Functions <i>B.M. Mohan, Vertika Singh</i>	293
63.	Fuzzy ARTMAP Technique for Quality Evaluation of Tea using Electronic Nose <i>Dibyendu Bhattacharyya, Anil Kumar Bag, Bipan Tudu, Nabarun Bhattacharyya, Rajib Bandhopadhyaya</i>	297
64.	An Intelligent Approach for Multi-Sensor Data Validation and Fusion Using Fuzzy Logic <i>S. Saha, U. Kar and J. Sil</i>	302
65.	A Ziegler-Nichols PID Controller With Auto tuning Feature <i>Chandhal Dey, Rajani K. Mudt</i>	307
Technical Session 3A: Sensors and Transducers		
66.	Modelling & Simulation of Laser Material Processing and Predicting Melt Pool Geometry and Temperature Distribution <i>M A Sheikh</i>	312
67.	Simulation of Loopless Deflection Routing Algorithms in Label Switched Optical Networks using SimEvents <i>G Pavan Kumar, Vinod Chandra</i>	317
68.	Metal Oxide Gas Sensor under UV radiation : Theory and Experiment <i>Sunita Mishra, Indrajeet Boiragi, C Ghanshyam</i>	320
69.	Modeling and Simulation of SMART CMOS MEMS Pressure Sensor <i>C. RoyChaudhuri, N.Futane, H.Saha</i>	324
70.	Study of an IC Based Flow Transducer <i>S. C. Bera, N. Mandal</i>	329
71.	Study of Electrode Polarisation Impedence Type Transducer for The Measurement of Flow Rate of a Conducting Liquid <i>S. C. Bera, B.Chakraborty, N. Mandal, R. Sarkar</i>	332
72.	Study of a Magneto-Optic Element as a Displacement Sensor <i>S. Chakraborty, S.C. Bera</i>	336
Technical Session 3B: Control Theory		
73.	Design of H [∞] -Optimal Robust Controller for a Singularly Perturbed System <i>Debasish Mondal</i>	339
74.	The Gauss-Hermite Filter and the Central Difference Filter for Bearing Only Tracking. <i>Manas Kumar Bera, Saurabh Pal</i>	344
75.	Robust Control of Inverted Pendulum System by Convex Optimization: An LMI Approach <i>Sharmistha Mandal, A. Sutradhar</i>	349
76.	Microprocessor based Identification of Sampled Data System with/without Hold Device using a Set of Sample-and-Hold and Dirac Delta Functions <i>Anindita Senguptaa, Anish deb, Sudipta Mandal</i>	354
77.	Robust control of stochastic system via Lyapunov Approach and Linear Matrix Inequalities (LMIs) <i>Selma Ben Attia, Salah Salhi, M.Ksouri</i>	359
78.	New Approach for Static Output Feedback Problem <i>Neila Béditout, Salah Salhi, M.Ksouri</i>	363
79.	A Parameter Plane Design Methodology for Two-Loop Lateral Missile Autopilot <i>Mousiki Kar (Deb), Kalyankumar Datta, Shyamal Kumar Goswami</i>	368
Technical Session 3C: Induction Machines		
80.	Eigen-Frequency Improvement of Induction Machine Using PI Controller <i>S. Ekram, A. K. Sen, B. Sarkar</i>	373
81.	A New Integrated Motor Starter for Induction Motor	377

	<i>J. P. Tewari, R. K. Singh, Naveen Nischal Chava</i>	
82.	Current and Vibration Analysis of Induction Motor for Detection of Broken Rotor bar <i>B. Kundu, P.P. Pal, P. Chattopadhyay, G. Bandyopadhyay</i>	380
83.	Decoupled Control of Linear Induction Motor <i>S. N. Mahendra, K. Chaudhary, Akshay K Rathore, Pankaj Chaudhary</i>	384
84.	Fault Identification of An Induction Motor by Fractal Analysis Technique <i>Dilip Dey, P. B. Duttagupta, S. Sengupta</i>	389
85.	Multi-Class Fault Identification of Induction Motor by Using Support Vector Machine <i>Dilip Dey, P. B. Duttagupta, S. Sengupta</i>	393
86.	Diagnosis of Fault Due to Unbalanced Rotor of an Induction Motor by Analysis of Vibration and Motor Current Signatures <i>Subrata Karmakar, S.K. Ahamed, M.Mitra, S. Sengupta</i>	399
Technical Session 3D: General Applications-I		
87.	The Motion of Spherical Shock Waves in Self-gravitating Heat Conducting Medium <i>R. P. Yadav, Ratnesh Kumar, Virendra K. Gangwar</i>	404
88.	Sizing and Optimization Of Hybrid Renewable Power System <i>S. C. Gupta, Y. Kumar, Gayatri Agnihotri</i>	407
89.	Performance Comparison of a PV Powered Water-Pumping System with and without Maximum Power Point Tracker <i>Abu Tariq, M. S. Jamil Asghar</i>	412
90.	Modeling and Analysis of Particle Movement in a Common Enclosure Gas Insulated Bus Duct Under Unbalanced Voltages <i>G. V. Nagesh Kumar, J. Amarnath, B. P. Singh</i>	417
91.	Maximum Power Point Tracking Using Perturb and Observe Algorithm <i>Vineeta Agarwal, Alok Kumar Vishwakarma, B.K. Pandey</i>	422
92.	Open Circuit VMPPT with current compensation for low power photovoltaic cell <i>Vineeta Agarwal, Alok Kumar Vishwakarma, B.K. Pandey</i>	427
93.	An Approach for Attribute Data Measurement from a Network of Electrical Equipments as an Application of GIS <i>Epsita Das, Susmita Kundu, J. N. Bera, R. Bramhachari</i>	431
<i>Author Index</i>		
VOL II		
Technical Session 4A: Power Electronics Applications		
94.	Automated Control Of Electric Locomotives <i>Srinivasa Rao, Gorantla, S. Sao, M. V. Ramesh</i>	435
95.	Role of Electromagnetic and Radio Frequency Noise Suppressor for High Frequency Inverter Operated Induction Heating Equipment <i>Nitai Pal, Pradip Kumar Sadhu, Dilip Kumar Mitra, Rupendranath Chakrabarti</i>	440
96.	Performance Analysis of H.F. Mirror Inverter for Energy Efficient Induction Cooking Appliance Range <i>Pradip Kumar Sadhu, Nitai Pal, Rupendranath Chakrabarti, T. K. Chatterjee</i>	444
97.	Design of Speed Control of DC Series Motor using Fuzzy PID Controller <i>Barwal Shweta and K.K Garg</i>	449
98.	Microcontroller Based High Frequency Inverter <i>M. G. Warl, V. K. Sharma, R. D. Kharadkar</i>	453
99.	A Constant Switching Frequency Hysteresis Current Controller for Single-Phase Voltage-Source Inverters <i>M. Ahmadi, H. Heydari, and A. Rahmati</i>	456
100.	Predictive Current Control of an Inverter-Fed a 25kA Current Injection Transformer System <i>M. Ahmadi, H. Heydari, A. Rahmati</i>	461
101.	Fuzzy Logic Based Extended Dynamic Braking of Electric Locomotive <i>R. S. Bhaipai, Rajesh Gupta</i>	466

Technical Session 4B: Biomedical Instrumentation		
102.	Real Time Data Acquisition System for Three Axis Force Measurements of Needle Insertion into Soft Tissue, its Modeling and Simulation <i>Debajit Bharali, Sohini Roy, Ajay K. Yagati, Sunil Kumar, Sujoy K. Guha</i>	471
103.	Automated Detection and Classification of Cerebral Palsy Gait using Support Vector Machines <i>M. Shiva Kumar, M. Sukumar</i>	476
104.	Single Channel Computerized ECG Recorder and Extraction of Relevant Parameters from the ECG-A DSP Based Approach <i>Monisha Chakraborty, Bipan Tudu, Debashis Das</i>	479
105.	Effect of Stimulus Parameters and Spontaneous Otoacoustic Emissions on Transient Evoked Otoacoustic Emission Measurement for Hearing Screening <i>Sukesh Kumar A, Jyothiraj V. P</i>	483
106.	Stochastic Model of Haematopoiesis <i>Probir Kumar Dhar, Abhik Mukherjee, Durjoy Majumder</i>	488
107.	Design And Simulation of Signal Generator For A New Noninvasive RF Heartbeat Detection System <i>S. Shabu, Roshna.R</i>	493
108.	A Methodology for Studying the Characteristics of Expansion of Stent Like Structures in a Hyper Elastic Artery Model <i>Naveen Kumar KU, Sujesh Sreedharan, CG Nandakumar, Muraleedharan CV</i>	498
Technical Session 4C: Electric Drives		
109.	ANN - Based Current Control of A Voltage Source PWM Inverter <i>R. Arulmozhiyal, K. Baskaran</i>	503
110.	A Simulink Based Dynamic Modeling and Analysis of High Performance Induction Motor Drive <i>Rajesh Kumar, R. A. Gupta, S. V. Bhargale</i>	507
111.	A PFC Based High Performance Induction Motor Drive <i>Rajesh Kumar, R. A. Gupta, S. V. Bhargale</i>	512
112.	Constant v/f Control of Combined Inverter-Induction Motor Drive <i>S. P. Muley, M. V. Aware</i>	517
113.	Observer-Based Sensorless Control of A Vector Controlled Five-Phase Induction Motor Drive <i>M. Rizvan Khan, Atif Iqbal, Mukhtar Ahmad</i>	521
114.	Simulation of Space Vector Theory Based Variable Speed Operation of a PMSM Drive System Using Predictive Current Control <i>A. Lekshmi, R. Sankaran, S. Ushakumari</i>	528
115.	New Current Control of PMSM Drives in Synchronously Rotor Reference Frame <i>M. Kadjoudj, M.E. Benbouzid, and C. Ghenni</i>	533
116.	Modelling of PWM-Inverter fed Induction Motor Drive and Simulation Analysis of Motor Terminal Overvoltages <i>B. Basavaraja, D. V. S. S. Siva Sarma</i>	538
117.	Speed Control of DC Drives for Controlling Tension of Steel Strips in Steel Strip Manufacturing Industries <i>S. K. Sen, B. R. Das, S. Banerjee, S. K. Basak, S. K. Mondal</i>	542
Technical Session 5A: Power System		
118.	Power Vector Coordinated Multilateral Trades <i>Sudha Balagopalan, S Ashok and KP Mohandas</i>	547
119.	High Speed Fault Identification in A HVDC System Using Wavelet Modulus Maxima <i>M. Sushama, Ch.Prasanth Babu, A.Jaya Lakshmi, G. Tulasi Ram Das</i>	552
120.	Design of an Optimum Controller for DVR to Compensate Unbalanced Voltage Sag <i>M. R. Shakarnai, A. Kazemi, B. Mahdian</i>	556
121.	On Line Three Phase Power Factor Estimation under Nonsinusoidal Unbalanced and Time Varying Condition <i>Arghya Sarkar, K. K. Mazumdar, S. Sengupta</i>	561
122.	Power Factor Control of Distribution System by Using DSTATCOM <i>J. Ramanyaneya Reddy, S. Jagadish Kumar, CH. Siva Kumar</i>	566

123.	A PC based simulated frequency relay for real time protection of power system <i>T. K. Sengupta, A. Das, A. K. Mukhopadhyay</i>	570
124.	A Novel Particle Swarm Optimized AGC for Restructured Three Area Power System <i>Ranjit Roy, S. P. Ghoshal</i>	575
125.	Development Of a Numeric Adaptive Relay For Transformer Overload Protection <i>Pratap Chandra Karfa, J.K. Das, K. Das (Bhattacharya)</i>	580
126.	Study For Monitoring And Control Of Power System Parameters Using Geographical Information System <i>Susmita Dey (Chaudhuri), Anushree Roy, Sumana Chowdhuri, Jitendra Nath Bera</i>	585
Technical Session 5B: Transmission and Distribution		
127.	Fuzzy System Approach to Power Purchase in a Power Pool of A Deregulated Power System. <i>Ajoy K Chakraborty, C. K. Roy, P. B. Duttagupta</i>	589
128.	Feeder Reconfiguration and Capacitor Placement for Loss Reduction of Distribution System Using Genetic Algorithm <i>P. V. Prasad, S. SivaNagaraju, N. Sreenivasulu</i>	594
129.	A New Approach to Calculate Frequency Dependent Impedance of Grounding Electrodes <i>S. M. Shahrtash, N. Ramezani</i>	598
130.	An offline Simulation Study of Security Analysis of a Multibus Power System Using Load-Flow Based Technique <i>Sangita Das Biswas, Kabir Chakraborty, Tanimu Bhattacharya, Bishakha Nandi</i>	605
131.	Voltage Sag and Unbalance Mitigation in Distribution Systems Using Multi-level UPQC <i>H. R. Toodeji, S. M. Ale Emran, N. Farokhnia, H. Askarian, S. H. Fathi, G. B. Gharehpetian, M. Abedi</i>	610
132.	Electromagnetic Field Effect on Metallic Particle Contamination in a Common Enclosure Gas Insulated Bus duct <i>G. V. Nagesh Kumar, J. Amarnath, B. P. Singh, K. D. Srivatsava</i>	616
133.	PD Detection and Location in Cable Networks Based on Traveling Waves Indices <i>S. M. Shahrtash, F. Haghighi</i>	621
134.	Reduced Order LQG Controller for Distribution Static Compensator used for Load Voltage Control of Distribution System <i>Rajesh Gupta, Arindam Ghosh</i>	628
135.	Concept and Benefits of Microgrid System with Modeling and Simulation <i>Prasenjit Basak, S.P. Chowdhury, and S. Chowdhury</i>	633
136.	Assessment of Transmission Line Losses through Power Flow Tracing in a Deregulated Multi-Bus Power System <i>Ashim Kumar Dey, Narendra Nath Sinha, J.K.Das, S. Sengupta</i>	637
Technical Session 5C: VHDL and Embedded System		
137.	Simulation of Random Early Detection Algorithm Using VHDL <i>Nilay Khare, Kavita Khare</i>	642
138.	An Efficient Simulator for Power Grid Analysis in VLSI Chips <i>Vishnu Vardhan, Sandeep K. Dey, Susmita Sur-Kolay, Debasis Mitra, Bhargab B. Bhattacharya</i>	646
139.	VHDL Simulation of A Memory Efficient, High Speed Huffman Decoder: Extension to FPGA Implementation <i>Bijoy Kumar Upadhyaya, P. Venkateswaran, S. K. Sanyal, R. Nandi</i>	651
140.	Hardware/Software Partitioning Problem in Embedded System Design Using Particle Swarm Optimization Technique <i>Amit Konar, Alakananda Bhattacharya</i>	656
141.	A CPLD Based Gold Code Generator <i>S. Chattopadhyay, S. K. Sanyal</i>	660
142.	Protection from Buffer Overflow with External Hardware in an Embedded System <i>Ashim Datta, S. Sengupta</i>	664
143.	Transmission of ECG Signal Using Microcontroller Based Wireless Bi-phase Modulation Technique <i>R. Gupta, C. Das, A. Mondal, J. N. Bera, M. Mitra, T. K. Mitra</i>	669

Technical Session 6A: ANN		
144.	Type Identification of Unknown Thermocouple Using Probabilistic Neural Network <i>Palash Kundu, Gautam Sarkar</i>	673
145.	Application of Neuro-Fuzzy Controller in HVAC System <i>A. K. Pal</i>	678
146.	Voltage Stability Evaluation using Artificial Neural Networks <i>P. Aruna Jeyanthi, D. Devaraj, N. Albert Singh</i>	683
147.	Electrical Fault Supervision in Induction Motors Using Neural Networks and Multiple Models Approach <i>IDER Zahir, Mendil Boubekour</i>	688
148.	ANN Application for Identification of Minimal Loss Feeder Reconfiguration <i>P. L. Muthukarthik, P. S. Venkataramu, T. Ananthapadmanabha</i>	694
149.	Nonlinear Dynamic Time Series Modeling using Genetically Optimized Evolving Fuzzy Neural Network <i>Jayashri Vajpai, Arun JB</i>	699
Technical Session 6B: General Application-II		
150.	Effect of Axial Magnetic Field on Temperature Variation of Self-Gravitating Gas Atmosphere Perturbed by Strong Shock Wave <i>R. P. Yadav, Virendra K. Gangwar, Sandeep Bharti, Satyendra Prakash, P. S. Rawat</i>	704
151.	Temperature Rise in the Cell Phone User's Head <i>R. Seetharaman, N. Kumaravel</i>	710
152.	Simulation And Analysis Of Micro-Resonators Using Sugar <i>S. Meenatchisundaram, G. Uma, M. Umapathy, B. S. Sathyanarayana, P. R. Venkateswaran</i>	712
153.	An Analytical Approach to Study Dynamics of Beat-up Mechanism of a Loom <i>A. Rastgoo, A. Mirdehghan</i>	717
154.	Three Dimensional Free Vibration Analysis of Transradially Isotropic Thermoelastic Sphere <i>J. N. Sharma, Nivedita Sharma</i>	722
155.	Direct Simulation of Forced Convection in Porous Media <i>Mohammad Hassan Rahimian, Abdullah Abasiun</i>	726
Technical Session 6C: Electrical Machines		
156.	Damping of Low Frequency Oscillations in Alternators using Neuro Fuzzy Logic Controller <i>F. Shamila, N. Albert Singh, K. A. Muraleedharan, K. Gomathy</i>	731
157.	Simulation of an Adjustable Speed Synchronous Motor fed from Sinusoidal Currents <i>Soumya Ray, Kaushik Mukherjee, Nikhil Mondal, Sujit K. Biswas</i>	736
158.	The Superiority of Interleaved Windings in a 25kA Current Injection Transformer <i>S. M. Pedramrazi, H. Heydari</i>	741
159.	Low Cost Controller for Switched Reluctance Motor <i>A.K. Dhakar, Amitava Das</i>	746
160.	PC Based Remote Speed Control and Condition Monitoring of DC Motor <i>S. Chowdhuri, J. N. Bera, G. Sarkar, S. Phoujdar</i>	751
Technical Session 7A: Electronics and Software Based Applications		
161.	Amplitude Control in Sinusoidal Oscillator <i>H. Mechergui, A. Haddouk</i>	755
162.	Quality Control In Distributed Software Systems <i>Rusakov M. A.</i>	761
163.	An Efficient Architecture for Low Density Parity Check Code Decoder <i>Saheeda P. A.</i>	764
164.	VLSI Architecture for Implementing Hearing Aid Algorithms <i>P A Saheeda, Reena M Roy</i>	768
165.	A Soft Computing Paradigm for Handwritten Digit Recognition with Application to Bangla Digits <i>Nibaran Das, Ram Sarkar, Subhadip Basu, Mahantapas Kundu, Mita Nastpuri,</i>	771

	<i>Dipak Kumar Basu</i>	
166.	Efficient Nanodevices for Advanced Ultradense VLSI Systems <i>Subir Kumar Sarkar, T. Datta, Ankush Ghosh, J. C. Singh, G. Prakash, Debasis Samanta</i>	775
167.	Communication Security through Cryptography and Performance Evaluation of Three Encryption/Decryption algorithms <i>Awadhesh Kumar Singh</i>	778
168.	A Novel Design Of Low Power Low Voltage Full Adder Using 14 MOSFETS <i>Manash Chanda, Swapnadip De, Amrit Ghosh, Devmalya Banerjee, Pijush Btswas</i>	782
Technical Session 7B: Image Processing		
169.	Statistical-Mechanical Modeling of Digital Halftoning <i>Jun-ichi Inoue, Yohei Saika, Masato Okada</i>	786
170.	Illumination Normalization Using DCT Coefficients Re-scaling and Adaptive Histogram Equalization for Face Recognition <i>Virendra P. Vishwakarma, Sujata Pandey, M. N. Gupta</i>	791
171.	Robust Face Recognition with PCA using Cascaded Correlation Neural Networks <i>J. Dheeba, N. Herald Anantha Rufus, N. Albert Singh</i>	796
172.	Face Recognition Using Back Propagation Algorithm <i>V.S. Dixit, Shweta Kundra Bhatta</i>	800
173.	An Application Module Using Eigenfaces for Face Recognition <i>S. Tripathi, R. Agrawal, M. K. Saini, A. K. Jain, S. Basu, R. Ramchandani, A. Gupta</i>	805
174.	Equivalence between Two Layout-Variant Document Images Without Reading <i>P. Nagabhushan, Sahana D. Gowda</i>	809
175.	Wavelet And Dct-Based Image Coding & Reconstruction For Low Resolution Implementation <i>Swanirbhar Majumder, Md. Anwar Hussain</i>	814
Technical Session 7C: Communication and Microwave		
176.	Microstrip Leaky-Wave Antenna With Arbitrary Metallic Strip Radiating Characteristics <i>Z. Mekkiout, H. Baudrand</i>	819
177.	Modeling of Process of Interaction of The Enterprises on The Basis of A Web-Services by Means of Java-Technologies <i>G. Jumatova</i>	822
178.	Performance Analysis of Neuro-Predictive Controller for Nonlinear Chemical Process <i>S. Paruya</i>	824
179.	Study of the Microwave Absorption Behaviour of Ceramic Material at X-Band Frequencies <i>S. K. Srivastava</i>	829
180.	Secure Communication in Power System Using Chaos Masking <i>Kabir Chakraborty, K.S.Sherpa, and S.Sengupta</i>	832
181.	A New Demodulation Scheme for AM Signals based on Sliding DFT <i>P. Sumathi, P. A. Janakiraman</i>	836
182.	Demonstration of Highly Efficient Transmission in Sixty Degree Sharply Bend Waveguide Based on Photonic Crystal at 1.5 μm Wavelength <i>L. Dekkiche, R. Naoum</i>	840
183.	Effect of Demodulator Filter Roll-off Factor on the Quality of QPSK Modulated Mobile Communication System <i>S. Chattopadhyay, S. K. Sanyal</i>	844
Invited Speeches		
184.	The Role of Measurement Automation on Accident Prevention and Industrial Safety <i>T. K. Mitra</i>	849
185.	The Changing Face of Power Electronics <i>Sujit K. Biswas</i>	851
186.	Beyond CMOS: Problems and Prospects of Nanodevices for VLSI Circuits <i>Subir Kumar Sarkar</i>	855
187.	Mobile GIS, Communication & Concurrent Safety for Intelligent Transport Systems	859

	<i>Rabindranath Bera</i>	
188.	HVDC-Link Modeling in OPF using Newton's Method: IIDVC-LCC <i>Enrique Acha</i>	864
189.	Indian Electricity Sector <i>D Sanyal</i>	873
190.	Utility applications of a RTDS® Simulator <i>Paul Forsyth, Rick Kuffel</i>	877
191.	Modelling the auditory system: an interesting challenge <i>Christian Berger-Vachon</i>	882
192.	Patteren Recognition: A Universal Problem Solving Discipline <i>B B Chaudhuri</i>	883
<i>Author Index</i>		

Technical Session 1A

Power System Stability

An Offline Simulation Method to Identify the Weakest Bus and Its Voltage Stability Margin in a Multibus Power Network

Kabir Chakraborty¹, and Sangita Das Biswas²

¹ Department of Electrical Engineering, Tripura University, Tripura, India, e-mail: kabir_jishu@rediffmail.com.

² Department of Electrical Engineering, Tripura University, Tripura, India, e-mail: sangitadasbiswas@rediffmail.com

Abstract—In this paper the reactive power sensitivity is proposed as an index for finding out the weakest load bus in a multibus system. P-V and P-Q curves have been plotted for finding out the voltage collapse point of the weakest load bus. The result is also verified by determining the value of determinant of Jacobian matrix. A method for computing voltage stability margin for the load buses is also proposed. Test results indicating the effectiveness of proposed method are presented.

Key words—Contingency, (dV/dQ) Index, voltage collapse point, voltage stability margin.

I. INTRODUCTION

THE topic voltage stability in power system study has been paid great attention in recent years as the voltage collapses have taken place around the world. Increasing interconnection of power network has led to an increasingly complex system which has to operate close to limits of voltage stability. The evaluation of voltage stability limit is an important part of study. A number of algorithms have been proposed for voltage stability limit evaluation.

Voltage collapse may be explained as inability of power system to supply the required reactive power or by an excessive absorption of reactive power by system itself [1,2]. Voltage collapse is characterized by a slow variation in system operating point; due to the increase in the load in such a way that the voltage magnitude gradually decreases until a sharp accelerated change occurs. Voltage magnitudes do not give a good indication of proximity to voltage stability limit [3]. Some of the important voltage stability and voltage collapse prediction methods are:

1. Voltage collapse index base on closely located power flow solution pairs [4].
2. Voltage collapse index based on sensitivity analysis [5], [6].
3. Voltage collapse index based on a normal load flow solution [1].
4. Minimum singular value of N-R power flow Jacobian matrix.

5. Global security indicator for an equivalent power network [7].

In this paper an attempt has been made to identify first the weakest load bus in a power system, from the voltage stability point of view. dV/dQ indicator has been employed to identify the weakest bus. Using off line simulations, V vs. P and V vs. Q profiles have been plotted at the weakest bus for a typical 25 bus – 35 line test system [14]. The critical values of power and voltages being obtain, determinant of Jacobian has been utilized to corroborate the findings. The simulation has been developed using FDLF method of load flow analysis and an attempt has been made to determine the voltage stability margin of the weakest bus following stipulated contingencies in the assumed power system. The investigation reveals that it is possible to identify the weakest load bus in any multibus network and it is possible to compute the voltage stability margin at that load bus using the developed technique.

II. DETERMINATION OF VOLTAGE STABILITY USING SENSITIVITY INDICATOR

The basic equation used in Newton-Raphson method is

$$\begin{bmatrix} \Delta P \\ \Delta Q \end{bmatrix} = \begin{bmatrix} J_1 & J_2 \\ J_3 & J_4 \end{bmatrix} \begin{bmatrix} \Delta \theta \\ \Delta |V| \end{bmatrix} \quad (1)$$

But power system transmission lines have a very high X/R ratio; for such a system, real power change ΔP are less sensitive to change in the voltage magnitude and are most sensitive to the change in phase angle $\Delta \theta$. Similarly, reactive power is less sensitive to changes in phase angle and is mainly dependent on changes in voltage magnitudes. Therefore it is reasonable to set element J_2 and J_3 of the Jacobian matrix to zero. Thus equation (1) becomes

$$\begin{bmatrix} \Delta P \\ \Delta Q \end{bmatrix} = \begin{bmatrix} J_1 & 0 \\ 0 & J_4 \end{bmatrix} \begin{bmatrix} \Delta \theta \\ \Delta |V| \end{bmatrix} \quad (2)$$

Where the diagonal and off diagonal elements of J_4 are

$$\frac{\partial Q_i}{\partial |V_i|} = -2|V_i||Y_{ii}|\sin\theta_{ii} - \sum |V_j||Y_{ij}|\sin(\theta_{ij} - \partial i + \partial_j) \quad (3)$$

$$\frac{\partial Q_i}{\partial |V_i|} = -|V_i||Y_{ii}|\sin(\theta_{ii} - \partial i + \partial_j) \quad i \neq j \quad (4)$$

Here equation (3) i.e. the diagonal element of J_4 indicate the reactive power sensitivity of i-th bus. $\partial Q_i/\partial |V_i|$ also indicates the degree of weakness for the i-th bus as $\partial Q_i/\partial |V_i|$ being high $\partial |V_i|/\partial Q_i$ became low, indicating minimum change in $|V_i|$ for variation in Q status of the bus. Thus $\partial Q_i/\partial |V_i|$ being higher, the degree of weakness of i-th bus becomes lesser [15].

III. IDENTIFICATION OF VOLTAGE COLLAPSE POINT

Identification of voltage collapse point is obtained using the conventional P-V and Q-V curves [8],[9]. A series of load flow (LF) simulation with successively increased load at a constant power factor is usually required to generate the P-V curve of a particular bus. However there is a critical point beyond which there is no load flow solution and the load flow method would not converge. Such a load point represents the 'knee' point of the P-V curve. The Q-V curve is also plotted from the results of a series of load flow simulations with the power of the candidate bus is kept constant.

However, there is a minimum voltage beyond which the load flow algorithm will again fail to converge and it represents the 'knee' point of the Q-V curve.

The above voltage stability problem is also analyzed using singularity criterion of Jacobian matrix [10], [11]. The minimum singular value of load flow Jacobian matrix has been proposed as an index for quantifying proximity to the voltage collapse point. It is an indicator available for normal load flow calculations. The determinant of Jacobian is determined for different values of P keeping Q constant at a particular value and P vs. $|J|$ graph is plotted. At a particular value of P, $|J|$ will have minimum value and beyond that magnitude of P, it is not possible to obtain $|J|$. This particular value of P is said to be the maximum real power loading limit for the concerned bus. Similarly increasing Q keeping P constant, the determinant of J is determined and Q Vs $|J|$ is plotted to find the maximum reactive loading condition for that system.

Voltage stability margin (VSM) is the measure of the security level of the bus, if the value of VSM is high then the bus is more secured and vice versa.

$$VSM = (V_w(\text{base case}) - V_w(\text{critical value})) / V_w(\text{critical value})$$

Where V_w is the bus voltage of the weakest bus of the system.

IV. SIMULATION

Simulations were carried out on a 25- bus, 35- line test system [14]. The aim of the simulation was to compare the performance of the different indices used to identify the

proximity of voltage collapse point of the weakest bus of the system.

The diagonal elements of $[J_4]$ are obtained first to find the weakest bus of the system

Table I: Bus number and its corresponding dV/dQ_i values.

BusNo	dV/dQ_i
2	0.0494
3	0.0396
4	0.0895
5	0.0351
6	0.0314
7	0.0325
8	0.0231
9	0.0457
10	0.0400
11	0.0577
12	0.0507
13	0.0268
14	0.0363
15	0.0169
16	0.0190
17	0.0189
18	0.0504
20	0.0357
21	0.0257

From this simulation it is observed that the bus number 4 is the weakest bus of the system and the bus number 15 is the strongest bus of the system from the voltage stability point of view.

Next the voltage collapse point is determined, P is increased keeping Q constant and P-V curve is drawn; also Q is increased keeping P constant and Q-V curve is drawn. The determinant of Jacobian for each value of P and Q is determined. As below Fig.1, fig.2, fig.3 and fig 4 represent the corresponding curves for bus number 4. The critical values area

$$P_{\text{crit}} = 1.97 \text{ pu at } V = 0.6245 \text{ pu}$$

$$Q_{\text{crit}} = 1.45 \text{ pu at } V = 0.6289 \text{ pu}$$

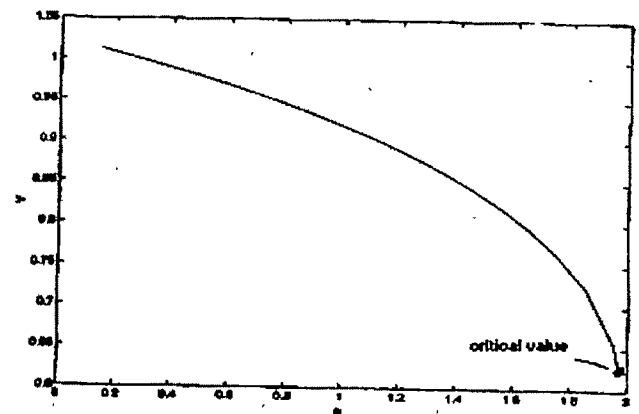


Fig. 1, P vs. V curve of bus no.4

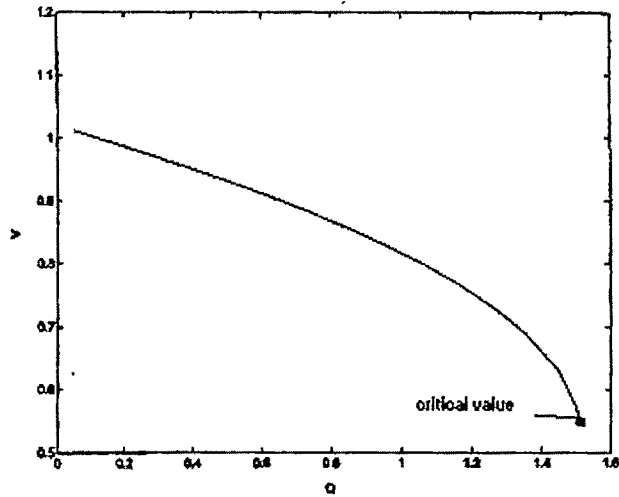


Fig. 2, P vs. Q curve of bus no. 4

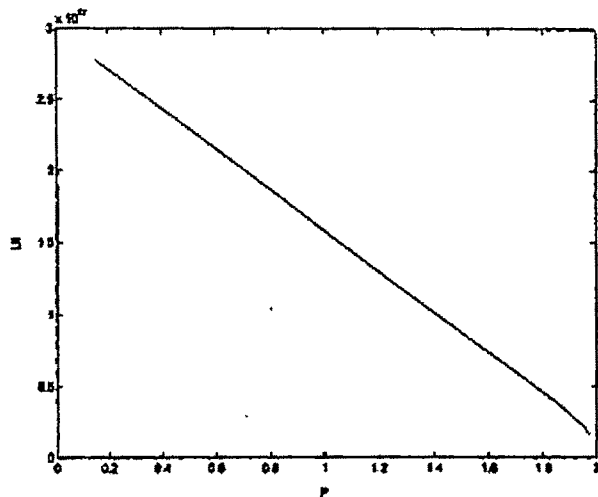


Fig.3, P vs. $|J|$ curve of bus no.4

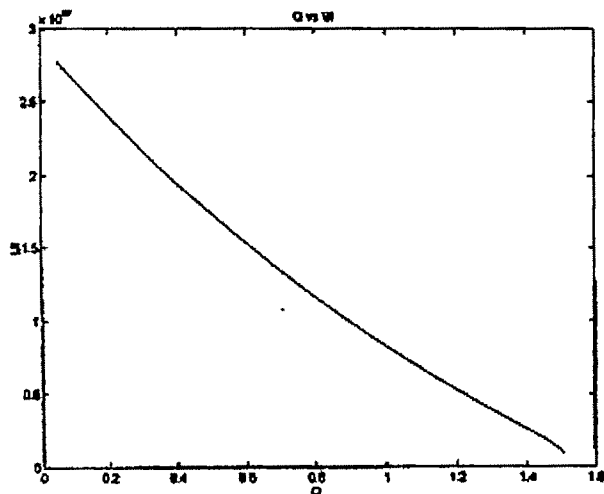


Fig. 4, Q vs. $|J|$ curve of bus no.4

Voltage stability margin (VSM) of the above case are VSM (P) =0.62 and VSM (Q) =0.85.

Contingency test have been done on that particular bus by tripping the line connected to it and corresponding VSM is calculated.

Case-I Tripping line 5(1-4)

Table-II: different values of P and its corresponding values of V and $|J|$.

P	V	$ J $
0.15	0.9215	1.4380e+051
0.25	0.8734	1.0431e+051
0.35	0.8099	6.6385e+051
0.45	0.7082	3.0436e+051
0.48	0.6507	1.8989e+051
0.49	0.6165	1.4191e+051

Table-III: different values of Q and its corresponding values of V and $|J|$.

Q	V	$ J $
0.05	0.9215	1.4380e+051
0.15	0.8513	9.5538e+050
0.25	0.7609	5.3895e+050
0.35	0.6038	1.6934e+050
0.36	0.5688	1.2578e+050

In this case, VSM (P) =0.495 and VSM (Q) =0.6197.

Case-II: Tripping line 33(5-4)

Table-IV: different values of P and its corresponding values of V and $|J|$.

P	V	$ J $
0.15	1.0154	5.9790e+051
0.25	1.0031	5.7652e+051
0.35	0.9899	5.5418e+051
0.45	0.9757	5.3082e+051
0.55	0.9604	5.0635e+051
0.65	0.9438	4.8067e+051
0.75	0.9257	4.5363e+051
0.85	0.9057	4.2504e+051
0.95	0.8835	3.9461e+051
1.05	0.8582	3.6189e+051
1.15	0.8288	3.2615e+051
1.25	0.7930	2.8600e+051
1.35	0.7456	2.3812e+051
1.45	0.6574	1.6411e+051
1.46	0.6351	1.4773e+051

Table-V: different values of Q and its corresponding values of V and |J|.

Q	V	J
0.05	1.0154	5.5979e+051
0.15	0.9921	5.6535e+051
0.25	0.9675	5.3166e+051
0.35	0.9431	4.9657e+051
0.45	0.9132	4.5989e+051
0.55	0.8828	4.2129e+051
0.65	0.8490	3.8030e+051
0.75	0.8115	3.3615e+051
0.85	0.7676	2.8747e+051
0.95	0.7130	2.3135e+051
1.05	0.6321	1.5703e+051
1.09	0.5645	1.0386e+051

In case-II, VSM (P) =0.66 and VSM (Q) = 0.87.

V. DISCUSSION

The simulation results for the test system indicate that the magnitude of the load bus system as well as the determinant of [J] decreases gradually with increase in system load. The changes are more rapid when the system approaches the voltage collapse point. The simulation also shows the contingency result by tripping the line connected to the weakest bus.

Simulation results for voltage stability margin (VSM) indicate that the proposed method provides quit accurate values of VSM. In case-II, i.e. when the line 33 is tripped then the value of VSM is higher then the two other cases ,that means in that case bus number 4 is more secured.

VI. CONCLUSION

In this investigation, the role of dV/dQ as a voltage stability index has been highlighted. This index has been used to identify the weakest bus in the test system. P-V and Q-V characteristic of the weakest bus are being plotted and critical values of P, Q and V being obtained, the voltage stability margins have been computed for the test system under heavy loading condition as well as under contingent condition of line trip. In this investigation, it has been revealed that it is possible to compute contingency ranking of line(s) connected to the load buses applying the concept if voltage stability margin to the corresponding load bus. The developed method can be used for offline study of static voltage stability and security of a multibus power network.

APPENDIX

The work is done with the following data and the limit of the PV buses is $-0.1 \leq Q \leq 0.4$

Table-VI: Line data

Line no.	Branch p-q	Line charging Y_{F1}	Impedence Z_{F1}	Turn-ratio a
1	1-24	j0.0179	0.0720+j0.2876	1.0
2	1-16	j0.0337	0.0290+j0.1379	1.0
3	1-17	j0.0148	0.1012+j0.2794	1.0
4	1-19	j0.0224	0.1487+j0.3897	1.0
5	1-4	j0.0573	0.1085+j0.2245	1.0
6	1-2	j0.0873	0.0753+j0.3593	1.0
7	25-6	j0.0186	0.0617+j0.2935	1.0
8	25-7	j0.0155	0.0511+j0.2442	1.0
9	25-8	j0.0175	0.0579+j0.2763	1.0
10	24-13	j0.0085	0.0564+j0.1487	1.0
11	24-14	j0.0185	0.1183+j0.3573	1.0
12	23-19	j0.0113	0.0196+j0.0514	1.0
13	23-20	j0.0220	0.0382+j0.1007	1.0
14	23-21	j0.0558	0.0970+j0.2547	1.0
15	22-10	j0.0557	0.0497+j0.2372	1.0
16	22-17	j0.1335	0.0144+j0.1269	1.0
17	22-19	j0.0140	0.0929+j0.2442	1.0
18	6-13	j0.0040	0.0263+j0.0691	1.0
19	7-8	j0.0078	0.0529+j0.1465	1.0
20	7-12	j0.0110	0.0364+j0.1736	1.0
21	8-9	j0.0118	0.0387+j0.1847	1.0
22	8-17	j0.0572	0.0497+j0.2372	1.0
23	9-10	j0.0085	0.0973+j0.2698	1.0
24	10-11	j0.0135	0.0898+j0.2359	1.0
25	11-17	j0.0161	0.1068+j0.2807	1.0
26	12-17	j0.0135	0.0460+j0.2196	1.0
27	14-15	j0.0044	0.0281+j0.0764	1.0
28	15-16	j0.0148	0.0256+j0.0673	1.0
29	17-18	j0.0122	0.0806+j0.2119	1.0
30	18-19	j0.0132	0.0872+j0.2294	1.0
31	20-21	j0.0354	0.0615+j0.1613	1.0
32	21-5	j0.0238	0.0414+j0.1087	1.0
33	5-4	j0.0169	0.2250+j0.3559	1.0
34	5-3	j0.0567	0.0970+j0.2595	1.0
35	3-2	j0.0317	0.0472+j0.1458	1.0

Table-VII: Generation, load, and voltage at buses

Bus no.	Generation		Load		Voltage		Type of Bus
	P_g (p.u.)	Q_g (p.u.)	P_L (p.u.)	Q_L (p.u.)	V_i (p.u.)	δ_i (rad)	
1	-	-	0.00	0.00	1.030	0.0	Slack
2	0.0	0.0	0.25	0.08	-	-	PQ
3	0.0	0.0	0.15	0.05	-	-	PQ
4	0.0	0.0	0.15	0.05	-	-	PQ
5	0.0	0.0	0.20	0.07	-	-	PQ
6	0.0	0.0	0.15	0.05	-	-	PQ
7	0.0	0.0	0.15	0.05	-	-	PQ
8	0.0	0.0	0.25	0.00	-	-	PQ
9	0.0	0.0	0.15	0.05	-	-	PQ
10	0.0	0.0	0.15	0.05	-	-	PQ
11	0.0	0.0	0.05	0.00	-	-	PQ
12	0.0	0.0	0.10	0.00	-	-	PQ
13	0.0	0.0	0.25	0.08	-	-	PQ
14	0.0	0.0	0.20	0.07	-	-	PQ
15	0.0	0.0	0.30	0.10	-	-	PQ
16	0.0	0.0	0.30	0.10	-	-	PQ
17	0.0	0.0	0.60	0.20	-	-	PQ
18	0.0	0.0	0.15	0.05	-	-	PQ

19	0.0	0.0	0.15	0.05	-	-	PQ
20	0.0	0.0	0.25	0.08	-	-	PQ
21	0.0	0.0	0.20	0.07	-	-	PQ
22	1.784	0.5	0.25	0.08	1.007	-	PV
23	0.480	-	0.30	0.10	1.015	-	PV
24	1.513	-	0.50	0.17	1.050	-	PV
25	0.936	-	0.10	0.03	1.002	-	PV

ACKNOWLEDGMENT

The authors are thankful to Prof. Avijit Chakraborty of BESU, West Bengal, for providing his support technically.

REFERENCES

- [1] P.Kessel and H.Glavitsch "Estimating the Voltage Stability of Power System" IEEE Trans. On power delivery, Vol. PWRD-1, No.3 July/1986, pp. 346-354
- [2] An Analytical Investigation of Voltage Stability of an EHV Transmission Network based on Load Flow - A. Chakrabarti and P.Sen. Journal of Electrical Engg., Institution of Engg. (I, Vol.-76, May 1995)
- [3] H.K. Clark "New Challenges: Voltage Stability" IEEE Power ENG. Rev., April 1990, pp. 33-37,
- [4] Y.Tamura, H.Mori and S.Lwanoto "Relationship between voltage instability and multiple load flow solution in electrical system" IEEE Trans. Vol. PAS-102, pp. 115-125.
- [5] Crisan and M. Liu " Voltage collapse prediction using an improved sensitivity approach", Electrical power system research ,1984, pp. 181-190
- [6] C.K.Chanda, S.Dey, A.Chakrabarti and A.K.Mukhopadhyay; Determination of Bus Security Governed by Sensitivity Indicator in a Reactive Power Constrained LPS System. Journal of Engg &Material Science, India, Vol. IX August 2002.
- [7] S.Dey, C.K.Chanda and A.Chakrabarti; Development of a Global Voltage Security Indicator and Role of SVC on it in LPS System. Journal of Electric Power System Research, USA, Vol.68 2004
- [8] C.W Taylor, Power System Voltage Stability, McGraw-Hill, 1994
- [9] R.J Koessler, Voltage instability/ Collapse-An overview, IEE Colloquium on voltage collapse, Digest No. 1997/101, 1997, pp. 1/6-6/6.
- [10] P.A Lof, T.Smed, G. Anderson, D.J Hill, "Fast calculation of a voltage stability index", IEEE Trans. Power System. 7(1), 1992, pp. 54-64.
- [11] T.Tiranuchit, R.J Thomas, "A posturing strategy against voltage in stabilities in electrical power system", IEEE Trans. Power System.3 (1), (1998), pp.87-93.
- [12] M.H Haque, "Novel Method of assessing voltage stability of a power system using stability boundary in P-Q plane." Electrical Power System Research 64 (2003) ,PP. 35-40.
- [13] A.K. Shina, D. Hazarika, "Voltage collapse proximity indicating index using diagonal element of Jacobian matrix", IEEE Trans, 2000, pp. 480-485.
- [14] D.P. Kothari, J.S. Dhillon, "Power system optimization", Prentice-Hall India, 2004
- [15] Abhijit Chakraborty, Sunita Haldar, "power System Analysis Operation and Control", Prentice-Hall India, 2006
- [16] Hadi Saadat, Power system analysis, TATA MCGRAW-HILL,2004

A Review of Analytical Techniques for Determination of Voltage Stability in a Multi-bus Power System

Suman Saha¹, Abhijit Chakroborti², C.K.Chanda³, A.B.Chowdhury⁴

Department of Electrical Engineering; Bengal Engineering and Science University; Shibpur, Howrah- 711 103, India

email: the_suman@yahoo.co.in, a_chakroborti55@yahoo.co.in, ckc_math@yahoo.co.in, ab_choudhury@yahoo.com

Abstract—In this paper an attempt has been made to review a few important voltage stability indicators namely, L-index, Jd, Sp, Sq, V-I indicator and VSM indicator. Though numerous researches have been reported so far in voltage stability of power system, in this paper the authors have tried to explore the applicability of a few of them which are found to be very effective in off line simulation of static voltage stability in a multi-bus power system. The simulation in this work has been conducted on the IEEE-30 bus system and a comparative review of these indicators has been presented.

Key words—power system stability, stability indices, voltage stability.

I. INTRODUCTION

WITH the increase of loadings of existing power transmission system the problem of voltage stability in the complex power-grid has become a major concern in power system planning and operations. In addition to this aspect, economic and operational factors have forced operation of power system close to operating limit there are many incidents of system blackout due to voltage collapse in the last quarter of 20th century [1]. The problem of voltage collapse is characterized by a slow variation in system operating point due to increase in the loads in such a way so that the magnitude of the bus voltage gradually decreases until a critical point is achieved. Beyond this critical point there is a sharp accelerated voltage collapse. The voltage collapse in its simplest concept is explained as the inability of the power supply system to transmit adequate amount of reactive power or the excessive absorption of reactive power by the system itself [2]. There are two different approaches for analyzing voltage stability problems of power systems static analysis and dynamic analysis. In the static approaches the voltage stability

problems are analyzed through steady state model and techniques [3, 4]. On the other hand, the dynamic approaches reveal the voltage collapse mechanism, i.e. why and how voltage collapse occurs. In this approaches it is required to include dynamic models and techniques [4, 5]. In voltage stability studies it has been found that voltage magnitude alone do not give a good indication of proximity to voltage collapse. Steady state voltage stability or static voltage stability being an important aspect, several works have been reported in the past to highlight the development of static voltage stability indicators [6, 7, 8, 9, 10, 11].

In this paper an attempt has been made to explore the applicability of a few important voltage stability indices:

- (a) L-index (voltage collapse index based on load flow solution) [12, 13]
- (b) Jd index (diagonal element ratio dependent index) [13]
- (c) Sp, Sq index (sensitivity based voltage collapse index [7])
- (d) V-I index (static voltage stability index) [14]
- (e) VSM indicator (voltage stability margin indicator) [14]

Simulations have been performed on IEEE-30 bus system and comparative results have been reported, in this paper for these stability indices.

II. THEORY

A. L-index [12,13]

L-index can be computed from the following equations

$$L_j = \left| 1 - \sum_{i=1}^n F_{ji} \frac{\bar{V}_i}{V_j} \right| \quad (1)$$

where $j = g + 1, \dots, n$ and all the terms within the sigma on the RHS of equation are complex quantities. The values F_{ji} are obtained from the Y-bus matrix as follows

where \bar{I}^G , \bar{I}^L and \bar{V}^G , \bar{V}^L represent currents and voltages at the generator nodes and load nodes. Arranging equation as

$$\begin{bmatrix} \bar{V}^L \\ \bar{I}^G \end{bmatrix} = \begin{bmatrix} \bar{Z}^{LL} & \bar{F}^{LG} \\ \bar{K}^{GL} & \bar{Y}^{GG} \end{bmatrix} \begin{bmatrix} \bar{I}^L \\ \bar{V}^G \end{bmatrix} \quad (2)$$

where $\bar{F}^{LG} = -[\bar{Y}^{LL}]^{-1}[\bar{Y}^{LG}]$

are the required values, we find that the L-index for a given load condition can be computed for all load buses and the maximum of the L-index gives the proximity of the system to voltage collapse. An L index value away from 1 and close to 0 indicates an improved voltage stability margin. The equation for the L-index for the jth node can be rewritten as

$$L_j = \left| 1.0 - \sum_{i=1}^g F_{ji} \frac{V_i}{V_j} \angle \theta_{ji} + \delta_i - \delta_j \right| \quad (3)$$

$$L_j = \left| 1.0 - \sum_{i=1}^g \frac{V_i}{V_j} (F_{ji}^r + F_{ji}^m) \right|$$

$$L_j^2 = \left[1.0 - \sum_{i=1}^g \frac{V_i}{V_j} F_{ji}^r \right]^2 + \left[\sum_{i=1}^g \frac{V_i}{V_j} F_{ji}^m \right]^2$$

For the L-index the bus angles can be considered to be constant for a given load condition, while the F_{ij} values are fixed for a given network configuration. Hence the only variables are system node voltage magnitudes.

n is the total number of buses with
 1,2,..., g generator buses (g),
 g+1, g+2, ..., g+s SVC buses (s),
 g+s+1, ..., n remaining buses (r = n - g - s)
 t number of OLTC transformers

B. Ratio of diagonal element (J_d)[13]

Diagonal element of the jacobian matrix being positive, the ratio of maximum to minimum value can be used as an index.

$$J_D \approx \frac{J_{MAX}}{J_{MIN}} \quad (4)$$

Where J_{MAX} is the maximum value of the diagonal element,

and J_{MIN} is the minimum value of the diagonal element.

C. Sensitivity based voltage collapse index. (S_p, S_q). [7]

The value of diagonal elements $\left[\frac{\partial Q_i}{\partial V_i} \right]$ and $\left[\frac{\partial P_i}{\partial \delta_i} \right]$ gets reduced, if the load is increased, thus the deviation in value of $\frac{\partial Q_i}{\partial V_i}$ and $\frac{\partial P_i}{\partial \delta_i}$ from its no-load value at any particular loading conditions can be used as an index of voltage stability for the load bus i.

Using these criteria two voltage stability indices are proposed.

$$S_p = \frac{\left[\frac{\partial P_i}{\partial \delta_i} \right]_{[FOR THE SPECIFIED LOAD]}}{\left[\frac{\partial P_i}{\partial \delta_i} \right]_{[AT NO LOAD CONDITION]}} \quad (5a)$$

$$S_q = \frac{\left[\frac{\partial Q_i}{\partial V_i} \right]_{[FOR THE SPECIFIED LOAD]}}{\left[\frac{\partial Q_i}{\partial V_i} \right]_{[AT NO LOAD CONDITION]}} \quad (5b)$$

D. V-I curve as a stability index [14]

Voltage versus current curve or V-I characteristic is presented as a tool to assess the voltage stability limit. It requires only bus voltage and current data at present; the above data are processed through the least squares method to establish the V-I characteristic. The extrapolated part of the characteristic is then used to estimate the critical load at the verge of voltage collapse.

Now we consider a general power system with a local load bus or voltage uncontrolled bus as shown in Fig.1. Its Thevenin equivalent can represent the rest of the system, and such an equivalent of the system is shown in fig.2 below. The load of the local bus is considered as $\bar{S} = S \angle \theta$ and is represented by shunt impedance

$Z = Z \angle \theta$ In the equivalent system.

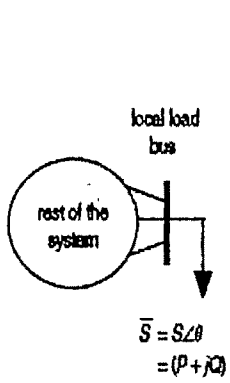


Fig: 1

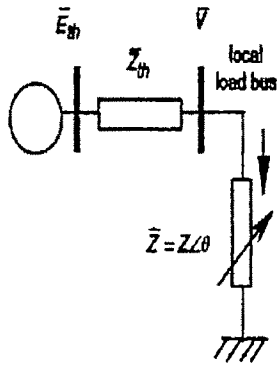


Fig: 2

By changing the load impedance we can vary the load voltage, current and power. A typical variation of load voltage against the load current is obtained by varying Z at a constant angle θ is shown in Fig.2 and is called the V-I characteristic of the bus. The complex load of the bus can be written as $\bar{S} = S \angle \theta = VI^*$ however, the magnitude of load apparent power S is the product of load voltage and current magnitudes i.e. $S = VI$.

E. Voltage stability margin indicator [14]

For a given operating condition, the VSM ξ_i of a load bus i , in a general power system can be defined as:

$$\xi_i = \frac{S_i^{\sigma} - S_i^0}{S_i^{\sigma}}$$

Here, S_i^{σ} is the critical load of bus i , and S_i^0 is the initial load by assuming that the load of all buses is increased uniformly. The procedure of estimating the critical load, at the present operating point, through the V-I characteristic is described in the following. Consider that the V-I characteristic of the bus, around the present operating point, can be represented by the following m -th order polynomial:

$$V = f(I) = a_0 + a_1 I + a_2 I^2 + \dots + a_m I^m$$

The magnitude of load apparent power S of the bus is the product of voltage and current magnitudes and is given by:

$$S = VI = f_1(I) = a_0 I + a_1 I^2 + a_2 I^3 + \dots + a_m I^{m+1}$$

As noted earlier, the value of the maximum load can be determined by sliding the operating point along the V-I characteristic (fig:5) until the shaded area becomes maximum. Alternatively, the condition of the maximum load can be written as:

$$\frac{\partial S}{\partial I} = 0$$

$$a_0 + 2a_1 I + 3a_2 I^2 + \dots + (m+1)a_m I^m = 0$$

The feasible solution of this provides the value of current at the maximum load point and is called the critical current I^{σ} .

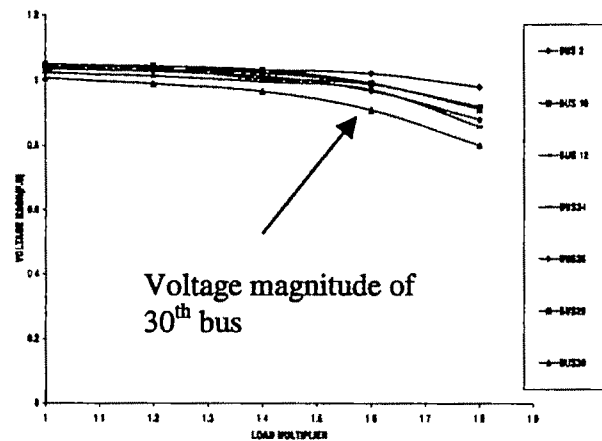
Thus, the value of the maximum or critical load S^{σ} can be obtained by substituting I^{σ} in $S^{\sigma} = f_1(I^{\sigma})$

The above techniques of finding the VSM and critical load can also be applied to other load buses of the system. When the system load increases uniformly and approaches the critical value, the voltage instability first occurs at the weakest bus. So the bus that has the lowest value of VSM may be considered as the weakest bus and is vulnerable to voltage collapse, in this investigation the voltage stability indices have been applied to assess the voltage stability of an IEEE-30 bus system.

III. SIMULATIONS AND RESULTS

In the first part of the work investigation have been conducted to obtain the weakest bus in the assumed IEEE-30 bus system. For this purpose simulations have been conducted to determine the voltage magnitude of the respective load buses. Then we have applied this useful indicator in order to find the status of voltage stability in these buses. In the next part of the work the voltage stability limit of the weakest bus has been assumed applying the respective indicators.

Fig: 3 represent the voltage profile of the heavily loaded load buses. For clarity the voltage profile of a few has been displayed and it has been revealed that the voltage magnitude at bus no-30 has the worst profile.



Bus voltage magnitude with load multiplier

Fig: 3

The L-index indicators for all load buses of 30-bus network have been computed from the base load case with continuous higher loading. Fig-4 represents the profile of L-index of the load buses, where it is evident that the bus 30 is the weakest bus.

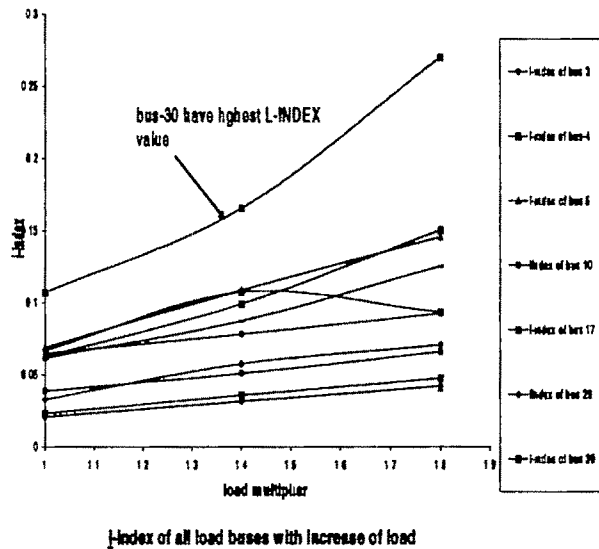


Fig-4

In this investigation the J_d indicator has also been applied which confirm that bus 30 is the weakest bus in the network. Once the weaknesses of bus-30 have been diagnosed, the voltage stability limit of this bus has been computed by Using V-I curves. The voltage stability margin has also computed for bus-30. The respective profile here been shown in Fig: 5&6.

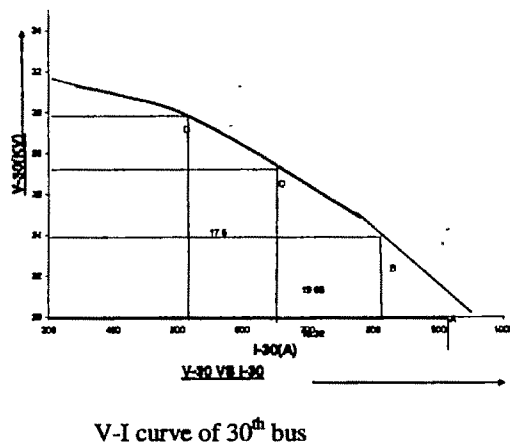
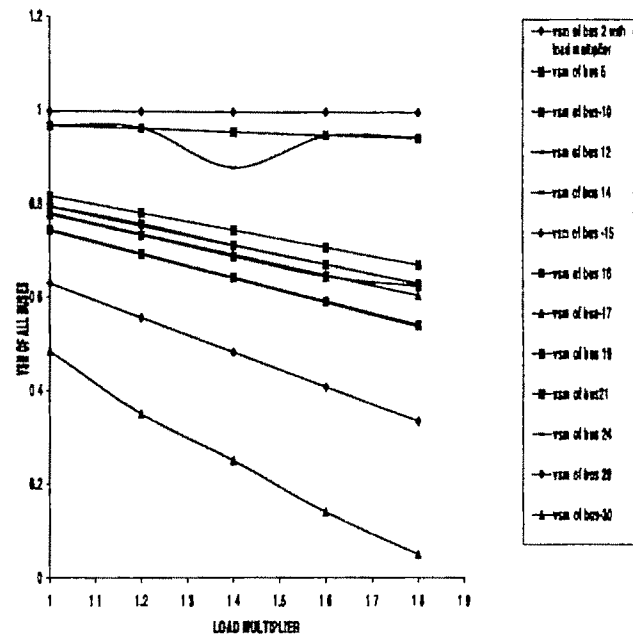


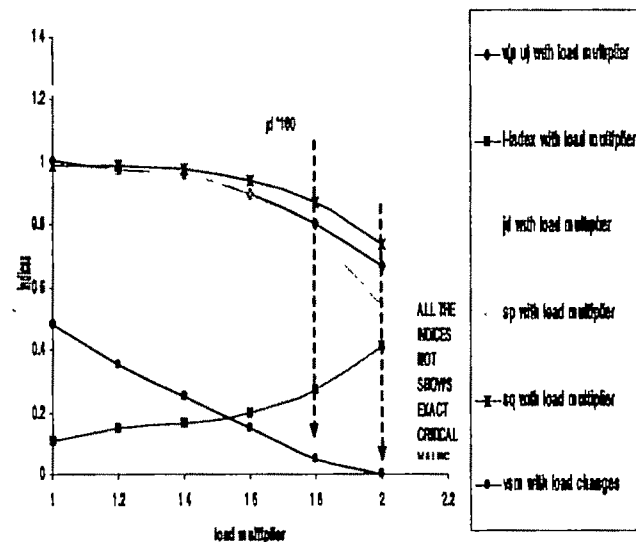
Fig-5



VSM of all buses with load multiplier

Fig-6

In all these simulations the findings reveal the voltage stability limit of weakest bus. Another indicator (S_p, S_q) has also been computed and the profile of all these indicators have been displayed



Characteristic of some indices with load multiplier

Fig: 7

III. CONCLUSION

The investigation reveals that it is possible to identify the weakest bus in a multi-bus system using L-index and VSM in addition to voltage magnitude study. Once the weak bus is identified in the next step it is possible to obtain the voltage stability limit following load increase and using the indicators Sp, Sq, Jd, VSM, L-index and V-I indicators.

Comparison of these indicators reveal that VSM is the most accurate to pinpoint the stability limit as well as to identify the weakest bus followed by L-index, Sp, Sq and Jd indicators.

REFERENCES

- [1] IEEE Committee Report, "Voltage stability of power system: Concepts, analytical tools and industrial experiences," IEEE Publication No. 90TH0358-2-PWR, New York, 1990.
- [2] Kessel P, Glavitsch H "Estimating the voltage stability of a power system". IEEE Trans Power Delivery 1986; PWRD-1(3):346-54
- [3] Taylor, C.W.: "Power system voltage stability" (McGraw Hill, New York, 1994)
- [4] Vu, K.T., Liu, C.C.: "Shrinking stability regions and voltage collapse in power systems", IEEE Trans. Circuit Syst., 1992, 39, (4), pp. 271-289
- [5] Vu, K.T., Liu, C.C., Taylor, C.W., and Jimma, K.M.: "Voltage instability: Mechanism and control strategies", Proc. IEEE, 1995, 83, (11), pp. 1442-1445.
- [6] Carpenter J, Girard R, Scano E Voltage collapse proximity indicators Computed from an optimal load flow. Proceeding of Eighth PSCC Conference, August 1984. p. 671-8.
- [7] Crisan, Liu M. Voltage collapse prediction using an improved sensitivity approach. Electrical Power Syst Res 1984:181-90.
- [8] Lof PA, Anderson G, Hill DJ. Voltage stability indices of stressed power system. IEEE Trans Power Syst 1993;8(1):326-35.
- [9] Savulescu CS. Qualitative indices for the system voltage and reactive power control IEEE Trans Power Apparatus and Syst 1976;PAS-95(4):1413-21.
- [10] Sunita Dey, C.K.Chanda, A. Chakrabarti "Development of a global voltage security (VSI) and role of SVC on it longitudinal power supply (LPS) System" Jnl EPSR 68(2004) pp 1-9 ELSEVIER, USA.
- [11] A.Chakrabarti, "Reactive Power Limitations in Voltage stability of an EHV system and its Microcomputer Based on Line Control" Jnl. Of the Institution of Engineers (I), Vol.-72, pt EL-1, April 1991.
- [12] Dobson I, Scott G, Alvarado FL Sensitivity of the loading margin to voltage collapse with respect to arbitrary parameters. IEEE Trans Power Syst 1997; 12(1): 262-72.
- [13] A K.Sinha, D.Hazarika "A comparative study of voltage stability indices in a power system", . ELSEVER-Sept-1999 Electrical power and energy systems 22(2000) 589-596.
- [14] Haque, M.H.: "Use of V-I Characteristic as a tool to assess the static voltage stability limit of a Power system" IEB Proc - Gener. Transm. Distrib., Vol.151. No.1 January 2004
- [15] Haque, M.H.: 'On-line monitoring of maximum permissible loading of a power system within the Voltage stability limits', IEE Proc., Gener Transm. Distrib., 2003, 150, (1), pp 107-112
- [16] Pai, M.A., "Computer techniques in power system analysis", Tata Mc Graw-Hill publishing company limited, New Delhi. 2006

Bulk Power System Reliability Evaluation Using Fuzzy Logic

K.Thippeswamy¹ and B.K.Keshavan²

¹ Research scholar (VTU), Dept. of Electrical Engg. Govt. Polytechnic, TUMKUR – 572 103, Karnataka State, India,
Email: thippeswamyk@rediffmail.com

² Professor & Head, Dept. of Electrical Engg, J.N.N.College of Engg, SHIMOGA-577 204, Karnataka State, India.,
Email: keshavanbk@yahoo.com

Abstract— Many methods have been proposed in literature for determining the reliability indices of bulk power system. The most significant parameter in the bulk power adequacy assessment are overall system “load curtailment indices”. Many utilities have difficulty in interpreting the calculated load curtailment indices as the existing models do not always consider realistic and practical operating conditions. Linear programming approach has been proposed for the load curtailment. A simple linear programming formulation is found to be inadequate in satisfying realistic system objectives and constraints. The present paper models uncertainties in load and generation as fuzzy numbers. The load curtailment indices are calculated using fuzzy linear programming. The results of the IEEE 14 bus system are presented to show the effectiveness of the proposed system.

Key words— Fuzzy logic, linguistic variables, reliability and bulk power system

I INTRODUCTION

The Power system continually experiences changes in its operating state. An emergency state may occur as a result of sudden increase in system demand, unexpected outages of generators or transmission lines or failure in any of the system components. Alleviation of the transmission line over load is a critical problem in power system operation; hence a control action strategy is necessary effectively to reduce the line over loads to the security limits in minimum time. The possible corrective control actions are generation rescheduling, load shedding, inter change arrangements and network switching etc neglecting economic considerations.

The reliability of bulk power systems (generation plus high voltage transmission, also called composite power systems) is an umbrella concept and not, per se, a measure of expected system performance. It is evaluated through indices relating to two of its attributes, adequacy and security. Adequacy is the

ability of the system to supply the aggregate electric power and energy requirements of the customers, within component ratings and voltage limits, taking into account planned and unplanned component outages. Security is the ability of the system to withstand Sudden disturbances such as the unanticipated losses of the system components. The most significant qualitative indices in bulk power system adequacy assessment are those that relate to load curtailment at both the individual bus and overall system levels. These indices can be extended to recognize additional factors, such as customer interruption cost and reliability cost/reliability worth considerations [1, 2].

Many methods have been proposed in literature [3] for determining the reliability indices of bulk power system. Many of the models considered are overly approximate and uses infeasible solution methods that are not sufficiently accurate. Many utilities have difficulty in interpreting the expected load curtailment indices, as the existing models are based on adequacy analysis and in many cases do not consider realistic operating conditions. The objective is to incorporate security considerations in power system reliability evaluation to determine which of the contingencies cause component limit violations and / or major system shifts, and to determine the severity of the contingencies.

Different methods have been proposed for performing load curtailment during emergencies. Useful load curtailment algorithms have been proposed [4,5,6]. Linear programming approaches used in these algorithms have the main drawback of treating the constraints as crisp values that have to be met all times, and most of these gives infeasible solutions. One way to resolve this problem is to allow in a least square sense, however, this approach does not usually produce realistic solutions when the problem is infeasible or almost infeasible. There is a need more than ever to develop realistic models that take advantages of the “soft” characteristics of the problem and calculate more accurately the “true” magnitude of the power system security margins [7].

Uncertainties in load and generations are modeled as fuzzy numbers from fuzzy set theory. Trapezoidal membership functions are defined for the constraints, such as voltage

magnitude of the buses. In this paper a fuzzy linear programming approach is used for computation of load curtailment (the adequacy and security) indices. The results obtained by this method are more realistic than the results of the existing methods.

II FUZZY LOGIC

Fuzzy logic is basically a multi valued logic that allows intermediate values to be defined between conventional evaluations like "good" and "bad", "yes" and "no", "true" and "false", "black" and "white", "tall" and "short" etc. Notions like very tall or too short or fairly good can be mathematically formulated and processed by the computers. Fuzzy logic is the super set of conventional (Boolean) logic that has been extended to handle the concept of partially truth. A partially true statement may be indexed any value between "completely true" and "completely false".

The basic requirement of a power flow program is to organize a set of input data, which describes the system parameters, line parameters, bus injection and initial state variables. Conventionally these inputs are assigned values that are crisp in nature. However, in many systems this may prove to be unrealistic as these parameters show imprecision and uncertainty. In such cases, the information need be qualitatively soft in nature. Fuzzy set theory offers a way to understand these problems and also allows incorporating ones own intuition, intelligence and knowledge from past experience in solving them. It is felt that these uncertainties can be properly modeled with the help of fuzzy set theory and fuzzy reasoning.

A fuzzy set \tilde{A} in the universe of discourse "U" can be defined as a set of ordered pairs, where each subset includes some element 'x' and its membership function $\mu_{\tilde{A}}$. The membership function $\mu_{\tilde{A}}$ indicates the degree that 'x' belongs to \tilde{A} . This relationship is expressed in a mathematical form as:

$$\tilde{A} = \{(x, \mu_{\tilde{A}}(x)) \mid x \in U\}$$

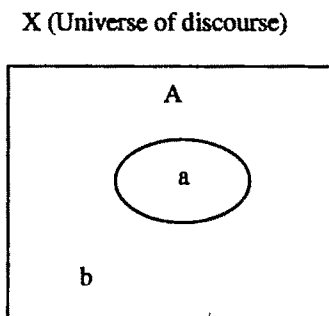


Fig 1. Crisp Set Boundary

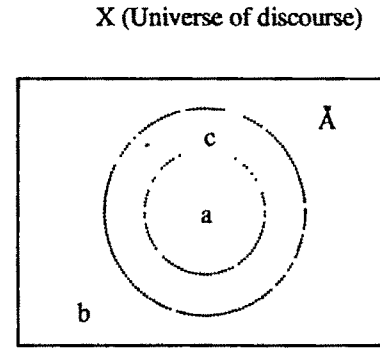


Fig 2. Fuzzy Set Boundary

In fuzzy set theory there exists several forms of distribution functions (e.g., triangular, trapezoidal, ramp, exponential etc.) to suit the need and requirement of the problem [8, 9].

III FUZZY APPROACH TO OPTIMIZATION

When Fuzzy set theory is used to solve real problems, the following steps are generally followed [10].

- Step 1: The problem to be solved should first be stated mathematically / linguistically.
- Step 2: For a variable, there is a specific value with the greatest degree of satisfaction evaluated from empirical knowledge and a certain deviating is acceptable with decreasing degree of satisfaction until a value that is completely unacceptable. The two values corresponding to the greatest and least degree of satisfaction are termed thresholds.
- Step 3: Proper forms of membership functions are constructed. Many forms of membership functions are available such as linear, piece wise linear trapezoidal parabolic, and so on. The membership functions should reflect the change in degree of satisfaction with the change in variables evaluated by experts.
- Step 4: In terms of the practical decision-making process by human experts, a proper fuzzy operation is selected so that the results obtained are like those obtained by experts. The interpretation of results using fuzzy systems is based on domain expert reasoning. Therefore, at this level a hybrid fuzzy set-expert system scheme is desirable. It helps to remove any ambiguity that may occur in problem solving.

IV POWER SYSTEMS MODEL

For the purpose of power system studies, we need to develop the mathematical model of the power system network. In order to develop fairly accurate models of the power system network, it is necessary that the model should reflect correctly

the terminal behavior of each component of the network for the purpose (i.e., study) for which the model has been developed. This is because the terminal behavior of the power system components differs from normal i.e., steady state condition to abnormal i.e., transient condition.

The power system is modeled using load flow equations [11]:

$$P_I = \sum |V_I| |V_J| Y_{IJ} \cos(\delta_J - \delta_I + \theta_{IJ}),$$

$$Q_I = \sum |V_I| |V_J| Y_{IJ} \sin(\delta_J - \delta_I + \theta_{IJ}),$$

Where,

δ_i = bus angle at i

V_i = bus voltage at i

P_i = bus Power injection at i

Q = reactive power at bus I

The summation is over the system buses.

V OBJECTIVE FUNCTION & CONSTRAINTS

The Linear programming for minimum load curtailment [12] is,

Objective function:

$$\text{Min. Sum} = \sum_{i=1}^N X_i$$

Such that,

$$\sum X_i + \sum P_{Li} + \sum P_i = 0 \quad \dots\dots\dots \text{Active power balance.}$$

$$|T_L| = T_L^M \quad \dots\dots\dots \text{Thermal limit.}$$

$$P_i^m \leq P_i \leq P_i^M \quad \dots\dots \text{Active power generation limit.}$$

$$0 \leq X_i \leq P_{Li} \quad \dots\dots\dots \text{Load curtailment limit.}$$

Where,

N load is the no. of load points in the system.

X_i is the load curtailment.

P_i is the power generation.

and P_{Li} is the load at bus i .

In this model both the generation shift and the load shed are used as variables. The main advantages of this model is that for each of those contingencies which violate the over load constraint, both the generation rescheduling as well as the amount of load shed can be found from a single run.

VI FUZZY MODELING OF OBJECTIVE FUNCTION & CONSTRAINTS

6.1 Objective function:

The attribute to be minimized is the load curtailment under certain generation and load requirements. This is modeled by taking this as the crisp value.

6.2 Security constraints:

It is reasonable to consider violations of branch flow limits, bus voltage limits and generator VAR limits.

6.2.1 Voltage Magnitude:

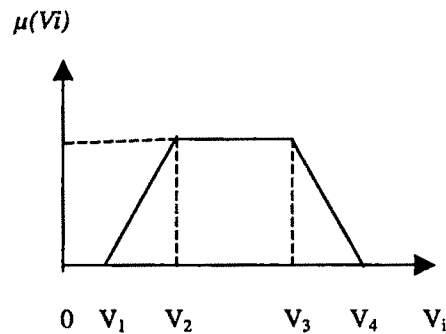


Fig 3. Load voltage magnitude constraint

The uncertainty in generation is depicted in fig 3. The voltage possibility signifies four break points i.e., V^1 , V^2 , V^3 , V^4 and their possibilities. This representation of voltage occurs with the experiences in power system indicating that as the system demand decreases, the load bus voltage would be required at generator to maintain specific voltages.

$$V_{min} \leq V_1 \leq V_2 \leq V_3 \leq V_4 \leq V_{max}.$$

6.2.2 Line flow constraint:

The thermal operating limits of transmission lines and transformers limits, the amount of current flow through them can be expressed as:

$$(\delta_k - \delta_i) \leq \theta_j.$$

Where j is the branch connecting the buses k and i

6.2.3 Real power generation constraint:

The real power generation constraints are modeled as fuzzy sets. This is modeled by a trapezoidal membership function, the limits being the minimum value and the maximum values.

6.2.4 Reactive power constraint:

The reactive power generation at the slack or PV bus is

$$Q_k^m \leq Q_k \leq Q_k^M$$

Where, 'm' and 'M' refers to the minimum and maximum values respectively.

VI ALGORITHM

The proposed methodology starts from an operating point that satisfies the power balance equation [13]. The scheme for calculating reliability indices is presented in fig 4.

- Step 1:* Select the contingency and identify the generation and power flow limits violation.
- Step 2:* Run fuzzy LP DC load flow, where it will curtail load due to generation deficiency.
- Step 3:* Run AC load flow to check for power flow and bus voltages.
- Step 4:* Select the most severe power flow violation (where load curtailment is necessary) and include the related constraints in fuzzy LP model.
- Step 5:* Determine the load curtailment indices.

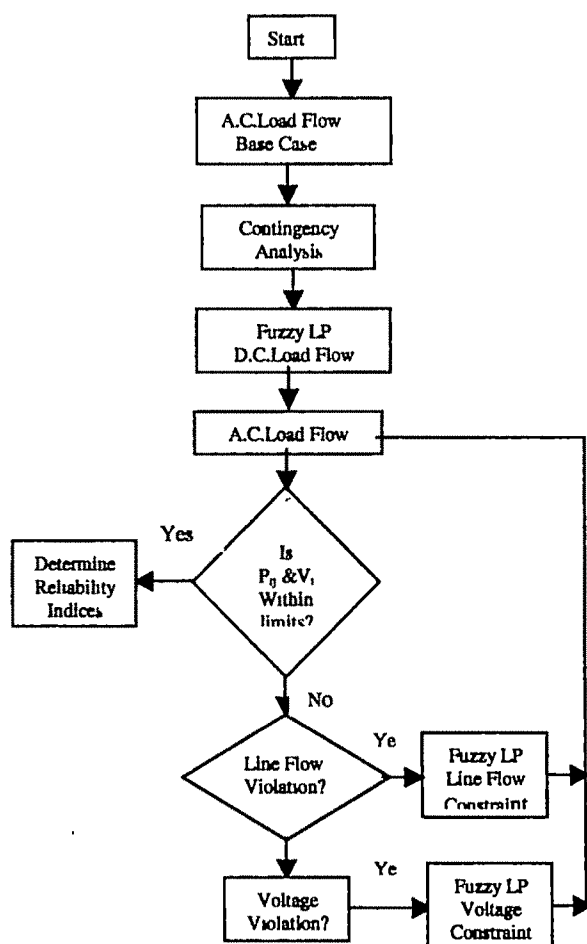


Fig 4. Scheme for Calculating Reliability Indices

VIII RESULTS

The quantitative reliability evaluation of a composite generation and transmission system involves the simulation and investigation of all possible element outage conditions for evaluating the reliability indices at each bus. The load curtailment at different buses for different contingencies has been determined. The results are tabulated in Table I, II, III and IV.

Table I: Maximum Load Curtailment Indices

Bus No.	Load Curtailed (MW)	Contingency Lines out
3	94.20	3&6
4	47.80	1&2
6	11.20	12&18
9	29.50	17&18
10	9.00	12&18
11	3.50	12&18
12	6.10	17&19
13	13.50	11&18
14	14.90	12&15

Table II: Maximum Duration of Load Curtailment Indices

Bus No.	Hours	Contingency Lines out
3	9.16	11&18
4	4.86	3&4
5	9.16	11&18
6	81.65	17&19
9	81.65	17&18
10	81.65	17&18
11	81.65	17&19
12	81.65	17&19
13	81.65	17&19
14	81.65	17&18

Table III: Maximum Energy Curtailment Indices

Bus No.	Energy Curtailed (MWh)	Contingency Lines out
3	457.40	3&6
4	231.97	1&2
5	36.88	1&2
6	914.49	17&19
9	2408.71	17&18
10	734.86	17&18
11	285.78	17&19
12	498.07	17&19
14	1216.6	17&19

Table IV: Average Bus Indices of the System

Bus no.	Load Curtailed (MW)
4	18.28
11	1.9145
13	12.3825
14	14.89

X CONCLUSIONS

The problem encountered in the reliability evaluation of a composite generation and transmission system is the overload of transmission lines. The simplest solution to this problem is to allow these elements to operate in the overloaded condition. This assumption results in optimistic reliability indices especially when the overload is heavy and persists for a longer duration. An alternative solution is to remove the overloaded component and continue to analyze the remaining system until no other element is overloaded, or until the total system has failed. This approach results in pessimistic reliability indices which may suggests expensive and unnecessary investment. A practical solution is to alleviate the line overloads by generation rescheduling and load shedding. Hitherto linear programming approach has been proposed for generation rescheduling and load curtailment.

REFERENCES

- [1].Roy Billinton & Ronald N Allan "Reliability evaluation of power systems", 2nd edition , plenum press, Newyork and London, 1994.
- [2].A panel discussion sponsored by the application of probability methods subcommittee of the PES, "Bulk Power System Reliability Assessment Why and How?", IEEE Transactions on Power Apparatus and systems, Vol.PAS-101, No.9, September 1982, pp3439-3456.
- [3].Billinton.R and E.Khan,"A Comparision of existing computer programs for composite System Adequacy Evaluation",CEA Transactions, 28, part-3,1989.
- [4].Chan.S.M and Schweppe.F.C, "A Generation reallocation and load shedding algorithm", IEEE Transactions on Power Apparatus and Systems, PAS-98, 1979, pp26-34.
- [5].Medicherla T.K.P, Billinton.R and sachdev.M.S "Generation Rescheduling and Load Shedding to Alleviate Line Overloads Analysis", IEEE Transactions on Power Apparatus and Systems, PAS-98, 1979, pp1876-1884.
- [6].A.Thanikachalam and J.R.Tudor "Optimal Rescheduling of Power for System Reliability", IEEE Transactions on Power Apparatus and Systems, PAS-90,Sep/Oct.1971, pp2186-2192.
- [7].Dipti srinivasan, A.C Liew and C.S. Chang "Application of Fuzzy systems in power system",Electric power system research, Vol.35,1995,pp39-43.
- [8].L.A.Zadeh, "Fuzzy sets", International journal of information and Control, Vol. 8, 1965, pp338.
- [9].Thimothy Ross , "Fuzzy logic with engineering applications", Mc Graw Hill, International publication, 1997.
- [10].J.A.Momoh & K.Tomsovic, "Over view and literature survey of fuzzy set theory in power systems", IEEE Transactions on Power Systems, Vol.10,No. 3, August1995pp1676 1690. [11].J. Endrenyi , "Reliability modeling in electric power systems", John Wiley & sons, 1978.
- [12].R.Billinton and E.Khan , "A Security Based Approach to Composite Power System Reliability Evaluation",IEEE Transactions on Power Systems, Vol.7, No.1, Feb.1992.
- [13]. Ajit K Verma, H.M.Ravikumar & B.K. Keshavan, "A Fuzzy Logic approach to security based bulk power system reliability evaluation", Electric Machines and Power systems,28:45-54, 2000

Stability Investigation of Power System and Its Stabilization by a Coordinated Application of Power System Stabilizers in Multi-machine Systems

N. Albert Singh¹, F. Shamila², K.A.Muraleedharan³ and K.Gomathy⁴

¹ Research Scholar, University of Kerala, Trivandrum India e-mail: albertsingh@rediffmail.com

² Research Scholar, University of Kerala, Trivandrum, India e-mail:shamisalm@yahoo.com

³ Professor, N. I. College of Engineering, Kumarakoil, TamilNadu, India

⁴ Professor, N. I. College of Engineering, Kumarakoil, TamilNadu, India

Abstract— Power system stabilizers (PSS) are used to generate supplementary control signals for the excitation system in order to damp the low frequency power system oscillations. To overcome the drawbacks of conventional PSS (CPSS), numerous techniques have been proposed in the literature. Based on the analysis of existing techniques, this paper presents the stabilization of multi-machine power system based on coordinated adaptive neuro-fuzzy network based power system stabilizer (ANFPSS) design. The proposed system consists of a neuro fuzzy controller, which is used to generate a supplementary control signal to the excitation system. The proposed method has the features of a simple structure, adaptivity and fast response. The proposed controller is evaluated on a multi-machine power system under different operating conditions and disturbances to demonstrate its effectiveness and robustness. Eigenvalue analysis shows that the undamped modes are sensitive to excitation control while speed governors have little influence on damping.

Key words— Neuro-Fuzzy Networks, Power System Stabilizer (PSS), Dynamic Stability.

I. INTRODUCTION

POWER system stabilizers are used to generate supplementary control signals for the excitation system in order to damp the low frequency inter-area and intra-area oscillations [1]. Conventional power system stabilizer is widely used in existing power systems and has made a contribution in enhancing power system dynamic stability. The parameters of CPSS are determined based on a linearized model of the power system around a nominal operating point where they can provide good performance. Since power systems are highly nonlinear systems, with configurations and parameters that change with time, the CPSS design based on the linearized model of the power system cannot guarantee its performance in a practical operating environment.

To improve the performance of CPSSs, numerous techniques have been proposed for their design, such as using intelligent optimization methods (simulated annealing, genetic algorithm, tabu search) [2]-[4], fuzzy [5]-[6], neural networks and many other nonlinear control techniques. The intelligent

optimization algorithms are used to determine the optimal parameters for CPSS by optimizing an eigenvalue based cost function in an offline mode. Since the method is based on a linearized model and the parameters are not updated online, therefore they lack satisfactory performance during practical operation. The rule-based fuzzy logic control methods are well known for the difficulty in obtaining and adjusting the parameters of the rules especially online. Recent research indicates that more emphasis has been placed on the combined usage of fuzzy systems and other technologies such as neural networks to add adaptability to the design [7]. Currently, most of the nonlinear control based methods use simplified models to decrease complexity of the algorithms. Considering the complexity of practical power systems, more realistic model with less computation time is required for effective robust control over a wide range of operating conditions.

As power systems are nonlinear, and also are prone to variations in its operating states over a wide range, the conventional PSS cannot provide optimal performance as the operating point changes. The fusion of ideas from fuzzy control and neural networks had acknowledged a significant role in improving controller performances. Fuzzy logic has proven effective for complex, non-linear and imprecisely defined systems. The common bottleneck in fuzzy logic is the derivation of fuzzy rules and the parameter tuning for the controller. The neural networks have powerful learning abilities, optimization abilities and adaptation. The fuzzy logic and neural networks can be integrated to form a connectionist Adaptive network based Fuzzy logic controller. The proposed Adaptive Neuro-Fuzzy based PSS (ANFPSS) is designed for a multimachine machine power system network.

The generator speed deviation and its derivative are taken as inputs to the controller. This paper also presents the results of a stability investigation of a power system by coordinated power system stabilizers (PSSs). The effects of the existing controllers on system stability are studied. If no PSSs are present, the damping of various swing modes in the system will be very poor and low frequency oscillations present.

The power system model is described in section II. The design of the coordinated adaptive neuro-fuzzy network

controller is described in section III. The Implementation process and simulation studies are described in section IV.

II. POWER SYSTEM MODELLING

For any electric power system dynamic study, a proper mathematical model must be chosen. There are only a limited number of system components important to the dynamic study: the synchronous generator, the governor and the excitation system.

A. Synchronous generator

The three armature phase windings on the stator of the synchronous machine are replaced by two equivalent armature windings, a d-winding on the d-axis and a q-winding on the q-axis by Park's transformation. The models mainly differ in the number of windings considered along d and q-axis. The third order model [8] represented by the following equations is used for the representation of synchronous generator.

$$\dot{\omega} = 1/M (T_m - T_e - T_d) \quad (1)$$

$$\dot{\delta} = \omega_b(\omega - 1) \quad (2)$$

$$\dot{e}_q' = \frac{1}{T_{do}} [E_{fd} - e_q' - (x_d - x_d') i_d] \quad (3)$$

and the auxiliary equations are

$$T_e \equiv P_e \equiv \frac{e_q' V_t}{x_d} \sin \delta + \frac{V_t^2 (x_d' - x_q) \sin 2\delta}{2 x_d x_q} \quad (4)$$

$$e_q' = V_t + j x_d' i_d + j x_q' j i_q \quad (5)$$

B. Modeling of Excitation System

The excitation system is considered to be of continuously acting IEEE Type-1 excitation system [8]. The CPSS consists of two phase-lead compensation blocks, a signal washout block, and a gain block. The input signal is the rotor speed deviation $\Delta\omega$ [18]. The block diagram of the CPSS is shown in fig.1

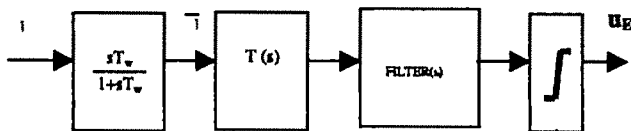


Fig.1 Block Diagram of CPSS

III. ADAPTIVE NEURO-FUZZY PSS

The Adaptive Network Based Fuzzy Logic PSS is designed with two inputs, the generator speed deviation $\Delta\omega$ and its derivative $\Delta\dot{\omega}$, and one control output (u_E). The training data is viewed to be very complex hence seven linguistic variables for each input variable were used to get the desired performance. The linguistic variables are specified by

Gaussian membership functions and as a result 49 rules are devised. The rule-base contains the fuzzy IF-THEN rules of sugeno's first order type [9] in which the output of each rule is a linear combination of input variables plus a constant term. The final output is the weighted average of each rule's output. The universe of discourse for the input-output variables is normalized and the gain parameters chosen based on input-output space are $\Delta\omega$ gain=1.0, $\Delta\dot{\omega}$ gain=0.08, u_E gain=0.1

The architecture of the ANFPSS sensing $\Delta\omega$ and $\Delta\dot{\omega}$ is shown in Fig. 2. where node functions in each layer are as described below.

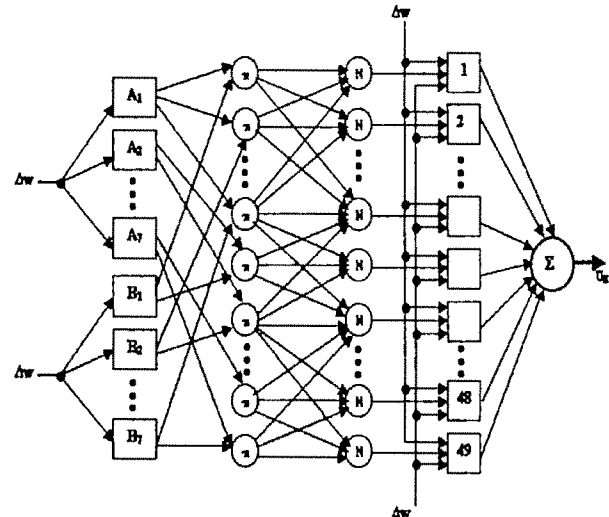


Fig 2. Architecture of ANFPSS

Layer 1:

Each node in this layer is an adaptive node performing Gaussian membership function.

$$o_{1,i} = \mu_{A,i}(x_i) = \exp \left[-\frac{(x_i - c_v)^2}{\sigma_j^2} \right] \quad \text{where } i=1, 2, \dots, 7, j=1, 2, \dots, 7$$

x_i is the input to this layer and c_v is the center of the membership function.

Layer 2:

Every node in this layer represents the firing strength of the rule.

$$o_{2,i} = w_i = \mu_{A,i}(x_i) \wedge \mu_{B,i}(y_i) \quad i=1 \dots 7.$$

Eventually the nodes of this layer perform fuzzy AND operation.

Layer 3:

The nodes of this layer calculate the normalized firing strength of each rule.

$$o_{3,i} = \bar{w}_i = \frac{w_i}{\sum w_i} \quad i=1 \dots 49.$$

w_i —firing strength of a rule.

Layer 4:

The nodes in this layer output the weighted consequent part of the rule table.

$$o_{4,i} = \bar{w}_i f_i = \bar{w}_i (p_i x + q_i y + r_i) \quad i=1, \dots, 49$$

where $\{p_i, q_i, r_i\}$ is the parameter set of this node.

Layer 5:

The single node in this layer computes the overall output as the summation of all the incoming signals.

$$O_{5,i} = \sum w_i f_i / \sum w_i \quad i=1 \dots 49.$$

where $O_{5,i}$ denote the output of the 'i'th node in layer 5.

5.

The learning algorithm for the connectionist network structure consists of two separate stages of a learning strategy, which combines unsupervised learning and supervised gradient-descent learning procedure. In phase one a self-organized learning scheme is used to locate initial membership functions and to find the presence of fuzzy logic rules. In phase two a supervised learning scheme is used to optimally adjust the parameters of membership functions for desired output. The back-propagation algorithm is used for the supervised learning. To initiate the learning scheme, training data and the desired or guessed coarse of fuzzy partition (i.e., the size of the term set of each input/output linguistic variable) must be provided from the outside world [9].

The ANFPSS training is done assuming that there is no expert available and the initial values of the membership functions parameters are equally distributed along the universe of discourse and all consequent parts of the rule table set to zero. The ANFPSS starts from zero output and during training it gradually learns the rules and functions as close to the desired controller. Thus during training the network structure update membership functions and rule base parameters according to the gradient descent update procedure.

The ANFPSS was trained by data's created from Power System Stabilizers designed for various operating conditions in which the generator output ranging from 0.2 to 1.0 pu and power factor ranging from 0.85 lead to 0.4 lag. The wide spectrum of possible disturbances used for the training are: reference voltage and infinite bus voltage disturbances in the range of -0.05 pu to 0.05 pu, torque variations from -0.15 pu to 0.15 pu, three phase fault transients, transmission line with different line reactance disturbances, different machine inertia disturbances and one transmission line outage. A total of 4512 input-output data pairs are created for the training of ANFPSS.

IV. SIMULATION STUDIES

The performance of the designed ANFPSS was investigated on a power system model of the three machine nine bus system [10] with third generator considered as the infinite bus. A single-machine part of the schematic diagram of the multi-machine system used for simulation studies is shown in Fig 3.

The Simulink and Fuzzy Logic toolbox of MATLAB [11, 12] are used for modeling the power system and designing the ANFPSS respectively. A number of studies have been performed to investigate the effect of PSS designed by the Adaptive Network Based Fuzzy Logic control approach. The control output for both the ANFPSS and CPSS was limited to 0.15 pu.

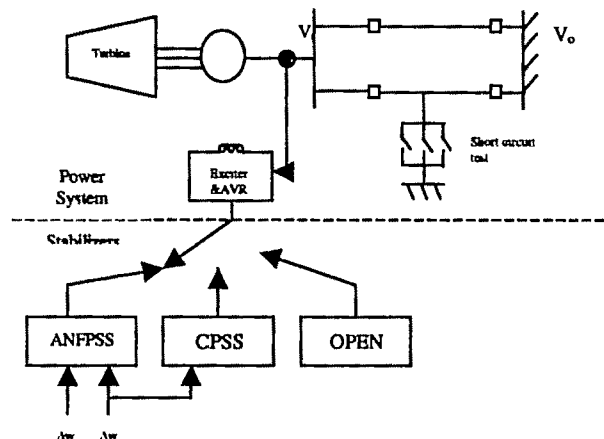


Fig.3 System model for Simulation Studies

Load test:

With the generator operating at an active power of 0.4 pu and a reactive power of 0.9 p.u lag a 0.01 pu step increase in input torque reference was applied in all the machines. The disturbance is large enough to cause the system to operate in the non-linear region. System response without PSS and with the CPSS and ANFPSS under these conditions was shown in Fig 4 & 5. The system without stabilizer is highly oscillatory. Although the CPSS is effective in damping the oscillations, the ANFPSS settles the oscillations smoothly and quickly.

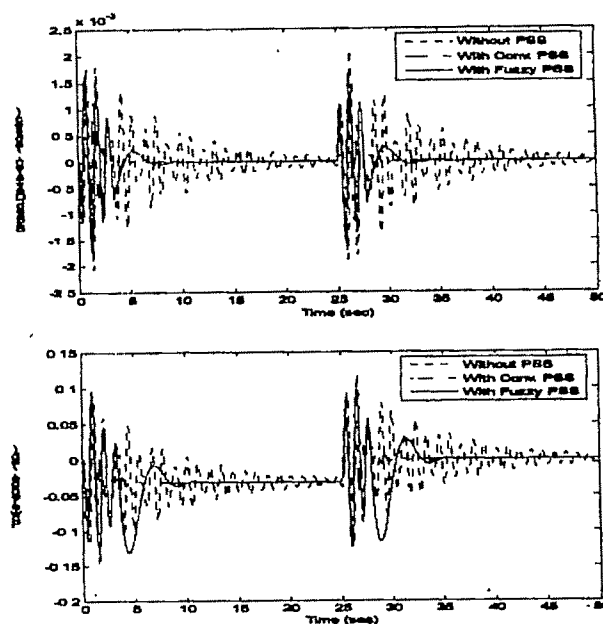


Fig.4 Simulation results for load test at an active power of 0.4 pu and reactive power 0.9 pu a 0.01 pu step increase in input torque reference in generator 1.

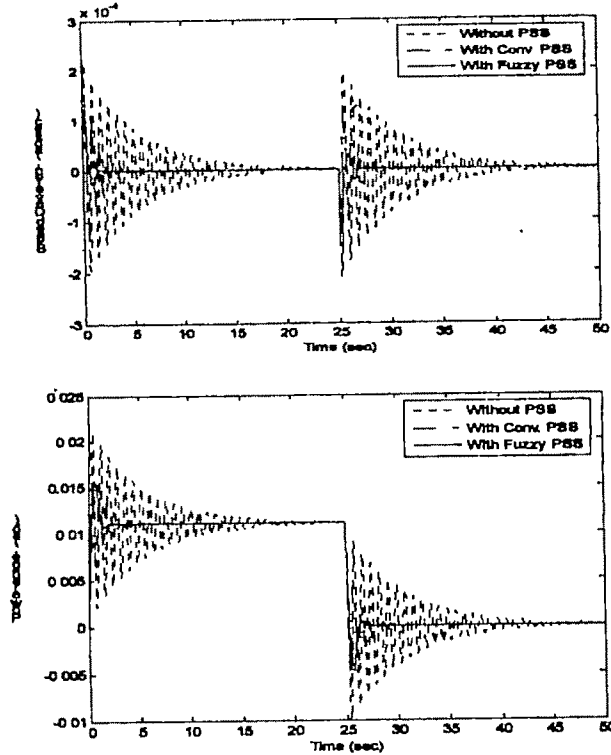


Fig:5 Simulation results for load test at an active power of 0.4 pu and reactive power 0.9 pu a 0.01 pu step increase in input torque reference in generator 2.

Leading pf Load test:

When the generator is operating at a leading power factor, the situation is much more difficult because the stability margin is reduced. However, in order to absorb the capacitive charging current in a high voltage power system, it may become necessary to operate the generator at a leading power factor. It is therefore desirable that the controller be able to guarantee stable operation of the generator under leading power factor condition.

With the generator operating at an active power of 0.9 pu and reactive power 0.8 lead, a 0.01 pu step increase in torque reference was applied at 1s. The results given in Fig 6 & 7 show that the oscillation of the system is damped out rapidly by the ANFPSS.

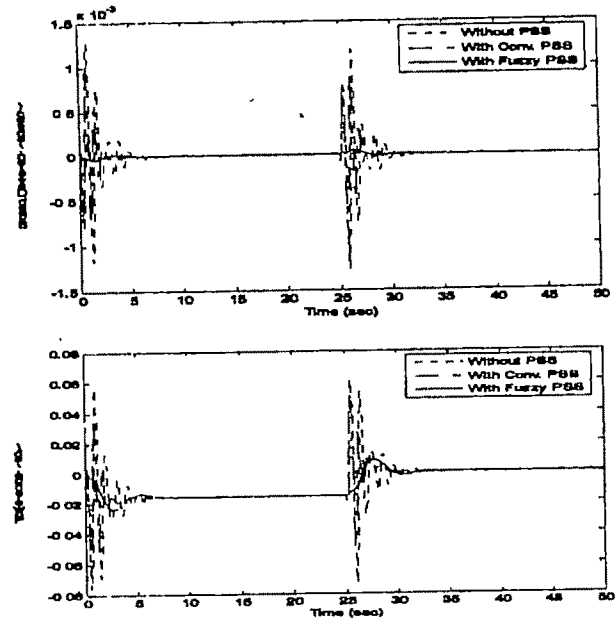


Fig:6 Simulation results for leading power factor load test at an active power of 0.9 pu and reactive power 0.8 pu a 0.01 pu step increase in input torque reference in generator 1

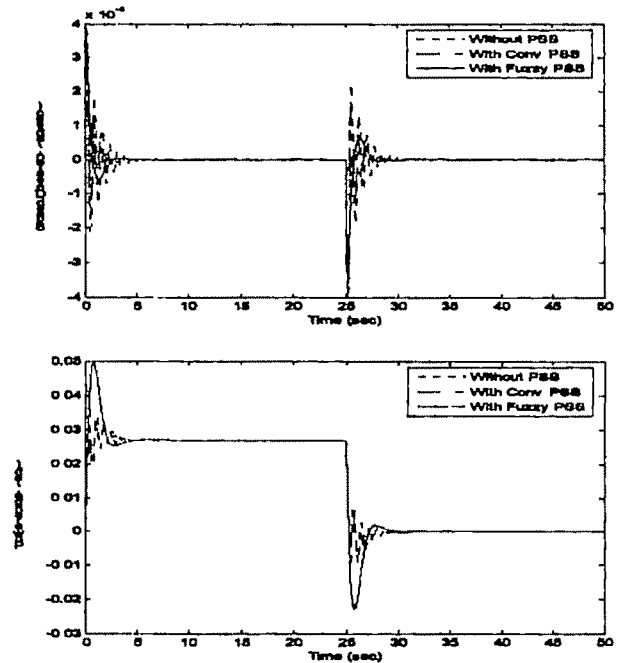


Fig:7 Simulation results for leading power factor load test at an active power of 0.9 pu and reactive power 0.8 pu a 0.01 pu step increase in input torque reference in generator 2

Eigenvalue Analysis

The following analysis is conducted without PSSs in service. The purpose is to identify the best sites for PSS installation. Two operating conditions for eigenvalue analysis are considered; the normal operation and the operating condition when one of the double circuit lines is tripped. Table I shows the eigenvalues, frequencies of swing modes and their participating generators for both situations.

Table:1

System	Eigen values without PSS	Eigen values with ANFPSS
Generator 1	-0.019649 + 5.5135i -0.019649 - 5.5135i -10.187 + 30.384i -10.187 - 30.384i	-7.9744 + 30.044i -7.9744 - 30.044i -1.6696 + 5.027i -1.6696 - 5.027i -0.34535 -11.114
Generator 2	-0.055556 + 7.4902i -0.055556 - 7.4902i -10.189 + 29.132i -10.189 - 29.132i	-7.0511 + 28.824i -7.0511 - 28.824i -2.2753 + 6.7059i -2.2753 - 6.7059i -0.34106 -11.828

V. CONCLUSION

To overcome the drawbacks of conventional power system stabilizers, an adaptive coordinated neuro-fuzzy network control based power system stabilizer design is presented in this paper. The proposed method is evaluated on a 9 bus three machine power system. The design of the proposed controller is based on only the speed deviation of the generator. Therefore, the computations involved in the network design are minimal. This is desirable for practical hardware implementation on the power station platforms. Simulation results for different kinds of disturbances and operating conditions demonstrate the effectiveness and robustness of the controller. Such a nonlinear adaptive PSS will yield better and fast damping under small and large disturbances even with changes in system operating conditions. Better and fast damping means that generators can operate more close to their maximum generation capacity thus ensuring that generators remain stable under sever faults such as three phase short circuits.

APPENDIX

List of Symbols:

δ	:	Rotor angle.
ω	:	Rotor angular velocity.
E_{fd}	:	Exciter output voltage
M	:	Inertia constant
T_m	:	Mechanical torque
T_e	:	Electrical torque
T_d	:	Damping torque
$T_{do'}$:	d-axis open circuit time constant
x_d'	:	d-axis transient reactance
x_d	:	d-axis component of synchronous reactance
x_q	:	q-axis component of synchronous reactance
i_d, i_q	:	d and q axis currents
V_t	:	Generator terminal voltage

REFERENCES

- [1] E.V.Larsen and D.A.Swann, "Applying Power System Stabilizers", *IEEE Trans. on PAS*, Vol 100, pp.3017-3041, 1981.
- [2] Abido, M.A., "Robust design of multi-machine power system stabilizers using simulated annealing," *IEEE Trans. on Energy Conversion*, Vol. 15, No. 3, pp. 297-304, 2000.
- [3] Do Bonfim, A.L.B., Taranto, G.N. and Falcao, D.M., "Simultaneous tuning of power system damping controllers using genetic algorithms," *IEEE Transaction on Power Systems*, Vol. 15, No. 1, pp. 163-169, 2000.
- [4] Abdel-Magid, Y.L., Abido, M.A. and Mantaway, A.H., "Robust tuning of power system stabilizers in multi-machine power systems," *IEEE Transactions on Power Systems*, Vol. 15, No. 2, pp. 735 -740, 2000.
- [5] K.A.El-Metwally, G.C.Hancock O.P.Malik, "Implementation of a Fuzzy Logic PSS using a micro controller and Experimental Test Results", *IEEE Trans. on Energy Conversion*, Vol.11, pp.91-96, 1996.
- [6] Hariri, A. and Malik, O.P., "A fuzzy logic based power system stabilizer with learning ability," *IEEE Trans. on Energy Conversion*, Vol. 11, No. 4, pp. 721 -727, 1996.
- [7] Hiyama, T. and Tomsovic, K., "Current status of fuzzy system applications in power systems," *Proceedings of the IEEE SMC99*, Tokyo, Japan, pp. 527-532, 1999.
- [8] Y.N.Yu, "Electric Power System Dynamics", Academic Press, New York, 1983
- [9] C.T.Lin, C.S.George Lee, "Neural-Network Based Fuzzy Logic Control and Decision system". *IEEE Trans.on Computers*, Vol.40, pp.1320-1336, 1991.
- [10] P.M.Anderson and A.A.Fouad, "Power system control and stability", Vol-1, IOWA State University Press, USA, 1981.
- [11] Ned Gulley, J.S.R.Jang, "Fuzzy Logic Tool Box for use with MATLAB, User's Guide", The MATH WORKS Inc, Jan.1995.
- [12] "Simulink Dynamic System Simulation Software, User's Guide", The MATH works Inc, Jan.1995.

Incorporating Static Synchronous Series Compensator in Optimal Reactive Power Allocation for Improving Voltage Stability Margins

P. Kanta Rao¹ and K. Vaisakh²

Dept. of Electrical Engineering, SRKR College of Engineering, BHIMAVARAM, AP 534 204 INDIA
Dept. of Electrical Engineering, Andhra University, VISAKHAPATNAM, AP 530 003 INDIA (e-mail: vaisakh_k@yahoo.co.in)

Abstract—The reactive power allocation aspect has received considerable attention in present day power system operation. The voltage magnitudes throughout a system are very important, as they must be high enough to support loads, and low enough to avoid equipment breakdown. Reactive power dispatch can be defined as the control of generator excitation, variable transformer tap settings, and adjustable VAR compensating devices to improve the system voltage profile, and thereby to minimize the active power losses in the system. At heavy/light load periods, voltage control is provided by the controllable reactive sources. These reactive power controls, which are scattered throughout the transmission network, function in co-ordination. In this paper, a sequential method for optimum allocation of reactive power in day-to-day operation of power systems in presence of SSSC is presented. The technique will try to utilize fully the reactive power sources in the system to improve the voltage profile and to minimize the voltage stability indices. The method involves successive solution of steady state power flows and optimization of reactive power control variables using linear programming techniques. The proposed method has been applied to few systems and the results obtained on a 24-bus real-life system are presented for illustration.

Index Terms—Optimal reactive power allocation, Voltage stability, Power loss, Controlled voltage source

I. INTRODUCTION

OVER the past 30 years, a number of power system optimization methodologies consist of a power flow solution integrated together with an optimization algorithm. The optimal power flow problem is the minimization of the fuel cost, system losses, or any other appropriate objective function, while maintaining acceptable system performance in terms of limits on generator active and reactive power outputs, outputs of reactive power

compensating devices, transformer tap settings, or bus voltage levels, etc [1, 2, 3, 4, 5]. When the objective function is minimized, the optimal power flow results in an economic dispatch through optimum allocation of real power generation. It also determines the reactive power outputs of generators and other VAR sources, as well as the transformer tap settings.

To handle large-scale problems, the idea of decomposition of problem into active power optimization and reactive power optimization is also used by many investigators [6,7,8, 9]. The active power optimization problem is to minimize the production cost under the assumption that system voltages are held constant, and the reactive power optimization problem is to minimize the transmission loss under the assumption that the active power generation is held constant. Due to the loose coupling between the two problems, the sequential optimization provides a considerable advantage over the simultaneous optimization of all the control variables.

In the recent years voltage stability issues have received considerable focus due to the several voltage stability crisis situations having occurred all around the globe. Economic competition, sometimes, results in paying less attention to security features of the overall system. A power flow can have any number of operating limit violations. Methods to understand the voltage instability phenomenon and quantify the stability indices have been reported in works [10,11,12]. In [13] a voltage stability indicator has been discussed whose value changes between zero (no load) and one (voltage collapse). The indicator incorporates the effect of all other loads in the system on the evaluation of index at individual load buses. The overall voltage stability of the system could be identified by the largest value of the index evaluated amongst all the load buses. This indicator can also be used as a normalized quantitative measure, for estimation of the voltage stability margin from the operating point.

In this paper, the authors have used this capability of the indicator. Works in the direction of developing algorithms to incorporate stability issues into power system operational analysis are going on. The reported work [14] attempts to

formulate the incorporation of the transient angle stability, into an OPF routine, as an additional constraint. In this paper the authors have proposed and formulated an algorithm to include the voltage stability margin as objective into the optimal reactive power allocation.

Controlling the power flows in the network, under normal operation and network contingencies, helps to reduce flows in heavily loaded lines, reduce system power loss, and improve stability and performance of the system without generation rescheduling or topological changes [15, 16]. A controlled voltage source installed in a line helps to increase or decrease the power flow in a line for improving real power loss reduction, voltage profiles, and voltage stability.

In this paper, a sequential method for optimum allocation of reactive power in day-to-day operation of power systems in presence of SSSC. The technique will try to utilize fully the reactive power sources in the system to improve the voltage profile and to minimize the real power losses and voltage stability indices. The method involves successive solution of steady state power flows and optimization of reactive power control variables using linear programming techniques.

II. VOLTAGE STABILITY INDICATOR

Consider an n-bus system having 1, 2...g, generator buses (g), and g+1,g+2...n the load buses(r=n-g-s) and t number of OLTC transformers. The transmission system can be represented using a hybrid representation, by the following set of equations

$$\begin{bmatrix} V_L \\ I_G \end{bmatrix} = H \begin{bmatrix} I_L \\ V_G \end{bmatrix} = \begin{bmatrix} Z_{LL} & F_{LG} \\ K_{GL} & Y_{GG} \end{bmatrix} \begin{bmatrix} I_L \\ V_G \end{bmatrix}$$

V_L, I_L are the voltage and current vectors at the load buses

V_G, I_G are the voltage and current vectors at the generator buses

$Z_{LL}, F_{LG}, K_{GL}, Y_{GG}$ are the sub-matrices of the hybrid matrix H.

The H matrix can be evaluated from the Y bus matrix by a partial inversion, where the voltages at the load buses are exchanged against their currents.

$$\begin{bmatrix} I_G \\ I_L \end{bmatrix} = \begin{bmatrix} Y_{GG} & Y_{GL} \\ Y_{LG} & Y_{LL} \end{bmatrix} \begin{bmatrix} V_G \\ V_L \end{bmatrix}$$

This representation can then be used to define a voltage stability indicator at the load bus [13], namely L_j which is given by,

$$L_j = \left| 1 + \frac{V_{0j}}{V_j} \right| \quad (1)$$

where,

$$V_{0j} = - \sum_{i \in G} F_{ji} V_i \quad (2)$$

The term V_{0j} is representative of an equivalent generator comprising the contribution from all generators.

The index L_j can also be derived and expressed in terms of the power terms as the following.

$$L_j = \left| \frac{S_{j+}^*}{Y_{jj+} V_j^2} \right| \quad (3)$$

where,

$$S_{j+} = S_j + S_{jcorr} \quad (4)$$

* indicates the complex conjugate of the vector

$$S_{jcorr} = \left(\sum_{\substack{i \in \text{Loads} \\ i \neq j}} \frac{Z_{ji}^* S_i}{Z_{jj} V_i} \right) V_j \quad (5)$$

$$Y_{jj+} = \frac{1}{Z_{jj}} \quad (6)$$

The complex power term component S_{jcorr} represents the contributions of the other loads in the system to the index evaluated at the node j. The L -indices for a given load condition are computed for all load buses. The equation for the L -index for j-th node can be written as

$$L_j = \left| 1.0 - \sum_{i=1}^{i=g} \left| F_{ji} \right| \frac{|V_i|}{|V_j|} \angle \theta_{ji} + \delta_i - \delta_j \right| \quad (7)$$

$$L_j = \left| 1.0 - \sum_{i=1}^{i=g} \frac{|V_i|}{|V_j|} (F_{ji}^r + jF_{ji}^m) \right| \quad (8)$$

* Indicates the complex conjugate of the vector

$$V_i = |V_i| \angle \delta_i, V_j = |V_j| \angle \delta_j, \quad (9)$$

$$\begin{aligned} F_{ji} &= |F_{ji}| \angle \theta_{ji} \\ F_{ji}^r &= |F_{ji}| \cos(\theta_{ji} + \delta_i - \delta_j), \\ F_{ji}^m &= |F_{ji}| \sin(\theta_{ji} + \delta_i - \delta_j) \end{aligned} \quad (10)$$

It can be seen that when a load bus approaches a steady state voltage collapse situation, the index L approaches the numerical value 1.0. Hence for an overall system voltage stability condition, the index evaluated at any of the buses must be less than unity. Thus the index value L gives an indication of how far the system is from voltage collapse. This feature of this indicator has been exploited in our proposed algorithm to evolve a voltage collapse margin incorporated OPF routine.

In the conventional optimal power flow approach, the objective is to minimize the total amount of load curtailment considering the load flow system constraints like line flow, voltage magnitude, the maximum active and reactive power generation etc. The control variables for the OPF evaluation are the real and reactive power generation of each generation bus and the real and reactive load at each load bus.

Power Flow Control With Controlled Voltage

III. POWER FLOW CONTROL WITH UPFC

Better utilization of existing power system capacities by installing new power electronic controllers such as FACTS has become imperative. FACTS controllers are able to change, in a fast and effective way, the network parameters in order to achieve better system performance. FACTS controllers, such as phase shifter, shunt, or series compensation and the most recent developed converter-based power electronic controllers, make it possible to control circuit impedance, voltage angle, and power flow for optimal operation performance of power systems, facilitate the development of competitive electric energy markets, stimulate the unbundling the power generation from transmission and mandate open access to transmission services, etc. With the practical applications of the converter-based FACTS controllers—STATCOM, SSSC, and UPFC in power systems, computer modeling of these is of great concern for the planning, operation planning, and control analysis of the FACTS controllers.

IV. MULTICONTROL FUNCTIONAL MODEL OF THE SSSC

A. Operation Principles of the SSSC

A SSSC usually consists of a coupling transformer, an inverter, and a capacitor. As shown in Fig. 1, the SSSC is series connected with a transmission line through the coupling transformer. It is assumed here that the transmission line is series connected with the SSSC via its bus. The active and reactive power flows of the SSSC branch entering the bus are equal to the sending end active and reactive power flows of the transmission line, respectively. In principle, the SSSC can generate and insert a series voltage, which can be regulated to change the impedance (more precisely reactance) of the transmission line. In this way, the power flow of the transmission line or the voltage of the bus, which the SSSC is connected with, can be controlled.

B. Equivalent Circuit and Power Flow Constraints of the SSSC

An equivalent circuit of the SSSC as shown in Fig. 2 can be derived based on the operation principle of the SSSC. In the equivalent, the SSSC is represented by a voltage source in series with a transformer's impedance. In the practical operation of the SSSC, V_{se} can be regulated to control the power flow of line $i - j$.

It is proposed to improve the performance of the system by in presence of UPFC using all of its advantages. The UPFC equivalent circuit for steady state model is shown in Fig. 1

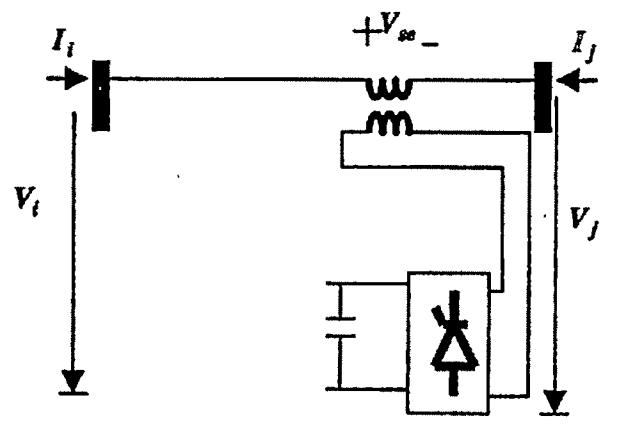


Figure 1. SSSC operating principles

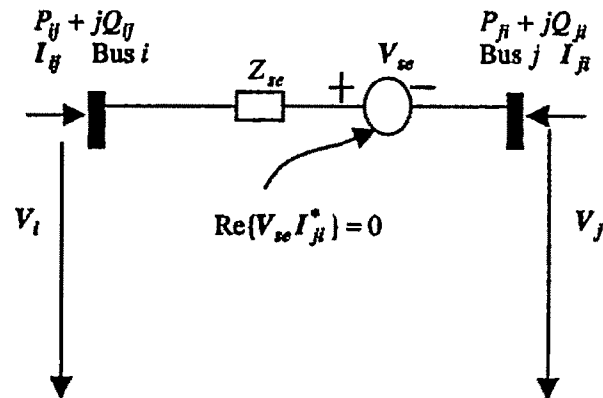


Figure 2. SSSC equivalent circuit

In the equivalent circuit, $V_{se} = V_{se} \angle \theta_{se}$, $V_i = V_i \angle \theta_i$, $V_j = V_j \angle \theta_j$, then the power flow constraints of the SSSC are:

$$P_{ij} = V_i^2 g_{ii} - V_i V_j (g_{ij} \cos(\theta_i - \theta_j) + b_{ij} \sin(\theta_i - \theta_j)) - V_i V_{se} (g_{ij} \cos(\theta_i - \theta_{se}) + b_{ij} \sin(\theta_i - \theta_{se}))$$

$$Q_{ij} = -V_i^2 b_{ii} - V_i V_j (g_{ij} \sin(\theta_i - \theta_j) - b_{ij} \cos(\theta_i - \theta_j))$$

$$\begin{aligned}
 & -V_i V_{se} (g_{ij} \sin(\theta_i - \theta_{se}) - b_{ij} \cos(\theta_i - \theta_{se})) \\
 P_{ji} = & V_j^2 g_{jj} - V_i V_j (g_{ij} \cos(\theta_j - \theta_i) + b_{ij} \sin(\theta_j - \theta_i)) \\
 & + V_j V_{se} (g_{ij} \cos(\theta_j - \theta_{se}) + b_{ij} \sin(\theta_j - \theta_{se})) \\
 Q_{ji} = & -V_j^2 b_{jj} - V_i V_j (g_{ij} \sin(\theta_j - \theta_i) - b_{ij} \cos(\theta_j - \theta_i)) \\
 & + V_j V_{se} (g_{ij} \sin(\theta_j - \theta_{se}) - b_{ij} \cos(\theta_j - \theta_{se})) \quad (5)
 \end{aligned}$$

Where $g_{ij} + jb_{ij} = 1/Z_{se}$, $g_{ii} = g_{ij}$,

$b_{ii} = b_{ij}$, $g_{jj} = g_{ij}$ and $b_{jj} = b_{ij}$

The operating constraint of the SSSC (the active power exchange via the dc link) is

$$PE = \text{Re}(V_{se} I_{ji}^*) = 0$$

where

$$\begin{aligned}
 \text{Re}(V_{se} I_{ji}^*) = & -V_i V_{se} (g_{ij} \cos(\theta_i - \theta_{se}) - b_{ij} \sin(\theta_i - \theta_{se})) \\
 & + V_j V_{se} (g_{ij} \cos(\theta_j - \theta_{se}) - b_{ij} \sin(\theta_j - \theta_{se}))
 \end{aligned}$$

of the shunt voltage source.

V. OPTIMAL REACTIVE POWER ALLOCATION

Minimization of voltage stability indices in a system forms the basis for the reactive power optimization problem. The model uses linearized sensitivity relationships to define the problem. The constraints are, the linearized network performance equations relating to control and dependent variables and the limits on the control variables.

The control variables are:

- The transformer tap settings (T)
- The generator excitation settings (V)
- The Switchable VAR compensator (SVC) settings (Q)

The dependent variables are:

- The reactive power outputs of the generators (Q)
- The voltage magnitudes of the buses other than the generator buses (V)

It is assumed that,

- 1,2,...,g are the generator buses,
- g+1,g+2,...,g+s are the SVC buses, and
- g+s+1,g+s+2,...,n are the remaining buses.

The optimization problem can then be defined as,

$$\text{Minimize } \sum (1 - L_j)^2 = Cx$$

Subject to

$$b_{\min} \leq b = Sx \leq b_{\max}$$

$$\text{and } x_{\min} \leq x \leq x_{\max}$$

Where, C is the row matrix of linearized loss sensitivity coefficients and S is the linearized sensitivity matrix relating the dependent and control variables and are evaluated using the load flow sensitivity matrix and the results of the load flow analysis [1, 2]. A linear programming technique is applied to the above problem to determine the optimum settings of the

control variables

The control vector in incremental variables is defined as

$$X = [\Delta T_1, \dots, \Delta T_2, \Delta V_1, \dots, \Delta V_g, \Delta Q_{g+1}, \dots, \Delta Q_{g+s}]'$$

And the dependent vector in incremental variables as

$$b = [\Delta Q_1, \dots, \Delta Q_g, \Delta V_{g+1}, \dots, \Delta V_{g+s}, \dots, \Delta V_n]'$$

A. Computational Procedure

This section presents the computational steps followed in the program developed for the optimization of reactive power allocation in an AC power system, the following are the steps used to obtain the optimal reactive power allocation in the system for improvement of system stability.

Step 1: Input -data relating to system

- Network, Scheduled load and generation
- Upper and lower limits and step size for transformers tap settings, generator excitation settings and Switchable VAR compensator settings
- Upper and lower limits on the generator reactive powers and voltage magnitudes at buses other than the generator buses.

Step 2: Perform the power flow (or output of the state estimation) to obtain the values of voltage violations in the system and advance the VAR control iteration count.

Step 3: Check for the satisfactory voltage profiles in the AC system

Step 4: Compute the column matrices b^{\max} , b^{\min} of the dependent variables.

Step 5: Compute the column matrices x^{\max} , x^{\min} of the control variables.

Step 6: Modify the matrices x^{\max} and x^{\min} to reasonably small ranges.

Step 7: Compute the sensitivity matrix (S), relating the dependent variables and control variables.

Step 8: Compute the row matrix (C) of the objective function sensitivities wrt the control variables.

Step 11: Solve the optimization problem using the linear programming technique.

Step 12: Obtain the optimum settings of the control variables.

Step 13: Perform the load flow with the optimum settings of the control variables.

Step 14: Check for satisfactory limits on the dependent variables.

Step 15: Check for the significant change in the objective function

Step 16: Print the results.

VI. TYPICAL SYSTEM STUDIES AND RESULTS

A system of 24 buses (typical of Indian practical system including the voltage levels of 220kV and 400kV) is considered for studies as shown in Fig.3. There are 4

generators in the system connected at buses 1, 2, 3, and 4. There are 7 tap regulating transformers, 4 non-regulating transformers, and 17 transmission lines in the system. The loads are present at 220 kV side of regulating transformers. About 4 numbers of buses are considered as Switchable VAR Compensator (SVC) buses. The system has about 2620MW, 980 MVAR peak load. Results for real and reactive power allocation obtained for the peak load condition are presented.

A. Base Case

The initial power flow studies are carried out without locating CVS in any transmission line, and the results under peak load condition are given in Table I. In this case, it is observed that a low voltage profile in the system with the voltages of about 16 buses is not being within acceptable limits (0.95-1.05 p. u.). There is no generator exceeding the maximum Q limits and the minimum Q limit and is given in Table II.

TABLE I
SYSTEM-GRID TOTALS

Parameters	Initial
Total P Gen.(MW)	2684.98
Total Q Gen. (MVAR)	1046.30
Total P Load (MW)	2620
Total Q Load (MVAR)	980
Total P Loss(MW)	64.94

TABLE II
GENERATORS Q (MVAR) LIMITS

Generator No.	Max. MVAR	Min. MVAR	Actual MVAR
1	950.0	-150.0	518.0
2	320.0	-100.0	34.6
3	400.0	-100.0	193.2
4	400.0	-100.0	300.4

B. ORPA Without CVS Location

The proposed algorithm for reactive power optimization is applied to improve the situation. The step size taken for both the regulating transformers and generators excitations is 0.0125 p.u. The total number of SVC buses selected for the compensation is about 4. After nine iterations of the VAR optimization the voltages at all the buses have been brought within the satisfactory operable limits (0.95-1.05 p.u.). The summarized results initial and after optimization (final) for the system are presented in Tables III and IV.

TABLE III
SYSTEM-GRID TOTALS WITHOUT CVS

Parameters	Initial	Final
Total P Gen. (MW)	2684.98	2677.07
Total Q Gen. (MVAR)	1046.30	773.54
Total P Load (MW)	2620	2620
Total Q Load (MVAR)	980	980

Total P Loss (MW)	64.94	57.07
Reduction in 'P' loss (MW)	7.87	
$\sum (1 - L_j)^2$	Before ORPA	1.4225
	After ORPA	0.6112

TABLE IV
GENERATORS Q (MVAR) LIMITS WITHOUT CVS

Generator No.	Max. MVAR	Min. MVAR	Actual MVAR
1	950.0	-150.0	588.27
2	320.0	-100.0	-92.29
3	400.0	-100.0	00.58
4	400.0	-100.0	276.98

C. UPFC Location in line 18-22 without ORPA

In this case, it is proposed to improve the system performance by locating CVS in a transmission line connected between buses 18-12. The initial real and reactive line flows in this transmission line 170MW and -10MVAR respectively. Four cases are considered for increasing the real and reactive line flows in the line 18-22 from initial real and reactive line flows and are given by

Case 1: 185MW, 7.5 MVAR

Case 2: 200MW, 10 MVAR

The summarized results for the four cases are given in Tables V, VI, and VII.

TABLE V
SYSTEM-GRID TOTALS WITH CVS

	Initial	Final
Total P Gen. (MW)	2684.98	2670.23
Total Q Gen. (MVAR)	1046.30	978.39
Total P Load (MW)	2620	2620
Total Q Load (MVAR)	980	980
Total P Loss (MW)	64.94	50.23
Reduction in 'P' loss(MW)	14.71	

Case 3: 215MW, 15 MVAR

Case 4: 225 MW, 25MVAR

TABLE VI
GENERATORS Q (MVAR) LIMITS WITH CVS

Generator No.	Max. MVAR	Min. MVAR	Actual MVAR
1	950.0	-150.0	507.46
2	320.0	-50.0	022.70
3	400.0	-100.0	184.83
4	400.0	-100.0	263.40

TABLE VII
REAL POWER LOSS

	With CVS Location, without ORPD			
	Case1	Case2	Case3	Case 4
'P' Loss (MW)	58.05	55.93	53.96	50.23

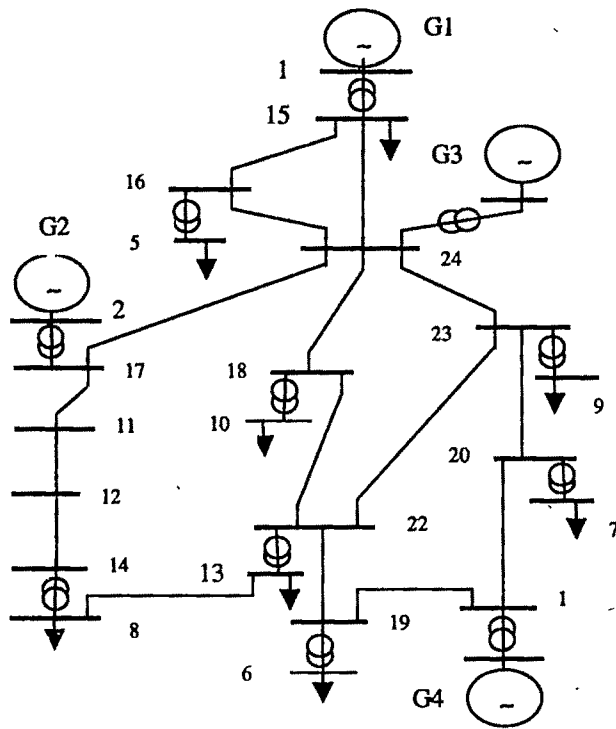


Figure 3 Practical 24-bus Equivalent EHV system

D. ORPA with UPFC Location in line 18-22

In this case, it is proposed to improve the system performance by locating CVS in a transmission line connected between buses 18-12 and by carrying out the reactive power optimization. Four cases, same as in the previous subsection C, are considered for increasing the real and reactive line flows in the line 18-22 from initial real and reactive line flows.

The summarized results are given in the Tables VIII, XI, and X. The improvements of voltage profiles and voltage stability indices are shown in Figures 3 and 4.

TABLE VIII
SYSTEM-GRID TOTALS

Parameters	Initial	Final
Total P Gen. (MW)	2684.98	2658.99
Total Q Gen. (MVAR)	1046.30	720.53
Total P Load (MW)	2620	2620
Total Q Load (MVAR)	980	980
Total P Loss (MW)	64.94	38.98
Reduction in 'P' loss (MW)	25.6	

TABLE IX
GENERATORS Q (MVAR) LIMITS

Generator No.	Max. MVAR	Min. MVAR	Actual MVAR
1	950.0	-150.0	580.97
2	320.0	-100.0	-100.00
3	400.0	-100.0	-03.32
4	400.0	-100.0	245.28

TABLE X
REAL POWER LOSS AND VOLTAGE STABILITY MARGINS

	ORPD with UPFC Location			
	Case1	Case2	Case3	Case 4
'P' Loss (MW)	46.46	44.33	42.31	38.98
$\sum(1-L_i)^2$	1.1072	1.1955	1.1826	1.1692

From the above Tables VIII-X, it can be observed that by optimizing the reactive power sources in presence of a controlled voltage source, the real power loss has been drastically reduced from initial loss 64.95MW to 38.98MW giving a total reduction in loss of 25.6 MW. Also the reactive power outputs of the generators and voltage profiles are well within the limits. The improvement of voltage profiles in all the cases is shown in figure 4.

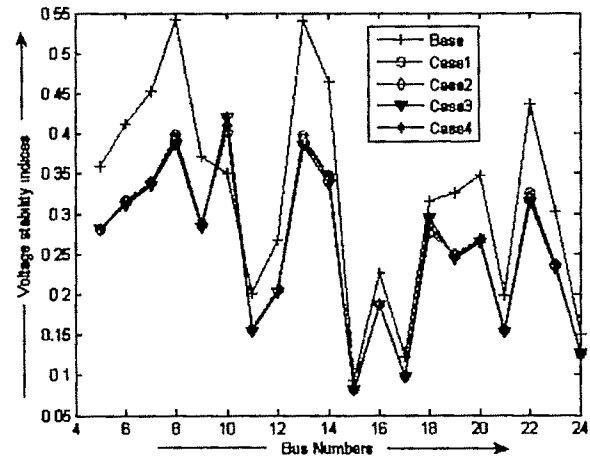


Fig.4 Voltage stability indices before and after optimization

E. ORPD with UPFC Location in line 18-22 under Line 20-23 outage Contingency

In this case, it is proposed to improve the system performance by locating UPFC in a transmission line connected between buses 18-12 under the line 20-23 outage contingency by carrying out the reactive power optimization. Four cases, same as in the previous subsection C, are considered for increasing the real and reactive line flows in the line 18-22 from initial real and reactive line flows. The summarized results are given in the Tables XI, XII, and XIII.

TABLE XI
SYSTEM-GRID TOTALS

Parameters	Initial	Final
Total P Gen. (MW)	2699.37	2659.21
Total Q Gen. (MVAR)	1365.11	804.69
Total P Load (MW)	2620	2620
Total Q Load (MVAR)	980	980
Total P Loss (MW)	79.37	39.20
Reduction in 'P' loss (MW)	40.17	

TABLE XII
GENERATORS Q (MVAR) LIMITS

Generator No.	Max. MVAR	Min. MVAR	Actual MVAR
1	950.0	-150.0	403.64
2	320.0	-100.0	005.67
3	400.0	-100.0	115.86
4	400.0	-100.0	279.52

TABLE XIII
REAL POWER LOSS AND VOLTAGE STABILITY MARGINS

	ORPD with UPFC Location			
	Case1	Case2	Case3	Case 4
'P' Loss (MW)	48.15	45.53	43.05	39.20
$\sum (1-L_i)^2$	1.1221	1.1041	1.1842	1.1633

From the above Tables XI-XII, it can be observed that by optimizing the reactive power sources in presence of a controlled voltage source under network contingency, the real power loss has been drastically reduced from initial loss 79.37MW to 38.20MW giving a total reduction in loss of 41.17 MW. Also the reactive power outputs of the generators and voltage profiles are well within the limits. The improvement of voltage stability indices in all the cases is shown in Figure 5.

VII. CONCLUSIONS

A multi-control functional model for the SSSC suitable for power flow control is used in this paper. The model has explored the multicontrol options of the SSSC such as 1) the active power flow on the transmission line; 2) the reactive power flow on the transmission line; 3) the bus voltage; and 4) the impedance (precisely reactance) of the transmission line, etc. Furthermore, within the model, the operating voltage and current constraints of the SSSC have been fully considered.

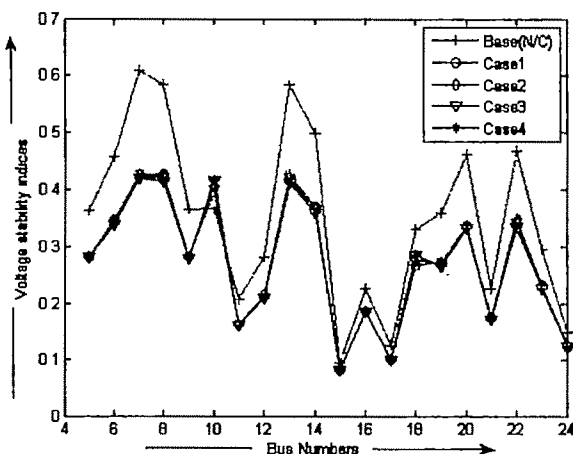


Fig.6 Voltage stability indices before and after optimization (ORPD with UPFC)

An algorithm for optimum allocation of reactive power in a practical system with an objective of improving the loss reduction, voltage profiles and voltage stability indices has been presented in this paper. The developed algorithm has been tested on typical sample systems and results for a

practical real-life equivalent system of 24-bus are presented. The proposed algorithm is demonstrated to give encouraging results for improving the operational conditions of the system under both peak load and light load conditions. The results on the equivalent practical system illustrate the application of the approach for large power systems.

VIII. REFERENCES

- [1] J.Carpentier, "Optimal power flows", *Electric Power and Energy Systems*, Vol.1, No.1, April 1979, pp.3-15.
- [2] A Monticelli, M V F Pereira, and S Granville, "Security constrained optimal power flow with post contingency corrective rescheduling", *IEEE Trans. on PS*, Vol 2, No.1, August 1987, pp.175-182..
- [3] A Mohamed and G B Jasmon, "Realistic power system security algorithm", *Proc. of IEE Gen. Tr. and Distrib.*, Vol.135, No.2, 1988, pp.98-106.
- [4] Milan Bjelorglic, Milan S Calovic, and Borivoje, S Babic, "Application of Newton's optimal power flow in voltage/reactive power control", *IEEE Trans. on PS*, Vol.5, No.4, 1990, pp.1447-1454.
- [5] A.M.Chebbo, M.R.Irving, and M.J.H.Stirling, "Reactive power dispatch incorporating voltage stability", *Proc. IEE, Gen.Tr. Distrib.*, Vol 139, No.3, 1992, pp.253-260.
- [6] Lee, K.Y., J. L. Ortiz, Y. M. Park, and L. G. Pond, "An Optimization Technique for Reactive Power Planning of Subtransmission Network under Normal Operation", *IEEE Trans. on PAS*, Vol. PWRS-1, May 1986, pp. 153-159.
- [7] Maurice K. Mangoli and K.Y. Lee, "Optimal long term reactive power planning using decomposition techniques", *Electric Power System Research*, Vol.26,1993, pp.41-52.
- [8] K H Abdul Rahman and S M Shahidehpour, "A fuzzy based optimal reactive power control", *IEEE Trans. on PS*, Vol 8, No.2, May 1993.
- [9] J L M Ramos, A G Exposito, J C Cerezo, E M Ruiz, and Y C Salinas, "A hybrid tool to assist the operator in reactive power/voltage control and optimization", *IEEE Trans. on PS*, Vol.10, No.2, 1995, pp.760-768.
- [10] C.W. Taylor, "Power System Voltage Stability", McGRAW-Hill, Inc., 1994
- [11] V Ajjarapu, C Christy, "The continuation power flow: A tool for steady state voltage stability analysis", *IEEE Trans. on Power Systems*, Vol. 7, No.1, February 1992.
- [12] G.K. Morison, B. Gao, P. Kundar, "Voltage stability analysis using static and dynamic approaches", *IEEE Tran. on Power Systems*, Vol. 8, No.3, August 1993.
- [13] P Kessel, H Glavitsch, "Estimating the voltage stability of a power system", *IEEE Trans on Power Delivery*, vol. PWRD-1, No.3, July 1986, pp. 346-354
- [14] D Gan, R.J Thomas, R.D. Zimmerman, "Stability constrained OPF", *IEEE Trans. on Power Systems*, vol. 15, no.2, May 2000, pp. 535-540
- [15] R. Fuerte-Esquivel, and E.Acha, "Unified power flow controller. a critical comparison of Newton-Raphson power flow studies", *IEE Proc. Gen. Transm. Distrib.*, Vol.144, No.5, 1997, pp. 437-444.
- [16] [16] Chen, H., Wang, Y., Zhou, R, "Analysis of voltage stability enhancement via unified power flow controller", *Proceedings of POWERCON conference*, Vol.1, 4-7, Dec.2000, pp. 403-408.
- [17] Laszlo Gyugyi "Dynamic compensation of ac transmission lines by solid-state synchronous voltage sources" *IEEE Transactions on Power Delivery*, Vol. 9, No. 2, April 1994
- [18] C.R. Fuerte-Esquivel E.Acha Unified power flow controller: a critical comparison of Newton-Raphson UPFC algorithms in power flow studies *IEE Proc -Gener. Transm. Distrib.*, Vol. 144, No. 5, pp.437-444 September 1997
- [19] Bansilal, D.Thukaram, K. Parthasarathy, "Optimal reactive power dispatch algorithm for voltage stability improvement", *Elect. Power and Energy Systems*, vol.6, no. 2, pp. 461-468, 1996.
- [20] D. Thukaram, L. Jenkins and K. Visakha Optimum allocation of reactive power for voltage stability improvement in AC-DC power systems, *IEE Proc -Gener. Transm. Distrib.*, Vol. 153, No. 2, pp.237-246 March 2006

Analysis of Voltage Control Stability Indices of Radial Distribution in Modern Power System

S.Sao¹, SrinivasaRao.Gorantla², M.V.Ramesh³

Vignan's engineering college, Vadlamudi Email:drsao53@yahoo.co.in
Vignan's engineering college, Vadlamudi Email:srinivas_gorantla@rediffmail.com
P.V.P.S.Institute of technology, Vijayawada Email:vmaddukuri@yahoo.com

Abstract: The occurrence of voltage collapse is very much dependent upon the maximum load that can be supported at a particular load bus. Any attempt to increase the load beyond this point could force the entire system into instability, leading to voltage collapse. This would indicate that the power system physically could not support the amount of the connected load. This work demonstrates the use of voltage stability index (VSI) and Fast Voltage Stability Index (FVSI), in order to estimate maximum loadability of a particular load node in the system. The process involves an evaluation of voltage stability condition of a system by computing the VSI and FVSI for each line. The point at which FVSI closed to a predetermined FVSI limit indicates the maximum possible connected load to a node termed as maximum loadability. The operating margin in a system can also be estimated by taking the difference between the load at the base case and the maximum load. The estimated maximum loadability on several load nodes allows the identification of a weak node in the system. The load nodes were ranked according to their maximum loadability, where the load node having the smallest maximum loadability was ranked highest, hence this node was identified as the weakest bus because it can withstand only a small amount of load increase before causing voltage collapse. This technique was tested on the IEEE Reliability Test System (RTS) and results proved that the proposed technique is able to estimate the maximum loadability in a system, exceed the maximum loadability, hence violating the voltage stability limit. Unfortunately, most of the conventional load flow methods are unsuitable for distribution systems because they are mostly based on the general meshed topology of a typical transmission system, where as most distribution systems have a radial or tree structure. Voltage instability phenomenon in power networks is highly nonlinear in nature posing operational as well as prediction problems in power systems. The main concern of researchers in this area today is that there appears no computationally efficient analytical tool for voltage stability analysis.

Key words: Voltage stability index, MATLAB, IEEE 69-node System

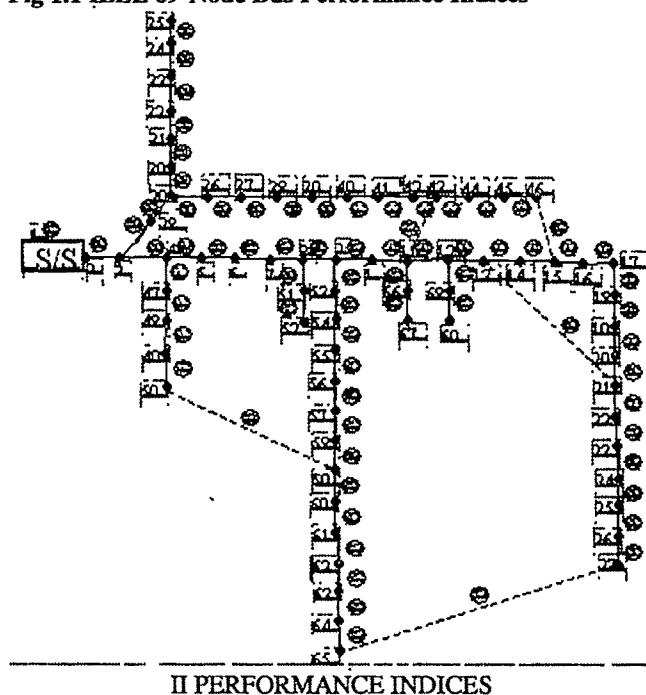
I. INTRODUCTION

THE modern power distribution network is constantly being faced with an ever-growing load demand. Distribution network experience distinct changes from a low to

high load level everyday. Numerous problems have to be attended in monitoring the operation of such system, which includes various switching operations for shifting loads, etc. In addition, most modern networks have to operate taking into consideration the minimization of losses so as to achieve high efficiency. In certain industrial areas, it has been observed that under certain critical loading conditions, the distribution system experience voltage collapse. Voltage collapse is a local phenomenon. It occurs at a bus within the area with high loads and low voltage profile. Due to the rapid growth in power demand, voltage collapse has been experienced. When such incident occurs, some industrial loads will be disconnected through automatic cut-off switches resulting in severe interruptions. Hence, it is a major concern in power distribution networks, which have surfaced fairly. Unfortunately, most of the conventional load flow methods are unsuitable for distribution systems because they are mostly based on the general meshed topology of a typical transmission system, where as most distribution systems have a radial or tree structure. Methods like the Newton-Rapson method and Gauss-Seidal method do not exploit the radial structure of the distribution system and require the solution of a set of equation, where size is of the order of the number of buses. This would result in more computation time. In addition, the Ybus matrix is very sparse, and this implies wastage of computer memory storage. Hence, conventional methods are not efficient for distribution systems. Another is due to the higher R/X ratio of distribution systems. This is a factor, which causes the distribution system to be ill condition for conventional power flow methods, especially the Fast Coupled Newton method, which diverges in most cases. Developing algorithm for solving load flow problems for radial distribution system is an on going process. As already said conventional load flow methods of transmission systems are not suitable for distribution systems. Many researches have suggested modified versions of the conventional load flow methods for solving distribution network by considering it as ill conditioned power network. They include admittance matrix, Jacobin, Trigonometric functions that results in large computational time. In this paper, a simple load flow technique is proposed for solving radial distribution networks using sparsity technique. It requires simple algebraic equation for

calculating the receiving end node voltage. Voltage instability phenomenon in power networks is highly nonlinear in nature posing operational as well as prediction problems in power systems. The main concern of researchers in this area today is that there appears no computationally efficient analytical tool for voltage stability analysis. M.Chakravorty and D.Das have offered a new technique for the voltage instability analysis, solving the earlier difficulties in mathematical modeling. They have proposed an efficient model for voltage stability analysis, in particular the use of the voltage stability index (VSI). Through this index one can measure the level of voltage stability and thereby instability. Appropriate action may be initiated if the index indicates a poor level of voltage. Most of the voltage stability condition was conducted using voltage stability index or proximity as measuring instruments.

Fig 1.1 IEEE 69-Node Bus Performance Indices



As far as islanding to be considered as one of the remedial measures for blackouts, determination of the criteria based on which the decision for islanding is important. In particular the vulnerability of the distributed distribution line or/and the transmission line has to be estimated and the most critical ones have to be identified to achieve at a effective forced island formation. For this, the most important electrical parameter, voltage is taken into consideration. The sensitivity factors are termed as performance indices. Different distribution lines are ranked with highest priority given to the least stable system. Some indices work better for particular power systems under particular operating conditions. Hence a combination such indices always give a clear-cut idea or view about the system sensitivity. Good indices can produce fast and accurate results. The main purpose of framing these indices is to give a cut-off point between stable and unstable contingencies in the ranking

phenomenon. To arrive at this the contingencies are predetermined before actual calculation of these indices. These indices are calculated for the predetermined period of time and for a predetermined set of operating conditions. We are considered are two performance indices. They are

- 1) Voltage stability index (VSI)
- 2) Fast voltage stability index (FVSI)

As the load increases drastically the stress imposed upon the power system also increases. This stressed condition may immediately reflect upon the system voltage. Voltage collapse prediction is important in power system planning and operation. The voltage level variation with time is shown in Fig. 2.1. It cannot be used to calculate the index, as it is inadequate for large system. So the degree of stability is used to calculate the index called Fast Voltage Stability Index. Apart from the load variations, line outages could also contribute to voltage collapse considerably

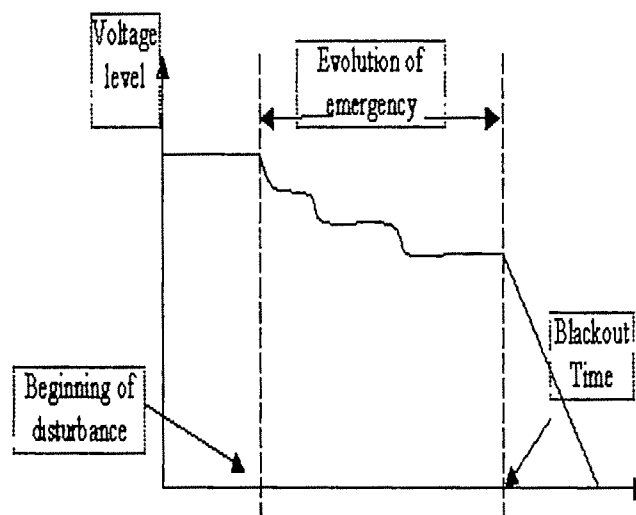


Fig 2.1

So the severity of the voltage instability condition in a power system due to line outages is also calculated. For an outage on any line in the system, the index is calculated for every other line taking into consideration the different operating conditions. Then these indices are sorted in the descending order to identify which line is the most liable one to the collapse for a given outage on any line under concern. The same analysis is repeated for every other possible line outage. The contingency, which yields the highest value of the FVSI mostly exceeding unity, is given the highest ranking. The ranking of contingencies assists in identifying the outage, which gives the most affecting voltage stability. Apart from the analysis the weakest bus and the strongest bus can also be identified for any loading condition taking in to consideration the maximum permissible loading limit.

III INDEX FORMULATION

Voltage stability index is an instrument to analyze the voltage stability. This index speeds up the analysis and hence called Fast Voltage Stability Index [FVSI]. It can be either referred to



a bus or a line but here it refers to a transmission line. For safer operation of the system it is preferred that FVSI should be less than unity. FVSI value closed to 1.00 indicates that the particular line is on the verge of instability. When the FVSI value exceeds unity it indicates that the corresponding transmission line or the bus is highly unstable and highly prone to collapse. Let us consider a two-bus system as shown in Fig 3.1

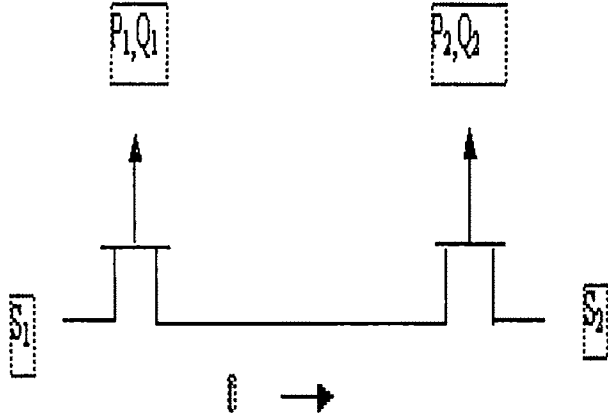


Fig 3.1

$$S(1)=P(1)+jQ(1) \quad S(2)=P(2)+jQ(2) \quad Z=R+jX$$

The line current can be expressed as

$$I = \frac{V_1 \angle \delta_1 - V_2 \angle \delta_2}{R + jX} \quad \dots (3.1)$$

The complex power is expressed as $S_2 = V_2 \cdot I^*$

$$\therefore I_2 = \{S_2 / V_2\}^* \quad \dots (3.2)$$

Equating the expression

$$\left\{ \frac{S_2}{V_2} \right\} = \frac{V_1 \angle \delta_1 - V_2 \angle \delta_2}{R + jX} \quad \dots (3.3)$$

$$\left\{ \frac{P_2 + jQ_2}{V_2 \angle \delta_2} \right\} = \frac{V_1 \angle \delta_1 - V_2 \angle \delta_2}{R + jX} \quad \dots (3.4)$$

$$\frac{P_2 - jQ_2}{V_2 \angle -\delta_2} = \frac{V_1 \angle \delta_1 - V_2 \angle \delta_2}{R + jX} \quad (3.5)$$

Cross-multiplying the above expression

$$\{P_2 - jQ_2\} \{R + jX\} = V_2 \angle -\delta_2 \{V_1 \angle \delta_1 - V_2 \angle \delta_2\} \quad (3.6)$$

$$RP_2 - jRQ_2 + jXP_2 + XQ_2 = V_1 V_2 \angle -\delta_2 - V_2^2 \angle -\delta_2 \quad (3.7)$$

$$\{RP_2 + XQ_2\} - j\{RQ_2 - XP_2\} = V_1 V_2 \{ \cos(\delta_1 - \delta_2) - j \sin(\delta_1 - \delta_2) \} - V_2^2 \quad \dots (3.8)$$

Equating the real and imaginary parts

$$RP_2 + XQ_2 = V_1 V_2 \cos(\delta_1 - \delta_2) - V_2^2 \quad \dots (3.9)$$

$$XP_2 - RQ_2 = -V_1 V_2 \sin(\delta_1 - \delta_2) \quad (3.10)$$

$$P_2 = \frac{-V_1 V_2 \sin(\delta_1 - \delta_2) + RQ_2}{X} \quad (3.11)$$

This quadratic equation when solved gives the solution for

$$FVSI = \frac{4Z^2 Q_2}{V_1^2 X \{ (R/X) \sin(\delta_1 - \delta_2) + \cos(\delta_1 - \delta_2) \}^2} \leq 1$$

In general this formula is sufficient for a system to be stable. This index is used for analyzing the stability of any line and the instant at which it jumps to unstable condition when load changes or any line outage occurs. The voltage stability index computes the proximity of a bus in the distribution network to voltage collapse. Using the VSI one can easily identify the node that is most vulnerable to voltage collapse and thereby it is possible to initiate appropriate action. It is shown that the node having minimum voltage stability is most prone to voltage collapse. The mathematical expression for VSI is simple and it is derived from the load flow equation for the fig1.3

The mathematical expression for VSI is simple and it is derived from the load flow equation

$$|V_{i+1}| = \sqrt{\{ (r_{ij} P_{i+1} + x_{ij} Q_{i+1}) - 0.5 |V_i|^2 \}^2 - (r_{ij}^2 + x_{ij}^2) (P_{i+1}^2 + Q_{i+1}^2)} \quad (3.12)$$

$$A = \{ (r_{ij} P_{i+1} + x_{ij} Q_{i+1}) - 0.5 |V_i|^2 \}^2 \}$$

$$B = \{ (r_{ij}^2 + x_{ij}^2) (P_{i+1}^2 + Q_{i+1}^2) \} - (r_{ij} P_{i+1} + x_{ij} Q_{i+1}) - 0.5 |V_i|^2$$

Where, Node no., $i=1, 2, \dots, nd$ Branch no., $j=1, 2, \dots, nd-1$

$nd = \text{total no. of nodes}$

$$B(j) - A(j) \geq 0 \quad (3.13)$$

$$(B(j) - A(j))^2 \geq 0 \quad \dots (3.14)$$

$$[B^2(j) - A^2(j)] + 2A^2(j) - 2B(j)A(j) \geq 0, \quad \dots (3.15)$$

$$[B^2(j) - A^2(j)] \geq 2A(j)[B(j) - A(j)] \quad (3.16)$$

The left hand side of equation (3.3) is derived from

$$B^2(j) - A^2(j) = \{ A^2(j) - Z^2(j) * (P^2(m2) + Q^2(m2)) \} - A^2(j) = -Z^2(j) * (P^2(m2) + Q^2(m2)) \quad (3.17)$$

From equation 3.13 and (3.14)

$$-Z^2(j) * (P^2(m2) + Q^2(m2)) \geq 2A(j)[B(j) - A(j)] \quad (3.18)$$

But $Z^2(j) * (P^2(m2) + Q^2(m2))$ cannot be negative

$$B(j) - A(j) > 0 \quad \text{and} \quad Z^2(j) * (P^2(m2) + Q^2(m2)) \leq -$$

$$2A(j)[B(j) - A(j)] \quad (3.19)$$

$$P(m2) \times R(j) + Q(m2) \times X(j) - 0.5 \times |V(m1)|^2 < 0$$

$$0.5 \times |V(m2)|^2 - P(m2) \times R(j) - Q(m2) \times X(j) > 0 \quad (3.20)$$

$$VSI = \frac{P(m2) \times R(j) + Q(m2) \times X(j) - 0.5 \times |V(m1)|^2}{0.5 \times |V(m2)|^2 - P(m2) \times R(j) - Q(m2) \times X(j)}$$

Where VSI is the voltage stability index of the ($m=2,3,4,\dots$) for secure and stable operation SI of ($m2$)>0 for all nodes the node where SI ($m2$) is found to be minimum the most sensitive to the voltage collapse.

IV. RESULTS

To demonstrate the effectiveness of the proposed method, to examples consisting 69 node and 33 node radial distributaries systems are considered

FVSI: The load at each node is increased gradually and the node at which the voltage collapse occurs is identified. It is observed that when the load was increased gradually, the Maximum value of FVSI is occurring at minimum voltage node i.e node 65, as given in the table (4.1).

Table 4.1 Critical loads at node 65 for different load conditions

Vpu	Critical loading condition			
	TPL(MW)	TOL(MVAr)	Max FVSI	Vmin p.u
1	8.471884	19.146875	0.999947	0.043107
1.05	9.334747	21.095137	0.999950	0.045445
1.1	10.244614	23.149693	0.999920	0.047864

VSI: The load at each node is increased gradually and the node at which the voltage collapse occurs is identified. It is observed that when the load was increased gradually, the minimum value of VSI is occurring at minimum voltage node i.e. node 65, as given in the table (4.2)

Table 4.2 Critical loads at node 65 for different load conditions

Vpu	Critical loading condition			
	TPL(MW)	TOL(MVAr)	Min VSI	Vmin p.u
1	10.836552	25.333562	0.000082	0.065851
1.05	11.733499	27.460156	0.000022	0.065462
1.1	13.63304	30.092259	0.000984	0.072461

FVSI: The load at each node is increased gradually and the node at which the voltage collapse occurs is identified. The test is repeated for three different substation voltage levels. It is observed that when the load was increased gradually, the Maximum value of FVSI is occurring at minimum voltage node i.e. node 27, as given in the table (4.3)

Table 4.3 Critical loads at node 27 for different load conditions

Vpu	Critical loading condition			
	TPL(KW)	TOL(KW)	Max FVSI	Vmin
1	15312.616629	10827.448384	0.999918	0.084797
1.05	16969.961130	11997.376933	0.999949	0.089307
1.1	18700.507345	13214.560927	0.999907	0.095021

VSI :The load at each node is increased gradually and the node at which the voltage collapse occurs is identified. The test is repeated for three different voltage levels. It is observed that when the load was increased gradually, the minimum value of VSI is occurring at minimum voltage node i.e. node 27, as

given in table (4.4).

Table 4.4 Critical loads at node 27 for different load conditions

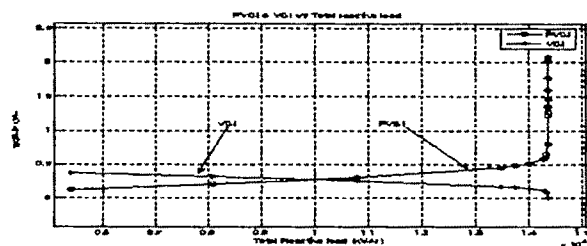
Vpu	Critical loading condition			
	TPL(KW)	TOL(KW)	Min VSI	Vmin
1	37814.630388	27683.214312	0.000049	0.086564
1.05	41816.932833	30592.550568	0.000051	0.092942
1.1	47884.742139	35110.972818	0.000015	0.102500

To demonstrate the effectiveness of the proposed the method, a 69 node radial distribution network is considered. in the present work, the study of voltage collapse at a particular node of the given distribution network is done by using different load compositions, i.e., constant power, constant current, constant impedance and exponential loads respectively and comparative study is made. The load at each node is increased gradually and the node at which the voltage collapse occurs is identified. This test is carried out for the four different types of load. For each load type, the test is repeated for the two different substation voltage levels.

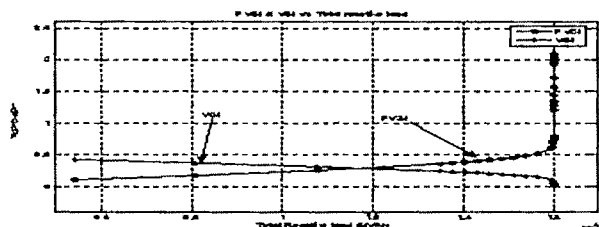
Case-I FVSI :A comparison in voltage behavior for different types of loads as well as for different voltage level has been made. When the load was increased gradually, maximum of Fast voltage stability index (FVSI) are occurring at node 65. Therefore, it can be concluded the node 65 is most sensitive to voltage collapse. It was observed that node 65 has the minimum voltage of 0.91953p.u.

Case-II VSI: A comparison in voltage behavior for different voltage level has been made. When the load was increased gradually, minimum of voltage stability index (VSI) are occurring at node 65. Therefore, it can be concluded the node 65 is most sensitive to voltage collapse. It was observed that node 65 has the minimum voltage of 0.91953p.u. Graph (4.4), (4.5) and (4.6) show the plots of total reactive power load (TQ) against VSI and FVSI at node 65 with different sub station voltage levels. The critical loading points or collapse points are indicated beyond which a small increment of load causes the voltage collapse. Another observation made from the shape of the plots is that the voltage stability index of a node varies almost linearly decreasing with reactive power loading and the Fast voltage stability index of a node varies almost linearly increasing with reactive power loading. The VSI and hence voltage at that node are minimum for constant power load and maximum for constant impedance load and for constant current load lies in between these two values. The FVSI and hence the voltage at that node are maximum and minimum respectively for constant power load and maximum for constant impedance load and for constant current load lies in between these two values.

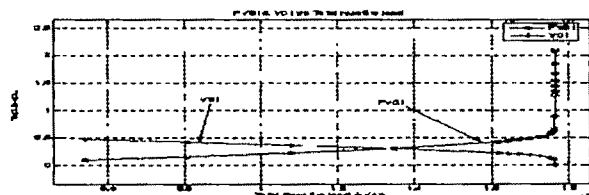
The results are shown in the graphs 4.1,4.2,4.3,4.4



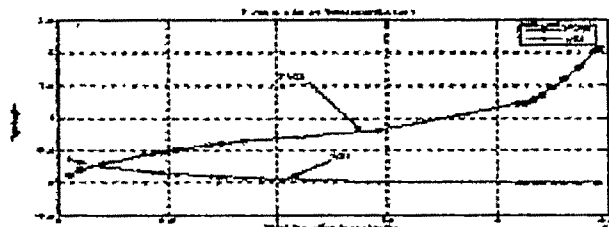
Graph (4.1) represents 1.0 p.u. Substation Voltage



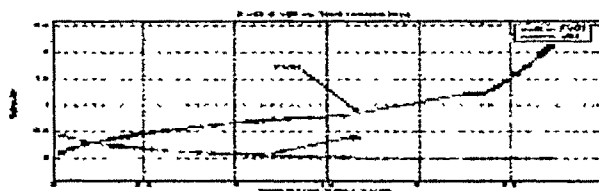
Graph (4.2) represents 1.05 p.u. Substation Voltage



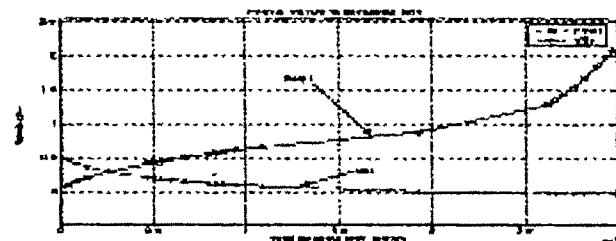
Graph (4.3) represents 1.1 p.u. Substation Voltage



Graph (4.4) represents 1.2 p.u. Substation Voltage



Graph (4.5) represents 1.05 p.u. Substation Voltage



Graph (4.6) represents 1.2 p.u. Substation Voltage

V. CONCLUSION

In this work, the algorithm for load flow solution of radial distribution network has been extended to determine voltage stability index (VSI) and Fast Voltage Stability Index (FVSI). An efficient algorithm is proposed for radial distribution with the indices of VSI and FVSI. With the expressions for VSI and FVSI, it is possible to compute the indices at every node and identified the node at which the value VSI is minimum and FVSI is maximum, is most sensitive to voltage collapse. Effectiveness of the proposed technique has been demonstrated through a 69-node radial distribution network. The VSI and FVSI (and hence the voltage) at a particular node has been found to vary linearly with change in load till the critical collapse point is reached. Beyond this critical point the load flow method is found to fail as voltage collapses abruptly with very small changes in load. It is observed that the critical point for FVSI is occurring before the critical point for VSI. Hence FVSI is most sensitive to change in loads than the VSI.

ACKNOWLEDGMENT

Dr.S.Sao. Would like to thank Dr.G.kesava Rao ,Professor ,for Dept of Electrical & Electronics Engineering Vignan's Engineering college vadlamudi for his participation in technical discussions. He also thanks president of this institution for providing facilities in completing this project. He also thanks Head of the institution and Head of the department of Electrical & Electronics Engineering in Vignan's Engineering college, vadlamudi. for providing facilities in completing this project.

REFERENCES

- [1] W.F. Tinney and C.S.Hart, "Power flow solution by Newton's method", IEEE Trans.on Power Apparatus and system, Vol.PAS-86, Nov 1967, pp.1449-1460.
- [2] B.Stott and O.Alzac, "Fast decoupled load flow", IEEE trans. On Power Apparatus and Systems, Vol. PAS-93, 1974, pp. 859-869
- [3] S.I. Wamoto and Y. Tamura, "A load flow calculation method for ill-conditioned power system", Vol. PAS -100, 1981, pp 1736-1740.
- [4] M.Chakravorty and D.Das, "Voltage stability analysis of radial distribution networks," Electrical Power and Energy system, Vol.23, pp. 129-135, 2001.
- [5] S.S.Vadhera, "Power System Analysis and Stability", Khanna Publications.
- [6] Ismail Musirin and Titik Khawa Abdul Rehman, "On-line voltage stability based contingency ranking using Fast Voltage stability index", IEEE Trans, 2002.
- [7] A simple approach to voltage stability assessment in radial networks Gubina, F.; Strmcnik, B.Power Systems, IEEE Transactions on Volume 12, Issue 3, Aug 1997 Page(s):1121 - 1128
- [8] Impact of Distributed Generation on the Stability ofElectrical Power Systems Ahmed M. Azmy and István Erlich, Member, IEEE.
- [9] Assessment of voltage instability through multiple load solutions Snchepakar member IEEE & V.V katwekar member IEEE
- [10] Real-Time System Stability Monitoring in the Transmission Network of Bosnia and Herzegovina Dusko Vickovic1, Roland Eichler2, Savu C. Savulescu3.
- [11] An enhanced Radial Basis Function Network for voltage stability monitoring considering multiple contingencies Saikat Chakrabartia and Benjamin Jeyasurya
- [12] Stability of Power Systems with LargeAmounts of Distributed Generation valerijs knazkins

Assessment of Voltage Stability in Longitudinal Power Supply System

S. Halder nee Dey¹, A. Chakrabarti² and A. De²

¹ Electrical Engineering Department, Jadavpur University, Kolkata-32, India e-mail:sunitaju@yahoo.com

² Electrical Engineering Department, Bengal Engineering and Science University, India, e-mail:a_chakrabarti55@yahoo.com

Abstract—In this paper an analytical technique to determine voltage stability limit being developed using the optimal power flow (OPF) Newton method, the effects of varying load condition on voltage stability limit have been observed using the proposed criterion of singularity of the Hessian in the optimal power flow equations. Magnitude of reactive power sensitivity at a load bus to assess the bus voltage stability has also been explored using optimal power flow technique. The proposed technique has been applied in a typical six bus weak system and an IEEE 14 bus system to assess the weakest bus in the network and to determine voltage stability limit using the OPF.

Key words—Voltage stability, Hessian, Optimal power flow

Notations used:

α_i, β_i and γ_i are the cost coefficients and

P_{g_i} = real power generation at i -th generator bus,

NG = total number of generators,

F_{c_i} = cost of generation at i -th generator and

$F_{c_{total}}$ = total cost of generation in the system.

$Y_{ik} = G_{ik} + jB_{ik}$ = ik -th element of $[Y_{BUS}]$ matrix,

$|V_i|$ = voltage magnitude of i -th bus, δ_i = voltage angle of i -th bus

$|V_k|$ = voltage magnitude of k -th bus and δ_k = voltage angle of k -th bus

I. INTRODUCTION

The problem of voltage control and voltage stability has been a topic of great interest since late of last century [4,8,9,15]. This aspect attained further momentum of research in voltage stability related investigations in longitudinal power supply (LPS) systems [3,10,12]. The system voltage stability being a dynamic phenomenon [7,11], frequently voltage stability is threatened in weak power systems due to dynamic load increase and/or line trip. Literature survey reveals related developments of the physical concepts and

mathematical backgrounds of voltage stability on basis of load flow solution feasibility [1,12], singularity of Jacobian [9], bifurcation technique [13] and optimal power flow [2,6] etc. It has nowadays been an accepted proposition that singularity of the Jacobian in the load flow solution indicates critical state of voltage and the voltage stability index can be obtained from feasibility of the solution to power flow equations for each of the buses [4,5] in multibus power network.

Optimal power flow has diverse fields of application in power system operation and control in terms of power generation and as well as stable operation of power system [6]. Voltage stability may be assessed using optimal power flow calculation and corrective measures may also be taken [2] accordingly.

In this paper Newton's method of optimal power flow has been used to assess voltage stability in a weak six bus system as well as in a robust IEEE 14 bus system. Weakest buses of the test systems being detected checking the magnitude of reactive power sensitivities of those buses [16], determinant of the Hessian matrix $[H]$ has been taken as an indicator to assess voltage stable states of the system considering all marginal costs as well as all operational constraints of the system.

II. THEORY

The cost function ($F_{c_{total}}$) of a N -bus power system having NG number of fossil fuel units is given by

$$F_{c_{total}} = \sum_{i=1}^{NG} F_{c_i} = \sum_{i=1}^{NG} \alpha_i \left(P_{g_i} \right)^2 + \beta_i P_{g_i} + \gamma_i$$

unit of cost /hr,

The aim of optimal power flow (OPF) is to optimise the cost function subjected to following constraints:

(i) active power balance in the network

$$P_i(|V|, \delta) - P_{g_i} - P_{load_i} = 0 \quad \text{for } i = 1, 2, 3, \dots, N$$

where P_i = active power injection at i -th bus and is a function of $|V|$ and δ . For load buses [i.e., for $i = (NG+1)(NG+2), \dots, N$], $P_{g_i} = 0$;

(ii) reactive power balance in the network

$$Q_i(V, \delta) - Q_{g_i} - Q_{load_i} = 0 \text{ for } i = (NG+1), \dots, N$$

where Q_i = reactive power injection at i -th load bus and is also a function of $|V|$ and δ ; Q_{g_i} = reactive power generation at i -th bus;

(iii) security related constraints (also called soft constraints); these constraints are as follows

(a) limits on real power generations, i.e.,
 $P_{g_{i_{min}}} \leq P_{g_i} \leq P_{g_{i_{max}}} \text{ for } i = 1, 2, 3, \dots, NG,$

(b) limits on reactive power generations, i.e.,
 $Q_{g_{i_{min}}} \leq Q_{g_i} \leq Q_{g_{i_{max}}} \text{ for } i = 1, 2, 3, \dots, NG,$

(c) limits on voltage magnitudes of load buses
 $|V_i|_{min} \leq |V_i| \leq |V_i|_{max} \text{ for } i = (NG+1), \dots, N$
 and

(d) limits on voltage angles of all of the above buses excluding slack bus $\delta_{i_{min}} \leq \delta_i \leq \delta_{i_{max}} \text{ for } i = 2, 3, \dots, N.$

The real power injection at bus- i can be expressed as [14]

$$P_i = \sum_{k=1}^N |V_i V_k| [G_{ik} \cos(\delta_i - \delta_k) + B_{ik} \sin(\delta_i - \delta_k)] \quad (1.1)$$

Now reactive power injection at bus- i [14] is given by

$$Q_i = \sum_{k=1}^N |V_i V_k| [G_{ik} \sin(\delta_i - \delta_k) - B_{ik} \cos(\delta_i - \delta_k)] \quad (1.2)$$

The constraint minimization problem can be transformed into an unconstrained one by increasing the load flow constraints into objective function. The additional variables are known as *Lagrange multiplier functions* (or *incremental cost functions*) in power system optimisation. The Lagrangian function then becomes

$$\begin{aligned} L(P_g, |V|, \delta) = & \sum_{i=1}^{NG} F_c(P_{g_i}) \\ & + \sum_{i=1}^N \lambda_{p_i} [P_i(V, \delta) - P_{g_i} + P_{load_i}] \\ & + \sum_{i=NG+1}^N \lambda_{q_i} [Q_i(V, \delta) - Q_{g_i} + Q_{load_i}] \end{aligned} \quad (2)$$

where λ_{p_i} and λ_{q_i} are Lagrangian multiplier for active power and reactive power balance at the i -th bus respectively.

The optimisation problem can be solved, only if the following equations are optimally satisfied;

$$\frac{\partial L}{\partial P_{g_i}} = \frac{\partial F}{\partial P_{g_i}} - \lambda_{p_i} \text{ for } i = 1, 2, 3, \dots, NG \quad (3.1)$$

$$\frac{\partial L}{\partial \delta_i} = \sum_{k=1}^N \left[\lambda_{p_k} \frac{\partial P_k}{\partial \delta_i} \right] + \sum_{k=NG+1}^N \left[\lambda_{q_k} \frac{\partial Q_k}{\partial \delta_i} \right]$$

$$\text{for } i = 2, 3, \dots, N \quad (3.2)$$

Also from equation (2) we can write

$$\frac{\partial L}{\partial \lambda_{p_i}} = P_i(V, \delta) - P_{g_i} + P_{load_i} \text{ for } i = 1, 2, 3, \dots, N \quad (3.3)$$

$$\text{and } \frac{\partial L}{\partial |V_i|} = \sum_{k=1}^N \left[\lambda_{p_k} \frac{\partial P_k}{\partial |V_i|} \right] + \sum_{k=NG+1}^N \left[\lambda_{q_k} \frac{\partial Q_k}{\partial |V_i|} \right] \quad (3.4)$$

for $i = (NG+1), \dots, N$

Further to this,

$$\frac{\partial L}{\partial \lambda_{q_i}} = Q_i(V, \delta) - Q_{g_i} + Q_{load_i} \text{ for } i = (NG+1), \dots, N \quad (3.5)$$

Any small variation in control variables about their initial values can be obtained by forming total differentials as shown below:

$$\begin{aligned} & \sum_{k=1}^{NG} \frac{\partial^2 L}{\partial P_{g_i} \partial P_{g_k}} \Delta P_{g_k} + \sum_{k=2}^N \frac{\partial^2 L}{\partial P_{g_i} \partial \delta_k} \Delta \delta_k \\ & + \sum_{k=1}^N \frac{\partial^2 L}{\partial P_{g_i} \partial \lambda_{p_k}} \Delta \lambda_{p_k} + \sum_{k=NG+1}^N \frac{\partial^2 L}{\partial P_{g_i} \partial \lambda_{q_k}} \Delta \lambda_{q_k} \\ & + \sum_{k=NG+1}^N \frac{\partial^2 L}{\partial P_{g_i} \partial |V_k|} \Delta |V_k| = - \frac{\partial L}{\partial P_{g_i}} \end{aligned} \quad (4.1)$$

for $i = 1, 2, 3, \dots, NG$

$$\begin{aligned} & \sum_{k=1}^{NG} \frac{\partial^2 L}{\partial \delta_i \partial P_{g_k}} \Delta P_{g_k} + \sum_{k=2}^N \frac{\partial^2 L}{\partial \delta_i \partial \delta_k} \Delta \delta_k \\ & + \sum_{k=1}^N \frac{\partial^2 L}{\partial \delta_i \partial \lambda_{p_k}} \Delta \lambda_{p_k} + \sum_{k=NG+1}^N \frac{\partial^2 L}{\partial \delta_i \partial \lambda_{q_k}} \Delta \lambda_{q_k} \\ & + \sum_{k=NG+1}^N \frac{\partial^2 L}{\partial \delta_i \partial |V_k|} \Delta |V_k| = - \frac{\partial L}{\partial \delta_i} \text{ for } i = 2, 3, \dots, N \end{aligned} \quad (4.2)$$

$$\begin{aligned} & \sum_{k=1}^{NG} \frac{\partial^2 L}{\partial \lambda_{p_i} \partial P_{g_k}} \Delta P_{g_k} + \sum_{k=2}^N \frac{\partial^2 L}{\partial \lambda_{p_i} \partial \delta_k} \Delta \delta_k \\ & + \sum_{k=1}^N \frac{\partial^2 L}{\partial \lambda_{p_i} \partial \lambda_{p_k}} \Delta \lambda_{p_k} + \sum_{k=NG+1}^N \frac{\partial^2 L}{\partial \lambda_{p_i} \partial \lambda_{q_k}} \Delta \lambda_{q_k} \\ & + \sum_{k=NG+1}^N \frac{\partial^2 L}{\partial \lambda_{p_i} \partial |V_k|} \Delta |V_k| = - \frac{\partial L}{\partial \lambda_{p_i}} \text{ for } i = 1, 2, 3, \dots, N \end{aligned} \quad (4.3)$$

$$\begin{aligned} & \sum_{k=1}^{NG} \frac{\partial^2 L}{\partial |V_i| \partial P_{g_k}} \Delta P_{g_k} + \sum_{k=2}^N \frac{\partial^2 L}{\partial |V_i| \partial \delta_k} \Delta \delta_k \\ & + \sum_{k=1}^N \frac{\partial^2 L}{\partial |V_i| \partial \lambda_{p_k}} \Delta \lambda_{p_k} + \sum_{k=NG+1}^N \frac{\partial^2 L}{\partial |V_i| \partial \lambda_{q_k}} \Delta \lambda_{q_k} \\ & + \sum_{k=NG+1}^N \frac{\partial^2 L}{\partial |V_i| \partial |V_k|} \Delta |V_k| = - \frac{\partial L}{\partial |V_i|} \end{aligned} \quad (4.4)$$

for $i = (NG+1), \dots, N$

$$\begin{aligned}
 & \sum_{k=1}^{NG} \frac{\partial^2 L}{\partial \lambda_{q_i} \partial P_{g_k}} \Delta P_{g_k} + \sum_{k=2}^N \frac{\partial^2 L}{\partial \lambda_{q_i} \partial \delta_k} \Delta \delta_k \\
 & + \sum_{k=1}^N \frac{\partial^2 L}{\partial \lambda_{q_i} \partial \lambda_{p_k}} \Delta \lambda_{p_k} + \sum_{k=NG+1}^N \frac{\partial^2 L}{\partial \lambda_{q_i} \partial \lambda_{q_k}} \Delta \lambda_{q_k} \\
 & + \sum_{k=NG+1}^N \frac{\partial^2 L}{\partial \lambda_{q_i} \partial |V_k|} \Delta |V_k| = - \frac{\partial L}{\partial \lambda_{q_i}} \\
 & \text{for } i = (NG+1), \dots, N \quad (4.5)
 \end{aligned}$$

Equations (4.1-4.5) can be written in matrix form as shown in equation (5.1);

$$\begin{bmatrix} H_{P_g P_g} & 0 & H_{P_g \lambda_p} & 0 & 0 \\ 0 & H_{\delta \delta} & H_{\delta \lambda_p} & H_{\delta \lambda_q} & H_{\delta |V|} \\ H_{\lambda_p P_g} & H_{\lambda_p \delta} & 0 & 0 & H_{\lambda_p |V|} \\ 0 & H_{|V| \delta} & H_{|V| \lambda_p} & H_{|V| \lambda_q} & H_{|V| |V|} \\ 0 & H_{\lambda_q \delta} & 0 & 0 & H_{\lambda_q |V|} \end{bmatrix} \begin{bmatrix} \Delta P_g \\ \Delta \delta \\ \Delta \lambda \\ \Delta \lambda_q \\ \Delta |V| \end{bmatrix} = \begin{bmatrix} J_{P_g} \\ J_{\delta} \\ J_{\lambda_p} \\ J_{|V|} \\ J_{\lambda_q} \end{bmatrix} \quad (5.1)$$

$$\text{or, } [H][\text{Change in control variables}] = [J] \quad (5.2)$$

Where $[H]$ and $[J]$ are conventional Hessian and Jacobian matrices respectively. Starting from initial data of an interconnected power system optimal power flow solution may be achieved by solving equation (5.1 or 5.2) using iterative process. In this method there is no need to separate load flow study; moreover this method has been observed to be faster with more accuracy as in optimal power flow, both power generations and voltages are calculated simultaneously considering the economics of operation with all system constraints taken into account.

Again, $\partial Q_i / \partial |V_i|$ being the reactive power sensitivity of the i -th bus, it inherently indicates the degree of weakness for the i -th bus (as with $\partial Q_i / \partial |V_i|$ being high, $\partial Q_i / \partial |V_i|$ becomes low indicating minimum change in $|V_i|$ for variation in Q -status of the bus). Thus in a multibus power network, at bus- i , $\partial Q_i / \partial |V_i|$ being higher, the degree of weakness of the i -th bus becomes lesser. $\partial Q_i / \partial |V_i|$ can be calculated from equation (1.2) and comparing the magnitudes of all

$\partial Q_i / \partial |V_i|$ the weakest bus in the system can be identified. Also with the determinant of Hessian matrix ($[H]$ matrix in equation (5.2) approaching zero, there will be a large change in control parameters of this state and therefore the critical point of optimal power flow solution, beyond which there will be no possible generation; can be identified. This state also represents the voltage stability limit.

III. SIMULATION

The proposed theory has been applied to a sample 6 bus, 8 lines interconnected transmission line model (typically similar to that of a sub-grid in LPS systems) as well as in a IEEE 14 bus test system. The flowchart for the system simulation has been shown in Fig.1.

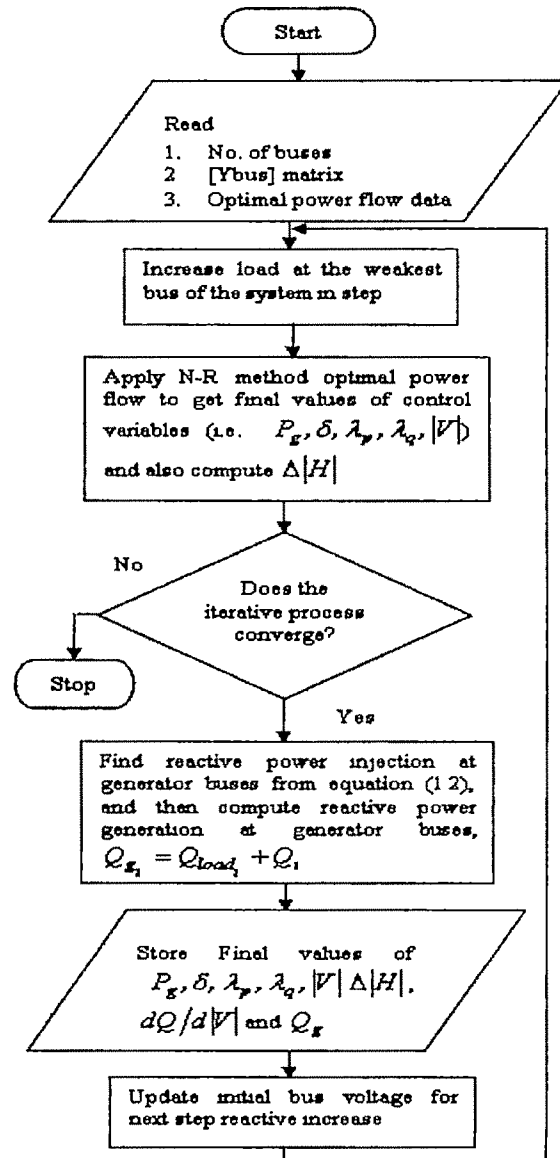


Fig. 1: Flow chart of the proposed method

Table 1a and Table 1b exhibit the p.u. impedances and line charging susceptances of the respective systems.

Table 1a - Impedances and line charging (in p.u.) for six bus test system

Line no	Bus-code p-q	Line impedance Z_{pq}	Line charging susceptance $B_{pq}/2$	Off-normal tap ratio of transformer
1	1-3	$0.04 + j0.30$	$j0.010$	
2	2-3	$0.03 + j0.20$	$j0.010$	
3	3-4	$0.04 + j0.20$	$j0.010$	
4	3-5	$0.04 + j0.20$	$j0.010$	
5	4-5	$0.03 + j0.15$	$j0.010$	
6	5-6	$0.06 + j0.30$	$j0.010$	
7	1-2	$j0.4$		$1.05 + j0.0$
8	2-6	$j0.2$		$1.02 + j0.0$

Table 1b - Impedances and line charging (in p.u.) for IEEE 14 bus test system

Line no.	Bus-code p-q	Line impedance Z_{pq}	Line charging susceptance $B_{pq}/2$	Off-normal tap ratio of transformer
1	1-2	$0.01938 + j0.05917$	$j0.02640$	
2	2-3	$0.04669 + j0.19797$	$j0.02190$	
3	2-4	$0.05811 + j0.17652$	$j0.01870$	
4	1-5	$0.05403 + j0.22304$	$j0.02460$	
5	2-5	$0.05685 + j0.17388$	$j0.01700$	
6	3-4	$0.06701 + j0.17103$	$j0.01730$	
7	4-5	$0.01335 + j0.04211$	$j0.0064$	
8	7-8	$0.0 + j0.17615$	$j0.0$	
9	7-9	$0.0 + j0.11001$	$j0.0$	
10	9-10	$0.03181 + j0.09450$	$j0.0$	
11	6-11	$0.09498 + j0.19690$	$j0.0$	
12	6-12	$0.22291 + j0.25381$	$j0.0$	
13	6-13	$0.06615 + j0.13027$	$j0.0$	
14	9-14	$0.12711 + j0.57038$	$j0.0$	
15	10-11	$0.05205 + j0.19207$	$j0.0$	
16	12-13	$0.022092 + j0.19988$	$j0.0$	
17	13-14	$0.17093 + j0.34802$	$j0.0$	
18	4-7	$0.0 + j0.20912$		0.978
19	4-9	$0.0 + j0.55618$		0.969
20	5-6	$0.0 + j0.25202$		0.978

In each of the simulations the weakest bus has been detected by observing the magnitude of $\partial Q/\partial V$ for the respective bus (for weakest bus this value being the minimum). Results revealed that bus number 6 is the weakest bus in the six bus system while bus number 14 is the weakest bus in the IEEE 14 bus system. In order to make the system more realistic, dynamic loading has been applied in each part.

Fig.2a and Fig.2b exhibit the profile of the values of determinant of the Hessian with respect to the increase in reactive load at the respective buses in the two test systems. The 'nose's of the characteristics of $\Delta|H|$ against reactive loading at load bus are obviously the points of singularities. An extended simulation reveals that enhancement of both active and reactive load reduces $\Delta|H|$ more rapidly and thereby pushing the system towards quicker voltage instability (Fig.2a) since the critical limit of stability is governed by the zero value of determinant of $[H]$.

Fig.3a and Fig.-3b show the profiles of bus voltage magnitudes at the weakest buses of the respective systems with variation of reactive loading at the designated weakest buses. It may be observed that following higher reactive

power demand the bus voltage collapses at the critical state of voltage stability. Enhancement of both active and reactive load reveals same observations similar to those obtained in Fig.-2a and Fig.-2b.

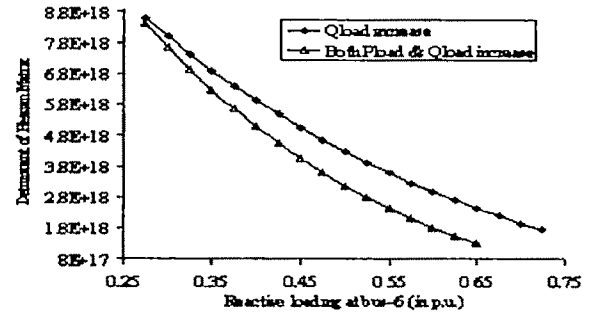


Fig.2a: Profiles of determinant of Hessian matrix with variation of reactive loading at bus-6 under different operating conditions (six bus system)

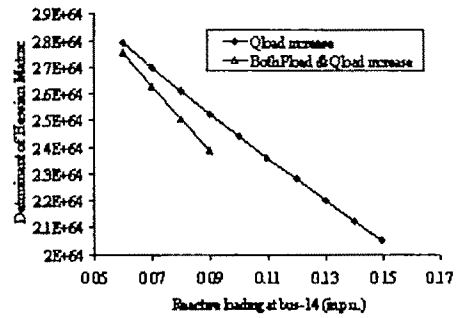


Fig.2b: Profiles of determinant of Hessian matrix with variation of reactive loading at bus-14 under different operating conditions (IEEE 14 bus system)

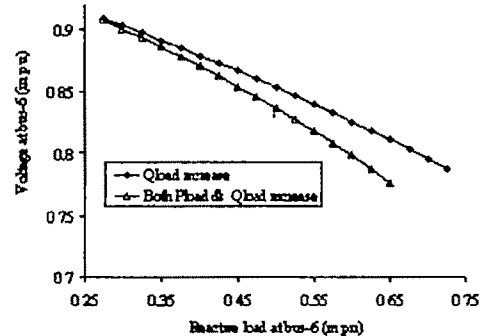


Fig.3a: Profiles voltage at bus-6 with increase in reactive load at bus-6 under different operating conditions (six bus system)

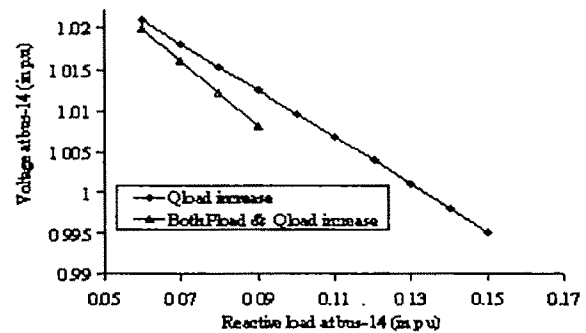


Fig.3b: Profiles voltage at bus-14 with increase in reactive load at bus-14 under different operating conditions (IEEE 14 bus system)

Fig.-4a and Fig.-4b exhibit the change in reactive power sensitivity of the weakest bus in the system with increase in reactive load at that bus. From the figures it is clear that as the system become more and more stressed, the reactive power sensitivities of the load buses reduce thus leading the system towards voltage instability. This effect is more pronounced in case when the bus is weaker. This process is fastest in the case when both active and reactive loads are increasing at the concerned bus and the effect may be vulnerable to the bus voltage if the process is uncontrollable.

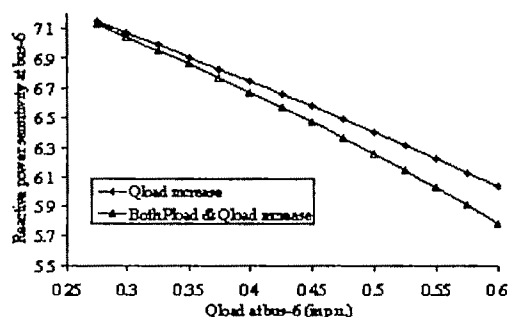


Fig.4a. Profiles reactive power sensitivity at bus-6 with increase in reactive load at bus-6 under different operating conditions (six bus system)

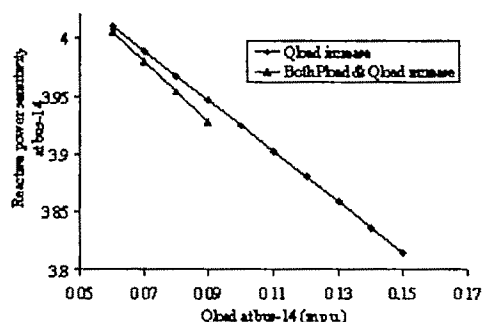


Fig.4b. Profiles reactive power sensitivity at bus-6 with increase in reactive load at bus-6 under different operating conditions (IEEE 14 bus system)

IV. CONCLUSION

This investigation reveals that there is a strong interconnection of voltage stability with optimal operation of the system. Voltage stability of a system can be assessed in better way by adopting optimal power flow algorithm, as in OPF algorithm, all the operational constraints of a power system are tied together (i.e., angle instability, voltage stability and economic operation of the system). Assessment of degree of weakness in terms of voltage stability of a load bus, using reactive power sensitivity, has also been found to be very effective in optimal power flow technique. The developed method finds application in both LPS and robust power systems.

V. REFERENCES

1. Y. Tamura, H. Mori and S. Iwamoto, "Relationship between voltage stability and multiple load flow solutions in electric power system", *IEEE transactions on Power Apparatus and Systems*, vol. PAS-102, no 5, pp. 1115-1125, May'1983.
2. J. Carpentier, R. Girard and E. Scano, "Voltage collapse proximity indicators computed from an optimal power flow", *Proceedings of 8th Power System Computation Conference (PSCC)*, September'1984, Helsinki, Finland.
3. F. Aboites and G. Arrey, "Security assessment in the operation of longitudinal power system", *IEEE Transactions on Power System*, vol. PWRS-1, no 2, May'1986.
4. A. Tiranuchit and R. J. Thoms, "A posturing strategy against voltage instabilities in electric power systems", *IEEE transaction on Power Systems*, vol. PWRS-3, no.1, pages 87-93, February'1988.
5. P.W. Sauer and M. A. Pai, "Power system steady state stability and the load flow Jacobian", *IEEE transaction on Power Systems*, vol.5, Nov'1990.
6. M. Huneault and F. D. Galiana, "A survey of the optimal power flow literature", *IEEE Transactions on Power Systems*, vol.6, no.2, pp. 762-770, 1991.
7. J. Deuse and M. Stubbe, "Dynamic simulation of voltage collapses", *IEEE Transactions on Power Systems*, vol.8, pages 894-904, 1993.
8. C. W. Taylor, "Power system voltage stability", *EPRI Power System Engineers Series*, McGraw Hill, 1994.
9. J. Bian and P. Rastgoufard, "Power system voltage stability and security assessment", *Electric Power System Research*, no. 30, pp.197-201, 1994.
10. A. Chakrabarti, D. P. Kothari and A. K. Mukhopadhyay, *Performance, Operation and Control of EHV power transmission system* (Book), 1st Edition 1995, (Wheeler Publication, New Delhi, India)
11. M. A. Pai, P. W. Sauer and B. C. Lesieutre, "Static and dynamic nonlinear loads and structural stability in power systems", *IEEE proceedings*, vol.83, pp.1562-1572, special issue on nonlinear phenomena in power systems, 1995.
12. T. J. Overbye, "Computation of a practical method to restore power flow solvability", *IEEE Transactions on Power Systems*, vol.10, pp. 280-287, 1995.
13. C. A. Canizares, "On bifurcations, voltage collapse and load modelling", *IEEE Transactions on Power Systems*, vol.10, no.1, pp. 512-522, Feb'1995.
14. A. Chakrabarti, Sumita Halder, *Power system analysis operation and control* (Book), Prentice Hall of India Pvt. Ltd. Publication, New Delhi, India, 1st Edition 2000.
15. Z. Feng V. Ajjarapu, and D.J. Maratukulam, "A comprehensive approach for preventive and corrective control to mitigate voltage collapse", *IEEE transactions on Power Systems*, Vol. 15, no. 2, May 2000, pp.791-797.
16. I. Musirin, T.K. Abdul Rahman, "Estimating Maximum Loadability for Weak Bus Identification Using FVSI", *IEEE Power Engineering Review*, November 2002, pp.50-52.

Single Cycle Mathematical Model for Harmonic Power in d-q Plane

Surajit Chattopadhyay¹, Madhuchhanda Mitra² and Samarjit Sengupta²

¹ Hooghly Engineering and Technology College (WBUT), Hooghly, WB, India-712103 e-mail: surajit_2004@indiatimes.com

² Department of Applied Physics, University of Calcutta, Kolkata, India e-mail: samarsgp@rediffmail.com

Abstract—This paper presents a single cycle mathematical model for harmonic power in d-q plane. Sampled power system data have been transformed into d-q plane. Fundamental frequency has been identified with the help of an arbitrary reference signal and then on the basis of this fundamental frequency some other specific reference signals have been defined. In d-q plane, sampled voltage and current data are plotted against those reference signals. Areas covered by the curves have been calculated, wherefrom, contribution of harmonic components in active power and reactive power have been measured.

Key words—Active power, d-q plane, harmonic power, reactive power.

I. INTRODUCTION

HARMONIC generation has increased to a great extent with the increase in complexity and use of semiconductor devices in power system. This harmonic generation degrades the quality of electric power, which refers to maintaining the near sinusoidal waveform of power distribution bus voltages and currents at rated magnitude and frequency. Contribution of harmonics has increased due to the use of power converter; nonlinear loads like switch-mode-power-supplier and phase control rectifiers in distribution and transmission networks. The other major contributors to poor power quality are harmonics component of reactive power. Solid-state control of ac power using high-speed switches is the main source of harmonics whereas different non-linear loads contribute to excessive drawl of reactive power from supply. It leads catastrophic consequences such as long production downtimes, mal-function of devices and shortened equipment life. A lot of problems are created by current harmonic like equipment overheating, motor failure, machine vibration, capacitor fuses blown, excessive neutral currents, inaccurate power metering, etc.

Researches are going on for long to study the effects of unbalance and harmonics on power quality in a power system [1]-[3]. In a non-sinusoidal and unbalanced environment, some practical definitions have also been suggested [4]-[6]. A new approach for designing power acceptability curve has been

proposed [7]. In such conditions measurement and monitoring of power quality in respect of its unbalance and harmonics have been presented in different publications [8]-[13] and different modern mathematical tools have also been utilized to estimate the unbalance in power in a system [15]-[17]. There are several existing methods for the detection of the current harmonics like fast Fourier transform (FFT), instantaneous p-q theory, synchronous d-q reference theory, analog or digital filters, etc [14], [18]-[24]. In some cases passive filters are also used, but they are having the drawbacks of bulky components, fixed compensated characteristics, sensitivity to line impedance, and series and parallel resonance with system.

In this paper a single cycle mathematical model for harmonic power in d-q plane has been presented. Sampled power system data have been transformed into d-q plane. Fundamental frequency has been measured with the help of an arbitrary reference signal and then on the basis of this fundamental frequency some other specific reference signals have been defined. In d-q plane, sampled voltage and current data are plotted against those reference signals. Areas covered by the curves have been calculated, wherefrom, contribution of harmonic components in active power and reactive power have been measured.

II. MATHEMATICAL MODEL

A. Area and Power

Let us define two sinusoidal waveforms

$$x(t) = \sum_{m=1,2,3,\dots} X_m \sin(m\omega t - \phi_m) \quad (1)$$

$$y(t) = \sum_{n=1,2,3,\dots} Y_n \sin(n\omega t - \theta_n) \quad (2)$$

where, m and n are order of harmonics in x(t) and y(t), respectively and ω is fundamental frequency. ω is assumed to be constant in one complete cycle. The area covered by these two waveforms in x-y plane in one complete cycle will be

$$\begin{aligned} A_{TOTAL}^{x-y} &= \int x \times dy \\ &= k_1 \times \sum_{n=m} n X_m Y_n \sin \phi_{mn} \quad (3) \end{aligned}$$

$$\text{where, } \phi_{mn} = \phi_m - \theta_n$$

The area covered in xy-t plane in one complete cycle is

$$\begin{aligned}
 A_{TOTAL}^{xy-t} &= \int x \times y dt \\
 &= \int \sum_{m=1,2,3,\dots} X_m \sin(m\omega t - \phi_m) \\
 &\quad \times \sum_{n=1,2,3,\dots} Y_n \sin(n\omega t - \theta_n) dt \\
 &= k_2 \times \sum_{n=m} X_m Y_n \cos \phi_n \quad (4)
 \end{aligned}$$

where, $\phi_{mn} = \phi_m - \theta_n$ and k_2 is a constant

B. Voltage and Current in d-q Plane

In presence of harmonics, voltages and currents in Park domain can be derived from phase voltage multiplying by Park transformation matrix as follows

$$\begin{aligned}
 \begin{bmatrix} V_d \\ V_q \\ V_0 \end{bmatrix} &= \begin{bmatrix} \sum_{m=1,2,3,\dots} V_{dm} \sin(m\omega t - \phi_{dm}) \\ \sum_{m=1,2,3,\dots} V_{qm} \sin(m\omega t - \phi_{qm}) \\ V_0 \end{bmatrix} \\
 &= \sqrt{\frac{2}{3}} \begin{bmatrix} \cos \theta & \cos\left(\theta - \frac{2\pi}{3}\right) & \cos\left(\theta - \frac{4\pi}{3}\right) \\ -\sin \theta & -\sin\left(\theta - \frac{2\pi}{3}\right) & -\sin\left(\theta - \frac{4\pi}{3}\right) \\ \frac{1}{2} & \frac{1}{2} & \frac{1}{2} \end{bmatrix} \\
 &\quad \times \begin{bmatrix} \sum_{m=1,2,3,\dots} V_{Rm} \sin(m\omega t - \phi_{Rm}) \\ \sum_{m=1,2,3,\dots} V_{Ym} \sin(m\omega t - \phi_{Ym}) \\ \sum_{m=1,2,3,\dots} V_{Bm} \sin(m\omega t - \phi_{Bm}) \end{bmatrix} \quad (5)
 \end{aligned}$$

Similarly, currents in d-q plane can be written as

$$\begin{bmatrix} i_d \\ i_q \\ i_0 \end{bmatrix} = \begin{bmatrix} \sum_{n=1,2,3,\dots} I_{dn} \sin(n\omega t - \theta_{dn}) \\ \sum_{n=1,2,3,\dots} I_{qn} \sin(n\omega t - \theta_{qn}) \\ I_0 \end{bmatrix}$$

$$\begin{aligned}
 &\sqrt{\frac{2}{3}} \begin{bmatrix} \cos \theta & \cos\left(\theta - \frac{2\pi}{3}\right) & \cos\left(\theta - \frac{4\pi}{3}\right) \\ -\sin \theta & -\sin\left(\theta - \frac{2\pi}{3}\right) & -\sin\left(\theta - \frac{4\pi}{3}\right) \\ \frac{1}{2} & \frac{1}{2} & \frac{1}{2} \end{bmatrix} \\
 &\quad \times \begin{bmatrix} \sum_{n=1,2,3,\dots} I_{Rn} \sin(n\omega t - \theta_{Rn}) \\ \sum_{n=1,2,3,\dots} I_{Yn} \sin(n\omega t - \theta_{Yn}) \\ \sum_{n=1,2,3,\dots} I_{Bn} \sin(n\omega t - \theta_{Bn}) \end{bmatrix} \quad (6)
 \end{aligned}$$

C. Assessment of Fundamental Frequency

For distortion factor analysis contribution of fundamental and harmonic components should be isolated. A reference signal has been defined for assessment of fundamental component of voltage waveform as

$$R_{V1}(t) = \sin \omega_1 t \quad (7)$$

Here, ω_1 is fundamental frequency of the reference signal. Fundamental frequency of the reference signal ω_1 must be equal to the fundamental frequency ω of the real signal collected from the power system, which is initially an unknown quantity. To select the value of ω_1 , at first take, $\omega_1 = 50 \pm \Delta\omega$, where, $\Delta\omega$ is a small incremental value. If this reference signal is plotted against any one signal of v_d , v_q , i_d and i_q which have been derived from the real power system data, then the starting and ending point will not meet each other. There will be a finite gap between these two points as shown in fig. 1.

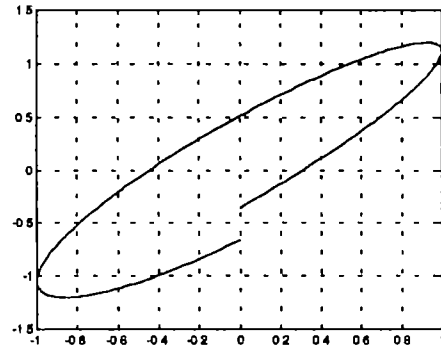


Fig. 1 Curves formed by R_{V1} and v_d having unequal fundamental frequency

If ω_1 is changed gradually by changing $\Delta\omega$ in such a way that the starting and ending points come closer to each other then, it can be said that ω_1 is approaching towards ω . When starting and ending points come at minimum distance from each other, ideally zero, then it can be said that $\omega_1 = \omega$. Then the reference signal for assessment of fundamental component of voltage waveform becomes

$$R_{v1}(t) = \sin \omega t \quad (8)$$

Similarly, the reference signal for assessment of fundamental component of current waveform is

$$R_{i1}(t) = \sin \omega t \quad (9)$$

D Reference Signal for Assessment of Harmonic Rows

To determine the harmonics components of voltage and current waveform, let us define the following two reference signals.

The reference signal for assessment of m^{th} order harmonic component of voltage waveform is

$$R_{vm}(t) = \sin m\omega t \quad (10)$$

The reference signal for assessment of n^{th} order harmonic component of current waveform is

$$R_{in}(t) = \sin n\omega t \quad (11)$$

D. Harmonic Power

Area covered by curve v_d and R_{vm} waveforms in $v_d - R_{vm}$ plane will be

$$A_{dm}^{v_d - R_{vm}} = k_1 V_{dm} \sin \phi_{dm} \quad (12)$$

Area formed by curve in $v_d - R_{vm}$ -t plane will be

$$A_{dm}^{v_d R_{vm} - t} = k_2 V_{dm} \cos \phi_{dm} \quad (13)$$

Using (12) and (13)

$$V_{dm} = \sqrt{(K_1 A_{dm}^{v_d - R_{vm}})^2 + (K_2 A_{dm}^{v_d R_{vm} - t})^2} \quad (14)$$

$$\phi_{dm} = \tan^{-1} \left(\frac{K_1 A_{dm}^{v_d - R_{vm}}}{K_2 A_{dm}^{v_d R_{vm} - t}} \right) \quad (15)$$

Area covered by curve in $i_d - R_{in}$ plane will be

$$A_{dn}^{i_d - R_{in}} = k_1 I_{dn} \sin \theta_{dn} \quad (16)$$

Area formed by curve in $i_d - R_{in}$ -t plane will be

$$A_{dn}^{i_d R_{in} - t} = k_2 I_{dn} \cos \theta_{dn} \quad (17)$$

Using (16) and (17)

$$I_{dn} = \sqrt{(K_1 A_{dn}^{i_d - R_{in}})^2 + (K_2 A_{dn}^{i_d R_{in} - t})^2} \quad (18)$$

$$\theta_{dn} = \tan^{-1} \left(\frac{K_1 A_{dn}^{i_d - R_{in}}}{K_2 A_{dn}^{i_d R_{in} - t}} \right) \quad (19)$$

In active and reactive power only harmonics components of same order contribute. Using (14), (15), (18) and (19), reactive and active power contributed by n^{th} order of voltage and current harmonics are written as

$$Q_{dn} = \frac{1}{2} V_{dm} I_{dn} \sin(\phi_{dm} - \theta_{dn})$$

$$= \frac{1}{2} \sqrt{(K_1 A_{dm}^{v_d - R_{vm}})^2 + (K_2 A_{dm}^{v_d R_{vm} - t})^2} \times \sqrt{(K_1 A_{dn}^{i_d - R_{in}})^2 + (K_2 A_{dn}^{i_d R_{in} - t})^2}$$

$$\times \sin \left(\tan^{-1} \left(\frac{K_1 A_{dm}^{v_d - R_{vm}}}{K_2 A_{dm}^{v_d R_{vm} - t}} \right) - \tan^{-1} \left(\frac{K_1 A_{dn}^{i_d - R_{in}}}{K_2 A_{dn}^{i_d R_{in} - t}} \right) \right) \quad (20)$$

$$P_{dn} = \frac{1}{2} V_{dm} I_{dn} \cos(\phi_{dm} - \theta_{dn})$$

$$= \frac{1}{2} \sqrt{(K_1 A_{dm}^{v_d - R_{vm}})^2 + (K_2 A_{dm}^{v_d R_{vm} - t})^2} \times \sqrt{(K_1 A_{dn}^{i_d - R_{in}})^2 + (K_2 A_{dn}^{i_d R_{in} - t})^2}$$

$$\times \sin \left(\tan^{-1} \left(\frac{K_1 A_{dm}^{v_d - R_{vm}}}{K_2 A_{dm}^{v_d R_{vm} - t}} \right) - \tan^{-1} \left(\frac{K_1 A_{dn}^{i_d - R_{in}}}{K_2 A_{dn}^{i_d R_{in} - t}} \right) \right) \quad (21)$$

Similarly,

Area formed by curve in $v_q - R_{vm}$ plane will be

$$A_{qm}^{v_q - R_{vm}} = k_1 V_{qm} \sin \phi_{qm} \quad (22)$$

$$\text{or, } V_{qm} \sin \phi_{qm} = K_1 A_{qm}^{v_q - R_{vm}} \quad (23)$$

Area formed by curve in $v_q - R_{vm}$ -t plane will be

$$A_{qm}^{v_q R_{vm} - t} = k_2 V_{qm} \cos \phi_{qm} \quad (24)$$

Using (23) and (24)

$$V_{qm} = \sqrt{(K_1 A_{qm}^{v_q - R_{vm}})^2 + (K_2 A_{qm}^{v_q R_{vm} - t})^2} \quad (25)$$

$$\phi_{qm} = \tan^{-1} \left(\frac{K_1 A_{qm}^{v_q - R_{vm}}}{K_2 A_{qm}^{v_q R_{vm} - t}} \right) \quad (26)$$

Area formed by curve in $i_q - R_{in}$ plane will be

$$A_{qn}^{i_q - R_{in}} = k_1 i_{qn} \sin \theta_{qn} \quad (27)$$

Area formed by curve in $i_q - R_{in}$ -t plane will be

$$A_{qn}^{i_q R_{in} - t} = k_2 i_{qn} \cos \theta_{qn} \quad (28)$$

Using (27) and (28)

$$i_{qn} = \sqrt{(K_1 A_{qn}^{i_q - R_{in}})^2 + (K_2 A_{qn}^{i_q R_{in} - t})^2} \quad (29)$$

$$\theta_{qn} = \tan^{-1} \left(\frac{K_1 A_{qn}^{i_q - R_{in}}}{K_2 A_{qn}^{i_q R_{in} - t}} \right) \quad (30)$$

Using (25), (26), (29) and (30), reactive and active power contributed by n^{th} order of voltage and current harmonics are written as

$$Q_{qn} = \frac{1}{2} V_{qn} I_{qn} \sin(\phi_{qn} - \theta_{qn})$$

$$= \frac{1}{2} \sqrt{(K_1 A_{qn}^{v-R_{qn}})^2 + (K_2 A_{qn}^{v-R_{qn}-1})^2} \times \sqrt{(K_1 A_{qn}^{i-R_{qn}})^2 + (K_2 A_{qn}^{i-R_{qn}-1})^2}$$

$$\times \sin \left(\tan^{-1} \left(\frac{K_1 A_{qn}^{v-R_{qn}}}{K_2 A_{qn}^{v-R_{qn}-1}} \right) - \tan^{-1} \left(\frac{K_1 A_{qn}^{i-R_{qn}}}{K_2 A_{qn}^{i-R_{qn}-1}} \right) \right) \quad (31)$$

$$P_{qn} = \frac{1}{2} V_{qn} I_{qn} \cos(\phi_{qn} - \theta_{qn})$$

$$= \frac{1}{2} \sqrt{(K_1 A_{qn}^{v-R_{qn}})^2 + (K_2 A_{qn}^{v-R_{qn}-1})^2} \times \sqrt{(K_1 A_{qn}^{i-R_{qn}})^2 + (K_2 A_{qn}^{i-R_{qn}-1})^2}$$

$$\times \cos \left(\tan^{-1} \left(\frac{K_1 A_{qn}^{v-R_{qn}}}{K_2 A_{qn}^{v-R_{qn}-1}} \right) - \tan^{-1} \left(\frac{K_1 A_{qn}^{i-R_{qn}}}{K_2 A_{qn}^{i-R_{qn}-1}} \right) \right) \quad (32)$$

III. EXPERIMENTATION

Proposed block diagram representation of experimental setup is shown in fig. 2. On line data from power system is captured through current and potential transformers. After sampling, they are collected through a data acquisition system (DAS). They are transformed into Park domain (d, q) by Park transformation matrix and analyzed by developing suitable program. Harmonic power has to be assessed from the areas formed in d-q plane.

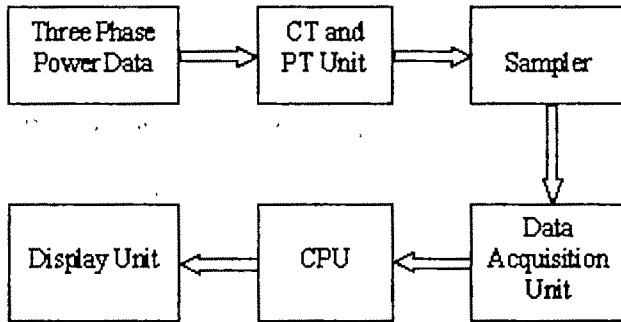


Fig. 2 Block Diagram of Proposed Experimental Setup

IV. SIMULATED RESULTS

The above area based approach have been verified through computer simulation. Phase voltage and current consisting of highest 23rd order of harmonics have been simulated as given in right hand sides of (5) and (6). From these known data, active power and reactive power for three phase system have been calculated as shown by true values in table -1 and 2. The simulated data have been sampled and transformed into Park plane using Park transformation matrix. Different areas have been formed and then three phase active and reactive powers have been calculated using (20, 21, 31, 32). They have been

compared with the corresponding true values and errors have been calculated comparing with true values. Satisfactory results with very small errors have been found which are presented in table-1 and 2.

Table 1
Total active power contributed by harmonic components

Active power (True Value)	Active Power	ERROR
0.1485	0.1485	0.0000
0.1672	0.1673	0.0001
0.1734	0.1736	0.0002
0.3351	0.3352	0.0001
0.2930	0.2930	0.0001

Table 2
Total reactive power contributed by harmonic components

Reactive Power (True Value)	Reactive Power	ERROR
0.1550	0.1549	0.0001
0.2407	0.2407	0.0000
0.5034	0.5035	0.0001
0.5560	0.5560	0.0000
0.1609	0.1608	0.0001

Accuracy increases with the increase of sampling rate of the data acquisition system. For analysis of a three-phase power system instead of using three phase voltages (v_R , v_Y and v_B) and three line currents (i_R , i_Y and i_B) use of v_d , v_q , i_d and i_q has reduced the computation effort by two-third ratio.

V. CONCLUSIONS

Small values of error speak of the acceptability of the above methods. In three-phase power system consisting of three voltage waveforms and three current waveforms, use of the Park domain consisting of two voltage waveforms and two current waveforms, has reduced the computational task to a great extent. Also in the above method fundamental frequency (ω) is assumed to be constant only for one complete cycle and may change in next cycle, which is more advantageous in real system analysis than other existing methods where (ω) is to be constant throughout the process. Thus the above method and d-q plane for three-phase system may be, in future, a good platform for harmonic power measurement.

REFERENCES

- [1] IEEE Working Group, "Power Quality-Two Different Perspective", IEEE Transaction on Power Delivery, Vol. 5, No. 3, July 1990, PP-1501-1513.
- [2] Ferrero, A. and Superti-Purga, G., "A new approach to the definition of Power components in three-phase systems under nonsinusoidal conditions", IEEE Transactions on Instrumentation and Measurement, Vol. 40, No. 3, pp. 568-577, June 1991
- [3] Akagi H., Nabae A., "The p-q theory in three-phase systems under non-sinusoidal conditions", European transactions on electrical power engineering, vol. 3, no1, pp. 27-31, 1993.

- [4] Ferrero A., Morando A. P., Ottoboni R., Superti-Furga G., Willems J. L., "On the meaning of the Park power components in three-phase systems under non-sinusoidal conditions", *European transactions on electrical power engineering*, vol. 3, no. 1, pp. 33-43, 1993.
- [5] A. Domijan, G.T. Heydt, A.P. S. Meliopoulos, "Direction of Research on Power Quality", *IEEE Transaction on Power Delivery*, Vol. 8, No. 1, January 1993, PP-429-436.
- [6] P. P. Barker, T. A. Short, C. W. Burns, J. J. Burke, C. A. Warren, J. J. Siewierski, R. T. Mancao, "Power Quality Monitoring of a Distribution System", *IEEE Transaction on Power Delivery*, Vol. 9, No. 2, April 1994, PP-429-436.
- [7] A. K. Ghosh, D. L. Lubkeman, "The Classification of Power System Disturbances Waveforms using a Neural Network Approach", *IEEE Transaction on Power Delivery*, Vol. 1, No. 1, January 1995, PP-109-115.
- [8] A. Cavallini, G.C. Montanari, "Stochastic Evaluation of Harmonics at Network Buses", *IEEE Transaction on Power Delivery*, Vol. 10, No. 3, July 1995, PP-1606-1613.
- [9] S. Santoso, E. J. Powers, W. M. Grady, P. Hofman, "Power Quality Assessment via Wavelet Transform Analysis", *IEEE Transaction on Power Delivery*, Vol. 11, No. 2, April 1996, PP-924-910.
- [10] D. D. Sabin, D.L. Brooks, A. Sundaram, "Indices for Assessing Harmonics Distortion from Power Quality Measurement: Definitions and Benchmark Data", *IEEE Transaction on Power Delivery*, Vol. 14, No. 2, April 1999, PP-489-496.
- [11] G. T. Heydt, P. S. Fjeld, C. C. Liu, D. Pierce, L. Tu, G. Hensley, "Application of the Windowed FFT to Electric Power Quality Assessment", *IEEE Transaction on Power Delivery*, Vol. 14, No. 4, October 1999, PP-1411-1416.
- [12] A. M. Gaouda, M. M. A. Salama, M. R. Sultan, A. Y. Chikhani, "Power Quality Detection and Classification Using Wavelet-Multi-resolution Signal Decomposition", *IEEE Transaction on Power Delivery*, Vol. 14, No. 4, October 1999, PP-1469-1475.
- [13] S. Santoso, E. J. Powers, W. M. Grady, A. C. Parsons, "Power Quality Disturbance Waveform Recognition Using Wavelet-Based Neural Classifier- Part1: Theoretical Foundation", *IEEE Transaction on Power Delivery*, Vol. 15, No. 1, January 2000, PP-222-228.
- [14] S. Santoso, E. J. Powers, W. M. Grady, A. C. Parsons, "Power Quality Disturbance Waveform Recognition Using Wavelet-Based Neural Classifier- Part2: Theoretical Foundation", *IEEE Transaction on Power Delivery*, Vol. 15, No. 1, January 2000, PP-229-235.
- [15] S. Santoso, E. J. Powers, W. M. Grady, A. C. Parsons, "Characterization of Distribution Power Quality Events with Fourier and Wavelet Transform", *IEEE Transaction on Power Delivery*, Vol. 15, No. 1, January 2000, PP-247-256.
- [16] S. H. Jaramillo, G. T. Heydt, E. O'Neill-Carrillo, "Power Quality Indices for Aperiodic Voltages and Currents", *IEEE Transaction on Power Delivery*, Vol. 15, No. 2, April 2000, PP-784-790.
- [17] A. Jouanne, B. Banerjee, "Assessment of Voltage Unbalance", *IEEE Transaction on Power Delivery*, Vol. 16, No. 4, October 2001, PP-782-790.
- [18] J. Kyei, R. Ayyanar, G. Heydt, R. Thallam, J. Blevins, "The Design of Power Acceptability Curves", *IEEE Transaction on Power Delivery*, Vol. 17, No. 3, July 2002, PP-828-833.
- [19] Leva, S. and Paolo Morando, A., "Waves and complex power in transmission lines", *IEEE Transactions on Power Delivery*, Vol. 18, No. 4, pp.1320-1327, Oct 2003
- [20] Surajit Chattopadhyay, Madhuchhanda Mitra, and Samarjit Sengupta, "Intelligent Power Quality Monitoring in an Electric Power System", *AMSE Best of 2004- volume*, pp. 146-156, 2004.
- [21] M. K. Ghartemani, M. R. Iravani, "Measurement of Harmonic/ Inter-Harmonics of Time Varying Frequencies", *IEEE Transaction on Power Delivery*, Vol. 20, No. 1, January 2005, PP-23-31.
- [22] S. Leva, A. P. Moronado, D. Zaninelli, "Evaluation of the Line Voltage Drops in Presence of Unbalance, Harmonics and Inter-harmonics: Theory and Applications", *IEEE Transaction on Power Delivery*, Vol. 20, No. 1, January 2005, PP-390-396.
- [23] J. A. L. Ghijselen, A. P. M. Van den Bossche, "Exact Voltage Unbalance Assessment Without Phase Measurement", *IEEE Transaction on Power Systems*, Vol. 20, No. 1, February 2005, PP-519-520
- [24] R. Carbone, F. D. Rosa, R. Langella, A. Testa, "A New Approach for the Computation of Harmonics Produced by Line-Commuted

AC/DC/AC Converters", *IEEE Transaction on Power Delivery*, Vol. 20, No. 3, July 2005, PP-2227-2234

LIST OF SYMBOLS AND ABBREVIATIONS

R_{vm} = reference signal generated for assessment of harmonic component of voltage of order m

R_{in} = reference signal generated for assessment of harmonic component of current of voltage of order n

ω =angular frequency

m=order of voltage harmonics

n=order of current harmonics

n_H =order of highest harmonics

ϕ_m =phase angle of voltage of harmonics of order m

θ_n = phase angle of current of harmonics of order n

ϕ_{mn} = phase angle difference between voltage harmonic of order m and current harmonics of order n

ϕ_{Ym} =phase angle of voltage of harmonics of order m in phase Y

θ_{Yn} = phase angle of current of harmonics of order n in phase Y

$A_{dm}^{V_d-R_{vm}}$ =Area covered by curve V_d and R_{vm} waveforms in $V_d - R_{vm}$

$A_{dm}^{V_d R_{vm}-t}$ =Area formed by curve in $V_d - R_{vm} -t$ plane

$A_{dn}^{I_d-R_{in}}$ =Area covered by curve in $i_d - R_{in}$ plane

$A_{dn}^{I_d R_{in}-t}$ =Area formed by curve in $i_d - R_{in} -t$ plane

$A_{qm}^{V_q-R_{vm}}$ =Area formed by curve in $V_q - R_{vm}$ plane

$A_{qm}^{V_q R_{vm}-t}$ =Area formed by curve in $V_q - R_{vm} -t$ plane

$A_{qn}^{I_q-R_{in}}$ =Area formed by curve in $i_q - R_{in}$ plane

$A_{qn}^{I_q R_{in}-t}$ =Area formed by curve in $i_q - R_{in} -t$ plane

Q_{dn} = reactive power contributed by harmonic component with frequency of order n along d axis

Q_{qn} = reactive power contributed by harmonic component with frequency of order n along q axis

P_{dn} = active power contributed by harmonic component with frequency of order n along d axis

P_{qn} = active power contributed by harmonic component with frequency of order n along q axis

DAS=Data Acquisition System

Technical Session 1B

Process Control

A Novel approach for the Design of Stabilizing PI Controllers

M.Siva Kumar¹, B.J.J Raju², A.Sarada Devi³, P.Naga Manasa⁴

¹shri Vishnu Engg college for womenBhimavaram. e-mail: shivamangipudi2@rediffmail.com

^{2,3,4}shri Vishnu Engg college for womenBhimavaram.

Abstract- In this paper, a simple method for the design of the parameters of a PI controller, which stabilize control system with fixed parameters, is given. The proposed method is based on plotting the stability boundary locus in the (k_p, k_i) -plane and then computing stabilizing PI controllers. The method presented does not require sweeping over the parameters and also does not need a linear programming to solve a set of inequalities. Thus, it has several important advantages over existing results. The developed method is illustrated with a typical numerical example available in literature.

Keywords - Stabilization, PI control, frequency gridding.

I. INTRODUCTION

THERE has been a great amount of research work on the tuning of PI, PID and lag/lead controllers since these types of controllers have been widely used in industries for several decades (see [1-5] and references therein). However, many important results have been recently reported on computation of all stabilizing P, PI and PID controllers after the publication of work by Ho *et al.* [6-9]. A new and complete analytical solution, which is based on the generalized version of the Hermite-Biehler theorem, has been provided in [6] for computation of all stabilizing constant gain controllers for a given plant. A linear programming characterization of all stabilizing PI and PID controllers for a given plant has been

obtained in [7,9]. This characterization besides being computationally efficient has revealed important structural properties of PI and PID controllers. For example, it was shown that for a fixed proportional gain, the set of stabilizing integral and derivative gains lie in a convex set. This method is very important since it can cope with systems that are open loop stable or unstable, minimum or non-minimum phase. However, the computation time for this approach increases in an exponential manner with the order of the system being considered. It also needs sweeping over proportional gain to find all stabilizing PI and PID controllers which is a disadvantage of the method. An alternative fast approach to this problem based on the use of the Nyquist plot has been given in [10-11]. An extension of the method given in [7] to the lag/lead controller structure has been given in [12]. A parameter space approach using singular frequency concept has been given in [13] for design of robust PID controllers. More direct graphical approaches to this problem based on frequency response plots have been given in [14-15]. However, the frequency gridding has become the major problem for this approach. On the other hand, compensator design in classical control engineering is based on a plant with fixed parameters.

In this paper, a new approach is given for design of stabilizing PI controllers in the parameter plane, (k_p, k_i) -plane. The result of [11] is used to avoid the problem of frequency gridding. Thus, a very fast way of calculating the stabilizing values of PI controllers for a given SISO control system is given.

II. ALGORITHM FOR THE PROPOSED METHOD

Consider the single-input single-output (SISO) control system of Figure 1 where

$$G(s) = \frac{N(s)}{D(s)} \quad (1)$$

is the plant to be controlled and $C(s)$ is a PI controller of the form

$$C(s) = k_p + \frac{k_i}{s} = \frac{k_p s + k_i}{s} \quad (2)$$

The problem is to compute the parameters of the PI controller of Eq. (4) which stabilize the system of Figure 1.

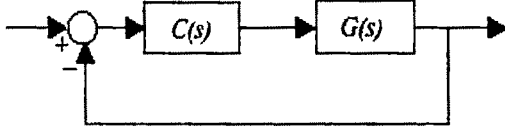


Figure 1: A SISO control system

Decomposing the numerator and the denominator polynomials of Eq. (3) into their even and odd parts, and substituting $s = j\omega$, gives

$$G(j\omega) = \frac{N_e(-\omega^2) + j\omega N_o(-\omega^2)}{D_e(-\omega^2) + j\omega D_o(-\omega^2)} \quad (3)$$

The closed loop characteristic polynomial of the system can be written as

$$\begin{aligned} \Delta(s) = & [k_i N_e(-\omega^2) - k_p \omega^2 N_o(-\omega^2) - \omega^2 D_o(-\omega^2)] \\ & + j[k_p N_e(-\omega^2) + k_i \omega N_o(-\omega^2) + \omega D_e(-\omega^2)] = 0 \end{aligned} \quad (4)$$

Then, equating the real and imaginary parts of $\Delta(s)$ to zero, one obtains

$$k_p(-\omega^2 N_o(-\omega^2)) + k_i(N_e(-\omega^2)) = \omega^2 D_o(-\omega^2) \quad (5)$$

and

$$k_p(N_e(-\omega^2)) + k_i(\omega N_o(-\omega^2)) = -D_e(-\omega^2) \quad (6)$$

Let

$$\begin{aligned} Q(\omega) &= -\omega^2 N_o(-\omega^2) \\ R(\omega) &= N_e(-\omega^2) \\ S(\omega) &= N_e(-\omega^2) \\ U(\omega) &= N_o(-\omega^2) \\ X(\omega) &= \omega^2 D_o(-\omega^2) \\ Y(\omega) &= -D_e(-\omega^2) \end{aligned} \quad (7)$$

Then, Eq. (7) and Eq. (8) can be written as

$$\begin{aligned} k_p Q(\omega) + k_i R(\omega) &= X(\omega) \\ k_p S(\omega) + k_i U(\omega) &= Y(\omega) \end{aligned} \quad (8)$$

From this equation

$$k_p = \frac{X(\omega)U(\omega) - Y(\omega)R(\omega)}{Q(\omega)U(\omega) - R(\omega)S(\omega)} \quad (9)$$

and

$$k_i = \frac{Y(\omega)Q(\omega) - X(\omega)S(\omega)}{Q(\omega)U(\omega) - R(\omega)S(\omega)} \quad (10)$$

Solving these two equations simultaneously, the stability boundary locus, $l(k_p, k_i, \omega)$, in (k_p, k_i) -plane can be obtained. The stability boundary locus divides the parameter plane $((k_p, k_i)$ -plane) into stable and unstable regions. Choosing a test point within each region, the stable region which contains the values of stabilizing k_p and k_i parameters can be determined

III. NUMERICAL EXAMPLE

Example 1: Consider the control system of Figure 1 with transfer function

$$G(s) = \frac{N(s)}{D(s)} = \frac{s^3 + 4s^2 - s + 1}{s^5 + 2s^4 + 32s^3 + 14s^2 - 4s + 50} \quad (11)$$

Which has 2 right-half plane poles and 2 right half plane zeros. From Eq. (9) and Eq. (10)

$$K_p = \frac{-\omega^8 + 23\omega^6 + 94\omega^4 - 210\omega^2 + 50}{-\omega^6 - 18\omega^4 + 7\omega^2 - 1} \quad (12)$$

and

$$K_i = \frac{2\omega^8 - 117\omega^6 - 20\omega^4 - 46\omega^2}{-\omega^6 - 18\omega^4 + 7\omega^2 - 1} \quad (13)$$

The aim is to compute all the stabilizing values of k_p and k_i which make the characteristic polynomial of Eq. (4) Hurwitz stable. For a range of frequency, the stability boundary locus can be easily computed.

For example, for $\omega \in [0.45, 7.8]$, $l(k_p, k_i, \omega)$ is shown in Figure 2. From this figure it can be seen that there are a few regions namely R1, R2, R3, R4 and R5 in which one needs to choose a test point in order to find the stability region. For example, choosing a test point within region R5 such as $k_p = 13$ and $k_i = 25$, it can be calculated that the characteristic polynomial has two right half plane complex roots, therefore, the system is unstable for these values of parameters. Thus, the region R5 is not a stability region. It has been computed that the only stabilizing region is the region denoted by R1.

For example, for $k_p = 5$ and $k_i = 20$ within region R1, the characteristic polynomial is

$$\Delta(s) = s^6 + 2s^5 + 37s^4 + 54s^3 + 71s^2 + 35s + 20$$

which is a stable polynomial. The all stabilizing values of k_p and k_i are shown in Figure 3.

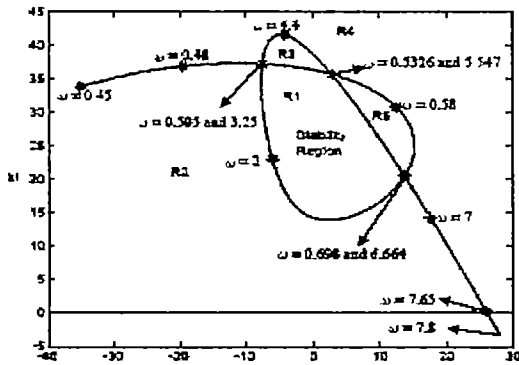


Fig 2: Stability boundary locus

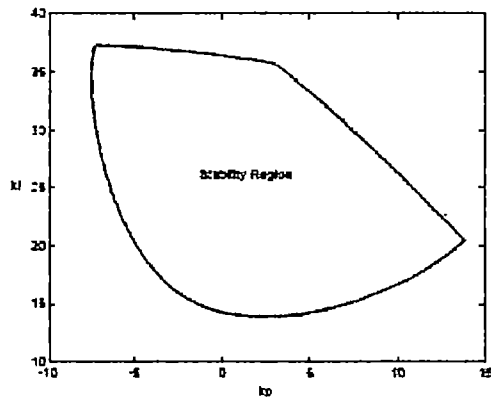


Fig 3: All stabilizing PI controllers

This example show that the method is very fast and effective, however, frequency gridding becomes important. An efficient approach to avoid frequency gridding can be obtained by using the Nyquist plot based approach of [11]. In this case, it is only necessary to find real values of ω that satisfy

$$\text{Im}[G(s)] = 0 \quad (14)$$

where $s = j\omega$. Thus, the frequency axis can be divided into finite number of intervals and then by testing each interval the stability region can be computed. To illustrate this consider the following example.

Example2:

$$G(s) = \frac{s-1}{s^2+0.8s+0.2} \quad (15)$$

Form Eq. (9) and Eq. (10)

$$k_p = \frac{1.8\omega^2 + 0.2}{-\omega^2 - 1} \quad (16)$$

and

$$k_i = \frac{-\omega^4 + 0.6\omega^2}{-\omega^2 - 1} \quad (17)$$

The stability boundary locus for 100 frequency points within $\omega \in [0, 10]$ is shown in Figure 4. From this figure it is not possible to determine the region of stability. However, for $G(s)$

of Eq.(15), the real frequency values which satisfy Eq. (12) is 0.77rad/sec. Thus the frequency axis can be divided into two intervals such as $\omega \in (0, 0.77)$ and $\omega \in (0.77, \infty)$. For 100 points within $\omega \in [0, 0.9]$, $l(k_p, k_i, \omega)$ is shown in Figure 5 where it can be seen that there are stabilizing values of k_p and k_i when $\omega \in (0, 0.77)$ as shown in Figure 5. For $G(s)$ of Eq. (11), $\text{Im}[G(j\omega)] = 0$ for $\omega = 7.65$. Thus, one needs to plot stability boundary locus for ω changing between 0 and 7.65. Then, stabilizing region can be computed as shown in example 1. The step response of the system with the stabilizing PI controller is shown in fig 6.

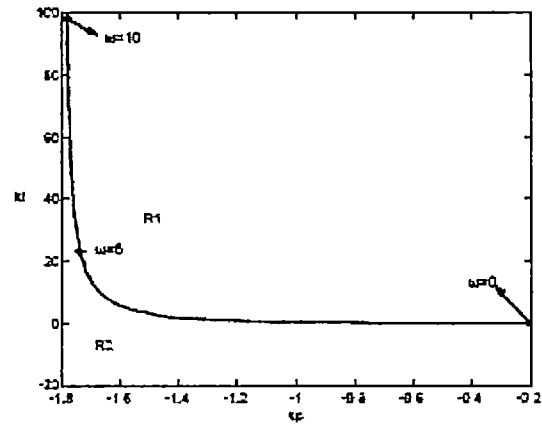


Fig 4: Stability boundary locus

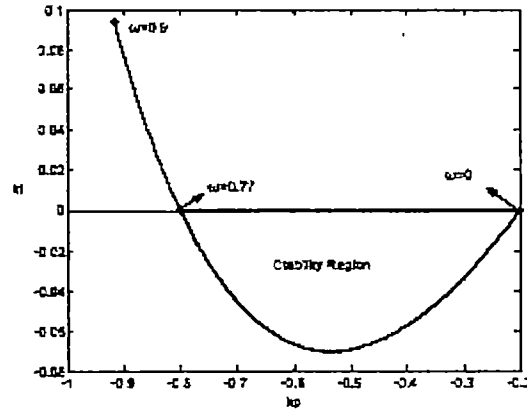


Fig 5: Stability boundary locus

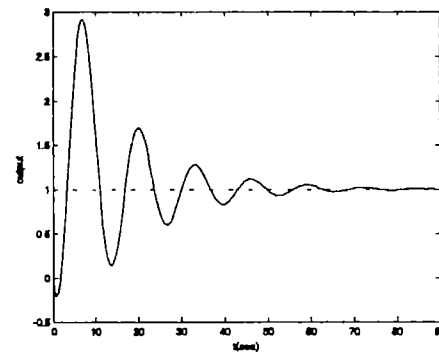


Fig 6: Step response of the system with PI controller of Ex2.

IV. CONCLUSIONS

In this paper, a new approach has been presented for the design of the boundaries of the limiting values of stabilizing PI controllers parameters that guarantee stability. The approach is based on the stability boundary locus which can be easily obtained by equating the real and the imaginary parts of the characteristic equation to zero. The method presented does not require sweeping over the parameters. Also, it does not need linear programming to solve a set of inequalities.

Therefore, the method has advantages over existing results. Illustrated examples clearly show the effectiveness of the proposed method.

REFERENCES

- [1] Ziegler, J. G. and N. B. Nichols, "Optimum settings for automatic controllers," *Trans. ASME*, vol. 64, pp. 759-768, 1942.
- [2] Astrom, K. J., T. Hagglund, C. C. Hang and W.K. Ho, "Automatic tuning and adaptation for PID controllers- a survey," *Control Eng. Pract.*, vol. 1, pp. 699-714, 1993.
- [3] Astrom, K. J. and T. Hagglund, *PID Controllers: Theory, Design, and Tuning*. Instrument Society of America, 1995.
- [4] Zhuang, M. and D. P. Atherton, "Automatic tuning of optimum PID controllers," *IEE Proc. Part D*, vol. 140, pp. 216-224, 1993.
- [5] Ho, W. K., C. C. Hang and L. S. Cao, "Tuning of PID controllers based on gain and phase margin specifications," *Automatica*, vol. 31, pp. 497-502, 1995.
- [6] Ho, M. T., A. Datta and S. P. Bhattacharyya, "A new approach to feedback stabilization," *Proc. of the 35th CDC*, pp. 4643-4648, 1996.
- [7] Ho, M. T., A. Datta and S. P. Bhattacharyya, "A linear programming characterization of all stabilizing PID controllers," *Proc. of Amer. Contr. Conf.*, 1997.
- [8] Ho, M. T., A. Datta and S. P. Bhattacharyya, "A new approach to feedback design Part I: Generalized interlacing and proportional control," *Dept. of Electrical Eng., Texas A&M Univ., College Station, TX, Tech. Report TAMU-ECE97-001-A*, 1997.
- [9] Ho, M. T., A. Datta and S. P. Bhattacharyya, "A new approach to feedback design Part II: PI and PID controllers," *Dept. of Electrical Eng., Texas A&M Univ., College Station, TX, Tech. Report TAMUECE97-001-B*, 1997.
- [10] Munro, N. and M. T. Söylemez, "Fast calculation of stabilizing PID controllers for uncertain parameter systems," *Proc. Symposium on Robust Control*, Prague, 2000.
- [11] Söylemez, M. T., N. Munro and H. Baki, "Fast calculation of stabilizing PID controllers," *Automatica*, vol. 39, pp. 121-126, 2003.
- [12] Tan, N. and D. P. Atherton, "Feedback stabilization using the Hermite-Biehler theorem," *International Conf. on the Control of Industrial Processes*, Newcastle, UK, 1999.
- [13] Ackermann, J. and D. Kaesbauer, "Design of robust PID controllers," *European control Conference*, pp. 522-527, 2001.
- [14] Shafiei, Z. and A. T. Shenton, "Frequency domain design of PID controllers for stable and unstable systems with time delay," *Automatica*, vol. 33, pp. 2223-2232, 1997.
- [15] Huang, Y. J. and Y. J. Wang, "Robust PID tuning strategy for uncertain plants based on the Kharitonov theorem," *ISA Transactions*, vol. 39, pp. 419-431, 2000.
- [16] Kharitonov, V. L., "Asymptotic stability of an equilibrium position of a family of systems of linear differential equations," *Differential Equations*, Vol. 14, pp. 1483-1485, 1979.
- [17] Ghosh, B. K., "Some new results on the simultaneous stabilization of a family single input, single output systems," *Syst. Contr. Lett.*, Vol. 6, pp. 39-45, 1985.

Improving Automation Benefits of Process Control System using Performance Evaluation by Statistical Analysis

S. G. Hingmire , S. G. Karad and D. S. Karanjkar
Dr. Babasaheb Ambedkar Tech. University, Raigad (M.S.), India.
hsomesh@yahoo.co.uk

Abstract - In this era of the new World – a world of International Competition, - process control can bring substantial benefits by improving quality of products, increasing yields, production rates and uptime and decreasing cycle time. However, this does not happen automatically by simply installing the most modern control equipment, as we experienced when distributed control system became available in the 1980s. Many companies installed distributed control systems expecting improved performance, only to find later that it was not significantly better than before. One of the reasons was that the control strategies had not been improved; they just duplicated the old analog systems. What is needed is to take advantage of the power of the new digital systems and upgrade the control strategies to gain concrete business benefits, not just to ensure stable operation of equipment. Companies are now going back and reevaluating how process control is applied and looking for ways to increase productivity through improved control. Thus an approach for a process control loop performance assessment is proposed. This approach was developed to collect performance data of the process control system and then to use this data to calculate performance and capability index. Based on this performance matrix, the recommendation for the improvement is displayed. Efficient algorithms for performance assessment are developed and evaluated by simulations using MATLAB.

Key words - Key Performance Indices (KPI), Mathematical Modeling, Performance Assessment, Process Monitor, Statistical Process Control, Simulation, Statistical Matrices.

I. INTRODUCTION

A. Global Scenario

In globally competitive Process Industries such as Chemicals, Petrochemicals, and Pharmaceuticals, Corporate Management is looking for Technology to help in improving the bottom line because

- i) Markets which were guaranteed few decades ago are now threatened by International competition
- ii) Product life cycles are much shorter and technology is changing at an un wavering rate.
- iii) Production needs to be faster, less expensive on a per unit basis and of high quality.

The olden days when products had a long life cycle, the domestic market was secured and the economical conditions

could be predicted are all gone. We are in a new world – a world of international competition.

B. Role of Automation in Process Control system

For the past 20 years, modern distributed control systems (DCS) have been used to keep process facilities running within acceptable operating limits. In a modern process industry several thousands regulatory control loops work in a coordinated fashion to ensure that the process remains in control. Previously, maintenance and process control teams within process companies have been challenged to keep these assets working optimally. Survey has shown that in many organizations, more than 50% of the regulatory control loops are either in manual or completely ineffective in minimizing variability within the process. Most often it is due to one or more of the following technical problems.

- a) Hardware issues such as valve and sensor faults
- b) Improperly tuned control loops.
- c) Improper control strategy.
- d) Mismatch in user requirement specifications
- e) Improper process design.
- f) Plant disturbances and loop interactions.

C. Problem

These problems, unfortunately, prevent operators from running the plant at or near the most profitable operating points or constraints in the process resulting in lost revenue in the form of throughput, quality gives away, energy consumption and product yield. The response to this problem by some organizations has been—when problems occur and they are a priority, fix them otherwise leave them alone. Others have implemented rigorous “Preventive Maintenance” strategies to address performance problems on

scheduled basis. It is practically impossible with the maintenance

resources available on a site to visit each loop frequently enough to keep them all working optimally 100% of the time. There is no such single methodology, which monitors the performance of process as well as control system.

Corporations world wide are discovering that one solution to this problem based on the current conditions or performance of

these assets, maintenance is applied to only those that are misbehaving impacting the process negatively and costing business money.

This present work aims in finding how process control should be applied or improved to gain business benefits.

D. Objectives

The objectives of the present work are:

1. To understand the necessity of performance monitoring of Process Control System.
2. To identify the KPI's of Process Control Systems.
3. To devise performance monitoring methodology.
4. To implement and conduct trials through simulation using MATLAB

E. Motivation & Solution

In order to achieve the objectives of the present work we prepared the detailed survey report based on literature survey, user feed back & consultants' views. This detailed survey report gives the overall information about process control system. This comprehensive survey report also consists of various performance parameters, which include

- System overview
- Expansion requirements
- Standards
- Data analysis requirement
- Alarm requirement
- Data display
- Process control
- Operators interface
- Maintenance
- Quality Control

The collection of data based on this survey report from various process industries like Chemical, Petrochemical and Pharmaceutical.

F. Key Performance Matrices

Each plant has certain matrices that are important to the bottom line. It is important to prioritize loops in the plant so that engineering personnel can make the best use of their time they will be working on the area as that will give make the greatest economic impact to the plant.

Key performance matrices will vary from plant to plant. One possible set of performance matrices is the variability.

II. PROCESS CONTROL SYSTEM PERFORMANCE ANALYSIS METHODOLOGY

A. Analysis to Identify Control Improvements

Customer feed back is then transformed in to internal business metric that will be used to monitor and drive improvements in process performance. These are defined as key business drivers and are given below.

Key Business Drivers

- Use as metrics to assess performance.
- Quality = Product properties conform to customer wants, measured by C_p and P_p indices.
- % First pass, first quality yield = make product right the first time.
- Through put = Rate at which product is made.
- Cycle time = elapsed time from receiving raw material to shipping the finished product.
- % Uptime = Time process is available to run at full rates.

The first step is to receive feedback from the customer and transform it into specific business matrix or goals. (in terms of product quality, yield, throughput, uptime and so forth) This task requires a close working relationship with the customer and falls largely on operations management, but could include technical specialists as well.

B. Identify Key Product Properties and Process Variables

In the first step of the analysis the business metrics are transformed into key product properties (flows, pressures, temperatures etc..) that must be measured and controlled to ensure that

- ♦ Product quality meets the customer specifications.
- ♦ Production rates, uptime and cycle time are achieved so that product orders are filled on time.
- ♦ First-pass, first quality yields are achieved to minimize rework and costs

In other words, the key product properties and process variables are the ones that have the greatest impact on meeting the business goals. Prime examples of process variables are reactor temperature, reactor feed ratio, and distillation column temperature. Product properties are things like density and viscosity and may be measured and controlled on line or may be measured in the laboratory and not controlled directly. In the latter case we have to identify the process variables that have the greatest impact on the product property. In addition to identifying the key variables, the associated steady-state targets, or set points, and the allowable ranges of variability must be determined. It is then the job of the controls to maintain the key variables at their respective targets within the prescribed ranges of variability.

C. Identify the Need for Improved Measurement and Control

The second step in the analysis identifies which of the key variables are in need of improved control. Assessing variability does this; since reducing variability is the basis, on which we will achieve improved performance.

Impact of Process variability on Business goal is as given below-

- Better consistency in product properties ➤ Product quality

- Tighter conformance to desired set points > yield
- Run closer to constraints > through put
- Faster transitions from one grade to another > Cycle time
- Avoid Process conditions which lead to fouling etc > up time.

There are three ways we can reduce variability. They are -

- Make frequent adjustments to process by automatic control > APC
- Monitor key variables to signal special cause, identify cause and eliminate it > SPC
- Change the process.

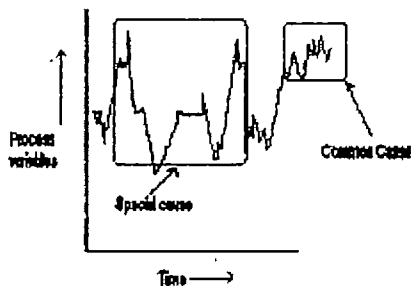


Fig. 1 Special cause and common cause variability

First, an understanding of the types of variability and their sources is necessary to determine how to reduce it. Special causes of variability are gross upsets in the process. Examples are large changes in raw material composition, operating blunders, and equipment malfunctions. It is the job of Statistical Process Control (SPC) to identify when a special cause has occurred so it can be identified and removed. Automatic Process Control (APC) on the other hand, compensates for these upsets by adjusting a process variable to counteract the effect. What actually occurs is the controls transfer the variability from where it matters to where it does not matter. For example, to maintain the reactor temperature, the controls will transfer the variability to reactor coolant flow and temperature. If feasible, chronic special causes should be removed rather than rely on control to compensate for them. However, the analysis described here identifies the improvements in process control that are needed to compensate for the special causes.

The other type of variability is called common cause variability and is inherent or built-in to the process. This kind of variability is frequent, random and generally small so it is sometimes referred to as 'process noise'. Some common causes are turbulence, machine vibration, steam supply pressure variations and small random variations in raw material composition. Process control is not recommended to compensate for common cause variability because it may result in over all control and create instability. A better approach is to identify the cause if it cannot be ignored and to make a process change to correct for it. For example, changing the process design, replacing equipment and adding damping or filtering to

the measurement to remove the variability are, often, remedies. The difference between the Special Cause and Common cause variability is shown below in Fig. 1

The range may be a product specification range for a quality variable or the allowable variability range for a process variable. Again the ranges are chosen to meet the business goals. C_p and P_p assume that the mean of the variable (also called average) is at the midpoint of the range. C_{pk} and P_{pk} are used when the variable is not midrange and it is important to reflect that, if the specification is one sided that is, there is either a high specification or a low specification.

The desired value for the indices depends on the needs of the customer but as a rule, a value of 2.0 is considered world class. A value of above 1.5 is also considered very good. Values of approximately 1.0 are just adequate and below 1.0 are poor.

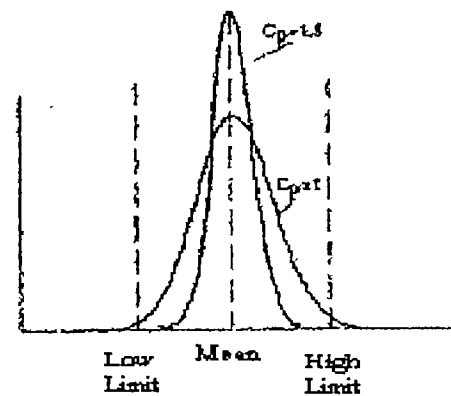


Fig. 2 Histograms Comparing C_p 's

Fig. 2. illustrates graphically the effect of the numerical value of the index. A value of 1.0 means that 99.73% of the data are within the specification if the mean is a mid range but there is no room for error in the process. A higher value allows some leeway in the position of the controller set point and allows some variation in the process without violating specifications.

The Capability Index is compared with the Performance Index to identify where control can be improved. The indices are calculated for each key product property and process variable and then compared, as per the capability and performance matrix as shown in Fig. 3 below.

		Does Performance meet capability?	
		No $P_p < C_p$	Yes $P_p \geq C_p$
Does Capability Meet Customer Needs?	No $C_p < \text{goal}$	Change Process Improve Control	Change Process
	Yes $C_p > \text{goal}$	Improve Control	Little Incentive For Improvements

Fig. 3 Capability and Performance Matrix

- If the capability index is below the goal, a process change is needed.
- If the performance index is less than capability, a process control improvement is needed.

D. Estimate Benefits for the Improvements

The final list of improvement opportunities may be large enough to require a prioritization to make sure funds and resources are used effectively. One method of prioritization is to rank candidate improvements according to stake and feasibility.

Prioritizing Opportunities

- Identify process control opportunities
- Estimate % reduction in variability
- Estimate impact on business drivers and estimate savings
- Assess feasibility
- Prioritize

The control assessment just completed may suffice to assess cost feasibility and technical feasibility. What may be needed in addition is to estimate the economic benefits to the business for each improvement. [8]

III. MATHEMATICAL MODELING OF CASCADE CONTROL OF JACKETED STIRRED TANK REACTOR.

The cascade control of jacketed stirred tank Reactor is shown in the Fig. 4 below. In this, the temperature of the reactor is measured and compared with the desired reactor temperature. The output of this reactor temperature controller is a set point to the jacket temperature controller. The jacket temperature controller manipulates the jacket flow rate. Notice that two measurements (reactor temperature and jacket temperature) are made but only one manipulated variable (jacket flow rate) is ultimately adjusted.

In this strategy, the reactor temperature controller is the primary (master or outer loop) controller. While the jacket temperature controller is the secondary (slave or inner loop) controller. This is effective because the jacket temperature dynamics are normally significantly faster than the reactor temperature dynamics. An inner loop disturbance, such as jacket feed temperature, will be 'felt' by the jacket temperature before it has a significant effect on the reactor temperature. This inner loop (secondary) controller then adjusts the manipulated variable before a substantial effect on the primary output has occurred.

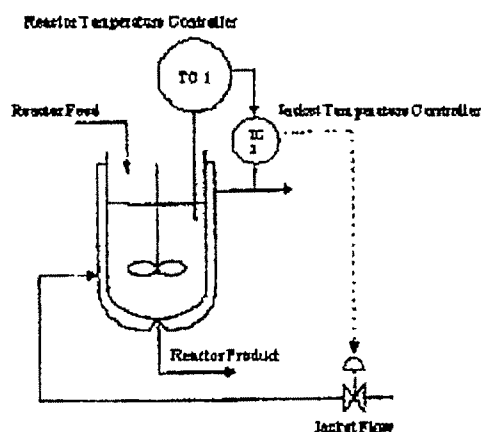


Fig. 4 Stirred Tank Reactor Cascade Control

IV. SIMULATION OF THE SYSTEM

A two state model for jacketed stirred tank reactor is built using 'SIMULINK', which is a very powerful block diagram simulation language. Here, reactor temperature is the key performance indicator, which is given to statistical process control algorithm. The simulation model for cascade control of a jacketed chemical reactor is shown in Fig. 5

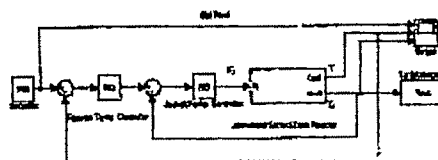


Fig. 5 The simulation model for cascade control of a jacketed chemical reactor

V. RESULT & ANALYSIS

System: Jacketed Stirred Tank Reactor.

Key Process variable : Reactor Temperature (T)

Set Point : 125°F, Lower Limit : 120°F, Upper Limit : 130°F

Sr No	System Status	C _p	P _p	Comment
1	Process disturbance	1.5185	0.1462	Improve Process & Control
2	Control Disturbance	3.2495	0.2866	Improve Control

Table 1 Test results of performance analysis using simulation model

Page 1
11Y39-41-204

$p = 100$;
 $q = 50$;
 $r = 200$;
 $s = 10$;
 $t = 5$;
 $u = 100$;
 $v = 50$;
 $w = 100$;
 $x = 50$;
 $y = 100$;
 $z = 50$;
 $aa = 100$;
 $ab = 50$;
 $ac = 100$;
 $ad = 50$;
 $ae = 100$;
 $af = 50$;
 $ag = 100$;
 $ah = 50$;
 $ai = 100$;
 $aj = 50$;
 $ak = 100$;
 $al = 50$;
 $am = 100$;
 $an = 50$;
 $ao = 100$;
 $ap = 50$;
 $aq = 100$;
 $ar = 50$;
 $as = 100$;
 $at = 50$;
 $au = 100$;
 $av = 50$;
 $aw = 100$;
 $ax = 50$;
 $ay = 100$;
 $az = 50$;
 $ba = 100$;
 $bb = 50$;
 $bc = 100$;
 $bd = 50$;
 $be = 100$;
 $bf = 50$;
 $bg = 100$;
 $bh = 50$;
 $bi = 100$;
 $bj = 50$;
 $bk = 100$;
 $bl = 50$;
 $bm = 100$;
 $bn = 50$;
 $bo = 100$;
 $bp = 50$;
 $bq = 100$;
 $br = 50$;
 $bs = 100$;
 $bt = 50$;
 $bu = 100$;
 $bv = 50$;
 $bw = 100$;
 $bx = 50$;
 $by = 100$;
 $bz = 50$;
 $ca = 100$;
 $cb = 50$;
 $cc = 100$;
 $cd = 50$;
 $ce = 100$;
 $cf = 50$;
 $cg = 100$;
 $ch = 50$;
 $ci = 100$;
 $cj = 50$;
 $ck = 100$;
 $cl = 50$;
 $cm = 100$;
 $cn = 50$;
 $co = 100$;
 $cp = 50$;
 $cq = 100$;
 $cr = 50$;
 $cs = 100$;
 $ct = 50$;
 $cu = 100$;
 $cv = 50$;
 $cw = 100$;
 $cx = 50$;
 $cy = 100$;
 $cz = 50$;
 $da = 100$;
 $db = 50$;
 $dc = 100$;
 $dd = 50$;
 $de = 100$;
 $df = 50$;
 $dg = 100$;
 $dh = 50$;
 $di = 100$;
 $dj = 50$;
 $dk = 100$;
 $dl = 50$;
 $dm = 100$;
 $dn = 50$;
 $do = 100$;
 $dp = 50$;
 $dq = 100$;
 $dr = 50$;
 $ds = 100$;
 $dt = 50$;
 $du = 100$;
 $dv = 50$;
 $dw = 100$;
 $dx = 50$;
 $dy = 100$;
 $dz = 50$;
 $ea = 100$;
 $eb = 50$;
 $ec = 100$;
 $ed = 50$;
 $ee = 100$;
 $ef = 50$;
 $eg = 100$;
 $eh = 50$;
 $ei = 100$;
 $ej = 50$;
 $ek = 100$;
 $el = 50$;
 $em = 100$;
 $en = 50$;
 $eo = 100$;
 $ep = 50$;
 $eq = 100$;
 $er = 50$;
 $es = 100$;
 $et = 50$;
 $eu = 100$;
 $ev = 50$;
 $ew = 100$;
 $ex = 50$;
 $ey = 100$;
 $ez = 50$;
 $fa = 100$;
 $fb = 50$;
 $fc = 100$;
 $fd = 50$;
 $fe = 100$;
 $ff = 50$;
 $fg = 100$;
 $fh = 50$;
 $fi = 100$;
 $fj = 50$;
 $fk = 100$;
 $fl = 50$;
 $fm = 100$;
 $fn = 50$;
 $fo = 100$;
 $fp = 50$;
 $fq = 100$;
 $fr = 50$;
 $fs = 100$;
 $ft = 50$;
 $fu = 100$;
 $fv = 50$;
 $fw = 100$;
 $fx = 50$;
 $fy = 100$;
 $fz = 50$;
 $ga = 100$;
 $gb = 50$;
 $gc = 100$;
 $gd = 50$;
 $ge = 100$;
 $gf = 50$;
 $gg = 100$;
 $gh = 50$;
 $gi = 100$;
 $gj = 50$;
 $gk = 100$;
 $gl = 50$;
 $gm = 100$;
 $gn = 50$;
 $go = 100$;
 $gp = 50$;
 $gq = 100$;
 $gr = 50$;
 $gs = 100$;
 $gt = 50$;
 $gu = 100$;
 $gv = 50$;
 $gw = 100$;
 $gx = 50$;
 $gy = 100$;
 $gz = 50$;
 $ha = 100$;
 $hb = 50$;
 $hc = 100$;
 $hd = 50$;
 $he = 100$;
 $hf = 50$;
 $hg = 100$;
 $hh = 50$;
 $hi = 100$;
 $hj = 50$;
 $hk = 100$;
 $hl = 50$;
 $hm = 100$;
 $hn = 50$;
 $ho = 100$;
 $hp = 50$;
 $hq = 100$;
 $hr = 50$;
 $hs = 100$;
 $ht = 50$;
 $hu = 100$;
 $hv = 50$;
 $hw = 100$;
 $hx = 50$;
 $hy = 100$;
 $hz = 50$;
 $ia = 100$;
 $ib = 50$;
 $ic = 100$;
 $id = 50$;
 $ie = 100$;
 $if = 50$;
 $ig = 100$;
 $ih = 50$;
 $ii = 100$;
 $ij = 50$;
 $ik = 100$;
 $il = 50$;
 $im = 100$;
 $in = 50$;
 $io = 100$;
 $ip = 50$;
 $iq = 100$;
 $ir = 50$;
 $is = 100$;
 $it = 50$;
 $iu = 100$;
 $iv = 50$;
 $iw = 100$;
 $ix = 50$;
 $iy = 100$;
 $iz = 50$;
 $ja = 100$;
 $jb = 50$;
 $jc = 100$;
 $jd = 50$;
 $je = 100$;
 $jf = 50$;
 $jj = 100$;
 $jh = 50$;
 $ji = 100$;
 $jj = 50$;
 $jk = 100$;
 $jl = 50$;
 $jm = 100$;
 $jn = 50$;
 $jo = 100$;
 $jp = 50$;
 $jq = 100$;
 $jr = 50$;
 $js = 100$;
 $jt = 50$

0713-99 ELI:AM KATLAS BROOKLYN #106-44 Page 1

27. 11/19/2008
28. 11/19/2008

40

14096

१०५

4.160

८५५-

4. 结论

1990

438E

• 1000 minutes per program control

中

The proposed methodology is a disciplined approach for improving the performance of a manufacturing process by identifying process control improvements aimed at bringing business value and not just ensuring smooth operation. This approach should not be applied only once but used for continuous improvement on a periodic basis. This is the only way to ensure that the benefits from process control are sustained over the long term. This proposed methodology monitors the performance indices as well as identifies improvements required, if any. This methodology has been analyzed with simulation studies.

We are highly grateful to Dr. A.A.Ghatol, Vice-chancellor, Dr. Babasaheb Ambedkar Technological University, Lonere (Maharashtra). The support extended by various companies allowing us to conduct the survey is gratefully acknowledged.

[1] Pradeep B. Deshpande and Raymond H Ash, "Computer Process Control," Second Edition, pp 1-30, ISA Handbook. U.S. (1988).
[2] Carlos A. Smith And Armando B. Corripio, "Principles & Practice Of Automatic Process Control," First Edition, John Wiley & Sons, Canada (1985).

- 51

Performance of Orifice Plates in Transient Cavitating Flow: Experimental Study

¹K.S. Sumam, ²S.G. Thampi, ³N. Sajikumar

¹ Sr.Lecturer in Civil Engineering, Government Engineering College, Thrissur-680009, Kerala, India and research scholar, NIT Calicut, Kerala, India
Email:sumamkottickatt@yahoo.com

² Assistant professor in Civil Engineering, NITC Calicut, Kerala, India

³ Assistant professor in Civil Engineering, Government Engineering College, Thrissur-680009, Kerala, India

Abstract-Transient cavitation is a widespread phenomenon occurring in piping system due to the drop of system pressure subsequent to pump failure or sudden change in operating condition of the system. Differential flow measuring devices based on the principle of pressure drop gives erroneous results in transient cavitating flow. This erroneous behaviour of flowmeters could result in grave problems like unacceptable proportioning of ingredients in chemical/pharmaceutical industry. In addition, it affects economy in the case of industries dealing with costlier liquids. This necessitates the evaluation of the performance of flow measuring devices during transient cavitating flow. Free gases may also get released in the system at low pressure in association with transient flow. In this study, an experimental approach is taken which qualitatively assess the performance of orifice plates in transient gaseous and vaporous cavitating flow.

Key words-Flow measurement, Pressure drop, Flowmeters, Bubbly flow

I. INTRODUCTION

THE use of square edged orifice plate has been well established in various industries for measuring fluid flow in normal conditions. This choice can be explained by its simple design, low cost and relatively significant accuracy achievable in measuring differential pressure. As a rule, flow meters are calibrated in fully developed pipe flow. For a practical use of the meter, existence of the same state of flow at the position of the meter must be secured. This requires providing certain lengths of straight pipe upstream and downstream of the meter, as specified in technical norms. These requirements are often not met in practice; the meter is then subjected to flow that is not fully developed, and measurement errors arise [1]. In addition, sudden operating conditions of flow regulating devices (transient conditions) will also disturb the flow profile. The effects of upstream velocity profile upon the performance of orifice flow meters have always been important in flow measurement [2]. Besides, flow in industrial piping system often contain small amount of gases either in free or in dissolved form. When the system undergoes fast depressurization during transient flow, flashing of dissolved gases in the liquid phase occurs ([3], [4]). The presence of

even a small amount of free gas - entrained or released - in the liquid increases the compressibility appreciably compared to that in pure liquid. This in turn reduces the speed of pressure wave in the flowing liquid [5]. The effect of free air on wave speed is more significant under low pressure conditions when its volume is greater than that under high pressure conditions. When pressure reduces beyond the vapour pressure of the flowing liquid it evaporates, transforming single phase flow into multi- phase, thereby maintaining the line pressure at vapour pressure [6]. Hence it is obvious that the accuracy of a standard orifice plate can be affected by a multitude of factors, such as swirl, sudden change in the axial velocity profile (transient condition), presence of second phase, turbulence, flow conditioner orientation, and placement. The present study evaluates the performance of orifice plate during transient cavitating flow.

II. PRINCIPLE OF FLOW MEASUREMENT

The principle of the method of measurement is based on the fact that insertion of the orifice plate into a pipe line in which a fluid is running full, causes a static pressure difference between the upstream side and the throat or downstream side of the device. The rate of flow can be determined from the measured value of this pressure difference and from a knowledge of the characteristics of flowing fluid as well as circumstances under which the device is being used.

The rate of flow can be determined using the following formula [7], which is given below.

$$q_m = \alpha \xi \frac{\pi}{4} d^2 \sqrt{2 \Delta p \rho} \quad (1)$$

in which q_m is the mass flow rate, α the flow coefficient, ξ expansion factor, d the diameter of the orifice, Δp the differential pressure (dp) and ρ is the density of the flowing fluid. Due to the transient condition, the normal pressure of the flowing system gets fluctuated leading to the reduction of flow rate. In addition, presence of a little percentage entrained air in the system and the gas release due to low pressure transients will also decrease the performance of the flow meters. How the interaction of gas bubbles and a liquid affects the functioning of a valve is investigated [8]. In this study, the density of the gas-liquid mixture was considered to be a function of the pressure. It was observed

that the presence of bubbles in the flow, produce a blocking effect due to the expansion of bubbles consequent to reduction in pressure. This reduces mass flux up to ten percentages. Similarly, the differential flow meters which were designed for the flow measurement of single phase fluid will not behave in normal way in the presence of small fraction of gases though its volume fraction is very less. In this connection, the amount of error or the necessary correction factors introduced in the measuring system are of very high magnitude. The present study qualitatively assesses the differential pressure rise across the orifice during transient condition.

III. DETAILS OF EXPERIMENTAL STUDY

The experimental work was carried out at an installation in the Water Flow Laboratory of Fluid Control Research Institute (FCRI), Palakkad, India. The schematic diagram of the experimental set up is as shown in Fig.1. A constant rate of flow was maintained in the pipe from a constant head tank with a head of 17.0m.

The line pressure at the upstream end was measured using a static pressure gauge. Flow rates in the line were adjusted using the control valve (CV), which was fitted at the downstream end of the pipe after the QAV (Fig.1). Sufficient time was given during every run for the development of steady flow conditions before the commencement of the valve operation. The entire sets of experiments were conducted at ambient temperature which varied between 31 to 33°C.

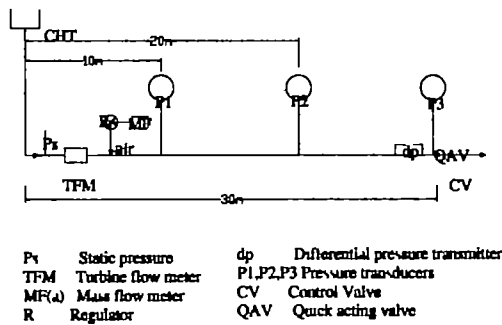


Fig. 1 Schematic diagram of the experimental setup (FCRI)

Transient cavitating flow was generated by the sudden closure of a butterfly valve (QAV) mounted at the end of the pipe. The valve closure time was measured by means of a photo switch and was found to range from 0.02 to 0.021s in all the tests. This time is less than or equal to the period of the pressure wave.

A. Data collection and instrumentation

A data acquisition system (DAS) with a resolution of 12-BITS is used. The capability of the DAS card is 12.5 lakhs sample/second. The sampling rate is constant for single channel or multiple channels. An important factor that affects the shape of the pressure characteristics is the time interval Δt at which pressure is recorded. Hence the time interval chosen to record pressure oscillations following cavity collapse should be no longer than 10^{-5} s [6]. The pressure

transducers were selected based on the expected maximum pressure at the points where pressure is measured along the pipeline. On the upstream side, a static pressure gauge having linear performance characteristics was fitted for measuring the steady state pressure. A Turbine Flow Meter (TFM) was used to measure the water flow rate. The unit of display of the TFM was shown as frequency in Hz. Discharge measurement was also checked gravimetrically. Compressed and regulated air flow rate was measured by using a Mass Flowmeter (MF). The specifications of pressure transducers, TFM, and MF are given in Table 1.

B. Initial Setting of the Experiment

The steady state velocity v_0 varied from 0.3m/s to 1.35m/s, facilitating different initial pressures at the terminal valve. Initial velocity and pressure in the system were controlled by means of the control valve (CV). Online density and temperature measurements were carried out continuously. The pressure transducers P1 and P2 (Fig.1) were also used to measure pressures during the transient condition.

Table.1 Specification of the Components of the Experimental Setup

Equipment	Quantity	Display Unit	Calibration Equation	Uncertainty
Pressure Transducer-P1	Pressure (0-12 bar)	0-10 volt	$1.1942 \times \text{volt} - 0.0507$	$\pm 0.02 \text{ bar}$
Pressure Transducer-P2	Pressure (0-25 bar)	0-10 volt	$2.488 \times \text{volt} - 0.2917$	$\pm 0.026 \text{ bar}$
Turbine Flowmeter (TFM)	Discharge (0-50 m ³ /hr)	Hz	Frequency/38.12	$\pm 0.01 \text{ Hz}$
Thermal Mass Flowmeter (MF)	Mass flow rate (0-22 lpm)	Direct	Direct	$\pm 0.1\%$

C. Measurement of Friction Factor for G.I Pipe

The pressure drop in steady state between points 1 and 2 (Fig.1) were measured for different flow rates by using the pressure transducers P1 and P2. The flow rate was regulated by adjusting the control valve (CV). The length of the pipeline between the pressure transducers P1 and P2 was also measured. The Darcy-Weisbach equation was then used for calculating the friction factor f for these pipes.

D. Experimental Data Collected in the Study

Transient conditions were created by the sudden closure of a quick acting valve (QAV), which was fitted at the downstream end of the G.I pipe with internal diameter $D = 52.76 \text{ mm}$, Length $L = 30 \text{ m}$, wall thickness $e = 3.7 \text{ mm}$. Orifice plate used has a beta ratio of 0.5. As qualitative assessment of performance of orifice meter under transient cavitating flow is envisaged, the experiments were conducted under two phase flow condition. The two phase flow condition was to examine cavitating flow, was generated by introducing air into the liquid flow.

IV. RESULTS AND DISCUSSIONS

As qualitative assessment of performance of orifice plate under cavitating flow was envisaged, the experiments were to be conducted under two phase flow condition. The two phase flow condition, so as to simulate the flow under cavitating flow, can be generated by introducing the air into the flow. As the flow is directly proportional to the differential pressure (dp), the variation of dp had to be analysed for different flow conditions. Hence, experiments were conducted for different flow rates of water and air. Pressure curves were measured instantaneously at the valve as well as across the orifice plate by means of pressure transducers shown in the Fig.1.

Two sets of experiments were carried out. In the first case (Table.2), air mass fraction was fixed as a constant value and water flow rate was varied from 0.0032 to 0.0039 in three steps. The column number (4) of Table.2 indicates how shall the maximum dp across the orifice vary with respect to the flow rates. Fig. 2 shows such variation. It was found that the maximum differential pressure across the orifice during transient condition increases with flow rate. Column number (5) of the same table indicates the variation in maximum dp occurred after the pass of negative phase of pressure wave. These dp values are higher than the respective values in the fourth column, indicative of the increase in dp under cavitation. In order to verify the presence of cavitation, the pressure variation noted at the quick acting valve for a typical case (E3) is plotted in Fig.3. The second peak in the variation of pressure has a higher peak than the first, and hence, validates the proposition that cavitation has occurred. A typical variation of dp across the orifice is also plotted in Fig.4. As could be seen from the figure that the dp varies drastically during transients; the variation is hectic in case of cavitation.

When the water flow rate increases, pressure drops to sub atmospheric and a high magnitude, secondary pressure peaks (up to 12 bar) occurs, once the negative wave passes (Table 2, Fig. 3 and Fig.4). It is approximately 16 times higher than steady state differential pressure. However, this dp variation could not be indicative of the flow variation as flow reversal with such large magnitude could not happen instantaneously.

In the second case (Table. 3), water flow rate was fixed as a constant value and air mass fraction was increased. Differential pressure across the orifice was measured and plotted against air flow rate (Fig. 5). It was found that differential pressure, beyond certain percentage of air mass flow rate, drops down with sharp slope. It might be due to the heterogeneity of air-water mixture when air mass fraction was increased. i.e. the flow changes from homogeneous flow of air-water mixture into layered flow. In addition, compressibility is directly affected by the increase in air content. The reduction in the ratio of maximum differential pressure to steady state dp also decreases with the increase in air mass flow rate. All these can be explained in terms of the reduction in water hammer pressure due to the increase in air content and consequent increase in compressibility.

All these results point towards the uncertainties involved in the measurement techniques based on the differential pressure while it is being used under transient and

cavitating conditions. A point to be noted that even the transient flow could affect the differential pressure to larger extent. Hence, the flow measurement during transient condition, which is inevitable in normal situation in a industrial flow line, can lead to instantaneous erroneous results to the extent of many folds. Though the current study does not assess the error involved in the measurement of flow, it qualitatively indicates even low transients can also lead to erroneous results.

Table. 2 Study of Differential Pressure Variation Across the Orifice plate for Increasing Water Flowrate

Experimental Run	Water Flow Rate (m ³ /s)	Air Flow rate (In mass fraction)	Maximum dp Across Orifice		dp/ (dp) _s
			First peak	Second Peak	
E ₁	0.0032	0.034	4.23	2.58	3.4
E ₂	0.0036	0.034	5.9	12	15.8
E ₃	0.0039	0.034	8	12	15.8

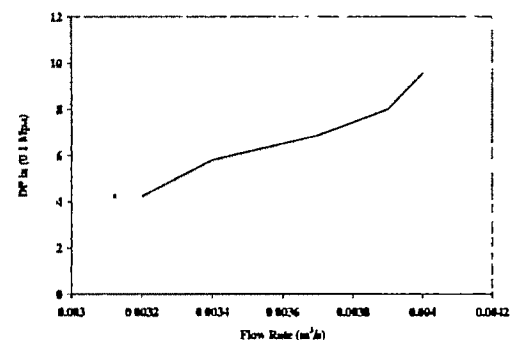


Fig. 2 DP variation across the orifice plate with increasing water flow rate (Table.2)

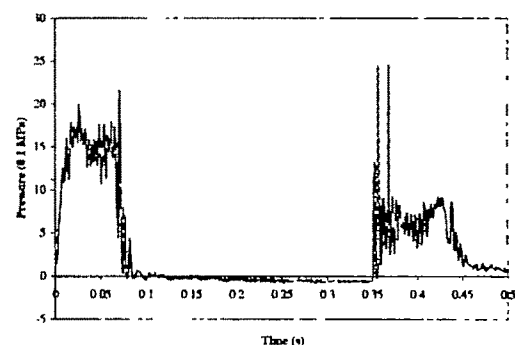


Fig. 3 Pressure peak at valve (Table. 2, E3))

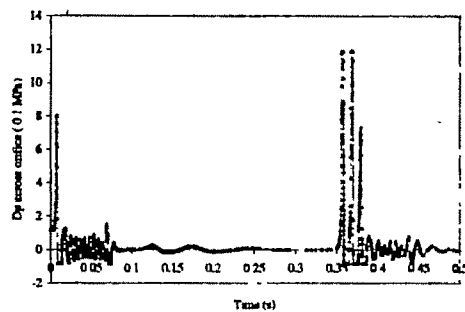


Fig. 4 dp variation across orifice plate (Table. 2, E3))

Table. 3 Study of Differential Pressure Variation Across the Orifice plate for Increasing Air Flowrate

Experi- mental Runs	Water Flow Rate (m ³ /s)	Air Flow Rate (In mass fraction)	Maximum dp Across Orifice		Ratio dp/ (dp) _s
			First peak	second peak	
E ₁	0.004	0.032	9.55	12	12
E ₂	0.0038	0.055	8.2	5	8.2
E ₃	0.0038	0.08	7.5	1.5	7.5
E ₄	0.0038	0.1	7.0	0.5	7
E ₅	0.0038	0.13	1.5	0.2	1.5

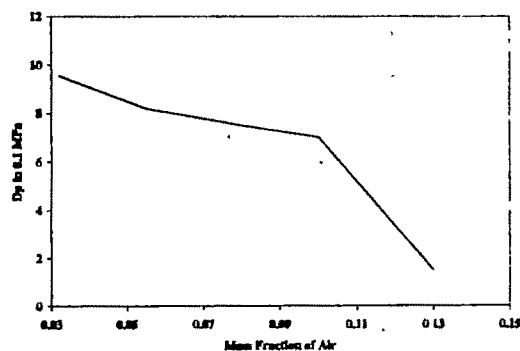


Fig. 5 Maximum DP across the orifice Vs mass fraction of air under constant flow rate of water

V. CONCLUSION

The use of orifice meter in transient cavitating conditions can lead to erroneous instantaneous flow estimation, amounting to many folds of the normal flow. Hence, the orifice meter is to be cautiously used where the chance of occurrence of transients and cavitation is more.

ACKNOWLEDGMENT

The authors acknowledge the financial assistance provided by the Kerala State Council for Science, Technology & Environment (KSCSTE) to carry out this work. The writers also acknowledge the Fluid Control Research Institute, Kerala, India for having spared their facility in conducting the experiment.

REFERENCES

1. C. Wildemann, W. Merzkirch and K. Gersten "A universal, nonintrusive method for correcting the reading of a flow meter in pipe flow disturbed by installation effects", *Trans. of ASME, Fluids Engrg.*, 2002, vol. 124, pp. 650-656.
2. C.L. Morrison, K.R. Hall, M.I. Macek, L.M. IHFE, L.L. DeOTTF and J.F. Haugliif "Upstream velocity profile effects on orifice flow meters, *Flow Meas. Instrum.*, 1994, vol.5, no.2, pp. 87-92.
3. J. A. Swaffield, "A study of the influence of air release on column separation in an aviation cavitation kerosene pipeline," *Proc. Inst. of Mech Engrs.*, Thermodynamics and Fluid Mechanics Group, vol. 186, pp. 693-703, 1972.
4. C. Kranenburg, "Gas release during transient cavitation in pipes," *J. of Hydr. Div.*, ASCE, vol. 100, pp. 1383-1398, 1974.
5. T. S. Lee and K. L. Ngho, "Air entrainment effects on the pressure transients of pumping systems with weir discharge chamber," *J. of Fluids Engrg.*, vol.124, pp.1034-1043, 2002.
6. Mitosek, M. (2000). Study of transient vapour cavitation in series pipe systems. *J. Hydr. Engrg.*, ASCE, 126(12), 904 - 911.
7. Measurement of fluid flow by means of pressure differential devices, Part 1, ISO 5167-1, 1991.
8. Campagne, C. V. L., Nicodemus, R., Bruin, G. J. D., and Lohse, D. (2002). A method for pressure calculation in ball valves containing bubbles. *J. Fluids Engrg.*, ASME, 124, 765-771.

Design of H_∞ based Robust Controller for AVR System

V. Mukherjee¹, Bijoy K. Mukherjee², and S.P. Ghoshal³

¹Electrical Engineering Department, Asansol Engineering College, Asansol, India, e-mail: vivek_agamani@yahoo.com

²Electrical Engineering Department, Asansol Engineering College, Asansol, India, e-mail: vj_bec@rediffmail.com

³Electrical Engineering Department, National Institute of Technology, Durgapur, India, e-mail: spghoshalnitdgp@yahoo.com

Abstract- In process plants, such as, thermal power plants, biomedical instrumentation etc. Proportional-Integral-Derivative (PID) controllers are being widely accepted. Proper tuning of such controllers is of prime requirement as far as their applications are concerned. Earlier works concentrate upon intelligent methods of tuning of such controllers. In the process of optimization of the PID controller gains, Particle Swarm Optimization (PSO) / Genetic Algorithm (GA) have been used as the optimizing tools. Researchers are modifying the PSO techniques with an aim to have better computational efficiency. Authors' earlier work deals with the determination of off-line, nominal, optimal PID gains of a PID controller of an Automatic Voltage Regulator (AVR) for nominal system parameters and step reference voltage input using modified PSO and binary coded GA. On-line terminal voltage response for varying off-nominal, on line system parameters has been obtained by applying fast acting Sugeno Fuzzy Logic (SFL). It has been also observed that the on-line computational burden of SFL is remarkably low.

However, in these works it has been observed that the controller parameters are required to be continuously updated their values with the change in system operating conditions. Even if we keep the controller parameter values constant, the system performance under change in reference voltage degrades substantially. On the other hand, fixed parameter robust controllers are capable of yielding satisfactory performance under continuously changing operating conditions.

The present work, thus, deals with the design of an H_∞ robust damping controller based on mixed- sensitivity theory for the AVR system so as to make the system insensitive to plant parameter variations as well as external disturbances. It is observed that the proposed H_∞ controller works satisfactorily under change in system operating conditions and system parameter variations. It is also found that the proposed H_∞ controller can also optimally eliminate the effects of external disturbances.

Key words — AVR, H_∞ optimal control, mixed-sensitivity problem, PSO

NOMENCLATURE

K_a amplifier gain

K_d	derivative gain of PID controller
K_e	exciter gain
K_g	generator gain
K_i	integral gain of PID controller
K_p	proportional gain of PID controller
K_s	sensor gain
$S(s)$	sensitivity function
$T(s)$	complementary sensitivity function
u	control output
$W_1(s)$	sensitivity weighting function
$W_2(s)$	uncertainty weighting function
y	measured output
$z = \begin{bmatrix} Z_1 \\ Z_2 \end{bmatrix}$	controlled output
ΔV_{ref}	incremental change in reference voltage
ΔV_t	incremental change in terminal voltage
ω	exogenous input
σ	singular value
τ_a	amplifier time constant (sec)
τ_e	exciter time constant (sec)
τ_g	generator time constant (sec)
τ_s	sensor time constant (sec)

I. INTRODUCTION

IN process control plants, chemical plants, power plants, Proportional-Integral-Derivative (PID) controllers are being extensively used owing to their simplicity. Past decades have witnessed ample advancements and researches in the arena of the application of PID controller in the process industries with an aim to mitigate the requirements of the end users. Improper tuning of such controllers requires a high degree of industrial expertise. For this reason, considerable interests are being paid towards the usage of intelligent approaches for the proper tuning of PID controllers. Neural Network [1], Fuzzy base approach [2], [3] Genetic Algorithm (GA) [4], Neuro-fuzzy approach [5], Evolutionary Computational techniques [6], [7] etc. are just a few among the numerous approaches adopted by the researchers for the tuning of the parameters of PID controllers.

Particle Swarm Optimization (PSO) [8], [9] is a population based evolutionary algorithm. The simulation of social behavioral pattern of organism, instead of the survival of the fittest, is the underlying concept of PSO. Here each candidate solutions (called *particles*) then fly through the search space. The velocity is constantly adjusted with the corresponding particle's and its companions' experience. It is expected that the particle will move towards better solution areas.

The issues of model uncertainty and disturbances were not directly addressed in the classical control paradigm. In classical control design, it is presumed that these effects are reduced by the use of feedback. However, in some cases where high quality control action is required, these issues are required to be addressed directly. Different robust control techniques started to evolve from such needs from early 1980's among which, H_∞ optimal control [10] is one. In H_∞ controller design technique, the plant uncertainty and external disturbances are considered & an optimized fixed parameter controller is obtained to meet the conflicting demands of stability under plant uncertainties and performance of the nominal model. The H_∞ controller yields satisfactory performance for all the plant models within a given bound.

In the present work, the following observations are made:

1. In the prevailing literature [6], [7] it is found that the PID controller parameters need to be changed with the change in operating conditions. It is also found that with the fixed gain settings of the PID controller, the system performance deteriorates considerably.
2. If we go for H_∞ controller to replace the swarm intelligent PID controller for AVR system, it is revealed that there is no such need of on-line tuning of the controller. At the same time, the required performance objective is fulfilled.
3. The H_∞ based controller also yields better disturbance rejection.

II. SYSTEM MODELING

The main cause behind the wide acceptability of PID controllers by the industry houses is lying in their simplicity. Its main focus here is reduction/elimination of steady state error as well as an improvement in the dynamic response. Reduction/elimination of steady state error is achieved by adding a pole at the origin with the help of integral controller, there by increasing the system type by one. Transient response improvement may be visualized from the action of derivative

controller which adds a finite zero to the open loop transfer function. As modeled in this paper, the transfer function of PID controller [7] is

$$G(s) = K_p + \frac{K_i}{s} + K_d s \quad (1)$$

Table I depicts parameters of PID controller & AVR model as considered in this work, transfer function of each item including limits of parameters [6]. In [6], Zve-Lee Gaing has

taken the generator transfer function as $\frac{K_g}{1 + \tau_g s}$ where K_g depends on load (0.7 to 1.0) and $1.0 \text{ sec} \leq \tau_g \leq 2.0 \text{ sec}$. The same model has been taken in the present work.

TABLE I
PARAMETERS OF PID CONTROLLER & AVR MODEL WITH
TRANSFER FUNCTION AND PARAMETER LIMITS

Item	Transfer Function	Parameter Limits
PID Controller	$G(s) = K_p + \frac{K_i}{s} + K_d s$	$0.2 \leq K_p, K_i, K_d \leq 2.0$
Amplifier	$TF_{\text{amplifier}} = \frac{K_a}{1 + \tau_a s}$	$10 \leq K_a \leq 40$ $0.02 \text{ sec} \leq \tau_a \leq 0.1 \text{ sec}$
Exciter	$TF_{\text{exciter}} = \frac{K_e}{1 + \tau_e s}$	$1 \leq K_e \leq 10$ $0.4 \text{ sec} \leq \tau_e \leq 1.0 \text{ sec}$
Generator	$TF_{\text{generator}} = \frac{K_g}{1 + \tau_g s}$	K_g depends on load (0.7 to 1.0) $1.0 \text{ sec} \leq \tau_g \leq 2.0 \text{ sec}$
Sensor	$TF_{\text{sensor}} = \frac{K_s}{1 + \tau_s s}$	$0.001 \text{ sec} \leq \tau_s \leq 0.06 \text{ sec}$

III. AVR WITH PID CONTROLLER

Incorporating the models of Table I, a composite AVR system along with PID controller is obtained. The block diagram representation is shown in Fig. 1. Equation of the incremental change in terminal voltage with an incremental change in reference voltage input is as in (2).

$$\left[\Delta V_{\text{ref}}(s) - \left(\frac{K_s}{1 + \tau_s s} \right) \Delta V_t(s) \right] \left[\left(\frac{K_a}{1 + \tau_a s} \right) \left(\frac{K_e}{1 + \tau_e s} \right) \left(\frac{K_g}{1 + \tau_g s} \right) \left(K_p + \frac{K_i}{s} + K_d s \right) \right] = \Delta V_t(s) \quad (2)$$

$$\text{i.e.} \quad \frac{\Delta V_t(s)}{\Delta V_{\text{ref}}(s)} = \frac{(s^2 K_d + s K_p + K_i)(K_a K_e K_g)(1 + s \tau_s)}{s(1 + s \tau_a)(1 + s \tau_e)(1 + s \tau_g)(1 + s \tau_s) + (K_a K_e K_g K_s)(s^2 K_d + s K_p + K_i)} \quad (3)$$

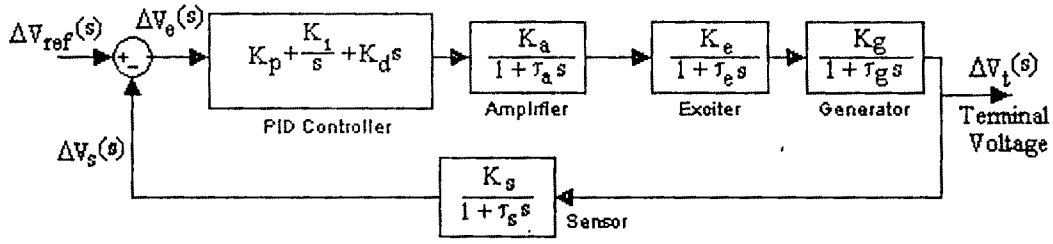


Fig. 1. Block diagram of AVR system along with PID controller.

IV. H_∞ MIXED-SENSITIVITY PROBLEM

In the mixed-sensitivity problem [10], the sensitivity function $S(s)$ and complementary sensitivity function $T(s)$ both are made small. Keeping $S(s)$ small implies good disturbance rejection and good reference (set point) tracking performance. Keeping $T(s)$ small, on the other hand, implies robustness with respect to multiplicative uncertainty and noise rejection.

However, the fundamental trade-off in such a design arises from the fact that $S(s) + T(s) = 1$, $\forall \omega > 0$ meaning that both the functions cannot be minimized at each frequency. In H_∞ mixed-sensitivity problem, a fixed order optimal controller is sought that makes $S(s)$ & $T(s)$ small in the sense of their H_∞ norm in low & high frequency ranges respectively. The sensitivity & uncertainty weighting functions $W_1(s)$ & $W_2(s)$ respectively gives a measure of the upper bound on $S(s)$ & $T(s)$ respectively.

Fig. 2(a) shows the block diagram representation of the mixed-sensitivity problem which is then cast into the general Linear Fractional Transformation (LFT) framework as shown in Fig. 2 (b) where the generalized plant P is given by as in (4).

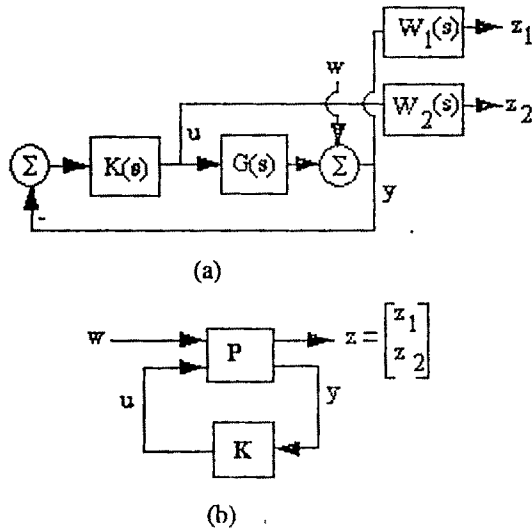


Fig. 2. Mixed-sensitivity problem. (a) Block diagram representation, (b) Linear Fractional Transformation representation.

$$P = \begin{bmatrix} W_1 & : & W_1 & G \\ 0 & : & W_2 & G \\ \dots & & \dots & \dots \\ -1 & : & -G \end{bmatrix} \quad (4)$$

The Transfer Function from $\omega \rightarrow z$ is then given by as in (5).

$$T_{zw} = P_{11} + P_{12}K(1 - P_{22}K)^{-1}P_{21} = \begin{bmatrix} W_1 S \\ W_2 T \end{bmatrix} \quad (5)$$

Keeping $\|T_{zw}\|_\infty < \gamma$ implies keeping $\|W_1 S\|_\infty < \gamma$ and $\|W_2 T\|_\infty < \gamma$, where γ is a small fraction. Here, $\|T_{zw}\|_\infty$ means that H_∞ norm of T_{zw} which is defined as $\|T_{zw}\|_\infty = \sup_\omega \bar{\sigma}(T_{zw}(j\omega))$ where $\bar{\sigma}$ denotes the maximum singular value. For SISO system, H_∞ norm is calculated as the peak value of the Bode magnitude plot. Though the weighting functions $W_1(s)$ & $W_2(s)$ directly come from the problem formulation, sometimes it is useful to treat them as tuning parameters for better design.

V. DESIGN OF H_∞ OPTIMAL CONTROLLER

In Fig. 3,

$$G(s) = \frac{K_a}{(1 + \tau_a s)} \times \frac{K_e}{(1 + \tau_e s)} \times \frac{K_g}{(1 + \tau_g s)} \times \frac{K_s}{(1 + \tau_s s)} \quad (6)$$

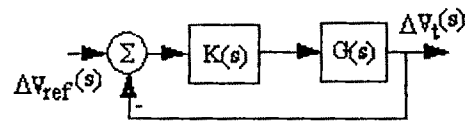


Fig. 3. Unity feedback structure of the AVR system.

The sensitivity weighting function, $W_1(s)$ is chosen for the present problem as in (7), corresponding to settling time ≤ 2.1 sec, % overshoot ≤ 2 % and steady state error to step input ≤ 0.5 %.

$$W_1(s) = \frac{25s^2 + 39.13s + 15.31}{s^3 + 5.247s^2 + 1.253s + 0.0766} \quad (7)$$

The uncertainty weighting function, $W_2(s)$ is chosen as in (8) based on the model uncertainty considered and with some trial and error.

$$W_2(s) = \frac{s^4}{10^8} \quad (8)$$

Frequency response of $W_1^{-1}(s)$ & $W_2^{-1}(s)$ is depicted in Fig. 4. From this figure it is observed that $|W_1^{-1}(s)| + |W_2^{-1}(s)| > 1.0, \forall \omega$

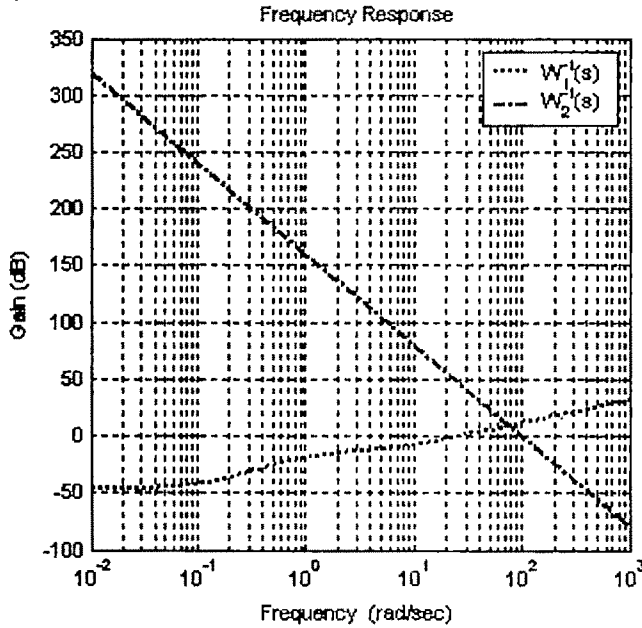


Fig. 4. Frequency plot of $W_1^{-1}(s)$ and $W_2^{-1}(s)$.

For these parameters an H_∞ controller is designed using robust control toolbox of MATLAB 7.1 [11]. The transfer function of the obtained H_∞ controller is given as in (9).

$$K(s) = \frac{234048.6599(s+100)(s+10)(s+2.5)}{(s+1.159)(s+1)(s+0.5987)} \quad (9)$$

$$= \frac{(s+5)(s^2 + 0.2475s + 0.01531)(s^2 + 224.6s + 1.553 \times 10^4)}{(s^2 + 50.58s + 1.013 \times 10^4)}$$

VI. SIMULATION RESULTS & DISCUSSIONS

From the earlier work [7], optimal transient response characteristic in respect of step response of incremental change in terminal voltage for the AVR system with varying

values of K_g & τ_g ($K_g = 0.7, \tau_g = 1.0$); ($K_g = 0.8, \tau_g = 1.2$); ($K_g = 0.9, \tau_g = 1.4$); ($K_g = 1.0, \tau_g = 2.0$)) is shown in Fig. 5. This figure indicates that the system performance deteriorates with the change in K_g & τ_g values. Thus, it is clear that the controller requires continuous tuning under varying load condition.

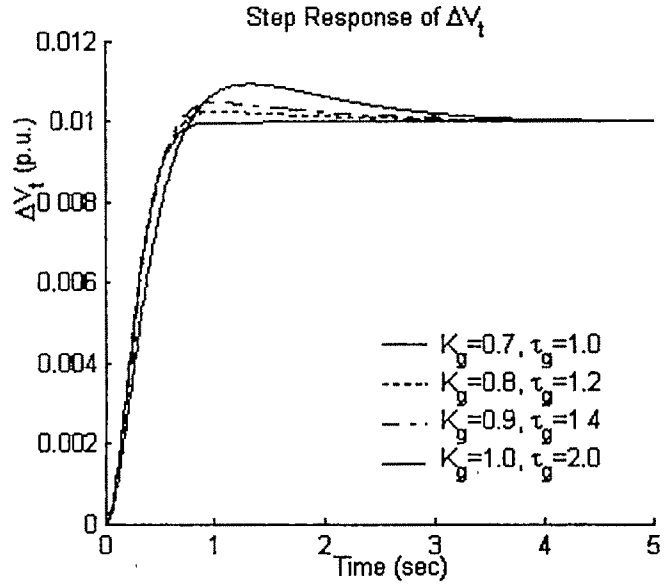


Fig. 5. Step response of incremental change in terminal voltage of PID controller based AVR system for different values of K_g & τ_g .

In Fig. 6, step response of incremental change in terminal voltage of the H_∞ optimal controller based AVR system for varying load conditions (same parameter variation as in Fig. 5) is shown. From Fig. 6 it is clear that the system performance remains almost unaltered under system parameter variations.

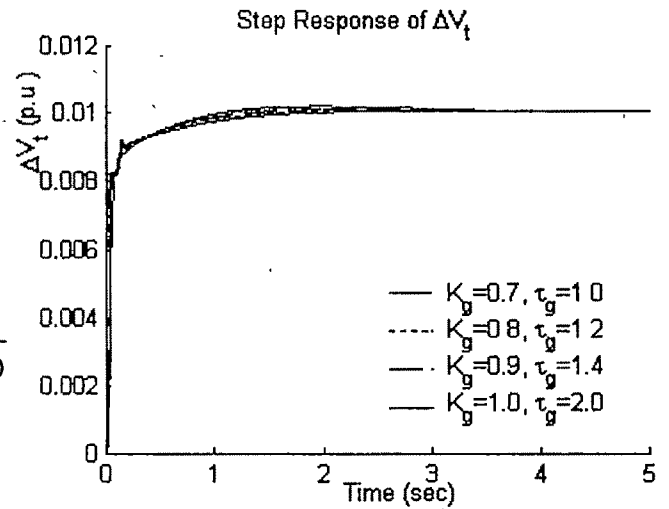


Fig. 6 Step response of incremental change in terminal voltage of H_∞ controller based AVR system for different values of K_g & τ_g .

The Bode magnitude plot of the sensitivity functions of the closed loop system considering PID controller and H_{∞} controller based AVR system is shown in Fig. 7. showing better disturbance rejection for the H_{∞} controller based AVR system.

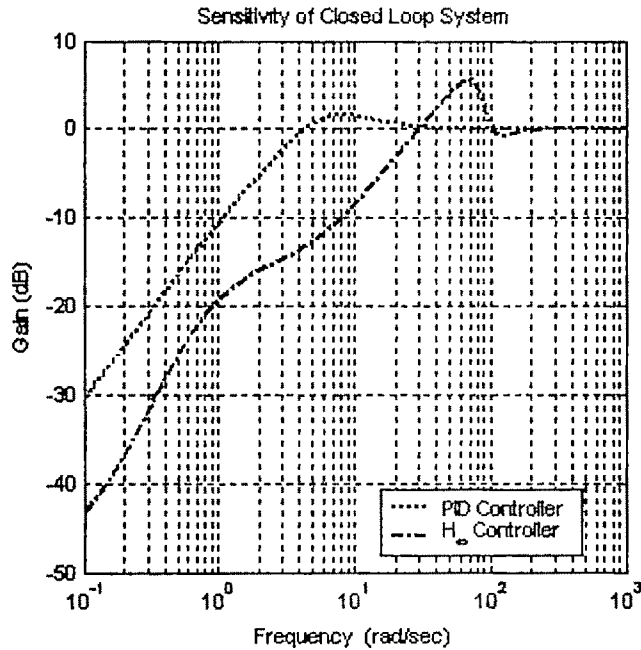


Fig. 7. Bode magnitude plot of the sensitivity functions of the closed loop systems.

VII. CONCLUSION

The present work concludes with the followings:

- a) Swarm intelligent PID controller parameters for the AVR system need to be changed with the change in operating conditions. The system performance deteriorates considerably with the fixed gain settings of the PID controller for the AVR system.

- b) Replacement of the swarm intelligent PID controller by H_{∞} controller for AVR system needs no on-line tuning of the controller. H_{∞} controller performs faithfully within the prescribed objective criterion.
- c) Better disturbance rejection in H_{∞} based controller is noticed.

REFERENCES

- [1] Q. H. Wu, B. W. Hogg and G. W. Irwin, "A neural network regulator for turbo generators," *IEEE Trans. Neural Networks*, vol. 3, 1992, pp. 95-100.
- [2] S. H. Qin and G. Borders, "A multi-region fuzzy logic controller of nonlinear process control," *IEEE Trans. Fuzzy System*, vol. 2, 1994, pp. 74-81.
- [3] George K. I. Mann, Bao-Gang Hu, and Raymond G. Gosine, "Analysis of direction fuzzy PID controller structures," *IEEE Trans. Systems, Man, and Cybernetics-Part B*, 29 vol. 3, 1999, pp. 371-388.
- [4] R. A. Krohling and J. P. Rey, "Design of optimal disturbance rejection PID controllers using genetic algorithm," *IEEE Trans. Evolutionary Computation*, vol. 5, Feb. 2001, pp. 78-82.
- [5] Ganesh Kumar Venayagamoorthy, Ronald G. Harley and Donald C Wunsch, "Implementation of adaptive critic-based neurocontrollers for turbo generators in a multimachine power system," *IEEE Trans. Neural Networks*, vol. 14, issue 5, Sept. 2003, pp. 1047-1064.
- [6] Zwe-Lec Gaing, "A particle swarm optimization approach for optimum design of PID controller in AVR system," *IEEE Trans. Energy Conversion*, vol. 19, issue 2, June 2004, pp. 384-391.
- [7] V. Mukherjee and S. P. Ghoshal, "Intelligent particle swarm optimized fuzzy PID controller for AVR system," *Electric Power System Research*, available on line, 8 January 2007.
- [8] J. Kennedy, R. C. Eberhart, "Particle swarm optimization," in *Proc. IEEE Int. Conf. Neural Networks*, Perth, Australia, 1995, pp. 1942-1948.
- [9] R. C. Eberhart and Y. Shi, Eberhart "Particle swarm optimization: developments, applications and resources," in *Proc. IEEE International Conference Neural Networks 1995*; vol. 4, 1995, pp. 1942-1948.
- [10] K. Zhou and J.C. Doyle, *Essentials of robust control*. New Jersey: PrenticeHall, 1997.
- [11] *Robust Control Toolbox Users' Guide*. The Math Works Inc., USA, 2005.

Study of Energy Losses of a High Capacity Boiler and Design of Flue Gas Heat Recovery Unit for the Optimum Efficiency of a Thermal Power Plant

S. C. Bera¹, and M. S. Bhowmick²

¹ Instrumentation Engineering Section, Applied Physics, University of Calcutta, Kolkata - 700 009, India, e-mail: scb152@indiatimes.com,

² Assistant Plant Engineer & Energy Auditor, RCF Thal, Alibag- 402208, India, e-mail: msbhowmick776@rediffmail.com

Abstract— The efficiency of a thermal power plant or captive power plant mainly depends on the energy losses in the steam generation unit of the plant in addition to other losses in the steam turbine section. In the present paper the energy losses in the steam generation unit of a naphtha and natural gas based captive power plant have been studied. From the online data of a running plant, the probable losses have been calculated and it has been observed that the considerable part of the losses is due to the flue gas as well as the hydrogen content of fuel. Again the heat loss in flue gas is contributed by air leakage in rotary air (RA) heaters to a large extent. The theoretical equations used to calculate these losses are presented in the paper and from these equations the efficiency of the plant has been indirectly calculated. On the other hand, the efficiency has been calculated by direct method from the enthalpy of the output steam and the heat content of the fuel. The efficiency values obtained from these methods almost coincide. This ensures the accuracy of the loss calculations by indirect method. From these calculations an alternative technique to reduce the energy losses in place of the RA heater section and get the optimum efficiency of the plant has been suggested in the paper.

Key words— Captive power plant, Direct Method, Energy Conservation, Efficiency, Indirect Method, Rotary Air (RA) heater, Steam Generation Unit.

I. INTRODUCTION

IN a thermal power plant, demineralised and deaerated water is heated in the water tube of a boiler drum by burning solid, liquid or gaseous fuels in the furnace. In order to increase the efficiency of this power plant the flue gas obtained from the furnace is utilised to increase the temperature of combustion air in a heat exchanger. In many plants, the rotary air (RA) heaters [1 - 5, 7-9] are used to heat

the combustion air by flue gas. But the air leakage in rotary air heater produces a considerable amount of heat loss in the form of heat carried by the leakage air into the flue gas and also in the form of more electric energy consumed by the FD and ID fans to supply the leakage air. Again the increase in hydrogen content in the fuel produces increase of water vapour, which carries large amount of lost energy due to its higher value of latent heat and thermal capacity. These losses along with the other losses decrease the efficiency of the power plant. Hence improving this heat recovery process after Economiser sections may increase the efficiency of the power plant. This increase of efficiency of a power plant is directly related with the plant economy. So many works are still being reported on the performance and efficiency of a thermal power plant. Hiroshi Miyama¹, Hitoshi Kaji¹, Yasuo Hirose², Norio Arai [9] have analysed heat transfer characteristics of a rotary regenerative combustion system (RRX). N. Ghodsipour and M. Sadrameli [8] have performed experimental and sensitivity analysis of a rotary air preheater for the flue gas heat recovery.

In the present paper the energy losses in a steam generation unit of a typical naphtha and natural gas based captive power plant have been studied. From the online data of a running plant, the probable losses have been calculated and it has been observed that the flue gas and the hydrogen content of fuel are responsible for a considerable part of heat loss. Another important reason of heat loss is due to leakage air in rotary air (RA) heaters. The theoretical equations used to calculate these losses are presented in the paper and from these equations the efficiency of the plant has been indirectly calculated. From the enthalpy of the output steam and the heat content of the fuel, the efficiency has also been calculated by direct method. It has been observed that the efficiency obtained from indirect method almost coincides with that obtained from direct

method. This ensures the accuracy of the loss calculations by indirect method. From these calculations an alternative technique of improving the efficiency of the plant has been suggested in the paper.

II. METHOD OF APPROACH

A. Calculations of Heat Losses in RA heater:

Let the fuel flow rate in boiler furnace be A ton/h and the theoretical air requirement per ton of fuel for stoichiometric combustion of fuel be B ton. Therefore total theoretical air requirement for stoichiometric combustion of fuel will be (A*B) ton/h. But in practice, theoretical air is not sufficient for complete combustion. This excess air requirement depends upon the type of fuel as well as upon the design of the burners. Let the excess oxygen be a_1 % by volume, which is measured by online oxygen analyzer that is mounted in the path of flue gas exit from the boiler. Hence the percentage amount of excess air is given by the formula

$$b_1 = [a_1 / (21 - a_1)] * 100. \quad (1)$$

Therefore total air supplied to the boiler which is called the combustion air is given by,

$$C = (1 + b_1 / 100) * A * B \quad (2)$$

Normally 77% by weight of nitrogen and 23% by weight of oxygen are present in air. So in C ton combustion air, the amount of oxygen is 0.23 C ton.

In a RA heater, as the disk slowly rotates, some amount of cold air passes to the hot gas path due to seal leakage and also some amount of hot gas may directly mix with the cold air.

Let the amount of total flue gas be X tons, in which X_1 ton directly mixes with the combustion air and X_2 ton goes to stack which contains a_1 % oxygen by volume.

$$\text{i.e., } X = X_1 + X_2 \quad (3)$$

Let the total cold air discharges from the FD fan be Y ton, in which Y_1 ton directly goes to the furnace as a combustion air and Y_2 ton goes to the stack as a leakage air.

$$\text{i.e., } Y = Y_1 + Y_2 \quad (4)$$

Let the excess oxygen percentage at the outlet of RA heater be a_2 % by volume and furnace infiltration air leakage be Le_1 , which contains 23% oxygen by weight or 21% oxygen by volume. Now from the oxygen balance equation, oxygen supplied through the combustion air is equal to the total oxygen required for the complete combustion. Therefore,

$$a_3 X_1 + 0.23 Y_1 + 0.23 Le_1 = 0.23 C \quad (5)$$

Where, a_3 = excess oxygen percentage by weight = 23 $a_1/21$
Again from the total flue gas calculation,

$$X_2 = Y_1 + A + Le_1 \quad (6)$$

The oxygen balance equation at the outlet of RA heater is given by,

$$a_3 X_2 + 0.23 Y_2 = a_4 (X_2 + Y_2) \quad (7)$$

Where, a_4 = excess oxygen percentage by weight = 23 $a_3/21$

$$\text{Or, } Y_2 = [(a_4 - a_3) / (0.23 - a_4)] X_2 \quad (8)$$

Combining the equations (6) and (8), we get

$$Y_2 = [(a_4 - a_3) / (0.23 - a_4)] (Y_1 + A + Le_1) \quad (9)$$

Let the inlet flue gas temperature at RA heater be T_1 and the outlet flue gas temperature after heat transfer to cold air and mixing with leakage cold air from the RA heater be T_2 . Let the inlet cold air temperature be T_4 (which is the ambient temperature) and after heat gain from the RA heater combustion hot air outlet temperature be T_3 .

Hence the heat transfer by hot flue gas to the cold combustion air

$$= X_1 * C_{p1} * (T_1 - T_3) + X_2 * C_{p2} * (T_1 - T_2) + HL_1 \quad (10)$$

(where, HL_1 = heat loss in RA heater)

This heat is gained by the cold air and the total heat gained by the cold air

$$= Y_1 * C_{p3} * (T_3 - T_4) + Y_2 * C_{p4} * (T_2 - T_4) \quad (11)$$

where, C_{p1} , C_{p2} , C_{p3} , and C_{p4} are the specific heats at constant pressure in the respective temperature zones as stated in the above equations.

Therefore from the heat balance (10), & (11), we get

$$X_1 * C_{p1} * (T_1 - T_3) + X_2 * C_{p2} * (T_1 - T_2) + HL_1 = Y_1 * C_{p3} * (T_3 - T_4) + Y_2 * C_{p4} * (T_2 - T_4) \quad (12)$$

Neglecting the variation of Cp with temperature, $C_{p1} = C_{p2} = C_{p3} = C_{p4} = C_p$.

Therefore, (12) can be written as,

$$X_1 * (T_1 - T_3) + X_2 * (T_1 - T_2) + HL_1 = Y_1 * (T_3 - T_4) + Y_2 * (T_2 - T_4) \quad (13)$$

For Ideal Case, if we assume negligible infiltration of leakage air Le_1 into the furnace, and very small heat loss HL_1 in the RA heater compared to the heat transferred to combustion air, then (5), (6), (8) and (13) can be written as simplified forms by the following (14), (15), (16), and (17) respectively.

$$a_3 X_1 + 0.23 Y_1 = 0.23 C \quad (14)$$

$$X_2 = Y_1 + A \quad (15)$$

$$Y_2 = [(a_4 - a_3) / (0.23 - a_4)] * (Y_1 + A) \quad (16)$$

and

$$X_1 * (T_1 - T_3) + X_2 * (T_1 - T_2) = Y_1 * (T_3 - T_4) + Y_2 * (T_2 - T_4) \quad (17)$$

Combining (15), (16) & (17), we have,

$$X_1 * (T_1 - T_3) + (Y_1 + A) * (T_1 - T_2) = Y_1 * (T_3 - T_4) + [(a_4 - a_3) / (0.23 - a_4)] * (Y_1 + A) * (T_2 - T_4) \quad (18)$$

The equation (18) can be written as simplified form,

$$B_1 X_1 + B_2 Y_1 = B_3 \quad (19)$$

where $B_1 = (T_1 - T_3)$,

$$B_2 = [(T_1 + T_4 - T_2 - T_3) - (a_4 - a_3) * (T_2 - T_4) / (0.23 - a_4)]$$

$$\text{and } B_3 = [(a_4 - a_3) * (T_2 - T_4) / (0.23 - a_4)] - (T_1 - T_2) * A,$$

All of which are constants for a particular boiler at particular load conditions.

Therefore total energy loss due to leakage air = $Y_2 \times C_p \times (T_2 - T_4) / 1000$ MKCal/H

(20)

From (14), and (19), we can easily find the value of X_1 and Y_1 and from these two known values we can easily find the

amount of flue gas X_2 and the leakage air Y_2 from the equations (15) & (16) respectively. Solving these equations, we can easily diagnose the problem of RA heater & different losses.

B. Calculation of Heat Losses in other Units

Let us consider the following losses which are applicable to liquid, gas and solid fired boilers as per standard formulas:

- L1- Loss due to dry flue gas (sensible heat)
 - L2- Loss due to hydrogen in fuel (H_2)
 - L3- Loss due to CBD (Continuous Blowdown) flow
 - L4- Loss due to moisture in fuel (H_2O)
 - L5- Loss due to moisture in air (H_2O)
 - L6- Loss due to carbon monoxide (CO)
 - L7- Loss due to surface radiation, convection and others.*
- The following losses are applicable to solid fuel fired boiler in addition to above
- L8- Unburnt losses in fly ash (Carbon)
 - L9- Unburnt losses in bottom ash (Carbon)

C. Calculation of Boiler Efficiency by Indirect Method from Heat Losses

The efficiency is the difference between the energy input to the boiler and the heat losses calculated.

$$\text{Boiler efficiency} = 100 - (L1+L2+L3+L4+L5+L6+L7+L8+L9) \quad (21)$$

D. Calculation of Boiler Efficiency by Direct Method from Enthalpy of Steam

$$\text{Boiler efficiency} = \frac{Q \times (H-h)}{q \times \text{GCV}} \times 100 \quad (22)$$

Where, Q = Quantity of steam generated per hour (kg/hr)

q = Quantity of fuel used per hour (kg/hr)

GCV = Gross calorific value of the fuel (kCal/kg)

H = Enthalpy of steam (kCal/kg)

h = Enthalpy of feed water (kCal/kg)

III. CASE STUDY

The present study has been made in a typical steam generation plant of naphtha and natural gas based fertilizer plant at the Thal Unit of Rashtriya Chemicals and Fertilizers Limited, Maharashtra, India during running condition of the plant in order to examine the effect of RA heater losses and to investigate about the effect of RA heater on the efficiency of thermal power plant. A number of studies have been made of which the observations during April'2006 are listed in the following Table-I.

A. Experimental report of the effect of RA heater of the captive power plant at Thal Unit, India in April '2006:

TABLE-I

Fuel	Naphtha
Evaporation rate (T/H)	235.9
Fuel (Naphtha) Consumption (T/H)	A= 14.734
Air to fuel ratio (T/T)	B= 15.2

Excess O_2 % by vol / by wt. in RAH inlet	3.2/3.5
Excess air in RA heater Inlet (%)	17.8
Excess O_2 % by vol/by wt and air in RA heater Outlet (%)	5.5/6.0 35.5
Total Theoretical Combustion air (T/H)	A* B = 224.0
Total air with 17.8% excess air Furn. (T/H)	264.0
Hot air to windbox Temperature ($^{\circ}C$)	180
RA heater Inlet Temperature ($^{\circ}C$)	255
RA heater Outlet Temperature ($^{\circ}C$)	114.5
Ambient Temperature ($^{\circ}C$)	30
Atomizing steam flow rate (T/H) (appx.)	1.0

From (14), we get

$$X_1 * 0.035 + Y_1 * 0.23 = 264.0 * 0.23$$

$$\text{Or, } 35X_1 + 230Y_1 = 60720 \quad (23)$$

From (15), we get

$$X_2 = Y_1 + 15.7 \quad (24)$$

From (16), we get

$$Y_2 = [(0.060 - 0.035) / (0.23 - 0.060)] * (Y_1 + 15.7)$$

$$\text{Or, } Y_2 = 0.147 * (Y_1 + 15.7) \quad (25)$$

From (11), we get

$$X_1 * C_{p1} * (255 - 180) + X_2 * C_{p2} * (255 - 114.5) = Y_1 * C_{p3} * (180 - 30) + Y_2 * C_{p4} * (114.5 - 30)$$

$$\text{Or, } 75 C_{p1} * X_1 + 140.5 C_{p2} * X_2 = 150 C_{p3} * Y_1 + 84.5 C_{p4} * Y_2 \quad (26)$$

Now taking $C_{p1}=C_{p2}= 0.24$, $C_{p3}=C_{p4}=0.23$, the above equation is reduced to

$$18X_1 + 33.7X_2 = 34.5Y_1 + 19.4Y_2 \quad (27)$$

From (33), (34), and (36), we get

$$18X_1 + 33.7(Y_1 + 15.7) = 34.5Y_1 + 19.4 * 0.147 * (Y_1 + 15.7)$$

$$\text{or, } 18X_1 - 3.7Y_1 = -484.3 \quad (28)$$

Now solving (23), and (28), we get

$$X_1 = 26.5 \text{ T/H, } Y_1 = 260.0 \text{ T/H, } X_2 = 275.7, \text{ \& } Y_2 = 40.5 \text{ T/H.}$$

Total air flow = $Y_1 + Y_2 = 300.5 \text{ T/H}$ & leakage air = 40.5 T/H .

Also for this amount air leakage causes energy losses due to carrying heat = $40.5 * 0.23 * (114.5 - 30) / 1000 = 0.787 \text{ MKCal/H}$ i.e., **6296 MKCal/Annum** (taking 8000 Hours per annum).

B. Calculation of Heat Losses in other Units

- % Heat loss due to flue gas = $21.5 * 0.24 * (114.5 - 30) / 11500 = 3.79\%$
- % Heat loss due to hydrogen in fuel = $9 * 0.145 \{ 584 + 0.45(114.5 - 30) \} / 11500 = 7.06\%$
- % Heat loss due to CBD = $4.0 * (351 - 189) / (14.734 * 11500) = 0.38\%$
- % Heat loss due to moisture in air = $\{ 21.7 * 0.025 * 0.45(114 - 30) * 100 \} / 11500 = 0.2\%$ (Taking 0.025 Kg/Kg of dry air).
- % Heat loss due to other unaccounted losses likely unburnt, moisture in fuel, & radiation losses ($L4+L6+L7$) = 1.5% (approximately)
- For liquid & gaseous fuels $L8 \text{ \& } L9 = 0.0\%$

C. Calculation of Boiler Efficiency by Indirect Method from Heat Losses

$$\text{Boiler efficiency} = 100 - (3.79 + 7.06 + 0.38 + 0.2 + 1.5) = 87.07\% \quad (29)$$

D. Calculation of Boiler Efficiency by Direct Method from Enthalpy of Steam

Steam flow rate – 235.9 MT/H, Naphtha flow rate – 14.734 MT/H, Enthalpy of Final steam from boilers – 811 Kcal/Kg. Enthalpy of LT Inlet Water – 189 Kcal/Kg
Boiler Efficiency = $\{235.9 * (811 - 189) * 100\} / (14.734 * 11500) = 86.6\%$ (30)

IV. MODIFICATION OF THE PLANT TO INCREASE EFFICIENCY:

Since the different units of a Thermal Power Plant have fixed losses as discussed above which can not be reduced further even for best design, so the only means of increasing the efficiency of a thermal power plant is to economically reuse the lost heat carried by the flue gas. The heat carried by the flue gas consist of two major parts, one of which is the heat content of the water vapour and the other is the heat content of excess air of furnace and leakage air of RA heater. An alternative technique is using heat exchanger in place of RA heater. In this technique two heat exchangers instead of two RA heaters are proposed to be used, where heat exchanger (HEX-2) is used as a pre heater of the FD fan output air and heat exchanger (HEX-1) is used for reheating this pre heated air before it enters the furnace up to about 240 °C instead of 180 °C to 200 °C (depending on the boiler steam load) as in the case of RA heater systems. The ID fan is to be installed between HEX-1 and HEX-2 in order to avoid the effect of condensed water vapour. The corrosion effect of the condensed water vapour on the duct and chimney material may be avoided by using better water resistant material or by using a suitable water trap at the outlet of the HEX-2. The relevant calculations for heat exchangers of moderate efficiency of 80% are stated below.

A. Design Data of Heat Exchanger-1 Flue Gas side for full Load condition:

Design data of boiler with natural gas fuel:

Fuel	Natural Gas (NG)		Naphtha	
	MCR	75%	MCR	75%
Evaporation rate (T/H)	275.0	206.5	275.00	206.50
Fuel Consumption (T/H)	16.45	12.35	17.20	12.90
Air to fuel ratio (T/T)	17.35	17.35	15.2	15.2
Excess air in Furnace (%)	8.0	8.0	10.0	10.0
Excess air in RAH i/l (%)	10.0	10.0	12.0	12.0
Excess air in RAH o/l (%)	20.0	20.0	22.00	22.00
Total Comb. air (T/H)	285.5	214.3	261.4	196.1
Air to FD Fan (T/H)	308.3	231.4	287.5	215.7
RA heater Inlet air (T/H)	314.1	237.7	292.8	219.6
RAH Outlet air (T/H)	342.6	257.2	318.9	239.2
Leakage air in RAH	28.5	19.5	26.1	19.6
Total FD air flow (T/H)	336.8	250.9	313.6	215.7
Hot air to WB Temp (°C)	200	168	200	168
RAH Inlet Temp (°C)	272	251	272	251
RAH O/L Temp. (°C)	135	135	135	135
Flue gas at ID fan T (°C)	130	130	130	130

B. Calculation of Heat Losses according to Design Data with NG Fuel in other Units:

GCV of NG = 12000 Kcal/Kg.

m = Mass of dry flue gas in Ton/Ton of fuel = $(336.8 + 16.454) / 16.454 = 21.5$

II2 % in Naphtha = 24

Cp = Specific heat of superheated steam in kCal/kg °C = 0.45

Cp = Specific heat of flue gas in kCal/kg = 0.24

1) % Heat loss due to flue gas = $21.5 * 0.24 * (130.0 - 30) * 100 / 12000 = 4.30\%$

2) % Heat loss due to hydrogen in fuel = $9 * 0.24 * \{584 + 0.45(130 - 30)\} * 100 / 12000 = 11.32\%$

3) % Heat loss due to CBD = 0.0 %

4) % Heat loss due to moisture in air = $\{20.5 * 0.025 * 0.45(130 - 30) * 100\} / 12000 = 0.19\%$ (Taking 0.025 Kg/Kg of dry air).

5) % Heat loss due to other unaccounted losses (L4+L6+L7) = 1.5% (approximately)

6) For liquid & gaseous fuels L8 & L9 = 0.0%

C. Calculation of Boiler Efficiency by Indirect Method from Heat Losses

Boiler efficiency = $100 - (4.30 + 11.32 + 0.0 + 0.19 + 1.5) = 82.69\%$ (31)

D. Design of Heat exchangers & Calculation of Boiler Efficiency by Indirect Method in new scenario:

As the maximum air requirement for gas firing, so we should design heat exchangers HEX-1 & HEX-2 with higher air flow.

Let be the design data for HEX-1:

Air to FD fan = 308.3 T/H, LT outlet flue gas flow = $(314.1 + 16.5) = 330.6$ T/H, Inlet Temperature – 272 °C, Outlet Temperature – 140 °C, Ambient Temperature – 30 °C

NG contains (approximately)– 75% C & 24% H₂

In this flue gas, there is some water vapour present, which comes from H₂ in fuel (for NG & Naphtha) (and atomizing in steam for Naphtha firing). Total wt. of water vapour for NG = $(9 * 24 * 16.45) = 35.5$ T/H

Total heat given by flue gas in HEX-1 = $\{295.1 * 0.24 * (272 - 140)\} + \{35.5 * 0.45 * (272 - 140)\} = 11.457$ MKCal/H.

Let be the Design Data for Heat Exchanger-2 (HEX-2) in Flue Gas side:

Inlet Temperature – 140 °C, Outlet Temperature – 95 °C

Total heat given by flue gas – $295.1 * 0.24 * (140 - 95) = 3.187$ MKCal/H. With this heat, some parts of the water vapour will be condensed and given up latent heat with the sensible heat. If we consider 18 % of the water vapour are condensed, then heat given by water vapour = $\{35.5 * 0.45 * (140 - 100)\} + \{0.18 * 35.5 * \{540 + 1.0 * (100 - 95)\}\} + \{0.82 * 35.5 * 0.45 * (100 - 95)\} = 4.187$ MKCal/H.

Therefore total heat given up by the flue gas in HEX-2 side = $(3.187 + 4.187) = 7.374$ MKCal/H.

Let be the Design Data for HEX-2 in Combustion Air side:

If we take 80% overall heat transfer efficiency of exchanger, then heat taken by cold air of 30 °C and rise the temperature up to in HEX-2 bc = $\{0.80 * 7.374 * 1000 / (308.3 * 0.23)\} + 30$

=113.2 °C, by which HEX-2 approach will be in the range of 27-28 °C.

Let be the Design Data of Heat Exchanger-1(HEX-1) Combustion Air side:

If we take 80% overall heat transfer efficiency of exchanger, then heat taken by hot air of 113.2 °C and rise the temperature up to in HEX-1 be={0.80*11.457 *1000/ (308.3*0.23)} + 113.2 (approximately) = 242.5 °C, by which HEX-1 approach will be in the range of 30 °C.

Temperature Condition	HEX-1		HEX-2	
	Inlet	Outlet	Inlet	O/L
Flue gas from Boiler to HEX-1 & HEX-2 Temp. (°C)	272	140	140	95
Cold air from FD fan to HEX-2 & HEX-1 Temp (°C)	113.2	242.5	30	113.2

E. Calculation of Boiler heat Losses according to New Design Data with NG Fuel in new scenario:

- 1) % Heat loss due to flue gas = {(17.35*1.08) +1.0}*0.24* (95-30)*100/12000 = 2.56 %
- 2) % Heat loss due to hydrogen in fuel = [.82*9*0.24 {584 +0.45(95-30)} + {0.18*9*.24(95-30)}]*100/12000 = 9.26 %
- 3) % Heat loss due to CBD = 0.0 %
- 4) % Heat loss due to moisture in air = {18.7*0.025*0.45(95-30)*100}/12000 =0.10% (Taking 0.025 Kg/Kg of dry air).
- 5) % Heat loss due to other unaccounted losses likely unburnt, moisture in fuel, & radiation losses (L4+L6+L7)= 1.5% (approximately)
- 6) For liquid & gaseous fuels L8 & L9 = 0.0%

F. Calculation of Boiler Efficiency by Indirect Method from Heat Losses::

Boiler efficiency = 100 – (2.56 + 9.26 + 0.0 + 0.10 + 1.5) = 86.58 % (32)

G. Design Data of Heat exchangers (HEX-1 & HEX-2) & Calculation of Boiler Efficiency by Indirect Method from Heat Losses in new scenario with present Load Condition and Naphtha Fuel:

Temperature Condition	HEX-1		HEX-2	
	Inlet	Outlet	Inlet	O/L
Flue gas from Boiler to HEX-1 & HEX-2 Temp. (°C)	255	125	125	92
Cold air from FD fan to HEX-2 & HEX-1 Temp.(°C)	111.8	234.1	30	111.8

H. Calculation of Boiler Efficiency by Indirect Method from Heat Losses::

- 1) % Heat loss due to flue gas = 19.0*0.24* (92-30)/11500 = 2.46 %
- 2) % Heat loss due to H₂ in fuel = [.65*9*0.145* {584+0.45(92-30)} + {0.35*9*.145(92-30)}]/11500 = 4.76%
- 3) % Heat loss due to CBD = 4.0 * (351 – 189)/(14.734* 11500) = 0.38%
- 4) % Heat loss due to moisture in air = {19*0.025*0.45(92-30)*100}/11500 =0.11% (Taking 0.025 Kg/Kg of dry air.
- 5) % Heat loss due to other unaccounted losses = 1.5%

Boiler efficiency = 100 – (2.46 + 4.76 + 0.38 +0.11+1.5) = 90.79% (33)

Therefore increase in efficiency = 90.79 – 87.07= 3.72% (34)

Saving Calculation against RA heater:

If we now take the present steam specific consumption 0.865 MKCal/T of net steam, after installation of heat exchanger in place of RA heater increase in efficiency will be 3.72% and at that time specific consumption will be 0.8296 MKCal/H. Therefore fuel & power saving will be (0.865 – 0.8296) = 0.0354 MKCal/H.

If we take total boiler load is 450 T/H gross steam, then net steam is 358.4 T/H.

Therefore net fuel & power saving will be =0.0354 * 358.4 =12.687 MKCal/H, causes total energy saving per annum (taking 8000 hrs) be 101499 MKCal/H. (35)

V. DISCUSSIONS

From the calculation of efficiency by direct and indirect method as shown (29) & (30) is found that the efficiency value is almost the same in the two methods. This proves that different losses calculated by the theoretical (14 – 28) are almost accurate. The proposed technique tends to increase the efficiency of the plant by a considerable amount from 87.07 %to 90.79 %, which tends to compensate the cost increase due to use of higher cost material in the outlet duct and chimney.

REFERENCES

- [1] Babcock & Wilcox Co.: "Steam, Its Generation and Use"
- [2] Foster Wheeler Power Project Ltd: " Operation, Maintenance & Controls"
- [3] Babcock & Wilcox , USA - "Instruction Manual for watertubes boilers"
- [4] P. Chattopadhyay : " Boiler Operation Engineering (Questions & Answers)" McGrawHill Company, 2nd Edition, 2001.
- [5] Bela, G. Liptak: " Process measurement and Analysis" 3rd edition, Butterworth Heinman Ltd..
- [6] Energy Hand book, Second edition, Von Nostrand Reinhold Company - Robert L.Lofness
- [7] Furtado Heloisa Cunha, May Lain Le: "High Temperature Degradation in Power Plant and Refineries" Material Research: Vol-7, Issue-1, pp:103-110: 2004
- [8] N. Ghodsi-pour and M. Sadrameli: "Experimental and Sensitivity Analysis of a Rotary air Preheater for the flue gas heat recovery" Journal on ScienceDirect Applied Thermal Engineering, Volume 23, Issue 5, April 2003, Pages 571-580
- [9] Hiroshi Miyama ¹, Hitoshi Kaji ¹, Yasuo Hirose ², Norio Arai: "Heat transfer Characteristics of a rotary regenerative combustion system (RRX)" 1999 Scripta Technica, Heat Trans Jpn Res, vol. 27(8): 584-596, 1998.
- [10] K.R. Shanmugam, P. Kulshreshtha : " Efficiency analysis of coal based thermal power generation in India during post reform era" International Journal of Global Energy: Vol.-23, pp:15-28, 2005.
- [11] F.A. Polyvoda, V.I. Kabakov: " Two stage fuel oxidation and comparison of water catalytic boilers with Fluidised Bed and fixed layer" International Journal of Global Energy: Vol.-22, pp:51-56, 2004. Energy Hand book, Second edition, Von Nostrand Reinhold Company - Robert L.Lofness

A Report on Modification of Burner Management System of a Steam Generation Unit in Naphtha and Natural Gas based Fertilizer Plant

S. C. Bera¹ and M. S. Bhowmick²

¹ Instrumentation Engineering Section, Applied Physics, University of Calcutta, Kolkata - 700 009, India, e-mail: scb152@indiatimes.com,

² Assistant Plant Engineer & Energy Auditor, RCF Thal, Alibag- 402208, India, e-mail: msbhowmick776@rediffmail.com

Abstract— Burner Management System (BMS) is a safety system for power generation companies that enables the safe start-up, operation, and shut down of the multiple-burner furnace section of a boiler. A good burner management system increases personnel safety and improves furnace protection with its sequencing and interlocking control design. The systems are designed to meet national and international standards (like National Fire Protection Association (NFPA) 85C, ISA S84.01, TUV, and IEC 1508) and regulations and also for fail-safe operation. In the present paper an investigation has been carried out to improve the burner management systems of the thermal power plant. Some modifications have been carried out in the air register damper and gun retraction system of BMS. The modified system has already been installed in 275 MT/H capacity boilers. The advantage of the modified system in terms of the smooth safe operation, reliability, energy saving and efficiency of the thermal power plant has been presented in this paper.

Key words— Air Register Damper, Burner Management System (BMS), Efficiency, Gun Retraction System, Thermal Power Plant.

I. INTRODUCTION

A Burner Management System (BMS) is a safety system for thermal power plant that enables the safe start-up, operation, and shut down of the multiple-burner furnace section of a boiler. These systems are designed to work efficiently with a variety of fuels including natural gas, oil, pulverized coal, solvents, off gases, biomass and other solid fuels for maximum reliability, flexibility and safety of thermal power plant. These systems are also designed to meet national and international standards and regulations. The proper designing of BMS increases the overall efficiency of the power plant and also decreases the maintenance cost as well as smooth operation of boilers. The modern Burner Management System (BMS) is PLC based system and is implemented based on the logic for safe and reliable startup

operation and shutdown of burners in the boiler. This is used for complete combustion of fuel with proper mixing of combustion air in the furnace of thermal power plant. For safety purposes, fuel addition should be limited by the amount of available combustion air, and combustion air may need minimum limiting for flame stability.

Due to this proper design of BMS, there is always air rich mixture in furnace and hence leads to safe operation of boiler [1 - 6]. Many works [7 - 15] are still being reported on the performance and efficiency of a thermal power plant. K.R. Shanmugam, P. Kulshreshtha [12] have analysed the efficiency of coal based thermal power plants in India have indicated that the average Technical Efficiency (TE) is about 73%. F.H. Cunha & M. L. Le [7] have analysed the effect of high temperature in degradation of power plants. F.A. Polyvoda, V.I. Kabakov [11] have analysed the effect of power plant on pollution of environment.

In the present paper some modified scheme in air register damper and gun retraction system of BMS has been proposed in order to eliminate the problems of a typical PLC based Burner Management System. The first part of the work consists of identifying the problems of the system, which was already installed in a running plant at RCF, Thal Unit. In the second part of the work these problems have been analysed and the defects of the control system have been identified. In the third part of the work a modified burner management system has been incorporated keeping the other existing control loops logics. In the last part of the work this modified control system has been tested online. The report of all these works is presented in this paper. It has been observed that all the problems of the earlier systems have been eliminated.

II. CASE STUDY

Circular Naphtha / Gas Dual Fuel Burner:

The circular burners serve the purpose of atomizing the liquid fuel naphtha to a fine spray, mixing the fuel intimately with combustion air and impart to this mixture the turbulence necessary to ensure complete combustion. An electric igniter imparts the necessary ignition energy to start the combustion of the pilot flame. The burners have provision for firing gas through gas spuds that are so located that surround the atomizer assembly.

The essential components are as under:-

- A) Air register assembly
- B) Gun retraction system for naphtha burner with atomizer sprayer cap and diffuser
- C) Gas fired lighter assembly
- D) Gas burner
- E) Flame scanner
- F) Sliding view ports
- G) Associated components for control function.

A. Air Register Dampers:

The air register assembly consists of a series of vanes surrounding the diffuser axially. The vanes overlap each other in the closed position and are inter connected by a linkage arrangement such that all vanes, also called doors, are operable simultaneously by means of a power cylinder provided at the burner front. The vanes swing through 55 Degrees to the full open position. The purpose of the air register damper is to provide a swirling effect to the combustion air entering from the windbox. This swirling effect is essential for the intimate mixing of fuel and combustion air for complete and efficient combustion.

Closing of the air register damper results into increase in windbox to furnace differential pressure and consequent higher velocities of air entering from windbox. Besides, the entry of air from the register damper becomes more tangential. This increases the swirling of the atomized fuel. Thus, the air register provides a vital tool for adjusting the flame into a desired shape. The air register vanes can be adjusted shaft by moving the adjusting handle spanning 90 degree movement. The registers are designed to impart a clockwise or counter clockwise swirl, as seen from burner front.

The air register dampers are operated from the air register cylinder with Bells Positioner. There is a three-position feedback by two proximeter switches attached with this system to indicate 20 % and 100% opening.

B. Gun Retraction System

The naphtha burner is mounted centrally in the air register damper assembly. The burner assembly can be axially adjusted to shape the flame as desired and then the burner can be locked in position by a set bolt. On multi-burner installations, the diffuser can be withdrawn from the naphtha firing position when neither gas nor naphtha is being fired (this is called

retracted position). This ensures that the diffuser as well as naphtha gun tips are well protected from the direct heating of the furnace. Auto gun positioning system is provided to facilitate above. The burner coupling mechanism is such that it facilitates easy and quick removal of the burner gun whenever required.

An effective combustion of the fuel naphtha requires that the naphtha be atomized into fine particles and effectively mixed with the correct quantity of combustion air. The burner supplied, is fitted with Y jet atomizer tip and uses steam as the atomizing medium. The atomized fuel and air mix thoroughly by the swirling air passing through the diffuser. The pressure of the atomizing steam is always maintained 1.2 to 1.5 kg/cm² higher than the naphtha pressure. In order to supply correct quantity of steam over the operating range, a constant pressure differential control loop is provided to control the steam flow in proportion to the naphtha flow

Study of the Existing Air Register Damper & Gun Retraction System and Identification of the Operational Problems:

A. Air Register Dampers:

The original scheme is at burner startup, air register damper should be at 20 % opening position to let the pilot flame establish and once the pilot flame stabilized, fuel valve opens for this burner and air register damper starts opening to 100%. Again when burner is tripped or stopped, air register damper closes fully. For naphtha firing, after tripping of naphtha burner air register damper should be at 20% position for clearing sequence to be started to ensure that no fuel is present in the hose and in the gun. All the sequencing is done by two numbers of 3 way solenoid valves with two regulators, which are set at 0.4 Kg/cm² for 20% opening and at 1.2 kg/cm² for 100% opening to give the signal to positioner. Another regulator is set at 4.5 kg/cm² and is used to supply the air to positioner.

It was observed for many burners that after giving burner firing command, air register was not moving to 20 % position from fully closed position. However, pilot flame is coming smoothly, may be due to passing of air from register vanes.

PLC Logic Scheme for Air Register Damper operation:

For Burner-3C,

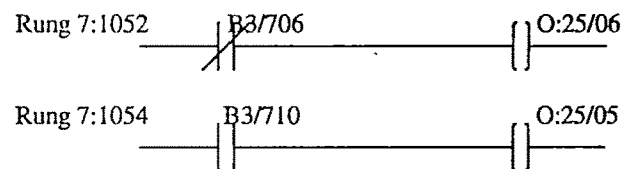
Outputs- O:25/05 & O:25/06

Inputs – I:33/14, I:33/05

For full closing: Both Outputs energized.

For 20% Opening: O:25/06 only energized and O:25/05 should be De-energised.

For 100% Opening: Both Outputs De-energised.



Problems Faced:

In the above type of air register damper operation, following problems are faced during startup of the burners.

- 1) Operation is not reliable as dampers get stuck up at different positions.
- 2) High failure rate of Bells positioner and also unavailability of this positioner spares. (Although single problem is not yet found in the cylinder).
- 3) Burner start-up problems. (Due to stuck up at 100%, pilot flame is not stabilised and as a result burners are not started and also clearing is not possible)
- 4) Air losses in positioner due to continuous venting.

B. Gun Retraction System:

In dual fired burners, gas is entered in the burner chamber from a separate pipe & after that it is distributed through 8 nos of guns of gas spuds for each burner, while Naphtha is entered along with atomizing steam through only one Naphtha gun. Gun retraction systems is used to position the Naphtha gun at different positions for different fuel firing conditions i.e., when burner is fired with natural gas, then gun position should be at gas position, for naphtha firing it should be at combination position and when burner is off it is at retracted position. There are three positions viz. retracted, gas and combination for feedback & three proximeter switches are used to indicate the three positions. Gas position is set at 2 to 3 inches behind the combination firing position for the very reason of protecting the naphtha gun spud from direct heating in case of gas firing. Retracted position is at sufficiently longer distance behind gas position.

Gas position is set at 2 to 3 inches behind the combination firing position for the very reason of protecting the naphtha gun spud from direct heating in case of gas firing. Retracted position is at sufficiently longer distance behind gas position.

PLC Logic Scheme for Gun Retraction System operation:

For Burner-3C,

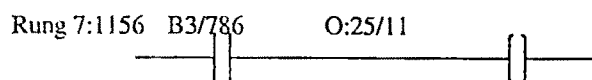
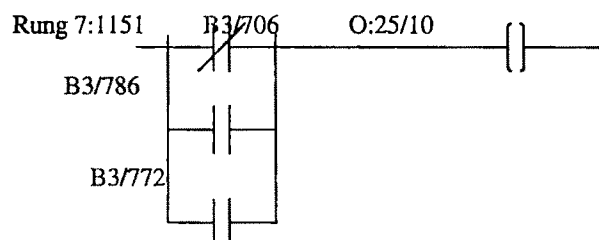
Outputs- O:25/10 (for Gas Position) & O:25/11 (for Naphtha & Combination Position)

Inputs – I:34/17 (for Retracted Position), I:33/06 (for Gas Position), & I:34/00 (for Naphtha & Combination Position)

For Retracted Position: Both Outputs De-energized.

For Gas Position: O:25/10 only Energized and O:25/11 should be De-energised.

For Naphtha & Combination Position: Both Outputs Energised.



Problem Faced:

To achieve these three positions, double piston & double cylinder type actuator is employed along with two 4-way solenoid valves. This system consists of many moving parts & is proved to be very prone to failure. At every start up or shut down of burner problems like gun stuck up, flexible air hose braking, proximity switch malfunction, stopper plate damage are observed.

III. MODIFICATIONS

A. Modified Scheme of Air Register Dampers:

After studying the above problems and brainstorming, the air register damper system is modified in one of the burners of one boiler. This is running successfully without any problems from few months.

The scheme is as follows:

- 1) Positioner is bypassed.
- 2) One 4-way SOV in place of two 3-way SOV is mounted for 100% signal.
- 3) One Air Filter Regulator is used in place of three regulators connected to supply the 4-way SOV.
- 4) Two air tubes directly connected to the cylinder for opening and closing from SOV.

PLC Logic Modified Scheme for Air Register Damper operation:

Output- O:25/11

Inputs – I:33/14, I:33/05

For full closing or setted position: O:25/11 energized.

For 100% Opening: O:25/11 De-energised.

Rung 7:1052 Deleted



By incorporating above modifications air register damper is now operated at two positions i.e. full open and setted position (i.e. at full close or at 10 – 20 % as per requirement).

B. Modified Scheme of Gun Retraction Systems:

After studying and analyzing above problems and also brainstorming, gun retraction system is being modified in one of the burner. The boiler is running successfully without any problems from few months. Starting and stopping of burner is verified many times and is successful.

The scheme is as follows:

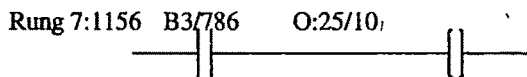
1. Gas position is removed. (i.e., naphtha gun remains at retracted position when burner is ON with gas firing). This will also ensure protection of naphtha gun spud from overheating.

2. As only two positions of gun are required, one 4-way SOV is used in place of two 4-way SOVs and T-off the air for both the cylinders (if required).

PLC Logic Modified Scheme for Gun Retraction System operation:

Output- O:25/10 (for Naphtha & Combination Position)
 Inputs – I:34/17 (for Retracted Position), & I:34/00 (for Naphtha & Combination Position)
 For Retracted Position: O:25/10 De-energized.
 For Naphtha & Combination Position: O:25/10 Energized.

Rung 7:1151 Deleted



By above modifications gun retraction system is now operated at two positions i.e. retracted position and naphtha combination position.

IV. EXPERIMENTS

The proposed modified air register damper and gun retraction system has been designed and incorporated in the PLC based conventional control system installed in the 275 MT/H capacity steam generation plant of RCF, Thal, Maharashtra, India. It has been observed that most of the difficulties of air register damper and gun retraction system remove as mentioned above. With this solution not only above problem solved, but also saving electrical energy, saving instrument air, reduction in inventory etc. are listed below.

Advantages and benefits of above modification for air register damper:

- 1) Positioner is not required i.e. reduced maintenance & maintenance cost as well.
- 2) Saving of instrument Air in the positioner due to continuous venting.
- 3) Saving power (current in one SOV, Relay).
- 4) Reduction in inventory of SOV, Relay, 2-regulators, one output, etc.

Advantages and benefits of above modification for gun retraction system:

- 1) Bypass gas position, minimize maintenance & maintenance cost.
- 2) Saving of instrument Air losses.
- 3) Saving power (current in one SOV, Relay.)
- 4) Spare savings of 4-way SOV, Relay, proximity switch & P&F amplifier, one output, one input, cables, tubing etc.
- 5) Protection of gun tip.

V. DISCUSSIONS

From the above modifications now BMS operation as well as maintenance procedure is improved. Now air register damper and gun retraction system of a burner is smooth operated and causes less/no burner starting problems in the boiler.

REFERENCES

- [1] Babcock & Wilcox Co.: "Steam, Its Generation and Use"
- [2] Foster Wheeler Power Project Ltd: " Operation, Maintenance & Controls"
- [3] Babcock & Wilcox, USA - "Instruction Manual for watertubes boilers"
- [4] P. Chattopadhyay : " Boiler Operation Engineering (Questions & Answers)" McGrawHill Company, 2nd Edition, 2001.
- [5] Bela, G. Liptak: " Process measurement and Analysis" 3rd edition, Butterworth Heinman Ltd..
- [6] Energy Hand book, Second edition, Von Nostrand Reinhold Company - Robert L Loftness
- [7] Furtado Heloisa Cunha, May Lain Le: "High Temperature Degradation in Power Plant and Refineries" Material Research: Vol.-7, Issue-1, pp:103-110: 2004.
- [8] N. Ghodsipour and M. Sadrameli: "Experimental and Sensitivity Analysis of a Rotary air Preheater for the flue gas heat recovery" Journal on ScienceDirect Applied Thermal Engineering, Volume 23, Issue 5, April 2003, Pages 571-580
- [9] Hiroshi Miyama¹, Hitoshi Kaji¹, Yasuo Hirose², Norio Arai: "Heat transfer Characteristics of a rotary regenerative combustion system (RRX)" 1999 Scripta Technica, Heat Trans Jpn Res, vol. 27(8). 584-596, 1998.
- [10] United States Patent 3968569: "Clearance monitoring probe for rotary regenerative heat exchanger", <http://www.freepatentsonline.com/3968569.html>
- [11] F.A. Polyvoda, V.I. Kabakov: " Two stage fuel oxidation and comparison of water catalytic boilers with Fluidised Bed and fixed layer" International Journal of Global Energy: Vol.-22, pp:51-56, 2004. Energy Hand book, Second edition, Von Nostrand Reinhold Company - Robert L.Loftness
- [12] K.R. Shanmugam, P. Kulshreshtha : " Efficiency analysis of coal based thermal power generation in India during post reform era" International Journal of Global Energy: Vol.-23, pp:15-28, 2005.
- [13] Azevedo, J.L.T., and Pereira, J.C.F.- "Flow Patterns Around and Inside a Bubble Growing in a Gas-Fluidised Bed". Chemical Engineering Science 46 (1): 155-165, 1991.
- [14] Saraiva, P.C., Azevedo, J.L.T. and Carvalho, M.G.- "Mathematical Simulation of a Circulating Fluidised Bed Combustor", Combustion Science and Technology-1993. A presentedo no First International Conference on Clean Combustion Technology, Vilamoura, 3-6/9/1991.
- [15] Afgan, N.H., He, X., Carvalho, M.G. and Azevedo, J.L.T. "Knowledge based system for fouling assesment of power plant boiler", Journal of Heat And Technology, 1999.

Position Control System of a Motorized Valve in a Process Plant using PLC

S. Chattopadhyay*, S. Pal*, U. Chakraborty* and S. C. Bera[#]

*Department of Electrical Engineering, NITTTR, Kolkata [Under MHRD, Govt. of India]
Block-FC, Sector-III, Salt Lake City, Kolkata-700 106, India
E-mail: subrata0507@sify.com, pal_sagarika@yahoo.co.in

[#]Instrumentation Engineering Section, Department of Applied Physics, University of Calcutta
92, Acharya Prafulla Chandra Road, Kolkata - 700 009

Abstract- In any control loop of a process plant, the motorized valve, used as a final control element, may be required to be positioned according to the set point decided by the process requirement. There are various types of position control techniques of a motorized valve. In the present paper, a position control scheme of a motorized valve has been described using Programmable Logic Controller (PLC). The final calibration data reported in the paper reveal the linearity and reliability of the control system.

Key words- Position control, Motorized valve, PLC, Control loop.

1. INTRODUCTION

THE final control element in any control loop of a process plant may be pneumatic, hydraulic or electric motor types [1], [2]. Pneumatic or hydraulic controllers are now being replaced by microprocessor based or PC/PLC based controllers in order to avoid maintenance problem. Again the pneumatic or hydraulic control valves need converters, which are required to convert electric voltage or current signals coming out from controllers. In order to overcome higher maintenance and manufacturing costs of these converters, the electric motor actuated control valves or motorized valves are now being used instead of pneumatic or hydraulic valves since they are driven directly by the analog DC voltage or current signal or digital signal from the electronic controller [1], [2], [11]. There are different position control techniques of a motorized valve such as firing angle control of a thyristor drive unit, armature control of DC motor [1], [2] [11], stepping motor [3], [5], linear motor control [6], PC based control [8], etc.

The Programmable Logic Controller (PLC) normally is desired to work with digital I/O and sequence control. Normally PI and PID control schemes are accepted in various types of control applications [9], [10] [12]. PC Based position control schemes have wide applications in process plant [8]. In recent years it has been more common to integrate control actions into PLC systems [11]. The analog I/O of a PLC can be used to achieve PID control [12].

In the present paper the analog I/O of a PLC has been used to achieve the PID control of position of a permanent magnet DC motor actuated control valve. The valve is operated by the analog DC output voltage signal from PLC based PID controller. The valve position has been calibrated by using a

DC voltage signal from PLC based PID controller and the calibration results are reported in the paper. From these experimental studies, the repeatability and linearity of the proposed control system are found to be within tolerable limits.

II. METHOD OF APPROACH

The developed motorized control valve consists of 12 volts, 10-RPM PMDC motor, which drives a Teflon seated valve in a 20 mm line at a reduced speed of 3 RPM by a gearbox [Rack and Pinion]. This valve is positioned by an analog voltage signal in the range of 0-5 V from PLC. The motor is rotated in both directions by using the analog signal obtained from PLC based controller. The analog signal at the O/P of the PLC is unidirectional, so separate circuit schematic has been developed for direction control of the DC motor.

One analog input to the PLC is the set point signal i.e. the desired valve position. Actual valve position signal, which is obtained from the servo potentiometer attached to the motor, is fed to the other analog input to the PLC. Analog output from the PLC which is the PID controlled output, is used to move and position the valve motor as per the requirement. The designed circuit for direction control of the motor consists of an instrumentation amplifier, an opto-isolated phototransistor assembly and a relay assembly. The instrumentation amplifier provides the switching action signal to the opto-isolated phototransistor assembly and the motor is rotated in both directions by alternately changing the motor coil connections by means of relay contacts. The block diagram of the system is shown in Fig. 1.

III. DETAIL CIRCUIT ANALYSIS

The detailed circuit diagram is shown in Fig. 2. Here PLC is acting as the main controller. Its analog output, which is the controlled variable, is in the range 0-5 volt i.e. unidirectional. This unidirectional output can not be used directly to change the valve position because the valve motor should run in both directions to move the valve actuator either towards full opening or towards the full closing depending on the requirement of the process. To achieve the bi-directional movement of the valve motor, the output from PLC is fed to one input of an instrumentation amplifier and the feedback

signal from position servo potentiometer attached to the valve motor shaft is fed to the other input of the same amplifier.

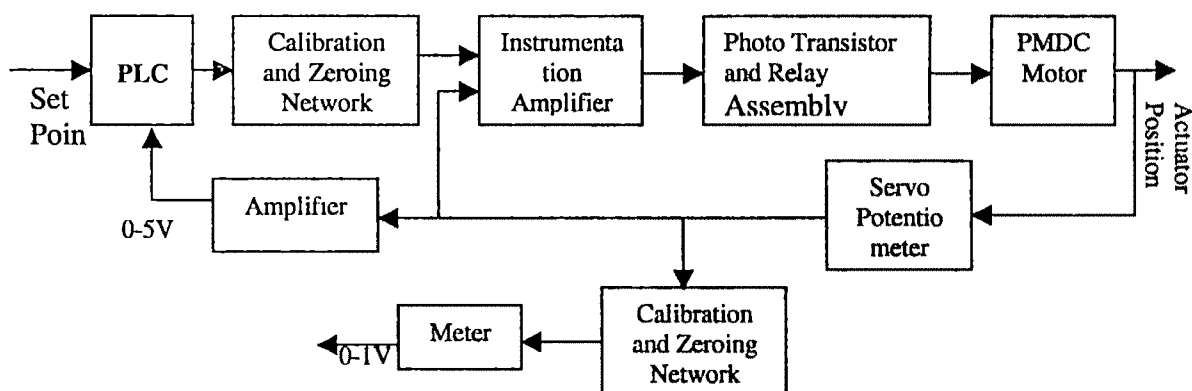


Fig. 1: Block Diagram of the System

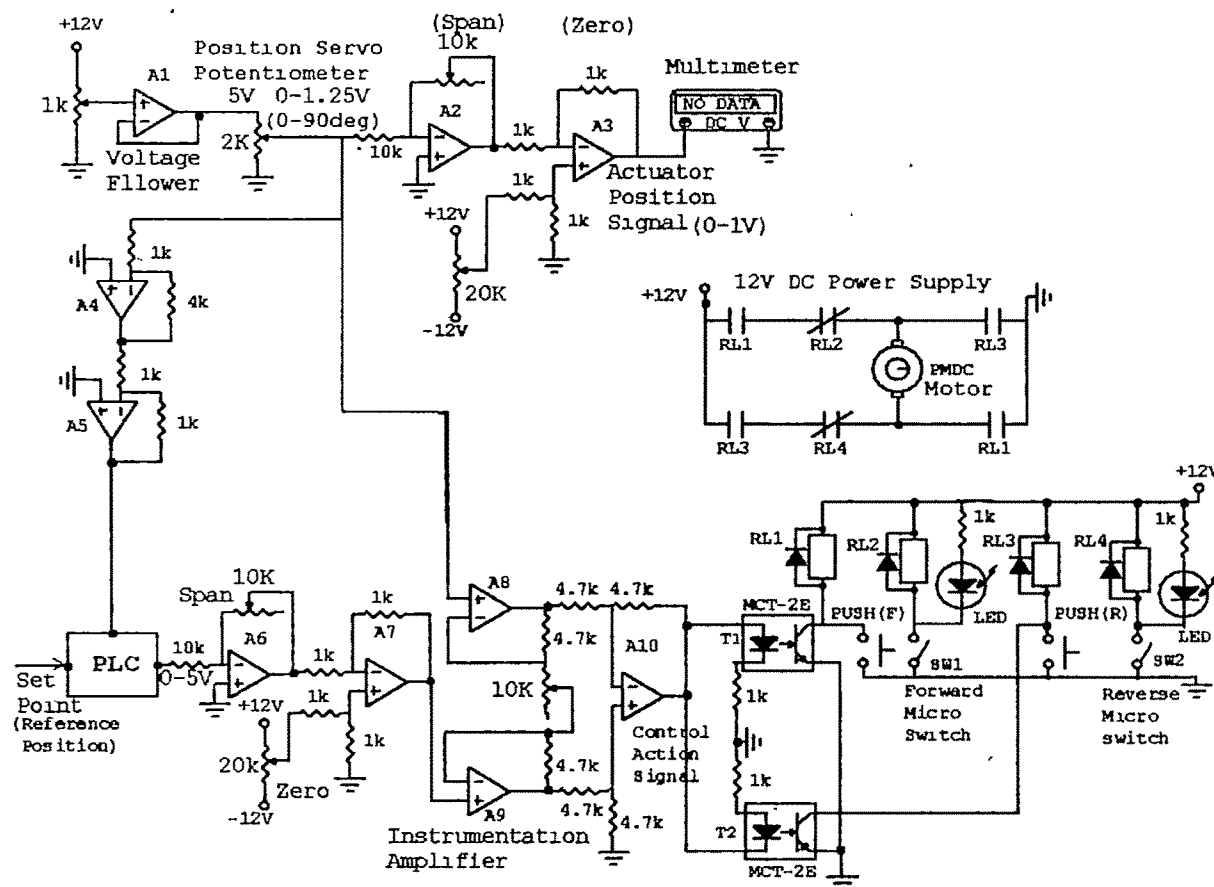


Fig. 2: Detailed Circuit Diagram

Thus the output signal of the instrumentation amplifier will change the polarity depending on the magnitude of the two input signals. This signal will act as the control action signal to the opto-isolated phototransistor assembly (T1 and T2). When T1 will be 'on', relay RL1 will be activated which will send the current through the motor in one direction and when T2 will be 'on', relay RL3 will be activated which will send

the current through the motor in the opposite direction. Relays RL2 and RL4 connected in series with RL1 and RL3 are normally closed and can be activated through two micro switches, which will operate at the maximum and the minimum position of the valve to avoid the damage of the system. Thus the valve motor will rotate through the activated

relays in both directions according to the valve position requirement within the process.

IV. CONTROLLER OPERATION

PID or Three-Mode Controller [9,10] is one of the most powerful but complex controllers, where the operation combines the proportional, integral and derivative modes. This system can be used for virtually any process condition. The analytic expression is

$$P = K_p e_p + K_p K_i \int_0^t e_p dt + K_p K_d \frac{de_p}{dt} + P_i(0) \quad (1)$$

Where

P = Controller output as percent of full scale

e_p = Error of the controlled variable from the set point

K_p = Proportional gain (% per %)

K_i = Integral gain ((% /s)/ %)

K_d = Derivative gain (% -s/ %)

$P_i(0)$ = Controller output at $t=0$

Programmable Logic Controller or PLC is an industrial computer that accepts inputs from switches and sensors, evaluates these in accordance with a stored program and generates outputs to control machines and processes. As PLC can accept and provide discrete and analog values, the analog

input and output may be current or voltage signal and PLC converts the signal to an integer between 0 and 32768 [2^{16} for 16 bit data bus] and vice versa.

The ladder diagram developed for PID control using PLC Software is shown in Fig. 3. In the diagram each rung consists of different functional blocks and output from each block is stored in registers addressed as %R0000N where N is register number. Power flows from left side to right side. After execution of 1st rung one analog input (Set Point value) is entered in to PLC processor through IN terminal (INPUT 2), which is an integer in between 0 to 32786 depending on the magnitude of the signal. This integer value is converted in to a real number for appropriate scaling which is done by "INT TO REAL" and "DIV REAL" function blocks. After appropriate scaling the real value output is again converted into integer value by "REAL TO INT" function block and stored in Register whose address is %R00008. Similarly the measured value or process value i.e. another analog input goes to PLC after execution of 3rd rung and is stored in register address %R00014. PID controlled operation is performed in rung 2 by PID ISA function block where set value (SP) and process value (PV) are coming from %R00008 and %R00014 respectively. In PID ISA function block "MAN", "UP" and "DN" terminals are always off (ALW_OFF) for automatic operation. Controlled variable (CV) is stored in %R00015 that is an integer and can be again scaled in rung 4. The content of the register %R00015 will go to the analog output terminal of PLC to be fed to the appropriate output device.

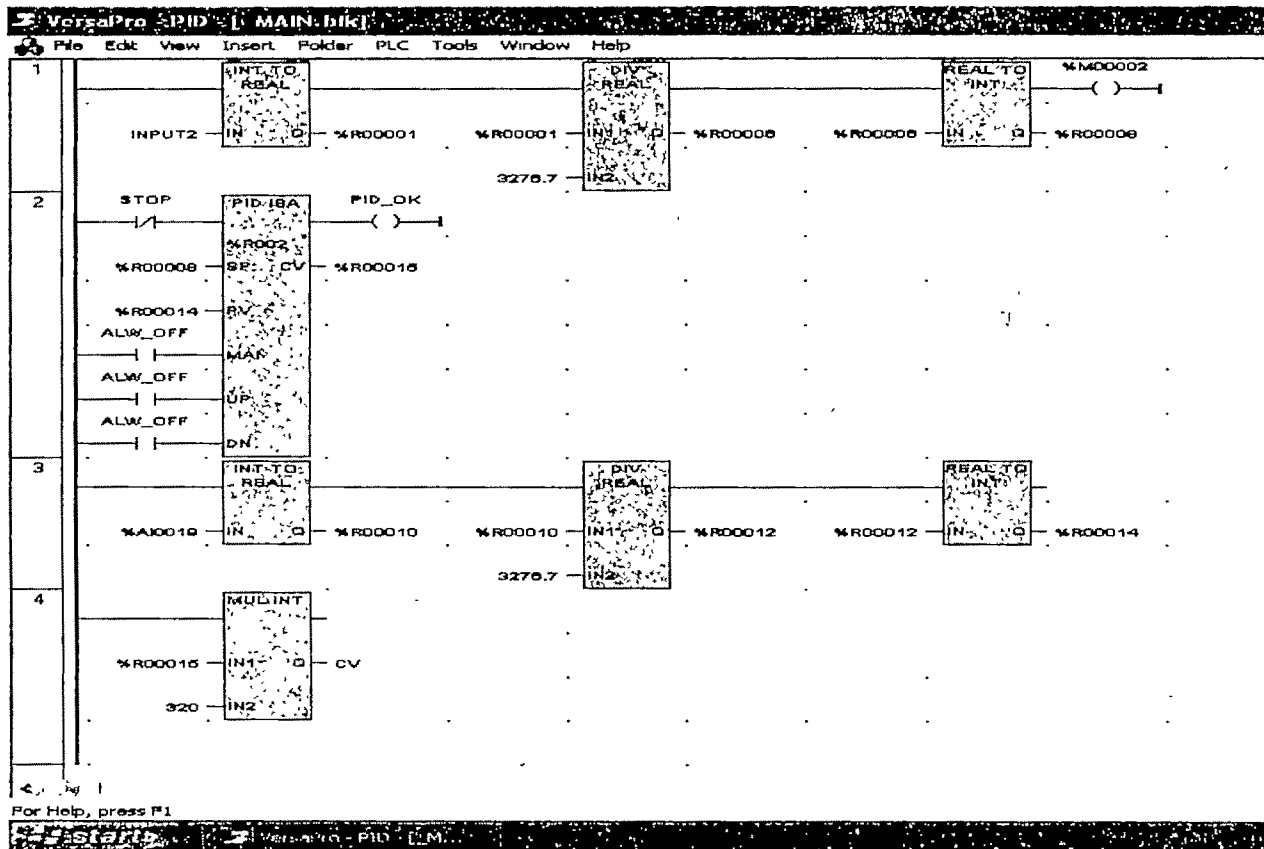


Fig. 3 Ladder diagram for PID control using VersaPro software

Tuning of controller [2,4,7,8,12] is the process of setting gains to achieve desired performance. The tuning sets the loop gains by optimizing the response to the command. Higher loop gains will improve command response and they also improve the disturbance response.

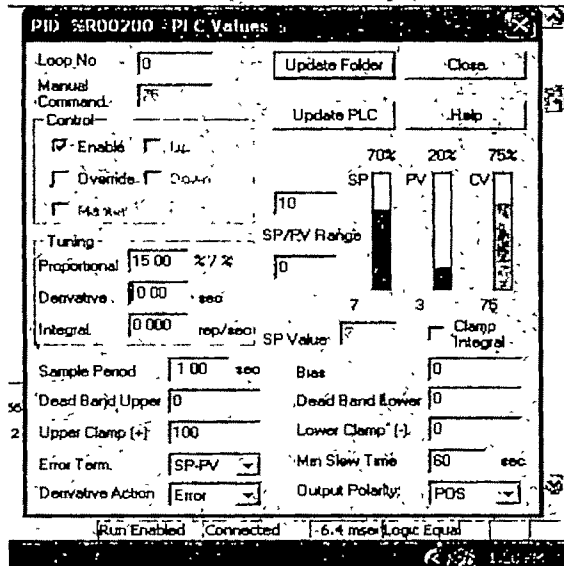


Fig. 4: Controller Tuning Window

In PLC based PID controller provisions are there to set the tuning parameters such as controller gains and can be viewed the corresponding controller out. Set point value (SP), Process value (PV) and controlled variable (CV) - all are clearly observable during tuning and thus gain setting is very easier in this system. The typical controller-tuning window for tuning of PLC based PID controller is shown in Fig. 4.

From the Fig. 4, it is clear that proportional gain, derivative gain, and integral gain can be set by the user and variation in set point (SP), process variable (PV) and controlled variable (CV) all will be observed from the same window.

V. EXPERIMENTAL RESULTS

Before experimentation the limit switches SW1 and SW2 is placed on the valve body so that the motor stops at full open and full close positions. During the experiment the valve shaft is moved in the forward or reverse direction by the manual push button switches F(M) and R(M). After the perfect alignment of the valve, the linear position of the valve shaft was indicated on a circular scale and the valve was calibrated by using a variable DC voltage source at the input instead of an actual signal from a controller. The minimum and the maximum rotations of the valve shaft are adjusted by zero and span adjustment potentiometers. Now the controlled output signal from PLC was connected to the position control unit and the set point in PLC was increased in steps and at each step the actual valve position was observed in both increasing and decreasing modes. The valve characteristics thus obtained by plotting the valve position against set point voltage is

shown in Fig. 5. The percentage error from the linearity is found to lie within $\pm 0.4\%$, as shown in Fig. 6.

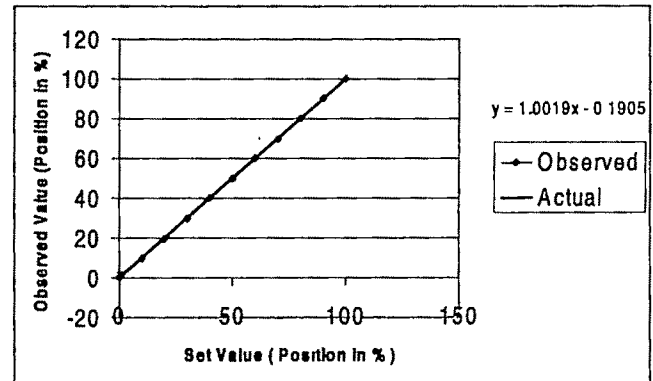


Fig. 5 The valve position characteristic

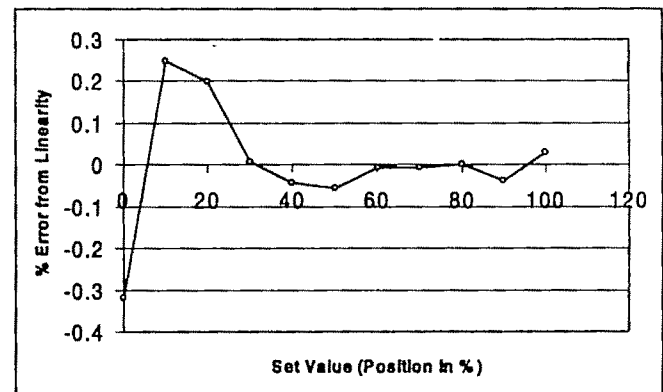


Fig. 6: The % error from linearity (analog position control system)

VI. DISCUSSIONS

From the valve position characteristic as shown in Fig.5, it is found that the characteristic is quite linear. The percentage error from linearity is within tolerable limit as shown in Fig.6. From experiment repeatability of the experimental data is obtained. The opto isolated phototransistor switches used to run the valve motor is less costly than the conventional thyristor drive units.

The controller is the PLC itself. A few key characteristics make the PLC advantageous over other controllers. Firstly, PLC is designed to communicate directly with the process to be controlled and PLC recognizes these inputs and outputs as part of its system at a fixed address. Secondly programming and reprogramming is much easier with PLC based controller. Thirdly such types of controllers are designed to operate in demanding industrial environment such as high noise, high vibration, high temperature and high humidity. These three factors are largely responsible for the wide acceptance of PLC as controller. They require no special programmer; no air conditioned rooms and no special input output systems to be designed.

REFERENCES

- [1] B.G Liptak (Ed), "*Instrument Engineers Hand Book*", vol.11, Ssec.4.1, Pneumatic-vs- Electronics, sec. 4.3, "Pneumatic Controllers", Chilton, Philadelphia, 1970
- [2] D.M. Considine, " *Process Instruments and Control handbook*", 2nd.ed., Mc.Graw Hill Book Company, 1974
- [3] J. D Usry, " Stepping Motors for Valve Actuation", *Instrum Technol.*, vol 24, no. 3, pp.-58, 1977.
- [4] M.F Hordeski, "Adapting Electric Actuators to Digital Control," *Instrum Technol.*, vol. 24, no.3, pp. -53, 1977.
- [5] S. J. Baily, "Stepping Controls Mature as Digital Actuators", *Control Eng* , vol. 26, no.8, 1979.
- [6] T. X Mei and R. M. Goodall, " Position Control for a subsea pump system driven by a linear Motor", *Control Engineering Practice*, vol.3, issue.9, pp-1209, 1995.
- [7] Shila Ming- Chang and Tseng Shy-I, " Identification and position control of Servo pneumatic cylinder", *Control Engineering Practice*, vol.3, issue 9, pp. -1209, 1995.
- [8] S.C. Bera and J. K. Ray, "PC based position control system of a Motorized valve in a Process Plant," *Proceedings of International Conference C.I.I.C 2001*.
- [9] R.A.Wright, C. Kravaris and N. Kazantzis, " Model Based Synthesis of nonlinear PI and PID Controllers." *AIChE journal*, vol 47, no 8, 2001.
- [10] M. Li, F. Wang and F. Gao, " PID - Based Sliding Mode Controller for Nonlinear Processes." *Ind. Eng. Chem. Res. - 2001*, vol. 40, no. 16, pp. 2660 - 2667.
- [11] Ashraf Salah , El Dm Zem El Din, "PLC Based Speed Control of DC Motor ", Power electronics and Motion control Conference , 2006, IPEC '06 CES/IEEE 5th International, Vol-2, 1-16 Aug. 2006. Page 1-6.
- [12] S. Chattopadhyay, S. Pal and S. C. Bera. "PLC Based Continuous Voltage Control System of a DC Generator", Proceedings of the Conference on 'Emerging Trends in Electrical Technology, ETET-2006.

Technical Session 1C

Power Electronics : Simulation

Design, Analysis and Simulation of DC-to-DC Flyback Converter

R. A. Gupta, Rajesh Kumar, Saurabh Goyal, Parikshit Yadav
Malaviya National Institute of Technology, JLN Marg, Jaipur, INDIA 302 017
e-mail rkumar_mnit@rediffmail.com

Abstract—In this paper, design, analysis and simulation of Flyback Converter based Switched Mode Power Supply is presented. In the design approach Voltage range of 100V (AC) to 265V (AC) is considered. The low frequency (50HZ, single-phase) input is converted to a high frequency (50 KHz) and then it is processed via high frequency Transformer and the secondary of this transformer is designed to give out AC voltage, which is again rectified and filtered out to give 24V DC, 5A output. A closed loop Flyback converter is designed and simulated. The designing of transformer in MATLAB is also discussed. Finally the Total Harmonic Distortion (THD) and the spectrum analysis of the output voltage at various loads are presented.

Keywords — Flyback Converter, Rectifier, Saw Tooth, Firing pulses, MOSFET, Total Harmonic Distortion (THD), Spectrum analysis, PWM, CCM.

I. INTRODUCTION

VIRTUALLY every piece of electronic equipment, e.g. computers and their peripherals, calculators, Television and other instruments are powered from a DC power source either in the form of a battery or a DC power supply. Since power supplies are widely used in electronic equipments there has always been a quest to improve the quality of power available from these sources. Among the currently existing transformer-coupled switching mode DC to DC converters, the Flyback converter is the simplest topology, since no choke is required only one power switch is used and the high-frequency power transformer with unifilar windings is employed. In addition to these structural advantages, it also possesses the merits of easy to obtain wide-range output voltage and multiple-output voltage with good transient response. Switching power supplies uses a high frequency switch (a MOSFET or a Transistor) with varying Duty cycle obtained from PWM (pulse width modulation) principle of feedback and instantaneous correction to maintain constant output voltage. A filter filters out the output variations caused by switching [2]. But here we will be dealing with the DC-DC conversion part of the SMPS. We have designed a closed loop DC-DC Flyback converter.

II. FLYBACK CONVERTER CIRCUIT

The basic circuit of the Flyback converter is shown in fig. 1. The major differences between other topologies and Flyback on the account of transformer construction are (a) No extra winding unlike the forward converter that employs a reset winding (b) The primary and secondary windings are wound in opposite direction. When the MOSFET switch is turned on

for a period T_{on} , the current in the primary winding rises linearly and the energy is stored in the primary winding and when the MOSFET switch is turned off for a period T_{off} , the energy stored is transferred to the secondary winding. The fly back-switching regulator accepts a DC voltage input and provides a regulated output voltage of opposite polarity.

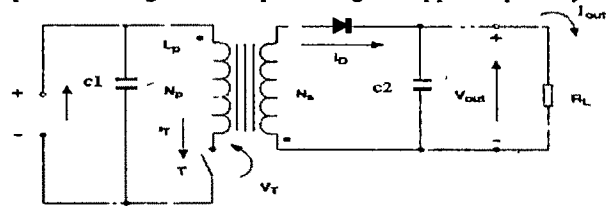


Fig 1: Basic circuit of Flyback converter

The main problem which comes into picture is the design of high frequency transformer because we need a transformer in which the two windings are wound for opposite polarity as for T_{on} energy is stored in the primary and for T_{off} it is dissipated in the secondary [1]. But in MATLAB we have a transformer with same polarities on both windings. So we have used the transformer and the Diode and capacitor are reversed. Also the parameters of the transformer need to be in per unit system.

II. DESIGN OF FLYBACK CONVERTER

Input parameters:

$V_{line}^{min} = 100VAC$, $V_{line}^{max} = 265VAC$, Line frequency = 50Hz, Maximum duty cycle ratio $D_{max} = 0.45$, Power conversion efficiency $\eta = 80\%$, The efficiency is assumed to be 80%, because of various losses during switching and also in transformer.

Output parameters:

$V_{out} = 24V$, $I_{out} = 5A$, Maximum Output Power = $V_{out} I_{out} = 24 \times 5 = 120W$.

Therefore Maximum Input Power will be

$$P_{in} = \frac{P_{out}}{\eta} = \frac{120}{0.8} = 150W$$

The minimum dc link voltage is given by:

$$V_{DC}^{Min} = \sqrt{2(V_{line}^{Min})^2 - \frac{P_{in}(1-D_{ch})}{C_{dc}f_l}} \quad (1)$$

$$V_{lms}^{Min} = 100V, P_{in} = 150W$$

D_{ch} is the DC link capacitor charging duty cycle, it is typically taken as 0.2

$$D_{ch} = 0.2, f_l = 50 \text{ Hz}$$

It is typical to select the DC link capacitor as $3\mu F$ per watt of the input power.

$$C_{dc} = 150 \times 3 = 450 \mu F$$

Therefore from equation 1, $V_{dc}^{Min} = 122V$

The maximum dc link voltage is given by:

$$V_{dc}^{Max} = \sqrt{2}V_{line}^{Max} = 375V \quad (2)$$

The designing of the SMPS is done for the minimum input voltage $V_{dc}^{Min} = 122V$ and it is open loop.

V_m and the nominal MOSFET voltage V_{dc}^{nom} is calculated as:

$$V_{ro} = V_{dc}^{Min} \times \frac{D_{max}}{(1-D_{max})} = 100V \quad (3)$$

$$V_{dc}^{nom} = V_{rn} + V_{dc}^{Min} = 222V \quad (4)$$

It can be seen, from the above equations that as D_{\max} decreases, the voltage stress on the MOSFET decreases. However this increases the voltage stress on the rectifier diodes used on the secondary side. So it is typical to set D_{\max} as 0.45.

Transformer Design

One of the most important factors in the design of a Flyback converter power supply is the design of the transformer. Although we call it a transformer it is not actually a true transformer, but more an energy storage device, where during the period of time when the primary switch is on energy is stored in the air gap of the core, and during the off time of the primary switch, this energy is transferred to the outputs. Current flows in either the primary or secondary winding, but not both at the same time. Therefore it can be thought of more as an inductor with secondary windings added. Usually gap is introduced between the cores to increase the energy storage capacity. Ferrite is the most widely used core material for commercial SMPS (Switched mode power supply) applications. The type of the core should be chosen with regard to system requirements including number of outputs, physical height, and cost. An EE core has been selected because of its low cost and its typical application in auxiliary power battery charger. But in the MATLAB Simulink we have linear transformer with same polarity [4]. So to get the same effect we reverse the diode and capacitors.

When MOSFET is switched on the current in the secondary side of transformer will not flow because the secondary diode is in reverse bias and during this period the capacitors discharge across the load or the voltmeter and when the MOSFET is switched off the inductance forces reversal of the polarities on all the windings. Therefore, the secondary diode conducts and the capacitors are charged and the secondary voltage induced appears across the load too or the voltmeter

Primary winding inductance L_m is obtained as:

$$L_m = \frac{(V_{dc}^{Min} \times D_{max})^2}{2P_{in} f_s K_{RF}} \dots\dots\dots (5)$$

Switching frequency $f_s = 50\text{KHz}$

K_{RF} is the ripple factor and for CCM operation $K_{RF} < 1$. We have taken $K_{RF} = 0.38$. The K_{RF} is defined below in the fig. 3

Once L_m is determined, Maximum Peak current and RMS current of the MOSFET are calculated as:

$$I_{EDC} = \frac{P_{in}}{V_{dc}^{Min} D_{max}} = 150 / 122 \times 0.45 = 2.73 A \quad (6)$$

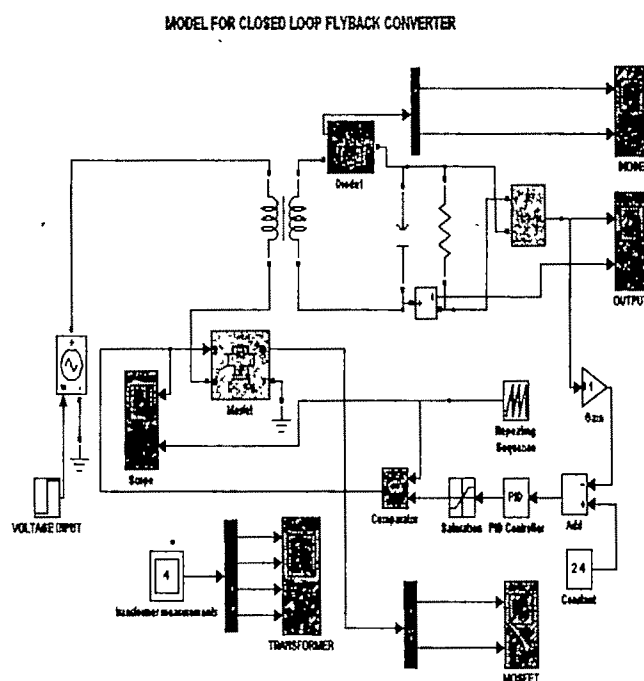
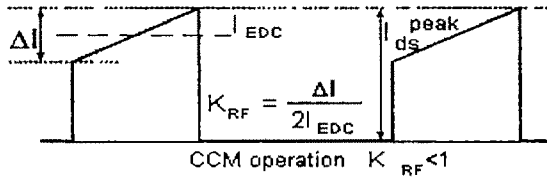


Fig. 2. MATLAB model of Closed loop Flyback Converter

The Flyback converter is thus modeled for 122V. The model is given an input supply through a battery of 122V. Thus assuming ideal condition and no disturbances; it behaves like a DC-DC converter with input of 122V and an output of 24V and 5A. The circuit of Flyback converter designed in MATLAB is shown in fig. 2.

Primary Side Design

When the MOSFET is turned off, the input voltage V_{dc} together with the output voltage reflected to the primary side of transformer (V_m) is imposed on the MOSFET.



$$L_m = \frac{(122 \times 0.45)^2}{2 \times 150 \times 50 \times 10^3 \times 0.38} = 530 \mu H$$

$$\Delta I = \frac{V_{dc}^{Min} D_{max}}{L_m f_s} = 122 \times 0.45 \times 10^3 / 530 \times 50 = 2.07 A \quad (7)$$

$$I_{dc}^{peak} = I_{EDC} + \frac{\Delta I}{2} = 2.73 + 1.035 = 3.76 A \quad (8)$$

$$I_{ds}^{rms} = \sqrt{[3(I_{EDC})^2 + (\frac{\Delta I}{2})^2] \frac{D_{max}}{3}} = 1.88 A \quad (9)$$

The limiting value of the MOSFET current should be greater than the peak value of the MOSFET current with a tolerance of 12%. So we have chosen the limiting current as $I_{Lm} = 6A$. From the Ferrite magnetic core database, we have selected an EE core with the following specifications: $B_{sat} = 0.44 T$, $A_w = 255 mm^2$, $A_e = 233 mm^2$. The minimum number of turns in the primary winding to avoid saturation is calculated as-

$$N_p^{min} = \frac{L_m I_{Lm} \times 10^6}{B_{sat} \times A_e} \text{ (Turns)} = 36 \quad (10)$$

Secondary Side Design:

Now next step is to determine the turn ratio between the primary side and the feedback controlled secondary side as the reference

The turn ratio between the primary and the secondary winding is calculated as-

$$n = \frac{N_p}{N_s} = \frac{V_{ro}}{(V_o + V_d)} = 100/24.9 = 4.01 \quad (11)$$

The number of primary turns assumed must be greater than N_p^{min} . Assuming N_p as 40 we get number of secondary turns as:

$$N_s = \frac{N_p}{n} = 40/4.01 = 10 \text{ turns}$$

The RMS value of secondary side current is given by:

$$I_{sec}^{rms} = I_{ds}^{rms} \sqrt{\frac{(1-D_{max})}{D_{max}}} \times \frac{V_{ro}}{V_o + V_d} = 8.34 A \quad (12)$$

Since current density should be less than $10 A/mm^2$, so from the wire gauge table we should select the wire of proper thickness. The wire diameter should not be more than $1 mm$

to avoid severe eddy current losses as well to make winding easier. So we choose Primary Winding of 26SWG and Secondary Winding of 24SWG. While choosing the wire diameter care must be taken that window area of core A_w is enough to accommodate the wirings.

Specifications of the wire chosen for Transformer Windings:

Radius of wire of the Primary is $\phi_p = 0.226 mm$

Radius of wire of the Secondary is $\phi_s = 0.283 mm$

Resistivity of the wire of Primary is $\rho_{pn} = 134.5 \mu\Omega/mm$

Radius of wire of the Secondary is $\rho_{sc} = 84.21 \mu\Omega/mm$

Number of strands for Primary winding is $\lambda_p = 3$

Number of strands for Secondary winding is $\lambda_s = 5$

Current Density is given by:

$$J = \frac{I_{RMS}}{A_s} A/mm^2 \quad (13)$$

Where, A_s is the area of the winding for single turn.

Current Density of the Primary Winding is calculated as

$$A_s(pri) = \pi * (\phi_p)^2 * \lambda_p = 0.48 mm^2$$

$$J_{pri} = \frac{1.88}{0.48} = 3.916 A/mm^2 = 19.256 mm^2$$

Where, $A_c(pri)$ is the copper winding area for the Primary winding. Current Density of the Secondary Winding is calculated as

$$A_s(sec) = \pi * (\phi_s)^2 * \lambda_s = 1.258 mm^2$$

$$J_{sec} = \frac{8.34}{1.258} = 6.629 A/mm^2$$

$$A_c(sec) = \pi * (\phi_s)^2 * \lambda_s * N_s = 12.58 mm^2$$

Where, $A_c(sec)$ is the copper winding area for the Secondary winding. So the required winding area is given by

$$A_{wr} = \frac{A_c}{K_f}$$

Where, A_c is the total winding area, K_f is the Fill Factor and its value lies between 0.2 – 0.25. Here we have assumed $K_f = 0.2$

The total copper winding area is equal to

$$A_c = A_c(pri) + A_c(sec) = 31.836 mm^2$$

Therefore, the required winding area is equal to

$$A_{wr} = \frac{A_c}{K_f} = 31.836/0.2 = 159.18 mm^2$$

So the calculated value of A_{wr} is less than $233 mm^2$ (A_w) chosen.

Calculation of Resistance of the Windings:

Calculating the length of primary winding from the Core data,
Mean Length per Turn (MLT) = 78.5 mm

Length of primary winding = Number of Turns of Primary Winding x MLT

$$= 40 * 78.5 = 31400 \text{ mm}$$

$$R_{pn} = \frac{\rho_{pn} * N_p * MLT}{\lambda_p} = 0.14077 \Omega$$

Length of secondary winding = Number of Turns of Secondary Winding x MLT

$$= 10 * 78.5 = 785 \text{ mm}$$

$$R_{Sec} = \frac{\rho_{Sec} * N_s * MLT}{\lambda_s} = 0.013221 \Omega$$

Output Block:

The Output block consists of a Diode rectifier and a filter that consists of a Capacitor. Capacitors are placed in parallel in order to reduce ESR (effective series resistance). Also the voltage rating of Capacitors should be high enough to withstand the voltage spikes.

Output filters capacitor is calculated as:

$$C_{out} = \frac{65 * \Delta I}{V_{ripple}} \mu F \quad (14)$$

Where, ΔI is the difference between the maximum and minimum value of the output current and is equal to 2A.

$$V_{ripple} \text{ (Desired)} = 90mV, C_{out} = 1445 \mu F$$

III. FEEDBACK LOOP

Consider the negative feedback loop for a Flyback converter in fig above. Consider that initially PI controller is not there then, for slow or dc variations of the output voltage V_o , the loop is, of course, stable. A small or slow variations of the output voltage V_o due to either line input or load changes will be sensed by the gain block which brings down the voltage to a level comparable to reference voltage (V_{ref}) and its further sensed by the inverting end of the error amplifier (comparator) and compared to a reference voltage at the non inverting end (positive end) of error amplifier. This will cause a small change in the DC voltage level V_{ea} at the output of the error amplifier and also at the input to the pulse width modulator (PWM).

The PWM, as described here to fore, compares the DC voltage level V_{ea} at the input of the PWM generator to the repeating sequence (Sawtooth generator). The pulse fixes the on time of the MOSFET. Thus a slow increase in input voltage V_{dc} causes a slow increase in output voltage V_o . The increase in the output voltage causes an increase in voltage sensed by comparator and hence a decrease in the output of the error amplifier (V_{ea}). Since T_{on} is the time from the start of the triangle to the time till it is equal to V_{ea} . So decrease in the V_{ea} causes decrease in on time of MOSFET (T_{on}) and when T_{on} decreases output voltage V_o decreases. Thus restores output voltage V_o to its original value. Similarly, of course, a decrease in input voltage V_{dc} causes an increase in on time of MOSFET (T_{on}) to maintain output voltage V_o constant. It

must be insured that polarities are such that an increase in output voltage V_o causes a decrease in on time of MOSFET (T_{on}). The circuit thus provides negative feedback and a stable circuit for low frequencies. For making the loop stable at higher frequencies we use PI controller and PI controller needs to be tuned. Once PI controller is tuned the closed loop Flyback converter is designed. Now the output of the Flyback converter will remain constant when there is any variation in the input voltage or the output load.

IV. SIMULATION RESULTS AND DISCUSSION

The Simulation Results of the DC-to-DC Flyback Converter are presented below and discussed. The waveforms for the Output Voltage and Current for Input voltage=122V and a load of 4.8 Ω are shown in figure4. It takes a small time Δt to go to the final value and this delay is due to the magnetization of the transformer and the inherent delay of the diodes and switching delays. The Ripple in the Output Voltage is $0.06V_{pp}$. The Fourier analysis and harmonic spectrum of the output voltage is also presented in figure4. The output voltage contains DC component of magnitude 24.01 and only even harmonics are present whose magnitude decreases with the increase in order. The Total Harmonic Distortion (THD) of the output Voltage is 0.06%. The Waveforms for the Current in and Voltage across the MOSFET switch are shown in figure3. The peak Current in the MOSFET is 3.76A and the variation in the Current is 2.07A. The Current raises from 1.69A to 3.76A in the ON state in a Ramp fashion since we are considering Continuous Conduction Mode (CCM) and it is 0A in the OFF state. The Voltage across the MOSFET comes to be 0V in the ON state and 222V when it is switched OFF.

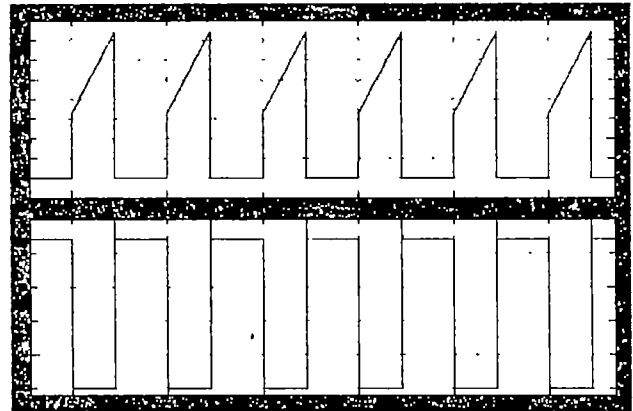
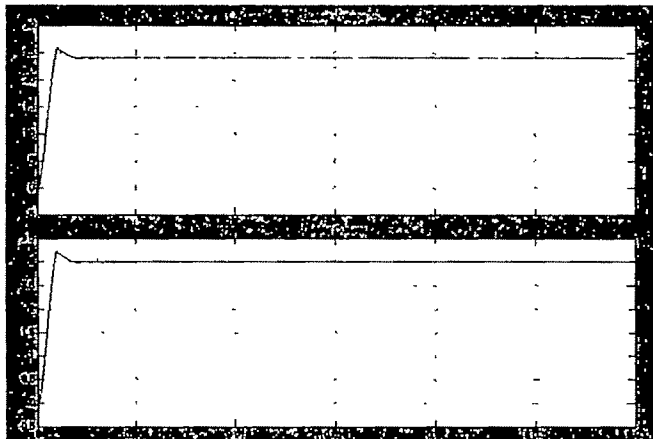


Fig.3: Waveforms for the Current and Voltage across the MOSFET switch

The input voltage is varied from 110V (AC) to 265V (AC) and their equivalent DC Voltages are applied to the MATLAB model and load is varied from 3A (8 Ω) to 5A (4.8 Ω). Finally, transient analysis is done for the variations in the input Voltage. Figure5 shows the Variation in Output Voltage and Current when input Voltage varies from 122V to 375V at 0.01 Seconds and Figure17 shows the Variation in Output Voltage and Current when input Voltage



- [5] Liaw, C.M. (1996), Research on integration of switch mode power supplies. Project report of National Science Council, NSC 85-2622-E-007-011, Taiwan, ROC.
- [6] Mammano, B. (1990), isolating the control loop. *Unitrode power supply Design Seminar SEM-700*, 1990, 2-1 to 2-15.
- [7] Kazimierzuk, M.K., and Nguyen, S. T. (1995) Small-Signal Analysis of open-loop PWM Flyback DC-DC converter for CCM. In *Proceedings of the IEEE 1995 National Aerospace and Electronics Conference*, 1995, 69-76.
- [8] V. Vorperian, "Simplified analysis of pwm converter using model of PWM switch: part I and II", *IEEE Trans. on Aerospace and Electronic Frequency (Hz) Systems*, vol. 26, no. 3, pp. 490-505, 1990.

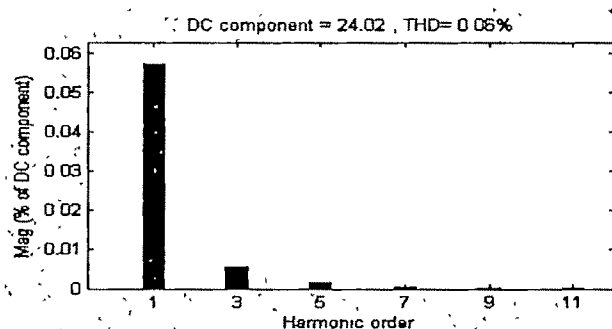


Fig 4 Output Voltage and Current for 122V, 5A, 4.8Ω and Harmonic spectrum of Output Voltage

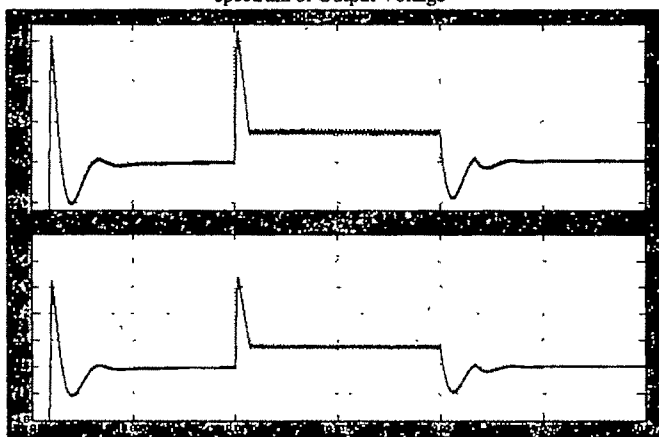


Fig. 5. Variation in Output Voltage and Current when input Voltage varies from 122V to 375V at 0.01 Seconds.

V REFERENCES

- [1] R. A. Gupta, Rajesh Kumar, Saurabh Goyal and Parikshit Yadav (2007) "Design, Analysis and Simulation of DC-DC Fly back Converter", Published in *IEEE sponsored International Conference on RACE, India*.
- [2] Mohan, N., Undeland, T.M., and Robbins, W. P. (1995) *Power Electronics: Converters, applications and Design*. New York: Wiley, 1995.
- [3] A. I. Pressman, *Switching Power Supply Design*. New York: Mc Graw Hill, 1997.
- [4] Liaw, C.M., Chiang, S.J., Lai, C. Y., Pan, K.H., Leu, G.C., and Hsu, G.S (1994) Modeling and Controller Design of a current mode controlled Converter. *IEEE transactions Industrial Electronics*, 41, 2 (Apr 1994), 231-240.

Modeling of a 3-Phase Current Controlled Inverter With Observer-Feedback and Decoupling

Dipanwita Gangopadhyay¹, K.Selvajyothi², P.A.Janakiraman³

¹Indian Institute of Technology, Madras, Chennai, India, e-mail: dipanwita.iitm@gmail.com.

²Indian Institute of Technology, Madras, Chennai, India, e-mail: selvajyothi@yahoo.com

³Electrical Engineering, Indian Institute of Technology, Madras, Chennai, India, e-mail: pajraman@iitm.ac.in.

Abstract— In current control systems using a 3-phase inverter, the Direct and the Quadrature components of the output Current, (I_d, I_q), show interaction with each other mainly due to the power factor of the load impedance. The interaction can be minimized by rotating the feed back vector (I_d, I_q) through the power factor angle. The feedback variables are filtered to remove the switching noise from percolating through the current control system, using a new a two-phase observer. The observer does not show any steady state magnitude or phase error in the current. The resulting two decoupled systems can be easily studied for stability and tuned for their PI settings. The PWM saturation has also been considered. The design procedure is studied with particular reference to the load impedance and power factor variations.

Key words— Current control, Decoupling, Direct and Quadrature components, Three-phase PWM inverter, Two-phase Observer, Stability.

I. INTRODUCTION

POWER Electronics being the technology of efficiently processing electric power, energy conversion techniques [1] form its main focus. The highly important topic of power switching deals with DC/AC Pulse Width Modulated (PWM) inverters which are widely used [2], [3], [4], [5]. Conventionally, the control circuitry for the inverters, have used PI (Proportional + Integral) controllers. Three major classes of regulators which have been popular are (1) Hysteresis, (2) Linear PI and (3) Dead-beat regulators with a further sub-classification into stationary ABC frame and synchronous-frame implementations [6]. All high performance control strategies have exhibited coupling problems [5], [7]. The most fundamental entity in variable speed drive systems is the current control loop [7]. Fast and accurate current loops with appropriate reference currents enable a machine to act as an ideal torque-source. The alternative arrangements of Trajectory Tracking loops exhibit a quick response, which are simple to fabricate [8]. However,

using PI controllers, it is difficult to realize small tracking errors for sinusoidal reference signals. The tuning process has been ad-hoc till recently [9]. Filters similar to the Luenberger Observer [10] have been recently employed for filtering out the switching harmonics in the feed back path without causing any steady state error.

Many methods for controlling voltage source inverters, which connect the photovoltaic (PV) cells to the power-grid, have been described in technical literature [11]. The feed forward and feedback decoupling methods have been modeled. Decoupled power control has been an active area of research in which active and reactive powers have been independently controlled in the synchronous frame.

One of the basic problems in inverter control by PWM is that of saturation, because distortion will appear when the controller enters into the saturation region. Further, instability also may occur, which can be overcome by applying Popov's criterion [12] while designing the controller.

In this paper modeling of a decoupled current controlled three-phase voltage source inverter is presented. A new two-phase observer has been employed for filtering the feedback signals. Decoupling of the control system by rotation of the feedback current vector is described in detail.

II. THREE PHASE VOLTAGE SOURCE INVERTER

The traditional three-phase full bridge voltage source inverter (VSI) is shown in Fig. 1. The main objective of this static power converter is to produce sinusoidal output current and voltage waveforms from a dc power supply. Six switches $S_1, S_2, S_3, S_4, S_5, S_6$ are activated by the PWM signals.

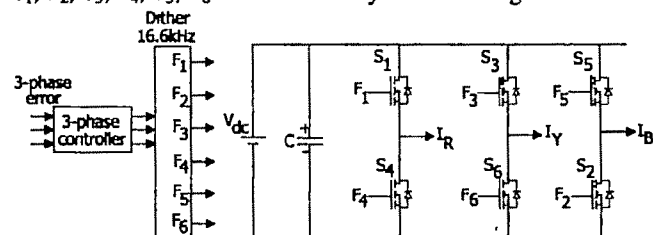


Fig.1. Schematic of Three-phase Voltage Source Inverter

III. CURRENT CONTROL SCHEME

The two-phase observer performs the filtering of the measured, instantaneous *unfiltered* three phase currents of the inverter. The basic aim is to build a decoupled controlled current source, for which the reference vector is composed of Direct and Quadrature components of the desired current. The feed back variables are also in the synchronous rotating frame. A PI controller is used to make the steady state error between the reference and the *feed back signals* zero.

The three-phase line current of the inverter is converted to its alpha (α) and beta (β) components using Clarke transform.

$$\begin{bmatrix} I_\alpha \\ I_\beta \end{bmatrix} = \begin{bmatrix} 1 & -0.5 & -0.5 \\ 0 & 0.866 & -0.866 \end{bmatrix} \begin{bmatrix} I_R \\ I_Y \\ I_B \end{bmatrix} \quad (1)$$

These I_α and I_β signals are passed through a two-phase observer for filtering out the switching noise. Now, the output signals from the observer are transformed from stationary to synchronous frame using Park transform.

$$\begin{bmatrix} I_d \\ I_q \end{bmatrix} = \begin{bmatrix} \cos\theta & \sin\theta \\ -\sin\theta & \cos\theta \end{bmatrix} \begin{bmatrix} I_\alpha \\ I_\beta \end{bmatrix} \quad (2)$$

The reference for I_d can be set at a desired peak value and the reference for I_q , at zero.

Considering the open loop block diagram shown in Fig. 2, the difference between the reference and feedback vectors is processed through two PI controllers to achieve zero steady state error at fundamental frequency as well as waveform fidelity.

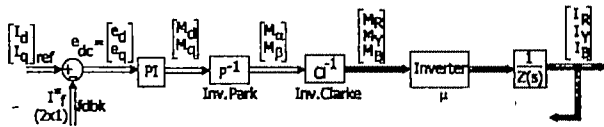


Fig 2. Open Loop Block diagram of Current Loop.

Let the PI controller output be $\begin{bmatrix} M_d \\ M_q \end{bmatrix}$. These are the control

signals in the [d,q] domain which are to be later transformed back to stationary [α , β] frame again; using inverse Park transform.

$$\begin{bmatrix} M_\alpha \\ M_\beta \end{bmatrix} = \begin{bmatrix} \cos\theta & -\sin\theta \\ \sin\theta & \cos\theta \end{bmatrix} \begin{bmatrix} M_d \\ M_q \end{bmatrix} \quad (3)$$

where $\theta = \omega.t$, and $\omega = 100\pi (\cong 314)$ rad/s

The two-phase signals are transformed back to three-phase by inverse Clarke transform.

$$\begin{bmatrix} M_R \\ M_Y \\ M_B \end{bmatrix} = \begin{bmatrix} 1 & 0 \\ -0.5 & 0.866 \\ -0.5 & -0.866 \end{bmatrix} \begin{bmatrix} M_\alpha \\ M_\beta \end{bmatrix} \quad (4)$$

IV. A NEW TWO-PHASE OBSERVER

A two-phase observer, as shown in Fig. 3, having a complex pole-pair is used to filter out switching noise or harmonic contaminated signals without introducing any pronounced delay or proportional gain.

It has been studied from the simulation results that the use of two separate single-phase observers instead of a composite two-phase observer results in loosely bound two-phase as well as three-phase waveforms due to inefficient timing adjustments between the two-phase signals. The two output signals of the observer after transformations to the synchronous frame give rise to two dc signals for use as feedback signals for the closed loop system.

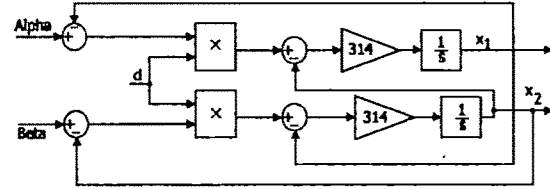


Fig.3. Schematic of the Two-Phase Observer.

A. Observer Design

The system generating the sinusoidal signals is assumed to be $\dot{X} = AX$ where $X = [x_1, x_2]^T$. The observer differential equation is given by: $\dot{\hat{X}} = A\hat{X} + D.E$

$$\text{i.e., } \begin{bmatrix} \dot{\hat{x}}_1 \\ \dot{\hat{x}}_2 \end{bmatrix} = \begin{bmatrix} 0 & \omega \\ -\omega & 0 \end{bmatrix} \begin{bmatrix} \hat{x}_1 \\ \hat{x}_2 \end{bmatrix} + \begin{bmatrix} d_1 \cdot \omega & 0 \\ 0 & d_2 \cdot \omega \end{bmatrix} \begin{bmatrix} e_1 \\ e_2 \end{bmatrix} \quad (5)$$

$$\text{where } A = \begin{bmatrix} 0 & \omega \\ -\omega & 0 \end{bmatrix} \quad D = \begin{bmatrix} d_1 \cdot \omega & 0 \\ 0 & d_2 \cdot \omega \end{bmatrix},$$

x_1 = real current (i.e. $I_m \sin \omega t$),

x_2 = orthogonal current (i.e. $I_m \cos \omega t$), error $E = X - \hat{X}$

and $\begin{bmatrix} \hat{x}_1 \\ \hat{x}_2 \end{bmatrix}$ are the estimates of x_1 and x_2

The elements of matrix [D] are obtained by suitable observer pole placement procedure. Considering $d = d_1 = d_2$ observer transfer function becomes:

$$\frac{\hat{X}(s)}{X(s)} = [sI - A + D]^{-1} D = \frac{d \cdot \omega}{(s + d \cdot \omega)^2 + \omega^2} \begin{bmatrix} s + d \cdot \omega & \omega \\ -\omega & s + d \cdot \omega \end{bmatrix} \quad (6)$$

The roots of the characteristic equation give the observer poles i.e., $(s + d \cdot \omega)^2 + \omega^2 = 0$ which gives $(s_1 = -d \cdot \omega + j\omega)$ and $(s_2 = -d \cdot \omega - j\omega)$.

This means that the observation error damps out with a time constant $\tau = 1/(d \cdot \omega)$ in an oscillatory manner.

B. Pole Placement

Though the observer poles can be made dependent on the power factor of the load, it results in a wide range of values for the observer poles, greatly influencing observer performance. Poles closer to the origin give better filtered waveform but the response is highly sluggish, while poles farther away from the origin make the system fast acting but at the same time showing higher noise sensitivity. So it is preferred to fix the poles at such a position that for a wide range of power factor, it will give a nice trade off between noise elimination and speed of response. Here, the real part of the observer poles are selected to be at $d \cdot \omega = -2\omega$ where $\omega = 100\pi (\cong 314)$ rad/s.

V. NON INTERACTING CONTROL

The two-phase output current signals are found to be coupled due to the combined effect of the inverter and the star connected three-phase R-L load. Fig.4 shows that the resultant load voltage (V_L) and current (I_L) signals are not in phase and the phase difference is θ , which is the load power factor angle. This brings in the idea of rotation of feedback current signals by an angle θ to make it in phase with voltage signals. The current vector $I_L = [I_d, I_q]^T$ in synchronous frame is rotated by θ using the rotation matrix.

$$\begin{bmatrix} I_{dn} \\ I_{qn} \end{bmatrix} = \begin{bmatrix} \cos\theta & -\sin\theta \\ \sin\theta & \cos\theta \end{bmatrix} \begin{bmatrix} I_d \\ I_q \end{bmatrix} \quad (7)$$

The interactions between the rotated (direct and quadrature) signals I_{dn} and I_{qn} as well as V_d and V_q become negligible due to this arrangement. However, the true load current will not be

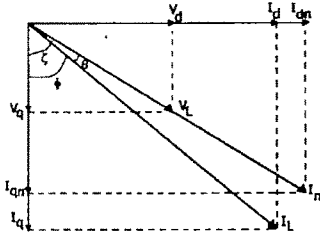


Fig.4. Load Current and Voltage vectors in the d-q Plane.

in phase with the reference current signal. This deficiency would be automatically taken care of in the outer voltage control loop. Now, the above decoupling technique clearly shows the need for online power factor estimation.

A. On line power factor estimation

From fig. 5, we see that the components of the rotated vector I_n resolved on to the d and q axes are

$$I_{qn} = |I_n| \cos \zeta = I \cos \zeta \quad \text{and} \quad I_{dn} = |I_n| \sin \zeta = I \sin \zeta \quad (8)$$

where ζ is the angle between V_L and V_q and $|I_n| = |I_L| = I$

Now, $V_q = |V_L| \cos \zeta = V \cos \zeta$ and

$$V_d = |V_L| \sin \zeta = V \sin \zeta \quad (9)$$

$$I_{qn} = I \cdot \frac{V_q}{V} \quad , \quad I_{dn} = I \cdot \frac{V_d}{V}$$

Thus, even for unknown load, knowing only the instantaneous values of V_d , V_q , I_d , I_q the proper rotation of current signal through power factor angle can be achieved by the following procedure. Now, the instantaneous value of the power factor can be obtained as follows:

$$\begin{aligned} \cos \theta &= \cos [(\phi + \theta) - \phi] \\ &= \cos \zeta \cos \phi + \sin \zeta \sin \phi \end{aligned} \quad (10)$$

$$= \frac{V_q}{V} \cdot \frac{I_q}{I} + \frac{V_d}{V} \cdot \frac{I_d}{I} = \frac{V_d \cdot I_d + V_q \cdot I_q}{V I} \quad (11)$$

B. Modeling of decoupled system

The major advantage of the decoupling of the signals I_d , I_q is that it results in two separate and identical block diagrams, if

we use the rotated current signals for feed back. Thus the order of the system to be analyzed gets reduced, simplifying the stability analysis. In the following discussion, each and every part of the system has been modeled by using the equivalent transfer functions or gain elements.

The transfer function of the observer in the stationary frame was found to be

$$\frac{\hat{X}(s)}{X(s)} = \frac{d\omega}{(s+d\omega)^2 + \omega^2} \begin{bmatrix} s+d\omega & \omega \\ -\omega & s+d\omega \end{bmatrix} \quad (12)$$

where, $d\omega$ is the real part of the observer pole.

The corresponding system behavior in the synchronous frame could be modeled by a transfer function having only one pole per channel as: $\frac{1}{1+s\tau}$ (13)

where, $\tau = \frac{1}{d\omega}$, the observer time constant in the d-q model.

C. Closed loop decoupled current control system

With the observer and rotation matrix operating in the feed back, the system shown in Fig.5 splits into two independent loops due to decoupling. We need to analyze only one of the two resulting loops as far as the stability is concerned.

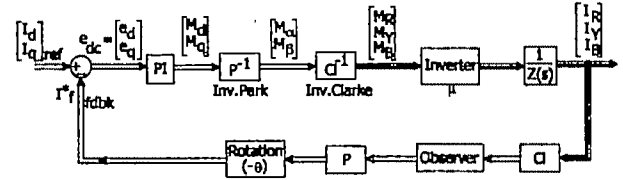


Fig.5. Closed Loop Current Control System with Decoupling.

Let the Inverter Gain be: μ

Let the PI controller transfer function be a $[2 \times 2]$ diagonal matrix

$$[PI] = K \cdot \left(K_p + \frac{K_i}{s} \right) [I]_2 \quad (14)$$

where, $[I]_2$ is a 2×2 Identity matrix.

The Park and Clarke transforms and their inverses operate symmetrically on either side of the Inverter. The feed back current vector can be obtained by the following sequence of operations:

1. The error vector in the synchronous frame is processed by a PI controller (diagonal matrix) block followed by Inverse-Park, Inverse-Clarke transform.
2. The result from the above is processed by $[\mu / Z]$, which is a (3×3) diagonal matrix representing the Inverter.
3. Further processing is carried out symmetrically, with Clarke, Observer and Park Transforms followed by negative rotation by power factor angle.

Considering the open loop transfer function of the scheme shown in Fig. 5.

The rotated feed back Current vector is given symbolically by:

$$I_r^* = [Park] \cdot [Obs] \cdot [CI] \cdot [\mu / Z] \cdot [CI^{-1}] \cdot [Park^{-1}] \cdot [PI] \cdot e_{dc} \quad (15)$$

$$= K' \cdot \frac{1}{Z} \cdot (\text{Park} \cdot \text{Obs} \cdot \text{Park}^{-1}) \cdot \text{PI} \cdot e_{dc} \quad (16)$$

where $K' = 1.5 \mu$

$$= K \cdot \left(\frac{K'}{R+sL} \right) \cdot \left(\frac{1}{1+s\tau} \right) \cdot \left(K_p + \frac{K_i}{s} \right) [I]_2 e_{dc} \quad (17)$$

where $[I]_2$ is the 2×2 Identity matrix.

$$= (K \cdot G) [I]_2 e_{dc} = (K \cdot G) \cdot [I]_2 (I_{ref} - I^*_f) \quad (18)$$

The scalar G is given by:

$$G = \frac{K' \cdot K_p}{\tau \cdot L} \cdot \frac{\left(s + \frac{K_i}{K_p} \right)}{s \cdot \left(s + \frac{1}{\tau} \right) \left(s + \frac{R}{L} \right)} = \frac{K' \cdot K_p}{\tau \cdot L} \cdot \frac{(s+b)}{s \cdot (s+p)(s+a)} \quad (19)$$

where $b = (K_i / K_p)$; $a = (R / L)$; $p = (1 / \tau)$

Therefore, the characteristic equation is $1 + KG = 0$. (20)

D. Root Locus based Design

Now, the poles and zeroes of the closed loop system can be placed using the equi-dominance criterion so that all the closed loop poles will have the same negative real parts. As far as the Observer is concerned, its pole has already been placed to be at $s = -2\omega = -p$ (say). Let $K_p = 1$

Referring to Fig. 6, using the equi-dominance criterion,

$$\frac{-p-a+b}{3-1} = -b \quad (21)$$

$$K_i = b = \frac{1}{3} (a + 2\omega), \quad a = 4\omega = \frac{R}{L}; \quad \frac{\omega \cdot L}{R} = 0.25 \quad (22)$$

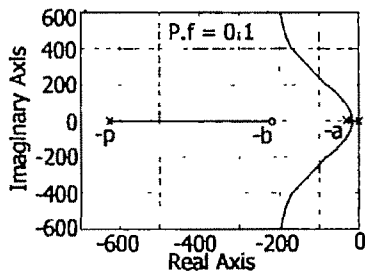


Fig 6. Root Locus for a power factor of 0.1.

Now, the open-loop pole location corresponding to the admittance $[1/Z]$, migrates as the power factor changes. This means both the parameters 'a' and 'b' which are now related by the equi-dominance criterion, move along negative real axis. Interestingly, for a critical value of $b = p$, the pole-zero cancellation takes place, which is to be generally avoided. The critical power factor $Pf_c = \cos(\tan^{-1}(0.25)) = 0.97$ (23) Hence, for highly resistive loads, a smoothing series inductor on the load side would solve this problem.

VI. POPOV'S CRITERION FOR TUNING PI CONTROLLER

The three-phase inverter can be visualized as a *linear gain element*, subject to saturation as shown in Fig.7. The gain and saturation are a function of the d.c source voltage E and the amplitude of the triangular carrier D . The PI controller transfer

function has been written as: $K \cdot \left(K_p + \frac{K_i}{s} \right)$ with $K_p = 1$

and integral controller tuned on the basis of the root locus design. The tuning of the controller can be completed, if the value of K can be specified. For a linear model, the critical value of K can be obtained from the Nyquist Criterion. However as the Inverter moves into the nonlinear zone, a better frequency domain criterion like that of Popov can be used to determine the maximum allowable gain K .

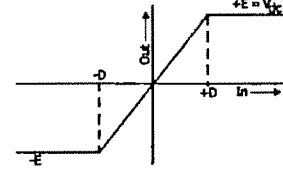


Fig.7. Equivalent I/O Characteristic for PWM scheme in inverters

Now, the characteristic equation is $1 + K \cdot G = 0$.

The Popov's criterion can be stated as:

$$\frac{1}{K_{max}} = \max \{ -\text{Re} (G(j\omega)) \} \quad (24)$$

From the Popov's criterion, we can obtain the value of K_{max} corresponding to different power factors in the range $0.05 < pf < 0.97$ for a fixed impedance of 10 Ohms.

VII. SENSITIVITY OF PI CONTROLLER TO LOAD PARAMETERS

For the current control of three-phase inverters, $K_p = 1$ and

$$K_i = \frac{1}{3} \left(\frac{R}{L} + 2\omega \right) = \frac{\omega}{3} (\cot \theta + 2) = \frac{\omega}{3} \left(\frac{1}{\tan \theta} + 2 \right) \quad (25)$$

So, K_i is independent of $|Z|$. It depends only on the power factor as shown in Fig. 8(a). Fig. 8(b) shows the change in the value of overall gain, K with respect to power factor for the fixed impedance value $|Z|$ in Ohms. And overall gain, K is directly proportional to impedance i.e. $|Z|$, as shown in Fig. 8(c), for a fixed load power factor.

VIII. SIMULATION RESULTS

A. Validation of Two-phase Observer and its Model

The Observer and model are fed with a step change in the two-phase sinusoidal input (stationary frame) and the extracted I_d and I_q corresponding to synchronous frame were plotted for the observer as in Fig. 9. Model also gave the same response. Obviously the step inputs are in the synchronous frame and the response is also seen in the same frame.

B. Validation of P.f Estimator and decoupled Model

Fig.10 shows the estimated power factor by simulation for a load of power factor 0.5. Model is derived at after decoupling the current controlled three-phase inverter. Then a disturbance is given to the two-phase sinusoidal input. Corresponding decoupled I_d and I_q of the system and model are coinciding as shown in Fig.11.

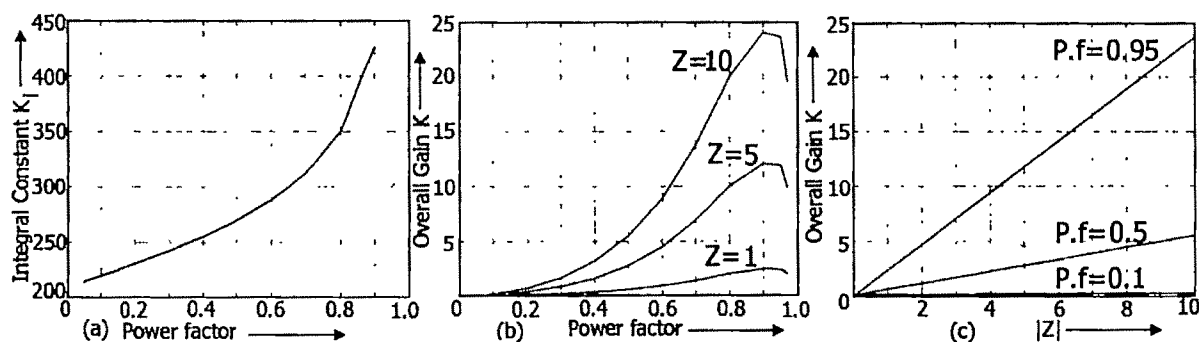


Fig.8 (a) Sensitivity of K_i w.r.t power factor. (b) Sensitivity of overall gain K w.r.t power factor. (c) Sensitivity of overall gain K w.r.t impedance.

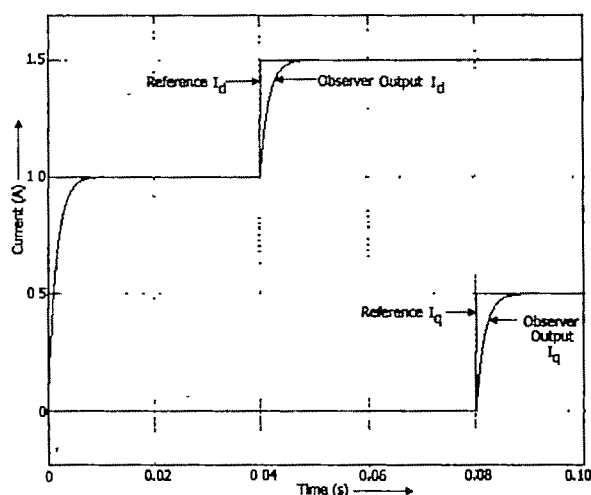


Fig.9 Transient Response of Observer in I_d and I_q Channels.

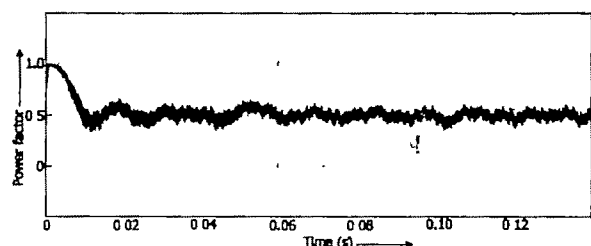


Fig 10. Estimated Power factor for an actual load power factor of 0.5.

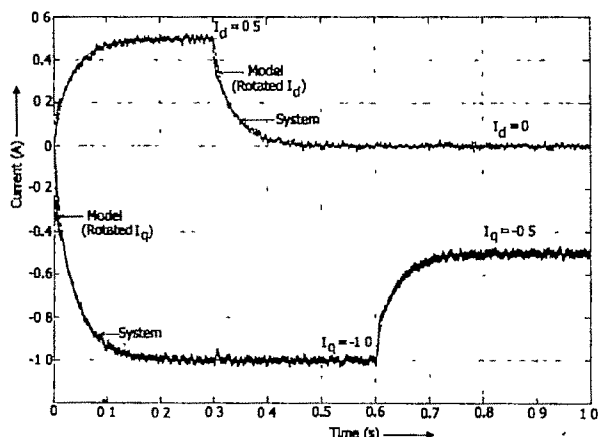


Fig 11 System and Model show Decoupled Transient Response in current

IX. CONCLUSION

The new feed back scheme consisting of a new two-phase observer and rotation matrix in the feed back path of the control system that resulted in decoupled current control in the Synchronous Frame for a three phase inverter. Stability analysis is quite simple because, the direct and the quadrature loops have become independent. Tuning the controllers is no more tedious and arbitrary, but the well known analysis and synthesis tools for the single-input single output control systems can be easily extended to the inverters supplying low power factor loads.

REFERENCES

- [1] F. Blaabjerg, Z. Chen, S.B. Kjaer, "Power Electronics as Efficient Interface in Dispersed Power Generation Systems", *IEEE Trans. on Power Electronics*, Vol. 19, issue 5, Sept.2004, pp: 1184-1194.
- [2] J. Holtz, "Pulsewidth modulation for electronic power conversion", *Proceedings of the IEEE*, Vol. 82, Issue 8, Aug. 1994 pp: 1194 - 1214.
- [3] J.-O.Krah, J.Holtz, "High-performance current regulation and efficient PWM implementation for low-inductance servo motors", *IEEE Trans. on Ind. Applications*, Vol. 35, Issue 5, Sept.-Oct. 1999 pp:1039 - 1049.
- [4] M.P. Kazmierkowski and L. Malesani, "Guest Editorial Special Section On PWM Converter Current Control", *IEEE Trans. on Industrial Electronics*, Vol.45, issue 5, Oct.1998, pp:689 - 690.
- [5] M.P.Kazmierkowski, L.Malesani, "Current control techniques for three-phase voltage-source PWM converters: a survey", *IEEE Trans. on Industrial Electronics*, Vol. 45, Issue 5, Oct. 1998 pp:691 - 703.
- [6] D.N. Zmood, D.G.Holmes, "Stationary frame current regulation of PWM inverters with zero steady-state error", *IEEE Trans. on Power Electronics*, Vol.18, Issue 3, May 2003 pp: 814 - 822.
- [7] R. E. Betz, B. J. Cook, and S. J. Henriksen, "A digital current controller for three-phase voltage source inverters," in *Conf. Rec. IEEE-IAS Annu Meeting*, New Orleans, LA, 1997, pp: 722-729.
- [8] J.Holtz, B.Beyer, "The trajectory tracking approach-a new method for minimum distortion PWM in dynamic high-power drives", *IEEE Trans. on Ind. Appl.*, Vol. 30, Issue 4, July-Aug. 1994 pp:1048 - 1057.
- [9] B.Saritha, P.A.Janakiraman, "An Observer for Three-Phase Current Estimation Using Non uniform Current Samples", *IEEE Trans. on Power Electronics*, Vol.22, No.2, March 2007, pp: 686-692.
- [10] George H. Ellis, "Observers in Control Systems: A Practical Guide", Published 2002 Elsevier.
- [11] M.Milosevic, G.Andersson, S.Grabic, "Decoupling Current Control and Maximum Power Point Control in Small Power Network with Photovoltaic Source", *Power Systems Conference and Exposition, 2006. PSCE '06. 2006 IEEE PES Oct 29 -Nov. 1* pp:1005 - 1011.
- [12] P.A Janakiraman and P.Rao, "Application of Popov's criterion to signal stabilization in discrete systems", *IEEE Trans. on Automatic Control*, Vol 15, issue 1, Feb 1970, pp:142 - 143.

Switch Mode Rectifier with Improved Power Factor and High Quality Input Waveforms

P.K.Gujarathi, Dr.M.V.Aware

Army Institute of Technology,Diggi Hills,Pune,Maharashtra ,India. e-mail:pritamgujarathi@rediffmail.com
Vishveswaraya National Institute of Technology, Nagpur,Maharashtra,India.email:mva_win@yahoo.com

Abstract—Advances in power electronics and high-performance electrical technology are driving a move toward switch-mode circuits for ac-dc conversion. The efficient control of these circuits is an ongoing research challenge. Switch mode ac/dc converters have been shown to be superior to thyristor phase controlled rectifiers in terms of power factor and input/output voltage and current harmonics. It is necessary and essential to maintain the dc output voltage constant in many applications of the rectifier. The paper presents the design, operation, analysis & simulation of the single phase half & full bridge switch mode rectifiers. A Simple control strategy is proposed to utilize the voltage input to make the near unity power factor at input side of the rectifier. Simulation is carried out in Matlab/Simulink & results of Single phase (Half & Full Bridge) are presented. The simplified voltage control of the switch mode rectifier ensures the improvement in the current waveform of the source. The ripple free dc output is obtained and maintained constant, while nearly sinusoidal input currents are drawn from the source. The Results obtained confirms the effectiveness of Control strategy..

Key words—Harmonics, Power converters, Switch-mode Rectifier (SMR), Unity power factor.

I. INTRODUCTION

ADVANCES in power electronics and high-performance electrical technology are driving a move toward switch-mode circuits for ac-dc conversion. The efficient control of these circuits is an ongoing research challenge, and to date has focused on the more popular voltage-driven converter/conversion between polyphase alternating current and direct current is ubiquitous in electrical applications. The switch-mode converter circuit, using IGBT's or similar devices, is in common use for dc-ac inversion and is becoming increasingly popular also for ac-dc conversion, as controlled switching devices become cost competitive with traditional thyristor technology. Switch-mode Converters offer several advantages over thyristor converters, including high input power factor and negligible low-frequency harmonics. They

also comply the standards and recommended guidelines such as IEEE-519 and IEC-555 to maintain the power quality.

II. SWITCH MODE RECTIFIER (SMR)

A. Basic Principle Of Switch Mode Rectifier (SMR)

The basic principle of SMR converters in case of inverting as well as rectifying mode has explained, consider only fundamental component neglecting switching frequency harmonics the rectifying mode of operation is shown when converter voltage V_{an} applied leads the E_a by an angle δ the active real component of I_{ap} of I_a is in phase with E_a and so converter is operating in inverter mode. Now power is fed back to utility and power flows from load to converter the phase angle of (as well as magnitude) of ac voltage produce by converter can be controlled. If converter voltage v_{an} is now made to lag e_a by the same angle δ as before (keeping v_{an} constant) the phasor diagram is shown the active component of I_{ap} of I_a is now 180° out of phase with E_a , resulting rectifying mode of operation where power flows from dc side of converter to inverter(motor).

In fact V_{an} can be controlled both in magnitude and phase (direction), thus allowing control over the current magnitude and power level, assuming that e_a cannot change instantaneously, and Fig 6.1 shows the Locus of v_{an} phasor, which would keep magnitude of current constant.

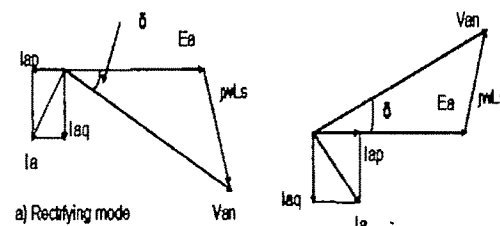


Fig.1 Principle of SMR

A single phase half bridge SMR is shown in Fig. 2(a) in positive half cycle of ac voltage, input current increases when S2 is on and decreases when S2 is off and D1 is forced to conduct. in negative half cycle corresponding switches are S1 and D2 .By turning on and off the respective switch for proper duration, the input current can be controlled to follow a sinusoidal waveform. The equivalent circuit of SMR looking into switching rectifier is shown in Fig.2 (b) below.

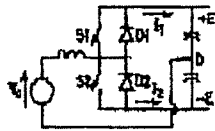


Fig.2(a) Circuit diagram

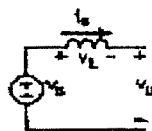


Fig.2(b)Equivalent circuit

B. Types and Operation of Switch Mode Rectifier (SRM)

The power circuit configuration of bi-directional switch mode rectifier is as shown in Fig.2 (a) and Fig.3. This configuration can work in first two quadrants. Quadrant one operation is rectifying operation and quadrant two operations as inverting operation.

The half bridge configuration uses two switching devices and two diodes, while the full bridge configuration uses four switching & four diodes. At the converter input terminals, the half bridge configuration produces bipolar voltage waveform, which is a two-level waveform($\pm V_{dc}/2$), while the full bridge configuration produces unipolar voltage waveform, which is a three level waveform[$+v_{dc}/2$ or $-v_{dc}/2$]. The unipolar voltage waveform has less harmonic content as compared to the bipolar voltage waveform.

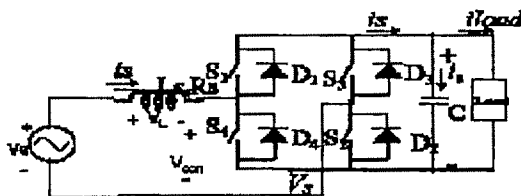


Fig.3 Full Bridge SMR

During Cycle	When Switches ON	When Switches OFF	During Cycle	When Switches ON	When Switches OFF
Positive Half Cycle	S1 Operated	D1 ON	Positive Half Cycle	S1 & S2 Operated	D1 & D2 ON
Negative Half Cycle	S2 Operated	D3 ON	Negative Half Cycle	S3 & S4 Operated	D3 & D4 ON

Table.1 Operating Modes for Half Bridge & Full Bridge Configuration

During regeneration, current reversal takes place; here operating modes are just opposite of powering modes.

III. ANALYSIS OF SWITCH MODE RECTIFIER (SMR)

In Full Bridge SMR (Fig 4(b)), is defined with a direction and inductance L_s is included to reduce the ripple in is at a finite switching frequency. From fig 4 (b):

$$V_s = V_{con} + V_L \quad (1)$$

Where, $V_L = L_s (di/dt)$

Assuming V_s to be sinusoidal, the fundamental-frequency components of V_{con} and is in Fig 4 (b), can be expressed as phasors V_{con1} and I_{s1} , respectively. Choosing V_s arbitrarily as the reference phasor $V_s = V_s e^{j\theta}$, at the line frequency $\omega = 2\pi f$

$$V_s = V_{con1} + V_{L1} \quad (2)$$

Where, $V_{L1} = j\omega L_s I_{s1}$

A Phasor diagram corresponding to equation (2) is shown in Fig 4.

Where, I_{s1} lags V_s by an arbitrary phase angle θ .

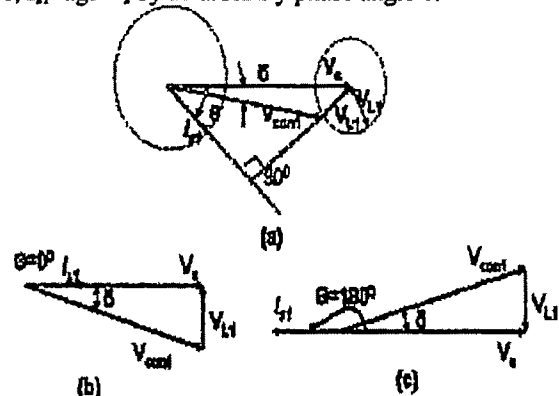


Fig.4: (a) General Phasor Diagram, (b) Rectification at Unity Power Factor, (c) Inversion at Unity Power Factor.

The real Power P supplied by the ac source to the converter is

$$P = V_s I_{s1} \cos \theta \quad (3)$$

From Fig 4(a),

$$V_{L1} \cos \theta = \omega L_s I_{s1} \cos \theta = V_{con1} \sin \delta$$

$$= \frac{V_s^2}{\omega L_s} \left(\frac{V_{con1}}{V_s} \sin \delta \right) \quad (4)$$

The reactive Power Q supplied by the ac source is positive. It can be expressed as

$$Q = V_s I_{s1} \sin \theta \quad (5)$$

From Fig 4(a),

$$V_s - \omega L_s I_{s1} \sin \theta = V_{con1} \cos \delta \quad (6)$$

$$= \frac{V_s^2}{\omega L_s} \left(1 - \frac{V_{con1}}{V_s} \cos \delta \right) \quad (7)$$

Note that Q is sum of the reactive power absorbed by the converter and the reactive power consumed by the inductance L_s . However, at very high switching frequencies, L_s can be made to be quite small; thus, Q can be approximated as the reactive power absorbed by the converter.

$$|s| = \frac{V_s - V_{con1}}{\omega L_s} \quad (8)$$

From above equation it is clear that for the given line voltage and chosen value of L_s , desired values of P and Q is obtained by controlled the magnitude and the phase of V_{con1} . From Fig 4(a), shows how V_{con1} can be varied, keeping the magnitude of I_{s1} constant. The two circles are traced by the loci of I_{s1} and V_{con1} phasors.

From fig 4 (b) & (c), in both cases

$$V_{con1} = \sqrt{V_s^2 + (\omega L_s I_{s1})^2} \quad (9)$$

If high switching frequency is used, only a small inductance L_s is needed. Therefore equation (2)

$$V_{con1} \approx V_s \quad (10)$$

To limit input ripple in input current, the dc bus voltage V_{dc} shown in Fig 3, must be greater than the peak of the input ac voltage

$$V_{dc} > \sqrt{2} V_s \quad (11)$$

IV. CONTROL SCHEME OF SWITCH MODE RECTIFIER (SMR)

The control principle of above scheme for sinusoidal line current at unity power factor is shown in Fig.5. The command dc link voltage V_{dref} is compared with the actual dc link voltage V_d and error is fed to PI controller/p of which is multiplied with line voltage waveform V_s to generate the command I_s^* (i.e. current will follow the voltage waveform to get unity power factor), which is compared with triangular carrier waveform at high frequency to get PWM signals to switches.

V. DESIGN OF FULL BRIDGE SMR

For Design of Full Bridge SMR, the following specification has taken,

2KVA, single phase, 220volts, 50hertz, Output voltage = 400volt.

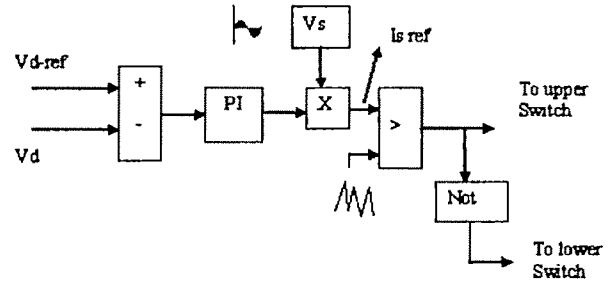


Fig 5. Control Scheme of Switch Mode Rectifier (SMR)

Following assumptions are considered for Design of Full Bridge SMR.

1. Line voltage varies sinusoidal and is given by the expression $V_s = V_p \sin \omega t$, Where, V_p is peak voltage.
2. For unity power factor operation, neglecting switching Components, $i_L = I_p \sin(\omega t)$, Where, I_p is peak line current.
3. Converter losses are neglected.
4. In half bridge, the two capacitors has same value.
5. Assuming zero switching losses.
6. Input inductor L_s may be determined knowing the switching frequency (say 25 kHz), to get 2.5% ripple in the Input current.

The dc bus capacitor must be designed to satisfy the following criteria-

1. To comply with the minimum ripple requirement of the dc bus voltage.
2. To limit the dc bus voltage fluctuations during load or input voltage transients.

From the Design Calculations, The minimum capacitance of 1100 μF is required & minimum inductance of 6 mH is required

VI. SIMULATION OF SMR

Simulations of SMR in both configurations are presented (Half Bridge & Full Bridge SMR). Simulation is carried out to maintain output DC Voltage to 100 V. A detail understanding of control strategy along with PI controller behavior is presented. Simulation parameter are set with variable step and solved with ode23b (stiff/TR-Df2). A parameter values like inductor, capacitor etc are considered from design. The Results of simulation of Half Bridge SMR is Shown in Fig. 6.

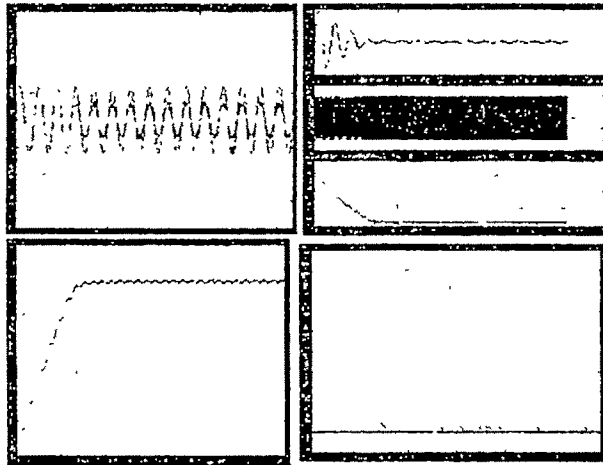


Fig.6 Source Voltage & Current, Response of PI Controller, DC Voltage and Error.

The Simulation results of full bridge SMR with Vdc ref changed from 100 V to 80 V after 0.2sec is shown in Fig.7.

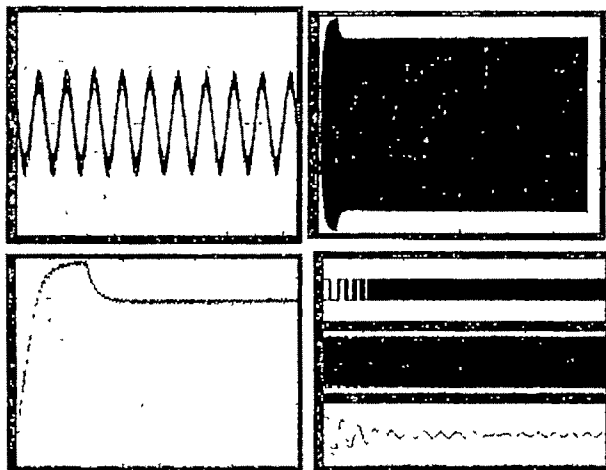


Fig.7 Source Voltage & Current, Vcon DC Voltage and Response of PI Controller.

It can be seen from above simulation that DC voltage is maintained constant according to command value. There is almost unity power factor at utility and sinusoidal currents at source input. To maintain sinusoidal current at input it is found that there is change in control voltage with source current value is maintained constant. The pulses for upper and lower will get changed to adjust the DC link voltage constant. The behavior of PI controller can be seen that, for step change in command value how settles down to zero value depending upon system characteristics, response it behaves like under damped, over damped etc. it is also observed that as the proportional gain is varied system settles down earlier gain to its final value. Also the THD has shown to be 9%.

VII.CONCLUSION

The paper presents the design; operation, analysis & simulation of the single phase half & full bridge switch mode rectifiers. A Simple control strategy is proposed to utilize the voltage input to make the near unity power factor at input side of the rectifier. Simulation is carried out in Matlab/Simulink & results of Single phase (Half & Full Bridge) are presented. The simplified voltage control of the switch mode rectifier ensures the improvement in the current waveform of the source. The ripple free dc output is obtained and maintained constant, while nearly sinusoidal input currents are drawn from the source. The Results obtained confirms the effectiveness of Control strategy. The prototype Laboratory model is under development stage.

REFERENCES

- [1] Lo, Y. K., Chen, C. L., "Three-phase four wire voltage controlled AC line conditioner with unity input power factor and minimized output voltage harmonics," *Electric Power Appl.*, Volume 142, No 1, Jan.1995 Page(s):43 – 44
- [2] Manias, S., "A novel SMR topology" *Industry Applications Society Annual Meeting, 1990., Conference Record of the 1990 IEEE 7-12 Oct.1990* Page(s):1113 - 1118 vol.2
- [3] Tsai, W. L., Sun, Y.Y., Shieh, W. S., "A Modelling and control of single phase switching mode rectifiers with near-optimum dynamic regulation" in *International Conference on Industrial Electronics, Control and Instrumentation, 1991., Proceedings.IBCON '91., 1991,* Page(s):501 – 506.
- [4] Dawande, M., Dubey G K., "Switching techniques for switch mode rectifier Power Electronics and Drive Systems," 1999. PEDS '99. *Proceedings of the IEEE 1999 International Conference on Volume 1, 27-29 July 1999* Page(s):167 - 173 vol.1.
- [5] B. K. Bose, "Power Electronics and Variable Frequency Drives," New York, IEEE Press, 1996.
- [6] R. Krishna, "Electrical Motor Drives-Modeling, Analysis and Control," Printace Hall of India 2003.
- [7] Matlab/Simulink Help.

Simulation and Design of an Active Power Filter for SCR Converter

Prabal Deb¹, Shilpi Bhattacharya², Sujit K. Biswas³

¹ Guru Nanak Institute of Technology, India, e-mail: deb_prabal@yahoo.com

² Narula Institute of Technology, India, e-mail: shilpihatt@yahoo.com

³ Electrical Engineering Department, Jadavpur University, India, e-mail: sujit_biswas@hotmail.com

Abstract— Power electronic converters operating from the AC mains supply are widely used in applications ranging from DC drives to HVDC. The objective of the paper is to study, simulate and design an active power filter capable of compensating predetermined current harmonics. The basic structure of the shunt active filter is a PWM voltage source inverter using 6 IGBTs. This converter is connected to the terminals of nonlinear load and controlled in such a way that it generates specific current harmonics. These generated harmonics are injected into the source in antiphase to the harmonics generated by the load. Thus cancellation takes place, so that these harmonics are not drawn from the source. In this paper, harmonic waveforms are generated in MATLAB software based on Fourier series of the ideal wave shapes created at the supply lines due to non-linear loads. The power circuit and the control circuits are developed in MATLAB /Simulink. Finally a fundamental design of the active filter has been made.

Key words—Active Power Filter, Harmonic Compensation, SCR Converter, THD

I. INTRODUCTION

THE idea of active filter was introduced by Gyugyi *et al* [1] in 1976. The term active filter is a generic one and is functional to a multitude of power electronic systems comprising power switching devices and other energy storage circuit elements, such as inductors and capacitors. A large number of low power electronic appliances houses power electronic converters, which may be as simple as a diode rectifier, a SCR based rectifier or bigger units comprising high power bulk rectifiers, cycloconverters used in adjustable speed drives, arc furnaces and in innumerable number of industries. However small and simple the unit may be, the characteristics are sufficient to introduce sufficient harmonics into the power system, resulting in currents which are far from being sinusoidal. Such non-sinusoidal currents are a serious threat to the entire power network that includes very important elements such as relays and transformers. Harmonics in the net may result in faulty operation of these electrical devices.

Active power filters are basically used to recompense for the harmonics introduced into the power lines due to loads with non-linear characteristics. These are designed to implement the well established concept of injecting the equal and opposite distortion current waveform to the power supply bus-bar system in order to enhance the power quality of the bus bar.

The primary idea is to make the power supply current near sinusoidal, the measure of which is the total harmonic distortion. The lower the THD, the better is the shape of the synthesized sinusoidal current at the source.

Since the basic configuration of the active filter involves a power switching circuit, a control strategy is a prerequisite for driving the power switch accordingly to generate the desired harmonic wave shape. Hence, keeping this in mind, two such methods can be used here to command the power switching circuit. One is the hysteresis control technique, where the error function is centered in a predefined hysteresis band. When the error tries to cross the upper or lower hysteresis limit, the controller makes an appropriate switching decision to restrict the error within the prescribed band. The other method is the one in which the error is compared with a fixed high frequency triangular carrier signal. The intersection of these two waveforms determines the switching instants of the switching device. Though both the approaches have been widely used but the former suffers from a serious demerit of operating the switch at an unknown variable frequency. Here, the active filter has been tested applying both the control methods in a simulated environment.

Basically, active power filters have been realized using two types of converters voltage source inverters (VSI) and current source inverter (CSI). Current fed pulse-width modulated inverter bridge structure is considered reliable but has higher losses and requires an inductor at the dc side. The other active power filter based on VSI has a self supporting dc voltage bus with a large dc capacitor. This converter topology is well accepted as compared to the CSI version since it is lighter, cheaper and expandable to multilevel and multistep versions, to boost the operation with lower switching frequency. Also in high power applications capacitor is more suited than an inductor.

Consequently, the active power filter considered here for simulation purpose is a three-leg current controlled voltage source converter. This forms the major power circuit shown in Fig.1, which is designed here using IGBT's owing to their capability to operate at a relatively high power at high switching frequency.

This paper presents the concept of using a fixed set of harmonic to compensate for the input current harmonics drawn by a SCR converter, rather than attempt to compensate for a large number of harmonics.

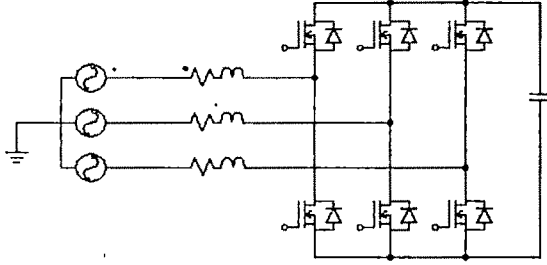


Fig.1: Power Circuit of Active Power Filter

II. INPUT CURRENTS OF A SCR CONVERTER

A SCR converter operating at different delay angles draws non-sinusoidal currents, which are high in harmonic content. The input currents i_a , i_b , i_c have rectangular waveforms with an amplitude I_d . The current waveform of phase-a is phase shifted by an angle α , which is the delay angle. Using the Fourier components the currents i_a , i_b and i_c can be expressed as :

$$i_a = \sqrt{2}I_{s1} \sin(\omega t - \alpha) - \sqrt{2}I_{s5} \sin[5(\omega t - \alpha)] - \sqrt{2}I_{s7} \sin[7(\omega t - \alpha)] + \sqrt{2}I_{s11} \sin[11(\omega t - \alpha)] + \sqrt{2}I_{s13} \sin[13(\omega t - \alpha)] - \sqrt{2}I_{s17} \sin[17(\omega t - \alpha)] - \sqrt{2}I_{s19} \sin[19(\omega t - \alpha)] + \dots \quad (1)$$

$$i_b = \sqrt{2}I_{s1} \sin(\omega t - \alpha - 120) - \sqrt{2}I_{s5} \sin[5(\omega t - \alpha - 120)] - \sqrt{2}I_{s7} \sin[7(\omega t - \alpha - 120)] + \sqrt{2}I_{s11} \sin[11(\omega t - \alpha - 120)] + \sqrt{2}I_{s13} \sin[13(\omega t - \alpha - 120)] - \sqrt{2}I_{s17} \sin[17(\omega t - \alpha - 120)] - \sqrt{2}I_{s19} \sin[19(\omega t - \alpha - 120)] + \dots \quad (2)$$

$$i_c = \sqrt{2}I_{s1} \sin(\omega t - \alpha + 120) - \sqrt{2}I_{s5} \sin[5(\omega t - \alpha + 120)] - \sqrt{2}I_{s7} \sin[7(\omega t - \alpha + 120)] + \sqrt{2}I_{s11} \sin[11(\omega t - \alpha + 120)] + \sqrt{2}I_{s13} \sin[13(\omega t - \alpha + 120)] - \sqrt{2}I_{s17} \sin[17(\omega t - \alpha + 120)] - \sqrt{2}I_{s19} \sin[19(\omega t - \alpha + 120)] + \dots \quad (3)$$

In the above, only the non-triplen odd harmonics h are present and

$$h = 6n \pm 1, n = 1, 2, K$$

The rms value of the fundamental frequency component is,

$$I_{s1} = 0.78I_d$$

and the rms values of the harmonic components

$$I_{sh} = \frac{I_{s1}}{h} \quad \text{where } h = 6n \pm 1$$

The rms value of the phase current can be calculated as [2]:

$$I_s = \sqrt{\frac{2}{3}} I_{s1} = 0.816 I_d$$

Hence the THD is obtained as 31.08% considering the source inductance to be zero.

III. ACTIVE-FILTER SET-UP

Conventionally, shunt active power filters have been recognized as a solution to minimize the harmonic content for existence of non-linear loads (diode, thyristor converters etc.). The basic principle is the creation and injection of the harmonic currents up to a desired order into the system. The efficiency and effectiveness is dependent on the control scheme. Several techniques of controlling an active filter have been proposed in [3-5] to attain the desired degree of harmonic compensation.

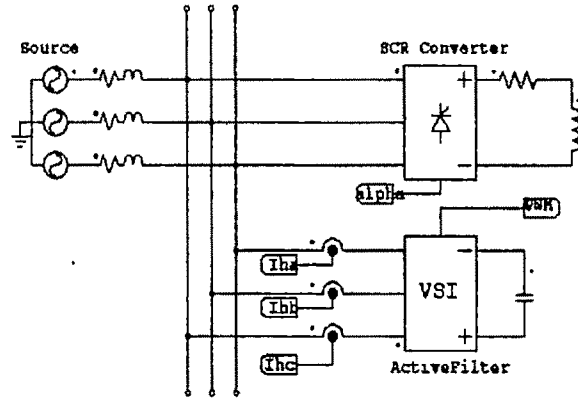


Fig.2: Simulation Block Diagram

The maximum harmonic order that an active power filter is able to compensate defines the filter bandwidth. The current becomes near sinusoidal after compensation. There are many pre-established current control pulse-width modulation techniques having their own merits and demerits. One of them is the tolerance-band control which is simple to implement but the switching frequency varies along the current waveform. In this study the reference currents are generated in Matlab with the aid of equations (1-3) and eventually fed to the controller. The line currents are sensed and ultimately fed to the controller. In the controller these two currents are compared and the error function is utilized in producing the pulse-width modulated signals for switching the six IGBT's, configured as a three-phase VSI. Although the study has been verified using both the control techniques i.e. hysteresis control and fixed frequency control methodologies, here the results of the latter only is included.

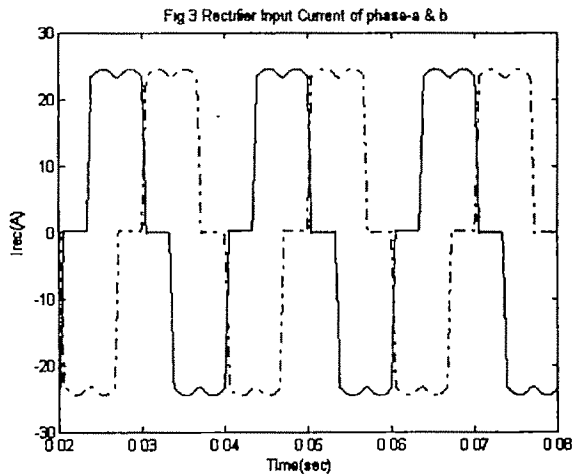
IV. SIMULATION AND RESULTS

A digital simulation of the entire active power filter set-up is accomplished in MATLAB/Simulink. The harmonic currents as given in the equations above are used to generate the harmonic wave shapes of the three phases and are fed into the system as the reference currents. The control system as discussed has been developed in this work as simulink subsystems of the main power circuit. The major components of the active filter i.e., line inductor and dc bus capacitor needs a trade-off for proper compensation from the actual design criteria. Thus to obtain the best values of the line inductor and dc capacitor, rigorous simulations were performed to ascertain the performance of the active power filter.

Table-I
Main Parameters of the Simulated System for Non-Linear load

System Parameters	Numerical Values
System Voltage	110V, 3-phase, 50Hz
Load	R-L load
DC Bus Capacitor	2500 μ F
Line Reactor	1mH

The shunt active filter has been simulated considering ideal power switches and later extended to actual practical converter using IGBT's. The study and simulation has been done for a non-linear load realized using a SCR based converter for delay angles 0 to 60 deg. The simulation results at 30 deg and 60 deg only are shown here.

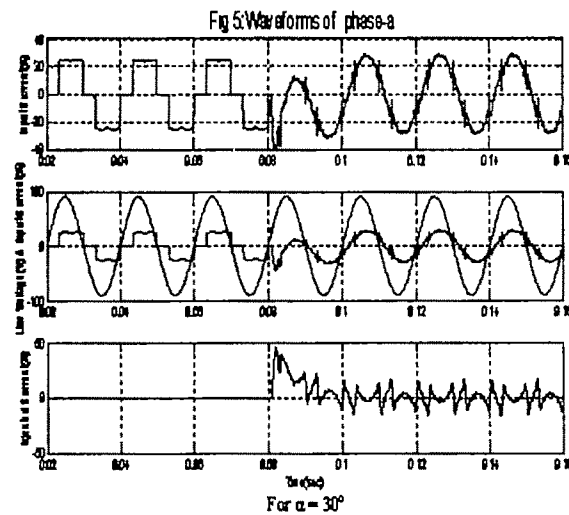
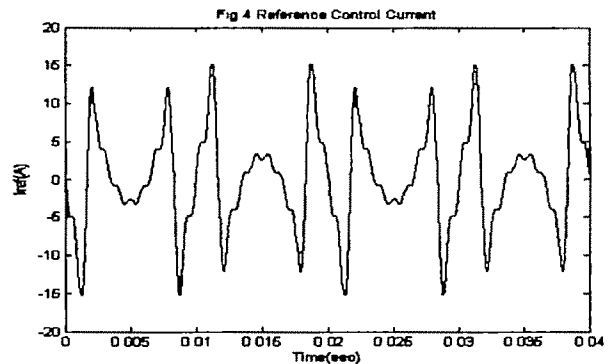


For a triggering angle $\alpha = 30^\circ$ as shown in Fig.5, the active filter was switched on at $t = 80$ ms. The results for $\alpha = 60^\circ$ are shown in Fig.6. The current drawn by the rectifier is also shown separately in Fig.3. The sudden change of the somewhat quasi-square nature of current into a near sinusoidal one after switching on the active filter, can be easily observed. Fig.4 shows the reference current generated by the controller and the actual compensation current of phase 'a' is as shown in Fig.5. The dc bus capacitor of the power circuit is self sufficient and charges to around 350V, maintaining its charge. There is a marked decrease in the total harmonic distortion after inclusion of higher harmonic orders in the reference

current waveform, as illustrated in Table-II. The actual total harmonic distortion of the current drawn from the supply by the non-linear load without use of the active filter is about 31%. The simulation results also asserts that use of very small value passive filter brings about remarkable change in the input current wave shape i.e. making it very close to a sinusoidal waveform.

Table-II

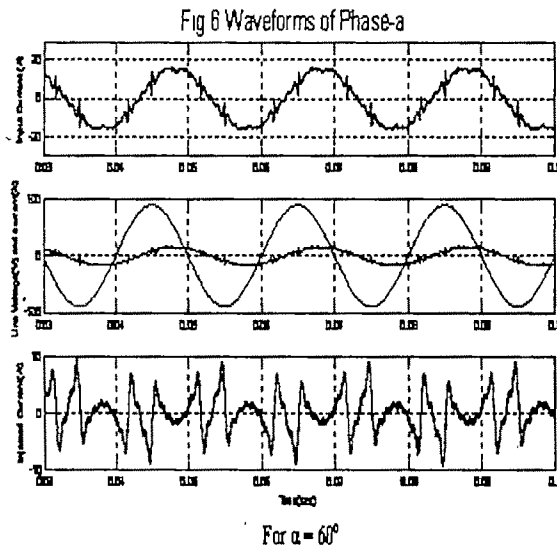
Harmonic Order	Calculated THD	Actual THD in Simulation
$5^{th}+7^{th}$	18.12%	17.76%
$5^{th}+7^{th}+11^{th}+13^{th}$	13.68%	14.48%
$5^{th}+7^{th}+11^{th}+13^{th}+17^{th}+19^{th}$	11.16%	12.41%



A small value inductor at the input of the rectifier reduces the THD to a value of around 10%. The Simulink block diagram (Fig.2) consists of the main load circuit wherein, the active filter is in shunt. The SCR converter can be operated at various delay angles from the block 'alpha' and the gate of the IGBT 's (which are in bridge configuration in the VSI block) are driven by current controlled PWM pulses generated by the current controller. The inductor currents of the VSI can be

sensed by current transducers. I_{ha}, I_{hb}, I_{hc} are sensed and fed to the current controller where they are compared with the respective phase reference currents and processed to drive the VSI in such a manner so as that actual inductor currents are able to track the reference current. The SCR converter can be operated at various delay angles from the block 'alpha' and the gate of the IGBT 's (which are in bridge configuration in the VSI block) are driven by current controlled PWM pulses generated by the current controller. The reference control current as shown, is a composite current, generated considering all major harmonics as referred in Table-II.

As seen above, the reference current generated by the controller is a very complex waveform having multiple peaks and the frequency which is programmed to coincide with the frequency of the ac supply.



V. DESIGN OF THE SHUNT ACTIVE-POWER FILTER

The power circuit implemented in this work is a three-leg current controlled voltage source inverter topology with a dc bus capacitor and a set of input reactors. The current controller forces the inverter as a controlled current source. The dc side of the inverter as mentioned is an energy element rather than a power supply, as the shunt active filter can be controlled to supply the losses in the inverter from the ac network side.

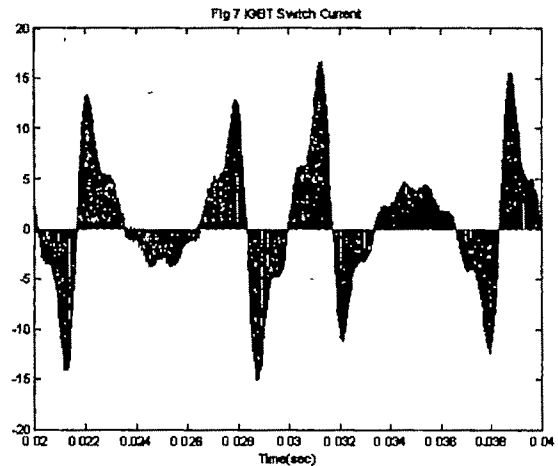
Hence power circuit design of the shunt active filter involves the selection of the value of the filter capacitor, filter inductor, the controllable switches and the nominal value of the capacitor voltage. Although for simulation purpose, the switches considered were ideal initially but later on, the design was extended to using MOSFET as well as IGBT (Insulated Gate Bipolar Transistor). Owing to their behavior to support unipolar voltage and bipolar current, an IGBT with antiparallel diode is used here to realize the switches. The peak current that flows through the device is the instantaneous value of the maximum inductor current, so the device has to have a peak current rating accordingly. The voltage rating of the power switches has to sustain the maximum dc bus voltage.

The inductor and the capacitor values should take into account switching frequency of the VSI, which should be high enough to eliminate harmonics upto a certain frequency. Theoretically, the switching frequency of the IGBT's should be twice of the maximum harmonic frequency to be eliminated. Some basic criteria are followed while designing the reactor and the dc capacitor values.

The peak amplitude of the injected current of the high frequency components is to be restricted to an acceptable value of the rated value of the load current. The instantaneous di/dt generated by the shunt active filter should be greater than the di/dt of the harmonic component of the load so that proper harmonic neutralization is possible. The tracking of the filter inductor current with the generated reference current improves when the filter inductor value is made smaller. The mathematical design equations are as given below as detailed in [6].

$$\frac{I_{af}}{I_1} = \frac{V_{af}}{I_1 \cdot (f_s / f) \cdot \omega L_f} < (3-5)\% \quad (4)$$

$$\sqrt{2}V + L_f \left| \frac{di}{dt} \right|_{load} < V_{dc} \quad (5)$$



where, I_{af} is the r.m.s value of the converter current at the switching frequency f_s , V_{af} is the r.m.s value of converter output voltage at f_s and I_1 is the r.m.s value of fundamental load current.

As discussed earlier and supported by the equations (4) & (5), a low value of reactor is suitable, as a high di/dt is preferable for maximum nullification of harmonics, ultimately leading to a improved wave shape at the source and lower THD. However, in that case, a high switching frequency is required to minimize the input current ripple. So there is a fundamental compromise on the choice of the filter inductor based on these lines. Here, a thorough and rigorous simulation has been carried out to achieve at the most accurate solution to the design of the reactor. The case is similar for the dc bus voltage also. To acquire a high di/dt the dc voltage can be

increased which again increases the high frequency ripple in the input source current.

The variation of dc bus voltage can be expressed as:

$$\Delta V_{dc} = v_{dc \max} - v_{dc \min}$$

$$= \frac{\left[\sum (v_{s,j} i_{j,h}) dt \right]}{CV_{dc}} \dots$$

..... $h = 3, 5, \dots$

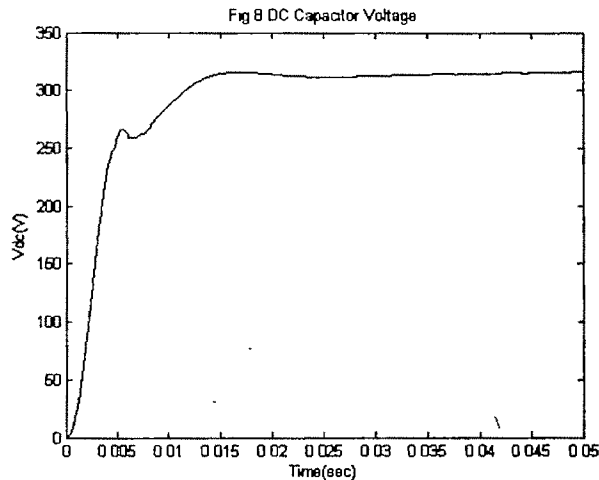
(6)

The capacitor value is mathematically expressed as [6],

$$C = \frac{\Delta \left[\sum (v_{s,j} i_{j,h}) dt \right]}{r_v V_{dc}^2}$$

$$r_v = \frac{\Delta V_{dc}}{V_{dc}}$$
(7)

r_v = % ripple of dc bus voltage.



The perfect value of dc bus capacitor is obtained by simulation as it is also load dependent. Here the study has been carried out with $L_f = 1\text{mH}$ and $C = 2500\mu\text{F}$. It is also observed that a filter inductor as low as 0.5mH also suffices but the current ripple increases in that case, also a higher value of inductor 2mH also gives suitable tracking of the desired current at a high switching frequency of 30KHz . Beyond this value the current is never able to follow the template and thus results in a high THD and complete failure of the active filter. The active filter circuit is also tested with various capacitors ranging from $1500\mu\text{F}$ to around $4000\mu\text{F}$ and it is seen to operate successfully.

VI. CONCLUSION

The study and simulation shown in this paper imparts an exhaustive investigation on the shunt active power filters. The Matlab simulation here gives an in-depth justification of the operation of the active power filters in a non-linear load which is a SCR converter associated in elimination of certain selected harmonics for a known load. The waveforms are

examined for various triggering angles ranging from $(0-60\text{deg})$ with satisfactory results.

In the latter half, the basic design of an active power filter is analyzed and the fundamental structure of the entire set-up is discussed.

REFERENCES

- [1] L. Gyugyi and E. Stycula, "Active AC filters," in *Conf. Rec. IEEE-IAS Annu.Meeting*, 1976, pp.529-525.
- [2] Mohan, N, Undeland, T. M. and Robbins, W. P: "Power electronics : converters, applications and design" (J. Wiley & Sons, 2003).
- [3] L. Rosseto and P. Tenti, "Using ac fed PWM converters as instantaneous reactive Power Compensators", *IEEE Trans. Power Electronics*, Vol 7, No.1, pp224-229, 1992.
- [4] J. C Montano and P. Salmeron, "Identification of Instantaneous current components in Three Phase System", *IEE Proc. Vol. 146No.5*, pp227-223, 1999.
- [5] H. Agaki, S. Ogasawara and H. Kim, "The Theory of Instantaneous Power in Three Phase Four-Wire Systems. A Comprehensive Approach" *Proc. IEEE-IAS Annual Meeting*, pp.431-439, 1999.
- [6] F. A. Talukdar, S. Choudhury, S. K. Biswas, "An instantaneous three-phase four-wire filter strategy", *Proc. IEEE PEDS 2001*, vol 2, 2001.

SiC based Buck Boost Converter

Vineeta Agarwal¹, and Neeraj Verma²

¹ MotiLal Nehru National Institute of Technology, Allahabad, INDIA e-mail: Vineeta_agarwal123@rediffmail.com

Abstract – An attempt has been made to analyze a current controlled buck-boost converter with a SiC diode using a software package ORCAD PSPICE. The simulation results indicate that both in charging mode as well as in discharging modes, the converter with SiC diode has a better performance compared to that with Si diode. The turn-on switching losses are found to be reducing to a great extent when SiC (CSD10060) diode as compared to that of the Si (MUR840) diode has been used. However, there is very little improvement for turn-off switching losses with a SiC diode. The SiC diodes reverse recovery losses have been found to be very low as compared to that of the Si diodes. This is because of very low or negligible value of the reverse recovery current flowing through SiC diode. Due to the reduction in the total losses comprising of switch and the diode losses in the case of the SiC (CSD10060) diode as compared to the Si (MUR840) diode, the overall efficiency of the buck boost converter is increased about 3 to 5 percent.

Key words—Buck-Boost Converter, Current Controlled, Inductor Current, Silicon Carbide (SiC)

1. INTRODUCTION

Wide band gap SiC power devices have the potential for reliable operations at higher junction temperatures, higher voltages, higher frequencies and thus higher power densities than what can be achieved with Si devices [1]. These advantages enable the SiC technology-based power conversion systems (PCM) to be made smaller, lightweight, more efficient and robust [2]. Recent studies predicted that the volume of a power converter system could be reduced five times through the utilization of SiC power devices [3]. SiC high-frequency diodes are ideal for military aircraft requiring lightweight high-performance electronic radar systems, gasoline engines, dynamic voltage restorers, static VAR compensators, high voltage dc (HVDC) transmission, and flexible ac transmission systems (FACTS) [4]. Use of SiC high power diodes in DC-DC converter enables high temperature operation, which is a desired feature in many applications [5].

In this paper an attempt has been made to evaluate the performance of Silicon and Silicon Carbide diode in a Buck-Boost Converter as it imposes a variety of switching stresses on the device [6]. The converter uses average current mode controlled scheme [7]. The overall performance of the converter is compared on the basis of the switch current during turn-on and turn-off period, reverse recovery current of the diodes, turn-on and turn-off switching losses, conduction losses, temperature rise, and weight/size of heat sink etc. Simulations are done for both SiC diode converter and its Si

counterpart. Simulation results reflect the better performance with SiC diode. With the same heat sink size and ambient temperature, great advantages in efficiency and junction temperatures are expected in the SiC-based converter [8].

II. PRINCIPLE OF OPERATION

Figure 1 shows the schematic diagram of a current controlled buck-boost converter. The power switch, S, is an n-channel MOSFET and output diode D_m is a SiC diode. The inductor, L, and capacitor, C, make the effective output filters whereas the resistor, R_L , represents the load seen by the power stage output. The current mode control is used in an inner loop while an outer control loop sets the reference current through output voltage feedback. Such control logic has the dual aim, regulating the output voltage, as well as limiting the inductor current [9]. The voltage error amplifier compares the reference voltage, V_{ref} and the voltage feedback signal, to generate a error signal V_{error} . Inductor current is sensed through a resistor. The resulting voltage is compared with voltage V_{error} that sets the desired inductor current signal V_{CA} . This signal V_{CA} is compared with a saw tooth ramp in PWM comparator to determine the duty cycle of the switch. Output of PWM comparator is fed to gate of MOSFET through RS flip-flop.

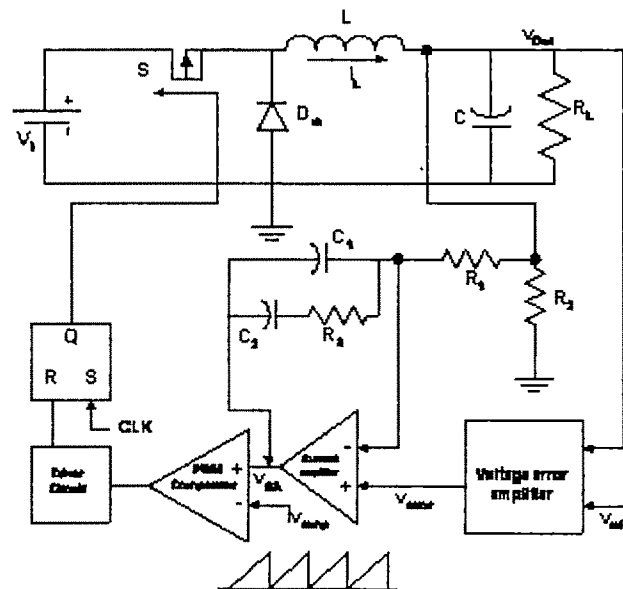


Fig. 1 Schematic diagram of current controlled buck-boost converter.

Figure 2 shows the comparator voltage waveforms when the current amplifier gain is optimized using the slope matching criteria [10].

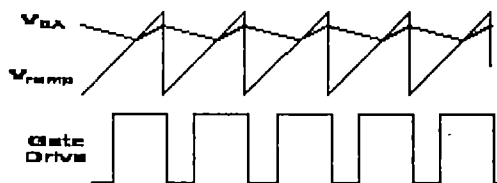


Fig - 2. Comparator Voltage Waveforms

III. SIMULATION RESULTS

The circuit of Fig.1 is simulated on the software package PSPICE. In order to minimize the circuit components, and to improve the performance of the overall circuit, high speed PWM controller IC SG1825 has been used. The operational amplifier IC TL082 is designed to offer a wider selection than any previously developed operational amplifier family. The MOSFET used in the simulation is IRF540; silicon (Si) diode is MUR840 and Silicon Carbide (SiC) diode is CSD10060. The voltage reference circuit used in the control circuit sets up the inductor level. The minimum voltage reference applied is 3.6 V and the corresponding average inductor current level is 1.5A and for the maximum voltage reference of 5.3 V, the corresponding average inductor current level is 4.87A.

Fig 3 shows the inductor current in the converter when input voltage (V_i) = 40 V and voltage reference V_{ref} is equal to 3.6V. The value of the output voltage has been found approximately 29.6 V as shown in Fig. 4

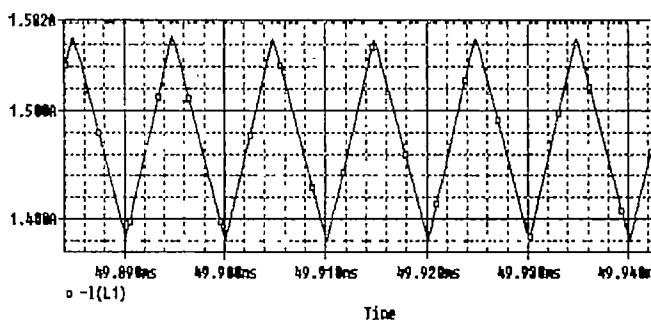


Fig. 3. Inductor current ($V_i = 40$ V)

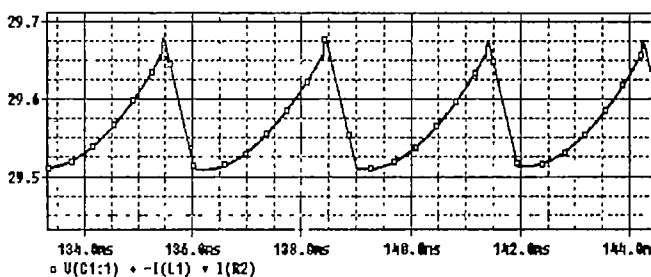


Fig. 4. Output Voltage, V_o

Fig. 5 and 6 show the waveforms of the current through the switch during turn-on for MUR840 and CSD10060 diodes respectively (for $I_L = 1.5$ A). It has been observed that there is a huge reduction in the transient current through the MOSFETs when SiC diode (CSD10060) is used as compared to the Si diode (MUR840). This is possible only because of very low reverse current that flows during turn-off of the SiC (CSD10060) diode as compared to the Si (MUR840) diode.

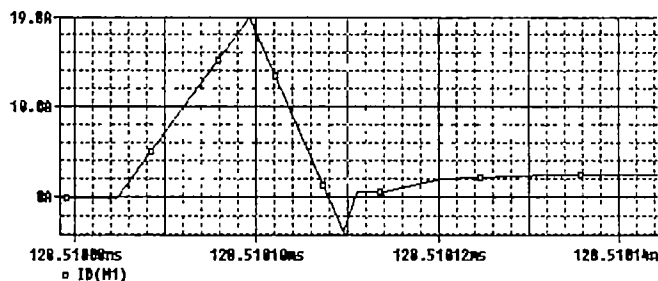


Fig. 5. Switch current during turn-on period when MUR840 is used

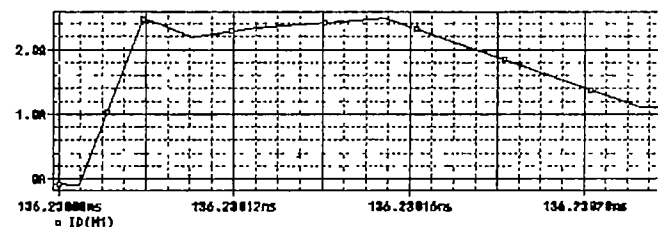


Fig. 6. Switch current during turn-on period when CSD10060 is used

The reverse recovery current flowing through Si diode and the SiC diode is shown in Fig. 7 and Fig. 8, respectively. This shows that there is a large reduction in the MOSFETs turn-on losses.

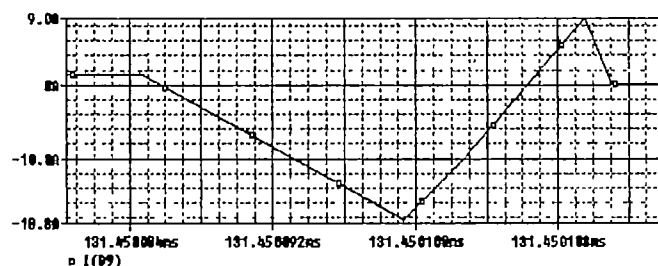


Fig. 7 Reverse Recovery Current through MUR840 (Si diode)

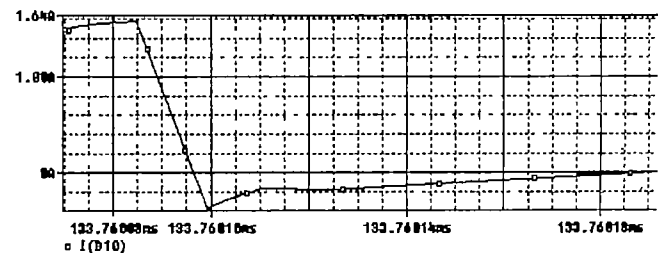


Fig 8. Reverse Recovery Current through CSD10060 (SiC diode)

The power dissipation during turn-on and turn-off period of the MOSFETs for the Si (MUR840) and the SiC (CSD10060) diodes are shown in the Fig. 9 and Fig. 10 respectively. It was found that when Si diode is used there is large power dissipation in the switch but when SiC diode was used the power dissipation in the MOSFET is largely reduced.

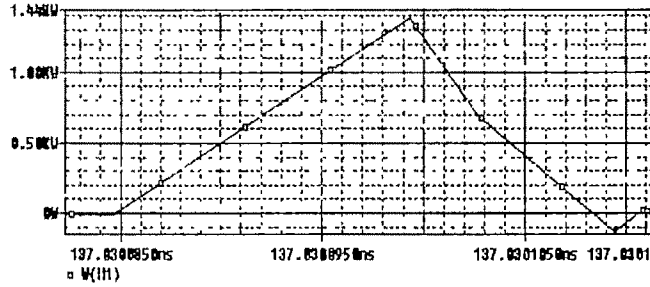


Fig. 9 MOSFET turn-on losses when MUR840 diode is used

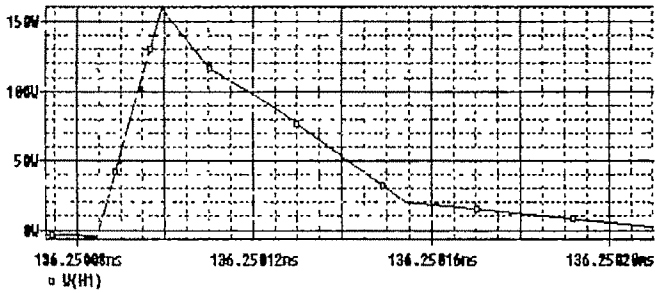


Fig. 10 MOSFET turn-on losses when CSD10060 diode is used

The power dissipation in MOSFET during turn-off period is shown in the Fig. 11 and Fig. 12 respectively. No significant changes have been observed in the losses of the MOSFET during turn-off.

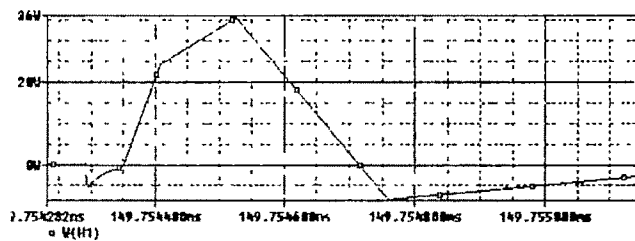


Fig. 11 MOSFET turn-off losses when MUR840 diode is used

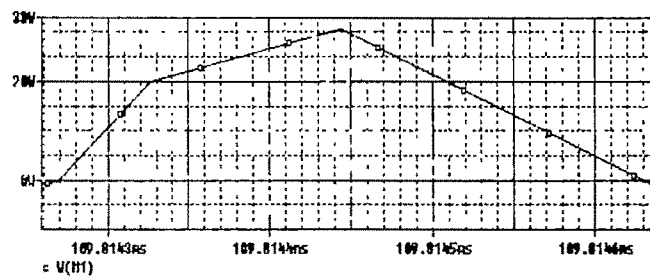


Fig. 12 MOSFET turn-off losses when CSD10060 diode is used

The losses associated with the diodes themselves are shown in Fig. 13 and Fig. 14 for the Si (MUR840) and the SiC (CSD10060) diodes respectively. The figures show that the losses of the SiC diode (CSD10060) is low as compared to the Si diode (MUR840).

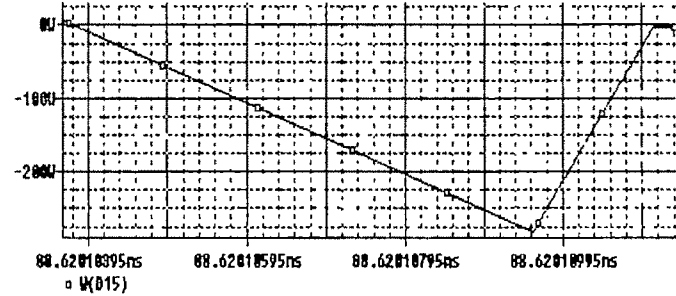


Fig. 13 Si (MUR840) diode losses during MOSFET's turn-on

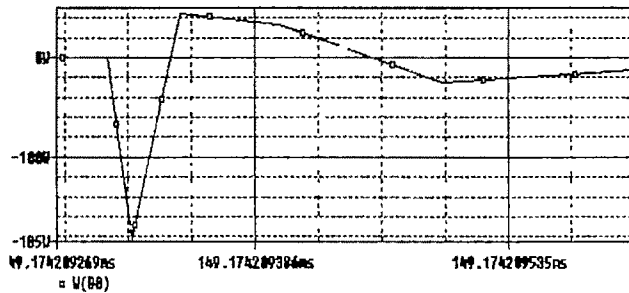


Fig. 14 SiC (CSD10060) diode losses during MOSFET's turn-on

IV. EXPERIMENTAL RESULTS

A prototype of current controlled buck boost converter is developed as shown in Fig. 15. It consists of a n-channel MOSFET (IRF-9530) and SiC diode CSD10060. The converter has following design specification:

- Input voltage range (V_i): 10 - 30 V
- Regulated output voltage (V_o): 20 V
- Switching frequency (f_s): 100 kHz.
- Output power (P_o): 20W
- Peak to peak ripple inductor current (ΔI): 0.2A
- Peak to peak ripple output voltage (ΔV): 0.5V
- Load resistance, R_L : 45 Ω

The converter is operated under continuous mode, so the required value of critical inductance for continuous conduction mode operation is calculated from (1), with $D = 0.5$, $R_L = 45 \Omega$, $f_s = 100\text{kHz}$, as:

$$L_c = \frac{(1-D)R_L}{2f_s} = 112.5 \mu\text{H} \quad (1)$$

Using (2), the value of the inductance is obtained as

$$L = \frac{V_i D}{f_s \Delta I} = 500 \mu H \quad (2)$$

The above inductance is larger than the required value of the critical inductance. This confirms the operation of the buck boost converter in the continuous conduction mode. The value of the capacitor used here is, $C = 2200 \mu F$.

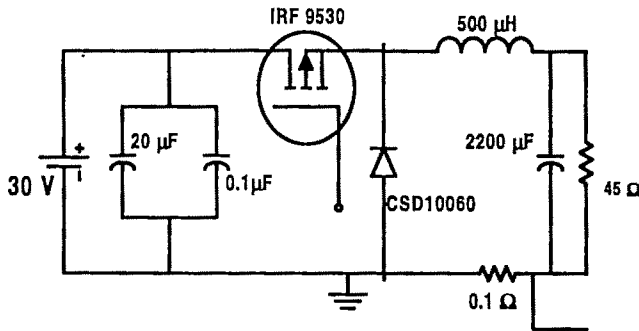


Fig. 15 Power circuit of the buck-boost converter

Two input capacitors of $20\mu F$ (350V, electrolytic) and another $0.1 \mu F$ (400V ceramic), connected in parallel, are also used. A standard resistance (0.1Ω 10A) has been used to take out the current signal from the power circuit and feed into the current controller.

Figure 16 shows the block diagram of the current controller circuit. Output voltage of the buck boost converter is fed to the error amplifier. Other input to error amplifier is the reference voltage, 2.5 V. For error amplifier IC TL084 (JFET-input operational amplifiers) is used. Output of the error amplifier, I_{ref} and the amplified inductor current are fed to the current comparator (LM311). The output of LM311 is now fed to the input terminal of the inverter (IC 7404). Finally the output of the D flip flop is given to the driver circuit of the MOSFET.

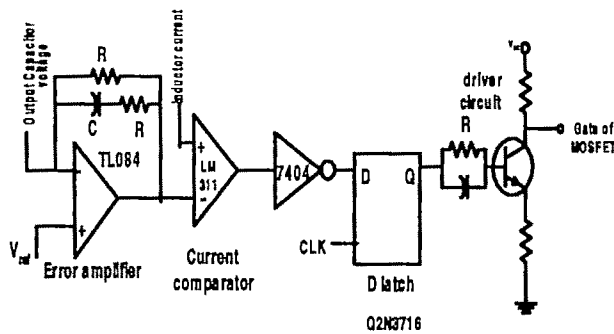


Fig. 16. Current Controller Circuit

Experimental results are obtained by observing inductor current waveforms at variable input supply voltage (V_i). Fig. 17 shows inductor current waveform, I_L , for $V_i = 30 V$. It is seen that inductor current state repeats after each clock cycle. The inductor current is bounded by the current reference value of 1.5 A. The value of the output voltage has also been shown in Fig. 17 by the bottom trace.

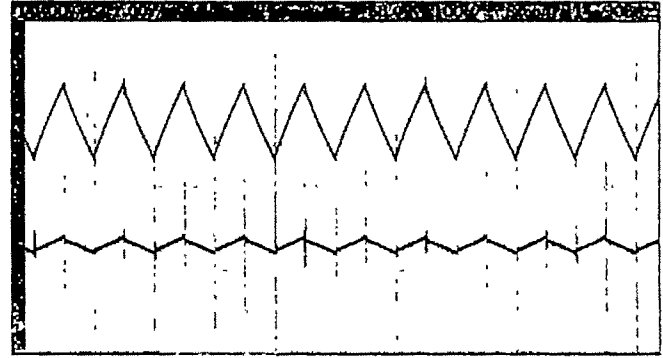


Fig. 17 Inductor current (Top trace) and Output voltage (bottom trace)

The overall efficiency of the converter is obtained for both types of converter. It is found to be 88 % when Si diode is used as compared to 92.6% when SiC diode has been replaced. Thus, the performance improves with SiC diodes.

VI. CONCLUSIONS

A buck boost converter has been designed which uses the SiC semiconductor diode. It has been observed that turn-on MOSFETs losses are reduced to a great extent when SiC (CSD10060) diode is used as compared to that of the Si (MUR840) diode. However, there is a little improvement in the MOSFETs turn-off losses. The SiC diodes reverse recovery losses are very low as compared to that of the Si diodes. This is due to the very low or negligible value of the reverse recovery current flowing through the SiC diode as compared to the reverse recovery current flowing through the Si diode. Due to the reduction in the total losses comprising the MOSFET and the diode losses in the case of the SiC (CSD10060) diode as compared to the Si (MUR840) diode, the overall efficiency of the buck boost converter is increased. The efficiency of the converter is about 3 to 5 percent higher in the case of the SiC diode as compared to the Si diode.

VII. REFERENCES

- [1] Burak Ozpineci and M. Tolbert Leon, " Characterization of SiC Schottky Diodes at Different Temperatures", *IEEE Power Electronics Letters*, Vol. 1, No. 2, June 2003.
- [2] M. Hernando, J. Sebastian, P. Villegas, A. Fernandez, J. Garcia, M. Rascon, "Comparing Si and SiC diodes performance in a commercial AC-to-DC rectifier with power factor correction", *Power Electronics Specialist Conference, 2003. PESC '03. 2003 IEEE 34th Annual Volume 4*, 15-19 June 2003, Page(s): 1979 - 1983.

- [3] Anant Agarwal, Ranbir Singh, Sei-Hyung, James Richmond, Craig Capell, Scott Schwab, Brice Moore and John Palmour, "600 V, 1-40 A, Schottky diodes in SiC and their applications", Application note from CREE Inc. 2004
- [4] Ranbir Singh, James Richmond, "SiC power Schottky diodes in power factor correction circuits", Application note from CREE Inc.
- [3] M. Trivedi, M.; Shenai, K., Neudeck, P.G.; "High-speed switching performance and buck converter operation of 4H-SiC diodes", High Performance Devices, 2000. Proceedings 2000 IEEE/Cornell Conference on 7-9 Aug. 2000 Page(s): 69 – 78.
- [4] Allen R. Hefner, Ranbir Singh, Jih-Sheng Lai, David W. Berning, Sebastian Bouche, Christophe Chapuy, "SiC power diodes provide breakthrough performance for a wide range of applications", IEEE transaction on Power Electronics, Vol. 16, No. 2, March 2001, pp 273-279
- [5] Trivedi, M.; Shenai, K.; "Hard- and soft-switching buck converter performance of high-voltage 4H-SiC and Si P-I-N diodes", Industry Applications Conference, 2001. Thirty-Sixth IAS Annual Meeting. Conference Record of the 2001 IEEE Volume 1, 30 Sept.- 4 Oct., 2001 Page(s): 391 – 395
- [6] Dallas T. Morissette, A. James Cooper, R. Michael, M. Melloch, Gary . M. Dolny, Praveen Shenoy, M. Zafrani and Jon Gladish, "Static and dynamic characterization of large area high current density SiC Schottky diodes", IEEE transaction on Electron Devices, Vol. No. 48, No. 2, Feb, 2001.
- [7] B. Ozpineci, L. M. Tolbert, S. K. Islam, Md. Hasanuzzaman, "Effects of Silicon Carbide power devices on HEV PWM inverter losses", IECON'01: the Annual Conference of the IEEE Industrial Electronics Society.
- [8] D.T. Morissette, J. A. Cooper, "Theoretical comparison of SiC PIN and Schottky diodes based on power dissipation considerations", IEEE Transactions on Electron Devices, Volume 49, Issue 9, Sept. 2002 Page(s): 1657 – 1664.
- [9] A. Blasser, M. H. Kherahwala, M. Ghezzi, R.L. Steigerwald, N.A. Evers, J. Chow Kretchmer, "A comparative evaluation of new silicon carbide diodes and state-of-the-art silicon diodes for power electronic applications", "IEEE Transactions on Industry Applications", Volume 39, Issue 4, Page(s): 915 – 921. July-Aug 2003
- [10] G. Spiazzi, S. Buso, M. Citron, M. Corradin, R. Pierobon,, "Performance evaluation of a Schottky SiC power diode in a boost PFC application", IEEE Transactions on Power Electronics, Volume 18, Issue 6, Page(s). 1249 – 1253. Nov. 2003

Simulation of a Novel Zero Voltage Transition (ZVT) Technique Based Boost Power Factor Correction (PFC) Converter with EMI Filter

P. Ram Mohan¹, M. Vijaya Kumar² and O. V. Raghava Reddy³

¹ Associate Professor, E.E.E Dept, G.Pulla Reddy Engg. College, Kurnool, Andhra Pradesh, India

² Professor, JNTU College of Engineering, Anantapur, Andhra Pradesh, India

³ Scientist, ISRO Satellite Centre, Bangalore, India
rammohan_cdp@yahoo.co.in

Abstract—A novel Zero Voltage Transition (ZVT) technique based closed loop control of Boost Power Factor Correction (PFC) converter with Electro Magnetic Interference (EMI) Filter is presented in this paper. It operates at a fixed frequency while achieving zero voltage turn-on of the main switch and zero current turn-off of the boost diode. This is accomplished by employing resonant operation only during switch transitions. During the rest of the cycle, the resonant network is essentially removed from the circuit and converter operation is identical to its non-resonant counterpart. The principle of operation and simulation results of proposed converter are presented in this paper. The power factor is improved to near 0.99 using the proposed converter.

Key words— Power Factor Correction, Electro Magnetic Interference, Zero Voltage Transition, Common Mode, Differential Mode

I. INTRODUCTION

THE demand for power, which is increased tremendously over last few decades, has forced the power engineers to establish reliable network in order to supply quality power to the consumers. Power factor, which is defined as the cosine of the phase angle between the voltage and current signals, plays a key role in delivering quality power to the consumers. [1]

Over the years lot of research has been carried out for the control of the power factor. This research got a tremendous boost with the strides made in the miniaturization of the electronic industry. The component of input current normal to voltage across the load resistance wastes power in the resistance of the source generator.

In power supplies with a capacitor filter across the input bridge rectifier, the input line current consists of very narrow spikes with the fast rise and fall time. These current spikes have a high rms value, waste power and give rise to RFI/EMI problems. Power supplies with such input line currents have poor "power factor".

Power Factor Correction seeks to eliminate such line current spikes and force input current to be sinusoidal, in phase with input voltage and to generate a fairly well regulated DC output

voltage somewhat greater than the peak of the incoming sine wave. [2,3]

Generally EMI problems arise due to the sudden changes in voltage (dv/dt) or current (di/dt) levels in a waveform. In diode rectifier, the line current can be pulse of short duration and the diode recovery current pulse can generate transient voltage spikes in the line inductance. A conductor carrying dv/dt wave acts like an antenna and sensitive signal circuit and appear as noise. The EMI problems create communication line interference with sensitive signal electronic circuits. [4]

II. BASIC BOOST POWER FACTOR CORRECTION CONVERTER

Boost converters can be operated in either the discontinuous or continuous mode. But the continuous-mode boost topology is far better suited to yield relatively smooth, ripple-free half sinusoids of input line current in this application. This can be seen from Figure 1, which shows a continuous-mode boost converter fed from a constant DC input voltage.

In the continuous-mode of Figure 1, the inductor L_1 is made significantly larger. Then the Q_1 current (Figure 1c) has the shape of a large step of current with a slow upward ramp on it, and the D_1 current has the shape of a large step with a slow downward ramp. And importantly, there is no gap of zero current between the end of a turnoff and the next turn-on. Input line current (Figure 1e) is now the sum of the I_{Q1} and I_{D1} currents and if the ramps are made small by using a large L_1 , the line input current over one switching cycle is then a constant I_{av} with very small peak-to-peak ripple of ΔI . The input power is $V_{IN}I_{av}$.

Now for an AC input, such a continuous-mode boost converter is used after the input bridge rectifier output. At any point on the half sinusoid input voltage, the Q_1 ON time will be forced by a PWM control chip to boost that instantaneous voltage to the desired DC output voltage. A DC voltage error amplifier, a DC reference voltage, and a pulse with modulator in the control chip modulate the Q_1 ON time in a negative feedback loop, to yield a constant DC output voltage throughout the half sinusoidal input voltage.

The instantaneous input line current will be sensed by a sensing resistor R_s and will be proportional to the instantaneous voltage throughout the half sinusoid. During any one ON time, current flows through L_1 , Q_1 and R_s back to the negative end of the bridge and during the following OFF time it flows through L_1 , D_1 , R_0 and C_0 in parallel and R_s back to the negative end of the bridge. By making L_1 large, the peak-to-peak ripple current throughout each switching cycle is kept small. Depending on switching speed of Q_1 , there may be very narrow spikes on the half sinusoids of current monitored in R_s . If present, these may cause an RFI problem. But a very small capacitor (in the vicinity of 1.0mF) across R_s easily eliminates them.

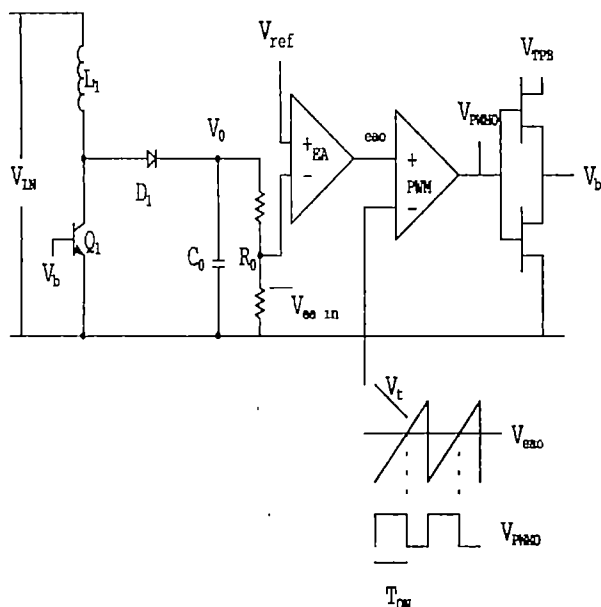


Figure 1a

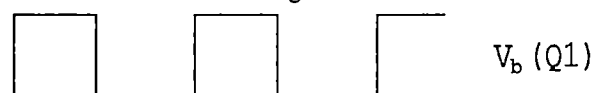


Figure 1b



Figure 1c

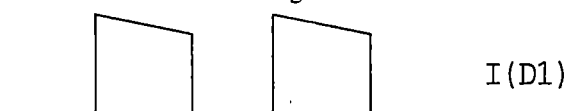


Figure 1d

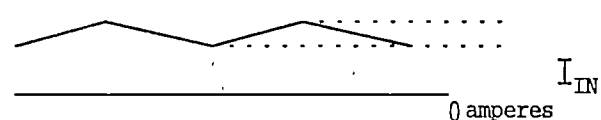


Figure 1e

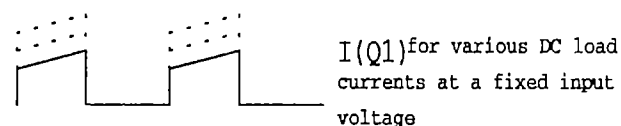


Figure 1f

Figure 1: Continuous conduction mode Boost Converter and wave forms of Q_1 and D_1 for various DC load currents at a fixed DC input voltage

III. ZERO VOLTAGE TRANSITION (ZVT) TECHNIQUE

In order to increase the switching frequency while maintaining acceptable efficiency, several soft switching techniques have been developed. Most of these resonant techniques increase the semiconductor current and/or voltage stress, leading to larger devices and increased conduction losses due to greater circulating current. [5]

The Zero Voltage Transition (ZVT) technique allows the increase in switching frequency without the associated increase in switching losses, while overcoming most of the disadvantages of the resonant techniques. ZVT converters operate at a fixed frequency while achieving zero voltage turn-on of the main switch and zero current turn-off of the boost diode. This is accomplished by employing resonant operation only during switch transitions. During the rest of the cycle, the resonant network is essentially removed from the circuit and converter operation is identical to its non-resonant counterpart. [6-8]

This technique allows an improvement in converter efficiency over the traditional boost converter, as well as operating the boost diode with reduced stress due to controlled di/dt at turn-off. This technique programs the input current of the converter to follow the line voltage so that the power factor is improved to 0.99.

The power stage of proposed Boost PFC converter with ZVT technique is shown in fig.1. The diode rectifier, inductor L , switch Q_{MAIN} , diode D_1 , capacitor C_0 and the load forms the basic boost converter. The switch Q_{ZVT} , diode D_2 , diode D_3 , inductor L_r and capacitor C_r forms the ZVT circuit. This ZVT circuit provides active snubbing of the diode and main switch of the basic boost converter.

The ZVT switch is turned on before turning on the main switch. This initiates a resonant process, which creates zero voltage switching conditions for the main switch. The time intervals where the ZVT circuit is active are very short when compared to the switching period. Hence, except for the commutation intervals, the waveforms of the ZVT technique based boost PFC converter are the same as traditional boost converter.

The timing diagram of ZVT technique is shown in fig.2. This figure shows the gate pulses for main switch Q_{MAIN} , ZVT switch Q_{ZVT} , drain to source voltage and drain current of main switch, current through resonant inductor L_r , voltage across diode D_1 and the current through diode D_1 .

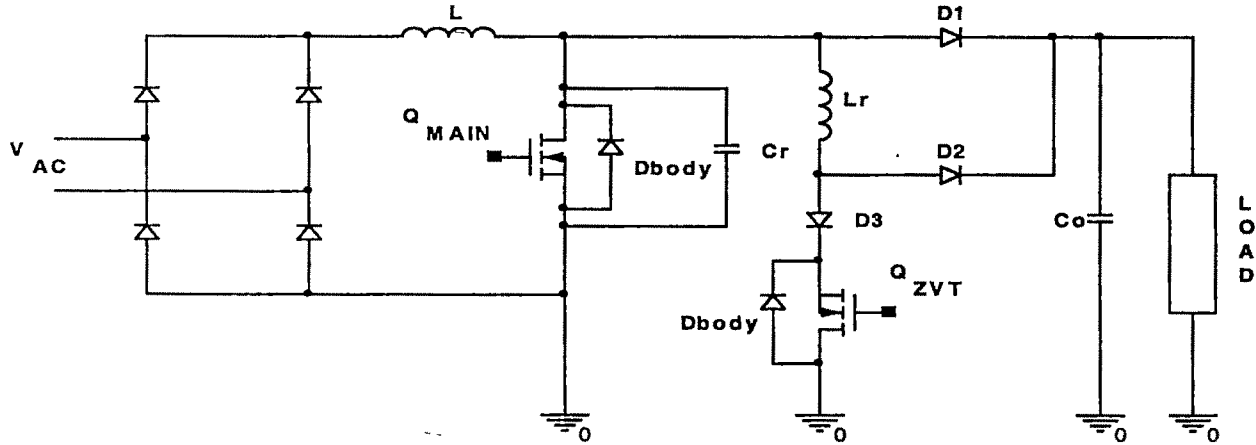


Figure 2. Power Circuit of ZVT technique based Boost PFC converter

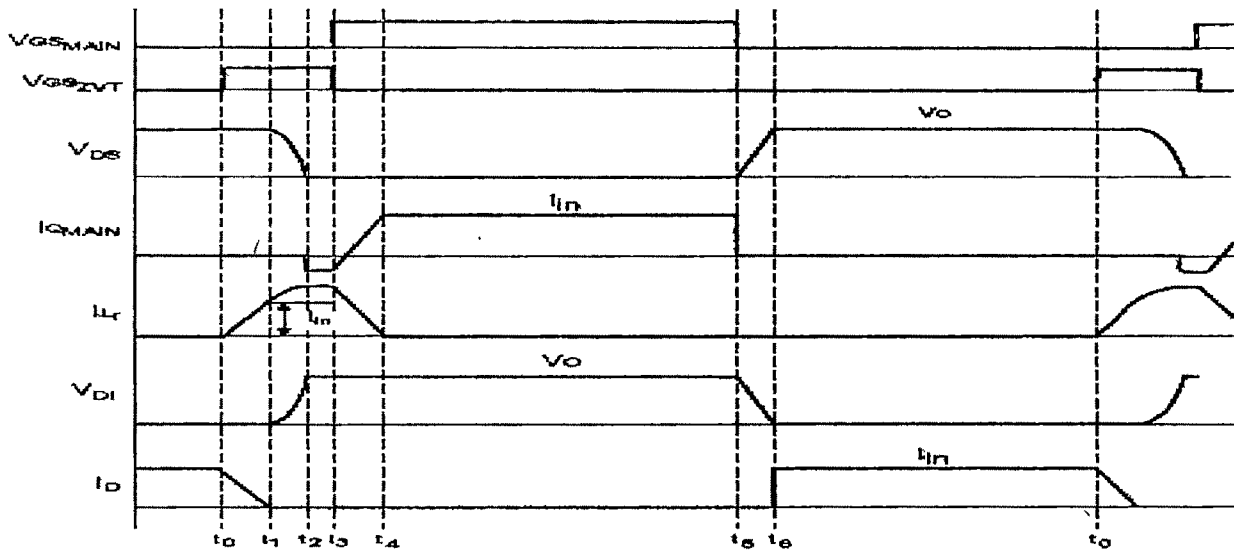


Figure 3. Timing Diagram

IV. MODES OF OPERATION

A. Mode 1 ($t_0 - t_1$):

During the time prior to t_0 , the main switch Q_{MAIN} is off and diode D_1 is conducting the full load current. At t_0 , the ZVT switch Q_{ZVT} is turned on. Then the current through the resonant inductor L_r i.e. I_{Lr} ramps up linearly to the value I_{in} i.e. the input current. During this time the current through diode D_1 i.e. I_D ramps down. When the diode current reaches zero, the diode D_1 turns off (i.e. soft switching of D_1). In the practical circuit some reverse recovery of the diode will occur since the diode needs time to remove the junction charge. During this interval, the voltage across the resonant inductor L_r is V_0 .

B. Mode 2 ($t_1 - t_2$):

At the instant t_1 , the current I_{Lr} reaches I_{in} . Now, the resonant inductor L_r and resonant capacitor C_r will begin to resonate.

This resonant cycle discharges C_r until its voltage equals to zero. The dv/dt of the drain to source voltage of the main switch i.e. V_{DS} is controlled by C_r . The current I_{Lr} continues to increase while C_r discharges. At the end of this period, the body diode of the main switch turns on and hence the voltage V_{DS} reaches zero. The time required for the voltage V_{DS} to reach zero is $1/4$ of the resonant period.

C. Mode 3 ($t_2 - t_3$):

At the instant t_2 , the body diode of the main switch turns on and the voltage V_{DS} reaches zero. Now, the main switch Q_{ZVT} can be turned on since the voltage across it i.e. V_{DS} is zero. The current through the body diode is being driven by the resonant inductor L_r and it freewheels through body diode and L_r during this interval.

D. Mode 4 ($t_3 - t_4$):

At the instant t_3 Q_{MAIN} is turned on and the Q_{ZVT} is turned off. After Q_{ZVT} is turned off, the energy in L_r is discharged linearly through diode D_2 to the load.

E. Mode 5 ($t_4 - t_5$):

At the instant t_4 , the current in diode D_2 reaches zero. When this occurs, the circuit is operated like a conventional boost converter.

F. Mode 6 ($t_5 - t_6$):

This mode operation is also exactly similar to a conventional boost converter. At the instant t_5 , the main switch Q_{MAIN} is turned off. The voltage V_{DS} ramps up to V_0 . The diode D_1 begins to supply the current to the load.

From the modes of operation, it is clear that the main switch is turned on when the voltage across it is zero and the boost diode is turned off when the current through it is zero. Hence, the phenomenon is named as Zero Voltage Transition (ZVT) technique.

The main power stage components of the above converter experience no more voltage or current stress than normal boost converter. The main switch and boost diode both experience soft switching transitions. Having significantly reduced the switching losses, the operating frequency can be increased without an efficiency penalty. The diode also operates with much lower losses and hence the reliability increases.

The design specifications for the proposed ZVT based Boost PFC Converter are

AC input Voltage = $V_s = 170 - 250$ Volts

DC output Voltage = $V_0 = 400$ V

Output Power = $P_{out} = 1000$ W

Switching Frequency = $F_s = 250$ KHz

Efficiency = $\eta = 95\%$

The designed values of different components in the converter circuit are

$L = 200\mu H$; $C_0 = 1600\mu F$; $L_r = 8\mu H$; $C_r = 0.47nF$

V. ELECTRO MAGNETIC INTERFERENCE (EMI) FILTER

The Electro Magnetic Interference can be transmitted in two forms: radiation and conduction. The switching converters supplied by the power lines generate conducted noise into the power lines that is usually several orders of magnitude higher than the radiated noise into free space. Conducted noise consists of two categories commonly known as the differential mode and the common mode.

The differential mode noise is a current or a voltage measured between the lines of the source that is line-to-line voltage. The common mode noise is a voltage or a current measured between the power lines and ground that is line-to-ground voltage [8]. An EMI filter is needed to reduce the differential mode and common mode noises. The EMI Filter for Boost PFC converter is shown in figure 4.

For CM Noise,

$$f_{R,CM} = 1/(2\pi\sqrt{2C_y * L_{CM}}) \quad - (1)$$

$$L_{leakage} = 0.5\% \text{ to } 2\% \text{ of } L_{CM} \quad - (2)$$

For DM Noise,

$$f_{R,DM} = 1/(2\pi\sqrt{2L_D C_X}) \quad - (3)$$

$$L_{DM} = (L_D - L_{leakage}) / 2 \quad - (4)$$

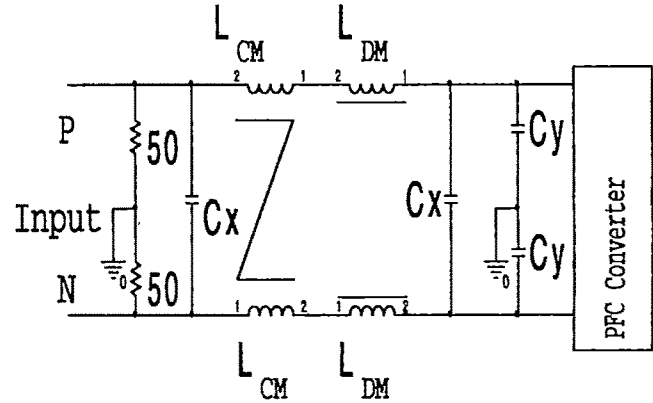


Figure 4. EMI Filter for PFC Converter

The PFC converter has the predicted noise level and EMI which includes total noise, common mode and differential mode noises. In general, the corner frequencies of EMI noises in the PFC circuits are 28 KHz for CM noise and 20.5 KHz for DM noise. The designed values are L_{CM} is 4.9mH and L_{DM} is 40μH.

VI. RESULTS

The proposed ZVT based Boost PFC converter is simulated using the software ORCAD-PSPICE software of version 9.2.

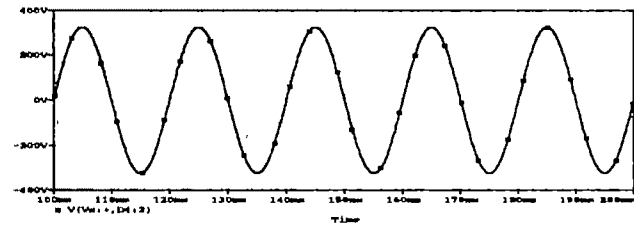


Figure 5. Input Voltage waveform without EMI Filter

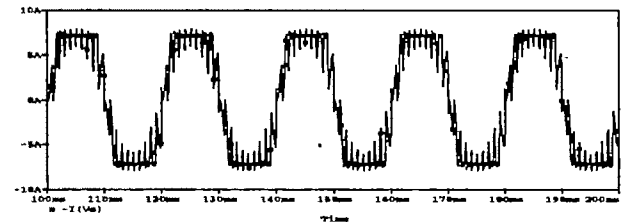


Figure 6. Input Current waveform without EMI Filter

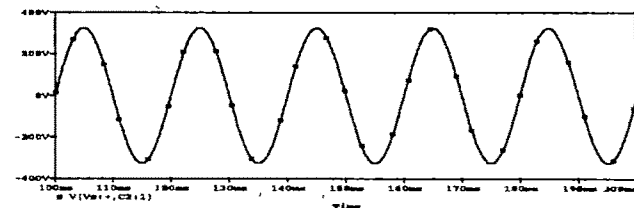


Figure 7. Input Voltage waveform with EMI Filter

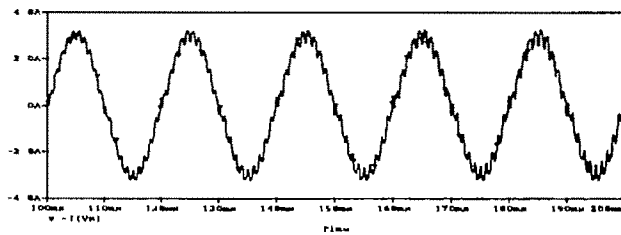


Figure.8. Input Current waveform with EMI Filter

Figure 5 shows the input voltage waveform without EMI Filter. Figure 6 shows the input current waveform without EMI Filter. In this figure, there is more noise and more spikes. Figure 7 shows the input voltage waveform with EMI Filter. Figure 8 shows the input current waveform with EMI filter. Here, the noise and spikes are reduced because of Filter. Here, the power factor is around 0.99, efficiency is 95% and the noise and spikes are also reduced.

VII. CONCLUSION

A Boost Power Factor Correction (PFC) Converter with EMI Filter employing Zero Voltage Transition (ZVT) technique is proposed. The proposed converter is simulated and the simulation results are presented in this paper. Power factor is improved upto 0.99 (lag) without compromising the efficiency because of the active snubber.

REFERENCES

- [1] Vlad Grigore, "Topological Issues in Single -Phase Power Factor Correction", Dissertation for the degree of Doctor of Science in Technology at Helsinki University of Technology (Espoo, Finland) on November, 2001.
- [2] M.A Geisler, "Predicting power factor and other input performances for switching power supplies", Proc. IEEE-Applied Power Electronics Conf. (APEC'90), 1990, pp.579-587.
- [3] C.Zhou, R.B Ridley, F C.Lee, "Design and analysis of a hysteresis boost power factor correction circuit", Proc. IEEE-Power Electronics Specialists Conf. (PESC'90), 1990, pp 800-807.
- [4] Fu-Yuan Shih, Dan Y Chen, Yan-Pei Wu, Yie-Tone Chen, "A Procedure for Designing EMI Filters for AC Line Applications" IEEE Transactions on Power Electronics, Vol 11, No. 1, January 1996.
- [5] L.H Dixon, "Average Current Mode Control of Switching Power Supplies", Unitrode Power Supply Design Seminar Manual SEM700, 1990
- [6] G.C.Hua, C.S.Leu, Y.M Jiang, and F C. Lee, "Novel Zero Voltage Transition PWM Converters", IEEE Transactions on Power Electronics, vol.9, no 2, pp 213-219, Mar 1994.
- [7] G.Moschopoulos, P Jain, G.Joos, "A novel zero voltage switched PWM boost converter", Proc. IEEE-Power Electronics Specialists Conf. (PESC'95), 1995, pp 694-700.
- [8] J. P. Noon, "A 250kHz, 500W Power Factor Correction Circuit Employing Zero Voltage Transitions", Unitrode Power Supply Design Seminar Manual SEM1000, 1994.

Design and Simulation of 30 Watt Phase Modulated Converter

Rajesh Babu Kollipara¹, P. K. Chaturvedi² and K. C. Pradhan²

¹ PG Student, Electrical Engineering Deptt, SATI, Vidisha (MP)

² Lecturer, Electrical Engineering Deptt, SATI, Vidisha (MP)

³ Professor, Electrical Engineering Deptt, SATI, Vidisha (MP)

Abstract— Switched Mode Power Supplies [SMPS] have become the natural choice for most of the power supplies, due to their higher efficiency and increased power density. Most of the present commercial SMPS, operate with a switching frequency of around 50 kHz, using hard switching PWM topologies. Power densities of these SMPS, can be increased manifold, if the switching frequencies are increased. Hence the technology is evolving towards switching frequencies of the order of a few MHz. In the Hard switching PWM topologies, the switching losses increase proportionately with the frequency, and hence they are not practical at these frequencies.

This paper explains the mechanism of switching losses in the hard switched topologies of power converters and briefly reviews the various soft switching topologies to address the problems of switching losses. In particular, Resonant Transition Converters are discussed as they combine the low switching loss characteristics of resonant converters and the low conduction loss and constant frequency characteristics of the PWM converters. The various parameters affecting Zero Voltage Switching are discussed. Design equations to obtain suitable values for these parameters are derived. With these values as the initial estimates, simulation is used iteratively, to obtain the most satisfactory design parameters. The design parameters and simulation results of a 30 W converter with rating (5V / 6A), switching at 250 kHz are presented. Simulation has been performed in Matlab environment.

Key words— Phase Modulated Converter, Zero Voltage Switching, Zero Current Switching,

I. INTRODUCTION

SWITCHED Mode Power Supplies (SMPS) with their higher efficiency and reduced size, have almost totally replaced the traditional linear regulated power supplies. Significant progress in the fields of circuit topologies, semiconductor power devices, control theory and integrated circuits, have made the switch mode power supplies, with typical switching frequencies of about 20 - 100 kHz, a mature technology. However, the recent remarkable advances in Integrated Electronics have greatly reduced the size of many electronic systems. Computers, automotive and telecommunication systems are a few examples, where the power supply has already become the critical component, owing to its size. It is well recognized that higher power densities are possible with higher switching frequencies. Since the size of the main

components in SMPS, like the power transformer and energy storage elements, depend strongly on the switching frequency, significant savings in size is possible at high frequencies. As 'Frequency goes up, size comes down', is a belief that has been the main motivating factor for switching at high frequencies. In the Pulse Width Modulated [PWM], square wave converters widely employed at present, the power devices are required to turn on and turn off the entire load currents, abruptly, during each switching. High device voltage and current overlap during these switching transitions, resulting in high switching loss and device stress. Figure 1 shows the equivalent of the typical switching conditions encountered in most PWM converters.

As seen in the Fig. 1(b) during turn-off, the moment the current begins to fall, the voltage across the switch rises to the maximum (since the freewheeling diode begins to conduct). During the turn-on process too, the device voltage remains at its peak (again due to the conduction of freewheeling diode), till the current rises to its maximum value. Hence, high device voltage and current overlap during both the transitions resulting in significant losses. The switching losses increase linearly with frequency, since switching transitions occur more frequently in a given time.

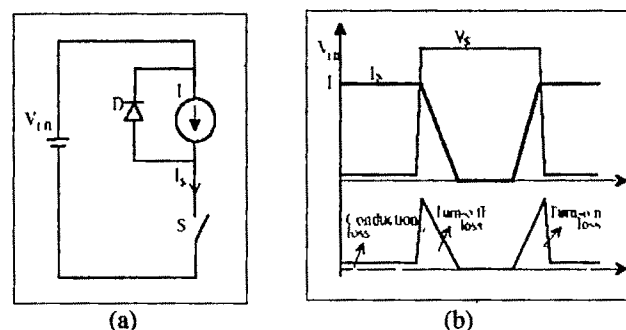


Fig. 1 Switching transitions in PWM converters (a) Equivalent circuit (b) switching waveform.

The presence of the parasitic elements like the stray inductance of the circuit and the junction capacitance of the semiconductor devices, force the devices to experience voltage spikes during turn-off and current spikes during turn-on and due to this there will be high switch stress during switching. Another serious drawback of switched mode converters, is the Electro Magnetic Interference [EMI] produced by the large di/dt and dv/dt during the switching transitions. At higher switching frequencies, this problem becomes more severe. The

switching losses increase linearly with frequency, since switching transition occurs more frequently in a given time. The losses in the drive circuit which are usually negligible in the 50 kHz range, become significant at higher frequencies. Soft switching of a converter topology should have the following two features in order to achieve soft switching.

- (1) Switch transitions should occur only when either the device current and /or the device voltage is zero,
- (2) The energy stored in the parasitic elements are fully recovered.

The Resonant Transition Converters, being proposed, combine the low switching loss characteristics of the resonant converters and the constant frequency and low conduction loss characteristics of the PWM converters. The resonant 12 transitions are achieved, relying mainly on the parasitic inductances and capacitances, and by adopting suitable switching strategies. The Phase Modulated Full Bridge Converter [PMC], which has been chosen for study and implementation in this work, belongs to the class of resonant transition converters. Some of the salient features of PMC are as follows.

- Zero Voltage Switching for all the four Mosfets of the full bridge.
- Constant frequency operation.
- Soft switching is obtained relying mainly on the parasitic elements, like the magnetizing and leakage inductance of transformer and the junction capacitance of the Mosfets.
- Phase shift control used in PMC, is identical to the duty ratio control used in PWM converters

II. ANALYSIS OF COMPLETE CYCLE OF OPERATION

Figure 2 shows the schematic diagram of the Phase Modulated Converter used in analysis and simulation. Capacitors C1 to C4 represent the output capacitances of the Mosfets together with any external snubber capacitors added. L_m and L_{lk} represent the magnetizing and leakage inductances respectively of the transformer. Zero voltage switching demands that, before a Mosfet is switched on, its output capacitance be completely discharged. The following three equations are general and are valid in all the intervals.

$$L_m \frac{d}{dt} I_m = V_{pri} \quad (1)$$

$$I_{pri} = I_m + I_{refl} \quad (2)$$

$$I_{refl} = (I_{dp} - I_{dn}) / n \quad (3)$$

A. Positive Power Transfer Interval

The inverter intervals are determined solely by the switching sequence of the devices. In the first interval, known as the positive power transfer interval, the diagonal switches S4 and S3 conduct, transferring power to the load. The equations that are valid for this interval are

$$V_{C1} = V_{C2} = V_{DC} \quad (4)$$

$$V_{C3} = V_{C4} = 0 \quad (5)$$

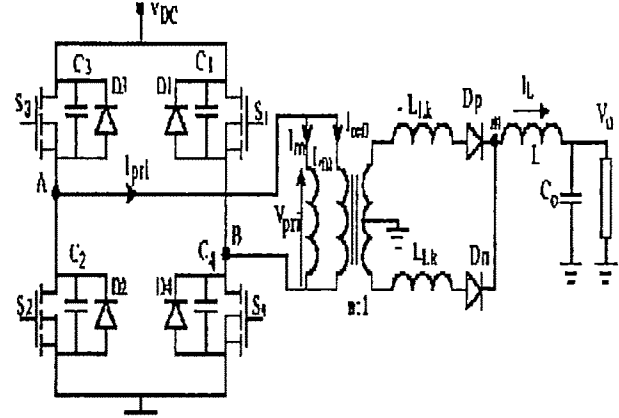


Fig. 2 Schematic diagram of phase modulated converter.

$$V_{pri} = V_{DC} \quad (6)$$

B. Transition from Power Transfer to Freewheeling Mode

The second interval is the transition interval from power transfer mode to the Freewheeling mode. This interval begins when S4 is switched off. There are two important factors to be considered in this interval as:

1. Turn-off process of S4
2. Discharge of the capacitance across S1, which is the next switch to be turned on.

As the gate voltage of S4 falls below the threshold level, the primary current which was initially flowing through S4, now begins to flow through C4 and C1.

$$\frac{d}{dt} V_{C4} = \frac{I_m + I_{refl}}{2C} \quad (7)$$

$$V_{C4} = V_{DC} - V_{C1} \quad (8)$$

$$V_{pri} = V_{C1} \quad (9)$$

$$\text{where } C_1 = C_2 = C_3 = C_4 = C$$

C. Freewheeling Interval

This interval starts when S1 is turned on. Since the body diode D1 is conducting when the gate drive to S1 is applied, this is truly a zero voltage turn-on transition. Even after gate drive is applied to S1, the diode D1 continues to conduct. The magnetizing current remains at its positive peak throughout the interval.

$$V_{pri} = V_{C1} = V_{C3} = 0 \quad (10)$$

$$V_{C2} = V_{C4} = V_{DC} \quad (11)$$

Though the transformer voltages remain zero in this interval, the leakage inductance ensures that only Dp is forward biased and Dn reverse biased. Hence the reflected

load LLK current still remains in the positive direction. The interval 3 ends when S3 is turned off.

D. Transition From Freewheeling To Power Transfer Mode

Interval 4 begins when S3 is turned off. The turn-off process of S3 is similar to the one explained in interval 2. It is a nearly lossless transition, as the output capacitances limit the voltage rise while the current is falling.

$$\frac{d}{dt} V_{C3} = \frac{I_{pri}}{2C} \quad (12)$$

$$V_{C2} = V_{DC} - V_{C3} \quad (13)$$

$$V_{pri} = -V_{C3} \quad (14)$$

From ZVS considerations, the Transition from the Freewheeling mode to the Power Transfer mode is the crucial interval. Since S2 is the next switch to be turned on, C2 has to be fully discharged. This discharge process is assisted by the primary current, made of the load component and the magnetizing component. In this the Freewheeling to Power Transfer transition, as C2 begins to discharge, the transformer voltages become negative. The secondary side diode Dn, thus begins to conduct. Due to the leakage energy, the diode Dp also continues to conduct. The load component of the primary current which is proportional to the difference between these two currents, begins to reduce, and eventually becomes negative. The magnetizing current component also reduces due to the negative voltage, but at a much slower rate, since the magnetizing inductance is relatively large. The design of the magnetizing and the leakage inductances should ensure that VC2 is completely discharged, before the sum of the magnetizing current and the reflected load current becomes negative. The duration of interval 4 is equal to the TDelay, and ends when S2 is switched on with zero volts across it. As stated earlier, the design of the transformer inductances should ensure that C2 is completely discharged and D2 begins to conduct within this time interval. The intervals 5, 6, 7 and 8 correspond to the negative half cycle and are similar to the intervals 1, 2, 3 and 4 respectively.

III. DESIGNING OF ZERO VOLTAGE SWITCHING (ZVS)

For any given line and load conditions the various factors affecting ZVS are, the magnetizing current, the leakage inductance, the dead time TDelay, and the capacitance across the Mosfet. Higher magnetizing current is good from a purely ZVS point of view. However, much higher magnetizing current results in higher peak and rms. Currents through the Mosfets, hence increasing the conduction losses. The design of magnetizing inductance should be done considering these two conflicting requirements. However, much large leakage inductance results in longer overlap intervals. This increases the primary current and hence the conduction losses. For ZVS to be achieved, the maximum allowable is the time in which

the TDelay primary current reverses direction. At light loads, the time taken for the reversal is more compared to heavy loads. Therefore should preferably be made load TDelay dependant - it should be high at light loads and small at higher loads. Larger capacitance across the Mosfets, helps to reduce the turn-off losses by limiting the voltage rise, while the device current is falling. Hence with a view to minimize turn-off losses, external capacitors may be added, apart from the intrinsic capacitance COSS of the Mosfets. However, during the turn-on process, larger capacitance demands more energy to be stored in the magnetizing and leakage inductances, to be fully discharged. Hence from the ZVS point of view, smaller capacitance is preferred. Design strategy to achieve zero voltage switching is as follows. The following two conditions have to be satisfied to achieve ZVS, at any given load:

$$(i) (I_m + I_{refl}) \sqrt{L_{eq}/2C} \geq V_{DC} \quad (15)$$

$$(ii) T_{Delay} = (\pi/2) \sqrt{2CL_{eq}} \quad (16)$$

Hence the design strategy is to

- Select TDelay considering the switching frequency and Mosfet characteristics. (IRF9540)
- Calculate the value of Leq from Eq.16, with the above value of TDelay
- With the above value of LLk, calculate from Eq.15, the peak magnetizing current required at any load down to which ZVS is required. From the value of peak magnetizing current (Im pk), obtain the value of magnetizing inductance (Lm) needed.

IV. SIMULATION RESULTS

A 30 Watt converter operating at 250 kHz frequency with input voltage of 50v after simulation gives output voltage of 5V and maximum output current of 6A. But if minimization of loss consideration is taken into account output current should be 5A. These results are as shown in the figures given below.

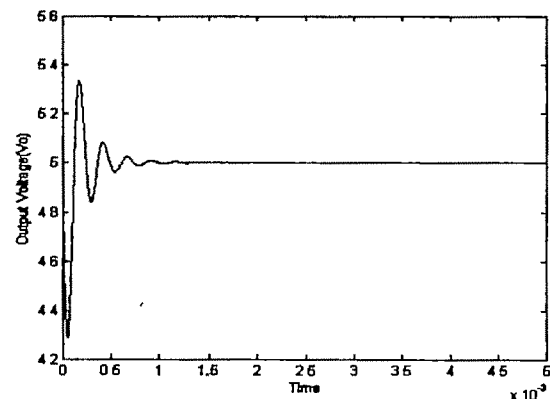


Fig. 3. Transient and steady state output voltage.

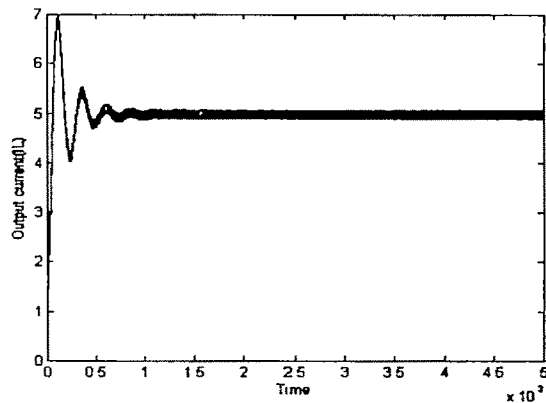


Fig. 4. Transient and Steady state output current.

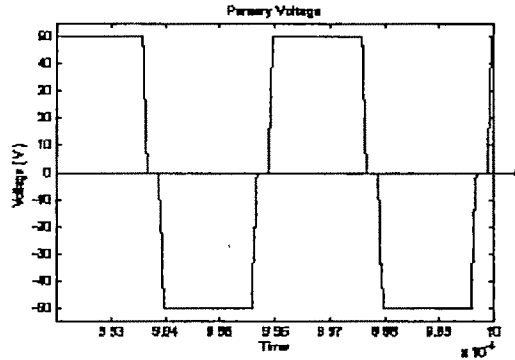


Fig. 5 Primary voltage.

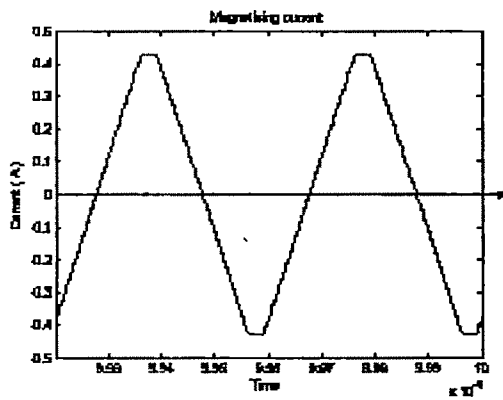


Fig. 6. Magnetizing current.

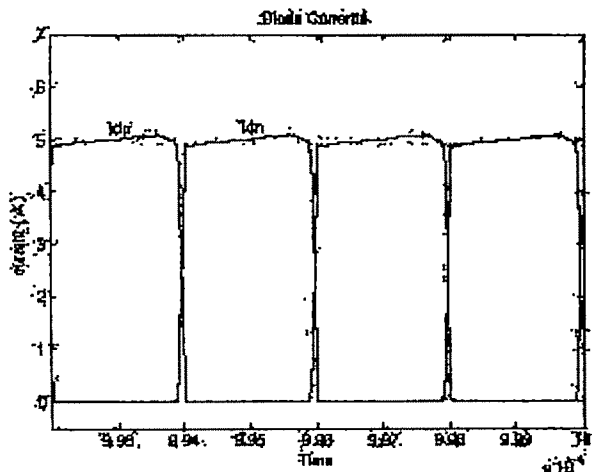


Fig. 7. Diode currents

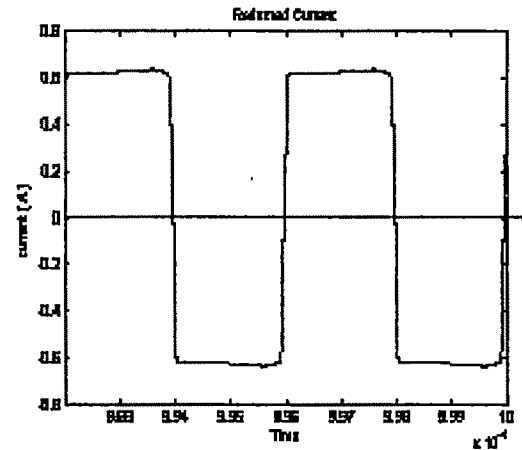


Fig. 8. Reflected load current

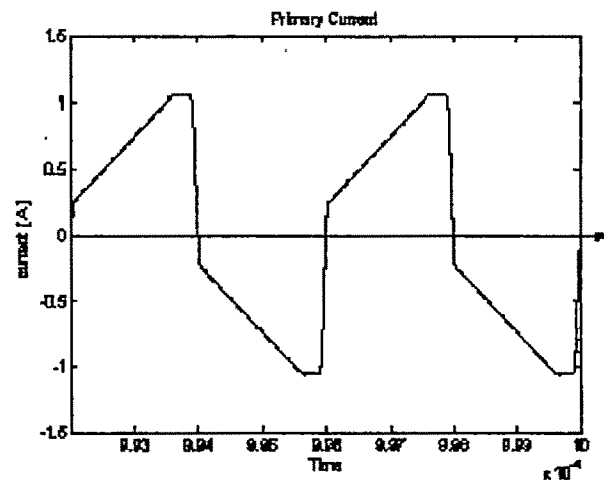


Fig. 9. Primary current.

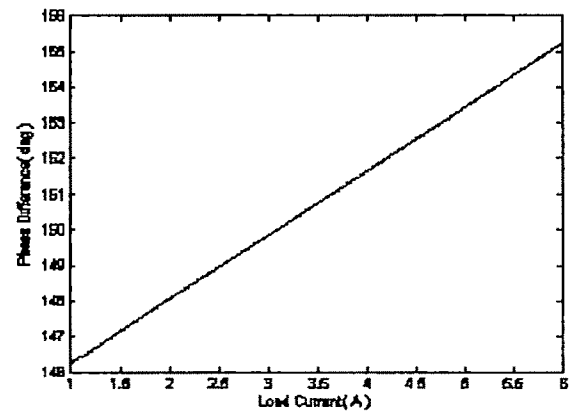


Fig. 10. Phase difference Vs load current.

Loss Curves: The Total Mosfet losses, sum of conducting losses and switching losses for each load at each ZVS load limit is plotted. From graph it is clear that ZVS Limit of 5 A has least losses for entire load range.

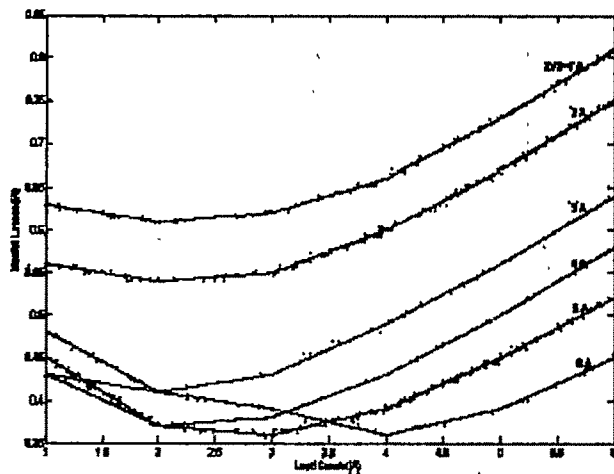
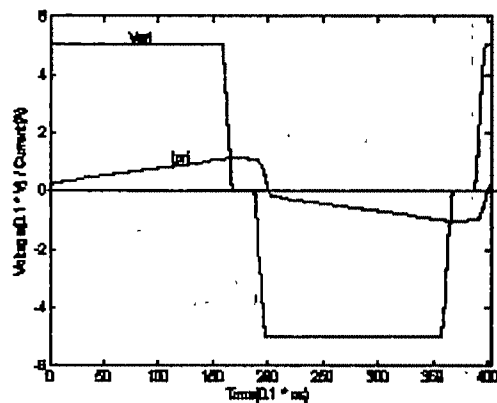
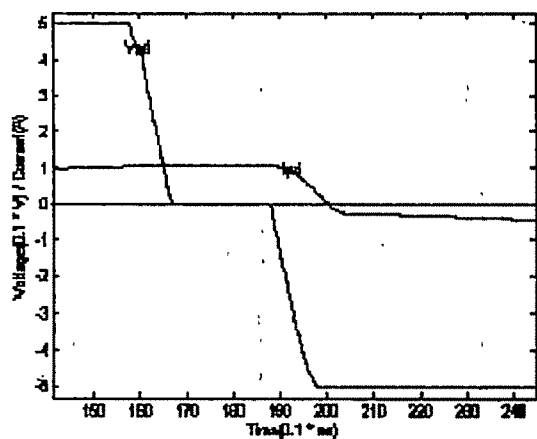


Fig. 11. Loss curves for different ZVS limits.

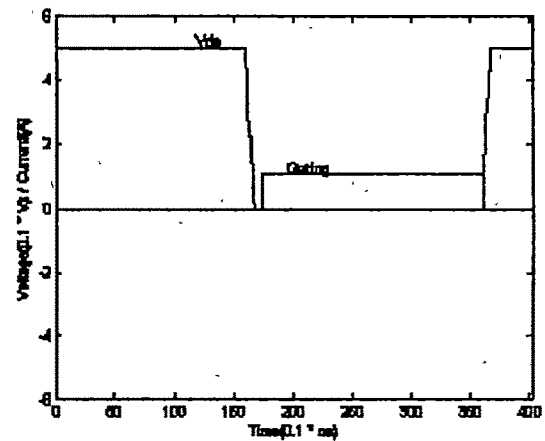
In order to minimize losses in entire load range Zero Voltage Switching Limit plays a vital role. The ZVS limit is 5A for this converter as seen from loss curves. For ZVS limit of 5 A and $I_o = 5$, the transformer primary voltages and currents, are plotted below. It can be seen clearly that voltage reaches -50 V before current becomes negative.



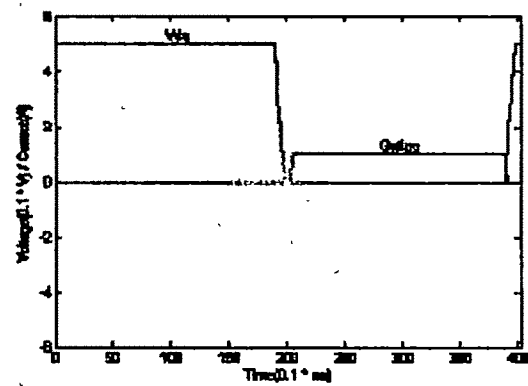
(a)



(b)



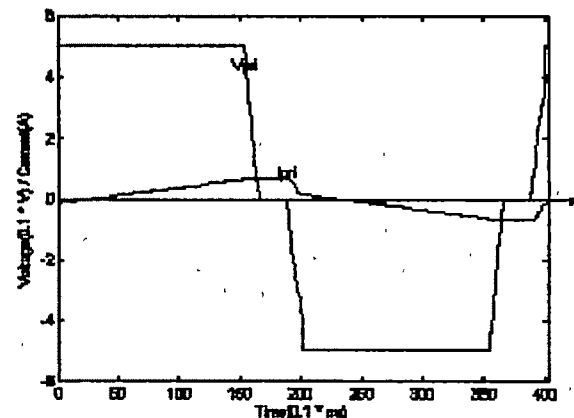
(c)



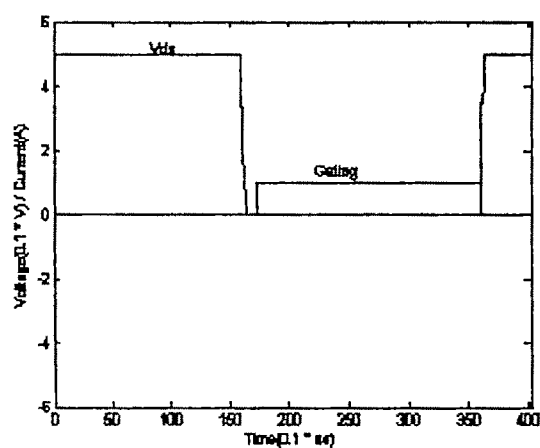
(d)

Fig. 12. (a) Transformer primary voltage and current for ZVS
(b) Zooming the negative going transition
(c) Right leg Mosfet VDS vs. Gate signal
(d) Left leg Mosfet VDS vs. Gate signal

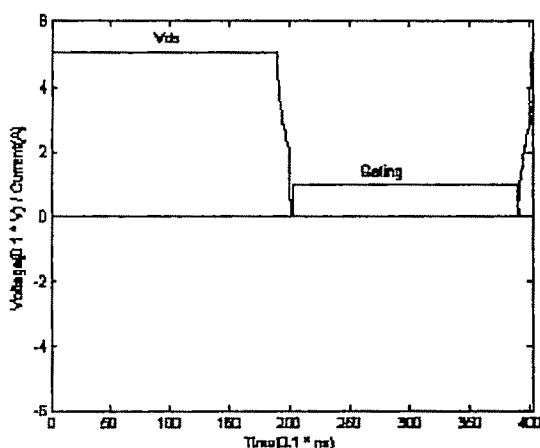
For ZVS limit of 5 A and $I_o = 1$ A, the transformer primary voltages and currents are plotted. Non-ZVS transitions can be observed.



(a)



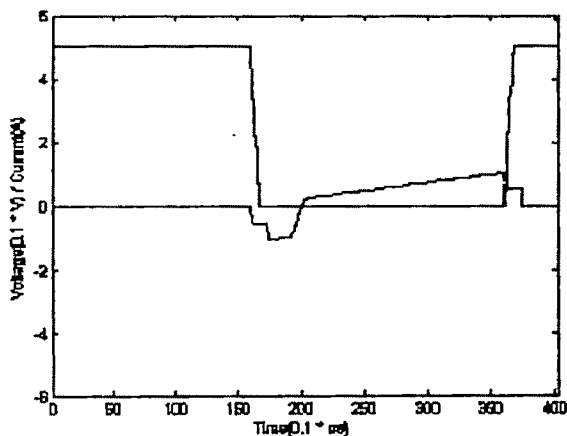
(b)



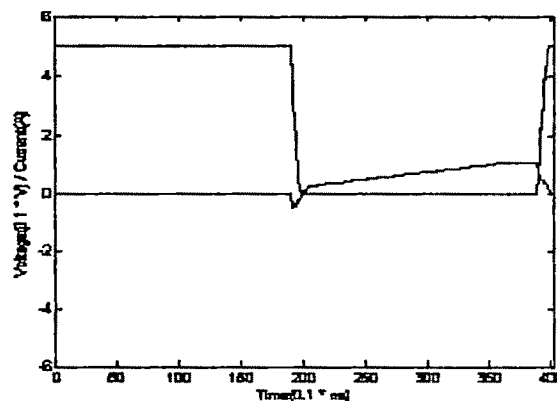
(c)

Fig. 13 (a) Transformer primary voltage and current for Non- ZVS
(b) Right leg Mosfet VDS vs. Gate signal
(c) Left leg Mosfet VDS vs. Gate signal

At the outset, the currents through right and left leg Mosfets seem symmetrical. Following plots show they are unsymmetrical.



(a)



(b)

Fig. 14 (a) Right leg Mosfet Vds Vs. primary current
(b) Left leg Mosfet Vds Vs primary current

V. CONCLUSION

On the basis of simulation results, it may be concluded that at power levels high enough to justify the use of four switches and at voltage levels high enough for the advantages of the ZVS to be significant, the Phase Modulated full bridge Converter, with the proper choice of ZVS LIMIT, is potentially the most suitable topology. It may confidently be predicted that the PMC will be a standard topology of the future for high frequency SMPS and other applications.

REFERENCES

- [1] A. Rajapandian, V. Ramanarayanan, "A 250 kHz / 560W Phase Modulated Converter", IEEE Proc. Power Electronics, Drives and Energy Systems (PEDES) Conf. 1996 Record.
- [2] V. Ramanarayanan, "Switched Mode Power Conversion", Class notes, Dept. of Electrical Engg., Indian Institute of Science.
- [3] Unitrode Application Notes U-136A, Bill Andreycak "Phase Shifted Zero Voltage Transition Design Considerations", 1997
- [4] J. Sabate et al, "Design considerations for high voltage, high power, full bridge ZVS PWM converter", IEEE Applied Power Electronics Conf. 1990 Record, pp 275-284.
- [5] N. Mohan, Undeland and Robbins, "Power Electronics : Converters, Applications and Design", John Wiley and sons, Newyork.

Technical Session 1D

GA and its Applications

Qualitative GA Based Identification and Control of 2DOF Inverted Pendulum

Alireza Rezazade and Mohsen Modarres

Shahid Beheshti University, Alireza.rezazade@gmail.com, Mohsen.Modarres@gmail.com

Abstract—In many systems qualitative knowledge of the system behavior is sufficient for introducing a robust and sufficiently accurate response. This paper, presented a method for qualitative parameter and model estimation and control of dynamic systems. In this method a qualitative model for dynamic systems is introduced as a graph and then the optimal path for shortest control time is obtained with the aid of genetic algorithm. This method is well examined by a complicated two degree of freedom inverted pendulum system and the responses are presented. The main advantages of this method are, increasing the robustness of the controlled system, more easily implementation of the control via a single LUT, rule based control generation for expert control methods like fuzzy control.

I. INTRODUCTION

ROBUST control of dynamic discrete time systems is very important in modern control. Almost all physical systems are in some sense, nonlinear and also variable with time and state of the operation. This makes the control to deviate from the desired operation conditions. Another theme that forces the designer to deal with the systems qualitatively is the limitation on the accuracy of the sensor. In most applications we need accuracy only in near of target response and during transient, it is not vital to sense the states in high precision. Qualitative identification and control of system, is a method to observe the system behavior in the next time step, when a special amount of excitation is applied to the system [7], [8]. The first step of the method is weighted quantization that is, to split the state space of the desired system to special sections. The sectioning of the state space must be made such that in desired points the resolution of state observation meets the designer conditions. In such cases it is recommended that the sections become finer around the set points. Each section must be numbered. The second step is to split the input space to quantized values. The next step is to find out the state transition from one quantized state to others in application of all of quantized inputs. The result of the process is a graph that represents the actual system qualitatively. Genetic algorithm is used to find a path in this complicated graph to find the optimal inputs for shortest response time [3], [4]. Finally the application result of the method to 2DOF inverted pendulum is presented.

II. GENERAL DESCRIPTION

A. Weighted quantization of state and input space

Quantization is a major task in qualitative control. In most of systems in far states conditions the resolution of state space splitting can be very low so that the system only knows that its states are far from the set point so that it acts with the highest saturated input to compensate the errors. So we can partition the far states in state space in wide sense. On the other hand in the near state conditions, the system must converge to final state with sufficient accuracy. So the state space in these regions must be fine partitioned. The quantization of the input(s) is the same as the above method. In figure 1 there is an example of this quantization for a D.C. motor [9]. In this example, the states of motor are speed of the motor, $X_1 = \omega - \omega_0$ and the armature current, $X_2 = i_a - I_A$ and the input is armature voltage, v_a .

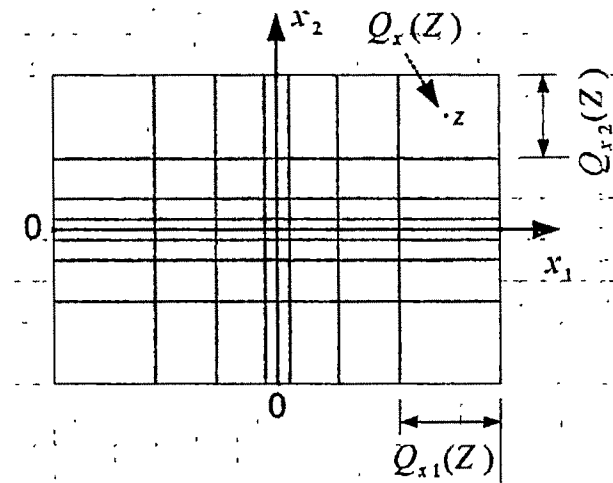


Fig. 1. State space non uniform quantization of a dynamic state system.

B. State transition calculation with Monte- Carlo method

State transition is the most important part of the qualitative system identification. State transition means that if the system is in state or node i on time t_0 , what is the state on time $t_0 + T_s$ in the application of special quantize input. T_s is the sample time of discrete time quantized system. Each quantized state or node for example in fig.1 is a square region in state space but the map of this region is not necessarily a square region and may overlap with many state regions as maintained in fig.2. To find out the overall transition states, a statistic method must be used. General state space equation is:

$$x[(k+1)T_s] = f(x[kT_s], u[kT_s]) \quad (1)$$

The quantized states or nodes are defined as in fig. (1):

$$Q_{x_i}(z_j) = \{x_i | g_j \leq x_i \leq g_{j+1}\} \quad (2)$$

Where g_j is the edge of each region in quantization.

In n -dimension system we have the quantized state or node as:

$$Q_x(z) = Q_{x_1}(z) \otimes Q_{x_2}(z) \otimes \dots \otimes Q_{x_n}(z) \quad (3)$$

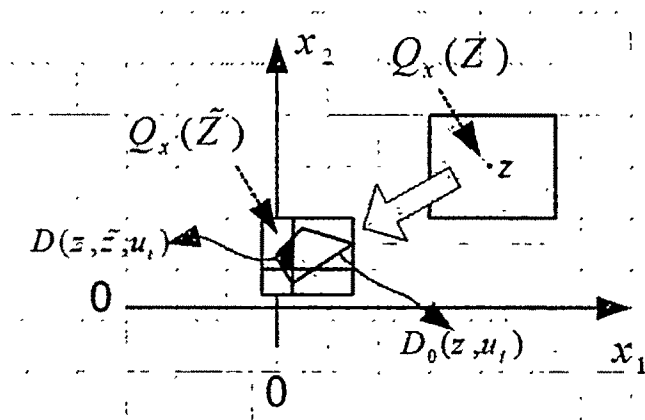


Fig. 2. State transition of a dynamic discrete event system, when u_i is as input to the system.

As it is clear in fig.2, z state ($Q_x(z)$) is mapped to more than one state and we can weight the transition of the state transition diagram, proportional to the probability of the accruing of next state. In fig.2, $D_0(z, u_i)$ is the map of the primary state, z , and $D(z, \tilde{z}, u_i)$ is the intersection of $D_0(z, u_i)$ and the node \tilde{z} . The transition probability is defined as:

$$p(z, \tilde{z}, u_i) = \frac{\int_{D(z, \tilde{z}, u_i)} dx}{\int_{D_0(z, u_i)} dx} \quad (4)$$

so in (4), the integration is taken with Monte Carlo statistic integration.

C. Monte- Carlo algorithm

Monte- Carlo algorithm is a statistic method and it can be used off-line for evaluation of (4). This algorithm is summarized as follow [9]:

1. Point generation in $Q_x(z)$ domain. These points are distributed uniformly in the region and quantity of them, must be much enough for good estimation of the integrals in (4).
2. Application of the system map of eq.(1) on the pre-defined points.
3. Counting the mapped points in each of the $Q_x(\tilde{z})$ regions and divide them by the total number of points.

The resulting is the calculation of $p(z, \tilde{z}, u_i)$. This procedure must calculate for each u_i .

III. GRAPH REPRESENTATION OF DYNAMIC SYSTEM

The result of the algorithm of section II is a complicated table that can be interpreted as a graph. In this graph, each quantized region in state space is a node and branches between nodes represent the possibility of transient of the former state to the proceeding one. On each branch, the input that caused this transient and its probability of occurrence is labeled [7]. This theme is sketched typically in fig.3.

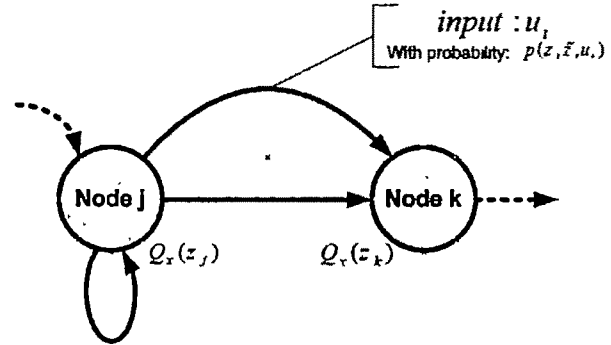


Fig. 3. Graph representation of dynamic system

This graph estimates the dynamic behavior of the system.

IV. CONTROL RULE GENERATION WITH GA

A. Control strategy

The next step is to find out a control strategy from the graph representation of the system. This control effort is in a specified set of inputs that are quantized. We have:

$$[u(k)] = g([x(k)]) \quad (5)$$

Where $[\cdot]$ means the quantized value. The control law, $g(\cdot)$, should be selected to maximize the probability of reaching final state that is $Z=0$, in minimum time. The objective function is the following equation:

Maximize:

$$\lim_{k \rightarrow \infty} \text{prob.} \{ [x(k)] = 0 \}$$

subject to:

$$x(k+1) = f(x(k), u(k)) \quad (6)$$

B. Genetic algorithm as an efficient optimization method

Genetic Algorithm is a searching process based on the laws of natural selection and genetics. The GA operates entirely differently from conventional optimization procedures; provides further flexibility and robustness [5], [6]. In addition, the GA approach has several advantages such as a reduced computational complexity, faster convergence and guaranteed global optima in most cases. A typical GA cycle is shown in Fig.4. Each gene which is the inputs in this problem, can be coded as a binary or floating-point string of l length. In this study, a binary string is used. A chromosome consists of all genes.

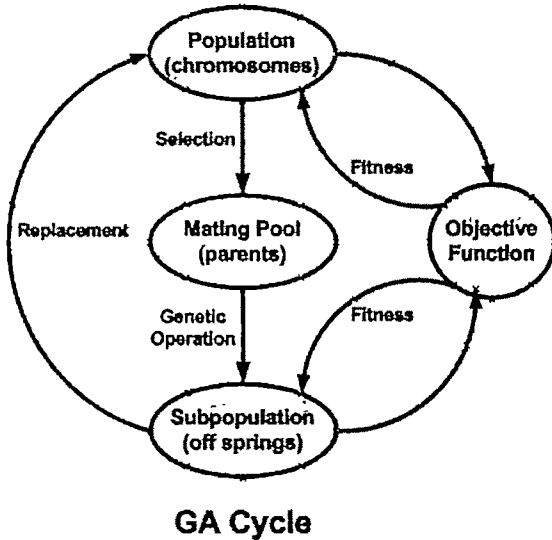


Fig.4.A simple GA cycle

A. Objective Function

The objective function, the function to be optimized, provides the mechanism for evaluating each string. In section IV, objective functions are defined in proper positions.

B. Selection

Selection model is nature's survival-of-the-fittest mechanism that is: fitter solutions survive while weaker ones perish. The selection mechanism that has been applied in this study is Roulette-wheel selection which is the most common and easy-to-implement selection mechanism [17]. It should be noted that in this work, this method is modified in combination with

elitist strategy where a definite number of best solutions are copied into the succeeding generation.

C. Genetic Operations

Crossover is a recombination operator that combines subparts of two parent chromosomes to produce offspring that contain some parts of both parents' genetic material. A probability term (p_0) is set to determine the operation rate. That is, a floating number (between 0 and 1) for each chromosome is assigned randomly. If this number is smaller than p_0 , this chromosome goes into *crossover*. A crossover point is randomly selected and the portions of two chromosomes on the two sides of this point are exchanged to form the offspring. Mutation is an operator that introduces variations into the chromosome. This variation can be global or local. The operation occurs occasionally (usually with a small probability p_m) but randomly alters the values of a string position. Each bit of a bit-string is replaced by a randomly generated bit if a probability test is passed. Figure.5 shows a typical crossover and mutation operation.

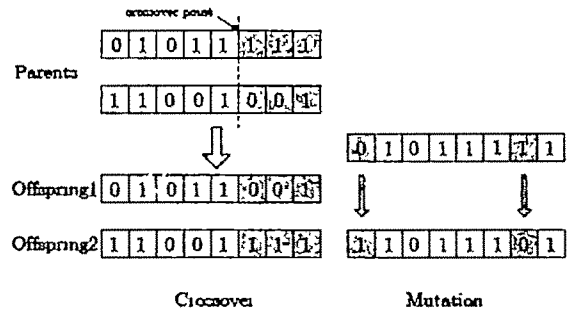


Fig.5. A typical crossover and mutation operation

Such a GA cycle is repeated until a desired termination criterion is reached (in this case, a predefined number of generations are produced) [4].

V. 2DOF INVERTED PENDULUM EXAMPLE

A. Model description

The problem of balancing a two degree of freedom (DOF) pendulum has been a benchmark problem in demonstrating and motivating various control design techniques [1], [2]. From a control design perspective, a challenging and difficult problem is presented as the system is nonlinear and the open-loop is unstable. In addition, need for a sensor system to measure the inclination angles of the pendulum contribute to the complexity of the balancing problem. A spherical pendulum system based on a X-Y table was designed and constructed. Then, a control model was developed by projecting the system onto the x-z and y-z planes of the inertial coordinate system. These projections were treated independently and were controlled individually by the x- axis and y- axis, respectively. Two stabilization controllers were designed for each planar inverted pendulum. In fig.6 the schematic of the system is presented. The table is

equipped with special DC motors as actuator and the pendulum is fixed in a cart and it can rotate free in all directions. The sensors of angles are a track ball mouse.

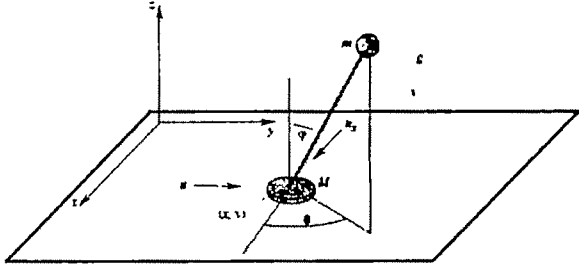


Fig.6 schematic of the 2DOF inverted pendulum

Actually, different friction terms should be added into the dynamics model in a practical implementation. Two friction terms are considered in our model, one is the viscous friction when carriage M performs its linear motion on the ball screw; the other is the viscous friction when the pendulum rotates around its pivot. Let the modified dynamics model of a spherical inverted pendulum as following:

$$(M_x + m)x'' + \frac{1}{2}ml\alpha''\cos\alpha - \frac{1}{2}ml\alpha'^2\sin\alpha + c_{Mx}x' = \tau_x \quad (7)$$

$$\frac{1}{2}mlx''\cos\alpha + \frac{1}{3}ml^2\alpha'' + c_{Mx}\alpha' - \frac{1}{2}mgl\sin\alpha = 0 \quad (8)$$

$$(M_y + m)y'' + \frac{1}{2}ml\beta''\cos\beta - \frac{1}{2}ml\beta'^2\sin\beta + c_{My}y' = \tau_y \quad (9)$$

$$\frac{1}{2}mly''\cos\beta + \frac{1}{3}ml^2\beta'' + c_{My}\beta' - \frac{1}{2}mgl\sin\beta = 0 \quad (10)$$

Where,

M_x : Mass of carriage respective to x-axis;

M_y : Mass of carriage respective to y-axis;

m : Mass of pendulum;

l : Length of pendulum;

x : Linear displacement of carriage in x direction;

y : Linear displacement of carriage in y direction;

α : Inclination angle of pendulum on xz projection;

β : Inclination angle of pendulum on yz projection;

c_{Mx}, c_{My} : Viscous friction coefficient for motion of carriage in x and y directions, respectively;

c_{Mx}, c_{My} : Viscous friction coefficient for rotary motion of pendulum on xz and yz projections, respectively;

τ_x, τ_y : Force provided by the motors to implement linear motion in x and y direction, respectively.

B. Practical System

The performance of the experimental hardware played very important part in this project. The flexible motion of the X-Y table, and the reliability of the sensor system were the decisive factors in the success of the whole system. Fig.7 is a schematic description of the overall system. And the practical system is shown in fig.8. The control box is FPGA based and designed to negotiate with windows based computer with fast USB port. The sensors of pendulum are two digital encoders in a track

ball mouse. The actuators that produce forces are DC motors that are coupled to the system.

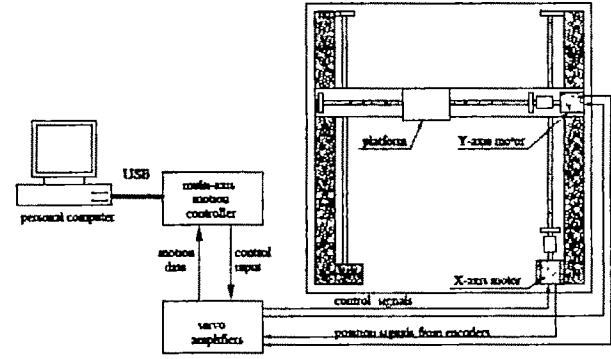


Fig.7 Overall schematic of X-Y table system for experiments of spherical inverted pendulum

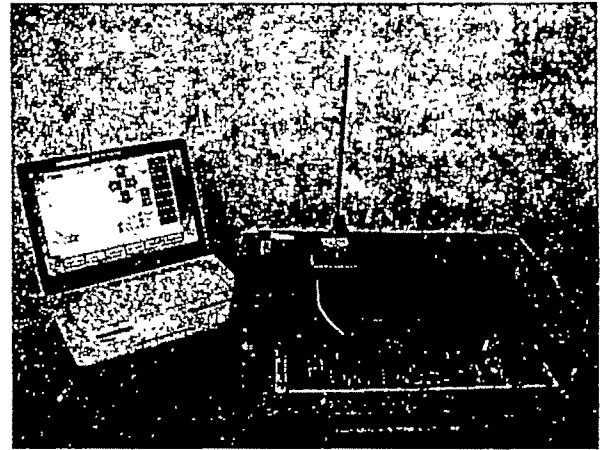


Fig.8 Picture of the working 2DOF inverted pendulum

B. Practical Results

As it is indicated earlier, around the set point, X and Y axis are approximately independent and the system converted to two one dimensional inverted pendulum. First of all, 3 dimensional (α, α', x) space and (β, β', y) space, and also the inputs, τ_x and τ_y must be partitioned and quantized properly. The each set of equations, can be converted to a special graph. The first one is sketched in fig.9. In the next step the optimized path with minimum travel time, is obtained with genetic algorithm. This path defines the proper inputs and the application of them to actuators, are done and the final results are presented in fig.10. The responses depend on the quantization process and that how fine we define the near final set point parameters.

ACKNOWLEDGMENT

This research is financial supported by Research office of Shahid Beheshti University.

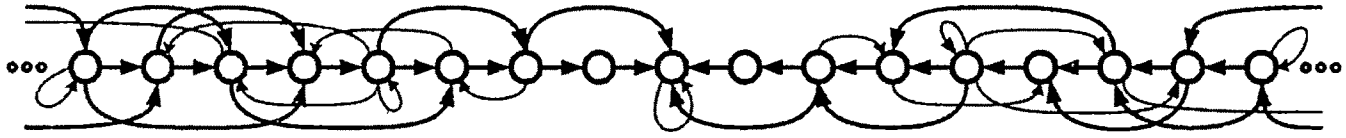


Fig.9 the $x - \alpha$ portion of system graph

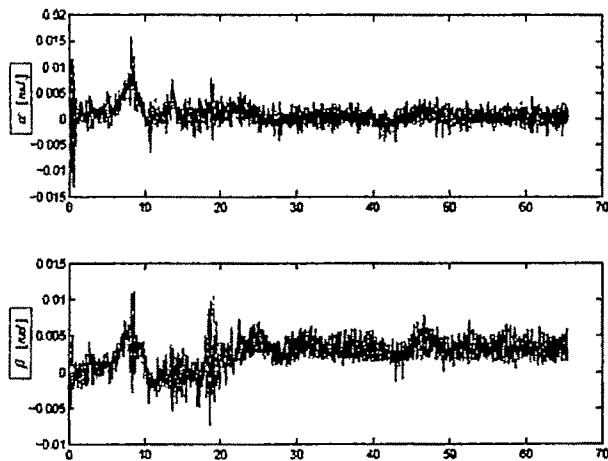


Fig.10 alpha and beta Resulted from the qualitative control

REFERENCES

- [1] K. J. Åström and K. Furuta, "Swinging up a pendulum by energy control," in *Proc. 13th IFAC World Congress*, San Francisco, CA, 1996.
- [2] Angeli, D., "Almost global stabilisation of the inverted pendulum via continuous statefeedback," *Automatica* 37, 1103-1108, 2001.
- [3] Ali Reza Rezazade, Arash Sayyah, Mitra Aflaki, "Optimization of THD and Suppressing Certain Order Harmonics in PWM inverters using Genetic Algorithms," *IEEE International Symposium on Intelligent Control (ISIC) October 4 to October 6, 2006, in Munich, Germany*.
- [4] Arash Sayyah, Mitra Aflaki, Ali Reza Rezazade, "GA-Based Optimization of Total Harmonic Current Distortion and Suppression of Chosen Harmonics in Induction Motors," *SPEEDAM SYMPOSIUM 23-26 May 2006 - Taormina (Italy)*.
- [5] Ali Reza Rezazade, Arash Sayyah, Mitra Aflaki "Optimal PWM for Minimization of Total Harmonic Current Distortion in High-Power Induction Motors using Genetic Algorithms," *SICE - ICASE International Joint Conference 2006 EXCO(Busan Exhibition & Convention Center), Busan, KOREA*.
- [6] Ali Reza Rezazade, Arash Sayyah, Mitra Aflaki "Modulation Error Observation and Regulation for use in Off-line Optimal PWM Fed High Power Synchronous Motors," *1st IEEE Conference on Industrial Electronics and Applications (ICIEA 2006), Singapore on 24 - 26 May 2006*.
- [7] Lichtenberg, G., Lunze, J., Scheuring, R., Schroder J., "Prozessdiagnose mittels qualitativer Modelle am Beispiel eines Wasserdampfverdichters," *Automatisierungstechnik* 47, 101-109, 1999.
- [8] Lunze, J., "Qualitative modeling of linear dynamical systems with quantized state measurements," *Automatica* 30, 417-431, 1994.
- [9] Ali Reza Rezazade, P. Jafar, "Qualitative rule base generator and its application in DC motor control," *Electrical engineering international conference, Tehran, Iran, 2003*.

An Object Oriented Neural Network Model Optimized by Genetic Algorithm for Microwave FETs

Anil Ahlawat¹, Rajesh Tyagi¹, Sujata Pandey¹ and Manoj Pandey²

¹ Department of Computer science and Engineering,
Amity School of Engineering and Technology, GGS Indraprastha University, New Delhi, India
e-mail: a_anil2000@yahoo.com, sujata.pandey@hotmail.com

² Institute of Technology and Management, Sector 23, Gurgaon, India

Abstract—A variant of Backpropagation algorithm is proposed for feed-forward neural networks training. The proposed algorithm improve the Backpropagation training in terms of quick convergence of the solution depending on the slope of the error graph and increase the speed of convergence of the system. Using the proposed algorithm, a simple, accurate and fast multilayer feed forward artificial neural network (ANN) model for S-parameter extraction of an InGaAs/InP PHEMT is developed.

The Genetic algorithm is applied to predict the most optimized set of S-parameters. The developed ANN model has demonstrated excellent precision and accurately models the microwave characteristics of the InGaAs/InP PHEMT. Furthermore, the developed ANN model requires a very small computational time compared with numerical models, which is very attractive for microwave applications. In addition, the model is suitable for physical-parameter extraction from available measured data. In order to verify the validity of the ANN model, a comparison between the measured S-parameters and the S-parameters calculated by the neural network was carried out under arbitrary chosen bias conditions are plotted and excellent fit between the simulated data and experimental data is observed.

Key words—Backpropagation algorithm, feed forward neural network training, Genetic algorithm, S-parameters.

I. INTRODUCTION

FEED-forward neural networks (FNN) have been widely used for various tasks, such as pattern recognition, function approximation, dynamical modeling, data mining, and time series forecasting, [1-3]. The back-propagation algorithm has been investigated many times with minor variations [4-7]. However, even to date, there are still a great number of problems that cannot be solved efficiently by the majority of the training algorithms that have been proposed over the years, using standard simple feed-forward network architectures. A number of different kind of BP based learning algorithms, such as an on-line neural-network learning algorithm for dealing with time varying inputs [8], fast learning algorithms based on gradient descent of neuron space [9], second derivative based non-linear optimization methods [10], conjugate gradient methods [11] and genetic algorithms [12,13] avoid use of any gradient information. Levenberg–Marquardt algorithm [14-16] is the most powerful and a popular second derivative based

algorithm that have been proposed for the training of feed-forward networks which combines the excellent local convergence properties of Gauss-Newton method near a minimum with the consistent error decrease provided by (a suitably scaled) gradient descent faraway from the solution. In first-order methods (such as gradient descent), a local minimizer problem is overshooted with the inclusion of momentum term. The momentum term actually inserts second-order information in the training process and provides iterations whose form is similar to the conjugate gradient (CG) method. The major difference of Backpropagation with the conjugate gradient method is that the coefficients regulating the weighting between the gradient and the momentum term are heuristically selected in BP, whereas in the CG algorithm these coefficients are adaptively determined. However, these algorithms also share problems [17] present in the standard Backpropagation algorithm and may converge faster in some cases and slower in others. Comparison of the speeds of convergence of different schemes for implementing Backpropagation is not clear-cut, though a discussion on benchmarking of the algorithms can be found [18].

In this paper, a proposal for a variant of back-propagation algorithm for FNN with time-varying inputs has been presented which is capable of overcoming the shortcomings of the BP as discussed above.

A simple, fast and robust algorithm for simultaneously determining the weights and architecture of a neural network model - the structured genetic algorithm is taken and applied to the small signal modeling of InGaAs/InP PHEMT.

II. PROPOSED VARIANT OF BACKPROPAGATION ALGORITHM

Assume a network with N inputs and M outputs. Let x_i be the input to i^{th} neuron in input layer, B^j be the output of the j^{th} neuron before activation, y_j be the output after activation, b_j be the bias between input and hidden layer, b_k be the bias between hidden and output layer, w_{ij} be the weight between the input and the hidden layers, and w_{jk} be the weight between the hidden and output layers. Let i , j and k be the indexes of the input, hidden and output layers respectively.

The response of each unit is computed as:

$$B_j = b_j + \sum_{i=1}^n x_i \cdot w_{ij} \quad (1)$$

$$y_j = (1 / (1 + \exp(-B_j))) \quad (2)$$

Weights and bias between input and hidden layer are updated by the following equations:

For input to hidden layer, for $i = 1$ to n ,

$$w_{ij}(t+1) = w_{ij}(t) + S(\eta \delta_j y_i + S \alpha (w_{ij}(t) - w_{ij}(t-1))) \quad (3)$$

$$b_j(t+1) = b_j(t) + S(\eta \delta_j + S \alpha (b_j(t) - b_j(t-1))) \quad (4)$$

Where, δ_j is the error between the input and hidden layer and calculated as:

$$\delta_j = y_j (1 - y_j) \cdot \sum_k \delta_k w_{jk} \quad (5)$$

Weights and bias between hidden and output layer are updated by the following equations:

For hidden to output layer, for $j = 1$ to h ,

$$w_{jk}(t+1) = w_{jk}(t) + S(\eta \delta_k y_j + S \alpha (w_{jk}(t) - w_{jk}(t-1))) \quad (6)$$

$$b_k(t+1) = b_k(t) + S(\eta \delta_k + S \alpha (b_k(t) - b_k(t-1))) \quad (7)$$

and δ_k is the error between the hidden and output layer and calculated as:

$$\delta_k = y_k \cdot (1 - y_k) \cdot (d_k - y_k) \quad (8)$$

where η is a positive constant, called the learning rate ($\eta < 1$) and α is the momentum coefficient, which is used to ensure a rapid convergence and to avoid the solution's convergence to local minimums and δ is the error and S is the speed factor, is used to increase the speed of convergence of the system.

III. NEURAL NETWORKS AND GENETIC ALGORITHMS FOR S-PARAMETER MODELING

This section of the paper presents an alternative method of using neural networks in modeling. The training method used, has the advantage of being relatively insensitive to the parameters of the algorithm and initial conditions. It can also be used for the simultaneous determination of weight values and the optimum number of neurons, a feature that could be useful for the automation of the training process. The training method uses a hierarchical representation for the genetic structure in which the neurons are represented as a high-level layer of genes controlling a lower level layer of weight genes. One other advantage of using our training method is that it has a randomizing mechanism called mutation which can be manipulated to escape from local minima traps thus avoiding the problem encountered in gradient descent methods.

The algorithm as described here assumes a feed forward neural network with one hidden layer.

1. Initialize a population of N arrays with small real random numbers. These arrays represent the weights between the input and hidden neurons.

2. For each individual, calculate the activation of the hidden neurons. Then calculate the output layer weights by using

linear regression to solve for the "best fit" of the activation to the output data.

3. Evaluate the fitness of each member to use the mean square error of the solution obtained in the previous step. Select individuals for reproduction based on their fitness values. Perform crossover and mutation operations. Evaluate the fitness of every member in the population. If the termination condition is not met, go to step 3. Else, select the best individual and exit.

Based on the training mechanism, the sets of S -parameters for a set of input parameters are determined and the same values are used as initial population for Genetic algorithm. As the Genetic algorithm runs, it attempts to solve the problem by repeatedly proposing new solutions. The fittest solutions are recombined with older solutions to form new solutions. The fitness function is defined over the genetic representation and measures the quality of the represented solution. Operations of Genetic algorithm (Selection, Crossover, Mutation, and Termination) are applied on a set of calculated data having same input but different outputs and the combination close-set to the actual result is selected.

The results are obtained using scattering parameters as shown below.

$$S_{ij}(m) = F[V_{ds}, I_{ds}, f_{op}]$$

$$S_{ij}(\text{ang}) = F[V_{ds}, I_{ds}, f_{op}]$$

Where i, j individually take disjoint values from the given set $G = [1, 2]$.

The model is based on the three layers (one input layer, one hidden layer and one output layer) feed forward architecture as shown in figure 1.

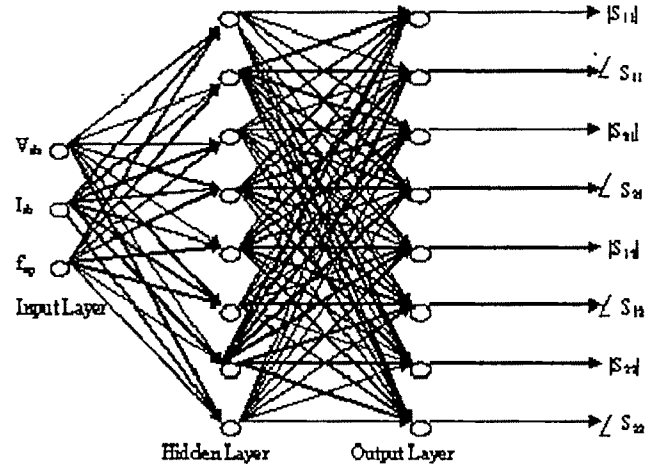


Figure 1: Neural network configuration for S -parameter modeling.

The number of neurons in the hidden layer was optimized so as to obtain a close agreement with the experimental results. A training set of data, which consisted of a set of variables at multiple frequencies measured at multiple biases, are then used to model the network. The learning rate is set and the neural network model is subjected to an initial set of

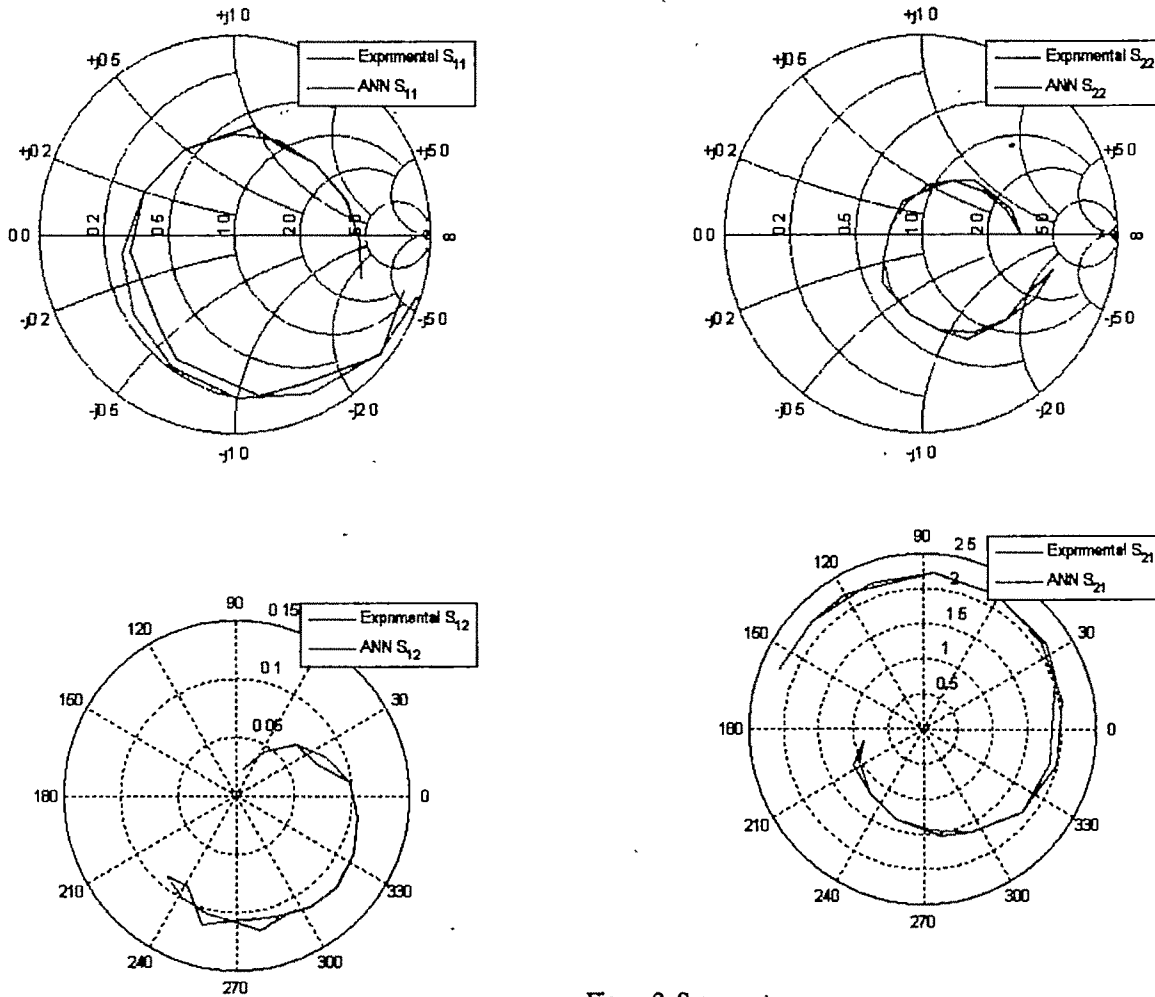


Figure 2: S parameters.

weights. The weights are adjusted to minimize the mean squared error of the outputs by using the training algorithm.

IV. RESULTS AND DISCUSSION

The algorithm proposed in this paper were tested on the training of standard multilayer feed forward networks (FNNs) and applied to several problems. The FNN simulator was implemented in Visual Basic .NET.

In the present paper, we have developed a neural network model for the S-parameters of an InGaAs/InP PHEMT (figure 2). The input parameters are the drain to source voltage, drain current and frequency of operation and the output parameters are S-parameters corresponding to magnitude and angle respectively.

The neural network model consists of three layers (one input layer, one hidden layer and one output layer). Training has been done using a modified back propagation algorithm with genetic algorithm. Training the network involves the determination of suitable values for the interconnection between the neurons in the different layers so that the error between the measured outputs of the network and the desired

outputs are minimized. The number of neurons in the hidden layer was optimized so as to obtain a close agreement with the experimental results. A training set of data, which consisted of a set of variables at multiple frequencies measured at multiple biases, are then used to model the network. The learning rate is set and the neural network model is subjected to an initial set of weights. The weights are adjusted to minimize the mean squared error of the outputs by using the training algorithm.

S-parameters are the reflection and transmission coefficients between the incident and reflection waves. They describe completely the behavior of a device under linear conditions at microwave frequency range.

The result for the InGaAs/InP PHEMT is shown in figure 2, where all the S-parameters (S_{11} , S_{12} , S_{21} , S_{22}) are plotted and compared with the experimental data [19]. Excellent agreement with the experimental data shows the validity of our model.

V. CONCLUSION

The variant in BP has been proposed for the training of feed forward neural networks. The convergence properties of the algorithm has been studied and the conclusion was reached that new algorithm is globally convergent. The proposed

algorithm was tested on available training tasks. The neural network method has been applied to the modeling of S-parameters and shown to give results that have been verified by comparing with experimental results. Thus, the neural network modeling technique can be applied to a variety of microwave circuits. It also has been demonstrated that transistors can be modeled by training neural networks with genetic algorithm.

Thus a neural network based model is developed that can be used to determine the microwave parameters of an InGaAs/InP PHEMT with a greater accuracy and at a faster rate.

ACKNOWLEDGMENT

The authors are thankful to Amity School of Engineering and Technology for providing the Software and Hardware for the development of the simulator.

REFERENCES

- [1] J. M. Zurada, "Introduction to artificial neural systems," *M. G. Road, Mumbai: Jaico*, (2002).
- [2] P. Mehra and B. W. Wah, "Artificial neural networks: concepts and theory," *IEEE Comput. Society Press*, (1992).
- [3] Bob Waterbury, "Artificial intelligence expands frontiers in asset management, condition monitoring and predictive maintenance systems make AI pay off with lower maintenance costs, improved forecasting, and fewer unplanned shutdowns," *Putman Media*, (November 16, 2000).
- [4] D.B. Parker, "Learning logic, technical report TR-47," *Center for Computational Research in Economics and Management Sciences, MIT*, (1985).
- [5] D.E. Rumelhart, G.E. Hinton, and R.J. Williams, "Learning internal representations by error propagation," *Parallel Distribution Processing*, vol. 1, pp. 318-362. MIT Press, Cambridge, MA (1986).
- [6] P.J. Werbos, "The roots of backpropagation," *John Wiley and Sons, Inc.*, New York (1994).
- [7] T. Nitta, "An analysis on decision boundaries in the complex-backpropagation network," *IEEE World Congress on Computational Intelligence*, vol. 2, pp. 934-939, Orlando, FL, June 1994, IEEE Computer Society Press.
- [8] Y. Zhao, "On-line neural network learning algorithm with exponential convergence rate," *Electron. Lett.*, vol. 32, no. 15, pp. 1381-1382 (July 1996).
- [9] G. Zhou and J. Si, "Advanced neural network training algorithm with reduced complexity based on Jacobian deficiency," *IEEE Trans. Neural Networks*, vol. 9, pp. 448-453 (May 1998).
- [10] D.B. Parker, "Optimal algorithms for adaptive networks: second order backpropagation, second order direct propagation and second order Hebbian learning," *First IEEE International Conference on Neural Networks*, San Diego, pp. 593-600 (1987).
- [11] E.M. Johansson, F.U. Dowla, and D.M. Goodman, "Backpropagation learning for multi-layer feed-forward neural networks using the conjugate gradient method," *Intl. J. Neural Systems*, vol. 2: pp. 291-301 (1992).
- [12] D.J. Mortana and L. Davis, "Training feed-forward networks using genetic algorithms," *In Proceedings of 11th Intl. Joint Conf. in Artificial Intelligence (IJCAI)*, Detroit, MI, pp. 762-767, Morgan Kaufmann, San Mateo, CA (1989).
- [13] D. Whitley and T. Hanson, "Optimizing neural networks using faster, more accurate genetic search," *Proceedings of 3rd Intl. Conf. Genetic Algorithms*, pp 391-396, Morgan Kaufmann, San Mateo, CA (1989).
- [14] R. Parisi, E. D. Di Claudio, G. Orlandi, and B. D. Rao, "A generalized learning paradigm exploiting the structure of feed-forward neural networks," *IEEE Trans. Neural Networks*, vol. 7, pp. 1450-1459, Nov. (1996).
- [15] M. T. Hagan and M. B. Menhaj, "Training feed-forward neural networks with the Marquardt algorithm," *IEEE Trans Neural Networks*, vol. 5, pp. 989-993, Nov. (1994).
- [16] X. Yu, M. O. Efe, and O. Kaynak, "A general backpropagation algorithm for feed-forward neural networks learning," *IEEE Trans. Neural Networks*, vol. 13, no 1, pp. 251-254 (January 2002).
- [17] S. Saarinen, R. Brambley, and G. Cybenko, "Ill-conditioning in neural network training problems," *SAIM J. Sci. Comput.*, 14(3):693-714 (May 1993).
- [18] S. E. Fahlman, "Faster-Learning variations on backpropagation: an empirical study in D. Touretzky, G. Hinton, and T. eds. Sejnowski," *Proceedings of the 1988 Connectionist Models Summer School*, Morgan Kaufmann, 38-51(1998).
- [19] Experimental-data [online]; <http://www.agilent.com>.

Genetic Algorithm Driven Modeling of Defect States in Poly-Thiophene (PT) and Poly-Selenophene (PS) under Zero Band-Gap Constraint

Rahul Sharma and S. P. Bhattacharyya

Department of Physical Chemistry, Indian Association for the Cultivation of Science,
Jadavpur, Kolkata – 700032, India.

Abstract— A Su-Schrieffer-Heeger type of Hamiltonian is used to model defect states in Poly-Thiophene and Poly-Selenophene. Genetic Algorithm is invoked to find minimum energy structures with or without the imposition of zero band-gap constraint. Polaronic defects do not reduce the neutral PT band-gap sufficiently. Bipolarons on the other hand reduce the band-gap significantly (≈ 0.6 eV). Under zero band-gap constraint, bipolaron doped PTs produce slightly higher energy structures that have vanishingly small band gap. It could be that conducting states of doped PTs and PSs are the equivalents of 'zero band gap' constrained, slightly metastable structures reported here.

Key words— Doped Polythiophene, Polyselenophene, Genetic Algorithms, Constrained optimization problem.

I. INTRODUCTION

POLYTHIOPHENES (PTs) are known to exhibit metallic conduction under doping.

These molecules can be synthesized rather easily, are chemically stable and can be easily hole-doped. Naturally, PTs have attracted a lot of attention of experimentalists and theoreticians alike [1]–[14]. Neutral PTs are semiconductors with a band-gap of 2 eV. The photoelectron spectrum of PTs reveal the presence of π -bands and the Fermi-level is about 1.2 eV above the valence band. Doping probably creates bipolaronic or polaronic defect states reducing the band-gap to a very low value. The optical transition in PTs at low levels of doping indicate electron-phonon coupling (defects). At higher levels of doping the optical properties of PTs begin to display metallic properties [15]–[19].

There is little doubt that the polaronic or bipolaronic defects represent the main charge storage mechanism in hole doped PTs. There is indication however, that with increasing level of

hole doping the band gap first diminishes and then rises as saturation doping is reached. At high levels of doping, the predicted band gaps do not indicate the presence of a metal-like conducting structure. Previously, we studied the problem using a modified form of Su-Schrieffer-Heeger Hamiltonian for representing the π -electron Hamiltonian [20]–[23] and the Simulated Annealing Method (SAM) [24]–[26] for locating the global minimum on the total energy surface [27]–[28]. It appeared that a lattice like regular arrangement of bipolarons represented the doped states at high level of hole doping and the state practically had zero band gap. If the system is allowed to evolve theoretically on the PES for a very long time, the defect state turns out to evolve further into a state that is less symmetric and the band gap increases significantly above the near zero value. Although there is non-zero density of states at Fermi energy, the band gap is a bit too high.

Our main focus in the present communication has been to develop a Genetic Algorithm [29]–[30] driven method for searching the potential energy surfaces of doped PTs and PSs generated by the Su-Schrieffer-Heeger Hamiltonian under the *imposed constraint of zero-band gap*. The purpose has been to explore

- (i) if bipolaronic defects can simultaneously produce zero-band gap, non-zero density of states at Fermi energy and a correct disposition of the HOMO and LUMO for charge migration,
- (ii) whether enforcing zero-band gap constraint, distorts the bipolaronic charge distribution across the PT or PS chains;
- (iii) whether polaronic defects could lead to metallic conduction.

II. METHOD

We start with the SSH Hamiltonian (H) where

We thank the D. S. T., Government of India, New Delhi, for generous funding.

$$H = H_e + H_I \quad (1)$$

H_e is the π -electron Hamiltonian defined as follows

$$H_e = \sum_n \alpha_n a_n^\dagger a_n + \frac{1}{2} \sum_{nm} V_{nm} a_n^\dagger a_n + H.C. \quad (2)$$

H_I represents contribution from the σ -framework as defined below:

$$H_I = \sum_n \frac{P_n^2}{2M} + \frac{1}{2} \sum_{nm} f(R_{nm}) \quad (3)$$

α_n is π -electron self-energy at the n^{th} site, V_{nm} represents the distance (R_{nm}) dependent hopping interaction between the n^{th} and the m^{th} sites, n, m running over all atom pairs joined by σ -bonds. The form of V_{nm} chosen is

$$V_{nm} = -Ae^{\frac{R_{nm}}{B}} \quad (4)$$

where A, B are parameters taken from the literature [8],[33].

$f(R_{nm})$ is the elastic energy of the σ -bond between the n^{th} and the m^{th} atoms and is represented as follows:

$$f(R_{nm}) = -AD_{nm}(R_{nm} - R_{nm}^0 + B)e^{\frac{-R_{nm}}{B}} \quad (5)$$

where A, B and D_{nm} are parameters of the model.

Under the frozen core approximation the lattice term reduces to potential energy term and is given by

$$E_I = \frac{1}{2} \sum_{n,m} f(R_{nm}) \quad (6)$$

The π MOs are built up from the atomic $2p_z, 3p_z(4p_z)$ orbitals as follows

$$\phi_i^\pi = \sum_{k=1}^N |k\rangle c_{ki} \quad (7)$$

c_{ki} are the variational parameters.

The total energy of the chain is the sum of π -energy and the σ framework potential (number of occupied MOs, $n_{occ} = N/2$)

$$E_T = E_\pi + E_I \quad (8)$$

where

$$E_\pi = \sum_{k=1}^{n_{occ}} n_k \epsilon_k \quad (9)$$

$$= \sum_n q_n \alpha_n + 2 \sum_{n < m} V_{nm} P_{nm}, \quad (10)$$

n_k is the occupation number of the k^{th} π -MO and E_I is already defined.

P_{nm} s are the elements of the charge density bond order matrix defined as

$$P = \sum_{k=1}^{n_{occ}} C_k C_k^\dagger \quad (11)$$

$$q_n = P_{nn} \quad (12)$$

Our main task is now to find out the set of $\{R_{nm}\}$ and the corresponding $\{c_k\}$ s that minimize the total energy subject to

the constraint that $\Delta E = (E_{n_{occ}+1} - E_{n_{occ}}) = 0$. It essentially means that we have a constrained variational problem at hand and we propose to solve the constrained variational problem by Genetic Algorithm driven search on the constrained potential energy surface of the PTs and PSs. The basic search variables are the distance between distinct adjacent atom pairs (R_{nm}) which are collected in strings $\{S_I\}$ where

$$S_I = (R_{12}, R_{13}, \dots, R_{ij}, R_{kl}, \dots, R_{n-1,n}) \\ = S_I(x_1, x_2, \dots, x_N) \quad (13)$$

A collection of m -such strings constitute the population which is allowed to evolve under the standard GA operations like selection, crossover, mutation and diversification. The scaled fitness function of the problem is defined through the objective function which is

$$F_{obj} = (E_T\{R_{nm}\} - E_L)^2 + (\epsilon_{n_{occ}}\{R_{nm}\} - \epsilon_{n_{occ}+1}\{R_{nm}\})^2 \quad (14)$$

where E_L is an estimated lower bound to the total energy (improvable), $\epsilon_{n_{occ}}$ is orbital energy of the HOMO, $\epsilon_{n_{occ}+1}$ is the orbital energy of the LUMO. The fitness function is given by ($\lambda > 0$)

$$F = e^{-\lambda F_{obj}} \quad (15)$$

which clearly scales between 0 and 1, the value $F=1$ is reached only if the band-gap is zero, and the energy $E_T = E_L$.

We use a fitness proportional selection and arithmetic crossover and mutation with probabilities $P_c = 0.8, P_m = 0.01$, respectively. Diversification has been carried out at every generation with diversification probability $P_d = 10^{-4}$ [31]–[32].

To begin with all the m -starting strings are evaluated for their fitness values (F_1, F_2, \dots, F_m) and a selection is carried out to prepare the mating pool. The post selection mating pool is expected to have more copies of better individuals with higher fitness and therefore have higher average fitness.

The crossover (with probability P_c) has been carried out by randomly selecting a pair of strings from the mating pool and selecting a site for crossover similarly. If the k^{th} site is chosen for crossover, the process of crossover generates two strings, S_I', S_J' as follows:

$$S_I \longrightarrow S_I'(x_1, x_2, x_3, \dots, x_k', x_{k+1}', \dots, x_N') \quad (16)$$

$$S_J \longrightarrow S_J'(y_1, y_2, y_3, \dots, y_k', y_{k+1}', \dots, y_N') \quad (17)$$

where

$$x_i' = f x_i + (1-f) y_i \quad (18)$$

$$y_i' = (1-f) x_i + f y_i \quad (19)$$

$$l = k, 2, \dots, N, 0 < f < 1.$$

The mixing parameter f is chosen randomly in the specified range. Each post crossover string is made to undergo mutation with a probability $P_m = 0.01$ and intensity Δ_k as follows:

$$x_k' = x_k + (-1)^l r_k \Delta_k \quad (20)$$

where l is a randomly chosen integer, r_k is a random number ($0 < r_k < 1$) and Δ_k is the mutation strength or intensity (user controlled). After carrying out crossover and mutation operations, fitness of m new strings are evaluated and the best m strings from among the m -parents and m -offsprings are chosen for the next generation in what is known as a strongly elitist GA [13], [14]. The geometrical parameters of each string are used to compute the H_π matrix which is diagonalized and the eigenvalues and eigenvectors are used to compute the fitness value. The entire sequence of operations of selection, crossover and mutation are carried out repeatedly till the string with the highest fitness does not show any improvement over 1000 generations. The geometrical parameters (x_1, x_2, \dots, x_N) coded by the string with the highest fitness define the structure of the polythiophene chain. The corresponding H_π is constructed, diagonalized, the eigenvalues, eigenvectors, charge densities are computed and analyzed.

III. RESULT AND DISCUSSION

The parameters of the model are reported in Table I [8], [33]

TABLE I: Parameters of the Model Used

PT	A	B	C	α_c	α_s	R_{c-c}^*	R_{c-s}^*
	123.6	0.3776	7.814	0.0	-4.0	1.557	1.782
PS	A	B	C	α_c	α_s	R_{c-c}^*	R_{c-s}^*
	176.6	0.3565	8.105	0.0	-3.44	1.578	1.932

The Genetic Algorithm used population size of $m=10$, single point arithmetic crossover with $P_c = 0.8$ and multi point arithmetic mutation operator along with roulette wheel selection. The GA was parallelized under Master-Slave architecture (1 master + 10 slave nodes, with a gigabit switch connecting the slave and master nodes).

TABLE II: Data for the optimized 100 ring, neutral and bipolaron doped (unconstrained and band gap constrained), PT chain

Doping level	Energy	HOMO	LUMO	Band Gap	Fermi Level
Minimum Energy Structure (Bipolaron)					
0	-5141.137	-1.03595	1.40883	2.44478	0.18644
1	-5140.046	-0.80216	-0.18476	0.61739	-0.49346
2	-5138.955	-0.80227	-0.18476	0.61751	-0.49351
3	-5137.864	-0.80017	-0.18476	0.61541	-0.49247
4	-5136.773	-0.79871	-0.18483	0.61387	-0.49177
5	-5135.682	-0.79838	-0.18490	0.61347	-0.49164
6	-5134.591	-0.79616	-0.18626	0.60990	-0.4912
Band Gap Constrained Structure (Bipolaron)					
1	-5139.706	-0.60410	-0.57619	0.027910	-0.59014
2	-5138.603	-0.60267	-0.60267	8.892×10^{-4}	-0.60267
4	-5136.428	-0.58138	-0.58138	1.552×10^{-4}	-0.58138
6	-5134.347	-0.62204	-0.51529	0.10675	-0.56867

The optimized energy (E_T), band gap, Fermi energy, etc. of neutral polythiophene chain of 100 PT units together with its bipolaron doped counterparts are reported in Table II. Table III reports the corresponding data for the unconstrained polaronic defect states.

TABLE III: Data for the unconstrained polaron doped, 100 ring PT chains

Doping Level	Energy	HOMO	LUMO	Band Gap	Fermi Level
Minimum Energy structure (Polaron)					
1	-5138.869	-0.56040	0.92719	1.48761	0.18339
2	-5137.727	-0.54322	0.90922	1.45245	0.18300
3	-5136.606	-0.54322	0.90923	1.45246	0.18300
4	-5135.458	-0.54330	0.90919	1.45249	0.18294

Fig. 1: Density of States for band-gap constrained structure of two-bipolaron doped 100 ring PT

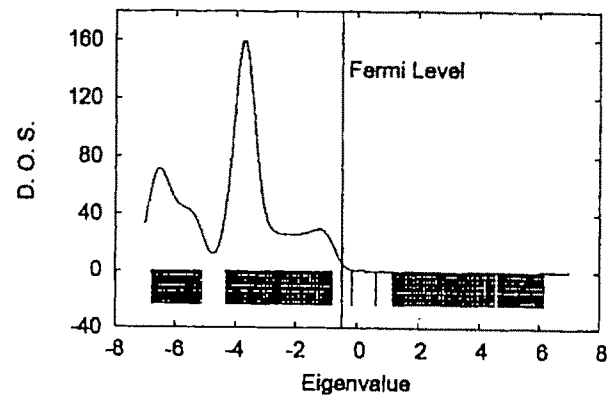
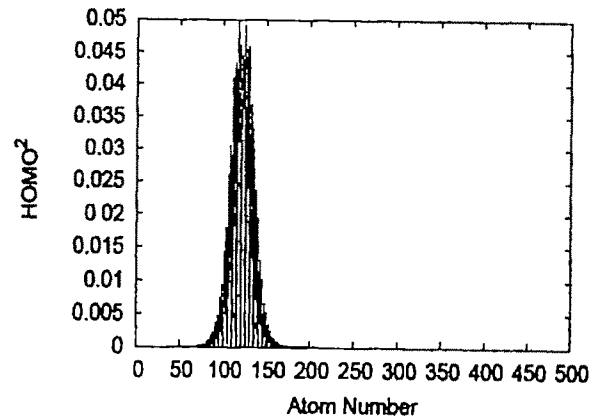
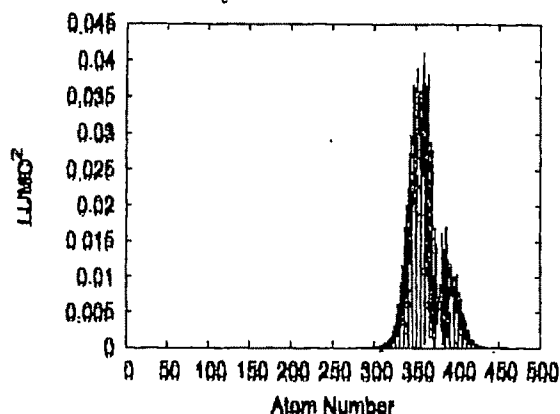


Fig 2: HOMO density distribution for two-bipolaron doped 100 ring PT



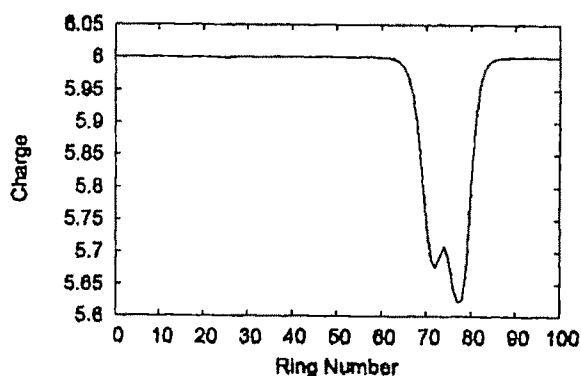
It is clearly seen that polaronic defects do not reduce the band gap to a level where metallic conduction could set in (2 eV to 1.4 eV). Bipolaron doping brings the band gap down to ≈ 6 eV, independent of the doping level. There is non-zero density of states at the Fermi energy and HOMOs are highly delocalized. When zero-band gap constraint is used during optimization, the band gap practically vanishes first and reappears with much reduced values at higher levels of doping.

Fig 3: LUMO density distribution for two-bipolaron doped 100 ring PT



These states have slightly higher energy relative to the unconstrained state and are therefore metastable. The double bipolaron-doped constrained polythiophene chain of 100 rings may be taken up as a test case. The band gap is $8.9 \times 10^{-8} \text{ eV}$ and the Fermi energy is -0.60267 eV . The density of states at Fermi energy is shown in fig. 1. while the HOMO and the LUMO are displayed in fig. 2 and 3. The distribution of electron density (charge) of two 'bipolaron' is shown in fig. 4. The defect appears to be localized over 20 PT units of the chain. The HOMO and LUMO are localized in different contiguous regions of the chain, providing the probability of charge migration from one part of the chain to the other when a bias voltage is applied.

Fig 4: Charge distribution for two-bipolaron doped 100 ring PT



Polyselenophene presents a similar scenario (Table IV). It could be that the hole doped conducting PTs and PSs are metastable structures that resemble the zero-band gap constrained structures predicted by us at low doping levels, which too are metastable. The globally stable doped structures are probably semiconducting. Detailed X-Ray and neutron diffraction studies on the doped PTs and PSs can settle the picture unambiguously.

TABLE IV: Data for the optimized 100 ring, neutral and bipolaron doped (unconstrained and band gap constrained), PS chain

Doping level	Energy	HOMO	LUMO	Band Gap	Fermi Level
Minimum Energy Structure (Bipolaron)					
0	-4962.4576	-0.95167	1.12719	2.07886	0.08776
1	-4961.2087	-0.94774	-0.17149	0.77624	-0.55961
2	-4959.9598	-0.94674	-0.17150	0.77524	-0.55912
3	-4958.7109	-0.94547	-0.17153	0.77394	-0.55850
4	-4957.4619	-0.94413	-0.17152	0.77260	-0.55782
5	-4956.2130	-0.94284	-0.17183	0.77101	-0.55734
6	-4954.9641	-0.94098	-0.17297	0.76800	-0.55698
Band Gap Constrained Structure (Bipolaron)					
2	-4958.9698	-0.64010	-0.61397	0.026123	-0.62703
4	-4956.5074	-0.62477	-0.59108	0.03368	-0.60792
6	-4954.3540	-0.73568	-0.62402	0.11163	-0.67984

The bipolaron doped band gap constrained structures of PSs are not globally optimal. Further evolution could reduce the band gaps and energies

IV. CONCLUSION

Genetic Algorithm driven zero band gap constrained optimization of bipolaron doped PTs and PSs indicate the existence of metastable conducting structures at low doping level. The unconstrained bipolaron doped structures are stable may not be metallic, even at the saturation level of doping.

ACKNOWLEDGMENT

The authors thank Dr. P. Chaudhury for his helpful suggestions and discussions.

REFERENCES

- [1] M. Kobayashi, J. Chen, T. C. Chung, F. Moraes, A. J. Heeger and F. Wudl, "Synthesis and properties of chemically coupled poly(thiophene)", *Synth. Met.*, vol-9 (1984), pp-77.
- [2] T. C. Chung, J. H. Kaufman, A. J. Heeger and F. Wudl, "Charge storage in doped poly(thiophene): Optical and electrochemical studies", *Phys. Rev. B*, vol-30 (1984), pp-702.
- [3] M. Logdlund, R. Lazzaroni, S. Stafstrom, W. R. Salaneck and J. L. Bredas, "Direct observation of charge-induced π -electronic structural changes in a conjugated polymer", *Phys. Rev. Lett.*, vol-63 (1989), pp-1841.
- [4] Y. Jugnet, G. Tourillon and T. M. Duc, "Evidence of Intrinsic Extended π -Bonding Band and Metallic like Behavior in Undoped and Doped Electropolymerized Poly (3-methylthiophene) Films", *Phys. Rev. Lett.*, vol-56 (1986), pp-1862.
- [5] K. Kaneto, Y. Kohno and K. Yoshino, "Absorption spectra induced by photoexcitation and electrochemical doping in polythiophene", *Solid State Commun.*, vol-51 (1984), pp-267.
- [6] Z. Vardeny, E. Ehrenfreund, O. Brafman, M. Nowak, H. Schaffer, A. J. Heeger and F. Wudl, "Photogeneration of confined soliton pairs (bipolarons) in polythiophene", *Phys. Rev. Lett.*, vol-56 (1987), pp-671.
- [7] (a) K. E. Ziemelis, A. T. Hussain, D. D. C. Bradley and R. H. Friend, "Optical spectroscopy of field-induced charge in poly (3-hexyl thiophene) metal-insulator-semiconductor structures: Evidence for polarons", *Phys. Rev. Lett.*, vol-66 (1991), pp-2231.
(b) G. Tourillon, D. Gourier, P. Garnier and D. Vivien, "Electron spin resonance study of electrochemically generated polythiophene and derivatives", *J. Phys. Chem.*, vol-88 (1984), pp-1049.
(c) G. Horowitz, A. Yassar and H. J. Von Bardeleben, "ESR and optical spectroscopy evidence for a chain-length dependence of the

- charged states of thiophene oligomers. Extrapolation to polythiophene", *Synth. Met.*, vol-62 (1994), pp-245.
- [8] F. C. Lavarda, M. C. dos Santos, D. S. Galvao, B. Lak, "Insulator-to-metal transition in polythiophene", *Phys. Rev. B*, vol-49 (1994), pp-979.
- [9] J. Cornil, D. Beljonne and J. L. Bredas, "Nature of optical transitions in conjugated oligomers II. Theoretical characterization of neutral and doped oligothiophenes", *J. Chem. Phys.*, vol-103 (1995), pp-842.
- [10] S. Stafström and J. L. Bredas, "Evolution of the electronic structure of polyacetylene and polythiophene as a function of doping level and lattice conformation", *Phys. Rev. B*, vol-38 (1988), pp-4180.
- [11] D. Giri, K. Kundu, "Theoretical study of the evolution of electronic band structure of polythiophene due to bipolaron doping", *Phys. Rev. B*, vol-53 (1996), pp-4340.
- [12] Ch. Ehrendorfer and A. Karpfen, "Spatial Extension of a Bipolaronic Defect in Oligothiophenes and in Polythiophene: A Combined Semiempirical and ab Initio Study", *J. Phys. Chem.*, vol-98 (1994), pp-7492.
- [13] J. L. Bredas and A. J. Heeger, "Theoretical investigation of gas-phase torsion potentials along conjugated polymer backbones: polyacetylene, polydiacetylene, and polythiophene", *Macromolecules*, vol-23 (1990), pp-1150.
- [14] A. J. W. Tol, "The instability of a bipolaron versus two polarons: charge localization in cyclo-dodecathiophene", *Synth. Met.*, vol-74 (1995), pp-95.
- [15] (a) D. Bertho and C. Jouanin, "Polaron and bipolaron excitations in doped polythiophene", *Phys. Rev. B*, vol-35 (1987), pp-626.
(b) D. Bertho, A. Leghdir and C. Jouanin, "Energetic study of polarons and bipolarons in polythiophene: Importance of Coulomb effects", *Phys. Rev. B*, vol-38 (1988), pp-12531.
- [16] S. Radhakrishnan, R. Parthasarathi, V. Subramaniam and N. Somanathan, "Quantum chemical studies on polythiophenes containing heterocyclic substituents: Effect of structure on the band gap", *J. Chem. Phys.*, vol-123 (2005), pp-164905.
- [17] M. van Fassen and P. L. de Boei, "Excitation energies of pi-conjugated oligomers within time-dependent current-density-functional theory", *J. Chem. Phys.*, vol-121 (2004), pp-10707.
- [18] J. Clark, C. Silva, R. H. Friend, F. C. Spano, "Role of Intermolecular Coupling in the Photophysics of Disordered Organic Semiconductors: Aggregate Emission in Regioregular Polythiophene", *Phys. Rev. Lett.*, vol-98 (2007), pp-206406.
- [19] K. D. Meisel, H. Vocks, P. A. Bobbert, "Polarons in semiconducting polymers: Study within an extended Holstein model", *Phys. Rev. B*, vol-71 (2005), pp-205206.
- [20] P. Chaudhury and S. P. Bhattacharyya, "Evolution of defect states in doped polythiophene: A study based on the method of simulated annealing", *Int. J. Quant. Chem.*, vol-91 (2003), pp-663.
- [21] W. P. Su, J. R. Schrieffer and A. J. Heeger, "Solitons in Polyacetylene", *Phys. Rev. Lett.*, vol-42 (1979), pp-1698.
- [22] (a) W. P. Su, J. R. Schrieffer and A. J. Heeger, "Soliton excitations in polyacetylene", *Phys. Rev. B*, vol-22 (1980), pp-2099,
(b) J. L. Bredas, R. R. Chance and R. Silbey, "Comparative theoretical study of the doping of conjugated polymers: Polarons in polyacetylene and polyparaphenylene", *Phys. Rev. B*, vol-26 (1982), pp-5843.
- [23] M. C. dos Santos and J. L. Bredas, "Nonlinear excitations in permigraniline, the oxidized form of polyaniline", *Phys. Rev. Lett.*, vol-62 (1989), pp-2499.
- [24] S. Kirkpatrick, C. D. Gelatt and M. P. Vecchi, "Optimization by Simulated Annealing", *Science*, vol-220 (1983), pp-671.
- [25] S. Kirkpatrick, "Optimization by simulated annealing: Quantitative studies", *J. Stat. Phys.*, vol-34 (1984), pp-975.
- [26] R. Car and M. Parrinello, "Unified Approach for Molecular Dynamics and Density-Functional Theory", *Phys. Rev. Lett.*, vol-55 (1985), pp-2471.
- [27] P. Dutta, D. Mazumdar and S. P. Bhattacharyya, "A random walk to local minima and saddle points on a potential energy surface. A strategy based on simulated annealing", *Chem. Phys. Lett.*, vol-250 (1991), pp-238.
- [28] P. Dutta and S. P. Bhattacharyya, "Simultaneous optimization of linear and non-linear parameters of a trial wavefunction: the efficacy of the method of simulated annealing", *Chem. Phys. Lett.*, vol-184 (1991), pp-330.
- [29] J. H. Holland, 1975, *Adaptation in Natural and Artificial Systems*, University of Michigan Press, Ann Arbor, MI.
- [30] D. E. Goldberg, 1989, *Genetic Algorithms in Search, Optimization and Machine Learning*, Addison Wesley, Reading, MA.
- [31] S. Nandy, P. Chaudhury and S. P. Bhattacharyya, "Diagonalization of a real-symmetric Hamiltonian by genetic algorithm: A recipe based on minimization of Rayleigh quotient", *J. Chem. Sci.*, vol-116 (2004), pp-285.
- [32] R. Saha and S. P. Bhattacharyya, "On Directly Solving Radial Schrödinger Equation for the Ground States of Two Electron Atoms or Ions by Genetic Algorithm", *J. Theo. Comp. Chem*, vol-3 (2004), pp-325.
- [33] N. Marcal and B. Laks, "Insulator-to-metal transition in polyselenophene", *Int. J. Quant. Chem.*, vol-95 (2003), pp-230.

Optimum Design of Stewart Platform by Using Genetic Algorithm

R. Kaviani¹ and A. Rastgo²

¹ B Sc. Student, Faculty of Mechanical Engineering, University of Tehran, e-mail: r.kaviani@me.ut.ac.ir

² Associate Professor, Faculty of Mechanical Engineering, University of Tehran, e-mail: arastgo@ut.ac.ir

Abstract—Motivated by the need for optimization of parallel mechanisms, this paper presents a new strategy in optimum design of a six-degree-of-freedom (6-DOF) manipulator, Stewart platform. First a closed form technique is used for the forward kinematic analysis of the platform's motion. The optimum platform is the one which is singularity-free, response optimized, without interference of legs and having improved dexterity, workspace volume, lower moving mass and higher load capacitance of the bearings. A genetic algorithm (GA) code developed considering the first five of these characteristics simultaneously as the objective function which is derived by a new technique and is based upon the simulation of the whole model. As stiffness, higher load bearing and acceleration with lower quantity of moving mass is usually mentioned as potential advantage of parallel mechanism, such parameters as we will see don't have much influence on the final optimal solution.

Key words—Genetic Algorithm, Modelling and Simulation, Optimization, and Stewart Platform.

I. INTRODUCTION

PARALLEL robots have become a large area of interest in the field of robotics. Although parallel mechanisms have reduced volume of workspace in comparison with serial mechanisms they have higher accuracy, velocity and rigidity [1]. These mechanisms are of various kinds but the most famous one is the Stewart-Gough manipulator which has applications in flight simulation, telescopes, satellite dish positioning, machine tool technology and a lot more [2]. Stewart platform has been a field of interest for years. Some modifications have been suggested for its design especially by Stoughton and Arai [3], [4]. Different works have been done on kinematic analysis of the problem [5]-[9]. As we will show the forward kinematic problem has 40 possible solutions (real and complex) [10]. Su brought a new method for singularity analysis of Stewart platform using genetic algorithm (GA) considering the square of determinant of Jacobian matrix of the platform [11].

In this work, we modeled the platform in ADAMS and mentioned the positions of legs as design variables. The plant was then exported to Simulink to design the PID controllers and also the Jacobian matrix of the platform was derived. We

developed a GA code for the optimization of all of these as a multi objective decision functions together with optimal control design. The results gained were checked and taken as a set of design points and the resulted model was analyzed with ANSYS.

II. FORWARD DISPLACEMENT ANALYSIS OF GENERAL STEWART MECHANISM

First let's go through the displacement analysis of Stewart platform. This helps us understand the mechanism better. We will see that deriving a general objective function neither in explicit nor in implicit form for optimization is not possible. Forward displacement analysis of the mechanism is considered, so we can get familiar with rotation matrix of the platform which is in relation with the singularity points. Consider the 6-DOF general Stewart mechanism shown in Fig. 1. The six inputs are provided at the prismatic joints in each leg, which in turn controls the location and orientation of the upper platform. For both moving and fixed platforms, the spherical joints P_i and X_i , $i = 1, \dots, 6$, are not restricted to lie in a plane. The notation and the loop-closure equations are given as follows (see Fig. 2).

Let \vec{x}_j denote the vector from the origin of the global system to the grounded spherical pair X_j , \vec{p}_j denote the vector (expressed in moving frame) from the origin of the coordinate frame attached to the platform at P_1 to the spherical pair P_j , \vec{l}_j denote the vector from the ground spherical pair X_j to moving spherical pair P_j expressed in the base coordinate frame with l_x , l_y , and l_z being the x -, y - and z -components of vector \vec{l}_j , $[R]$ is the 3×3 rotational matrix (of direction cosines) denoting the orientation of the moving frame relative to the base frame, and x_j , l_1 , l_j and p_j denote the magnitudes of the vectors \vec{x}_j , \vec{l}_1 , \vec{l}_j and \vec{p}_j , respectively.

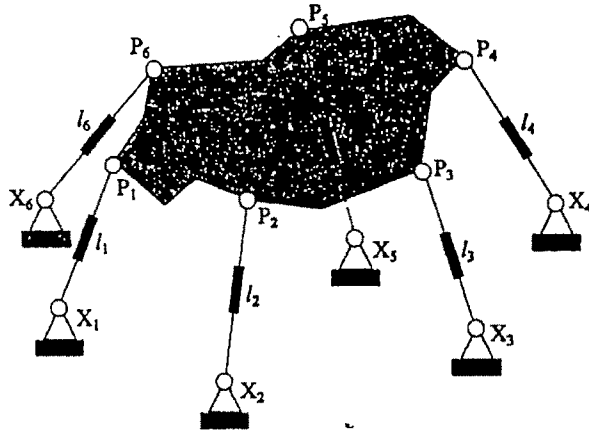


Fig1. A 6-DOF general Stewart mechanism.

Then, the loop-closure equations for the mechanism are:

$$\vec{l}_j = \vec{l}_1 + [R]\vec{p}_j - \vec{x}_j, \quad j = 2, \dots, 6 \quad (1)$$

Equating the magnitudes of the vectors on the left- and right- hand-side of (1) as:

$$\vec{l}_j \cdot \vec{l}_j = (\vec{l}_1 + [R]\vec{p}_j - \vec{x}_j) \cdot (\vec{l}_1 + [R]\vec{p}_j - \vec{x}_j) \quad (2)$$

leads to:

$$l_j^2 = l_1^2 + x_j^2 + p_j^2 + 2\vec{l}_1 \cdot [R]\vec{p}_j - 2\vec{x}_j \cdot [R]\vec{p}_j - 2\vec{l}_1 \cdot \vec{x}_j \quad (3)$$

and after expanding:

$$\begin{aligned} & 2h_1(p_{xj}) + 2h_2(p_{yj}) + 2h_3(p_{zj}) \\ & + p_j^2 + l_1^2 + x_j^2 - l_j^2 \\ & - 2[(p_{xj})r_1 + (p_{yj})r_2 + (p_{zj})r_3]x_{j1} \\ & - 2[(p_{xj})r_4 + (p_{yj})r_5 + (p_{zj})r_6]x_{j2} \\ & - 2[(p_{xj})r_7 + (p_{yj})r_8 + (p_{zj})r_9]x_{j3} \\ & - 2l_{x1}(x_{j1}) - 2l_{y1}(x_{j2}) - 2l_{z1}(x_{j3}) \\ & = 0 \quad j = 2, \dots, 6 \end{aligned}$$

Where:

$$\begin{aligned} h_1 &= l_{x1} \cdot r_1 + l_{y1} \cdot r_4 + l_{z1} \cdot r_7 \\ h_2 &= l_{x1} \cdot r_2 + l_{y1} \cdot r_5 + l_{z1} \cdot r_8 \\ h_3 &= l_{x1} \cdot r_3 + l_{y1} \cdot r_6 + l_{z1} \cdot r_9 \end{aligned} \quad (5)$$

and $(r_1, r_2, r_3), (r_4, r_5, r_6), (r_7, r_8, r_9)$ represent the three rows of-

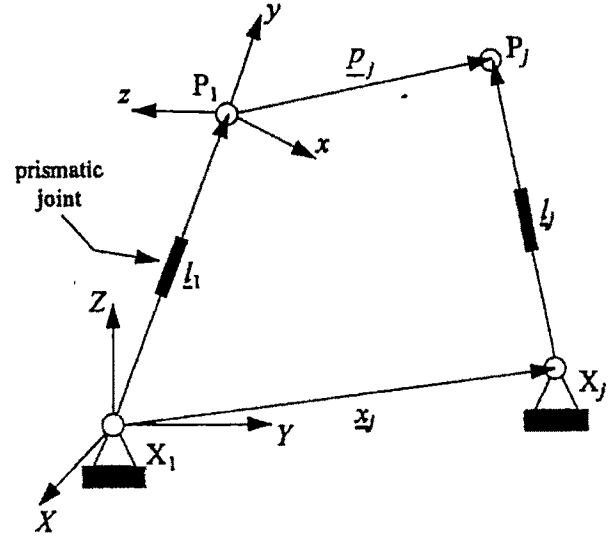


Fig2. A loop of general Stewart mechanism.

the rotation matrix $[R]$. Since $[R]$ is orthogonal, the rows and columns of $[R]$ satisfy the following dot- and cross-product relations:

$$\begin{aligned} r_1^2 + r_4^2 + r_7^2 &= 1 \\ r_2^2 + r_5^2 + r_8^2 &= 1 \\ r_3^2 + r_6^2 + r_9^2 &= 1 \\ r_7^2 + r_8^2 + r_9^2 &= 1 \end{aligned} \quad (6)$$

$$\begin{aligned} r_1 \cdot r_2 + r_4 \cdot r_5 + r_7 \cdot r_8 &= 0 \\ r_1 \cdot r_3 + r_4 \cdot r_6 + r_7 \cdot r_9 &= 0 \\ r_2 \cdot r_3 + r_5 \cdot r_6 + r_8 \cdot r_9 &= 0 \end{aligned} \quad (7)$$

$$\begin{aligned} r_7 &= r_2 \cdot r_6 - r_3 \cdot r_5 \\ r_8 &= r_3 \cdot r_4 - r_1 \cdot r_6 \\ r_9 &= r_1 \cdot r_5 - r_2 \cdot r_4 \end{aligned} \quad (8)$$

The constant length condition of vector l_1 is expressed as:

$$l_1^2 = l_{x1}^2 + l_{y1}^2 + l_{z1}^2 \quad (9)$$

(4) The direct kinematics problem can now be stated as follows: for specified leg lengths l_j , for $j=1, \dots, 6$, determine all possible assembly configurations (real and complex) of the mechanism in terms of the x -, y - and z -components of the reference leg x_1, y_1, z_1 and the nine elements r_1, \dots, r_9 of the rotational matrix $[R]$.

The system of equations (4) to (9) represents a system of 19 equations in 15 unknown variables, namely $r_1, \dots, r_9, x_1, y_1, z_1, h_1, h_2$ and h_3 . The method we use here for solving this system of equations is Sylvester- Gröbner hybrid method [10]. Although only fifteen equations ((4), (5) and (9) and any 6-

Table.I Numerical data for Stewart mechanism

$p_{x1}=0$	$p_{y1}=0$	$p_{z1}=0$
$p_{x2}=2$	$p_{y2}=3$	$p_{z2}=3$
$p_{x3}=3$	$p_{y3}=5$	$p_{z3}=0$
$p_{x4}=1$	$p_{y4}=0$	$p_{z4}=4$
$p_{x5}=4$	$p_{y5}=2$	$p_{z5}=1$
$p_{x6}=2$	$p_{y6}=1$	$p_{z6}=3$
$x_{x1}=0$	$x_{y1}=0$	$x_{z1}=0$
$x_{x2}=2$	$x_{y2}=3$	$x_{z2}=0$
$x_{x3}=3$	$x_{y3}=4$	$x_{z3}=4$
$x_{x4}=5$	$x_{y4}=1$	$x_{z4}=2$
$x_{x5}=0$	$x_{y5}=2$	$x_{z5}=3$
$x_{x6}=4$	$x_{y6}=0$	$x_{z6}=5$
$l_1=12$	$l_2=12$	$l_3=10$
$l_4=14$	$l_5=12$	$l_6=10$

equations from (6)–(8)) are needed to derive the closed-form I/O polynomial for this mechanism, the fact that additional equations are used may actually improve the reduced Gröbner basis computational efficiency, provided that the given over constrained system of equations is finitely solvable. In fact, 11 additional relations can be derived from the dot- and cross products of the orthogonal vectors of the rotational matrix [R] that can be adjoined to (4)–(9) to derive the same reduced Gröbner basis. It should be emphasized that the reduced Gröbner basis and the number of generators used to setup the Sylvester's matrix is independent of the initial number of equations used to derive the reduced Gröbner basis provided that the initial system of equations is finitely solvable.

Using the degree lexicographic (dlex) term ordering with $r_5 < r_1 < r_2 < r_3 < r_4 < r_6 < r_7 < r_8 < r_9 < r_{10} < r_{11} < r_{12} < r_{13} < r_{14} < r_{15} < r_{16} < r_{17} < r_{18} < r_{19} < r_{20} < r_{21} < r_{22} < r_{23} < r_{24} < r_{25} < r_{26} < r_{27} < r_{28} < r_{29} < r_{30} < r_{31} < r_{32} < r_{33} < r_{34} < r_{35} < r_{36} < r_{37} < r_{38} < r_{39} < r_{40}$, yields a reduced Gröbner basis G with 68 polynomials. For the numerical data given in Table. I, the 68 polynomials in G are not reported herein due to space limitations but they can be found in Almadi [12].

Suppressing the unknown r_5 , G can be viewed as a linear system of 68 equations in 68 unknown monomials $r_2^3, l_{z1}r_4^2, r_1r_4^2, r_4^2r_3, r_4^2r_6, r_7r_4^2, r_9r_4^2, r_4^3, l_{z1}^2, r_1l_{z1}, r_1^2, r_3l_{z1}, r_1r_3, r_3^2, l_{z1}r_6, r_1r_6, r_3r_6, r_6^2, l_{z1}r_7, r_1r_7, r_3r_7, r_7r_6, r_7^2, l_{z1}r_8, r_1r_8, r_3r_8, r_8r_6, r_7r_8, r_8^2, l_{z1}r_9, r_1r_9, r_3r_9, r_9r_6, r_7r_9, r_8r_9, r_9^2, r_2l_{y1}, r_1l_{z2}, r_2r_3, r_2r_6, r_2r_7, r_2r_8, r_2r_9, r_2^2, l_{z1}r_4, r_1r_4, r_4r_3, r_4r_6, r_7r_4, r_8r_4, r_9r_4, r_2r_4, r_4^2, h_1, h_2, h_3, l_{x1}, l_{y1}, l_{z1}, r_1, r_3, r_6, r_7, r_8, r_9, r_2, r_4$ and 1, with the polynomial coefficients expressed in terms of r_5 .

$$\begin{bmatrix} g_1 \\ \vdots \\ g_{68} \end{bmatrix} = \begin{bmatrix} 68 \times 68 \\ a_{ij} \in k[r_5] \end{bmatrix} \begin{bmatrix} r_2^3 \\ l_{z1}r_4^2 \\ \vdots \\ 1 \end{bmatrix} \quad (9)$$

Since $G=\{g_1, \dots, g_{68}\}=0$, (25) reduces to $SX=0$ where S is the 68×68 Sylvester's (or coefficient) matrix and X is the

6831 column matrix of the unknown variables (the 68 monomials). The vanishing of the Sylvester's matrix determinant, i.e., $|S|=0$, yields the following univariate resultant:

$$\begin{aligned} F_{110} = & r_5^{40} - 40.34068436r_5^{39} + 2613.674295r_5^{38} \\ & + 48741.59612r_5^{37} - 428723.4299r_5^{36} \\ & - 4274132.197r_5^{35} - 83540302.79r_5^{34} \\ & - 1100933043r_5^{33} + 0.1759214513e11r_5^{32} \\ & + 0.1965350860e12r_5^{31} + 0.1048048526e13r_5^{30} \\ & - 0.2345420202e14r_5^{29} + 0.1519869349e15r_5^{28} \\ & - 0.2532142007e16r_5^{27} + 0.5763041011e16r_5^{26} \\ & - 0.1262508992e18r_5^{25} + 0.1708093186e19r_5^{24} \\ & - 0.1280226550e20r_5^{23} + 0.1277021571e21r_5^{22} \\ & - 0.1438435067e21r_5^{21} + 0.2959635899e22r_5^{20} \\ & - 0.5268108151e23r_5^{19} + 0.7036209479e23r_5^{18} \\ & - 0.4607232515e24r_5^{17} + 0.9532463122e25r_5^{16} \\ & - 0.1808866634e26r_5^{15} + 0.2100680317e27r_5^{14} \\ & - 0.2058612826e28r_5^{13} + 0.6893379360e28r_5^{12} \\ & - 0.3848331827e29r_5^{11} + 0.1749687727e30r_5^{10} \\ & - 0.3684514761e30r_5^9 + 0.1092764420e31r_5^8 \\ & - 0.2122101006e31r_5^7 + 0.1577335438e31r_5^6 \\ & + 0.5167452234e31r_5^5 + 0.4545748611e31r_5^4 \\ & - 0.9804725966e31r_5^3 + 0.9522001983e31r_5^2 \\ & - 0.1610650914e32r_5 + 0.9994869958e31 \\ & = 0 \end{aligned} \quad (10)$$

Here F_{110} is the 40th degree I/O polynomial for the forward kinematics problem of the general Stewart mechanism and it is devoid of any extraneous factors. Two items are worth mentioning at this point. First, it is not necessary that the smallest variable in the dlex term order should be hidden to set up the Sylvester's matrix even though it is the case with the example above where r_5 is suppressed. Second, it may be noted that the forty solutions could also have been obtained by solving the generalized eigenvalue problem (9) instead of expanding the determinant of the Sylvester's matrix. The reason for expanding the determinant of S to derive the univariate I/O polynomial is that this polynomial contains a wealth of other information about Stewart's mechanism such as its singular and unstable configurations which can be determined by analyzing discriminants of (9). Hence, the Stewart mechanism has 40 possible solutions (real and complex) since the I/O polynomial in (10) is a 40th order polynomial and the remaining unknown variables are linear and expressed explicitly in r_5 . It should be noted that since [R] is a direction cosine matrix, the elements (r_i) of this matrix must satisfy the additional constraint $|r_i| \leq 1$. Otherwise, the solution is considered to be complex since $\cos^{-1}(r_i > 1)$ or $\sin^{-1}(r_i > 1)$ leads to complex values.

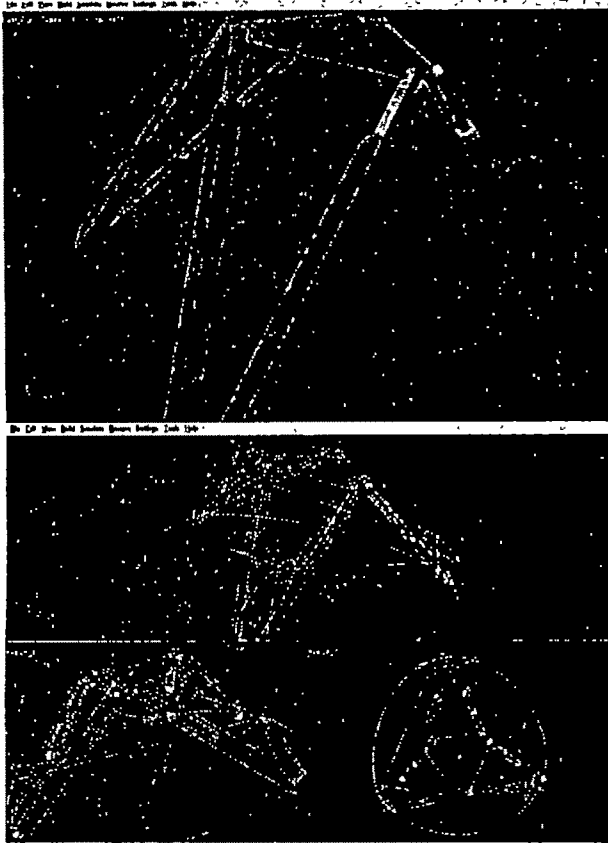


Fig3. Stewart platform model in ADAMS

III. MODELLING THE SYSTEM IN ADAMS

As mentioned before we must perform a stress strain analysis on the model. So modelling the dynamical system in simmechanics was not sufficient. As this model was a three dimensional one first a simple model was sketched with SolidWorks 2006 and exported to ADAMS (See Fig.3.). This model was primitive and without much details. So all of the joints, contacts and actuators were been added. Later we used AdamsFlex and performed a stress analysis with ANSYS on one leg. But for exporting to MATLAB and Simulink we eliminate those flexible bodies to save time in design of controllers and optimum design of legs' base points. In fact running a GA code on a Simulink model takes a lot of time. The most important thing in model was that design points which were in use for determining the base point positions were a kind of design variables and we should change it in various iterations to find the optimum solution. As there is no control over them when this model is exported to Simulink, we defined some arcs as constraints and defined six motions (displacement) for each base point along them. So the simulation were been done in two stages. First the base point moves as it reaches to desired place. And long enough after that the desired input motion was been generated from Simulink to ADAMS plant. At first this may seem a little inappropriate but later it can be seen that this is in a good agreement with real platforms if such arc type constrains were build in a rail type base. This can be a proper modification to

the classic Stewart platform manipulator.

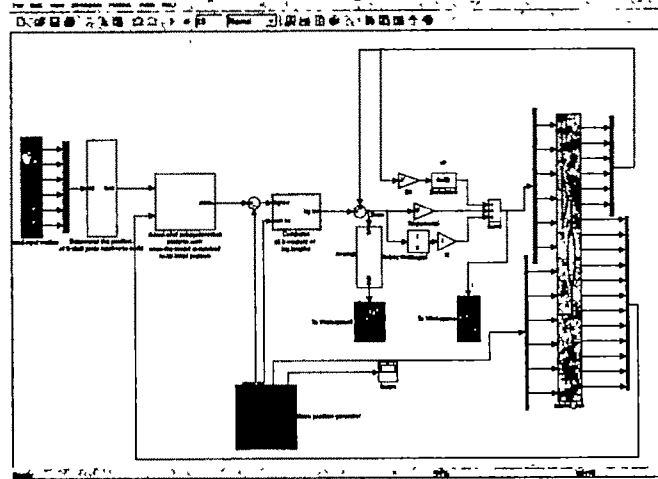


Fig4. View of the complete model in Simulink

IV. ANALYSIS OF STEWART PLATFORM USING SIMULINK

Now again consider the Stewart mechanism. We saw in spite of using one of the best methods of analytical algorithms, it'll take us so much time just to perform position analysis of that Stewart mechanism. So we put the model described in section 3 as a unit (subsystem) of the control system. A schematic view of the model is shown in Fig. 4.

This model can be simulated with any input data and running the model every time leads to results which are needed. For example by generating 6 random input signals (equal to the degree of freedom in addition to the position of 6 design variable point mentioned earlier) for the mechanism, we'll have results gained after simulation and thus the curves of displacement, velocity, angular velocity, and acceleration of the platform's CG can be taken and analyzed. Note that to verify our results, we defined the input variables as those taken in Table I. Then by the results gained we computed the rotation matrix and substituted r_5 in (10) with the value gained from the resulted rotation matrix and we saw that the value of F_{10} is equal to zero. Note that we choose all axis orientations like those defined in section II. In any case reaching to such answers is difficult in practice considering the round-off error. See [13] and [14] for analysis of such mechanisms.

V. OPTIMUM DESIGN OF PLATFORM

First we should define the objective functions. As usually in design of such manipulators price is not of great importance, we concentrate more on minimization of actuating forces, errors that will be explained later and stress. The last of those cannot be simultaneously studied with other two. In facing a multi-objective optimization problem, some methods like vector evaluated GA (VEGA) are usually used. We used weighted sum method which we find it more reliable in spite of being more time-consuming for this objective function. At last we wrote a function to find the pareto set out of the results (see Fig. 5). Thus we started with optimization of an objective function (as a MATLAB M-file). And by running the GA code

several times we received to candidate solutions (pareto-

```
function [xs,fs]=Final_Main
xsize=21; j=10*ones(xsize,1); UB=20*ones(xsize,1); LB=-
20*ones(xsize,1);
N=50; Pc=0.7; Pm=0.001; xsize=size(1,1); num=20;
for i=1:num+1
    w1=(i-1)/num;
    w=[w1,1-w1];
    [x,F,f]=Final_GA_Main(N,Pc,Pm,xsize,1,UB,LB,w);
    xs(i,:)=x; fs(i)=f;
end
[xs,fs]=Final_Problem01_pareto(xs,fs);
plot(fs(1,:),fs(2,:),'*'); xlabel('f1'); ylabel('f2');

function [Xs,Fs]=Final_pareto(xs,fs)
num=size(xs,2); A=[xs;fs];
i=0; j=0;
while (i<size(A,2))
    i=i+1; temp1=A(3,i); temp2=A(4,i);
    while (j<size(A,2))
        j=j+1;
        if and(temp1<A(3,j),temp2<A(4,j))
            A(:,j)=[]; j=j-1;
            if j<i i=i-1; end
        end
    end
    j=0;
end
Xs=A(1:num,:);
Fs=A(3 4,:);
```

Fig5. MATLAB Code for finding the Pareto set

set). Considering each of them as a new set of variables stress-strain analysis (by finite element method using ANSYS) has applied to the ADAMS model. The results showed that all of the candidate solutions were passed the stress criteria. This shows the advantage of parallel manipulators over others. But let's discuss a little bit more about decision function for the Simulink model. The design variables here were K_i , K_d , K_t and 6 motions that were equivalent to the position of the legs' bases. Here we face two problems. First one is a static optimum problem and second is the optimum control design. If we want to solve them separately; first one can be solved by MATLAB genetic algorithm toolbox and the second one with MATLAB optimum control design toolbox. But this way leads to lots of iterations. So for saving time we developed a GA code suitable for this kind of problem and write an M-file that includes the whole design function. This function is resulted from summation of the errors of the lengths of the legs and penalty criterion (as the actuating forces must not exceed from some specific value relative to prismatic joint and actuators). The error is defined as $\| ([R]p_t + p) - p_b \| - l_n$, where R is the rotation matrix for the top plate, p is the position of the origin of the top plate, p_t is the leg attachment point at the top plate, p_b is the leg attachment point at the base, and l_n is the nominal (reference) distance between the top and base attachment points. The magnitudes of errors are being averaged and summed (RMS) after long enough period of time that mentioned earlier. The maximum magnitude of actuating force is mentioned for penalizing the function. The function is also penalized by the inverse of the square of determinant of Jacobian matrix of the platform. In developing the GA code

time for running the program considered mainly. A simple GA code (with tuning parameters taken in Fig. 5) results to a set of design variables including 6 position vector (=18 variables) of the leg's bases and 3 PID controller values.

VI. RESULTS AND DISCUSSION

Results showed that the modified Stewart platform manipulator that has been discussed shows much better dexterity. In addition as in this work we designed the PID controllers and other geometrical parameters simultaneously; the final solution is both singularity-free and response optimized. In addition it needs less number of iterations than using the classical trial and error method. Note that in our work K_i , K_d , K_t values were taken equal for all six legs. For extension of this work these values can be taken different for each leg. So that number of design variables increases from 21 to 36. In this case the final design value set will be more appropriate. However using same PID controllers for all 6 legs is very usual in practice.

REFERENCES

- [1] H Zohour and A. Aryaei, "Forward and inverse kinematic Analysis of a SRU parallel manipulator with two legs", MSc. thesis, Sharif University, Tehran, Iran, pp. 3-5, 2003.
- [2] D. Stewart, "A platform with Six degrees of freedom", UK Institution of Mechanical Engineers Proceedings, vol. 180, Pt 1, No 15, 1965-66.
- [3] R. Stoughton and T. Arai, "A modified Stewart platform with improved dexterity", IEEE Transactions on Robotics and Automation, vol. 9, pp. 166-73, 1993.
- [4] R. Stoughton and T. Arai, "Optimal sensor placement for forward kinematics evaluation of a 6-DOF parallel link manipulator", IEEE Transactions on Robotics and Automation, vol. 2, pp. 785-790, Nov 1991.
- [5] B. Dasgupta and P. Choudhury, "A general strategy based on the Newton-Euler approach for the dynamic formulation of parallel manipulators", Elsevier Science Ltd, Mechanism and Machine Theory, vol. 34, pp 801-824, 1999.
- [6] L.W Tsai, "Solving the inverse dynamics of a Stewart-Gough manipulator by the principle of virtual work" ASME Transactions, Journal of Mechanical Design, vol. 122, pp. 3-9, March 2000.
- [7] G. Lebert, K. Liu and F.L Lewis, "Dynamic analysis and control of a Stewart platform manipulator", Journal of Robotic Systems, vol. 10, No. 5, pp. 629-655, 1993.
- [8] X. Zhao and S. Peng, "Direct displacement analysis of parallel manipulator", Journal of Robotics, vol. 17, pp. 341-345, 2000.
- [9] P. Nauma and K J Wardron, "Direct kinetics solution of a Stewart platform", IEEE Transactions on Robotics and Automation, vol. 6 pp. 438-444, 1990.
- [10] A K. Dhingra, A.N. Almadi and D. Kohil, "A Gröbner-Sylvester hybrid method for closed-form displacement analysis of mechanisms", Journal of Mechanical Design, ASME, vol. 122, Dec 2000.
- [11] Y.X. Su, B.Y. Duan and B. Peng, R.D. Nan, "Singularity analysis of fine-tuning Stewart platform for large radio telescope using genetic algorithm", Elsevier Science Ltd, Mechatronics, vol. 12, pp. 413-425, 2003.
- [12] A.N. Almadi, "On new foundations of kinematics using classical and modern algebraic theory and homotopy", Ph.D. Thesis, University of Wisconsin-Milwaukee, 1996.
- [13] H. Zohour, H. Pendar and M. Vakil, "Inverse and forward kinematics and singularity analysis of a spherically actuated platform manipulator with 3 SPU Legs", MSc. thesis, Sharif University, Tehran, Iran, 2003.
- [14] H. Tavakolnia, K. Sugimoto and H. Zohour, "A Computational Algorithm with High Generality for Simulation of Parallel Mechanisms", ASME Transactions, Journal of Mechanical Design, Paper No: MD-05-1190, Jan 2006.

Optimization of Surface Roughness in End Milling of Stainless Steel (SS 304) Using Genetic Algorithm

Anayet U Patwari¹, A.K.M. Nurul Amin², and Ishtiyah M. Hossain³

^{1,2,3}Department of Manufacturing and Materials Engineering
Faculty of Engineering, International Islamic University Malaysia
Kuala Lumpur, Malaysia
Corresponding author e-mail: aupatwari@hotmail.com

Abstract—Surface roughness and dimensional accuracy plays an important role for the better performance of any machined part. Cutting at high speed, depth of cut and feed, of course, will increase the production rate; however, it will sacrifice the machining quality, such as surface roughness values. It is very important to establish a functional relationship between the surface roughness with the cutting parameters and to optimize the same. This paper presents an approach to optimize the surface finish in end milling of stainless steel using coated TIN insert under dry conditions and full immersion cutting. In this optimization technique, Genetic Algorithm is used to predict the optimum cutting conditions leading to the least surface roughness value. MATLAB 7.0 toolbox for GA is used to develop GA program. A mathematical quadratic model based on response surface methodology is used as a fitness function for the GA. The developed optimization technique proposed in this study is coupled with RS model. The developed optimization technique is effective and can be efficiently used in other machining problems. The experimental results indicate that the proposed optimization model made good agreement with the calculated one.

Key words—coupled RSM with GA, coated TIN, optimization, surface roughness.

I. INTRODUCTION

METAL cutting is one of the important and widely used manufacturing processes in engineering industries. The study of metal cutting focuses, among others, on the features of tools, input work materials, and machine parameter settings influencing process efficiency and output quality characteristics (or responses). A significant improvement in process efficiency may be obtained by process parameter optimization that identifies and determines the regions of critical process control factors leading to desired outputs or responses with acceptable variations ensuring a lower cost of manufacturing [1]. Determination of optimal cutting parameters is one of the most important elements in any

process planning of metal parts. The selection of optimal cutting parameters, like depth of cut for each pass, feed and speed, is very important issue for every machining process. In workshop practice, cutting parameters are selected from machining databases or specialized handbooks, but the range given in these sources are actually starting values, and are not the optimal values. To ensure the quality of machining products, and to reduce the machining costs and increase the machining effectiveness, it is very important to select the machining parameters. A machinability model may be defined as a functional relationship between the input of independent cutting variables (speed, feed, depth of cut) and the output known as responses (tool life, surface roughness, cutting force, etc) of a machining process [2]. Response surface methodology (RSM) is a combination of experimental and regression analysis and statistical inference. RSM is a dynamic and foremost important tool of design of experiment (DOE), wherein the relationship between response(s) of a process with its input decision variables is mapped to achieve the objective of maximization or minimization of the response properties [3].

Many researchers used different techniques for the optimization of different machining parameters for the optimum surface finish. Taraman [4] used Response Surface Methodology (RSM) for predicting surface roughness. A family of mathematical models for tool life, surface roughness and cutting forces were developed in terms of cutting speed, feed, and depth of cut. Hasegawa et al., [5] conducted 3^4 factorial design to conduct experiments for the surface roughness prediction model. They found that the surface roughness increased with an increase in cutting speed. Sundaram and Lambert [6 -7] considered six variables i.e speed, feed, depth of cut, time of cut, nose radius and type of tool to monitor surface roughness. Mital and Mehta [8] conducted a survey of surface roughness prediction models developed and factors influencing surface roughness. They found that most of the surface roughness prediction models

were developed for steels. Boothroyd [9] investigated effect of speed, feed, depth of cut etc., on steel. Baradie [10] also emphasized the use of RSM in developing a surface roughness prediction model for turning grey cast iron. But optimization of the combined effects of the different process parameters is an important factor for the optimum surface quality. In this paper, an optimization technique is proposed based on coupled RSM and Genetic algorithm for the optimum cutting parameters for the prediction of surface roughness.

II. EXPERIMENTAL DETAILS

In this study, cutting tests are carried out for end milling in dry conditions on vertical machining centre with 20mm diameter tool holder fitted with a single Coated TiN insert. Machining was performed with full immersion. The roughness of SS304 was measured by Mitutoyo SURFTEST SV-500. In this work, down milling method was employed in end milling due to some advantages like better surface finish, less heat generation, larger tool life, better geometrical accuracy.

A. Coding of the independent variables:

The independent variables at different levels were coded taking into considerations the limitation and capacity of the cutting tools. Levels of independent and coding identification are presented in Table 1, for experiment using Coated TiN inserts, respectively.

Table1. Coding Identification for end milling using Coated TiN cemented carbide insert

Levels Coding	Lowest -1	Low -1	Centre 0	High +1	Highest +1
x_1 , cutting speed, V (m/min)	59.5	71	109.2	168	200.78
x_2 , axial depth of cut, a (mm)	1.005	1.15	1.59	2.2	2.516
x_3 , feed, f (mm/tooth)	0.039	0.05	0.089	0.16	0.204

B. Experimental Design:

The design of the experiments has an effect on the number of experiments required. Therefore, it is important to have a well-designed experiment to minimize the number of experiments which often are carried out randomly. In the experiment, small central composite design was used to develop the surface roughness model. The analysis of mathematical models was carried out using Design-expert 6.0.8 package [11]. Cutting conditions in coded factors and the surface roughness values obtained using TiN coated cemented carbide insert are presented in Table 2.

Table2. Surface Roughness results and cutting conditions in coded factors

Standard Order	Type	Coding of Level			R_a , Surface Roughness (μm)
		x_1	x_2	x_3	
1	Factorial	1	1	-1	0.52
2	Factorial	1	-1	1	0.59
3	Factorial	-1	1	1	0.92
4	Factorial	-1	-1	-1	0.3
5	Centre	0	0	0	0.32
6	Centre	0	0	0	0.35
7	Centre	0	0	0	0.34
8	Centre	0	0	0	0.33
9	Centre	0	0	0	0.34
10	Axial	-1.414	0	0	0.65
11	Axial	1.414	0	0	0.51
12	Axial	0	-1.414	0	0.32
13	Axial	0	1.414	0	0.34
14	Axial	0	0	-1.414	0.25
15	Axial	0	0	1.414	0.98

III. DEVELOPMENT OF SECOND ORDER MODEL USING CCD DESIGN

The Fit and summary test which are shown in Table 3, indicate that the quadratic model CCD models was more significant than linear model and it also proved that linear model has a significant lack of fit (LOF). Therefore, the quadratic model was chosen in order to develop the CCD model.

Table3. Fit and Summary test of the second order CCD model

Sequential Model Sum of Squares					
Source	Sum of Squares	Mean Square	F Value	Prob > F	Suggested
Mean	10.67377	1.067377			
Block	0.030703	0.030703			
Linear	1.415965	3.0471988	4.61538	0.0283	
2FI	0.18703	3.0062343	0.522255	0.6805	
Quadratic	0.830962	3.0276987	238.237	< 0.0001	Suggested
Cubic	0	0			Aliased
Residual	0.004651	4.0001163			
Total	13.14308	15.0876205			

The second order surface roughness model (coded form) is given as:

$$\hat{y}_2 = -1.10 - 0.086x_1 + 0.021x_2 + 0.48x_3 + 0.28x_1^2 + 0.20x_2^2 + 0.17x_1x_2 - 0.23x_1x_3 - 0.11x_2x_3 \dots \dots \dots (1)$$

IV. GENETIC ALGORITHMS

Genetic algorithms are a family of computational models inspired by evolution. These algorithms encode a potential solution to a specific problem on a simple chromosome-like data structure and apply recombination operators to these structures so as to preserve critical information. Genetic algorithms are often viewed as function optimizers, although the range of problems to which genetic algorithms have been applied is quite broad. An implementation of a genetic algorithm begins with a population of (typically random) chromosomes. One then evaluates these structures and allocates reproductive opportunities in such a way that those

chromosomes which represent a better solution to the target problem are given more chances to "reproduce" than those chromosomes which are poorer solutions. The "goodness" of a solution is typically defined with respect to the current population. This particular description of a genetic algorithm is intentionally abstract because in some sense, the term genetic algorithm has two meanings. In a broader usage of the term, a genetic algorithm is any population-based model that uses selection and recombination operators to generate new sample points in a search space.

A. Optimization problem formulations:

The objective of the optimization is to achieve minimum surface roughness by adjusting the cutting condition with the help of numerical optimization technique. Genetic algorithms are search algorithms for optimization, based on the mechanics of natural selection and genetics [12]. The optimization problem in this study will be solved by coupling the RSM surface roughness model with the GA algorithm. In the solutions of the optimization techniques GA will begin with a set of chromosomes (bit strings) which will be randomly generated or selected.

The entire set of these chromosomes will comprise a population. The chromosomes will evolve several iterations or generations and will make new generation called offspring using crossover and mutation technique. The chromosomes will be evaluated using fitness criteria and the best one will be kept and other will be discarded. The optimization will be formulated in the standard mathematical format:

Find: V (cutting speed), a (depth of cut), f (feed)

Minimum: $R_a(V, a, f)$

Subject to constraints: $R_a \leq R_{a \text{ min}}(\mu m)$

Within ranges: $(v_{\min} \leq v \leq v_{\max})$,
 $(a_{\min} \leq a \leq a_{\max})$,
 $(f_{\min} \leq f \leq f_{\max})$

In this work, MATLAB 7.0 Toolbox GA was used to develop GA program. The GA was written in MATLAB programming language selects chromosomes based on objective value and level of constraint violation.

B. Optimization by genetic algorithm

In this work, MATLAB 7.0 Tool box for GA is used to develop the GA program [13]. The critical parameter for GA are the size of the population, mutation, generations and all their values are listed in Table 4. The developed quadratic CCD coded model is used as a fitness function for the GA. The GA program written in MATLAB language selects the chromosomes based on the objective value and the level of constraint violation.

Table 4: GA Parameters

Subject	Values
Population sizes	50
Scaling Function	Rank
Function	Stochastic Uniform
Crossover function	Scattered
Crossover fraction	0.8
Mutation: Function	Gaussian
Scale	1.0
Shrink	1.0
Stopping criteria: generation	300

C. Optimization results and discussion:

By solving the optimization problem, the GA predicts the optimum roughness is $0.22 \mu m$ for the machining of stainless steel SS304. The best optimum conditions leading to minimum surface roughness are shown in Table 5. The predicted optimum conditions by GA will be further validated with physical measurement. The performance of fitness value with every generation and the best individuals' performance are shown in figure 1 in coded form. From the experimental results the surface roughness with the optimum cutting parameters as predicted by GA shows good agreement.

Table 5: Best cutting condition found in GA

Parameters	Values
Optimized Cutting conditions:	
Cutting speed, m/min	63.84 m/min
Depth of cut, mm	1.149 mm
Feed mm/tooth	0.0495 mm/tooth
Response	Results
Roughness (Predicted by GA)	0.22057 μm
Roughness (Experimental)	0.20 μm

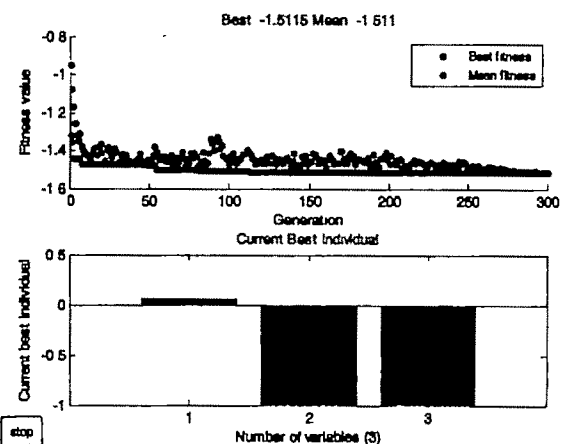


Figure 1: The performance of fitness value with generation and the best individual's performance of variables in coded form.

V. CONCLUSIONS

This research paper discussed the development of an optimization technique by coupled RSM with GA for improving the surface quality of stainless steel (SS304) using coated TiN insert. The general conclusions can be summarized as follows:

The two-stage effort of obtaining a surface roughness model by surface response methodology, and optimization of this model by Genetic Algorithms, has resulted in a fairly useful method of obtaining process parameters in order to attain the required surface quality.

The CCD model developed by RSM using Design Expert package are able to provide accurately predicted values of surface roughness close to actual values found in the experiments. The equations are checked for their adequacy with a confidence level of 95%. The application of the GA approach to obtain optimal machining parameters will be quite useful in the production of good quality surface finish.

ACKNOWLEDGMENT

The authors wish to thank the Research Centre IIUM and Ministry of Higher Education, Malaysia for their financial support to the FRGS Project- No: 0106-23.

REFERENCES

- [1] D.C. Montgomery, Design and Analysis of Experiments, 6th ed., 1997, Wiley, New York.
- [2] LA Choudhury, M.A. El-Baradie, 'Machinability assessment of Inconel 718 by factorial design of experiment coupled with response surface methodology', Journal of Material Processing and Technology 95, pp. 30 – 39, 1999
- [3] Box. G.E.P, Wilson. K.B, 'On the experimental attainment of optimal conditions', Journal of the Royal Statistical Society, 1951, B, 13, pp. 1-45.
- [4] K. Taraman, Multi machining output—multi independent variable turning research by response surface methodology. International Journal of Production Research 12 (1974), pp. 233–245.
- [5] M. Hasegawa, A. Seireg and R.A. Lindberg , Surface roughness model for turning. Tribology International December (1976), pp. 285–289
- [6] R.M. Sundaram and B.K. Lambert , Mathematical models to predict surface finish in fine turning of steel, Part I. International Journal of Production Research 19 (1981), pp. 547–556
- [7] R.M. Sundaram and B.K. Lambert , Mathematical models to predict surface finish in fine turning of steel, Part II. International Journal of Production Research 19 (1981), pp. 557–564
- [8] A. Mital and M. Mehta , Surface roughness prediction models for fine turning International Journal of Production Research 26 (1988), pp. 1861–1876
- [9] M. Hasegawa, A. Seireg and R.A. Lindberg, Surface roughness model for turning. Tribology International December (1976), pp. 285–289.
- [10] M.A El Baradie , Surface roughness model for turning grey cast iron (154BHN), Proceeding of Institution of Mechanical Engg, Part B. Journal of Engineering/Manufacture 207 (1993), pp. 43–54.
- [11] Design-Expert Software, Version 6.0.8, User's Guide, Technical Manual, Stat-Ease Inc , 2000, Minneapolis, MN.
- [12] Randy L.Haupt, Practical Genetic Algorithms, John Wiley, New York, 1998.

Genetic Algorithm Based Tabu Search Method for Solving the Unit Commitment Problem with Cooling – Banking Constraints

C.Christober Asir Rajan¹

¹ Pondicherry Engineering College, Pudhucherry, INDIA e-mail: asir_70@hotmail.com.

Abstract— This paper presents a new approach to solving the short-term unit commitment problem using Genetic Algorithm Based Tabu Search Method with Cooling - Banking constraints (GATSCB). The objective of this paper is to find the generation scheduling such that the total operating cost can be minimized, when subjected to a variety of constraints. This also means that it is desirable to find the optimal generating unit commitment in the power system for the next H hours. A Thermal Power Station in India demonstrates the effectiveness of the proposed approach; extensive studies have also been performed for different power systems consist of 10, 26, 34 generating units. Numerical results are shown comparing the cost solutions and computation time obtained by using the Genetic Algorithm method and other conventional methods like Dynamic Programming, Lagrangian Relaxation and Simulated Annealing and Tabu Search in reaching proper unit commitment.

Key words— Unit Commitment, Genetic Algorithm, Tabu Search, Lagrangian Relaxation, Dynamic Programming.

I. INTRODUCTION

ELECTRICITY generating companies and power systems has the problem of deciding how best to meet the varying demand for electricity, which has a daily and weekly cycle. The short-term optimization problem is how to schedule generation to minimize the total fuel cost or to maximize the total profit over a study period of typically a day, subject to a large number of constraints that must be satisfied. The daily load pattern for a given system may exhibit large differences between minimum and maximum demand. Therefore enough reliable power generation to meet the peak load demand must therefore be synchronized prior to the actual occurrence of the load. Thus it is clear that it is not proper and economical to run all the units available all the time. Since the load varies continuously with time, the optimum condition of units may alter during any period. Therefore the problem of determining the units of a plant that should operate for a given load is the

problem of unit commitment. For total number of units of higher order, the problems associated with unit commitment have generally been difficult to solve because of uncertainty of particular aspects of the problem. For instance the availability of fuel in precise, load forecast variable costs affected by the loading of generator units and the losses caused by reactive flows are some of the unpredictable issues. There are other problems of inconsistency that affect the overall economic operation of the electric power station. In order to reach a feasible solution for Unit Commitment Problem (UCP), different considerations must be considered.

TS have the ability to avoid entrapment in local minima. TS employ a flexible memory system (in contrast to 'memory less' systems, such as Simulated Annealing and Genetic Algorithm, and rigid memory system such as in branch - and - bound). Explicit interest is given to the short - term memory constituent of TS, which has provided solutions superior to the best obtained with other methods for a variety of problems.

Research endeavors, therefore, have been focused on; efficient, near-optimal UC algorithms, which can be applied to large-scale, power systems and have reasonable storage and computation time requirements. A survey of existing literature [1-21] on the problem reveals that various numerical optimization techniques have been employed to approach the complicated unit commitment problem. More specifically, these are the Dynamic Programming method (DP), the Mixed Integer Programming method (MIP), the Lagrangian relaxation method (LR), the Branch and Bound method (BB), the Expert system (ES), the Fuzzy Theorem method (FT), the Hop Field method (H), the Simulated Annealing method (SA), the Tabu Search (TS), the Genetic Algorithm (GA), the Artificial Neural Network (ANN), and so on. The major limitations of the numerical techniques are the problem dimensions, large computational time and complexity in programming.

The DP method [1-2], [13] is flexible but the disadvantage is the "curse of dimensionality", which results it may leads to more mathematical complexity and increase in computation time if the constraints are taken in to consideration. The MIP methods [3-4] for solving the unit commitment problems fail

when the number of units increases because they require a large memory and suffer from great computational delay. The LR approach [5-8], [20] to solve the short-term UC Problems was found that it provides faster solution but it will fail to obtaining solution feasibility and solution quality problems and becomes complex if the number of units increased. The BB method [9] employs a linear function to represent fuel cost and start-up cost and obtains a lower and upper bounds. The difficulty of this method is the exponential growth in the execution time for systems of a practical size. An ES algorithm [10], [13] rectifies the complexity in calculations and saving in computation time. But it will face the problem if the new schedule is differing from schedule in database. In the FT method [11], [13] using fuzzy set solves the forecasted load schedules error but it will also suffer from complexity. The H neural network technique [12] considers more constraints but it may suffer from numerical convergence due to its training process. SA [14], [21] is a powerful, general-purpose stochastic optimization technique, which can theoretically converge asymptotically to a global optimum solution with probability one. But it will take much time to reach the near-global minimum. The TS [15-16], [21] is an iterative improvement procedure that starts from some initial feasible solution and attempts to determine a better solution in the manner of a greatest – decent algorithm. However, TS is characterized by an ability to escape local optima by using a short-term memory of recent solutions. GA [13], [17-21] is a general-purpose stochastic and parallel search method based on the mechanics of natural selection and natural genetics. It is a search method to have potential of obtaining near-global minimum. And it has the capability to obtain the accurate results within short time and the constraints are included easily. The ANN [12] has the advantages of giving good solution quality and rapid convergence. And this method can accommodate more complicated unit-wise constraints and are claimed for numerical convergence and solution quality problems. The solution processing in each method is very unique.

From the literature review, it has been observed that there exists a need for evolving simple and effective methods, for obtaining an optimal solution for the UCP. Hence, in this paper, an attempt has been made to couple GA with TS for meeting these requirements of the UCP, which eliminates the above-mentioned drawbacks. The GA combines good solution quality for TS with rapid convergence for GA. The GA Based TS (GATS) is used to implement and locate optimal or near-optimal solutions to typical optimization problems such as UCP. By doing so, it can help to find the optimum solution rapidly and efficiently. However they take long time to finally reach the global solution. Many advanced operators are proposed to reduce the search time to acceptable values. But these sophisticated operators are problem specific and sensitive to the problem parameters. Hence, local search and hybrid combinations of different methods have been proposed to obtain a robust optimization method. The application on the

Utility System (US) in India and IEEE 10, 26, 34 unit test system shows that we can find the optimal solution effectively and these results are compared with the conventional methods.

II. PROBLEM FORMULATION

The objective is to find the generation scheduling such that the total operating cost can be minimized, when subjected to a variety of constraints [24]. The major component of the operating cost, for thermal and nuclear units, is the power production cost of the committed units and this is given in a quadratic form in (1).

$$F_u(P_u) = A_u P_u^2 + B_u P_u + C_u \text{ Rs/hr} \quad (1)$$

Where

A_u, B_u, C_u ~ the cost function parameters of unit i (Rs./MW²hr, Rs./MWhr, Rs/hr)

$F_u(P_u)$ ~ production cost of unit i at a time t (Rs/hr)

P_u ~ output power from unit i at time t (MW)

The start up cost depends upon the down time of the unit, which can vary from a maximum value, when the unit i is started from cold state, to a much smaller value, if the unit i has been turned off recently. The start up cost calculation depends upon the treatment method for the thermal unit during down time periods. The start-up cost S_u , is a function of the down time of unit i as in (2).

$$S_u = S_0[1 - D_i \exp(-T_{off_i}/T_{down_i})] + E_i \text{ Rs} \quad (2)$$

Where

S_0 ~ unit i cold start – up cost (Rs)

D_i, E_i ~ start – up cost coefficients for unit i

The overall objective function of the UCP is in (3).

$$F_T = \sum_{t=1}^T \sum_{i=1}^N (F_u(P_u)U_{it} + S_{it}V_{it}) \text{ Rs/hr} \quad (3)$$

Where

U_{it} ~ unit i status at hour $t = 1$ (if unit is ON) = 0 (if unit is OFF)

V_{it} ~ unit i start up / shut down status at hour $t = 1$ if the unit is started at hour $t = 0$ otherwise.

F_T ~ total operating cost over the schedule horizon (Rs/Hr)

S_{it} ~ start up cost of unit i at hour t (Rs)

A. Constraints

Depending on the nature of the power system under study, the UCP is subject to many constraints, the main being the load balance constraints and the spinning reserve constraints. The other constraints include the thermal constraints, fuel constraints, security constraints etc. [24]

1) Load Balance Constraints

The real power generated must be sufficient enough to meet the load demand and must satisfy the following factors in (4).

$$\sum_{i=1}^N P_{it} U_{it} = PD_t \quad (4)$$

Where

PD_t ~ system peak demand at hour t (MW)

N ~ number of available generating units

$U(0,1)$ ~ the uniform distribution with parameters 0 and 1

$UD(a,b)$ ~ the discrete uniform distribution with parameters a and b

2) Spinning Reserve Constraints

The spinning reserve is the total amount of real power generation available from all synchronized units minus the present load plus the losses. The reserve is considered to be a pre specified amount or a given percentage of the forecasted peak demand. It must be sufficient enough to meet the loss of the most heavily loaded unit in the system. This has to satisfy the equation in (5).

$$\sum_{i=1}^N P_{\max,i} U_i \geq (PD_t + R_t); 1 \leq t \leq T \quad (5)$$

Where

$P_{\max,i}$ ~ Maximum generation limit of unit i

R_t ~ spinning reserve at time t (MW)

T ~ scheduled time horizon (24 hrs.)

3) Thermal Constraints

The temperature and pressure of the thermal units vary very gradually and the units must be synchronized before they are brought online. A time period of even 1 hour is considered as the minimum down time of the units. There are certain factors, which govern the thermal constraints, like minimum up time, minimum down time and crew constraints.

a) Minimum up time:

If the units have already been shut down, there will be a minimum time before they can be restarted and the constraint is in (6).

$$Ton_i \geq Tup_i \quad (6)$$

Where

Ton_i ~ duration for which unit i is continuously ON (Hr)

Tup_i ~ unit i minimum up time (Hr)

b) Minimum down time:

If all the units are running already, they cannot be shut down simultaneously and the constraint is in (7).

$$Toff_i \geq Tdown_i \quad (7)$$

Where

$Tdown_i$ ~ unit i minimum down time (Hr)

$Toff_i$ ~ duration for which unit i is continuously OFF (Hr)

4) Must Run Units

Generally in a power system, some of the units are given a must run status in order to provide voltage support for the network.

III. TABU SEARCH

A. Overview

To solve the UCP, two types of variables require being determined. The unit's status variables U and V, which are integer variables and the units, output power variables P that are continuous variables. The problem can then be

decomposed into two sub problems, a combinatorial problem in U and V and a non-linear optimization problem in P. TS are used to solve the combinatorial optimization and the non-linear optimization is solved via a quadratic programming routine [15]. The proposed algorithm contains three major steps:

- First, generating randomly feasible trial solutions
- Second, calculating the objective function of the given solution by solving the EDP.
- Third, applying the TS procedures to accept or reject the solution in hand.

B. Tabu Search General Algorithm

Step(0): Assume that the fuel costs to be fixed for each hour and all the generators share the loads equally.

Step(1): By optimum allocation find the initial feasible solution (U_i, V_i).

Step(2): Demand is taken as the control parameter.

Step(3): Generate the trial solution.

Step(4): Calculate the total operating cost, F_t , as the summation of running cost and Start up – shut down cost.

Step(5): Tabulate the fuel cost for each unit for every hour.

IV. GENETIC ALGORITHM

A. Introduction

The GA is essentially a search algorithm based on the mechanics of natural selection and natural genetics. It combines solution evaluation with randomized, structured exchanges of information between solutions to obtain optimality. GA is a robust approach because no restrictions on the solution space are made during the search process. The power of this algorithm comes from its ability to exploit historical information structures from previous solution guesses in an attempt to increase performance of future solution structures [22-23].

By simulating "the survival of the fittest" criterion of Darwinian evaluation among chromosome structures, the optimal solution is searched by randomized information exchange. While randomized, GA is not a simple random walk. It effectively exploits historical information to speculate on new search points with expected improved performance. In every generation, a new set of artificial chromosomes is created using bits and pieces of the fittest of the old ones. The three prime operators associated with the GA are reproduction, crossover and mutation [22-23].

B. Unit Commitment Using GA

1. Initial binary coded solutions are produced at random to form the initial population.
2. Calculate the total power production cost of the committed units as given in (1) by solving the EDP.
3. Calculate and scale the fitness function and assigned to the initial population as given in (2).
4. Check the convergence criterion is satisfied. If yes go to stop. Otherwise, go to next step.
5. Copy the best solution of every generation.

6. Create the offspring with the application of rules for generating randomly feasible solutions by means of the crossover and mutation operations.

V. GA BASED TS ALGORITHM

In the TS technique for solving UCP, Initial Operating Schedule status in terms of maximum real power generation of each unit is given as input. As we know that TS is used to improve any given status by avoiding entrapment in local minima, the offspring obtained from the GA algorithm is given as input to TS and the refined status is obtained. And in this method, no advanced operators are required.

- Step(1): Get the demand for 24 hours and no. of iterations to be carried out.
- Step(2): Generate population of parents (N) by adjusting the existing solution to the given demand to the form of state variables.
- Step(3): Unit down time makes a random recommitment.
- Step(4): Check for constraint in the new schedule.
- Step(5): Perform ELD and calculate the total production cost for each parent.
- Step(6): Has iteration count reached? If yes go to Step (10) else go to step (7).
- Step(7): Using the basic GA generates new population.
- Step(8): Improve the status of the new population and update it by TS algorithm.
- Step(9): Select the best N number of population for next iteration.
- Step(10): Stop if stopping criterion is satisfied. Otherwise go to Step(5).
- Step(11): For the units, which are in the off states, calculate the cost for both cooling and banking.
- Step(12): Compare the cooling and banking costs, if banking cost is lesser than cooling, bank the unit.
- Step(13): Print the optimum schedule.

VI. SIMULATION RESULTS

A US in India with seven generating units, each with a capacity of 210MW, has been considered as a case study. A time period of 24 hours is considered; the unit commitment problem is solved for these seven units and also compared with IEEE 10, 26, and 34 generating unit power systems. The required inputs for solving the UCP are briefed here.

TABLE I
DAILY GENERATION OF SEVEN UNITS IN MW

Hour	Unit 1	Unit 2	Unit 3	Unit 4	Unit 5	Unit 6	Unit 7
1	840	0	0	100	101	140	150
2	757	0	0	100	100	147	150
3	773	0	0	100	113	150	150
4	773	0	0	100	113	150	150
5	770	0	0	100	110	150	150
6	778	0	0	100	118	150	150
7	757	0	0	100	100	147	150
8	778	0	0	100	118	150	150
9	770	0	0	100	110	150	150
10	764	0	0	100	104	150	150
11	598	0	0	99	97	142	0
12	595	0	0	100	96	139	0
13	543	0	0	100	99	144	0
14	538	0	0	99	97	142	0
15	535	0	0	100	96	139	0
16	464	0	0	0	116	150	0
17	440	0	0	0	101	148	0
18	439	0	0	0	97	142	0
19	466	0	0	0	116	150	0
20	463	0	0	0	113	150	0
21	460	0	0	0	110	150	0
22	434	0	0	0	93	139	0
23	530	0	0	0	120	150	0
24	840	0	0	100	101	140	150

TABLE II
DAILY GENERATION OF 10,26,34 UNIT TEST SYSTEM

Hour	10 Unit	26 Unit	34 Unit
1	103	1820	1025
2	100	1800	1000
3	90	1720	900
4	85	1700	850
5	103	1730	1025
6	140	1910	1400
7	197	2030	1970
8	280	2600	2800
9	285	2600	2830
10	315	2600	3130
11	330	2600	3300
12	360	2380	3600
13	328	2590	3275
14	295	2570	2930
15	230	2500	2300
16	235	2500	2330
17	272	2350	2725
18	330	2480	3300
19	330	2380	3300
20	280	2600	2800
21	213	2600	2125
22	163	2480	1630
23	130	2130	1300
24	115	1850	1120

TABLE III
GENERATION SYSTEM OPERATION DATA

Unit	P _{max} (MW)	P _{min} (MW)	C ₁ (Rs./hr)	C ₂ (Rs./hr/MW)	C ₃ (Rs./hr/MW ²)	R ₁ (Rs./hr)	R ₂ (Rs./hr)	R ₃ (Rs./hr)
1	15	80	750	70	0.255	42.50	20.5	10
2	20	80	1250	70	0.198	30.50	20.5	10
3	30	100	2000	70	0.198	37.00	26.5	10
4	25	120	1600	70	0.191	47.00	32.5	10
5	30	150	1400	70	0.104	34.50	32	9
6	30	150	4900	45	0.0473	141.00	37.5	4.5
7	75	200	4100	80	0.074	113.50	33	2.5

The total number of generating units, the maximum real power generation of each unit and the cost function parameters of each unit are tabulated for a day, respectively, as shown in Table I for US and Table III for US. The daily load data of 10, 26, 34 unit test systems are shown in Table II. The status of unit i at time t and the start-up / shut - down status obtained are the necessary solutions and are obtained for SA, TS, GA, GATS, DP, LR methods for US. The comparison of the total costs and Central Processing unit (CPU) time is shown in Table IV for US, 10, 26, and 34 generating unit power systems. "Fig. 4" represents the convergence of the proposed GATS method for different generations. "Fig. 5" gives the plot of optimal solution for various mutation rates.

TABLE IV
COMPARISONS OF COST AND CPU TIME FOR UTILITY, 10, 26, 34 SYSTEMS

System	Method	Total Cost (\$)	CPU Time (sec)
7 Unit (Utility)	SA	0.94780	84
	TS	0.95531	110
	GA	0.92002	64
	GATS	0.91525	55
	GATS (Cooling & Banking)	0.91220	53
	DP	1.00000	130
IEEE 10 Unit	LR	0.97843	115
	SA	0.94422	200
	TS	0.95322	230
	GA	0.91602	181
	GATS	0.91054	176
	GATS (Cooling & Banking)	0.90766	169
IEEE 26 Unit	DP	1.00000	260
	LR	0.97183	235
	SA	0.93906	1810
	TS	0.94887	1820
	GA	0.91082	1782
	GATS	0.90534	1771
IEEE 34 Unit	GATS (Cooling & Banking)	0.90128	1765
	DP	1.00000	1860
	LR	0.96642	1858
	SA	0.93500	6800
	TS	0.94382	6842
	GA	0.90472	6790
GATS (Cooling & Banking)	GATS	0.90124	6770
	DP	0.90003	6762
	LR	1.00000	6865
	LR	0.96197	6824

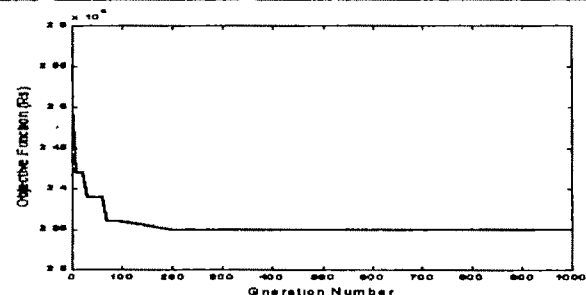


Fig. 4. Convergence of the GATS algorithm

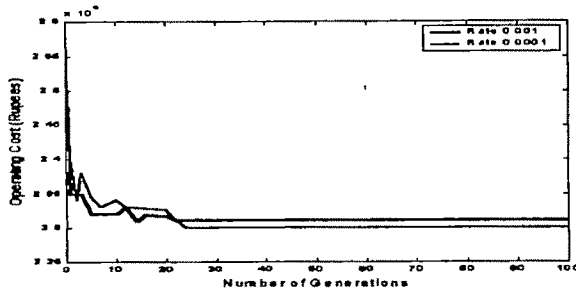


Fig. 5. Optimal solution for various mutation rate

The proposed GATSCB approach was compared to the related methods in the references indented to serve this purpose, such as the DP and LR with a zoom feature, the SA, TS and the GA approaches. And with the use of Tabu Search method, the status is improved by avoiding the entrapment in local minima. By means of stochastically searching multiple points at one time and considering trail solutions of successive generations, the GATSCB approach avoids entrapping in local optimum solutions. Also, disadvantages of huge memory size required by the SA method are eliminated. Moreover, intellectual schemes of encoding and decoding entailed by the GA approach are not needed in the proposed GATSCB approach. The problem of power unbalance previously existing in the solution of GA is circumvented as well in this paper. The main limitation in the implementation of the GA model is that the performance of the system mainly depends on the selection of genetic parameters and these vary from system to system. In comparison with the results produced by the referenced techniques, the GATSCB method obviously displays a satisfactory performance with respect to the quality of its evolved solutions and to its computational requirements. From these results, the GATSCB method had lesser total cost and took lesser CPU time in all the power systems considered including US.

VII. CONCLUSION

In this proposed method to the unit commitment problem the essential process simulated in the procedure are mutation, competition, and selection. The mutation rate is computed as a function of the ratio of the total cost by the schedule of interest to the cost of the best schedule in the current population. The best solutions to form the basis of the subsequent generation are selected from among the parents and the offspring in the current population. In this proposed work, the parents are obtained from a pre-defined set of solution's i.e. each and every solution is obtained from the Tabu Search method. Then, a random recommitment is carried out with respect to the unit's minimum down times.

In comparison with the results produced by the referenced techniques (Genetic Algorithm, Dynamic Programming, Lagrangian Relaxation, Simulated Annealing and Tabu Search), the GATSCB method obviously displays a satisfactory performance. There is no obvious limitation on the size of the problem that must be addressed, for its data structure is such that the search space is reduced to a minimum; No relaxation of constraints is required; instead, populations of feasible solutions are produced at each generation and throughout the process.

VIII. REFERENCES

- [1] W.L.Snyder, H.D.Powell, and C.Rayburn, "Dynamic Programming approach to Unit Commitment", *IEEE Trans. Power Systems*, Vol.3, No.2, pp. 339-350, 1987.
- [2] Y.Y.Hsu., Su, C.C.Liang, C.C.Lin.C.J. and C.T.Huang., "Dynamic Security Constrained Multi-Area Unit Commitment", *IEEE Trans. Power Systems*, Vol.6, pp.1049-1055, 1991.
- [3] Samer Takriti and John R.Birge, "Using Integer Programming To Refine Lagrangian - Based Unit Commitment Solutions", *IEEE Trans. Power Systems*, Vol.15, No.1, pp.151-156, 2000.
- [4] M.R.Mohan, K.Kuppusamy, M.Abdullah Khan, "Optimal Short-term Hydro-Thermal Scheduling using Decomposition Approach and Linear Programming Method", *International Journal of Electrical Power and Energy Systems*, Vol. 14, No.1, pp.39-44, 1992.
- [5] J.M.Ngundam, F.Kenack, T.T.Tahetse, "Optimal Scheduling Of Large - Scale Hydrothermal Power Systems Using The Lagrangian Relaxation Technique", *International Journal of Electrical Power & Energy Systems*, Vol. 22, No.1, pp.237-245, 2002.
- [6] A.G.Bakirtzis, C.E.Zoumas, "Lambda of Lagrangian relaxation solution to unit commitment problem", *IEE Proc. Generation, Transmission and Distribution*, Vol.147, No.2, pp.131-136, 2000.
- [7] Chuan-ping Chang, Chih-wen Liu, Chun-chang Liu, "Unit Commitment by Lagrangian Relaxation and Genetic Algorithms", *IEEE Trans. Power Systems*, Vol.15, No.2, pp.707-714, 2000.
- [8] R.Nieva, A.Linda., and I.Guillen, "Lagrangian Reduction Of Search Range For Large Scale Unit Commitment", *IEEE Trans. Power Systems*, Vol.2, pp.465-473, 1987.
- [9] A.I.Cohen and M.Yoshimura, "A Branch and Bound Algorithm for Unit Commitment", *IEEE Trans. Power and Apparatus*, Vol. 102, No.2, pp.444-451, 1983.
- [10] Z.Ouyang, SM.Shahidepour, "Short term Unit Commitment Expert System", *International Journal of Electrical Power System Research*, Vol. 20, pp.1-13, 1990.
- [11] C.C.Su, Y.Y.Hsu, "Fuzzy Dynamic Programming: an application to Unit Commitment", *IEEE Trans. Power Systems*, Vol.6, No.3, pp.1231-1237, 1991.
- [12] H.Sasaki, M.Watanabe, J.Kubokawa, N.Yorino, "A solution method of Unit Commitment by artificial neural networks", *IEEE Trans. Power Systems*, Vol.7, No.3, pp.974-981, 1992.
- [13] N.P.Padhy, "Unit Commitment using Hybrid Models: A Comparative Study for Dynamic Programming, Expert Systems, Fuzzy System and Genetic Algorithms", *International Journal of Electrical Power & Energy Systems*, Vol.23, No.1, pp 827-836, 2000.
- [14] A.H.Mantawy, Youssef L. Abdel-Magid, Shokri Z. Selim, "A Simulated Annealing Algorithm For Unit Commitment", *IEEE Trans. Power Systems*, Vol. 13, No. 1, pp. 197-204, 1998.
- [15] A.H.Mantawy, Youssef L. Abdel-Magid, Shokri Z.Selim, "A Unit Commitment By Tabu Search", *IEE Trans. Generation, Transmission and Distribution*, Vol. 145, No. 1, pp.56-64, 1998.
- [16] Whei-Min Lin, Fu-Sheng Cheng, Ming-Tong Tsay, "An Improved Tabu Search for Economic Dispatch With Multiple Minima", *IEEE Trans. Power Systems*, Vol.17, No.1, pp.108-112, 2002.
- [17] Yong-Gang Wu, Chun-Ying Ho, Ding-Yi Wang, "A Diploid Genetic Approach to Short-Term Scheduling of Hydro-Thermal System", *IEEE Trans. Power Systems*, Vol.15, No.4, pp.1268-1274, 2000.
- [18] Ying-Yi Hong, Chih-Yuan Li, "Genetic Algorithms Based ED for Cogeneration Units Considering Multipiant Multibuyer Wheeling", *IEEE Trans. Power Systems*, Vol.17, No.1, pp.134-140, 2002.
- [19] K.S.Swarup, S.Yamashiro, "Unit Commitment Solution Methodology Using GA", *IEEE Trans. Power Systems*, Vol.17, No.1, pp 87-94, 2002.
- [20] Chuan-Ping Cheng, Chih-Wen Liu, Chun-Chang Liu, "Unit Commitment By Lagrangian Relaxation And Genetic Algorithms", *IEEE Trans. On Power Systems*, Vol.15, No.2, pp. 707-714, 2000.
- [21] A.H.Mantawy, Youssef L. Abdel-Magid, Shokri Z.Selim, "Integrating Genetic Algorithms, Tabu Search, And Simulated Annealing For The Unit Commitment Problem", *IEEE Trans. On Power Systems*, 1999, 14(3), pp. 829-836.
- [22] David E. Goldberg, *Genetic Algorithms In Search, Optimisation And Machine Learning*, Eastern Press: Addison-Wesley, 1999.
- [23] Melanie Mitchell, *An Introduction To GA*, U.S.A : MIT Press, 2002.
- [24] A.J.Wood and B.F.Woolenberg, *Power Generation And Control 2nd Edn.*, New York: John Wiley and Sons., 1996.

Automated Active Filter Design using Genetic Algorithm

Rupaban Subadar¹, and Swanirbhar Majumder²

Electronics and Communication Engineering Department, NERIST (Deemed University), Arunachal Pradesh

¹e-mail: rupaban@yahoo.com ²e-mail: swanirbhar@gmail.com

Abstract—Decision-making features occur in all fields of human activities such as scientific and technological and affect every sphere of life. Active filter design and modeling using genetic algorithms for aiding the optimization process is the main idea of this work. The strength of genetic algorithm when combined with a workable method of optimization has been discussed here. The principles, strengths, and weaknesses of Genetic Algorithm's applied to sizing circuit parameters to meet performance specifications are discussed and a software implementation is introduced. Using this, we can design any kind of filter (HPF & LPF). We have also incorporated the code for generation of Band Pass and Band Stop filters. But as these filters are more complex to design so to get the best output we need to increase the population size as well as the maximum generation size

Key words— Band pass, band stop, high pass, low pass filter design and modeling, Genetic Algorithm (GA).

I. INTRODUCTION

THE past several years have witnessed a sharp increase in work with reconfigurable hardware systems. Reconfigurability is essential in a general-purpose GA engine because certain GA modules require changeability (e.g. the function to be optimized by the GA). Thus a hardware-based GA is both feasible and desirable. The use of reconfigurable hardware for the design of GA was seen in projects. In Stephan Scott's behavioral-level implementation of a GA, [1] the targeted application was optimization of an input function. In some GA it was designed and implemented on a PLD, using Altera hardware description language (AHDL). In some, a number of GAs were designed and implemented in a text compression chip. In another case, the GA was implemented in hardware on a Splash 2 reconfigurable computer. The problem selected for implementation is the famous Traveling Salesman Problem (TSP).

Splash2 consisted of an interface board and a collection of processor array boards. Its basic unit of computation was the processor, which consisted of four Xilinx 4010 FPGA's [2] and associated memories. The performance differences between Hardware [3] and Software versions of Genetic Algorithm in solving Travelling Salesman Problem (TSP) [7] were further analyzed by Paul Graham and Brent Nelson in

their thesis. The new Xilinx XC6216 was also used to accelerate the GA performance in those cases. It was used to accelerate the most time-consuming fitness task of GA by embodying each individual of evolving population into hardware. The memory bottleneck is inevitable since GA requires a large memory to store the population. As a result, high-speed memory may be used making the hardware expensive or low-cost memory reducing performance. Therefore, in contrast to the Simple GA, the Compact GA [5] [6] [8] was more suitable for hardware implementation. In the current work, all the research done in hardware implementation of GA is combined to create a system which attempts to achieve significant speedup over software GA due to pipelining and parallelization. It also attempts to minimize the logic resources used within FPGA [4] [9].

SCAM (Symbolic Circuit Analysis in MATLAB) is used here. But the SCAM program cannot simply read a schematic diagram so we need to develop a method for representing a circuit textually. This can be done using a device called a netlist that defines the interconnection between circuit elements similar to SPICE [10] (Simulation Program with Integrated Circuit Emphasis). Thus we take our results and use them in MATLAB[®] for other calculations. This is especially true when working with transfer functions. Obtained on applying the genetic algorithm

II. WORKING

The working step of the algorithm devised is started with the initial inputs about the frequency and gain specification to be achieved. This is followed by specification of parameters for running the first generation genetic algorithm (GA-I). This GA-I is run to optimize the circuit topology. Thereby the transfer function after simulating the best circuit topology is obtained. After obtaining the transfer function the second generation algorithm (GA-II) is executed to optimize the component values of the circuit simulated. The best fit component is taken and frequency response of the circuit is deduced and plotted.

For the first generation genetic algorithm or GA-I, a circuit is randomly generated, it is then checked whether it is valid or not. If it is not again one circuit topology is randomly generated till it is valid. After getting the valid circuit topology it is added with the initial population. Then the initial population is counted if it is not equal to twenty one more valid circuit topology is generated and added with the initial population till it is twenty. These twenty circuit topologies make the present generation. From this generation we find out the scores of each circuit topologies. After that it is checked whether any termination condition has occurred or not. The three termination conditions used in our algorithm:

1. minimum score value = 0
2. minimum score remain same for last consecutive five
3. total number of generation = 10

If the termination condition has occurred the algorithm returns the best circuit in the present population and it is stopped. If termination condition does not occur, two circuits having least score are taken out and stored in the next generation we call them as elite kids. Next using roulette selection we chose 28 parents from the present population and create crossover kids from them. To make our generation with 20 kids we required more 4 kids and we get this through mutation. After that we combine the crossover kids, mutated kids and elite kids to form the next generation. Now this becomes our present generation and it goes till the 100.

To find the score we firstly take the bit pattern that we have achieved and then decode it. Then the circuit configuration is written on a file. After that scam function is called it simulate the circuit. Next we find the transfer function of the circuit. After that we find the frequency response of the circuit from 0.1rad/sec to 10rad/sec at regular interval of 0.1rad/sec. next we find the absolute value of the error between the desired and actual frequency response. Then the difference is taken as error which we have termed as score and it is returned and it is stopped

To find the crossover kids, the two best parents are taken according to least score. Then randomly the crossover point is chosen. Then the two parents are combined on the basis of crossover point. Then the kids are checked for validity. If they are not valid then again a randomly generated crossover point is selected and combined till it is valid. In this way 14 crossover kids are returned and are generated.

To find the mutated kids, one parent is taken according to least score. Then randomly the mutation point is chosen with a probability less than 0.01. The bits are altered at mutated points. Then the kids are checked for validity. If they are not valid then again a randomly generated mutated point is selected and bits are altered till it is valid. In this way 4 mutated kids are returned and are generated

To optimize the component values, after the first

optimization we got a circuit topology which had a frequency response nearest to our desired response. In this optimization we take the previous circuit and use the genetic algorithm to optimize the component values such that the error is further reduced. This GA runs with the following parameters.

1. minimum score value = 0
2. minimum score remain same for last consecutive fifty
3. total number of generation = 100

The only differences between this and the previous optimization are that, the type of encoding used previously was bit string, but in the present one it is double vector and here after the creation of the next generation kids we do not need to validate the circuit.

III. RESULTS

For the high pass filter if we are interested in $F_c=700$ Hz, pass band gain between 0.9 to 1.1 and stop band gain of 0 to 0.5. For this we feed our software with the following inputs as in figure 1

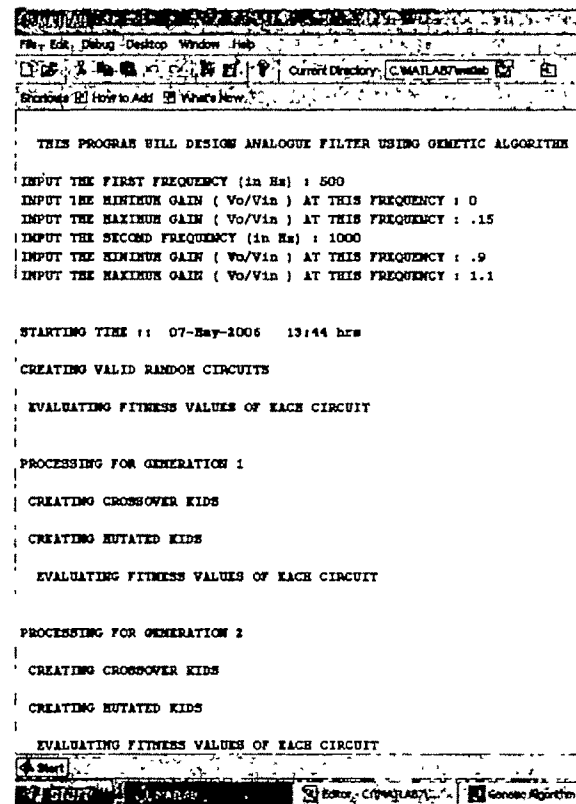


Figure 1: Inputs for High Pass Filter Design

The algorithm runs for around 30mins. During this time it performed two genetic optimizations. The first one was for optimizing the circuit topology. This optimization was performed with a population size of 20 and maximum generation of 10. The second optimization was to optimize the circuit component values and number of components. These

we get in figure 2 based on which we have the circuit of figure 3. This optimization was performed with a population size of 50 and maximum generation of 100.

The graph obtained after using our algorithm and the graph obtained by simulating AIM SPICE will show the comparison and how effectively our algorithm worked. The graphs obtain by using two processes are shown in figures 4 and 5 for the High Pass filter.

Thus we were able to design a high pass filter with desired specifications using genetic algorithm. The performance of the algorithm could be increased by increasing the population limit as well as the maximum generation limit

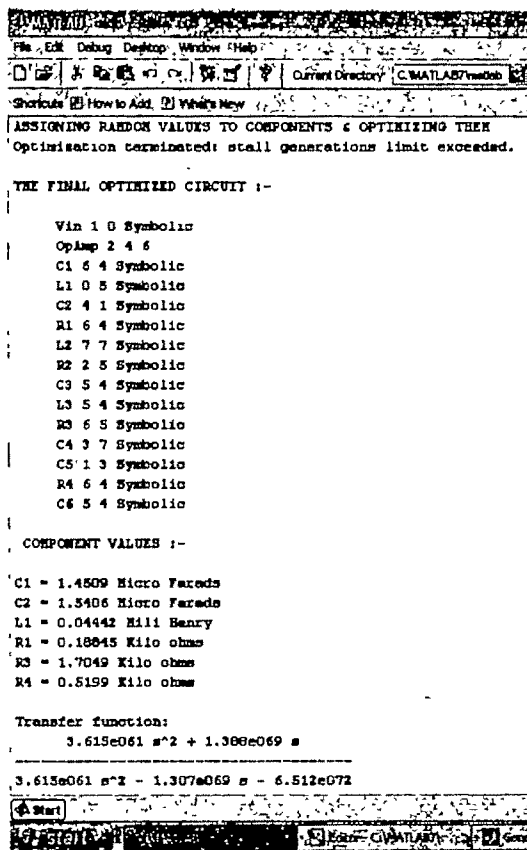


Figure 2: Circuit details of High Pass Filter after optimization

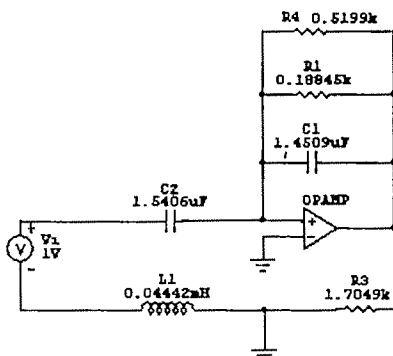


Figure 3: Circuit Diagram of the High Pass Filter optimized



Figure 4: High pass filter response using genetic algorithm

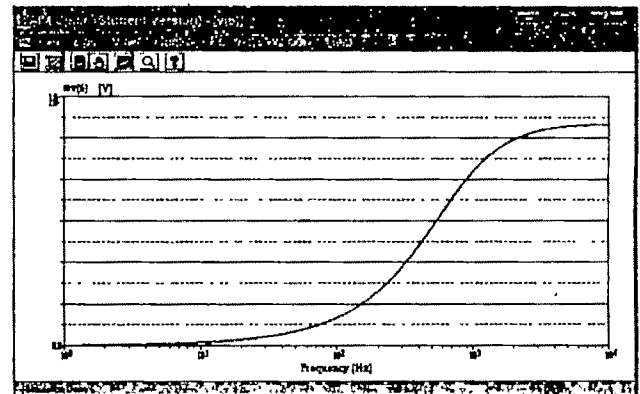


Figure 5: High pass filter response using AIM SPICE

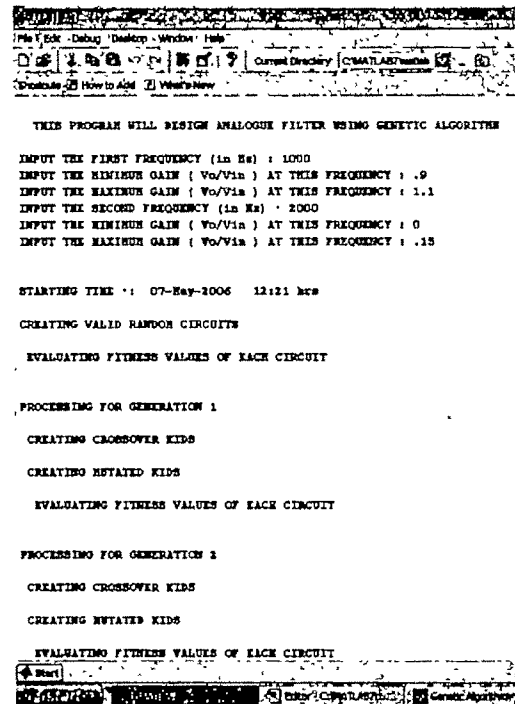


Figure 6: Inputs for Low Pass Filter Design

Now if we are interested in designing a Low pass filter with the parameters $F_c=1700$ Hz, pass band gain of 0.9 to 1.1 and stop band gain of 0 to 0.15. For this we feed our software with the following inputs as shown in figure 6.

The algorithm ran for around 35 minutes. During this time it performed two genetic optimizations. The first one was for optimizing the circuit topology. This optimization was performed with a population size of 20 and maximum generation of 10. The second optimization was to optimize the circuit component values and number of components. These we get in figure 7 based on which we have the circuit of figure 8. This optimization was performed with a population size of 50 and maximum generation of 100.

The graph obtained after using our algorithm and the graph obtained by simulating AIM SPICE will show the comparison and how effectively our algorithm worked. The graphs obtained by using two processes are shown in figures 9 and 10 for the Low Pass filter.

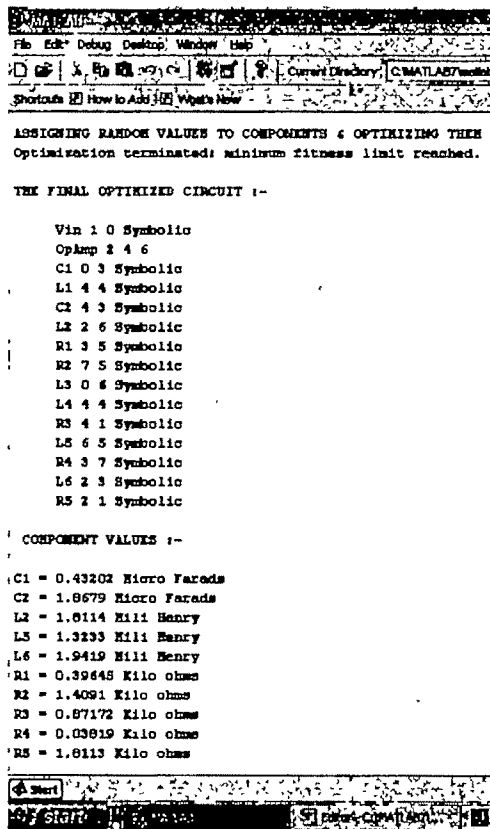


Figure 7: Circuit details of Low Pass Filter after optimization

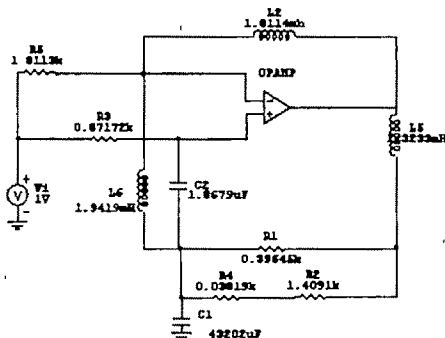


Figure 8: Circuit Diagram of the Low Pass Filter optimized

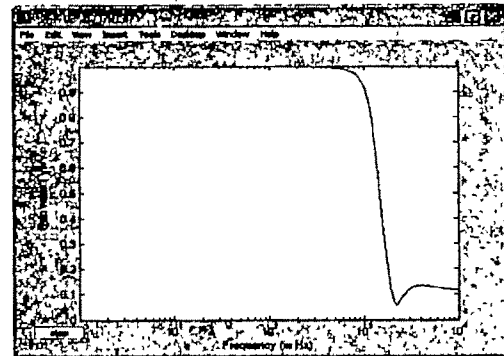


Figure 9: Low pass filter response using genetic algorithm:

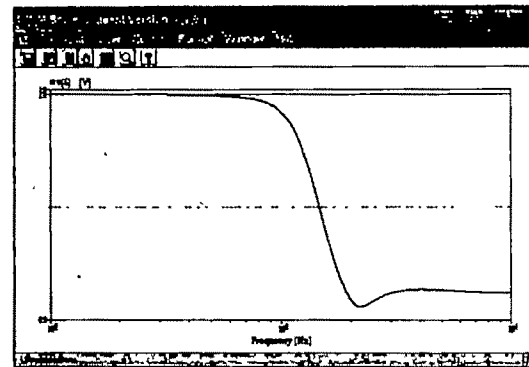


Figure 10: Low pass filter response using AIM SPICE

IV. CONCLUSION AND DISCUSSION

Using these algorithms we can design any kind of high and low pass filters and have also incorporated the code for generation of band pass and stop filters. But for the more complex designs, to get the best output we need to increase the population size as well as the maximum generation size. Compared to normal design time taken, this type circuit generation takes lesser time. This method of generation of Active Filters can also be used to find many new dimensions in the field of Filter Design.

Genetic Algorithms are a powerful algorithmic paradigm for evolutionary computing. Future work involves using more efficient ways to combine a local search heuristic with GA to produce high quality solutions in less time, especially for the circuit placement problem.

Here in our algorithm we are using two separate optimizations, one for circuit topology and the other for component values and number of components. For future work we can think of building a hybrid algorithm. There we can use nested genetic optimizations. In the nested optimization algorithm we can implement the second optimization inside the first optimizations. It means that during the circuit topology optimization the component values are also optimized. This can be handled by a more advanced side of Genetic Algorithm which is known as MULTIPLE OBJECTIVE GENETIC ALGORITHM (MOGA)

REFERENCES

- [1] Scott, *et. al*, "Behavioral-level implementation of a GA"
- [2] G. Koonar S. Areibi M. Moussa, "Hardware Implementation of Genetic Algorithms for VLSI CAD Design"
- [3] M. Rabinovich, K. Robarge, J. Sznyd, and J. Carletta, "An Experimental Evaluation of Algorithms For VLSI Partitioning"
- [4] Kenneth V. Noren and John E. Ross, "Analog Circuit Design using Genetic Algorithms"
- [5] James B. Grimbleby, "Hybrid Genetic Algorithms for Analogue Network Synthesis"
- [6] James B. Grimbleby, "Automatic Synthesis of Active Electronic Networks using Genetic Algorithms"
- [7] G.Andal Jayalakshmi et al, "A Hybrid Genetic Algorithm – A New Approach to Solve Traveling Salesman Problem"
- [8] Mike Davis, Luoping Liu, and John G. Elias, "VLSI Circuit Synthesis using a Parallel Genetic Algorithm"
- [9] Goldberg, D. E., "Genetic Algorithms in Search, Optimization and Machine Learning", Addison-Wesley
- [10] Zebulum, R.S., Pacheco, M.A., Vellasco, M., "A Multi- Objective Optimisation Methodology Applied to the Synthesis of Low-Power Operational Amplifiers", to appear in the Proc. of the Int. Conf. on Microelectronics and Packaging, Brazil,

Technical Session 2A

FACTS

Dynamic Stability Analysis of Power System Using Thyristor Controlled Series Capacitor

P. Bera¹, D. Das² and T.K.Basu³

¹Marine Engineering & Research institute, Kolkata, India (e-mail: partha_bera@rediffmail.com)

²Electrical Engineering Department, Indian Institute of Technology, Kharagpur, India (e-mail: ddas@ee.iitkgp.ernet.in)

³Electrical Engineering Department, Indian Institute of Technology, Kharagpur, India (e-mail: tkb@ee.iitkgp.ernet.in)

Abstract— In this paper, the application of thyristor controlled series capacitor (TCSC) in damping power system oscillation is investigated. Analysis is carried out considering independent operation of TCSC equipped with conventional lead-lag controller and proportional-integral-derivative (P-I-D) controller. A genetic algorithm (GA) based method is proposed to tune the parameters of conventional phase lead-lag power system stabilizer (CPSS) and TCSC controllers. It also ensures that for any operating condition within a pre-specified domain, the system remains stable when subjected to a small disturbance. A quadratic performance index is considered to measure the quality of system dynamic performances within the tuning process. The solution thus obtained is robust. Dynamic performances considering conventional phase lead-lag power system stabilizer (CPSS) and TCSC are compared. Analysis reveals that independent operation of TCSC equipped with P-I-D controller improves the dynamic performances significantly as compared to that of conventional power system stabilizer

Key words— Power system stabilizer; TCSC; Genetic algorithm.

I. INTRODUCTION

LOW frequency oscillations are very common phenomenon when large power systems are interconnected by relatively weak tie-lines. These oscillations may sustain and grow to cause system separation due to inadequate damping of electromechanical modes. Several approaches have been reported in the literature to provide the damping torque required for damping machine oscillations. DeMello and Concordia [1] proposed the concept of synchronous machine stability as affected by a lead-lag compensator usually called power system stabilizer (PSS), for damping the machine oscillations. Although PSSs provide supplementary feedback stabilizing signals in the excitation systems and enhance the dynamic stability of power system by increasing the system damping of low frequency oscillations associated with the electromechanical mode but they are liable to cause a great variation in the voltage profile and may even result in leading power factor operation under severe disturbance condition [2]. Many researchers have made significant contribution in conventional lead-lag PSS design [3-7]. Recently many approaches based on optimal control, variable structure control

and intelligent control have been proposed for PSS design [8-11]. The recent advances in power electronics have led to the development of the flexible alternating current transmission systems (FACTS). One of the promising FACTS devices is thyristor controlled series capacitor (TCSC) and has found application in improving power system stability [12-20].

In the present work, a comprehensive assessment of the effects of the excitation and TCSC control when applied independently is carried out. The controller design problem is formulated as an optimization problem with the aim of getting the optimal or near optimal settings of the controller parameters. Two types of control schemes for TCSC are proposed for single machine infinite bus (SMIB) power system.

II SYSTEM INVESTIGATED

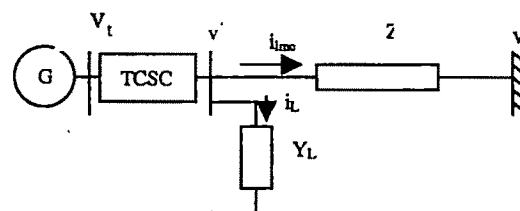


Fig. 1. Single machine infinite bus (SMIB) power system equipped with TCSC.

A special case of practical power system is that of a generator or a group of generators sending power through a transmission line to a much bigger power network, which can be represented by the model of the SMIB system. Studying the simplest power system model is always important because it can often provide insight into the problem which can help the study of more complex power system. Fig.1 shows a SMIB power system with TCSC. Parameters of this system are given in Appendix.

The operating condition for SMIB system is completely defined by the values of the real power, P and the reactive power, Q , at the generator terminal. P and Q are assumed to vary over the following ranges [21]:

$$0.4 \leq P \leq 1.2; \quad -0.2 \leq Q \leq 0.6;$$

This encompasses almost all practically occurring operating conditions.

III STRUCTURE OF CPSS

The typical structure of a conventional PSS consists of a gain, a washout unit, phase compensation units and an output limiter which is shown in Fig. 2 [2]. The washout unit is used to avoid steady changes of the input signal modifying the terminal voltage.

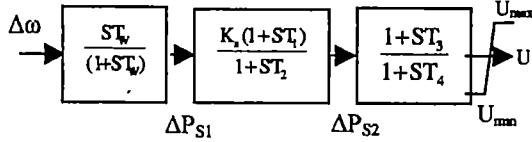


Fig. 2 Conventional power system stabilizer

To provide pure damping, the CPSS should have appropriate phase-lead characteristics to compensate the phase-lag between the generator exciter input and electrical output torque. Two lead-lag blocks are used in this paper although the number and characteristics of phase compensation units could be modified according to the design requirements.

The gain and time constants of the phase compensation units therefore need to be determined such that the system should give good dynamic performances. In order to restrict the level of the generator terminal voltage fluctuation during transient conditions, limits are imposed on power system stabilizer output. To ensure maximum contribution of the stabilizer, use of relatively large positive limits, i. e., 0.1 pu to 0.2 pu and negative limits of -0.05 pu to -0.1 pu is reported [2]. In the present work maximum positive and negative limits are considered as 0.2 pu and -0.1 pu respectively.

IV STRUCTURE OF TCSC CONTROLLER

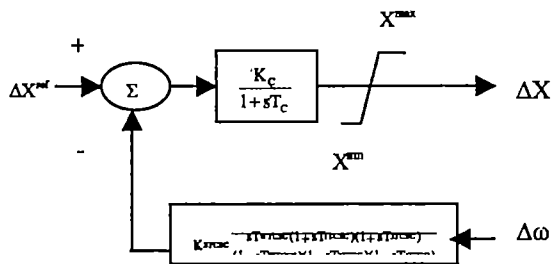


Fig.3: Block diagram of TCSC equipped with Lead-Lag Controller

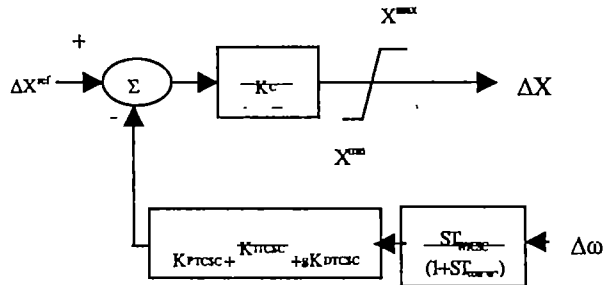


Fig.4: Block diagram of TCSC equipped with P-I-D Controller

Fig.3 shows TCSC with conventional phase lead-lag controller. Fig. 4 shows the TCSC with P-I-D controller. The

best location of the TCSC is at the generator terminal as it gives the greatest change of electrical distance between the generator and the disturbance point [11]. Hence the speed deviation $\Delta\omega$ is available and used as the input signal to both PSS and TCSC controller. This makes the proposed controllers easy for implementation. In these figures $\Delta\Phi_{ref}$ is the reference angle and K_C and T_C are the gain and time constant of TCPS.

VI OBJECTIVE FUNCTION

Scalar integral performance indices have proved to be the most meaningful and convenient measures of dynamic performances [22,23]. Penalizing only the speed excursions, an objective function based on the integral squared error (ISE) criterion is considered in this study and is given by

$$J = \int_0^{\infty} (\Delta\omega)^2 dt \quad (1)$$

This objective function has a characteristic in that a large initial error is weighted heavily and errors occurring late in the transient response are penalized lightly. J measures the performance of the CPSS and controllers of TCSC; particularly with respect to system damping for a set of parameter settings and operating conditions (P, Q).

In order to introduce a degree of robustness to the CPSS over a wide operating region, a new measure of performance, the average performance index J_{avg} that quantifies the mean performance of a particular CPSS or controllers of TCSC settings over the whole operating horizon, is introduced. Thus, if N_{PQ} is the number of operating points in the domain D , we have,

$$J_{avg} = \frac{1}{N_{PQ}} \sum_{P,Q \in D} \int_0^{\infty} (\Delta\omega)^2 dt \quad \forall P, Q \in D \quad (2)$$

The above performance criterion is implemented within the genetic search process, for obtaining the globally optimal parameter settings of the CPSS and controllers of TCSC. For the purpose of this study, operating domain $D \{D \in P = [0.4, 1.2] \text{ and } Q = [-0.2, 0.6] \text{ in pu}\}$ with a step size of 0.05 pu is considered in each case. Therefore total number of operating point is 256 in P-Q plane.

VII GENETIC ALGORITHM

Genetic algorithms (GAs), a way to randomly search for the best answer to tough problems were first suggested by John Holland in his book in Natural and Artificial systems [24]. Over the last few years, it is becoming important to solve a wide range of search, optimization and machine learning problems. Here genetic algorithm is used to optimize the objective function and hence to design the gain K_s and time constants (i.e. T_w , T_1 , T_2 , T_3 and T_4). Constraints are also imposed on these parameters.

Different population sizes (40,50,60,70 & 80), were considered and it has been observed that the population size of 60 were satisfactory. After selecting the population size, the effect of mutation and crossover probabilities were examined.

Different combination of mutation probabilities (0.0001, 0.001, 0.005 & 0.01) and the crossover probabilities (0.6, 0.8, 0.9 & 1.0) were tested and it was found that $P_c = 1.0$ and $P_m = 0.005$ give the best performance for all the operating conditions. It is worth mentioning here that the bit size (gene length) of each variable is 10 (i.e., $\lambda=10$).

VIII OPTIMUM PARAMETERS

To investigate the ability of CPSS and TCSC controller to damp out the low frequency oscillations associated with the electromechanical mode, three different control schemes are examined.

(a) Optimum parameters of CPSS

In this case, five unknown parameters are optimized. These parameters are K_{SPSS} , T_{1PSS} , T_{2PSS} , T_{3PSS} and T_{4PSS} . Value of T_{WPSS} is pre-specified and is taken as $T_{WPSS} = 10$ seconds. Optimum values of these parameters are tabulated in Table-1.

Table-1: Optimum gain and parameters of the CPSS

Parameters of CPSS					
K_{SPSS}	T_{1PSS}	T_{2PSS}	T_{3PSS}	T_{4PSS}	T_{WPSS}
3.332	0.612	0.049	0.236	0.065	10

(b) Optimum Parameters of Lead-Lag Controller of TCSC

In this case, five unknown parameters are optimized. T_{WTCSC} is pre-specified and is taken as $T_{WTCSC} = 10$ seconds. Optimum values of K_{STCSC} , T_{1TCSC} , T_{2TCSC} , T_{3TCSC} and T_{4TCSC} are given in Table-2.

Table-2: Optimum gain and parameters of the Lead-Lag Controller for TCSC

Parameters of Lead-Lag Controller of TCSC					
K_{STCSC}	T_{1TCSC}	T_{2TCSC}	T_{3TCSC}	T_{4TCSC}	T_{WTCSC}
2.652	0.639	0.018	0.347	0.024	10

(c) Optimum Parameters of P-I-D Controller of TCSC

In this case, proportional (K_{PTCSC}), integral (K_{ITCSC}) and derivative (K_{DTCSC}) gains of P-I-D controller are optimized. Value of T_{WTCSC} is pre-specified and is taken as $T_{WTCSC} = 10$ seconds. The optimum values of these gains are given in Table-3.

Table-3: Optimum gain settings of the P-I-D controller for TCSC

Gains of P-I-D Controller of TCSC			
K_{PTCSC}	K_{ITCSC}	K_{DTCSC}	T_{WTCSC}
23.50	0.040	2.94	10

IX DYNAMIC RESPONSES

Fig.5 shows the comparison of dynamic responses for $P = 0.9$ pu and $Q = 0.5$ pu considering CPSS and TCSC equipped with lead-lag controller. From Fig.5, it is observed that TCSC equipped with lead-lag controller gives better dynamic performances in terms of settling time as compared to that of CPSS. However, peak deviation is slightly more considering TCSC equipped with lead-lag controller as compared to that of CPSS.

Fig.6 shows the comparison of dynamic responses for $P = 0.9$ pu and $Q = 0.5$ pu considering CPSS and TCSC equipped with P-I-D controller. From Fig.6, it is seen that TCSC equipped with P-I-D controller gives much better dynamic performances as compared to that of CPSS.

Fig.7 shows the comparison of dynamic responses for $P = 0.9$ pu and $Q = 0.5$ pu considering TCSC equipped with P-I-D controller and TCSC equipped with lead-lag controller. From Fig.7, it is seen that TCSC equipped with P-I-D controller gives much better dynamic performances.

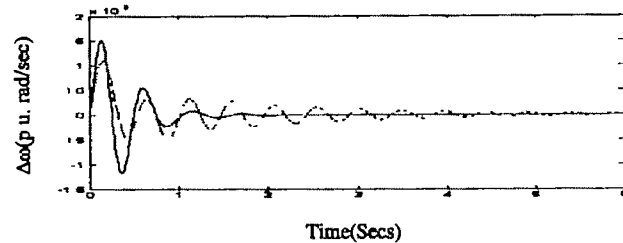


Fig.5: Dynamic responses of SMIB system considering optimum parameter settings of TCSC equipped with lead-lag controller & CPSS ($\Delta T_m = 0.05$). (—CPSS, — TCSC equipped with lead-lag controller)

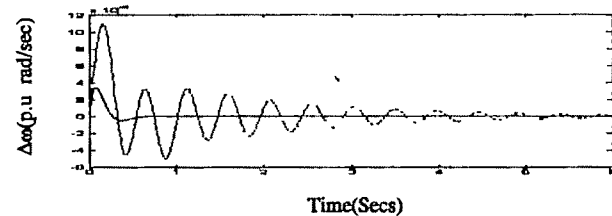


Fig.6: Dynamic responses of SMIB system considering optimum parameter settings of TCSC equipped with P-I-D controller & CPSS ($\Delta T_m = 0.05$). (—CPSS, — TCSC equipped with P-I-D controller)

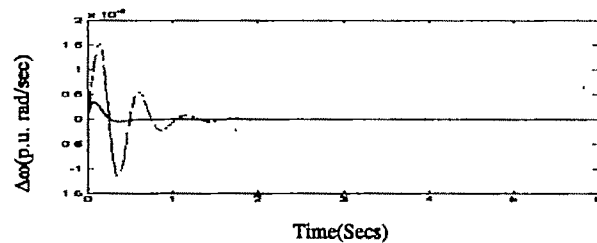


Fig.7: Dynamic responses of SMIB system considering optimum parameter settings of TCSC equipped with P-I-D controller & TCSC equipped with lead-lag Controller ($\Delta T_m = 0.05$). (—TCSC equipped with lead-lag controller, — TCSC equipped with P-I-D controller)

Similar findings were also observed for all other operating conditions within the range mentioned in Section-2. Therefore, it may be concluded that TCSC equipped with P-I-D controller can be an alternative of the conventional PSS for providing much better dynamic responses.

Fig.8 shows the system responses to a 3-phase transient fault of six cycle duration, at the generator terminals considering conventional lead-lag power system stabilizer (CPSS), TCSC equipped with lead-lag controller and TCSC equipped with P-I-D controller. From Fig.8, it is seen that the TCSC equipped with P-I-D controller gives better dynamic

performances in terms of peak deviation and settling time. Similar findings were also observed within the range of operating conditions as mentioned in Section-2.

X CONCLUSIONS

In this study, dynamic stability analysis for single machine infinite bus (SMIB) power system has been carried out considering conventional phase lead-lag power system stabilizer (CPSS), independent operation of TCSC equipped with lead-lag controller and independent operation of TCSC equipped with P-I-D controller. Investigations reveal that independent operation of TCSC equipped with P-I-D controller gives better dynamic performances compared to that obtained with CPSS and independent operation of TCSC equipped with lead-lag controller. It was found that CPSS, independent operation of TCSC equipped with lead-lag controller and independent operation of TCSC equipped with P-I-D controller do not adversely affect the transient stability and damps out the oscillations following fault clearing. However, performance of independent operation of TCSC equipped with P-I-D controller is much better following fault clearing.

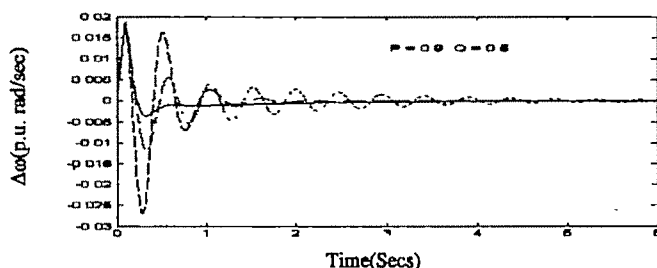


Fig.8: System responses for a three phase six cycle fault at generator terminal considering CPSS, TCSC equipped with (i) Lead-Lag controller (ii) P-I-D controller (— CPSS, ---- TCSC equipped with Lead-Lag Controller, TCSC equipped with P-I-D Controller)

XI APPENDIX

The parameters of the system investigated are as given below:

$M = 4.74$ pu, $D = 0$, $T'_{do} = 5.9$ Secs., $K_A = 400$, $T_A = 0.05$ Secs., $K_E = -0.17$, $T_E = 0.95$ Secs., $K_F = 0.025$, $T_F = 1.0$ Secs.; $x_d = 1.70$ pu, $x'_d = 0.245$ pu, $x_q = 1.64$ pu, $R = 0.02$ pu, $X = 0.4$ pu, $G = 0$, $B = 0$, $f = 50$ Hz.

REFERENCES

- [1] F.P. deMello and C. Concordia, "Concepts of synchronous machine stability as affected by excitation control", IEEE Transactions on Power Apparatus and Systems, Vol. PAS-88, April 1969, pp.316-329.
- [2] P. Kundur, M. Klein, G. J. Rogers, M. S. Zywno, "Application of power system stabilizers for enhancement of overall system stability", IEEE Transactions on Power Apparatus and Systems, Vol. 4, No 2, May 1989, pp 614-626.
- [3] R. J. Fleming, M.A. Mohan, K. Parvatisam, "Selection of parameters of stabilizers in multimachine power systems", IEEE Transactions on Power Apparatus and Systems, Vol PAS-100, No 5, May 1981, pp2329-2333.
- [4] M. A. Abido, "Parameter optimization of multimachine power system stabilizers using genetic local search", Electrical Power & Energy Systems Vol. 23, 2001, pp. 785-794.
- [5] Y. L. Abdel-Magid, M. A. Abido and A. H. Mantawy, "Robust tuning of power system stabilizers in multimachine power systems", IEEE Transactions on Power Systems, Vol. 15, No.2, May 2000, pp 735-740.
- [6] P. Zhang and A. H. Coonick, "Coordinated synthesis of PSS parameters in multimachine power systems using the method of inequalities applied to genetic algorithms", IEEE Transactions on Power Systems, Vol. 15, No.2, May 2000, pp 811-816.
- [7] X. Lei, H. Huang, S.L. Zheng, D Z Jiang, Z.W. Sun, "Global tuning of power system stabilizers in multi-machine systems", Electrical Power System Research, Vol. 58, 2001, pp.103-110.
- [8] I. Robandi, K. Nishimori, R. Nishimura and N. Ishihara, "Optimal feedback control design using genetic algorithm in multimachine power system", International Journal of Electric Power & Energy Systems, Vol. 23, 2001, pp. 263-271.
- [9] A. S. R. Murty and S. Parameswaran, K. Ramar, "Design of decentralized variable structure stabilizers for multimachine power system", Electric Power and Energy Systems, Vol. 18, No.8, 1996, pp.535-546.
- [10] P. Srikanth Rao and I. Sen, "Robust pole placement stabilizer design using linear matrix inequalities", IEEE Transactions on Power Systems, Vol. 15, No.1, February 2000, pp. 313-319.
- [11] P. Shamsollahi and O. P. Malik, "Design of a neural adaptive power system stabilizer using dynamic back-propagation method", International Journal of Electric Power & Energy Systems, Vol. 22, 2000, pp. 29-34.
- [12] N. Yang, Q. Liu and J. D. McCalley, "TCSC controller design for damping interarea oscillations" IEEE Transactions on Power Delivery, Vol. 13, No. 4, November 1998, pp. 1304- 1310.
- [13] S. K. Tso, J. Liang and X. X. Zhou, "Coordination of TCSC and SVC for improvement of power system performance with NN-based parameter adaptation", Electric Power and Energy Systems, Vol. 21, 1999, pp.235-244
- [14] B. H. Li, Q. H. Wu, D. R. Turner, P. Y. Wang and X. X. Zhou, "modeling of TCSC dynamics for control and analysis of power system stability", Electric Power and Energy Systems, Vol. 22, 2000, pp.43-49
- [15] K. M. Son and J. K. Park, "On the Robust LQG Control of TCSC for Damping Power System Oscillations", IEEE Transactions on Power Systems, Vol. 15, No. 4, November 2000, pp. 1306-1312.
- [16] L. Pan, Ali Fellachi and K. Schoder, "Selection and design of a TCSC control signal in damping power system inter-area oscillations for multiple operating conditions", Electric Power System Research, Vol. 62, 2002, pp. 127-137.
- [17] M. Ishimaru, R. Yokoyama, G. Shirai and T. Niumura, "Robust thyristor-controlled series capacitor controller design based on linear matrix inequality for a multi-machine power system", Electric Power and Energy Systems, Vol. 24, 2002, pp.621-629.
- [18] A. D. Del Rosso, C. A. Canizares and V. M. Dona, "A study of TCSC controller design for power system stability improvement", IEEE Transactions on Power Systems, Vol. 18, No. 4, November 2003, pp. 1487 - 1496.
- [19] J. Chen, T. T. Lie and D. M. Vilathgamuwa, "Enhancement of power system damping using VSC-based series connected FACTS controllers", IEE Proc.-Gener. Transm. Distrib., Vol. 150, No. 3, May 2003, pp. 353 - 359.
- [20] H. F. Wang, "Design of non-negatively interactive FACTS-based stabilizers in multi-machine power systems", Electric Power System Research, Vol. 50, 1999, pp. 169-174.
- [21] P. Srikanth Rao and I. Sen, "Robust pole placement stabilizer design using linear matrix inequalities", IEEE Transactions on Power Systems, Vol. 15, No.1, February 2000, pp313-319.
- [22] W.C. Schultz and V.C. Rideout, "Control system performance measures: past, present and future", IRE Transactions on Automatic Control, AC-6, 1961, pp 22-35.
- [23] K. Ogata, "Modern Control Engineering", A book, Printice-Hall, Englewood cliffs, NJ, 1970, pp. 293-313
- [24] J.H. Holland, "Adaptation in Nature and Artificial Systems", University of Michigan Press, Am Arbor, I

Simulation and Modeling of GA Optimized Distribution Static Compensator for Power Quality Improvement

Deepika Masand, Shailendra Jain, and Gayatri Agnihotri

National Institute of Standards and Technology, Bhopal.
Email:deepikajai@rediffmail.com

Abstract— The ever increasing power distribution demands in terms of quality and reliability has led to the employment of FACT devices at the distribution end. Converter based FACTS controllers prove to be viable alternatives to the Thyristor based first generation FACTS controllers. Distribution Static Compensator (DSTATCOM) is one such converter based shunt controller which has the potential to compensate for reactive power and to suppress harmonic distortions as well, due to its larger bandwidth. In this paper, an offline genetic algorithm (GA) based dc loop parameter tuning technique is applied to a DSTATCOM used for reactive power compensation and harmonic suppression for linear and nonlinear loads. The optimization of parameters is carried out relative to the performance index. Optimization by hit and trial and by genetic algorithms is compared for a defined system. The DSTATCOM is simulated using MATLAB/Power System Blockset and the DC Loop Controller is optimized using GAOT toolbox for MATLAB.

Key words— AC/DC bus voltage regulation, DC loop controller DSTATCOM, Genetic Algorithms, Integral Square Error.

I. INTRODUCTION

REACTIVE power compensation is an important aspect in the control of distribution systems. Reactive current in addition to increasing the distribution system losses, introduces various power quality problems like, harmonics, voltage sag, swell and poor load power factor. A Distribution Static Compensator (DSTATCOM) proves to be a viable solution for the mitigation of power quality problems [1-2]. A DSTATCOM is basically a voltage source converter based FACTS controller sharing many similar concepts to that of a

STATCOM used at the transmission level [3]. The difference being that the STATCOM handles only fundamental reactive power and provides voltage support while as a DSTATCOM is employed at the distribution level for effective load compensation. The paper presents modeling and simulation of a DSTATCOM for power quality improvement. The modeling is based on synchronous reference frame which decomposes the system into d- axis and q-axis coordinates, and then applying small signal disturbances, which helps in simplifying the controller design [4]. The DSTATCOM performance is based on decoupled current control where it is treated as a current source. In order to achieve unity power factor operation for linear/ nonlinear loads, the supply currents must feed only the real power to the load. This is achieved by generating a reference active component of current by monitoring the variation in dc link voltage. This is because the capacitor voltage increases/decreases with the increase/decrease of the volt amperes of the load.

Additionally in order to achieve voltage regulation, the supply currents must slightly lead the supply voltages, in order to cater to the distribution line losses. Then the reference current is the sum of the active and reactive component of current. This reference reactive component of current is obtained by monitoring the deviation of ac voltage at the PCC. The reference reactive current is assigned zero value during unity power factor operation. A hysteresis current controller is used for generating the switching signals to the voltage sourced converter.

This paper also presents a systematic procedure for the optimum design of the PI controller parameters using both empirical (hit and trial) and Genetic Algorithm based tuning method for reference dc link voltage regulation. This offline parameter optimization is carried out relative to a performance index, which is the Integral Square Error (ISE) [5]. The fitness is reciprocal of the error and is evaluated using Genetic

Algorithm Optimization Toolbox (GAOT) toolbox [6]. On comparing the dc link voltage response by both the methods, during switch on and load perturbation, for linear nonlinear loads the performance of the GA based optimization is better than the empirical method. All the simulations are carried out using MATLAB/Sim Power systems environment.

II. MODELING OF DSTATCOM AND COMPENSATION SCHEME

A DSTATCOM is a controlled reactive source which includes a Voltage Source Converter (VSC) and a DC link capacitor connected in shunt, capable of generating and /or absorbing reactive power. The modeling of DSTATCOM is based on the synchronous reference frame method, which justifies the decoupled current control scheme [7]. Fig.1 shows the simplified single line diagram of a DSTATCOM, comprising of a dc link capacitor (C_{dc}), IGBT based VSC, filter inductance (R_f , L_f) and the PCC voltage $V_{s(abc)}$. $V_{c(abc)}$ and $i_{c(abc)}$ are compensator voltages and currents respectively.

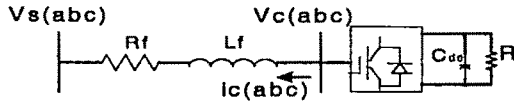


Fig. 1 Simplified model of DSTATCOM

The equations of the AC side of the single line diagram shown in fig.1, is given as,

$$V_{c(abc)} = V_{s(abc)} + R_f i_{c(abc)} + L_f \frac{d(i_{c(abc)})}{dt} \quad (1)$$

In order to convert the above equation to synchronous reference frame, the following transformation matrix 'K' is used,

$$K = \frac{2}{3} \begin{bmatrix} \cos(\omega t + \theta) & \cos(\omega t + \theta - \frac{2\pi}{3}) & \cos(\omega t + \theta + \frac{2\pi}{3}) \\ \sin(\omega t + \theta) & \sin(\omega t + \theta - \frac{2\pi}{3}) & \sin(\omega t + \theta + \frac{2\pi}{3}) \\ \frac{1}{\sqrt{2}} & \frac{1}{\sqrt{2}} & \frac{1}{\sqrt{2}} \end{bmatrix}$$

Transforming quantities in equation 1, to the synchronous reference frame, and substituting in equation (1),

$$K^{-1}V_{c(dq0)} = K^{-1}V_{s(dq0)} + R_f(K^{-1}i_{c(dq0)}) + L_f \frac{dK^{-1}(i_{c(dq0)})}{dt} \quad (2)$$

simplifying and writing the d-q terms separately,

$$L_f \frac{d(i_{cd})}{dt} = -R_f i_{cd} + \omega L_f i_{cq} + (V_{cd} - V_{sd}) \quad (3)$$

$$L_f \frac{d(i_{cq})}{dt} = -R_f i_{cq} - \omega L_f i_{cd} + (V_{cq} - V_{sq}) \quad (4)$$

writing in matrix form,

$$\frac{d}{dt} \begin{bmatrix} i_{cd} \\ i_{cq} \end{bmatrix} = \begin{bmatrix} -R_f/L_f & \omega \\ -\omega & -R_f/L_f \end{bmatrix} \begin{bmatrix} i_{cd} \\ i_{cq} \end{bmatrix} + \frac{1}{L_f} \begin{bmatrix} V_{cd} - V_{sd} \\ V_{cq} - V_{sq} \end{bmatrix} \quad (5)$$

Here V_{cd} and V_{cq} , which are compensator voltages in d-q axis depends upon the switching states of the converter and the dc link voltage. Since a hysteresis current controller is used the switching states are dependant upon the error during current tracking. These voltages are given as,

$$\begin{bmatrix} V_{cd} \\ V_{cq} \\ 0 \end{bmatrix} = K \frac{V_{dc}}{3} - \begin{bmatrix} 2 & -1 & -1 \\ -1 & 2 & -1 \\ -1 & -1 & 2 \end{bmatrix} \begin{bmatrix} S_a \\ S_b \\ S_c \end{bmatrix} \quad (6)$$

Here S_a , S_b and S_c are the switching states of switches in phase A,B and C. Since d-q axes are not stationary, and they follow the trajectory of the voltage vector, within this synchronous rotating frame, $v_s = v_{sd}$ and $v_{sq} = 0$, using the definition of Instantaneous Reactive Power Theory, the instantaneous active and reactive powers are described as :

$$\begin{aligned} p &= v_{sd} i_{cd} + v_{sq} i_{cq} = v_{sd} i_{cd} = v_s i_{cd} \\ q &= v_{sq} i_{cd} - v_{sd} i_{cq} = -v_{sd} i_{cq} = -v_s i_{cq} \end{aligned} \quad (7)$$

Equation (7) shows that DSTATCOM performance is controlled by the active and reactive component of current i_{cd} and i_{cq} . The controller based on the above model is shown in Fig.2, comprising of an outer loop consisting of ac and dc voltage controllers [8]. Three phase ac supply voltages and dc link voltages are sensed and fed to two PI controllers, the outputs of which decide the amplitude of the reference reactive and active current to be generated by the DSTATCOM. In order to achieve unity power factor operation for linear/ nonlinear loads, the supply currents must feed only the real power to the load. This is achieved by the reference active component of current by monitoring the variation in dc link voltage. This is because the capacitor voltage increases/decreases with the increase/decrease of the voltamperes of the load. Additionally in order to achieve voltage regulation, the supply currents must slightly lead the supply voltages, in order to cater to the distribution line losses. Then the reference current is the sum of the active and reactive component of current. This reference reactive component of current is obtained by monitoring the deviation of ac voltage at the PCC. This ac/dc voltage regulation can be achieved by conventional PI controllers or Fuzzy Controllers.

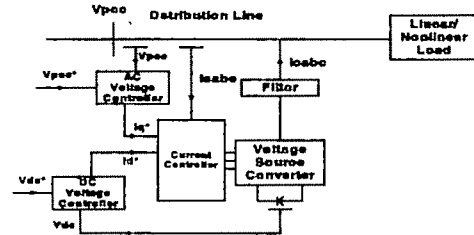


Fig.2 Control of DSTATCOM

The inner loop current controller as shown in Fig.3, gives switching commands to the VSC. The direct and the quadrature reference currents obtained from the outer loop are transformed into abc frame by dq0_abc transformations. A phase locked loop (PLL) is used to synchronize the control loop to the ac supply so as to operate the dq0_abc reference frame. The transformed abc reference currents and the sensed line currents are fed to the inner loop current controller which is a carrier less hysteresis controller. The switching are obtained as:

If $I_{sa} > (I_{sa}^* + h)$, upper switch of inverter leg corresponding to phase 'a' is ON and the lower switch is OFF.

If $I_{sa} < (I_{sa}^* - h)$, upper switch of inverter leg corresponding to

phase 'a' is OFF and the lower switch is ON.

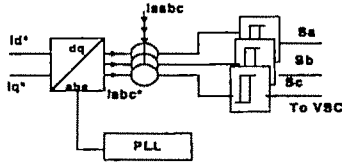


Fig. 3 DSTATCOM current controller

Similarly the switching state of the other phases is calculated and the three currents are regulated within the assigned tolerance band 'h' of their respective values. The tracking becomes better if the hysteresis band is narrower, but then the switching frequency is increased which results in increased switching losses. Therefore the choice of the hysteresis band should be a compromise between the tracking error and the inverter losses [9]. The main advantage of tracking control is that it is simple, robust and exhibits an automatic current limiting capability.

III. IMPLEMENTATION OF DC VOLTAGE LOOP

As observed in the previous section, the DC voltage loop contributes towards, achieving power factor correction and harmonic mitigation for linear nonlinear loads. The block diagram of DC voltage loop is shown in fig. 4. In order to eliminate the steady state error in the dc link voltage, a PI controller is used..

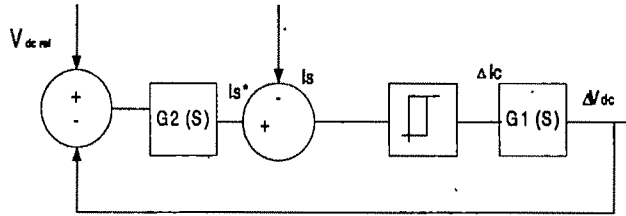


Figure 4. Block Diagram of DC Voltage Loop

Where,

G1 is the transfer function of the PWM converter

G2 is the gain of the PI controller

From eq.(7) the input active power of the converter at the AC side in dq0 frame is calculated as:

$$P_{ac} = 3 \left(V_s I_{cd} + I_{cd}^2 R + \frac{d}{dt} \frac{1}{2} L I_{cd}^2 \right) \quad (8)$$

The active power of the converter on the dc side is:

$$P_{dc} = \frac{V_{dc}^2}{R} + V_{dc} C_{dc} \frac{dV_{dc}}{dt} \quad (9)$$

The power at the AC and DC terminals of the converter are equal, giving the following power balance equation.

$$P_{ac} = P_{dc} \quad (10)$$

The transfer function of the PWM converter at a particular operating point in steady state is obtained by assuming the PCC voltage as stable and applying small signal perturbation [4,11].

$$G1(s) = \frac{\Delta V_{dc}}{\Delta I_{cd}} = \frac{3(V_s + 2RI_{cd} + I_{cd}L_s s)}{2V_{dc}/R + sC_{dc}V_{dc}}$$

$$G2(s) = K_p + \frac{K_i}{s}$$

where,

K_p = proportional gain which determines the voltage response.

K_i = integral gain which defines the damping factor of the loop.

A second order transfer function can be found for the closed loop system. The controller parameters found empirically by hit and trial are obtained as 9 and 30 respectively.

A. GA based parameter tuning

Genetic Algorithms are powerful search methods based on the mechanics of natural genetics. They employ operations found in natural genetics to guide itself through the paths in the search space. Generally for a given optimization problem, a standard GA consists of the following [10]:

1. Chromosomal representation of the solution to the problem.
2. A means of generating an initial population of solutions.
3. A fitness function, which ranks the solutions according to their fitness.

GA's basically start with an initial population containing a number of chromosomes, whose performance is evaluated using the fitness function. The algorithm is repeated for many generations, the offspring being improved with each generation by the use of genetic operators and finally terminates when reaching at the individual, which is the optimum solution to the problem.

For parameter optimization GA is initiated by a population pool of chromosomes which are randomly set initially. Each chromosome here represents a string of k_p and k_i which can be represented as a binary or a real valued string. The fitness of each chromosome is calculated with the view to minimize the performance index. The performance index chosen is 'Integral Square Error' (ISE), which removes the negative error components and the fitness is calculated as the inverse of the Integral Square Error. The optimized values of K_p and K_i obtained in each generation, and are used calculate the error w.r.t. unit step response. The fitness is evaluated as the reciprocal of the error, as the GA's are used to find the maxima. This whole process has been carried out using GAOT toolbox, where the size of the population, GA operators such as selection scheme, crossover, mutation can easily be specified. The flow chart of the GA assisted PI controller tuning is shown in fig. 5. The properties of GA using GAOT for dc loop parameter optimization are given in Table I.

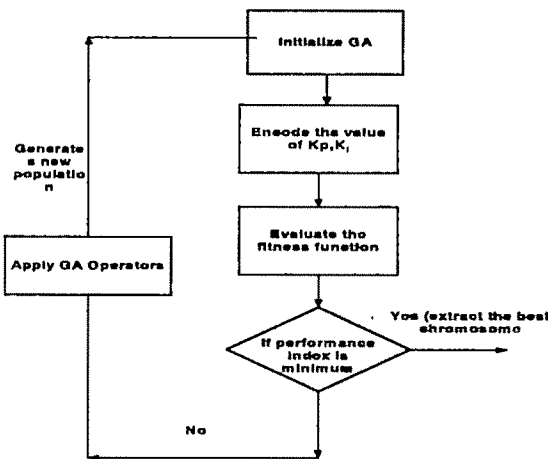


Fig 5 Flowchart for GA assisted PI tuning

TABLE 1
GA PROPERTIES

Property	Value
Population Size	60
Generations	100
Selection	Normalized Geometric Selection
Crossover	Arithmetic Crossover
Mutation	Non Uniform Mutation
Mutation Rate	0.01%

The optimized K_p and K_i are found as 9.996 and 38.243 respectively. Fig. 6 shows the convergence of K_p and K_i to their final values through a given number of generations. It is observed that the value of K_p settles by 40 generations but K_i tends to settle down after 80 generations. Comparing the step response of an empirical and an optimized controller the settling time and the rise time of the latter is less than the former as shown in fig.7. This offline parameter optimization, based on fitness function is less tedious and gives a better system response. The variation of dc link voltage based on the above PI parameters for linear/nonlinear load is discussed in the subsequent section.

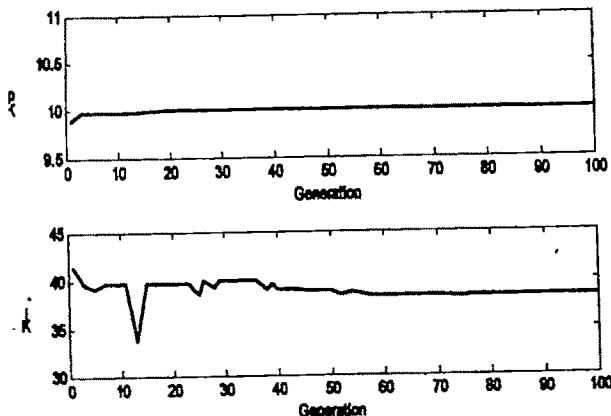


Fig6. Variation of K_p and K_i with generations

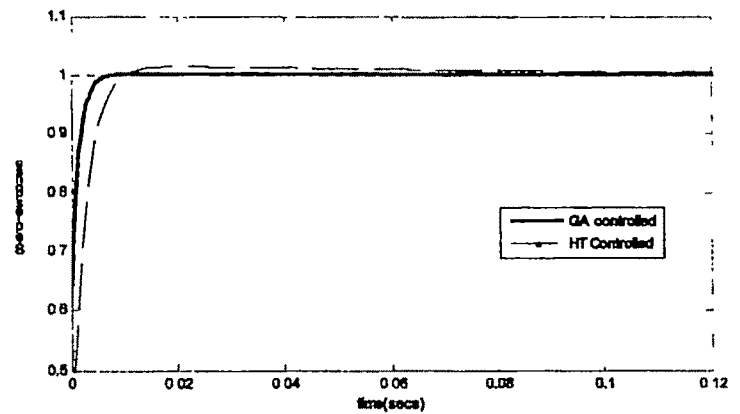


Fig. 7 Step response of both the controllers

IV. SIMULATION RESULTS

The simulation of controllers is carried out in MATLAB/Power system blockset. The system parameters are mentioned in Appendix 1. Fig. 7 shows that the dc link voltage response of the optimized controller is better than the empirical controller, and the voltage settles down to the reference value within 0.02 secs. The response of optimized DSTATCOM with lagging varying linear load of 22KVA for reactive power compensation and power factor correction is shown in fig.9. Even though the load is suddenly reduced by 22% between 0.25 secs.-0.32secs, the source currents are in phase with the source voltage ($V_{sa}/5$ for better clarity) and the dc link voltage is also maintained regulated at 650V after a short transient.

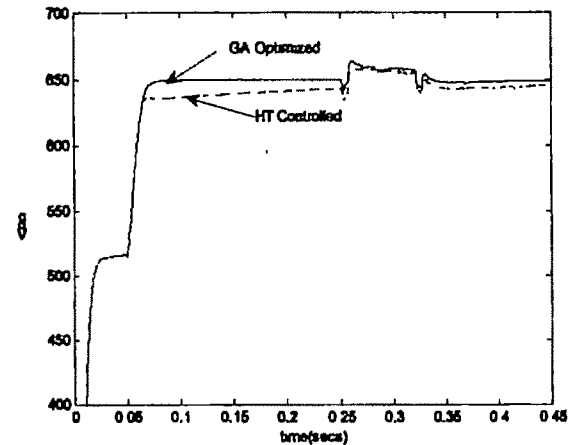


Fig. 8 DC Link Voltage Response for both the controllers (linear load)

Similarly in case of a nonlinear load also the transient response of dc link voltage with the optimized controller is better and the voltage settles down to the reference value within 0.02 secs as shown in fig.10.

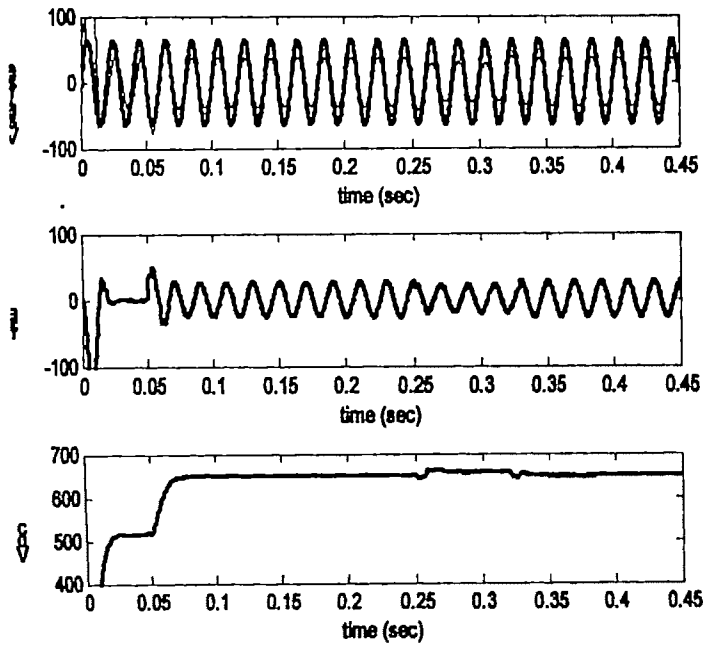


Fig. 9 Response of GA Optimized DSTATCOM for a linearly varying load

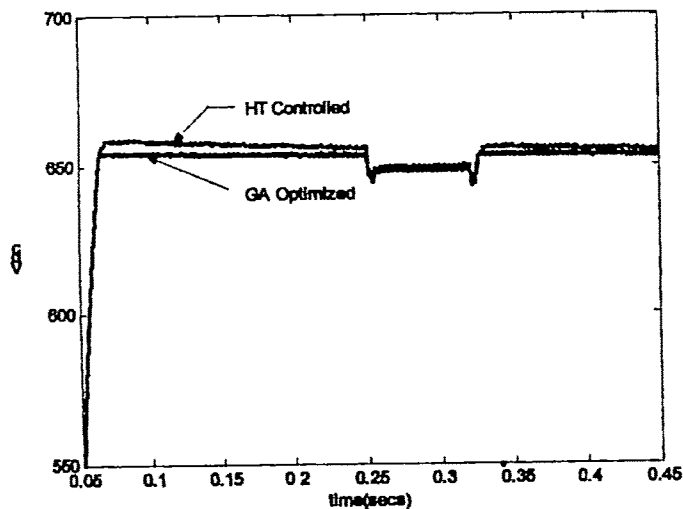


Fig. 10 DC Link Voltage Response for both the controllers (nonlinear load)

Fig 11 shows the response for a nonlinearly varying load, and unity power factor operation and harmonic suppression is maintained even during load change between 0.25 secs-0.32secs. The total harmonic distortion in source current is reduced to 2.94% as shown in fig.12

V. CONCLUSION

Proper parameter tuning in DSTATCOM is an important criteria for obtaining fine control performance, better dynamic response and harmonic suppression. The offline parameter optimization of the dc voltage loop is better than the empirical method as observed by the simulations. The tuning method can be extended to multi objective optimization when extending the application of a DSTATCOM for voltage

regulation in addition to power factor correction and harmonic mitigation at the distribution end.

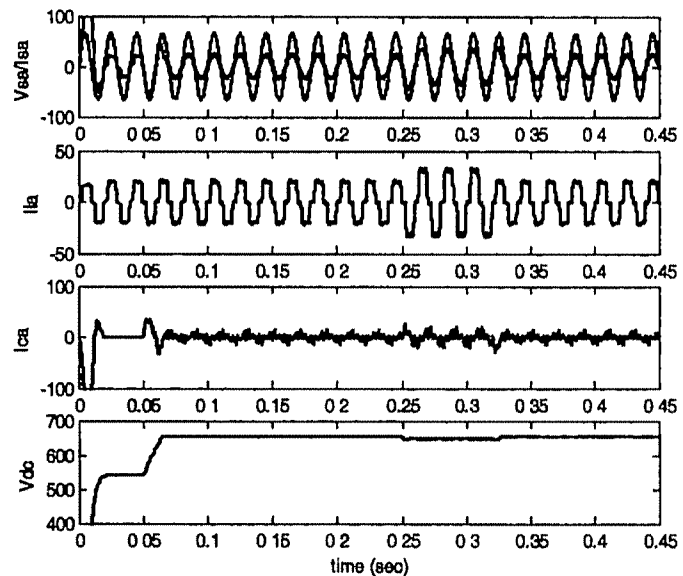


Fig. 11 Response of GA Optimized DSTATCOM for a linearly varying load

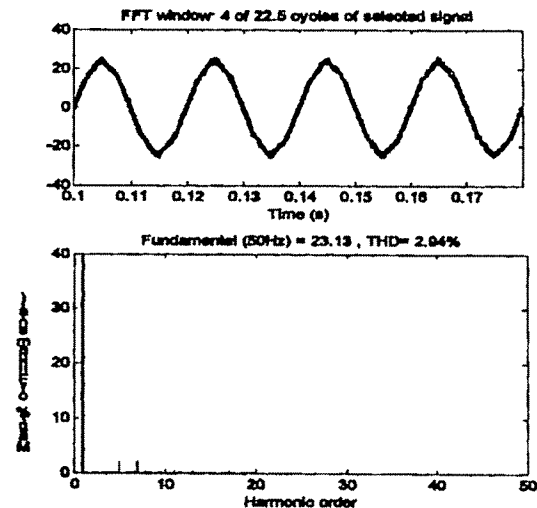


Fig. 11 Frequency spectrum of the source current after compensation

APPENDIX I

SYSTEM PARAMETERS

$V_s=400V(L-L)$, source impedance $X/R=6$, filter impedance $L_c=4.5mH$, $R_c=0.2ohms$, dc capacitance $=3000\mu F$, $V_{dc}(ref)=650V$, Linear load 22KVA at 0.83 lagging, nonlinear load: $R_1=30ohms$, $L_1=20e-3H$, $R_2=18ohms$, $L_2=7.5e-3H$

REFERENCES

- [1] Gyui L, "Dynamic Compensation of AC Transmission lines by solid state synchronous voltage sources", IEEE Trans. Power Delivery, vol.9, No 2, pp.904-911, 1994
- [2] Pasrba, Reed, Takeda, Aritsuka, "FACTS and Custom Power Equipment for the enhancement of Power Transmission System and Power Quality", VII SEPOPE, Brazil, May 21-26, 2000
- [3] N.G.Hingorani and L Gyuyi, "Understanding FACTS-Concepts and Technology of Flexible AC Transmission Systems", (Inst Of Elect. Electronic Engg. Press) 1998
- [4] Yongan Deng, V.K.Sood, L.Lopes, "STATCOM model in EMTF EV using Hysterisis Current Controlled Voltage Source

- Converter(VSC)",IEEE Canadian Conference on Electrical and Computer Engineering, 2005,pp. 517-522
- [5] T.O.Mahony,C.J.Downing,K.Fatla, "Genetic Algorithms for PID Parameter Optimization: Minimizing Error Criteria,Process Control and Instrumentation 2000,26-28 July2000,University of Strathclyde,Pg 148-153
 - [6] C.Honck,J.Joines and M.Kay " A Genetic Algorithm Toolbox for function optimization:A Matlab Implementation," NCSU-IE TR 95-05,1995
 - [7] C.Schauder and H.Mehta, "Vector Analysis and Control of Advanced Static VAR Compensators",IEE proceedings-C,vol.140,pp.299-306,July 1993
 - [8] SenKK,"STATCOM-Theory,Modelling &Applications", in IEEE PES 1999 Winter Meeting Proceedings ,pp 1177-1183
 - [9] A.Ghosh and G.Ledwich, "Power Quality Enhancement Using Custom Power Devices, (Kluwer Academic Publishers), London 2002.
 - [10] Goldberg,D.E.: Genetic Algorithms in Search ,Optimization and Machine Learning.Addison-Weasley Publishing Company,Inc.1989
 - [11] Kishore Chatterjee, B.G.Fernandes, and G.K.Dubey, " An Instantaneous Reactive Volt-Ampere Compensator AND harmonic Suppressor System", IEEE Trans. Power Electronics, vol 14, No.2,pp 381-391, March 1999

Improvement of Voltage Stability Margins with OPF Incorporating Static Series Synchronous Compensator

L.R.Srinivas¹, and ²K.Vaisakh

¹Dept. of Electrical Engineering, SRKR College of Engineering, Bhimavaram, AP 77843 INDIA.

²Dept. of Electrical Engineering, AU College of Engineering, Andhra University, VISAKHAPATNAM 530 003 INDIA
(e-mail: vaisakh k@yahoo.co.in)

Abstract— The static synchronous series compensator (SSSC) is one of the recently developed flexible ac transmission system (FACTS) controllers. The SSSC coupled with a transformer is connected in series with a transmission line, which can be used for steady state control of one of the following parameters: 1) the active power flow on the transmission line; 2) the reactive power flow on the transmission line; 3) the voltage at the bus; and 4) the impedance (precisely reactance) of the transmission line. Furthermore, the model can also take into account the voltage and current constraints of the SSSC. The detailed implementation of such a multicontrol functional model in Newton power flow algorithm is presented. A special consideration of the initialization of the variables of the SSSC in power flow analysis is also proposed. Numerical examples on the IEEE 30-bus system, are used to illustrate the feasibility of the SSSC model and performance of the Newton power flow algorithm. Power system-security enhancement is a remedial action against possible network overloads in the system following the occurrence of contingencies. Line overload can be removed by means of generation re-dispatching and by adjustment of FACTS devices such as phase shifting transformers, thyristor controlled series compensators and unified power flow controller (UPFC). The paper presents an algorithm for OPF for identifying the optimal values of UPFC series and shunt voltage source magnitudes and its angles. The locations of UPFC are selected based on sensitivity analysis. Simulation results on IEEE 30-bus test system are presented and compared with the results of other conventional approaches.

keywords—OPF, system security, unified power flow controller, voltage stability

I. INTRODUCTION

TRANSMISSION line overloads can be alleviated by rerouting power flows in the system. A linearized relationship between power flow in the overloaded lines and the generated power has been used to reschedule the power generation earlier. A computationally simple algorithm has been developed in [1] for real-time security control. In [2], a fuzzy set-theory-based approach has been proposed for overload alleviation through real power-generation rescheduling. A generation-shift sensitivity factor was used to determine the change in generation required at a generator

busbar. Although these approaches are fast in rescheduling the power generation, it may lead to overloading in other lines.

For secure operation of the system without any limit violation, complete modelling of the system through load-flow equations and operational constraints is necessary. Apart from generation rescheduling, adjustment of phase angles of-phase shifting transformers will also result in a change in line flow pattern. This paper presents an optimal power flow with phase shifter for overload alleviation. The locations of phase shifters are identified based on sensitivity analysis.

In the recent years voltage stability issues have received considerable focus due to the several voltage stability crisis situations having occurred all around the globe. Economic competition, sometimes, results in paying less attention to security features of the overall system. System security/stability has become one of an important issue in the context of deregulation because of the increased demand and competition.

A power flow can have any number of operating limit violations. When such situations occur, the violations can be alleviated by appropriate or various corrective actions. The analytical process of evolving this procedure is known as optimal power flow [3]. The current practice is to use the constraints based on the operating limits imposed by bus voltages, branch flows, power transfers over interfaces, etc. The system troubles in contingency analysis are violations of such constraints. Controls may include generator, real power phase shifter angles etc. The objective of the corrective action algorithm is to observe all constraints while minimizing the weighted sum of the control movement. The Newton based approach to OPF was proposed in [4]. In [5] the authors have formulated the OPF extension to take into effect the contingencies that occur in power systems. The non-solvability of the Newton process due to the singularity of the Jacobian matrix is got over by modifying the OPF through load shedding or by relaxing some in-equalities [6].

Methods to understand the voltage instability phenomenon and quantify the stability indices have been reported in works [7,8,9]. In [10] a voltage stability indicator has been discussed whose value changes between zero (no load) and one (voltage collapse). The indicator incorporates the effect of all other loads in the system on the evaluation of index at individual load buses. The overall voltage stability of the system could be identified by the largest value of the index evaluated amongst

all the load buses. This indicator can also be used as a normalized quantitative measure, for estimation of the voltage stability margin from the operating point.

Works in the direction of developing algorithms to incorporate stability issues into power system operational analysis are going on. The reported work [11] attempts to formulate the incorporation of the transient angle stability, into an OPF routine, as an additional constraint. Controlling the power flows in the network, under normal operation and network contingencies, helps to reduce flows in heavily loaded lines, reduce system power loss, and improve stability and performance of the system without generation rescheduling or topological changes [15, 16]. An UPFC installed in a line helps to increase or decrease the power flow in a line for improving real power loss reduction, voltage profiles, and voltage stability.

The OPF solution gives the optimal settings of all controllable variables for a static power-system-loading condition. A number of mathematical-programming-based techniques have been proposed to solve the OPF problem. These include the gradient method [12,13,14]. Newton method and linear programming [15,16]. In [17, 18] mixed-integer linear programming has been applied to identify the location of the phase shifter and FACTS devices in order to improve the loadability of the system. The gradient and Newton methods suffer from the difficulty in handling inequality constraints. To apply linear programming, the input-output function is to be expressed as a set of linear functions, which may lead to loss of accuracy. Also, difficulties are encountered in incorporating directly the discrete variables related to the phase-shifting transformers. In [19], a rule-based OPF with phase shifter has been proposed to alleviate the line overload. The principal shortcoming of a rule-base approach is that the construction of rules requires extensive help from skilled knowledge engineers. Also, it does not provide a continuous fabric over the solution space.

The paper presents an algorithm for OPF for identifying the optimal values of UPFC series and shunt voltage source magnitudes and its angles. The locations of UPFC are selected based on sensitivity analysis. Simulation results on IEEE 30-bus test system are presented and compared with the results of other conventional approaches.

II. VOLTAGE STABILITY MARGIN

Consider an n-bus system having 1, 2...g, generator buses (g), and g+1,g+2...n the load buses(r=n-g-s) and t number of OLTC transformers. The transmission system can be represented using a hybrid representation, by the following set of equations

$$\begin{bmatrix} V_L \\ I_G \end{bmatrix} = H \begin{bmatrix} I_L \\ V_G \end{bmatrix} = \begin{bmatrix} Z_{LL} & F_{LG} \\ K_{GL} & Y_{GG} \end{bmatrix} \begin{bmatrix} I_L \\ V_G \end{bmatrix}$$

where

V_L, I_L are the voltage and current vectors at the load buses

V_G, I_G are the voltage and current vectors at the generator buses

$Z_{LL}, F_{LG}, K_{GL}, Y_{GG}$ are the sub-matrices of the hybrid matrix H.

The H matrix can be evaluated from the Y bus matrix by a partial inversion, where the voltages at the load buses are exchanged against their currents. This representation can then be used to define a voltage stability indicator at the load bus, namely L_j which is given by,

$$L_j = \left| 1 + \frac{V_{0j}}{V_j} \right| \quad (1)$$

where,

$$V_{0j} = - \sum_{i \in G} F_{ji} V_i \quad (2)$$

The term V_{0j} is representative of an equivalent generator comprising the contribution from all generators.

The index L_j can also be derived and expressed in terms of the power terms as the following.

$$L_j = \left| \frac{\dot{S}_{j+}}{Y_{jj+} V_j^2} \right| \quad (3)$$

where,

$$S_{j+} = S_j + S_{jcorr} \quad (4)$$

* indicates the complex conjugate of the vector

$$S_{jcorr} = \left(\sum_{\substack{i \in Load \\ i \neq j}} \frac{\dot{Z}_{ji} S_i}{Z_{ji} V_i} \right) V_j \quad (5)$$

$$Y_{jj+} = \frac{1}{Z_{jj}} \quad (6)$$

The complex power term component S_{jcorr} represents the contributions of the other loads in the system to the index evaluated at the node j.

It can be seen that when a load bus approaches a steady state voltage collapse situation, the index L approaches the numerical value 1.0. Hence for an overall system voltage stability condition, the index evaluated at any of the buses must be less than unity. Thus the index value L gives an indication of how far the system is from voltage collapse. This feature of this indicator has been exploited in our proposed algorithm to evolve a voltage collapse margin incorporated OPF routine. The L -indices for a given load condition are computed for all load buses. The equation for the L -index for j-th node can be written as

$$L_j = \left| 1.0 - \sum_{i=1}^{l=g} F_{ji} \left| \frac{V_i}{V_j} \right| \angle \theta_{ji} + \delta_i - \delta_j \right| \quad (7)$$

$$L_j = \left| 1.0 - \sum_{i=1}^{l=g} \left| \frac{V_i}{V_j} \right| (F_{ji}^r + jF_{ji}^m) \right| \quad (8)$$

* Indicates the complex conjugate of the vector

$$V_i = |V_i| \angle \delta_i, V_j = |V_j| \angle \delta_j, \quad (9)$$

$$F_{ji} = |F_{ji}| \angle \theta_{ji} \quad (10)$$

$$F_{ji}^r = |F_{ji}| \cos(\theta_{ji} + \delta_i - \delta_j),$$

$$F_{ji}^m = |F_{ji}| \sin(\theta_{ji} + \delta_i - \delta_j)$$

It can be seen that when a load bus approaches a steady state voltage collapse situation, the index L approaches the numerical value 1.0. Hence for an overall system voltage stability condition, the index evaluated at any of the buses must be less than unity. Thus the index value L gives an indication of how far the system is from voltage collapse. This feature of this indicator has been exploited in our proposed algorithm to evolve a voltage collapse margin incorporated OPF routine.

III. POWER FLOW CONTROL WITH UPFC

Better utilization of existing power system capacities by installing new power electronic controllers such as FACTS has become imperative. FACTS controllers are able to change, in a fast and effective way, the network parameters in order to achieve better system performance. FACTS controllers, such as phase shifter, shunt, or series compensation and the most recent developed converter-based power electronic controllers, make it possible to control circuit impedance, voltage angle, and power flow for optimal operation performance of power systems, facilitate the development of competitive electric energy markets, stimulate the unbundling the power generation from transmission and mandate open access to transmission services, etc. With the practical applications of the converter-based FACTS controllers—STATCOM, SSSC, and UPFC in power systems, computer modeling of these is of great concern for the planning, operation planning, and control analysis of the FACTS controllers.

IV. MULTICONTROL FUNCTIONAL MODEL OF THE SSSC

A. Operation Principles of the SSSC

A SSSC usually consists of a coupling transformer, an inverter, and a capacitor. As shown in Fig. 1, the SSSC is series connected with a transmission line through the coupling transformer. It is assumed here that the transmission line is series connected with the SSSC via its bus. The active and reactive power flows of the SSSC branch entering the bus are equal to the sending end active and reactive power flows of the

transmission line, respectively. In principle, the SSSC can generate and insert a series voltage, which can be regulated to change the impedance (more precisely reactance) of the transmission line. In this way, the power flow of the transmission line or the voltage of the bus, which the SSSC is connected with, can be controlled.

B. Equivalent Circuit and Power Flow Constraints of the SSSC

An equivalent circuit of the SSSC as shown in Fig. 2 can be derived based on the operation principle of the SSSC. In the equivalent, the SSSC is represented by a voltage source in series with a transformer's impedance. In the practical operation of the SSSC, V_{se} can be regulated to control the power flow of line $i-j$.

It is proposed to improve the performance of the system by in presence of UPFC using all of its advantages. The UPFC equivalent circuit for steady state model is shown in Fig.1

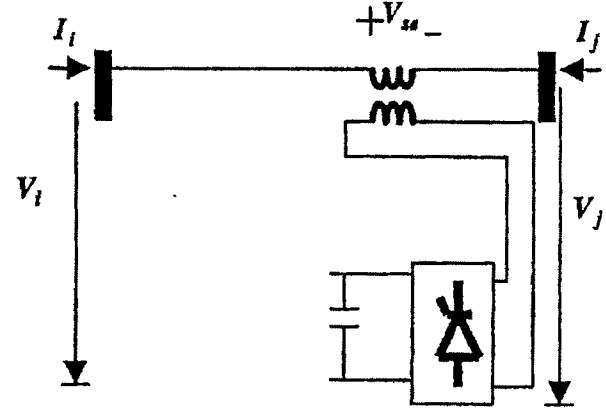


Figure1. SSSC operating principles

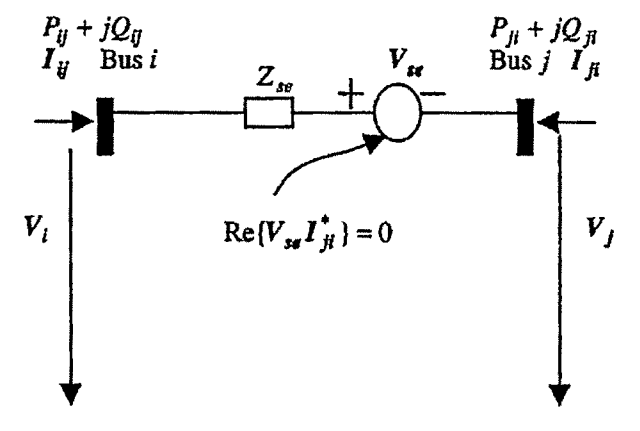


Figure 2 SSSC equivalent circuit

In the equivalent circuit, $V_{se} = V_{se} \angle \theta_{se}$, $V_i = V_i \angle \theta_i$, $V_j = V_j \angle \theta_j$, then the power flow constraints of the SSSC are:

$$P_u = V_i^2 g_{ii} - V_i V_j (g_{ij} \cos(\theta_i - \theta_j) + b_{ij} \sin(\theta_i - \theta_j))$$

$$\begin{aligned}
 & -V_i V_{se} (g_{ij} \cos(\theta_i - \theta_{se}) + b_{ij} \sin(\theta_i - \theta_{se})) \\
 Q_{ij} = & -V_i^2 b_{ij} - V_i V_j (g_{ij} \sin(\theta_i - \theta_j) - b_{ij} \cos(\theta_i - \theta_j)) \\
 & -V_i V_{se} (g_{ij} \sin(\theta_i - \theta_{se}) - b_{ij} \cos(\theta_i - \theta_{se})) \\
 P_{ji} = & V_j^2 g_{ij} - V_i V_j (g_{ij} \cos(\theta_j - \theta_i) + b_{ij} \sin(\theta_j - \theta_i)) \\
 & + V_j V_{se} (g_{ij} \cos(\theta_j - \theta_{se}) + b_{ij} \sin(\theta_j - \theta_{se})) \\
 Q_{ji} = & -V_j^2 b_{ij} - V_i V_j (g_{ij} \sin(\theta_j - \theta_i) - b_{ij} \cos(\theta_j - \theta_i)) \\
 & + V_j V_{se} (g_{ij} \sin(\theta_j - \theta_{se}) - b_{ij} \cos(\theta_j - \theta_{se})) \quad (5)
 \end{aligned}$$

Where

$$g_{ij} + jb_{ij} = 1/Z_{se}, g_{ii} = g_{ij},$$

$$b_{ii} = b_{ij}, g_{jj} = g_{ij} \text{ and } b_{jj} = b_{ij}$$

The operating constraint of the SSSC (the active power exchange via the dc link) is

$$PE = \text{Re}(V_{se} I_{ji}^*) = 0$$

where

$$\begin{aligned}
 \text{Re}(V_{se} I_{ji}^*) = & -V_i V_{se} (g_{ij} \cos(\theta_i - \theta_{se}) - b_{ij} \sin(\theta_i - \theta_{se})) \\
 & + V_j V_{se} (g_{ij} \cos(\theta_j - \theta_{se}) - b_{ij} \sin(\theta_j - \theta_{se}))
 \end{aligned}$$

of the shunt voltage source.

V. OPF FORMULATION INCORPORATING VOLTAGE STABILITY MARGIN AND UPFC

The OPF problem formulation, which we have used, is presented herewith. In order to keep the load power factor as a constant, we assume that when a certain amount of real load has been shed at one bus, the corresponding reactive load will also be shed in the same proportions. The conventional formulation of the optimal-power-flow (OPF) problem determines the optimal settings of control variables such as real power generations, generator terminal voltages, transformer tap settings and phase-shifter angles while minimising an objective function such as fuel cost given in (2).

$$\text{Objective: } F_T = \sum (a_i P_{gi}^2 + b_i P_{gi} + c_i) \quad (2)$$

The minimization problem is subjected to the constraints

$$P_i = \sum_{j=1}^n V_i \|V_j\| (G_{ij} \cos \delta_{ij} + B_{ij} \sin \delta_{ij}) \quad (3)$$

$$Q_i = \sum_{j=1}^n V_i \|V_j\| (G_{ij} \sin \delta_{ij} - B_{ij} \cos \delta_{ij}) \quad (4)$$

$$P_{gi}^{\min} \leq P_{gi} \leq P_{gi}^{\max} \quad (5)$$

$$Q_{gi}^{\min} \leq Q_{gi} \leq Q_{gi}^{\max} \quad (6)$$

$$0 \leq Q_{li} \leq Q_{lireq} \quad (7)$$

$$|V_i|_{\min} \leq |V_i| \leq |V_i|_{\max} \quad (8)$$

$$P_{gi\min} \leq P_{gi} \leq P_{gi\max} \quad (9)$$

$$Q_{gi\min} \leq Q_{gi} \leq Q_{gi\max} \quad (10)$$

$$P_{ij}^2 + Q_{ij}^2 \leq S_{ij\max}^2 \quad (11)$$

$$V_{cR}^{\min} \leq V_{cR} \leq V_{cR}^{\max}$$

$$V_{vR}^{\min} \leq V_{vR} \leq V_{vR}^{\max}$$

$$0 \leq \theta_{cR} \leq 2\pi$$

$$0 \leq \theta_{vR} \leq 2\pi$$

$$L_i \leq L_{crit} \quad (12)$$

Where

P_{gi} : real power generation at bus i

Q_{gi} : reactive power generation at bus i

$|V_i|$: voltage magnitude at bus i

$|V_j|$: voltage magnitude at bus j

G_{ij}, B_{ij} : real/reactive part of the ij^{th} element of the bus admittance matrix

δ_{ij} : angle difference between the voltage phasor at bus i and bus j

$P_{gi\min}, P_{gi\max}$: minimum/maximum real power generation at generation bus i

$Q_{gi\min}, Q_{gi\max}$: minimum/maximum reactive power generation at generation bus i

$|V_i|_{\min}, |V_i|_{\max}$: minimum/maximum voltage magnitude at bus i

P_{ij}, Q_{ij} : real/reactive power flow through transmission line ij

$S_{ij\max}$: maximum apparent power flow allowable through the ij^{th} line

$|V_{cR}|_{\min}, |V_{cR}|_{\max}$: minimum/maximum voltage magnitude of UPFC series voltage source

$|V_{vR}|_{\min}, |V_{vR}|_{\max}$: minimum/maximum voltage magnitude of UPFC shunt voltage source

$\theta_{cR}|_{\min}, \theta_{cR}|_{\max}$: minimum/maximum voltage angle of UPFC series voltage source

$\theta_{vR}|_{\min}, \theta_{vR}|_{\max}$: minimum/maximum voltage angle of UPFC shunt voltage source

L_i is the index L evaluated at the ith bus other than the generation buses

L_{crit} is the threshold value of the index acceptable for the system

VI. SIMULATION RESULTS

The method is applied to IEEE-30 bus test system Two different cases are considered for the study. In the first case, the proposed algorithm was applied to obtain the optimal-control variables in the IEEE 30-bus system under normal conditions. In the second case, the proposed algorithm was applied under line outage.

A. Normal Operation

The UPFC is placed at 3 different locations i.e., at line 15-14, line 22-21, and line 25-24 in the bus system. The solutions were compared in all the three cases, as given in the Table 1

Table 1 OPF results in 3 different locations under normal operation

	UPFC Location		
	15-14	25-24	22-21
Total 'P' gen	293.7525	293.6976	293.6531
Total 'Q' gen	112.5378	112.0164	111.6473
Total 'P' loss	10.7339	10.3480	10.2936
V _{min}	0.9410	0.9460	0.9520
δ_{max}	-3.673	-3.687	-3.989
δ_{min}	-16.342	-15.814	-16.161
V _{CR}	0.0208	0.0235	0.0480
θ_{CR}	-3.2478	-7.8187	-2.1202
L _j	0.321	0.325	0.351
Cost of Gen \$/MWhr	810.897	811.021	811.045

B. Under line 11-8 network contingency

The method is applied under the transmission line 11-8 outage contingency condition and the results obtained are given in Table 2.

Table 2 OPF results in 3 different locations under network contingency

	UPFC Location		
	15-14	25-24	22-21
Total 'P' gen	296.92	299.136	301.213
Total 'Q' gen	122.17	128.13	134.78
Total 'P' loss	13.901	15.795	17.854
V _{min}	0.950	0.943	0.950
δ_{max}	-5.71	-6.10	-6.986
δ_{min}	-19.78	-20.66	-22.28
V _{CR}	0.0453	0.4351	0.0507
θ_{CR}	21.34	45.087	23.496
L _j	0.342	0.353	0.362
Cost of Gen \$/MWhr	814.726	816.034	817.045

VII. CONCLUSIONS

This paper has proposed, an optimal power flow incorporating the UPFC for system security and voltage stability margin enhancement. The paper presents an OPF algorithm for identifying the optimal values of UPFC series and shunt voltage source magnitudes and its angles. The locations of UPFC are selected based on sensitivity analysis. Simulation results on IEEE 30-bus test system are presented and compared with the results of other conventional approaches.

VIII. REFERENCES

- [1] Lachs, W.R.: 'Transmission line overloads: real-time control', Proc.IEEE, 1987, 134, (5), pp. 342-347
- [2] Udupa, A.N., Purushothama, G.K., Parthasarathy, K., and Thukaram, D.: 'A fuzzy control for network overload alleviation', Electr. Power Energy Syst., 2001, 23, pp. 119-129
- [3] H.W.Dommel, W.F. Tinney, "Optimal power flow solutions", IEEE PAS, vol. 87, Oct 1968, pp. 1866-1876.
- [4] D.I Sun, B. Ashley, A Hughes, W.F. Tinney, "Optimal power flow by Newton Approach", IEEE Trans. Power System, vol. 103, 1984, pp. 2684-2880.
- [5] O Alsac, B Stott, "Optimal power flow with steady state security", IEEE PAS, vol. 93, May 1974, pp. 745-751.
- [6] O Alsac, J Bright, M Prais, B Stott, "Further developments in LP-based OPF", IEEE Trans. on Power Systems, vol. 5, no. 3, Aug 1990, pp. 697-711.
- [7] C.W. Taylor, "Power System Voltage Stability", McGRAW-Hill, Inc., 1994
- [8] V Ajarapu, C Christy, "The continuation power flow: A tool for steady state voltage stability analysis", IEEE Trans. on Power Systems, Vol. 7, No.1, February 1992.
- [9] G.K Morison, B Gao, P. Kundar, "Voltage stability analysis using static and dynamic approaches", IEEE Tran. on Power Systems, Vol 8, No.3, August 1993.
- [10] P Kessel, H Glavitsch, "Estimating the voltage stability of a power system", IEEE Trans on Power Delivery, vol. PWRD-1, No.3, July 1986, pp. 346-354
- [11] D Gan, R J Thomas, R D. Zimmerman, "Stability constrained OPF", IEEE Trans. on Power Systems, vol. 15, no.2, May 2000, pp. 535-540.
- [12] Alsac, O., and Scott, B.: 'Optimal load flow with steady state security', IEEE Trans., 1974, PAS-93, pp. 745-751
- [13] Lee, K.Y., Park, Y.M., and Ortiz, J.L.: 'Fuel-cost minimization for both real and reactive power dispatches', IEE Proc., 1984, 131C, (3), pp. 85-93
- [14] Mangoli, M.K., and Lee, K.Y.: 'Optimal real and reactive power control using linear programming', Electr. Power Syst. Res., 1993, 26, pp. 1-10
- [15] Scott, B., Alsac, O., Bright, J., and Paris, M.: 'Further developments in LP-based optimal power flow', IEEE Trans., 1990, PWRD-5, (3), pp. 697-711
- [16] Lima, G.M. et al.: 'Phase shifter placement in large-scale systems via mixed Integer programming', IEEE Trans., 2003, PWRD-18, (3), pp. 1029-1034
- [17] Kumar, A., and Parida, S.: 'Enhancement of power system Loadability with location of FACTS controllers in competitive electricity markets IEE Proc.-Gener. Transm. Distrib., Vol. 152, No. 6, November 2005
- [18] using MILP. Proc. Int. Conf. Energy, Information Technology and Power Sector, Kolkata, Jan. 2005, pp. 515-523
- [19] Momoh, J.A., Zhu, J.Z., Boswell, G.D., and Hoffman, S.: 'Power system security enhancement by OPF with phase shifter', IEEE Trans., 2001, PWRD-16, (2), pp. 287-293.

Multi-Area Unit Commitment Using Dynamic Programming Approach and Checking of Dynamic Stability

Rambabu.Ch
 ,Vignana's Engg.College
 Vadlamudi-522213 Guntur(Dt)
 email:Rams_Babu2001@yahoo.com

Abstract- This project presents new approach for multi-area unit commitment which takes power system dynamic stability limit into account. In the proposed dynamic security constrained commitment method, dynamic programming is first employed to perform unit commitment on whole system. The eigenvalues for the resultant yearly generation schedules are examined to see if they satisfy the specified dynamic security criterion. If the dynamic security requirement is not met at certain hours, an iterative algorithm is employed to reduce the inter-area line flows gradually and to perform area red patch and, if necessary, area unit commitment, in order for the resultant generation schedule to satisfy the dynamic security requirement.

The goal of the presented approach is to achieve a multi-area generation schedule which not only meets the conventional requirements of having lowest fuel costs with the spinning reserves and steady-state transmission capacity limits satisfied, but also offers dynamic performance through the enforcement of dynamic security constraint. The effectiveness of the proposed approach is demonstrated by unit commitment of a utility system.

Keywords - Dynamic stability, economic operation, unit commitment, dynamic security

1. INTRODUCTION

THE objective of unit commitment is to determine the optimum schedule of a utility's generating units that minimize total generating costs. In addition to providing sufficient generation to meet the load demand, certain operating constraints such as spinning reserve margin, minimum up time and down time, and must run units and normally considered in standard unit commitment routines. In the past two decades, several approaches such as priority lists, branch-and-bound method, dynamic programming, and Lagrangian relaxation have been proposed for unit commitment.

To "commit" a generating unit is to "turn it on;" that is, to bring the unit up to speed, synchronize it to the system,

and connect it so it can deliver power to the network. The problem with "commit enough units and leave them on line" is one of economics.

For a given demand the units to be committed, for determine so that the fuel cost is minimized.

The generic UC problem can be formulated as:

Minimize the Operational cost

Subjected to:

- Minimum up - time and down-time constraint
- Crew constraints
- Ramp rate limits

2. DYNAMIC PROGRAMMING APPROACH TO UNIT COMMITMENT

In conventional dynamic programming (DP) approach, an objective function is to be minimized subject to some constraints such as power generation-load balance, spinning reserve requirement, minimum up time, minimum down time, and crew constraints. The objective function of to be minimized is written as

$$\text{COST} = \sum_{K=1}^N \sum_{I=1}^I [\text{FCOST}_i(G_i(K)) + \text{SCOST}_i] \quad (1)$$

Where
 COST = total cost over the study period

I = number of thermal units
 $\text{FCOST}_i(G_i(K))$ = cost of producing G_i at unit I during stage K

SCOST_i = start up cost for thermal unit i

The generation-load balance equation as

$$\sum_{i=1}^I G_i(K) + GHYDRO(K) \geq L(K), K=1,2,\dots,N$$

(2)

Where

GHYDRO(K) = total power from hydro units at stage K

L(K) = load demand at stage K

The spinning reserve requirement as follows

$$\sum_{i=1}^I RES_i(K) + RES(K) \geq REQ(K) \quad (3)$$

Where

RES_i(K) = spinning reserve of thermal unit i at stage K

RES(K) = total spinning reserve from hydro units

REQ(K) = required spinning reserve at stage K

In multi-area unit commitment, an additional constraint with regard to the maximum allowable power flows over the inter area trunk must be imposed. In other words, we have

$$P_{\ell}(K) \leq P_{\ell}^c(K) \quad (4)$$

Where

$P_{\ell}(K)$ is the power flow over trunk line ℓ at hour K and $P_{\ell}^c(K)$ is the corresponding transmission capacity limit.

To obtain a commitment schedule with lowest cost, a recursive algorithm has been derived to compute the minimum cost at stage K (hour K) with state I

$$F_{COST}(K, I) = \min_{(L)} [PCOST(K, I) + SCOST(K-1, L) ; K, I) + FCOST(K-1, L)] \quad (5)$$

Where

$F_{COST}(K, I)$ = least total cost to arrive at state (K, I)

$PCOST(K, I)$ = production cost for state (K, I)

$SCOST(K-1, L ; K, I)$ = transition cost from state (K-1, L) to state (K, I)

3. CONSTRAINTS IN UC

Due to increased competition on power companies there has been new interest to optimization methods by which production and distribution costs could be minimized. Optimal

electric power plant scheduling can provide substantial savings in both fuel and operational costs. The problem is to find the optimal combination of power generation for each power consumption situation, i.e. a schedule, when the costs of each generator unit and other relevant economic and technological parameters are known.

Many constraints can be placed on the unit commitment problem. The list presented here is by no means exhaustive.

1. Spinning Reserve

Spinning reserve is the term used to describe the total amount of generation available from all units (i.e., spinning) on the system, minus the present load and losses being supplied. Spinning reserve must be carried so that the loss of one or more units does not cause too far a drop in system frequency. Quite simply, if one unit is lost, there must be ample reserve on the other units to make up for the loss in a specified time period.

2. Thermal Unit Constraints

Thermal units usually require a crew to operate them, especially when turned on and turn off. A thermal unit can undergo only gradual temperature changes, and this translates into a time period of some hours required to bring the unit on-line. As a result of such restrictions in the operation of a thermal plant, various constraints arise, such as:

a. Minimum up time

once the unit is running, it should not be turned off immediately.

b. Minimum down time

once the unit is determined there is a minimum time before it can be recommitted.

c. Crew constraints

if a plant consists of two or more units, they cannot both be turned on at the same time since there are not enough crew members to attend both units while starting up.

3. Other constraints

d. Hydro-constraints

Unit commitment cannot be completely separated from the scheduling of hydro-units.

e. Must Run

Some units are given a must-run status during certain times of the year for reason of voltage support on the transmission network or for such purposes as supply of steam for uses outside the steam plant itself.

f. Fuel constraints

A system in which some units have limited fuel, or else have constraints that require them to burn a specified amount of fuel in a given time, presents a most challenging unit commitment problem.

4. UNIT COMMITMENT SOLUTION METHODS

The commitment problem can be very difficult. As a theoretical exercise, let us postulate the following situation.

- * We must establish a loading pattern for M periods.
- * We have N units to commit and dispatch.
- * The M load levels and operating limits on the N units are such that any one unit can supply the individual loads and that any combination of units can also supply the loads.

The most talked -about techniques for the solution of the unit commitment problem are

1. Priority-list schemes,
2. Dynamic programming (DP) [Forward and Backward],
3. Lagrange relation (LR),
4. Genetic algorithms,
5. Lp-solve,
6. Simplex algorithm with exclusive condition,
7. Simplex algorithm with penalty function,
8. Branch-And-Bound,
9. Separable programming,
10. Expert systems / Artificial neural networks.

5. RESTRICTED SEARCH PATHS IN DP ALGORITHM

The restricted search paths in dynamic programming algorithm with $N=3$ and $X=5$ is shown in below.

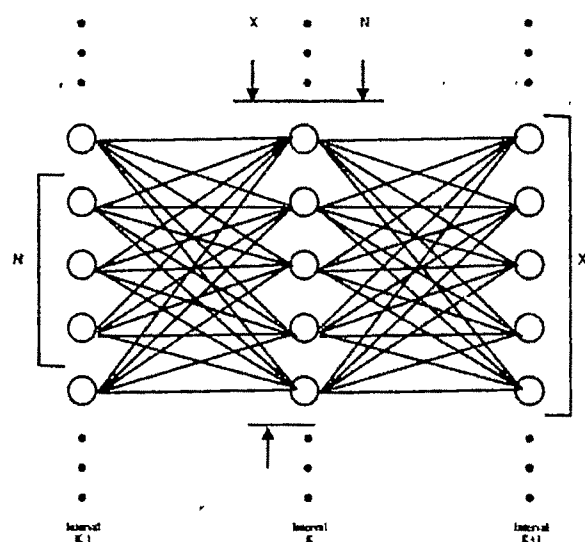


Fig 1

Where

X = number of states to search each period

N = number of strategies, or paths to save at each step.

These variables allow control of the computational effort (see fig 1).For complete enumeration, the maximum number of the value of X or N is $2^n - 1$.

For example ,with a simple priority -list ordering , the upper bound on X is n , the number of units.Reducing the number N means that we are discarding the highest cost schedules at each time interval and saving only on the lowest N paths or strategies. There is no assurance that the theoretical optimal schedule will be found using a reduced number of strategies and search range (X value) ; only experimentation with a perticular program will indicate the potential error associated with limiting the values of X and N below their upper bounds.

6. DYNAMIC SECURITY CONSTRAINT UNIT COMMITMENT

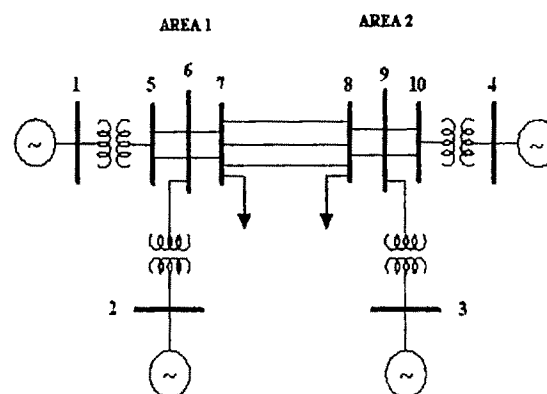


Fig 2 one-line diagram of 4 generator 10 bus system

7. THE DYNAMIC SECURITY CONSTRAINED UNIT COMMITMENT ALGORITHM

The dynamic security constrained unit commitment algorithm proceeds the following steps.

Step1.

Perform unit commitment for the whole system, dynamic programming taking the constraints such as generation balance, spinning reserve requirement ,minimum up and down times, into account .The yearly generation schedule, which is referred to as the generation schedule ,does not take the dynamic security constraint into account.

Step2.

Starting from the generation schedule at the first hour to compute the eigen values for the oscillation mode of poorest damping for the generation schedule at the present hour K , $\sigma(K) \pm j\omega(K)$.The particular mode of concern be identified based on past experience with the system through an examination of the frequency and eigen values of the oscillation mode. In the present study, the oscillation mode of special interest to us is an inter-area mode with frequency of around 1 Hz which affects all generation the three areas.

Step3.

Check if the generation schedules at the present hour the dynamic stability requirement. In other words, we have to examine if $\sigma(K) \leq \sigma_R$, where σ_R is a prespecified stability criterion determined based on system requirement and past experience. In the present study, we employ a value of -0.15 for σ_R . This has been considered from our past experience with the system that a real part of -0.15 for the eigen values associated with the worst damped mode of yield satisfactory dynamic responses for the system under disturbance conditions. However, the selection of σ_R system dependent. Different values of σ_R may be used for different systems. The value of σ_R will also affect the operating cost of the resultant generation schedule.

If $\sigma(K) \leq \sigma_R$, then dynamic stability requirement is satisfied by the present generation schedule and there is a need to change the present schedule. Proceed to check for generation schedule at the next hour until the schedule at the last hour has been examined.

If $\sigma(K) > \sigma_R$, then dynamic stability criterion is not met by the present generation schedule. Go to next step to modify the present schedule.

Step4.

Reduce the inter-area line flows by a certain amount. Determine the total generation at each area which is the sum of the load demand at that area and the next outgoing flow from the area. Perform area economic dispatch for each of the three areas in the system. Note that only the amount of power generation for the units on-line is redispatched; the on-off status of each unit remains unchanged at the moment.

If the stability requirement ($\sigma(K) \leq \sigma_R$) is met by the new generation schedule after redispatch, proceed to the generation schedule at the next hour ($K=K+1$). Otherwise reduce the inter-area line flows further until area economic dispatch is not possible with the current on-line units. In this case, further reduction in inter-area line flows is possible only through area unit commitment. Since the total generation for each area has been determined, the commitment schedules for the generating units in one area are modified by re performing unit commitment on the units in that area. It is noted that, in performing area unit commitment at hour K, the generation schedules for hours 1 through (K-1) remain unchanged. Once the new generation schedule for hour K is reached by area unit commitment, go to step3 to see if it satisfies the dynamic stability requirement.

9. INPUT DATA

FOUR UNITS ARE TO BE COMMITTED TO SERVE A 4-H LOAD PATTERN. DATA ON THE UNITS AND THE LOAD PATTERN IS CONTAINED IN TABLE.

UNIT COMMITMENT DATA 4 HOURS / 4 UNITS

I. TABLE -- 1

unit	max MW	min MW	Incremental heat rate	no-load cost (R/h)	start-up cost (R)	incremental cost (R/Mw hr)	min up time (h)	min. down time
1	80	25	10440	213	350	20.88	4	2
2	250	60	9000	585.62	400	18	5	3
3	300	75	8730	684.74	0	17.46	5	4
4	60	20	11900	252	0	23.8	1	1

Load pattern

II. TABLE--2

Hour	LOAD (MW)
1	450
2	530
3	600
4	540

10. OPTIMUM COMMITMENT SCHEDULE

Table - 3

•The eigenvalues for the worst-damped mode and the inter-area line flows .

H	1	2	3	4
1	0	0	25	25
2	150	230	265	275
3	300	300	300	300
4	0	0	0	0
Total generation	450	550	550	600

$$(\sigma(H) \pm j \omega(H)) = -42.86623345968889$$

-42.25655140046127

-31.03787403281116

-25.85244211373193 +11.11882658359965i

-25.85244211373193 -11.11882658359965i

-21.77426873901444

-12.86182895431045

-12.61339168755754

-3.52738152807112 + 8.67345508545868i swing mode 1

-3.52738152807112 - 8.67345508545868i swing mode 2

-2.51253992704980 + 6.30365587622010i swing mode 3

[inter area mode]

-2.51253992704980 - 6.30365587622010i

-5.05521791694474

-0.57873531456900 + 3.80502727858256i

-0.57873531456900 - 3.80502727858256i

2.85825846983292

0.59209414413774

0.00000000000004

• -Line-- Power at bus & line flow -Line loss--
Transformer from to MW Mvar MVA MW
Mvar tap 1 699.415 128.834 711.182

5 699.429 128.860 711.200 4.768 57.212

2 700.000 144.484 714.756

6 700.000 144.536 714.766 5.008 60.099

3 700.000 156.337 717.246

9 700.000 156.370 717.253 5.043 60.518

4 721.720 136.452 734.506

10 721.720 136.463 734.508 5.085 61.024

5 0.000 0.000 0.000

1 -694.661 -71.647 698.346 4.768 57.212

6 694.661 71.647 698.346 11.948 104.464

6 0.000 0.000 0.000

2 -694.992 -84.437 700.102 5.008 60.099

7 1377.705 51.620 1378.672 19.425 188.432

5 -682.714 32.817 683.502 11.948 104.464

7 -1159.000 88.000 1162.336

8 199.281 -48.812 205.172 3.033 -64.453

6 -1358.281 136.812 1365.153 19.425 188.432

8 -1575.000 112.000 1578.977

7 -196.248 -15.642 196.870 3.033 -64.453

9 -1378.752 127.642 1384.648 20.096 186.480

9 0.000 0.000 0.000

3 -694.957 -95.852 701.536 5.043 60.518

8 1398.848 58.839 1400.085 20.096 186.480

10 -703.892 37.014 704.864 12.743 112.453

10 0.000 0.000 0.000

4 -716.635 -75.439 720.594 5.085 61.024

Total loss

87.149 766.229

11. CONCLUSIONS

A new approach has been developed for dynamic security constrained unit commitment. In the proposed approach, a dynamic security criterion is first specified. Then, an iterative algorithm is developed to yield a generation schedule which not only minimizes total operating cost but also satisfies the dynamic stability requirement. Results obtained from this study reveal that, in some cases where the inter-area line flows exceed their dynamic stability limits the conventional dynamic programming approach may result in a generation schedule with insufficient system damping. The proposed method has been applied to the unit commitment of a utility system.

12. REFERENCES

1. Yuan-Yih Hsu ,Ching-Ching Su, Chih-Chien Liang, Chia-Jen Lin,Chiang-Tsung Huang,"Dynamic Security Constrained Multi-Area Unit Commitment", IEEE Transaction on Power systems,vol. 6,No. 3, August 1991.
2. A.J.Wood and B.F. Wollenberg, Power Generation,Operation and Control,Wiley,1984.
3. Gerald B. Sheble and George N.Fahd (1994) " Unit Commitment Literature Synopsis" , IEEE Trans . PAS .VOL .5 ,pp. 128-135.
4. J.L. Kerr , R.H .,Scheidt, Fontana,A. J., and Wiley,J.K. (1996) "Unit Commitment", IEEE Trans.PAS.VOL.5, pp.417-421.
5. Hadi saadat, 'Power System Analysis', Tata Mc Graw Hill Publishing Company Limited,2002., 'Power System Analysis'

Ratings of FACTS Devices for Power Flow Control in Power System Network

Subrata Majumdar¹, P.K.Chattopadhyay², and A.K.Chakrabarty³

¹ Electrical Engineering Department, College of Engineering & Management, Kolaghat, India, e-mail: sagarnil2@rediffmail.com

² Electrical Engineering Department, Jadavpur University, Kolkata, India, e-mail: pkchattopadhyay@ee.jdvu.ac.in

³ Electrical Engineering Department, College of Engineering & Management, Kolaghat, India e-mail: akcalll@yahoo.co.in

Abstract—This paper focuses a new approach to steady state power flow control using multiple flexible A.C. transmission systems (FACTS) equipped devices. Generalized nodal admittance model has been presented for Series Compensator, Phase Shifter, Static Var Compensator(SVS) and tap changing transformer. The proposed method is based on load flow and line flow equations and best suited for evaluating the ratings of individual FACTS devices when multiple FACTS devices are installed in a network to enhance the power transmission capability of selected lines very close to line limits. A Newton Raphson load flow programme has been developed on MATLAB platform and tested for modified IEEE-14 bus system.

Key Words: FACTS, TCSC, TCPAR, Power flow Controllers

I. INTRODUCTION

THE global liberalization trend in all economic sectors throughout the world acts as vital force in favour of deregulation in the Electric Supply Industry (ESI) and demands new concept and technologies to best suit the existing power system resources without compromising the system security [1]. Under these circumstances, efficient control of the power system network is essential. Installation of flexible AC transmission system (FACTS) appears to be the most appropriate solution for controlling power flow in the network because of its excellent flexibility and versatility [2,3].

With the advancement in Power electronics, FACTS devices are being utilized to achieve many objectives in an electric power system [4,5]. It can be used to reduce power flow in the overloaded lines by using excess capacity of the alternative paths. This helps to increase the power transfer capability of existing lines under normal condition very close to their thermal limits. In many situations it becomes necessary to increase the power transfer capability of some lines with the installation of facts devices. In this paper authors have developed an algorithm for proper choice of multiple FACTS devices parameters in the power network to enhance the power transfer capability of existing lines under normal condition

very close to their line limits. This algorithm has been applied for modified IEEE 14- bus system [6].

II. MODELING OF FACTS DEVICES

Facts technology opens up new opportunities for controlling line power flows, minimizing losses and maintaining bus voltages at desired level in a power system network. These are done by controlling one or more of the interrelated system parameters including series impedance, shunt impedance, current, voltage, phase angle etc. with the insertion of facts controllers in a power system network. Facts controllers may be categorized into three types;

- Series Controllers
- Shunt Controllers
- Combined Series-Shunt Controllers

Only one FACTS device of a given type per branch may be allowed.

2.1. Thyristor-Controlled Series Compensator (TCSC)

The TCSC is modeled with variable series reactance. The equivalent circuit of TCSC is shown in Fig.1

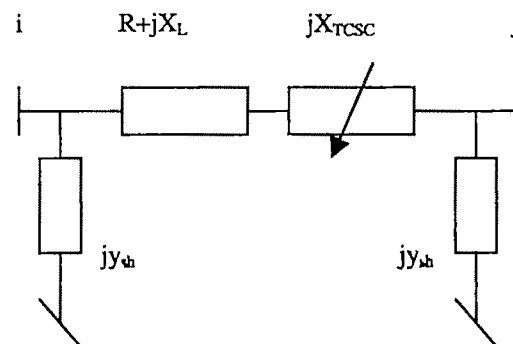


Fig.1. Equivalent circuit of TCSC

Increasing or decreasing the net series impedance of a line by varying the value of TCSC will greatly affect the active power flow. The value of TCSC (X_{TCSC}) is function of the reactance of the line X_L where the device is located. The maximum value of capacitive type TCSC is fixed at $-0.8X_L$. For inductive type, the maximum value is $0.2X_L$ [7]. This

type device can be cost-effective means of controlling the power flow when the angle between two bus voltages is small

2.2. Thyristor-Controlled Phase Shifting Transformer (TCPST)

Like TCSC it is also a series type compensator. The model of the transmission line with TCPST is shown in Fig.2.

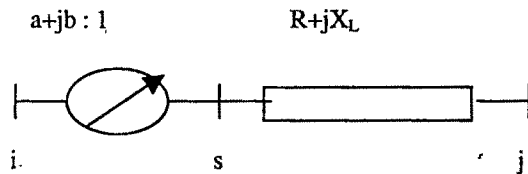


Fig.2. Equivalent circuit of TCPST.

This device can control the voltage phase shift angle. By varying the voltage phase shift angle, active power flow is controlled. The active power flow of a overloaded line can be decreased with negative phase shift and that of a under-loaded line can be increased up to almost the rating capacity. The range of the phase shift angle is

$$-15 \text{ deg.} \leq \delta_{TCPST} \leq 15 \text{ deg.}$$

2.3. Static Var Compensator (SVC)

The SVC is represented by a shunt variable susceptance inserted in the bus or at the mid point of the line. This device is used to maintain bus voltages at desired level. The compensator is inductive if reactive power has to be absorbed and capacitive if reactive power has to be supplied to maintain the voltage level within specified limit.

III. MODIFICATION OF BUS ADMITTANCE MATRIX

Let a line has series impedance $z = R + jX_L$. When a variable series x_{TCSC} is inserted in the line then series admittance of the line will be modified as

$$y = 1 / [R + j(X_L - x_{TCSC})] \quad (1)$$

and the bus admittance matrix can be written as

$$[Y_{bus}] = [Y] + [Y_{sh}]; \quad (2)$$

Where $[Y]$ is a square matrix of net series admittance and $[Y_{sh}]$ is a diagonal matrix of half line charging usceptance. Insertion of TCPST having a complex tapping ratio $a + jb$ will modify $[Y]$ as

$$[Y_{mod}] = \begin{bmatrix} Y_s / \tau_s^2 & -Y_g / \tau_s^* \\ -Y_g / \tau_s & Y_s \end{bmatrix} \quad (3)$$

Where, $\tau_s = a + jb$
 $= \tau_s \angle \phi$

Now, if a SVC is also connected to a bus then modified bus admittance matrix can be written as

$$[Y_{bus}]_{mod} = [Y_{mod}] + [Y_{sh}] + [B_{SVC}] \quad (4)$$

Where $[B_{SVC}]$ is a diagonal matrix of variable shunt susceptance (b_{SVC}).

IV. EXAMPLE

The proposed method has been tested for special IEEE 14-bus system as shown in Fig.3. Four FACTS devices are inserted in four lines in the given system. FACTS1 and FCTS4 are TCSC devices. FACTS2 and FACTS3 are TCPST devices. These four devices are connected to increase the active power flows of the selected lines very close to its thermal limits and to find out the minimum values of the devices parameters. The FACTS devices are inserted progressively one at a time. A capacitive type shunt compensator is also connected in bus no. 9. The line parameters and bus parameters are given in tables 1 and 2.

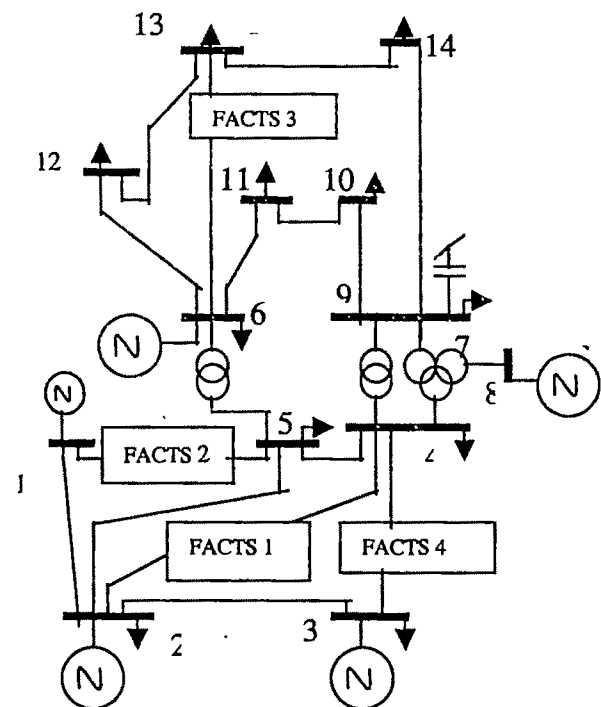


Fig.3. Special IEEE 14-busbar system network with FACTS devices

V. METHOD OF SOLUTION

In this approach nodal admittance matrix is modified considering the presence of series compensators, phase shifter, static Var compensator and tap setting transformer in the power system network. A Newton Raphson load flow programme has been developed on

Table.1:Line parameters of the modified IEEE-14 bus system

Line Nos	i	j	R	X_L	y_{ch}	t_i
1	1	2	0.01938	0.05917	0.0264	1.000
2	2	3	0.04699	0.19797	0.0219	1.000
3	2	4	0.05811	0.17632	0.0187	1.000
4	1	5	0.05403	0.22304	0.0246	1.000
5	2	5	0.05695	0.17388	0.0170	1.000
6	3	4	0.06701	0.17103	0.0173	1.000
7	4	5	0.01335	0.04211	0.0064	1.000
8	5	6	0.00000	0.25202	0.0000	0.932
9	4	7	0.00000	0.20912	0.0000	0.978
10	7	8	0.0000	0.17615	0.0000	1.000
11	4	9	0.0000	0.55618	0.0000	0.969
12	7	9	0.0000	0.11001	0.0000	1.000
13	9	10	0.03181	0.0845	0.0000	1.000
14	6	11	0.09498	0.1989	0.0000	1.000
15	6	12	0.12291	0.25581	0.0000	1.000
16	6	13	0.06615	0.13027	0.0000	1.000
17	9	14	0.12711	0.27038	0.0000	1.000
18	10	11	0.08205	0.19207	0.0000	1.000
19	12	13	0.22092	0.19988	0.0000	1.000
20	13	14	0.17093	0.34802	0.0000	1.000

Table 2: Bus parameters of modified IEEE-14 bus system

Bus Nos	Voltage (V)	Generated Power(P_g)	Real Power Demand (P_d)	Reactive Power Demand (Q_d)	b_{svc}
1	1.05	0.0	0.000	0.000	0.000
2	1.02	0.4	0.220	0.130	0.000
3	1.01	0.7	0.950	0.200	0.000
4	1.00	0.0	0.450	-0.040	0.000
5	1.00	0.0	0.080	0.020	0.000
6	1.01	0.3	0.120	0.075	0.000
7	1.00	0.0	0.000	0.00	0.000
8	1.03	0.6	0.000	0.00	0.000
9	1.00	0.0	0.300	0.180	0.190
10	1.00	0.0	0.090	0.060	0.000
11	1.00	0.0	0.035	0.018	0.000
12	1.00	0.0	0.060	0.018	0.000
13	1.00	0.0	0.135	0.060	0.000
14	1.00	0.0	0.150	0.050	0.000

MATLAB platform. Conventionally, installation of one fact device increase the dimension of Jacobean matrix by one. In the proposed techniques dimension of Jacobean matrix is kept unaltered. The line flow equations are solved and checked for convergence after ensuring the convergence of load flow solution for small increment of the values of facts devices. Thus the number of equations to be solved in each iteration reduces and consequently takes less time.

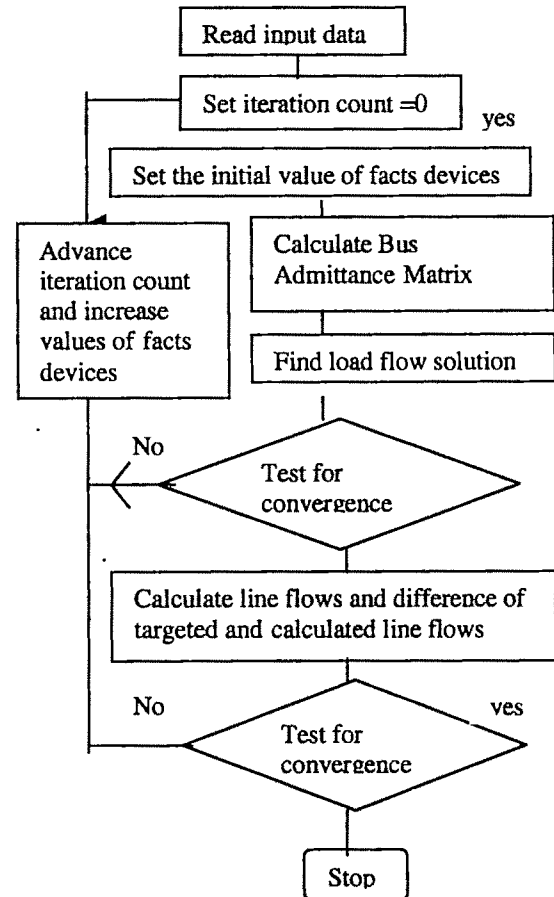


Fig 4. Flow Chart For Newton-Raphson Load Flow Program.

Five cases are studied with the given example. The active power flows and bus voltage profiles for all the above five cases are given in table nos. 3 & 4 respectively.

CASE-0: No facts devices are used.

CASE-1: A series capacitor (FACTS1) is connected in line number 3 to increase the real power flow of line.3 to 25 MW. The optimal value of reactance of series capacitor is - 0.0681 p.u.

CASE-2: A series capacitor (FACTS1) is connected in line number 3 to increase the real power flow of line 3 to 25 MW and a phase shifter (FACTS2) is connected in line number 4 to increase the real power flow of line number 4

Table-3: The controlled line flows of modified IEEE-14 bus system:

			Case-0	Case-1	Case-2	Case-3	Case-4
Line Nos	i	j	Line Flows In MW	Line Flows In MW	Line Flows In MW	Line Flows In MW	Line Flows In MW
1	1	2	39.27	40.86	31.16	32.27	32.19
2	2	3	21.72	20.19	17.25	17.31	16.90
3	2	4	19.56	25.00	24.99	25.00	25.20
4	1	5	21.96	20.43	30.04	30.09	30.19
5	2	5	15.31	12.98	6.44	7.46	7.58
6	3	4	3.49	4.99	7.88	7.83	8.23
7	4	5	18.40	14.83	17.55	13.79	3.99
8	5	6	10.32	10.09	10.30	15.12	15.15
9	4	7	14.48	14.34	14.47	16.81	16.83
10	7	8	60.01	60.01	60.01	60.00	60.00
11	4	9	3.70	3.78	3.71	2.37	2.36
12	7	9	45.53	45.67	45.54	43.19	3.17
13	9	10	7.91	8.05	7.93	11.45	11.44
14	6	11	4.65	4.51	4.63	1.12	1.13
15	6	12	7.34	7.32	7.34	3.06	3.06
16	6	13	16.34	16.27	16.34	35.06	35.08
17	9	14	11.31	11.40	11.32	4.10	4.09
18	10	11	1.12	0.98	1.10	2.40	2.39
19	12	13	1.26	1.25	1.26	9.20	9.21
20	13	14	3.90	3.81	3.90	11.22	11.23

Table 4: Bus voltages of modified IEEE-14 bus system :

Bus No.	Case-0 Voltage	Case-1 Voltage	Case-2 Voltage	Case-3 Voltage	Case-4 Voltage
1	1.0500	1.0500	1.0500	1.0500	1.0500
2	1.0156	1.0158	1.0200	1.0200	1.0200
3	1.0100	1.0100	1.0100	1.0100	1.0100
4	1.0030	1.0029	1.0055	1.0050	1.0055
5	1.0029	1.0029	1.0055	1.0045	1.0049
6	1.0143	1.0142	1.0167	1.0146	1.0149
7	1.0183	1.0183	1.0198	1.0185	1.0188
8	1.0300	1.0300	1.0300	1.0300	1.0300
9	1.0119	1.0119	1.0138	1.0111	1.0115
10	1.0046	1.0045	1.0066	1.0041	1.0045
11	1.0059	1.0058	1.0081	1.0060	1.0063
12	0.9992	0.9991	1.0016	0.9920	0.9923
13	0.9953	0.9951	0.9976	0.9962	0.9966
14	0.9857	0.9857	0.9879	0.9852	0.9856

to 30 MW. The optimal values of reactance of series capacitor is -0.1115p.u. and angle of phase shift is 2.2541degree.

CASE-3: A series capacitor (FACTS1) is connected in line number 3 to increase the real power flow of line 3 to 25 MW, a phase shifter (FACTS2) is connected in line number

4 to increase the real power flow of line number 4 to 30 MW and another phase shifter (FACTS3) is connected in line number 16 to increase its real power level to 35 MW. The optimal values of three devices are respectively 0.1099 p.u, 2.1203 degree and 6.0172 degree.

CASE-4: A series capacitor (FACTS1) is connected in line number 3 to increase the real power flow of line 3 to 25 MW, a phase shifter (FACTS2) is connected in line number 4 to increase the real power flow of line number 4 to 30 MW, a second phase shifter (FACTS3) is connected in line number 16 to increase its real power level to 35 MW and another capacitor (FACTS4) is connected in line number 6 to increase its real power flow to 8.5 MW. The optimal values are found -0.1105p.u, 2.1203 degree, 6.0172 degree and -0.0358 p.u respectively.

VII. CONCLUSION

This paper presented a simple and efficient operating scheme of four FACTS Devices which helped to improve the line capability in a coordinated way. The simultaneous use of several kinds of FACTS devices is the most efficient solution to increase the system loadability. It is also observed that this algorithm helped to arrive at the optimal ratings of the FACTS devices for steady operation of a power network. The proposed algorithm works satisfactorily for larger systems as well.

VIII. REFERENCES

- [1] Y. Xiao, Y. H. Song and Y. Z. Sun, "Power Flow Control Approach to Power Systems with Embedded FACTS Devices" IEEE Trans. on Power systems Vol. 17, No. 4, Nov. 2002.
- [2] N. G. Hingorani and L. Gyugyi, "Understanding FACTS Concepts and Technology of Flexible A.C Transmission System" Piscataway : IEEE Press, 1999.
- [3] C.R. Fuerte-Esquivel and E. Acha, "A Newton Type Algorithm for the Control of Power flow in Electrical Power Network." IEEE Trans. on Power Systems Vol. 12, No. 4 Nov. 1997.
- [4] S.Y. Ge and T.S. Chung, "Optimal Active Power Flow incorporating Power Flow Control Needs in Flexible A.C. Transmission Systems" IEEE Trans. on Power Systems, Vol. 14, No. 2, May, 1999.
- [5] S. H. Song, J.U. Lim and Seung-II Moon, "Installation and Operation of FACTS Devices for Enhancing Steady -State Security" Electric Power Systems Research, Vol. 70, pp. 7 – 15, 2004.
- [6] P. Yan and A. Sekar, "Steady -State Analysis of Power System having Multiple FACTS Devices using Line-Flow- Based Equations." IEE Proc. Genr, Transm, Distb, Vol. 152, No. 1, Jan. 2005.
- [7] S. Gerbex, R. Cherkaoui, and A. J. Germond, "Optimal Location of FACTS Devices to Enhance Power System Security "

Design of STATCOM Controller Based on State Predominant Approach

R. K. Pandey and Akashdeep Agrawal

Dept. of Electrical Engineering, Institute of Technology, Banaras Hindu University, Varanasi, India.
Email. rpsneh@yahoo.co.in

Abstract— This paper presents the development of multimachine model in state space framework along with the STATCOM. The state space model of Multi Machine Power System (MMPS) has been obtained. The design of controller based on a novel state predominant concept utilizing the pole placement/LQR control has been proposed. The state predominant pole placement/LQR controller response has been compared with the classical design of STATCOM controller with a supplementary lag-lead controller.

Keywords— FACTS, STATCOM, small signal stability, damping controllers, Phillips-Heffron model.

I. INTRODUCTION

In the present scenario of growing power system, network stability has become a thought of great concern as power oscillations are very common phenomenon due to different operating and changing conditions prevailing in the network. The power transfer in an integrated power system is constrained by transient stability, voltage stability and small signal stability. These constraints limit a full utilization of available transmission corridors. Flexible AC Transmission System (FACTS) is the technology that provides required corrections of the transmission functionality in order to fully utilize the existing transmission facilities and hence, minimizing the gap between the stability limit and thermal limit.

The static synchronous compensator (STATCOM) is based on the principle that a voltage-source converter generates a controllable AC voltage source behind a transformer-leakage reactance so that the voltage difference across the reactance produces active and reactive power exchange between the STATCOM and the transmission network. The STATCOM is one of the important FACTS devices and can be used for dynamic compensation of power systems to provide voltage support and stability improvement [1-4]. A unified Phillips-Heffron model [5] of a power system is established for three major types of FACTS devices such as Static VAR Compensator (SVC), Thyristor Controlled Series Compensator (TCSC) and Thyristor Controlled Phase

Shifter (TCPS). The model has been used for the analysis and design of damping functions of these three FACTS devices. Here, the Phillips-Heffron model [3] of power systems installed with a STATCOM is derived; which turns out to have the similar configuration as of unified model for SVC, TCSC and TCPS. There are fundamental differences between these FACTS devices. The first is between SVC and TCSC as controlled-impedance sources and the STATCOM and TCPS as controlled-voltage sources. The second difference is that STATCOM has been developed from a switch-mode voltage-source converter configuration with an energy-storage device.

The Phillips-Heffron model of power system has been used for decades for the analysis and design of PSS [6, 7]. This paper proposes a mathematical model of STATCOM in multi machine power network. The application of STATCOM has come in the power utilities in a big way; however the design of the controller with best possible tracking characteristics has not been analyzed properly. The possible control variables are me and de control of shunt VSC which enables the reactive power modulation in accordance with the load variation. The tuning of the control variables needs an approach which is linked with the deviation of states such as rotor angle of machine $\Delta\delta$, angular speed of the machine $\Delta\omega$, bus voltage of the generator $\Delta E_q'$, field excitation of the synchronous generator (ΔE_{FD}) and the dc voltage of the dc link capacitor (ΔV_{dc}) of STATCOM. A good control scheme is one which provides sufficient damping to the deviated states in minimum time; this is true from control view point if all the states are damped accordingly. The design of the controller utilizing the LQR/pole placement control theory has been done based on this principle, in which the most deviated state is fed back with suitable optimal gain along with the required gain for the other states as well. This ensures good tracking of the signal with change in loading criterion. The paper presents entire analysis in a systematic way supported by extensive simulated results with suitable arguments.

II. MATHEMATICAL MODELLING OF MMPS

The block diagram of two machine system has been shown in Fig. 1 where G1 and G2, represents two generator, I_{1L} & I_{2L}

armature current, V_{11} & V_{12} terminal voltages, x_{1L} & x_{2L} are the transmission impedance which are connected between two terminal. δ_1 is the torque angle between E'_{q1} and V_{11} , δ_2 is the angle between E'_{q2} and V_{12} . STATCOM is connected between two generators. V_L is the voltage of the bus where the STATCOM is connected, V_o is the STATCOM voltage bus after step down transformer (STD) where x_e is the step down transformer reactance, I_{Lo} is STATCOM current.

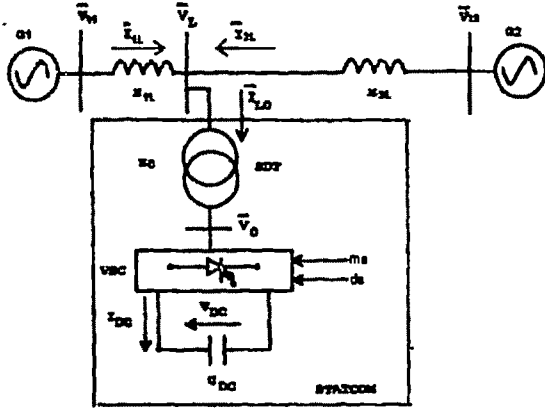


Fig. 1 STATCOM installed in a two machine power network

A. Linearized Equations of Generators

The linearized equations of the generator are obtained from the fundamentals from Phillips Heffron Model [2, 6].

First Generator

The equations are obtained as

$$I_{1L} = I_{1Ld} + jI_{1Lq} \quad V_{11} = V_{11d} + jV_{11q} \quad (1)$$

$$V_{11} = V_{11} (\sin \delta_1 + j \cos \delta_1) \quad (2)$$

$$\text{where } \delta_1 = \angle(E'_{q1}, V_{11}) \quad (3)$$

The armature current of the first generator in d-q components of the current are obtained as

$$I_{1Lq} = \frac{V_{12} \sin(\delta_1 - \delta_2) + \frac{x_{2L}}{x_e} m e V_{dc} \cos de}{(x_{1L} + x_{2L} + x_{1L} \frac{x_{2L}}{x_e}) + (1 + \frac{x_{2L}}{x_e}) x_{q1}} \quad (4)$$

$$I_{1Ld} = \frac{E'_{q1} - V_{12} \cos(\delta_1 - \delta_2) - \frac{x_{2L}}{x_e} m e V_{dc} \sin de}{(x_{1L} + x_{2L} + x_{1L} \frac{x_{2L}}{x_e}) + (1 + \frac{x_{2L}}{x_e}) x'_{d1}} \quad (5)$$

Initial torque angle of first generator is given as

$$\delta_1 = \sin^{-1} ((I_{1Lq} x_{qeq1} - m e V_{dc} x_{2L} \cos(de)) / (x_e V_{11})) \quad (6)$$

where, V_{dc} is the STATCOM voltage and m_e is the modulation index

Second Generator

The equations are obtained as

$$I_{2L} = I_{2Ld} + jI_{2Lq} \quad V_{12} = V_{12d} + jV_{12q} \quad (7)$$

$$V_{12} = V_{12} (\sin \delta_2 + j \cos \delta_2) \quad (8)$$

$$\text{Where, } \delta_2 = \angle(E'_{q2}, V_{12}) \quad (9)$$

The armature current of the generator in d-q components results as

$$I_{2Ld} = \frac{E'_{q2} - V_{11} \cos(\delta_2 - \delta_1) - \frac{x_{1L}}{x_e} m e V_{dc} \sin de}{(x_{1L} + x_{2L} + x_{2L} \frac{x_{1L}}{x_e}) + (1 + \frac{x_{1L}}{x_e}) x'_{d2}} \quad (10)$$

$$I_{2Lq} = \frac{V_{11} \sin(\delta_2 - \delta_1) + \frac{x_{1L}}{x_e} m e V_{dc} \cos de}{(x_{1L} + x_{2L} + x_{2L} \frac{x_{1L}}{x_e}) + (1 + \frac{x_{1L}}{x_e}) x_{q2}} \quad (11)$$

Initial torque angle of second generator are determined as

$$\delta_2 = \sin^{-1} ((I_{2Lq} x_{qeq2} - m e V_{dc} x_{1L} \cos(de)) / (x_e V_{11})) \quad (12)$$

d-q components of the STATCOM current can be determined from (4), (5), (10) and (11) as I_{Loq} and I_{Lod} .

The first generator constants are calculated as

$$K_{11} = \frac{(V_{11d} - x'_{d1} I_{1Lq})(x_{d11} - x_{d1}) V_{dc} \sin de}{x_{d11}} + \frac{(V_{11q} + x'_{q1} I_{1Ld})(x_{q11} - x_{q1}) V_{dc} \cos de}{x_{q11}}$$

$$K_{21} = (I_{1Lq} + \frac{V_{11d} (x_{2L} + x_e)}{x_{d11}})$$

$$K_{31} = 1 + \frac{(x'_{d1} - x_{d1})(x_{2L} + x_e)}{x_{d11}}$$

$$K_{41} = \frac{-(x'_{d1} - x_{d1})(x_{d11} - x_{d1}) V_{12} \sin(\delta_1 - \delta_2)}{x_{d11}} \quad (13)$$

When STATCOM is installed in power network; K_{pe1} , K_{pde1} are represented, the STATCOM control input constants, K_{pd1} is representing the STATCOM voltage control constant to control the power output of the first generator is obtained as

$$K_{pe1} = \frac{(V_{11d} - x'_{d1} I_{1Lq})(x_{d11} - x_{d1}) V_{dc} \sin de}{2x_{d11}} + \frac{(V_{11q} + x'_{q1} I_{1Ld})(x_{q11} - x_{q1}) V_{dc} \cos de}{2x_{q11}}$$

$$K_{pde1} = \frac{(V_{11d} - x'_{d1} I_{1Lq})(x_{d11} - x_{d1}) m e V_{dc} \cos de}{2x_{d11}} + \frac{(V_{11q} + x'_{q1} I_{1Ld})(x_{q11} - x_{q1}) m e V_{dc} \sin de}{2x_{q11}}$$

$$K_{pe1} = \frac{(V_{11d} - x'_{d1} I_{1Lq})(x_{d11} - x_{d1}) m e \sin de}{2x_{d11}} + \frac{(V_{11q} + x'_{q1} I_{1Ld})(x_{q11} - x_{q1}) m e \cos de}{2x_{q11}} \quad (14)$$

constants K_{qe1} , K_{qde1} are representing the STATCOM control input constants, K_{qd1} is representing the STATCOM voltage control constant which is used to control the internal voltage of the generator. These constants are calculated to result as

$$K_{qe1} = - \frac{(x'_{d1} - x_{d1})(x_{d11} - x_{d1}) m e \sin de}{2x_{d11}}$$

$$K_{qde1} = - \frac{(x'_{d1} - x_{d1})(x_{d11} - x_{d1}) V_{dc} \sin de}{2x_{d11}}$$

$$K_{qde1} = - \frac{(x'_{d1} - x_{d1})(x_{d11} - x_{d1}) m e V_{dc} \cos de}{2x_{d11}} \quad (15)$$

K_{S1} and K_{61} are obtained as

$$K_{61} = \frac{(V_{11q} / V_{11})(x_{d11} + x'_{d1}(x_{2L} - x_e))}{x_{d11}}$$

$$K_{S1} = \frac{(V_{11d} / V_{11}) x_{q1}(x_{q11} - x_{q1}) V_{dc} \cos(\delta_1 - \delta_2)}{x_{q11}} - \frac{(V_{11q} / V_{11}) x'_{d1}(x_{d11} - x_{d1}) V_{dc} \cos(\delta_1 - \delta_2)}{x_{d11}} \quad (16)$$

constants K_{ve1} , K_{vde1} are representing STATCOM control input and K_{vd1} is representing STATCOM voltage control constant which controls the terminal voltage of generator and given as

$$K_{ve1} = \frac{(V_{1d}/V_{1n})x_{q1}(x_{q1}-x_{q1})V_{dc} \cos de}{2x_{q1}} - \frac{(V_{1q}/V_{1n})x_{d1}(x_{d1}-x_{d1})V_{dc} \sin de}{2x_{d1}}$$

$$K_{vde1} = \frac{(V_{1d}/V_{1n})x_{q1}(-x_{q1}+x_{q1})meV_{dc} \sin de}{2x_{q1}} - \frac{(V_{1q}/V_{1n})x_{d1}(x_{d1}-x_{d1})meV_{dc} \cos de}{2x_{d1}}$$

$$K_{vd1} = \frac{(V_{1d}/V_{1n})x_{q1}(x_{q1}-x_{q1})me \cos de}{2x_{q1}} - \frac{(V_{1q}/V_{1n})x_{d1}(x_{d1}-x_{d1})me \sin de}{2x_{d1}} \quad (17)$$

K_{71} and K_{81} are obtained as

$$K_{71} = \left(\frac{3}{4C_{dc}} \right) \left\{ \frac{meV_{12} \sin(\delta_1 - \delta_2)(\cos de)x_{d1}}{x_{d1}} - \frac{meV_{12} \cos(\delta_1 - \delta_2)(\sin de)x_{q1}}{x_{q1}} \right\}$$

$$K_{81} = \left(-\frac{3}{4C_{dc}} \right) \frac{x_{1L} me \cos de}{x_{d11}} \quad (18)$$

Similarly, the second generator constants are calculated as obtained for first generator and written as

$$K_{12} = \frac{(V_{1d}-x'_{d2}I_{2q})(x_{q2}-x_{q2})V_{1n} \sin(\delta_2 - \delta_1)}{x_{d2}} + \frac{(V_{1q}+x'_{q2}I_{2d})(x_{q2}-x_{q2})V_{1n} \cos(\delta_2 - \delta_1)}{x_{q2}}$$

$$K_{22} = (I_{2Lq} + \frac{V_{12d}(x_{1L} + x_s)}{x_{d22}})$$

$$K_{32} = 1 + \frac{(x'_{d2} - x_{d2})(x_{1L} + x_s)}{x_{d22}}$$

$$K_{42} = \frac{-(x'_{d2} - x_{d2})(x_{d22} - x_{d22})V_{1n} \sin(\delta_2 - \delta_1)}{x_{d22}}$$

$$K_{52} = \frac{(V_{1d}-x'_{d2}I_{2q})(x_{q2}-x_{q2})V_{dc} \sin de}{2x_{d2}} + \frac{(V_{1q}+x'_{q2}I_{2d})(x_{q2}-x_{q2})V_{dc} \cos de}{2x_{q2}}$$

$$K_{62} = \frac{(V_{1d}-x'_{d2}I_{2q})(x_{q2}-x_{q2})meV_{dc} \cos de}{2x_{d2}} + \frac{(V_{1q}+x'_{q2}I_{2d})(x_{q2}-x_{q2})meV_{dc} \sin de}{2x_{q2}}$$

$$K_{72} = \frac{(V_{1d}-x'_{d2}I_{2q})(x_{q2}-x_{q2})me \sin de}{2x_{d2}} + \frac{(V_{1q}+x'_{q2}I_{2d})(x_{q2}-x_{q2})me \cos de}{2x_{q2}}$$

$$K_{82} = -\frac{(x'_{d2} - x_{d2})(x_{d22} - x_{d22})me \sin de}{2x_{d22}}$$

$$K_{92} = -\frac{(x'_{d2} - x_{d2})(x_{d22} - x_{d22})V_{dc} \sin de}{2x_{d22}}$$

$$K_{102} = -\frac{(x'_{d2} - x_{d2})(x_{d22} - x_{d22})meV_{dc} \cos de}{2x_{d22}}$$

$$K_{62} = \frac{(V_{12q}/V_{12})(x_{d22} + x'_{d2}(x_{1L} - x_s))}{x_{d22}}$$

$$K_{12} = \frac{(V_{1d}/V_{1n})x_{q2}(x_{q2}-x_{q2})V_{1n} \cos(\delta_2 - \delta_1)}{x_{q2}} - \frac{(V_{1q}/V_{1n})x_{d2}(x_{d2}-x_{d2})V_{1n} \cos(\delta_2 - \delta_1)}{x_{d2}}$$

$$K_{22} = \frac{(V_{1d}/V_{1n})x_{q2}(x_{q2}-x_{q2})V_{dc} \cos de}{2x_{q2}} - \frac{(V_{1q}/V_{1n})x_{d2}(x_{d2}-x_{d2})V_{dc} \sin de}{2x_{d2}}$$

$$K_{32} = \frac{(V_{1d}/V_{1n})x_{q2}(-x_{q2}+x_{q2})meV_{dc} \sin de}{2x_{q2}} - \frac{(V_{1q}/V_{1n})x_{d2}(x_{d2}-x_{d2})meV_{dc} \cos de}{2x_{d2}}$$

$$K_{42} = \frac{(V_{1d}/V_{1n})x_{q2}(x_{q2}-x_{q2})me \cos de}{2x_{q2}} - \frac{(V_{1q}/V_{1n})x_{d2}(x_{d2}-x_{d2})me \sin de}{2x_{d2}}$$

$$K_{72} = \left(\frac{3}{4C_{dc}} \right) \left\{ \frac{meV_{11} \sin(\delta_2 - \delta_1)(\cos de)x_{d2}}{x_{d2}} - \frac{meV_{11} \cos(\delta_2 - \delta_1)(\sin de)x_{q2}}{x_{q2}} \right\}$$

$$K_{82} = \left(-\frac{3}{4C_{dc}} \right) \frac{x_{1L} me \cos de}{x_{d22}}$$

STATCOM constant K_9 , K_{10} and K_{11}

$$K_9 = \left(\frac{3}{4C_{dc}} \right) \left\{ \frac{me \sin de (me \cos de)x_{d1} + me \cos de (me \sin de)x_{q1}}{2x_{d1}} + \frac{me \sin de (me \cos de)x_{d2} + me \cos de (me \sin de)x_{q2}}{2x_{d2}} \right\}$$

$$K_{10} = \left(\frac{3}{4C_{dc}} \right) \left\{ \frac{V_{dc} \sin de (me \cos de)x_{d1} + V_{dc} \cos de (me \sin de)x_{q1}}{2x_{d1}} + \frac{V_{dc} \sin de (me \cos de)x_{d2} + V_{dc} \cos de (me \sin de)x_{q2}}{2x_{d2}} \right\}$$

$$K_{11} = \left(\frac{3me}{4C_{dc}} \right) (I_{Ldq} \cos de - I_{Ld} \sin de)$$

$$+ \left(\frac{3}{4C_{dc}} \right) \left\{ \frac{meV_{dc} \cos de (me \cos de)x_{d1} - meV_{dc} \sin de (me \sin de)x_{q1}}{2x_{d1}} + \frac{meV_{dc} \cos de (me \cos de)x_{d2} - meV_{dc} \sin de (me \sin de)x_{q2}}{2x_{d2}} \right\} \quad (19)$$

III. STATE SPACE MODEL OF MMPS

The state space model of the MMPS with STATCOM can be derived to arrive in the form of

$$\dot{X} = Ax + Bu \quad (20)$$

$$u = [u_{E1} \ u_{E2}]$$

where A is the state matrix, B is the STATCOM control input matrix and u_{E1} & u_{E2} are the supplementary control inputs. The state matrix elements can be found according to the relation

$$\begin{bmatrix} \Delta \delta_1 \\ \Delta \omega_1 \\ \Delta E'_{q1} \\ \Delta E'_{fd1} \\ \Delta V_{dc} \\ \Delta \delta_2 \\ \Delta \omega_2 \\ \Delta E'_{q2} \\ \Delta E'_{fd2} \end{bmatrix} = [A] \begin{bmatrix} \Delta \delta_1 \\ \Delta \omega_1 \\ \Delta E'_{q1} \\ \Delta E'_{fd1} \\ \Delta V_{dc} \\ \Delta \delta_2 \\ \Delta \omega_2 \\ \Delta E'_{q2} \\ \Delta E'_{fd2} \end{bmatrix} + [B] \begin{bmatrix} \Delta me \\ \Delta de \end{bmatrix} \quad (21)$$

where δ_1 , ω_1 , E'_{q1} , E'_{fd1} are the state variable of the first generator similarly δ_2 , ω_2 , E'_{q2} , E'_{fd2} are the state variable of the second generator, V_{dc} is state variable of STATCOM. The control variables are me and de where me is modulation index of PWM based voltage source converter, de is firing angle of voltage source converter.

The state matrix of first generator is

$$[A_1] = \begin{bmatrix} 0 & \omega_s & 0 & 0 & 0 \\ -\frac{K_{11}}{M_1} & -\frac{D_1}{M_1} & -\frac{K_{21}}{M_1} & 0 & -\frac{K_{p1}}{M_1} \\ -\frac{K_{41}}{T'_{d01}} & 0 & -\frac{K_{31}}{T'_{d01}} & \frac{1}{T'_{d01}} & -\frac{K_{q1}}{T'_{d01}} \\ -\frac{K_{d1}K_{s1}}{T_{d1}} & 0 & -\frac{K_{d1}K_{s1}}{T_{d1}} & -\frac{1}{T_{d1}} & -\frac{K_{d1}K_{q1}}{T_{d1}} \\ K_{71} & 0 & K_{81} & 0 & -K_9 \end{bmatrix}$$

The state matrix of second generator is

$$[A_2] = \begin{bmatrix} 0 & \omega_0 & 0 & 0 & 0 \\ -\frac{K_{12}}{M_1} & -\frac{D_2}{M_2} & -\frac{K_{22}}{M_2} & 0 & -\frac{K_{pd2}}{M_2} \\ -\frac{K_{42}}{T_{d02}} & 0 & -\frac{K_{12}}{T_{d02}} & \frac{1}{T_{d02}} & -\frac{K_{pd2}}{T_{d02}} \\ -\frac{K_{A2}K_{12}}{T_{A2}} & 0 & -\frac{K_{A2}K_{62}}{T_{A2}} & -\frac{1}{T_{A2}} & -\frac{K_{A2}K_{1d2}}{T_{A2}} \\ K_{72} & 0 & K_{82} & 0 & -K_9 \end{bmatrix}$$

$$[A] = \begin{bmatrix} & & & & 0 & 0 & 0 & 0 \\ & & & & 0 & 0 & 0 & 0 \\ & & [A_1] & & 0 & 0 & 0 & 0 \\ & & & & 0 & 0 & 0 & 0 \\ 0 & 0 & 0 & 0 & & & & \\ 0 & 0 & 0 & 0 & & & & \\ 0 & 0 & 0 & 0 & & & & \\ 0 & 0 & 0 & 0 & & & & \\ & & & & & [A_2] & & \end{bmatrix}$$

The state variables have been expressed in Δ as small perturbation. The control input matrix of first generator is $[B_1]$, control input matrix of second generator is $[B_2]$.

$$B_1 = \begin{bmatrix} 0 & 0 \\ -\frac{K_{pe1}}{M_1} & -\frac{K_{pde1}}{M_1} \\ \frac{K_{qe1}}{T_{d01}} & -\frac{K_{qde1}}{T_{d01}} \\ -\frac{K_{A1}K_{1e1}}{T_{A1}} & -\frac{K_{A1}K_{1de1}}{T_{A1}} \end{bmatrix} \quad B_2 = \begin{bmatrix} 0 & 0 \\ -\frac{K_{pe2}}{M_2} & -\frac{K_{pde2}}{M_2} \\ \frac{K_{qe2}}{T_{d02}} & -\frac{K_{qde2}}{T_{d02}} \\ -\frac{K_{A2}K_{1e2}}{T_{A2}} & -\frac{K_{A2}K_{1de2}}{T_{A2}} \end{bmatrix}$$

$$[B] = \begin{bmatrix} & [B_1] \\ [B] = K_{ee} & K_{ede} \\ & [B_2] \end{bmatrix}$$

For the system with supplementary control u_{E1} & u_{E2} the equation can be written as

$$X = Ax + Bu + B_F u_F \quad (22)$$

Where A is system state matrix, B is STATCOM control input matrix and B_E is supplementary control matrix, so A_c the controlled system matrix. $[A_{c1}]$ and $[A_{c2}]$ are the controlled system matrix of the first and second generators respectively

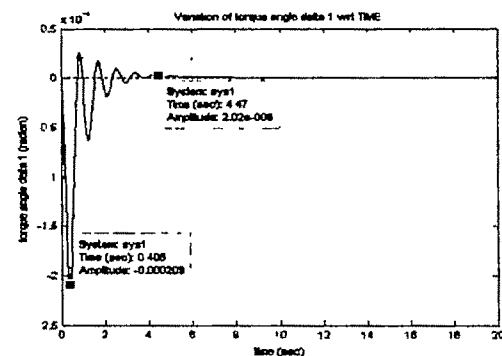
$$[A_1] = \begin{bmatrix} & & & & 0 & 0 \\ & & & & 0 & 0 \\ & & & & 0 & 0 \\ & & & & 0 & \frac{K_d}{T_d} \\ & & & & 0 & 0 \\ \frac{K_1}{M_1} & \frac{D_1}{M_1} & \frac{K_2}{M_1} & 0 & \frac{K_{w1}}{M_1} & \frac{1}{T_w} & 0 \\ \frac{K_{c1}K_{v1}T_{11}}{MT_{21}} & \frac{K_{c1}DT_{11}}{MT_{21}} & \frac{K_{c1}K_{v1}T_{11}}{MT_{21}} & 0 & \frac{K_{c1}K_{v1}T_{11}}{MT_{21}} & \frac{K_{c1}(1-\frac{T_{11}}{T_c})}{T_{21}} & \frac{1}{T_{21}} \end{bmatrix}$$

$$[A_2] = \begin{bmatrix} & & & & 0 & 0 \\ & & & & 0 & 0 \\ & & & & 0 & 0 \\ & & & & 0 & \frac{K_{A2}}{T_{A2}} \\ & & & & 0 & 0 \\ \frac{K_{I1}}{M_1} & \frac{D_1}{M_1} & \frac{K_{I2}}{M_1} & 0 & \frac{K_{P2}}{M_1} & \frac{1}{T_w} & 0 \\ \frac{K_{C1}K_{I1}T_{I1}}{M_1T_{I1}} & \frac{K_{C1}D_1T_{I1}}{M_1T_{I1}} & \frac{K_{C1}K_{I1}T_{I2}}{M_1T_{I2}} & 0 & \frac{K_{C1}K_{P2}T_{I2}}{M_1T_{I2}} & \frac{K_{C1}(1-\frac{T_{I1}}{T_w})}{T_{I2}} & \frac{1}{T_{I2}} \end{bmatrix}$$

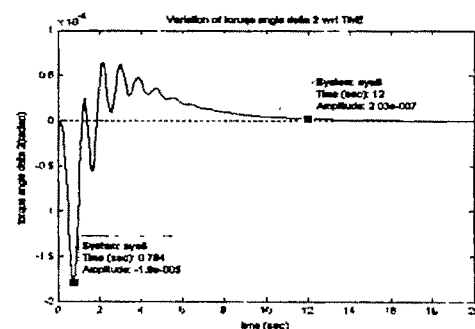
$$[A_c] = \begin{bmatrix} & & & 0 & 0 & 0 & 0 \\ & & & 0 & 0 & 0 & 0 \\ & & [A_{c1}] & 0 & 0 & 0 & 0 \\ & & & 0 & 0 & 0 & 0 \\ 0 & 0 & 0 & 0 & & & \\ 0 & 0 & 0 & 0 & & [A_{c2}] & \\ 0 & 0 & 0 & 0 & & & \end{bmatrix}$$

IV. CASE STUDY OF MMPS

The case study of the sample system [2] has been carried out with STATCOM with the concept of state predominant approach in which the large deviated states are highly weighted compared to other states. Both Pole placement and LQR control approach have been studied on the sample power system.

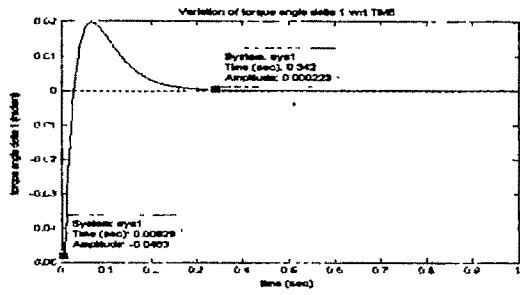


(a)

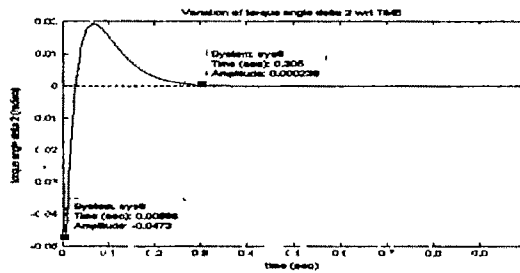


(b)

Fig. 2 Response of supplementary controller (a) δ_1 and (b) δ_2

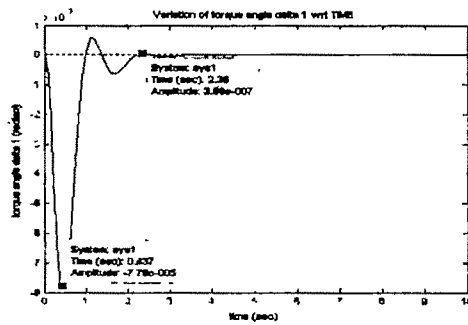


(a)

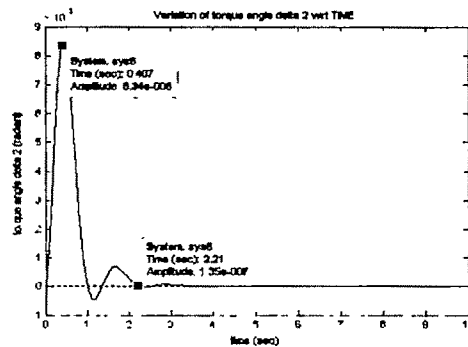


(b)

Fig. 3 Response of state predominant pole placement controller (a) δ_1 and (b) δ_2



(a)



(b)

Fig. 4 Response of state predominant LQR controller (a) δ_1 and (b) δ_2

V. CONCLUSIONS

This paper develops a state space model for MMPS. This model has been used to design the controllers based on state predominant approach. The simulation study reveals that the concept of state predominant will be an effective control strategy to have the cost effective controllers along with adequate damping characteristics within minimum acceptable time and peak overshoots. This can be used in power system oscillation damping in open access power system. The design of the reactive power controllers for multi machine case with the supplementary control strategy, Pole Placement Design and LQR approach based on the state predominant concept has been carried out. The concept of state predominant has been introduced that is linked with the changing weights of Q matrix as the states are deviated most. The system control design must be carefully carried out with changing dynamics of either side machine or even transmission line in which the STATCOM has been embedded. The most vulnerable state variable is E_q' at either side and need to be properly regulated with suitable feedback. However, the V_{dc} is also resulting to abnormal value during control (in case control response time is kept relatively small as design criterion) and needs proper control while other state feedback variables are maintained. The most deviated states have been attached very large weight which implies that the large gain will provide the high priority to the signal concerned for regulating the system dynamics. This is to mention that with the concept introduced for LQR design, the settling time of the response is well defined and also the only compromise has to be made in magnitude of peak overshoot/undershoot. In order to obtain the fast/minimum settling time for a given perturbation, the peak overshoot/undershoot will certainly increase. Since LQR control is the optimal control based on the state feedback, the stabilization of the system is guaranteed and moreover the system control tracks the error dynamics fast compared to other controllers proposed.

VI. REFERENCES

- [1] Gyugyi L., Hingorani N. G., Nannery P. R. and Tai T., "Advanced Static VAR Compensator using Gate Turn Off Thyristors for Utility Applications", CIGRE Paris, 1990.
- [2] Gyugyi L., "Reactive Power Generation and Control by Thyristor Circuits", pp. 521-532, IA-15, (5), IEEE Trans. 1979
- [3] Wang H. F., "Applications of Damping Torque Analysis to STATCOM Control", pp. 197-204, International Journal of Electrical Power and Energy Systems, 2000.
- [4] Hingorani, N.G., and Gyugyi, L., "Understanding FACTS: Concepts and Technology of Flexible AC Transmission Systems", IEEE Press, New Jersey, 1999.
- [5] Heffron W G., Phillips R A. "Effect of Modern Amplidyne Voltage Regulator on Under Excited Operation of Large Turbine Generator", pp. 692-697, AIEE Trans 1952.
- [6] Yu Y.N.: "Electric Power System Dynamics", Academic Press-1983.
- [7] H.F.Wang, F.J.Swift and M.LI, 'An Unified Model for the Analysis of FACTS Devices in Damping Power System Oscillations Part II Multi-Machine Power Systems', IEEE Trans on Power Delivery, Vol 13, No.4, pp1355-1362, 1998.

Normal Form Analysis of Stressed Power System Incorporating STATCOM

Ramtin Hadidi¹, Abbaq Kazemi²

^{1&2} Centre of Excellence for Power Systems Automation and Operation, Electrical Engineering Department,
Iran University of Science and Technology, Iran
e-mail: ¹ramtin_hadidi@yahoo.com & ²kazemi@iust.ac.ir

Abstract—When a stressed power system is subjected to a disturbance, it exhibits complex dynamic behavior. The complexity of this behavior depends on the power system structure, system loading, and type and location of disturbance. The approach presented in this study provides an analytical functional relationship describing the nonlinear coupling between the natural modes. This functional relationship is demonstrated here for system with second order nonlinearities. By using the normal form of vector fields approach, an explicit solution which contains nonlinear information explicitly, up to the order in which the analysis is carried out, is obtained.

In this paper, a comprehensive analytical technique based on normal form theory is proposed for the study of nonlinear interaction in stressed power system incorporating FACTS controllers. Emphasis is being placed on the analysis and simulation of STATCOM at critical system buses which is new in the literature. A second order representation of the power system is derived that considers the explicit representation of synchronous machines and STATCOM in the state representation. On the basis of this model, normal form theory is used to study nonlinear power system behavior following large disturbance. A simplified 4-machine, 2-area test system is used to illustrate the proposed methodology.

Key words— Normal Form, Nonlinear dynamics, STATCOM, Stressed Power System

I. INTRODUCTION

POWER system is inherently a nonlinear system. It is a general practice in small signal analysis to linearize the dynamic equations of this system and deduce dynamic behaviors and stability properties and design controllers based on linear system theory. The stressed power system following a large disturbance, exhibits complex dynamic behavior, not detectable from linear system analysis[1].

The analysis of small-signal behavior involves the study of system characteristics in the vicinity of essentially stable equilibrium points. However, small-signal stability analysis is based on a first-order (linear) approximation of the nonlinear power system differential-algebraic equations in the neighborhood of an operating point. It has been suggested that in certain cases, such as when the system is stressed, linear analysis techniques might not provide an accurate picture of the power system modal characteristics and complex phenomena, involving interaction between the fundamental modes of the system may occur[2].

A number of recent studies [3-5] have shown that under certain ranges of operating conditions the system modes may interact nonlinearly leading to second (or higher) order resonances and hence the onset of more complex dynamical phenomena. It is shown that some oscillation frequencies may appear in stressed power systems which are not predictable by linear modal analysis. This makes techniques that extend the domain of applicability of small-signal stability analysis an attractive proposition for advancing the understanding of power system dynamics. Recently, the technique of normal forms of vector fields has been used to analyze the complex behavior of the power systems [3-7]. With this technique, it is possible to obtain the simplest form of a set of non-linear differential equations and hence, to identify and study the nature of system oscillations using conventional linear analysis methodologies [8-9].

The study of nonlinear modal interaction arising from the application of FACTS devices on the transmission network, however, has not been satisfactorily addressed [10]. In this paper, an analytical technique based on normal form theory is proposed for the study and control of non-linear oscillations in power systems incorporating FACTS controllers. Emphasis is being placed on the analysis and simulation of STATCOM at critical system buses.

The remainder of the paper is structured as follows. In Section II the system dynamic model are discussed and the

dynamic equations are obtained. Sections III briefly review normal form technique method and show the solutions of the differential equation obtained using these method. The proposed procedure is demonstrated on a sample 2-areas test system and the analytical results are shown and discussed in Section IV. The conclusions of the work are presented in Section V.

II. POWER SYSTEM MODEL

The electrical network obtained for an n-machine system is as shown in Fig. 1. Nodes 1,2,...,n are the internal machine buses. The magnitudes E_i , $i=1,2,...,n$ are held constant during the transient in classical stability study. A number of assumptions are made in the classical-machine-model analysis of this paper: mechanical power is constant; loads are represented by constant; and impedance is reduced to generator terminal [11].

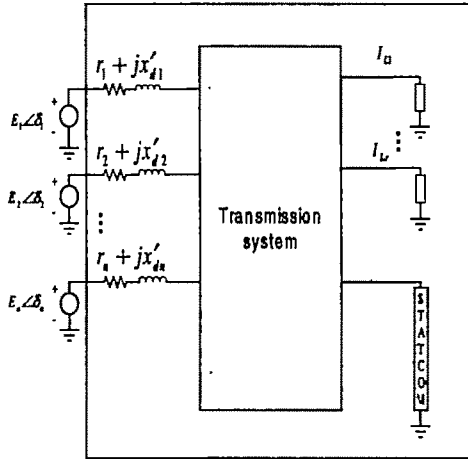


Fig. 1 Representation of a multimachine system (classical model)

A. Generator Model

The generator equation for the classical model are given by

$$\dot{\omega}_i = \frac{\omega_s}{2H_i} [P_m - P_{ei} - D_i \omega_i] \quad (1)$$

$$\delta = \omega_i - \omega_s \quad i = 1, 2, \dots, n \quad (2)$$

Where P_{ei} is the power into the network at node i , ω_i is rotor speed of generator i , δ_i is rotor angle of generator i , D_i is the damping factor and ω_s is synchronous speed.

B. STATCOM Model

The implemented STATCOM model is a current injection model [12]. The STATCOM current is always kept in quadrature in relation to the bus voltage so that only reactive power is exchanged between the ac system and the STATCOM. The dynamic model is shown in Fig. 2. The differential equation and the reactive power injected at the STATCOM node are given, respectively, by

$$i_{sh} = \frac{1}{T_r} [K_r (V_{ref} - V) - i_{sh}] \quad (3)$$

$$Q = -i_{sh} V \quad (4)$$

Where K_r is the STATCOM gain, T_r is the time constant of STATCOM and V_{ref} is the reference voltage.

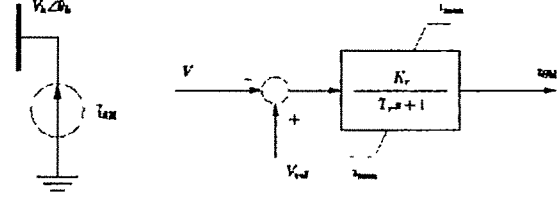


Fig.2 STATCOM circuit and control block diagram

Then the state vector is given by

$$X = [\delta_1 \delta_2 \dots \delta_n \omega_1 \omega_2 \dots \omega_n i_{sh1} i_{sh2} \dots i_{shn}] \quad (5)$$

III. NORMAL FORM

The dynamic equations governing the generators and the STATCOM have the general form

$$\dot{X} = F(X) \quad (6)$$

where X is the state vector and F is an analytic vector field.

We expand (6) as a Taylor series about a stable equilibrium point X_{SEP} and obtain using again X and x_i as the state variables.

$$\dot{x}_i = A_i x + \frac{1}{2} X^T H' X + H.O.T \quad (7)$$

where A_i is i th row of Jacobian A which is equal to

$$A_i = \left[\frac{\partial F}{\partial X} \right]_{x_{sep}} \quad \text{and} \quad H' = \left[\frac{\delta^2 F_i}{\delta x_j \delta x_k} \right]_{x_{sep}} \quad \text{is Hessian matrix.}$$

Denote by J the (complex) Jordan form of A , and by U the matrix of the right eigenvalues of A . Then the transformation $X=UY$ yields for the linear and the second order terms of (7) the equivalent system

$$\dot{y}_j = \lambda_j y_j + \sum_{k=1}^N \sum_{l=1}^N C_{kl}^j y_k y_l \quad (8)$$

where

$$C^j = \frac{1}{2} \sum_{p=1}^N V_p^T [U^T H' U] = [C_{kl}^j] \quad (9)$$

and V denotes the matrix of associated left eigenvectors. If the second order non-resonance condition holds, i.e. if $\lambda_j + \lambda_k = \lambda_l$ for any combination of eigenvalues of A , then the normal form transformation of (8) is defined by [4], [6]

$$Y = Z + h_2(Z) \quad (10)$$

where

$$h_2^j(z) = \sum_{k=1}^N \sum_{l=1}^N h_{2,kl}^j Z_k Z_l \quad (11)$$

$$h_{2,kl}^j = \frac{C_{kl}^j}{\lambda_k + \lambda_l - \lambda_j} \quad (12)$$

In Z-coordinates, the system (8) takes on the form

$$\dot{z}_j = \lambda_j z_j \quad (13)$$

(13) together with the nonlinear (2nd order) transformation (10) describe the simplest 2nd order approximation of the system (6). This procedure can be continued with higher order resonances and corresponding transformation. Large h_2 coefficients describe a strong functional dependence between the corresponding modes. This fact can be seen from writing the solutions of (13) explicitly

$$Z_j(t) = Z_{j0} e^{\lambda_j t} \quad (j=1, \dots, N) \quad (14)$$

The solution for (8) are then given by

$$y_j(t) = Z_{j0} e^{\lambda_j t} + \sum_{k=1}^N \sum_{l=1}^N h_{2_{kl}}' Z_k Z_l e^{(\lambda_k + \lambda_l)t} \quad (15)$$

where z_{j0} is the initial condition of the normal form variable z_j . For the solution of the original system (6), (15) yields

$$x_i(t) = \sum_{j=1}^N u_{ij} Z_{j0} e^{\lambda_j t} + \sum_{j=1}^N u_{ij} \left[\sum_{k=1}^N \sum_{l=1}^N h_{2_{kl}}' Z_k Z_l e^{(\lambda_k + \lambda_l)t} \right] \quad (16)$$

where

$$Y_o = U^{-1} X_o \quad (17)$$

$$Z_o = Y_o - h_2(Z_o) \quad (18)$$

Previous work [3-7] shows that the presence of nonlinear modal interaction has strong impact on system performance. To quantify the extent to which modes interact nonlinearly, use the interaction index (II) defined in [6], [13]. The relative amount of the second-order nonlinearity at mode j can be computed by $\left| \frac{y_j(t)}{z_j(t)} \right|$. By insertion (14) and (15) and some

simplification

$$II^1(j) = \left| \frac{\max_{k,l} h_{2_{kl}}' Z_k Z_l}{Z_{j0}} \right| \quad (19)$$

where $\max_{k,l} h_{2_{kl}}' Z_k Z_l$ is the complex form when the largest values of $|h_{2_{kl}}' Z_k Z_l|$ occurs. This index is also measures of normalized magnitude of nonlinear interaction.

IV. CASE STUDY

The developed procedures are applied to the 2-area, 4-machine test system from [14], modified to consider different operating conditions. Fig. 3 shows a single-line diagram of the system under investigation. The generator data and system parameters are given in the [13], [14].

A. Simulated Conditions

An ample range of operating conditions was simulated to fully characterize nonlinear behavior and modal interaction. To stress the system, the load in Area 2 was increased in discrete steps. The load in Area 1 was then modified to achieve a given tie line power transfer.

From this analysis, two main operating scenarios to

investigate the presence of nonlinear modal interaction were examined: A base condition with a 300-MW power transfer between the interconnected areas and a high stress condition obtained by increasing the level of power transference to about 400 MW. Table I summarizes the operating conditions for the above operating conditions. For 0.31 second one of the lines between buses 5 and 6 is opened and then closed to simulate a fault. Increasing fault-on time to 0.32 second made this system unstable. For the purpose of analysis, a single STATCOM was placed in the system at bus 5. The method introduced in [9, 15] is used to implement STATCOM. For STATCOM T_r is set to .05 second and three STATCOM control gain, $K_r=1, 80, 160$, are used.

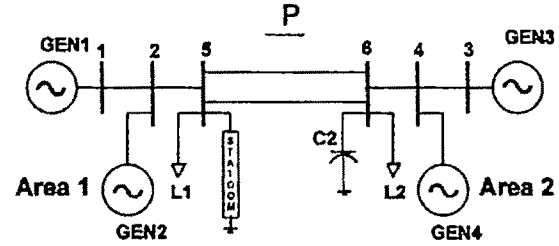


Fig. 3 Schematic of the study system

Table 1 Summary of Operation Conditions

Operation Scenario	Power Transfer (MW)	Load Area 1 (MW)	Load Area 2 (MW)
Base	300	1069	1615
Stressed	400	969	1715

B. Linear Analysis

Table 2 shows the system eigenvalues obtained from linear part of the normal form analysis. These eigenvalues are for base condition and $K_r=1$. Fig. 4 depicts the root-loci of electromechanical modes showing the effect of STATCOM on system damping. It is seen that STATCOM improves the damping of inter-area modes 6 and the local plant mode 4 and has a small positive contribution to the local plant mode 2.

Table 2 Eigenvalues of the test system for the base case and $K_r=1$

Mode	Real Part	Imaginary part
1	-20.5081	0
2,3	-0.11508	± 8.6184
4,5	-0.40051	± 8.6077
6,7	-0.3467	± 2.7
8	0	0
9	-0.3489	0

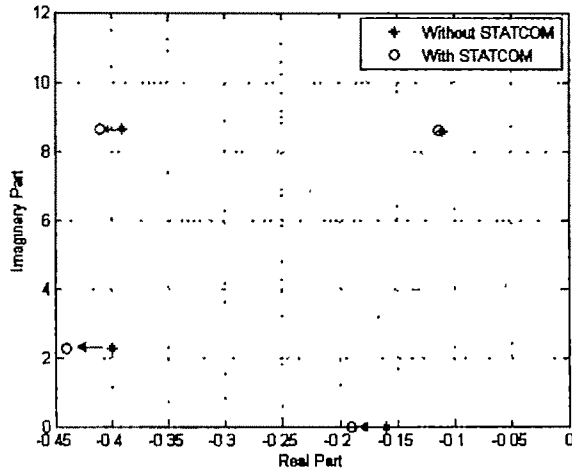


Fig. 4 Root-loci of system electromechanical modes

C. Nonlinear Modal Interaction

The procedure developed in Section III was used to quantify nonlinear modal interaction between the STATCOM control mode and the electromechanical modes. Table 3 synthesizes the two largest second-order normal form coefficients $|h_{2'_{kl}}|$ along with the product $|h_{2'_{kl}} Z_{ko} Z_{lo}|$ associated with critical modes as a function of the STATCOM gain. A large value of the product $|h_{2'_{kl}} Z_{ko} Z_{lo}|$ compared to the term z_j^0 indicates a strong interaction between mode j and modes k and l . The analysis of second-order normal form coefficients in Table 3 reveals a strong nonlinear modal interaction between inter-area mode 6 and the STATCOM control mode 1 especially for high STATCOM gains and stressed operating conditions. The mechanism of interaction was found to be rather complex and depends on several factors such as the control setting and the system operation condition. It is also noted from this analysis that the STATCOM control mode 1 interacts with modes 6 and the local mode 4 revealing the importance of STATCOM on system damping.

Table 4 Nonlinear modal interaction index for Stressed condition

Mode J	$II^1(j)$		
	$K_r=1$	$K_r=80$	$K_r=160$
1	0.0316(9,1)	0.9393(1,6)	1.9080(1,6)
2	0.2081(2,9)	0.1841(6,6)	0.1808(6,6)
4	0.0609(6,6)	0.0845(6,6)	0.087(6,6)
6	1.0320(6,9)	0.2263(6,7)	0.1979(6,7)
9	2.5834(6,7)	4.9907(6,7)	5.0487(6,7)

Table 4 depicts the interaction indices as a function of the STATCOM setting. The analysis of interaction indices confirms previous findings revealing a strong interaction between the STATCOM mode and inter-area mode 6. Clearly, for the study system, interaction coefficients increase for high-gain operation of the STATCOM indicating a greater contribution of the STATCOM to system nonlinear performance. Furthermore, eigenvalues analyses suggest that increased nonlinear interaction actually helps in enhancing system stability. Time domain simulation is presented in Fig.5

for various STATCOM gains and different operation condition for one of the state variables.

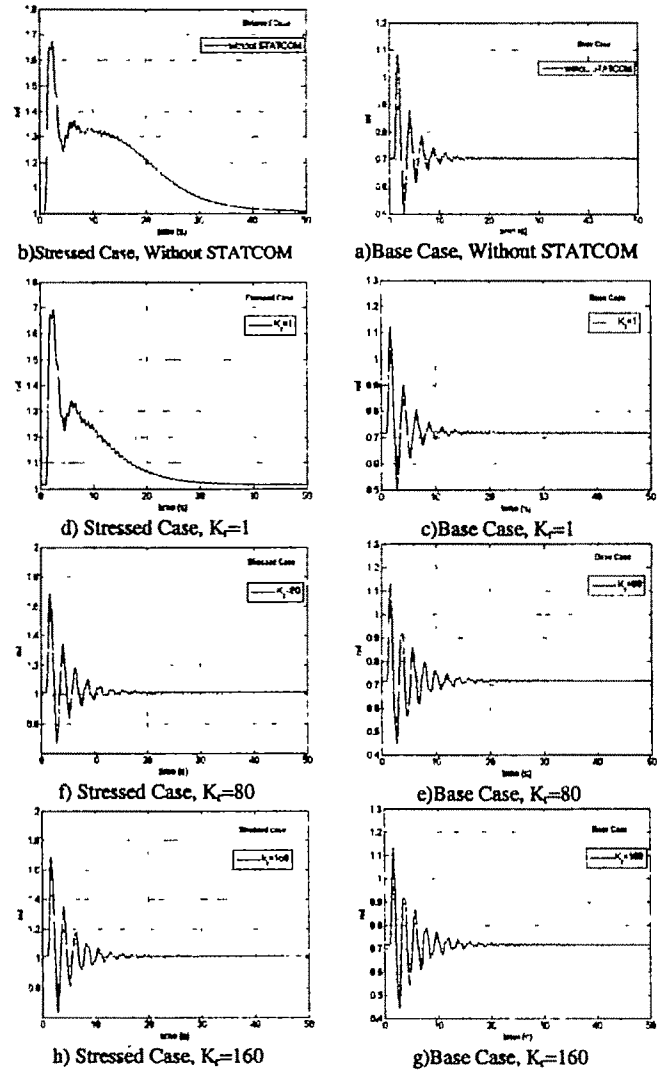


Fig.5 Relative rotor angle of generator 1 in different operation condition and different STATCOM gain

V. CONCLUSION

This paper reports on the experience in the study of nonlinear modal interaction in stressed power systems using STATCOM. A second order representation of the power system is derived that considers the explicit representation of synchronous machines and STATCOM in the state representation. Study experience shows that STATCOM can influence nonlinear system behavior especially under stressed condition and high STATCOM gains. STATCOM's control mode can significantly interact with inter-area mode and also local modes. This modal interaction can actually aid to enhance system stability.

Table 3 Second order non-linear coefficients at different operation conditions and STATCOM gains

Mode	K_r	Base Case		Stressed Case	
		$ h_{2k}^2 $	$ h_{2k}^2 Z_{k0} Z_{k0} $	$ h_{2k}^2 $	$ h_{2k}^2 Z_{k0} Z_{k0} $
1	1	0.0028(2,3)	0.0024(2,3)	0.0015(1,9)	0.0169(1,9)
		0.0024(7,7)	0.0160(6,7)	0.0028(2,3)	0.0150(6,7)
	80	0.1343(1,6)	4.3498(1,6)	0.1823(1,6)	15.7391(1,6)
		0.0696(2,2)	3.8032(1,9)	0.0739(1,9)	14.6289(1,9)
	160	0.2418(1,6)	12.0619(1,6)	0.0247(1,2)	36.9499(1,6)
		0.0861(1,9)	12.0879(1,9)	0.0179(1,4)	32.9458(1,9)
2	1	0.02(2,6)	0.1027(6,6)	0.0069(2,2)	0.2234(2,9)
		0.0161(6,6)	0.0475(2,7)	0.0205(2,7)	0.168(6,6)
	80	0.0098(2,6)	0.1225(6,6)	0.0076(2,3)	0.2818(6,6)
		0.0075(2,3)	0.0415(2,6)	0.0089(6,6)	0.3060(6,6)
	160	0.0057(2,9)	0.0176(2,9)	0.0069(5,4)	0.0953(4,9)
		0.0061(6,6)	0.0144(6,7)	0.0034(6,7)	0.1054(6,6)
4	1	0.0059(4,4)	0.0156(2,9)	0.0014(2,9)	0.1554(6,6)
		0.0059(4,4)	0.0166(2,9)	0.0021(4,6)	0.0241(4,7)
	80	0.0059(4,5)	0.0404(6,6)	0.0016(6,7)	0.1675(6,6)
		0.0059(4,5)	0.0404(6,6)	0.0016(6,7)	0.1675(6,6)
	160	0.0247(2,3)	0.1679(6,9)	0.0975(6,6)	1.4345(6,7)
		0.0203(6,9)	0.3825(6,7)	0.0975(6,7)	3.9580(6,9)
6	1	0.0223(6,7)	0.2733(6,6)	0.0439(6,7)	1.1658(6,7)
		0.0077(6,9)	0.243(6,9)	0.0180(6,9)	1.0979(6,9)
	80	0.0159(6,7)	0.2412(6,6)	0.0338(6,7)	1.1590(6,7)
		0.0056(2,3)	0.2464(6,9)	0.0145(6,9)	1.0493(6,9)
	160	4.3439(2,3)	3.8376(2,3)	26.3(2,3)	30.3059(2,3)
		3.5156(6,7)	22.3751(6,7)	3.82(6,7)	56.1887(6,7)
9	1	0.3711(2,3)	1.2654(2,5)	0.6556(2,3)	1.5355(2,3)
		0.8263(4,5)	47.9543(6,7)	0.2833(3,4)	58.9492(6,7)
	80	0.1327(2,3)	1.6553(2,5)	0.7430(5,5)	2.7538(4,5)
		0.8765(4,5)	57.0314(6,7)	0.0163(4,4)	62.5543
	160				

REFERENCES

- [1]. N. Pariz, H. M. Shanechi, and E. Vaahedi, "Explanation and validation stressed power systems behavior using modal series" *IEEE Transaction on power systems*, vol. 18, pp. 778-785, May 2003.
- [2]. V. Vittal, N. Bhatia, and A. A. Fouad, "Analysis of inter-area mode phenomenon in power systems following large disturbance" *IEEE Transaction on Power System*, vol. 6, no. 4, pp. 1515-1521, Nov. 1991.
- [3]. Starrett, S. K., V. Vittal, A. A. Fouad, and W. Kliemann, "A methodology for the analysis of nonlinear, interarea interactions between power system natural modes of oscillation utilizing normal forms", *Proceedings of the 1993 International Symposium on Nonlinear Theory and Its Application*, Vol. 2, pp. 523-538, Sheraton Waikiki Hotel, Hawaii, December 5-10, 1993
- [4]. C. M. Lin, V. Vittal, W. Kliemann, and A. A. Fouad, "Investigation of modal interaction and its effects on control performance in stressed power systems using normal forms of vector fields," *IEEE Transaction on Power System*, vol. 13, no. 2, pp. 781-787, May 1996.
- [5]. J. Thapar, V. Vittal, W. Kliemann, and A. A. Fouad, "Application of the normal form of vector fields to predict interarea separation in power systems," *IEEE Transaction on Power System*, Vol. 12, no. 2, pp. 844-850, May 1997
- [6]. G. Jang, V. Vittal, and W. Kliemann, "Effect of nonlinear modal interaction on control performance: Use of normal forms technique in control design, Part I, II" *IEEE Trans. Power System*, vol. 13, no. 2, pp. 401-413, May 1998
- [7]. S. Liu, A. R. Messina, and V. Vittal, "Assessing placement of controllers and nonlinear behavior using normal form analysis", *IEEE Trans Power Syst.*, vol. 20, no. 3, pp. 1486-1495, Aug. 2005.
- [8]. H. M. Shanechi, N. Pariz, and E. Vaahedi, "General nonlinear modal representation of large scale power systems," *IEEE Transaction on Power System*, Vol. 18, No. 3, pp. 1103-1109, August 2003.
- [9]. J.J. Sanchez Gasca, V. Vittal, M.J. Gibbard, A.R. Messina, D.J. Vowles, S. Liu, U.D. Annakkage: "Inclusion of higher order terms for small signal (modal) analysis: committee report task force on assessing the need to include higher order terms for small signal (modal) analysis", *IEEE Tran. On power systems*, Vol. 20, No. 4, p.p. 1886-1904, November 2005.
- [10]. E. Barocio, A. R. Messina, "Normal form analysis of stressed power systems: incorporation of SVC models", *Journal Electrical Power and Energy Systems* 25, pp. 79-90, 2003.
- [11]. Anderson, P.M., and A. A. Fouad, *Power System Control and Stability*. New York: IEEE Press, 1994.
- [12]. Chun, L., Qirong, J., Xiaorong, X. and Zhonghong, W., "Rule-based control for STATCOM to increase power system stability", *Power System Technology, Proceedings 1998 International Conference on POWERCON*, pp. 372-376, 1998.
- [13]. Liu, S. "Assessing placement of controllers and nonlinear behavior of Electrical Power System using normal form Information", Ph.D. Thesis, Iowa State University, Ames, Iowa, 2006.
- [14]. Kundur, P., *Power System Stability and Control*. New York: McGraw-Hill Inc., 1994
- [15]. H. F. Wang, "Modeling multiple FACTS devices into multi-machine power systems and applications", *Journal Electrical Power and Energy Systems* 25, pp. 227-237, 2003

A Homogeneous Model of SSSC in Power Network

R. K. Pandey and N. K. Singh

Dept. of Electrical Engineering, Institute of Technology, Banaras Hindu University, Varanasi, India.
Email: rpsneh@yahoo.co.in, nks_ltbhu@yahoo.com

Abstract— In this paper a mathematical model of static synchronous series compensator (SSSC) in a single machine infinite bus power system is proposed. This model can be used for a detailed performance analysis of power system oscillations damping capabilities of SSSC, under different line loading conditions and under different reactive power requirements of the system, and can be used in order to design SSSC based damping controller.

Index Terms— FACTS, SSSC, small signal stability, damping controllers, Phillips-Heffron model.

I. INTRODUCTION

FLEXIBLE AC transmission systems (FACTS), which are the result of recent rapid development in power electronics technology, are being put in use in modern power systems for providing power transmission capacity enhancement and improvement of system stability. With their use it has become easily possible to improve both the dynamic and static performance of the power system [1, 2]. There are many types of FACTS devices, such as Unified Power Flow Controller (UPFC), Static Synchronous Compensator (STATCOM), Static Synchronous Series Compensator (SSSC), Thyristor Controlled Phase Shifter (TCPS), Static Var Compensator (SVC), etc. All of these devices can be used to improve power flow over the transmission line and power system oscillations damping [3, 4]. The SSSC can be implemented through static synchronous voltage source converter (VSC). The VSC is simply an array of solid state switches operated from a dc voltage source so as to produce a three phase set of synchronous, nearly sinusoidal output voltage with independently controllable amplitude and phase angle. From the basic physical law, amplitude and angle control implies the capability of VSC to exchange active and reactive power at its ac output terminals. Since the input terminal of VSC is dc, it clear that only the active power it exchange can be supplied from these terminal. Hence VSC can be considered as an ideal generator that can be operated with small dc capacitor in self-sufficient manner

to exchange reactive power with ac terminal. SSSC is VSC connected in series with power transmission line through a transformer, produces a controllable voltage in quadrature with the line current and has the bi-directional compensation capability i.e. the capability of dynamically changing its reactance characteristic from capacitive to inductive mode. When SSSC inject an ac voltage leading the line current it emulates an inductive reactance in series with transmission line causing power flow as well as the line current to decrease as the level of compensation increases, now SSSC is operating in inductive compensation mode. If SSSC inject an ac voltage lagging the line current it emulates an capacitive reactance in series with transmission line causing power flow as well as the line current to increase as the level of compensation increases, now SSSC is operating in capacitive compensation mode. The SSSC can exchange real power with transmission line, when injected voltage is having an angle other than $\pm 90^\circ$, with line current. The exchange of real power requires the dc terminal of SSSC to be coupled with an energy source or sink. Thus SSSC is one of the important 'FACTS' devices and it can be used for dynamic compensation of power systems to provide voltage support and stability improvement, damping of low frequency power system oscillations [5]. The damping function of SSSC is required to be investigated thoroughly for the proper on line applications in the changing operating point conditions.

The Phillips-Heffron model of power system has been used for decades for the analysis and design of PSS [7, 8]. This paper proposes a mathematical model of STATCOM in single machine infinite bus power network. Here the linearised Phillips-Heffron model of the power system installed with STATCOM, developed by linearizing the non-linear model around operating point is being used. The application of proposed model has been demonstrated by taking an example of SMIB power network

II. SINGLE MACHINE INFINITE BUS NETWORK

Figure 1 show a single machine infinite bus power system installed with SSSC. The SSSC based on pulse width modulation (PWM) technique is being considered, as in figure 1, it consists of a solid-state synchronous voltage-source converter VSC series connected through a transformer BT having leakage reactance X_b and DC capacitor C_{dc} . The

VSC generate a controllable AC voltage. Here m_b and δ_b are the two input control parameter of the SSSC, where m_b - Amplitude modulation ratio and δ_b -Phase angle of series VSC. Figure 2 shows the equivalent circuit of SSSC, where the series connected converter VSC and the transformer BT has been replaced by a synchronous voltage source V_B in series with the transformers leakage reactance X_b .

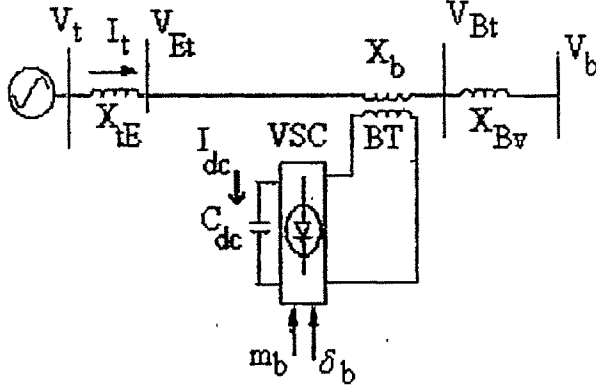


Fig.1 SMIB power network with SSSC.

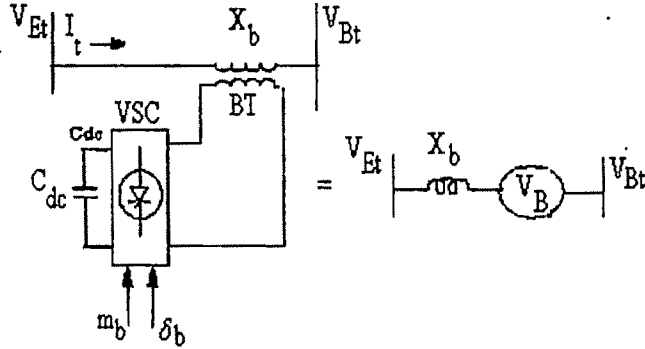


Fig.2 Equivalent circuit of SSSC.

III. PROPOSED MODEL OF SSSC

Consider DC link, phase 'a' of transformer ET and the corresponding arm of VSC-E then the expression for voltage is $V_{Ba} = km_b V_{dc} \cos(\omega t - \delta_b)$, the expression for voltage of phase 'b' and 'c' are similar but have phase shift of $2\pi/3$ and $4\pi/3$ respectively. The dynamics of DC link capacitor is $\frac{dV_{dc}}{dt} = \frac{1}{C_{dc}} I_{dc}$. On applying Park's transformation dynamic model of SSSC is [7]

$$\bar{V}_B = km_b V_{dc} e^{j\delta_b} \quad (1)$$

$$\frac{dV_{dc}}{dt} = \frac{I_{dc}}{C_{dc}} = \frac{km_b}{C_{dc}} [I_d \cos \delta_b + I_q \sin \delta_b] \quad (2)$$

The following expressions from figure 1 are very clearly evident

$$\bar{V}_t = jX_{tE} \bar{I}_t + \bar{V}_{Et} \quad (3)$$

$$\bar{V}_{Et} = \bar{V}_B + jX_{Bv} \bar{I}_t + jX_{Bv} \bar{I}_t + \bar{V}_b \quad (4)$$

$$\bar{V}_t = jE'_q - jI_d X'_d + I_q X_q \quad (5)$$

Making use of above equations from 1 to 5 the d- and q-components of I_E and I_B are obtained as

$$I_d = \frac{1}{X_{bd}} E'_q - \frac{1}{X_{bd}} V_b \cos \delta - \frac{1}{X_{bd}} km_b V_{dc} \sin \delta_b \quad (6)$$

$$I_q = \frac{1}{X_{bq}} V_b \sin \delta + \frac{1}{X_{bq}} km_b \cos \delta_b V_{dc} \quad (7)$$

$$\text{Where } X_{bd} = X_{Bv} + X'_d + X_{tE}$$

$$X_{bq} = X_{Bv} + X_q + X_{tE}$$

The non-linear differential equations from which the well known Phillips-Heffron linear model of a single-machine infinite-bus model is derived [8, 9] are

$$\dot{\delta} = \omega_0 \Delta \omega \quad (8)$$

$$\Delta \dot{\omega} = \frac{(P_m - P_e - D \Delta \omega)}{2H} \quad (9)$$

$$\dot{E}_q = \frac{(-E_q + E_{qe})}{T'_{d0}} \quad (10)$$

$$E_{qe} = \text{Re } g(s)(V_{t0} - V_t) = \frac{K_A (V_{t0} - V_t)}{(1 + sT_A)} \quad (11)$$

$$\text{Where } P_e = \frac{E'_q V_b \sin \delta}{X_{d\Sigma}} - \frac{V_b^2 (x_q - x'_d) \sin 2\delta}{2X_{d\Sigma} X_{qE}}$$

$$E_q = \frac{X_{d\Sigma} E'_q}{X_{d\Sigma}} - \frac{(x_d - x'_d) V_b \cos \delta}{X_{d\Sigma}}$$

$$V_{td} = \frac{x_q V_b \sin \delta}{X_{q\Sigma}}; \quad V_{tq} = \frac{X_L E'_q}{X_{d\Sigma}} + \frac{V_b x'_d \cos \delta}{X_{d\Sigma}}$$

$$X'_{d\Sigma} = x'_d + X_L$$

$$X_{q\Sigma} = x_q + X_L$$

$$X_{d\Sigma} = x_d + X_L$$

Where X_L is the impedance of the transmission line, and the transfer function of the voltage regulator $\text{Reg}(s)$ is assumed to be first order linear loop. When a FACTS device is installed in system above equations, (10) to (13) must be modified in order to analyze the effect of device on the system performance. Linearizing equations (2), (6) and (7) and the non-linear

differential equations (8) to (11) of the power system and making use of the following current equation $I_t = I_d + jI_q$, the linearised model is obtained as

$$\Delta \dot{x} = A\Delta x + B\Delta u \quad (12)$$

Where

$$\Delta x = \begin{bmatrix} \Delta \delta \\ \Delta \omega \\ \Delta E'_q \\ \Delta E_{FD} \\ \Delta V_{dc} \end{bmatrix} \quad \Delta u = \begin{bmatrix} \Delta m_b \\ \Delta \delta_b \end{bmatrix}$$

$$A = \begin{bmatrix} 0 & \omega_0 I & 0 & 0 & 0 \\ -K_1 & -D & -K_2 & 0 & -K_{pd} \\ M & M & M & 0 & M \\ -K_4 & 0 & -K_3 & 1 & -K_{qd} \\ T_{d0} & 0 & T_{d0} & T_{d0} & T_{d0} \\ -K_A K_5 & 0 & K_A K_6 & 1 & K_A K_{vd} \\ T_A & 0 & T_A & T_A & T_A \\ K_7 & 0 & K_8 & 0 & -K_9 \end{bmatrix}$$

$$B = \begin{bmatrix} 0 & 0 \\ K_{pb} & K_{pdb} \\ M & M \\ -K_{qb} & -K_{qdb} \\ T_{d0} & T_{d0} \\ K_A K_{vb} & K_A K_{vdb} \\ T_A & T_A \\ K_{cb} & K_{cdb} \end{bmatrix}$$

From equations (3) and (5), we can write

$$\begin{aligned} V_{Et} &= jE'_q - jI_d X'_d + I_q X_q - jX_{tE} I_t \\ &= jE'_q - jI_d X'_d + I_q X_q - jX_{tE} (I_d + jI_q) \\ V_{Et} &= jE'_q - jI_d X'_d + I_q X_q - jX_{tE} I_d + X_{tE} I_q \end{aligned} \quad (13)$$

Also, we can write

$$\begin{aligned} V_{Et} &= V_B + jX_{bb} I_t + V_b \\ &= (V_{Bd} + jV_{Bq}) + jX_{bb} (I_d + jI_q) \\ &\quad + V_b \sin \delta + jV_b \cos \delta \end{aligned}$$

Where $X_{bb} = X_b + X_{Bv}$

$$\begin{aligned} V_{Et} &= V_{Bd} + jV_{Bq} + jX_{bb} I_d - I_q X_{bb} \\ &\quad + V_b \sin \delta + jV_b \cos \delta \end{aligned} \quad (14)$$

From equations (13) and (14), on equating real and imaginary parts we have

$$V_{Bd} = X_{bq} I_q - V_b \sin \delta \quad (15)$$

$$V_{Bq} = E'_q - X_{bd} I_d - V_b \cos \delta \quad (16)$$

From equation (1) we can write,

$$\bar{V}_B = km_b V_{dc} (\cos \delta_b + j \sin \delta_b) = V_{Bd} + jV_{Bq} \quad (17)$$

Hence from equations (19) on equating real and imaginary parts we can write for SSSC input control parameters m_b, δ_b as,

$$m_b = \frac{\sqrt{V_{Bd}^2 + V_{Bq}^2}}{kV_{dc}} \quad (18)$$

$$\delta_b = \tan^{-1} \left(\frac{V_{Bq}}{V_{Bd}} \right) \quad (19)$$

On placing values from equations (15) and (16) into equations (18), linearizing and making use of the linearised equations for I_q and I_d , after some mathematical manipulations one can write

$$\begin{aligned} N1\Delta m_b + N8\Delta \delta_b &= N9\Delta E'_q \\ &\quad + N10\Delta V_{dc} + N11\Delta \delta \end{aligned} \quad (20)$$

On placing values from equations (15) and (16) into equations (19), linearizing and making use of the linearised equations for I_q and I_d , after some mathematical manipulations one can write

$$\begin{aligned} M5\Delta m_b + M6\Delta \delta_b &= M7\Delta E'_q \\ &\quad + M8\Delta V_{dc} + M9\Delta \delta \end{aligned} \quad (21)$$

From equation (20) and (21), one can write m_b and δ_b in terms of the state variables hence in matrix form

$$[Y][\Delta u] = [Z][\Delta x] \quad (22)$$

$$\text{Where } Y = \begin{bmatrix} N7 & N8 \\ M5 & M6 \end{bmatrix}$$

$$Z = \begin{bmatrix} N11 & 0 & N9 & 0 & N10 \\ M9 & 0 & M7 & 0 & M8 \end{bmatrix}$$

The values of the elements of matrices Y and Z are given in appendix 2.

From equation (22) and equation (12) the following can be written

$$\Delta \dot{x} = A_{NEW} [\Delta x] \quad (23)$$

Where $A_{NEW} = [A + BY^{-1}Z]$

The proposed model, given by equation (23) above, can be used for detailed performance analysis of SSSC installed in single machine infinite bus power network. For the derivation of homogeneous model of SSSC installed in multi-machine system, the same procedure is required to be followed, the difference is while writing equation (3), (5) and (13), (14) due care must be taken, they are required to be written for the multi-machine case.

IV. SIMULATION RESULTS

In order to investigate further and to demonstrate effectiveness of proposed model, an example power system is

Table 1: Eigenvalue obtained from proposed model

0.8pu	1.0e+002 *	1.0e+002 *
	-2.8298	-2.5459
	-0.9061	-0.8592
	-0.0193 + 0.1991i	-0.0322 + 0.1430i
	-0.0193 - 0.1991i	-0.0322 - 0.1430i
1.0pu	1.0e+002 *	1.0e+002 *
	-2.8287	-2.8805
	-0.9081	-0.9055
	-0.0183 + 0.1970i	-0.0168 + 0.1875i
	-0.0183 - 0.1970i	-0.0168 - 0.1875i
1.2pu	1.0e+002 *	1.0e+002 *
	-2.8275	-2.9043
	-0.9103	-0.9132
	-0.0172 + 0.1941i	-0.0156 + 0.1866i
	-0.0172 - 0.1941i	-0.0156 - 0.1866i
1.4pu	1.0e+002 *	1.0e+002 *
	-2.8262	-2.9615
	-0.9126	-0.9221
	-0.0163 + 0.1902i	-0.0105 + 0.1943i
	-0.0163 - 0.1902i	-0.0105 - 0.1943i

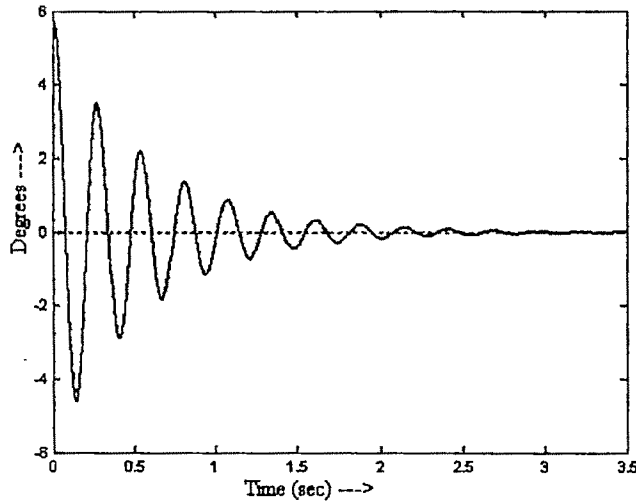


Fig.3: Variation of $\Delta\delta$

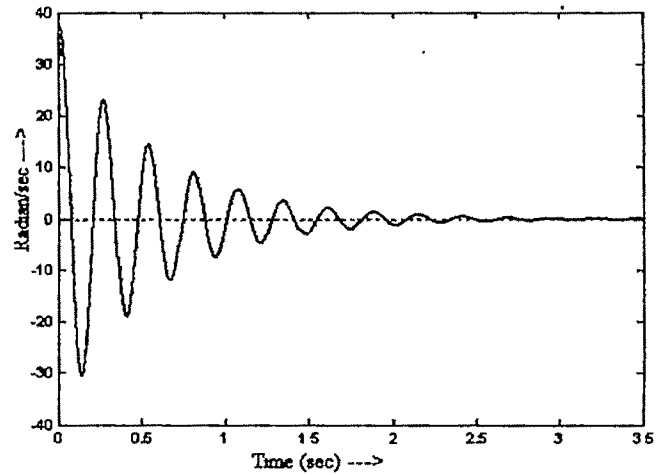


Fig.4: Variation of $\Delta\omega$

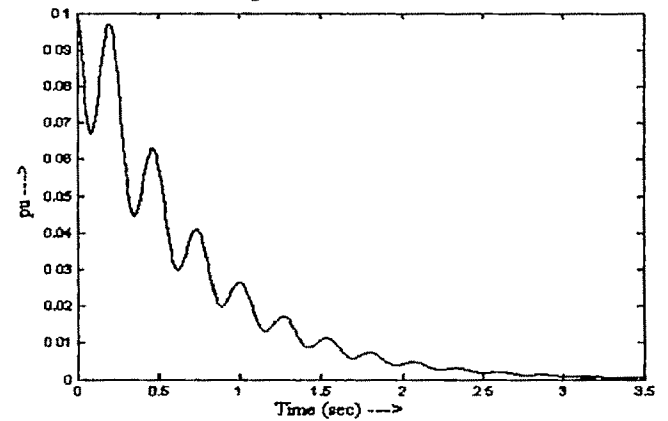


Fig.5: Variation of $\Delta E'_q$

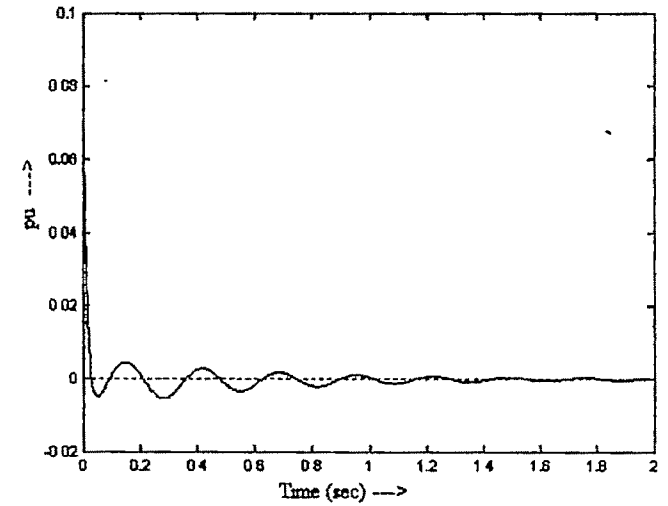


Fig.6: Variation of $\Delta E'_{Fd}$

taken, parameters of which are given in appendix 1, detail performance analysis has been carried out. In any power system, transmission line loading varies over wide range; hence it is extremely important to investigate effect of variation of line loading condition on dynamic performance of system. Keeping in view of this fact, eigenvalue from modified model has been calculated on line loading of 0.8pu, 1.0pu, 1.2pu and 1.4pu, refer to table 1. It has been observed

that eigenvalue as obtained from model of system as given in equation (14), refer to column 2 of table 1, and the eigenvalue as obtained from proposed model of system as written in equation (23), refer to column 3 of table 1, are not having any appreciable difference. This fact strongly establishes and validates effectiveness of proposed model. Figures 3 to 7 show initial condition response of example power system as obtained with proposed model of SSSC.

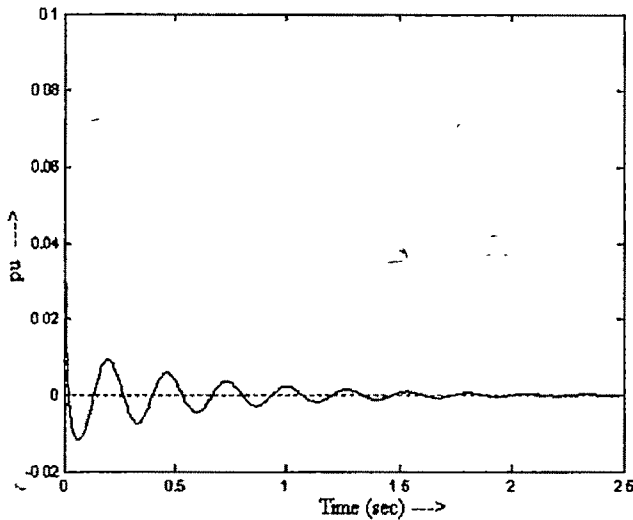


Fig.7: Variation of ΔV_{dc}

V. CONCLUSIONS

This paper presents a mathematical model of SSSC installed in single machine infinite bus system. The proposed model can be used for detailed performance analysis of power system oscillations damping capabilities of SSSC under changing line loading conditions and reactive power requirements of the network. The tuning of the control parameters m_b and δ_b of SSSC can be done utilizing this model. This concept of modeling can be extended on the modular basis for the multi-machine system.

APPENDIX 1

$$\begin{aligned} X_d &= 1.0, X_q = 0.6, X'_d = 0.3, X_e = 0.03, X_b = 0.03 \\ X_{te} &= 0.3, X_{bv} = 0.3, C_{dc} = 300\mu F, V_{dc}^0 = 1.0, \\ E'_q &= 1.024, T_{d0} = 5.044 \text{ sec}, V_b = 1.0, \delta = 40^\circ \\ M &= 8.0, D = 0.0, K_A = 10.0, T_A = 0.01 \text{ sec}, \end{aligned}$$

APPENDIX 2

$$\begin{aligned} N7 &= N1 - N4.D5 - N5.Q5 \\ N8 &= -(N4.D6 - N5.Q6) \\ N9 &= N3 + N4.D1 \\ N10 &= N4.D4 + N5.Q4 - N2 \\ N11 &= N6 + N4.D3 + N5.Q3 \\ M5 &= -(M2.D5 + M3.Q5) \\ M6 &= M1 - M2.D6 - M3.Q6 \\ M7 &= 1 + M2.D1 \\ M8 &= M2.D4 + M3.Q4 \\ M9 &= M4 + M2.D3 + M3.Q3 \end{aligned}$$

The parameters used in above equations are given as under

$$N1 = 2k^2 V_{dc}^2 m_b; \quad N2 = 2k^2 V_{dc} m_b^2$$

$$\begin{aligned} N3 &= 2E'_q - 2V_b \cos \delta - 2I_d X_{bd} \\ N4 &= 2X_{bd}^2 I_d + 2X_{bd} V_b \cos \delta - 2E'_q X_{bd} \\ N5 &= 2X_{bq}^2 I_q - 2X_{bq} V_b \sin \delta \\ N6 &= 2E'_q V_b \sin \delta - 2I_d X_{bd} V_b \sin \delta - 2I_q X_{bq} V_b \cos \delta \\ M1 &= I_q X_{bq} \sec^2 \delta_b - V_b \sin \delta \cdot \sec^2 \delta_b \\ M2 &= -X_{bd}; \quad M3 = -X_{bq} \tan \delta_b \\ M4 &= V_b \sin \delta + V_b \cos \delta \cdot \tan \delta_b \\ D1 &= 1/X_{bd}; \quad D2 = -D1; \quad D3 = D1 V_b \sin \delta \\ D4 &= D2 k m_b \cdot \sin \delta_b; \quad D5 = D2 k V_{dc} \cdot \sin \delta_b \\ D6 &= D2 k m_b V_{dc} \cos \delta_b; \quad Q1 = 1/X_{bq} = Q2 \\ Q3 &= Q2 V_b \cdot \cos \delta; \quad Q4 = Q1 k m_b \cdot \cos \delta_b \\ Q5 &= Q1 k V_{dc} \cdot \cos \delta_b; \quad Q6 = -Q1 k m_b V_{dc} \cdot \sin \delta_b \end{aligned}$$

REFERENCES

- [1] Larsen, E.V., Sanchez-Gasca, J.J., Chow J. H.: "Concept for design of FACTS controllers to damp power swings", IEEE Trans., 1995, PWRS-10(2), pp 948-955.
- [2] Noroozian M., Anderson G.: "Damping of power system oscillations by use of controllable components", IEEE Trans., 1994, PWRD-9, pp. 2046-2054.
- [3] Gyugyi, L., "Dynamic compensation of ac transmission line by solid- synchronous voltage sources", IEEE Trans. On PD., Vol. 9, No. 2, pp. 1994, 904-911.
- [4] Hingorani, N.G., and Gyugyi, L., "Understanding FACTS: concepts and technology of flexible ac transmission systems", IEEE Press, New Jersey, 1999.
- [5] Gyugyi, L., Schauder, C. D. and Sen K. K., Concordia C., "Static Synchronous Series Compensator: a solid state approach to the series compensation of transmission lines", IEEE Trans. on Power Delivery no.1, 1997 pp. 406-417.
- [6] Heffron W.G., Phillips R.A. "Static Synchronous Series Compensator: theory modeling and applications", IEEE Trans. on Power Delivery, no 1, 1998, pp. 241-246.
- [7] Nabavi-Niaki A., Irvani M.R.: "Steady-state and dynamic models of Unified Power Flow Controller (UPFC) for power system studies", IEEE Trans., 1996, PWRS-4, pp. 1937-1943
- [8] DeMello F.P., Concordia C., "Concept of synchronous machine stability as affected by excitation control", IEEE Trans., 1969, PAS-2, pp. 316-329.
- [9] Heffron W.G., Phillips R.A. "Effect of modern amplidyne voltage regulator on under excited operation of large turbine generator", AIEE Trans., 1952, pp. 692-697.
- [10] Kalyan K. Sen and Eric J. Stacey, "UPFC - Unified Power Flow Controller: Theory, Modeling, and Applications," IEEE Transactions on Power Delivery, vol. 13, No. 4, October 1998, pp. 1453-1460.
- [11] Narain G. Hingorani and Laszlo Gyugyi, Understanding FACTS, Concepts and Technology of Flexible AC Transmission Systems, IEEE Press, 2000
- [12] Yu Y.N.: "Electric Power System Dynamics", Academic Press-1983.

SSSC Based Power Oscillation Damping Controller

R. K. Pandey and N. K. Singh

Dept. of Electrical Engineering, Institute of Technology, Banaras Hindu University, Varanasi, India.
Email: rpsneh@yahoo.co.in, nks_itbhu@yahoo.com

Abstract— The paper presents a comparative analysis of the approaches namely Minimum Singular Value (MSV), Hankel Singular Value (HSV), Direct Component of Torque (DCT) and residue for finding the most appropriate control input parameters of Static Synchronous Series Compensator (SSSC) for damping power system oscillations. The basic objective of the paper is to identify the control parameters of SSSC in order to provide damping in power network with changing system conditions. The results presented in this paper are studied widely on single machine infinite bus. The results show the suitability of this approach in tuning the SSSC control parameters.

Keywords—FACTS, SSSC, Damping controllers, Phillips-Heffron model.

I. INTRODUCTION

INCREASED demands on transmission, absence of long-term planning and need to provide open access to generating companies and customers have created tendencies toward less security and reduced quality of supply. The FACTS technology is essential to alleviate some but not all of these difficulties. The FACTS technology opens up new opportunities for controlling power and enhancing usable capacity of present, as well as new and upgraded, lines. The possibility that current and therefore power through a line can be controlled enables a large potential of increasing capacity of existing lines. These opportunities arise through ability of FACTS controllers to control interrelated parameters that govern operation of transmission systems including series impedance, shunt impedance, current, voltage, phase angle and the damping of oscillations. For operational reliability and profitability more efficient utilization and control of existing transmission system infrastructure along with interconnection is required. When large power systems are interconnected by relatively weak tie lines, low frequency oscillations are observed. These oscillations may sustain and grow which may result in system separation in case of inadequate damping. FACTS devices may be beneficial in utilization of existing transmission system infrastructure along with fast damping of low frequency oscillations as well. It has been well recognized

that FACTS devices are adequate for permitting existing transmission corridor to be loaded without degrading both the dynamic and static performance of network. It has been strongly established and proved that these FACTS based stabilizers [1, 2] can offer an alternative choice to power system stabilizers (PSS). There are many types of FACTS devices, such as Unified Power Flow Controller (UPFC), Static Synchronous Compensator (STATCOM), Static Synchronous Series Compensator (SSSC), Thyristor Controlled Phase Shifter (TCPS), Static Var Compensator (SVC), etc. These devices can be used to improve power system oscillations damping [3, 4]. SSSC is solid state voltage source inverter, which generate controllable AC voltage connected in series with power transmission line in power system. The injected voltage is in quadrature with line current and emulates capacitive or inductive reactance so as to have effect on power flow through transmission line [5, 6]. It can be used for effective and efficient power flow control, loop-flow control, enhancement of transient stability, mitigation of low frequency power system oscillations and voltage (reactive power) regulation. The damping capabilities of SSSC need through investigation for proper on line applications in changing operational environment of power network. The Phillips-Heffron model of power system has been used extensively for analysis and design of PSS [7, 8]. For small signal stability studies of single-machine infinite-bus (SMIB) power network, linear model of Phillips-Heffron has been used for years, providing reliable results. Although model is linear, it is quite accurate for studying low frequency oscillations and stability of power systems. It has also been successfully used for designing and tuning classical Power System Stabilizers.

In this paper Phillips-Heffron model of SMIB power system with SSSC, developed by linearising non-linear equations around nominal operating point has been used. Since small signal stability is essentially viewed as stability affected by perturbations valid within boundary of nominal operating point domain, linearised power system model is relevant for system studies mapped in domain of small perturbations. In this paper eigenvalue analysis technique has been used as this is powerful tool for analyzing oscillatory instability and yields information about frequency and damping of each oscillation mode.

II. SSSC IN POWER NETWORK

Figure 1 shows single machine infinite bus power system installed with SSSC. Main circuit of SSSC based on pulse width modulation (PWM) technique consists of series connected transformer BT, solid-state synchronous voltage-source converter (VSC) and DC capacitor C_{dc} . Here m_b and δ_b are two input control parameter of SSSC, where m_b - Amplitude modulation ratio and δ_b - Phase angle of VSC. Figure 2 shows equivalent circuit of SSSC in figure 1, where series connected VSC and transformer BT has been replaced by synchronous voltage source V_B in series with transformers leakage reactance X_b . Considering DC link, phase 'a' of transformer BT and corresponding arm of VSC then expression for voltage is $V_{Ba} = km_b V_{dc} \cos(\omega t - \delta_b)$, here k is constant depends upon converter structure. The expression for voltage of phase 'b' and 'c' for VSC are similar but have phase shift of $2\pi/3$ and $4\pi/3$ respectively. The dynamics of DC capacitor is $\frac{dV_{dc}}{dt} = \frac{1}{C_{dc}} I_{dc}$. On applying Park's transformation on three phase equations of SSSC, dynamic model of SSSC is [9]

$$\bar{V}_B = km_b V_{dc} e^{j\delta_b} \quad (1)$$

$$\frac{dV_{dc}}{dt} = \frac{I_{dc}}{C_{dc}} = \frac{km_b}{C_{dc}} [I_d \cos \delta_b + I_q \sin \delta_b] \quad (2)$$

From figure 1 following expressions can be written

$$\bar{V}_t = jX_{tE} \bar{I}_t + \bar{V}_{Et} \quad (3)$$

$$\bar{V}_{Et} = \bar{V}_B + jX_{Bv} \bar{I}_t + jX_{Bv} \bar{I}_t + \bar{V}_b \quad (4)$$

$$\bar{V}_t = jE'_q - jI_d X'_d + I_q X_q \quad (5)$$

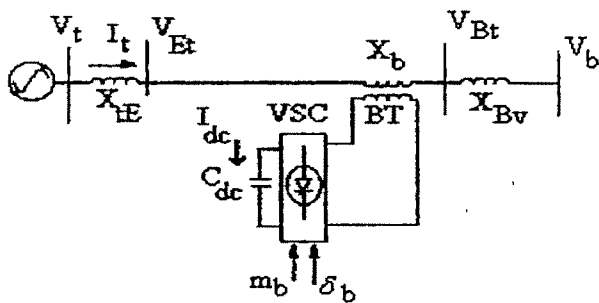


Fig.1 SMIB power network with SSSC

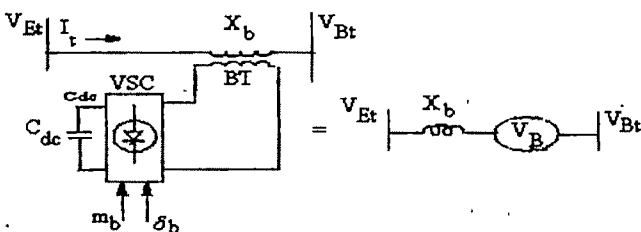


Fig.2 Equivalent circuit of SSSC

Using (1 to 5) d- and q- components of current I_t can be obtained. The non-linear differential equations from which Phillips-Heffron linear model of single-machine infinite-bus is derived [7, 8] are

$$\dot{\delta} = \omega_0 \omega \quad (6)$$

$$\omega = \frac{(P_m - P_e - D \omega)}{2H} \quad (7)$$

$$\dot{E}'_q = \frac{(-E'_q + E_{qe})}{T_{d0}} \quad (8)$$

$$\dot{E}_{qe} = \text{Re } g(s)(V_{t0} - V_t) = \frac{K_A(V_{t0} - V_t)}{(1 + sT_A)} \quad (9)$$

$$\text{Where } P_e = \frac{E'_q V_b \sin \delta}{X_{d\Sigma}} - \frac{V_b^2 (x_q - x'_d) \sin 2\delta}{2X_{d\Sigma} X_{qE}}$$

$$E_q = \frac{X_{d\Sigma} E'_q}{X_{d\Sigma}} - \frac{(x_d - x'_d) V_b \cos \delta}{X_{d\Sigma}}$$

$$V_{td} = \frac{x_q V_b \sin \delta}{X_{q\Sigma}}; \quad V_{tq} = \frac{X_L E'_q}{X_{d\Sigma}} + \frac{V_b x'_d \cos \delta}{X_{d\Sigma}}$$

$$x'_{d\Sigma} = x'_d + x_L; \quad x_{q\Sigma} = x_q + x_L; \quad x_{d\Sigma} = x_d + x_L$$

Where X_L is the impedance of the transmission line, and the transfer function of the voltage regulator $\text{Reg}(s)$ is assumed to be first order linear loop. When a FACTS device is installed in system above equations, (6 to 9) must be modified in order to analyze the effect of device on the system performance.

Linearising (2), equations for d- and q- components of current I_t and the non-linear differential equations (6 to 9) of power system, linearised power system model can be obtained as

$$\Delta \dot{x} = A \Delta x + B \Delta u \quad (10)$$

$$\text{Where } \Delta x = [\Delta \delta \quad \Delta \omega \quad \Delta E'_q \quad \Delta E_{FD} \quad \Delta V_{dc}]^T$$

$$\Delta u = [\Delta m_b \quad \Delta \delta_b]^T$$

This state-space model of SSSC for SMIB power network has been used for detailed damping performance analysis.

III. SELECTION OF INPUT SIGNAL FOR SSSC BASED STABILIZER

The damping controllers are designed to produce an electrical torque in phase with speed deviation. The adequate design of SSSC controller is essential to have an effective oscillation damping for reliable system operation. This necessitates proper methodology for tuning control parameters of SSSC, in this process it is required to select most effective control input parameter out of two input parameters of SSSC, i.e., m_b and δ_b to be modulated as dynamical conditions are changing in network in order to arrive at effective and robust damping control design criterion. The speed deviation $\Delta \omega$ is considered as input to damping controllers. Two types of SSSC based damping controllers are defined based on signal contribution such as damping controller based on SSSC control parameter m_b will be named as damping controller- m_b , damping controllers based on δ_b will be named as

damping controller- δ_b , respectively. In this paper a method is proposed for the selection of most suitable control input signal for mode of oscillation under consideration. The proposed method uses minimum singular value (MSV), hankel singular value (HSV), direct component of torque (DCT) and residue as indicators to find most effective control input signal.

A. Minimum Singular Value (MSV)

To measure controllability of oscillation mode by given input, concept of singular value decomposition (SVD) [10] can be used. Mathematically, if G is an $m \times n$ complex matrix then there exist unitary matrices W and V with dimensions of $m \times m$ and $n \times n$ respectively such that G can be written as

$$G = W \Sigma V^H, \text{ where } \Sigma = \begin{bmatrix} \Sigma_1 & 0 \\ 0 & 0 \end{bmatrix}; \text{ this is } m \times n \text{ matrix and } \Sigma_1 \text{ defined as } \Sigma_1 = \begin{bmatrix} \sigma_1 & 0 & \dots & 0 \\ 0 & \sigma_2 & \dots & 0 \\ \vdots & \vdots & \ddots & \vdots \\ 0 & 0 & 0 & 0 \end{bmatrix}, \text{ where } r = \min \{m, n\}$$

and $\sigma_1, \dots, \sigma_r$ are singular values of G , placed diagonally in descending order, i.e. $\sigma_1 \geq \sigma_2 \geq \dots \geq \sigma_r$. This property can be utilized to comment on modal controllability. In present case, matrix B in (10) can be written as $B = [B_1, B_2]$ where B_i is column matrix corresponding to i -th input. The minimum singular value of matrix $[sI - A : B_i]$ indicates capability of i -th input to control mode associated with eigenvalue λ . Thus minimum singular value of matrix $[sI - A : B_i]$ corresponding to two inputs of SSSC can be calculated. The input that has highest value of minimum singular value corresponding to it will be selected as most effective and responsive input parameter for design of SSSC based damping controller.

B. Hankel Singular Value (HSV)

In control theory, eigenvalue define system stability, whereas Hankel singular values define "energy" of each state in system. In order to find which combination of input-output contains more information about internal states of system, one possible method can be calculation of controllability and observability indices of system such as Hankel Singular Value (HSV). Mathematically, for stable state-space system (A, B, C, D) , Hankel singular values are defined as $\sigma_H = \sqrt{\lambda_i(PQ)}$, where P and Q are Controllability and Observability Grammians satisfying relation $AP + PA^T + BB^T = 0$ and $A^T Q + QA + C^T C = 0$. For selecting most suitable input parameter, HSV corresponding to each input m_b, δ_b can be calculated, input having highest value of HSV corresponding to it can be selected as most suitable input signal.

C. Direct Component of Torque (DCT)

The damping torque contribution [11] from SSSC based damping controller to electromechanical oscillation loop is

$\Delta T_D = T_D \omega_0 \Delta \omega$, where T_D is damping torque coefficient.

From figure 3 it is seen that damping torque contribution by SSSC based damping controller have a part of it which directly applies into electromechanical oscillation loop of generator and its sensitivity can be measured by coefficient K_P , this can be taken as direct component of torque (DCT) and other part of it applies through field circuit of generator and its sensitivity is related to deviation of field voltage is much smaller as compared to DCT because it is attenuated by two filters before it forms damping torque. This fact can be utilized to select most appropriate input of SSSC. The input that has highest value of DCT corresponding to it can be selected as most effective input parameter.

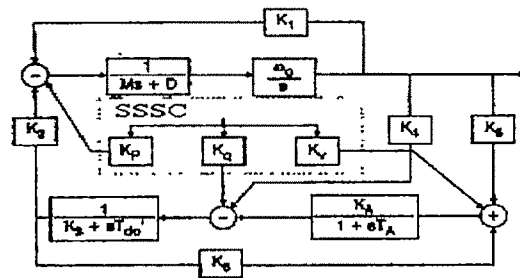


Fig.3: Phillips-Hefron model of power system with SSSC.

D. Residue

The state space equation for power system with SSSC is

$\Delta \dot{x} = A \Delta x + B \Delta u$. For any eigenvalue $\lambda_i = -\sigma_i \pm j\omega_i$, the oscillation mode of interest, there is right-eigenvector ϕ_i satisfying equation $A\phi_i = \lambda_i\phi_i$ and left-eigenvector ψ_i satisfying equation $\psi_i A = \lambda_i\psi_i$. The i^{th} mode is controllable by j^{th} input if product of $\psi_i B_j$ defined as controllability index is non zero and i^{th} mode is observable in j^{th} output if product of $C_j \phi_i$ defined as observability index is non zero. A mode of interest must be controllable by selected input and observable in selected output for control to have effect on mode of oscillation. A scalar quantity R_i defined as residue of particular mode i , product of mode's controllability and observability index, will give measurement of mode's sensitivity to feedback between output and input. The figure 4 shows closed loop system where $G(s)$ represent power system and $H(s)$ represent SSSC based damping controller. The transfer function $H(s)$ of damping controller can be taken as $H(s) = KH_1(s)$, where K is positive constant gain and $H_1(s)$ is transfer function of controller's blocks. The objective of SSSC based power oscillation damping controller is to improve damping ratio of selected oscillation mode i by changing eigenvalue λ_i . Hence change in eigenvalue $\Delta \lambda_i$ must be real negative value in order to move real part of eigenvalue λ_i to left half of complex plane. From figure 4,

change in eigenvalue λ_i after action of damping controller can be represented as $\Delta\lambda_i = R_i K H_i(\lambda_i)$. Hence, for same value of gain of feedback loop larger value of residue will provide larger change in corresponding mode of oscillation. Hence it can be concluded that best signal for damping controller is one which has largest residue for mode of oscillation under consideration. The input that has highest value of residue corresponding to it can be selected as most responsive control input parameter.

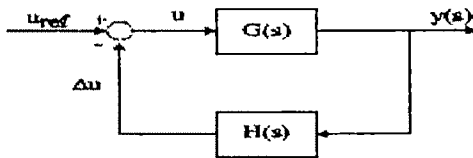


Fig. 4: Closed loop system with SSSC-based damping controller

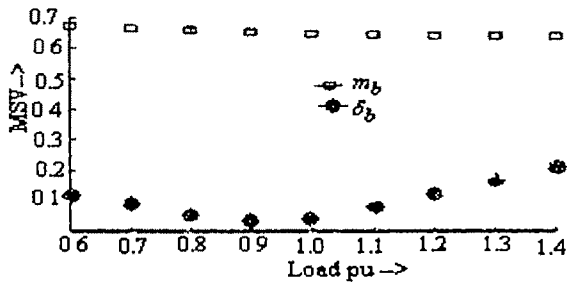


Fig 5: MSV corresponding to parameters of SSSC

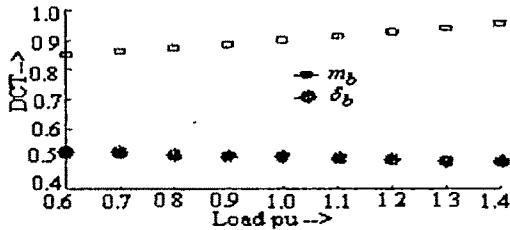


Fig.6: DCT corresponding to parameters of SSSC

The figure 5 to 8 shows variations of MSV, DCT, Residue and HSV corresponding to input of SSSC. It is seen from figure 5 to 8, that MSV, DCT, Residue and HSV corresponding to input m_b is highest hence controllability of oscillation mode through this input is much better as compared to other input, thus it can be concluded that, this is most effective input parameter to be modulated while designing SSSC based damping controller. It is seen from figure 6 that DCT corresponding to input m_b of SSSC increases as load increases, hence it can be proposed that controllability of oscillation mode with damping controller- m_b get improved with increase in line loading, i.e. the damping performance of this controller is improving as line loading is increasing. It is also seen that range of change in MSV and DCT corresponding to input m_b is much smaller as compared to range of change in these values corresponding to input δ_b , thus

it can be concluded that damping performance of damping controller- m_b is much more robust as compared to that of damping controller- δ_b , as far as change in line loading is concerned.

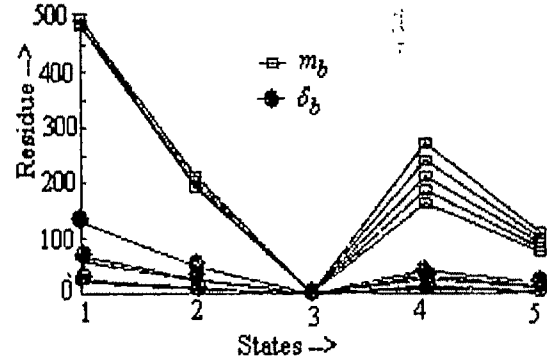


Fig.7: Residue corresponding to parameters of SSSC

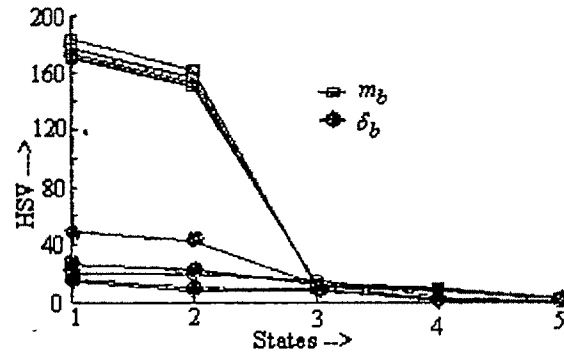


Fig.8: HSV corresponding to parameters of SSSC

IV. SIMULATION RESULTS

In order to investigate further and to demonstrate proposed method for selection of most appropriate control input parameters of SSSC, an example power systems – single machine infinite bus has been considered for study, parameters of which are given in appendix, detailed performance analysis of above two SSSC based damping controllers has been carried out. In any power system, transmission line loading varies over wide range, hence it is extremely important to investigate effect of variation of loading condition on dynamic performance of system. Keeping in view of this fact, response of system under consideration has been obtained. Figures 9 and 10 show response of $\Delta\delta$ state of system as obtained with above proposed two types of SSSC based damping controllers, over wide variation in loading condition from 0.6pu to 1.4pu. It can be clearly observed and concluded from response shown in figure 9 and 10, that any of SSSC based damping controller provide satisfactory performance over wide range of variations in loading conditions. From figure 10 for damping controller- δ_b it is observed that responses are hardly affected in terms of settling time, but this is not case with damping controller- m_b , there is an appreciable change in settling time of response with variations of line loading. From response, as in figure 9 and 10 for damping controller- m_b and damping controllers- δ_b

respectively, it is observed that there is an appreciable larger change in final operating point of system with variations of line loading in case of damping controllers- δ_b as compared to that with damping controller- m_b . Hence one may conclude that damping controller- m_b has highest controllability over the oscillation mode of interest, which is evident from maximum value of MSV, HSV, DCT and Residue corresponding to input m_b , and damping performance of damping controller- m_b is much more robust as compared to that of damping controller- δ_b , which is evident from smaller range of change in MSV with line loading, corresponding to input m_b .

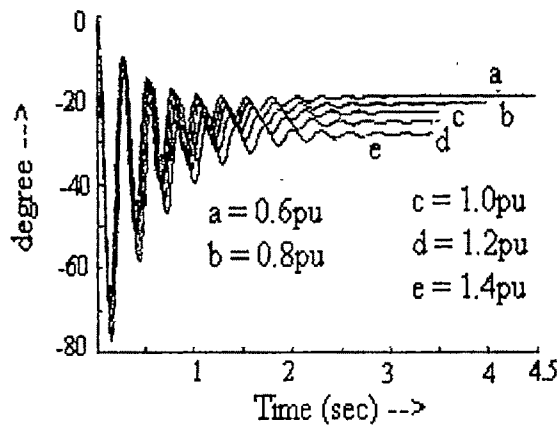


Fig.9: $\Delta\delta$ with damping controllers- m_b

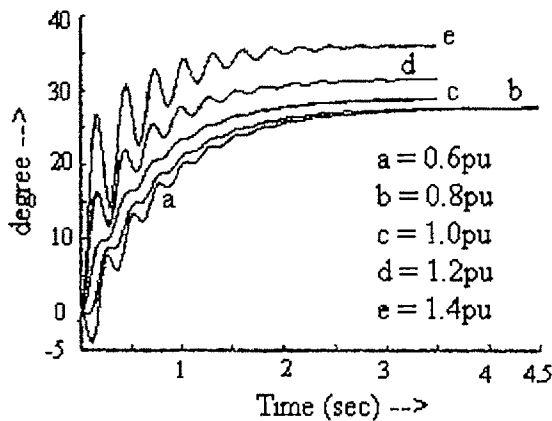


Fig.10: $\Delta\delta$ with damping controller- δ_b

V. CONCLUSIONS

This paper presents an investigation into the selection of most appropriate control parameter of SSSC to ensure adequate damping as dynamic changes occur in power network. This has been done by comparative analysis through various analytical techniques such as MSV, HSV, DCT and Residue based approaches. In this paper, power system stability enhancement with use of SSSC based damping controllers, i.e., damping controller- m_b and damping controller- δ_b has been investigated and it has been found that

damping controller- m_b has highest controllability over oscillation mode of interest and as far as robustness of damping controllers to wide variations of line loading conditions is concerned damping controller- m_b is more appropriate damping controllers as compared to damping controller- δ_b .

APPENDIX

$$X_d = 1.0, X_q = 0.6, X_d' = 0.3, X_e = 0.03, X_b = 0.03$$

$$X_{IE} = 0.3, X_{BV} = 0.3, C_{dc} = 300 \mu F, V_{dc}^0 = 1.0,$$

$$E_q' = 1.024, T_{d0}' = 5.044 \text{ sec}, V_b = 1.0, \delta = 40^\circ$$

$$M = 8.0, D = 0.0, K_A = 10.0, T_A = 0.01 \text{ sec},$$

REFERENCES

- [1] Larsen, E.V., Sanchez-Gasca, J.J., Chow J. H.: "Concept for design of FACTS controllers to damp power swings", IEEE Trans., 1995, PWRS-10(2), pp. 948-955.
- [2] Noroozian M., Anderson G.: "Damping of power system oscillations by use of controllable components", IEEE Trans., 1994, PWRD-9, pp. 2046-2054.
- [3] Gyugyi, L., "Dynamic compensation of ac transmission line by solid- synchronous voltage sources", IEEE Trans. On PD., Vol. 9, No. 2, pp. 1994, 904-911.
- [4] Higorani, N.G., and Gyugyi, L., "Understanding FACTS: concepts and technology of flexible ac transmission systems", IEEE Press, New Jersey, 1999.
- [5] Gyugyi, L., Schauder, C. D. and Sen K. K., Concordia C., "Static Synchronous Series Compensator : a solid state approach to the series compensation of transmission lines", IEEE Trans. on Power Delivery no 1, 1997 pp. 406-417.
- [6] Heffron W.G., Phillips R.A. "Static Synchronous Series Compensator . theory modeling and applications", IEEE Trans. on Power Delivery, no. 1, 1998, pp. 241-246.
- [7] DeMello F.P., Concordia C., "Concept of synchronous machine stability as affected by excitation control", IEEE Trans., 1969, PAS-2, pp. 316-329.
- [8] Heffron W.G., Phillips R.A. "Effect of modern amplidyne voltage regulator on under excited operation of large turbine generator", AIEE Trans , 1952, pp 692-697
- [9] Nabavi-Niaki A , Irvani M.R . "Steady-state and dynamic models of Unified Power Flow Controller (UPFC) for power system studies", IEEE Trans., 1996, PWRS-4, pp 1937-1943.
- [10] A. M. A. Hamdan, "An Investigation of the Significance of Singular Value Decomposition in Power System Dynamics," Int. Journal of Electrical Power and Energy Systems, Vol. 21, 1999, pp. 417-424.
- [11] Yu Y.N., "Electric Power System Dynamics", Academic Press-1983

Technical Session 2B

Biomedical Signal Processing

Erythrocyte Shape Investigation and Analysis Using Image Processing Technique

Umalakshmi A¹, Rajeshwari S¹, Sandhya Rao¹, Shilpa G.S¹, Mallikarjuna Swamy M.S²,
Manjunatha M³ and Mallikarjun S. Holi¹

¹Dept of Biomedical Engg, Bapuji Institute of Engg and Technology, Davangere-577004, Karnataka, India. e-mail: msholi@yahoo.com

²Dept. of Instrumentation Tech., Sri Jayachamarajendra College of Engg, Mysore-570006, Karnataka, India. e-mail:
ms_muttad@yahoo.co.in

³Dept. of Instrumentation Tech, Bapuji Institute of Engg and Tech., Davangere-577004, Karnataka, India e-mail. m_manj@yahoo.com

Abstract— Erythrocytes or RBC's (Red Blood Corpuscles) are circular, biconcave, non-nucleated discs which carry the oxygen throughout the body. An abnormality of any kind in the RBC's usually become fatal; especially the shape of the corpuscles on the whole should be normal for proper intake of oxygen, to be carried throughout the body for metabolic activity. The objective of the current work is to investigate and analyse the erythrocyte shape in normal and disease state by image processing techniques. The peripheral blood smear slides of normal subjects and patients suffering from anemia and jaundice are collected. Images of these slides were obtained by using the trinocular research microscope fitted with a camera which is interfaced to the computer for digitization. The acquired images are processed by median filtering, Gaussian filtering, edge detection and thresholding to obtain the binary image to find the shape of RBC. To analyze the shape of the erythrocyte, the edges which are the areas with strong intensity contrast is found by implementing Canny edge detection algorithm, which is a multistage process, where the first step is to filter out any noise in the original image by using Gaussian filter. The next step is to find the edge strength by taking the gradient of the image. It is found from the results that there is a significant change in the shape of erythrocytes, area of the cell (A), perimeter (P) and form factor (FF) under normal and diseased condition. There is significant difference in the all the parameters for normal and diseased cells. The image processing algorithm developed in the present work is found to be very useful in the diagnosis of several diseases in which shape of the erythrocyte will change with pathologic condition.

Key words— Canny edge detection, Erythrocyte, Form factor, Median Filtering.

I. INTRODUCTION

NORMAL RBC's are circular in shape from the front view, discoid or dumb-bell shaped from the side view, 6-8 μ m in diameter, and have a central pallor due to their biconcave shape. Target cells are pathological RBC's having a dark center surrounded by a light band which is encircled by a

darker ring. It may be caused by increased cholesterol and lecithin content, bile insufficiency, liver disease, splenectomy or anemia. Sick cell disease is an inherited blood disorder that is caused by the presence of a mutation in the gene that encodes for the protein, haemoglobin. A little change in haemoglobin causes it to form long rods in the RBC when it gives away oxygen. These rigid rods change the red cell into a sickle cell. There are several *in vivo* mechanisms, which induce changes in erythrocyte membrane lipids and proteins and their interior, leading to alteration in erythrocyte shape, which in turn affects the deformability [1]. Hypercholesterolemic process induces changes in the erythrocyte membrane. This is primarily attributed to accumulation of cholesterol in the membrane. These observations show that the gradual change in erythrocyte shape, as observed microscopically, may reflect the effect of cholesterol in the arterial vessels [2]. Erythrocyte deformability is an inherent property attributed to the size and shape of these cells. Basically, the erythrocytes contain excess surface area than that required to hold their volume and thus allowing these cells to undergo various shape transformations while flowing through the cardiovascular system. Any deviation from the discoidal shape alters the deformability of these cells. Hence variation in morphometric parameters such as surface area and perimeter may show the extent of changes in the flow properties of these cells [2].

II. METHODOLOGY

The peripheral blood smear slides of patients suffering from anemia and jaundice are collected. Images of these slides were obtained by using the trinocular research microscope fitted with a camera and interfaced to the computer for digitization as shown in Fig.1. In order to obtain a clearer image, the slides were oil immersed [3]. The level of magnification of the various lenses in the microscope and camera are as follows; objective lens-100x, eye piece-10x, camera lens-5x, total magnification-5000x.

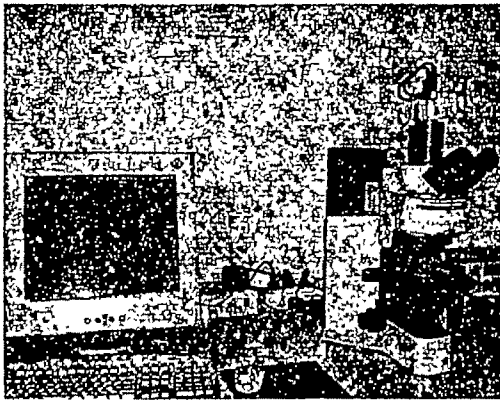


Fig.1 Trinocular research microscope fitted with a camera and interfaced to computer.

The sequence of operations in proposed algorithm to analyse the shape of the erythrocytes is shown in Fig. 2.

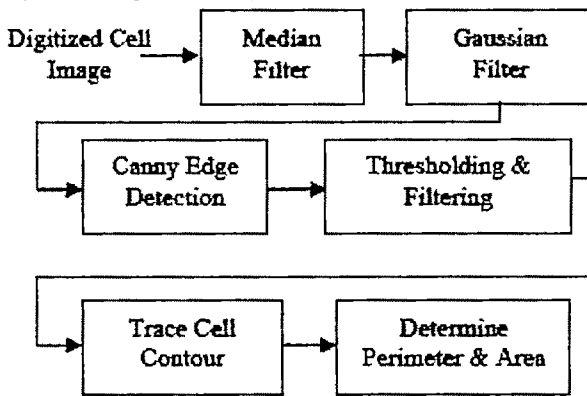


Fig.2 The sequence of operations implemented to analyse the shape of erythrocyte.

A. Median Filter

Filtering is a non-linear signal enhancement technique for the smoothing of signals, the suppression of impulse noise, and preserving the edges. It is implemented to an image using a mask of odd length, the mask moves over the image and at each center pixel the median value of the data within the window is taken as the output [4].

The median filter considers each pixel in the image in-turn and looks at its nearby neighbours to decide whether or not it is representative of its surroundings. Instead of simply replacing the pixel value with the mean of neighbouring pixel values, it replaces it with the median of those values. When performing median filtering, each pixel is determined by the median value of all pixels in a selected neighborhood. The median is calculated by first sorting all the pixel values from the surrounding neighborhood into numerical order and then replacing the pixel being considered with the middle pixel value [4].

B. Gaussian Filter

The Gaussian smoothing operator is a 2D convolution operator. The Gaussian filter uses a kernel that represents the

shape of the Gaussian (bell shape) curve. A 2D isotropic [i.e. circularly symmetric] Gaussian has the form;

$$G(x, y) = (1/2\pi\sigma^2) \exp(-(x^2 + y^2)/2\sigma^2) \quad (1)$$

The idea of Gaussian smoothing is to use 2D distribution as a point spread function, this is achieved by convolution of pixels, we have to produce the discrete approximation of Gaussian function before convolution. Theoretically, Gaussian distribution is non-zero everywhere, requiring infinitely large convolution kernel. But practically it is effectively zero and more than 3 standard deviation from the mean, so we can truncate the kernel at this point. The degree of smoothing is determined by the standard deviation of the Gaussian. Gaussian filter outputs a 'weighted average' of each pixel neighborhood, with the average weighted more towards the value of the central pixels. Thus, produces greater smoothing and preserves edges. The size of Gaussian kernel mask is a function of the parameter, ' σ ', and size of the kernel mask determines the range of frequencies that are removed by the Gaussian filter.

C. Edge Detection

Edges in images are areas with strong intensity contrasts – a jump in intensity from one pixel to the next. Edge detecting an image significantly reduces the amount of data and filters out useless information, while preserving the important structural properties in an image.

D. Canny Edge Detection

This is a multi-step edge detection procedure considered to be the ideal edge detection algorithm for images that are corrupted with white noise. The optimality of it is related to three criteria:

- Detection criterion expresses that important edges should not be missed and there should be no spurious responses.
- Localization criterion says that the distance between the actual and located position of the edge should be minimal.
- One response criterion minimizes multiple responses to a single edge (i.e. when there are two responses to a single edge one of them should be considered as false).

The Canny edge detector is used for detection of the edges (segmentation) and gives the result as the contour of the cell. Algorithm of Canny edge detection technique is as follows:

- a. The noise is filtered out using Gaussian filter.
- b. Image edges are detected using Sobel edge detector by selecting a small window (mask) of size (n×n) from original array and set threshold value for edge detection.
- c. Multiply all the elements of window with gradient operators and sum the results.
- d. If the sum is greater than threshold, edge is detected, so retain this value and otherwise it will be zero, due to the property of masks.
- e. Repeat above steps for the whole area.
- f. End of algorithm.

Based on these criteria, the Canny edge detector first smoothens the image to eliminate the noise and later finds the

image gradient to highlight regions with high spatial derivatives. The algorithm then tracks along these regions and suppresses any pixel that is not at the maximum. The gradient array is now further reduced by hysteresis. Hysteresis is used to track along the remaining pixels that have not been suppressed. Hysteresis uses two thresholds and if the magnitude is below the first threshold, it is set to zero (made a nonedge). If the magnitude is above the high threshold, it is made an edge. If the magnitude is between the 2 thresholds, then it is set to zero unless there is a path from this pixel to a pixel with a gradient above threshold 2.

E. Stages of the Canny Edge Detection Algorithm

Noise Reduction: The first step is to filter out any noise in the original image before trying to locate and detect any edges. So the Gaussian filter can be computed using a simple mask, it is used exclusively in the Canny algorithm. Once a suitable mask has been calculated, the Gaussian smoothing can be performed using standard convolution methods. A convolution mask is usually much smaller than the actual image. As a result, the mask is slid over the image, manipulating a square of pixels at a time. The larger the width of the Gaussian mask, the lower is the detector's sensitivity to noise. The localization error in the detected edges also increases slightly as the Gaussian width is increased. **Edge Strength Detection:** After smoothing the image and eliminating the noise, the next step is to find the edge strength by taking the gradient of the image. The Sobel operator performs a 2D spatial gradient measurement on an image. Then, the approximate absolute gradient magnitude (edge strength) at each point can be found [4].

Sobel Edge Detection: The sobel operator performs a two dimensional special gradient measurement on an image and so emphasizes regions of high spatial gradient that corresponds to edges. The most commonly used method of differentiation (sharpening) in image processing applications is the gradient. The gradient magnitude gives the amount of the difference between pixels in the neighborhood (the strength of the edge). The gradient orientation gives the direction of the greatest change, which presumably is the direction across the edge (edge normal). The value of the gradient is proportional to the difference in gray level between adjacent pixels. The gradient operation reduces all the constant white regions to zero [black], leaving only the points associated with the abrupt changes in gray level. The Sobel operator uses a pair of 3x3 convolution masks, one estimating the gradient in the x-direction (columns) and the other estimating the gradient in the y-direction (rows). They are shown as Sobel masks as in Fig 3 and Fig.4. The G_x gives the derivative in the x-direction and G_y gives the derivative in the y-direction. The magnitude, or edge strength, of the gradient is then approximated using the formula:

$$G = |G_x| + |G_y| \quad (2)$$

Z_1	Z_2	Z_3
Z_4	Z_5	Z_6
Z_7	Z_8	Z_9

Fig. 3 A 3x3 region of an image (z's are the gray level values).

-1	-2	-1
0	0	0
1	2	1

G_x

-1	0	1
-2	0	2
-1	0	1

G_y

Fig. 4 Sobel masks for horizontal and vertical direction.

For finding the direction we use;

$$\alpha(x, y) = \tan^{-1}((\partial f / \partial y) / (\partial f / \partial x)) \quad (3)$$

Non-maximum Suppression: After the edge directions are known, non-maximum suppression now has to be applied. Non-maximum suppression is used to trace along the edge in the edge direction and suppress any pixel value (sets it equal to 0) that is not considered to be an edge. This will give a thin line in the output image.

Hysteresis: Hysteresis is used as a means of eliminating streaking. Streaking is the breaking up of an edge contour caused by the operator output fluctuating above and below the threshold. If a single threshold, $T1$ is applied to an image, and an edge has an average strength equal to $T1$, then due to noise, there will be instances where the edge dips below the threshold. Equally it will also extend above the threshold making an edge look like a dashed line. To avoid this, hysteresis uses 2 thresholds, a high and a low i.e. $T1$ and $T2$ with $T1 > T2$. Any pixel in the image that has a value greater than $T1$ is presumed to be an edge pixel. If the pixel value is below $T2$ is set to zero. And if the magnitude is between the 2 thresholds, then it is set to zero unless there is a path from this pixel to a pixel with a gradient above $T2$.

Thresholding: For the calculated gradient to be declared as an edge, the value should above a certain threshold. So the number of pixels declared as edges would be dependent on the threshold. There is no specific algorithm for choosing a threshold. The threshold is dependent on the image and the mask. Hence, the threshold is not a constant factor.

F. Calculation of Perimeter, Area and Form Factor:

For calculation of area (A), the contour of the cell is filled up with pixels. By counting the number of these and multiplying with pixel area, the area of the cell is determined. Similarly, by counting the number of pixels along the perimeter (P) and then multiplying with pixel length, the

perimeter of the same cell is determined. Based on these, the ratio P/A and the form factor (FF) are calculated.

$$\text{Form Factor} = \frac{P^2}{4\pi A} \quad (4)$$

The parameter FF is the measure of compactness or roundness of the cell and its variation indicates the deviation of the shape in the image from that of a normal cell [5].

III RESULTS AND DISCUSSION

The results obtained after the implementation of the algorithm are as shown in the Table 1 and Table 2, and in Fig.5. It is observed that there is a significant difference in the values P , A and P/A parameters between normal and diseased cells ($p < 0.001$). The parameter FF is found to be one of the best parameters which significantly differentiate the normal and diseased cells ($p < 0.0001$) and can be used as one of the diagnostic parameters. The algorithm has also been implemented for the study of the shape of sickle cells and the parameters calculated are found to be significantly different from that of normal cells [6].

Table 1. The parameters calculated for normal cell images obtained from trinocular microscope.

Normal Cells n=3	P (μm)	A (μm^2)	P/A	Form Factor (FF)
Sub 1	201.5	3916.8	0.051	0.825
Sub 2	203.4	3871.9	0.053	0.850
Sub 3	196.6	3538.3	0.056	0.858
mean	200.5	3775.7	0.053	0.844
SD	3.508	206.8	0.003	0.017

Table 2 The parameters calculated for target cell images obtained from trinocular microscope.

Target cells n=3	Pathology	P (μm)	A (μm^2)	P/A	Form Factor (FF)
Sub 1	Malaria	242.2	5806.9	0.042	0.803
Sub 2	Jaundice	244.2	5745.4	0.043	0.825
Sub 3	Hemolytic anemia	214.6	4674.6	0.046	0.784
mean	-	233.7	5408.9	0.044	0.804
SD	-	16.5	636.7	0.002	0.021

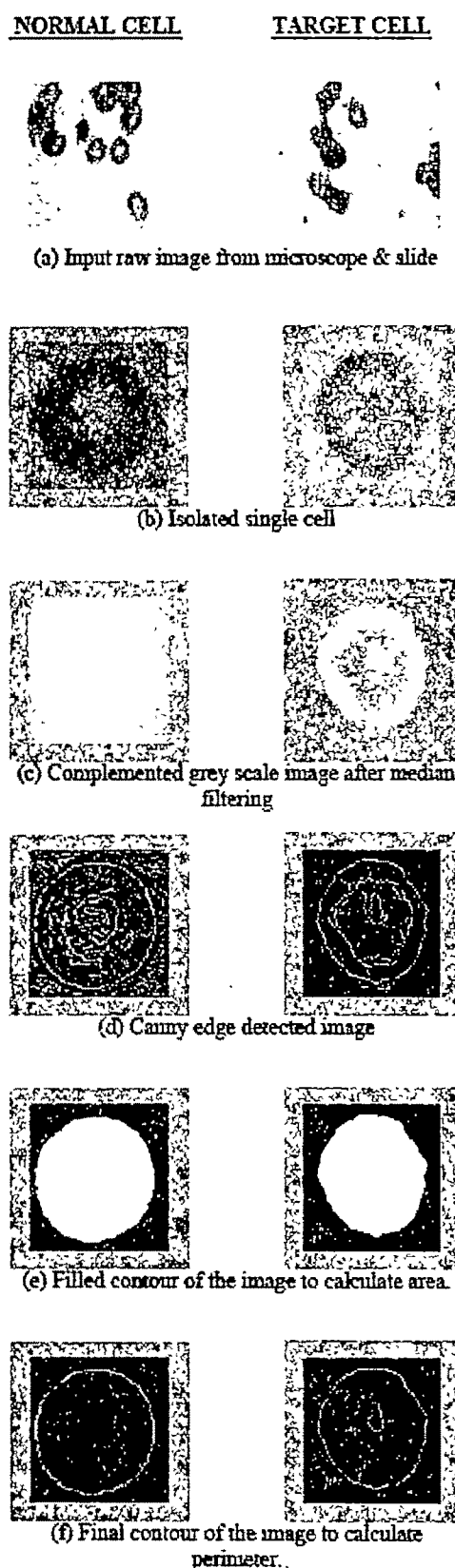


Fig. 5 Images obtained at different stages of implementation of algorithm for normal and pathological cell (target cell).

The applications of this project are especially in detection of structural changes in erythrocytes which are generally seen in pathological conditions such as malaria, sickle-cell anemia, jaundice, liver diseases. In many developing countries, microscopy is not reliable because the microscopists are insufficiently trained and supervised and are overworked, and moreover the microscopes and reagents are of poor quality. Conversely in non-endemic countries laboratory technicians are often unfamiliar with malaria and may miss the parasites. Image processing technique developed in the present work may help in overcoming these difficulties. This technique helps in diagnosis of many abnormalities which are obscure even after normal enhancement of the image, therefore eliminating any chance of errors during diagnosis of any problem, through simple and fast techniques.

IV CONCLUSIONS

In the present work an image processing algorithm has been developed and implemented for tracing the contour to find the shape of normal and abnormal erythrocytes, and to find the parameters perimeter, area and form factor. It is found that the normal and abnormal cells can be easily differentiated with help form factor. The image processing algorithm developed in the present work is found be very useful in the diagnosis of several diseases in which shape of the erythrocytes will change with pathologic condition.

REFERENCES

- [1] Marchesi, V. T., The red cell membrane skeleton: recent progress, *Blood*, 1983, 61(1), pp.1-11.
- [2] Vaya, A., Martinez, M., Sloves, P., Barbera, J. L. and Aznar, J., *Clin. Hemorheol.*, 1996, 16, 515-522.
- [3] Dennis A. Noe and Robert C. Rock, *Laboratory Medicine: The Selection and Interpretation of Clinical Laboratory Studies*, Williams & Wilkins, January 1994.
- [4] Gonzalez R.C and Woods R.B, 'Digital Image Processing', 3e, Pearson Education, pp.123-137.
- [5] John Bernard Henry, *Clinical Diagnosis and Management by Laboratory Methods*, W.B. Saunders Company; 19e, 1996.
- [6] Red blood cells and multiple sickle cells. Available: <http://health.allrefer.com/health/cbc-red-blood-cells-multiple-sickle-cells.html>.

Computer based Investigation of Hearing Disorders through Distortion Product Otoacoustic Emission Analysis

Jyothiraj V. P and Sukesh Kumar A

¹ Dept. of Electronics and Communication Engineering, College of Engineering, Trivandrum, Kerala, India
e-mail: vpj27@yahoo.com, sukeshkumarcet@yahoo.com

Abstract—Distortion product otoacoustic emissions (DPOAEs) are a series of combination tones generated in the ear when stimulated with two pure tones of frequency f_1 and f_2 (in audio range). The most prominent distortion product is the cubic difference tone at $2f_1-f_2$. Maximum level of the DPOAE signals are observed when the frequency ratio f_2/f_1 is chosen to be 1.22. The objective of this study is to determine the DPOAE response characteristics from normal and hearing impaired subjects and to investigate the relation among spectra of evoking tones, the measurement parameters of DPOAEs and audiometric status. The DSP platform controls the microphone/speaker system which generates the acoustical stimuli for presentation to the ear canal and collects the acoustic responses recorded in the ear canal. The signal processing problem involves estimation of the weak DPOAE response under two strong stimuli and background noise. A total of 43 DPOAE responses from neonatal to adult subjects are analyzed. The DPOAE data of both adults and children are compared with individual pure tone audiometric data to investigate how DPOAE responses differentiated ears with normal hearing from impaired ears. DPOAE assessment provides detailed frequency specific information on cochlear function. This property of DPOAEs is used for clinical applications to find hearing impairment and hearing screening.

Key words—DPOAE, Hearing disorders, OAEs, Stimulus.

I. INTRODUCTION

THE human ear can not only perceive sound passively but produces sound actively. Otoacoustic emissions (OAEs) is defined as low intensity sound that originates from the cochlea and that can be recorded in the outer ear canal. OAE was first reported by Kemp in 1978[1]. The outer hair cell (OHC) system of cochlea is responsible for the generation of OAEs

and OHC mobility is the cellular basis of this phenomenon [2] atleast for mammals. OAEs are considered to have clinical utility as a sensitive measure of cochlear function, being generated only when the cochlea is functioning normally or nearly normal. Screening and monitoring of cochlear function have been the two most important areas of clinical application.

OAEs are classified according to the type of stimulation to induce them (1) spontaneous otoacoustic emission (SOAEs) (2) evoked otoacoustic emissions (EOAEs). The SOAEs are narrow band and low level signals which are generated without acoustic stimulation, whereas EOAEs occur during or after external acoustic stimulation [3]. The most outstanding features of EOAEs with respect to their suitability as a clinical test are that they can be measured simply, non invasively and readily in the outer ear canal by a sensitive microphone. There are several subclasses of EOAEs based primarily on the stimuli used to evoke them. These include (i) transient evoked OAEs (TEOAEs) (ii) distortion product OAEs (DPOAEs). TEOAEs are delayed response to acoustic transient stimuli such as clicks or tone burst.

The DPOAEs are inter modulation-distortion response produced by the ear in response to two simultaneous pure tone stimuli referred to as the primary tones f_1 and f_2 with levels L_1 and L_2 . The primaries are related in frequency separation of f_2 from f_1 commonly called f_2/f_1 ratio, i.e., typically 1.22 [4]. The most frequently measured acoustic inter modulation-distortion product is at the frequency $2f_1-f_2$ i.e., the cubic difference tone [5], although the cochlea also produces concurrently DPOAEs at other frequencies (e.g., f_2-f_1 , $2f_2-f_1$, $3f_1-2f_2$) in response to such bitonal stimulation [6]. Indeed, the only emitted distortion component utilized to clinical purpose has been $2f_1-f_2$ because it is the largest DPOAE. The amplitude of a DPOAE depend upon the level of the eliciting stimulus.

In clinical applications of DPOAE, data are most commonly presented as DPOAE level frequency functions (often called DPOAE audiogram or DPgram), in which DPOAE level is measured as a function of primary tone frequency for fixed level primaries. The DPOAE level frequency function allows the status of a given cochlea to be assessed in a frequency specific manner, by comparison of DPOAE level at each frequency in the test ear to DPOAE level measured in a population of normally hearing individuals. Cochlear impairment is indicated at those frequencies at which DPOAE levels in the test ear are below the range of response in the normal population [7].

The amplitude of DPOAEs depends systematically upon the parameters of the stimulus tones i.e., frequency, frequency separation and level difference. DPOAE can be recorded in ear with hearing loss upto 50 dB. This study is focused to find DPOAE response characteristics and to investigate the relationship among spectra of evoking tones, the measurement parameters of DPOAEs and audiometric data. By analyzing properties of DPOAE response it can be possible to find subjects suffering from noise induced hearing loss, the influence of ototoxic drugs to hearing and cochlear disorders etc. This work is an extension of authors earlier work [8].

II. MATERIALS AND METHODS

A. DPOAE Measurement System

A schematic of computer-based DPOAE measurement system is shown in the Fig. 1.

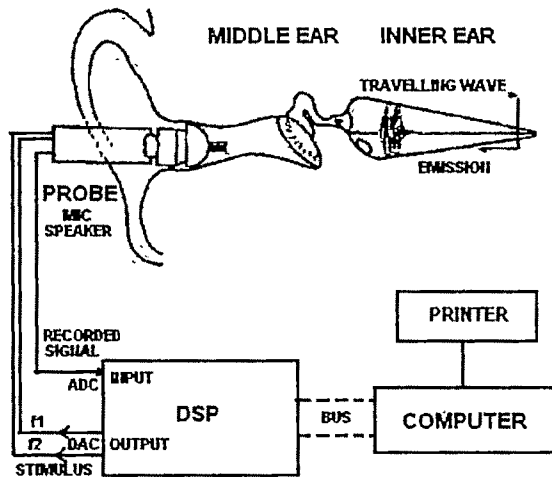


Fig. 1. Schematic of a computer based DPOAE measurement setup.

The DPOAE response is measured via a probe that is sealed into the ear canal using a removable rubber or foam ear tip. The probe incorporates two miniature speakers and one high sensitivity miniature microphone. Two speakers are required to elicit DPOAEs, so that the two stimulus tones are mixed acoustically rather than electrically, to prevent generation of artifactual intermodulation-distortion products by a single

speaker when driven simultaneously by tones. The DSP platform controls the microphone/speaker system, which generates the acoustical stimuli for presentation to the ear and collects the acoustic responses recorded in the ear canal. The two primary tones f_1 and f_2 are digitally synthesized and presented to ear canal through digital to analog converter and miniature speaker system to elicit DPOAEs. The responses are collected through miniature microphone, and fed to the DSP platform through analog to digital converter for further signal processing [9].

The signal processing problem involves estimation of weak DPOAE under two strong stimuli and the background noise, which in some cases can be higher than that of the DPOAE itself. Traditionally, use fast fourier transform to filter the signal into narrow frequency bands, and to detect any emission present. The intensity levels and frequency of the test tones and averaging time to process the signal can be determined by the tester through the adjustable setting maintained in OAE instrument. The noise floor level is further reduced by using a low noise environment such as a sound proof room for DPOAE measurement.

B. DPOAE Acquisition and Analysis

DPOAEs are measured from 43 subjects like normal, hearing impaired, and normal having other diseases. To conduct DPOAE test, two primary tones at frequency f_1 and f_2 and levels L_1 and L_2 were presented. The frequency ratio f_2/f_1 was fixed at 1.22. The stimulus levels were held constant at $L_1 = 65$ dB SPL and $L_2 = 55$ dB SPL. These values have been shown to give large amplitude and thus easily detectable [10]. The following variables were analyzed. (i) the estimated DPOAE level (DP) measured at the $2f_1 - f_2$ frequency with f_2 at frequencies 2, 3, 4 and 5 KHz [11], [12]. (ii) the noise level (NF) estimated from the 4 Fourier components nearest to but not including the $2f_1 - f_2$ frequency. (iii) the estimated DPOAE signal to noise ratio (SNR) is defined as the difference between estimated DPOAE level and estimated noise level. Fig. 2. shows the spectra of ear canal sound pressure detected by microphone.

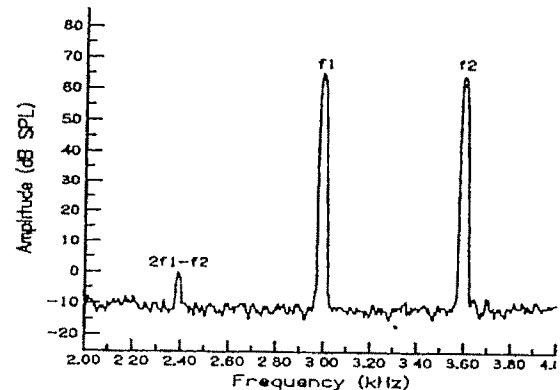


Fig. 2. Spectra of ear canal sound pressure from the ear of a normal hearing adult.

The measurement of DPOAEs was restricted to frequency of 2 KHz and higher, because DPOAE at lower frequencies (0.5 to 1 KHz) have been shown to require very long average time to be reliably recorded [13]. An automatic regime was followed in which each frequency (2, 3, 4 and 5KHz) were measured twice, averaged for 2 seconds each time. Therefore, the total test time approximately equals 8 seconds. Another protocol is 4 sec average time at each of 4 frequencies and total test time is equal to 16 seconds. The shorter test time protocol offers an advantage when testing young children or uncooperated subjects, who will tend to move considerably during test. The longer averaging time test protocol offers an advantage when testing in noisy environments. The tester can select the approximate test protocol on the subject being tested and the test environments. In this study, pure tone audiometric data are also collected from the hearing subjects (adults and children) using both air conduction and bone conduction methods. This data are compared with DPOAE data for detailed frequency specific analysis and diagnosis.

III. RESULTS AND DISCUSSIONS

OAEs have been regarded as an energy leakage from the cochlea. OAEs may provide an objective assessment of the OHCs. Especially DPOAEs yield frequency specific response in a format comparable to the audiogram. In this study, amplitude of DPOAEs are measured in diabetics who have no hearing loss and the results are compared with normal control groups. The result shows that the values of the DPOAEs are decreased in diabetic subjects with normal hearing than in the normal controls. Fig. 3. shows the DPOAE responses obtained from diabetic and control subjects. Because DPOAE is an objective tool for detecting functional alteration of outer hair cells of cochlea, these results indicate that there would be an invisible pathology of cochlea hair cells in diabetic subjects with normal hearing. Therefore DPOAE could predict the occurrence of sub clinical diabetic cochlear dysfunction.

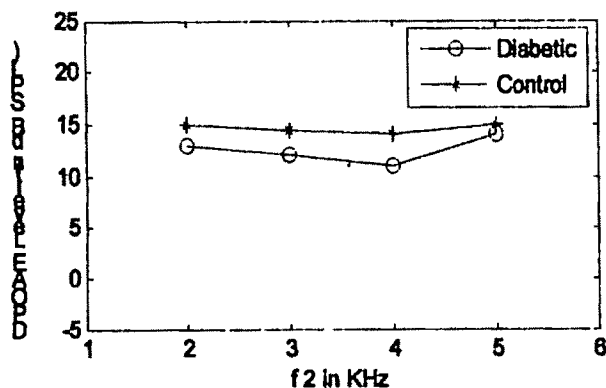


Fig. 3. DPOAE responses in diabetic and control subjects.

Table I gives the DPOAE data of 28 year old female subject with sensorineural hearing loss (left ear) and normal right ear.

Table. I.

f2 KHz	L1 dB	L2 dB	Left Ear			Right Ear		
			DP dB	NF dB	SNR	DP dB	NF dB	S N R
2	65	55	-4	-17	21	-2	-18	16
3	65	55	-4	-2	16	8	-19	26
4	65	55	-9	-20	11	3	-20	23
5	65	55	-20	-20	0	-3	-20	17

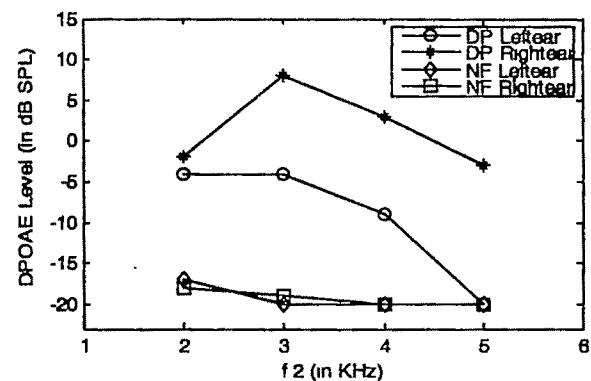


Fig. 4. DP gram of a 28 years female subject with hearing loss (left ear) and normal right ear and NF plot indicates corresponding noise level.

The result of data analysis shows that the high frequency DP response of the left ear is poorer when compared with that of right ear. The right ear provides DP response at all frequency range. i.e., right ear is functionally normal. In DPgram of left ear, DPOAE response level decreases with increase of frequency. At 5 KHz the DPOAE level is only noise level. i.e., SNR is zero. This analysis shows that left ear have high frequency hearing loss. i.e., sensorineural hearing loss. Pure tone audiometric data also shows same results. i.e., the threshold of hearing at high frequency region is higher compared with lower frequency region.

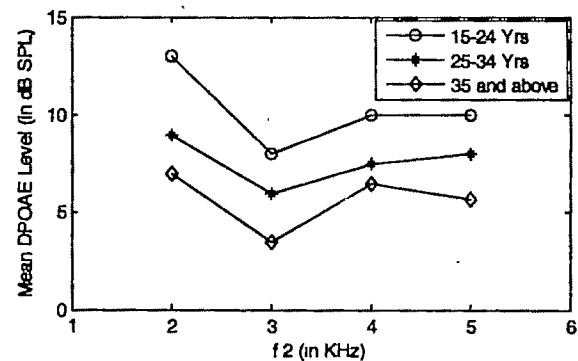


Fig. 5. Variation of DPOAE response level with age and frequency.

The influence of age on DPOAE amplitude is shown in Fig. 5., ears are divided into three groups: 15-24 Yrs, 25-34 Yrs and 35 Yrs and older. In pure tone analysis behavioral threshold increased significantly with age at and above 3 KHz. The DPOAE amplitude decreased with increasing age at all frequencies. Hearing screening and monitoring of cochlear functions are two most important areas of clinical applications. DPOAEs are objective, easy, rapid and noninvasive method and are then ideal for large scale population screening. Apart from the above use the method is used for screening difficult to test subjects such as children, developmentally delayed patients and the elderly with dementia or other medical problems. Other DPOAE clinical applications are (i) to estimate influence of ototoxic drugs to hearing. (ii) to investigate tinnitus. (iii) detection of cochlear disorders. (iv) detection of neuroma tumors and other central auditory disorders.

IV. CONCLUSION

Distortion product otoacoustic emission should be viewed as additional, objective audiological technique and may be the most powerful tool when used in conjunction with neural evoked potential, immittance measurement and pure tone audiometry.

ACKNOWLEDGMENT

The authors are grateful to the Director, Kerala ENT Research Foundation (KERF), Kollam, Kerala and the Director, National Institute of Speech and Hearing (NISH), Trivandrum, Kerala for being provided the facility to carry out the above work.

REFERENCES

- [1] D. T. Kemp, *Otoacoustic emissions in perspective*, Thieme Medical publishers, New York, 1978, pp. 1-20.
- [2] W. E. Brownell, "Outer hair cell electro motility and otoacoustic emissions," *Ear.Hear.*, vol. 11, 1990, pp. 82-92.
- [3] D. T. Kemp, 1978, "Stimulated acoustic emissions from within the human auditory system," *Journal of Acoustic Society of America*, 64, no. 5, pp. 1386-1391.
- [4] F. P. Hiris, Lonsbury, and B. L. Maertlin., "Acoustic distortion product in human systematic changes in amplitude as a function f2/f1 ratio," *Journal of Acoustic Society of America*, 85, 1989, pp 280-286.
- [5] Hauser, and Probst, "The influence of systematic primary tone level L2-L1 on the acoustic distortion and mission 2f1-f2 in normal human ears," *Journal of Acoustic Society of America*, 89, pp 280-286
- [6] J. O. Pickles, "Active mechanical processes in the cochlea : Cochlear emissions," in *An introduction to the physiology of hearing*, 2nd ed. , London: Academic, pp 141-145.
- [7] Marta Parazzini, Pado Galloni, R. Alessandra. Bazzale et.al., "Quantitative indices for the assessment of the repeatability of DPOAE in laboratory animals," *IEEE Trans. Biomedical Engg.*, vol. 53, no. 8, pp. 1550-1556, August 2006.
- [8] V. P. Jyothiraj, and A. Suresh Kumar, "Detection and analysis of otoacoustic emissions for diagnosis of hearing disorders," presented at the 2004 16th Kerala science congress, Kozhikode, Kerala.
- [9] Minghui Du, F. H. Y. Chan, F. K. Lam, and Jun Ren, 1998, " Design consideration of a multi-function otoacoustic emission measurement system", *Proceedings of the 20th Annual International Conference of the IEEE Engineering in Medicine and Biology Society*, 20, no. 4, pp. 1928-1931

- [10] S. A. Gaskill, and A. M. Brown, "The behavior of the acoustic distortion product 2f1-f2 from the human ear and its relation to auditory sensitivity," *Journal of Acoustic Society of America*, 88 (2), 1990, pp 821-831.
- [11] W. K. Ma, and Y. T. Zhang, "Estimation of distortion product otoacoustic emissions," *IEEE Trans. Biomedical Engg.*, vol. 46, no.10, pp. 1261-1264, 1999
- [12] A. K. Zirani, and A. Konard, " A novel method of estimation of distortion product otoacoustic emission signals," *IEEE Trans Biomedical Engg.*, vol 51, no 5, pp. 864-868, 2004.
- [13] M. P. Gorga, S. T. Neely, B M Bergman, K. L. Beauchaina, J. R. Kaminsk, and Z. Liu, "Towards understanding the limits of distortion product otoacoustic emission measurements," *Journal of Acoustic Society of America*, 96(5), 1994, pp 2639-2648

Diagnosis of Eye Diseases Using Medical Imaging

Sheeba O¹ and Suresh Kumar A².

¹ T.K.M. college of Engineering, Kerala, India e-mail: shb_odattil@yahoo.com.

² Dept. of Electronics & Communication College of Engineering, Thiruvananthapuram, Kerala State.

Abstract— Image processing of fundus images has the potential to play a major role in the diagnosis of Age Related Macular Degeneration and Diabetic Retinopathy. Drusen that appear as abnormal white yellow deposition on the retina are the signs of development of Age Related Macular Degeneration (AMD). Early signs of Diabetic Retinopathy are formation of lipids (pale fatty deposits) on the retina and scar tissue forming from the mass of ruptured blood vessels. With the help of digital fundus camera retina images can be captured. An algorithm has been developed for the automatic detection and mapping of the drusen deposits in the case of AMD and the lipids and scar tissue in the case of Diabetic Retinopathy. The results help the doctor to make the accurate diagnosis and provide the information regarding the efficacy of treatment very faster during the course of disease.

Key words — Image processing, Macular Degeneration, Diabetic Retinopathy and drusen

I. INTRODUCTION

MACULAR degeneration is a group of diseases characterized by a breakdown of the macula. Age-related macular degeneration (AMD) is a disease characterized by the progressive loss of central vision. It is currently the leading cause of irreversible blindness in the industrialized world, afflicting an approximately 1 in 20 people over the age of 60 years [1]. The macula is the center portion of the retina that makes central vision and visual acuity possible [2]. The drusen can become larger and increase in number, which may lead to sight threatening complications [3], [4]. Diabetic retinopathy is a potentially blinding complication of diabetes that damages

the eye's retina. Diabetic retinopathy is the leading cause of blindness and visual impairment in adults in developed societies. Approximately 2% of all individuals who have

diabetes become blind after 15 years, and severe visual impairment develops in 10% of individuals with diabetes. Diabetic retinopathy occurs when diabetes damages the tiny blood vessels in the retina. At this point, most people do not notice any changes in their vision. Some people with diabetic retinopathy develop a condition called macular edema. It occurs when the damaged blood vessels leak fluid and lipids onto the macula. The fluid makes the macula swell, blurring vision. As the disease progresses, it enters its advanced, or proliferate, stage. Fragile, new blood vessels grow along the retina and in the clear, gel-like vitreous that fills the inside of the eye. Without timely treatment, these new blood vessels can bleed, cloud vision, and destroy the retina.

Digital fundus cameras are used to capture the retinal images. Then image processing is done so as to detect the presence of drusen and to find the affected area in both macular degeneration and diabetic retinopathy. This work is an extension of the earlier works of the authors [5], [6], [7].

II. METHODOLOGY FOR DRUSEN DETECTION

The main steps of the proposed algorithm are non-uniform illumination compensation, enhancement and segmentation. The enhancement and thresholding [8] operators for drusen segmentation are adaptive and based on histogram analysis. In particular, the local thresholding operator is designed from a rigorous analysis of the local histogram [9], as to exploit the important characteristics of the signal distribution that differentiate drusen from background and overcome the inefficiencies of other histogram based segmentation schemes. The next processing step aims at enhancing the contrast of the retina's image. In histogram equalization all display intensities are approximately equally represented. The intention is that ranges of pixel values are allocated portions of the display intensity range according to the frequency with which they appear in the image [10], [11]. The simplest way to form a binary image is by thresholding. Pixels with intensities less

than or equal to the threshold become one component of the binary image, and those with intensities greater become the other. The main problem in the classic segmentation methods like thresholding and edge detection is the choice of thresholds as well as scale factors [12],[13]. Here we use the concept of mathematical morphology as a tool for extracting the image components and also morphological reconstruction that involves two images.

III. MORPHOLOGICAL OPERATIONS

Mathematical morphology is an approach to image analysis based on set theory [14]. Here two fundamental morphological operations, dilation and erosion are used in terms of intersection of an image with a translated shape for extracting features from an image. Dilation is an operation that "grows" objects in an image. A shape referred to as a structuring element controls the extent of growing. The erosion of a set by a structuring element is the set of pixel positions for which a structuring element placed with its reference point there will be contained completely within the set. An opening is similar to erosion, except that it consists of all points lower-case, points of the structuring element when the structuring element can be placed within a set. Dilation is an erosion of the background of a set. Erosion "shrinks" objects in an image. Dilation and erosion [15] can be used in various combinations. Here we make use of the most common combination opening and closing. In morphological opening, erosion removes small objects and the subsequent dilation tends to restore the shape of the objects that remain. In our problem we make use of gray-scale morphology where dilation and erosion are defined in terms of minima and maxima of pixel neighborhoods. The digital image functions are of the form $f(x, y)$ and $b(x, y)$, where $f(x, y)$ is the input image, the $b(x, y)$ is the structuring element, itself a sub image function. The gray-scale dilation of f by structuring element b , denoted $f \oplus b$ is defined as

$$(f \oplus b)(x, y) = \max \{ (x - x', y - y') + b(x', y') / (x', y') \in D_b \} \quad (1)$$

where D_b is the domain of b , and $f(x, y)$ is assumed to equal $-\infty$ outside the domain of f . The structuring element is rotated about its origin and translated to all locations in the image. At each translated location the rotated structuring element values are added to the image pixel values and the maximum is computed. The gray-scale dilation is performed using flat structuring elements in which the value of b is 0 at all coordinates over which D is defined. That is $b(x', y') = 0$ for $(x', y') \in D$. Thus the gray-scale dilation equation simplifies to

$$(f \oplus b)(x, y) = \max \{ f(x - x', y - y') / (x', y') \in D \} \quad (2)$$

Thus flat gray-scale dilation is a local maximum operator, where the maximum is taken over a set of pixel neighbors

Morphological filtering simplifies a segmented image to facilitate the search for objects of interest. This is done by smoothing out object outlines, filling small holes, eliminating small projections, and using other similar techniques. Dilation allows objects to expand, thus potentially filling in small holes and connecting disjoint objects. Erosion shrinks objects by etching away (eroding) their boundaries. These operations can be customized for an application by the proper selection of the structuring element, which determines exactly how the objects will be dilated. The dilation process is performed by laying the structuring element on the image and sliding it across the image in a manner similar to convolution. The difference is in the operation performed. It is best described in a sequence of steps:

1. If the origin of the structuring element coincides with a '0' in the image, there is no change; move to the next pixel.
2. If the origin of the structuring element coincides with a '1' in the image, perform the OR logic operation on all pixels within the structuring element.

With a dilation operation, all the '1' pixels in the original image will be retained, any boundaries will be expanded, and small holes will be filled.

The morphological operations can be extended to gray-level images in different ways. The easiest method is to simply threshold the gray-level image to create a binary image and then apply the existing operators. For many applications this is not desired because too much information is lost during the thresholding process. Another method that allows us to retain more information is to treat the image as a sequence of binary images by operating on each gray level as if it were the 1 value and assuming everything else to be 0. Laying them on top of each other and "promoting" each pixel to the highest gray-level value coincident with that location can then combine the resulting images.

Dilations can be made directional by using less symmetrical structuring elements. e.g. a structuring element that is 10 pixels wide and 1 pixel high will dilate in a horizontal direction only. Similarly, a 3x3 square structuring element with the origin in the middle of the top row rather than the center will dilate the bottom of a region more strongly than the top.

IV. IMAGE RECONSTRUCTION

Grayscale dilation with a flat disk shaped structuring element will generally brighten the image. Bright regions surrounded by dark regions grow in size, and dark regions surrounded by bright regions shrink in size. Small dark spots in images will disappear as they are 'filled in' to the

surrounding intensity value. Small bright spots will become larger spots. Small dark spots in images will disappear as they are 'filled in' to the surrounding intensity value. Small bright spots will become larger spots. The effect is most marked at places in the image where the intensity changes rapidly and regions of fairly uniform intensity will be largely unchanged except at their edges. An image can have multiple regional maxima or minima image peaks or valleys can be used to create marker images that are used in morphological reconstruction. In an image, every small fluctuation in intensity represents a regional minimum or maximum.

To remove the less significant minima and maxima but retain the significant minima and maxima, a threshold level 'h' is specified that suppresses all maxima whose height is less than h or whose minima are greater than h [16].

Morphological reconstruction can be thought of conceptually as repeated dilations of the marker image until the contour of the marker image fits under the mask image. In this way, the peaks in the marker image "spread out", or dilate. Each successive dilation is constrained to lie underneath the mask. When further dilation ceases to change the image, processing stops. The final dilation is the reconstructed image.

V. PROGRAM METHODOLOGY

Here the software was developed using MATLAB. This work is intended to diagnose both Age related Macular Degeneration (AMD) and Diabetes retinopathy (DR). First the disease to be diagnosed is chosen. The images obtained from fundus photography covers a large area of the eye than we actually require including the iris. Only the region of the eye that is affected by the disease is selected. Thus, a window is obtained that consists of the affected part of the eye and other unwanted details among which blood vessels are prominent. Drusen that differ slightly from the background regions are correctly segmented without losing their size and actual shape. Once the noisy images are segmented by thresholding, successive application of opening and closing operations are performed to improve the image. For removing the blood vessels structures that are lighter than their surroundings and that are connected to the image border are selected and then suppressed. A background image generated is then subtracted from the obtained gray image to improve the visibility of the effected area. The contrast of this image is then increased. This enhanced grey image is then converted o a binary image based on a threshold. This image clearly distinguishes the affected parts from the others. Based on this the area of the affected region is obtained for both Diabetic Retinopathy & Macular Degeneration. The flowchart is shown in fig (1). Tests were conducted on many images both for diabetic retinopathy and macular degeneration with satisfactory results.

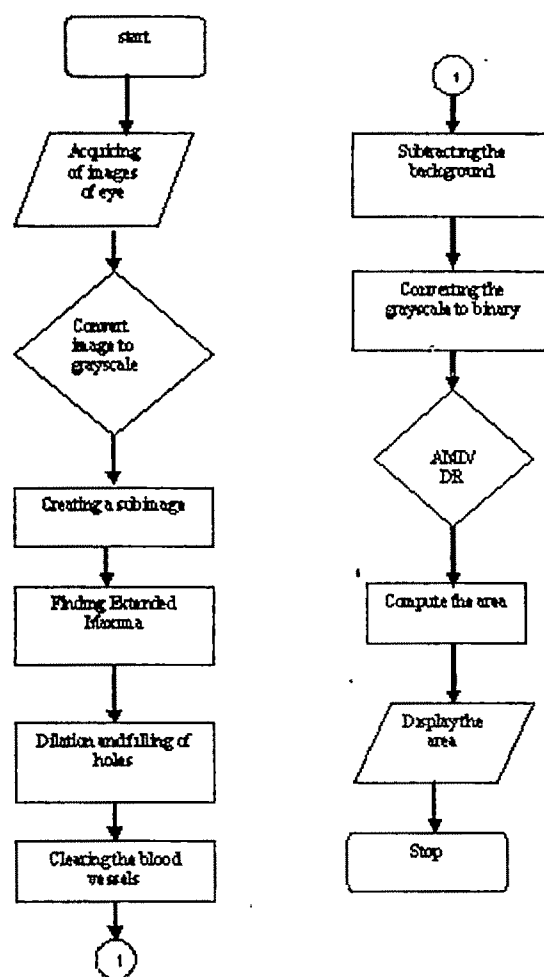


Fig (1).

Fig (2) shows sample images for diabetic retinopathy and the affected area. Fig (3) shows sample images for macular degeneration, number of drusen and the affected area.

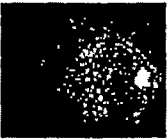




Images	Affected area
	4.47825mm ²
	2.2011mm ²
	3.58042mm ²
	2.75489mm ²
	1.38143mm ²

Fig (2)

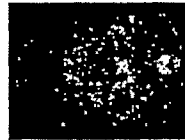
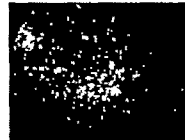



Images	Affected area
	2.49624mm ²
	1.13368mm ²
	1.58355mm ²
	15.6991mm ²
	2.06719mm ²

Fig (3)

VI. CONCLUSION

Diabetic retinopathy and Age-related macular degeneration are the leading causes of preventable vision loss in the country. Image processing of fundus images has the potential to play a major role in the early diagnosis of age related macular degeneration and diabetic retinopathy. Incorporation of image processing technologies in the field of ophthalmology presents a wide range of possibilities in a time when specialized Examiners are over-stretched and when there is a demand for improving the quality of medical care in

a vision-impaired population with a high probability of increasing in numbers during the next quarter of the century. An automated and reliable method for finding out the drusen exudates, lipids have been done here. Quantification of drusen is essential to the study of age related macular degeneration. Similarly, the quantification of exudates, lipids are essential to the study of diabetic retinopathy. Current techniques are relatively imprecise, subjective, and labor intensive. By applying our findings, we have developed a reproducible, validated automated method for leveling the background and obtain segmenting by a uniform threshold. Robustness and accuracy in comparison to human graders have been evaluated on a small image database. The results are encouraging and a

clinical evaluation will be undertaken in order to be able to integrate the presented algorithm as a tool for diagnosis of diabetic retinopathy

ACKNOWLEDGMENT

The authors would like to thank Dr. Mahesh G. for his valuable suggestions. Drusen images are courtesy of Giridhar Eye Institute, Cochin

REFERENCES

- [1] David S.Shin, Noreen B Javornik, Jeffrey W. Berger, *Computer-assisted, interactive fundus image processing and macular drusen quantitation* (Ophthalmology, 106,6,1999).
- [2] Glasbey C.A and Horgan G.W, *Image Analysis for the Biological Science* (Wiley, 1995).
- [3] Deng G., Cahill L.W. and Tobin G.R. *The study of Logarithmic Image Processing Model and its Application to image Enhancement*
- [4] Green R.W, *Histopathology of age related macular degeneration.* (Molec. Vis 27-36, 1999).
- [5] Sheeba.O, Dr.Sukeshkumar.A *Image Analysis for the detection of Drusen Deposits on Human Retina. National Conference on Industrial Automation – Emerging Trends* 21 & 22 Jan 2005. Easwari Engg College, Chennai
- [6] Sheeba.O, Dr.Sukeshkumar.A, Dr.Mahesh.G *Processing of Retinal images in Age Related Macular Degeneration. National conference on Bioinformatics Computing (NCBC '05) field* 18-19 March 2005. Deemed university, Patiala.
- [7] Dr.Mahesh.G., Dr A.Giridhar, Sheeba.O, Dr.Sukeshkumar *Drusen Segmentation – Validation and Analysis of Fellow Eyes of End stage Wet Age Related Macular Degeneration. First Conference of Ophthalmic Association of South India and Sri Lanka and 32nd Annual Conference of Kerala Society of ophthalmic surgeons.* NOV 25,26,27 2005.
- [8] Otsu Nobuyuki "A threshold Detection Method from gray level histograms", vol.SMC-9, no.1, January 1979.
- [9] Zimmerman S., Johnson D., Arrighi F. and Rupp M, (*Comput.Biol. Med.* 16(3) 223, 1986).
- [10] Kirkpatrick JNP, Spencer T, Manivannan A., et al., *Quantitative image analysis of macular drusen from fundus photographs and scanning laser ophthalmoscope images* Eye, 9, 48-55, 1995.
- [11] Morgan WH., Cooper RL. Constable JJ, Eikelboom RH., *Automated extraction and quantification of macular drusen from fundal photographs.* Aust NZJ *Ophthalmology*, 22, 7-12 (1994).
- [12] Peli E., Lahav M, *Drusen measurements from fundus photographs using computer image analysis, Ophthalmology* 1986, 93, 1575-80 (1986).
- [13] Pitas, A.N Venetsanopoulos, *Nonlinear Digital Filters*, Kluwer Academic Publishers (1990)
- [14] Evans J.R. (2001) *Risk factors for age related macular degeneration.* Prog Retin.Eye Res. 20, 227-253.
- [15] Gonzalez R.C., Woods R.E. 'Digital Image Processing', 1993.
- [16] Soille P., *Morphological Image Analysis: Principles and Applications* (Springer-Verlag, 1999, pp.170-171).

Effect of Fractal Image Compression on Screening for Diabetic Retinopathy

David. J¹, Sukesh Kumar. A² and Harsha. A³

¹ College of Engineering, Trivandrum, INDIA e-mail: jdavid@cet.ac.in

² College of Engineering, Trivandrum, INDIA e-mail: suresh@cet.ac.in

³ College of Engineering, Trivandrum, INDIA e-mail: harsha appukutan@gmail.com

Abstract—Diabetic retinopathy is the leading cause of blindness in working age population. Early detection of diabetics reduces the risk of blindness. This work aimed to assess the effect of fractal image compression on the accuracy of grading of diabetic retinopathy. Fractals are widely used in medical imaging. The storage and transmission of medical images can be facilitated using fractal image compression. It has a lot of advantages over JPEG compression. The characteristics features of different retinal images, some with no retinopathy, some with background, some with pre proliferate, and some with proliferate retinopathy are taken. The images are then subjected to fractal image compression by 90%, 80%, 70%, and 0%. Fractal image compression performed both in time domain and frequency domain is compared with JPEG compression. The images were decompressed at the receiver side and graded on a portable computer. Two masked graders assessed the images for grade of retinopathy and image quality. The sensitivity and specificity of retinopathy grading were calculated and the parameters are compared before and after fractal image compression with JPEG compression.

Key words—Fractals, exudates, optic disc, vessel extraction, JPEG compression, iterated function systems (IFS).

1 INTRODUCTION

THE leading causes of retina-related vision impairment and blindness in the working age population are diabetic retinopathy, age-related macular degeneration (AMD), and glaucoma. [1]. It is estimated that more than 8,000 diabetic patients become blind every year from retinal complications [2]. Much of this blindness can be prevented if the retinopathy is detected early enough for the treatment with laser photocoagulation. During clinical examination, the ophthalmologist analyzes the fundus photographs and looks out for abnormal

signs such as exudates and hemorrhages which may lead to retinopathy [3].

Giving due consideration to the increase of diabetes, as well as to the fast advances in computer hardware and software technique, the development of a cost-effective PC-based retinal image analysis system offers a potential of being very useful in the mass screening of diabetic retinopathy. This system may not only provide objective diagnosis to the doctor, but also extend his capability and productivity during clinical examination. The storing of retinal images is performed by using fractal image compression.

Fractal encoding is largely used to convert bit map images to fractal codes. Fractal decoding is just the reverse, in which a set of fractal codes are converted to bit map. The encoding process is extremely computationally intensive. Millions or billions of iterations are required to find the fractal patterns in an image. Depending upon the resolution contents of the input bitmap data, and output quality, compression time, and file size parameters selected, compressing a single image could take anywhere from a few seconds to few hours (or more) on even a very fast computer. Decoding a fractal image is much simpler process. The difficult process is finding all the fractals during the encoding process. All the decoding process needs to do is to interpret the fractal codes and translate them into a bitmap image.

METHODS

The fundus photographs were taken with a fundus camera during mass screening. These photographs were then scanned by a flat-bed scanner and saved as a 24-bit true color BMP file of 512x512 pixels. The image files were then analyzed using the algorithms described in the following section: 1. Detection of optic disc and exudates area. 2. Vessel extraction. 3. Fractal image compression. 4. Fractal image decompression.

The basic block diagram to describe the methodology is shown in figure (1).

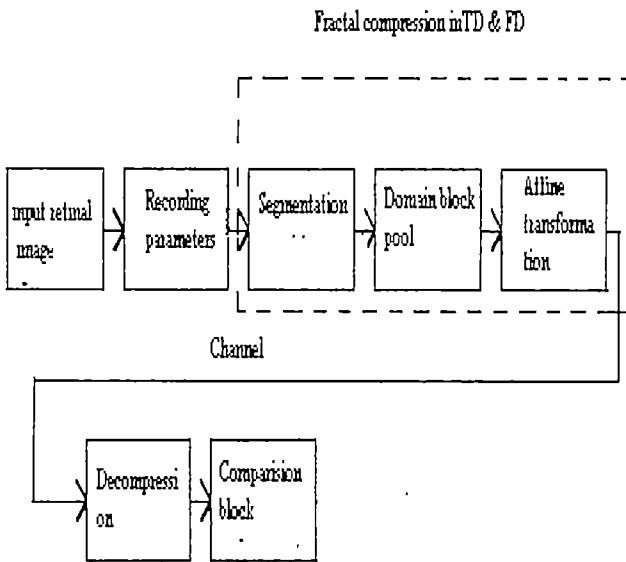


fig (1)

II. PROCEDURE

A. Detection of optic disc and exudates area

The retinal image obtained from the fundus camera is converted to gray level image. Pre-processing of the resultant gray level image is done to reduce the intensity variations and noise present in the image. The next step to be done is the removal of optic disc and exudates areas.

Exudates are the primary signs of diabetic retinopathy which are mainly cause of blindness and could be prevented with an early screening process. The exudates can be identified on the ophthalmoscope as areas with hard white or yellowish colors with varying sizes, shapes and locations. They normally appear near the leaking capillaries within the retina [4]. Exudates are one of the most common occurring lesions in diabetic retinopathy. The shape, brightness and location of exudates vary a lot among different patients. Techniques in the exudates detection can be classified into three categories: thresholding, edge detection and classification.

The thresholding method is straightforward, but the automatic selection of the threshold is difficult. The main concern of the methods based on edge detection is how to distinguish the edges of exudates from the edges of vessels and other lesions. Statistical classification and neural network were also attempted, which are cataloged into the classification approach. It is still difficult for these methods to detect exudates robustly in fundus images.

The optic disc is the brightest part in the normal fundus image that can be seen as a pale, round or vertically slightly oval disc. It is the entrance region of blood vessels and optic nerves to the retina and it often works as a landmark and reference for the other features in the retinal fundus image.

Usually in the normal eye, physical diameter of the optic disc is about 1.5mm [5] on average. The location of the optic disc is essential in retinal image analysis to measure distance and identify other anatomical parts in retinal images.

B. Exudates detection

The illumination in fundus images is not homogeneous; a fundus image is divided into sixty-four sub-images. Exudates detection is performed in each sub image. The color difference of an object can be defined as:

$$D(i, j) = (L(i, j) - L_r)^2 + (u(i, j) - u_r)^2 \quad (10)$$

Where $L(i, j)$ and $u(i, j)$ are the colors of pixel (i, j) in the component L and u respectively. L_r and u_r are the reference colors of the object. The reference color is determined as the gravity center of the object [6]. Mean squared filter is used to remove noise. A combined method of region growing and edge detection, which includes seed selection, edge detection and growing criteria, is employed here to detect the exudates. It is noted that some local minima are from the retinal background since the retinal background is uneven. Local minima below a certain threshold are chosen as the seeds. The edges in a sub-image are detected by the Canny edge detector. As some weak edges still cannot be detected, other features are examined besides checking if the region has reached an edge. Three criteria are employed:

- The gradient of the pixel is lower than a threshold T1;
- The difference between the pixel value and the mean value of the region is lower than a threshold T2;
- The difference between the pixel value and the value of the seed is lower than a threshold T3.

C. Optic disc detection

The optic disc is the exit point of retinal nerve fibers from the eye, and the entrance and exit point for blood vessels. Since the blood vessels passes through the optic disc, the blood vessel regions have to be replaced with optic disc pixels [7]. The blood vessel regions are replaced with the nearest, highest grey level pixels by gray level morphological closing operation using the square structuring element of size slightly bigger than the blood vessel width (1/40 of retinal diameter). Histogram is taken for this closed image which is used for segmentation of the brighter regions using thresholding method.

Images having bi-modal histogram can be segmented in to the background and foreground objects by threshold value by maximizing the between-class variance. But the histogram of a retinal image will be a multimodal due to the presence of many features such as arteries, veins, optic disc, fovea and exudates. Hence a multilevel threshold method has to be employed to extract the optic disc and exudates in retinal images.

D. Vessel Extraction

Vessel tracking in fundus images is of significant importance for many reasons. First, it provides a map of the retinal vessels of the eye, from which a reference frame may be derived that would ease the process of associating objects (e.g. lesions, anatomical structures) with absolute coordinates. Second, it allows the localization of stable anchor points (such as bifurcations) needed for image registration [8]. Third, it allows the characterization of veins and thus the potential detection of a very specific pathology called venous beading (tortuosity in veins that reflect the progress of diabetic retinopathy). Finally, it turns out to be helpful to other recognition algorithms by facilitating the removal of the vascular network. (For instance, algorithms dedicated to the detection of micro-aneurysms are known to 'get confused' by the presence of vessels.)

Vessel extraction is done by using connected component method. In the connected component method the connected areas are extracted from the background image. In this method the gradient of adjacent pixels are evaluated first and after that the region property of the image is applied. The blood vessel shows connected graph nature. So one of the region properties such as the area of the connected regions are extracted with the help of a filter. From the extracted vessel the width of the vessel is calculated and checked with the standard one to detect whether the patient is diabetic or not.

E. JPEG Image Compression.

JPEG compression includes both lossless and lossy modes [9]. The acceptable solutions of this compression problem are based on the human visual system and the fact that the human eye is insensitive to certain changes in an image, and tolerant of a wide range of approximations [9]. The JPEG compression takes advantage of the fact that a loss of data is acceptable.

There are basically four steps in the JPEG algorithm. First it is necessary to break the $M \times N$ image into local blocks, most popularly into 8×8 blocks. Second, these blocks need to be transformed, using the cosine transform, in order to identify the high frequency components. The cosine transforms exchanges raw spatial information for information on frequency content. Then a quantizing method, or a "rounding" procedure, needs to be applied to the transformed coefficients. The high frequencies are usually reduced considering the human eye is insensitive to high frequencies. The fourth step is encoding the output of the quantizing step. The JPEG standard uses Huffman and arithmetic coding [9].

F. Fractal image compression

1. Iterated Function Systems

Iteration is a process, or set of rules, which one repeatedly applies to an initial state. Iterated Function Systems set the foundation for Fractal Image Compression. The basic idea of an Iterated Function System is to create a finite set of

contraction mappings, written as affine transformations, based on what image one desires to create [10]. If these mappings are contractive, applying the IFS to a seed image will eventually produce an attractor of that map. It does not matter what the seed image is for the mappings, the same fixed point will be produced regardless.

2. Algorithm for Fractal Image Compression.

1. Input a binary image, call it M .
2. Cover M with square range blocks. The total set of range blocks must cover M , without overlapping.
3. Introduce the domain blocks D ; they must intersect with M . The sides of the domain blocks are twice the sides of the range blocks.
4. Define a collection of local contractive affine transformations mapping domain block D to the range block R .
5. For each range block, choose a corresponding domain block and symmetry so, that the domain blocks n the range block.
6. Write out the compressed data in the form of a local IFS code.
7. Apply a lossless data compression algorithm to obtain a compressed IFS code.

G. Fractal Denoising

In fractal denoising the relation between a noisy image and its noiseless counterpart is found out specifically in terms of their respective fractal gray-level map coefficients. This relationship provides a method of estimating the fractal parameters of the noiseless image from those of the noise free image [11]. From the former a fractal representation of the noiseless image can be reconstructed.

III. RESULT AND DISCUSSION

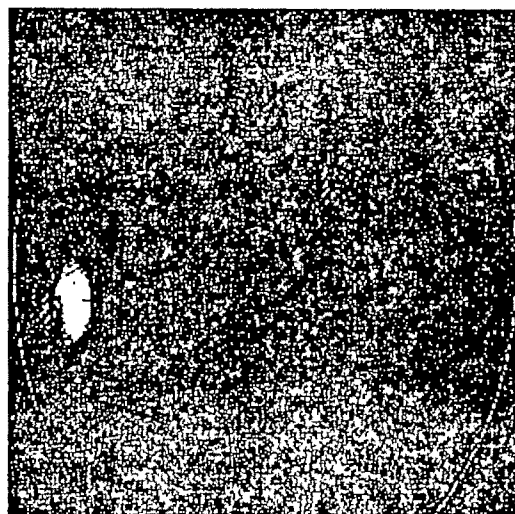
The retinal images were taken with a fundus camera during mass screening. These images saved as a 24-bit true color BMP file of 512×512 pixels. The first process performed is the feature extraction process. The preprocessing of the retinal images is done for removing the noise effect and averaging the intensity variations. Extraction of exudates and optic disc is done next and after that vessel extraction is performed. The features obtained are stored and compared with the standard values to check whether the patient is diabetic or not. This is done by checking the vessel width with the standard value of 1.5 mm and also by measuring the exudates area we can measure the rate of diabetic. The resultant images are then subjected to both JPEG and fractal image compression by 90%, 80%, 70% and 0%. Histogram

matching compare the PSNR values of both compression techniques. After JPEG and Fractal image decompression the features are extracted from the resultant image and are compared with the features extracted from the original image. The error is found to be small in fractal image compression compared to JPEG and provide good compression ratios.

Considering that each pixel requires 8 bits to store the values of 0 to 255, to store an 256×256 image pixel by pixel would require 65536 bytes (around 65KB). Using 'Fractal Encode' and 'Fractal Decode' with any chosen error, to store an image of this size with a range block size of 4×4 pixels only requires 11776 bytes. The compression ratio is better than 5:1. Of course, increasing the range block size to 8×8 pixels improves the compression to only 2688 bytes, with a compression ratio of approximately 24:1. The larger range block sizes allow higher compression ratios. The time needed to produce the attractor image is based on how much error is allowable in the transformations. The larger the error, the quicker the compression obtained. The use of the image will determine the required amount of compression and image quality.

The result of fractal image compression and JPEG compression and their histogram matching will be produced in the middle of October

Detection of optic disc and exudates



Gray equivalent of the retinal image

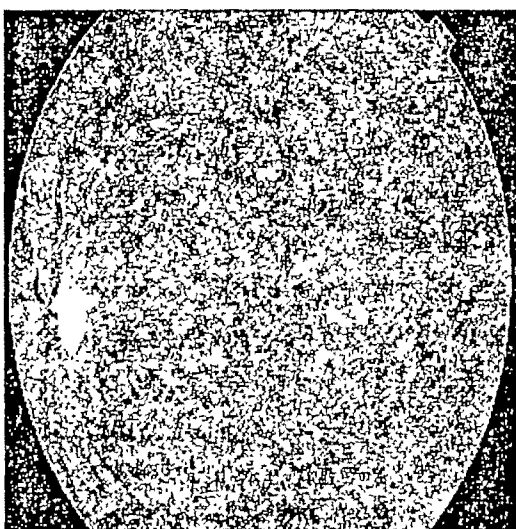


Image after Vessel extraction



IV. CONCLUSION

The effect of fractal image compression on screening of diabetic retinopathy is explained here. By providing fractal image compression the on line communication of doctors to see the current condition of the patient and able to provide a better diagnosis. This is done by taking the advantage of fractal image compression such as smaller size for storing the physical data and also provides faster data rates compared to other types of compression. The error occurred between the data before after compression is less in the case of fractal image compression compared with JPEG compression and also provide good compression ratio.

REFERENCES

- [1] Michal Sofka, and Charles V. Stewar t, "Retinal Vessel Extraction Using Multiscale Matched Filters, Confidence and Edge Measures," IEEE Transactions on Medical Imaging Vol 25, No 12, December 2006
- [2] R. Klein, etc., "Vision Disorders in Diabetes," US Department of Health and Human Services, 1985, ch.8, pp.1-2
- [3] J.J. Kanski, "Clinical Ophthalmology." Butterworths, 1989 ch. 10, pp 320-313.
- [4] Akara Sopharak, Bunyarit Uyyanonvara, "Automatic Exudates Detection from Non-Dilated Diabetic Retinopathy Retinal Image using Fuzzy C-Means Clustering," WACBE World conference on Bioengineering 2007 Bangkok, Thailand
- [5] M. Lalonde, M. Beaulieu, and L. Gagnon . " Fast and Robust optic disc detection using pyramidal decomposition and Hausdorff-based template matching," IEEE Transaction on Medical imaging Vol. 20 ,No. 11, pp. 1193-1200, November 2001
- [6] G. Luo, O. Chutatape, H. Li and S. M. Krishnan, "Abnormality detection in automated mass screening system of diabetic retinopathy," Proceedings of 14 th IEEE Symposium on computer based medical systems, 2001, pp. 132-137 .
- [7] D. Kavitha, S. Sneha Devi, "Automatic detection of optic disc Exudates in retinal images," Proceedings of ICISIP -2005.
- [8] Zhi-Wen Xu, Xia-Xin Guo, Xiao-Ying Hu, "The blood vessel recognition of ocular fundus," Proceedings of 2005 international conference 18-21 august 2005
- [9] Jhonson. Jr, "Introduction to Information Theory and data compression," CRC press
- [10] Bransley, Michel, "Fractals Everywhere," Academic press 1998.
- [11] Bransley, Michel and Lyman p. Hard, "Fractal Image compression," AK Peters, Ltd, 1993.

Protein Secondary Structure Prediction through Combination of Decisions from Multiple MLP classifiers

Piyali Chatterjee¹, Subhadip Basu², Mahantapas Kundu², Mita Nasipuri², Dipak Kumar Basu²

¹ Computer Science & Engg Department, Netaji Subhas Engineering College, Garia, e-mail: chatterjee_piyali@yahoo.com

² Computer Science & Engg, Jadavpur University, e-mail: nasipuri@vsnl.com

Abstract— A novel technique for protein secondary structure prediction is presented here. Instead of using a single sequence window of residues, five such windows of sizes 5,7,9,11,13 residues are used here for prediction of structural states of the *central residues* of the windows separately with Multi Layer Perceptron (MLP) based classifiers trained on the basis of a powerful 8-element *feature set*. Prediction decisions thus produced are finally combined through *majority voting* to reach a consensus on the *structural states* of the unknown protein. The structural states targeted by this technique include *helix*, *β -strands* and *turn*. On being tested on proteins from SWISS-PROT Protein Data Bank, the performances of the present technique are found more or less comparable with that of the three important existing methods, viz., GOR4 [12], NN-PREDICT [13], and SIMPA96 [14].

Keywords—Protein secondary structure, Classifier combination, Majority voting.

I. INTRODUCTION

Proteins are formed with chains of amino acids to constitute the core materials of living cells, which are responsible for most of the biological function of the cells. Protein secondary structure prediction is an important area of Bioinformatics. It is required for rational drug design by interpolating activities of an unknown protein from the functions of a group of known proteins of the identical structures.

Each protein folds into a 3D structure through interactions of neighboring amino acid sequence. Folding makes a protein biologically active. It begins with interactions between close neighbors of an amino acid sequence to form helical structures known as *α -helices*. Amino acid chains are aligned into *sheets*, through more distant interactions, which are called *β -sheets*.

Regions between *α -helices* and *β -sheets* are called *loops*. The loops bent to follow the shape of a hairpin in the protein chain form the structure called *turn*. A turn may be as short as two amino acids in length. A region of the secondary structure that is not an *α -helices*, *β -sheets* or a recognizable turn is commonly referred to as A coil. All these structures discussed so far are called *secondary protein structures* [1].

Secondary Protein structures further fold to form tertiary protein structures with additional amino acid interactions. For prediction of secondary protein structures, information about the amino acid sequence of the protein is necessary. And, for prediction of tertiary protein structures information about the secondary protein structure is necessary

II. A BRIEF REVIEW OF THE PAST WORK

In the early days of research on protein structure prediction i.e., in mid and late 1950s, techniques like X-ray crystallography and NMR spectroscopy were applied for this work. Such methods are not only expensive but also very time consuming.

The work on protein structure prediction has been going on for nearly last fifty years. Algorithmic procedures for prediction of secondary protein structures were started to evolve from late 1970s. In this connection, some of the important contributions came from Chou and Fasman [2], Qian and Sejnowski [5], GORIV [3], NN-PREDICT [7], SIMPA96[14], Rost and Sander[7]. Propensity values of different amino acids for forming different secondary structures play a key role in secondary protein structure prediction in general. All the algorithmic methods evolved so far for secondary protein structure prediction mainly differ in how *residue* information from amino acid sequences are used. Each element of an amino acid sequence representing a specific monomer of the corresponding protein, is called a *residue*. Out of various algorithmic methods for secondary protein structure prediction, the older ones mostly depend on single residue statistics expressed by their propensity values. The modern methods mostly depend on information from a

group of adjacent residue, i.e., an amino acid sequence *window*, and sets of *homologous sequences*. Homologs are proteins having similar structures due to their shared ancestry.

The work by *Chou and Fasman* [2] represents an important piece of old method. Search for contiguous regions of residues with a high probability of forming a secondary structure feature is central to this work. The accuracy of such method was later found to be overestimated, as the databases used for supplying the statistical information could not be made sufficiently exhaustive due to the low number of known protein structures.

In the pioneering work of Qian and Sejnowski [5], secondary protein structures are predicted through two levels of refinements. In the *first level*, probabilities for forming three secondary structures, i.e., α -helices, β -sheets and loop region are produced through a neural network supplied with the residue identities i.e., identities of constituent amino acids of a 13 residue sequence window coded with a 20 bit coding per residue. The neural network predicts the probabilities for forming the said three secondary protein structures by the central amino acid of the sequence window supplied to it. The process is repeated by sliding the sequence window residue by residue on the amino acid sequence of the unknown protein requiring structure prediction. On completion of this process, i.e., at the end of first level activities, probabilities of forming the three secondary structures by the constituent residues of the sliding window, which may also be considered as certainty of first level prediction decision are supplied to another network for obtaining refined prediction decisions about the secondary protein structures of an unknown protein at the second level. It is again performed through a window-by-window manner. The combined average performance of the two-cascaded neural network is experimentally observed to be 64.3% on a test set of non-homologous proteins. This is the best possible performance on the training set of non-homologous proteins, as reported in [5].

Prediction of the secondary structure of the central amino acid on the basis of information theoretic measure is central to a series of GOR methods developed throughout the period of 1970s to 1980s [3][4][9][15].

What is common to all the first three versions of GOR methods is that the structural state of a central amino acid is determined there on the basis of the maximum information sum produced by the neighboring residues on the central residue. In GOR IV method, the difference between the information sum for each structural state and that for the set of its complementary states is considered before determining the state of a central amino acid. The state, for which the maximum information difference is produced, is finally selected for the central amino acid. Here also the information equations remain complexly conditioned as in GOR III method. On a database of 267 proteins, the mean accuracy of GOR IV method was observed as 64.4% for a three-state prediction i.e., for α -helices, β -sheets and coil. However, there is no scope for utilizing evolutionary information in GOR IV method.

One of the important neural network based second generation methods is *NN-PREDICT*[6][7]. A two layer feed forward neural network is used there for secondary protein structure prediction from amino acid sequences. The technique is reported to have obtained the best-case prediction of 79% for the class of all-alpha proteins.

SIMPA96 is also another important window based method, which uses training data of short fragments, each of length equal to the window size, collected from protein sequences of known structures but minimal sequence similarity. For predicting secondary structures of an unknown protein fragments of equally sized sequences, extracted from unknown proteins, are compared with training data using Nearest neighbor method in search of the most similar fragments.

Rost & Sander [11] made some significant upgradations in the neural network based paradigm for protein secondary structure prediction. In their work, they have used *multiple protein sequence alignment* with appropriate cut-offs to supply more enriched information about the protein secondary structure, compared to what can be supplied with a single sequence to the neural network. Multiple protein sequence alignments are generated from the *training database for utilizing evolutionary information in secondary structure prediction*. In the work of Rost and Sander, they have also addressed the problem of inadequacy in the *length distribution* of the predicted helices and strands by introducing a *second-level* neural network for *structure-to-structure* prediction. But this can enhance the overall accuracy only marginally. For final prediction of a protein secondary structure, a *voting* method is followed with the responses of 12 different neural networks working parallelly on the same input. With this, additional two percentage points in overall accuracy are gained. In testing the performance of their method, Rost and Sander prepared a database of 130 representative protein chains of known structures. In this database, no two sequences can have more than 25% identical residues. With seven fold cross validation of results, the overall three-state prediction accuracy of the method is observed as 69.7%. It was three percentage points above the highest value (66.4% [8]) reported previously. This is all about the brief descriptions of some of the important past works leading to protein secondary structure prediction.

III. MOTIVATION

In the light of the above discussion, it appears that there is still some scope for studying how best multiple attributes or features of constituent *residues* of an amino acid sequence, such as amino acid type, hydrophobic value, structural propensity values, probabilistic measures of forming structures by each amino acid type can be utilized for *sequence to structure* prediction. A good tradeoff can be made among different window sizes by adopting a standard technique for *combination* of prediction decisions obtained individually with various window sizes about the *structural*

state of each residue. The work presented here mainly concentrates on these two aspects, i.e., how best different features of contiguous residues within a window can be utilized to decide about the structural state of the central amino acid therein and how prediction decisions about the structural state of each residue obtained with different window sizes can be combined.

IV. THE PRESENT WORK

In this work, three MLPs are employed for separately producing prediction decisions about the three structural states of the central residue of a hypothetical window placed over the amino acid sequence of a protein under consideration. In doing this, the necessary feature values representing the four types of features, as mentioned before, are extracted from each residue of the currently selected window and then supplied to the three MLPs separately. The total number of feature values, considered for this work, is 8. The number of inputs to each of the three MLPs becomes the product of the said number of features and the window size. And the number of outputs of the MLP becomes two, i.e., one for a particular structural state and the other for all other structural states. So, each of three MLPs employed for this work is required for recognizing one of the three above mentioned structural states viz., helix, β strand, turn.

A. The Feature Set

The following are the descriptions of the four types features (F_0 - F_7) use in the present work.

1) *Amino Acid Type (F_0)*: Each residue position in a protein may bear one of the twenty amino acids, viz. A, R, N, D, C, Q, E, G, H, I, L, K, M, F, P, S, T, W, Y, V. They are coded with values varying from 0.05 to 1 in steps of 0.05.

2) *Hydrophobicity Value (F_1)*: Hydrophobic values of all the amino acids are shown in Table I of the Appendix. For conducting experiments, hydrophobic values are *normalized* in the range from 0 to 1.

3) *Structural Propensity Value (F_2 - F_4)*: Each amino acid in a protein chain has its own structural propensity value to form a particular secondary structure. Structural propensity values of each amino acid for forming helix, β -strand and turn are given in Table I in the Appendix. In this work, these structural propensity values of an amino acid residue, are considered as 3 features. These values are also normalized here within the range from 0 to 1.

4) *Probability of forming a structure by each Amino Acid type (F_5 - F_7)*: The statistical knowledge about how frequently a particular amino acid forms each of the three said structures in the training data is also considered here for prediction of protein secondary structures. In doing this, the probability that each amino acid can form a particular secondary structure in the training data is computed for all the twenty amino acids and the three secondary structures, under consideration for this work, which are considered as three features here.

B. Deciding about the window sizes

Many methods examine different sequence windows of 13-17 residues and assume that the central amino acid in a window will adopt a conformation that is determined by side groups of all the amino acids in the window. The length for helices varies from 5 to 40 residues whereas that for β -strands varies from 5 to 10 residue [15]. Generally, helices are of longer lengths compared to strands and turns. Considering this, experiments for the present work are conducted by varying the window size from 5 to 13 residues in steps of 2.

C. The MLP as a classifier

Each of the above mentioned three MLPs is trained with a training set consisting of data from the two complementary classes in equal proportion.

For determining the structural states of residues of an unknown protein chain, the set of *feature values* extracted from a *window* of *residues* of the same protein is supplied to the three MLPs separately, whose outputs classifies the *central residue* of the window with some degree of *confidence*. Considering the maximum of these outputs from three MLPs, the structural state of the central residue is determined. If this maximum output value becomes less than 0.5 then the structure of the central residue is recognized as a Coil.

D. Combination of Decisions obtained from different window sizes

In the present work, the secondary structure of each residue of an unknown protein is determined with five different window sizes. Every residue of the unknown protein is marked with five possible prediction decisions on its structural state corresponding to five different window sizes. To decide about the residue structures finally, a *majority voting* is to be conducted for each residue of the unknown protein. This is how the prediction decisions about the structural state of each residue, drawn with different window sizes, are finally combined to reach a consensus.

E. Results and discussion

To test the performances of the technique presented here, a database is formed by selectively collecting 58 annotated proteins from SWISS-PROT Protein Data Bank. These proteins were also used for the pioneering work of Qian and Sejnowski[5] With the protein database thus prepared, a *training data set* consisting of 53 proteins and a *test data set* consisting of rest of the 5 proteins are formed. In forming the test set, the proteins of test set 2, used by Qian and Sejnowski, are selected only except one, which is not available from SWISS-PROT data bank. The proteins of the test set thus formed have *homology* with the proteins of the training set, as investigated by Qian and Sejnowski [5] using the method of Kabsch and Sander.

To test the performances of the technique presented here, a database is formed by selectively collecting 58 annotated proteins from SWISS-PROT Protein Data Bank [10]. These proteins were also used for the pioneering work of Qian and

Sejnowski [5]. In fact, more proteins were used for that work. But not all of them are available from the SWISS-PROT Data Bank. The performance of the structure prediction technique as observed after voting is measured here on the basis of the following $Q_3 = (P_\alpha + P_\beta + P_{turn})/N$, where P_α , P_β , P_{turn} are the numbers of correctly predicted helices, β strands and turns in the residues respectively, and N is the total number of residues. Q_3 provides an *overall success rate* of the technique. The performances of the technique are also analyzed on the basis of certain parameters, viz., TP (i.e., Truly identified Positive instances of data), FN (i.e., Falsely identified as Negative instances of data) and FP (i.e., Falsely identified as Positive instances of data). All these are shown in Tables (I-V) for the five test proteins selected for this experimentation

Table I. Protein P00336, $Q_3=51.21\%$

P00336	+ve data	-ve data	TP(%)	FN(%)	FP(%)
helix	127	207	44.88	55.11	4.83
turn	15	319	40.00	60.00	9.09
strand	34	300	64.70	35.29	11.0

Table II. Protein P01009, $Q_3=51.21\%$

P01009	+ve data	-ve data	TP(%)	FN(%)	FP(%)
helix	108	310	71.29	28.70	19.03
turn	38	380	63.15	36.84	14.47
strand	143	275	32.88	67.13	3.27

Table III. Protein P02208, $Q_3=58.33\%$

P02208	+ve data	-ve data	TP(%)	FN(%)	FP(%)
helix	108	42	80.18	39.81	7.14
turn	10	140	50.00	50.00	15
strand	2	148	0.00	100.00	9.45

Table IV. Protein P00617, $Q_3=25.55\%$

P00617	+ve data	-ve data	TP(%)	FN(%)	FP(%)
helix	50	97	14.00	86.00	7.21
turn	19	128	47.36	52.63	18.75
strand	21	126	33.33	66.66	16.66

Table V. Protein P07195, $Q_3=46.21\%$

P07195	+ve data	-ve data	TP(%)	FN(%)	FP(%)
helix	147	187	48.29	51.70	13.90
turn	28	306	67.55	32.44	15.38
strand	39	295	35.95	64.04	12.54

To make a comparative assessment of the performances of the present technique, three of the existing techniques, viz., GOR4 [12], NN-PREDICT[13] and SIMPA96[14], are separately applied on the same test data, on which performances of the present technique are computed. The said three techniques are considered here mainly because of the

fact the tools based on these techniques are readily available through Internet for testing. To make a visual presentation of a comparative assessment of the present technique and the said three, Bar charts showing the performances for helices and β -strands are shown in Figs. (I-V) for all five test proteins. In all these figures, the bar charts labeled with 'MULTI-MLPs' are obtained by the present method.

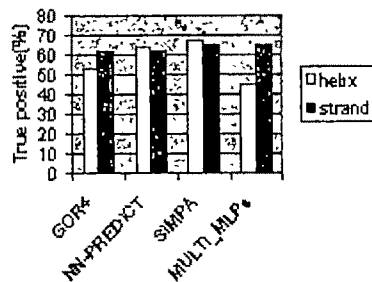


Fig I. Bar chart drawn with P0336

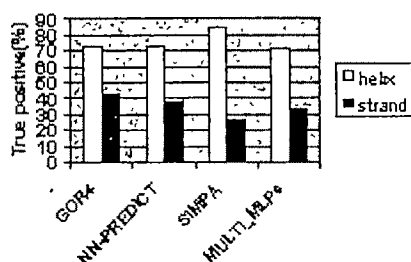


Fig II. Bar chart drawn with P01009

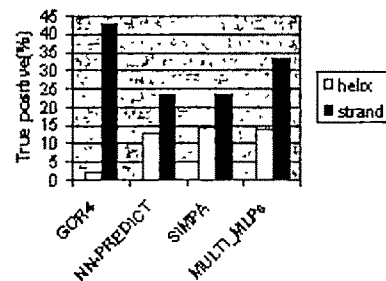


Fig III. Bar chart drawn with P00617

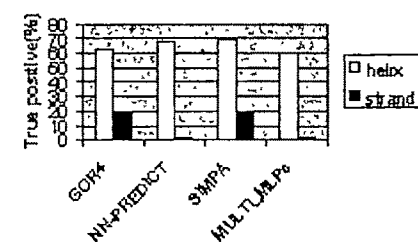


Fig IV. Bar chart drawn with P07195

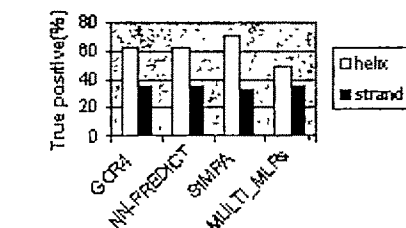


Fig V. Bar chart drawn with P02208

ACKNOWLEDGMENT

These *bar charts* are drawn for graphical representations of P_{α} , P_{β} for each of these four methods, including the present one. Since turns are not separately predicted in the said three of the existing methods, P_{turn} is not considered for drawing these bar charts. On analysis of the bar charts, it can be observed that, out of the five cases, in two cases, i.e., for Protein P01009 and P00617 the performances of the present technique are more or less comparable to that of the said three techniques. For β -strands, the performance of the present technique more or less excels that of the existing three techniques for Proteins P00336 and P07195. The present technique fails miserably on β -strand data collected from P02208. NN-PREDICT also does the same in this case. It is possibly because of presence of strands in P02208 data in a very small proportion.

V. CONCLUSION

In conclusion, it can be said that the performances of the present technique are more or less comparable with that of the three important existing methods, viz., GOR4, NN-PREDICT, and SIMPA96. This has been possible without incorporating evolutionary information through alignment of homologous proteins and adopting a second level structure-to-structure prediction paradigm. The power of the present technique mainly lies in the feature set selected for this work and the combined decision obtained from prediction decisions produced with 5 different window sizes.

APPENDIX

Table I. Amino Acid Propensity and hydrophobicity values

Amino Acid	Structural propensity			Hydrophobicity
	α -helices	β -sheets	turn	
A	1.40	0.75	0.80	1.8
R	1.20	0.90	0.90	-4.5
N	0.78	0.66	1.54	-3.5
D	1.00	0.66	1.40	-3.5
C	0.95	1.10	1.00	2.5
Q	1.17	1.00	0.95	-3.5
E	1.45	0.51	0.77	-3.5
G	0.63	0.85	1.60	-0.4
H	1.12	0.83	0.90	-3.2
I	1.00	1.57	0.47	4.5
L	1.30	1.20	0.60	3.8
K	1.22	0.70	1.02	-3.9
M	1.30	1.12	0.60	1.9
F	1.15	1.23	0.60	2.8
P	0.50	0.60	1.50	-1.6
S	0.72	0.95	1.40	-0.8
T	0.78	1.43	0.50	-0.7
W	1.03	1.26	0.90	-0.9
Y	0.74	1.40	1.00	-1.3
V	0.96	1.66	0.50	4.2

Authors are thankful to the "Center for Microprocessor Application for Training Education and Research", "Project on Storage Retrieval and Understanding of Video for Multimedia" of Computer Science & Engineering Department, Jadavpur University, for providing infrastructure facilities during progress of the work. Authors are also grateful to SWISS-PROT protein databank for online help. One of the authors, Mrs. P. Chatterjee is thankful to Netaji Subhas Engineering College, Garia for kindly permitting her to carry on the research work.

REFERENCES

- [1] David Mount., "Bioinformatics Sequence and Genome Analysis" second edition] 456
- [2] P.Y Chou and G.D. Fasman, "Prediction of Secondary Structure of Proteins from their amino acid sequence", *Advances in Enzymology and Related Areas of Molecular Biology*, 47:45-148,1978
- [3] J.Gannier, D.J.Osguthrope and B.Robson, "Analysis of the accuracy and implications of simple methods for predicting the secondary structure of globular protein", *Journal of Molecular Biology*, 120 97-120,1978.
- [4] J.Gannier,J.F. Gibrat and B.Robson, "GOR method for predicting protein secondary structure from amino acid sequence", *Methods in Enzymology*,266:540-553,1996
- [5] N. Qian, T.J. Sejnowski, "Predicting the secondary structure of globular proteins using Neural Network models", *Journal of Molecular Biology*, 202, 865-884,1988.
- [6] D.G. Kneller, F. E Cohen and R.Langridge, "improvements in protein secondary structure prediction by an enhanced neural network", *Journal of Molecular Biology*,214(1):171-182, Jul 1990
- [7] <http://www.cmpharm.ncsf.edu/%7Eenom/nnpredict.html>
- [8] B.Rost and C. Sander, "Prediction of protein secondary structure at better than 70% accuracy", *Journal of Molecular Biology*,232(2):584-599,Jul 1993.
- [9] J. Gibrat, J. Garnier, & B.Robson, " Further developments of protein secondary structure prediction using information theory—new parameters and consideration of residue pairs. *J Mol Biol*, 198 : 425-443, 1987.
- [10] <http://www.expasy.ch>
- [11] B.Rost, C. Sander, "Improved prediction of protein secondary structure by use of sequence profiles and neural networks", *Proc Natl. Acad Sci USA*, vol 90, 7558-7562, 1993.
- [12] http://npsa-pbil-ibcp.fr/cgi-bin/npsa_automat.pl?page=npsa_gor4.html
- [13] http://npsa-pbil-ibcp.fr/cgi-bin/npsa_automat.pl?page=npsa_nn.html
- [14] http://npsa-pbil-ibcp.fr/cgi-bin/npsa_automat.pl?page=npsa_simp96.html
- [15] Kloczkowski.A, Ting K-L, Jerigan RL, Garnier J, "Protein Secondary Structure Prediction based on the GOR algorithm incorporating multiple sequence alignment information", *Polymet* 2002;43:441-449

Study of EEG Signals under Photic Stimulation

Mohandas K P and Rameshkumar P

National Institute of Technology Calicut, Calicut, Kerala 673601, Email: kpmidas@yahoo.com

Abstract: EEG Signals have been used as one of the most effective methods for the diagnosis of brain disorders like epilepsy. As the onset of EEG cannot be easily predicted one of the ways of studying and classifying different types of brain disorders is to induce mild form of epilepsy by stimulating the eyes with light of controlled intensity and frequency. This is called photic stimulation. Nonlinear parameters such as correlation dimension and entropy can be used as measures for the state of the brain under different levels of epileptic conditions.

Key words—EEG signals, biomedical signal processing, nonlinear analysis of EEG

I. INTRODUCTION

ELECTROENCEPHALOGRAMS (EEG) have been used as an important clinical tool for the evaluation and diagnosis of brain disorders and mental activities. Even though the EEG is indicative of mental activities, the online analysis of a non-stationary EEG signal is a complicated process. Epilepsy is a chronic neurological condition characterized by recurrent seizures caused by abnormal cerebral nerve cell activity. Photic stimulation is a method of stimulating seizures in epilepsy patients by subjecting the patient to light flashes of varying intensity and then observing the changes in the pattern of EEG. Several attempts have been made in modeling of EEG signals using linear time series models. These have been found to be moderately adequate for detection of epileptic spikes in EEG signals to a reasonable extent. However in order to analyze the variation of EEG signals recorded under different conditions or for developing techniques for brain computer interfacing and for classifying the type of epileptic seizures, non-linear analysis of EEG signal provides a better means. In this paper, the non-linear parameters correlation dimension and entropy are employed to investigate the complexity of EEG signals. The study shows that these parameters can be effectively used to study the variation of EEG signals under different stimulated conditions. It is seen that the EEG signals exhibit chaotic behavior when it contains spikes.

II. EEG SIGNALS AND BRAIN DISORDERS

The main sources of EEG potentials are cortical neurons, which are arranged in layers beneath the cortical surface. Within each layer, neurons are aligned in bundles oriented

perpendicular to the cortical surface. EEG signals are continuous variations of summated cellular electrical potentials as a function of time and location. If two electrodes are applied to the surface of human brain, a sensitive instrument can show continuous fluctuation of electrical potential difference between two electrodes. The EEG is a measure of this potential, which represents signal containing information about the condition of brain. The shape of the wave may contain useful information about the state of brain. The analysis of recorded EEG can be done for estimation of brain state and for diagnosing brain diseases such as traumatic brain injuries, brain tumors, epilepsy, Alzheimer's disease, sleeping disorders, and other psychometric disorders. Analysis of recorded EEG data is presently the least expensive and most widely used way to effectively and non-invasively study human brain function.

The characteristics of EEG signals may be studied using different measures. One of the most common measure is the different frequency components such as alpha, beta, theta, delta and other components. These are identified by their features as follows:

Table 1. Components in EEG - Frequency Ranges

Components	Frequency Range Hz	State of the brain activity
Alpha	8 -13	Closely related to cerebral blood flow
Beta	18 -25, 14-16, 35-40	High amplitude in drowsiness, light sleep and rapid eye movements
Theta	6-7	Heightened emotional states
Gamma	30-100	Cognitive functions such as attention, learning and memory

III. ARTIFACTS AND THEIR REMOVAL

The recording of physiological signals is prone to a variety of extraneous influences that may add up to, or completely mask the signals of interest. These unwanted signals are usually referred to as 'artifacts' and they make it difficult for the physician to interpret the outcome of the recording and in some cases they lead to an erroneous diagnostic or misinterpretation of the information. Artifacts are generally divided into two groups: physiological and nonphysiological. Physiological artifacts usually arise from generator sources

within the body but not necessarily the brain such as due to eye movements, due to electrocardiographic, electromyographic, glossokinetic effects or artifacts due to physiological movements etc. Non-physiological artifacts come from a variety of sources, which includes instrumental artifacts, electrode artifacts, environmental artifacts etc.

IV. PHOTIC STIMULATION FOR EEG STUDIES

EEG is considered as the most useful and important test in confirming and diagnosing epilepsy. The recorded EEG data is analyzed and studied to get a clear idea about the kind of epilepsy the patient is suffering from. But some people with abnormal EEG results do not have epilepsy and some people who have epilepsy will have normal EEG results despite repeated tests. If the doctor suspects that a person has epilepsy but the EEG is normal then the patient may be subjected to a technique of stimulating the seizure called photic-stimulation. In this technique, pulsed light of variable intensity and frequency is shown to the eyes of the patient after the patient has been placed around 30cm from the photic stimulator device. Separate ten seconds trains of flashes are given for each frequency with intervals of seven seconds [1]. If we observe the EEG under photic stimulation we can observe seizure in the EEG waveform of the patient if the patient is suffering from photosensitive epilepsy. This recorded EEG data can be used for clinical analysis of the disease. The photic stimulation has shown itself to be very effective in the treatment of whole range of illness and complaints including migraine, insomnia, stress, seasonal affective disorder and attention deficit disorder [2].

Doctors treat epilepsy primarily with seizure-preventing medicines. Although seizure medications are not a cure, they control seizures in the majority of people with epilepsy. Surgery, diet (primarily in children), or electrical stimulation of the vagus nerve, a large nerve leading into the brain, may be options if medications fail to control seizures. Several drugs (called antiepileptic or anticonvulsant drugs) are prescribed to prevent seizures. Many factors are involved in choosing the right seizure drug. The goal of treatment is to stop seizures without side effects from the medicines [3,4]. Portable photic stimulation devices have been developed recently. Many researches are currently studying the effectiveness of pulsed light therapy or photic stimulation as treatment for brain disorder.

V. NONLINEAR PARAMETERS FOR EEG STUDIES

The importance of the biological time series analysis, which exhibits typically complex dynamics, has long been recognized in the area of nonlinear analysis. Several features of these approaches have been proposed to detect the hidden important dynamical properties of the physiological phenomenon [5]. The nonlinear dynamical technique is based on the concept of chaos and it has been applied to many areas including the area of medicine and biology. The nonlinear

analysis technique is found to be a better approach than traditional linear methods in characterizing intrinsic nature of EEG. Efforts have been made in determining non-linear parameters for pathological signals and it has been shown that they are useful indicator of pathologies. The chaotic behavior at neural level could be responsible for brain diseases such as insomnia, epilepsy and other brain disorder [5]. The analysis of nonlinear dynamics in EEG could improve medical diagnostics and the understanding of physiological processes. It can provide information about the timing and locations of inter ictal activity, the duration and pattern of spread of ictal discharge for patient with epilepsy and seizures. Automatic and real time seizure detection would be very useful in clinical practice. Thus automated methods for EEG analysis are attractive and beneficial to conventional visual analysis procedure. In analysis of EEG data here, different non-linear parameters such as correlation dimension and approximate entropy are used. A brief description of the non-linear parameters is given below.

Correlation dimension

The dimension of a graph, which gives information about the nature of the system, can be determined from experimental data. This is useful in understanding the system, particularly for deciding whether the system is periodic, chaotic or noisy. Correlation dimension is one of the most widely used measures of fractal dimension, which describes the dimensionality of the underlying process in relation to its geometrical reconstruction in phase space. According to Grassberger and Procaccia algorithm [5,6], construct a function $C(r)$ that is the probability that two arbitrary points on the orbits are closer together than r . This is done by calculating the separation between every pair of N data points and sorting them into bins of width dr proportional to r . Correlation dimension was calculated using the distance between each pair of points in the set of N number of points,

$$s(i, j) = |X_i - X_j| \quad (1)$$

A correlation function $C(r)$ is calculated using the formula,

$$C(r) = \frac{1}{N^2} (\text{Number of pairs of } (i, j) \text{ with } s(i, j) < r) \quad (2)$$

The $C(r)$ has been found to follow a power law $C(r) = k r^D$ then by definition correlation dimension CD is given by,

$$CD = \lim_{r \rightarrow 0} \frac{\log C(r)}{\log(r)} \quad (3)$$

The correlation dimension can also be estimated using a new method called Gaussian Kernel algorithm [7]. The Gaussian kernel algorithm allows one to simultaneously estimate the complexity of the deterministic structure (correlation dimension and entropy), the scale of noise contamination and the distribution of inter-point distance. The Gaussian kernel algorithm is employed in this work for evaluating the non-linear parameters correlation dimension and entropy [8].

Entropy

Entropy is the thermodynamic quantity describing the amount of disorder in the system [7]. From information theory perspective, the above concept of entropy is generalized as an amount of information stored in more general probability distribution. The theory was supported by the contributions by Shannon, Renyi and Kolmogorov. Entropy is determined from the embedded time series data by finding points on the trajectory that are close together in phase space but which occurred at different times. These two points are then followed in to the future to observe how rapidly they move apart from one another. Entropy reflects how well one can predict the behavior of each respective part of trajectory from the other. Higher the entropy indicates less predictable and closer approach to stochasticity. Entropy applied to EEG signal analysis it reflects the intra-cortical information flow in the brain.

Significance Of Non-Linear Parameters

The non-linear parameters can represent the complexity of the physiological signal such as EEG and ECG. If the complexity of a system is more, the correlation dimension takes a higher value [9]. It is well known that the dimension of EEG time series is closely related to the cognitive activity of the brain. The dimension increases with the degree of cognitive activity of the brain. During the condition of epilepsy the brain will not be involved in any type of cognitive activity hence the complexity of the brain reduces and the correlation dimension takes a lower value. This shows that correlation dimension can be employed as a direct measure of the complexity of brain.

A chaotic signal is a signal produced by an autonomous chaotic system in response to an initial condition that leads to aperiodic behavior. It is possible to use the nonlinear parameter as measure of the degree of chaos. Higher the value of correlation dimension implies that the system is periodic and lower the value indicates that the system is exhibiting a chaotic behavior. If the signal contains spikes the system loses its predictability and the correlation dimension takes a lower value implies the system exhibits a chaotic behaviour. An uncorrelated random noise is completely unpredictable, it essentially fills up any space in which it is embedded and therefore its correlation dimension is theoretically infinite. Correlated random noise is expected to have a high dimension also but dimension estimates from short data records of correlated noise can be surprisingly low. So filtering with a linear Finite Impulse Response filter has been shown not to seriously corrupt the estimate of correlation dimension and report that various non-linear filtering schemes improve the ability to determine correlation dimension in their particular applications. The correlation dimension will be overestimated if the amount of noise content in the signal is more. [9]

Entropy provides generalized measure of regularity of a system. A deterministic signal with high regularity has a higher probability. Such a signal will hold a smaller entropy

value; whereas a random signal has a very low regularity and will hold a high entropy value. In other words, a time series containing many repetitive patterns has relatively small entropy and a less predictable process has higher entropy value [6]. In the case of an EEG signal, a normal EEG pattern has many repetitive patterns so that such a signal will have relatively lower entropy value compared with any abnormality.

VI. RESULTS OF NON-LINEAR ANALYSIS

The non-linear analysis has been carried out on the three stage of the recorded EEG, which is normal, pre-photic and photic stimulated condition. The variation on these parameters has been studied. Here we employ the above discussed Gaussian kernel algorithm for finding the non-linear parameters.

Now considering the normal EEG data of patient 1, the correlation dimension and entropy is found with different values of embedding dimension ranging from 2 to 20, as shown in Fig.1. The correlation dimension holds a constant value for an embedding dimension in the range of 14-16 and 18-20 after a gradual rise in initial portion of the graph. Entropy holds more or less constant value after an embedding dimension of 4. The plot of EEG shows there is no spike content in the waveform and it indicates that it is a normal data. Now considering another set of EEG data of patient 1 before the photic stimulation and the above procedure for finding the non-linear parameters carried out. The variation in non-linear parameters under the pre-ictal stage is shown with different values of embedding dimension

Fig 2 shows the variation of correlation dimension for pre-photic EEG. It is seen that it takes a constant value for an embedding dimension of 10-12 and 18-20. The plot for EEG shows that there are some spike content in the waveform with high magnitude and sharp slope indicating the presence of disorder in the brain. Entropy does not follow any particular order of variation with embedding dimension in this case. For a particular embedding dimension the correlation dimension holds a higher value in the case of normal EEG compared to the one with spike content indicating that the complexity of brain is more in normal case. The higher the value of entropy in the second case shows that the system will become less predictable due to presence of spike. The same procedure finding the non-linear parameters carried out for the EEG data under photic condition that contains more number of spikes than previous two cases.

The Fig 3 shows that variation of correlation dimension and entropy with embedding dimension for EEG under photic stimulation. Correlation dimension takes approximately constant value for an embedding dimension of 10-12 and 14-20 range. The entropy decreases after an embedding dimension of 4 and bears constant value there after. The EEG plot shows that are many spike present in the data with high amplitude and sharp spike indicating the presence of abnormality. The Table II below shows the comparison of correlation dimension for three cases with an embedding

dimension of 10 and 20.

Table II Variation of correlation dimension with embedding dimension

Patient	Embedding dimension	Normal	Pre-photic	Photic
Patient-1	10	2.345	2.198	2.037
Patient-1	20	4.583	3.783	3.321

Table II shows that correlation dimension takes a lower value when there is spike content in the EEG compared to that of a normal EEG. This proves that the complexity of the brain is reduced during epilepsy or other brain disorders. It is well known that the complexity of brain will be more when we are thinking, or doing some cognitive tasks. Then, the correlation dimension takes a higher value. But on the onset of epilepsy, the brain will not be involved in any type of cognitive activity or even the patient may loose his consciousness due to which the complexity reduces and the correlation dimension takes a lower value. The comparison of the entropy value is given in Table III

Table III. Variation of entropy with embedding dimension

Patient	Embedding dimension	Normal	Pre-photic	Photic
Patient-1	10	-0.245	-0.204	-0.189
Patient-1	20	-0.276	-0.222	-0.207

The above procedure of non-linear analysis has been carried out for seven patients and parameters compared for a correlation dimension of 20. The seven patients considered here are of different kind seizure content in the EEG pattern. But the changes are occurring in the parameters in an ordered way in the sense that we can get a clear picture of how the parameters vary with spike content in the waveform. The table IV shows the variation of correlation dimension on different conditions for seven patients.. The values of non-linear parameters for the three cases such as normal, pre-photic and photic with an embedding dimension of 20 is shown in Fig 4 with the help of a bar graph to easily understand the variations.

The plot clearly indicates that the values of correlation dimension is lesser in the case of pre-photic condition when compared with that of normal because of the presence of spikes in less amount during pre-photic condition. When we compare the correlation dimension in the photic condition with that of normal, there is an appreciable difference between the two because of presence of more number of spikes during photic stimulation. The plot confirms that the complexity of brain is reduced in case of photic stimulated condition compared to that of normal and pre-photic condition. From the

above discussion, we can conclude that correlation dimension is a reliable measure of complexity of the brain.

Now consider the variation of the other non-linear parameters, entropy for the three stages such as normal, photic and pre-photic for an embedding dimension of 20. The table IV shows the variation of entropy on different conditions.

Table IV. Correlation dimensions of different patients for an embedding dimension of 20

Condition	Patient Number						
	1	2	3	4	5	6	7
Normal	4.58	4.58	3.76	3.61	4.41	3.71	4.68
Pre-photic	3.78	3.45	2.05	2.56	3.34	3.48	79
Photic	.32	3.53	1.87	2.34	3.34	3.33	3.20

The bar graph in Fig 5 shows the entropy takes a higher value in the case of pre-photic and photic stimulated condition compared with normal EEG. This is because the signal becomes less predictable when it contains spikes. In other words, a time series containing many repetitive patterns has relatively small entropy and a less predictable process has higher entropy value. A normal EEG pattern has many repetitive patterns so that such a signal will have relatively lower entropy value compared with any abnormality. Here during pre-photic and photic stimulated condition the EEG contains some spikes so that its predictability decreases tremendously. More the amount of spike contents in the EEG higher the deviation in parameters from that of normal EEG. There is a difference in the case of patient2 and 3, the values of entropy is higher in pre-photic stage than that in photic condition because this patients data contains more spikes during pre-photic condition itself.

VII. CONCLUSIONS

The above study shows that the non-linear parameters can successfully describe the complexity of the brain. There is a decrease in correlation dimension during pre-photic and photic condition compared with that of normal EEG. The reason behind the drop in correlation dimension during photic stimulated condition or during the onset of epilepsy is that the cortex become more inactive and less number of neurons will be available for the processing of information also brain is not involved in any type cognitive tasks or thinking. As we know that during thinking or doing some mathematical problem the brain will be in a more complex state and the measure of complexity that is correlation dimension takes a higher value. But during the onset of epilepsy the patient may loose his consciousness and control indicating that brain is not coordinating his action and the complexity measure takes a lower value.

Considering the other non-linear parameter entropy, which shows that, a predictable signal takes lower entropy value compared with a less predictable signal. In the case an EEG signal a normal EEG pattern have many repetitive pattern so that such a signal will have relatively lower entropy value compared with an EEG with any abnormality. Here, when the signal contains spikes, it loses its predictability compared with a normal EEG. In other words, entropy takes a higher value. During the onset of epilepsy the EEG data is characterized by large number of spikes in which case the parameter entropy will take a higher value. A more general abnormality-detecting algorithm can be built by considering number of patient's data under normal and abnormal conditions, which will help the physician in diagnosing brain disorder.

VIII. REFERENCES

- [1] D J Anderson Bsc, MBBS, "The treatment of migraine with variable frequency photo-stimulation", The journal of Head and Face pain, volume 29 page 154-march 1989.
- [2] www.webmd.com/nw/epilepsy/aa22249.asp
- [3] William J Marks, "Management of seizures and epilepsy including patient information handout". American family physician, Vol.57/No.7 April 1998
- [4] Elinor-Ben Menachem MD, PhD, "Predicting epileptic seizures: a quantitative approach". MedGenMed journal-2002
- [5] Kannathal Natarajan, Rajendra Acharya, U Fadillah Alias, Thelma Tibolena and Sadasivan K Puduserypady, "Non Linear analysis of EEG signal at different mental states", Bio Medical Engineering Online, March 2004, 3.
- [6] Rajendra Acharya U, Oliver Foust, N Kannathal, Tji Leng Chua, Swami Lakshminarayan, "Non linear analysis of EEG signal at various sleep stages", computer method and program in biomedicine 2005, Elsevier science Vol 80, 2005:37-45(9 pages)
- [7] Michael Small, Dejin Yu, Jennifer Simonotto, Robert G Harrison, Neil Grubb, K A A Fox, "Uncovering non linear structure in human ECG recordings" Chaos, Solitons and Fractals 13(2002), Pages 1755-1762
- [8] Liang Fang, HaoYang, Wei He, Heng-Ming Tai, "Non Linear analysis of EEG signals", IEET Trans.2002.
- [9] Eugene N.Bruce, "Biomedical Signal Processing and Signal Modeling". A Wiley-Interscience Publication, 2006.



Fig 5 Comparison of entropy for three states

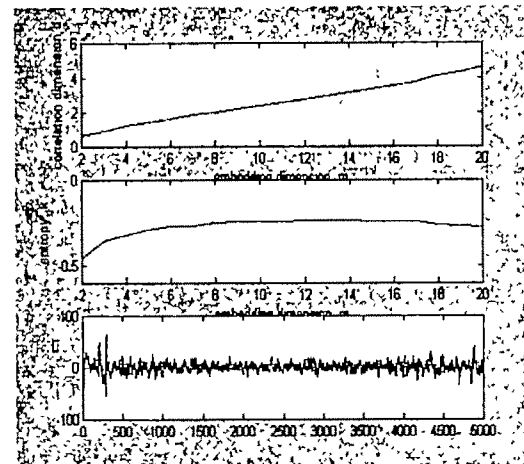


Fig 1. Variation of correlation dimension, entropy with embedding dimension for normal EEG

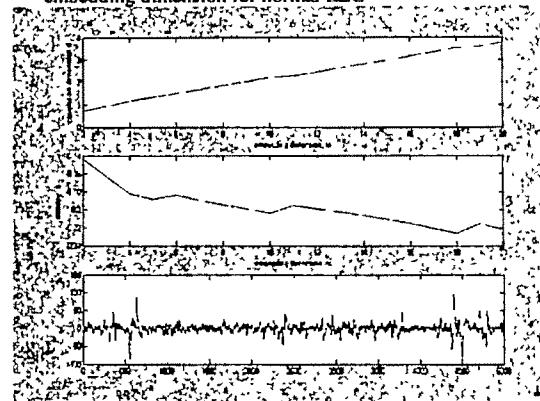


Fig.2 Variation of correlation dimension, entropy with embedding dimension for pre-Photic EEG

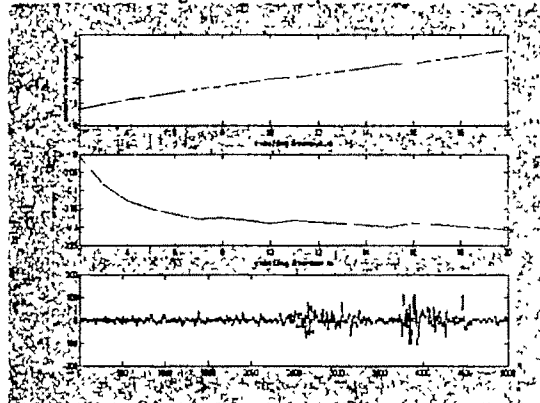


Fig 3. Variation of correlation dimension, entropy with embedding dimension for photic EEG

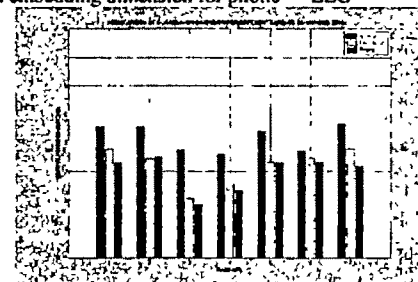


Fig 4 Comparison of correlation dimension for states

ECG Signal Processing for Analysis of Abnormalities based on QT Interval-A Novel Approach

Madhuchhanda Mitra¹, Saurabh Pal², and Swanirbhar Majumder³

¹ Dept. of Applied Physics, University of Calcutta, India. e-mail: madhuchhanda94@rediffmail.com

² Haldia Institute of Technology, India. e-mail: spal76@rediffmail.com

³ Electronics and Comm Engg. Department, NERIST, India. e-mail: swanirbhar@gmail.com

Abstract— Delay in cardiac repolarization causes ventricular tachyarrhythmias as well as Torsade de pointes (TdP). A feature of TdP is pronounced prolongation of the QT interval in the supraventricular beat preceding the arrhythmia. TdP can degenerate into ventricular fibrillation, leading to sudden death. Thus QT interval measurement and regular verification of the interval is important for analyzing cardiac health. A novel and simple approach to determine the duration of ventricular repolarization, i.e. QT interval of a recorded ECG wave is proposed here. Here a fully automatic method for measurement of QT interval is proposed, i.e. by five-point differentiation of ECG data and noting the slope change of the resulting graph. Points with zero slopes were considered as the end of respective waves. The algorithm is tested with physionet database. As per the analysis it was found that the algorithm provides accurate R to R duration & QT wave duration with error within $\pm 3\%$, in only some cases it is going upto $\pm 5\%$ and in a very few cases above that (which is very rare).

Key words—Torsade de pointes (TdP), supraventricular, ventricular fibrillation.

I. INTRODUCTION

THE QT interval is measured as the time interval between the onset of the QRS complex and the end of the T wave.

At the end of the T wave repolarisation is completed and the T wave voltage amplitude returns to the baseline [1]. The QT interval is thus a measure of the ventricular depolarisation and repolarisation. Some error may introduce in the QT interval measurement due to the fact that it may not return back to the base line or it may go below the base line along with the onset of U wave occasionally.

It is seen that many drugs prolongs cardiac repolarization which in turn increases the QT interval. This may lead to ventricular arrhythmia as severe as torsade de pointes (TdP) in some critical cases [2, 3]. Hence accurate measurement of the QT interval is very important for intensive cardiac care and also for pharmaceutical industry. A statistically significant increase in the mean QT interval (corrected for heart rate) as small as 6 milliseconds between baseline and maximal drug effect may be important as a signal of repolarisation abnormality [4]. There are manual methods being used to measure this QT interval but these are not so accurate as well as not repeatable in general. Rather automatic QT interval measurement techniques are more accurate and reproducible [5, 6]. Many researchers have performed several fundamental works on determination of QT interval along with other characteristic waves. Yan Sun, Kap Luk Chan and Shankar Muthu Krishnan have proposed a multiscale morphological derivative (MMD) transform-based singularity detector for the detection of fiducial points in ECG signal, where these points are related to the characteristic waves such as the QRS complex, P wave and T wave [7]. Laguna P, Jane R, Caminal P have developed a method where the intervals of clinical importance can be detected by a multilead QRS detector that locates each beat, using a differentiated and low-pass filtered ECG signal as input and the waveform boundaries are located in each lead.

Here in this discussion a five point differentiation technique [9] of an ecg is performed followed by an estimation of slope of each point of the differentiated wave. The method is simple and is verified with over 150 data of the physionet[10] database. A comparison study between the manual method and the proposed method is performed to check the accuracy of the proposed technique.

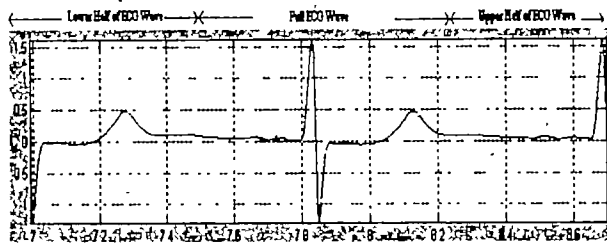


Fig 1 ECG Wave

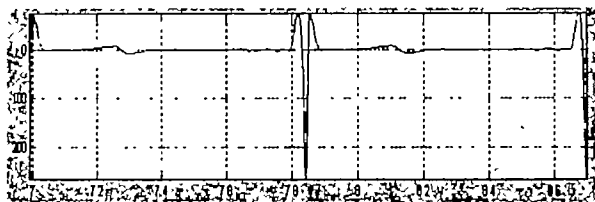


Fig 2 Differentiated ECG Wave

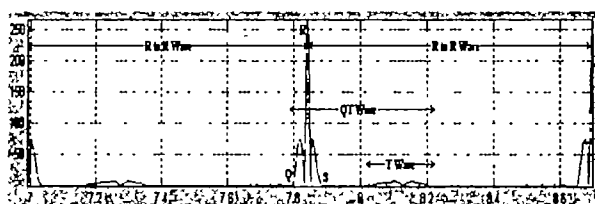


Fig 3 Absolute Value of Differentiated ECG Wave

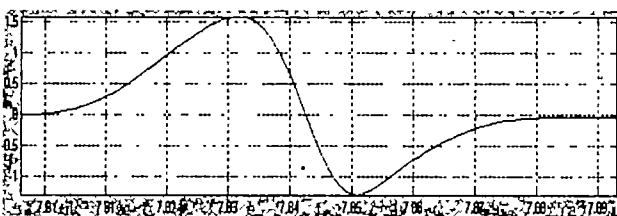


Fig 4 QRS Complex Detected

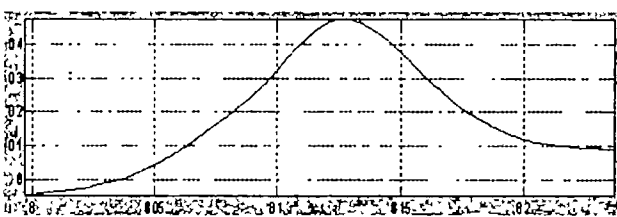


Fig 5 T Wave Detected

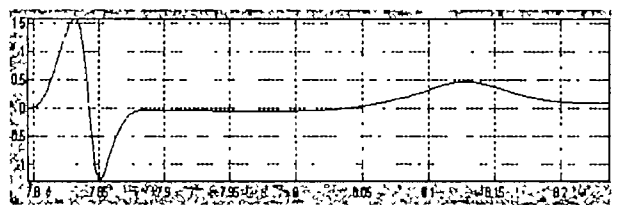


Fig 6 QT Wave Detected

II. PROCEDURE

From the physionet's site 15 seconds of the database for different patients containing 15000 samples at a rate of 1000 samples/ seconds were downloaded. These tab delimited database were converted to '.mat' (dot MAT) form for proper & faster accessing by MATLAB. Of all the lead voltages

available we were concerned about the V_2 chest lead as this is where the QT is significant. The wave plotted was smoothened with SPLINES and then 5 point differentiation was done on it. From the differentiated form of wave QRS complex was detected as shown in the Fig 3. The T wave was then detected from the differentiated data peaks as in Fig 3 here we use the absolute form of the differentiated data as this provides the same output even if the T wave is inverted. Thus from the start of QRS complex & end of T wave we get the QT wave. For the wave below of patient152/s0004_re we have $RR=0.852$ sec & $QT=0.441$ sec programmatically. While manually the R to R is same but the QT value is 0.422 thus providing an error of 4.5% for a difference of 0.19 seconds

III. RESULTS

Of the 550 databases of 294 patients available at (<http://www.physionet.org>) 166 databases comprising 52 different patients have been analyzed. A few randomly selected statistics are given here. The programmatically obtained durations of R to R & QT waves were compared with those obtained visually and manually detected values. Thus it was found that though R to R values got by 5 point differentiation are exactly equal to the manually detected values there are still some slight differences in the values of QT within $\pm 5\%$ error.

TABLE I

Comparison of some QT intervals detected programmatically with those detected manually

Sl No	Patient	RR	QT Duration		Error %
			Prog	Manual	
1	patient004/s0020are	0.738	0.35	0.353	0.85
2	patient005/s0021bre	0.636	0.309	0.315	1.905
3	patient011/s0039lre	0.673	0.372	0.359	3.62
4	patient015/s0152lre	0.882	0.382	0.384	0.521
5	patient024/s0083lre	0.940	0.376	0.376	0
6	patient027/s0151lre	0.777	0.366	0.365	0.274
7	patient044/s0142lre	0.666	0.315	0.315	0
8	patient048/s0171lre	0.615	0.319	0.319	0
9	patient050/s0215lre	0.881	0.417	0.411	1.46
10	patient152/s0004_re	0.852	0.441	0.422	4.502

IV. CONCLUSION

We here by conclude that of all the data that we have analyzed we have found 47 within 0 to 0.5% error, 29 with 0.5 to 1 % error, 34 with 1 to 2 % error, 23 with 2 to 3 % error, 14 with 3 to 5 % error, and only 19 with error above

5%. Thus out of 166 databases 133 were having less than 3 % error. This statistics is plotted in Fig. 7.

The algorithm devised to detect R to R is very effective as there is no error between the programmatically detected and the manually detected value, while in case of the QT we have it within 5% error limit & with 76 out of 166 databases having error less than 1% where the difference in time for error being less than 1% is 1 to 2 microseconds. But program would have been faster had it been programmed in C or C++, but this would have increased program complexity. So here we use MATLAB as it has inbuilt functions for SPLINES (for smoothening) and has user friendly file accessing & waveform plotting techniques compared to the C or C++ compilers.

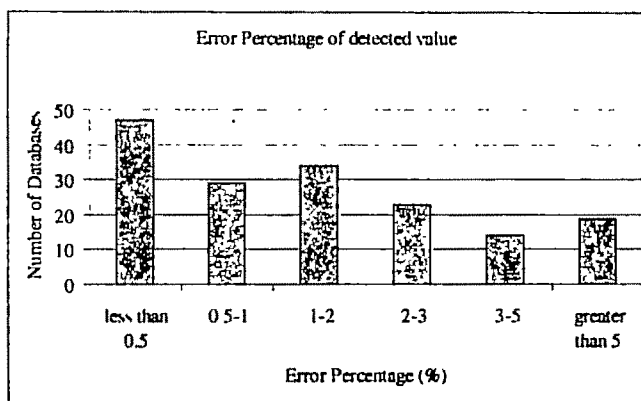


Fig 7 Error percentage Statistics of Detected Value of QT wave

REFERENCES

- [1] Moss AJ, Zareba W, Benhorin J, Malik M, Couderc J-P, Kennedy H, Locati Heilbron E, Maison-Blanche P. ICHNE guidelines for electrocardiographic evaluation of drug-related QT prolongation and other alterations in ventricular repolarisation: task force summary. *Ann Noninvasive Electrocardiol* 2001;6:333-41
- [2] Myerburg RJ, Castellanos A. Cardiac arrest and sudden death. In: Peter Libby, editor. *Braunwald's Heart Disease. A Textbook of Cardiovascular Disease*. 6. Saunders (W.B.) Co Ltd, 2001 pp 899-900
- [3] Haverkamp W, Breithardt G, et al. The potential for QT prolongation and proarrhythmia by non-antiarrhythmic drugs: clinical and regulatory implications. *European Heart Journal* 2000;21:1216-1231. doi: 10.1053/euhj.2000.2249
- [4] Pratt CM, Ruberg S, Moisanroth J, McNutt B, Woodward J, Hanis S, Ruskin J, Moye L. Dose response relation between terfenadine and the QTc interval on the scalar electrocardiogram: Distinguishing a drug effect from spontaneous variability. *American Heart Journal*. 1996;131:472-480. doi: 10.1016/S0002-8703(96)90525-6
- [5] Salvelieva I, Yi G, Guo X, Hnatkova K, Malik M. Agreement and reproducibility of automatic versus manual measurement of QT interval and QT dispersion. *Ame J Cardiol* 1998;81:471-477. doi: 10.1016/S0002-9149(97)00927-2
- [6] Kautzner J, Yi G, Camm AJ, Malik M. Short and long-term reproducibility of QT, QTc and QT dispersion measurements in healthy subjects. *PACE Pacing and Clinical Electrophysiology* 1994, 17:928-940
- [7] Yan Sun, Kap Luk Chan and Shankar Muthu Krishnan, Characteristic wave detection in ECG signal using morphological transform, *BMC Cardiovascular Disorder*, Vol 5, 2005
- [8] Laguna P, Jane R, Caminal P. Automatic detection of wave boundaries in multilead ECG signals: validation with the CSE database. *Comput Biomed Res*, 1994 Feb;27(1):45-60
- [9] F. B. Hilderbrand, "Introduction to Numerical Analysis; TMH edn, pg no: 82-84
- [10] <http://www.physionet.org>

Roughset Based Classification of Myocardial Infarction

Sucharita Mitra¹, M.Mitra², and B.B. Chaudhuri¹

¹ CVPR Unit, Indian Statistical Institute, Kolkata, India e-mail: sucharita_r@isical.ac.in, bbc@isical.ac.in

² Department of Applied Physics, University of Calcutta, Kolkata, India e-mail: mmaphy@caluniv.ac.in

Abstract—In this paper an attempt is taken to classify the Myocardial Infarction (MI) according to the location of the left ventricular cone where infarction actually occurs. For this purpose, 12 lead ECG PTB diagnostic database are considered. At first, the noises are eliminated from the signals with the help of smoothing and filtering techniques and then the clinically significant time-domain features are extracted according to a generated knowledgebase, developed from the opinion of reputed cardiologists and consultation of medical books. These extracted features are used as input parameters of a rough set based decision system for classification of normal and MI data and then for separation of MI according to its location in left ventricle.

Key words—Electrocardiogram, knowledgebase, Myocardial Infarction, rough set, time-domain features.

I. INTRODUCTION

THE most widely used signal in clinical practice is the ECG. It is frequently recorded, and widely used for the assessment of cardiac function. It was thus one of the first signals where biomedical signal processing techniques were applied upon [1,2]. ECG processing techniques have been proposed to effect pattern recognition [1,3,4], parameter extraction, denoising, baseline correction and arrhythmia detection[6]. Although QRS complex is the most prominent feature in ECG and can provide useful information about the heart status, other parts of the ECG (P-wave, T-wave, etc) are also significant in determining the health status. Recently, researches for P-wave and T-wave detection algorithms started to appear but a parameter extractor in obtaining most essential ECG parameters (PQRST) is still not very popular. Considering that all these can be integrated together, an Intelligent Home Health Care Embedded System (IHCS) with essential ECG parameters extraction that can provide diagnosis about health status of patients directly at home is proposed [9]. Neural networks (NN) based techniques are used for ECG pattern recognition and classification [7]. On the other hand, QRS detection is one of the most essential tasks in ECG analysis. A great research effort has been devoted in the development and evaluation of automated QRS detectors [8]. An algorithm using Slope Vector Waveform (SVW) for ECG QRS complex detection and RR interval evaluation has also

been reported. The algorithm consists two parts of operations. They are variable stage differentiation and non-linear amplification[10]. Another method has been reported where ECG signals were first decomposed using wavelet transform. The feature vectors were then extracted from these decomposed signals as normalized energy and entropy. To improve the classification of the feature vectors of normal and abnormal beats, the normal beats which occur before and after the abnormal beats were eliminated from the group of normal beats. Accordingly the important segments were detected [11].

An extensive variety of techniques including statistical pattern recognition, Expert Systems, Artificial Neural Networks, Wavelet Transform, Fuzzy and Neuro-fuzzy Systems are used for auto diagnosis of ECG signals. More recently, artificial neural network and Bi-group Neural Network classifiers have been used for signal classification [13,14]. Moreover, Fuzzy and hybrid neuro-fuzzy approaches are proposed for computerized electrocardiogram diagnosis and classification of myocardial infarction [15, 16]. Rough set theory is now becoming one of the most useful tools for soft computing and decision-making. Pawlak used rough set theory in Bayes' theorem and showed that it can apply for generating rule base to identify the presence or absence of disease. Discrete Wavelet Transform and rough set theory are used for classification of arrhythmia [12]. In this paper, a rough decision system is developed for rule optimisation to categorise MI automatically according to its location of the left ventricular cone where infarction actually occurs.

II. PROPOSED METHOD

A. Deletion of noises from ECG Signals

It is important to remove the noise before further analysis of ECG signal. The recorded ECG signals may be corrupted with six different types of noise. The contact noise is encountered in most of the cases of the existing PTB DB diagnostic database. Cubic spline technique for equal time interval is used to remove this contact noise. The spline interpolation formula which is used in this purpose is given below:

$$S(x) = \frac{1}{h} \left[\frac{1}{6} (x_{i+1} - x)^3 M_i + \frac{1}{6} (x - x_i)^3 M_{i+1} \right] + \frac{1}{h} (x_{i+1} - x) \left(y_i - \frac{h^2}{6} M_i \right) + \frac{x - x_i}{h} \left(y_{i+1} - \frac{h^2}{6} M_{i+1} \right)$$

Barring the smoothing process, a 50hz notch filter for the rejection of high frequency band due to power line oscillation has also been used.

Base line drift due to respiration was modeled as a sinusoid of frequency 0.15 to 0.4 Hz. Then a high pass filter of critical frequency 0.6 Hz is developed to block the low frequency noise signal. Both these FIR filters are designed by a matlab toolbox named FDATool (filter design and analysis toolbox). Among all the data (normal or abnormal) it is found that noise level varies from 10% to 30% and both smoothing and filtering techniques give good response to most of the data.

B. Development of Knowledgebase for clinically useful feature selection

With the help of 25 reputed cardiologists of different hospitals and clinical centers a knowledgebase regarding ECG interpretation is developed for selection of most clinically significant parameters, useful for disease classification. From opinion of those cardiologists and consulting different medical books [5,17,18] 12 most important time plane features are chosen for consideration and extraction. They are listed below:

1. Heart Rate, 2. PR interval, 3. P wave height, 4. P wave width, 5. QRS width, 6. QRS voltage, 7. QTc = (QT interval / Sqrt RR interval), 8. Pathologic or abnormal Q wave, 9. R wave Progression, 10. ST segment, 11. Reciprocity in T wave, and 12. T wave.

Beside these parameters, another important matter is the lead information where the abnormality has been found basically for MI classification.

C. Extraction of clinically significant parameters from ECG Signal

Accurate detection of the R-R interval between two consecutive ECG waves is very important for extraction of other parameters from ECG signals. For this purpose, the 2nd order derivative of the captured signal is computed by using 5-point Lagrangian interpolation formulas for differentiation [19]. The formula is given below :

$$f_0'' = \frac{1}{12h} (f_{-2} - 8f_{-1} + 8f_1 - f_2) + \frac{h^4}{30} f^{(5)}(\xi)$$

ξ lies between the extreme values of abscissas involved in the formula. After squaring the values of 2nd order derivative, a square-derivative curve having only high positive peaks of small width at the QRS complex region can be obtained. A small window of considerable length (say W) is taken to detect the area of this curve and we obtained maximum area at those peak regions. The local maxima of these peak regions are considered as R-peak [Fig 1]. Depending on the shape of

the signal a syntactic approach is developed for detection of P, Q, R and S waves. In order for accurate detection of P wave and ST segments base-line must be correctly identified. So isoelectric level detection algorithm is also implemented based upon the assumption that the isoelectric level of the signal lies on the area ~80ms left of the R-peak. In order to form the base array a minimum slope technique is employed for a window span of 30 ms around 80 ms left of the R peak. Then from the basepoint the R-R array is traversed towards left and the peak of P wave is determined implementing a heuristic procedure in conjunction with differentiated array and maximum area determination within predefined window. The ladder network type elimination criterion leads to demarcation of P wave. A zero crossing which is basically the isoelectric level crossing determines the starting of P segment [fig 2]. T wave detection and ST segment processing is also done based upon similar logical progression. To the right of the R peak a traversal is done to detect two zero crossings (ZCR1 & ZCR2). Then following similar analytical approach as P wave detection the ST segment is determined [fig 2]. ST segment begins at 60ms after the R-peak in normal sinus rhythm which is assumed based on the syntactic approach given in [14]. After determining P, QRS [fig 2] and T waves we also computed P height, Qheight, QRS complex height, QRS width, S height, T height.

D. Development of Roughset Decision System

A roughset decision system is developed from the extracted time domain features and lead information for classification of MI according to its location in myocardium. The most popular and widely used rough-set software tool box is ROSETTA [20,21]. This software supports different options of generating decision tables, reducts, discretization techniques, decision algorithms and classifications. For this reason we used this software for our experiment. Learning samples are processed in the following way. First a knowledge base is acquired for the data set i.e, for normal and abnormal data regarding both quantitative and qualitative natures of those extracted time-plane features. Knowledge base consists of objects, which are represented using conditional attributes and decision parameters. All the time plane features described above are get their specific attributes according to knowledgebase and lead position and used as the input parameters of the Decision tables, a portion of which is given in table I and II. Here, two consecutive decision tables are framed basically for generation of two sets of rules. The first set is for separation of normal and abnormal sets of data and the second one is for the classification of diseased data set (specially MI).

Consequently, the acquired data are quantized to convert real attribute values into discretized form allowing further rule processing. Based on the discrete values, attributes are analyzed in terms of discernibility investigation. Sets of attributes allowing partition of object classes are then revealed. These sets are called reducts. The ROSETTA system supports a variety of quantization as well as reduct and rule generation procedures however the details of these lie beyond the scope of this report. These processing parameters were chosen during a preliminary research aimed at optimizing the system efficiency and generation ability.

Table I. A portion of decision table1

Hand Run	PR Interval	PWave height	Pwave width	QRS width	QTc	QRS width	R wave Roc	Am Q waves	ST Segment	Recipro- city	T waves	Diases
String	String	String	String	String	String	String	String	String	String	String	String	String
B	A	N	N	N	N	N	A	P	E	Ab	+	V
B	A	N	N	N	N	N	A	P	E	P	+	V
B	N	N	N	N	N	N	A	P	E	P	+	V
B	N	N	N	N	N	N	A	P	D	P	+	V
N	N	N	N	N	N	N	A	Ab	E	Ab	+	N
N	N	N	N	N	N	N	N	Ab	I	Ab	+	N
T	N	N	N	N	N	N	N	Ab	I	Ab	+	N
T	N	N	N	N	N	N	N	Ab	I	Ab	+	N

Table II. A portion of decision table2

[illegible]

III. RESULT

In this experiment two consecutive rule sets are generated from two separate decision tables. Table I is generated by different time plane features after acquiring specific attribute values depending on the generated knowledgebase. Whereas, table II is generated mainly according to the lead positions where the specific abnormality is present. A rule with high accuracy and coverage factor is considered as a strong rule. The accuracy of a rule reflects how trustworthy its consequent is. A portion of the generated rule set from table I and the corresponding confusion matrix, which is generated using standard voting classifier are given below in the figures 3 and 4. Both trained and untrained samples for all the dataset (e.g. Normal, and Myocardial Infarction) are fed to the Inference system and the result obtained is given in table III. The numbers given in brackets in table III represent the number of properly classified samples versus all tested samples. The confusion matrix predicts cent percent accuracy for all the three set of trained data. Table III supports this prediction. Still, the present system is tested by three types of ECG data samples and encouraging result is obtained. In future the system will be tested by more number of samples and few other types of diseases.

The rule set from table II is given in figure 5. We select the optimum rule set by the similar manner for classification of MI according to the location of the left ventricular cone where infarction actually occurs. MI can be classified as Anterior(AN), Inferior(IN), Antero-lateral(AL), Infero-lateral(IL), Antero-septal(AS), Infero-septal(IS) etc.

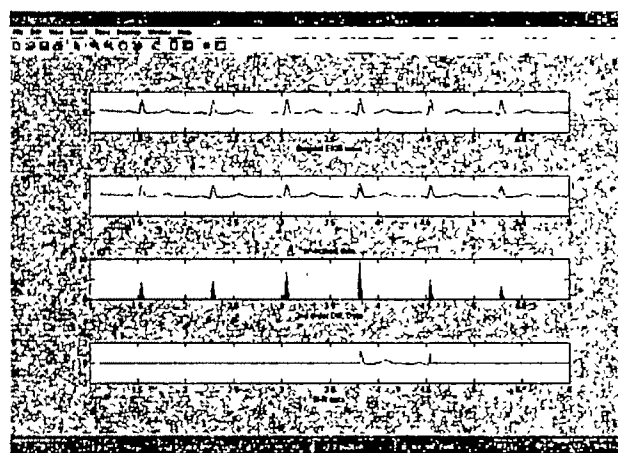


Fig 1. Plot of original ECG wave, corresponding smoothed differentiated and squared data and detected R-R data

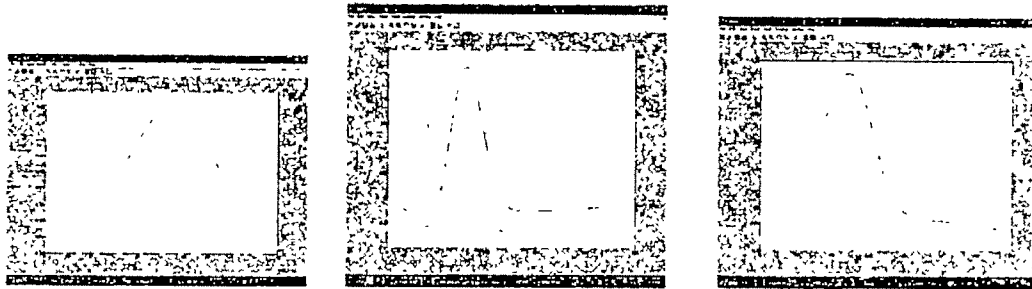


Fig.2 Detected P, QRS and T segments from the R-R interval showed in fig. 1

Table III. Result obtained from rule based rough set decision system

Type of Samples	No. of Trained Samples	No. of Untrained Samples	Accuracy for Trained Samples	Accuracy for Untrained Samples
Normal	19	31	100%(19/19)	100%(31/31)
Disease	14	26	100%(14/14)	96.1%(25/26)

Rules							
	Rule	LHS Support	RHS Support	RHS Accuracy	LHS Coverage	RHS Coverage	RHS Label
1	R_wave_Prog(A) => Disease(Y)	14	14	1.0	0.424242	1.0	1.0
2	R_wave_Prog(N) => Disease(N)	19	19	1.0	0.575758	1.0	1.0
3	ST_segmental(E) => Disease(Y)	12	12	1.0	0.363636	0.657143	1.0
4	ST_segmental(D) => Disease(Y)	2	2	1.0	0.080808	0.142857	1.0
5	ST_segmental(I) => Disease(N)	19	19	1.0	0.575758	1.0	1.0
6	Reciprocity(P) => Disease(Y)	12	12	1.0	0.363636	0.657143	1.0
7	Abn_Q_waves(P) => Disease(Y)	14	14	1.0	0.424242	1.0	1.0
8	Abn_Q_waves(Ab) => Disease(N)	19	19	1.0	0.575758	1.0	1.0
9	Heart_Rate(B) => Disease(Y)	6	6	1.0	0.161616	0.357143	1.0
10	Heart_Rate(T) => Disease(N)	7	7	1.0	0.212121	0.388421	1.0
11	QRS_width(A) => Disease(Y)	2	2	1.0	0.080808	0.142857	1.0
12	PR_interval(A) => Disease(Y)	6	6	1.0	0.161616	0.428571	1.0
13	T_waves(-) => Disease(Y)	2	2	1.0	0.080808	0.142857	1.0
14	PR_interval(N) AND Reciprocity(Ab) => Disease(N)	19	19	1.0	0.575758	1.0	1.0
15	Heart_Rate(N) AND Reciprocity(Ab) => Disease(N)	12	12	1.0	0.363636	0.631579	1.0

Fig. 3 Generated rules from decision table I

Predicted			
Actual	Y	N	
	14	0	1.0
	0	19	1.0
ROC	Class	Y	
	Area	1.0	
	Std. error	0.0	
	Thr. (0, 1)	0.628	
	Thr. acc	0.628	

Fig. 4 Confusion Matrix Output for Standard Voting Classifier

Rough Set Rules						
	Rule	LHS Support	RHS Support	RHS Accuracy	LHS Coverage	RHS Coverage
1	T wave S(L1,L3,V1,V2,V3,V4,V5,V6) ⇒ Disease(N)	4	4	1.0	0.125	0.5
2	T wave S(L1,L3,V4) ⇒ Disease(N)	4	4	1.0	0.125	0.5
3	T wave S(L1,L2,L3,V1,V2,V3,V4,V5) ⇒ Disease(N)	4	4	1.0	0.125	0.5
4	T wave S(L2,V1,V2,V3,V4,V5,V6) ⇒ Disease(L)	4	4	1.0	0.125	0.5
5	T wave S(L1,L3,V1,V2,V3,V4,V5,V6) ⇒ Disease(L)	4	4	1.0	0.125	0.5
6	T wave S(L3,V1,V2,V3,V4,V5,V6) ⇒ Disease(AS)	4	4	1.0	0.125	0.5
7	T wave S(L1,L2,V1,V2,V3,V4,V5,V6) ⇒ Disease(AS)	4	4	1.0	0.125	0.5
8	ST Seg E (L1,L2,V1,V2,V3,V4,V5,V6) ⇒ Disease(N)	4	4	1.0	0.125	0.5
9	ST Seg E (L1,V1,V2,V3,V4,V5,V6) ⇒ Disease(N)	4	4	1.0	0.125	0.5
10	ST Seg E (L1,V1,V2,V3,V4,V5,V6) ⇒ Disease(L)	4	4	1.0	0.125	0.5
11	ST Seg E (L1,L2,V1,V2,V3,V4) ⇒ Disease(AS)	4	4	1.0	0.125	0.5

Fig. 5 A Portion of Generated rule set from table 2

IV. CONCLUSION

Automatic detection of location of MI in the myocardium from ECG parameters is a challenging task for researchers. Here, one of the most useful and popular decision making soft computing tool roughset is used for meeting that dispute. Six different types of noises may corrupt those extracted ECG signals. So different smoothing and filtering techniques are adopted for making those signals almost noise free. A knowledge base about the time plane features and ECG interpretation is developed from various medical books and from the feed back of different reputed cardiologists. The time-plane features of ECG signals are extracted from each of the 12 lead ECG signals with the help of differentiation and syntactic approaches. A rule-based rough set decision system is developed from these time-plane features to make an inference engine for two phase ECG classification. At present, the system is tested with three types of ECG data- Normal, Myocardial Ischemia and Myocardial Infarction. In the first phase it is isolated the ischemia and MI data from normal data set and in the next phase it can classify the MI data according to the location of the left ventricular cone where infarction actually occurs. In future the system will be tested with large number and different types of dataset.

REFERENCES

- [1] A.Cohen, "Biomedical signal processing", CRC Press, Boca Raton, FL, 1988
- [2] P. Coumel, O.Garfeln, "Electrocardiography-Past and future", Annals NY Academy of Sciences, vol.601,1990.
- [3] J. Pan, W.J. Tompkins, "A real-time QRS detection algorithm", *IEEE Trans. Biomed Eng.* 32 (1985), pp 230-236.
- [4] G. Taddei, Constantino, R. Silipo, M. Emdin, C. Marchesi, "A system for the detection of ischemic episodes in ambulatory ECG", *Computers in Cardiology, IEEE Comput. Soc. Press* (1995),pp 705-708.
- [5] Ary L. Goldberger, "Clinical Electrocardiography, A Simlified Approach", 6th Edn., Harcourt India Pvt. Ltd.
- [6] N.V. Thakor, Z. Yi-Sheng, "Applications of adaptive filtering to ECG analysis: noise cancellation and arrhythmia detection", *IEEE Trans. Biomed Eng.* 38 (1991) pp785-794.
- [7] N. Maglaveras, T. Stamkopoulos, K. Diamantaras, C. Pappas, M. Strintzis, "ECG pattern recognition and classification using non-linear transformations and neural networks. a review", *International Journal of Medical Informatics*, vol. 82, 1998, pp. 191-208.
- [8] G.M. Friensen, T.C. Jannett, M.A. Jadallah, S.L. Yates, S.R. Quint and H.T. Nagle, " A comparison of the noise sensitivity of nine

QRS detection algorithms", *IEEE Trans. Biomed. Eng.*, vol BME-37, Jan, 1990, pp 85-89

- [9] Chi Chan W, Tang S, Hang Pun S, Vai M, Un Mak P, "ECG Parameter Extractor of Intelligent Home Healthcare Embedded System". *Conf Proc IEEE Eng Med Biol Soc* 2005 pp 110-113
- [10] X. Xu, Y. Liu, "ECG QRS complex detection using slope vector waveform (SVW) algorithm", *Conf Proc IEEE Eng Med Biol Soc.*, vol. 2, no. 1, 2004, pp. 3597-3600.
- [11] Matsuyama, MJonkman, de Boer, " Improved ECG signal analysis using wavelet and feature Extraction", *Methods Inf Med.* 46(2), 2007, pp.227-30
- [12] Z. Pawlak, " Bayes' Theorem Revised – The Rough Set View, New Frontiers in Artificial Intelligence", *Joint JSAI 2001 Workshop Post-Proceedings, Lecture Notes in Computer Science*, vol. 2253, 2001,pp 240-250.
- [13] G. Bortolan, C. Brohet, and S. Fusaro, "Possibilities of using neural networks for ECG classification", *J. Electrocardiol.*, vol 29, 1996, pp 10-16.
- [14] C.D. Nugent, J.A. Webb, N.D. Black, "Feature and classifier fusion for 12-lead ECG classification", *Med Inform Internet Med.*, vol 25, no 3, 2000, pp 225-35..
- [15] R. Degani, "Computerized Electrocardiogram Diagnosis: Fuzzy Approach ", *Methods of Inform. Med.*, vol31, 1992, pp 225-233.
- [16] P. Bozzola et al., "Ahybrid neuro-fuzzy system for ECG classification of myocardial infarction", *Comput. Cardiol.*, IEEE Comput. Soc. Press, Indianapolis, IN, 1996.
- [17] M.J. Goldman, " Principles of Electrocardiography", 11th Edn., Marugen Asia (Pvt) Ltd.
- [18] Hampton J.R.,The ECG Made Easy, 5th edn., Churchill Livingstone.
- [19] F.B. Hildebrand., "Introduction To Numerical Analysis", T M H edn., Tata McGraw-Hill Publishing Company Ltd., pp. 82-84.
- [20] L.Polkowski., A. Skowron., "Rough Sets in Knowledge Discovery", *Physica – Verlag*, Wurzburg, Wein, 1998.
- [21] A. ohm, "Discernibility and Rough Sets in Medicine : Tools and Applications". Ph.D. Thesis, Department of Computer and Information Science, Norwegian University of Science and Technology, Trondheim, NTNU Report, 1999:133, IDI Report 1999.

Pattern Grammar and Histogram Based ECG Features Extraction

Sucharita Mitra¹, M.Mitra², and B.B. Chaudhuri¹

¹ CVPR Unit, Indian Statistical Institute, Kolkata, India e-mail: sucharita_r@isical.ac.in, bbc@isical.ac.in.

² Department of Applied Physics, University of Calcutta, Kolkata, India e-mail: mmaphy@caluniv.ac.in

Abstract— A combination of histogram based and syntactic techniques are used for detection of different patterns of ECG waves and extraction of few important time-plane features, which are mainly used for ECG interpretation and classification. At first, an efficient, very simple and new approach for detection of both base line and QRS complexes from the horizontal and vertical histogram of ECG images plotted on computer screen is described. The vertical and horizontal histograms are generated from the number of ordinates for a particular abscissa at the vertical and horizontal direction respectively. The base line is determined at the maxima of the horizontal histogram whereas QRS or R peaks are determined from the local maximas of the maximum area zone of vertical histograms. A very high accuracy level is achieved for both the cases (99.5% for QRS and 92% for base line). This method is advantageous for online analysis because both QRS and base lines can be determined directly from ECG data on computer screen without computation of complex mathematical models even when ECGs are tilted due to respiration and in the presence of power line oscillation. After detection of R points and base points an efficient algorithm is developed using syntactic approaches for detection of P, Q, R, S and T waves and their different attributes which are useful for ECG interpretation.

Key words— Base line, ECG, Histogram, QRS complex, Syntactic Approach.

I. INTRODUCTION

PATTERN RECOGNITION approaches are widely used for the detection and analysis of ECG waves. Mainly, non-linear transformations of the ECG, principal component analysis (linear and non-linear), different ways to map the transformed data into n-dimensional spaces, and neural networks (NN) based techniques are used for ECG pattern recognition and classification [1]. Signal pattern comparison is also done for ECG signal analysis [2]. A significant point extraction algorithm, based on the analysis of curvature, that identifies data samples that represent clinically significant

information in the ECG waveform is reported. This method help in both data reduction as well as pattern matching[3,4]. Syntactic approaches are also used for ECG waveform detection [5]. Both the syntax and semantics of ECG grammar are used for P and T wave detection [6]. In another research, a learning system is reported to classify biomedical patterns grammatically [7]. In recent years, Wavelet transform is used to decompose ECG signal for detection of P wave by neural network [8]. In another case, it is used to obtain a multiresolution representation of some example patterns for ECG signal structure extraction. Neural Networks are trained with the wavelet-transformed templates providing an efficient detector even for temporally varying patterns within the complete time series [9]. Recently, multi-resolution wavelet transform, wavelet decomposition and continuous wavelet transform are also used for ECG feature extraction [15,16,17]. QRS detection is one of the most important tasks in time-plane ECG analysis. Accurate detection of QRS helps in detection of other time-plane features more accurately. Considerable research has been devoted to the development and evaluation of automated QRS detectors [10]. Hidden Markov Model [11], Wavelet transform [12] and Artificial Neural Network (ANN) [13] are also used for detection of QRS complexes from ECG signals. A slope vector waveform based ECG QRS detection algorithm which is ideal for a widely range of machine diagnosis applications, particularly, embedded real-time ECG monitoring is also reported [18]. Baseline detection is another essential task in ECG analysis for extraction of different time domain features. Most methods for base line or isoelectric line detection are based upon the assumption that the isoelectric level of the signal lies on the area ~80 ms left of the R-peak, where the first derivative becomes equal to zero for at least 10 ms or in the flattest 20 ms segment [14].

In the present paper a new and comparatively simple (with no such mathematical and computational complexities) algorithm for ECG time domain features extraction is described for future development of an automated online very simple ECG

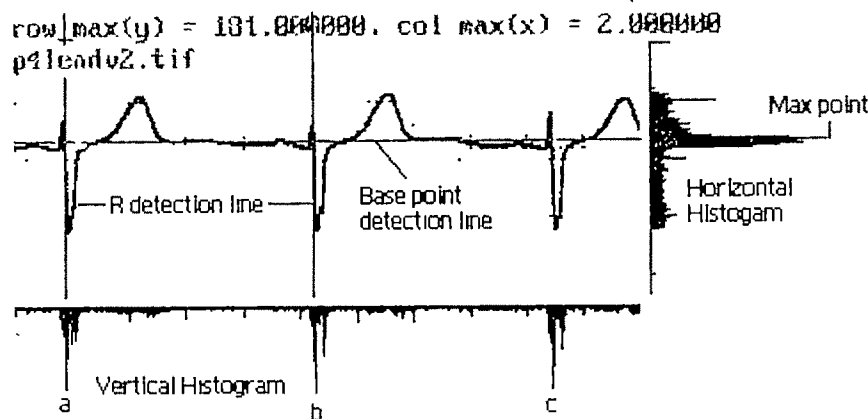


Fig 1 Vertical and Horizontal histogram of an ECG pattern of lead V2 of sample 4 where a, b, c are the maximum area zones

analyzing system. The method is based on the combination of both vertical and horizontal histogram and syntactic approaches and is especially useful for embedded real time ECG monitoring systems due to its simplicity and minimum involvement of mathematical and computational complexities. A high accuracy level is obtained in detection of baseline, QRS, P and T waves by this method even in the presence of noises like baseline drift due to respiration and power line oscillation (up to 15%).

II. METHODOLOGY

In the present work we consider the ECG plot appearing on computer screen that may be considered as a two-dimensional picture consisting of elements, organized in rows and columns, with values 0 (corresponds to points having no ordinate) and 1 (corresponds to points having ordinate).

A. Determination of Baseline from Horizontal Histogram

For a particular row the number of 1 is being computed for plotting of the horizontal histogram of ECG data. Since the baseline regions contain few almost straight line portions, then searching the maxima of this horizontal histogram, the baseline region can be obtained. Figure 1 and 2 show the baseline region of the plotted ECG signals.

B. Determination of QRS complex from vertical histogram

Similarly, the vertical histogram of an ECG data is being plotted after considering the number of 1 for a particular column. Each vertical histogram contains only high positive peaks of small width at the QRS complex region. A small window of considerable length (say W) is taken to detect the area of this curve and we obtained maximum area at the peak regions (fig. 1 and 2). So extracting the local maxima of the maximum area zone the R waves of each ECG signals can be detected. Two consecutive R waves and hence the total samples and a distance between them are also computed. So, the sampling period can easily be calculated for each signal. The accuracy of detection of QRS complex very much depends on W . Very high or very low values of W will decrease the accuracy. Hence an optimum value of W is

required. An experiment is being done for choosing the appropriate value of W with the considerable number of test samples of signals to achieve the maximum accuracy in detection of QRS.

C. Detection of P, Q, R, S and T waves by syntactic approaches

Depending on the slope reversals and shape of the each wave, a syntactic approach [22,23] is developed for detection of P, Q, R, S and T waves. The area of P, QRS and T waves are also computed. In syntactic pattern recognition, the task of recognition is essentially reduced to that of parsing a linguistic representation of the patterns to be recognized with a parser that utilizes a certain grammar, called "pattern grammar". We have formulated pattern grammar for each of the ECG complexes basically based on the slope reversals, aligned segments and the structural shape of each complex, using a priori knowledge of the ECG structure. This pattern grammar is given briefly in the detailed algorithm given below. Fig. 3 shows different features

which are extracted by the algorithm. After getting the S and T waves, the algorithm detects the ST segment by using standard assumptions which are in general agreement with the recommendation of the European ST-T database and with the observations in [19,20,21]. Once after getting to the beginning it computes the slope of the ST segments.

D. Detailed Algorithm

The step wise detailed algorithm is given below :

Step 1

Detect the base points and R points using horizontal and vertical histograms.

Step 2

Shift to the R point nearest to the base point region

Step 3 Find Q and S wave by finding the slope reversal followed by aligned segments at the left and right hand sides

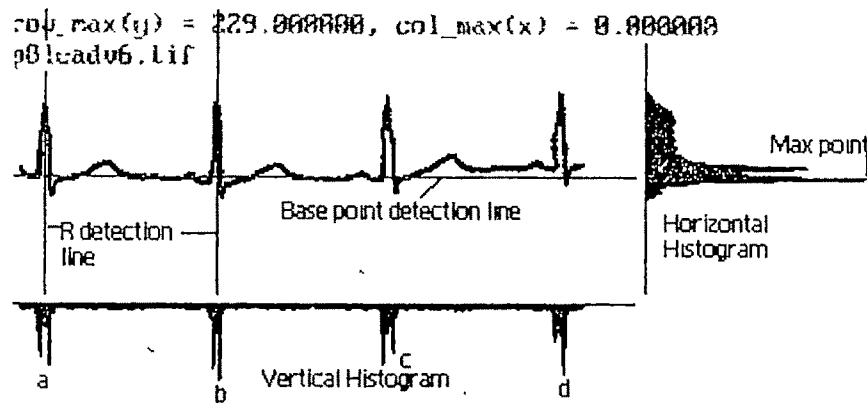


Fig 2 Vertical and Horizontal histogram of an ECG pattern of lead V2 of sample 4 where a, b, c, d are the maximum area zones

of R wave respectively.

Step 4

Determine the peak of the P wave by implementing a heuristic procedure in conjunction with differentiated array and maximum area determination within predefined window by traversing at the left of the base point in to the R-R array.

Step 5

Go to the P location and search the nearest zero crossing or aligned segment at the left of that position and mark it as the beginning of the P wave.

Step 6

Detect T wave by analytical approach as P wave by traversing at the right from S wave.

Step 7

Detect ST segment from the end of S to the beginning of T.

Step 8

Calculate the slope of ST segment.

Step 9

Determine the area of all the detected segments P, QRS, and T.

III. RESULT

A database of 12 lead ECG signals of 140 subjects (70 normal and 70 abnormal) was generated [24] and used for this work. The abnormal subjects have mostly myocardial infarction and ischemia. So, the algorithm was tested by 36 types of ECG waves. The system also tested for both noise free and noisy signals. The levels of both type of noises are increased from 0% to 15% and still we achieved 99.5% accuracy in an average in detection of QRS complexes and 92% for detection of baseline. The result obtained in different noise levels are given in table 1 and 2. A testing has been made for checking the accuracy in the detection of QRS. After detection of QRS complexes the heart rate of every signal is computed and is checked with the values given on paper ECG records.

After getting base points and R points the noises are removed by using appropriate filtering software and the P and T wave detection has been done in a noise free environment. The detection accuracy for P wave and T wave are 92.2% and

96.7% respectively. A portion of different extracted features are shown in table 3.

Table 1. QRS Detection Accuracy in Different Levels of Two type Noises

Noise Level (Power line Interference)	QRS Detection Accuracy	Noise Level (Base line shift)	QRS Detection Accuracy
0%	100%	0%	100%
5%	100%	5%	100%
10%	99.3%	10%	100%
15%	97.75%	15%	98.8%
Average	99.26%	Average	99.70%

Table 2. Baseline Detection Accuracy in Different Levels of Two type Noises

Noise Level (Power line Interference)	Base-line Detection Accuracy	Noise Level (Base line shift)	Baseline Detection Accuracy
0%	94.50%	0%	94.50%
5%	93.80%	5%	93.20%
10%	91.20%	10%	90%
15%	90.15%	15%	89.20%
Average	92.41%	Average	91.73%

IV. CONCLUSION

A method based on the combination of both vertical and horizontal histogram and syntactic approaches is described in this paper for detection of different patterns of ECG waves and extraction of few important time-plane features, which are mainly used for ECG interpretation and classification.

The algorithm is new and comparatively simple (with no such mathematical and computational complexities) and is

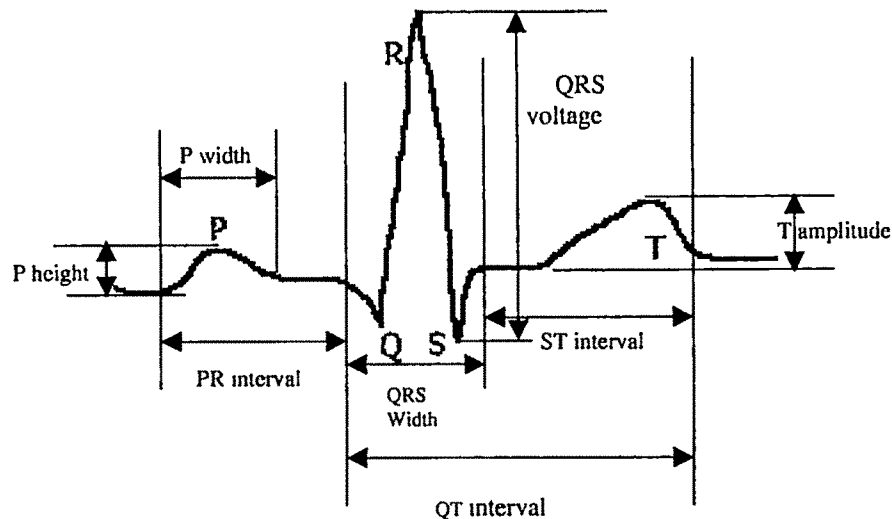


Fig 3 Different time domain features which are extracted

Table 3. Different features, which our algorithm extracts

Heart Rate	PR Interval	P Wave Height	P wave width	QRS width	QT Interval	RR Interval	QTc	QRS voltage
88	0.16	1.62	0.08	0.04	0.4	0.68	0.09	11
100	0.16	-0.2	0.04	0.08	0.36	0.64	0.09	3
79	0.17	1.2	0.08	0.04	0.36	0.72	0.08	7
56	0.24	1	0.08	0.04	0.36	1.08	0.07	3
63	0.16	0.2	0.04	0.04	0.36	0.76	0.08	8
83	0.24	-0.1	0.02	0.08	0.4	0.72	0.09	7
57	0.24	1	0.08	0.04	0.36	1.04	0.07	7
94	0.2	1	0.04	0.08	0.32	0.64	0.08	5
58	0.16	1	0.08	0.04	0.44	1.04	0.08	4
68	0.16	1	0.08	0.04	0.32	0.92	0.06	26

especially useful for embedded real time ECG monitoring systems. At first, a very simple vertical and horizontal histogram based approach is used for detection of R points and base level of ECG signal and then syntactic approaches are used for detection of P,Q,R,S and T waves of ECG signals. Problem arises to make a diagnostic decision from time plane ECG waves when they are corrupted by different noises. Different types of filters have been used to reduce those noises but that may result the loss of clinically significant data. The performance of the developed QRS and baseline detector is satisfactory especially in noisy environment and still we obtained a 99.5% and 92% accuracy in an average in detection of these. Whereas the detection accuracy for other two waves P and T are 92.2% and 96.7% respectively.

REFERENCES

- [1] N Maglaveras, T Stamkopoulos, K Diamantaras, C Pappas, M. Strintzis, "ECG pattern recognition and classification using non-linear transformations and neural networks: a review", *International Journal of Medical Informatics*, vol 82, pp 191-208, 1998.
- [2] R.D Bousseljot, D. Kreisler, "ECG analysis by signal pattern comparison", *Biomedical Engineering*, vol. 43, pp 156-157, 1998.
- [3] H.S Lee, Q.L. Cheng, N.V. Thakor, "ECG waveform analysis by significant point extraction in data reduction", *Comput Biomed Res*, vol. 20(5), pp. 410-427, 1987.
- [4] Q.L Cheng, H.S Lee, N.V. Thakor, "ECG waveform analysis by significant point extraction II. Pattern matching", *Comput Biomed Res*, vol. 20(5), pp.428-442, 1987.
- [5] A. Koski, M. Juhola, M. Meriste, "Syntactic recognition of ECG signals by attributes finite Automata In", *Pattern Recognition*, vol. 28(12), pp 1947-1940
- [6] Gabriella Kóka, János Csirik, Tibor Gyimóthy, "Learning the syntax and semantic rules of an ECG grammar", *Proceedings of fifth congress of the Italian Association for Artificial Intelligence*, Roma, September, 1997
- [7] Gabriella Kóka, Zoltán Alexin, Tibor Gyimóthy, "Learning Biomedical Patterns".
- [8] G Xie, Z Nie, H. Xiang, Z Zeng, "Detection of P wave through wavelet transform and neural network", *Journal of Biomedical Engineering*, vol 16(3), pp 320-323, 1999.
- [9] K. Sternickel, "Automatic pattern recognition in ECG time series", *Comput Methods Programs Biomed*, vol 68(2), pp 109-115, 2002
- [10] G.M. Friensen, T.C Jannett, M.A. Jadallah, S.L.Yates, S.R. Quint, H.T Nagle, "A comparison of the noise sensitivity of nine QRS detection algorithms", *IEEE Trans Biomed Eng.*, vol. BME-37, pp 85-89, 1990

- [11] D.A. Coast, R.M. Stern, G.G. Cano, S.A. Briller, "An approach to cardiac arrhythmia analysis using hidden Markov models", *IEEE Trans. Biomed. Eng.*, vol. BME-37, pp. 826-836, Sep. 1990.
- [12] S Kadamb, R Murray, GF Boudreaux-Bartels, "Wavelet transform-based QRS complex detector", *IEEE Trans Biomed Eng.* vol. 46 , pp 838-48, Jul, 1999
- [13] Yu X, Xu X, "QRS detection based on neural-network", *Journal of Biomed. Eng.*, vol. 17, pp.59-62, Mar , 2000
- [14] N. Maglaveras, T Stamkopoulos, C. Pappas, M Strintzis, "An adaptive back-propagation neural network for real-time ischemia episodes detection. Development and performance analysis using the European ST-T database", *IEEE Trans. Biomed. Eng.*, vol. 45, no 7, pp. 805-813, 1998.
- [15] S Mahmoodabadi, A Ahmadian, A M bolhasani, M Eslami, J Bidgoli., "ECG Feature Extraction Based on Multiresolution Wavelet Transform", *Conf Proc IEEE Eng Med Biol Soc.* , vol. 4, pp. 3902-3905, 2005.
- [16] A Matsuyama, M Jonkman, F de Boer., "Improved ECG signal analysis using wavelet and feature extraction", *Methods Inf Med.*, vol. 46, no. 2, pp 227-230, 2007.
- [17] Z , Ji, S Qin, C Peng, "Electrocardiographic signal feature extraction and its instrument development based on continuous wavelet transform", *Journal of Biomed. Eng.*... Vol. 23, no 6, pp.1186-90, 2006
- [18] X Xu, Y Liu, "ECG QRS Complex Detection Using Slope Vector Waveform (SVW) Algorithm," *Conf Proc IEEE Eng Med Biol Soc.*, vol. 5, pp. 3597-3600, 2004.
- [19] N Maglaveras, T Stamkopoulos, C. Pappas, M. Strintzis, "An adaptive back-propagation neural network for real-time ischemia episodes detection. Development and performance analysis using the European ST-T database", *IEEE Trans. Biomed.Eng.*, vol. 45 no 7, pp. 805-813, 1998.
- [20] R. Siiho, P. Laguna, C. Marchesi, R.G. Mark, "ST-T segment change recognition using artificialneural networks and principal component analysis", *proceedings Computers in Cardiology, IEEE Comput. Soc.Press*, pp.213-216, 1995.
- [21] F Jager, R.G. Mark, G.B. Moody, S. Divjak, "Analysis of transient ST segment changes during ambulatory monitoring using the Kauhuncn-Loeve transform", *proceedings Computers in Cardiology, IEEE Comput. Soc. Press*, pp. 691-694, 1992.
- [22] T. Pavlidis, "Structural Pattern Recognition", Springer-Verlag, Berlin, Heidelberg, Newyork, pp. 185-215, 1980.
- [23] P.Trahanias, E Skordalakis, "Syntactic pattern recognition of the ECG", *IEEE Trans. Pattern Anal. Mach. Intell.*, vol. PAMI-12, pp.648-657, July, 1990.
- [24] S Mitra, M. Mitra , "An Automated Data Extraction System From 12 Lead ECG Images", *Computer Methods and Programs in Biomedicine*, vol. 71(1), pp 33-38, 2003.

Technical Session 2C

Modeling and Simulation

First-Principles Modeling and Simulation of the Electronic and Magnetic Properties of C_8 , Si_8 and MnC_7 , $MnSi_7$

T. Benabdesselam, A. Tadjer, and B. Bouhafs

Modelling and Simulation in Materials Science Laboratory, Physics Department, Sciences Faculty,
University of Sidi Bel-Abbés, Sidi Bel-Abbés 22000, Algeria.
e-mail tassaditbenabdesselam@yahoo.fr.

Abstract— In this work, we report the structural, electronic and magnetic properties obtained in the study of the cubic binary alloys Mn_xC_{1-x} , Mn_xSi_{1-x} at the concentrations $x=0$ and $x=0.125$ (we used a cell of 8 atoms. Thus, one can study the alloys Mn_nC_{8-n} and Mn_nSi_{8-n} in a simple cubic structure according to the number of atoms $n=0$ and $n=1$). using the full-potential linearized augmented plane wave method (FP-LAPW) within the density functional theory framework. The structural properties calculated for C_8 and Si_8 were calculated at first hand to implement calculations for the alloys. Two different states: magnetic (ferromagnetic (fm)) and nonmagnetic (nm) for MnC_7 and $MnSi_7$, were studied. Our results show that the ferromagnetic state is energetically more stable than the nonmagnetic state with magnetic total moment of $2.3255\mu_B$ for the $MnSi_7$, whereas for MnC_7 the two states ferromagnetic and nonmagnetic are identical with magnetic total moment reduced to zero.

With a view of calculating the electronic and magnetic properties; we compared the electronic bands of the alloys MnC_7 and $MnSi_7$ with those of C_8 and Si_8 , respectively. For C_8 and Si_8 , the maximum of valence band is located at Γ point and the minimum of the conduction band is situated at X point, with, thus an indirect gap of 4.14eV and 0.45eV for C_8 and Si_8 respectively. But for the alloys MnC_7 and $MnSi_7$, we notice the appearance of a band splitting below the level Fermi contrary to C_8 and Si_8 respectively. Moreover, when comparing systems, we notice the disappearance of the gap in MnC_7 comparatively to the C_8 compound.

The calculations of the different densities of states, for the alloys under consideration, namely the MnC_7 , and the $MnSi_7$ show that the densities of states of spin-up and spin-down are symmetrical and metallic like, for the former while the densities of states of spin-up and spin-down are asymmetrical and metallic like for the latter, however we notice a difference of the densities of states at the Fermi level of 0.256states/eV for the latter, this suggests that the alloy the $MnSi_7$ is semi-magnetic.

Key words—DFT/LDA, FP-LAPW, Magnetic materials, semiconductors of group IV.

I. INTRODUCTION

THE development of the semiconductors doped by transition metals aroused much interests these last years. This is due to the enormous potential which has the magnetic semiconductors. These materials are often used in the *spintronic* devices [1-4]. particularly, much of works were concentrated on the Mn doped III-V semiconductors, where the ferromagnetism was experimentally observed [2] and confirmed later theoretically by the structural electronic analyses. [5-8] However, the origin of the ferromagnetism in the III-V semiconductors still always a question not elucidated and several mechanisms (such as the interaction of Ruderman-Kittel-Kasuya-Yoshida (RKKY) [4,9,10,11,12] were proposed. The semiconductors of group IV (C, Si...) became a significant material class which is used in the devices which function with the state of spin, i.e. which exploits the spin of the electron. Moreover for this reason they are known as *spintronic* devices. However, this material class was not intensively studied like those of the III-V and II-VI families.

The *spintronic* components constitute already a fundamental discovery for the information storage, development of faster microprocessors, and increase in the capacities of memories... etc [13-16]. In the *spintronic* applications; the materials containing impurities atoms must have a broad magnetic moment ($\geq 1 \mu_B$, where μ_B is the Bohr magneton) and high Curie temperatures (above the ambient temperature). Among materials already used in the *spintronic* applications, those magnetic doped semiconductors remain the favourite candidates offering a broad promising applicability [17-20,2]. Well on, there is other material classes which are also used the

spintronic applications, such as for example semi-metals [21]. This concept of semi-metallicity was highlighted for the first time by Groot et al [22] Which used the term «semi-metal» to describe the nature of the NiMnSb alloys and PtMnSb (of Heusler type), this term was then generalized by Pask et al [23] for MnC. The electronic structure of this material also reflects the "semi-metal" character in the structure zinc-blende. In this work we were interested in the study of the $Mn_{0.125}C_{0.875}$ and $Mn_{0.125}Si_{0.875}$ alloys in a cubic cell, comparing the different properties with those of C and Si. To have a good description of the electronic properties and especially the band structures, we using the full-potential linearized augmented plane wave method (FP-LAPW) based on density functional theory (DFT). This method already showed its effectiveness and its exactitude in the determination of the electronic and magnetic properties. Finally we conclude our analysis with a global conclusion.

II. RESULTS AND DISCUSSION

A. Details of calculations

All the presented calculations were performed using the FP-LAPW method implemented in the wien2k code [24]. we used the local density approximation (LDA) parameterized by Perdew and wang in our determination of the exchange-correlation potential[25]. Two cases: polarized spin and nonpolarized spin are considered.

For the alloys (Mn_xC_{1-x} and Mn_xSi_{1-x}), we used a cell of 8 atoms. Thus, one can study the alloys Mn_nC_{8-n} and Mn_nSi_{8-n} in a simple cubic structure according to the concentrations $x=0$ and $x=0.125$ ($n=0$ and $n=1$, where n is the number of atoms).

For C_8 and Si_8 , we chose muffin-tin radius of 1.4 u.a and 2.1 u.a respectively, While for the $Mn_{0.125}C_{0.875}$ alloy (MnC_7), we used $R_{MT}=1.4$ u.a for Mn and C, and for the $Mn_{0.125}Si_{0.875}$ alloy ($MnSi_7$), we chose muffin-tin radius of 2.1 a.u for Mn and Si. Plane waves are expanded with a vector up to $K_{max}=8/R_{MT}$ for Si and $Mn_{0.125}Si_{0.875}$, and $K_{max}=9/R_{MT}$ for C and $Mn_{0.125}C_{0.875}$, and an angular momentum expansion up to $L_{max}=10$. For the potential and charge density, integration over the irreducible Brillouin zone wedge was performed using 8k points according to the Monkhorst-Pack scheme[26].

B. Structural properties

TABLAU I

Structural properties of C_8 and Si_8 . Equilibrium lattice constant a_0 (u.a), total energy E_{tot} (Ry), Bulk modulus B (Mbar), and the Bulk modulus derivative B' .

	E_{tot} (Ry)	B (Mbar)	B'	a_0 (u.a)
C Nitre calc	-604 699	4 667	3 533	6 694
Expt				6 740 ^a
Nitre calc				6 727 ^b
				6 705 ^c

Si Nitre cal	-1614 543	0 977	4 127	10 249
Expt				10 259 ^a
Nitre calc				10 266 ^b
				10 261 ^c

^a experimental value reference. 27-28

^b Reference. 29

^c Reference. 30

TABLAU II

Equilibrium lattice constant a_0 (u a), energy total E_{tot} (Ry), Bulk modulus B (Mbar), the Bulk modulus derivative B' , total magnetic moment M (μ_B) and local magnetic moment M_{Mn} (μ_B) for $Mn_{0.125}C_{0.875}$ and $Mn_{0.125}Si_{0.875}$ calculated by the LDA

	E_{tot} (Ry)	B (Mbar)	B'	a_0 (u a)	M (μ_B)	M_{Mn} (μ_B)
$Mn_{0.125}C_{0.875}$ (nm)	-2853 286	3 71	2 46	6 72	-	-
(Fm)	-2853 286	3 65	3 10	6 72	0 (0)	0 (0)
$Mn_{0.125}Si_{0.875}$ (nm)	-6335 207	0 96	3 93	10 15	-	-
(Fm)	-6335 243	0 88	4 08	10 21	2.325	2 441

According to Table. I, we can note the undervaluation of the equilibrium lattice constant in contrast to its experimental value, and along Table. II, in the case of $Mn_{0.125}C_{0.875}$, we can note that the total energy and the equilibrium lattice constant are the same ones for the two states ferromagnetic (Fm) and nonmagnetic (Nm). This indicates that the $Mn_{0.125}C_{0.875}$ is nonmagnetic with a full null magnetic energy ($\Delta E_{mag}=E_{Fm} - E_{nm}=0$ eV/atome).

For the $Mn_{0.125}Si_{0.875}$, magnetic energy is not null (-0.0615eV/atom), this shows that the ferromagnetic state is the most stable state. One notices in this case that the Bulk modulus is small while the equilibrium lattice constant is large. This signifies that magnetism influence the structural properties considerably. The ferromagnetic state of the $Mn_{0.125}Si_{0.875}$ characterized by the total magnetic moment of 2.325 μ_B , is mainly due to the local magnetic moment of Mn.

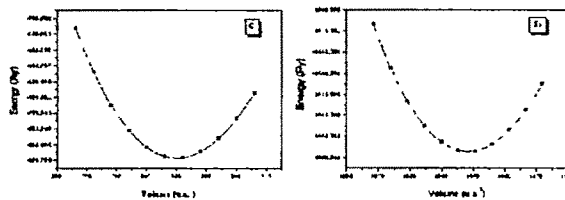


FIG. 1. Total énergies versus total volume for C and Si

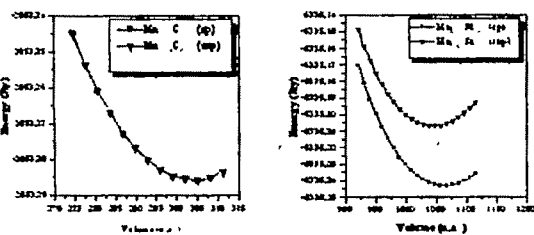


FIG. 2. Total energies versus total volume for alloys $Mn_{0.125}C_{0.875}$ and $Mn_{0.125}Si_{0.875}$ for the ferromagnetic (Fm) and nonmagnetic (Nm) states

C. Electronic and magnetic properties

C.1 Electronic and magnetic band structure

In comparing the electronic band structures of the $Mn_{0.125}C_{0.875}$ and $Mn_{0.125}Si_{0.875}$ alloys, with those of C and Si respectively, we can notice that for this later ones, the maximum of the valence band is at the Γ point while the minimum of the conduction band is situated at X point, which represents an indirect gap of 4.14eV and 0.45eV for C and Si respectively.

From Figs. 4 and 5, we notice the appearance of a band splitting below the Fermi level in $Mn_{0.125}C_{0.875}$ and $Mn_{0.125}Si_{0.875}$ contrary to C and Si compounds. Moreover, we can also remark the disappearance of the gap in $Mn_{0.125}C_{0.875}$ relatively to C.

The band structures of spin up and spin down are similar (Fig. 4), the lowest bands derive from the 2s states of the anion. With the lower part of the Fermi level, a doubly degenerated band is localized at the Γ (0 0 0) point, the main contributions are made up of the 2p states of the anion with a contribution of the 3d states of the cation. At the M point, just with the lower part of the Fermi level, the gap is null; On the other hand, in the vicinity of E_F , it is the hybridization of d states of the cation and p states of the anion which is dominant. We can also remark an overlapping in bands appearing with the top of the Fermi level, it derives from the 2p and 3d states of the anion and cation respectively.

From Fig. 5, we can remark that the band structures in both cases (up and down) are similar in the lowest area of the Fermi level, these bands are characterized by the 2s states of anion (Si). However, there is a distinction neighbouring the EF, in the spin down stats, appears a direct small gap at the point Γ (0 0 0) of 0.5eV below the Fermi level. While in the spin up case, a band overlapping appears, these bands result from d and p states of Mn and Si hybridizations.

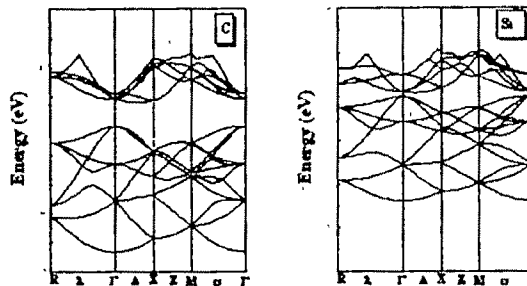


FIG. 3. Band structures of the cell of 8 atoms of C and Si.

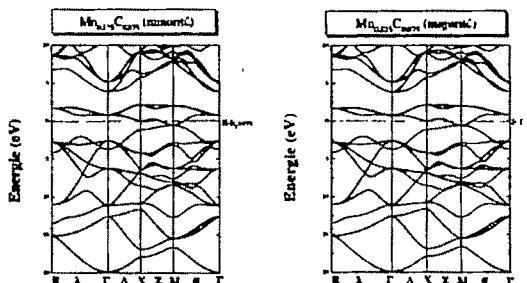


FIG. 4. Majority-spin and minority-spin band structures for $Mn_{0.125}C_{0.875}$.

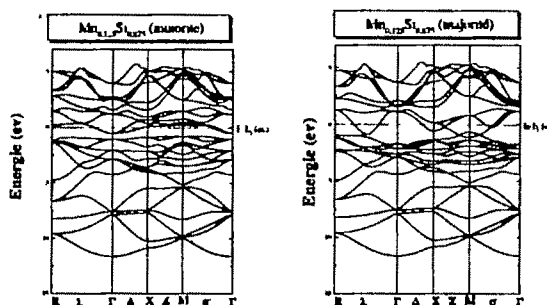


FIG. 5. Majority-spin and minority-spin band structures for $Mn_{0.125}Si_{0.875}$.

C.2 Density of states

The total densities state of C and Si expose two principal states separated by a gap: the first area, just with the lower part of the Fermi level, the main contributions are essentially due to the p states, while the second area is dominated by both s and p states. On the other hand in the alloys $Mn_{0.125}C_{0.875}$ and $Mn_{0.125}Si_{0.875}$, the changes in the density of state are more distinct comparatively to C and Si.

From Figs. 7 and 8, we can notice firstly that the densities of states of spin-up and spin-down are symmetrical for the $Mn_{0.125}C_{0.875}$ and asymmetrical for the $Mn_{0.125}Si_{0.875}$ compounds. The position of the Fermi level is also distinct in the two alloys.

Fig. 8 indicate the asymmetrical spin-up and down density of states, this implies a magnetic character which can be shown by the values of the density of states on the Fermi level. From these values, we can deduce the difference in spin-up and spin-

down densities of states which is of 0.256states/eV. In the case of spin down, the density of state is characterized by two regions separated by a low density states illustrating the small direct gap about 0.5eV. The first region is dominated by the 2p states of the anion, and a significant peak appearing below the Fermi level essentially due to 3d states of the Mn and a certain contribution to 2p states of Si. The second region is characterized by a centered peak in the neighbourhoods of 0.5eV. This area is dominated by the 3d states of the Mn, while the region of spin-up density of state in partitioned in tow different densities of states separated by a minimum. The first region with the lower part of the Fermi level is dominated by the 3d states of Mn, whereas the second region is essentially a contribution coming from Si(2p) and Mn(3d). In the vicinity of the Fermi level, a strong hybridization is due to d states of Mn and p states of Si. From the partial density of states of spin, we deduces that the magnetic moment of Mn is significant for the $Mn_{0.125}Si_{0.875}$, the fact is that the p states of Si are slightly hybridized with the d states of Mn, this induces that the $Mn_{0.125}Si_{0.875}$ alloy is semi-magnetic.

According to Fig. 7, we notice that the density of states of spin-up and down are symmetrical, therefore $Mn_{0.125}C_{0.875}$ is nonmagnetic. This density of states is characterized by two areas separated by a minimum of the density of states.

From the partial densities, one can define the character for each area. The first is dominated by the 2p states of the anion, the second area is dominated by the 2p states of the anion with a contribution of the d character of the cation. Finally, around the Fermi level, the contribution is due to the d states of Mn and p of C.

One can recall that hybridization between Mn and the group IV atoms, results from the states which are near the Fermi level. In particular, in the area of the gap for the elements of the group IV, if it is insulating or semiconductor (in our case C and Si).

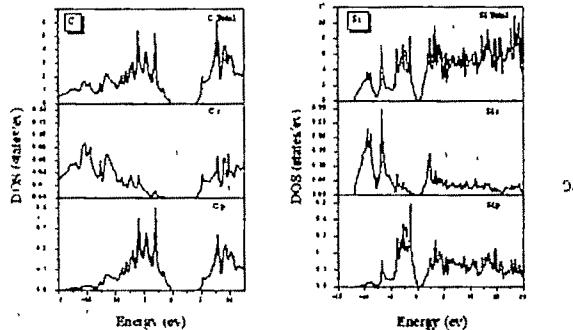


FIG. 6. Total and partial densities of states unit cell of 8 atoms of C and Si.

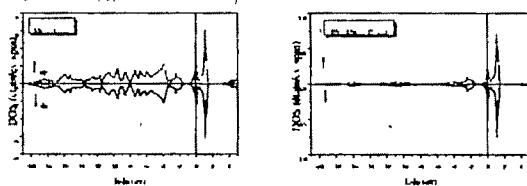


FIG. 7. Total and partial spin-up and spin-down densities of states of $Mn_{0.125}C_{0.875}$.

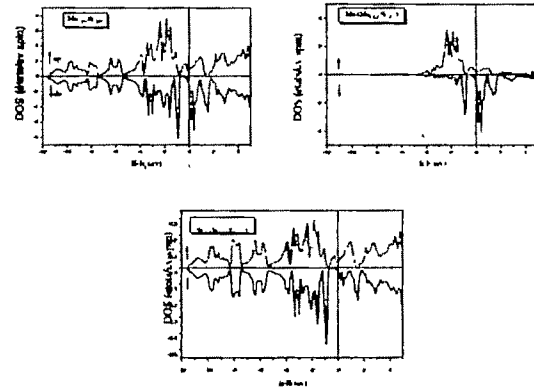


FIG. 8. Total and partial spin-up and spin-down densities of states of $Mn_{0.125}Si_{0.875}$.

III. CONCLUSION

In summary, we have studied the structural, electronic and magnetic properties of binary alloys Mn_xC_{1-x} , Mn_xSi_{1-x} , using the full-potential linearized augmented plane wave (FP-LAPW); for that we studied a mesh of 8 atoms For the Mn_xC_{1-x} and Mn_xSi_{1-x} alloys (Mn_nC_{8-n} and Mn_nSi_{8-n}) in the simple cubic structure according to the concentrations $x=0$ and $x=0.125$. The structural properties calculated for C and Si concurs with theoretical calculations but are underestimated compared to the experimental results. For $Mn_{0.125}C_{0.875}$ and $Mn_{0.125}Si_{0.875}$, we studied two different states: magnetic (ferromagnetic (Fm)) and nonmagnetic (Nm). Our results show that the ferromagnetic state is vigorously more stable than the nonmagnetic state for the $Mn_{0.125}Si_{0.875}$, but for $Mn_{0.125}C_{0.875}$, the two states ferromagnetic and nonmagnetic are identical. We notice that $Mn_{0.125}C_{0.875}$ alloy is nonmagnetic (Nm) with a total magnetic moment reduced to zero, and the $Mn_{0.125}Si_{0.875}$ alloy are ferromagnetic (Fm) with magnetic total moment of 2.3255 μ_B .

For the calculation of the electronic and magnetic properties for $Mn_{0.125}C_{0.875}$, our calculations shows that the densities of states of spin-up and spin-down are symmetrical with metallic character, which means that the connection carbon-carbon is more rigid (cannot be easily dissociated, the Mn can not broken this connection), while for the $Mn_{0.125}Si_{0.875}$, the densities of states of spin-up and spin-down are asymmetrical with metallic-like character, but with a difference of the

densities of states on the Fermi level of 0.256states/ev, which suggests that this alloy is semi-magnetic.

REFERENCES

- [1] H Ohno, *Science* **281**, 951 (1998)
- [2] Y Ohno, D K. Young, B Beschoten, F. Matsukura, H Ohno, and D D. Awschalom, *Nature (London)* **402**, 790 (1999)
- [3] R. Friederling, M. Keim, G Reuscher, W. Ossau, G. Schmidt, A Waag, and L W. Molenkamp, *Nature (London)* **402**, 787 (1999)
- [4] T Dietl, H. Ohno, F. Matsukura, J. Cibert, and D. Ferrand, *Science* **287**, 1019 (2000)
- [5] S. Sanvito, P. Ordejon, and N.A. Hill, *Phys. Rev B* **63**, 165206 (2001).
- [6] Y J Zhao, W T Geng, K.T. Park, and A J. Freeman, *Phys. Rev. B* **64**, 035207 (2001)
- [7] M Jam, L. Kronik, J R. Chelikowski, and V.V. Godlevsky, *Phys. Rev B* **64**, 245205 (2001)
- [8] M. van Schilfgaarde and O.N. Mityasov, *Phys. Rev B* **63**, 233205 (2001).
- [9] F Matsukura, H Ohno, A. Shen, and Y Sugawara, *Phys. Rev. B* **57**, R2037 (1998)
- [10] OH. Akai, *Phys Rev Lett* **81**, 3002 (1998).
- [11] J Inoue, S Nonoyama, and H. Itoh, *Phys. Rev. Lett.* **85**, 4610 (2000)
- [12] M Yagi, K Noba, and Y. Kayanuma, *J Lumin* **94 95**, 523 (2001)
- [13] G. A. Prinz, *Science* **282**, 1660. (1998)
- [14] P. Ball, *Nature (London)* **404**, 918 (2000)
- [15] P Grunberg, *Phys Today* **54**, 31 (2001)
- [16] S. A. Wolf, D. D Awschalom, R. A Buhrman, J M. Daughton, S von Molnar, M. L. Roukes, A Y Chitcheikanova And D. M. Treger, *Science* **294**, 1488 (1998).
- [17] T. Dietl, *Diluted Magnetic Semiconductors in Handbook of Semiconductors (North-Holland, New York, 1994), Vol. 3B.*
- [18] H Ohno, *Science* **281**, 951 (1998)
- [19] H. Ohno, *J Magn Magn. Mater.* **200**, 110 (1999).
- [20] Y. Ohno, D K. Young, B. Beschoten, F. Matsukura, H. Ohno, and D Awschalom, *Nature (London)* **402**, 790 (1999)
- [21] W E Pickett and J. S. Moodera, *Phys. Today* **54**, 39 (2001).
- [22] R. A de Groot, F M Mueller, P G. van Engen, and K. H. J Buschow, *Phys Rev Lett.* **50**, 2024 (1983).
- [23] J E Pask, L. H. Yang, W E. Pickett, and S. Dag, *Phys. Rev. B* **67** 224420 (2003).
- [24] P. Blaha, K Schwarz, G. K. H Madsen, D. Kvasnicka, and J. Luitz, *WIEN2K, An Augmented Plane Wave Plus Local Orbitals Program for Calculating Crystal Properties (Vienna University of Technology, Vienna, Austria, 2001).*
- [25] J P Perdew and Y. Wang, *Phys Rev B* **45**, 13244 (1992)
- [26] H J. Monkhost and J. D Pack, *Phys. Rev B* **13**, 5188 (1976). [27] K J Chang and M L Cohen, *Phys. Rev. B* **35**, 8196 (1987).
- [28] M T Ying, *Proceedings of the 17th International Conference On The Physics of Semi-conductors, San Francisco, edited by I D Chadi and W. A Harrison (Springer-Verlag, New York, 1985), p. 927.*
- [29] M T Yin, *Phys. Rev. B* **30**, 1773 (1984).
- [30] M T Yin and M L Cohen, *Phys. Rev B* **26**, 5668 (1982), and references therein

Symmetry Through Group Theory and Linear Transformation

Samir Zaki and Mohamed Mehrez

Retired Police Officer (General), Egypt, e-mail: samoad@hotmail.com

Abstract—The aim of this contribution is to show how through mathematical tools very interesting numerous symmetry figures could be produced. This paper will first discuss the symmetry of plane figures in terms of groups of rigid motions. Then illustration will be devoted to geometric representation of various types of matrix transformations. Representative patterns with various types of symmetry will be illustrated through figures and graphs. Numerical tables will also be used for explanation.

Key words- reflection, rotation, stretches, transformation.

I. INTRODUCTION

SYMMETRY is a common phenomenon in all sciences. It provides one of two main appealing applications of group theory. In common usage symmetry generally conveys two primary meanings. The first is an imprecise sense of harmonious or aesthetically-pleasing proportionality and balance; such that it reflects beauty or perfection. The second meaning is a precise and well-defined concept of balance or patterned self-similarity that can be demonstrated or proved according to the rules of a formal system; by geometry, through physics or otherwise. Although the meanings are distinguishable, in some contexts, both meanings of 'symmetry' are related and discussed in parallel. The discussion in this paper will deal with geometric transformations such as scaling, reflection, and rotation. The author will use geometric reasoning without bothering to carry the arguments back to axioms of geometry.

II. MATHEMATICAL MODEL for SYMMETRY

The set of all symmetry operations considered, on all objects in a set X , can be modeled as a group action $g : G \times X \rightarrow X$, where the image of g in G and x in X is written as $g.x$. If, for some g , $(g.x = y)$ then x and y are said to be symmetrical to each other. For each object x , operations

g for which $(g.x = x)$ form a group, the symmetry group of the object, is a subgroup of G . If the symmetry group of x is the trivial group then x is said to be asymmetric, otherwise symmetric. A general example is that G is a group of bijections $g : V \rightarrow V$ acting on the set of functions $x : V \rightarrow W$

by $(g.x)(V) = x(g^{-1}(V))$ (or a restricted set of such functions that is closed under the group action). Thus a group of bijections of space induces a group action on objects in it. The symmetry group of x consists of all g for which $x(V) = x(g(V))$ for all v . G is the symmetry group of the space itself, and of any object that is uniform throughout space. In a modified version for vector fields, we have $(g.x)$

$(V) = h(g.x((g^{-1}(V))))$ where h rotates any vectors and pseudo vectors in x , and inverts any vectors but not pseudo vectors according to rotation and inversion in g . The symmetry group of x consists of all g for which $x(V) = h(g.x((g(V))))$ for all v . In this case the symmetry group of a constant function may be a proper subgroup of G : a constant vector has only rotational symmetry with respect to rotation about an axis if that axis is in the direction of the vector, and only inversion symmetry if it is zero.

III. GEOMETRIC RELATIONSHIPS INVOLVING MATRIX TRANSFORMATIONS

Many matrix operations can be usefully represented geometrically if two or three dimensions are involved. At this point it seems useful to extend this line of geometric reasoning to other aspects of matrix transformations. In order to motivate the discussion, let us consider the small 9×2 matrix of synthetic data shown in Table 1. This matrix consists of nine points, positioned in two dimensions, as diagramed in Fig. 1.

Table 1 Original matrix X of nine points in two dimensions.

Point (code letter)	Dimension 1	Dimension 2
a	1	0
b	1	1
c	1	2
d	2	0
e	2	1
f	2	2
g	3	0
h	3	1
i	3	2
\bar{x}_j	2	1

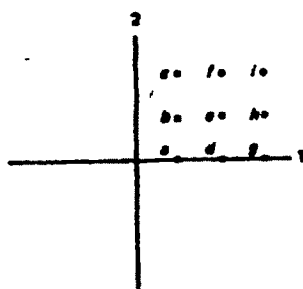


Fig. I Illustrates a square lattice arrangement of nine points of the matrix of table I.

We shall now describe a variety of operations on this synthetic data matrix, and show their effects geometrically. Thus the basic format to be followed consists of the transformation

$$X^* = XA \quad (1)$$

Where A assumes various special forms that exhibit simple geometric patterns, and each row vector in X is being postmultiplied by A to obtain each row vector in X^* .

A. Translation

Matrix translation has to do with the problem of relating a set of points to a particular origin in the space. Suppose, for example, that we wished to refer the nine points of Fig. 1 to a centroid - centered origin as shown in table 1, the mean of the points on the first dimension is 2; their mean on the second dimension is 1. By expressing each original value as a deviation from its mean, we arrive at matrix X_d as shown in Table II. Note that this simply involves a subtraction of \bar{x} whose entries represent the mean of the points on each dimension, from the original matrix X.

Table II Translation of matrix X to origin at centroid.

X	\bar{x}	X_d
$\begin{bmatrix} 1 & 0 \\ 1 & 1 \\ 1 & 2 \\ 2 & 0 \\ 2 & 1 \\ 2 & 2 \\ 3 & 0 \\ 3 & 1 \\ 3 & 2 \end{bmatrix}$	$\begin{bmatrix} 2 & 1 \\ 2 & 1 \\ 2 & 1 \\ 2 & 1 \\ 2 & 1 \\ 2 & 1 \\ 2 & 1 \\ 2 & 1 \\ 2 & 1 \end{bmatrix}$	$\begin{bmatrix} -1 & -1 \\ -1 & 0 \\ -1 & 1 \\ 0 & -1 \\ 0 & 0 \\ 0 & 1 \\ 1 & -1 \\ 1 & 0 \\ 1 & 1 \end{bmatrix}$

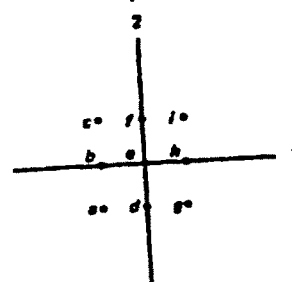


Fig. II Shows the effect of the translation geometrically.

A translation, then, involves a parallel displacement of every point to some new origin of interest. In this case the centroid of the points is the origin of interest.

B. Reflection

Reflection of a set of points entails multiplication of the coordinates of each point to be reflected by -1 .

For example, suppose we wished to reflect the nine points of Fig. II "across" axis 2. This can be accomplished by multiplying each of the coordinates on axis 1 by a -1 , as shown in Table III.

Table III Reflection of matrix X_d across axis 2.

$$\begin{bmatrix} -1 & -1 \\ -1 & 0 \\ -1 & 1 \\ 0 & -1 \\ 0 & 0 \\ 0 & 1 \\ 1 & -1 \\ 1 & 0 \\ 1 & 1 \end{bmatrix} \xrightarrow{\text{Reflection } \begin{bmatrix} -1 & 0 \\ 0 & 1 \end{bmatrix}} \begin{bmatrix} 1 & -1 \\ 1 & 0 \\ 1 & 1 \\ 0 & -1 \\ 0 & 0 \\ 0 & 1 \\ -1 & -1 \\ -1 & 0 \\ -1 & 1 \end{bmatrix}$$

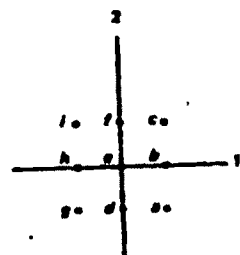


Fig. III Illustrates graphically the reflection of the nine points of Fig. II across axis 2.

Similarly, if desired, one could reflect the nine points across axis 1, it should be reiterated, however, that reflection typically involves an odd number of dimensions. If we were to reflect the points across both axis 1 and axis 2, the overall effect - called a reflection through the origin - is equivalent to a rotation of the points about an angle of 180° from their original orientation.

C. Axis Permutation

Permutation of a set of points, involves a matrix transformation that carries each coordinate value on axis 1 into a corresponding coordinate on axis 2, and vice versa.

This is illustrated in Table IV, and the effect is shown graphically in Fig. 1V.

Table IV Axis permutation of matrix X_d .

$$X_d = \begin{bmatrix} -1 & -1 \\ -1 & 0 \\ -1 & 1 \\ 0 & -1 \\ 0 & 0 \\ 0 & 1 \\ 1 & -1 \\ 1 & 0 \\ 1 & 1 \end{bmatrix} \xrightarrow{\text{Permutation}} \begin{bmatrix} -1 & -1 \\ 0 & -1 \\ 1 & -1 \\ -1 & 0 \\ 0 & 0 \\ 1 & 0 \\ -1 & 1 \\ 0 & 1 \\ 1 & 1 \end{bmatrix}$$

The permutation matrix that post-multiplies X_d produces an interchange of columns. However, if the permutation matrix pre-multiplies a matrix of pre-images, then the rows of the pre-images are interchanged.

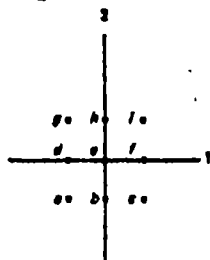


Fig. IV Illustrates the effect of axis permutation.

D. Central Dilation

Central dilation of a set of points entails scalar multiplication of the matrix of coordinates, which is equivalent to multiplication by a scalar matrix; that is, a diagonal matrix in which each diagonal entry involves the same positive constant λ , central dilation leads to a uniform expansion, if $\lambda > 1$, or a uniform contraction, if $\lambda < 1$, of each dimension. If $\lambda = 1$, then the scalar matrix becomes an identity matrix, and the point position remains as originally expressed.

Table V Shows application of a central dilation where $\lambda = 2$.

$$X_d = \begin{bmatrix} -1 & -1 \\ -1 & 0 \\ -1 & 1 \\ 0 & -1 \\ 0 & 0 \\ 0 & 1 \\ 1 & -1 \\ 1 & 0 \\ 1 & 1 \end{bmatrix} \xrightarrow{\text{Central dilation}} \begin{bmatrix} -2 & -2 \\ -2 & 0 \\ -2 & 2 \\ 0 & -2 \\ 0 & 0 \\ 0 & 2 \\ 2 & -2 \\ 2 & 0 \\ 2 & 2 \end{bmatrix}$$

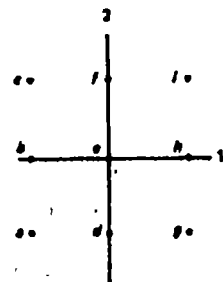


Fig. V Shows the result of central dilation where $\lambda = 2$.

According to the present case, each of the original axis is dilated to twice its original length.

E. Stretch

A stretch transformation of a set of points involves applications of a diagonal matrix where, in general, the diagonal entries are such that $\lambda_{ii} \neq \lambda_{jj}$. In contrast to central dilation, a stretch involves rescaling of points corresponding again to directions along the original axis.

For example, $\lambda_{11} = 2$ and $\lambda_{22} = 1$, the effect of this transformation is to stretch axis 1 to twice its original length, thus producing a lattice-like rectangle out of the original lattice-like square.

Table VI Illustrates a stretch of matrix X_d .

$$X_d = \begin{bmatrix} -1 & -1 \\ -1 & 0 \\ -1 & 1 \\ 0 & -1 \\ 0 & 0 \\ 0 & 1 \\ 1 & -1 \\ 1 & 0 \\ 1 & 1 \end{bmatrix} \xrightarrow{\text{Stretch}} \begin{bmatrix} -2 & -1 \\ -2 & 0 \\ -2 & 1 \\ 0 & -1 \\ 0 & 0 \\ 0 & 1 \\ 2 & -1 \\ 2 & 0 \\ 2 & 1 \end{bmatrix}$$

Here we shall restrict the term "stretch" to the case in which all $\lambda_{ii} > 0$. If some λ_{ii} were zero, those dimensions would be annihilated. A $\lambda_{ii} < 0$ would correspond to a stretching followed by reflection

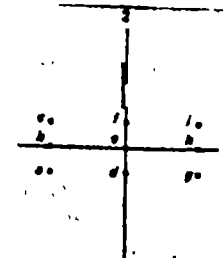


Fig. VI Shows the graphical results of the stretch transformation.

F. Rotation

Axis rotation involves application of rather special kind of matrix – an orthogonal matrix. An orthogonal matrix is distinguished by the properties: (a) the sum of squares of each column (row) equals 1, and (b) the scalar product of each pair of columns (rows) equals zero. In two dimensions an orthogonal matrix entails a rigid rotation of the original configuration of points about some angles Ψ . In the preceding example we rotate the points counter clockwise about an angle, $\Psi = 45^\circ$

Table VII Shows the application of the 45° counter clockwise rotation of matrix X_d

$$\begin{bmatrix} -1 & -1 \\ -1 & 0 \\ -1 & 1 \\ 0 & -1 \\ 0 & 0 \\ 0 & 1 \\ 1 & -1 \\ 1 & 0 \\ 1 & 1 \end{bmatrix} \xrightarrow{\text{Rotation}} \begin{bmatrix} 0 & -1.414 \\ -0.707 & -0.707 \\ -1.414 & 0 \\ 0.707 & -0.707 \\ 0 & 0 \\ -0.707 & 0.707 \\ 1.414 & 0 \\ 0.707 & 0.707 \\ 0 & 1.414 \end{bmatrix}$$

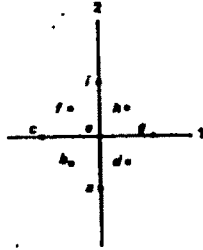


Fig. VII Summarizes the results graphically, of the 45° counterclockwise rotation of X_d .

Note that the zero point (intersection of the axes) can be viewed as a hub of a wheel and remains fixed during the rotation.

G. Shear

A shear transformation is characterized by the following form

$$\begin{bmatrix} 1 & 1 \\ 0 & 1 \end{bmatrix}$$

so that post multiplications of some matrix by a shear has the effect of adding columns. If we apply the shear to the matrix X_d , we obtain the coordinates shown in table VIII.

Table VIII Shows a shear transformation of matrix X_d .

$$\begin{bmatrix} -1 & -1 \\ -1 & 0 \\ -1 & 1 \\ 0 & -1 \\ 0 & 0 \\ 0 & 1 \\ 1 & -1 \\ 1 & 0 \\ 1 & 1 \end{bmatrix} \xrightarrow{\text{Shear}} \begin{bmatrix} -1 & -2 \\ -1 & -1 \\ -1 & 0 \\ 0 & -1 \\ 0 & 0 \\ 0 & 1 \\ 1 & 0 \\ 1 & 1 \\ 1 & 2 \end{bmatrix}$$

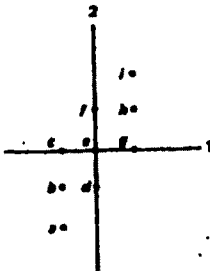


Fig. VIII Illustrates a shear transformation of matrix X_d .

IV. COMPOSITE TRANSFORMATIONS

The transformations described previously, each has been applied singly. It is instructive to see what happens when some of these transformations are applied on a composite bases. For illustrative purpose note the following case:

Rotation followed by Reflection.

If we multiply the following matrices,

$$\begin{bmatrix} 0.707 & 0.707 \\ -0.707 & 0.707 \end{bmatrix} \begin{bmatrix} -1 & 0 \\ 0 & 1 \end{bmatrix}$$

we obtain,

$$\begin{bmatrix} -0.707 & 0.707 \\ 0.707 & 0.707 \end{bmatrix}$$

The resultant matrix has a determinant of - 1, this type of matrix is called an improper rotation. Although it meets the conditions of an orthogonal matrix, its application actually involves a proper rotation, in which the determinant is 1, followed by reflection of axis 1.

Table IX Shows the result of this composite transformation.

$$\begin{bmatrix} -1 & -1 \\ -1 & 0 \\ -1 & 1 \\ 0 & -1 \\ 0 & 0 \\ 0 & 1 \\ 1 & -1 \\ 1 & 0 \\ 1 & 1 \end{bmatrix} \xrightarrow{\text{Improper rotation}} \begin{bmatrix} 0 & -1.414 \\ 0.707 & -0.707 \\ 1.414 & 0 \\ -0.707 & -0.707 \\ 0 & 0 \\ 0.707 & 0.707 \\ -1.414 & 0 \\ -0.707 & 0.707 \\ 0 & 1.414 \end{bmatrix}$$

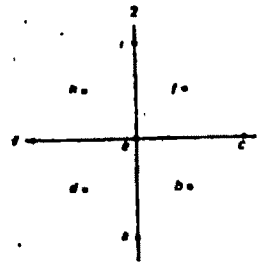


Fig. IX Shows the geometric of an improper rotation of matrix X_d .

REFERENCES

- [1] Michael Artin "Algebra" Third Printing 1996 Published by Asoke K. Ghosh, Printice - Hall of India Private Limited M. 97, Connaught Circus, New Delhi
- [2] Paul E. Green, J. Douglas Carroll " Mathematical Tools for Applied Multivariate Analysis " Academic Press 1976 New York
- [3] Rosen, Joe, 1995. Symmetry in Science. An Introduction to the General Theory. Springer-Verlag
- [4] Livio, Mario (2005). The Equation That Couldn't Be Solved: How Mathematical Genius Discovered the Language of Symmetry. New York: Simon & Schuster

Mathematical Modeling for Predicating the Mechanical Properties of Plain-Weft Knitted Fabric

H. R. Karimi¹, Ali .A. A. Jeddi², A. Rastgoo³

¹Faculty of Engineering, Islamic Azad University, Science and Research Branch, Tehran, Iran, e-mail: hamid_r_karimi@yahoo.com

²Department of Textile Engineering, Amirkabir University of Technology, Tehran 15914, Iran, e-mail: ajeddi@ut.ac.ir

³Mechanical Engineering Department University of Tehran, Iran, e-mail: arastgo@ut.ac.ir

Abstract— This paper presents a theoretical analysis for the tensile properties of plain weft-knitted fabric. Recently, many researchers have contributed to develop theoretical analysis methods, on elastic behavior for plain weft-knitted fabric. We propose the mathematical model based on the energy theorem with applied the Castigliano's theorem for predicting the initial modulus properties of plain weft-knitted fabric. We proposed the theoretical model to simulate the tensile properties of plain knitted fabric in different state of fabric and yarn specification (such as: yarn coefficient of friction, yarn bending rigidity, yarn modulus and structural parameter of fabric)

Key words—Castigliano's theory, initial modulus, mechanical properties, weft knitted fabric.

I. INTRODUCTION

THE way in which textile materials deform under the application of biaxial stresses play an important role both in their processing and in their end use. For this reason, various authors have investigated the tensile properties of plain weft knits [1], [2], [3], [4], [7], [8], [9], [10], [11], [12], [13], and most of these investigations were based on the micromechanics of knitted structure. The unit cell often a single loop, was used for these analysis, and the tensile properties of knitted fabrics were directly derived from the loop configuration and yarn properties. The model proposed by Leaf and Kandil [6] reported analysis of the initial load-extension behavior of plain-woven fabrics. In this paper, we propose a theoretical analysis based on the energy theorem by using Castigliano's theorem and the simple model for plain knitted fabric to predicate tensile properties of plain knitted fabric in relation with its geometry.

II. ANALYSIS

BASIC ASSUMPTION

First, we assume the plain knitted fabrics are made of naturally straight filament yarns, which can be considered as homogeneous elastic rods. This assumption is not very

realistic, but should be accepted for reason. The analysis focuses on the deformation of knitted fabrics at low loading conditions (compared to the load required to break the yarn).

In this condition the chief mechanism of deformation is the change of loop shape within the fabric. The resistance to extension of the fabric depends mainly on the bending and extension properties of the yarn. In this case, yarn compression effect is relatively small and can be ignored.

Second, we assume that the knitted fabric is formed with planar loop structure. All loops within the same fabric keep an identical configuration. No plastic deformation of the yarn takes place when the fabric is knitted from a yarn and later subjected to extension. The load-extension properties of a knitted fabric are directly derived from its loop configuration change.

Finally, with the same assumptions as Leaf's model [6] were taken for the yarn properties as following:

- They extend according to the law $T = E_y \epsilon_y$, where T the tension in the yarn is, E_y is the initial modulus of yarn and ϵ_y is the extension produced. The strain energy of extension per unit length of yarn is then $T^2 / 2\lambda$.
- Because of the force generated between the yarns when the fabric deform, the yarns will be compressed. In a real fabric, the compressive force will be distributed over the region of yarn contact, but in the model they are represented as point force. If the inter-yarn force is V and G is a shear modulus of yarn, we shall assume that $V = G\epsilon_d$ where $\epsilon_d D$ is the change in yarn diameter that takes place when the force V is applied. The strain-energy of compression is then $V^2 D / 2G$.
- The yarns bend with flexural rigidity B . The strain-energy per unit of yarn is then $M^2 / 2B$, where M is the applied bending moment.

THEORETIC ANALYSIS

Duo to the symmetry of the loop configuration, only a unit cell of the loop is analyzed.

A simple model for plain knitted fabric

We assumed that the fabric deformation is homogeneous all over the fabric. When normal stress is applied to a knitted fabric in the course or wale directions, when this happens, then the curved element of yarn will straighten except at the crossing points. The simplified model of knitted fabric is shown in (Fig.1).

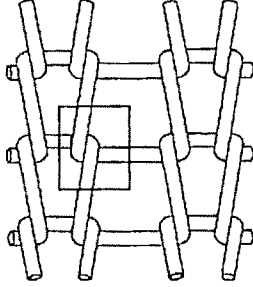


Figure 1 Schematic of simple model of knitted structure under biaxial stress.

As shown in (Fig.2) the unit cell of structure is divided in two segments (ABC, DEF) let: D = diameter of yarn, L = stitch length (length of yarn in one complete weave), C = course spacing, W = wale spacing, r = yarn radius, θ = yarn inclination ($\cos\theta = 2r/C$).

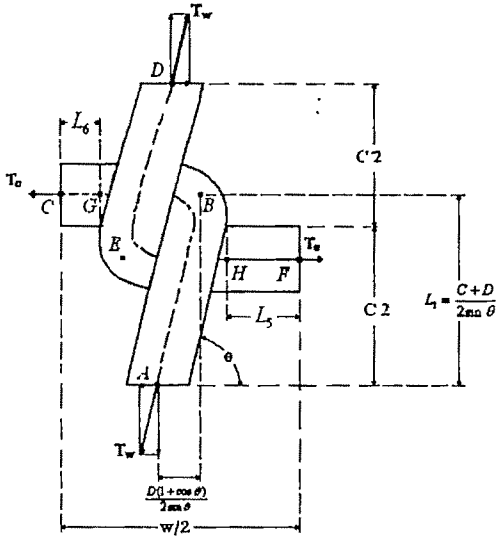


Figure 2 Schematic straight line model of unit cell of structure.

(A) The total strain energy in unit cell of structure (in YOX plane)

By considering the symmetrical properties of the loop and the force-equilibrium state (Fig.2) it can be seen that the T_w force is imposed at A and D points, while drive the force T_c is imposed at C and F points. There will be a point of inflexion

at A, so that the bending moment there is zero, with small deformation assumed, the moments at a point on GC at the distance s_1 and s_2 from A are approximately:

$$M_1 = (T_w \cos \theta) s_1 \quad (1)$$

$$M_2 = -(T_w \sin \theta) s_2 \quad (2)$$

And the bending strain-energy in the AB is therefore:

$$U_{B(M_1)} = \int_0^{\frac{C+D}{2}} \frac{M_1^2}{2B} ds = \frac{(C+D)^3}{24B} T_w^2 \cos^2 \theta \quad (3)$$

$$U_{B(M_2)} = - \int_0^{\frac{D(1+\cos\theta)}{2\sin\theta}} \frac{M_2^2}{2B} ds = - \frac{T_w^2}{24B} \left(\frac{D}{\sin\theta} (1+\cos\theta) \right)^3 \quad (4)$$

The total bending strain-energy in the AB is therefore:

$$U_{T(AB)} = U_{B(M_1)} + U_{B(M_2)} \quad (5)$$

The bending strain energy in DE is given by a similar expression, and hence the total bending strain energy in the unit cell ($U_{T(YOXplane)}$) shown in (Fig.2) is:

$$U_{T(YOXplane)} = U_{T(AB)} + U_{T(DE)} \quad (6)$$

(B) The total strain-energy in the ABC segments

The tension in the yarn ABC at two components AB and BC are respectively:

$$T = T_w \quad (7)$$

$$T = T_c \quad (8)$$

And the bending extension-energy in the AB and BC is therefore:

$$U_{ET(ABC)} = \frac{L_1 T_w^2}{2E_y} + \frac{L_2 T_c^2}{2E_y} \quad (9)$$

Finally the total strain-energy in the ABC segments is given as:

$$U_{T(ABC)} = U_{ET(ABC)} \quad (10)$$

(C) The total strain-energy in the DEF segments

We can use the same calculation for DEF segments therefore:

$$U_{ET(DEF)} = \frac{L_1 T_w^2}{2E_y} + \frac{L_2 T_c^2}{2E_y} \quad (11)$$

Thus the total strain-energy in the DEF segments is

$$U_{T(DEF)} = U_{CT(DEF)} \quad (12)$$

Finally the total strain energy for the unit cell (U_T) is obtained as follows:

$$U_T = U_{T(VOXplane)} + U_{T(ABC)} + U_{T(DEF)} \quad (13)$$

Calculation of Fabric Extension

The fabric extension in the wale direction is $\epsilon_w = \delta C / C$, so that

$$\epsilon_w C = \delta C = \partial U_T / \partial T_w \quad (14)$$

$T_w = T_c e^{-2\mu\alpha}$ (+ extension in wale wise direction, - extension in courses wise direction) which α = Angle at interlocking region (radian) and μ = Yarn friction coefficient.

If applied Castigliano's theory. Hence

$$\epsilon_w C = T_w \left\{ \frac{((L_2 + L_1)(e^{-2\mu\alpha}) + 2L_1)}{E_1} + \frac{1}{12B} \left((\cos^2 \theta (C + D)^3) - \left(\sin^2 \theta \left(\frac{D}{\sin \theta} (1 + \cos \theta) \right)^3 \right) \right) \right\} \quad (15)$$

and

$$E_1 \epsilon_w = \frac{T_w \sin \theta}{W / 2} \quad (16)$$

E_1 is the initial Young's modulus of the fabric in wale direction .

We can use the same calculation for the initial Young's modulus of the fabric in course wise direction (E_2).where

$$\epsilon_c W = T_c \left\{ \frac{((L_2 + L_1) + 2L_1(e^{-2\mu\alpha}))}{E_2} + \frac{e^{-2\mu\alpha}}{12B} \left((\cos^2 \theta (C + D)^3) - \left(\sin^2 \theta \left(\frac{D}{\sin \theta} (1 + \cos \theta) \right)^3 \right) \right) \right\} \quad (17)$$

and

$$E_2 \epsilon_c = \frac{T_c}{C} \quad (18)$$

III. RESULT AND DISCUSSION

In order to simulate the initial fabric modulus from Equations (16) and (18) it is necessary to know the yarn and

fabric characteristics (i.e., bending rigidity, diameter and coefficient of friction for yarn ,and course spacing, wale spacing and stitch length of fabric). We assumed seven range of course spacing and wale spacing for fabric and using Equation (24) to measure the stitch length. The assumed parameters of yarn are: coefficient of friction=0.15, modulus=0.4N/cm, diameter =0.2 mm, bending rigidity =0.4 N.mm². The simulated initial modulus values of fabrics are summarized in Table.1.

Table 1 Simulation of fabric modulus with varying of stitch length

Course Spacing(C) (mm)	Wale Spacing(W) (mm)	Predicating stitch length (L)(mm)	Predicted E1 (N/cm)	Predicted E2 (N/cm)
0.961	0.806	2.856	0.6571	0.1604
1.020	0.819	2.979	0.6563	0.1465
1.084	0.833	3.113	0.6544	0.1235
1.149	0.847	3.251	0.6517	0.1222
1.222	0.862	3.405	0.6486	0.1111
1.295	0.874	3.557	0.6477	0.1013
1.373	0.888	3.722	0.6448	0.0925

In next step we simulate the fabric modulus with varying the coefficient of friction in four states; the simulated data are shown in Table.2.

Table 2 Simulation of fabric modulus with varying of yarn-to-yarn coefficient of friction

Coefficient of friction=0.1		Coefficient of friction=0.2		Coefficient of friction=0.3		Coefficient of friction=0.4	
E1 (N/cm)	E2 (N/cm)	E1 (N/cm)	E2 (N/cm)	E1 (N/cm)	E2 (N/cm)	E1 (N/cm)	E2 (N/cm)
0.6700	0.1860	0.6426	0.1382	0.6058	0.1023	0.5673	0.0754
0.6692	0.1698	0.6417	0.1263	0.6076	0.0934	0.5664	0.0689
0.6673	0.1548	0.6399	0.1151	0.6058	0.0851	0.5646	0.0628
0.6646	0.1416	0.6373	0.1053	0.6033	0.0779	0.5662	0.0574
0.6614	0.1288	0.6342	0.0957	0.6004	0.0708	0.5596	0.0522
0.6604	0.1170	0.6335	0.0873	0.6001	0.0646	0.5596	0.0476
0.6503	0.1072	0.6026	0.0797	0.5976	0.0589	0.5575	0.0434

The similar manner was adopted to simulate of fabric modulus with varying yarn bending rigidity and yarn modulus in four different states and the results are tabulated in Tables.3 and 4.

Table 3 Simulation of fabric modulus with varylog of yarn bending rigidity

Table 4 Simulation of fabric modulus with varying of yarn modulus

Yarn Modulus ($E_y = 0.02$ N/cm)		Yarn Modulus ($E_y = 0.03$ N/cm)		Yarn Modulus ($E_y = 0.04$ N/cm)		Yarn Modulus ($E_y = 0.05$ N/cm)	
E1 (N/cm)	E2 (N/cm)	E1 (N/cm)	E2 (N/cm)	E1 (N/cm)	E2 (N/cm)	E1 (N/cm)	E2 (N/cm)
0.3337	0.0816	0.4967	0.1214	0.6571	0.1604	0.8510	0.1989
0.3333	0.0745	0.4961	0.1108	0.6563	0.1465	0.8140	0.1816
0.3223	0.0679	0.4946	0.1010	0.6544	0.1335	0.8116	0.1655
0.3310	0.0621	0.4926	0.0924	0.6517	0.1222	0.8084	0.1514
0.3294	0.0565	0.4902	0.0840	0.6486	0.1111	0.8045	0.1377
0.3289	0.0515	0.4896	0.0766	0.6477	0.1013	0.8035	0.1256
0.3274	0.0470	0.4874	0.0699	0.6448	0.0925	0.7998	0.1146

As it can be observed from the simulated results with increase the stitch length and the coefficient of friction of yarn-to-yarn, the fabric initial modulus are decreased, while it has a reversed result with the increase of yarn bending rigidity and yarn modulus. On the other hand, the predicted result from this theoretical analysis for E_1 and E_2 (Table 1) show a very higher values for initial modulus in wale wise than course wise which has a very good agreement with the previous researcher's analysis Kovar [5]. Kovar indicated that the friction effect on fabric deformation and say yarn-to-yarn slip is much more important in knitted fabric than in woven fabric deformation. In the direction of the wale, the frictional resistance of knitted fabric needs be overcome at the very beginning of the fabric elongation. It leads to step increased in load σ (stress) in the model approach (Fig.10, line 1) and higher initial modulus of deformation on the real fabric elongation (line 2). In course wise direction, the same effect is not observed (Fig.10, line3).

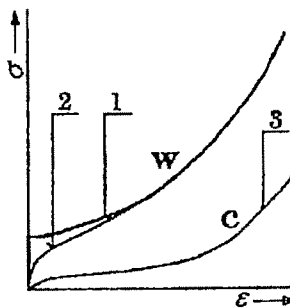


Figure 3 Effect of yarn-to-yarn slip and direction of load applied in knitted fabric stress-strain curve.

III. CONCLUSION

We have presented a mathematical model based on the energy theorem with applied the Castigliano's theorem for predicting the initial modulus properties of plain weft-knitted fabric in both wale wise and course wise directions. This

Yarn bending rigidity ($B = 3$ N.mm ³)		Yarn bending rigidity ($B = 4$ N.mm ³)		Yarn bending rigidity ($B = 5$ N.mm ³)		Yarn bending rigidity ($B = 6$ N.mm ³)	
E1 (N/cm)	E2 (N/cm)	E1 (N/cm)	E2 (N/cm)	E1 (N/cm)	E2 (N/cm)	E1 (N/cm)	E2 (N/cm)
0.6503	0.1586	0.6571	0.1604	0.6612	0.1615	0.664	0.1623
0.6495	0.1449	0.6563	0.1465	0.6604	0.1475	0.6632	0.1482
0.6476	0.132	0.6544	0.1335	0.6585	0.1344	0.6612	0.1351
0.645	0.1208	0.6517	0.1222	0.6558	0.123	0.6586	0.1236
0.642	0.1099	0.6486	0.1111	0.6526	0.1119	0.6554	0.1124
0.6411	0.1002	0.6477	0.1013	0.6518	0.102	0.6545	0.1025
0.6382	0.0914	0.6448	0.0925	0.6488	0.0931	0.6515	0.0935

model is useful to predict the fabric modulus with a given characteristics of the yarn used and fabric produced. This approach may lead to a reduction in the need for destructive testing. This topic will be discussed in detail and experimental result in further paper.

APPENDIX

As seen in Figure.2

$$HF + GC = L_3 + L_4 = \frac{W}{2} - \frac{2D}{\sin \theta} \quad (19)$$

$$DE = AB = L_1 = \frac{C + D}{2 \sin \theta} \quad (20)$$

$$BC = L_2 = L_3 + L_4 \quad (21)$$

$$BG = EH = L_4 = \frac{D}{2 \sin \theta} (1 + \cos \theta) \quad (22)$$

$$EF = L_3 = L_4 + L_4 \quad (23)$$

$$\frac{L}{2} = \frac{C}{\sin \theta} + \frac{W}{2} + D \cot \theta \quad (24)$$

REFERENCES

- [1] S. De Jong and R. Postle, "An energy analysis of the mechanics of weft-knitted fabrics by means of optimal-control theory Part2: Relaxed-fabric dimension and tensile properties of the plain-knitted structure," *J. Text. Inst.*, 10, 316-323, 1977.
- [2] B. Hepworth, "The biaxial load-extension behavior of a model of plain weft-knitting -Part1," *J. Text. Inst.*, 4, 101-107, 1987
- [3] H. Hong, M. de Araujo, R. Franguerio and O. Ciobanu, "Theoretical analysis of load-extension properties of plain weft-knits made from high performance yarns for composite reinforcement," *Text. Res. J.* 72(11), 991-996, 2002.
- [4] R. J. Bassett and R. Postle, "Experimental method for measuring fabric mechanical properties a review and analysis," *Text. Res. J.* 69(11), 866-875, 1999.
- [5] R. Kovar, "Stick-slip effect in knitted fabric deformation," International Textile Clothing and Design Conference, University of Zagreb, Dubrovnik, Croatia, 2002
- [6] G. A. V. Leaf and H. Kandil, "The initial load-extension behavior of plain-weave fabrics," *J. Text. Inst.*, 1, 1-7, 1980
- [7] Brian. M. MacRory, J. Roger. McCarth and Aidan B. McNamara, "Knitted fabric subjected to biaxial stresses-an experimental study," *Text. Res. J.* October, 908-911, 1967.
- [8] Brian. M. MacRory, J. Roger. McCarth and Aidan. B. McNamara, "The biaxial load-extension properties of plain weft-knitted fabrics- a theoretical analysis," *Text. Res. J.* October, 746-760, 1975.
- [9] Brian M. MacRory, J. Roger. McCarth and Aidan B. McNamara, "Experimental investigation of the biaxial load-extension properties of plain weft-knitted fabrics," *Text. Res. J.* April, 233-239, 1977.
- [10] P. Popper, "The theoretical behavior of a knitted fabric subjected to biaxial stresses," *Text. Res. J.* February, 148-157, 1966.
- [11] W. J. Shanahan and R. Postle, "A theoretical analysis of the tensile properties of plain-knitted fabrics Part1 The load-extension curve for fabric extension parallel to the courses," *J. Text. Inst.*, 4, 200-212, 1972

- [12] W. J. Shanahan and R. Postel, "A Theoretical analysis of the tensile properties of plain-knitted fabrics Part2: The initial load-extension behavior for fabrics extension parallel to the wales," *J. Text. Inst.*, 4, 254-260 1973.
 - [13] J. M. Whitney and J. L. Epting, Jr, "Three-dimensional analysis of plain knitted fabric subjected to biaxial stresses," *Text. Res. J.*, 1,143-147, 1966
-

A Simulation Model for Partial Discharge with Stochastic Features

P. Das

College of Engineering & Management, Kolaghat, West Bengal, India e-mail: prithwiraj_13dec@rediffmail.com

Abstract—A model based on Finite Difference Method (FDM) is proposed for simulation of Partial Discharge (PD) Patterns, in which three parameters are considered, viz. the critical field intensity for partial discharge occurrence E_c , residual field intensity E_r and size of the void. Discharge quantity at any instant is not only function of E_c , E_r but also depends upon the discharge area which is function of void size. In this paper Plane-Plane electrode system is considered and the void taken is a rectangular parallelepiped. PD simulations for different sizes of void inside the dielectric are carried out with constant E_c , considering occurrence of partial discharge, residual field to be stochastic in nature. The inception and extinction of PD, shape of PD patterns in relation to pulse amplitude and the amount of charge, which is released during PD for different void sizes, are studied and reported in this paper.

Key words—Finite Difference Method, Partial Discharge Simulation and Stochastic Parameters.

I. INTRODUCTION

A VARIETY of solid, gaseous, liquid and combinations of these materials are used as insulation in electric power apparatus and cables. Most of the insulators are not perfect. The imperfections act as weak parts of an insulator and are responsible for Partial Discharge (PD). Charge released during PD causes degradation of insulating material at various defects within the insulator and also at the interface between electrode and insulating material [1]. Partial Discharge is inherently a complex, stochastic process that exhibit significant statistical variation in the form of pulse amplitude, shape and time instant of PD occurrence [2]. PD pattern has been observed to be turtle like or rabbit like for void [3], [4] and wing-like (or triangle-like) patterns for electrical trees [5-6]. It also changes with material aging [7-8].

The turtle-like pattern was found considering the effect of time lag of PD [3] and the rabbit-like

pattern was obtained when probability of occurrence of the first PD after the change of pulse polarity was assumed to be less than that of other pulses [4]. The PD behavior in an artificial single channel was studied by an author [9] to show the growth of tree along the channel, tree along the channel.

In order to compute the field distribution within the specimen and to study PD mechanism, Finite Difference Method (FDM) is used in this work. Phase resolved plots, which directly reflect the statistical properties of PD, have been obtained and reported in this paper. Total charge released per half cycle with the change of void size is also observed in this study. A turtle-like PD pattern with periodicity is obtained in which stochastic variation of the PD magnitude is also reflected.

II. CHARGE RELEASED DURING PD

When a PD occurs in a void, a discharge channel of high conductivity is formed as shown in fig1 and as a result positive ions and electrons move in opposite directions. With the accumulation of charges on the void surfaces, the field intensity between the two discharge areas is reduced and PD ceases when the field intensity reaches the residual field intensity, E_r . In this study, simulations were carried out with probabilistic nature of E_r as well as partial discharge occurrence. The charge of a PD pulse can be expressed as

$$Q = \epsilon_r \epsilon_0 A (E - E_r) = [(\epsilon_r \epsilon_0 A) / d] (E - E_r) d \quad (1)$$

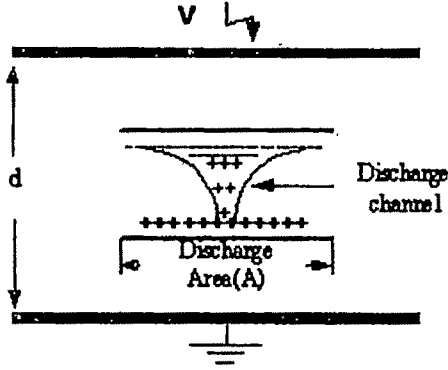


Fig1. Discharge channel due to PD in a void.

where A is the discharge area, d is the void thickness, ϵ_r is the relative permittivity of gas inside the void and $(\epsilon_r \epsilon_0 A)/d$ is the capacitance between the discharge areas. E_0 is the field intensity between the void surfaces at the time of PD occurrence.

III. MODEL USED FOR SIMULATION

In this section the simulation model used for PD has been discussed using Finite Difference Method considering a rectangular parallelepiped void inside a rectangular parallelepiped insulator with Plane-Plane electrode arrangement. The insulator is considered to be placed between a pair of electrodes. Fig2 shows the electrode-insulator-void configuration used in this simulation.

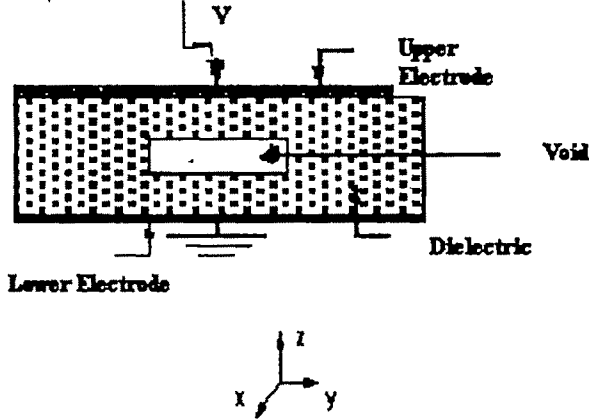


Fig2. Electrode-insulator configurations considered for PD simulation.

The mesh used in the simulation is a three dimensional one of size $(21 \times 21 \times 10)$ units. The electrode separation is taken as 10 units. One unit in the mesh corresponds to 0.20mm. The void dimension is varied from $(1 \times 1 \times 2)$ units to $(36 \times 36 \times 2)$ units in four steps which are termed as size1 to size 4 respectively. The relative permittivity of the insulating material (ϵ_{r1}) is 4, which is of epoxy resin and that of the gas inside the void (ϵ_{r2}) is 1. The peak value of the sinusoidal applied voltage is 12kV at 50 Hz. When the field intensity in the z-direction in the void exceeds the critical field intensity (E_c) for partial discharge occurrence, PD takes place and a narrow discharge channel is formed between the void surfaces. It is assumed that the opposite discharge surfaces are symmetrical and the discharge

extend symmetrically on the two surfaces of the void. As a result the positive and negative charges after PD extinction on the two void surfaces are also distributed symmetrically as in Fig1. After PD extinction, the charges left in the gas within the void move to the void surfaces because it is considered that the charges can reside only on the void surfaces.

IV. FINITE DIFFERENCE MODELLING

At first the total three dimensional zone of interest is discretised suitably into a mesh. In FDM the potential of any node (x,y,z) is expressed in terms of the potentials of the connected nodes. After satisfying Laplace's equation at (x,y,z) for a single-dielectric and equal nodal distances, the potential of the node (x,y,z) can be written as

$$v_{x,y,z} = [v_{x+1,y,z} + v_{x-1,y,z} + v_{x,y+1,z} + v_{x,y-1,z} + v_{x,y,z+1} + v_{x,y,z-1}] / 6 \quad (2)$$

The potential at any point (x,y,z) on the void surface can be expressed, considering two dielectric arrangement and the dielectric interface on the x-y plane, as follows.

$$v_{x,y,z} = [v_{x+1,y,z} + v_{x-1,y,z} + v_{x,y+1,z} + v_{x,y-1,z} + (2\epsilon_{r2}\epsilon_0 v_{x,y,z+1} + 2\epsilon_{r1}\epsilon_0 v_{x,y,z-1}) / (\epsilon_{r1}\epsilon_0 + \epsilon_{r2}\epsilon_0)] / 6 \quad (3)$$

The field distribution is calculated using the difference form of Laplace equation refers to (2) & (3). The boundary conditions for PD simulation are as follows.

- (a) $v = V_m \sin \omega t$
- (b) The field intensity in the discharge channel is E_0 ;
- (c) In presence of any charge accumulation due to PD, the potential at any point (x,y,z) on the void surface can be expressed as follows.

$$v_{x,y,z} = [v_{x+1,y,z} + v_{x-1,y,z} + v_{x,y+1,z} + v_{x,y-1,z} + (h\sigma_{x,y,z} + 2\epsilon_{r2}\epsilon_0 v_{x,y,z+1} + 2\epsilon_{r1}\epsilon_0 v_{x,y,z-1}) / (\epsilon_{r1}\epsilon_0 + \epsilon_{r2}\epsilon_0)] / 6 \quad (4)$$

where $\sigma_{x,y,z}$ is the surface charge density and h is the nodal distance.

- (e) Fringing effect is neglected on the four sides of the specimen on x-z and y-z planes, i.e. electric field intensity is considered to have only z component on those four boundaries.

The PD charge is equal to the difference between the induced charges on the electrode before and after PD. The field distribution can be calculated after PD using equation (4). If the conductivities on the surface and that of the insulating material are neglected, the charge distribution would not change until the next PD. The field intensity changes with the AC voltage, and the next PD occurs when the field intensity across the void again exceeds the discharge inception value (E_i). When E_r and occurrence of PD are considered to be stochastic in nature, the actual PD patterns are simulated using the above calculations repeated for large number of cycles.

V. ASSUMPTIONS TO INTRODUCE STOCHASTIC FEATURES TO PD

In this model, the stochastic behavior of PD is expressed in two different ways as mentioned below:

(a) This stochastic behavior is modeled by assuming the probability for PD occurrence as given below [10].

$$P(E) = f(E) \quad (E > E_c) \\ = 0 \quad (E < E_c) \quad (5)$$

where $P(E)$ is the probability for partial discharge occurrence in the void when the field intensity across the void is E , $f(E)$ is a chosen function and E_c is the critical field for partial discharge occurrence. For the present work $f(E)$ is expressed as follows.

$$f(E) = k_{probe} (E - E_c) \quad (6)$$

The critical field for PD inception is 3kV/mm which the breakdown strength of air at STP. In this work the value of K_{prob} is varied in such a way that PD inception takes place within the electrical field range of 3kV/mm to 5kV/mm. This is to introduce the effect of pressure and volume of air within the void, which is enclosed by insulating material.

(b) During or after PD, the random motion of the carriers may lead to diversity of charge distribution within the discharge area. This effect may be expressed by considering a random range of residual field E_r . It is assumed that the residual field in the segments between the two discharge areas is distributed randomly within a certain range.

$$E_r = E_{r0} \pm BN_r \quad (7)$$

Where N_r is a random number distributed uniformly between 0 and 1 and B is a constant.

VI. RESULTS AND DISCUSSIONS

The time period ($T=20ms$) of the applied sinusoidal voltage is divided into 3600 discrete time intervals such that each time interval is equal to 0.1 degree or 5.55 μs . Results in the form of phase resolved plots have been obtained, which show the effect of probability distribution function $f(E)$ and dimension of the void on PD respectively. Fig3. shows the phase resolved plot for void dimension (1×1×2) units. Due to small surface area of the void the possibility of number of discharge at a particular instant of time decreases. As a result instantaneous charge released and total charge released per half cycle are low compare to that of larger voids, which is reflected from fig4. The time lag between two consecutive discharges decreases with the increase of void size. Therefore the phase resolved plots for larger voids become much dense than that of smaller voids. It is also observed from fig3, fig4 & table1 that angle of inception of PD decreases and angle of extinction of PD increases with increasing dimension of void. This is because, as the dimension of the void increases, electric field within the void in z direction increases and along x-y direction decreases. Therefore critical electric field for PD occurrence is achieved at a comparatively lower voltage phase angle. As the void dimension increases, the possibility of PD occurrence from different parts of the void surface also

increases, as a result PD extinct at a higher voltage phase angle.

The effect of probability distribution function $f(E)$ on PD phenomenon is observed from fig4,5,6 & table2. It is observed from the phase resolved plots that the shapes of PD patterns become more cluster and variation of charge magnitudes become less with decrease in the value of K_{prob} . As the value of K_{prob} increases the stochastic variation of PD occurrence decreases and the stochastic variation of E_r becomes the dominating factor. As a result comparatively large variation in charge magnitudes are observed. Although the shapes of the PD patterns in each of the cases remains almost like a turtle.

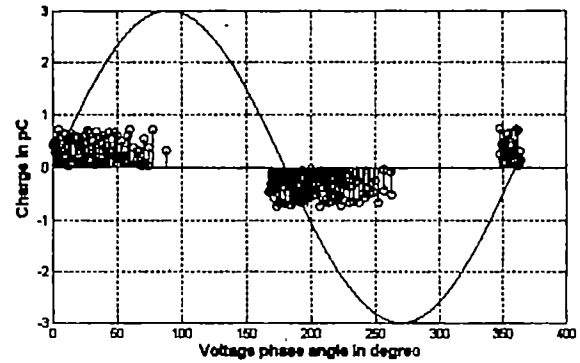


Fig3. Phase resolved plot for void dimension (1×1×2) units and $K_{prob}=5$.

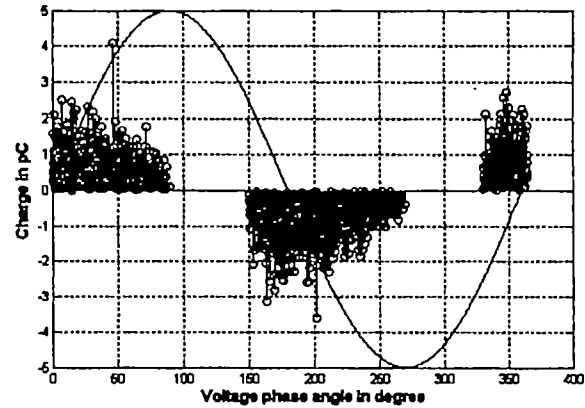


Fig4. Phase resolved plot for void dimension (25×25×2) units and $K_{prob}=5$.

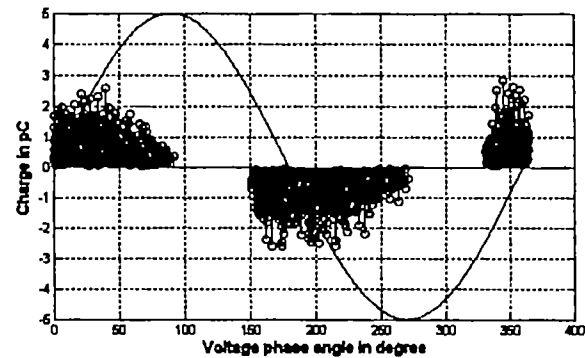


Fig5. Phase resolved plot for void dimension (25×25×2) units and $K_{prob}=0.5$.

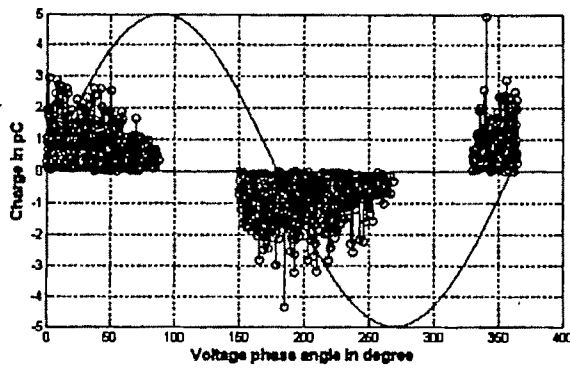


Figure6. Phase resolved plot for void dimension (25x25x2) units and $K_{prob}=50$.

Among three values of K_{prob} , the last value in table2 gives the most appropriate turtle shape which actually resembles with the shapes found by the authors of [3],[8]. Also the variation in the total amount of charge released per half cycle is very less as reflected from table2.

Table1. Variation of Angle of inception and extinction with Void Dimension for $K_{prob}=4.25$

Size of the void	Angle of inception of PD in degree	Angle of extinction of PD in degree
Size 1=(1x1x2)units	167.9	262.7
Size 2=(9x9x2)units	155.5	267.5
Size 3=(25x25x2)units	150.3	268.5
Size 4=(36x36x2)units	147.0	270.0

Table2. Variation of charge released per half cycle for different values of K_{prob} with void dimension (25x25x2) units

Value of K_{prob}	Charge released per half cycle in pC
60	207
5	210
0.6	220

With the increase of the dimension of the void, the surface area of the void increases, as a result PD takes place throughout the total area of the void surface. Therefore number of PD pulses and total charge released per half cycle at a particular instant of time increases, which is shown in fig7.

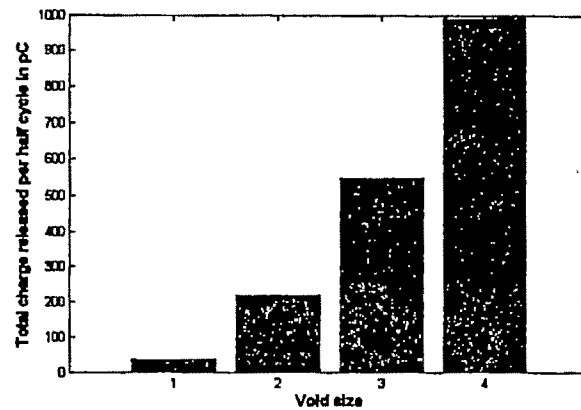


Fig7. Variation of total charge released per half cycle with different size of the void for $K_{prob}=5.0$ (1 to 4 represent void varying from size1 to size4).

VII. CONCLUSION

This simulation model provides information about inception, extinction and shape of PD patterns for different sizes of void when the conductivity of the void surface is low and the effect of charge migration in air is neglected. The time lag between two consecutive discharges is assumed to be determined by the charge distribution on the void surface. The stochastic nature of PD is reflected in simulation results, which tally closely with the experimental results of previous researchers.

REFERENCES

- [1] J. H. Mason "Discharges", *IEEE Trans. on EI*, Vol.13, pp.211-238, 1978.
- [2] R. J. Vanbrant, "Stochastic Properties of Partial Discharge Phenomena", *IEEE Trans. on EI*, Vol. 26, pp.902-948, 1991.
- [3] M. Hikita, K. Yamada, A. Nakamura and T. Mizutani, "Measurement of Partial Discharges by Computer and Analysis of Partial Discharge Distribution by Monte Carlo Method", *IEEE Trans. on EI*, Vol.25, No.3, pp.453-468, 1990..
- [4] F. Gutfleisch and L. Niemeyer, "Measurement and Simulation of PD in Epoxy Voids", *IEEE Trans. Dielectr. & EI*, Vol.2, No.5, pp.729-743, 1995.
- [5] Suwarno, H. Ichikawa, Y. Suzuoki, T. Mizutani and K. Uchida, "A Model for Electrical Treeing Discharge in Polyethylene", *International Symposium on Electrical Insulating Materials, Tokyo, Japan*, pp.443-446, 1995.
- [6] Suwarno, Y. Suzuoki, F. Komori and T. Mizutani, "Partial Discharge due to Electrical Treeing in Polymers: phase- resolved and time-sequence observation and analysis", *J. Phys. D: Appl. Phys.* Vol.29, pp.2922-2931, 1996.
- [7] K. Wu, H. K. Xie, Y. Suzuoki and T. Mizutani, "The Effects of Conductivity Distribution in Tree Channel on the Behavior of PD in Electrical Tree", *ISEI'98*, pp.701-704, 1998.
- [8] T. Ishida, M. Nagao, Y. Mizuno and K. Kosaki, "Swarming Pulsive Microdischarge Characteristics of Internal Void Specimen and Factors Affecting its Occurrence", *Trans. IEE Japan*, Vol.113-A, No.1, pp.43-51, 1993.
- [9] K. Wu, H. K. Xie, Y. Suzuoki and T. Mizutani "A Novel Physical Model for Partial Discharge in Narrow Channels", *IEEE Trans. on Dielectr. & EI*, Vol.6, No.2, pp.181-190, 1999.
- [10] Kai Wu, Tatsuki Okamoto and Yasuo Suzuoki, " A Simulation Model for PD Patterns in Voids with consideration of PD Discharge Areas", *IEEE Conference on EI and Dielectric Phenomena*, pp.649-652, 2000.

Developed Model of Exciter Mechanism in Vibrating Screen and its Influence on the Efficiency of Grading Particle in Iron Ore Production Line

A.Rastgo¹, H.Sohanian², and A.Aram³

¹ Associate Prof. of Mechanical engineering department, University of Teheran, Iran e-mail: arastgo@ut.ac.ir)

² M S student, Mechanical engineering department, University of Teheran Iran e-mail: hh_haghighi@yahoo.com

³ Scholar of Iran institute of mineral research

Abstract— Vibration of screen chamber has direct effect on the performance of screen. Different type of exciter mechanism used for this purpose. The modeling and simulation of the exciter make better prediction of its behavior. In this work, the excitation of the mechanism studied by developed model and the rule of a few parameters such as frequency, amplitude and spring stiffness investigated. The kinematics and dynamics analysis of exciter along with simulation of the screen chamber give several data to achieve better efficiency of screen for grading particle. Accordingly, the quantity and distribution of the feed to the screen can be related to the mechanical parameters of screen for higher efficiency. The result discussed and verified by the experimental analysis of iron ore production line.

Key words — exciter mechanism, vibrating screen, efficiency, and screen capacity.

I. INTRODUCTION

It is always necessary to control the size characteristic of particulate material that is fed to process equipment that separates the mineralogical components. Screens are used for this purpose. The usual industrial screen is vibrating screen. Vibrating screen machines for use in mineral processing industries are commonly used to separate minerals such as ores by size, usually after crushing. Several ingenious methods of movement and vibration of screen surface have been devised and employed in screening devices over the years.

High-frequency vibration is used in some devices, wherein the screen is vibrated on the order of 10,000 Hz and responds through rapid particle separation. Typically, these devices also utilize low-frequency vibration to assist in transporting and dispersing material across the screen unfiltered is collected. Another form of vibratory motion used is low-frequency vibration, typically, produced through counter-rotation of eccentric weights. Finally, some devices employ a method wherein the screen is vibrated at a frequency at or near one of its resonant frequencies, and is tuned closer and closer to that resonant frequency. This method advertises a low input power requirement because of the efficient natural of the resonant vibration, but requires massive components and foundation for resonant damage resistance. Similarly, the above-discussed low and high frequency vibration, devices are constructed of heavy components and foundations since they cannot guarantee that their operating frequency range will not coincide with any of device's resonant frequency modes. These heavy construction setups more power to impart a selected vibration regime than would a lighter construction. Unbalance vibrator with at least one pair of unbalanced masses disposed on the shaft is suitable in cases where the screen capacity may be varied. In order to evaluate the effects of exciter mechanism design and operating variables on the performance characteristics of screening operation, an analysis on parameters has been done. Better understanding of these factors will inevitably lead to more effective design and use of screens and will thereby improve accuracy and efficiency of such size separations. This paper presents a summary of the work and study on these parameters.

II. CHARACTERISATION OF PERFORMANCE

The primary objective for imparting vibrations to screen is to aid segregation of fines through the bed to the screen surface, dislodge accumulations at the apertures and to keep the screen active at all time. However, the shape of particles, moisture content and number of times a particle is able to approach the screening surfaces complicate the process [1]. The probability (p) of a particle passing through a screen has been shown by Gaudin [2] to be:

$$p = \left[\frac{L_A - d_p}{L_A + d_w} \right]^2 \quad (1)$$

Where d_p = the particle size of which 50% passed through a screen, d_w = diameter of wire and L_A = bar aperture.

This probability is affected by the amplitude, frequency and direction of vibration. These parameters depend on exciter mechanism used to move the screen. Miwa [3] has estimated the number of presentation (N_L) of particles on to the screen surface by considering the effective aperture (L_{AE}), the diameter of the wire (d_w) of screen, the length of screen (L) and taking a particle size, d_{50} at which 50% of the material of this size passes or is retain on the screen. The expression is given by:

$$N_L = \frac{1}{L} \left[\frac{0.833(L_{AE} + d_w)}{(L_{AE} - d_{50})} \right]^2 \quad (2)$$

The value of N_L includes vibration (amplitude and frequency) and other variables related to screening. Another equation is given by Gupta [1]:

$$m_r = \frac{M}{M_i} = (1 - p)^{N_L} \quad (3)$$

Where M_i = the initial mass of undersize in the feed stream. M = the mass of undersize remaining on the screen after N attempts.

The ratio (m_r) is directly depending to the efficiency of screen. Because of effect of amplitude and frequency on P and N_L , it is necessary to study on parameters that determine the relation between amplitude and, frequency.

III. SCREEN PERFORMANCE CRITERIA

Two criteria are used to assess screen performance, capacity and efficiency. Capacity is simply the quantity of material fed to the screen per unit time per unit area of screen surface. In reality capacity should be quoted along with efficiency. The basic purpose of screening is to separate particles larger or smaller than the other aperture of a screen. Efficiency is defined based on mass fraction of undersize in the oversize and mass fraction of oversize in the undersize. Capacity and efficiency are generally conflicting quantities. Any screen can have its capacity increased; but this is likely to be achieved at the expense of efficiency.

IV. DESCRIPTION OF EXCITER MECHANISM

The exciter has a cast housing and mounting base secured to mounts bolted to the side plate of screen. Pair of shafts is mounted for rotation in. The outer end of the shaft is provided with eccentric masses aligned on their respective shafts 180° out of phase Units. Fig.1 shows the exciter unit with unbalance weights.

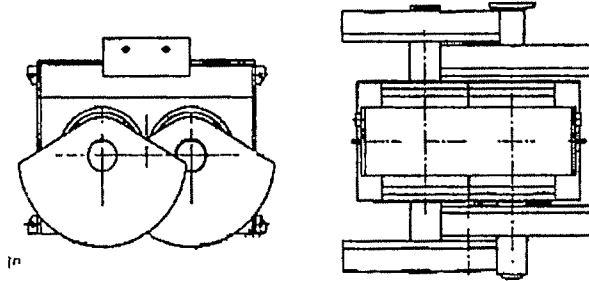


Fig.1

In vibratory power unit of this type position of moveable mass or weight member is changeable by rotating it relative to fixed mass. In these power units a regulation of the centrifugal forces, and thus due to changes in vibration amplitude, a regulation of the screening capacity between a maximum and minimum value can be obtained. Such regulation can however, not be affected during operation but can be affected only when the unit is at rest. If the two masses of each pair of are of equal size, the screening capacity can be adjusted equally with respect to the motor shaft, and zero, when the masses are oppositely directed and the generated centrifugal forces cancel each other.

The vibrating devices are mounted either at the feed end, center of screen frame or near the discharge end. The vibrations are controlled by large steel springs attached to the bottom of the frames. It has been determined that the direction of excitation should pass through the center of gravity of machine in use. However, as the screen wears or panels are changed or the machine is loaded with a mass of material and progressively shifts this mass, the center of gravity moves relatively to the direction of vibration. Fig.2 shows direction of vibration is normal to plane which the exciter is installed.

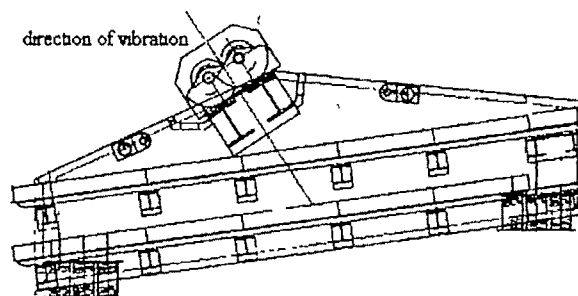


Fig.2

V. DYNAMIC ANALYSIS OF EXCITER

The exciter is explained with the following analysis. Assuming the forcing function to be sinusoidal, the acceleration of the screen motion may be expressed by (4):

$$a_i = -\frac{A_i}{2} \omega^2 \sin(\omega t) \quad (4)$$

Where a_i = screen acceleration

A_i = Screen stroke

$$\begin{aligned} \omega &= 2\pi f \text{ angular frequency} \\ &= \frac{N \cdot 2\pi}{60} \end{aligned}$$

Where N = the operating speed of the screen (rpm) and where a_i is at a maximum value when $\sin(\omega t) = 1$ and the force required to produce a desired maximum stroke A_i is given by the second Newton law:

$$\begin{aligned} F_i &= M_i \frac{A_i}{2} \omega^2 = \frac{W_i}{g} \frac{A_i}{2} \left(\frac{N \cdot 2\pi}{60} \right)^2 \\ &\xrightarrow{g=9.81 \frac{N}{m^2}} F_i = \frac{W_i A_i N^2}{1790.9} \end{aligned} \quad (5)$$

Where F_i = required force

M_i = mass of the screen

This force F_i is applied to the screen through the spring system and exciter mechanism. The forces generated by the rotating eccentric weights in fig.1, of the linear exciter may be computed as shown in (6):

$$F_w = \frac{W_w}{g} r \left(\frac{N \cdot 2\pi}{60} \right)^2 \quad (6)$$

Where F_w = force generated by eccentric weight.

W_w = total weight of eccentric weights.

r = distance from center of rotation to the center of gravity of the eccentric weight. Spring system force may be compute as shown in (7):

$$F_s = \frac{A_i}{2} C_e \quad (7)$$

Where C_e = spring system rate. Using equilibrium equation we have (8):

$$\begin{aligned} F_i &= F_s + F_w \Rightarrow -\frac{W_i A_i N^2}{1790.9} = -\frac{W_w r N^2}{895.44} - \frac{A_i}{2} C_e \\ A_i &= \frac{\frac{W_w r N^2}{895.44}}{\left(\frac{C_e}{2} - \frac{W_i N^2}{1790.9} \right)} \end{aligned} \quad (8)$$

Equation (8) shows the effect of parameters on amplitude of vibration. The exciter's parameters such W_w and r have most effect on screen stroke. It also shows that at frequencies higher than natural frequency of screen increase in frequency lead to decrease of amplitude of vibration. Using vibrating screen with exciter mechanism include unbalance weights we could change the amplitude of vibrating by changing the parameter (r). It should be noted that increasing the amplitude of vibration initially increases the percentage passing through a screen. After reaching a peak, a further increase of vibration decreases the amount passing through. It has also been determined that in constant amplitude or in frequency much higher than natural frequency change in frequency has little effect on the amount passing through the screen as shown in fig.3.

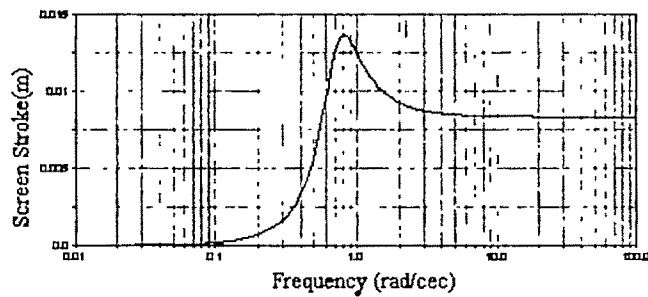


Fig.3

We are using ADAMS to simulate vibration screen motion. To study the effect of screen mass on the amplitude of vibration we change screen mass and measure position of center of gravity (cm). Fig.4 shows the effect of varing screen mass that may happen because of changing in screen capacity; on the amplitude of vibration .

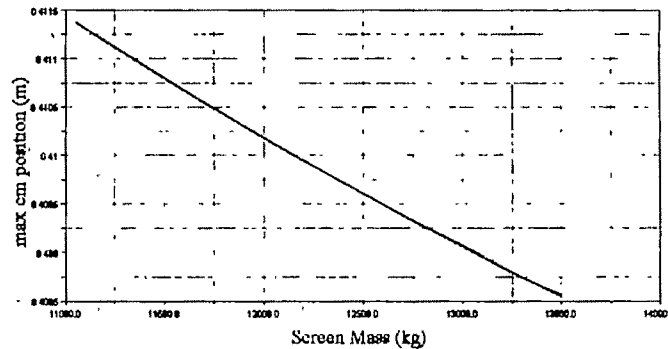


Fig.4

We can also see from (8) increase in screen mass lead to deacres in amplitude of vibration.

VI. EXPERIMENTAL STUDY

Maintaining of the target particle size distribution from a grinding circuit is a question of vital importance. Screen analyses show that there is a large variation in the particle size

distribution of the ore fed to the autogenously grinding circuits. The most important factor for this variation is difficult to point out, since the link between the mining face and the concentrator is very complex. Although, the blasted ore may have a relatively constant size distribution, the flow in draw points at the mining face is changing during loading. Thus, the size distribution of the loaded ore will vary. Since variations in feed ore rate influences the ground product; comparisons of the resulting particle size distributions of the product streams for the different capacity were carried out. For each capacity we should regulate vibrator to obtain better performance and efficiency. As can be seen in fig .5 for finest fraction ($< 3\text{mm}$) we have excellent efficiency.

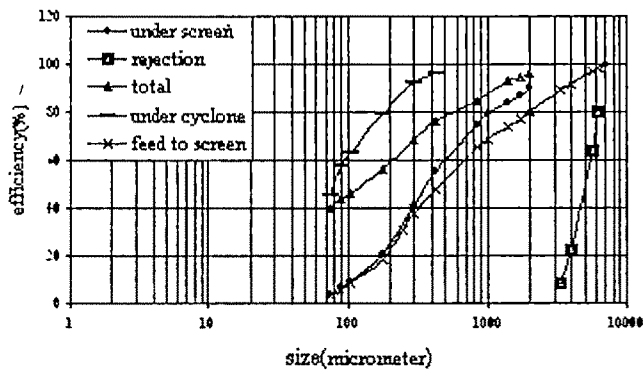


Fig.5

In industrial screening efficiencies of 100% is not achievable. Hence 90-95% efficiency is considered as the maximum for normal wire screens. During scale ping operations Colman [4] suggested that the efficiency should be taken as 80-85%.

VII. CONCLUSION

Screen exciter has direct effect on screen efficiency. Parameters such as frequency and amplitude of vibration are depending to exciter parameters such as weight of eccentric masses and distance from center of rotation to center of gravity of masses. Also we study on effect of increasing in screen mass on the amplitude of vibration. Equation (8) derives from dynamic analysis of exciter and relates parameters to each other. Experimental study show that by regulating vibrator unit we can reach to high efficiency.

ACNOWLEDGMENT

The studies of vibrating screen were performed under contract with Iran institute of mineral research.

REFERENCES

- [1] A.Gupta, Mineral Processing Design and Operations Elsevier, 2006.
- [2] A.M.Gaudian, Principles of Mineral Dressing, McGraw-Hill, 1939
- [3] S.Miwa, Chemical Engineering, Japan, 24(1960) 150.
- [4] K.G.Colman, Mineral Processing Handbook, N.L.Weiss(ed), SME/AIME, 1985 pp 3E 13-19.
- [5] A Eitmayer, Vibrational Dewatering Improvement by Superposed Capillary Suction, AA.Balkema, 2000.

Modulus of Highest Eigenvalue of a Polynomial

J.R.P. Gupta¹, Yogesh V. Hote¹, D.Roy Choudhury²

¹ Netaji Subhas Institute of Technology, Dwarka, New Delhi, INDIA,
e-mail: jrpg83@yahoo.com, y_hotel@yahoo.co.in

² Delhi Institute of Technology, Bawana Road, New Delhi, INDIA,
e-mail: d_roych@hotmail.com

Abstract—In this paper, a computationally efficient technique is proposed for determining the modulus of highest eigenvalue of a linear polynomial using Newton Raphson method and an algorithm for power of companion matrix.

Keywords—Eigenvalue, Polynomial, Newton Raphson method, Gerschgorin theorem.

I. INTRODUCTION

THE problem of finding regions that contain some or all eigenvalues of matrices or zeros of polynomial has a long history. Cauchy gave an easily calculated circular bound for complex coefficient polynomial zeros [1]. A bound for zero of the polynomial is also presented by Fujiwara [2]. A new improved bound based on Cauchy are given in [3-5]. For matrix eigenvalues, Gerschgorin Theorem is very powerful tool for improving existing bound. It can be used to find disks whose union contains all the eigenvalues of a complex matrix [6,7]. In [8], an algorithm for determination of power of companion matrix is developed. It is useful in determining the state transition matrix.

In this paper, we have determined improved bound of a polynomial by applying Gerschgorin theorem to various powers of companion matrices. We have observed that the higher the powers of companion matrix, more improvement in the bound. Further, this improved bound is used as initial approximation in Newton Raphson method for determining the modulus of highest eigenvalue. The proposed method is computationally efficient since very less iterations are needed in determining the power of companion matrix and hence in determining modulus of highest eigenvalue of a polynomial. It is useful in various control system applications [9-10].

II. BOUND FOR THE ZERO OF A REAL POLYNOMIAL USING DIFFERENT TECHNIQUES

A. Cauchy Bound [1]

Let $P(z)$ is a real polynomial. It is given below as

$$P(z) = z^n + \sum_{k=1}^n a_k z^{n-k} \quad a_k \in \mathbb{R} \quad (1)$$

be a real polynomial. The result due to Cauchy states that all the zeros of $P(z)$ lie in the circle

$$|z| < 1 + A \quad (2)$$

where,

$$A = \max_k \{|a_k|\}, k = 1, 2, \dots, n. \quad (3)$$

B. Fujiwara Bound [2]

The zeros of $P(z)$ satisfy $|z| \leq A$ if

$$A = 2 \max_{1 \leq k \leq n} \{|a_k|\}^{1/k} \quad (4)$$

C. Datta and Govil Bound [4]

Datt and Govil obtained an annulus containing all zeros of $P(z)$ and proved that $|z| \leq r$ for $A \geq 1/n$ with

$$R = 1 + A[1 - (1 + A)^{-n}] \quad (5)$$

where,

$$A = \max_k \{|a_k|\}, k = 1, 2, \dots, n. \quad (6)$$

D. Boese and Luther Bound [5]

All zeros of $P(z)$ lie in the disk $|z| \leq r$,

$$R = \min\{(1 + A)(1 - A)/[(1 + A)^{n+1} - nA], 1 + 2(nA - 1)/(n + 1)\} \\ A \geq 1/n \quad (7)$$

where,

$$A = \max_k \{|a_k|\}, k = 1, 2, \dots, n \quad (8)$$

III. GERSCHGORIN THEOREM [6]

The Gerschgorin theorem finds a region in the complex plane that contains all the eigenvalues of a square matrix. Let $A = [a_{ij}] \in \mathbb{C}^{n \times n}$. Assume that

$$R_i = \sum_{k=1, k \neq i}^n |a_{ik}|, i=1, \dots, n \quad (9)$$

and

$$C_i = \sum_{k=1, k \neq i}^n |a_{ki}|, i=1, \dots, n \quad (10)$$

then each eigenvalue of A is in at least one of the disks (row wise circles),

$$\{z \in \mathbb{C} : |z - a_{ii}| \leq R_i\} \quad (11)$$

So, each eigenvalue of matrix A must lie in the union of 'S' of these n circles in the s-plane.

Similarly, each eigenvalue of A is in at least one of the disks (column wise circles).

IV. POWER OF COMPANION MATRIX

An algorithm for power of companion matrix has been developed in [8]. It is based on partitioning of the matrices. Suppose, we know $[C]^r$, then, the next higher power of $[C]$, i.e., $[C]^{r+1}$, can be known by computing only a single row, which involves 'n' multiplications together with '(n-1)' additions.

It has been applied for determining the state transition matrix and also in determining the dominant eigenvalue of the system having distinct eigenvalues.

V. BOUND USING POWER OF COMPANION MATRIX AND GERSCHGORIN DISK

Now we will determine bound of a polynomial using Gerschgorin Theorem and algorithm for power of companion matrix. Let

$$P(z) = z^n + \sum_{i=1}^{n-1} c_i z^i; c_i \in \mathbb{C} \quad (12)$$

be a monic polynomial of degree n with real coefficients. Let

$$[C] = \begin{pmatrix} 0 & 1 & 0 & 0 & \dots & 0 & 0 \\ 0 & 0 & 1 & 0 & \dots & 0 & 0 \\ \vdots & \vdots & \vdots & \vdots & \dots & \vdots & \vdots \\ 0 & 0 & 0 & 0 & \dots & 0 & \vdots \\ 0 & 0 & 0 & 0 & \dots & 0 & 1 \\ -c_0 & -c_1 & -c_2 & 0 & \dots & -c_{n-2} & -c_{n-1} \end{pmatrix}$$

be a companion matrix for $P(z)$. It can be shown that the eigenvalues of A are the zeros of $P(z)$.

Applying recursive algorithm for power of companion matrix, the powers of $[C]$ can be developed. For simplicity, consider the matrix $[C]^2$. It is given as

$$[C]^2 = \begin{pmatrix} 0 & 0 & 1 & 0 & \dots & 0 & 0 \\ 0 & 0 & 0 & 1 & \dots & 0 & 0 \\ \vdots & \vdots & \vdots & \vdots & \dots & 0 & 0 \\ 0 & 0 & 0 & 0 & \dots & 0 & 1 \\ -c_0 & -c_1 & -c_2 & \dots & \dots & \dots & -c_{n-1} \\ c_0 c_{n-1} & c_1 c_{n-1} & -c_0 c_{n-2} & c_2 c_{n-1} & -c_1 & \dots & c_{n-1}^2 - c_{n-2} \end{pmatrix}$$

After applying Gerschgorin theorem to $[C]^2$, the zeros of $P(z)$ are contained in the three disks:

$$|z^2| \leq 1, \quad (13)$$

$$|z^2 + C_{n-2}| \leq \sum_{i=0}^{n-1} |C_i|, \quad (14)$$

$$|z^2 + C_{n-2} - C_{n-1}^2| \leq \sum_{i=0}^{n-2} |C_{n-1} C_i - C_{i-1}|; C_{-1} = 0 \quad (15)$$

Using the triangle inequality, we can consider larger regions so that:

$$|z^2| \leq 1, \quad (16)$$

$$|z^2| \leq \sum_{i=0}^{n-1} |C_i|, \quad (17)$$

$$|z^2| \leq \sum_{i=0}^{n-1} |C_{n-1} C_i - C_{i-1}|; C_{-1} = 0 \quad (18)$$

Consequently, all eigenvalues are contained in the disk of radius R, where

$$R = \max \left\{ 1, \sqrt{\sum_{i=0}^{n-1} |C_i|}, \sqrt{\sum_{i=0}^{n-1} |C_{n-1} C_i - C_{i-1}|} \right\} \quad (19)$$

This idea can be generalized as follows. Let $r \geq 2$ be a positive integer and assume that $D_r = C^r = [d_{ij}^{(r)}]$. Then, all zeros of P are contained in a disk of radius R, where,

$$R = \max \left\{ r, \sqrt[r]{\sum_{k=1}^n |d_{kk}^{(r)}|} \right\} \quad (20)$$

Analogous result holds if columns of D_r are used, i.e.,

$$R1 = \max \left\{ \sqrt[n]{\sum_{k=1}^n |d_k^{(r)}|} \right\} \quad (21)$$

VI. NEWTON RAPHSON METHOD

One of the most widely used methods of solving equations is Newton method. This method is based on a linear approximation of the function, but does so using a tangent to the curve. It is explained in various books [11]. Now the real problem is to consider starting initial estimate, which is not too far from a root. We can consider initial guess, which is determined from companion matrix of a polynomial and Gerschgorin theorem. It is useful in determination of modulus of highest zero of a polynomial. We find that less number of iterations is required in comparison with the conventional guess method, particularly in determination of highest eigenvalue. The algorithm and numerical example for Newton Raphson method are as given below.

A. Algorithm

Step1: Determine improved Gerschgorin bound for scaled companion matrix of a polynomial, i.e. z_0

Step2: Compute $p(z_0)$, $p'(z_0)$

If $(P(z_0) \neq 0)$ and $(P'(z_0) \neq 0)$

Repeat

Set $z_1 = z_0$

Set $z_0 = z_0 - P(z_0)/P'(z_0)$

Until $(|z_0 - z_1| < \text{tolerance value})$.

B. Example

Consider polynomial

$$s^3 + 7s^2 + 4s + 3 = 0 \quad (22)$$

$$[C] = \begin{bmatrix} 0 & 1 & 0 \\ 0 & 0 & 1 \\ -3 & -4 & -7 \end{bmatrix}$$

The bound using Gerschgorin Theorem for the above matrix C is a disk of radius of 8. Now we determine the improved Gerschgorin bound using an algorithm for power of companion matrix. So, we get $[C^2]$ and $[C^3]$, which are given below.

$$[C^2] = \begin{bmatrix} 0 & 0 & 1 \\ -3 & -4 & -7 \\ 21 & 25 & 45 \end{bmatrix}$$

$$[C^3] = \begin{bmatrix} -3 & -4 & -7 \\ 21 & 25 & 45 \\ -135 & -159 & -290 \end{bmatrix}$$

All the zeros are contained in the disk of radius R, where $R=7.2801$ when $[C^2]$ and $R=6.9932$ when $[C^3]$. As higher the power of C, radius will be nearer to the modulus of highest eigenvalue. We have determined modulus of highest eigenvalue considering initial guess as $x_0=0, -14$ and -6.9932 . The results are shown in Tab.1, Tab.2, and Tab.3 respectively. Initial approximation is considered as non-positive since all coefficients of the characteristics polynomial are positive. The largest eigenvalue in terms of magnitude is -6.4521 .

Iterations	x0	xnew	error
1	0	-0.7500	0.7500
2	-0.7500	-0.0195	0.7305
3	-0.0195	-0.8039	0.7844
4	-0.8039	-0.0912	0.7127
5	-0.0912	-1.0711	0.9799
6	-1.0711	-0.3406	0.7304
...
...
35	-6.4522	-6.4521	0.0001

Tab.1 Newton Raphson using Conventional approximation

Iterations	x0	xnew	error
1	-8.0000	-6.8929	1.1071
2	-6.8929	-6.5035	0.3894
3	-6.5035	-6.4529	0.0506
4	-6.4529	-6.4521	0.0008

Tab.2 Newton Raphson using improved Gerschgorin bound

Iterations	x0	xnew	error
1	-6.9932	-6.5266	0.4646
2	-6.5266	-6.4538	0.0728
3	-6.4538	-6.4521	0.0017

Tab. 3 Newton Raphson using Gerschgorin bound and from power of companion matrix.

From the above results, we have found that Gerschgorin bound using powers of companion matrix are required less iteration in comparison with conventional approximation method and Gerschgorin bound. The above iterations can also reduced for higher values of power of companion matrix.

REFERENCES

- [1] A.L. Cauchy, 'Exercices de Mathematique in Oeuvres,' (2), vol.9, 1829.
- [2] Fujiwara, M., 'Uber die obere Schranke des absoluten Betrages der Wurzeln einer algebraischen' Tohoku Math.J, 1916, 1(10), pp 167-171.
- [3] Joyal, A., et al.: 'on the locations of zero of polynomials', Canadian Math. Bulletin, 1967, (10), pp 53-63.
- [4] Datta, B., and Govil, N.K., 'On the location of the zeros of polynomial', J.Approx Theory, 1978, 24, pp.78-82.
- [5] Boese, F.G., and Luther, W.J.: 'A note on a classical bound for the moduli of all zeros of polynomial', IEEE Trans. Automatic Control, 1989, (34), pp 998-1001.
- [6] Erwin Kreyszig, "Advanced Engineering Mathematics," John Wiley and Sons,(ASIA), Ltd, (1999), 920-921.
- [7] Yogesh V Hote,D Roy Choudhury,J R.P Gupta, " Gerschgorin theorem and its applications in control systems problem," IEEE transaction on Industrial Electronics,2006,pp 2438-2433.
- [8] D Roy Choudhury, "Algorithm for power of Companion matrix and its applications,"IEEE transaction on automatic control,vol 18, no 2, 1973,pp 179-180.
- [9] A.Besharati Rad,Wai Lun, and K.M Tsang, "Self tuning PID controller using Netwon Raphson method,"IEEE conference on Industrial Electronics,1997,44(5),pp 717-725,2006.
- [10] Mark E. Schlarmann and Randall L Geiger, "Use of the Newton-Raphson Iteration to eliminate low frequency dipoles,"IEEE Transaction on circuit and systems, 2002,pp.535-538.
- [11] Gerald Wheatley, 'Applied Numerical Analysis, Pearson education, 2005

Heat and Mass Transfer with Interaction Effects Analysis between an External flow and a Capillary Porous Body

S. Larbi, M. Malki, and H. Belhaneche

Mechanical Engineering and Development Laboratory, Department of Mechanical Engineering
National Polytechnic School of Algiers, 10, avenue Hassen Badi, El-Harrach, Alger, ALGERIE
Fax : 213 21 52 29 73, E-mail : larbisalah@yahoo.fr

Abstract— The work presented in this paper consists in the analysis of interaction effects between an external laminar air flow and a porous medium where we are interested in these effects of interaction between the two mediums by means of intersection of two computer software; one characterizes the external flow and the other the porous structure. The results presented are related to the space-time evolution of convective heat and mass transfer coefficients, and the surface temperature. Obtained results are in good agreement with those of the literature.

Key words- porous media, external flow, heat and mass coefficients, surface temperature.

I. INTRODUCTION

In a great number of problems, as well in natural situations as in practical applications, interaction effects between fluid and structure can be encountered. Processes of drying and filtration, heat insulation, and the many problems of exchanges between the soil and the atmosphere are typical examples of these applications [1, 2, 3]

In these cases, it is possible to model the transport phenomena within the structure and its environment using the classical equations of the mechanics of the continuous mediums. The natural step consists in coupling the equations of transport in these mediums by expressing the continuity of the variables of state and the normal flux to the interface between the two mediums.

The mathematical modelling of these phenomena is in general very complicated. So, in order to simplify the study

we were interested to the interaction effects between an external laminar flow of air and a porous structure with well known thermo physical properties [6].

The present work consists in analysing the interaction effects between this external laminar flow and a porous structure. We were interested in the study of these effects of interaction between the two mediums by means of intersection of two computer software; one characterizes the external flow and the other the porous structure.

The results presented are related to the space-time evolution of the interfacial flow parameters for various Reynolds numbers and for different suction velocities, specially, the determination of the space-time evolution of convective heat and mass transfer coefficients, and the surface temperature.

II. MATHEMATICAL MODELING

Physical Model

The physical model studied is represented by the figure 1. We have considered the problem of exchange between an external flow of air and a porous medium initially at a temperature T_0 . The porous medium is placed in an enclosure, where, the conditions with the wall are adiabatic ($x = 0$ and $x = L_x$), the higher part ($y = 0$) is in contact with an external flow of air and the lower part ($y = L_y$) is isothermal. The temperature far from the plate is equal to T_∞ . In some cases of heat transfer problems in porous media, convective effects can be neglected in comparison with the conductive effects [1]. By taking into account the fact that the phase change heat transfer is negligible compared to that by conduction [6], then, the resulting equations are given as below.

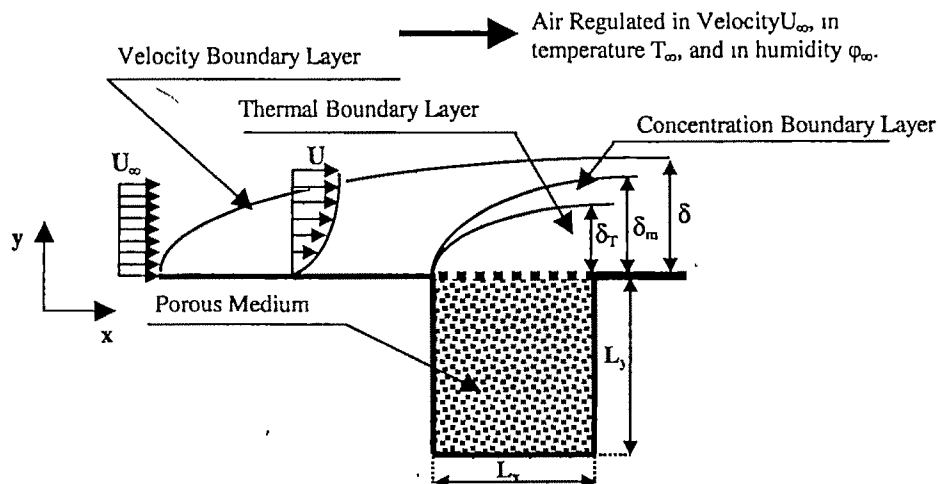


Fig. 1. Studied physical model.

Mathematical Model

Energy and mass balance equations in the porous medium are given by:

$$\begin{aligned} (\rho C_p)_{MP} \frac{\partial T_{MP}}{\partial t} &= \nabla \cdot (\lambda_{MP} \nabla T_{MP}) \\ \frac{\partial \omega}{\partial t} &= \nabla \cdot (D_\omega \nabla \omega + D_T \nabla T_{MP}) \end{aligned} \quad (1)$$

With: T_{MP} : the temperature of the porous medium; λ_{MP} : the thermal conductivity; ρ : the density; C_p : the heat-storage capacity at constant pressure; ω : the moisture content; D_ω and D_T : the mass coefficients of diffusion of the porous medium.

In a laminar flow case, equations characterizing mass, energy, and momentum transfer for the external flow are those of velocity, concentration, and thermal boundary layers. In a dimensionless form, they are written in the form

$$\begin{aligned} \frac{\partial u^*}{\partial x^*} + \frac{\partial v^*}{\partial y^*} &= 0 \\ \frac{\partial u^*}{\partial t^*} + u^* \frac{\partial u^*}{\partial x^*} + v^* \frac{\partial u^*}{\partial y^*} &= \frac{1}{Re} \frac{\partial^2 u^*}{\partial y^{*2}} \\ \frac{\partial v^*}{\partial t^*} + u^* \frac{\partial v^*}{\partial x^*} + v^* \frac{\partial v^*}{\partial y^*} &= \frac{1}{Re} \frac{\partial^2 v^*}{\partial y^{*2}} \\ \left(\frac{\partial \theta^*}{\partial t^*} + u^* \frac{\partial \theta^*}{\partial x^*} + v^* \frac{\partial \theta^*}{\partial y^*} \right) &= \frac{1}{Re \cdot Pr} \left(\frac{\partial^2 \theta^*}{\partial y^{*2}} \right) \\ \left(\frac{\partial C^*}{\partial t^*} + u^* \frac{\partial C^*}{\partial x^*} + v^* \frac{\partial C^*}{\partial y^*} \right) &= \frac{1}{Re \cdot Sc} \left(\frac{\partial^2 C^*}{\partial y^{*2}} \right) \end{aligned} \quad (2)$$

With: $t^* = \frac{t}{t_l}$; $t_l = \frac{L}{U_\infty}$ and

$$x^* = \frac{x}{L}, y^* = \frac{y}{L}, u^* = \frac{u}{U_\infty}, v^* = \frac{v}{U_\infty}, p^* = \frac{P}{\rho U_\infty^2}, \theta^* = \frac{T - T_\infty}{T_w - T_\infty}, C^* = \frac{C - C_\infty}{C_s - C_\infty}$$

Where: u and v : are the components of the vector velocity according to x and y ; T : the temperature; T_w : the wall temperature; P : the pressure; L : the length of the plate; t : the time; Re : the Reynolds number; Pr : the Prandtl number; Sc : the Schmidt

Initial and boundary conditions corresponding to the boundary layers are given by

$$\begin{aligned} \text{For: } t^* \leq 0; u^*(x, y) = 0, \theta^*(x, y) = 0 \text{ and } C^*(x, y) = 1 \\ \text{At: } y^* = 0; u^*(x, t) = 0, v^*(x, t) = V_0^*, \theta^*(x, t) = 1 \text{ and } C^*(x, y) = 1 \\ \text{When: } y^* \rightarrow 1; u^*(x, t) = 1; \theta^*(x, t) = 0 \text{ and } C^*(x, y) = 0 \end{aligned} \quad (3)$$

For the porous medium, boundary conditions are:

$$\begin{aligned} \text{For: } \left\{ \begin{aligned} x = 0; q_{MP} &= -\lambda_{MP} \frac{\partial T_{MP}}{\partial x} \Big|_{x=0} = 0; J_m = 0 \\ x = L_x; q_{MP} &= -\lambda_{MP} \frac{\partial T_{MP}}{\partial x} \Big|_{x=L_x} = 0; J_m = 0 \end{aligned} \right. \end{aligned} \quad (4)$$

$$\begin{aligned} \text{At: } \left\{ \begin{aligned} y = L_y; T_{MP}(x, L_y, t) &= T_l; J_m = 0, \text{ with: } T_l = \text{cst;} \\ y = 0; q_{MP} &= h_c(T_p - T_\infty) = -\lambda_{MP} \frac{\partial T_{MP}}{\partial y} \Big|_{y=0}; J_m = h_m(C_s - C_\infty) \end{aligned} \right. \end{aligned} \quad (5)$$

The initial condition is

$$\text{For: } t \leq 0; T_{MP}(x, y, 0) = T_0; \omega(x, y) = \omega_0 \quad (6)$$

Interfacial conditions between the external flow and the porous medium, are given by the below conditions [9]:

For: $0 \leq x \leq L_x$,

$$T_{ex}(x, 0, t) = T_{MP}(x, 0, t) \text{ and } q_{ex} = q_{MP} \quad (7)$$

$$\text{With: } \begin{cases} q_{ex} = h_c(T_p - T_\infty); J_m = (D_\omega \nabla \omega + D_T \nabla T_{MP}) \\ q_{MP} = -\lambda_{MP} \frac{\partial T_{MP}}{\partial y} \Big|_{y=0} \end{cases} \quad (8)$$

Where: h_c : the convective heat transfer coefficient; h_m : the mass transfer coefficient; q_{ex} : the external heat flow; J_m : the mass flow.

III. NUMERICAL SIMULATION

To calculate at any time and at each position the convective heat transfer coefficient " h_c ", we initialize the value of " h_c " by using an empirical relation related to the coefficient of convective heat exchange on a plane plate [3], given by:

$$Nu = 0.453 \cdot Re^{\frac{1}{4}} \cdot Pr^{\frac{1}{4}} = \frac{h_{emp} \cdot L}{\lambda} \quad (9)$$

The solution of the problem requires the resolution of the dynamic and thermal boundary layer equations as well as the equation of heat transfer in the porous environment. These equations are solved numerically by using an ADI method [4, 5].

IV. RESULTS AND DISCUSSIONS

The results presented are related to the space-time evolution of the convective heat transfer coefficient and of the surface temperature at times varying between 1 hour and 3 days. The properties of the air and of the porous medium are given by:

- For the air (external flow): $\lambda_{ex} = 2.65 \times 10^{-2}$ W/m K; Re , lies between 3000 and 10^4 ;

$Pr = 0.70734$. $T_0 = 30^\circ\text{C}$; $T_\infty = 30^\circ\text{C}$. $T_l = 10^\circ\text{C}$; $\omega_0 = 0.02\%$.

- For the porous medium: $\lambda_{MP} = 0.5$ W/m K;

$$\alpha = \lambda_{MP} / \rho C_p = 25 \times 10^{-8} \text{ m}^2/\text{s}.$$

The dimensionless suction velocity value, V^* , is chosen in order to satisfy the condition [2]: $V^* < \frac{1}{\sqrt{Re}}$.

We have taken two values of V^* equal to 0 and 10^{-4} for a Reynolds number equal to 3000 and V^* equal to 0 and $-3 \cdot 10^{-4}$ for a Reynolds number equal to 10^4 .

Convective heat transfer coefficients, empirical and averaged, are

$$\text{given by: } h_{emp} = \frac{0.453 \lambda_{ex} Re^{\frac{1}{4}} Pr^{\frac{1}{4}}}{L} \text{ and } h_{moy} = \frac{1}{L_y} \int_0^{L_y} h(x) dx = \frac{\sum_{m=1}^M h(m)}{m}$$

The determination of mass transfer coefficients, empirical and averaged is achieved by using the analogy between heat and mass transfer.

The figures (2 and 3) show the evolution of convective heat transfer coefficient in space and in time for Reynolds numbers, Re , equal respectively to 3000 and 10 000 and for a suction velocity equal to 0.

The figures (4 and 5) give the evolution of convective heat transfer coefficient in space and in time for Reynolds numbers, Re , equal respectively to 3000 and 10 000 and for a suction velocity equal to -10^{-4} . The figures (6 and 7) show the evolution of convective mass transfer coefficient in space and in time for Reynolds numbers, Re , equal respectively to 3000 and 10 000 and for suction velocities equal respectively to -10^{-3} and to -10^{-4} . The figures (8, and 9) show the evolution of convective mass transfer coefficient in space and in time for a Reynolds number equal to 3000, and for suction velocity, respectively equal to -10^{-3} and -10^{-4} .

For all figures, we can note an hyperbolic pace of the convective heat and mass transfer coefficients curves (h_c and h_m decrease when "x" increases). As we can underline, the influence of the effect of the leading edge (great value of the coefficient of exchange on the level of the leading edge), which has a consequence on a high value of heat flow in this zone. It is also noticed, that " h_{moy} " and " h_{emp} " are quantitatively different.

From the temporary point of view, we cannot note a significant evolution of the heat transfer coefficient during the process, while, we can note this influence on the mass transfer coefficient h_m . The importance of the Reynolds number on the convective heat transfer coefficient is quite obvious, which has a consequence on the increase of the temperature of the porous medium. The increase of the suction velocities does not have a notable effect on the coefficient of heat transfer.

The figures (10 and 11) show respectively the evolution of the surface temperatures for Reynolds numbers equal respectively to 3000 and 10 000 and for a suction velocity equal to 0. The figures (12 and 13), respectively, give the evolution of the surface temperatures Reynolds numbers equal to 3000 and 10 000 and for a suction velocity equal to -10^{-4} . The Figure 14, show the evolution of the surface temperature obtained by M. Prat [1] at four times, for a velocity and a temperature far from the wall respectively equal to : $U_{\infty} = 1\text{m/s}$ and $T_{\infty} = 20^{\circ}\text{C}$ and with an initial temperature : $T_0 = 10^{\circ}\text{C}$.

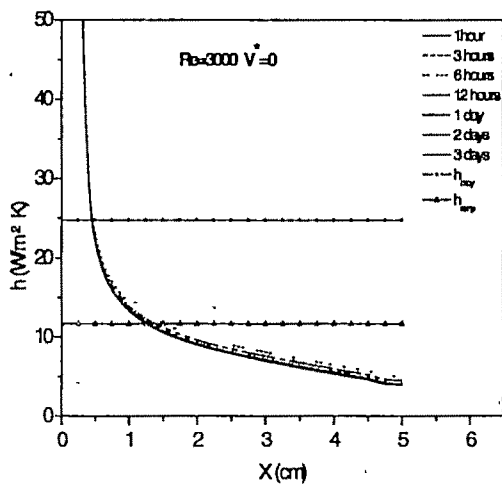


Fig.2. Evolution in time and in space of the convective heat transfer coefficient for: $Re = 3000$ and for $V^* = 0$.

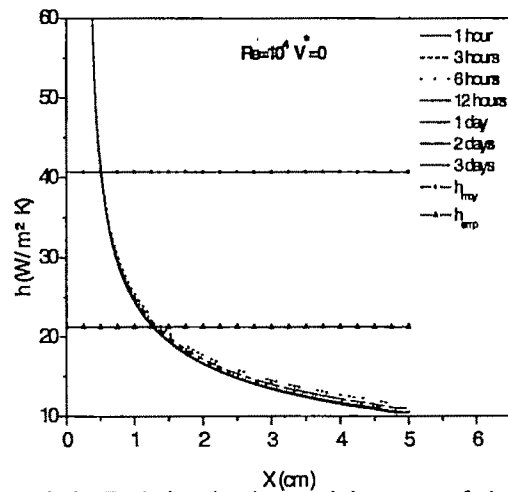


Fig.3. Evolution in time and in space of the convective heat transfer coefficient for: $Re = 10\,000$ and for $V^* = 0$

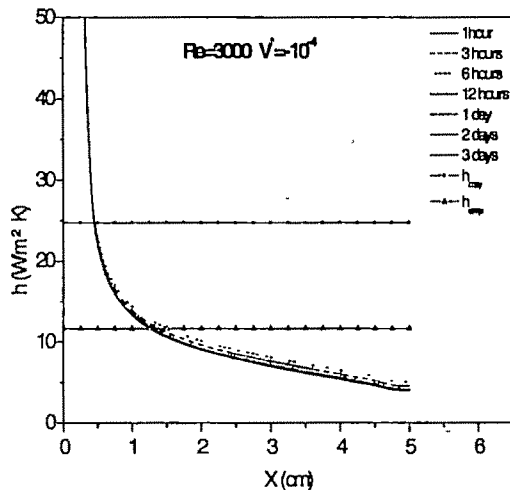


Fig.4. Evolution in time and in space of the convective heat transfer coefficient for: $Re = 3000$ and for $V^* = -10^{-4}$.

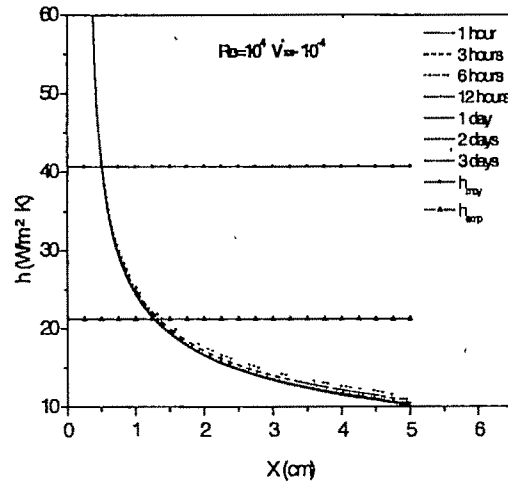


Fig. 5. Evolution in time and in space of the convective heat transfer coefficient for: $Re = 10\,000$ and for $V^* = -10^{-4}$.

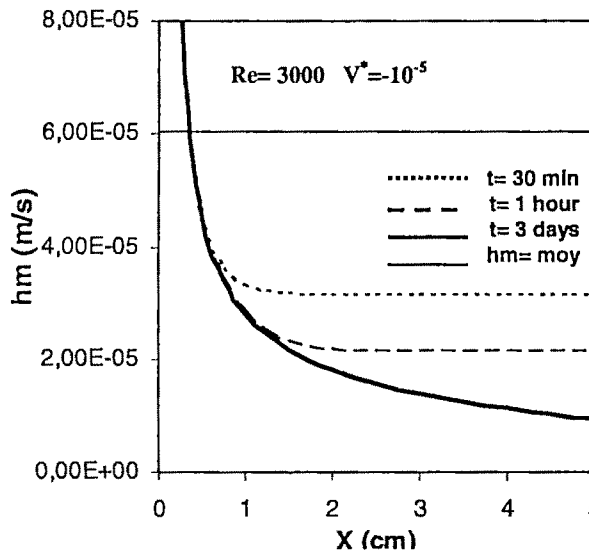


Fig.6. Evolution in time and in space of the convective mass transfer coefficient for: $Re=3000$, and for $V^*=-10^{-5}$

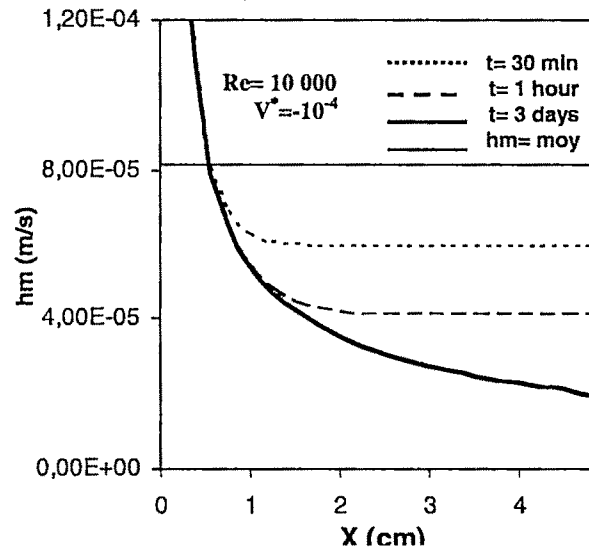


Fig.7. Evolution in time and in space of the convective mass transfer coefficient for: $Re=10000$, and for $V^*=-10^{-4}$

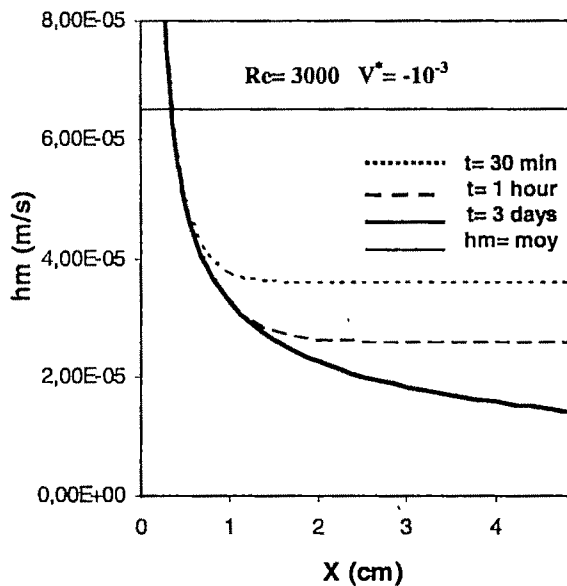


Fig.8. Evolution in time and in space of the convective mass transfer coefficient for: $Re=3000$, and for $V^*=-10^{-3}$

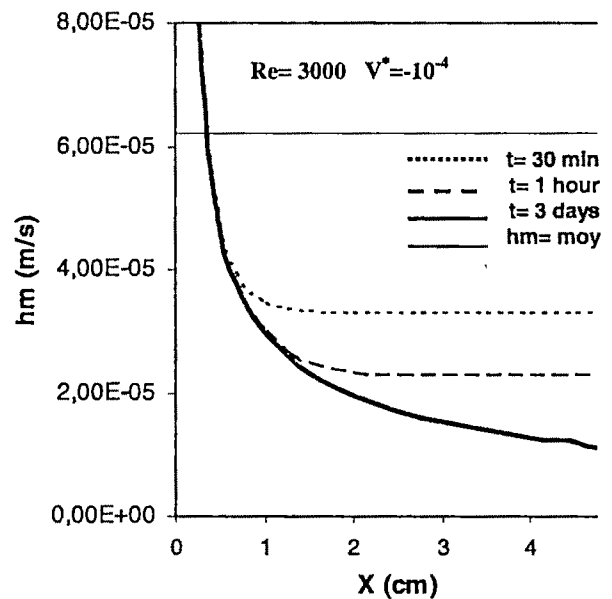


Fig.9. Evolution in time and in space of the convective mass transfer coefficient for: $Re=3000$, and for $V^*=-10^{-4}$

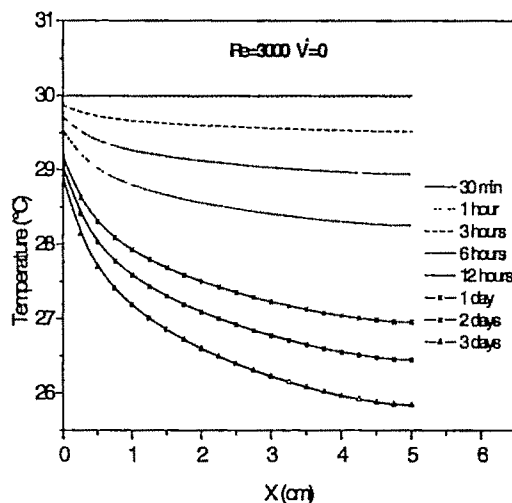


Fig.10. Evolution in time and in space of the surface temperature for: $Re=3000$, and for $V^*=0$.

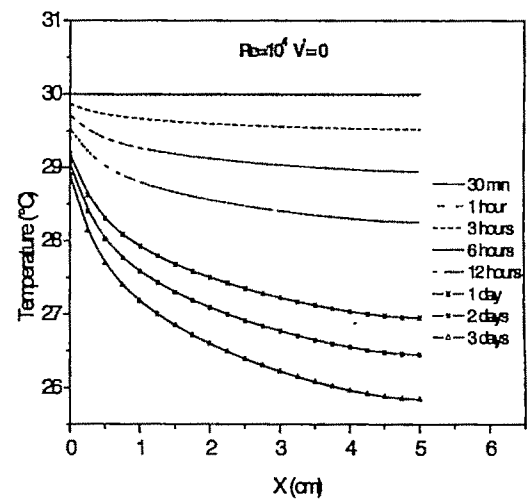


Fig.11. Evolution in time and in space of the surface temperature for: $Re=10000$, and for $V^*=0$.

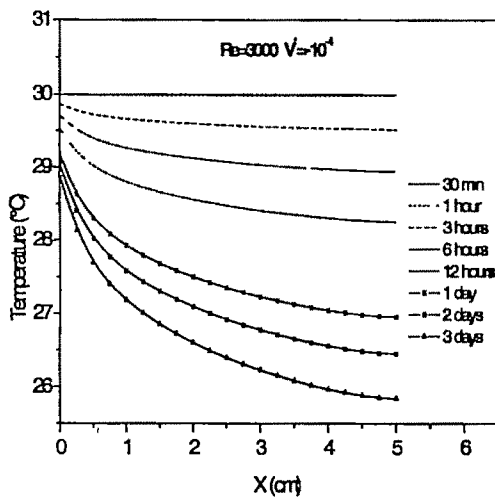


Fig 12. Evolution in time and in space of the surface temperature for: $Re=3000$, and for $V^*=-10^{-4}$.

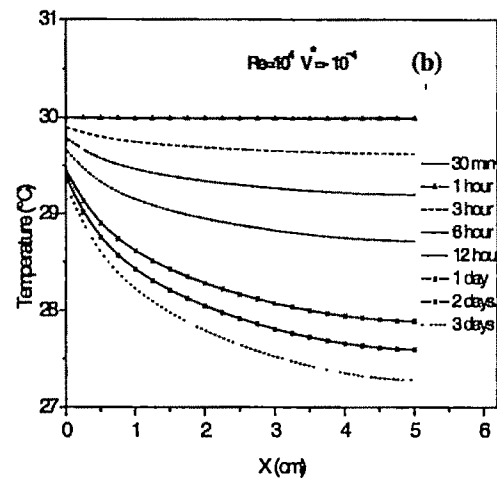


Fig.13. Evolution in time and in space of the surface temperature for: $Re=10000$, and for $V^*=-10^{-4}$.

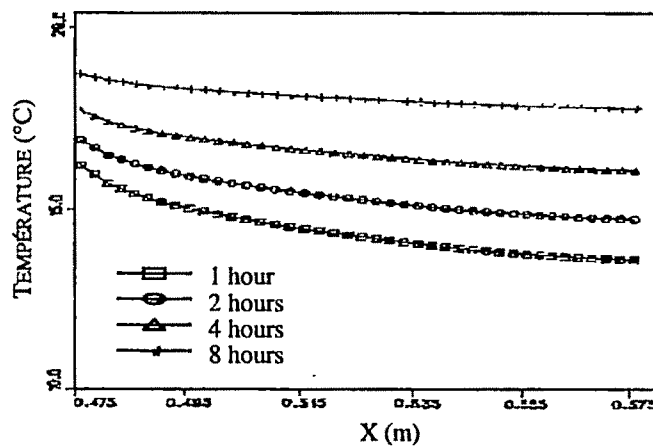


Fig. 14. Evolution of the surface temperature for: $U_{\infty}=1\text{m/s}$ and $T_{\infty}=20^{\circ}\text{C}$, according to [1].

V.CONCLUSION

Obtained results in this study, highlight particularly, the effect of interaction between two mediums (external flow and porous structure) with in particular an appreciable influence of the thermal leading edge effect. We can also note that: if we increase the Reynolds number, the convective heat transfer coefficient and the surface temperature increase, which generates a better heat exchange; The influence of the suction velocity on the convective heat transfer coefficient and the surface temperature are not important; One of the significant results of the interaction between an external flow and a porous environment, is to create a spatial non homogeneity on the distribution of the interfacial temperature and of a coefficient of exchange; Obtained results by our computer software are in the same physical signification as those of Prat [1].

REFERENCES

- [1] Prat, M., 'Modélisation des transferts en milieux poreux changement d'échelle et conditions aux limites', Thèse de doctorat Es- Sciences Physiques, Institut National Polytechnique de Toulouse, Toulouse, France, 1989.
- [2] Schlichting, H., 'Boundary layer theory', McGraw-Hill Book Company, New York, 1979.

- [3] Incropera, F.P., De Witt, D.P., 'Fundamentals of heat and mass transfer', John Wiley and Sons Inc., New York, 1984.
- [4] Carnahan, B., 'Applied Numerical Methods', John Wiley and Sons Inc., New York, 1969.
- [5] Peyret, R., Taylor, D., 'Computational Methods for Fluid Flow', Springer-Verlag, 1990.
- [6] S. LARBI, M. MALKI (2006). 'Determination of interfacial parameters between an external flow and a porous structure'. Third International Conference on Thermal Engineering ASME Conference Dhaka, 21- 23 December, 2006.

Extension Classification Method and Its Application

Yang Chunyan

Research Institute of Extension Engineering, Guangdong University of Technology, Guangzhou P.R.China
e-mail: wyw@gdut.edu.cn.

Abstract—Based on the definitions of extensible set and the constructing method of its dependent function, a sort of classification method under extension transformation, which is called extension classification method, is studied. It is different from the classification methods based on classical set, fuzzy set and rough set, and it is a sort of alterable classification method. According to a certain transformation, it can divide a universe of discourse into 5 parts: positive extension field, negative extension field, positive stable field, negative stable field and extension boundary. Moreover, the universe of discourse and the dependent function describing the degree that an object possesses certain character are alterable. It makes the classification more elaborate. The phenomenon that “there is a corresponding classification pattern for a given transformation” is illuminated from the angle of set theory. Taking the extension classification management on human resources as an example, its applied value will be explained. The classification method is a basic method of extension data mining. It makes the classification function of data mining richer.

Key words—extensible set, extension transformation, extension classification, data mining.

I. INTRODUCTION

SET is a tool that describes classification and identification of human brain for objective objects. Objective objects are complex and in incessant sport and variety. Hence, the classification and identification are not one mode but multifarious, and then the set theory describing them are not only but various^[1]. The diversity of set theory indicates that human beings can conduct multi-angle and multi-level thinking for different objective objects, and can create set to represent objects in different ways, also reflects the dynamic role of set methodology in representing objects.

For example, certain enterprise has definite demand for certain work-piece. For the machined work-pieces, we can divide them into standard and non-standard using the

classification method based on classical set. But in fact, there is a sort of re-workable work-pieces in non-standard work-pieces. For the work-pieces that measurements are bigger than stated standard, they can be changed into standard products by renewed machining; for the work-pieces that measurements are smaller than stated standard, they cannot be changed into standard products if only lathe them. All appearances, the wasters and re-workable products are different in nature in all non-standard products. Contrarily, if we change “renewed machining” into “electroplating”, then the set composed of re-workable products and wasters are just opposite to lathe them.^[2] The sort of problem cannot be described by classical set^[3], fuzzy set^[4] or rough set^[5]. Therefore, this classification lies on adopted transformation. A different transformation is corresponding with a different classification result. Our realistic world abounds with this sort of classification problem, so we must study the classification method based on transformation.

In realistic world, some classifying problems cannot be described by classical set and fuzzy set. They lie on adopted transformations. A transformation is corresponding with a classifying method. The classifying problems are abounding, so we must study the classifying methods based on transformations. Extensible set is a concept based on this sort of practical problems. It can describe both the mutual transform between “yes” and “no” and the degree that an object possesses certain character, that is, it can describe both the process in qualitative change and the process in quantitative change. The advance of extensible set has provided theoretical basis for making the process that people solve contradiction problems quantification, formalized and logical. It has also provided new mathematical tools for dealing with contradiction problems.

Extensible set^[6] is a concept based on this sort of practical problems. It can describe both the mutual transform between “yes” and “no” and the degree that an object possesses certain character, that is, it can describe both the process in qualitative change and the process in quantitative change. The advance of extensible set has provided theoretical basis for making the process that people solve contradiction problems quantification, formalized and logical. It has also provided new mathematical tools for dealing with contradiction problems.

This paper is supported by #70671031, National Natural Science Foundation of China and # 05001832, Guangdong Provincial Natural Science Foundation

In this paper, based on the definitions of extensible set and the constructing method of its dependent function, a sort of classification method under extension transformation, which is called extension classification method, is studied. It is different from the classification methods based on classical set, fuzzy set and rough set [17-19], and it is a sort of alterable classification method. According to a certain transformation, it can divide a universe of discourse into 5 parts: positive extension field, negative extension field, positive stable field, negative stable field and extension boundary. Moreover, the universe of discourse and the dependent function describing the degree that an object possesses certain character are alterable. It makes the classification more elaborate. The phenomenon that "there is a corresponding classification pattern for a given transformation" is illuminated from the angle of set theory. Taking the extension classification management on human resources as an example, its applied value will be explained.

II. EXTENSIBLE SET AND THE CONSTRUCTING METHOD OF ITS DEPENDENT FUNCTION

A. Definition of extensible set

Definition: Suppose U is a universe of discourse, u is a discretonal element in U , k is a mapping from U to real number field I , $T=(T_U, T_k, T_u)$ is a given extension transformation. Then

$$\tilde{E}(T) = \{ (u, y, y') \mid u \in T_U U, y=k(u) \in I, y' = T_k k(T_u u) \in I \}$$

is called an extensible set in U , $y=k(u)$ is a dependent function of $\tilde{E}(T)$, $y' = T_k k(T_u u)$ is an extension function of $\tilde{E}(T)$. Among which T_U is the transformation of U , T_k is the transformation of the dependent function, T_u is the transformation of element u (Here we need to prescribe: If $u \in T_U U - U$, then $y=k(u) \leq 0$).

If $T \neq e$, then

$$E_+(T) = \{ (u, y, y') \mid u \in T_U U, y=k(u) \leq 0, y' = T_k k(T_u u) > 0 \}$$

is called the positive extension field of $\tilde{E}(T)$;

$$E_-(T) = \{ (u, y, y') \mid u \in T_U U, y=k(u) \geq 0, y' = T_k k(T_u u) < 0 \}$$

is called the negative extension field of $\tilde{E}(T)$;

$$E_+(T) = \{ (u, y, y') \mid u \in T_U U, y=k(u) > 0, y' = T_k k(T_u u) > 0 \}$$

is called the positive stable field of $\tilde{E}(T)$;

$$E_-(T) = \{ (u, y, y') \mid u \in T_U U, y=k(u) < 0, y' = T_k k(T_u u) < 0 \}$$

is called the negative stable field of $\tilde{E}(T)$;

$$J_0(T) = \{ (u, y, y') \mid u \in T_U U, y' = T_k k(T_u u) = 0 \}$$

is called the extension boundary of $\tilde{E}(T)$.

According to the definition of extensible set, for a given extension transformation T , there must be a partition of the extensible set corresponding with it. The extensible set can be divided into 5 parts, that is, the positive extension field,

negative extension field, positive stable field, negative stable field and extension boundary.

$$V_+ = \{ u \mid u \in U, y=k(u) \leq 0, y' = k(T_u u) > 0 \}$$

is called the positive extension field of U as to T_u ;

$$V_- = \{ u \mid u \in U, y=k(u) \geq 0, y' = k(T_u u) < 0 \}$$

is called the negative extension field of U as to T_u ;

$$V_+(T) = \{ u \mid u \in U, y=k(u) > 0, y' = k(T_u u) > 0 \}$$

is called the positive stable field of U as to T_u ;

$$V_-(T) = \{ u \mid u \in U, y=k(u) < 0, y' = k(T_u u) < 0 \}$$

is called the negative stable field of U as to T_u ;

$$V_0(T) = \{ u \mid u \in U, y' = k(T_u u) = 0 \}$$

is called the extension boundary of U as to T_u .

B. Constructing method of dependent function

In an extensible set, $y=k(u)$ is a dependent function, it expresses the degree that the object $u \in U$ possesses certain characteristic. According to the different demand of each index in certain practical problem, $y=k(u)$ can be chosen as different forms, such as primary dependent function, simple dependent function, discrete dependent function or interval dependent function, etc.^[10]

According to document [10], the dependent function $y=k(u)$ can be established for single evaluating characteristic or multi evaluating characteristics.

In the case of single evaluating characteristic, if the characteristic value area can be described using two intervals $X_0 = \langle a, b \rangle$ and $X = \langle c, d \rangle$, and $X_0 \subset X$, we can construct a primary dependent function^[11] based on side-distance as follow:

$$k(x) = \begin{cases} \frac{\rho(x, x_0, X_0)}{D(x, X_0, X)} - 1, & \rho(x, X) = \rho(x, X_0) \\ & \text{and } x \notin X_0 \\ \frac{\rho(x, x_0, X_0)}{D(x, X_0, X)}, & \text{other conditions} \end{cases} \quad (1)$$

Where

$$D(x, X_0, X) = \begin{cases} \rho(x, X) - \rho(x, X_0), & \rho(x, X) \neq \rho(x, X_0) \\ & \text{and } x \notin X_0 \\ \rho(x, X) - \rho(x, X_0) + a - b, & \rho(x, X) \neq \rho(x, X_0) \\ & \text{and } x \in X_0 \\ a - b, & \rho(x, X) = \rho(x, X_0) \end{cases}$$

According to the place of x_0 in X_0 , we can choose one of the following formulas to calculate $\rho(x, x_0, X_0)$ ^[12]:

If $x_0 \in (a, \frac{a+b}{2})$, then

$$\rho(x, x_0, X_0) = \rho_l(x, x_0, X_0) = \begin{cases} a - x, & x \leq a \\ \frac{b - x_0}{a - x_0} (x - a), & x \in \langle a, x_0 \rangle \\ x - b, & x \geq x_0 \end{cases}$$

If $x_0 \in (\frac{a+b}{2}, b)$, then

$$\rho(x, x_0, X_0) = \rho_r(x, x_0, X_0) = \begin{cases} a-x, & x \leq x_0 \\ \frac{a-x_0}{b-x_0}(b-x), & x \in (x_0, b) \\ x-b, & x \geq b \end{cases}$$

If $x_0 = a$ or $x_0 = b$, then

$$\rho_l(x, a, X_0) = \begin{cases} a-x, & x < a \\ a_z, & x = a \\ x-b, & x > a \end{cases}$$

where

$$a_z = \rho_l(a, a, X_0) = \begin{cases} 0, & a \notin X_0 \\ a-b, & a \in X_0 \\ 0 \otimes (a-b), & a \notin X_0 \text{ and } a \in X_0 \end{cases}$$

$$\rho_r(x, b, X_0) = \begin{cases} a-x, & x < b \\ b_z, & x = b \\ x-b, & x > b \end{cases}$$

where

$$b_z = \rho_r(b, b, X_0) = \begin{cases} 0, & b \notin X_0 \\ a-b, & b \in X_0 \\ 0 \otimes (a-b), & b \notin X_0 \text{ and } b \in X_0 \end{cases}$$

If $x_0 = \frac{a+b}{2}$, then

$$\rho(x, x_0, X_0) \square \rho(x, X_0) = \left| x - \frac{a+b}{2} \right| - \frac{b-a}{2} = \begin{cases} a-x, & x \leq \frac{a+b}{2} \\ x-b, & x \geq \frac{a+b}{2} \end{cases}$$

In the case of multi evaluating characteristics, we need to establish a multi characteristic integrating dependent function. It has various forms, for example,

$$y = \sum_{i=1}^m \alpha_i k_i(x_i) \quad (2)$$

$$y = \bigwedge_{i=1}^m k_i(x_i) \quad (3)$$

$$y = \bigvee_{i=1}^m k_i(x_i) \quad (4)$$

Where each $k(x_i)$ can be chosen as different forms, such as primary dependent function, simple dependent function, discrete dependent function or interval dependent function, etc.

In formula (2), $\alpha_1, \alpha_2, \dots, \alpha_m$ are weight coefficients. They are used to express the importance of each evaluating characteristic. According to the importance of evaluating characteristics, they are given different weight coefficients.

Formula (3) expresses that the integrating dependent function is the minimum among dependent functions of all characteristics.

Formula (4) expresses that the integrating dependent function is the maximum among dependent functions of all characteristics.

Based on the above definition on extensible set and the constructing method of its dependent function, we can make an

alterable classification for all research objects. This classification method is called extension classification method.

III. BASIC STEPS OF EXTENSION CLASSIFICATION METHOD

Extension classification method is based on extension transformation. It includes ones based on element transformation in a universe of discourse, based on dependent rule transformation and based on the transformation of a universe of discourse.

Given the general steps of extension classification method as follow:

Step 1: Take the whole objects waiting be classified as a universe of discourse U , for \forall a transformation $T=(T_k, T_u)$, set up an extensible set in U

$$\tilde{E}(T) = \{ (u, y, y') \mid u \in U, y = k(u) \in I, y' = T_k k(T_u u) \in I \}$$

Step 2: Suppose $T=(T_k, T_u)=(e, e)$, that is, the transformation T is a unit transformation. Calculate the dependent function values of each object, and according to them, the universe of discourse can be divided into as follow:

$$V = \{ u \mid u \in U, k(u) > 0 \},$$

$$\bar{V} = \{ u \mid u \in U, k(u) < 0 \},$$

$$\bar{V} = \{ u \mid u \in U, k(u) < 0 \},$$

$$V_0 = \{ u \mid u \in U, k(u) = 0 \},$$

They are called the positive field, the negative field and the zero boundary of U respectively. This is a partition of the universe of discourse U . The partition is determinate for a determinate dependent function.

Step 3: Suppose $T=(T_k, T_u) \neq (e, e)$. For a determinate transformation T , calculate the dependent function values after actualizing the transformation T , and according to them, the universe of discourse can be divided into 5 parts as follow:

The positive extension field of U as to T :

$$V_+ = \{ u \mid u \in U, y = k(u) \leq 0, y' = T_k k(T_u u) > 0 \}$$

The negative extension field of U as to T :

$$V_- = \{ u \mid u \in U, y = k(u) \geq 0, y' = T_k k(T_u u) < 0 \}$$

The positive stable field of U as to T :

$$V_+ = \{ u \mid u \in U, y = k(u) > 0, y' = T_k k(T_u u) > 0 \}$$

The negative stable field of U as to T :

$$V_- = \{ u \mid u \in U, y = k(u) < 0, y' = T_k k(T_u u) < 0 \}$$

The extension boundary of U as to T :

$$V_0(T) = \{ u \mid u \in U, y' = T_k k(T_u u) = 0 \}$$

This is the partition of a universe of discourse as to a transformation. The partition is determinate for a determinate transformation and a determinate dependent function.

According to the above partition, the universe of discourse U can be divided into 5 parts. In this way, for a discrecional object in U , it must belong to certain sort among the above 5 sorts after given a transformation. The extension classification is done.

Step 4: Take turns analogy, suppose to actualize other transformation, then it must be corresponding with a new extension classification.

Step 5: For the demand of different value area of dependent function, we can still give a more particular partition. For example, for the following set

$$V_+ = \{ u \mid u \in U, y=k(u) \leq 0, y' = T_k k(T_u u) > 0 \},$$

If we want to divide the objects that their dependent function values are in $\langle 0, 1 \rangle$, $\langle 1, 5 \rangle$ and $\langle 5, +\infty \rangle$ after actualizing the above transformation into a sort respectively, then the three sorts are the following sets:

$$V_1 = \{ u \mid u \in U, y=k(u) \leq 0, y' = T_k k(T_u u) \in \langle 0, 1 \rangle \}$$

$$V_2 = \{ u \mid u \in U, y=k(u) \leq 0, y' = T_k k(T_u u) \in \langle 1, 5 \rangle \}$$

$$V_3 = \{ u \mid u \in U, y=k(u) \leq 0, y' = T_k k(T_u u) \in \langle 5, +\infty \rangle \}$$

Step 6: Suppose to actualize a transformation for the universe of discourse U , make $T_U U = U'$, then there is a new extension classification for the new universe of discourse U' , and repeat step 1 to 6.

IV. CASE ANALYSIS

Certain company's human resources department needs to actualize classifying management for its staff. The company originally classified its staff according to department, technical post, degree, technical sort, age, etc. Because the modern enterprise's productions are high tech ones, they make the relations among all departments and all types of work increasingly osculation. Therefore, the classifying management for human resources also needs to consider its changeability. Under exquisite marketing competition, the company's old productions have already not adapted the market demand, so the company decided to produce a sort of high tech new production.

We will give some classification methods on the company's human resources using extension classification method.

Suppose the company's staff form a universe of discourse U . For certain employee O , it can be expressed with matter-element $M \in U$, there is a multi-dimension matter-element expression as follow:

$$M = \begin{bmatrix} O, & \text{department } c_1, & v_1 \\ & \text{technical post } c_2, & v_2 \\ & \text{technical sort } c_3, & v_3 \\ & \text{degree } c_4, & v_4 \\ & \text{age } c_5, & v_5 \end{bmatrix} = \begin{bmatrix} O, & c_1, & v_1 \\ & c_2, & v_2 \\ & c_3, & v_3 \\ & c_4, & v_4 \\ & c_5, & v_5 \end{bmatrix}$$

Suppose the degree that a sort of technical level of the employee O accords with the demand that the company want to develop a high tech production is $y=k(M)$. When the universe of discourse U doesn't change, we can establish an extensible set as follow

$$\tilde{E}(T) = \{ (M, y, y') \mid M \in U, y=k(M) \in I, y' = T_k k(T_u M) \in I \}$$

Here, we adopt single evaluating characteristic dependent function, that is, we can adopt a primary dependent function to construct $y=k(M)$.

1) When we don't actualize any transformation, that is, $T=(T_k, T_M)=(e, e)$, we can divide staff of the company into 3 sorts:

$\bar{V} = \{ M \mid M \in U, k(M) < 0 \}$ expresses the employees who their technical levels don't accord with the demand that the company want to develop a high tech production;

$V = \{ M \mid M \in U, k(M) > 0 \}$ expresses the employees who their technical levels accord with the demand that the company want to develop a high tech production;

$V_0 = \{ M \mid M \in U, k(M) = 0 \}$ expresses the employees who their technical levels are on critical state, that is, they either accord with the demand or don't accord with the demand.

After making the above classification, we discovered that the employees in V failed to finish the task developing the high tech production. Hence, we must train the employees who don't accord with the demand, that is, renew to classify based on transformation, and then form a new developing group.

2) Actualizing corresponding technical training for the employees who don't accord with the demand, that is, making the following extension transformation

$$T_M M = \begin{bmatrix} O, & c_1, & v_1 \\ & c_2, & v_2 \\ & c_3, & v_3' \\ & c_4, & v_4 \\ & c_5, & v_5 \end{bmatrix} = M'$$

After training, test them and then confirm the degrees that they accord with the demand, that is, according to the value of $y' = k(T_M M)$, the employees can be divided into 4 sorts as follow:

$V = \{ M \mid M \in U, k(M) > 0 \}$ expresses the employees who formerly accorded with the demand.

$V_+ = \{ M \mid M \in U, y=k(M) \leq 0, y' = k(T_M M) > 0 \}$ expresses the employees who formerly disaccorded with the demand or were in critical state.

$V_- = \{ M \mid M \in U, y=k(M) < 0, y' = k(T_M M) < 0 \}$ expresses the employees who formerly disaccorded with the demand and still disaccord with the demand after training.

$V_0(T) = \{ M \mid M \in U, y=k(M) = 0, y' = k(T_M M) = 0 \}$ expresses the employees who formerly were in critical state and still are in critical state after training.

Under the above transformation T_M , the whole employees' set that accord with the demand is $V \cup V_+$. If the employees have

been enough to finish the task developing the high tech production, then the classification is over. If the employees' numbers have been more than demand ones, then we need to size the employees who accord with the demand according to their dependent function values, and then confirm persons selected.

3) For the employees who aren't employed after actualizing the above classification, they form a set U_1 , the company needs to consider how to allocate them. Therefore, the company is going to launch a culture service department. Here the former dependent rule is inapplicable. So we need to transform the dependent rule firstly, that is, make $T_k k = k'$, for example, consider the employees' social capability and education degree, and then classify them. The transformation can divide the employees in U_1 into 3 sorts as follow:

$$V_+ = \{M \mid M \in U, y=k(M) \leq 0, y'=k'(M) > 0\}$$

expresses the employees who disaccorded with the former demand or were in former critical state, and accord with the new demand after transforming the rule.

$$V_- = \{M \mid M \in U, y=k(M) < 0, y'=k'(M) < 0\}$$

expresses the employees who disaccorded with the former demand, and disaccord with the new demand after transforming the rule.

$$V_0(T) = \{M \mid M \in U, y=k(u)=0, y'=k'(u)=0\}$$

expresses the employees who formerly were in critical state, and still in critical state after transforming the rule.

In order to unite prepare and allocate within reason the employees of the company, we can take advantage of a new rule to classify for the employees in U who accorded with the former demand. Under the new rule, they can be divided into two sorts as follow:

$$V = \{M \mid M \in U, y=k(M) \geq 0, y'=k'(M) < 0\}$$

expresses the employees who accorded with the former demand or formerly were in critical state, and disaccord with the new demand after transforming the rule;

$$V_+ = \{M \mid M \in U, y=k(M) > 0, y'=k'(M) > 0\}$$

expresses the employees who accorded with the former demand, and still accord with the new demand after transforming the rule.

Under the transformation T_k , the set composed of the employees who accord with the new demand is $V_+ \cup V_-$. Here

the employees in V_+ can be as spare ones. If certain employee in V_+ is adapt to be a manage of the culture service department, then the employee can be prepared to the department.

4) If the above classification still didn't satisfy company's demand, then we can adopt the method transforming the universe of discourse U , that is, make $T_U U = U'$. The transformation will lead to reclassify for employees. For example, in the case of changeless rule, make an enlarging transformation for the universe of discourse U , that is, engage some high technical persons out of the company to join in the research group, or retain some pluralistic persons, and so on, they all can make the classification change and bring a new group.

In the example, the dependent function $y=k(M)$ describing quantificationally the degree that employees accord with demand can be established by using the constructing methods of dependent function according to the idiographic demand of enterprise.

V. CONCLUSIONS

Based on the classifying thought of extensible set, in this paper, a classification method based on extension transformation---extension classification method is provided. The method fits in with objects' classifying management in variable environment. The classification is detailed, its changeability is strong, and it can provide more classifying

modes in order to let manager choose. Therefore, the method possesses not only classifying function but also the function that assists manager to make classifying decision. The classifying management software using the method to program will provide a strong classifying management tool for managers. Using the method to research data mining, it must dig out more valuable knowledge from a mass of data.^[13]

The classification method is a basic method of extension data mining.^[14] It makes the classification function of data mining richer.

REFERENCES

- [1] Cai Wen, "Extension theory and its application", *Chinese Science Bulletin*, Vol. 44, No. 17, pp. 1538-1548, 1999.
- [2] Cai Wen, Yang Chunyan, *Extension Marketing*, Science and Technology Document Press, Beijing, 2000.
- [3] Zhu Wujia, Xiao Xi'an, *Conspectus on Mathematical Basis*, Nanjing University Press, Nanjing, 1996.
- [4] Hu Baoqing, *Foundation of Fuzzy Theory*, Wuhan University Press, Wuhan, 2006.
- [5] Hu Keyun, Lu Yuchang, Shi Chunyi, "Advances in rough set theory and its applications", *Journal of Tsinghua University (Sci & Tech)*, Vol. 41, No. 1, pp. 64-68, Jan. 2001.
- [6] Yang Chunyan, Zhang Yongjun, Cai Wen, "Extension set and its applications", *Mathematics in Practice and Theory*, Vol. 32, No. 2, pp. 301-308, Feb. 2002.
- [7] Li Xiongfei, Li Jun, *Data Mining and Knowledge Discovery*, Higher Education Press, Beijing, 2003.
- [8] Wang Hong, *Customer Value Analysis Based on Rough Set Data Mining Technology*, Economic Science Press, Beijing, 2006.
- [9] Cai Wen, Yang Chunyan, Lin Weichu, *Extension Engineering Methods*, Science Press, Beijing, 2003.
- [10] Yang Chunyan, Cai Wen, *Extension Engineering*, Science Press, Beijing, 2007.
- [11] Li Qiaoxing, Liu Sifeng, "A method to construct the general location value and general primary dependent function", *Systems Engineering*, Vol. 24, No. 6, pp. 116-118, June 2006.
- [12] Cai Wen, *Matter-element Model and Its Applications*, Science and Technology Document Press, Beijing, 1994.
- [13] Chen Wenwei, "Research on mining the mutative knowledge with extension data mining", *Engineering Science*, Vol. 8, No. 11, pp. 70-73, Nov. 2006.
- [14] Li Lixi, Yang Chunyan, Li Huawen, *Extension Strategy Generating System*, Science Press, Beijing, 2006.

Computation of Optimum Expansion Coefficients in Generalized Block Pulse Function Domain

Anish Deb¹, Gautam Sarkar¹, Nabanita Nath Chowdhury²

¹Department of Applied Physics, University of Calcutta, India. E-mail anishdeb2000@yahoo.co.in

²Electrical Engineering Department, Meghnad Saha Institute of Technology, Kalcutta, India. E-mail nabanita.nc@gmail.com

Abstract— In this paper, a method for computation of optimum expansion coefficients in generalized block pulse domain is suggested. A derivative based algorithm is developed and a subsequent computer program for computation of such coefficients for a few functions has been employed.

Key words—Block pulse functions, Generalized Block pulse coefficients, Mean integral square error.

I. INTRODUCTION

WITH the advent of piecewise constant basis functions (PCBF) [1] like Haar, Walsh, block pulse [2] and other related functions, scientists have understood the importance of function approximation with minimum error while dealing with a variety of problems. The quantitative judgment of quality of approximation until now is the mean integral square error (MISE). Of all PCBF's, the block pulse function (BPF) set [3] proved to be the most fundamental. Also, a generalized version of the BPF set [4-6] was found to be more powerful for certain applications including function approximation.

Until now, there is no definite method for computing the expansion coefficients of generalized block pulse functions an optimum manner. This helps in keeping the balance between the number (m) of component functions employed for

(GBPF) in an optimum manner. Here, we present an algorithm for computing GBPF coefficients, off-line as well as on-line, in function approximation and MISE. For any particular value of m , the GBPF set incurs less MISE [6] compared to conventional BPF set in most of the cases.

II. REVIEW OF FUNCTION APPROXIMATION VIA ORTHOGONAL FUNCTIONS

A time function can be synthesized completely to a tolerable degree of accuracy by using a set of orthogonal functions. Let

a time function $f(t)$ defined over a time interval $[0, T)$ be represented by an orthogonal function set $S_n(t)$. Then

$$f(t) = \sum_{n=0}^{\infty} c_n S_n(t) \quad (1)$$

where, c_n 's are the coefficients connected to the n^{th} member of the orthogonal function set.

Since only a finite number of terms of the series $S_n(t)$ can be considered for practical realization, the right-hand side of equation (1) has to be truncated and we have

$$f(t) \approx \sum_{n=0}^N c_n S_n(t) \quad (2)$$

when N is large, the accuracy of representation is good enough for all practical purposes. Also, it is necessary to choose the coefficients c_n 's in such a manner that the mean integral square error (MISE) is minimized. Thus,

$$\text{MISE} = \frac{1}{T} \int_0^T [f(t) - \sum_{n=0}^N c_n S_n(t)]^2 dt \quad (3)$$

This is realized by making

$$c_n = \frac{1}{T} \int_0^T f(t) S_n(t) dt \quad (4)$$

For a complete orthogonal function set, MISE in equation (3) decreases monotonically to zero as N tends to infinity.

III. REVIEW OF BLOCK PULSE FUNCTIONS (BPF) [3]

During the early 80's, the BPF set found its application in different areas of control theory, like system analysis and identification, parameter estimation, distributed system analysis, solving integral equations etc.

A set of block pulse functions, comprised of m equal width component functions, in the semi-open interval $t \in [0, T)$ is defined as

$$\psi_i(t) = \begin{cases} 1 & ih \leq t < (i+1)h \\ 0 & \text{otherwise} \end{cases}$$

where, $i = 0, 1, 2, \dots, (m-1)$ and the width of each block pulse function is $h=T/m$.

Any function $f(t)$ which is square integrable in the interval $[0, T)$, can be expanded via a block pulse series as

$$\begin{aligned} f(t) &= \sum_{i=0}^{\infty} c_i \psi_i = c_0 \psi_0 + c_1 \psi_1 + \dots + c_i \psi_i + \dots \\ &= C^T \Psi_{(m)}(t) \end{aligned} \quad (5)$$

where $c_0, c_1, \dots, c_i, \dots$ etc are the coefficients of the block pulse series to be determined from the equation

$$c_i = \frac{1}{h} \int_{ih}^{(i+1)h} f(t) \psi_i(t) dt \quad (6)$$

IV. GENERALIZED BLOCK PULSE FUNCTIONS (GBPF) AND THEIR REPRESENTATION [4-6]

The generalized block pulse functions are defined as

$$\psi_i(t) = \begin{cases} 1, & t_i \leq t < t_{i+1} \\ 0, & \text{elsewhere} \end{cases}$$

where, width of the i -th block pulse is $(t_{i+1}-t_i) = h_i$ (say)

Figure 1 represents a set of 4 GBPFs [4, 5] with unit amplitude and different widths h_i ($i=0, 1, 2 \dots m-1$). The nomenclature used until now in the literature has not been able to characterize a particular

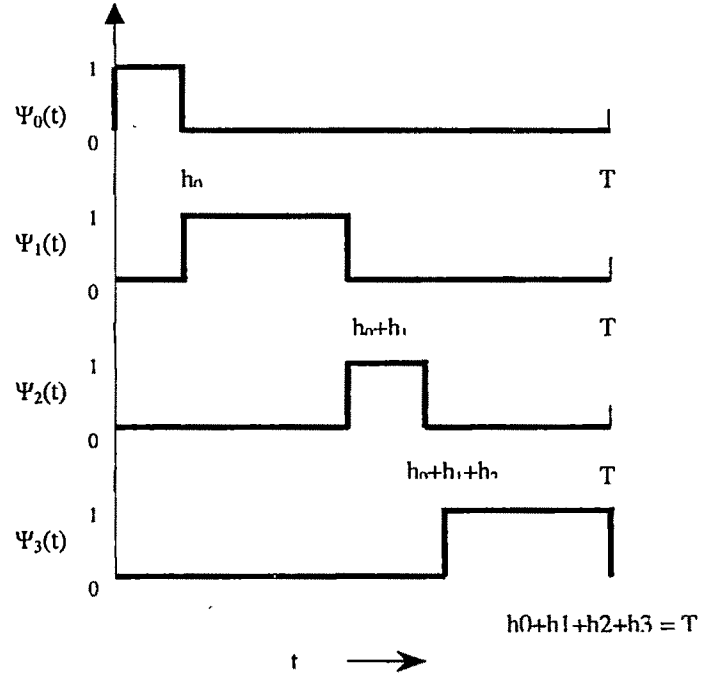


Figure 1: A set of generalized block pulse functions [4]

member of the GBPF set in a unique manner. From figure 1, it is observed that there are three characterizing properties [6] of any member of a GBPF set. These are:

- The distance of the member from the origin.
- The width of the member
- The total time interval under consideration.

These three properties can represent any member of the GBPF set uniquely. Thus, the i -th member of the GBPF set can be represented as

$$\psi_i \left[\sum_{j=0}^{i-1} h_j, h_i, \sum_{j=0}^{m-1} h_j \right] = \begin{cases} 1, & \sum_{j=0}^{i-1} h_j \leq t < \sum_{j=0}^i h_j \\ 0 & \text{elsewhere} \end{cases} \quad (7)$$

where the argument of ψ_i represents The distance of ψ_i from the origin, i.e.

$$\sum_{j=0}^{i-1} h_j$$

and when $i=0$, the summation is assumed to be zero, indicating a zero delay of ψ_0 from the origin.

- The width of ψ_i ($=h_i$);

- (ii) The total time interval T under consideration, i.e.

$$\sum_{i=0}^{m-1} h_i$$

For expansion of a square integrable function $f(t)$ in GBPF domain the i^{th} GBPF coefficient c_i is determined by the following relation.

$$c_i = \frac{1}{h_i} \int_{\sum_{j=0}^{i-1} h_j}^{\sum_{j=0}^i h_j} f(t) \psi_i(t) dt \quad (8)$$

V. THE PROPOSED DERIVATIVE CONCEPT

If we want to use generalized (i.e., unequal width) block pulse functions for function approximation, it seems to be a reasonable strategy to use derivatives of the function to be approximated. The proposed approach is somewhat *ad hoc* in manner and is based upon computation of derivatives of the function to be expanded via GBPF. That is, the widths of the block pulses depend upon the 'trends' of the function in different regions along the time scale.

First of all, the derivative of the function $f(t)$ is computed at $t=0$. Let us call this $f'(0)$. Then, with the slope $f'(0)$, we form a ramp function of the form

$$\{tf'(0) + C_1\}$$

where $C_1=f(0)$.

Now we check the difference between the function $f(t)$ and the above ramp function for different values of t along the time scale. When the magnitude of the difference of $[f(t) - \{tf'(0) + C_1\}]$ exceeds some predefined value ϵ (say), we stop at that time value (say, t_0) and call it the first sub-interval h_0 .

Now we repeat the process, as shown in fig. 2, and compute $f'(t_0)$ to form a different ramp function

$$\{tf'(t_0) + C_2\}$$

where $C_2 = f(t_0)$.

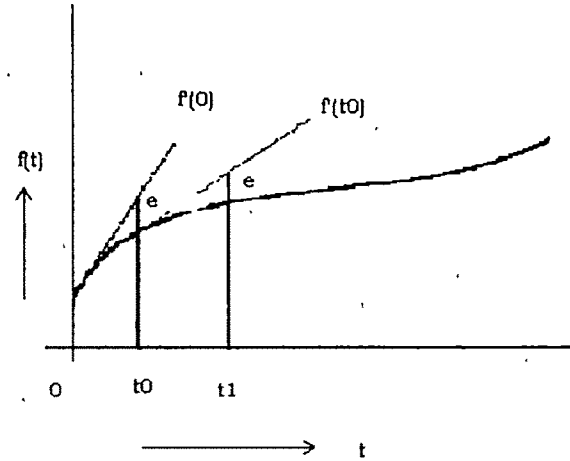


Fig. 2 : The derivative concept shown for a function $f(t)$.

Again, we check the difference between the function $f(t)$ and the ramp function $\{tf'(t_0) + C_2\}$ for different values of t . When the magnitude of the difference of $[f(t) - \{tf'(t_0) + C_2\}]$ exceeds ϵ , we stop at that time value t_1 (say) and call (t_1-t_0) the sub-interval h_1 .

Proceeding in this manner, we cover the whole time zone (say, T) under consideration and thus are able to find out all the generalized BPF sub-intervals $h_0, h_1, \dots, h_i, \dots, h_{(m-1)}$. A point to be noted is, the value of m , that is, the number of sub-intervals, is finally determined from the above strategy. Knowing the values of different sub-intervals $h_0, h_1, \dots, h_i, \dots, h_{(m-1)}$, the related GBPF coefficients can be determined from equation (8).

VI. SPECIAL CASES

VIA. Step Function Approximation : As the derivative of the step function is zero, it is obvious that this function should be approximated by equal width block pulses (using one block pulse or more). In this case, MISE is always zero.

VIB. Ramp function approximation : Consider a unit ramp function approximated via equal width BPF. Let the interval under consideration be $[0, T]$ and the number of component BPF's be m . Then, MISE is obtained as

$$\text{MISE} = \frac{1}{T} \int_0^T [f(t) - \sum_{i=0}^{m-1} c_i \psi_i(t)]^2 dt = T^2/12m^2 \quad (9)$$

Thus, we see that for such approximation, MISE is inversely proportional to the square of the number of block pulses employed for the expansion. As we increase the number of BPF's, MISE tends to decrease rapidly.

VII. THE DERIVATIVE BASED APPROACH : ALGORITHM

1. Start.
2. Compute the derivative $f'(t)$ of the function to be approximated.

3. Choose a set value ϵ on *ad hoc* basis.
4. Multiply the derivative value with t (and any intercept value C , as required) and compare it with the function value $f(t)$ at t .
5. Go on repeating step 4 with small increments in t until the magnitude of the difference between $[t f'(t)+C]$ and $f(t)$ crosses the predefined set value ϵ at time t_0 (say). Stop and declare that $h_0=t_0$.
6. Start from $t=t_0$ and repeat step 4 to find out t_1 , where the compared value again crosses the predefined value ϵ . Then declare $h_1=t_1-t_0$.
7. Go on repeating step 4 until the total time interval is covered. That is

$$\sum_{j=0}^{m-1} h_j \geq T$$

8. Compute the GBPF coefficients considering the generalized time intervals $h_0, h_1, h_2 \dots$ etc, using the following formula

$$c_i = \frac{1}{h_i} \int_{\sum_{j=0}^{i-1} h_j}^{\sum_{j=0}^i h_j} f(t) \psi_i(t) dt$$

9. Stop.

VIII. CASE STUDIES

The algorithm was tested for two functions. The first is a unit amplitude sine wave from 0 to π . The time interval chosen was $T = 1$ second. With $\epsilon = 0.01$, the method resulted in twelve sub-intervals, that is $m = 12$, and with the sub-intervals computed via this algorithm, the MISE for the GBPF approximated sine function turned out to be 4.273906E-03.

With equal-width BPF and $m=12$, the MISE was found to be 2.847905E-03. It is noted that the algorithm fails to come up with an MISE less than that obtained via conventional analysis. This is not surprising because the proposed method is based upon an *ad hoc* approach with regards to the value of ϵ .

As a second example, we chose the function $f(t) = 1 - \exp(-t)$. With $\epsilon = 0.008$, the MISE via GBPF analysis turned out to be 9.912886E-04, with $m=6$. With this computed m , the conventional analysis resulted in an MISE = 9.97997E-04.

IX. CONCLUSION

Since the present work is basically an *ad hoc* method it can not be claimed that this method will work successfully for all functions of square integrable nature. We have considered only two cases to prove our point, but it needs deeper investigation with different types of functions to establish the usefulness of the method for majority of functions. Another point to be mentioned is, the algorithm, while computing the widths of different sub-intervals, covered a time period very close to $T = 1$ s, but not exactly equal to 1s. This obviously has introduced slight error in the computation of MISE. If the program can be modified to take care of this drawback, the GBPF based result may be further improved.

The present work may be extended by employing a microprocessor for implementing this algorithm using any on-line signal and the MISE may be estimated and compared with conventional BPF expansion.

ACKNOWLEDGMENT

The authors acknowledge the support of Priyanka Roy and Debasish Biswas during preparation of this work.

REFERENCE

- [1] Beauchamp, K. G., *Applications of Walsh and related functions with an introduction to sequence theory*, Academic Press, London, 1984.
- [2] Deb, Anish, Sarkar, Gautam and Sen, Sunit K., Block pulse function, the most fundamental of all piecewise constant basis functions, *Int. J. Systems Sci.*, vol 25, no 2, pp 351-363, 1994.
- [3] Jiang, J. H. and Schaufelberger, W., *Block pulse functions and their application in control systems* LNCIS-179, Springer-Verlag, Berlin, 1992
- [4] Chang, Rong-Yeu, Chou, Chih-Kao and Wang, Maw-Ling, Solution of functional differential equations via generalized block pulse functions, *Int. J. Systems Sci.*, vol 16, no. 11, pp 1431-1440, 1985
- [5] Wang, Maw-Ling, Yang, Shwu-Yien and Chang, Rong-Yeu, Analysis of systems with multiple time-varying delays via generalized block pulse functions, *Int. J. Systems Sci.*, vol 18, no. 3, pp 543-552, 1987.
- [6] Deb, Anish, Sarkar, Gautam and Sen, S. K., Linearly pulse-width modulated block pulse functions and their application to linear SISO feedback control system identification, *Proc. IEE, Part D, Control Theory and Appl.*, vol 142, no. 1, pp 44-50, 1995

An Approach to Detect the Cause of Over Current in Power System Network Using Real Time Digital Simulation

A. K. Dhara, S. Chowdhuri, J. N. Bera, S. C. Kar, S. Sengupta,

Department of Applied Physics, University of Calcutta,

Abstract— Detection the cause of over current in power system network carried out at different means is absolutely essential to enhance the system reliability and to maintain continuity of supply. Unexpected over current causes serious problems for generation, transmission as well as distribution system. The primary reasons for over current are basically of two types viz. overload condition and/or fault condition. Here a simulation study has been carried out to detect the Cause of Over Current in Power System Network Using Real Time Digital Simulation

Key Words—Real Time Digital Simulation (RTDS), Different type of fault, over current, over load, Phase imbalance.

1. INTRODUCTION

THE main purpose of electrical power system is to efficiently generate, transmit and distribute electrical energy. The need of steady power supply with minimum power interruption and fast supply restoration has also increased. After design and before implementation of a new system simulation is required to study the system performance under normal and abnormal condition. In this paper we are going to detect the cause of over current created in the electrical network by analysis of harmonic component and sequence current. Real Time Digital Simulation (RTDS) software is powerful simulating software using worldwide for simulating power system and electric machine [1]. RTDS technologies was established and incorporated in Manitoba, Canada [2]. RTDS simulator is the hardware containing the processing and communicating devices performing simulation and RSCAD is the set of software modules which performs the graphical user interface to the RTDS. RSCAD represents a family of software tools consisting of individual modules that accomplish different tasks involved in operating the simulation. Through RSCAD the user can organize a project case, assemble circuit diagram using predefined and user defined power and control system component models and analyze the simulated result. Many high-speed processors are utilized in RTDS in parallel in order to realize and maintain required computational rates. RTDS cubicle can have many types of processor cards (WIF, 3PC, GPC, IRC, DIO, DOPTO) may be installed in each rack. As it is online simulation so we

can monitor current, voltage, real power, reactive power, frequency during runtime and we can set all parameter according our requirement.

II. SIMULATION HARDWARE

Analogue simulators use scaled down linear models of system elements, whereas a digital simulator models these same system elements, by solving the linear or nonlinear mathematical equations which describe the elements' dynamic behavior. To run an electromagnetic transient study a time step of approximately 50ps is required. A true system may require hundreds of millions of floating point operations per second (MFLOPS) to solve all the necessary equations at least once in a single time step. The most powerful computer workstations available today can run at only a few MFLOPS on an intermittent basis. Thus a special purpose device is required which uses parallel processing techniques capable of very high speed floating point arithmetic. The RTDS is made up of several standard cards viz GIGA Processor Card (GPC), Triple Processor Card (3PC), one inter-rack communication card (IRC) and one workstation interface card (WIC), Digital Input output Card (DOPTO), High precision analog Input Card (OADC) [2]. Any one rack can directly communicate with four other racks. Since there are only three types of card, and programmable VLSI devices are used to construct the cards, the cost of the RTDS is much less than for an analogue simulator of similar capability. This is a versatility which an analogue simulator cannot match. Each card is equipped with a processor capable of up to many MFLOPS. It also has hardware to allow interfacing to external signals. Analogue channels can be selected to monitor variables being computed on that card and these channels can be scaled on-line to suit the external device. An input channel can also accept a logic signal such as the closing of the test relay contacts to trigger breaker opening. relay under test The IRC card transfers data generated on its rack to other connected racks which need this information For the next time step. Transfer of information takes place at 500 Mhz. The WIC deals with the communication between the RTDS and the host computer network over an ethernet communication link. The data transfer rate is 10 Mhz. The WIC is not only involved in the

real time simulation but deals with the downloading of the case prior to the run. The RTDS for this study occupies one rack in the simulator cubicle..

III. SIMULATION SOFTWARE

The user interface to the RTDS is via the host workstation on which various high level software routines viz RSCAD are available to set up, run and analyze a case. RSCAD provides the ability to set up simulations, control, and modify system parameters during a simulation, data acquisition, and result analysis. The modules of RSCAD Software Suite include: FileManager, Draft, Time, Cable, RunTime and MultiPlot. Figure 1 is a "screen dump" from the host workstation of a system being assembled for another study using the input graphics routine called "DRAFT". The screen is divided into a right 'menu' or component selection area containing Icons representing all of the system elements which have been coded for the real time simulator, and an area on the left where the system is being assembled. With the aid of a mouse any desired component can be selected and dragged into the left area to be connected at the desired location. There are many more Icons available than are shown on the screen and again the complete menu can be examined by using the mouse in the right hand window to scroll up and down, left and right. When a particular Icon is incorporated in the circuit diagram the user is prompted on the screen to supply the necessary data for software. the item in question. Although only a portion of the entire circuit is visible on the screen, one can move around the whole circuit by scrolling with the mouse. When the compiler has completed its task the case is run up

IV. SIMULATION

In this figure there is a generator delivering 33kv to the generator bus. The generator bus is connected to a transmission line having length 100km. At the end of transmission line there is a distribution transformer, which transform 33kv to 11kv. At 11kv bus an induction machine is connected. We can set all possible parameter relating to induction machine, generator and transformer according to our requirement using RTDS. Let us assume there is an over current at receiving end bus. This situation may occur mainly due to two reasons, firstly due to overloading of induction machine, and secondly due to L-G, L-L, or L-L-G fault. With the help of Real Time Digital Simulation (RTDS), we will find out the actual cause of over current.

The block diagram of induction machine connected at receiving end is shown in fig.-2.and the parameter-monitoring table is shown in fig.-3. This table indicates that we can monitor all possible parameter.

V. PROCEDURE TO DETECT THE CAUSE OF OVERCURRENT

During overload condition current will increase largely but there will be no phase imbalance but during fault condition phase imbalance will occur. Using REAL TIME DIGITAL SIMULATION we can simulate the result of over current and fault condition and from the result we can detect the cause of over current. At first we will measure phase current of

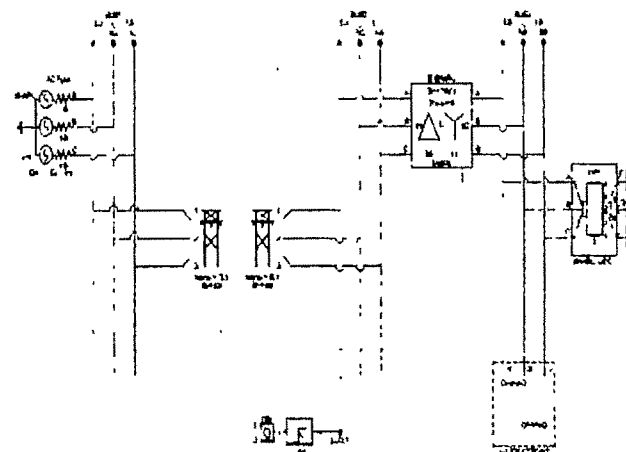


Fig.-1, Total electrical network.

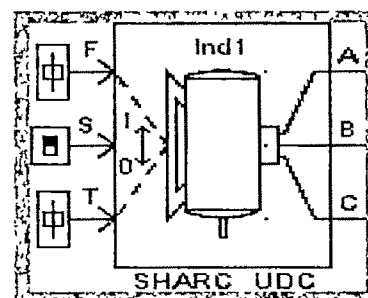


Fig.- 2, Block diagram of induction machine

RTDS SHARC SLD INDM				
SATURATION CURVES MONITORING SELECTIONS SIGNAL NAMES				
MOTOR ELECTRICAL PARAMETERS & MECHANICAL PARAMETERS				
CONFIGURATION				
Name	Description	Value	Unit	Min
name	Motor name	Ind1		
nm1	Number of Rotor Cages	One		
srcsp	Source of Speed Signal (F)	Fal		
srcsw	Source of Torque/Speed Mode (S)	Ru		
src1q	Source of Torque Signal (T)	Ru		
zroc	Force all initial currents to 0	No		
<input type="button" value="Update"/> <input type="button" value="Cancel"/> <input type="button" value="Cancel All"/>				

Fig.- 3, Parameter monitoring of induction machine

induction machine during normal condition and this is shown graphically in the fig.-4. From the figure it is obvious that phase current are balanced. During overload condition current will increase largely but there will be no phase imbalance and it is shown in fig.-5. We have increased mechanical load of induction machine. As a result current has increased from 0.98 KA to 1.25 KA. We have simulated L-L and L-L-L fault. In first case fault has occurred between phase A & phase B and the fault current is shown in fig.-6. During fault A-phase

current is reverse of B-phase current and it is 6.2 KA. So there is a phase imbalance here.

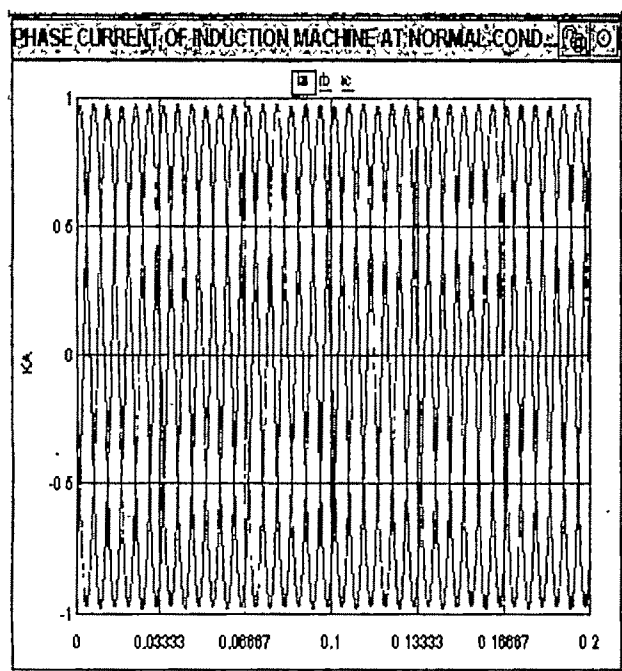


Fig.-4, Phase current of induction machine at normal condition

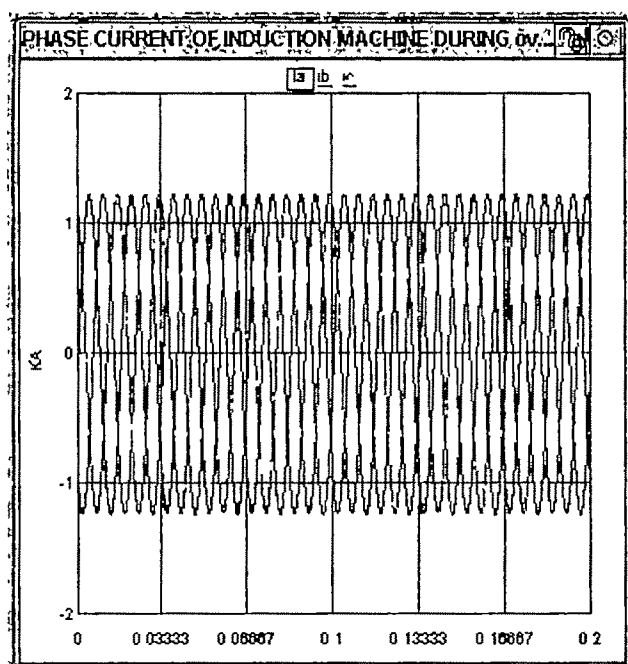


Fig.-5, Phase current of induction machine at overload condition.

In second case fault has occurred between phase A, phase B and phase C. The fault current is shown in fig.-7. During fault condition currents at different phases are totally unbalanced. So phase imbalance must be created during fault condition.

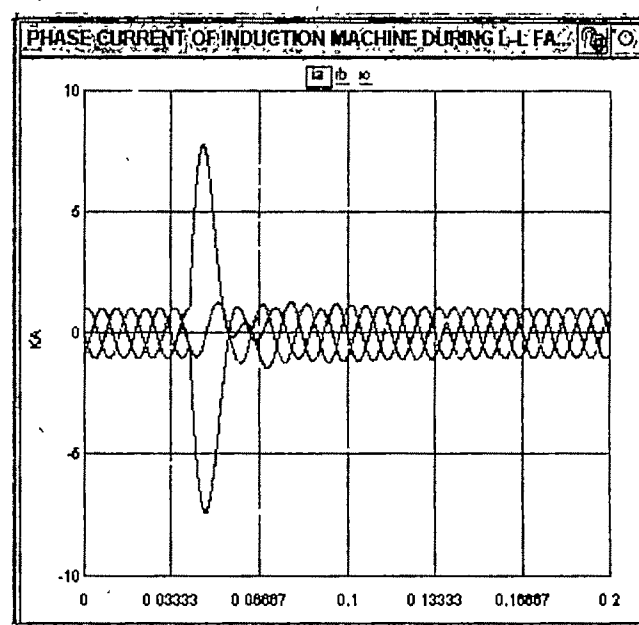


Fig.-6, Phase current of induction machine during L-L fault

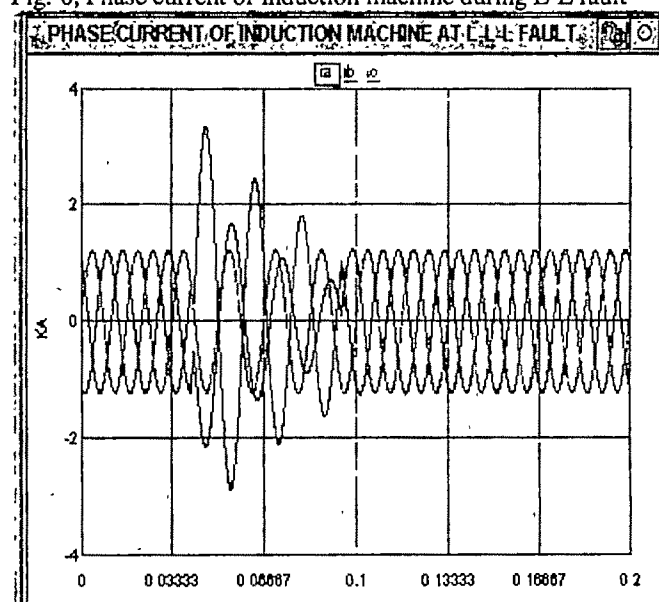


Fig.-7, Phase current of induction machine during L-L-L fault.

Table 1 gives the result of over Current in Power System Network due to different fault conditions as obtained using RTDS.

Cause	Normal Condition	120% overload condition	Line to Line (LL) fault	Line to line ground fault
Current (KA) (Maximum value)	1.0	1.2	7.8	Ia=3.8 Ib=1.8 Ic=1.0

Table 1: Results at different fault condition

VI.CONCLUSION

The following are the major inferences may be made .

1. The cause of over current in a particular busbar can be detected whether it is due to overload or fault situation.
2. The type of fault occurred can also be detected with the help of this RTDS power system simulating software.
3. Sequence component tool can also be utilized to categorise the fault or healthy condition.
4. Using DOPTO card different protection schemes can be adopted depending on the type of faults and simulation result can be visualised.

ACKNOWLEDGEMENT

The authors acknowledge the support provided by the University of Calcutta and also the TEQUIP fund for providing the RTDS Lab to carry out this research work.

REFERENCES:

- [1] Thiringer, "Comparison of Reduced Order Dynamic Models of Induction Machine" IEEE Tran. on Power System ,Vol -16, No-1, Feb. 2001
- [2] RTDS manual, RTDS Technologies, Manitoba.
- [3] Rosendahl, G.K., Wierckx, R.P., Maguire, T.L., Woodford, D.A., "A Parallel Machine for Real-Time PowerSystem Simulations". Canadian Conference on Electrical and Computer Engineering, Montreal, September, 1989.
- [4] Brandt, D., Wachal, R., Valiquette, R., Wiercks. R., "Closed loop testing of a joint var controller using a digital real-time simulator", IEEE PES Winter Power Meeting, New York, February 1991. Paper 91WM 240-242.

Technical Session 2D

Fuzzy Logic Applications

An approach for translation of Fuzzy Petri nets to Ladder Logic Diagrams

P.R. Venkateswaran¹, Jayadev Bhat², and S.Meenatchisundaram³

^{1&3} Instrumentation and Control Engineering Department, Manipal Institute of Technology, Manipal, INDIA, e-mail: prv_i@yahoo.com

² Chemical Engineering Department, Manipal Institute of Technology, Manipal, INDIA

Abstract— Discrete Event Systems are identified as systems which may change state over time, based on current state and state-transition rules, and where each state is separated from its neighbor by a step rather than a continuum of intermediate infinitesimal states. Often falling into this classification are information systems, operating systems, networking protocols, banking systems, business processes and telecommunications systems. Fuzzy Petri nets replaces conventional Petri nets for modeling Discrete Event Systems for better representation and description. This paper identifies logic for translation of fuzzy Petri net formalism for ladder code generation. The methodology derived from the analog operations available in a Siemens PLC and it can be shown from the results that the logic is universal and is applicable over all Programmable Logic Controllers.

Key words—Fuzzy Petri nets, Ladder Logic Diagrams, Programmable Logic Controller

I. INTRODUCTION

DISCRETE Event Systems present a challenging option to controller synthesis because they exhibit properties of concurrency, hybrid and sometimes, uncertainty. Hence, it is important to streamline the understanding of the flow of events in a Discrete Event System [1] and accordingly devise a controller. Fuzzy Petri net (FPN) [2] helps in handling the modeling of DES inclusive of uncertainties and vagueness. [3], [4] explains some typical framework for using FPN. The controller is synthesized from the model using supervisory control theory suggested in [5]. If the selected DES is in manufacturing or process control domain, then the controller is exercised through Programmable Logic Controller (PLC). PLC is an electronic device capable of executing decisions in sequential manner as programmed. [6] – [8] gives some of the application and issues arising out of implementation of controllers using PLC. The approaches followed in the literature can be consolidated as in Figure 1. Unfortunately, this approach is met with difficulties as listed, for example, in [6]. [7] approaches the design in a different way by providing a translation from Petri nets to Ladder Logic Programming for PLC. Since Petri net is insufficient to handle the mapping of DES into a model [3], FPN is chosen for modeling. When FPN

is chosen, the translation stated in [7] becomes invalid. This paper provides a valid translation for such cases with justification.

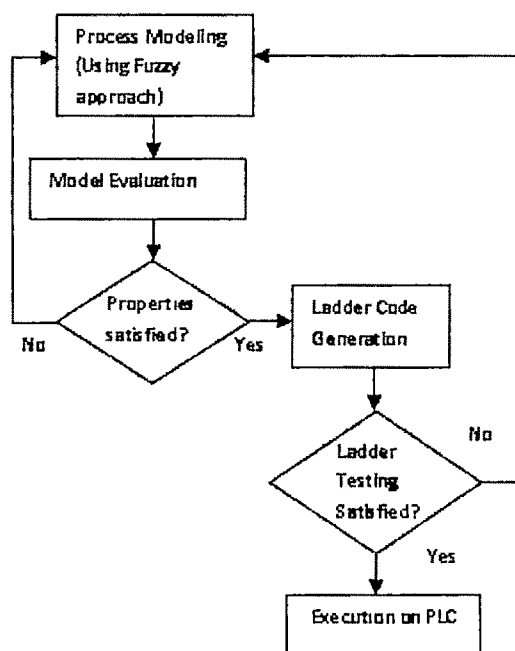


Fig.1. Approach to Controller design in FMS as DES.

II. FPN TO LLD CONVERSION

A. Fuzzy Petri nets

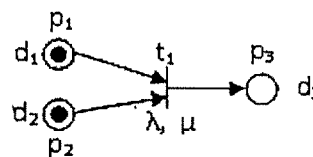


Fig.2. Fuzzy Petri net formalism

The graphical representation of Fuzzy Petri net is in Figure 2. Here, place p represents a proposition, transition t represents a fuzzy rule, arcs represent the relationship between a proposition and a rule and a token value is a truth state of the

proposition represents a fact. μ corresponds certainty factor which will determine the final truth value of the proposition. λ is the threshold value for the transition. If the result operation between two truth values d_1 and d_2 falls below the threshold, then the transition will not fire. The weights for the proposition of the model, the backward reasoning algorithm using this FPN model, membership functions for the model are discussed in [9], [4], [11] respectively.

B. FPN formalisms

The rule t in FPN is of the form:

IF A is A_i (for a time of T_i) and B is B_i **THEN** C is C_i (after time T_i).

This is a simple but important statement that needs to be understood clearly. Let us take the statement per se. The antecedent combines two conditions and the consequent is based on the result of these two conditions of antecedent. The question is what is meant by *combining* antecedents to map consequents. The logic that is likely to be used for deducing such *combination* in fuzzy is generalized into four forms for FPN in [11].

C. Translation of FPN into LLD

The logic of translation of FPN into LLD is listed in Table 1. [11] is used as reference for different types of rule structures provided. μ_i is used as a multiplier or as a threshold in different formalisms. Accordingly the logic may have to be adjusted in the operator as a compare operator like \leq instead of $|*$ as indicated here. In fact, in LLD parlance, the symbol $|*$ does not exist. For this work, it is unlikely a threshold will be introduced (value assigned is zero) and the symbol $|*$ is only indicative. The max and min operations are to be achieved by using sorting process as presently there is no provision for such logic in PLC.

D. Translation logic

Let Type 1 rule be considered for implementation. The case illustrates a set of inputs $d_{11}, d_{12}, d_{13} \dots d_{1n}$ represented logical AND operation. Conventional AND logic states that the output is true when all inputs are true. Translated into fuzzy relation (mamdani), the output will be the minimum of all input values. When the fuzzified input values are available, they are fed into the table in descending order. Then using sorting operation, the least value of the set is taken out for output. The box indicating *min* operation is in fact a combination of two operations here: *Table* and *Sort* operators. The output can be normalized with an associated weight μ_i as the multiplication factor. Table and Sort algorithms can be written as subroutines to be accessed.

III. IMPLEMENTATION

The first proposition (Type 1 rule) is taken for illustrative example for implementation. It is stated as follows:

Type 1: If d_1 AND d_2 , THEN d_3

In general, if we can deduce the logic for logical AND and logical OR, then it will be possible to execute all types of

rules. Type 1 stands for the execution of logical AND operation. The implementation of continuous fuzzy operation is possible if only if the Programmable Logic Controller has an analog extension module. All the instructions that are followed in this paper correspond to Siemens CPU226, EM231/232 and Step 7 V4.0 software. The case considered is for two inputs only and hence illustrated here with the program statement. Since only two values are received as inputs, they are stores at AIW0 and AIW2 using the MOVE instruction. They they are compared and the result is moved to the location AQW0.

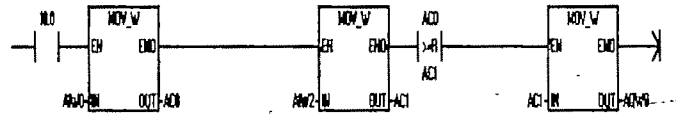


Figure 3. Implementation of AND logic using LLD (Rung 1)

The truth values d_1 and d_2 of place p_1 and p_2 are represented by inputs AIW0 and AIW2 respectively in word format. The input truth values are stored in AC0 and AC1 which are accumulator registers. The compare instruction compares the values and if AC0 is greater than AC1, then the value in AC1 is moved to the output register AQW0. If not, the following line of the program will provide AC0 as the output. Thus, the AND logic is simulated by converting the fuzzy Petri net model into a ladder logic program using the instructions available in the PLC instruction set [12].

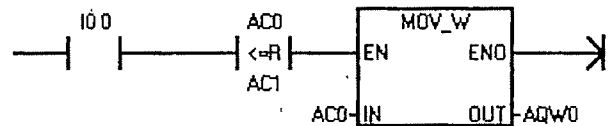


Figure 4. Implementation of AND logic using LLD (Rung 2)

The threshold is assumed to be zero. If any other threshold value is to be provided, another compare instruction can be introduced between the output and the result value. I0.0 is used as the enable switch for the operation. In a similar manner, the logic for rest of the types in the Table can be implemented.

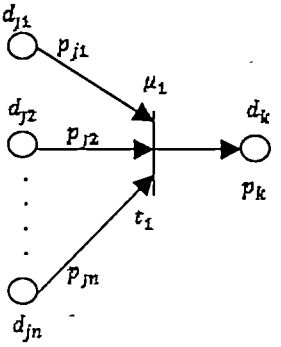
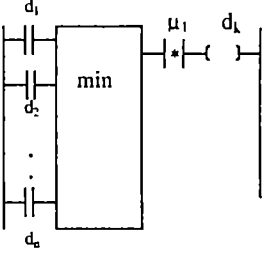
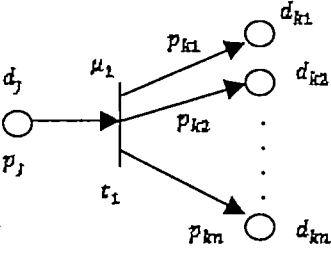
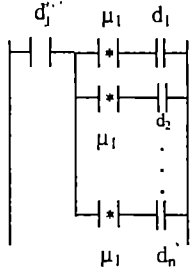
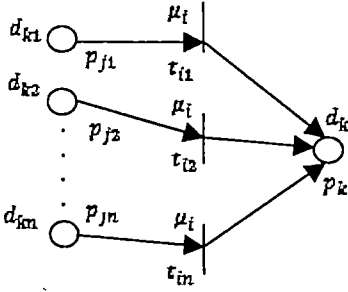
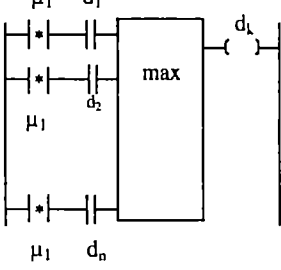
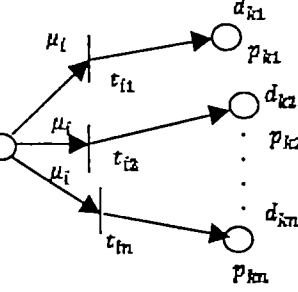
IV. CONCLUSION

The conversion of fuzzy Petri net formalism into ladder logic program for implementation in Programmable Logic Controller is suggested. It was implemented in Siemens S7 200 CPU226 PLC with analog modules EM231/232. The advantage of the suggested method is that it can be implemented using the simplest of PLC programming language. The possible drawback is the inconsistency of instructions across various manufacturers which may alter the implementation logic.

ACKNOWLEDGMENT

The first author gratefully acknowledges Dr. Narayana Iyer, Dean, R&D, NMAMIT, NITTE for his inspiring discussions on the topic of fuzziness in discrete event systems.

Table 1. Type of Fuzzy Logical Formalisms and suggested LLD Translation

S.No.	Logical Formalism	Fuzzy Petri net Formalism	Suggested LLD Translation
1.	Type 1 rule: $d_k = \min (d_{j1}, d_{j2}, \dots, d_{jn}) * \mu_i$		
2.	Type 2 rule: $d_{kn} = d_j * \mu_i$		
3.	Type 3 rule: $y_k = \max (y_{j1} * \mu_1, y_{j2} * \mu_1, \dots, y_{jn})$		
4.	Type 4 rule: <i>If d_j THEN d_k1 or d_k2) ...</i>		Rules of this type are normally unsuitable for control as they do not have specific implications [11]. Hence not pursued.

V. REFERENCES

- [1] Ard Overkamp and Jan H. van Schuppen, Control of Discrete Event Systems. Report BS – R9503, Department of Operations Research, Statistics and System Theory, National Institute for Mathematics and Computer Science, Amsterdam.
- [2] J. Cardoso, R. Valette, Didier Dubois Fuzzy Petri nets – An Overview, CNPq – Brazil grant #2000649/85-0.
- [3] A. J. Bugarin and Senen Barro, 'Fuzzy reasoning supported by Petri nets', IEEE Trans. on Fuzzy Syst. Vol.2, no.2, May 1994, pp.295-301.
- [4] W. Pedrycz, F. Gomide, 'A generalized Fuzzy Petri net Model', IEEE Tran. on Fuzzy Syst. vol 2, no.1, November 1994, pp 295-301.
- [5] P.J. Ramadage and W.M. Wonham, The Control of Discrete Event Systems, Proceedings of the IEEE, Vol.77, No.1, January 1989, pp.81 – 98.
- [6] Anders Hellgren, On the Implementation of Discrete Event Supervisory Control with focus on flexible Manufacturing Systems, Technical Report No. 422, Control and Automation Laboratory, Department of Signals and Systems, Chalmers University of Technology, Sweden, 2002.
- [7] Uzam, A.H. Jones, 'Discrete event control system design using Automation Petri nets and their ladder diagram implementation', In International Journal of Advanced Manufacturing systems, Special issue on Petri nets Applications in Manufacturing systems, vol.14, no 10, October 1998, pp 716-728.
- [8] D. Andreu, J.C. Pascal, R. Valette, 'Fuzzy Petri net based Programmable Logic Controller', ' IEEE Trans. on Syst. Man and Cybern Vol.27, no 6, December 1997, pp.952-961.
- [9] S M Chen, "Fuzzy backward reasoning using fuzzy Petri nets", IEEE Transactions on Systems, Man and Cybernetics (Part B), Vol.30, No.6, pp 846-856, Dec. 2000.
- [10] P Srinivasan and D. Gracanin, "Appropriate reasoning with fuzzy Petri nets", Proceedings of 2nd IEEE International conference on fuzzy systems, San Francisco, Vol.2, pp.396-401, Mar.1993
- [11] Shyi Ming Chen et al, Knowledge representation using Fuzzy Petri nets, IEEE Transactions on Knowledge and Data Engineering, Vol.2, No.3, September 1990, pp.311 – 319.
- [12] Siemens S7200 Manual, 2005.

An Approach to Relate and Optimize Metal Forming Process Parameters by Fuzzy Logic

S.L. Mahmood¹, Fazilatunnessa², M. H. Banna¹, M. Raju Hossain¹

¹ Department of Mechanical & Chemical Engineering, Islamic University of Technology (IUT), Board Bazar, Gazipur-1704, Dhaka, Bangladesh. mrajuh@msn.com, banna@iut-dhaka.edu

² Department of Computer Science and Engineering, Ahsanullah University of Science and Technology saimon@iut-dhaka.edu.

Abstract— Production of the desired shape is a significant part of the manufacturing process but the process is substantially nonlinear and mathematical model is very difficult to obtain. In this paper an attempt is made to show how to inter-relate the metal forming process parameters and optimize the input parameters (e.g. different types of forces) by adopting fuzzy logic. The inter-relation is done, by developing the fuzzy patches between input and output (product geometry) parameters and from there, the optimum process parameters can be computed. A method for determining the working conditions in the deep-drawing process by combining a method of optimization and Finite Element simulation is also included in this study.

Key words— Optimization; Metal forming process, Fuzzy logic, Simulation

I. INTRODUCTION

In forming processes the desired shape and size of an object are obtained through plastic deformation of materials. This is a very economical process as the desired shape, size and finish can be obtained without any significant loss of materials. Moreover apart of the input energy is fruitfully utilized in improving the strength of the product through work hardening [1]. Deformation processes exploits a remarkable property of metals – their ability to flow physically in the solid state without deterioration of properties. By simply moving the material to the desired shape, as opposed to removing the unwanted regions, there is little or no waste. The required forces however are often high. But the main problem involved in metal forming process is to predict the most suitable quantities of the process parameters which will produce the most satisfactory outcome.

Fuzzy logic is the most classical soft computing mathematical tool, that trades off between the imprecision and uncertainty on one hand and low solution cost, tractability and robustness on the other. Fuzzy logic uses the whole interval between 0

(False) and 1 (True) to describe any process parameters [2]. It is a system of logic developed for representing conditions that deal with degrees of membership and degrees of truth (cannot be easily described by the binary terms true and false). Fuzzy logic is determined as a set of mathematical principles for knowledge representation based on degree of membership. Thus, fuzzy logic is a very suitable solution to predict and optimize the process parameters in metal forming process in order to obtain the desired product geometry.

II. FEM SIMULATION

To complete the scheme for the development of finite element simulation, a preprocessor and a universal post processor development work is going on. A typical post processor developed in this project is shown in Figure 1.

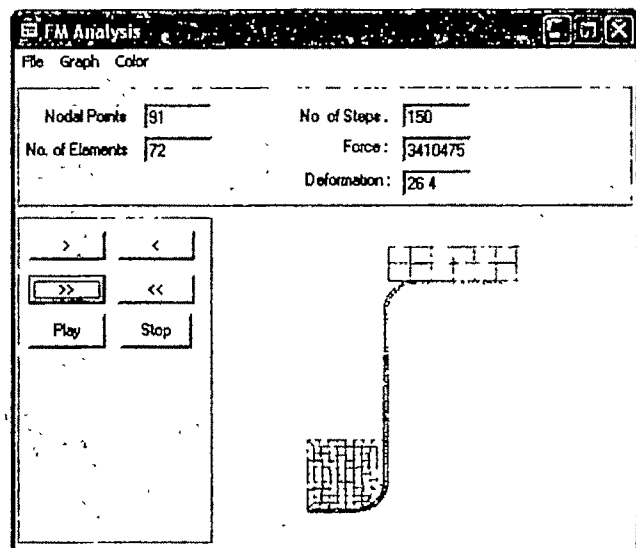


Figure 1 Development of a post processor for metal forming process.

III. METAL FORMING PROCESS

Metal forming process can be defined as a process in which plastic deformation of material takes place when the applied stress level exceeds a certain limit defined as yield stress. The stresses induced during the process are greater than the yield strength, but less than the fracture of the material. The typical forming processes are rolling, forging, drawing, deep drawing, bending and extrusion.

Variables involved in metal forming process

In general forming processes tend to be complex systems consisting of independent variables, dependent variables, and independent-dependent interrelations.

Independent variables are those aspects of the process which are generally selected or specified when setting up the process. Some of the independent variables are starting material, starting work piece geometry, tool or die geometry, starting temperature, speed of operation, amount of deformation etc.

After the deformation, the independent variables are specified and the process then determines the nature and values for a second set of variables known as dependent variables. Examples of these include forces and power requirements (also known as input parameters), material properties of the product, exit temperature, surface finish and precision (also known as output parameters), the nature of material flow etc.

IV. GENERAL APPROACH IN FUZZY LOGIC

Membership Function

The set of elements that have a non-zero membership is called the support of the fuzzy set. The function that ties a number to each element x of the universe is called the membership function $\mu(x)$. There are two alternative ways to represent a membership function in a computer, continuous or discrete. In the continuous form, the membership function is a mathematical function, possibly a program, which is used in this study. A membership function is for example may be bell-shaped (also called a Π curve), s-shaped (called an s curve), a reverse s-curve (called z curve), triangular, or trapezoidal. In this method membership function of each process parameters are plotted within the interval of 0 to 1. In the discrete form the membership function and the universe are discrete points in a list (vector). Sometimes it can be more convenient with a sampled (discrete) representation.

Fuzzy modeling

General approach in fuzzy modeling is to define the variables of relevance (in metal forming process which are called input and output process parameters) and define the subset intervals (Small - Medium, or Negative - Positive, or Left - Right). From there, shapes and the positions of fuzzy subsets therefore membership functions are chosen, through which fuzzy rules (If-then rules) are implemented.

The possible dependencies of the process parameters in metal forming process can be represented by the pattern recognition and classification shown in figure 2.

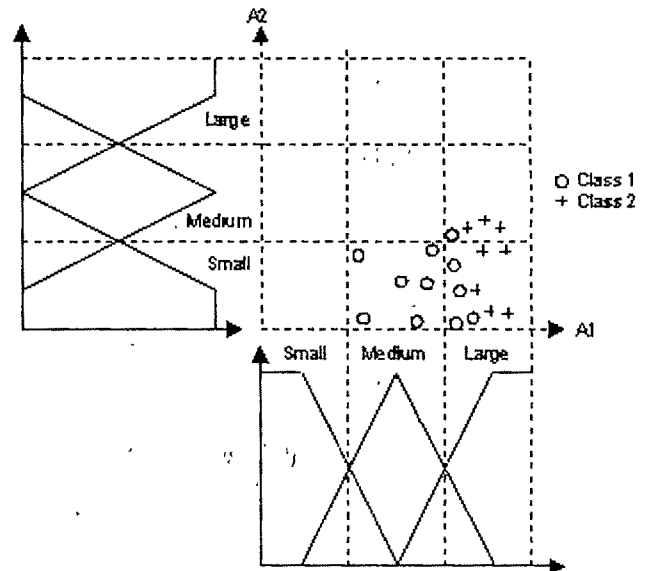


Figure 2 Pattern recognition and classification

Curve fitting procedure

Standard mathematical procedure of curve fitting results in a more or less acceptable solution. It is usually done by using fuzzy rules (patches). An increase in a number of rules increases the precision at the cost of a computation time needed to process more rules. This is the most classical soft computing dilemma that trades off between the imprecision and uncertainty on one hand and low solution cost, tractability and robustness on the other. A function covered by three patches produced by IF-THEN rules and modeled by two possible approximations (dashed and dotted curves) is shown in figure 3 by a solid line.

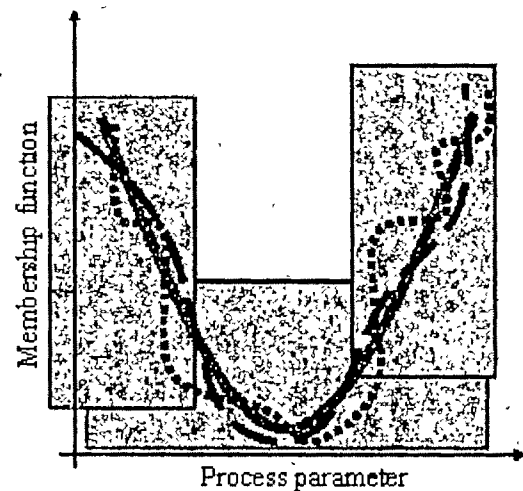


Figure 3 Standard mathematical curve fitting

In this paper polynomial regression fits data to the equation given below,

$$Y = A + B X + C X^2 + D \cdot X^3 + E \cdot X^4$$

here, Y is membership function, X is process parameter and A, B, C, \dots are constants.

V. CONTROL STRATEGY

Fuzzy logic may be considered as an assortment of decision-makings. The algorithm's outcome is ruled by a number of key decisions which are made in the algorithm. An extensive knowledge of the system is required to define the best decision. For the present project the problem is decomposed into a number of possible decisions by associating fuzzy logic functions with predefined input and output. The accuracy of the system depends on how many functions and how many rules are implemented. For example, in deep drawing process the most interesting thing is that fuzzy logic enables better optimization of the presence of strong disturbances (non-linearity) and the time varying parameters of the process. The fuzzy-program includes three stages [3], Input processing (Fuzzification); Control algorithms (Inference); Output processing (Defuzzification).

Control algorithm

The algorithm of the control program is shown in figure 4

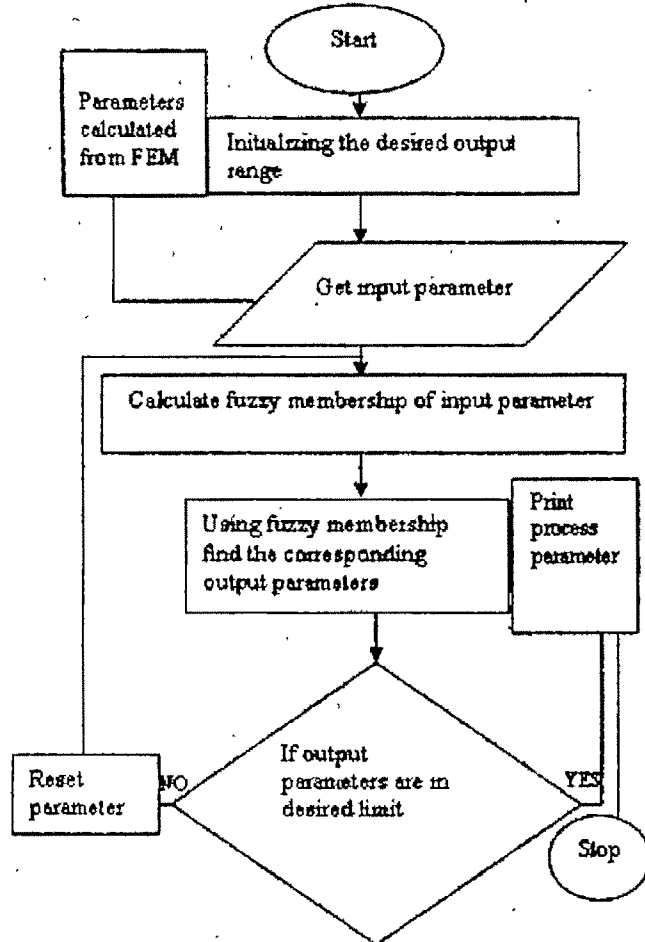


Figure 4 Algorithm used in the program for the prediction of optimized process parameters

Control description

The control program reads the input process parameters sent by simulation computer. In each simulation time step the

control program calculates the desired output for that step and then draws fuzzy triangles for both output and input parameters against the membership function shown in figure 5. Each time these functions are used as inputs for the fuzzy module. The control program calls the fuzzy module which calculates optimized input to ensure the desired output for that step. At the same time output parameter of the fuzzy module are sent to the simulation computer to start the next simulation step.

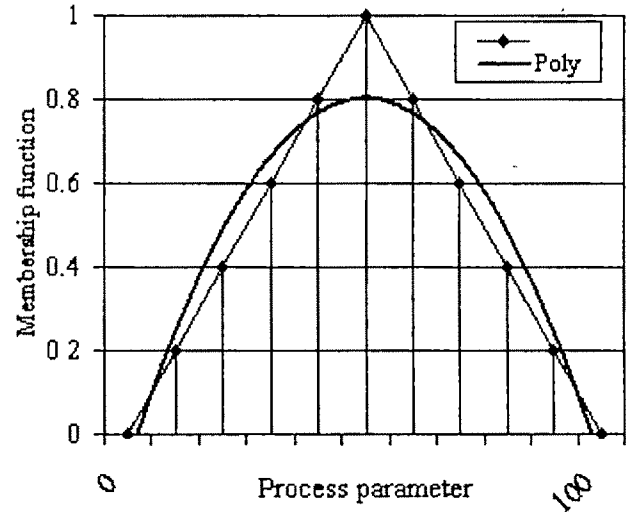


Figure 5 Adjectives of the consequent

The control is implemented by fuzzy PI. The classic PID control is defined by the error, its increments and its rates of integration in the following way [4, 5]:

$$e(n) = r(n) - y(n)$$

$$\Delta e(n) = e(n) - e(n-1)$$

$$u(n) = K_p \cdot e(n) + K_D \cdot \Delta e(n) + K_I \cdot \sum_{m=0}^n e(m)$$

The increment of the output signal is,

$$\Delta u(n) = u(n) - u(n-1)$$

$$\Delta u(n) = K_p \cdot \Delta e(n) + K_D \cdot \Delta^2 e(n) + K_I \cdot e(n)$$

Then in the fuzzy PI control the antecedents are $e(n)$ and $\Delta e(n)$ and the fuzzy output is $\Delta u(n)$.

VI. PREDICTION AND OPTIMIZATION OF PROCESS PARAMETERS IN DEEP DRAWING PREOCESS

Deep drawing (shown in figure 5) is a process in which a blank is forced into or through a die by a punch to form a hollow component that has essentially the same thickness as the original material. The most critical region of a deep drawn cup is the flange because of the circumferential stresses involved.

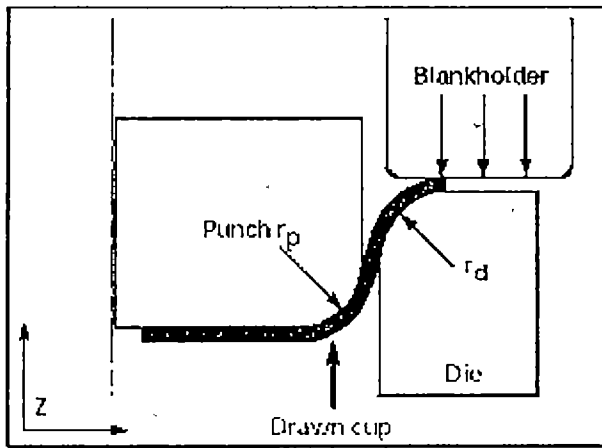


Figure 5 Die blank-holders and punch geometry

In deep drawing process, optimization of punch force and blank holder force is mandatory to ensure uniform thickness distribution throughout the drawn cup. Thus in this study punch force & blank holding force are considered as input variables and sheet thickness is considered as output variable.

Mathematical relationships

$$F = \sigma_r (e^{\mu n/2}) 2\pi R_p t$$

$$\left[P_H = 10^{-3} c[(DR-1)^3 + \frac{0.005d_0}{t}] \right]$$

$$\sigma_r = \mu P_H / \pi r_j t + 2k \ln(r_j / R_d)$$

$$P_H = \beta \pi r_j K$$

Computation software

Optimization software has been developed and interfaced with the preprocessor of the FEM scheme.

In this software, at first the range of the desired sheet thickness (in mm) is given as input as shown in figure 6. The software then determines the membership function for each thickness within the desired range and automatically plots the thickness vs membership function, which is a triangular shaped curve as shown in figure 7. It can also set the best fitted polynomial curve with the triangle and can generate the governing equation of the polynomial curve.

Similarly, using the above equations, the software then calculates the corresponding punch force & blank holding force and plot membership function against punch force and blank holding force.

Based on figure 4, algorithm is set in the program and the decisions are made using the polynomial equations shown in figure 7, 8 & 9. Figure 10 shows the calculation of the thickness based on optimized punch and blank holding force.

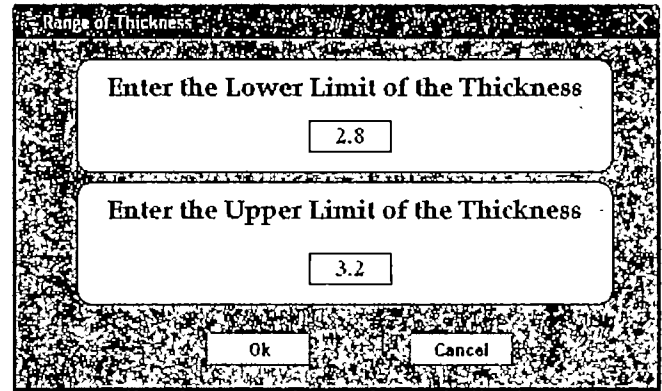


Figure 6 Allowable thickness range input window

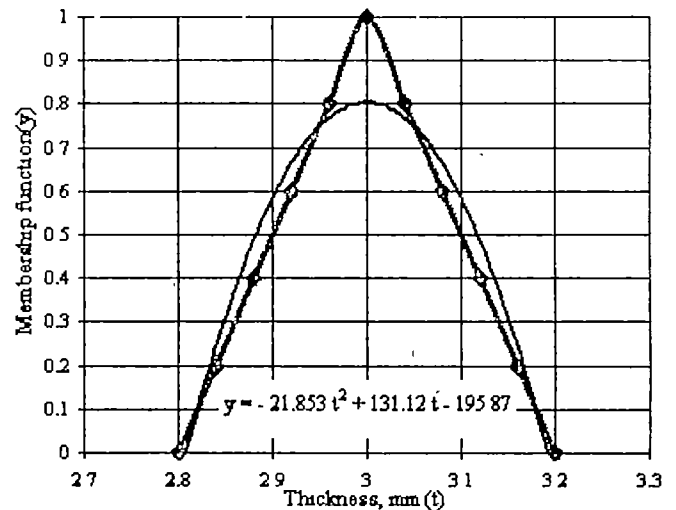


Figure 7 Thickness vs Membership function

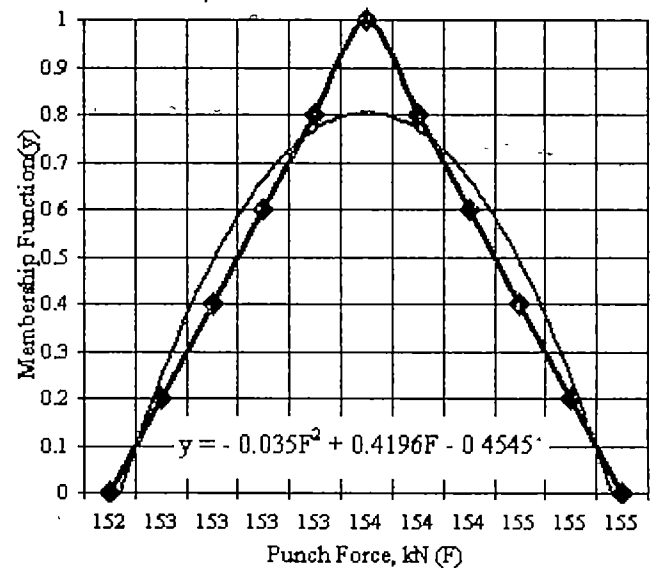


Figure 8 Punch force vs Membership function

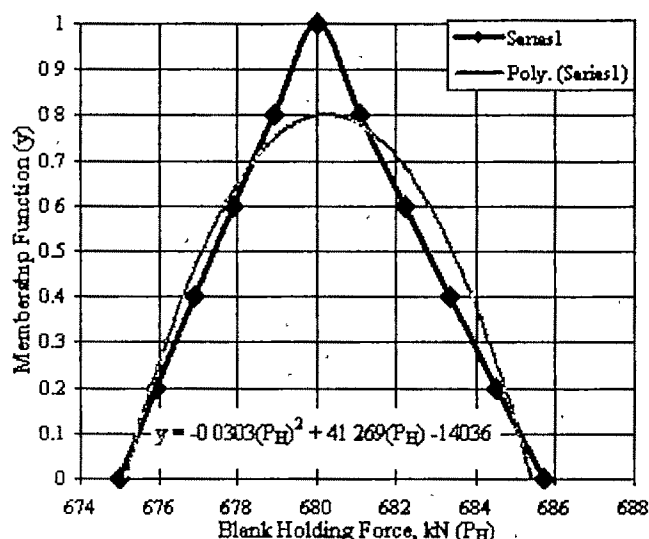


Figure 9 Blank holding force vs Membership function

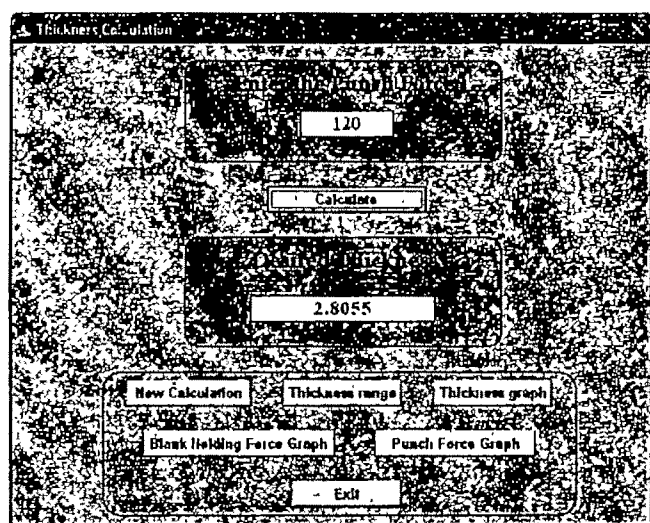


Figure 10 Thickness calculation window

VII. CONCLUSION

In metal forming process the required geometric shape and structure can be achieved by successful implementation of fuzzy logic, no matter how nonlinear the process is. But the problem that may arise is that, increasing the number of inputs increases the number of rules & computation time exponentially. Another major problem is the right choice of the variables. Successful implementation of fuzzy logic provides highly precision metal forming process. With the possibility of directly sensing work piece conditions during forming operations, it is conceivable that these measurements could be fed back to the metal-forming equipment for computer control of the forming equipment, thereby enabling real-time compensation for variations in initial work piece and equipment conditions.

VIII. REFERENCES

- [1] Kyung K. Choi, Nam H. Kim "Design optimization of Deep drawing process", American institute of Aeronautics and Astronautics", 4747, 1 – 5, 2000.
- [2] Zadeh, L. A. Fuzzy sets, *Inf. and control* 8: 338–353, 1965.
- [3] Geortchev V., R.Krusteva, D.Butcharov : "Fuzzy Logic Approach to Sensor Fusion" Proceedings of 2nd International Mechatronic Design and Modeling Workshop. METU. Ankara. TURKEY, 1995.
- [4] M.Mizumoto. "Realization of PID Controls by Fuzzy Control Methods" Fuzzy Sets and Systems, 70, 171-182, 1995.
- [5] C.L. Chen, P.C. Chen, C.K. Chen. "Analysis and design of Fuzzy control System." Fuzzy sets and systems, 57, 125-140, 1993.

IX. NOMENCLATURE

n	time instant
$e(n)$	objective function error
$r(n)$	target objective function value
$y(n)$	objective function value in n instant
$\Delta e(n)$	change rate of error
$u(n)$	control output
$\Delta u(n)$	change rate of control output
K_P	proportional gain
K_D	differential gain
K_I	integral gain
F	punch force
P_H	blank holder pressure
c	an empirical factor ranging from 2 to 3
DR	draw ratio (draw depth/punch diameter)
d_0	blank diameter
S_u	ultimate tensile strength
σ_r	radial stress
R_d	radius of the die
β	empirical factor ranging from .02 - .08
K	shear yield stress
μ	friction co-efficient (lets take 0.1)
R_p	radius of the punch
t	thickness of the sheet
r_j	radius of job
r_p	punch corner radius,
r_d	die corner radius,
r_o	blank radius,
C	clearance

Selection of Membership Functions in the Prediction of Shoot Length of Mustard Plant at Maturity

Satyendra Nath Mandal¹, J. Pal Choudhury², Dilip De³ and S. K. Mukherjee⁴

¹Kalyani Govt. Engg College/ Dept of I T, Kalyani, Nadia(W.B),India, satyen_kgec@rediffmail.com

²Kalyani Govt Engg College/ Dept. of I.T, Kalyani, Nadia(W.B),India, jnpc193@yahoo.com

³Bidhan Chandra Krishi Viswavidyalay, Kalyani, Nadia(W B),India,dilipde_bckv@gmail.com

⁴B. I T Mesra, Ranchi (Jharkhand),India, skmukherjee@bitmesra.ac.in

Abstract— The main objective of plantation is to produce maximum amount of fruit in any fields. By observing, the growth of initial stage, it is very difficult to ascertain the amount of fruits(in terms of seeds weight) of a mustard plant at maturity. The seeds weight of mustard plant at maturity dependent on some parameters of that plant, these are shoot length, number of leaves, number of roots and roots length etc. As the plant is growing, some leaves may be fall down and some new leaves may come, so it can not gives the idea to develop the relationship with the seeds weight at mature stage of that plant. It is not possible to find the number of roots and root length of mustard plant at growing stage, that will be harmful of this plant as roots goes deeper to deeper inside the land. Only the value of shoot length which increases in course of time can be measured at different time instances. As the growth of the plant is very uncertain, fuzzy environment can be considered for the prediction of Shoot length at maturity of the plant. Fuzzification plays a greater role for fuzzification of data, which is based on certain membership functions. Here an effort has been made to fuzzify the original data based on gaussian function, triangular function, and s-function . After that all fuzzified data are defuzzified to get normal form. Finally the error analysis(calculation of forecasting error and average error) indicates the membership function appropriate for fuzzification of data and use to predict the shoot length at maturity.

Key words— Fuzzification, defuzzification, gaussian function, triangular function, trapezoidal function, membership function

1 INTRODUCTION

IN the modern world, the activities of agriculture have a major role in the field of economy of the state as well as a of the country. But uncertainty exists in all the activities of agriculture. The farmer can not predict the amount of seeds to be produced at maturity of plants which they cultivate. Although, the amount of seeds of a plant at the stage of maturity depends on various parameter of that plant. Among them, the shoot length only gives the idea about the growth of

the plant. It gives the idea whether the plant is healthy or not. If the plant is not growing healthy, it must be destroyed otherwise that should be protected. In this paper, an effort has been made to predict the growth of shoot length using the

different fuzzy membership function and finally one of them is selected based on minimum error.

In order to handle the fuzzy data, it is necessary to convert the actual data into fuzzy data based on certain membership functions. Here the three membership functions e.g. trapezoidal, gaussian triangular, S-shapped and L-shapped functions are used. Now it is necessary to find out which of these membership functions is suitable for this shoot length data

A lot of research work has been carried out in the field of forecasting([1] - [5], [7] - [9], [11] - [14]), out of these certain work has been done using fuzzy logic ([1] - [5], [11] - [13]). Research work using neural networks has been done([6], [8] - [10], [14]). Work in the field of genetic algorithm has been carried on ([16], [18], [23]).

In the field of fuzzy logic, the fuzzification plays a greater role. The work related to the type of membership function used for fuzzification has not been done in agriculture field so far, That is the reason for making this effort in this paper.

A statistical survey has been conducted by a group of certain agricultural personnel on different mustard plant under the supervision of Prof. Dilip dey, Bidhan Chandra Krishi Viswavidyalay West Bengal, India. The data for shoot length of the initial stage(growing stage) of the plant are also available, which are measured at different time instances(after an interval of 7 days, 14 days, 21 days, 28 days). The ultimate aim is to select a suitable membership in fuzzy model which gives minimum error and estimated which plant is growing as per desire standard . These plant must be protected other wise it is to be destroyed. In this paper the models of fuzzy time series with different membership function have been tested on a particular type mustard plant and based on error analysis (calculation of average error) that membership function with minimum error is selected and that will be the suitable membership function to estimated the growth of mustard plant.

II. METHODOLOGY

A. Fuzzy Systems.

The characteristic function of a crisp set assigns a value of either 1 or 0 to each individual in the universal set, thereby discriminating members and nonmembers of the crisp set under consideration. This function can be generalized such that the value assigned to the elements of the universal set fall within a specific range and indicate the membership grade of these elements in the set in question. Larger values denote higher degrees of set membership. Such a function is called a membership function and the set defined by it a fuzzy set.

The range of values of membership functions is the unit interval [0, 1]. Here each membership function maps elements of a given universal set X, which is always a crisp set, into real numbers in [0, 1].

The membership function of a fuzzy set A is defined by $A: X \rightarrow [0, 1]$.

B. Fuzzy Time Series

Let $Y(t)$ ($t = \dots, 0, 1, 2, \dots$), a subset of R' , be the universe discourse on which fuzzy sets $f_i(t)$ ($i = 1, 2, \dots$) are defined and $F(t)$ is a collection of $f_1(t), f_2(t), \dots$. Then $F(t)$ is called a Fuzzy Time Series defined on $Y(t)$ ($t = \dots, 0, 1, 2, \dots$).

C. Functions for Fuzzification.

A Gaussian membership function is defined by

$$G(u; m, \sigma) = \exp\left[-\frac{(u-m)^2}{2\sigma^2}\right]$$

Where the parameters m and σ control the center and width of the membership function. A plot of the Gaussian membership function is presented in fig. 1.1

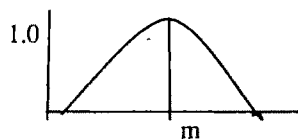


fig1.1. One typical form of the Gaussian function.

The Triangular membership function with straight lines can formally be defined as follows:

$$\begin{aligned} \Lambda(u; \alpha, \beta, \gamma) &= 0 & u < \alpha \\ &= (u - \alpha) / (\beta - \alpha) & \alpha \leq u \leq \beta \\ &= (\gamma - u) / (\gamma - \beta) & \beta \leq u \leq \gamma \\ &= 0 & u > \gamma \end{aligned}$$

One typical plot of the triangular membership function is given in fig 1.2

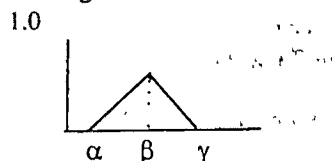


Fig1.2: One typical form of the Triangular membership function

Trapezoidal Function Furnished in figure 2

$$\begin{aligned} f(x, a, b, c, d) &= 0 & \text{when } x < a \text{ and } x > d \\ &= (x - a) / (b - a) & \text{when } a \leq x \leq b \\ &= 1 & \text{when } b \leq x \leq c \\ &= (d - x) / (d - c) & \text{when } c \leq x \leq d \end{aligned}$$

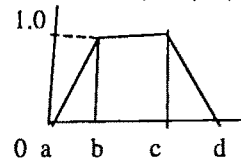


Fig 1.3 One typical form of the trapezoidal membership function

S-shaped built-in membership function s-shaped built-in membership function

$$\begin{aligned} S(u; \alpha, \beta, \gamma) &= 0 & u < \alpha \\ &= 2[(u - \alpha) / (\gamma - \alpha)]^2 & \alpha \leq u \leq \beta \\ &= 1 - 2[(u - \gamma) / (\gamma - \alpha)]^2 & \beta \leq u \leq \gamma \\ &= 1 & u > \gamma \end{aligned}$$

One typical form of the S-function is presented below

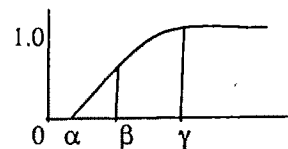


Fig 1.4 One typical form of the S-shaped membership function

This function is the converse of the typical γ -function. It can be mathematically expressed by

$$\begin{aligned} L(u; \alpha, \beta) &= 1 & u < \alpha \\ &= (\alpha - u) / (\beta - \alpha) & \alpha \leq u \leq \beta \\ &= 0 & u > \beta \end{aligned}$$

One typical form of the L-function is presented in below

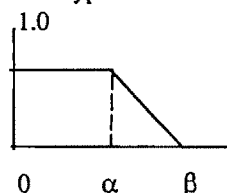


Fig 1.4 One typical form of the L-shaped membership function

The generalized Bell function depends on three parameters a, b , and c as given by

$$f(x; a, b, c) = 1 / (1 + ((x - c) / a)^{2b})$$

where the parameter b is usually positive. The parameter c locates the center of the curve.

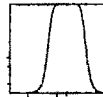


Fig 1.5 One typical form of the Bell membership function

D. Forecasting Error and Average Forecasting Error

The forecasted error and average forecasting error are calculated using the formula :-

Forecasting error = $[(\text{forecasted value} - \text{actual value}) / (\text{actual value})] \times 100 \%$

Average forecasting error = $(\text{sum of forecasting errors}) / (\text{total no of errors})$.

III. IMPLEMENTATION

Step 1.

The universe U is partitioned into five equal length(10) intervals. The intervals are chosen as $u_1 = [10, 20]$, $u_2 = [21, 30]$, $u_3 = [31, 40]$, $u_4 = [41, 50]$, $u_5 = [51, 60]$, $u_6 = [61, 70]$

Step 2.

The available data are fuzzified based on gaussian function which is furnished in Table I given below :-

Table I

Actual Shoot Length and Fuzzy Set							
Actual Shoot Length	A1	A2	A3	A4	A5	A6	Fuzzy Set
19	1.0	0.9	0.0	0.0	0.0	0.0	A1
24	0.6	1.0	0.4	0.0	0.0	0.0	A2
28	0.2	1.0	0.8	0.0	0.0	0.0	A2
33	0.0	0.7	1.0	0.3	0.0	0.0	A3
37	0.0	0.3	1.0	0.7	0.0	0.0	A3
41	0.0	0.0	0.9	1.0	0.1	0.0	A4
45	0.0	0.0	0.5	1.0	0.5	0.0	A4
49	0.0	0.0	0.1	1.0	0.9	0.0	A4
54	0.0	0.0	0.0	0.6	1.0	0.4	A5
57	0.0	0.0	0.0	0.3	1.0	0.7	A5
59	0.0	0.0	0.0	0.1	1.0	0.9	A5
63	0.0	0.0	0.0	0.0	0.7	1.0	A6
66	0.0	0.0	0.0	0.0	0.4	1.0	A6

Step 3.

The historical knowledge from Table I about the evolution of the shoot length is obtained to set up the forecasting model. The available data are transformed into linguistic values.

Using the symbols of Song and Chissom [3] , all the fuzzy logical relationships from Table I are obtained as follows :-

Table II

Fuzzy Logical Relationships

A1 \rightarrow A2 A2 \rightarrow A2 A2 \rightarrow A3 A3 \rightarrow A3
A3 \rightarrow A4 A4 \rightarrow A4 A4 \rightarrow A5 A5 \rightarrow A5
A5 \rightarrow A6 A6 \rightarrow A6

It is to note that the repeated relationships are counted for

only once.

Step 4.

By definition a time-invariant fuzzy time series has been developed([1], [3], [5]).

Let us define an operator 'X' of two vectors. Suppose C and B are row vectors of dimension m and $D = (d_{ij}) = C^T \times B$. Then the element d_{ij} of matrix D at row i and column j is defined as $d_{ij} = \min (C_i, B_j)$ (i, j = 1, , m) where C_i and B_j are the i-th and the j-th element of C and B respectively.

Let $R_1 = A_1^T \times A_2$, $R_2 = A_2^T \times A_3$, $R_3 = A_3^T \times A_4$, $R_4 = A_4^T \times A_5$, $R_5 = A_5^T \times A_6$, $R_6 = A_6^T \times A_7$, $R_7 = A_7^T \times A_8$, $R_8 = A_8^T \times A_9$, $R_9 = A_9^T \times A_{10}$, $R_{10} = A_{10}^T \times A_{11}$. Now a relation matrix R has been formed as $R(t, t-1) = R = U R_i$ (3) where U is the union operator.

The value of R as follows:-

0.6	1.0	0.6	0.2	0.0	0.0
0.6	1.0	1.0	0.7	0.1	0.0
0.2	0.7	1.0	1.0	0.5	0.1
0.0	0.3	0.7	1.0	1.0	0.6
0.0	0.0	0.1	0.6	1.0	1.0
0.0	0.0	0.0	0.3	0.7	1.0

Using R, the forecasting model is $A_i = A_{i-1} \cdot R$ where A_{i-1} is the shoot length of reading i - 1 and A_i is the forecasted shoot length of reading i and ' \cdot ' is the max - min operator.

Step 5.

The forecasted output is interpreted which are all fuzzy sets. Now it has been translated into a regular number(defuzzification). The predicted values for the shoot length are furnished in Table III.

Table III

Output Fuzzy Value and Estimated Value

Actual Shoot Length	Output Fuzzy Value	Estimated Value
19	-	-
24	[0.6 1.0 0.9 0.7 0.1 0.0]	25
28	[0.6 1.0 1.0 0.7 0.4 0.1]	30
33	[0.6 1.0 1.0 0.7 0.4 0.1]	30
37	[0.6 0.7 1.0 1.0 0.5 0.3]	40
41	[0.3 0.7 1.0 1.0 0.7 0.6]	40
45	[0.2 0.7 0.9 1.0 1.0 0.6]	50
49	[0.2 0.5 0.7 1.0 1.0 0.6]	50
54	[0.1 0.3 0.7 1.0 1.0 0.9]	50
57	[0.0 0.3 0.6 0.6 1.0 1.0]	60
59	[0.0 0.3 0.3 0.6 1.0 1.0]	60
63	[0.0 0.1 0.1 0.6 1.0 1.0]	60
66	[0.0 0.0 0.1 0.6 0.7 1.0]	65
	[0.0 0.0 0.0 0.4 0.7 1.0]	65

Step 6.

Finally the forecasted error and average forecasting error are calculated and furnished in Table IV. The average Error is 4.73 %

Table IV

Estimated Data and Error Based on Fuzzy Time Series using Gaussian function

Actual Value	Estimated Value	Error(%)
--------------	-----------------	----------

19	-	-
24	25	41.6
28	30	7.14
33	30	9.09
37	40	8.10
41	40	2.44
45	50	11.11
49	50	2.04
54	50	7.41
57	60	5.26
59	60	1.69
63	60	4.7
66	65	1.5
	65	

Average Error 4.73 %

The same effort has been applied using bell shaped, s-shaped, L shaped, trapezoidal, triangular membership functions. The results are as follows:-

Table -V

Estimated Data and Error Based on Fuzzy Time Series using bell shaped member function

Actual Value	Estimated Value	Estimated Error(%)
19	-	-
24	29	20.83
28	30	7.14
33	30	9.09
37	40	8.10
41	40	2.43
45	41	8.88
49	50	2.04
54	59	9.25
57	60	5.26
59	60	1.69
63	60	4.76
66	65	1.51
	65	

Average Error 6.23%

Table -VI

Estimated Data and Error Based on Fuzzy Time Series using S-shape member function

Actual Value	Estimated Value	Estimated error(%)
19	-	-
24	25	4.16
28	30	7.14
33	30	9.09
37	36	2.70
41	40	2.43
45	45	0
49	50	2.04
54	50	7.40
57	57	0
59	60	1.69
63	60	4.761
66	65	1.51
	65	

Average Error 3.30%

Table -VII

Estimated Data and Error Based on Fuzzy Time Series using L-shape member function

Actual Value	Estimated Value	Estimated Error(%)
19	-	-
24	29	20.83
28	30	7.14
33	34	3.03
37	40	8.10
41	44	7.31
45	50	11.11
49	50	2.04
54	55	1.85
57	57	0
59	57	3.38
63	57	9.52
66	61	7.57
	65	

Average Error 6.30%

Table -VIII

Estimated Data and Error using Triangular membership function

Actual Value	Estimated Value	Estimated Error(%)
19	-	-
24	29	20.83
28	33	17.85
33	34	3.03
37	40	8.10
41	44	7.31
45	44	2.22
49	49	0
54	57	5.55
57	57	0
59	57	3.38
63	57	9.52
66	61	7.57
	65	

Average Error 6.57%

Table -IX

Estimated Data and Error Based on Fuzzy Time Series using Trapezoidal member function

Actual Value	Estimated Value	Estimated Error(%)
19	-	-
24	29	20.83
28	30	7.14
33	30	9.09
37	35	5.40
41	35	14.63
45	40	11.11
49	40	18.36
54	40	25.92
57	55	3.50
59	55	6.77
63	60	4.76
66	65	1.51
	65	

Average Error 9.92%

IV. RESULT

It is found that the average error for S-shape function gives the minimum error. Therefore the S-shape function has to be used for fuzzification for this data set. The output forecasted data based on S-shape function can be used for the estimate the shoot length of mustard plant.

V. CONCLUSIONS

In normal statistical method, prediction is based on available data. If certain error may exist in the actual data, that error data will enter into the model and as a result the prediction will not be accurate. The fuzzification plays a major role in handling the data in fuzzy environment. The fuzzification is based on certain membership function. The selection of a particular membership function depends on the nature of data value to be used. If the selected membership function is not proper, the input fuzzy data is wrong and as a result the output fuzzy data (the data outputted from a mathematical model) will also be wrong and the defuzzified output data will be improper and error will be very high. Thus caution has to be needed for the selection of membership function. In future, the artificial neural network (ANN) base on the fuzzy input and Genetic Algorithm can be used to estimate error and based on the minimum error any of them can be selected to predict the shoot length of mustard plant

VI. REFERENCES

- [1] Q. Song and B. S. Chissom, "Forecasting enrollments with fuzzy time series part I", *Fuzzy Sets and Systems* 54(1993) 1 - 9.
- [2] J. Sullivan and William H. Woodall, "A Comparison of Fuzzy Forecasting and Markov Modelling", *Fuzzy Sets and Systems* 64(1994) 279 - 293.
- [3] Q. Song and B. S. Chissom, "Fuzzy Time Series and its Models", *Fuzzy Sets and Systems* 54(1993) 269-277.
- [4] H. Bintley, "Time Series analysis with REVEAL", *Fuzzy Sets and Systems* 23(1987) 97-118.
- [5] Q. Song and B. S. Chissom, "Forecasting enrollments with fuzzy time series - part II", *Fuzzy Sets and Systems* 62(1994) 1-8.
- [6] G. A. Tagliarini, J. F. Christ, E. W. Page, "Optimization using Neural Networks", *IEEE Transactions on Computers*, vol. 40, no 12, December '91 1347-1358.
- [7] T. K. Bhattacharya and T. K. Basu, "Medium range forecasting of power system load using modified Kalman filter and Walsch transform", *Electric Power and Energy Systems*, vol. 15, no 2, 109 -115, 1993.
- [8] F. G. Donaldson and M. Kamstra, "Forecast combining with Neural Networks", *Journal of Forecasting* 15(1996) 49-61.
- [9] J. V. Hansen and Ray D. Nelson, "Neural Networks and Traditional Time Series Methods: A Synergistic combination in state Economic Forecasts", *IEEE Transactions on Neural Networks* vol. 8, no 4, July 1997.
- [10] S. F. Brown, A. J. Branford, W. Moran, "On the use of Artificial Neural Networks for the analysis of Survival Data", *IEEE Transactions on Neural Networks*, vol. 8, no 5, Sept 1997.
- [11] M. Sugeno and K. Tanaka, "Successive Identification of a Fuzzy Model and its applications to prediction of a complex system", *Fuzzy Sets and Systems* 42(1991) 315-334.
- [12] L. Zuoyong, Chen Zhenpei, Li Jitao, "A model of Weather Forecast by Fuzzy Grade Statistics", *Fuzzy Sets and Systems* 26(1998) 275-281.
- [13] L. feng and Xu Xia Guang, "A Forecasting Model of Fuzzy Self Regression", *Fuzzy Sets and Systems* 58(1993) 239-242.
- [14] M. Ishikawa, T. Moriyama, "Prediction of Time Series by a Structural Learning of Neural Networks", *Fuzzy Sets and Systems* 82(1996) 167-176.
- [15] D.H.Goldberg, "Genetic Algorithms in Search, Optimization and Machine Learning", Addison Wesley Inc, 1999.
- [16] J. Paul Choudhury, Dr. Bijan Sarkar and Prof. S. K. Mukherjee, "Some Issues in building a Fuzzy Neural Network based Framework for forecasting Engineering Manpower", *Proceedings of 34th Annual Convention of Computer Society of India, Mumbai*, pp. 213-227, October -November 1999.
- [17] J. Paul Choudhury, Dr. Bijan Sarkar and Prof. S. K. Mukherjee, "Rule Base of a Fuzzy Expert Selection System", *Proceedings of 34th Annual Convention of Computer Society of India, Mumbai*, pp. 98-104, October - November 1999.
- [18] J. Paul Choudhury, Dr. Bijan Sarkar and Prof. S. K. Mukherjee, "A Fuzzy Time Series based Framework in the Forecasting Engineering Manpower in comparison to Markov Modeling", *Proceedings of Seminar on Information Technology, The Institution of Engineers(India), Computer Engineering Division, West Bengal State Center, Calcutta*, pp. 39-45, March 2000.
- [19] G. P. Bansal, A. Jain, A. K. Tiwari and P. K. Chanda, "Optimization in the operation of Process Plant through Genetic Programming", *IETE Journal of Research*, vol 46, no 4, July-August 2000, pp 251-260.
- [20] K. K. Shukla, "Neuro-genetic prediction of Software Development Effort", *Information and Software Technology* 42(2000), pp 701-713.
- [21] S. Bandyopadhyaya and U. Maulik, "An Improved Evolutionary Algorithm as Function Optimizer", *IETE Journal of Research*, vol 46, no 1 and 2, pp 47-56, 2000.
- [22] B. Banerjee, A. Konar and S. Mukhopadhyay, "A Neuro-GA approach for the Navigational Planning of a Mobile Robot", *Proceedings of International Conference on Communication, Computers and Devices (ICCD-2000)*, Department of Electronics and Electrical Engineering, Indian Institute of Technology, Kharagpur, December 2000, pp 625-628.
- [23] J. Paul Choudhury, Dr. Bijan Sarkar and Prof. S. K. Mukherjee, "Forecasting using Time Series Model Direct Method in comparison to Indirect Method", *Proceedings of International Conference on Communication, Computers and Devices (ICCD-2000)*, Department of Electronics and Electrical Engineering, Indian Institute of Technology, Kharagpur, December 2000, pp 655-658.
- [24] Satyendra Nath Mandal, Dr. J. Paul Choudhury, "Plant Growth Estimation using Neuro-Fuzzy Model", *Proceedings of ORSI-2006 Convention & OR Workshop in the 39th Annual Convention of Operational Research Society of India, Calcutta Chapter*.
- [25] Satyendra Nath Mandal, Dr. J. Paul Choudhury, "Neural Network versus Fuzzy Logic", *Proceedings of National Conference on Innovative Computational Intelligent & Security Systems*, Sona College of Technology, Salem, pp 31-39, February 2007.
- [26] Dr. J. Paul Choudhury, Satyendra Nath Mandal, Prof. Dilip Dey, Prof. S. K. Mukherjee, "Bayesian Learning versus Neural Learning : towards prediction of Pod Yield", *Proceedings of National Seminar on Recent advances on Information Technology (RAIT-2007)*, Department of Computer Science and Engineering, Indian School of Mines University, Dhanbad, India, pp 298-313, February 2007.
- [27] Dr. J. Paul Choudhury, Satyendra Nath Mandal, Prof. S. K. Mukherjee, "Shoot Length Growth Prediction of Paddy Plant using Neural Fuzzy Model", *Proceedings of National Conference on Cutting Edge Technologies in Power Conversion & Industrial Drives PCID*, Department of Electrical and Electronics Engineering, Bannari Amman Institute of Technology, Sathyaamangalam, Tamilnadu, India, pp 266-270, February 2007.
- [28] Dr. J. Paul Choudhury, Satyendra Nath Mandal, Prof. Dilip Dey, Prof. S. K. Mukherjee, "Soft Computing model: towards the forecasting of Pod Yield as compared to Statistical model", *International Conference on Information Technology, Haldia*, March 2007.

- [29] Dr J Paul Choudhury, Satyendra Nath Mandal, "Neuro-fuzzy GA model against statistical model on agriculture shoot length prediction", CD Proceedings of International Conference on Recent Advancements and Applications of Computer in Electrical Engineering, Engineering College Bikaner(India), March 2007.
- [30] Chandan Mishra, Rupak K Bhakat, Satyendra Nath Mandal, Dr J Paul Choudhury, "A Framework for predicting shoot length for mustard plant using suitable Soft Computing Method", CD Proceedings of WIE NSET 2007 1st IEEE WIE National Symposium on Emerging Technologies, Woman in Engineering Affinity Group, IEEE Calcutta Section, IEEE Woman in Engineering, Calcutta, June 2007
-

Behavior Modeling Based Fuzzy Controller for Combustion Control of Utility Boiler

T.R. Rangaswamy

Crescent Engineering College, Chennai 600 048, India e-mail: ramy49@vsnl.com

Abstract –The main objective of the combustion controller in a thermal power plant is to regulate fuel and air in proper ratio to maintain the desired steam pressure at the turbine inlet, irrespective of the changes in steam demand. The mathematical models hitherto developed for power plants are mostly too complicated to compute for control purposes. Moreover, the conventional fixed gain feed back control schemes have difficulty to cope with inherent time delay, nonlinearity due to uncertainty of the combustion process and frequent load changes. This paper deals with the design of behavior modeling approach to get the optimal PID controller parameters for the combustion control of utility boiler. Many steady state and dynamic behavioral responses in a thermal plant were analyzed for different load conditions. By integrating the steady state response obtained from the optimum PID parameters and knowledge of the experienced engineers, a fuzzy based air /fuel ratio controller was designed for combustion control. A lab scale experimental setup is fabricated in the laboratory for fuel and air control and tests were carried out for several load conditions. The dynamic changes of steam pressure, drum pressure, turbine first stage pressure and oxygen content in the flue gas due to load disturbance are derived from the computer simulated combustion system. The advantages of the proposed design upon the conventional controller are highlighted.

Key words– Combustion control, Behavior modeling, Fuzzy control, Air/Fuel ratio.

I. INTRODUCTION

THE utility boilers are large capacity steam generators used purely for the electrical power generation. In a Thermal power station, steam is produced in a boiler, is expanded in the prime mover (Turbine) and condensed in a condenser before feeding it into the boiler again. The turbine shaft is coupled with generator, which is used to produce electricity.

The combustion system consist of airflow and the fuel flow control loops that are driven by the firing rate demand signal through master steam pressure controller. Conventional PID (Proportional–Integral–Derivative) controller is not generally suitable for non-linear, higher order, time delayed and complex systems that have no precise mathematical models. Further it needs frequent tuning, which is not an easy task and is also time consuming. Several methods of tuning were suggested for the PID controller schemes [1].

To cope with varying dynamics of the system, PID controllers have been evolved to include adaptive features such as gain scheduling and self-tuning [2]. During the last decade, extensive research has been done on adaptive control theory, methods and applications. Several researchers [3]-[5] developed dynamic models for boilers. The complexity involved in obtaining the reasonably accurate models is high. If assumptions were made to reduce complexity in obtaining models, it would yield degraded performance of controllers. In order to utilize the robustness of the fuzzy system and advantages of the PID controller, a behavior modeling approach has been proposed to get optimum PID parameters. Based on the response obtained from the PID controllers, fuzzy controllers are designed for fuel and air flow for combustion in utility boiler.

The present paper is organized as follows: Section II deals with the design of behavior modeling approach to obtain optimum PID parameters for fuel and air controllers using fabricated hardware set up in the laboratory. Section III describes the design of the proposed fuzzy scheme. Section IV deals with the closed loop simulation responses of fuzzy and PID schemes for fuel and air control and Section V gives the summary & conclusions.

II. BEHAVIOR MODELING

In the behavior modeling based approach, the control signals obtained from a controller are determined by response behaviors [6] of controlled objects, rather than by analytical models. Since the design strategy of PID and fuzzy controller depends only on the response behavior [7], it can yield similar control results irrespective of mathematical models. In the present work, many behavior responses for load vs. pressure, fuel flow and airflow with respect to steady states and dynamic states were obtained from thermal power plant during real time operation. The following are the responses for different operation conditions are obtained. 1) Behavior during boiler start up and shut down, 2) behavior during positive and negative change in ramp load from 10% to 70%. 3) The open loop behavior for negative and positive step change in loads. 4) The behavior of air and fuel flow to maintain desired turbine inlet pressure and also boiler drum pressure during sudden load change due to grid disturbance. 5) Behavior during one of the major auxiliaries fails. There are two feed water pumps to feed the water to the boiler drum and two forced draft fans to supply

required air flow to the boiler at full load. If any one fails there is an automatic reduction of load to 60% of maximum continuous rating to avoid tripping of boiler due to low drum level and low airflow. 7) Behavior during island mode (house load mode) operation to keep the station auxiliaries in running condition.

After obtaining the behavior responses from power plant, real time simulations were carried out, by mimicking all the above-mentioned cases, on the lab scale experimental set-up for fuel and airflow.

A. Lab scale experimental set-up

In order to find out optimum PID controller parameters and also to carry out the closed loop studies of PID and fuzzy schemes for air and fuel flow, a lab scale experimental set-up is designed and fabricated. The lab scale experimental set-up is shown in Fig. 1.

The hardware design for the lab scale experimental set-up comprises of the oil pump, air compressor, rotameter, control valves, current to pressure (I/P) converter, differential pressure transmitter, orifice and pressure regulators. There are two distinct control loops for air and fuel control.

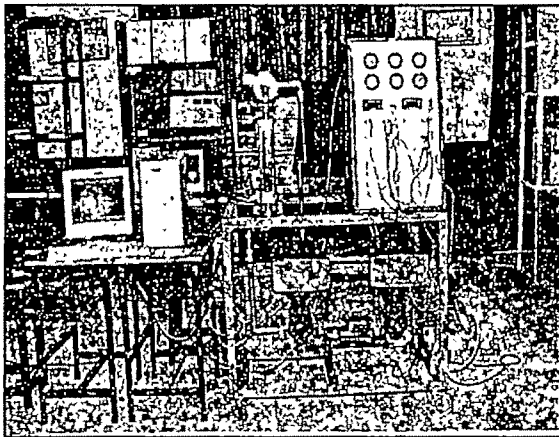


Fig.1. Hardware for the Experimental set up.

The following algorithm is proposed for mimicking each behavior response.

- Step 1: Initialize K_p , K_i and K_d the Proportional, Integral and Differential gains respectively of PID controller for both fuel and air flow.
- Step 2: Conduct experiments and plot the response for one behavior for different load conditions.
- Step 3: Find out deviations between behavior and experimental response at different sampling times.
- Step 4: Find average of all deviations.
- Step 5: Adjust K_p , K_i and K_d of the fuel and air controllers.
- Step 6: Repeat the experiment until deviations between behavior and experimental response become zero.
- Step 7: Note down the final value of K_p , K_i and K_d of the fuel and air controllers, which are taken as optimum PID parameters for particular behavior.

Repeat the procedure for all the behaviors mentioned above.

Using the above algorithm, simulations on the experimental setup for various behavior responses were carried out. The values of optimal PID parameters obtained by trial and error method are presented in Table I. These values are considered as optimum for particular behavior response because of satisfactory agreement with the real time response obtained from 210 MW thermal power plant.

Table I. Optimal PID controller parameters for different behavior responses

Behavior Response	PID parameters					
	K_p		K_i		K_d	
	Fuel	Air	Fuel	Air	Fuel	Air
Boiler Start-Up	2	1.5	1.8	1.2	0.3	0.4
10% change in ramp load from 60% to 100%	1.8	2	1.2	1	0.5	0.5
Open Loop Response for positive change in load.	1.8	1.7	1.5	1.2	0.3	0.5
Open Loop Response for negative change in load.	1.8	1.7	1.5	1.2	0.3	0.5
Sudden load change due to grid disturbance	2.5	1.7	1.5	1.2	0.3	0.5
Sudden run back of load due to auxiliary failure	2.5	2	2	1.8	0.5	0.5
Sudden Load throw off to House Load	3	2.5	2.5	2.1	0.5	0.5

Keeping the above optimum PID parameters as guidance, again several simulations were carried out on the lab-scale experimental set-up for all the behavior responses. Finally, one set of overall optimal PID controller parameter, which will mimic almost same way for all the types of dynamic behaviors mentioned above was found out. The overall optimum PID parameters obtained for air and fuel flow controllers suitable for any kind of dynamic behavior of combustion process in utility boiler is presented in Table II.

In order to improve the settling time and performance indices, an intelligent controller using fuzzy logic is designed. Steady state response obtained from those parameters can confidently be used to form membership functions and rule bases for designing fuzzy controllers without depending on the guidance from experts.

Table II. Overall Optimum PID controller parameters for fuel and air.

Control loop	K_p	K_i	K_d
Fuel Controller	1.75	1.0	0.2
Air Controller	1.5	0.8	0.2

III. PROPOSED FUZZY SCHEME.

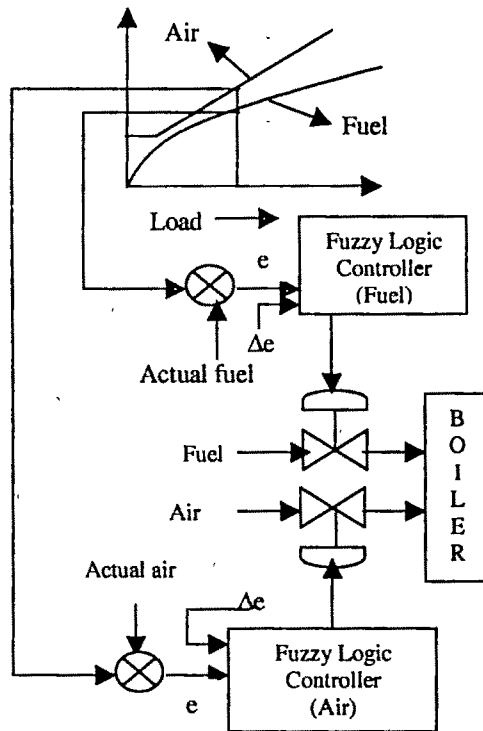


Fig 2. The proposed Fuzzy Controller.

The proposed fuzzy controller system for fuel and air control is shown in the Fig.2. The data collected from thermal power plant are stored and these are shown as two response graphs, one load vs. fuel flow and the other load vs. airflow (incorporated in Fig. 2). From the graphs, the fuel and air flow set points corresponding to the desired load are derived. The difference between the set point and the actual flow is computed as error signal. The error and change in error are taken as inputs to the proposed fuzzy controller.

Using overall optimum value of the PID parameters obtained from behavior response modeling technique as per Table.II, experiments were conducted on the lab scale set-up. Response was plotted for different load Vs fuel flow and airflow to find out the ranges for the triangular membership values using piecewise linear approximation method. The same procedure is repeated for the input and output variables of fuzzy based air and fuel controllers.

A. Fuzzification

Fuzzification converts the input data into suitable linguistic values [8]. The following are the range for the input variables for both fuel and air controls considered in the design of FLC.

Error (E) = - 50% to + 50%

Change in Error (ΔE) = - 25 %to + 25%

Control valve Position (U) = 10% to 100%

The number of linguistic levels for each linguistic variable is five.

Error (E) for fuel = {MN, N, Z, P, MP}

Change in error (ΔE) for fuel = {VS, S, M, L, VL}

Control valve position for fuel = {VS, S, M, L, VL}

Error (E) for air = {MN, N, Z, P, MP}

Change in error (ΔE) for air = {VS, S, M, L, VL}

Control valve position for air = {VS, S, M, L, VL}

The triangular membership functions are used to represent the linguistic terms.

A scale mapping is performed using triangular membership function, which transfers the range of input variables into corresponding universe of discourse. An element of each term set is mapped on the domain of corresponding linguistic variable.

B. Knowledge base

Knowledge base consists of database and rule base. Database provides necessary definitions, which are used to define linguistics control rules. In the present work 23 rules for fuel and 21 rules for air are framed while designing FLC scheme. All the rules are represented in the form of rule matrix as presented in Table III. The values inside the rule base matrix correspond to control valve position.

Table III. Rule base matrix for fuel and air controller.

		CHANGE IN ERROR				
		VS	S	M	L	VL
E R R O R	MN	VS	VS	S	M	L
	N	VS	S	S	M	L
	Z	—	—	VS	VS	M
	P	VS	VS	M	M	L
	MP	VS	VS	M	L	L

a) Fuel Control

		CHANGE IN ERROR				
		VS	S	M	L	VL
E R R O R	MN	—	VS	VS	S	M
	N	—	VS	S	S	M
	Z	—	—	S	M	L
	P	VS	VS	S	M	VL
	MP	S	S	M	L	VL

b) Air Control

C. Inference (Decision making logic)

Knowledge to perform deductive reasoning is called inference. Inference mechanism is to draw conclusion from rule base, which can produce an output from a collection of *if-then* rules. In the present work the inference mechanism is designed using Mamdani (min-max) method.

D. Defuzzification

Defuzzification [9] is the conversion of a fuzzy quantity to a precise quantity. In the present work Centroid method of defuzzification method is used.

$$\text{Crisp output } Z^* = \frac{\sum_{j=1}^n \mu_z(W_j)(W_j)}{\sum_{j=1}^n \mu_z(W_j)}$$

Where

$J = 1$ to N , the number of quantization levels.

$\mu_z(W_j)$ = Maximum value of membership function corresponding to J^{th} quantization level.

W_j = Value at which membership function reaches maximum value $\mu_z(W_j)$

The design parameters of FLC scheme are presented in Table.IV.

Table. IV. The design parameters of FLC scheme

Parameter	Value	
	Fuel Control	Air Control
No. of input variables	2	2
No. of fuzzy sets	5	5
No. of rules	23	21
Membership function	Triangular	Triangular
Defuzzification	Centroid	Centroid

IV. SIMULATION STUDIES

After designing fuzzy controllers for air and fuel, several closed loop simulations were conducted and studied the performance for both positive and negative changes in the set point as well as in the load perturbation. Fig. 3 (a-b) shows the responses for positive step change in the load set point from 21-63 MW for PID and fuzzy controllers.

Fig.3 (c-d) shows the response for negative step changes in the load set point from 110-42 MW for PID and fuzzy controllers. It is observed that, the time taken for settling is lesser than PID controllers for all the step changes in load with out off set.

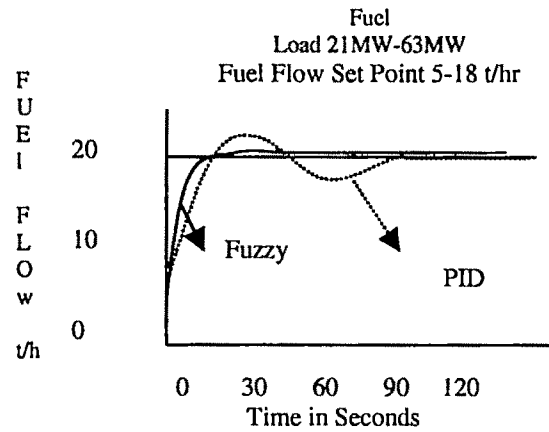


Fig.3 (a) Fuzzy/PID fuel flow response for 21 to 63 MW change in load

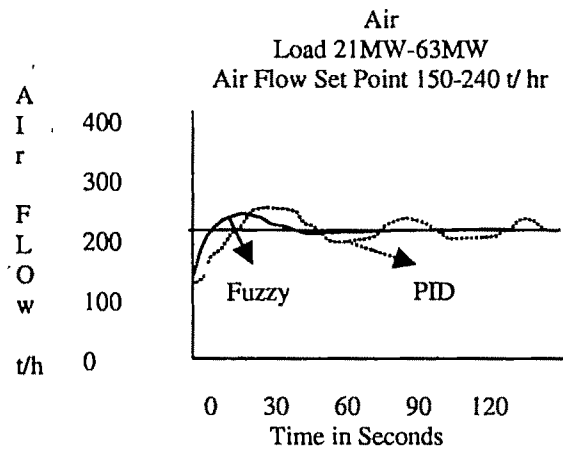


Fig.3 (b) Fuzzy/PID air flow response for 21 to 63 MW change in load

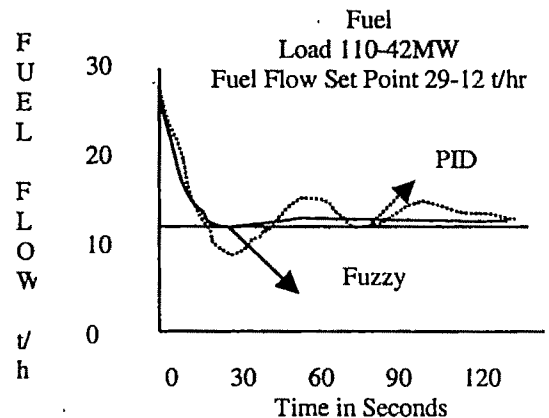


Fig.3 (c) Fuzzy/PID fuel flow response for 110 to 42 MW change in load

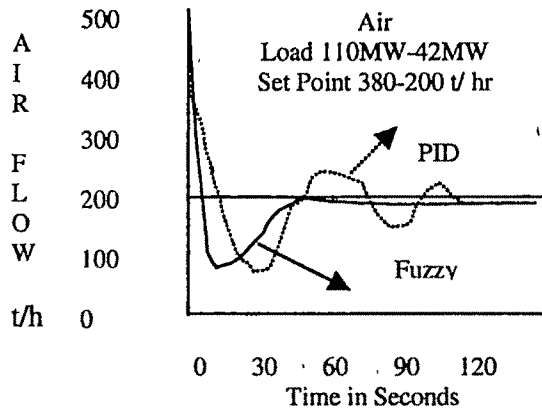


Fig.3 (d) Fuzzy/PID Air flow response for 110 to 42 MW change in load

The performance of two controllers namely PID and FLC are evaluated using error integral criteria. The Table V presents the comparison of the performance indices of the two control schemes.

Table V. ISE & IAE Comparison of for PID and Fuzzy Fuel flow schemes.

Step change in boiler load	Fuel Flow			
	PID		Fuzzy	
	ISE	IAE	ISE	IAE
21 MW – 42 MW 10%–20%	11212	14476	7543	9963
21 MW – 63 MW 10% – 30%	13765	14302	6498	9524
21 MW – 84 MW 10% – 40%	15484	19987	8847	8975
110 MW – 84 MW 50% – 40%	9012	11067	4657	9643
110 MW – 63 MW 50% - 30%	9846	16785	5574	9234
110 MW – 42 MW 50% - 20%	6549	16807	4756	9436

From Table V it is observed that the proposed fuzzy scheme for fuel has minimum integral square error (ISE) and integral absolute error (IAE) when compared with conventional controllers.

V. CONCLUSIONS

The inherent drawback of the requirement of *a priori* mathematical model for designing conventional schemes motivated the authors to apply behavior-modeling technique to obtain optimum parameters for the PID controllers for fuel and air for the combustion control of utility boiler, suitable for any kind of dynamic behavior. Steady state response obtained from those parameters are used to form membership functions and rule bases for designing fuzzy controllers without depending on the guidance from experts. The response of non-fuzzy control system has 26% overshoot for air and 39% for fuel flow. It settles down after about 83 and 74 steps of increment. The closed loop response of fuzzy scheme shows

satisfactory transient response with less overshoot and settles down after about 38 and 36 steps of increment for air and fuel respectively. This shows 50% improvement over conventional schemes in settling time for both air and fuel. The control output is smooth without any oscillations, which would increase the life of the control elements. Table V shows that the proposed fuzzy scheme, results in least ISE and IAE values for both positive and negative step changes in load showing 25% improvement for fuel control when compared to conventional schemes. The qualitative and quantitative comparisons of the performance of the various control schemes reveal the superiority of the behavior modeling based fuzzy controller over the conventional control scheme.

REFERENCES

- [1] Astrom K.J. & T.Hagghund, "Automatic tuning of simple regulations with specification on phase and amplitude margin", *Automatica*, Vol 20, pp.645-651, 1984.
- [2] Raul Garduno-Ramirez and Kwang Y.Lee, "Multi objective Optimal Power Plant Operation Through Coordinated Control with Pressure Set point Scheduling", *IEEE Transactions on Energy Conversion*, Vol. 16, No.2, pp 115-122, 2001.
- [3] Gordon Pellegrinetti and Joseph Bentsman, "Nonlinear Control Oriented Boiler Modelling", *IEEE Transactions on Control System Technology*, Vol. 4, No.1, pp 209-216, 1996.
- [4] M.E. Flynn and M.J.O Malley, "A Drum Boiler Model for Long Term Power System Dynamic Simulation", *IEEE Transactions on Power Systems*, Vol. 14, No.1, pp 209-216, 1999.
- [5] K.J. Astrom and R.D. Bell, "Drum, boiler dynamics", *Automatica*, Vol 36, pp 363-378, 2000.
- [6] Wei Li and Xiaoguang Chang, "A neuro-fuzzy controller for a stoker-fired boiler, based on behavior modeling", *Control Engineering Practice*, pp 469-481, 1999.
- [7] Li. W, "A method for design of a hybrid neuro fuzzy control system based on behavior modeling", *IEEE Trans. Fuzzy systems*, pp 128-137, 1997.
- [8] Timothy J. Rose, *Fuzzy logic with engineering application*, McGraw - Hill, Inc., Singapore, 1995
- [9] M. Chidambaram, *Computer control of process*, Narosa publishing house, India, 2002.
- [10] Sam G. Dukelow, *The Control of Boilers*, Instrument Society of America, 1991.

Numerical Solution of Takagi-Sugeno Fuzzy Model Based State Equations via Block Pulse Functions

B.M.Mohan¹, Vertika Singh²

¹ Department of Electrical Engineering, Indian Institute of Technology, Kharagpur - 721302, India e-mail: mohan@ee.iitkgp.ernet.in .

² Department of Electrical Engineering, Indian Institute of Technology, Kharagpur - 721302, India e-mail: vertikasingsh@gmail.com

Abstract—Block Pulse Functions (BPFs) approach is introduced in this paper to solve Takagi – Sugeno (TS) continuous fuzzy model based state equations. A recursive algorithm is proposed to solve the state equations. In view of the elegant and interesting properties of BPFs the proposed approach is computationally much simpler compared to that of Chebyshev polynomials of first kind [5, 6]. An illustrative example is included to demonstrate (i) the effectiveness of the proposed BPF approach and (ii) the superiority of the BPF approach over the Chebyshev polynomials approach in terms of computational time and memory requirement.

Key words—Block pulse functions, Chebyshev polynomials of first kind, Takagi – Sugeno fuzzy model.

I. INTRODUCTION

IN the analysis of TS fuzzy model based control systems we normally solve the TS fuzzy model based dynamic equations so that we can obtain the behavior of the fuzzy system to some nonzero initial conditions and input. In the recent past, orthogonal functions approach had become quite popular as a convenient and sharp tool in the analysis of dynamic systems [2, 3]. The main characteristic of this approach is that it converts calculus (differential, integral) into algebra in the sense of least – squares. It is somewhat similar to the well known Laplace transform technique in spirit. Moreover, it is easily implementable on a digital computer. However, the problem of solving TS fuzzy model based dynamic equations via orthogonal functions was unknown to the scientific community until the appearance of [5, 6] wherein Chebyshev polynomials of first kind are used. It is very important to note that the Chebyshev polynomial approach in [5, 6] is computationally not attractive as (i) it is non-recursive, (ii) it

makes use of Kronecker product of matrices and (iii) it involves inversion of a matrix of size nq where q is the number

of Chebyshev polynomials used and n is the order of the dynamic system.

In this paper we use BPFs and arrive at a recursive algorithm to solve TS fuzzy model based state equations. Interesting features of the algorithm are: (a) it is purely recursive, (b) it does not involve Kronecker product of matrices, (c) it involves inversion of a matrix of size n only, and (d) it is faster and requires low memory space. An illustrative example is given to demonstrate the superiority of the BPF approach.

II. TS CONTINUOUS FUZZY MODEL [4]

Rule i of continuous fuzzy system model is given by
IF $z_i(t)$ is M_{i1} and ...and $z_p(t)$ is M_{ip}
THEN $\dot{x}(t) = A_i x(t) + B_i u(t)$, $i = 1, 2, \dots, r$ (1)

with the initial state vector $x(0)$. Here M_{ij} is the fuzzy set, r is the number of model rules, $x(t) \in R^n$ is the state vector, $u(t) \in R^m$ is the input vector, $A_i \in R^{n \times n}$, $B_i \in R^{n \times m}$, and $z_1(t), \dots, z_p(t)$ are known premise variables that may be functions of state variables. Each linear consequent equation represented by $A_i x(t) + B_i u(t)$ is called a 'subsystem'.

Given a pair of $(x(t), u(t))$, the final output of the fuzzy system is given by

$$\dot{x}(t) = \frac{\sum_{i=1}^r w_i(z(t)) [A_i x(t) + B_i u(t)]}{\sum_{i=1}^r w_i(z(t))}$$

$$= \sum_{i=1}^r h_i(z(t)) [A_i x(t) + B_i u(t)] \quad (2)$$

where

$$z(t) = [z_1(t), z_2(t), \dots, z_p(t)]^T$$

$$w_i(z(t)) = \prod_{j=1}^p M_{ij}(z_j(t))$$

$$h_i(z(t)) = \frac{w_i(z(t))}{\sum_{i=1}^r w_i(z(t))} \quad (3)$$

for all t . The term $M_{ij}(z_j(t))$ is the membership grade of $z_j(t)$.

III. BLOCK PULSE FUNCTIONS AND THEIR PROPERTIES [2]

A q -set of BPFs are defined over $t \in [t_0, t_f]$ as follows :

$$B_i(t) = \begin{cases} 1 & \text{if } iDT \leq t < (i+1)DT, i = 0, 1, 2, \dots, q-1 \\ 0 & \text{otherwise} \end{cases}$$

where $DT = (t_f - t_0)/q$. An absolutely integrable function $f(t)$ can be approximately represented in terms of BPFs as

$$f(t) \approx \sum_{i=0}^{q-1} f_i B_i(t) = f^T B(t) \quad (4)$$

where $f = [f_0, f_1, f_2, \dots, f_{q-1}]^T$, block pulse coefficient vector

$B(t) = [B_0(t), B_1(t), B_2(t), \dots, B_{q-1}(t)]^T$, BPFs vector and

$$f_i = \frac{1}{T} \int_{iDT}^{(i+1)DT} f(t) dt$$

BPFs have the following integration operational property:

$$\int_{iDT}^{(i+1)DT} B(t) dt \approx HB(t) \quad (5)$$

where H is the operational matrix of integration, given by

$$H = DT \begin{bmatrix} 1/2 & 1 & L & 1 \\ 0 & 1/2 & L & 1 \\ 0 & 0 & O & M \\ 0 & 0 & K & 1/2 \end{bmatrix} \quad (6)$$

which is an upper triangular matrix of order qxq .

IV. SOLUTION OF TS FUZZY MODEL BASED STATE EQUATIONS

Assume that all the elements of $x(t)$ and $u(t)$ are absolutely integrable in

$kT \leq t < (k+1)T$ where $T = t_f - t_0$, a small time interval.

Define

$$t = kT + \eta \quad (7)$$

$$x_k = x(kT) \quad (8)$$

$$u_k = u(kT) \quad (9)$$

where $k = 0, 1, 2, \dots$ and $0 \leq \eta \leq T$. Then $x(t)$ and $u(t)$ in $kT \leq t < (k+1)T$ can be approximately represented in BPFs as

$$x(t) \approx \sum_{i=0}^{q-1} x_i^{(k)} B_i(t) = X^{(k)} B(t) \quad (10a)$$

$$\text{and } u(t) \approx \sum_{i=0}^{q-1} u_i^{(k)} B_i(t) = U^{(k)} B(t) \quad (10b)$$

where $X^{(k)} = [x_0^{(k)}, x_1^{(k)}, \dots, x_{q-1}^{(k)}]$, $n \times q$ block pulse coefficient matrix

and $U^{(k)} = [u_0^{(k)}, u_1^{(k)}, \dots, u_{q-1}^{(k)}]$, $m \times q$ block pulse coefficient matrix

Accuracy of final solution depends on the value of q , i.e. larger the value of q means better the accuracy.

Since T is assumed to be small, we assume [6] that the value of $h_i(z(t))$ in the interval $kT \leq t < (k+1)T$ is a constant and is considered to be $h_i(z(kT))$ itself. Then integrating Eq. (2) once with respect to t , we have

$$x(t) - x(kT) = \sum_{i=1}^r h_i(z(kT)) \int_{kT}^t [A_i x(\tau) + B_i u(\tau)] d\tau \quad (11)$$

Substituting Eq.(10) into Eq.(11), applying the notation in Eqs. (8) and (9), and making use of the property in Eq.(5) lead to

$$X^{(k+1)} - [x_k, x_k, x_k, \dots, x_k] = \sum_{i=1}^r h_i(z(kT)) [A_i X^{(k)} + B_i U^{(k)}] H \quad (12)$$

which can be rewritten as

$$X^{(k+1)} - \sum_{i=1}^r h_i(z(kT)) A_i X^{(k)} H = S^{(k)} \quad (13)$$

where $S^{(k)} = [x_k, x_k, x_k, \dots, x_k] + \sum_{i=1}^r h_i(z(kT)) B_i U^{(k)} H$,

which is an $n \times q$ known matrix.

Using Kronecker product [1], Eq.(13) can be rewritten as

$$\text{Vec}(X^{(k+1)}) = [I_{nq} - \sum_{i=1}^r h_i(z(kT)) H^T \otimes A_i]^{-1} \text{Vec}(S^{(k)}) \quad (14)$$

where I_{nq} denotes the identity matrix of order nq , \otimes denotes the Kronecker product, and

$$\text{Vec}(X^{(k)}) = [x_0^{(k)T}, x_1^{(k)T}, \dots, x_{q-1}^{(k)T}]^T$$

$$\text{Vec}(S^{(k)}) = [s_0^{(k)T}, s_1^{(k)T}, \dots, s_{q-1}^{(k)T}]^T$$

The algebraic formula in Eq.(14) involves inversion of a matrix of size $nq \times nq$ which becomes large if the value of q is chosen large. For better accuracy q should be sufficiently large. This point, equally valid for Chebyshev polynomials approach in [5, 6], can be regarded as the drawback of Kronecker product method of solving Eq.(14).

We now introduce a recursive method which is strictly applicable to BPF approach only. For this we first substitute the integration operational matrix H into Eq.(12), and obtain the following recursive relations after simplification :

$$x_0^{(k+1)} = (I_n - 0.5\Delta T \bar{A})^{-1} [x_k + 0.5\Delta T \bar{B} u_0^{(k)}] \quad (15a)$$

$$\begin{aligned} \mathbf{x}_j^{(k)} = & (I_n - 0.5\Delta T \bar{A})^{-1} [(I_n + 0.5\Delta T \bar{A})\mathbf{x}_{j-1}^{(k)} \\ & + 0.5\Delta T \bar{B}(\mathbf{u}_{j-1}^{(k)} + \mathbf{u}_j^{(k)})] \end{aligned} \quad (15b)$$

for $j = 1, 2, \dots, q-1$.

where $\bar{A} = \sum_{i=0}^r h_i(z(kT))A_i$ and $\bar{B} = \sum_{i=0}^r h_i(z(kT))B_i$

and I_n is the identity matrix of order n . Thus this approach involves inversion of a matrix of order $n \times n$ only. Moreover, it is recursive in nature. Having thus obtained $\mathbf{x}^{(k)}$ recursively, we compute $\mathbf{x}_{k+1} = \mathbf{x}[(k+1)T]$ in the following manner:

Since $\int_{t_k}^{t_{k+1}} B(t)dt = \Delta T[1, 1, \dots, 1]^T$,

at $t = t_j = (k+1)T$ Eq. (11) can be written as

$$\mathbf{x}_{k+1} = \mathbf{x}_k + \Delta T \sum_{j=0}^{q-1} [\bar{A} \mathbf{x}_j^{(k)} + \bar{B} \mathbf{u}_j^{(k)}]$$

which can be further rewritten as

$$\mathbf{x}_{k+1} = (I_n + 0.5\Delta T \bar{A})\mathbf{x}_{q-1}^{(k)} + 0.5\Delta T \bar{B} \mathbf{u}_{q-1}^{(k)} \quad (16)$$

So, the recursive algorithm to solve the TS fuzzy model based state equations is as follows:

Step1: Choose a small time interval $t_0 \leq t \leq t_f$. Set $k = 0$.

Step2: Compute $h_i(z(kT))$ for $i = 1, 2, \dots, r$

Step3: Compute $\mathbf{x}_j^{(k)}$ for $j = 0, 1, \dots, q-1$ from Eq. (15)

Step4: Compute the solution $\mathbf{x}[(k+1)T]$ from Eq. (16)

Step5: Set $k = k+1$ and go to Step2.

V. ILLUSTRATIVE EXAMPLE [5]

Consider the following TS fuzzy model based state equations:

Rule 1: if $z_1(t)$ is M_{11} and $z_2(t)$ is M_{12} then $\dot{\mathbf{x}}(t) = A_1 \mathbf{x}(t) + b_1 u(t)$

Rule 2: if $z_1(t)$ is M_{21} and $z_2(t)$ is M_{22} then $\dot{\mathbf{x}}(t) = A_2 \mathbf{x}(t) + b_2 u(t)$

Rule 3: if $z_1(t)$ is M_{31} and $z_2(t)$ is M_{32} then $\dot{\mathbf{x}}(t) = A_3 \mathbf{x}(t) + b_3 u(t)$

Rule 4: if $z_1(t)$ is M_{41} and $z_2(t)$ is M_{42} then $\dot{\mathbf{x}}(t) = A_4 \mathbf{x}(t) + b_4 u(t)$ (17)

with $\mathbf{x}(0) = [1 \ 1]^T$ where

$$\begin{aligned} \mathbf{z}(t) = & \begin{bmatrix} x_1^{-3}(t) \\ x_1^2(t) \end{bmatrix}, A_1 = \begin{pmatrix} 1 & 0 \\ 4 & -1 \end{pmatrix}, A_2 = \begin{pmatrix} 1 & 0 \\ 1 & -1 \end{pmatrix}, \\ A_3 = & \begin{pmatrix} 0.125 & 0 \\ 4 & -1 \end{pmatrix}, A_4 = \begin{pmatrix} 0.125 & 0 \\ 1 & -1 \end{pmatrix} \text{ and} \\ b_1 = & b_2 = b_3 = b_4 = \begin{pmatrix} 0 \\ 1 \end{pmatrix}. \end{aligned}$$

The fuzzy sets are $M_{11}(z_1(t)) = M_{21}(z_1(t)) = (z_1(t)-0.125)/0.875$, $M_{31}(z_1(t)) = M_{41}(z_1(t)) = (1-z_1(t))/0.875$, $M_{12}(z_2(t)) = M_{32}(z_2(t)) = (z_2(t)-1)/3$ and $M_{22}(z_2(t)) = M_{42}(z_2(t)) = (4-z_2(t))/3$.

The exact solution of the given state equations is $\mathbf{x}(t) = [(3t+1)^{1/3} \ 3t-1]^T$. Using the proposed BPF algorithm with $T = 0.001$ and $q = 4$ the solution of the TS fuzzy model based state equations in (17) is obtained and shown in Table 1 in which the exact solution and

the solution obtained via Chebyshev polynomials [5] are also shown for comparison purpose. It can be seen that the proposed BPF approach and Chebyshev polynomials approach produce identical result which is in close agreement with the exact result.

The computational time and memory requirement in the cases of Chebyshev approach and BPF approach are recorded in Table 2. All the computations are done using MATLAB 7.0 and Pentium 4 system. It is evident from Tables 1 and 2 that (i) BPF approach is as good as Chebyshev polynomials approach as far as accuracy of solution is concerned, and (ii) BPF approach is computationally superior to Chebyshev polynomials approach as it is faster and requires low memory space.

Table 1. Exact solution, Chebyshev solution and BPF

t	x(t)		x(t)	
	Exact	Chebyshev or BPF	Exact	Chebyshev or BPF
0.0	1.0000	1.0000	-1.0000	-1.0000
0.2	1.169779	1.169779	-0.400000	-0.400110
0.4	1.300591	1.300634	0.200000	0.199903
0.6	1.409439	1.409719	0.800000	0.799959
0.8	1.503694	1.503965	1.400000	1.400118
1.0	1.587401	1.587676	2.000000	2.000271
1.2	1.663103	1.663379	2.600000	2.600438
1.4	1.732478	1.732753	3.200000	3.200610
1.6	1.796701	1.796974	3.800000	3.800782
1.8	1.856635	1.856904	4.400000	4.400951
2.0	1.912931	1.913197	5.000000	5.001115

Table 2: Computational time and memory space

Approach	Time (in seconds)	Memory (in kilobytes)
Chebyshev	1.25	1.86
BPF	0.394	1.17

VI. CONCLUSION

A recursive algorithm for solving TS fuzzy model based state equations via BPFs has been presented. This algorithm is straightforward, purely algebraic and well adapted for computer implementation. The proposed BPF approach is as good as Chebyshev polynomials approach [5] if accuracy of solution is considered, and is superior to Chebyshev approach if speed of computation and memory space requirement are concerned. In view of the recursive nature of algorithm, low computing time and low memory requirement it is always advisable to work with the proposed BPF approach.

REFERENCES

- [1] J.W. Brewer, "Kronecker products and matrix calculus in system theory," IEEE Trans. Circuits and Systems, Vol. CAS-25, No. 9, pp. 772-781, 1978.
- [2] G.P. Rao, Piecewise Constant Orthogonal Functions and Their Application to Systems and Control, Springer - Verlag, Berlin, 1983
- [3] K.B. Datta and B.M. Mohan, Orthogonal Functions in Systems and Control, World Scientific, Singapore, 1995.

Fuzzy ARTMAP Technique for Quality Evaluation of Tea using Electronic Nose

Dibyendu Bhattacharyya¹, Anil Kumar Bag², Bipan Tudu³,
Nabarun Bhattacharyya⁴, and Rajib Bandhopadhyay⁵

^{1,2} Future Institute of Engineering and Management, Sonarpur Station Road, Kolkata-700150, India,
e-mail: ¹dib_ch@rediffmail.com, ²anilkumarbag@gmail.com

⁴Center for Development of Advance Computing, C-DAC, Kolkata-700 091, India, e-mail: ⁴nabarun.bhattacharya@kolkatacdac.in

^{3,5} Department of Instrumentation and Electronics Engineering, Jadavpur University, Salt Lake campus, Kolkata -700 098, India
e-mail: ³bt@ice.jusl.ac.in, ⁵rb@ice.jusl.ac.in

Abstract—Fuzzy ARTMAP (FAM) is neural network architecture based on the principle of adaptive resonance and fuzzy set theory. The network is capable of learning input-output domain associations in an on-line or an off-line fashion. As a special case, when the output domain consists of a collection of class labels, FAM can be used as a classifier. FAM enjoys several desirable properties of learning including the dual support for off-line (batch) and on-line (incremental) learning as well as the property of learning stability: using fast learning its training phase completes in a finite number of list presentations (epochs). When analyzing test results after classification with FAM it is found that even for highly overlapped classes the prediction accuracy is quite good and the online incremental learning capability of the ARTMAP network is good enough for catering a wide range without losing stability. The results show that FAM technique is very promising in terms of its possibility for incremental learning, generalization ability and much less time is required for training. In this paper, the algorithm has been applied to the datasets obtained from a gas sensor array in an electronic nose instrument with tea samples and the results are quite promising. In this particular application for quality evaluation of tea, incremental learning ability, which is inherent in FAM, is very much needed in order to use the electronic nose instrument for different types of tea produced in different countries all over the globe and this FAM promises to be an universal pattern classification algorithm for tea quality estimation using electronic nose.

Key words—Fuzzy ARTMAP, Gas sensor array, Electronic nose, Black tea.

I. INTRODUCTION

QUANTITATIVE gradation of tea quality is a difficult and tedious job as the tea quality depends upon the combined multidimensional effect of different innumerable attributes. Black teas produced at processing plants are tasted by expert

human panel called “Tea Tasters” and gradation of tea is carried out on the basis of marks given by these tasters. However, this gradation is highly subjective and it may widely vary due to different human factors like individual variability, decrease in sensitivity due to prolonged exposure, infection, adverse mental state at times etc.

Electronic nose technology has been successfully employed for recognition and quality analysis of various food and agro products, viz., wine [1], cola [2], meat [3], fish [4], etc. In tea quality classification, pioneering work had been done by Dutta et al. [5], where efficacy of electronic nose systems in classifying black tea aroma and flavour in different processing stages was established. Correlation of electronic nose data with the tea taster marks has been successfully carried out in [6]. Electronic nose has also been used successfully for detection of optimum fermentation time during tea processing [7]. Electronic nose using Fuzzy ARTMAP technique for pattern recognition has also been successfully employed for recognition and quality analysis various food and agro products [8] - [10].

In the present study, electronic nose based aroma and flavour categorization of black tea using Fuzzy ARTMAP technique has been attempted and promising results are obtained. The system has the potential to eliminate the problems associated with human panel tasting and, if this instrument is standardized for quality characterization of tea, it may serve as a very useful gadget for fast, reliable, non-invasive and continuous and real time monitoring of aroma of finished tea. Incremental learning feature of FAM has been utilized in the model and has been found to be quite advantageous for tea quality classification.

II. EXPERIMENTAL STUDY

A. Customized Electronic Nose Set-up for Tea

An electronic nose set-up has been specially made with an array of eight Metal Oxide Sensors (MOS) and headspace-

sampling module for tea aroma characterization. The block diagram for the electronic nose set-up developed has been shown in Fig. 1. The electronic nose consists of (a) sensor array, (b) micro-pump with programmable sequence control, (c) PC-based data acquisition and (d) olfaction software.

Specially designed sample holders made of glass have been used for the experimental runs. The glass sample holders may be fixed to the instrument by simple threaded fitting. For black manufactured tea, an array of Metal Oxide Semiconductor (MOS) sensors has been used for assessment of volatiles in the set-up. A series of experiments were carried out using a number of commercially available MOS sensors. From the response sensitivity of individual sensors, a set of eight gas sensors from Figaro, Japan [11] (TGS-832, TGS-823, TGS-831, TGS-816, TGS-2600, TGS-2610, TGS-2611 and TGS-2620) has been selected for odour capture from black tea. The outputs of the sensors are acquired in the PC through PCI Data Acquisition cards. The MOS sensors are conductometric in nature, and their resistance decreases when subjected to the odour vapour molecules. The change in resistance with respect to their original values ($\Delta R/R$) is converted into voltage and then taken to the PC through analog to digital converter cards for subsequent analysis in the computational models.

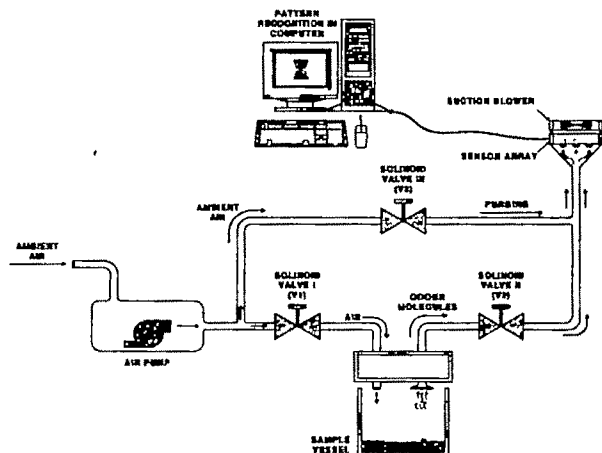


Fig.1: Customized electronic nose set-up

The experimental sniffing cycle consists of automated sequence of internal operations: (i) headspace generation, (ii) sampling, (iii) purging and (iv) dormancy before the start of the next sniffing cycle. Headspace generation ensures adequate concentration of volatiles released by tea within the sample holder by blowing regulated flow of air on the sample. During sampling, the sensor array is exposed to a constant flow of volatiles through pipelines inside the electronic nose system. During purging operation, sensor heads are cleared with blow of fresh air so that the sensors can go back to their baseline values. The programmable time dormancy cycle is the suspended mode of the electronic nose between two consecutive sniffing cycles.

The PC-based data acquisition and automated operation of all these cycles are controlled by the specially designed

software, called olfaction software. The software has got features like programmable sequence control, dynamic fermentation profile display, data logging, alarm annunciation, data archival, etc. The software has been developed in LabVIEW® of National Instruments. The software design is focused on features like minimum operator intervention in the production floor and user-friendly graphical user interface, so that operators with basic computer literacy can handle the instrument.

The experimental conditions for black tea aroma classification are given as:

Amount of each sample = 50 gms.

Headspace generation time = 30sec.

Collection time = 100sec.

Purging time = 100sec.

Air-flow rate = 5 ml / sec.

B. Sample collection

Experiments were carried out in two major tea-tasting centers in the city of Kolkata, the hub of tea auctioning and export in India. Experiments were done for approximately one-month duration each at M/s. Dalmia Tea Plantation & Industries Ltd. and M/s. Vikram India Ltd. Both the industries have multiple tea gardens spread across India and the teas produced in their gardens are sent everyday to the tea tasting centers for quality assessment. Both the centers had expert tea tasters and for our experiments one expert tea taster was deputed by the respective industries to provide taster's mark to each of the samples tested by the electronic nose.

The samples arriving at the testing centers on daily basis were tested with the electronic nose system. The identified tea tasters in the respective testing centres have evaluated all these samples and assigned scores to individual samples which have been considered as taster's mark for the correlation study with the computational network model. A sample tea taster score sheet is given in Table I.

Table I: Sample tea taster's score sheet

Sample code	SCORES (1 to 10)			
	Leaf quality	Infusion	Liquor	Aroma
VIKRAM240 806-01	7	5	3	5
VIKRAM260 806-10	6	5	5	8
DALMIA190 706-07	5	4	4	7
DALMIA280 706-03	7	5	6	6

While "leaf quality" and "infusion" scores are based on visual inspection of the samples by the tasters, the marks given against "liquor" is the combined perception of taste, briskness, and astringency of the sample. The scores assigned to

“aroma”, signify the smell and flavour of the samples. These aroma scores, therefore, have been considered by us for training the FAM model discussed in the next section.

III. THE FUZZY ARTMAP TECHNIQUE

A. Fuzzy ARTMAP Architecture

Fuzzy ARTMAP is a supervised ART network that performs incremental learning of recognition categories and multidimensional mapping in response to the arbitrary ordering of input patterns.

FAM consists of two fuzzy ART modules, ART_a and ART_b, which create stable recognition categories in response to any arbitrary sequences of the input patterns. These two ART modules are connected by an inter-art associative memory called the map field F_{ab} . The architecture of the Fuzzy ARTMAP is shown in the Fig.2.

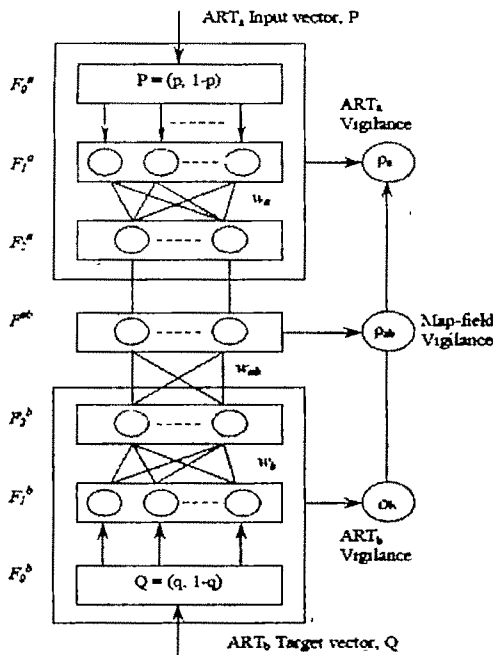


Fig. 2 The architecture of fuzzy ARTMAP

F_0^a and F_0^b layer are known as the pre-processing layer where the input patterns are preprocessed. Both the ART_a and ART_b modules have two major fields of nodes: a feature-matching field called F1 and a competitive coding field called F2. New node may be added in the F2 field when necessary to code the input patterns.

During supervised learning, ART_a receives a stream of input patterns, $\{P_a\}$ and ART_b receives a stream of target patterns, $\{P_b\}$ of the input patterns. During testing, the supervisory inputs at ART_b are omitted. ART_a inputs are used to recall a previously learned association with an ART_b output via the map field. For detailed review of this architecture is referred to Ref. [12], [13], and to Ref. [14].

B. Hypothesis selection, testing and searching

The m dimensional input pattern $p \in [1, 0]$ is converted into a $2m$ dimensional vector inserting the complement code of the vector in the F_0^a layer. Now the input patterns becomes $I = P = (p, p^c)$, where p^c is the complement code of p . The complement coding overcomes the category drift and the proliferation problem. This preprocessed input pattern is now propagated from F_1^a to F_2^a layer through a set of adaptive weights. The activation function of the j^{th} F_2^a node is defined by a choice function, $T_j(I)$, i.e.

$$T_j(I) = \frac{|I \wedge w_j^a|}{\alpha_a + |w_j^a|} \quad (1)$$

where α_a is the choice parameter of ART_a and w_j^a is the weight vector of the j^{th} F_2^a node. The node having the highest value, selected as the winner. If more than one maximum T_j exists, the one with the smallest index is chosen.

The output of the winning F_2^a node, denoted as node J , is then propagated back to the F_1^a layer through the adaptive weights. Then a vigilance test is carried out to measure the degree to which the input pattern, I , matches previously learned prototypes, i.e.

$$\frac{|I \wedge w_J^a|}{|I|} \geq \rho_a \quad (2)$$

There is a dimensionless parameter known as vigilance parameter, ρ_a , which determines the level of similarity. If vigilance test is satisfied, the network will enter into a resonance state so that the adaptive weights are tuned to the input pattern. If the vigilance test fails, a new search process is initiated and current winning node is disabled. This search process continues until a match is found or until all the F_2^a nodes have been exhausted. If none of the existing node satisfies the test, then a new node included in the F_2^a layer to encode the input patterns.

The same cycle also occurs for the ART_b and all the equation can be applied in ART_b by changing the subscripts.

C. Map-field activation

Map-field is used to form predictive associations between categories and to realize the match-tracking rule. The map-field is activated whenever ART_a or ART_b is active. Assuming the nodes J and K are the winning nodes in ART_a and ART_b respectively, an association is formed between J and K at the map-field via the map-field weight vectors. The output of the map-field, x^{ab} , is as follows:

$$x^{ab} = \begin{cases} y^b \wedge w_j^{ab} & \text{if the J-th } F_2^a \text{ node is} \\ & \text{active and } F_2^b \text{ is active} \\ w_j^{ab} & \text{if the J-th } F_2^a \text{ node is active} \\ & \text{and } F_2^b \text{ is inactive} \\ y^b & \text{if } F_2^a \text{ inactive and } F_2^b \text{ is active} \\ 0 & \text{if } F_2^a \text{ inactive and } F_2^b \text{ is active} \end{cases} \quad (3)$$

where y^b is the output of ART_b and w_j^{ab} is the weight vector that links node J in ART_a and the map field.

After the map-field output, x^{ab} , has found, a map-field vigilance test is then carried out to confirm the prediction by comparing the similarity between the predicted vector, x^{ab} , and the target vector, y^b , using:

$$\frac{|x^{ab}|}{|y^b|} = \frac{|y^b \wedge w_j^{ab}|}{|y^b|} \geq \rho_{ab} \quad (4)$$

where $\rho_{ab} \in [0,1]$ is the vigilance parameter of the map-field. If the nodes J and K have a link via the map-field, then the prediction is correct. However $x^{ab} = 0$, if the prediction w_j^{ab} is disconfirmed by y^b . Such a mismatch event triggers an ART_a search for a better category and this process is known as match-tracking.

D. Match-tracking

At the start of each input presentation, the ART_a vigilance parameter ρ_a equals to baseline vigilance $\bar{\rho}_a$. If

$$|x^{ab}| < \rho_{ab} |y^b| \quad (5)$$

then ρ_a is increase until it is slightly larger than $|I \wedge w_j^a| |I^{-1}|$, where I is the input to the F_1^a of ART_a, in complement coding form. When this occurs, will lead to failure of the current ART_a vigilance test, and a new cycle of hypothesis selection, testing and searching will be initiated to find a new winning node in ART_a. Hence, a prototype node that satisfies both the ART_a and map-field vigilance tests must be selected. If all the existing nodes are exhausted, the network creates a new none to learn the correct prediction.

E. Learning

Initially all the weight vectors w_j are set to one. Moreover, learning takes place by adjusting the weight vector of the winning node in ART_a according to

$$w_j^{a(new)} = \beta (I \wedge w_j^{a(old)}) + (1 - \beta) w_j^{a(old)} \quad (6)$$

where β is the learning parameter that determine the learning modes of the network.

The map-field weight vectors w_{jk}^{ab} that links F_2^a and F^b are initially satisfy

$$w_{jk}^{ab} = 1.$$

Once J learns to predict the ART_b category K, that association is permanent; i.e. $w_{JK}^{ab} = 1$ for all time.

IV. RESULTS

Experimentation with Fuzzy ARTMAP based electronic nose has been performed with three different tea grades. These teas were presented to electronic nose to produce 150 signature patterns for each tea. As there was eight sensors in the electronic nose the patterns were of dimension 8. FAM classifies these patterns. Clustering was done in three modes.

Different parameters were $\rho_a = 0.0$; $\rho_b = 0.8$;

$\rho_{ab} = 0.1$; $\alpha = 0.0$; and $\beta = 0.8$, where ρ , α , β indicates accordingly vigilance parameter, signal rule parameter, and learning parameter

In mode 1, the FAM was trained by a training set of 150 patterns that include first 50 patterns from each class. The same training set was then used as the test set. The result was as follows in the Table I.

Table I: Results obtained using FAM in mode 1

Total no of samples	No of samples used for training	No of samples used for testing	No of samples Miss - classified	accuracy
50	50	50	0	100%
50	50	50	3	94%
50	50	50	0	100%

In mode 2, the training set consists of 150 patterns that include first 50 patterns from each class. Testing was done with the remaining 100 patterns of each class. The result was as follows in the table II.

Table II: Results obtained using FAM in mode 2

Total no of samples	No of samples used for training	No of samples used for testing	No of samples Miss classified	accuracy
150	50	100	0	100%
150	50	100	15	85%
150	50	100	0	100%

In mode 3, the training set consists of 200 patterns that include first 50 patterns from each class and second 50 patterns of class 2. Testing was done with the patterns that are excluded from training patterns. The result was as follows in the Table III.

Table III: Results obtained using FAM in mode 3

Total no of samples	No of samples used for training	No of samples used for testing	No of samples Miss classified	accuracy
150	50	100	0	100%
150	100	50	4	92%
150	50	100	0	100%

V. CONCLUSION

The prediction accuracy of Fuzzy ARTMAP technique has been found to be quite good for highly overlapped classes and the online incremental learning capability of the ARTMAP network is good enough for catering a wide range without losing stability. The ARTMAP is a part of growing family of supervised self organizing network models that feature attentional feedback and stable code learning. In the presented study, our objective was to apply the FAM technique for quality estimation of black tea using electronic nose. Results obtained are quite encouraging and this technique seems to be, quite faster than the other algorithms.

REFERENCES

- [1] J. Lozano, J.P.Santos, M.Alexandre, L.Sayago, J.Gutierrez, and M.C.Horrillo, "Identification of typical wine aromas by means of an electronic nose," *IEEE Sensors Journal*, vol. 6, pp. 173-178, February 2006.
- [2] B.G.Kermani, S.S.Schiffman, and H.T.Nagle, "Performance of the Levenberg-Marquardt neural network training method in electronic nose applications," *Sensors and Actuators B: Chemical*, vol. 110, pp. 13-22, September 2005.
- [3] D.D.H.Boothe and J.W.Arnold, "Electronic nose analysis of volatile compounds from poultry meat samples, fresh and after refrigerated storage," *Journal of the Science of Food and Agriculture*, vol. 82, pp. 315-322, January 2002.
- [4] M.O'Connell, G.Valdora, G.Peltzer, and R.Martin Negri, "A practical approach for fish freshness determinations using a portable electronic nose," *Sensors and Actuators, B: Chemical*, vol. 80, pp.149-154, November 2001.
- [5] R. Dutta, K. R. Kashwan, M. Bhuyan E.L. Hines, and J.W. Gardner, "Electronic Nose based tea quality standardization," *Elsevier Science, Sensors and Actuators B-Chemical*, vol. 94, pp. 228-237, September 2003.
- [6] N.Bhattacharyya, R. Bandyopadhyay, M. Bhuyan, B. Tudu, D. Ghosh, A. Jana, "Electronic Nose for Black Tea Classification and Correlation of Measurements with "Tea Taster" Marks," *IEEE Trans. Instrumentation and Measurement* (to appear).
- [7] N.Bhattacharyya, S. Seth, B. Tudu, P. Tamuly, A. Jana, D. Ghosh, R. Bandyopadhyay, M. Bhuyan, and S. Sabhapandit, "Detection of optimum fermentation time for black tea manufacturing using electronic nose," *Sensors and Actuators, B: Chemical*, vol. 122, pp 627-634, March 2007.
- [8] E. Llobet, E. L. Hines, J. W. Gardner, P. N. Bartlett, and T. T. Mottram, "Fuzzy ARTMAP based electronic nose data analysis," *Sensors and Actuators, B: Chemical*, vol. 61, pp. 183-190, 1999.
- [9] J. W. Gardner, H. W. Shin, E. L. Hines, and C. S. Dow, "An electronic nose system for monitoring the quality of potable water," *Sensors and Actuators, B: Chemical*, vol. 69, pp. 336-341, 2000.
- [10] J. Brezmes, P. Cabré, S. Rojo, E. Llobet, X. Vilanova, and X. Correig, "Discrimination Between Different Samples of Olive Oil Using Variable Selection Techniques and Modified Fuzzy Artmap Neural Networks," *IEEE Sensors Journal*, vol. 5, pp. 463-469, June 2005.
- [11] www.figarosensor.com
- [12] G. Carpenter, S. Grossberg, N. Markuzon, J. Reynolds, and D. Rosen, "Fuzzy ARTMAP: a neural network architecture for incrementalsupervised learning of multidimensional maps," *IEEE Trans. Neural Networks*, vol. 3, pp. 698-713, 1992.
- [13] G.A. Carpenter, S. Grossberg, "Fuzzy ARTMAP: a synthesis of neural networks and fuzzy logic for supervised categorization and nonstationary prediction," in: R.R. Yager, L.A. Zadeh_Eds., *Fuzzy Sets, Neural Networks, and Soft Computing*, Van Nostrand-Reinhold, New York, 1994, pp. 126-165.
- [14] G.A. Carpenter, S. Grossberg, "A massively parallel architecture for a Self-organizing neural pattern-recognition machine," *Computer Vision Graphics and Image Processing*, vol. 37, pp. 116-165, 1987.

An Intelligent Approach for Multi-Sensor Data Validation and Fusion using Fuzzy Logic

S. Saha¹, U. Kar² and J. Sil³

¹Dept. of Electronics and Instrumentation, Techno India, Salt lake, Kolkata - 700091, India, imsankhadip@gmail.com

²Dept of Electrical Engineering, Netaji Subhash Engg. College, Garia, Kolkata - 700152, India, urmilakar@rediffmail.com

³Dept of Information Technology, Bengal Engg. and Science University, Shibpur, Howrah -711103, India, js@cs.becs.ac.in

Abstract— A large and complex control system may contain multiple sensors. Manufacturing and automation demand accuracy in sensor measurements. However, sensors often interact with uncertain environment and thereby, the performance of the sensors gets affected or damaged. The proposed system contains multiple sensors suitable for the measurement of process temperature as accurately as possible. A generic intelligent approach has been developed in this paper which processes the sensor data obtained from uncertain environment in order to remove measurement errors. Sensor data is represented here as Gaussian curves. The methods use fuzzy logic with statistical fundamentals in selecting the valid sensors while rejecting the invalid sensors. After validation of sensors corresponding values are fused to obtain accurate sensor data as much as possible. The system has been simulated and tested in MATLAB environment.

Key words— Data Fusion, Fuzzy rule based system, Measurement uncertainty, Validation,

I. INTRODUCTION

WITH the advancement of science and technology, modern instrumentation requires more and more advanced control as compared to the existing traditional ones. Sometimes we require accurate control over a system in spite of the insufficient and inaccurate data from the sensors due to uncertain environment. Traditional control system cannot do this task as they follow a specific mathematical equation and for that they require more accurate data. In case of industrial temperature control, conventional PID controller can do the job provided the data received from the sensors are error free. But in the real situation, one requires some intelligent approach of control using soft computing techniques [8], [2]. Researches are going on in this field for multi sensor data fusion [9]. In the paper fuzzy logic approach has been proposed with some statistical fundamentals [3], [4] to validate and fuse sensor data. Since the logic applied to the

system under consideration deals with one-dimensional data, it may also be applicable to many such control problems. However, the fuzzy inference engine has been designed and developed based on a collection of temperature sensor data.

The text contains the concept of measurement validation and multisensor data fusion, different forms of uncertainty, fuzzy modeling techniques and finally results and discussion.

A. Measurement validation

Validation can be described as a method for ensuring measurement's accuracy. A sensor signal can be validated with additional information or by statistical analysis. The information may be an infrequent reference signal (laboratory analysis or calibration signal) or a signal produced by mathematical process model. Sensor malfunction detection is an integral part of sensor signal validation. The information from malfunctioning sensor may be used independently or accompanied with other information to validate the measurement. Individual signals in a redundant set may often exhibit deviations from each other after a length of time. These differences could be caused by slowly time-varying sensor parameters, plant parameters, transport delays, etc.

B. Multi-sensor data fusion

Data fusion is a way to carry out dynamic data validation. Data fusion and integration are concepts for combining data from multiple sources to provide reliable and accurate information. The objective is to derive more information through combining than is present in any individual element of input data. Another aspect is to enhance the effectiveness of the sensor system by taking advantage of the co-operation of the multiple sensors.

Process data validation includes an expert system [1] with rules derived from operator's experience. The rules include normal operating ranges and minimum or maximum limits for each variable.

II. DIFFERENT FORMS OF UNCERTAINTY

A. Uncertainty

Uncertainty of measurement is defined formally as a parameter, associated with the result of a measurement that characterizes the dispersion of the values that could reasonably be attributed to the measurand. Another definition is the probability of a reading lying in a given range on either side of the mean value of that range. Uncertainty can also be understood as a distribution. The Gaussian distribution (figure 1) is normally used to represent the distribution of measurements and uncertainty of measurements.

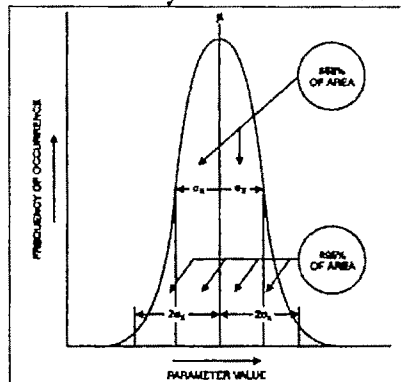


Figure 1 Gaussian distribution

Uncertainty of measurement can be characterized through measurement error, which consists of systematic error and random error. Systematic errors will always be corrected, whereas a random error cannot be corrected in a single measurement. The magnitude of a random error in a measurement is characterized by the amplitude distribution of the measurement and is typically represented as the confidence limit that is calculated from the standard deviation (σ) of the measurement error. Usually, 2σ (95 % in the case of the normal distribution) limits are used (see figure 1); for example, (1.3 ± 0.2) kg, where 1.3 kg is the mean, and 0.2 are the 2σ limits of uncertainty. Uncertainty of measurement represents well the random error of a single measurement, although it is insufficient as such to represent the uncertainty of a multivariate signal or a time series, where we need also information about the mutual and time dependences of measurement errors.

B. Sources of uncertainty

Uncertainty of measurement stands for random error, but its origin is not usually explained. Several sources of uncertainties are observed in sensor measurements due to lack of standardization of equipments, operator error, environmental behavior and malfunctioning of equipments and many others. Randomness of the measurement errors occurred due to the different uncertainties are modeled in the paper using normal distribution.

III. MODELING USING FUZZY LOGIC

The system attempts to implement fuzzy sensor fusion and interpretation by abstracting the sensor model as a Gaussian

distribution. We form fuzzy heuristic hypothesis about the validity and reliability of sensor data based on the standard deviation given to the sensor and the proximity of conflicting sensor readings using IF-AND-THEN rules. Fuzzy systems are particularly suitable for sensor fusion because quality judgments must be made at several levels. An expert must establish the intrinsic quality of a sensor reading a priori. The relative quality of redundant sensor information must be assessed online. A new measure of data quality must be expressed for the final output. The general block diagram is shown below (figure 2).

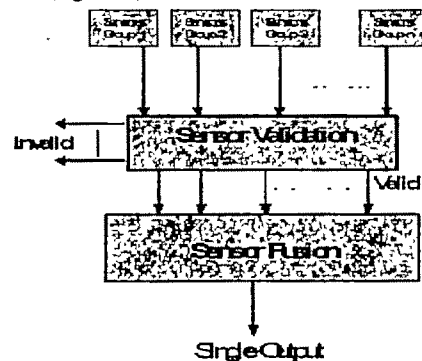


Figure 2 General block diagram

Sensors are modeled using Gaussian curves of equal area to denote sensor reliability. The mean of the curve is the current Sensor reading. The standard deviation of the curve is the reliability of that particular sensor. By fixing the area of curves, less reliable sensor readings will receive a lower weighting during the center of mass fusion algorithm. A crisp determination on sensor validity is made prior to fusion. The Sensors are modeled using the following equations.

$$N(x) = \frac{1}{\sigma\sqrt{2\pi}} e^{-\frac{(x-\mu)^2}{2\sigma^2}} \quad (1)$$

where

$$\mu = \frac{1}{n} \sum_{i=1}^n x_i \quad (2)$$

μ is the mean value, n is the number of measurements and x_i is the i^{th} measurement. The standard deviation can be calculated from:

$$\sigma = \sqrt{\frac{\sum_{i=1}^n (x_i - \mu)^2}{(n-1)}} \quad (3)$$

Sensor data are distributed using Gaussian curves (figure 3) of equal area to denote sensor reliability. The mean of the curve is the sensor reading and the standard deviation of the curve is the reliability of that particular sensor.

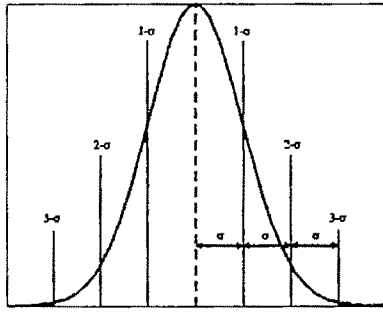


Figure 3 Gaussian distribution

A. Method 1

Mean and the standard deviation are used as inputs to the fuzzy inference engine (figure 4) while grade as fuzzy output in order to decide valid sensors of the system.

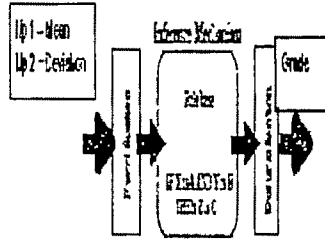


Figure 4 Fuzzy Inference Engine for Method - 1

The μ_k (mean) and σ_k (standard deviation) are defined as follows:

$$(x_k, y_k) = (\mu_k, \sigma_k) \quad \dots (4)$$

$$\text{and } z_k = \text{grade} \quad \dots (5)$$

The frame of *Mean* is

$$\langle \text{Mean}, L \text{ Mean}, X, \mu_{\mu k} \rangle$$

where *L Mean* is the set of linguistic values that *Mean* can take. We may use the following fuzzy subsets to describe the linguistic variables:

i.e. *L Mean* = { NegativePoor (NP), NegativeAccept (NA), Good (GD), Positive Accept (PA), Positive Poor (PP) }

The frame of the *standard deviation* is

$$\langle \text{StandardDeviation}, L \text{ StandardDeviation}, Y, \mu_{\sigma k} \rangle$$

The following fuzzy subsets are used for the *standard deviation*.

Very Very Small (VVS), Very Small (VS), Small (SL), Medium (MD), Large (LG), Very Large (VL), Very Very Large (VVL)

i.e. *L Standard Deviation* = { Very Very Small, Very Small, Small, Medium, Large, Very Large, Very Very Large }

We take the following frame for the fuzzy output *Grade*.

$$\langle \text{Grade}, L \text{ Grade}, Z, \mu_{z k} \rangle$$

i.e. *L Grade* = { Very Poor (VP), Poor (PR), Accept (AC), Good (GD), Very Good (VG) }

Figures 5, 6 and 7 represent fuzzy membership functions for mean, standard deviation and grade respectively.

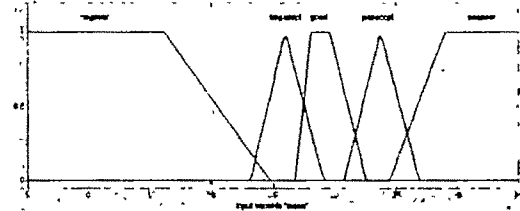


Figure 5 Fuzzy membership functions for Mean

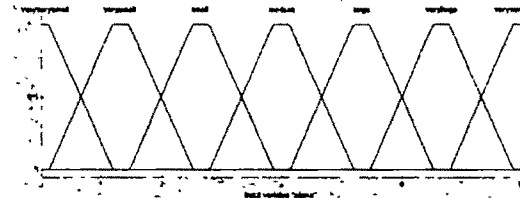


Figure 6 Fuzzy membership function for StandardDeviation

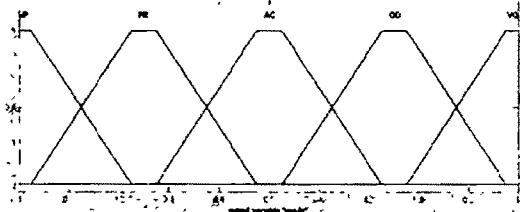


Figure 7 Fuzzy membership function for Grade

Table 1: Fuzzy Associative Memory (FAM) for Method 1

	NP	NA	GD	AC	VG	VG	VG
NP	NP	NP	NP	NP	NP	NP	NP
NA	NP	NP	NP	NP	NP	NP	NP
GD	NP	NP	NP	NP	NP	NP	NP
AC	NP	NP	NP	NP	NP	NP	NP
VG	NP	NP	NP	NP	NP	NP	NP
VG	NP	NP	NP	NP	NP	NP	NP

Depending on the input and output variables fuzzy decision table has been formed as shown in table 1. Fuzzy inference engine computes the grade according to the current input conditions of the sensor data. A predefined threshold value determines the accept/reject criteria of the sensors for validation, defined below

$$\text{Grade} = \text{Accept}, Z_c \geq \text{threshold}$$

$$\text{Reject}, Z_c \leq \text{threshold}$$

Valid sensors are fused where the sensor reading (*mean*) for each distribution is the centroid of its membership function. Therefore the fused mean can be obtained using the center-of-gravity method formulated in the following equation

$$\mu_{\text{fused}} = \frac{\int f^i(x_k) x_k dx_k}{\int f^i(x_k) dx_k} \quad (6)$$

Because each Gaussian curve has the same area (figure 8), the equation can be re-formulated as

$$\mu_{\text{fused}} = \frac{\text{summation of the sensor reading}}{\text{number of sensors}} \quad (7)$$

For calculating the value of fused value of the standard deviation, we have used the following equation. All sensors Gaussian curves are weighted and summed as follows

$$\sigma_{fused} = \sqrt{\frac{\sum_{i=1}^N \sum_{k=1}^M (x_k^i - \mu_{fused})^2 \times f^i(x)}{(N \times M - 1)}} \quad (8)$$

N is the number of the sensor number, M is the number of data points and $f^i(x)$ is the probability value. Here 500 data points are used to present the curve.

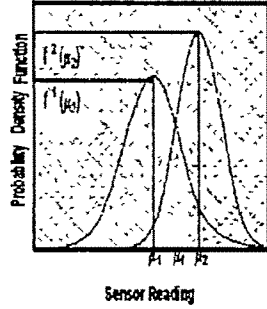


Figure 8 Gaussian curves for fused mean

B. Method II

In the second method the distance (between each mean and the fused mean) and the standard deviation are used as inputs to the fuzzy inference engine (figure 9) while weight as fuzzy output which is assigned to all the sensors.

Input 1 = standard deviation

Input 2 = the distance between each mean and the fused mean $[\mu_k - \mu_{fused}]$

Output = z_k (weight)

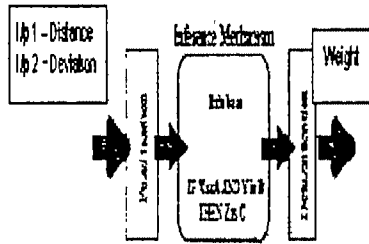


Figure 9 Fuzzy Engine for Method - 2

The frame of *Distance* is

$\langle \text{Distance}, \text{LDistance}, X, \mu_{dk} \rangle$

where *LDistance* is the set of linguistic values that Mean can take. We may use the following fuzzy subsets to describe the linguistic values:

VeryClose (VC), Close (CL), Medium (MD), Far (FR), VeryFar (VF)

i.e. *L Mean* = { VeryClose, Close, Medium, Far, VeryFar }

The frame of the *standard deviation* is

$\langle \text{StandardDeviation}, \text{LStandardDeviation}, Y, \mu_{dk} \rangle$

The following fuzzy subsets are used for the standard deviation.

VerySmall (VS), Small (SL), Medium (MD), Large (LG), VeryLarge (VL)

i.e. *LStandardDeviation* = { VerySmall, Small, Medium, Large, VeryLarge }

We take the following frame for the fuzzy output *Weight*.

$\langle \text{Weight}, \text{L Weight}, W, \mu_{wk} \rangle$

LWeight = { VeryHigh(VH), High(HI), Medium(MD), Low(LW), VeryLow(V) }

Fuzzy membership functions for standard deviation, distance and weight are represented in figures 10, 11 and 12 respectively.

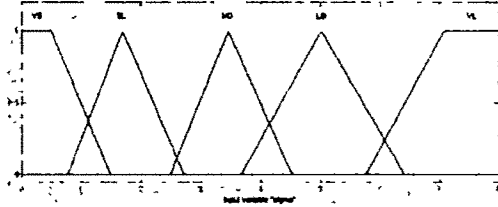


Figure 10 Fuzzy membership function for Standard Deviation

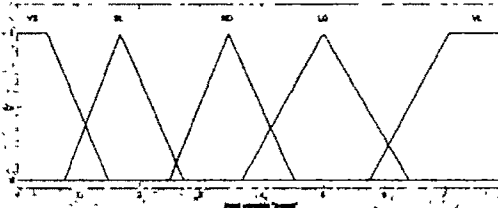


Figure 11 Fuzzy membership function for Distance

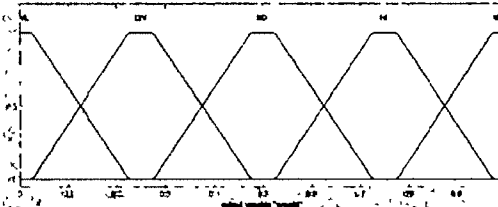


Figure 12 Fuzzy membership function for Weight

Table 2 : Fuzzy Decision Table for Method 2

	VS	SL	MD	LG	VL
VS	VS	SL	MD	LG	VL
SL	VS	SL	MD	LG	VL
MD	VS	SL	MD	LG	VL
LG	VS	SL	MD	LG	VL
VL	VS	SL	MD	LG	VL

The strength of all rules from the rule evaluation process is defuzzified using the center of gravity method. Therefore the fused mean can also be obtained using the center-of-gravity method formulated in the following equation

$$\mu_{fused} = \frac{\int f^i(x_k) x_k dx_k}{\int f^i(x_k) dx_k} \quad (9)$$

The fused standard deviation can be obtained by the weighted average of each sensor's standard deviation as the following equation

$$\sigma_{fused} = \frac{\int \sigma_i z_c^i}{\int z_c^i} \quad (10)$$

IV. RESULTS AND ANALYSIS

Five sensors are simulated with some random values. The data range for Gaussian distribution is set to between $(\mu - 3\sigma)$ and $(\mu + 3\sigma)$ which will contain 99.7% of the curve (figure 13). Sensor readings are given in table 1. Corresponding mean and deviation and the grade are also given in table 3

Table 3

SENSORS	Sensor 1	Sensor 2	Sensor 3	Sensor 4	Sensor 5
READINGS	36.32 35.048 35.011 37.592	59.15 60.02 56.57 61.73 62.01	-10.444 -9.4102 -11.6998 -9.5 -10.501 -10.001	13.535 17.532 13.326 17.41 13.59	20.385 23.015 17.775 22.9
ABSOLUTE DISTANCE	17.8095	41.6473	28.508	2.77007	2.77008
STANDARD DEVIATION	1.07317	2.20606	0.890452	2.00938	2.47976
WEIGHT	0.0831154	0.0860019	0.0736789	0.75	0.659414

Status (Accepting and rejecting criterion) of the sensors depending on the threshold value of 0.5 is given in the table 4.

Table 4

SENSORS	GRADE	
	Accepted	Rejected
Sensor 1		✓
Sensor 2		✓
Sensor 3		✓
Sensor 4	✓	
Sensor 5	✓	

Distance and standard deviation of the sensors and corresponding weight are given in the table 5.

Table 5

SENSORS	Sensor 1	Sensor 2	Sensor 3	Sensor 4	Sensor 5
READINGS	36.32 35.048 35.011 37.592	59.15 60.02 56.57 61.73 62.01	-10.444 -9.4102 -11.6998 -9.5 -10.501 -10.001	13.535 17.532 13.326 17.41 13.59	20.385 23.015 17.775 22.9
ABSOLUTE DISTANCE	17.8095	41.6473	28.508	2.77007	2.77008
STANDARD DEVIATION	1.07317	2.20606	0.890452	2.00938	2.47976
WEIGHT	0.0831154	0.0860019	0.0736789	0.75	0.659414

Fused Mean for the Validation Method-1 is 18.2487
Fused Sigma for the Validation Method is 2.47321
Fused Mean for the Validation Method-2 is 18.2487
Fused Sigma for the Validation Method-2 is 2.10813

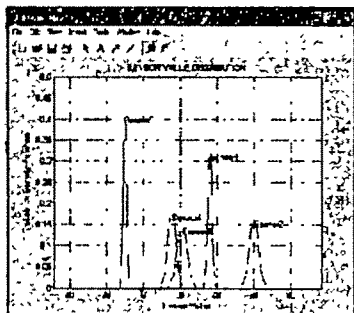


Figure 13 Distribution of 5 sensors

V. CONCLUSION

A generic fuzzy logic algorithm for validation and fusion process has been proposed for multiple sensors. Fuzzy inference engine has been developed assuming the sensors are temperature sensors. Although the intension and idea for the algorithm is based on the fact that the theoretical idea will be same for different type sensors but the model of the fuzzy inference engine will be different. This method is favorable as compared to other methods (Kalman Filter) because it preserves marginal sensor information. This algorithm could not be applied to real time environment. However this algorithm can efficiently be applied to quality judgments. For example to know the exact quality of the smoke of emission of car, a no of random test values from different test centers can be taken and the proposed algorithm can be applied to get the fused quality. The algorithm for validation and fusion method is tested in MATLAB (Version 6.5) software. MATLAB codes are generated for simulation purpose. Fuzzy logic architecture and rule base are generated in SIMULINK environment.

The proposed algorithm will be tested on the distributed networked sensors environment using Java socket programming to determine its functionality in an industrial environment.

ACKNOWLEDGMENT

This work was done under the networking programme of TEQIP (Technical Education Quality Improvement Programme) of GOI (Govt. of India).

REFERENCES

- [1] D. Driankov, H. Hellendoorn, and M. Reinfrank. An Introduction to Fuzzy Control. Springer-Verlag, New York, 1993.
- [2] T. Ross. Fuzzy Logic in Engineering Applications. McGraw-Hill, New York, 1995.
- [3] C. B. Gupta and Vijay Gupta, An Introduction to Statistical Methods, 23rd Edition, Vikash Publishing House Pvt. Ltd.
- [4] William G. Cochran, Sampling Techniques, Third Edition, Wiley Eastern Limited.
- [5] A.H.G. Al-Dhaher and D. Mackesy Multi-Sensor Data Fusion Architecture, 2004 IEEE.
- [6] P. Hsu, K. Lin, and L. Shen, "Diagnosis of Multiple Sensor and Actuator Failures in Automotive Engines," IEEE Transaction on Vehicular Technology, Vol. 44, No. 5, pp. 779-789, November 1995.
- [7] Nakamiti G. and Gomide F., Fuzzy Distributed Artificial Intelligence Systems, Technical Report RT-DCA 15/93, Department of Computer Engineering and Industrial Automation, University of Campinas-SP, Brazil, 1993.
- [8] Tenny R. P., Sandell N. R., Detection with Distributed Sensor, IEEE Trans on AFS-17, 4:501-509, 1981.
- [9] Richard R. Brooks and S. S. Iyengar, Multi-Sensor Fusion: Fundamentals and Applications with Software, Prentice Hall, Toronto, 1998.

A Ziegler-Nichols PID Controller with Auto-tuning Feature

Chanchal Dey¹ and Rajani K. Mudi²

¹ Department of Applied Physics, University of Calcutta, Calcutta 700009, India, e-mail: cdaphy@caluniv.ac.in

² Department of Instrumentation & Electronics Engineering, Jadavpur University, Calcutta 700098, India, e-mail: rkemudi@jee.ju.ac.in

Abstract—Ziegler-Nichols tuned PID controllers are usually found to provide unsatisfactory results for high-order and nonlinear systems. To overcome this limitation here we propose an auto-tuning scheme for Ziegler-Nichols tuned PID controller (ZNPID). All three individual parameters of ZNPID i.e., proportional (P), integral (I) and derivative (D) gains are updated continuously based on instantaneous process response. An intelligent factor α is introduced in gain expressions of P, I and D terms for their on-line modification. The value of α is calculated through a simple relation based on the instantaneous values of error (e) and change of error (Δe) of the process variable. In comparison with ZNPID and Refined Ziegler-Nichols tuning relations (RZNPID), our proposed scheme shows significant improvements in process responses during both the set point change and load variation simultaneously. Simulation study is made for second order linear and non-linear processes with dead time. In all cases performance indices (e.g., percentage overshoot, settling time, integral absolute error and time integral absolute error) show considerable improvements in their values compared to their respective counterparts of ZNPID and RZNPID.

Key words—Dead time, Intelligent parameter, PID controller, Ziegler-Nichols tuning.

I. INTRODUCTION

IN spite of various advancements in process control techniques, till today most of the controllers used in industry are of PID type [1].

The performance for many of them is quite poor due to, among other factors, inadequate tuning of the controller parameters [2]. Ziegler-Nichols (ZN) ultimate cycle method [3] is one of the most popular tuning methods to obtain reasonably good settings for PID controllers [4]. The superiority of ZN tuning formula has been found to be quite

satisfactory for first order processes, but they usually fail to

provide acceptable performance for high-order and non-linear systems [5].

To cope-up with such difficult control situations auto-tuning [6], [7] is a very desirable feature and almost every industrial PID controllers provides it nowadays [8]. Dynamics of the industrial processes are not completely known and are subject to change under various operating conditions. Hence to achieve a desired response we propose a scheme for on-line modifications of P, I and D components of ZNPID depending on the instantaneous values of e and Δe of the process variable. Similar types of auto-tuning schemes have also been tested in fuzzy control [9], [10].

In practical process control applications when a plant is operated under manual mode, an operator uses his expertise to adjust the controller gain according to the process conditions (i.e., e and Δe) to achieve the desired output. The basic strategy behind this gain manipulation is that when the process variable is moving away from the set value, controller takes aggressive action to bring it back to the desired value with minimum number of oscillations (i.e., smaller settling time). In a reverse situation when the process output is close enough to the desired value, control action is reduced to restrict the possible overshoot and undershoot in subsequent operating phases. In our proposed modified ZN tuned PID controller (MZNPID) we have tried to incorporate this gain modification strategy in a very simple way by introducing an on-line gain updating factor α in expressions of P, I and D components of ZNPID. The factor α is calculated continuously from the product of normalized values of process error (e_N) and change of error (Δe_N). The proposed method is tested with second order linear and non-linear dead-time processes and comparison is made with ZNPID and RZNPID [11] in terms of various performance indices- percentage overshoot (%OS), rise time (t_r), settling time (t_s), integral absolute error (IAE) and time integral absolute error (ITAE). Performance analysis reveals that the proposed MZNPID is capable of providing a significantly improved control performance under step set

point changes as well as sudden load disturbances.

II. THE PROPOSED CONTROLLER

A. Design of MZNPID

The initial setting for the proposed PID controller is based on ZN ultimate cycle tuning [3]. On introducing the gain updating factor α in the expressions of P, I and D terms they get modified continuously depending upon the current process conditions (i.e., e and Δe).

At the k^{th} sampling instant $e(k)$ and $\Delta e(k)$ are expressed as:

$$e(k) = r - y(k), \quad (1)$$

$$\Delta e(k) = e(k) - e(k-1), \quad (2)$$

where r is the desired response and $y(k)$ is the process output at k^{th} instant. The gain updating factor α can be defined as

$$\alpha(k) = e_N(k) \times \Delta e_N(k). \quad (3)$$

$$\text{Where, } e_N(k) = \frac{e(k)}{e_{\max}}, \quad (4)$$

$$\text{and } \Delta e_N(k) = e_N(k) - e_N(k-1). \quad (5)$$

Here, $e_N(k)$ and $\Delta e_N(k)$ are taken as the normalized values of $e(k)$ and $\Delta e(k)$ respectively, and e_{\max} is the maximum possible value of process error. Discrete form of conventional ZNPID at k^{th} sampling instant may be described as:

$$\begin{aligned} u(k) &= K_p \left[e(k) + \frac{\Delta t}{T_i} \sum_{i=0}^k e(i) + \frac{T_d}{\Delta t} \Delta e(k) \right] \\ &= K_p e(k) + K_i \sum_{i=0}^k e(i) + K_d \Delta e(k). \end{aligned} \quad (6)$$

In Eq. (6), K_p is the proportional gain, $K_i = K_p(\Delta t/T_i)$ is the integral gain and $K_d = K_p(T_d/\Delta t)$ is the derivative gain where T_i is the integral time, T_d is the derivative time and Δt is the sampling interval. K_p , T_i and T_d are calculated according to the ZN ultimate cycle tuning scheme.

In our proposed MZNPID, K_p , K_i and K_d will be modified continuously by gain updating factor α with the following relations:

$$K_p^m = K_p (1 + K_1 |\alpha|), \quad (7)$$

$$K_i^m = K_i (0.3 + K_2 \alpha), \quad (8)$$

$$K_d^m = K_d (1 + K_3 |\alpha|) \quad (9)$$

where K_p^m , K_i^m and K_d^m are modified proportional, integral and derivative gains respectively. K_1 , K_2 and K_3 are three positive constants, which are used to determine the required variations of K_p^m , K_i^m and K_d^m . Depending on the type of response desired to achieve in terms of some performance indices suitable values of K_1 , K_2 and K_3 are to be decided by

the designer either through trial and error or based on some prior knowledge about the process to be controlled. Thus MZNPID can be expressed as:

$$u^m(k) = K_p^m e(k) + K_i^m \sum_{i=0}^k e(i) + K_d^m \Delta e(k). \quad (10)$$

B. Block diagram of MZNPID

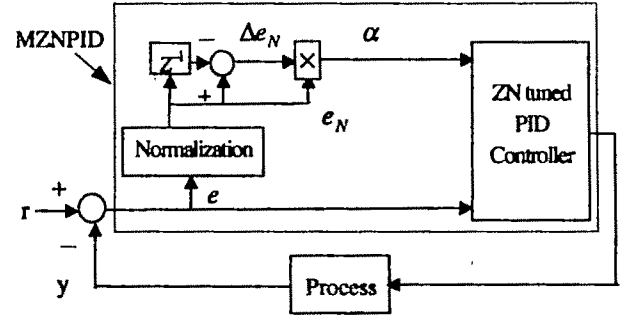


Fig. 1. Block diagram of proposed MZNPID.

The simplified block diagram of the proposed PID controller is shown in Fig. 1. It shows that the gain updating factor α , a function of process error (e) and change of error (Δe) continuously adjusts the parameters of ZNPID. From (3) it is found that α would vary within the range $[-1, 1]$ for all closed loop stable systems.

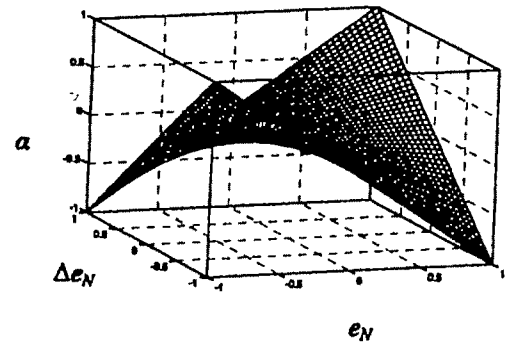


Fig. 2. Variation of α with e_N and Δe_N .

Fig. 2 shows the highly non-linear variation of α , which indicates that unlike ZNPID, MZNPID has a non-linear gain variations. Due to non-linear variation of P, I and D components of MZNPID leads to a non-linear control surface (Fig. 3b) in comparison with linear control surface (Fig. 3a) produced by ZNPID due to their fixed gains. Some important features of the proposed controller are: (i) traditional control structure is preserved so that the existing system can be easily modified into the proposed form just by introducing a gain

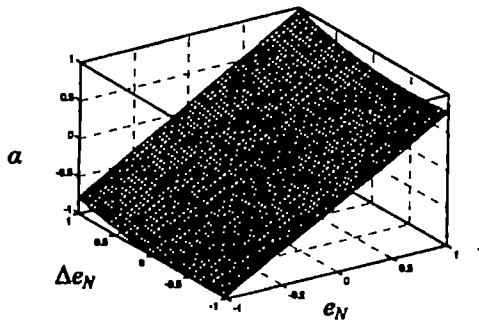


Fig. 3(a). Linear control surface of ZNPID.

updating factor, (ii) the gain updating factor is continuously modified depending upon the recent status of the process, (iii) gain modification scheme is independent of any mathematical model or any process performance parameter, (iv) easy to implement in process loop with conventional control equipments.

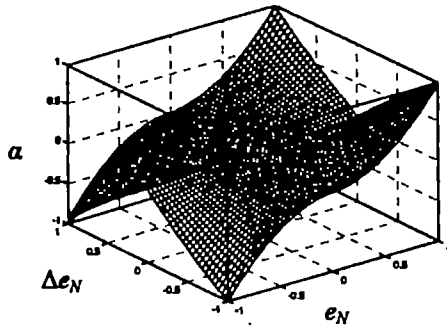


Fig. 3(b). Non-linear control surface of MZNPID.

C. Tuning mechanism

The objective of the proposed auto-tuning scheme is that, subsequent to any set-point change or load disturbance, the P, I and D parameters of the MZNPID would change continuously in such a manner that the process may have a quick recovery without a large number of oscillations. While designing MZNPID, the following important points are taken into consideration to provide the appropriate control action in different operating phases. For easy understanding, a typical close-loop response of a second-order under-damped system is illustrated in Fig. 4.

(i) When the controlled variable is far from the set-point and moving towards it, e.g., point A or C in Fig. 4, proportional gain should be reasonably large to reach the set-point quickly but at the same time integral gain should be small enough to prevent the large accumulation of control action, which may result in a large overshoot or undershoot in future. At the same time to prevent oscillations derivative gain should increase for higher damping. In such situations (i.e., e and Δe are of opposite sign), α becomes negative as per the relation (3), which will make the proportional gain

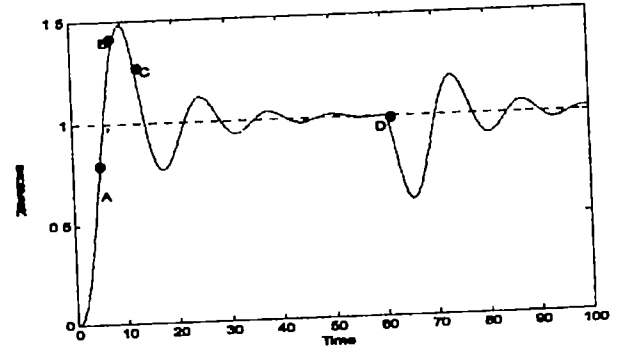


Fig. 4. Typical closed loop response of an under-damped second order process.

$k_p^m > K_p$, integral gain $k_i^m < K_i$ and derivative gain $k_d^m > K_d$ according to relation (7), (8) and (9) respectively. This type of gain variation will try to reduce the overshoot and/or undershoot for faster settling. Moreover, a reduced integral gain is important to avoid integral windup problem, especially, when the process dead-time becomes considerably large.

(ii) When the process variable is far from the set-point and moving further away from it (e.g., point B in Fig. 4), proportional as well as integral and derivative gains should be large enough to bring back the process variable to its desired value. Under such situations, both e and Δe have large values with the same sign, thereby making α large and positive according to relation (3). Such a large and positive α makes all three gain components larger than their respective initial values according to relations (7) to (9). As a result, the control action becomes more aggressive (i.e., $u^m > u$ according to relations (6) and (10)) during such operating phases. Therefore, MZNPID satisfies the need for a strong control action to improve the process recovery.

(iii) Industrial processes are often subjected to load variations. An efficient controller should provide a good regulation against such sudden changes in load, and restore the desired process state within a shortest possible time. This may be accomplished by increasing the controller gain. Observe that, at the event of any load disturbance, process will move away rapidly from the set-point, e.g., point D in Fig. 4. In such a situation, α becomes positive as both e and Δe are of the same sign. Therefore, all three components P, I and D of MZNPID will be increased according to relations (7), (8) and (9). These higher gains will help to provide a better load rejection.

From the previous discussion it is evident that our proposed auto-tuning scheme would provide improved transient and steady state behaviour under set point change and load variation. This control scheme is entirely independent of any process parameter or any predefined mathematical model; it depends only upon the recent process status (i.e., e and Δe). To get further improved performance for different types of processes an experienced process operator may use his expertise by selecting suitable values of K_1 , K_2 and K_3 that are implicitly present in controller expression (10).

III. RESULTS

Effectiveness of the proposed scheme is verified through simulation experiments on second order linear as well as nonlinear processes with dead-time (L). In addition to response characteristics, performance of the proposed MZNPID is compared with ZNPID and RZNPID with respect to a number of performance indices- %OS, t_r , t_s , IAE, and ITAE. The values of tuning parameters K_1 , K_2 and K_3 are empirically chosen as $K_1 = K_2 = 1$ and $K_3 = 12$. Fourth-order Runge-Kutta method is used for numerical integration with an interval of 0.1s. The detailed performance analysis for the mentioned processes is discussed below.

A. Second-order linear process

Transfer function of the second-order linear process is given by

$$G_p(s) = \frac{e^{-Ls}}{(1+s)^2} \quad (11)$$

Response characteristics for the process in (11) with $L = 0.2s$ under ZNPID, RZNPID, and MZNPID is shown in Fig. 5(a). Various performance indices are listed in Table I(a). Figure 5(a) and Table I(a) clearly reveal a significant performance improvement both in set point and load responses under MZNPID over ZNPID and RZNPID. For examples, %OS has been reduced from more than 60% to below 1%, and the t_r is reduced over 60% with respect to ZNPID. Moreover, Table I(a) and Fig. 5(a) indicate that the performance of MZNPID is better than that of RZNPID. To study the robustness of the proposed scheme a 50% higher value of dead-time, i.e., $L = 0.3s$ is considered with the same controller setting as that of $L = 0.2s$, and the corresponding responses and performance parameters are shown in Fig. 5(b) and Table I(b) respectively. Figure 5(b) and Table I(b) also depict the superiority of MZNPID over RZNPID and ZNPID.

B. Second-order non linear process

The performance of the proposed auto-tuner is tested for different nonlinear processes. One of them is described by

$$\frac{d^2 y}{dt^2} + \frac{dy}{dt} + 0.2y^2 = u(t-L) \quad (12)$$

Figure 6(a) shows the responses of (12) with $L = 0.3s$ under ZNPID, RZNPID and MZNPID. Table II(a) presents the various performance indices. Though the controllers are tuned for $L = 0.3s$, a higher value, i.e., $L = 0.4s$ is also considered keeping the controller's setting same. To check the robustness of the controllers for non-linear system, response characteristics for $L = 0.4s$ is illustrated in Fig. 6(b) and performance parameters are listed in Table II(b). From Fig. 6(b) and Table II(b) it is found that in case of MZNPID, %OS is reduced by more than 70%, and the steady state is reached faster, which reveals that unlike ZNPID and RZNPID, MZNPID is capable of providing more satisfactory performance under dead-time variation.

IV. CONCLUSION

A simple model independent auto-tuning scheme has been proposed for Ziegler-Nichols tuned PID controller. It continuously adjusts the controller (ZNPID) P, I and D components through a single nonlinear parameter α , defined on the instantaneous process states. It can be easily incorporated in an existing control loop. Effectiveness of the proposed controller (MZNPID) has been tested through simulation experiments for second order linear and non-linear processes. In each case, MZNPID has shown better performance both in transient and steady state conditions compared to ZNPID, and RZNPID. Robustness of the proposed scheme has been established by varying the dead-time without changing the controller parameters for a given process, and using the same values of K_1 , K_2 and K_3 for both the linear and non-linear processes in simulation experiments.

In the present study, we have used empirical values of K_1 , K_2 and K_3 . Further works may be done to find their more appropriate values. Stability analysis for this nonlinear controller (MZNPID) may also be tried to make this study more meaningful.

REFERENCES

- [1] K. J. Åström and T. Hägglund, "The future of PID control," *Control Engineering Practice*, vol. 9, pp. 1163–1175, 2001.
- [2] K. J. Åström and T. Hägglund, *PID Control-Theory, Design and Tuning*, North Carolina, USA: Instrument Society of America, 1995.
- [3] J. G. Ziegler and N. B. Nichols, "Optimum settings for automatic controllers," *ASME Trans*, vol. 64, pp. 759–768, 1942.
- [4] C. C. Hang, K. J. Åström, and W. K. Ho, "Refinements of Ziegler-Nichols tuning formula," *IEE Proc. -D*, vol. 138, pp. 111–118, 1991.
- [5] R. K. Mudi, C. Dey, and T. T. Lee, "An improved auto-tuning scheme for PI controllers," *ISA Trans.*, to be published.
- [6] S. K. Panda, J. M. S. Lim, P. K. Dash, and K. S. Lock, "Gain scheduled PI speed controller for PMSM drive," in *Proc. 23rd Int. Conference on IEEE Industrial Electronics Society IECON 1997*, New Orleans, USA, pp. 925–930.
- [7] R. K. Mudi and C. Dey, "An augmented Ziegler-Nichols tuned PI controller," in *Proc. Int. Conference on Computers and Devices for Communication CODEC 2004*, Calcutta, India.
- [8] R. R. Pecharrmán and F. L. Pagola, "Improved identification for PID controllers auto-tuning," in *Proc. 5th European Control Conference ECC 1999*, Karlsruhe, Germany.
- [9] R. K. Mudi and N. R. Pal, "A robust self-tuning scheme for PI and PD type fuzzy controllers," *IEEE Trans. Fuzzy Systems*, vol. 7, pp. 2–16, 1999.
- [10] R. K. Mudi and N. R. Pal, "A self-tuning fuzzy PI controller," *Fuzzy Sets and Systems*, vol. 115, pp. 327–338, 2000.
- [11] K. J. Åström, C. C. Hang, P. Persson, and W. K. Ho, "Towards intelligent PID control," *Automatica*, vol. 28, pp. 1–9, 1999.

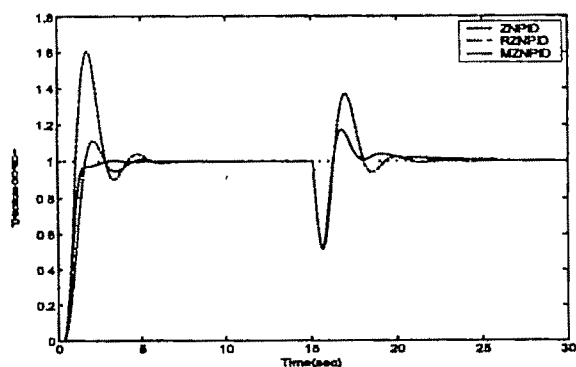


Fig. 5(a). Second order linear system, $L = 0.2s$ in (11).

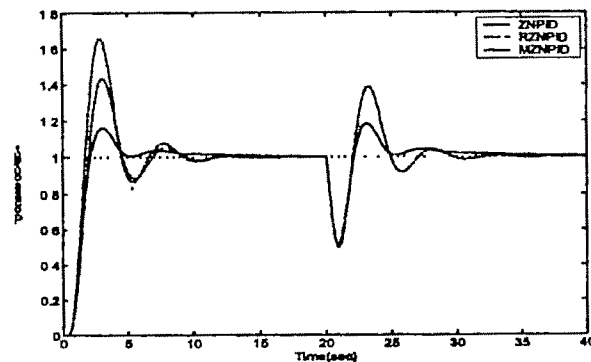


Fig. 6(a). Second order non-linear system, $L = 0.3s$ in (12).

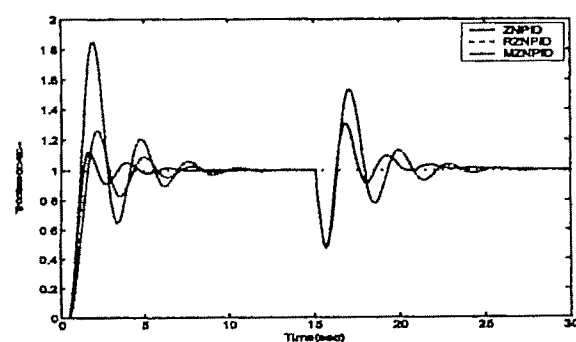


Fig. 5(b). Second order linear system, $L = 0.3s$ in (11).

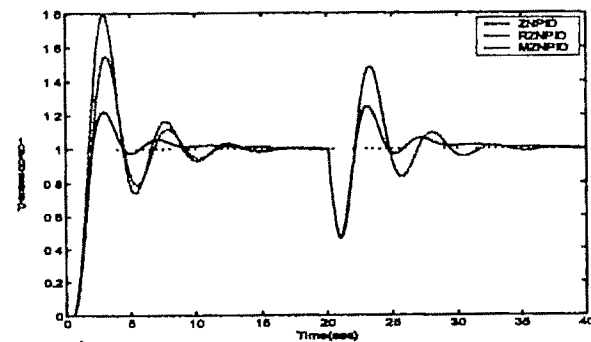


Fig. 6(b). Second order non-linear system, $L = 0.4s$ in (12).

$L=0.2s$	ZNPID	RZNPID	MZNPID
%OS	60.61	11.40	0.56
$t_r(s)$	1.00	1.50	1.30
$t_s(s)$	4.00	3.90	1.60
IAE	2.48	2.14	1.67
ITAE	15.93	14.94	12.07

Table I(a). Performance analysis for Second order linear system in (11).

$L=0.3s$	ZNPID	RZNPID	MZNPID
%OS	65.78	43.53	16.50
$t_r(s)$	1.50	1.70	1.80
$t_s(s)$	8.70	8.40	4.50
IAE	4.29	3.95	3.14
ITAE	41.40	39.99	33.20

Table II(a). Performance analysis for Second order non-linear system in (12).

$L=0.3s$	ZNPID	RZNPID	MZNPID
%OS	85.43	26.40	12.27
$t_r(s)$	0.90	1.30	1.10
$t_s(s)$	8.10	5.60	4.20
IAE	3.95	3.17	2.14
ITAE	30.51	27.68	16.67

Table I(b). Performance analysis for Second order linear system in (11).

$L=0.4s$	ZNPID	RZNPID	MZNPID
%OS	79.48	54.94	22.18
$t_r(s)$	1.40	1.60	1.70
$t_s(s)$	10.80	10.60	7.80
IAE	5.48	5.01	3.45
ITAE	58.31	56.05	37.15

Table II(b). Performance analysis for Second order non-linear system in (12).

Technical Session 3A

Sensors and Transducers

Modeling and Simulation of Laser Material Processing: Predicting Melt Pool Geometry and Temperature Distribution

M. A Sheikh

Laser Processing Research Centre, School of Mechanical, Aerospace & Civil Engineering, The University of Manchester, Manchester, M60 1QD, UK e-mail: m.sheikh@manchester.ac.uk

Abstract—This paper presents the enhanced thermal conductivity approach for modelling of laser melting processes. Here, Finite Volume Method (FVM) has been used to simulate the transient effects of a moving laser beam in the melting of mild steel (EN-43A). Experimental melt pool geometry has been compared with CFD model and enhanced thermal conductivity model.

Key words—Enhanced Thermal Conductivity Approach, Finite Volume Method, Laser Material Processing, Melt Pool Geometry.

1. INTRODUCTION

MANY laser manufacturing processes involve laser melting of material e.g. selective laser melting, welding, brazing, soldering, glazing, surface alloying, cladding etc. Modelling of these processes is extremely important for controlling these processes by predicting the melt pool geometry, thermal gradients, cooling rate, microstructure, and stress distribution etc. However, modelling of processes involving laser melting is not straightforward due to Marangoni and buoyancy convection within the melt pool.

It is well established that heat transfer in melt pool is influenced more by fluid flow than by heat conduction [1]. Fluid flow within the melt pool is dominated by thermo-capillary or Marangoni forces and hence conduction based models are not able to accurately predict the laser melting process, particularly in metals [1]. Thus any modelling attempt to investigate the effects of beam geometries on laser melting of metals should take into account melt pool convection due to thermo-capillary and buoyancy forces. Detailed CFD models

are therefore required to accurately predict the melt pool geometry and temperature distribution.

CFD modelling of melting processes require considerable expertise and computational resources. CFD models are also prone to errors due to uncertainties in the values of surface tension co-efficient and viscosity of material in the fluid state [2]. Model agreement can be improved by adjusting the values of surface tension coefficient and viscosity but to reach the correct figure, a sizeable computational effort is required. To simplify and speed up the modelling process, many researchers have used the enhanced thermal conductivity approach to account for melt pool convection. Here, instead of solving the intricate Navier-Stokes equations, only the energy equation is solved by enhancing the thermal conductivity beyond the melting temperature, to predict the melt pool geometry and temperature distribution. This approach has been used in the past for modelling laser cladding, laser welding [3-5] etc. However, researchers have used the values of enhanced thermal conductivity from literature which range from 2 times the original values to 420 times [3-5]. Due to this large bandwidth it is difficult to pick an accurate value from the available literature. Moreover, even if careful selection is made by looking at the materials and processing conditions, it is not known whether it would give the desired matching between the experimental and the predicted melt pool profile and temperature distribution. Thus there is a need to study the enhanced thermal conductivity approach and see its effectiveness.

This paper presents an analysis of the enhanced thermal conductivity approach for modelling laser melting processes. A finite volume model is constructed using a commercial software FLUENT to simulate the transient effects of a moving beam for laser melting of mild steel (EN-43A). Melt pool convection induced due to the Marangoni and buoyancy forces is taken into account in the CFD model, whereas enhanced thermal conductivity approach is used for the conduction model. Experimental melt pool geometry is compared with the CFD model and the enhanced thermal conductivity model to demonstrate the effectiveness of enhanced thermal conductivity approach.

II. FINITE VOLUME MODEL

A 3D finite-volume model, based on the Reynolds Averaged Navier Stokes Equations and the Enthalpy-Porosity technique was set-up in FLUENT for modelling of the laser melting process. The laser beam was input as surface heat flux. An 'area sector' approach [6] was used to simulate the moving laser beam instead of a moving wall approach. Necessary subroutines were added to handle the spatially varying heat flux to simulate the moving laser beam. For the normal heat transfer and enhanced thermal conductivity approach same model was used but only the energy equation was solved. In the enhanced thermal conductivity model, thermal conductivity values were enhanced by three to four times their original values. The enhancement in thermal conductivity k' is defined by (1) as:

$$k' = \alpha k \quad (1)$$

where k is the normal thermal conductivity value at the corresponding temperature and α is the enhancement factor which is defined as:

$$\alpha = \begin{cases} 1 & \text{if } T < T_{\text{liquidus}} \text{ \& } T_{\text{solidus}} \\ \text{multiplying factor} & \text{if } T > T_{\text{liquidus}} \end{cases}$$

where T_{liquidus} is the temperature at which solid formation begins and T_{solidus} is the temperature at which full solidification occurs.

Energy conservation equation for the complete single domain in enthalpy-porosity technique is written in terms of enthalpy and temperature, as in (2), [7]:

$$\frac{\partial}{\partial t}(\rho H) + \nabla \cdot (\rho \vec{u} H) = \nabla \cdot (k \nabla T) + \dot{q} \quad (2)$$

where H is enthalpy, ρ is density, \vec{u} is the fluid velocity and \dot{q} is the surface heat source. For enhanced thermal conductivity model k is replaced by k' in (2).

Enthalpy of material is computed as the sum of sensible enthalpy (h) and latent heat (ΔH), as in (3).

$$H = h + \Delta H \quad (3)$$

where

$$h = h_{ref} + \int_{T_{ref}}^T C_p dT$$

h_{ref} = Reference enthalpy

T_{ref} = Reference temperature

C_p = Specific heat at constant pressure

Latent heat content (ΔH) can be written in terms of latent heat of the material, as in (4) [7]:

$$\Delta H = \beta L \quad (4)$$

where β is the liquid fraction, which is defined as:

$$\beta = \begin{cases} 0 & \text{if } T < T_{\text{solidus}} \\ \frac{T - T_{\text{solidus}}}{T_{\text{liquidus}} - T_{\text{solidus}}} & \text{if } T_{\text{solidus}} < T < T_{\text{liquidus}} \\ 1 & \text{if } T > T_{\text{liquidus}} \end{cases}$$

Thermocapillary or Marangoni convection is treated as shear stress applied at wall. Shear stress applied at the wall is given by (5), [7]:

$$\tau = \frac{d\sigma}{dT} \nabla_s T \quad (5)$$

where τ is the shear stress, $d\sigma/dT$ is the surface tension gradient with respect to temperature and $\nabla_s T$ is the surface gradient. Shear stress given by (5) is then applied to momentum equations.

The governing equations are finally solved simultaneously using a segregated solver and employing SIMPLE algorithm to obtain temperature and velocity fields. Because of the complexity of the model simplifying assumptions have been made which are:

1. Liquid metal flow within the melt pool is Newtonian, incompressible and laminar.
2. As the power density is low and there is no external gas pressure, the free surface is assumed planar. Similar laser processes involving melting, have been modelled in the past with the assumption of planar free surface with reasonable accuracy.
3. Radiation effects are neglected

A circular laser beam with a diameter of 3.34 mm was used for the model. The power distribution of fiber optic coupled high power diode laser was close to top-hat; therefore a uniform power distribution was used in the model. The power density was set at 5.5 kW/cm^2 and the processing of a single surface track length of 20 mm was modelled. The scanning speed of laser was set at 5 mm/s.

The material used was bright drawn mild steel EN-43A (0.45-0.55 wt % C, 0.05-0.5 wt % Si, 0.70-1.00 wt % Mn, 0.060 wt % S, 0.060 wt % P), as supplied (average hardness of 220 HV). The size of the work piece was $50 \times 50 \times 10 \text{ (mm}^3\text{)}$. The ambient temperature was set at 20 °C. Temperature dependent material properties were used for the model [8, 9].

III. EXPERIMENTAL SET-UP

The laser source used was a 1.5 kW fiber coupled high power diode laser (LDL 160-1500) operating in the range of 800 - 980 nm, with a top hat (approximately uniform) power distribution and a circular laser spot.

The sample was sand blasted to improve the absorptivity of the laser beam. Ocean Optics SD 2000 fibre optic spectrometer was used to measure the reflectivity of the investigated material (EN-43A) at the abovementioned laser wavelengths. It was found to be between 41-43 % at room temperature.

A CNC table was used to move the material under the laser beam, and the table velocity was set at 5 mm/sec. The input power was adjusted according to the material absorptivity and fiber coupling in order to maintain the power density at 5.5 kW/cm^2 . A single colour Impac Pyrometer, requiring input of material emissivity, was used for temperature measurement in this study. The upper limit of pyrometer was 2000 °C (2273 K) while the lower limit was 250 °C (523 K). The temperature sensitivity at the lower limit was poor. Emissivity of material increases significantly close to melting temperature due to changing surface conditions and oxidation. Emissivity of molten mild steel of 0.50 (taken from literature) was therefore supplied as input to the pyrometer for accurate measurement of surface temperature. The temperatures recorded by the pyrometer below the melting temperature were therefore inaccurate and were not considered; only maximum

surface temperature was recorded. Figure 1 shows the schematic arrangement of experimental set-up.

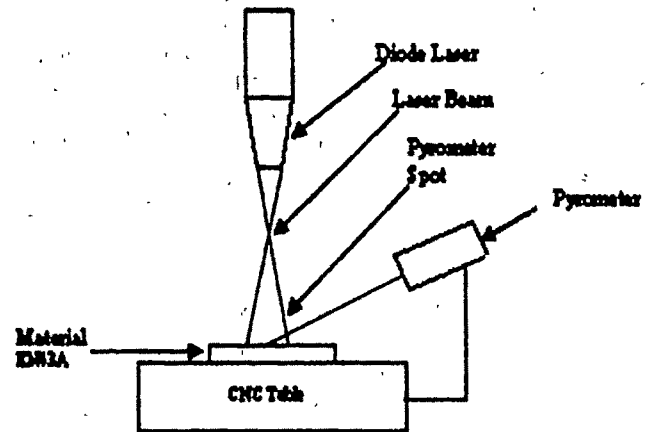


Fig 1. Schematic representation of the experimental set-up

IV. RESULTS & DISCUSSION

To analyse the effects of enhanced thermal conductivity approach for predicting the melt pool geometry and the temperature distribution, a comprehensive post-processing analysis was carried out on all the four models (i.e. CFD, heat transfer and two enhanced thermal conductivity models). The global co-ordinate system for the model was in the middle and on the top of the work-piece. Three orthogonal paths were created namely 'Along' (path along the scanning direction), 'Cross-sec' and 'Depth' for the purpose of analysis. A liquidus line has been superimposed on all the graphs to quickly see the temperature distribution above the melting temperature, the melt zone. Some of the results have also been compared with the experimental results.

Fig 2 shows the temperature distribution on the 'Along' path. Melt pool length can be estimated by looking at the temperature distribution above the liquidus line. It can be seen that the melt pool length predicted by all the four models is approximately similar. The maximum temperature predicted by the normal heat transfer model (*Circle HTx1*) is 2615 K, whereas the maximum temperature predicted by the CFD model (*Circle conv*) is 1946 K which is much closer to the experimentally measured temperature of 1992 K. The enhanced thermal conductivity models predict a temperature in between the CFD and the heat transfer model. The maximum temperature predicted by the four times model is 2069 K, which is less than the maximum temperature predicted by the three times model (i.e. 2127 K) is mainly due to the increased heat diffusion above the liquidus temperature. Although the maximum temperature predicted by the enhanced thermal conductivity models is less than the normal heat transfer model, nevertheless the temperature profile remains similar to

the normal heat transfer model.

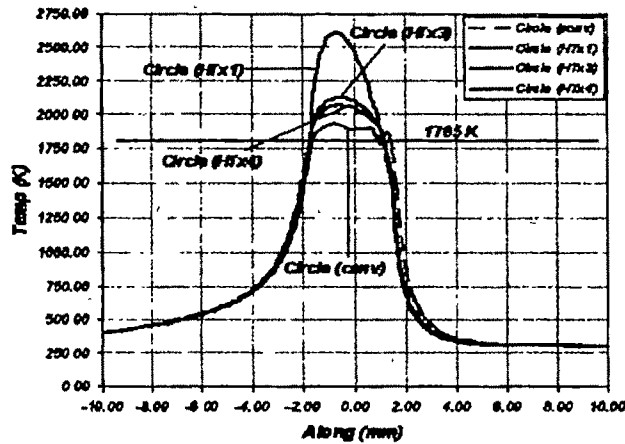


Fig 2. Temp vs distance on the 'Along' path

Fig 3 shows the temperature distribution on the 'Cross-sec' path. Melt pool width can be estimated by examining the temperature distribution above the liquidus line. It can be seen that the melt pool width predicted by all the models is approximately similar.

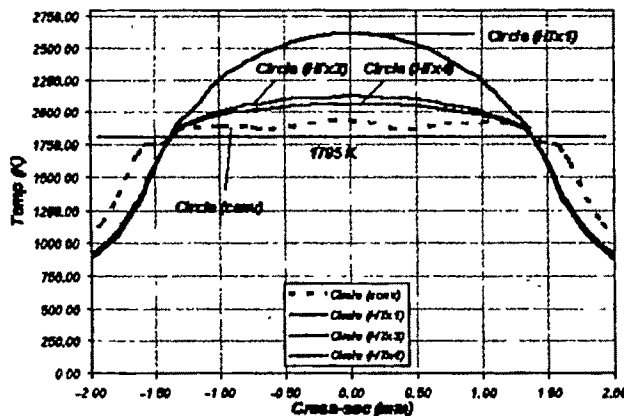


Fig 3. Temp vs distance on the 'Cross-sec' path

From Figures 2 and 3, it can be suggested that if the enhanced thermal conductivity value is further increased, the maximum surface temperature will approach that predicted by the experiments and the CFD model.

Fig 4 shows the temperature distribution on the 'Depth' path. Melt pool depth can be estimated by looking at the temperature distribution above the liquidus line. Unlike the 'Along' and the 'Cross-sec' paths, the melt pool depth predicted by the CFD model and the heat transfer models is significantly different. The melt pool depth predicted by the heat transfer and the enhanced thermal conductivity models is approximately five times higher as predicted by the fluid flow model (Table 1). This shows that increasing the thermal conductivity does not change the melt pool depth. This is mainly due to the energy balance. The melt pool volume

predicted by the heat transfer models (i.e. the normal heat transfer model and the enhanced thermal conductivity models) remains the same. The only effect of increased thermal conductivity is that it clips the maximum surface temperature due to the increased heat diffusion. Thus it can be said that the enhanced thermal conductivity model is not able accurately to predict the melt pool depth.

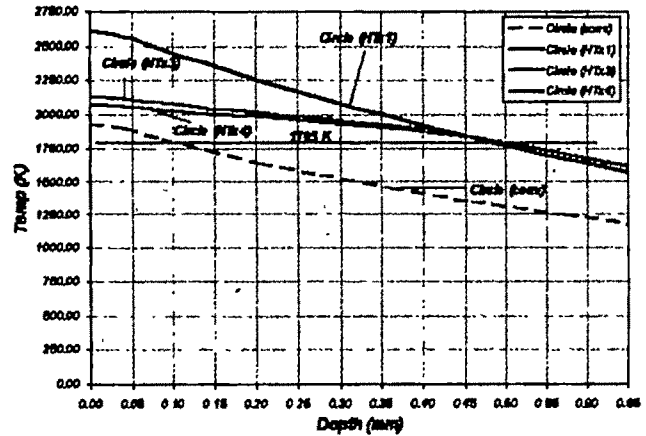


Fig 4. Temp vs distance on the 'Depth' path

Fig 5 compares the experimental melt pool profile and the cross-sectional melt pool profiles predicted by the CFD, heat transfer, and enhanced thermal conductivity models. It can be seen that the experimental pool profile is flatter and is in better agreement with the CFD model. The melt pool profile predicted by the normal heat transfer model and the enhanced thermal conductivity models is having a meniscus profile. Accurate prediction of melt pool profile is very important as the solidification microstructure would exist within the melt pool. Moreover the orientation of solidification microstructure is dictated by the melt pool profile. Thus if the predicted melt pool profile is not accurate the predicted orientation of the solidification microstructure will also be inaccurate.

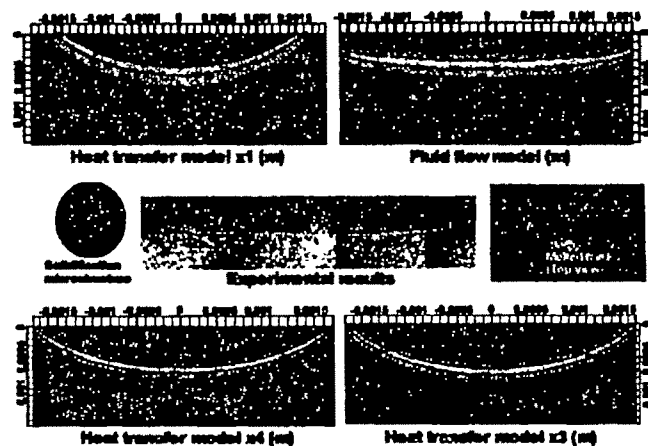


Fig 5. Comparison of melt pool profiles

Model	Max Temp (K)	Width (mm)	Depth (mm)
Experiment Results	1992	2.57	0.166
CFD Model	1946	3.08	0.132
Heat Transfer Model	2615	2.84	0.48
Enhanced thermal Conductivity model $\times 3$	2127	2.84	0.47
Enhanced thermal Conductivity model $\times 4$	2069	2.84	0.47

Table 1. Comparison of experimental and modelling results

V. CONCLUSIONS

Modelling of laser manufacturing processes involving laser melting is extremely important for controlling and optimising these processes. However, modelling of these processes is not straightforward due to Marangoni and buoyancy convection within the melt pool. Detailed CFD models are required to accurately predict the melt-pool geometry and temperature distribution. CFD modelling of melting processes require greater user expertise and longer computational times. To simplify and speed up the modelling process, many researchers have used the enhanced thermal conductivity approach to account for melt pool convection. Instead of solving the intricate Navier-Stokes equations, only the energy equation is solved by enhancing the thermal conductivity beyond the melting temperature, to predict the melt pool geometry and temperature distribution. However, researchers have used the values of enhanced thermal conductivity from the available literature without any validation. Moreover, it is not established whether the enhanced thermal conductivity is able to accurately predict the melt pool geometry and temperature distribution. The work presented in this paper has investigated the enhanced thermal conductivity approach to artificially simulate the fluid flow within the melt pool. A CFD model, a normal heat transfer model, and two enhanced thermal conductivity models have been developed using finite volume method.

It has been found that the enhanced thermal conductivity approach gives reasonable results on the work-piece surface. However, it is not able to accurately predict the melt pool depth and melt pool profile, which are of significant importance for any process involving laser melting.

REFERENCES

- [1] Mills, K. C., Koene, B. J., Brooks, R. F., and Shirali, A., 1998, "Marangoni Effects in Welding," in *The Royal Society*, pp. 911-925.
- [2] Eustathopoulos, N., Drevet, B., and Ricci, E., 1998, "Temperature Coefficient of Surface Tension for Pure Liquid Metals," *Journal of Crystal Growth*, vol. 191, pp. 268-274.
- [3] Toyserkani, E., Khajepour, A., and Corbin, S., 2004, "3-D Finite Element Modeling of Laser Cladding by Powder Injection: Effects of Pulse Shaping on the Process," *Optics and Laser in Engineering*, vol. 41, pp. 849-867.
- [4] Zhang, W., Kim, C.-H., and DebRoy, T., 2004, "Heat and Fluid Flow in Complex Joints During Gas Metal Arc Welding-Part II: Application to Fillet Welding of Mild Steel," *Journal of Applied Physics*, vol. 95, pp. 5220-5229.
- [5] Kim, C.-H., Zhang, W., and DebRoy, T., 2003, "Modeling of Temperature and Solidified Surface Profile During Gas-Metal Arc Fillet Welding," *Journal of Applied Physics*, vol. 94, pp. 2667-2679.
- [6] Sadler, S., Li, L., Sheikh, M. A., and Schmidt, M. J., 2006, "A Thermal History Analysis of Surface Heating of Mild Steel with Different Laser Beam Geometries," *Journal of Mechanical Engineering Science, IMechE Part C*, vol. 220, pp. 1549-1557.
- [7] Fluent, "Users Guide," vol. Vol 1,2 &3, pp. 2005.
- [8] Branger, G., Henry, G., and Sanz, G., *The Book of Steel*, Intercept Limited, 1996.
- [9] Kumar, A., Zhang, W., and DebRoy, T., 2005, "Improving Reliability of Modelling Heat and Fluid Flow in Complex Gas Metal Arc Fillet Welds-Part I: An Engineering Physics Model," *Journal of Physics D: Applied Physics*, vol. 38, pp. 119-126.

Simulation of Loopless Deflection Routing Algorithms in Label Switched Optical Networks Using SimEvents

G Pavan Kumar and Vinod Chandra

Department of Electrical Engineering, Indian Institute of Technology, Delhi,
New Delhi, 110016, INDIA, vchandra@ee.iitd.ernet.in

Abstract: Contention Resolution is an important issue in case of Packet Switched Optical Network. Two loopless deflection routing algorithms load insensitive and load sensitive, are simulated in a six node label switched optical network. Load insensitive deflection routing algorithm attempts to find the shortest path in term of the hop distance and does not consider the load information in the routing process. Load sensitive deflection routing algorithm takes the link load information into account and the deflection path is computed based on the estimated link load. Load cost is defined in terms of link load and bandwidth allocated. Simulation is done using a discrete event simulation tool SimEvents.

Key Words: *Loopless Deflection, Optical Networks*

I. INTRODUCTION

THE convergence of telecommunication and data communication has caused a paradigm shift in networking environment. The massive explosion in traffic generated by the Internet has driven the current trend, with Internet Protocol (IP) becoming the dominant protocol for data communication [1]. Electronic packet-switching technologies are capable of providing services based on various priority and buffering schemes, but the increasing transmission rates and high wavelength densities over each fiber will eventually make it very expensive to process each packet electronically at each node. All-optical switching technologies will enable packets to traverse nodes transparently without conversion to electronics. This technology has the potential to offer the flexibility of existing packet switched networks and also eliminate the cost of electronic conversion and processing at each node [2]. An important issue in case of photonic packet switched network is Contention Resolution. Contention occurs when two or more packets contend for same output port on same wavelength at the same time. Typically, contention in traditional electronic packet-switched networks is handled through buffering; however in optical domain, it is more difficult to implement buffers, since there is no optical equivalent of random-access memory. There are three dimensions for resolving contention: optical delay lines (ODL), space deflection and wavelength usage [2]. Both ODL and wavelength converters require extra hardware and control software, but deflection can be implemented with simple control software. In case of space deflection, packets that

lose the contention are routed to the node other than their preferred next-hop nodes, with an expectation that they will eventually be routed to their destinations.

II. DEFLECTION ROUTING ALGORITHMS

To achieve contention resolution in the space domain preferred and deflection routing tables are required for an optical router and following algorithms can be used to construct them.

A. Load insensitive deflection routing algorithm

This algorithm is based on k -shortest path algorithm and is independent of the link load in the network. It attempts to find the shortest path in term of the hop distance and does not consider the load information in the routing process. The preferred path and the deflection path between source s and destination d are the first and second shortest paths determined based on the hop count². Dijkstra's algorithm is used to determine these paths in NSF network.

B. Load sensitive deflection routing algorithm

This algorithm follows same method to compute the preferred path as the load insensitive algorithm. But to estimate the deflection path, the link cost parameter C_{ij} is used instead of shortest path.

$$C_{ij} = \lambda_{ij} / B_{ij} \quad (1)$$

where λ_{ij} is the estimated load and B_{ij} is the maximum bandwidth of link l_{ij} . The least cost path from source s to destination d is the deflection path in this case. Thus load sensitive deflection routing algorithm takes link load into account³. The link load is estimated based on the preferred path determined using Dijkstra's algorithm. Load sensitive case has been proposed in [3].

III. SIMULATION

The above mentioned algorithms are simulated for a six node label switched optical network shown in Figure 1 using SimEvents [4]. The number on each link in the network, multiplied by 10 km will give distance of the link. SimEvents extends Simulink in Matlab with tools for modeling and simulating discrete-event systems using queues and servers [4]. A *discrete-event simulation*, or event-based simulation, permits the system's state transitions to depend on asynchronous discrete incidents that are called *events*. These items are called *entities* in

SimEvents. Entities pass through a network of queues, servers, gates, and switches during a simulation. Entities can carry data, known in SimEvents as attributes [4].

In the simulation, each node is modelled as M/D/1 system with a maximum link transmission speed of 10 Gbps. The traffic is uniformly distributed at all nodes. The schematic of the simulation model for a node is shown in Figure 2. To simplify the simulation, labels are defined on a per-destination basis. By utilizing destination-based labeling, the number of label entries at each node can be kept to a minimum. Use of such deterministic labels will do away with the need of label swapping. So hop by hop routing can be used similar to IP routing [2, 5].

As shown in the schematic, at every node, packets are generated and labels are attached. An attribute for hop count is associated with the packet and initialized to zero in. Routing block contains the routing tables which are calculated based on the algorithms mentioned above. It also contains the collision detection block, which on detection of collision, routes the packet based on one of the deflection routing algorithms. For each destination label, the preferred port and deflection ports are precomputed using the deflection routing algorithms and the tables obtained using load insensitive and load sensitive algorithms for each node.

When the packet enters the node, if the hop counter is greater than 1, the packet is dropped to avoid packet getting into loops in the network. Once the packet enters the node, a single server serves it for the assigned service time, and then the hop count is updated. Also, the label of the packet is checked. If the label matches with the current node number, then the packet is sent to sink else it is sent to the routing block.

Each packet is associated with a timer tag before it leaves the node. When it enters the node, the timer tag is read and the delay is calculated. To simulate the delay, an infinite server with appropriate service time (Length of the link / Velocity of the signal in the fiber), is used in each link.

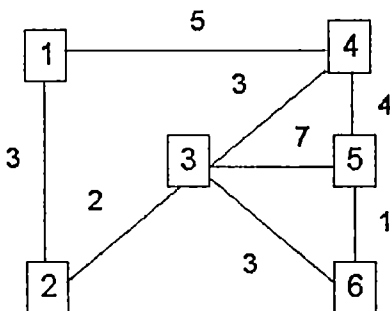


Fig. 1. Six node network used for simulation and analysis

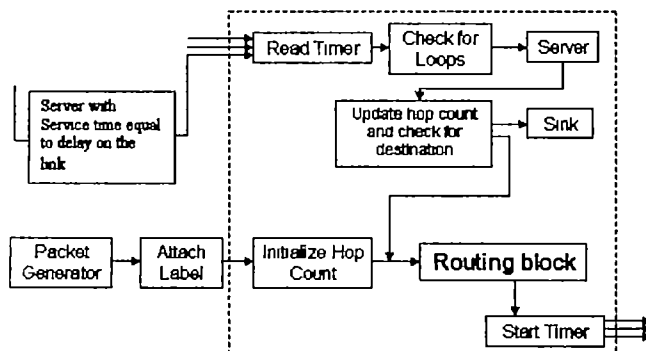


Fig. 2. Schematic of node used in the simulation

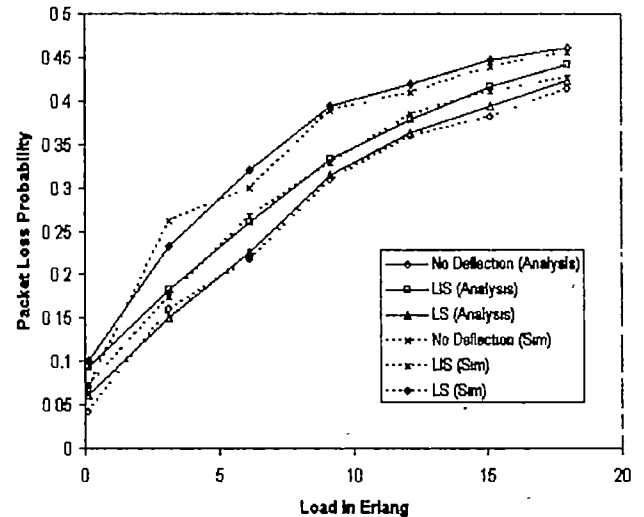


Fig. 3. Packet loss probability in the network under various loopless deflection routing algorithms

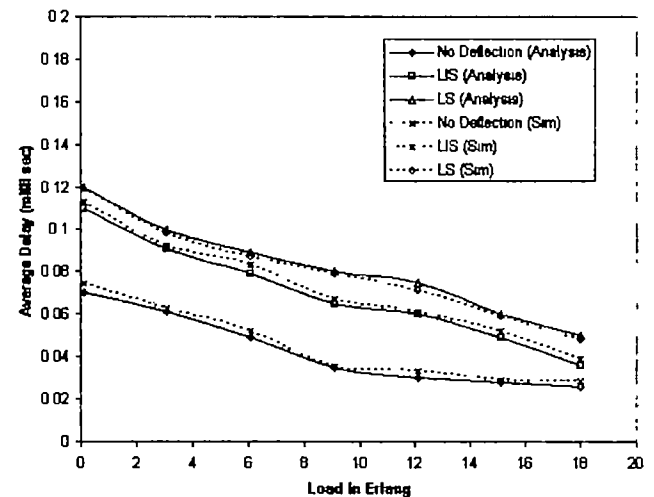


Fig. 4. Average delay in the network under various loopless deflection routing algorithms

IV. RESULTS AND CONCLUSIONS

Two loopless deflection routing algorithms are simulated using SimEvents. Destination based labels are used to do away with label swapping and simple hop by hop routing was used in which for a given destination label, the next node for the packet is decided from the routing table precomputed from the deflection routing algorithms.

Simulation results are shown in Fig. 3. and Fig. 4. In the case of load sensitive deflection routing, the path chosen is the one with least load. Since the load on these paths chosen is lower compared to that of the paths chosen by load insensitive deflection routing, the contention probabilities are less in load sensitive case leading to lower packet loss probabilities. From analysis, it is concluded that when the load is close to zero, the loss probabilities for both the cases are almost same. As the load increases, the loss probabilities are lower for load sensitive case, implying that load sensitive works more efficiently at

higher load conditions. At lower loads, the analysis overestimates the algorithms and the values from simulation do not match.

From simulation it is observed that, as the load increases, more number of packets get deflected due to increase in contention. Since only deflection alternative is assumed for every node, the extent of deflection is highly limited and more number of packets with increasing loads. This reduces the overall delay with increasing delay. Since the paths chosen by load sensitive deflection routing algorithm are longer compared to load insensitive deflection routing, the average delay is more for the former case.

REFERENCES

- [1] B. Mukherjee, *Optical WDM Networks* (Springer Series, 2006).
- [2] P. Jason, "An algorithm for loopless deflection in photonic packet-switched networks", *Proc. IEEE Int. Conf. Commun.*, 5, 2776-2780 (2002).
- [3] S. Yamano, Fei Xue, and S. J. Ben Yoo, "Load-Sensitive Deflection Routing for Contention Resolution in Optical Packet Switched Networks", *Proc. IEEE Int. Conf. Commun.*, 243-248 (2003).
- [4] Mathworks, User guide for SimEvents for use with Simulink, version 1(2006).
- [5] S J. Ben Yoo, "Optical-label switching, MPLS, MPLambdaS, and GMPLS", *Optical Networks magazine* (2003).

Metal Oxide Gas Sensor under UV radiation: Theory and Experiment

Sunita Mishra¹, Indrajeet Boiragi, and C Ghanshyam

¹Central Scientific Instruments Organization, Chandigarh-160 030, India, Email: s_mishra8@rediffmail.com

Abstract—The effect of ultraviolet radiation on the sensing mechanism of polycrystalline metal oxide gas sensor has been studied experimentally and theoretically. A theoretical model is developed and is verified experimentally. We found that increasing the UV radiation flux density and alcohol concentration increases the conductivity of the film by decreasing the resistance which results in the increase in sensitivity. The sensing characteristics of the sensor with and without UV radiation matched with the experimentally observed characteristics of the sensor but with a slightly different value. It may be due to the fact that the exact physical parameters of TGS 822 were not available and we have taken the approximate values of the parameters for the numerical calculations.

Key words—Grain boundary, Metal oxide sensor, Sensitivity, UV radiation.

I. INTRODUCTION

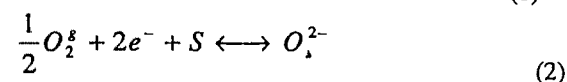
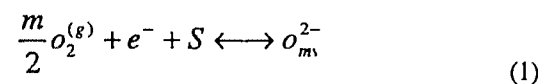
METAL oxide gas sensors have been extensively used for the detection of volatile, toxic and explosive gases. Its performance strongly depends on their electronic and structural properties of the surface when it is brought into contact with a gas. They show their sensing behavior around the temperature range of 175°–425°. To make it power efficient a number of effort has been made to lower the sensor operating temperature. J. Saura [1] studied the gas sensing properties of SnO₂ pyrolytic films under UV radiation and found that thermally treated SnO₂ are capable of fast detection of trichloroethylene and acetone vapors even at the room temperature. It has been observed that UV exposure enhances the performance of tin oxide film by decreasing the operating temperature and response and recovery time with no poisoning effect [2]. Many authors has studied the light enhancing properties of metal oxide thin film for oxygen and other reducing gases like CO at room temperature [3],[4]. It was found that illumination often influences the adsorption rate. Moreover, the time dependence of adsorption rate and activation energy may also be changed by illuminating the sensor with band gap energy light. The effect of UV radiation

exposure on the room temperature hydrogen sensitivity of nano-crystalline indium oxide (In₂O₃) doped tin oxide thin film gas sensor exhibited a very high sensitivity but at higher concentration of H₂ the sensitivity decreases by a small amount [5]. Mishra et al has studied the effect of UV radiation on the sensing mechanism of metal oxide gas sensor theoretically and found that it is possible to detect gases even at room temperature [6].

This paper deals with the experimental validation of the theoretical model developed for metal oxide gas sensor exposed under UV radiation. An experimental study has been done with TGS 822 gas sensor which is generally used for the detection of alcohol. Since the most common metal oxide that is used for sensor is tin oxide and also TGS 822 is based on tin oxide, the parameters used in the theoretical calculations is taken for tin oxide.

II. DETECTION MODEL

Tin oxide (SnO₂) is a wide band-gap semiconductor; $E_g = 3.5$ eV, with n type of conductivity due to the presence of bulk oxygen vacancies. The surface oxygen vacancies play the role of chemisorptions sites in the presence of atmospheric oxygen. We have used the assumption taken in [7]. Oxygen chemisorptions can be described as



where S is an unoccupied oxygen vacancy, superscript 'g' denotes a gaseous species, subscript 's' denotes a surface fixed species, O_m is a singly ionized oxygen atom coupled with a surface oxygen vacancy for $m=1$ or a singly ionized oxygen molecule for $m=2$, O_s^{2-} is a doubly ionized oxygen atom coupled with a surface oxygen vacancy e^- is an electron.

The concentration of surface oxygen vacancies, N_{oxy} , in the presence of atmospheric oxygen is evaluated by assuming that the bulk oxygen vacancies within a sheet of thickness δ at

surface are in fact surface vacancies with N_d as donor density. N_{oxy} for spherical grain of radius R is given as [7]

$$N_{oxy} = \Delta N = N_d \delta \left(1 - \frac{\delta}{2R} - \frac{\delta^2}{3R^2} \right) \quad (3)$$

Using the assumption that $2N_{oxy} = N_b R$, where N_b is the bulk concentration of electrons and (3) and (5), R is given as

$$R = \delta \left(1 + \frac{N_d}{N_b} \right) \left[1 + \left(\frac{N_d / N_b}{1 + (N_d / N_b)} \right)^{1/2} \right] \quad (4)$$

It is assumed that the resistance is mainly due to the neck resistance R_n and grain boundary resistance R_{gb} . When UV radiation falls on the SnO_2 polycrystalline film, electron hole pairs are generated in the grain depletion region. Using the depletion approximation and solving the Poisson's equation, the grain boundary barrier height is given as [6]

$$V_b = \frac{q}{\epsilon} \left[\frac{1}{2} N_d w^2 - \phi \tau \left(w + \frac{1}{\alpha} \exp(-\alpha w) \right) \right] \quad (5)$$

with w as depletion width, α as absorption coefficient, ϕ as UV radiation flux density, τ as minority carrier life time. Assuming that the conduction is mainly due to the thermionic emission [8] the current density across the grain boundary is given as [6]

$$J = q^2 N_d \left(\frac{1}{2\pi m_n K T} \right) \exp \left[\frac{-q^2 N_d w^2}{2\epsilon K T} \right] \cdot \exp \left[\frac{q^2 \phi \tau}{\epsilon K T} \left(w + \frac{1}{\alpha} \exp(-\alpha w) \right) \right] \quad (6)$$

Using the approximation that V_b is equal to electric field E across this boundary of grain size L , the grain boundary resistance can be expressed as [6]

$$R_{gb} = \frac{(2\pi m_n k_b T)^{1/2}}{(A_{gb} q^2 N_d)} \exp \left[\frac{-q^2}{\epsilon K T} \left(\frac{1}{2} N_d w^2 - \phi \tau \left(w + \frac{1}{\alpha} \exp(-\alpha w) \right) \right) \right] \quad (7)$$

Here A_{gb} is the cross-section of grain boundary; T is the operating temperature of the sensor and ϵ the permittivity of metal oxide.

For taking into account the neck grain conductivity it has been assumed that its carrier density in the depletion region is N_b . Hence the total neck grain current density is

$$I_N = \pi(R-w)^2 q N_b \mu_b E_N + \pi[R^2 - (R-w)^2] q N_d \mu_d E_N \quad (8)$$

where μ_b and μ_d are the electron mobility of the neutral grain body and the depletion region respectively and E_N is the electric field. Using V_b as in (5) and

$$N_b = N_d \exp \left(\frac{-q V_b}{K T} \right) \quad (9)$$

Neck grain resistance R_N is given as

$$R_N = [\pi(R-w)^2 q N_b \mu_b] \cdot \exp \left[\frac{1}{\epsilon} \left(\frac{q^2}{K T} \left(\frac{1}{2} N_d w^2 - \phi \tau \left(w + \frac{1}{\alpha} \exp(-\alpha w) \right) \right) \right) \right] + \pi[R^2 - (R-w)^2] q N_d \mu_d \quad (10)$$

Total sensor conductance is given by $R = R_N + R_{gb}$. Sensitivity of the metal oxide gas sensor S is defined as

$$S = \frac{R_{air}}{R_{gas}} \quad (11)$$

Here R_{air} and R_{gas} are the sensor resistance in air and in reducing gases respectively. For the present calculation following parameters have been used: $N_b = 3.5 \times 10^{24} \text{ m}^{-3}$, $m_0 = 0.275 m_0$ (electron rest mass) and $\alpha = 8 \times 10^6 \text{ m}^{-1}$.

III. EXPERIMENTAL STUDY

The sensing characteristics of tin oxide gas sensor TGS-822 was carried out under UV exposure. The sensor was illuminated with UV radiation from a mercury lamp with an of output power of 18 W/cm^2 . An optical fiber was used to guide the UV radiation directly on the sensor surface in order to avoid power loss. In order reduce the power loss further, the sensor cover was removed and placed in front of the optical fiber. During the period of experiment the distance between the sensor surface and the optical fiber was maintained at a constant distance. Ethanol was injected in the test chamber using a syringe. The volume of the test chamber was 5l. The test chamber has a small fan that is used for mixing the alcohol vapour with air. Electrical characterization was carried out by biasing the sensor with a 5 V DC power supply and measuring the sensor resistance by Model 485 Keithely Picoammeter. The heater voltage was applied to sensor using a regulated power supply and it was varied from 1V to the 4V. After every measurement, clean dry synthetic air was used to remove the contaminant from the sensor surface.

IV. RESULTS AND DISCUSSIONS

Numerical calculations have been carried out for the sensing characteristics of the film using the developed model and it was verified experimentally. Sensor temperature for TGS 822 as a function of heater voltage is calculated using the formula given as [9]

$$T = 102.83.V + 214.37(K) \quad (12)$$

Fig. 1 shows the variation of grain boundary barrier height V_b with adsorbed gas concentration under UV radiation theoretically. It is observed from the graph that with the increase in the adsorbed gas concentration and UV radiation flux density, V_b decreases. It is due to the fact that as UV radiation flux density and adsorbed gas concentration

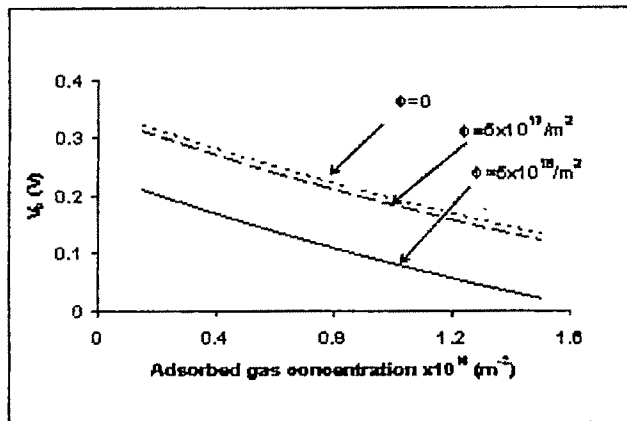


Fig. 1. Variation of grain boundary barrier height with adsorbed gas concentration

increases, number of electrons generated increases thereby decreasing the potential barrier. At the radiation flux densities of $5 \times 10^{17}/\text{m}^2$ and $5 \times 10^{18}/\text{m}^2$, grain boundaries barrier height decreases from 0.22V to 0.12V at the adsorbed gas concentration of $0.8 \times 10^{16}/\text{m}^2$.

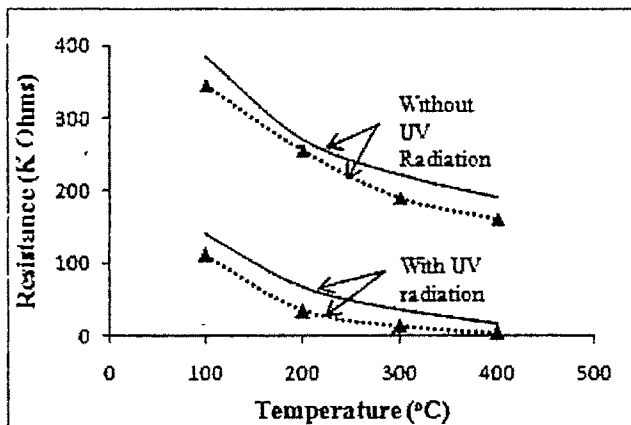


Fig.2 Plot of Resistance versus operating temperature of sensor. Solid and dotted lines are theoretical and experimental results respectively.

Fig.2 shows the variation of sensor resistance with operating temperature in the presence and absence of UV radiation at a flux density of $10^{18}/\text{m}^2$ and alcohol concentration of 600 ppm. It has been observed that the resistance decreases with the increase in the temperature. The difference in the resistance in the presence and absence of UV radiation is almost five times. Though the experimental and theoretical values have a quantitative difference but the nature of variation is same in both the cases. Decrease in the resistance shows an exponential behavior in both the cases.

Sensitivity versus temperature plot is shown in Fig.3. The UV radiation flux density was kept at $10^{18}/\text{m}^2$ and alcohol concentration at 600 ppm. The nature of the variation in experimental and theoretical data is same with a slight variation. Sensitivity first increases with temperature and after reaching a highest value it starts decreasing. This is because at

lower temperature, sensitivity is due to the speed of the chemical reaction and at higher temperature it is due to the diffusion of the gas molecules but at the intermediate temperature both process becomes equal and add to give maximum sensitivity. By exposing the sensor to UV radiation results in further increase in the sensitivity because UV radiation increases the electron concentration by creating the electron hole pairs thereby decreasing the sensor resistance.

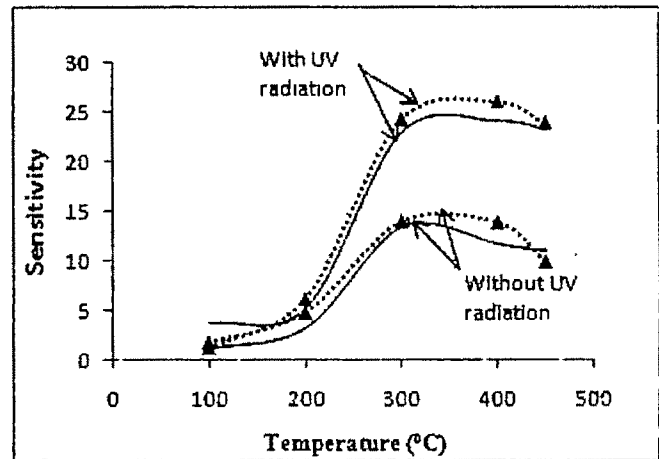


Fig.3. Sensitivity as a function of sensor operating temperature. Solid and dotted lines are theoretical and experimental results respectively.

Variation of sensitivity with alcohol concentration is plotted in Fig.4. As evident from the above results, UV radiation results in the enhancement of the sensitivity. These

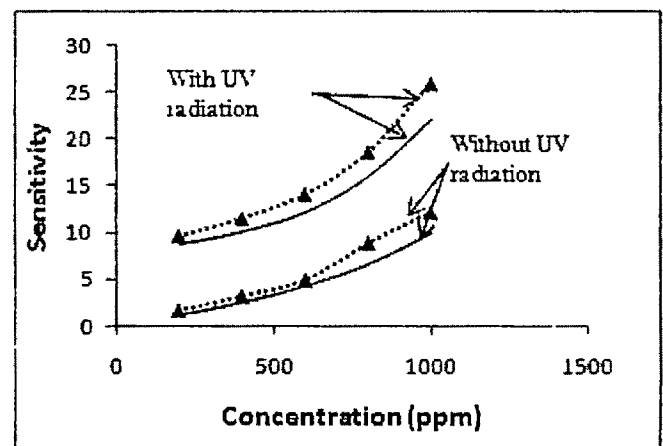


Fig.4 Graph between sensitivity and gas concentration. Solid and dotted lines are theoretical and experimental results respectively.

results are obtained at the UV radiation flux density of $10^{18}/\text{m}^2$ and at the temperature of 249.86°C . As the alcohol concentration increases sensitivity increases. The reason behind it is that as the alcohol concentration is increased, more and more gas molecules participate in the chemical reaction and diffusion, resulting in the decrease in the resistance. UV

radiation also enhances the sensitivity by adding the more number of electrons that further reduces the resistance of the sensor. In this plot also the nature of the graph of the experimental results match well with the theoretical results.

V. CONCLUSION

An analytical model has been developed for the metal oxide sensor and verified experimentally. It was seen that experimental results and the results obtained by the theoretical model shows the same graphical behavior with a little quantitative difference. This difference can be attributed to the fact that the exact physical parameters of the metal oxide used in TGS 822 sensor are not known and we have used the approximate values of the parameters. It has been observed that the UV radiation is capable of enhancing the sensitivity while keeping the experimental conditions same.

REFERENCES

- 1 J saura, "Gas sensing properties of SnO₂ pyrolytic films subjected to ultraviolet radiation," *Sensors and Actuators B*, vol.17 .pp 211-214 Feb. 1994.
- 2 E Comini, G. Faglia and G. Sberveglieri, "UV light activation of tin oxide thin films for NO₂ sensing at low temperatures" *Sensors and Actuators B*, vol.78 , pp .73-77, Aug.2001.
- 3 P. Camagni, G. Faglia, P. Galinetto, C. Perego, G. Samoggia and G. Sberveglieri, "Photosensitivity activation of SnO₂ thin film gas sensors at room temperature," *Sensors and Actuators B*, Vol. 31, pp.99-103, Feb 1996.
- 4 E. Comini, A. Cristalli, G. Faglia and G. Sberveglieri, "Light enhanced gas sensing properties of indium oxide and tin dioxide sensors," *Sensors and Actuators B*, Vol. 65, pp.260-263, June 2000
- 5 S Shukla, R Agarwal, H young, J. Cho, Sudipta Seal, L. Ludwig and C Parish, " Effect of ultraviolet radiation exposure on room-temperature hydrogensensitivity of nanocrystalline doped tin oxide sensor incorporated into microelectromechanical systems device," *J Appl. Phys.* vol.97, pp.054307-054320, Mar.2005
- 6 Sunita Mishra, C. Ghanshyam, N. Ram, R P. Bajpai and R. K. Bedi, "Detection mechanism of metal oxide gas sensor under UV radiation," *Sensors and Actuators B*, Vol. 97, pp.387-390, Feb.2004.
- 7 N Baisan and R.Ionescu , "The mechanism of the interaction between CO and an SnO₂ surface: the role of water vapour," *Sensors and Actuator B* , vol.12, pp. 71-75, March 1993.
- 8 S. M. Sze, in *Physics of Semiconductor Devices*, Wiley, New York, 1981, pp.255.
- 9 A. Lee and B. Reedy, "Application of radiometric temperature determination methods to semiconductor as sensors," *Sensors and Actuators B*, vol. 69, pp.37-45, Sept.2000

Modeling and Simulation of SMART CMOS MEMS Pressure Sensor

C. Roy Chaudhuri¹, N. Futane², and H. Saha²

¹ Bengal Engineering and Science University Shibpur, India e-mail: chirooreepam@yahoo.com

² Jadavpur University, Kolkata, India e-mail: sahairanmay@yahoo.com

Abstract—In this paper, coupled simulation for front end design of SMART CMOS MEMS pressure sensor has been proposed. This helps to reduce the design cycles for the development of integrated sensors and sensor array. A model of MEMS piezoresistive pressure sensor has been developed which has been linked dynamically with the low voltage low noise current mode instrumentation amplifier (IA) for signal conditioning. The results of the MEMS pressure sensor analytical model has been matched with the ANSYS results. The MOS model used for the simulation of the low noise micropower IA is 0.18 μ m dual threshold technology. The simulation of the integrated amplifier and MEMS has been done using TSPICE and the variation of the output voltage of the amplifier with different pressure for a particular dimension of the sensor has been obtained directly from the netlist.

Key words—Coupled simulation, dynamically linked library, integrated CMOS MEMS

I. INTRODUCTION

IN this paper, a new coupled circuit and mechanical simulator has been reported for the design and simulation of integrated CMOS MEMS pressure sensor. The mechanical simulator accepts the MEMS pressure sensor non-electrical parameter namely the radius and thickness of the diaphragms, geometry and doping concentration of the piezoresistors and the input parameters i.e. pressure to compute the value of the piezoresistors analytically. The analytical results have been matched with the ANSYS 10.0 simulation and the experimental results. The SPICE circuit simulator includes the analytical model of the mechanical simulator of the piezoresistor as a subcircuit in its netlist of low noise low voltage current mode instrumentation amplifier through dynamically linked library. The circuit simulator assigns connectivity of the piezoresistors in the Wheatstone Bridge configuration. The output of the Wheatstone Bridge is connected to the input of the current mode low noise instrumentation amplifier. The design parameters of both the

MOS transistors and of the MEMS pressure sensor can be adjusted in the SPICE circuit simulator to meet the desired specifications. This feature which enables the truly integrated front end design has been incorporated in the coupled circuit and mechanical simulator. This coupled simulation helps in the reduction of design cycles. There are reports on the development of coupled circuit simulator for high performance RF MEMS VCO [1] where MEMS is an intrinsic component of the circuit. However, coupled circuit simulators for MEMS pressure sensors where MEMS acts as the mechanical component has not been reported so far.

In this work we have proposed the design of integrated MEMS pressure sensor in the range of 0-300millibar for biomedical and other applications. The instrumentation amplifier coupled to MEMS based piezoresistive pressure sensor is low-voltage low-noise current mode instrumentation amplifier achieving low noise and low power. For this purpose the dual threshold 0.18 micron MOS devices have been considered using low power low voltage BSIM3 model.

II. DESIGN AND SIMULATION OF INSTRUMENTATION AMPLIFIER

A. Basic structure of current mode instrumentation amplifier

Conventional resistive feedback differential amplifiers (classical three operational amplifier structure) are not suitable when low power, low cost and high CMRR are simultaneously required[2]. These structures need operational amplifier with low output impedance to drive the feedback resistors, which implies high current and large power drain. In addition precisely matched resistors are needed to achieve high CMRR. One way to overcome this problem is use of current mode amplifier shown in fig 1[3].

From figure 1, we observe that the output voltage gain depends on the ratio between two resistors R_o and R_i and the current gain k , and is given by equation 1:

$$A_v = \frac{v_o}{v_i} = k * \frac{R_o}{R_i} \quad (1)$$

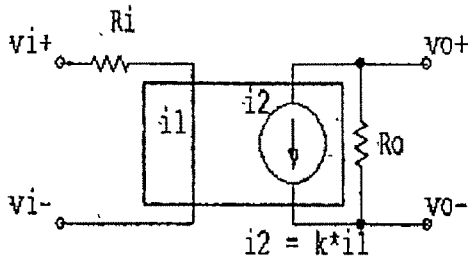


Fig.1 Concept of current mode amplifier

It is important to note that, contrary to classical configuration with three operational amplifiers, there is no global feedback and there is only one high impedance node, which simplifies the frequency compensation. Another advantage is that CMRR do not depends on the matching of resistors. The resistor count is also reduced, saving chip area.

B. Design of current mode instrumentation amplifier

The proposed instrumentation amplifier schematic is shown in fig 2[4]. M1 and M2 are two identical NMOS voltage follower. The input voltage is copied onto R_i and the current flowing through R_i is.

$$i_{R_i} = \frac{v_{in}}{R_i} \quad (2)$$

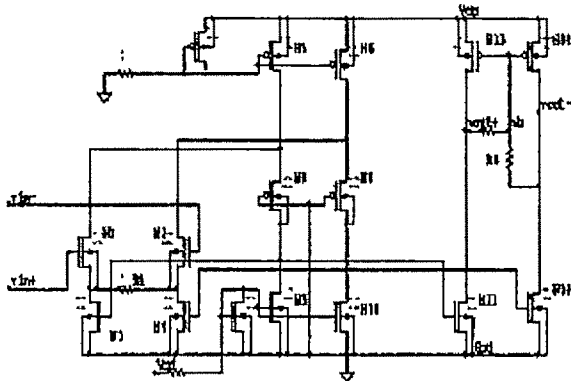


Fig.2 Schematic of the current mode amplifier

M1-M10 form a series-shunt feedback loop, which adjusts the gate voltages of M3 and M4 so that

$$i_3 = i_1 - i_{R_i} \quad (3a)$$

$$i_4 = i_1 + i_{R_i} \quad (3b)$$

where i_1 , i_3 and i_4 are currents through transistors M1, M3 and M4 respectively.

M3, M4, M1 and M12 are identical. Drain currents of M3 and M4 are copied to M11 and M12.

The common mode input range is

$$V_{d,s3} + V_{th} + V_{d,s1} < V_{common} < V_{dd} - V_{d,s5} + V_{th} \quad (4)$$

The differential input voltage range is determined by the bias current of first stage and R_i , that is

$$-i^*R < v_{in} < i^*R_i \quad (5)$$

C. Noise and voltage considerations

A simplified input referred flicker noise analysis of instrumentation amplifier from M1-M14 is [2]

$$V_n^2 = \frac{1}{2} \left(\frac{2}{g_m} + R_i^2 \right) * (g_{m5}^2 * V_{n5}^2 + g_{m9}^2 * V_{n9}^2) + 2 * V_{n1}^2 + \left(g_{m3}^2 * V_{n3}^2 + \frac{1}{2} * g_{m13}^2 * V_{n13}^2 \right) * R_i^2 \quad (6)$$

where $V_{n_i}^2$ denotes the flicker noise of transistor M_i and is given by

$$V_{n_i}^2 = \frac{K_i}{(W * L * f)} \Delta f \quad (7)$$

and g_{m_i} represents the transconductance of transistor M_i .

According to equations (6) and (7), in order to reduce the noise, g_{m_i} should be made high while the g_m of other transistors should be made low. This can be done by selecting appropriate aspect ratios of these transistors

M7 and M8 are in common gate configuration in cascade stage with M1 and M2 and contribute only negligible flicker noise [5]. For M3-6, M9-14, small size is preferred for low noise consideration. The minimum power supply voltage is

$$V_{dd} = V_{thn} + V_{dsat3} + V_{dsat7} + V_{dsat5} \quad (8)$$

PMOS transistors exhibits low flicker noise [6] and are preferred at input stage for low noise. However threshold voltage of targeted CMOS process, the threshold voltage of PMOS transistor is about 0.12V higher than that of NMOS. Hence for low voltage operation NMOS are used for input stage.

According to equation (6), small R_i should be used for low noise. However according to (5), the input range is directly proportional to R_i for fixed bias current. Thus trade-off among noise, input range and power consumption is required.

The simulations results of the ac analysis, input referred noise and dc analysis of the proposed low-voltage low-noise current mode instrumentation amplifier are shown in Fig.3,4 and 5 respectively. The power consumption of the amplifier for a gain of 30 (as indicated in Fig.5) is 82μW compared to a value of 300 μW in a three opamp configuration. The noise power is of the order of 2.0μV compared to 2.5μV in a conventional three opamp configuration.

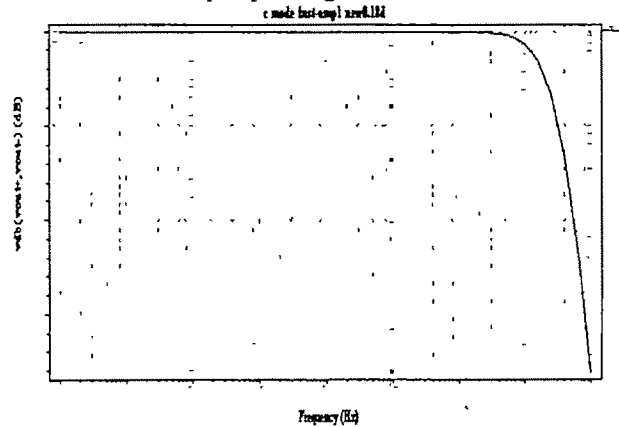


Fig.3 AC analysis

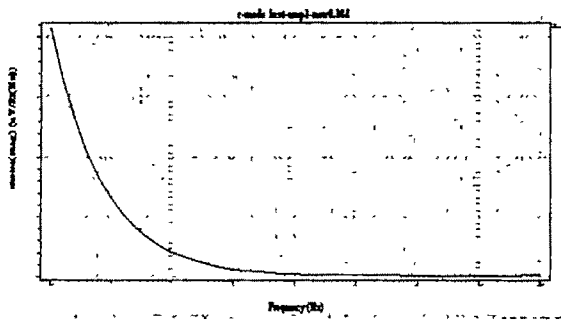


Fig. 4 Noise Analysis

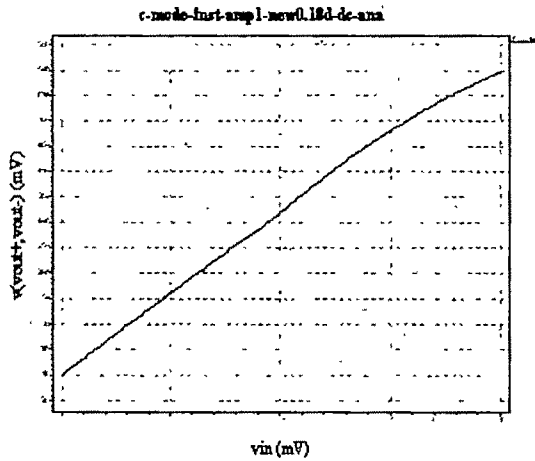


Fig. 5 DC analysis

III. MODELING OF MEMS PRESSURE SENSOR

In a piezoresistive MEMS pressure sensor as shown in Fig. 6, the resistance changes due to the change in resistivity on application of pressure. Normally the resistors are connected in a Wheatstone Bridge configuration so that the output voltage is maximized for a particular input pressure. The change in resistance for each of the piezoresistor is given by equation 9:

$$R' = R (1 \pm (\pi_l \sigma_l + \pi_t \sigma_t)) \quad (9)$$

where R is the initial resistance of the piezoresistor which depends on the doping concentration and dimensions of the piezoresistor, R' is the changed resistance, π_l and π_t are the longitudinal and transverse coefficients respectively, σ_l and σ_t are the longitudinal and transverse stresses respectively which are dependent on applied pressure and membrane dimensions given by [7]. The \pm sign indicates the nature of the stress—compressive or tensile. The value of the resistance R is given by [8]:

$$R = l / (A q n \mu) \quad (10)$$

where l is the length of the piezoresistor, A is the area of cross section, q is the electronic charge, n is the doping concentration and μ is the mobility of carriers, in this case holes.

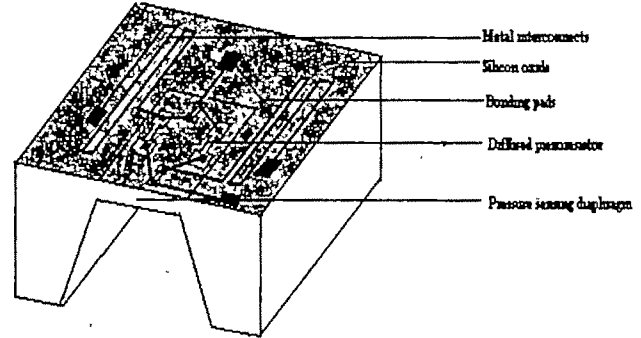


Fig. 6 Schematic of piezoresistive pressure sensor

The results of equations 9 and 10 are matched with the ANSYS v 10 simulation results. To obtain the change in resistance with the help of ANSYS, voltage has to be applied as the input across the piezoresistors and the current density plot is obtained. Electromechanical simulation needs to be done by choosing proper-coupled field elements. On application of pressure, the membrane bends and the change in current density is obtained. Fig. 7 shows the current density results of ANSYS after application of pressure of 0.8 bar on a piezoresistor of dimensions $75\mu\text{m}$ by $20\mu\text{m}$, doping concentration of 10^{18} atoms/cc, membrane dimensions of 2.5mm by 2.5mm by $50\mu\text{m}$.

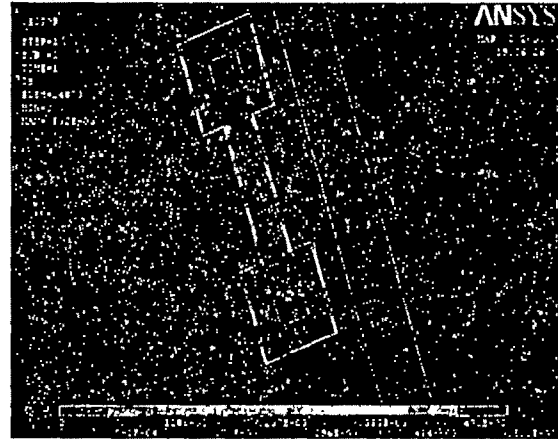


Fig. 7 ANSYS results

IV. INTEGRATED CMOS MEMS DESIGN AND SIMULATION

The analytical equations discussed in the previous section are linked dynamically with the netlist of the amplifier using TSPICE. Fig. 8 shows the schematic diagram of the functioning of the coupled simulator by using file processing and system calls. At the beginning of the netlist, the library file for the piezoresistor is called. In this file, the value of the piezoresistor is computed from the default design parameters, two nodes are assigned namely ANODE and CATHODE for the piezoresistor for its inclusion in the circuit described in the netlist. The connectivity between the resistors in the form of Wheatstone Bridge are assigned in the netlist and an input voltage is applied. The output voltage is then applied to the

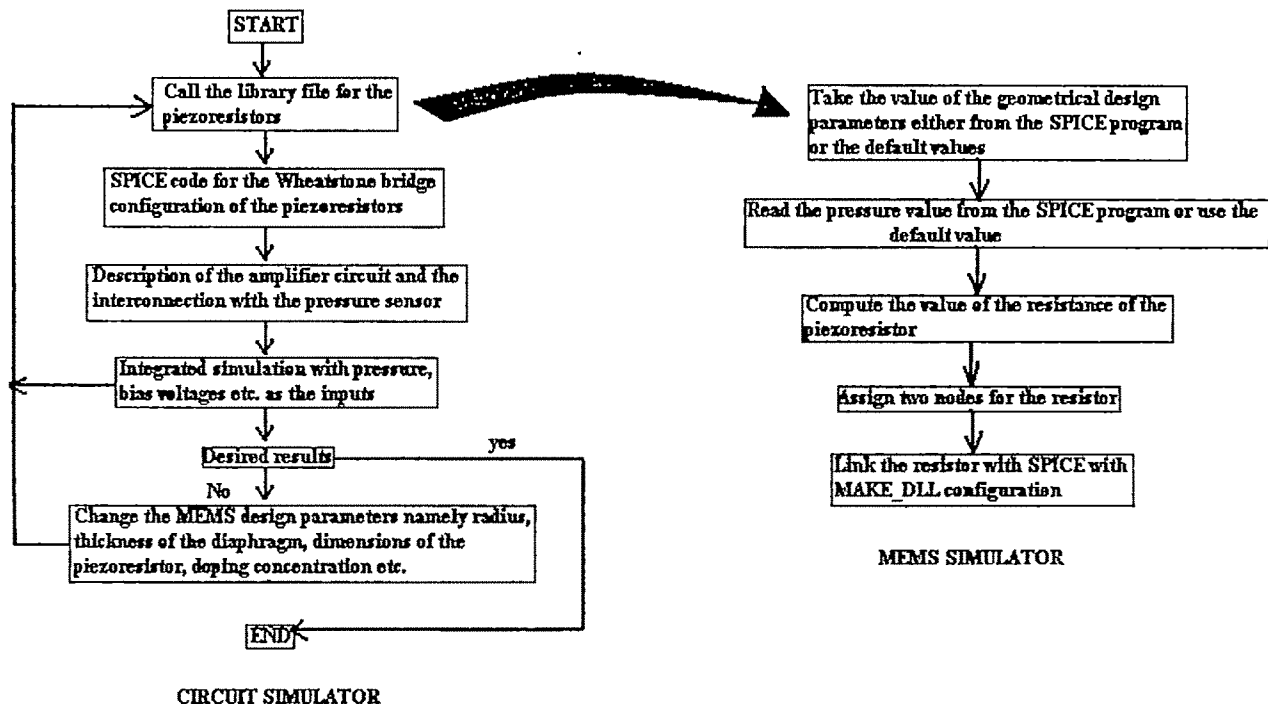


Fig.8 Flowchart of the integrated simulator

input of the amplifier discussed in Section II. If the output do not match some specifications, then the piezoresistor dimensions are altered in the netlist and the entire process is repeated. The output of the integrated simulation of the CMOS MEMS pressure sensor is shown in Fig.9 for different values of pressure and for piezoresistor of dimensions $75\mu\text{m}$ by $20\mu\text{m}$, doping concentration of 10^{18} atoms/cc, membrane dimensions of 2.5mm by 2.5mm by $50\mu\text{m}$.

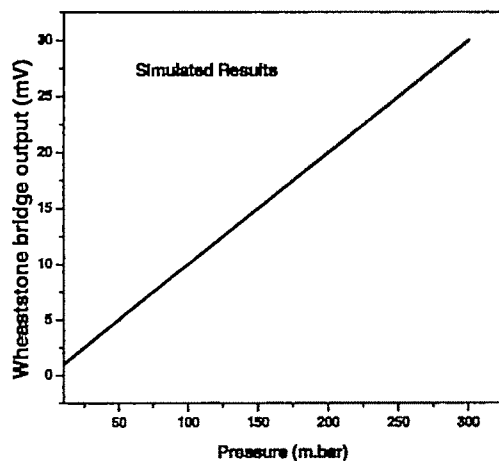


Fig.9 Integrated simulation results

V. CONCLUSION

In this paper, coupled simulation for front end design of SMART CMOS MEMS pressure sensor has been discussed. A model of MEMS piezoresistive pressure sensor has been developed which has been linked dynamically with the low voltage low noise current mode instrumentation amplifier (IA) for signal conditioning. The results of the MEMS pressure sensor analytical model has been matched with the ANSYS results for a piezoresistor of dimensions $75\mu\text{m}$ by $20\mu\text{m}$, doping concentration of 10^{18} atoms/cc, membrane dimensions of 2.5mm by 2.5mm by $50\mu\text{m}$. The MOS model used for the simulation of the low noise micropower IA is $0.18\mu\text{m}$ dual threshold technology. It has been observed that the power consumption and noise voltage of the current mode instrumentation amplifier is $82\mu\text{W}$ and $2\mu\text{V}$ compared to $300\mu\text{W}$ power and $2.5\mu\text{V}$ noise voltage of the conventional three opamp configuration. The simulation of the integrated amplifier and MEMS has been done using TSPICE and the variation of the output voltage of the amplifier with different pressure (upto 300mbar) for a particular dimension of the sensor has been obtained directly from the netlist.

ACKNOWLEDGMENT

The authors would like to acknowledge AICTE, govt. of India for their financial assistance in carrying out the work.

REFERENCES

- [1] M.Behera, V.Kratyuk, S.K.De, N.R Aluru, K.Mayaram, "Accurate Simulation of RF MEMS VCO Performance Including Phase Noise",

- Journal of Microelectromechanical Systems*, vol. 14, no.2, pp 313-325(2005).
- [2] P. E. Allen and D. Hollberg, *CMOS analog Circuit Design*, Oxford University Press, First Edition, 2004.
 - [3] Martin, R., Schreiner, S.; Vaz, F. A. "A CMOS IC for portable ECG acquisition systems" *IEEE Trans. On Instru and Meas*, Vol47, No.5, pp1191-1196, Oct.1989.
 - [4] Honglei Wu and Yong-Ping Xu "A low-voltage Low-noise Instrumentation amplifier for portable medical monitoring systems" *IEEE conference* 2005.
 - [5] Behzad Razavi, *Design of Analog CMOS Integrated Circuits*, McGraw Hills, 2001.
 - [6] C. Jacobson, I. Bloom, and Y. Nemirovsky, "1/f noise in CMOS transistor for analog applications from subthreshold to saturation" *Solid State Electronics*, vol-42, no 10, pp 1807-1817, 1998
 - [7] K. Matsuda, Y Kanda, *Proc Modeling and Simulation of Microsystems(MSM 98)*, Santa Clara, USA, 686 (1998)
 - [8] S.M Sze, *Physics of Semiconductor Devices*, Wiley Publishers (1998).

Study of an IC Based Flow Transducer

S. C. Bera¹ and N. Mandal²

¹Instrumentation Engineering Section, Applied Physics, University of Calcutta, 92, Acharya Prafulla Chandra Road, Kolkata, W.B. India
E-mail: scb152@indiatimes.com

²Department of Applied Electronics & Instrumentation Engineering, Asansol Engineering College, Sen-Raleigh Road, Kanyapur, Asansol, W.B. India E-mail: nirupama_cal@rediffmail.com

Abstract—Flow transducer is one of the most important transducer in process industry. In the anemometer type flow transducer, the effect of flow rate of a fluid on the heat transfer from a heated surface in contact with the flowing fluid is utilized in order to measure the mass flow rate of the fluid. In the present paper a modified IC based anemometer type flow transducer has been designed. Its performance has been studied experimentally. The results of the experimental study are presented in the paper. A linear characteristic in the streamline condition and a nonlinear characteristic in the turbulent condition with very good repeatability have been observed

Key words—Anemometer, flow transducer, heat transfer coefficient, temperature sensing IC.

I. INTRODUCTION

Flow transducers may be broadly classified into two major groups [1-3], which are volume flow transducers (like obstruction type flow transducers, electromagnetic type flow transducers, turbine type flow transducers etc.) and mass flow transducers (like anemometer type flow transducer, coriolis flow transducer etc). The orifice plates with DP transmitters [1-3] are still being used as the flow sensor of a process fluid through a pipeline since they are very simple and easy to design. Development of smart and intelligent flow meters like coriolis mass flow meters, multi variable flow meters [2-3] have recently become popular in industry. For the last few decades attempts are being made by various workers to design flow transducers by intelligent application of different physical phenomena. Various works on anemometric technique of flow measurement of a fluid in a pipeline are being reported in recent times. In hot wire anemometer [3-4] mass flow rate of a fluid is measured by measuring the

change in resistance of a constant current hot resistance wire immersed in the fluid. In a self-balancing bridge technique [1,3] the temperature of the fluid velocity sensor is kept at a constant value and the feedback current to restore equilibrium is taken as the measure of the index of the fluid velocity. The thermistor [1-3] running at constant voltage or current is also as flow sensor. H Fujita *et al*, [12] have used thermistor for low flow rate measurement. G.A.Sokolov *et al* [14] have used the microprocessor-based computation for a thermal type flow meter. L Spassov, *et al* [15] have used thermo-sensitive quartz resonator for liquid flow rate measurement, where frequency changes with flow rate. Using anemometric technique a digital flow meter has been developed by K. Oktamoto *et al* [13]. A highly accurate flow measurement technique using alternative direction method for thermal flow sensors has been developed by J. A. M. Michael *et al* [11]. A new technique of temperature compensation of hot wire anemometer has been reported by R.P.C.Ferreira *et al* [10] and the same group has reported the performance evaluation [8] of that sensor. A hot film anemometer in high pressure application has been studied by U.Schmid [9]. A surface micro machined out of plane hot wire anemometer has been developed by J. Chen *et al* [7]. W.R.M.Almeida *et al* [5] have utilized sigma delta modulation technique to develop an accurate thermo resistive anemometer.

In the present paper a modified anemometer type IC based flow transducers has been developed. In this technique the anemometric effect i.e. cooling effect of flowing fluid on the heat sink metallic surface of a temperature sensing IC unit like AD590 is utilized to measure the mass flow rate of the fluid. In order to compensate the temperature effect of the fluid, four identical IC units are used and mounted in the same diametrical plane along two perpendicular diametrical directions. Experiment has been carried out to find the characteristic of the flow sensor in both streamline and turbulence conditions. It has been observed that this characteristic is almost linear under streamline condition and a

definite nonlinear characteristic with an appreciable linear region has been observed for turbulent condition. Hence using a suitable linearization technique in the turbulent region the proposed sensor may be used as a detecting device for measuring the flow rate of a fluid

II. METHOD OF APPROCH

Two units of AD590 (AD1, AD2) are installed at the top and bottom and two other units of AD590 (AD3, AD4) are installed horizontally in the same diametrical plane of a PVC pipeline section used as the flow head as shown in figure 1 and mounted horizontally.

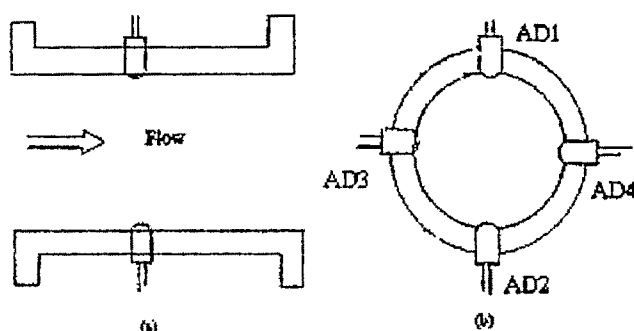


Figure1: Arrangement of four IC's in the pipeline

The flow tube is mounted in the horizontal position in such a way that it is always filled up with flowing fluid and four identical temperature sensing units (AD590) are mounted at equidistant apart in the same diametrical plane of the flow tube. Two sensing IC's are mounted along a horizontal diameter in the same diametrical plane and the other two IC's are mounted along the vertical diameter in the same plane. As a result the cooling effect of the fluid on the ICs along horizontal diametrical positions are more than that on the ICs along Vertical diametrical position. All the ICs are supplied from the same +5V dc source so that their heat supply rate is identical. The output of each IC is a current signal independent of load resistance upto a certain limiting value. This current signal in each IC is passed through a load resistance, which is identical in all of them. The dc voltage developed across each load resistance has been found to be related with fluid flow rate. Sum of the voltage signals developed for two horizontal IC's has been subtracted from that of the voltage signals for two vertical IC's by an adder and subtractor circuit as shown in figure 2. As a result the effect of temperature of the fluid is nullified and the resultant after this subtraction is a function of fluid flow rate only.

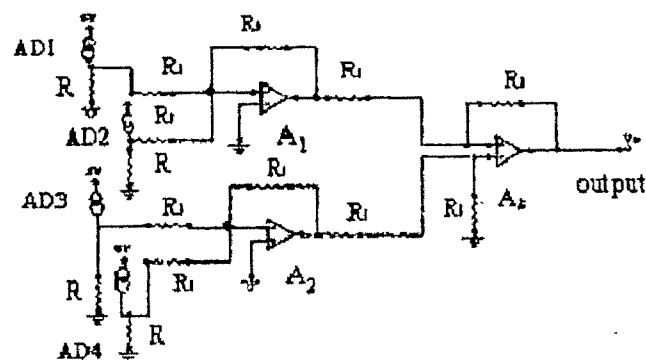


Figure2: Flow Transducer

III. DESIGN

The flow head is designed with a PVC pipe line section of length 80 cm, 30 cm outside diameter and 25cms inside diameter with flange joints at both ends as shown in Figure1(a). At the middle section of the flow head pipe, four IC units with metal sinks are mounted equidistant apart in the same diametrical plane as shown in Figure1 (b) in such a way that the metallic sink faces are just in contact with the flowing liquid and produces negligible obstruction to flow. Each IC is supplied from a stabilized +5V DC source through a load resistance of 1k. The DC voltage signals across the load resistances of top and bottom ICs (AD1 and AD2) are added by the adder circuit consisting of OP AMP A₁ and those across the load resistance of horizontal IC's (AD3, AD4) are added by the adder circuit consisting of OP AMP A₂ as shown in figure 2. The output of A₁ is subtracted from that of A₂ by the differential amplifier circuit consisting of OP AMP A₃ as shown in same figure.

IV. EXPERIMENT

The schematic of experimental setup is given in figure3. Clean water is taken as the experimental liquid. The water level of an overhead tank is maintained constant by feeding continuous water supply to the overhead water tank by a centrifugal water pump and allowing the excess water to discharge through a overflow line. Thus this facility maintained a fixed water head in the overhead water tank. The experimental flow head is installed horizontally in the discharge water line and the output is taken through a regulating valve. Water height of 15 feet is maintained for the entire experiment. The water at various mass flow rates is collected at the discharge end into a graduated measuring cylinder for a definite period of time. The amount collected per unit time is the actual mass flow. The corresponding flow transducer output in mV was measured at each flow rate by a digital 4 and ½ digit multimeter. The characteristic graph of

the transducer was then drawn by plotting mV output against flow rate. The characteristic thus obtained is shown in figure 4.

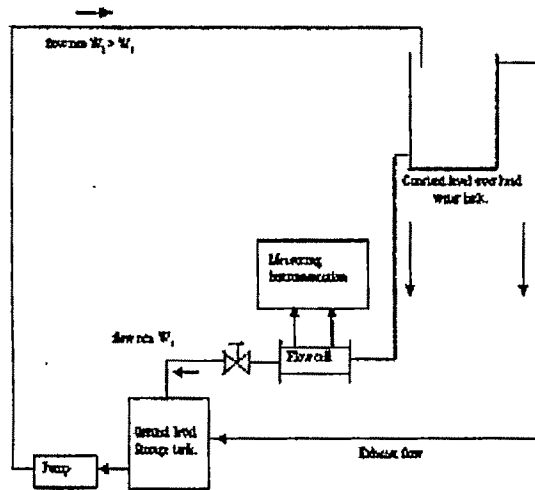


Figure3: Experimental setup

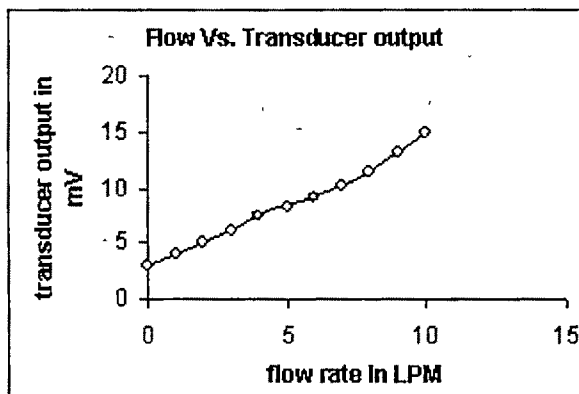


Figure 4: characteristic of flow transducer

V. DISCUSSION

It is found from figure (4) that the characteristic graph of the flow transducer is almost linear under streamline condition and it is nonlinear under turbulence condition of the liquid. The experiment was repeated for both increasing and decreasing flow rate and the same characteristic was obtained. The transducer characteristic was also found to be independent of liquid temperature.

By using a suitable linearization tech such as microprocessor based piece wise technique the characteristic can be made linear easily. Moreover the characteristic can be

utilized to determine the transition between streamline and turbulent condition of a flowing fluid through a pipeline.

REFERENCES

- [1] J. P. Bentley, Principles of Measurement Systems, 3rd ed. Singapore: Longman Singapore Publishers (pvt) Ltd., 1995.
- [2] E. O. Doebelin, Measurement System Application and Design, 4th ed., New York: McGraw-Hill, 1990.
- [3] R. C. Baker, Flow Measurement Handbook: Industrial Designs, Operating Principles, Performance and Applications. Cambridge, U.K., Cambridge Univ. Press, 2000.
- [4] Ulrich Buder, Andreas Berns, Ralf Petz, Wolfgang Nitsche, and Ernst Obermeier, "AcroMEMS Wall Hot-Wire Anemometer on Polyimide Substrate Featuring Top Side or Bottom Side Bondpads", IEEE Sensors Journal, vol. 7, no. 8, August 2007, pp 1095-1101
- [5] Almeida, W. R. M.; Freitas, Georgina M.; Palma, Ligia S.; Catunda, Sebastian Y.C.; Freire, Raimundo C. S.; Aboushady, Hassan; Santos, Francisco F.; Oliveira, Amauri; "A Constant Temperature Thermoresistive Sigma-Delta Anemometer", Instrumentation and Measurement Technology Conference Proceedings, 2007 IEEE, 1-3 May 2007, pp 1-6
- [6] C. Clark, M. Zamora, R. Cheesewright and M. Henry, "The dynamic performance of a new ultra-fast response Coriolis flow meter", J. flow meas. and inst, Elsevier science (U.K) Volume 17, Issue 6, pp. 315-414, 2006
- [7] Jack Chen, and Chang Liu, "Development and Characterization of Surface Micromachined, Out-of-Plane Hot-Wire Anemometer", Journal Of Microelectromechanical Systems, Vol. 12, No. 6, December 2003 979
- [8] Rômulo Pires Coelho Ferreira, Raimundo Carlos Silvério Freire, and Gurdip Singh Deep, "Performance Evaluation of a Fluid Temperature-Compensated Single Sensor Constant Temperature Anemometer", IEEE Transactions on Instrumentation and Measurement, Vol. 12, No. 5, October 2003, pp 1554-1558
- [9] Ulrich Schmid, "Theoretical and Experimental Investigations of a Novel Hot-Film Anemometer for High-Pressure Automotive Applications", IEEE Sensors Journal, Vol. 3, No. 2, April 2003, pp 229-240
- [10] Rômulo Pires Coelho Ferreira, Raimundo Carlos Silvério Freire, Gurdip Singh Deep, Jose Sérgio da Rocha Neto and Amauri Oliveira, "Hot-Wire Anemometer With Temperature Compensation Using Only One Sensor", IEEE Transactions on Instrumentation and Measurement, Vol. 50, No. 4, August 2001, pp 954-958
- [11] J.A.M. Michael, Van putten, H.P. Maurice Van putten and F.P. Anton Van Putten, "Highly accurate flow measurement with thermal flow sensors using the alternative direction method", IEEE, Vol-4, no-6, 1996, pp 527-530
- [12] Hiroyuki Fujita, Tadahiko Ohhashi, Masahiro Asakura, Mitsuhiro Yamada, and Kenzo Watanabe, "A Thermistor Anemometer for Low-Flow-Rate Measurements", IEEE Transactions on Instrumentation and Measurement, Vol. 44, No. 3, June 1995, pp 779-781
- [13] K. Oktamoto, T. Ohhashi, M. Asakura and K. Watanabe, "A digital anemometer", IEEE Trans on instrumentation and measurement, Vol-43, no 2, April 1994, pp 116-120.
- [14] G. A. Sokolov, Yu A Novichkov and A L Lyashenko, "thermal microprocessor flow meters", Thermal Engg(Russia), vol 41, no 6, 1994.
- [15] L. Spassov and Y. Yankov "An Application of a thermosensitive quartz resonator for liquid flow rate measurement", Rev Sci Instrum(USA), vol 65, no 3, 1994, pp 721-723

Study of Electrode Polarisation Impedance Type Transducer for the Measurement of Flow Rate of a Conducting Liquid

¹S. C. Bera, ²B.Chakraborty, ³N.Mandal and ³R.Sarkar

¹Instrumentation Engineering Section, Applied Physics, University of Calcutta,
92, Acharya Prafulla Chandra Road, Kolkata - 700 009, W B. India, E-mail : scb152@indiatimes.com

²Bidhan Chandra Kishore Viswavidyalaya, Kallyani, WB, India, Email: badulchak@yahoo.com

³Asansol Engineering College, Sen-Raleigh Road, Kanyapur, Asansol-713304, W B. India, E-mail : nirupama_cal@rediffmail.com

Abstract – The polarization impedance produced at the interface between a metallic electrode and an electrolyte is a function of current density, frequency of excitation and the flow rate of the electrolytic liquid. Utilizing this effect, the flow rate of a liquid has been measured. The transducer consists of four identical metallic electrodes placed at diametrical distance apart in pipeline made of insulating material like PVC, nylon, fibre, glass etc. The polarization impedance of the four electrodes form a Wheatstone bridge network and if any two diagonal electrodes are supplied from a sinusoidal ac source and the output is taken from the other two diagonal electrodes then the output signal will vary with the change of flow rate through the pipeline due to the effect of polarization impedance. In the present work the effect of electrode distance, frequency of excitation and magnitude of supply voltage on the proposed transducer has been experimentally studied. The experimental results are reported in the paper.

Keywords: conducting liquid, flows measurement, Lumped parameter bridge, polarization impedance

I. INTRODUCTION

THE measurement of volume flow rate of a conducting liquid is generally done in the process industries by using electromagnetic flow meters [4], [5], [6], [11] since this technique is very simple compared to the other methods. There are other techniques [4], [5], [6], [7] of this flow measurement like absorption type, turbine type, coriolis force type, target type, vortex type etc. But for the flow measurement of conducting liquid, the electromagnetic flow measurement technique is much easier and less costly compared to the other measurements. In this technique an intense magnetic field is

produced in the selected region of the flow tube by means of two coils excited from an ac or a dc source. Two sensing electrodes are placed on the diametrically opposite positions inside the tube in contact with the flowing liquid. The flowing liquid induces an e.m.f between the electrodes which is directly proportional to the flow. In the present paper a novel technique of measurement of flow of a conducting liquid has been described. In this technique no excitation coil is required. This technique consists of four metal electrodes inserted into the selected zone of the flow tube which are always in contact with the liquid and produce no obstruction to the liquid flow. This electrode system is excited from an a.c source and the output signal has been found to be linearly related with the liquid flow under streamline condition along with a small non-linear zone at turbulent condition. This output voltage has been amplified by an instrumentation amplifier and then rectified. The offset or zero adjustment network controls the offset of the rectified signal. This signal is then further amplified to voltage signal in the range of 0 - 5 volts and the non-linear zone is linearised by a microprocessor based piece-wise linearisation technique. The digital output signal of microprocessor is converted into analog signal and is then converted into 4 - 20 mA current signal for transmission. The design of the flow head and the calibration data before and after linearisation are reported in the paper. The experimental data are almost found to conform with the theoretical equations.

II. ANALYSIS

When two metal electrodes are immersed in a conducting liquid the polarisation effect [1],[3],[8],[9],[10],[13] at each electrode produces an electric double layer at each metal liquid interface across which there exists a difference in potential along with a polarisation impedance. If

a very small value of sinusoidal voltage signal be applied across the electrodes then this ac voltage signal is superimposed with the half cell potential [8] at each electrode and accordingly the flow of ions from one electrode to the other is obtained. The electric current due to this flow ions may be opposed by the dc polarisation impedance and the ohmic impedance of the liquid between the two electrodes. Again if there is a flow of liquid from one electrode to the other then the flow of a liquid elements along with the ions may be opposed by the viscous effect of the liquid produced by the velocity gradient. Hence the net impedance between the electrodes defined as the ratio of the supply voltage to the current may be assumed to be dependent on the electrode polarisation effect, ohmic effect and the velocity gradient of the liquid [8],[9],[10]. The dc polarisation effect non-linearly depends [9] on the electric current density and frequency of excitation and ohmic effect may be assumed constant for a particular system. When a liquid flows through a pipe line there exists a velocity gradient across the cross section of the pipe line which depends on the flow rate of the liquid if the polarisation effect and ohmic effect are assumed to be constant. In the present paper the effect of four electrodes inserted into a conducting liquid flowing through the pipe line with proper insulation at the diametrically opposite positions is studied. Since an impedance is always found to exist between any two of these electrodes, the four electrodes may be assumed to be equivalent to four lumped impedances as shown in fig. 1.

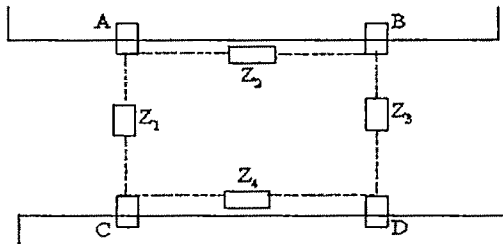


Fig 1 - Lumped parameter equivalent impedance network between four electrodes.

Now when a conducting liquid flows through the horizontal pipe under the streamline condition it may be assumed to have no component of its velocity along any diameter since it is perpendicular to the length of the pipe line. Hence the lumped parameter impedance Z_1 between the diametrically opposite electrodes A & C and Z_3 between the similar electrodes B & D may remain constant but the effective lumped impedance Z_2 between C & D or Z_4 between A & B tends to change due to the velocity gradient among the liquid layers between the electrodes.

Hence if any two diagonally opposite electrodes be supplied from a very small value sinusoidal stabilised ac source then the output across the other two electrodes may change due to the flow of the conducting liquid following the Wheat stone's bridge network principle. So for a small value supply voltage V_S at a fixed frequency applied between A and D and for a very high input impedance of the measuring circuit the bridge output voltage signal V_o may be given by

$$V_o = (Z_2 Z_4 - Z_1 Z_3) / (Z_1 + Z_4) (Z_2 + Z_3) V_S \quad (1)$$

For a very small value of ac voltage V_S and for the identical electrodes $Z_1 = Z_3$ and $Z_2 = Z_4$.

Let at any flow rate Q_0 of the liquid $Z_1 = Z_2 = Z_C$, $Z_2 = Z_4 = Z_0$ and at any other flow rate Q slightly different from Q_0 the value of Z_0 changes to Z_Q . Hence the Taylor series expansion of Z_Q may be given by

$$Z_Q = Z_0 + (Q)_{Q_0} \Delta Q + (Q)_{Q_0} \Delta Q^2 + \quad (2)$$

where $\Delta Q = Q - Q_0$

Let $(Q)_{Q_0} = \mu$ and $(Q)_{Q_0} =$

$$\text{Hence } Z_Q = Z_0 + \mu \Delta Q + \frac{\Delta Q^2}{\Delta Q^2} + \quad (3)$$

Under streamline conditions, the value of and the coefficient of higher order terms may be assumed to be very small. Hence for very small change (ΔQ) of flow rate, Z_Q may be given by

$$Z_Q = Z_0 + \mu \Delta Q \quad (4)$$

Hence putting $Z_1 = Z_3 = Z_C$ and $Z_2 = Z_4 = Z_Q$ in equation no. (1) the bridge output voltage for a liquid flowrate Q is given by

$$V_o = V_S [(Z_Q - Z_C) / (Z_C + Z_Q)] \quad (5)$$

From the equation nos (4) and (5) we get

$$V_o = V_S [(Z_0 + \mu \Delta Q - Z_C) / (Z_C + Z_0 + \mu \Delta Q)]$$

or

$$V_o = \{1 / (Z_C + Z_0)\} [(Z_0 - Z_C) + \{2Z_C / (Z_0 + Z_C)\} \mu \Delta Q - \mu^2 \Delta Q^2 / (Z_C + Z_0)^2] V_S$$

or

$$V_o = K_1 + K_2 \Delta Q + K_3 \Delta Q^2 \quad (6)$$

$$\text{where } K_1 = [(Z_0 - Z_C) / (Z_0 + Z_C)] V_S \quad (7)$$

$$K_2 = [2 \mu Z_C / (Z_0 + Z_C)] V_S \quad (8)$$

$$K_3 = [\mu^2 / (Z_C + Z_0)^2] V_S \quad (9)$$

Under the streamline conditions, the term

$K_3 = [\mu^2 / (Z_C + Z_0)^2] V_S$ may be assumed to be very small and hence for a very small change ΔQ of flow rate, the equation no. (6) may be written as

$$V_o = K_1 + K_2 \Delta Q$$

or

$$V_o = K_1 + K_2 (Q - Q_0) \quad (11)$$

Hence the bridge output voltage is linearly related with the incremental change in flow rate under the stream line condition. Under no flow condition $Q_0 = 0$ and for electrode separation along the pipe line equal to the pipe diameter, $Z_0 = Z_C$. Hence $K_1 = 0$ and the equation no. (11) is reduced to $V_o = K_2 Q$ (12)

Thus the bridge output voltage is linearly related with flow rate when the flow rate is very small and streamline.

Under the turbulent condition, the equation no. (3) may be given as

$$Z_Q = Z_0 + \mu \Delta Q + \Delta Q^2$$

Hence from equation (5) the bridge output voltage is given by

$$V_o = [(Z_0 + \mu \Delta Q + \Delta Q^2 - Z_C) / (Z_0 + \mu \Delta Q + \Delta Q^2 + Z_C)] V_S \quad (13)$$

Hence under turbulent condition, the bridge output voltage may be non linearly related with the incremental change of

flow rate. Therefore $Z_O + Z_C \gg \mu \Delta Q + \Delta Q^2$. So the bridge output voltage under turbulent condition may be given by

$$V_O = [(Z_O - Z_C \mu \Delta Q + \Delta Q^2) / (Z_O + Z_C)] [1 - (\mu \Delta Q + \Delta Q^2) / (Z_O + Z_C)]$$

or

$$V_O = K_1 + K_2 \Delta Q + K_3 \Delta Q^2 - K_4 \Delta Q^3 - K_5 \Delta Q^4 \quad (14)$$

$$\text{where } K_3 = [(2Z_C - \mu^2) / (Z_O + Z_C)^2] V_S \quad (15)$$

$$K_4 = [2\mu / (Z_O + Z_C)^2] V_S \quad (16)$$

$$K_5 = [2 / (Z_O + Z_C)^2] V_S \quad (17)$$

Since μ and ΔQ are small so K_4 and K_5 may be negligible and hence the above equation no. (14) may be written as

$$V_O = K_1 + K_2 \Delta Q + K_3 \Delta Q^2 \quad (18)$$

Hence the relation between the bridge output voltage and the incremental change of flow rate may be assumed to be parabolic under some conditions of turbulent flow.

III. DESIGN

The design of the flow head is very simple as shown in fig.2. It involves only the selection of the electrode material which is chemically inert to the flowing liquid. In the present design, the flow rate of water through a one inch pipe line has been measured. Hence the electrode material is selected to be stainless steel. Since outside and inside diameter of the pipe are 25mm and 20 mm respectively so length of each electrode is selected to be 15 mm with 2 mm insertion depth. The diameter of each electrode is selected to be 4 mm. These selections are made on a trial basis so that the obstruction to the flow is minimum. Each electrode is covered with PVC sleeve and is fitted with a 2 mm terminal screw. Each electrode is then mounted on the flow head along its line of symmetry through a proper hole so that the electrode may be inserted with tight shut up condition and there is no water leakage at the operating pressure. The small gap is sealed with araldite. The length of the flow head is selected to be three feet with flange connections at both ends of internal diameter exactly equal to that of the pipe line. The flow head is connected with the pipe line through insulating gasket of teflon sheet.

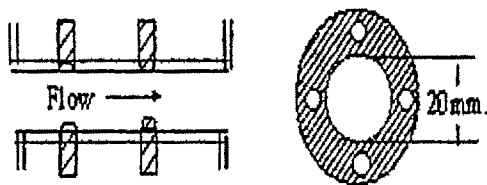


Fig.2 · Flow head of the bridge flow meter

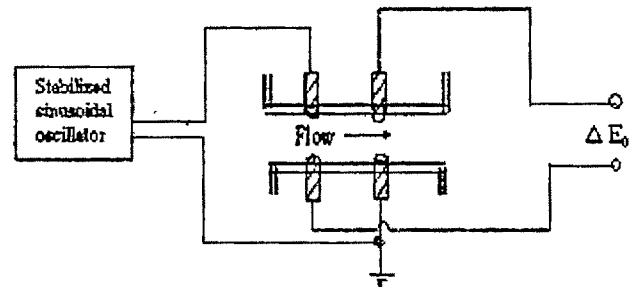


Figure 3 : Electrode polarization impedance type flow transducer

IV. EXPERIMENT

The experiment is performed by using tap water with the experimental set up as shown in fig.4. The flow through the pipe line is increased in small steps and in each step the signal conditioner output and the microprocessor output are noted in both increasing and decreasing modes. The static calibration graphs obtained from the experiment for the signal conditioner output and microprocessor output after linearisation are as shown in fig.5.

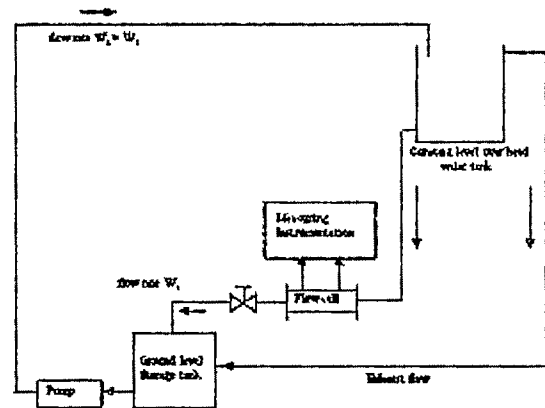


Fig.4 : Experimental setup of the bridge type flow meter

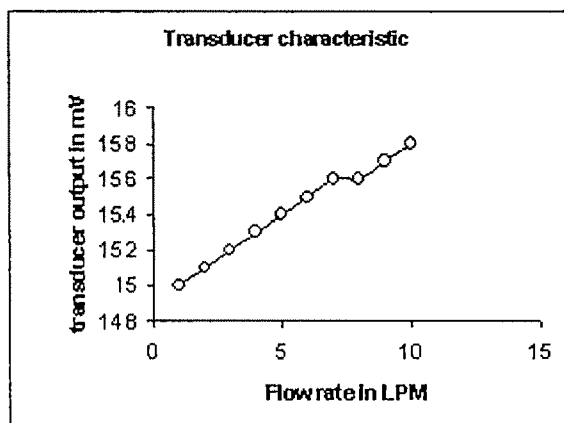


Figure 5. Transducer characteristic

V.DISCUSSION

The repeatability of the experimental data in the increasing and decreasing modes were found to be satisfactory. The calibration graph shown in fig.5 reveals that the nature of the graph is linear over large portion of the operating zone. The non-linearity may be due to the turbulence effect of flow. The nature of the graph appears to follow the theoretically derived equation (11) and (18). Thus the transducer output may be amplified by an AC amplifier and the amplified output after rectification, filtering, signal conditioning and linearization may be utilized to drive an analog or digital indicator calibrated in terms of flow rate of the liquid. The technique is very simple and requires no magnetic excitation field coils as in the case of an electromagnetic flow meter and hence it is very low cost.

REFERENCES

- [1] P.C. Raghav: 'Physical Chemistry' Science Book Agency, 3rd Edition, 1973.
- [2] John Borer: 'Instrumentation and Control for the process Industries' Book, Elsevier Applied Science Publishers, 1st edition, 1985
- [3] R. Bryon Bird, W.E. Stewart, and E.N. Lightfoot, 'Transport Phenomenon' Book. John Wiley and Sons, 1994.
- [4] Bela, G. Liptak: 'Process measurement and Analysis' 3rd edition, Butterworth Heinman Ltd, 1999.
- [5] Douglas M. Considine, 'Process Instruments and Control hand Book', 2nd edition, McGrawHill Company, 1974
- [6] John P. Bentley, 'Principles of Measurement Systems', 3rd edition, Longman Singapore Publishers (pte) Ltd, 1995.
- [7] E. O. Doebelin: 'Measurement System application and Design' 4th Edition, McGraw Hill Publishing Co., 1990
- [8] H.P. Schwan: 'Linear and non-linear platinum electrode polarisation equivalence of frequency and time domain behaviour', Medical and Biology eng and comp (GB) Vol 23, No 1, pp 28 - 37, Jan 1988
- [9] R.W. Simson, J.G. Berberian, H.P. Schwan: 'Non-linear AC and DC polarisation of platinum electrodes' IEEE Trans. on Biomed Eng. Vol. BME27, No.3, pp 166 - 171, March, 1980.
- [10] H.H. Sun, B. Oneral: 'A unified approach to represent neutral electrode polarisation' IEEE trans. on Biomed. Eng. Vol. BME30, No.7, pp 309 - 406, July 1983.

- [11] J. K. Roy, K. Naskar & S. C. Bera: 'Low Cost Microprocessor based Liquid level Transmitter using inductive pickup', J. I.E (I), Vol.80, May 1999
- [12] Peyman Mirtaheri, Sverre Grimnes, and Orjan G. Martinsen: 'Electrode Polarization Impedance in Weak NaCl Aqueous Solutions' IEEE Transactions on Biomedical Engineering, VOL. 52, NO. 12, 2005, pp 2093-2099

Study of a Magneto-Optic Element as a Displacement Sensor

S. Chakraborty, S.C.Bera*

Department of Electrical and Electronics Engineering, Birla Institute of Technology
Mesra, Ranchi-835215, Jharkhand, India (saibanry@yahoo.com)

*Instrumentation Engineering Section, Department of Applied Physics, University of Calcutta, 92, APC Road, Calcutta-700
009(scbl52@indiatimes.com)

Abstract— Displacement sensors are important components in many instrumentation systems but the existing electrical based systems suffer from electromagnetic interference, noise, low response etc. In the present paper, a magneto-optic element like Terbium Doped Glass (TDG) has been experimentally studied for its use as a displacement sensor. The experimental results are reported in the paper. The experimental data have been found to be in good agreement with the theoretical study.

Key words— Displacement sensor, Faraday rotation, Optical Current Transducer, and Polarization

I. INTRODUCTION

Displacement implies the establishment of a new position of a movable member as related to a stable, normal or reference position. The widely used displacement sensor is AC/DC Linear Variable Displacement Transducer (LVDT) [1]. The other types include linear potentiometers, magnetostrictive linear displacement transducers [1]. The magneto-optic based displacement sensor design is very recent. L. Brackenbury Maurice et al [2] designed a displacement apparatus using a magneto-optic sensor and position dependent magnetic field produced by superposing two magnetic fields. M.McElfresh et al [3] designed micro-position sensor using magneto-optic element. In this design a permanent magnet mounted on a movable stage is used to produce a relative motion between the moving magnetic field and the static magneto-optic element. The rotation of the plane of polarization due to Faraday effect is then measured by polarimetric / interferometric method. In our design the non-uniformity of the magnetic field at the end of a solenoid coil is utilized to produce the change in detected light intensity due to the displacement of the magneto-optic element placed in the non-uniform region of the magnetic field.

The potential advantages of immunity to EMI, electrical isolation, large bandwidth, ease of integration into digital control system, potentially low cost of displacement sensor over its non-optical counterpart, led to the development of magneto-optical based systems in recent years. The magneto-optic based displacement sensor utilizes the principle of Faraday rotation. Faraday Effect is observed in solids, liquids and gases [4] such as in glass, quartz, water, sodium vapor etc when subjected to a strong magnetic field. Magneto-optic garnet such as Yttrium Iron Garnet (YIG), Terbium Gallium Garnet (TGG) is widely used as magneto-optic medium. TGG is commercially used for producing large rotations in magneto-

optic laser isolators [5]. YIG bulk optics or YIG film [6] are used for current detectors. Since magneto-optic garnet materials are expensive and large size crystals are difficult to grow, several glass materials [7] are used as a Faraday rotator. In the present study, a displacement sensor is designed by utilizing the interaction of non-uniform magnetic field with magneto-optic element. In this system an input monochromatic beam of light is first passed through a polarizer and then through a Terbium Doped Glass (TDG) element placed outside the solenoid coil. The light beam is then passed through an analyzer with transmission angle at 90° to that of the input polarizer and is finally detected by a photo-detector. The D.C. current passing through the solenoid coil is kept at a fixed value and the magneto-optic element (TDG) is displaced axially towards the solenoid coil. As the TDG element comes close to the solenoid coil a stronger magnetic field is encountered which produces more rotation of the plane of polarization and the photo-detector output is measured. The increase in photo-detector output can be scaled with the linear displacement of the TDG element for a certain range and finally the saturation is obtained where magneto-optic element is completely inside the region of uniform magnetic field.

II. THEORY AND ANALYSIS

Schematic diagram of the magneto-optic measurement set up is shown in Fig.1.

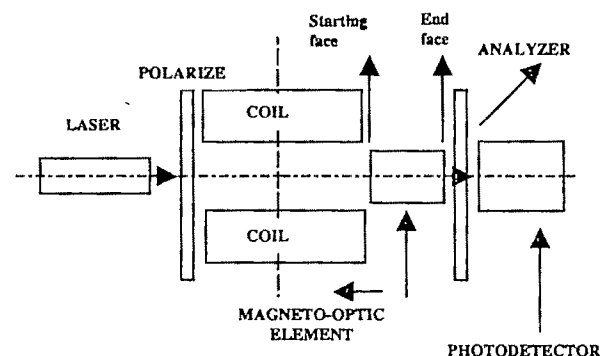


Fig 1 Schematic diagram of the magneto optic displacement measurement set up

Let the beam incident on the magneto optic element be linearly polarized with azimuth α_p has intensity I_0 . The Stokes

vector of the output beam from the analyzer can then be written as

$$S_{out} = I_0 M_{ana} M_{rot} S_{in} \quad \dots(1)$$

where M_{rot} and M_{ana} are respectively the Muller matrices [8] of Faraday rotator and analyzer and S_{in} is the normalized Stokes vector of the input linearly polarized beam which are given by the following equation no. (2), (3) and (4) respectively.

$$M_{rot} = \begin{bmatrix} 1 & 0 & 0 & 0 \\ 0 & \cos 2\theta & -\sin 2\theta & 0 \\ 0 & \sin 2\theta & \cos 2\theta & 0 \\ 0 & 0 & 0 & 1 \end{bmatrix} \quad \dots(2)$$

$$M_{ana} = \frac{1}{2} \begin{bmatrix} 1 & \cos 2\alpha_a & \sin 2\alpha_a & 0 \\ \cos 2\alpha_a & \cos^2 2\alpha_a & \cos 2\alpha_a \sin 2\alpha_a & 0 \\ \sin 2\alpha_a & \cos 2\alpha_a \sin 2\alpha_a & \sin^2 2\alpha_a & 0 \\ 0 & 0 & 0 & 0 \end{bmatrix} \quad \dots(3)$$

and

$$S_{in} = \begin{bmatrix} 1 \\ \cos 2\alpha_p \\ \sin 2\alpha_p \\ 0 \end{bmatrix} \quad \dots(4)$$

where α_a is the transmission angle of the analyzer and θ is the Faraday rotation.

Considering linearly horizontally polarized ($\alpha_p = 0^\circ$) monochromatic input beam and combining the equation nos. (1), (2), (3) and (4), the expression for detected intensity of the output beam is given by,

$$I = \frac{I_0}{2} [1 + \cos 2(\theta - \alpha_a)] \quad \dots(5)$$

When a linearly polarized light passes through a magneto-optic medium in a direction parallel to the magnetic field, the Faraday rotation is given by the relation [9]

$$\theta = V_{verdet} \int_{l_1}^{l_2} B(l, a) dl \quad \dots(6)$$

where V_{verdet} , L and $B(l_{coil}, a, n, I)$ are wavelength dependent Verdet constant of the TDG element, length ($L = l_2 - l_1$) of the magneto-optic medium and magnetic flux density (function of coil length(l), radius(a), number of turns(n), current strength(I)) of the air-core solenoid respectively.

For extinction position, $\alpha_a = 90^\circ$, and the above expression for intensity reduces to

$$I = I_0 \sin^2 \theta \quad \dots(7)$$

For theoretical computation of eq.6 and 7 the variation of magnetic flux density along the axis of the solenoid coil is measured by the axial Hall probe of a Gaussmeter (Make-M/s.Lab Magnet, India) from a distance of 40 mm (end face of magneto-optic element shown in Fig.1) and is shown by Fig.2.

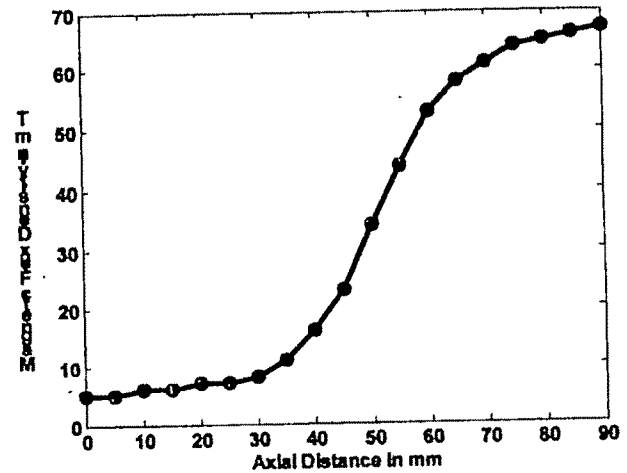


Fig.2 Variation of magnetic flux density $B(l_{coil}, a, n, I)$ with axial distance l for a direct current of strength of 2 Amp. The zero of the axial distance is 40 mm away from the solenoid.

The integration of eq.6 is carried out over the length (30 mm) of the magneto-optic element with the help spline interpolation (in MATLAB environment) from the data set of Fig.2. Finally eq.7 is computed by considering the verdet constant $V_{verdet} = 101.81$ radian/Tesla.Meter (for wavelength $0.5435 \mu\text{m}$ —Green HeNe Laser) of the magneto-optic element and shown by Curve-A of Fig.4. For computation the value of verdet constant is obtained from the typical value of verdet constant variation of TDG with wavelength (supplied by the manufacturer) with the help of shape preserving interpolation (in MATLAB Curve Fitting Tool Box). Curve-A of Fig.4 shows an increase in detected intensity when the starting face of the magneto-optic element is more than 10 mm inside the solenoid coil. The corresponding curve of Fig.2 shows that appreciable increase in magnetic flux density starts from the distance of 10 mm inside the solenoid coil. Thus as the magneto-optic element moves inside the solenoid coil the effective length of the element increases which produces more optical rotation and thus more intensity.

III EXPERIMENTAL RESULTS AND DISCUSSIONS

Experiment is carried out on the proposed magneto-optic displacement sensor with the experimental set-up as shown in Fig.3.

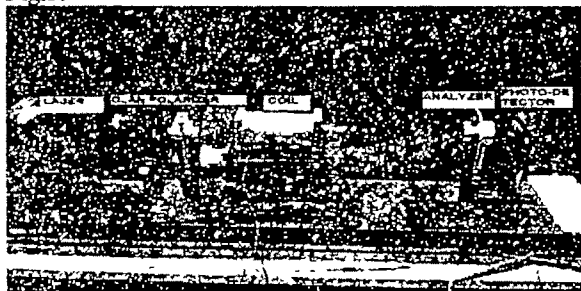


Fig.3 : Experimental set-up

Light from HeNe green laser (wavelength $0.5435 \mu\text{m}$) is first passed through a prism polarizer and then through a TDG cylinder of length 30 mm and diameter 10 mm placed outside the core of a multiple layer solenoid coil (copper) of length 95 mm with 2600 turns and wound on an aluminium cylinder of diameter 10 mm rested on two wooden spacers of thickness 5 mm each. The output beam is again passed through a film-type analyzer and detected by a photometric detector (Si-PIN Photodiode). The power from a stabilized DC power supply is supplied to the solenoid coil. 2 Ampere DC is passed through the solenoid coil. The transmission axes of the input polarizer and the analyzer are kept crossed.

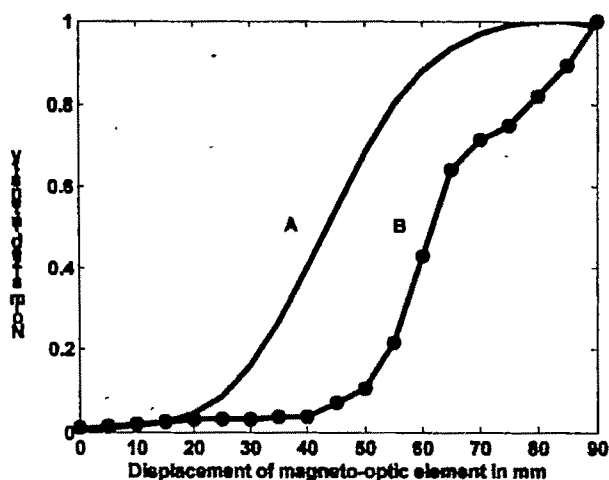


Fig.4 Theoretical (Curve-A) and Experimental (Curve-B) variation of normalized photodetector intensity with axial displacement of TDG. Zero x-axis position corresponds to end face of the magneto-optic element (of length 30mm) which is 40 mm away from solenoid coil. The starting face of the solenoid coil is at 10 mm away from the solenoid coil.

Curve-B of Fig.4 shows the experimentally obtained variation for the corresponding theoretical variation shown by Curve-A of Fig.4. The mismatch between theoretically and experimentally obtained variation shows that appreciable change in intensity is observed when the starting face of the magneto-optic element is around 40 mm inside the solenoid coil and is subjected to magnetic flux density of more than 25

mT. This calls for the use of photodetection circuit of higher sensitivity which can detect lower change in light intensity due to low value of angular rotation when subjected to low magnetic flux density. Both the theoretically and experimentally obtained variations tend to saturate at higher value of displacement implying complete entry to the region of uniform magnetic field.

IV. CONCLUSIONS

From the characteristic curves shown in Fig.4, it may be concluded that a magneto optic sensing element like terbium doped glass (TDG) can be utilized for designing a displacement sensor over a certain range of distance (approximately 15 mm, when the starting face of the magneto-optic element is displaced from a distance of 40 mm to 55 mm inside the solenoid coil, the corresponding distances are shown by 50mm to 65mm in Fig.4.) which shows sharp increase in detected intensity. The higher range of linearity is expected with high sensitivity photodetection system.

V. ACKNOWLEDGEMENT

The authors gratefully acknowledge the constant encouragement of senior colleagues of the Department of EEE, BIT, Mesra, Ranchi and Departments of Applied Physics and Applied Optics & Photonics of Calcutta University.

REFERENCES

- [1]. "Process/Industrial Instruments & Controls Handbook", D.M.Considine, Fourth Edition, McGraw-Hill, Inc., New York, 1993, Section-5
- [2]. L.B. Maurice et al, "Displacement apparatus using a magnetic optic sensor and position dependent magnetic field", United States Patent No.5859531, January 12, 1999
- [3]. M. McElfresh et al, "Micro-position sensor using Faraday Effect", United States Patent No. 7183765 B2, February 27, 2007
- [4]. Francis A. Jenkins and Harvey E. White, "Fundamentals of Optics", 4th edition, McGraw-Hill, New York, 1976
- [5]. G.B.Gillman, "A reliable faraday rotator with solid state switching", J. Phys. E: Sci. Instrum. Vol.10, 1977, pp959-960
- [6]. Hans Sohlstrom, "Fiber optic magnetic field sensors utilizing iron garnet materials", Royal Institute of Technology (KTH), Ph.D. Thesis, 1993
- [7]. B. Yi, B.C.B.Chu and K.S.Chiang, "Magneto-optical electric current sensor with enhanced sensitivity", Meas. Sci. Technology, Vol.13, 2002, pp N61-N63
- [8]. "Handbook of Optics-Vol-II", 2nd Edition, Michael Bass, Editor-in-Chief, McGraw-Hill Inc., New York, 1995, Chapter-33
- [9]. K. Lizuka, "Engineering optics", 2nd Ed., Springer-Verlag, 1983, Berlin

Technical Session 3B

Control Theory

Design of H_∞ -Optimal Robust Controller for a Singularly Perturbed System

Debasish Mondal

Haldia Institute of Technology, Purba Medinipur, India . email: baishalidebasish@rediffmail.com
Department of Applied Electronics and Instrumentation Engg.

Abstract— In this paper a complete theoretical study of the design of H_∞ -optimal robust controller for a LTI singularly perturbed system in continuous-time domain is considered. Here the full order plant is a two-time scale system. It is decomposed into reduced order slow and fast subsystem by applying similarity transformation. Then stabilizing slow and fast H_∞ controller is designed separately for fast and slow subsystem by solving the standard H_∞ control problem in Robust control *TOOLBOX* in *MATLAB*. Finally the composite controller is formed by combining the slow and fast controller. The validity of design of the composite H_∞ controller is established by comparing the magnitude bode- plot & step response with the H_∞ controller designed for the Full order plant. An illustrative Example (Two-tank chemical reactor) is given.

Key words— Augmented plant, Block-diagonal form, Ill-conditioning, Similarity transformation, Stiffness difficulties, Two-time scale system.

I. INTRODUCTION

SINGULAR perturbation techniques were used in control system design since 1960's. Linear state-feedback controller, LQR and LQG controller have already been designed [1] for singularly perturbed systems both in continuous-time and discrete-time domain. In this paper a complete theoretical study of the design of the H_∞ -optimal robust controller for LTI singularly perturbed system (Two-tank chemical reactor) in continuous time domain is considered. The standard H_∞ -control problem consists in finding a static-state feed back controller 'K' such that the H_∞ -norm of the closed-loop transfer function is less than a given positive number, under the constraint that 'K' stabilizes the generalized plant 'G'. Here the plant 'G' is a two-time scale (two-frequency scale) transfer function. In the singular perturbation method the original full-order plant 'G' is decomposed into slow (G_s) and fast (G_f) subsystem of order less than the

original plant by applying a similarity transformation. Then a stabilizing fast H_∞ -controller(K_f) is designed for fast subsystem to meet the high frequency design specification and a stabilizing slow H_∞ -controller(K_s) is designed for slow subsystem to meet the low-frequency specification separately, under the constraint $K_s(\infty)=K_f(0)$ [4]. The slow and fast controller is obtained by solving the standard H_∞ -control problem in Robust control *TOOLBOX* in *MATLAB*. Finally the composite controller (K_c) is formed by combining the slow (K_s) and fast (K_f) controller. The goal of this paper is to show the validity of the composite H_∞ controller, by comparing the magnitude bode-plot & step response with the H_∞ controller (K) designed for the Full order plant (G).

II. SINGULAR PERTURBATION TECHNIQUE

Let us now introduce the idea of singular perturbation technique from the systems and control perspective. Using the state variable representation for an LTI system

$$\dot{x}(t) = A_{11}x(t) + A_{12}z(t) + B_1u(t) \quad (1)$$

$$x(t=0) = x_0$$

$$\epsilon \dot{z}(t) = A_{21}x(t) + A_{22}z(t) + B_2u(t) \quad (2)$$

$$z(t=0) = z_0$$

Where, $x(t)$ and $z(t)$ are 'n' and 'm' dimensional state vectors, respectively. $u(t)$ is an 'r' dimensional control vector and ' ϵ ' is a small scalar parameter. The matrices A and B are of appropriate dimensions. The system (1) and (2) are said to be in the singularly perturbed form in the sense that by making $\epsilon = 0$ in (2) the degenerate system

$$\dot{x}^0(t) = A_{11}x^0(t) + A_{12}z^0(t) + B_1u(t) \quad (3)$$

$$x^0(t=0) = x_0$$

$$0 = A_{21}x^0(t) + A_{22}z^0(t) + B_2u(t) \quad (4)$$

$$z^0(t=0) \neq z_0$$

is a combination of "differential" system in $x^0(t)$ of order 'n' and "algebraic" system in $z^0(t)$ of order 'm'. The effect of degeneration is not only to "cripple" the order of the system

from $(n+m)$ to ' n ' by "dethroning" $z(t)$ from its original state variable status, but also to "desert" its initial conditions z^0 . This is a harsh "punishment" on $z(t)$ for having a close association (multiplication) with singular perturbation parameter ' ϵ '. We assume that the matrix A_{22} is non singular and hence we have a standard singular perturbation problem. The singularly perturbed problem has two widely separated characteristics roots giving rise to *slow* and *fast* components modes in its solution. The simultaneous presence of *slow* and *fast* phenomenon makes the problem 'stiff' from the numerical point of view.

III. LINEAR TIME-INVARIANT SINGULARLY PERTURBED SYSTEM AND IT'S (BLOCK DIAGONAL) DECOM-POSED FORM.

In the singular perturbation method the original full-order system is decomposed into slow and fast subsystems of order less than the original system. We shall take the following finite dimensional LTI model of singularly perturbed system.

$$\dot{x}(t) = A_{11}x(t) + A_{12}z(t) + B_1u(t) \quad (5)$$

$$x \in \mathbb{R}^n; u \in \mathbb{R}^r$$

$$\epsilon \dot{z}(t) = A_{21}x(t) + A_{22}z(t) + B_2u(t) \quad (6)$$

$$z \in \mathbb{R}^m$$

$$y(t) = C_1x(t) + C_2z(t) \quad (7)$$

$$x(t=0) = x_0; z(t=0) = z_0, \epsilon = \text{singular perturbation parameter.}$$

To obtain a complete de-coupled fast and slow subsystem of (5), (6) & (7) we shall take two new choice of state variables $\eta(t)$ and $\xi(t)$ for the fast and slow states respectively. In which the system appears in two distinct block- triangular form, these forms are called the "actuator form" and "sensor form" and are represented in Fig(1) where we temporary disregard the input 'u' and output 'y' and focus on the properties of the free system.

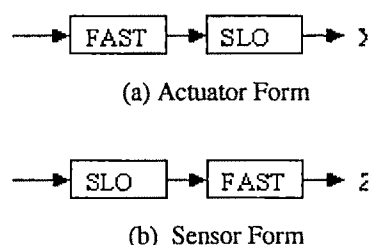


Fig. 1

The Actuator form:

The actuator form is the result of change of variables

$$\eta(t) = z(t) + L(\epsilon)x(t) \quad (8)$$

That is with the similarity transformation

$$\begin{bmatrix} x(t) \\ \eta(t) \end{bmatrix} = \begin{bmatrix} I_n & 0 \\ L(\epsilon) & I_m \end{bmatrix} \begin{bmatrix} x(t) \\ z(t) \end{bmatrix}$$

Which transform Eqn. (5)& (6) into

$$\begin{bmatrix} \dot{x}(t) \\ \epsilon \dot{\eta}(t) \end{bmatrix} = \begin{bmatrix} A_{11} - A_{12}L & A_{12} \\ R(L, \epsilon) & A_{22} + \epsilon LA_{12} \end{bmatrix} \begin{bmatrix} x(t) \\ \eta(t) \end{bmatrix} \quad (9)$$

The requirement is that the matrix $R(L, \epsilon)$ be zero, i.e. the $(m \times n)$ matrix (L, ϵ) satisfied the algebraic equation

$$R(L, \epsilon) = A_{21} - A_{22}L + \epsilon LA_{11} - \epsilon LA_{12}L = 0 \quad (10)$$

results in the system (9) assuming the upper block triangular form

$$\begin{bmatrix} \dot{x}(t) \\ \epsilon \dot{\eta}(t) \end{bmatrix} = \begin{bmatrix} A_{11} - A_{12}L & A_{12} \\ 0 & A_{22} + \epsilon LA_{12} \end{bmatrix} \begin{bmatrix} x(t) \\ \eta(t) \end{bmatrix} \quad (11)$$

The system (5) & (6) has been partially decoupled in (11) to a separate *fast subsystem*

$$\epsilon \dot{\eta}(t) = (A_{22} + \epsilon LA_{12}) \eta(t) \quad (12)$$

The unique solution of the Eqn (10) $L(\epsilon)$, exists and is approximated by

$$L(\epsilon) = A_{22}^{-1}A_{21} + O(\epsilon); O(\epsilon) \text{ stands for Order of } \epsilon, \text{ provided } A_{22} \text{ is non-singular.}$$

The Block-Diagonal form :

Starting with the actuator form (11) the change of variables

$$\xi(t) = x(t) - \epsilon H \eta(t) \quad (13)$$

results in

$$\begin{bmatrix} \dot{\xi}(t) \\ \epsilon \dot{\eta}(t) \end{bmatrix} = \begin{bmatrix} A_{11} - A_{12}L & S(H, \epsilon) \\ 0 & A_{22} + \epsilon LA_{12} \end{bmatrix} \begin{bmatrix} \xi(t) \\ \eta(t) \end{bmatrix} \quad (14)$$

and the requirement that the $(m \times n)$ matrix H satisfies the linear algebraic Eqn.-

$$S(H, \epsilon) = \epsilon(A_{11} - A_{12}L)H - H(A_{12} + \epsilon LA_{12}) + A_{12} = 0 \quad (15)$$

Which converts the system (14) to finally the Block-diagonal or decoupled form

$$\begin{bmatrix} \dot{\xi}(t) \\ \epsilon \dot{\eta}(t) \end{bmatrix} = \begin{bmatrix} A_{11} - A_{12}L & 0 \\ 0 & A_{22} + \epsilon LA_{12} \end{bmatrix} \begin{bmatrix} \xi(t) \\ \eta(t) \end{bmatrix} \quad (16)$$

The actuator form describes the exact *fast subsystems*, while the new block

$$\dot{\xi}(t) = (A_{11} - A_{12}L) \xi(t) \quad (17)$$

describes the *slow subsystem*

The unique solution of (15), $H(\epsilon)$ exists and is approximated by

$$H(\epsilon) = A_{12}A_{22}^{-1} + O(\epsilon) \quad (18)$$

Now the change of variables (8) and the present change of variables (13) together constitute a similarity transformation

$$\begin{bmatrix} x(t) \\ z(t) \end{bmatrix} = \begin{bmatrix} I_n & \epsilon H \\ -L & I_m - \epsilon LH \end{bmatrix} \begin{bmatrix} \xi(t) \\ \eta(t) \end{bmatrix} = T \begin{bmatrix} \xi(t) \\ \eta(t) \end{bmatrix}$$

Where $T = \begin{bmatrix} I_n & \epsilon H \\ -L & I_m - \epsilon LH \end{bmatrix}$ is the

transformation matrix operator. Therefore the "block-diagonal-form" or decoupled form of the Eqn (5), (6) & (7) can be written as

$$\begin{bmatrix} \dot{\xi}(t) \\ \varepsilon \dot{\eta}(t) \end{bmatrix} = \begin{bmatrix} A_s & 0 \\ 0 & A_f \end{bmatrix} \begin{bmatrix} \xi(t) \\ \eta(t) \end{bmatrix} + \begin{bmatrix} B_s \\ B_f \end{bmatrix} u \quad (19)$$

$$y = \begin{bmatrix} C_s & C_f \end{bmatrix} \begin{bmatrix} \xi(t) \\ \eta(t) \end{bmatrix} \quad (20)$$

s: stands for *Slow* system blocks.

f: stands for *Fast* system blocks.

Where $A_s = A_{11} - A_{12}L$

$$B_s = B_1 - \varepsilon HB_2 - \varepsilon LHB_2$$

$$C_s = C_1 - C_2 \varepsilon L$$

And $A_f = A_{22} + \varepsilon LA_{12}$

$$B_f = B_2 + \varepsilon LB_1$$

$$C_f = C_2 + \varepsilon C_1 H - \varepsilon C_2 LH$$

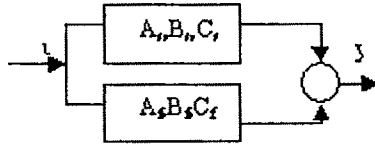


Fig (2) Decomposed system.

IV. H_∞ CONTROL FOR SINGULARLY PERTURBED SYSTEM.

Consider again a linear time-invariant system described by

$$\dot{x}(t) = Ax(t) + B_1 w(t) + B_2 u(t) \quad (21)$$

$$z(t) = C_1 x(t) + D_{11} w(t) + D_{12} u(t) \quad (22)$$

$$y(t) = C_2 x(t) + D_{21} w(t) + D_{22} u(t) \quad (23)$$

Where

$x(.) \in R^n$ is the state vector.

$w(.) \in R^{m1}$ is the disturbance vector.

$u(.) \in R^{m2}$ is the control vector.

$z(.) \in R^{p1}$ is the error vector.

$y(.) \in R^{p2}$ is the observation vector.

This system representation includes a plant augmented with frequency-dependent weights. The Transfer-function of the system is denoted by

$$\begin{aligned} G(s) &= \begin{bmatrix} G_{11}(s) & G_{12}(s) \\ G_{21}(s) & G_{22}(s) \end{bmatrix} \\ &= \begin{bmatrix} D_{11} & D_{12} \\ D_{21} & D_{22} \end{bmatrix} + \begin{bmatrix} C_1 \\ C_2 \end{bmatrix} [SI - A]^{-1} [B_1 \ B_2] \end{aligned} \quad (24)$$

The H_∞ control problem is to find an internally stabilizing compensator $u(s) = K(s)y(s)$, such that the H_∞ norm of the closed-loop transfer function $T_{zw}(s)$

$$= G_{11}(s) + G_{12}(s) K(s) [I - G_{22}(s) K(s)]^{-1} G_{21}(s) \quad (25)$$

satisfies the inequality $\|T_{zw}(s)\|_\infty < \gamma$ for some specified $\gamma > 0$. The solution of this problem is well known [5].

Aim of this paper is to analyze the case when the system (21)-(23) is a *standard singularly perturbed system*. In this case the matrices A, B, and C for $i=1, 2$, take the special form

$$A = \begin{bmatrix} A_{11} & A_{12} \\ A_{21} & A_{22} \\ \varepsilon & \varepsilon \end{bmatrix}; B = \begin{bmatrix} B_{11} \\ B_{12} \\ \varepsilon \end{bmatrix}; C = [C_{11} \ C_{12}]$$

Where ε is the small positive parameter all matrices are analytic functions of ε , and matrix A_{22} is non-singular at $\varepsilon = 0$. It follows that the transfer function $G(s, \varepsilon)$ defined by (24) is a two-frequency scale or two-time scale transfer function. It is shown in [6] that for any two-frequency scale compensator $K(s, \varepsilon)$, the closed loop transfer function T_{zw} is also two-frequency scale. Therefore we write T_{zw} as $T_{zw}(s, \varepsilon)$ and can be denoted its slow and fast transfer function by

$$T_{zw}(s) = T_{zw}(s, 0) \text{ and}$$

$$T_{zw}(p) = T_{zw}(p/\varepsilon, \varepsilon) \text{ } \varepsilon \rightarrow 0 \text{ respectively.}$$

The sequential procedure [4] for solving the H_∞ control problem starts by defining a fast problem for the plant $G_f(p)$. An internally stabilizing fast compensator $K_f(p)$ is designed such that $\|T_{zw}(s)\|_\infty < \gamma$. We assume that $K_f(0)$ is finite; that is the compensator has no poles at origin. Then we consider a slow problem for the plant $G_s(s)$. An internally stabilizing slow compensator $K_s(s)$ is designed such that $\|T_{zw}(s)\|_\infty < \gamma$ and $K_s(\infty) = K_f(0)$. Assuming, for the moment, that we have successfully designed $K_f(p)$ and $K_s(s)$, then a composite controller is formed as [4].

$$K(s, \varepsilon) = K_s(s) + K_f(p) - K_s(\infty) \quad (26)$$

It follows from the result of (26) that for sufficiently small values of ε , $K(s, \varepsilon)$ is an internally stabilizing two-frequency scale compensator such that $\|T_{zw}(s)\|_\infty < \gamma + O(\varepsilon)$.

To prove this inequality with $O(\varepsilon)$ requires a careful treatment which is done in [7].

The fast H_∞ control problem is a standard one and its solution exists under well-known condition [8]. The slow H_∞ control problem is the constrained H_∞ control problem due to the additional constraint $K_s(\infty) = K_f(0)$ and existence of its solution is already proved in [4].

V. MIXED SENSITIVITY APPROACH IN H_∞ - CONTROL THEORY.

The main use of H_∞ -control theory is in the synthesis of compensators which achieve frequency-domain loop-shaping specifications. In a typical setup we have a plant 'G' and want to design a compensator 'K' to achieve certain specifications on the sensitivity function $S = (1 + GK)^{-1}$ and the complementary sensitivity function $T = 1 - S$. By choosing appropriate filters W_1 , W_2 and W_3 , we formulate the problem as one of achieving $\|T_{zw}(s)\|_\infty < 1$

$$\text{Where } T_{zw} = \begin{bmatrix} W_1 S \\ W_2 S \\ W_3 T \end{bmatrix}$$

By defining Augmented plant as

$$P = \left[\begin{array}{c|c} W_1 & -W_1 G \\ 0 & W_2 \\ 0 & W_3 G \\ \hline I & -G \end{array} \right]$$

The transfer function T_{zw} , defined (24) will be the desired one, when the plant G is a two-frequency scale transfer function. Choosing the filters W_1 and W_3 as two-frequency scale transfer function yields an augmented-plant P which itself is a two-frequency scale transfer function and hence representable in the state space form (21)-(23) as a standard singularly perturbed system. The choice of W_1 , W_2 and W_3 depends upon the high- frequency and low-frequency specifications and to be match with the frequency-scale structure of the plant.

VI. DESIGN EXAMPLE (TWO-TANK CHEMICAL REACTOR).

We consider a LTI two-time scale system of Two-tank Chemical Reactor, which is described by

$$\begin{bmatrix} \dot{x}(t) \\ \dot{z}(t) \end{bmatrix} = \begin{bmatrix} -1/2 & 1/5 & 0 & 0 \\ 0 & -1/2 & 1/2 & 0 \\ 0 & 0 & 0 & 1/\epsilon \\ 0 & 0 & -1/\epsilon & -2/\epsilon \end{bmatrix} \begin{bmatrix} x(t) \\ z(t) \end{bmatrix} + \begin{bmatrix} 0 \\ 0 \\ 0 \\ 1/\epsilon \end{bmatrix} u; \quad y(t) = \begin{bmatrix} 1 & 0 & 0 & 1 \end{bmatrix} \begin{bmatrix} x(t) \\ z(t) \end{bmatrix}$$

Let $\epsilon=0.1$ is the singular perturbation parameter. We want to design slow, fast, composite and full-order controller separately to meet *Robust Performance* and *Robust Stability* specification through H_∞ -control theory. We choose the filters

$$W_1 = \frac{\beta(0.5s + 0.01)}{(2s + 0.01)(2\epsilon s + 1)}; \quad W_2 = [0.1];$$

$$W_3 = \frac{s(2\epsilon s + 1)}{(0.5s + 0.01)}; \quad \beta = \text{some constant}$$

To design full order controller we choose $\beta = 0.51$ and the whole problem is solved for $\gamma = 1$ using *Robust Control TOOLBOX in MATLAB*.

To design H_∞ controller for slow and fast sub- system, for the filters W_1 , W_2 and W_3 , put for $\beta=1$ and $\epsilon = 0$. and change the frequency scale of s to high frequency scale $s = p/\epsilon$ and then put $\epsilon = 0$ for the fast subsystem.

The obtained full order controller $K_{H_\infty}(s)$, slow controller $K_{sH_\infty}(s)$, Fast controller K_{fH_∞} and composite controller K_{cH_∞} are shown in sec.-VIII. The step response and magnitude Bode – plot of the composite and full-order controller are shown in Fig (3) and Fig (4). The response of the full- order controller and the composite controller are almost indistinguishable in the two plots.

VII. CONCLUSION

The modeling of the control systems usually calls for higher-order dynamics. Singularly perturbation techniques are the simplification of higher-order dynamic models. In this paper thus the separation of time scale from the full-order plant and design of reduced order model controller and finally getting a composite controller achieve the simplified design procedure and eliminates stiffness difficulties and problem of ill-conditioning, also prepares for a more efficient hardware and software implementation of the controller.

VIII. RESULT

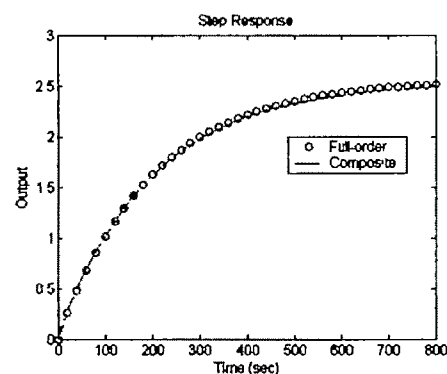


Fig.. 3

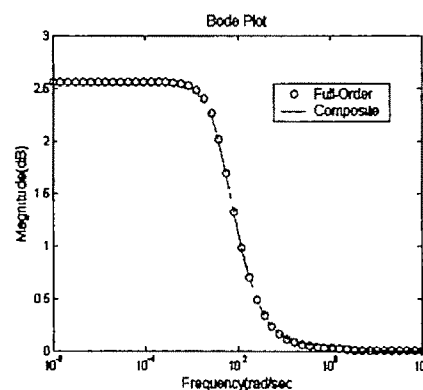


Fig. 4

Fast controller:

$$K_{fHo}(p) = \frac{5.803p^2 + 11.606p + 5.803}{p^3 + 120883p^2 + 6044.19p + 125.001}$$

Slow controller:

$$K_{sHo}(s) = \frac{0.415s^3 + 0.438s^2 + 0.127s + 0.006}{s^3 + 1.026s^2 + 0.277s + 0.006}$$

and $K_{fHo}(0) = K_{sHo}(\infty) = 0.4157$

Full-order controller:

$$K_{Ho}(s) = \frac{s^6 + 0.079s^5 + 0.483s^4 + 0.615s^3 + 0.295s^2 + 0.051s + 0.0009}{s^7 + 8.284s^6 + 21.464s^5 + 28.661s^4 + 18.033s^3 + 4.003s^2 + 0.090s + 0.0004}$$

Composite controller:

$$K_{cHo}(s) = \frac{s^6 + 0.272s^5 + 6.804s^4 + 8.338s^3 + 3.519s^2 + 0.466s + 0.008}{s^7 + 13.115s^6 + 73.127s^5 + 190.368s^4 + 144.912s^3 + 34.454s^2 + 0.787s + 0.003}$$

REFERENCES

- [1] Geray O, Looze D P. *Linear quadratic regulator loop shaping for high frequency compensation*; IEEE, Dec 1994, Vol 1, 887-891pp
- [2] Singh H; Brown R H; Naidu D S. *Unified approach to H_∞-optimal control of singularly perturbed system* Acc, Vol 4 1999, 2909-2913pp
- [3] Valery y Glizer, Emilia Fridman. *H_∞-control of linear singularly perturbed system with small state delay*; Journal of Mathematical analysis and application Vol 250; issue 1, Oct-2000, 49-85pp.
- [4] H.K Khalil, F.C Chen. *H_∞-control of two time scale system; control lett*, Vol. 19, 35-42pp, 1992.
- [5] J.C Doyle; K.Glover; P.P.khargonekar and B.A. Francis. *State space solution of standard H₂ and H_∞ control problem* IEEE Trans Auto. Control 34 (8) (1989) 831-847pp.
- [6] D.W.Luse and H.K.Khalil, *Frequency domain results for systems with slow and fast dynamics*, IEEE Trans Auto Control 30 (12) (1985) 1171-1179pp
- [7] D.W.Luse and J.A Ball, *Frequency -scale decomposition of H_∞ disk problem*, SLAM J. Control optim 27(1989).
- [8] K.Glover and J.C Doyle, *State-space formulae for all stabilizing controllers that satisfy an H_∞ norm bound relation risk sensitivity, system. control lett*. 11(1988) 167-172pp.
- [9] R.Y..Chiang and M.G. Safnov, *Robust control Toolbox user's gui de* (Math Works, South Natick, MA, 1988.
- [10] S.M.Sharuz, *Design of H_∞-optimal compensators for singularly perturbed systems*, in Proc IEEE conf on Decision Control, Tampa, FL (Dec 1989) 2397-2398.
- [11] M Suzuki and M.Miura, *Stabilizing feedback controllers for singularly perturbed linear constant system* . IEEE Trans. Auto. Control 21 (1) (1976) 123-124pp
- [12] J.L.Vian and M.E Sawan, *H_∞ control for singularly perturbed system* in Proc IEEE conf. on Decision Control, Brighton, England (Dec.1991) 1072-1074.
- [13] U K Mackenroth. *Robust control system Theory and Casestudy* (springer, Germany, 2004).

The Gauss-Hermite Filter and the Central Difference Filter for Bearing Only Tracking

Manas Kumar Bera¹, Saurabh Pal²

¹ Dept of Instrumentation Engineering, Haldia Institute of Technology, Haldia, Purba Medinipur, West Bengal, e-mail: bera_manas@yahoo.co.in.

² Dept of Instrumentation Engineering, Haldia Institute of Technology, Haldia, Purba Medinipur, West Bengal, e-mail: spal76@rediffmail.com

Abstract— Nonlinear estimation or filtering is the process of estimating and tracking the state of nonlinear stochastic system from Gaussian and non-Gaussian noisy observation data. We address the special case where only the observation model is nonlinear but the noises are additive and Gaussian. The extended Kalman filter (EKF) has been the standard technique usually applied here. But, for severe nonlinearities, the EKF can be very unstable and has poor performance. Bayesian filtering requires integration over probability density functions that cannot be accomplished in the closed form for the general nonlinear, Gaussian multivariate system. Hence approximations are required. Several numerical techniques are presented that give approximate solutions for these integrals, including Gauss-Hermite quadrature, and Central difference filter. Performance of extended Kalman filter (EKF), Gauss-Hermite filter (GHF), and Central Difference filter (CDF) as applied to the bearing only tracking problem have been compared. The performances of the filters are compared in terms of accuracy and computational load. With a simplified quantitative criterion for track-loss, relative occurrence of such track loss in batch Monte Carlo simulation has been used as a measure of robustness.

Key words— Bayesian filtering, Central Difference filter, Extended Kalman filter, Gauss-Hermite filter, Monte Carlo simulation.

I. INTRODUCTION

NONLINEAR filtering problems consist of recursively estimating the state of a nonlinear stochastic system based on a set of a noisy observation data. It has many significant applications in many diverse fields including economics, biostatics, and numerous statistical signal and array processing

engineering problem such as time series analysis, communications, radar and sonar target tracking and satellite navigation [1], [2], [3]. The Extended Kalman Filter (EKF) has become a standard technique used in a number of nonlinear state estimation. However, if the nonlinearities are significant, or the noise is non-Gaussian, the EKF gives poor performances. Recently, another real-time and accurate filter known as CDF and GHF for nonlinear filtering algorithms based on Gaussian distributions is reported [12]. The motivation for the present study to explore the possibility of using CDF and GHF for the 2D bearing-only target (BOT) tracking problem, and for performance comparison with EKF, we use identical truth model with Lin *et al* [8].

II. 2D BEARING ONLY TRACKING PROBLEM FORMULATION

The nonlinear BOT problem may be visualized by a situation, where a low flying aircraft is tracing an ammunition train or an enemy ship. The problem formulation is the same as in [1],[2],[8].

In our scenario, a moving observer which may be ownship or platform at an approximately known altitude measures bearings to a target at altitude zero, and subsequently processes these measurements to obtain estimates of the position and velocity of the target in earth fixed co-ordinate system. Both the ownship and the target are moving parallel in constant velocity and in the same horizontal plane, so it is a 2D tracking problem. The observer model is nonlinear and both process and measurement noises are Gaussian.

The non-linear BOT problem consider has two components, namely, the target kinematics and the tracking *platform* kinematics as shown in fig.1. The target moves along *x*-axis according to the following state space relations

$$x(k+1) = Fx(k) + G(k)w(k) \quad (1)$$

where $x(k) = \begin{bmatrix} x_1(k) \\ x_2(k) \end{bmatrix}$; $F(k) = \begin{bmatrix} 1 & T \\ 0 & 1 \end{bmatrix}$ and $G(k) = \begin{bmatrix} T^2/2 \\ T \end{bmatrix}$

where $x_1(k)$ and $x_2(k)$ represent the position along x-axis in meters and velocity in m/sec of the target respectively. $w(k)$ is independent zero mean Gaussian white acceleration noise sequence with variance $q = 0.01 \text{ m}^2/\text{s}^4$. The sampling period is denoted by $T=1\text{sec}$. The (unknown) true initial condition is

$$\underline{x}(0) = \begin{bmatrix} 80 \\ 1 \end{bmatrix}.$$

The target motion noise covariance matrix may be computed,

$$\begin{aligned} \text{as } Q(k) &= G(k)G^T(k)q = \begin{bmatrix} T^2/2 & T \\ T & 1 \end{bmatrix} q \\ &= \begin{bmatrix} T^4/4 & T^3/2 \\ T^3/2 & T^2 \end{bmatrix} q \end{aligned}$$

A tracking platform with an airborne sensor moves according to the following discrete time equations:

$$x_p(k) = \bar{x}_p(k) + \Delta x_p(k) \quad k=0,1,\dots,n_{\text{step}} \quad (2)$$

$$y_p(k) = \bar{y}_p(k) + \Delta y_p(k) \quad k=0,1,\dots,n_{\text{step}} \quad (3)$$

where $\bar{x}_p(k)$ and $\bar{y}_p(k)$ are the (known) average platform position co-ordinates and perturbations $\Delta x_p(k)$ and $\Delta y_p(k)$ are the mutually independent zero mean Gaussian white noise sequences with variances $r_x = 1 \times 10^{-2} \text{ m}^2$ and $r_y = 1 \times 10^{-2} \text{ m}^2$, respectively. The mean positions of the platform are:

$$\bar{x}_p(k) = 4kT \text{ and } \bar{y}_p(k) = 20$$

The sensor measurement is

$$z_m(k) = z(k) + v_s(k)$$

Where

$$z(k) = h[x_p(k), y_p(k), x_1(k)] = \tan^{-1} \frac{y_p(k)}{x_1(k) - x_p(k)} \quad (4)$$

is the bearing between the x axis and the line of sight (LOS) from the sensor to the target and $v_s(k)$ is the zero mean Gaussian white measurement noise sequence with variance $r_s = (3^\circ)^2$. The sensor noise is assumed to be independent of the sensor platform perturbations and sampling interval.

The random component of platform motion induces additional errors in the measurements, which is nonadditive and already embedded in (5). The effect of these errors can be approximated as additive noise by expanding the nonlinear measurement equation as

$$z_m(k) = h[x_p(k), y_p(k), x_1(k)] + v_s(k)$$

$$\equiv h[\bar{x}_p(k), \bar{y}_p(k), x_1(k)] + v(k) \quad (5)$$

where $v(k)$ is the equivalent additive measurement noise given approximately by small perturbation theory as

$$v(k) = \frac{[\bar{y}_p \Delta x_p + \{x_1(k) - \bar{x}_p(k)\} \Delta y_p]}{[x_1(k) - \bar{x}_p(k)]^2 + \bar{y}_p(k)^2} + v_s(k), \quad (6)$$

with variance $R(k)$. $R(k)$ is calculated considering $\Delta x_p(k)$, $\Delta y_p(k)$ and $v(k)$ are mutually independent as

$$R(k) = E[v(k)^2] = \frac{\bar{y}_p(k)^2 r_x + [x_1(k) - \bar{x}_p(k)]^2 r_y}{\{[x_1(k) - \bar{x}_p(k)]^2 + \bar{y}_p(k)^2\}^2} + r_s \quad (7)$$

A. Filter Initialization

Traditionally, tracking filters are initialised from first few measurements.

From the measurement equation taking inverse transformation

$$\hat{x}_1(k) = g[z(k), \bar{x}_p(k), \bar{y}_p(k)] = \bar{x}_p(k) + \frac{\bar{y}_p(k)}{\tan(z(k))}$$

The initial position estimate $\hat{x}_1(0)$ may be obtained from the first measurement $z_m(0)$ and platform mean positions as in [8]

$$\hat{x}_1(0) = \bar{x}_p(0) + \frac{\bar{y}_p(0)}{\tan(z_m(0))}$$

from which

$$P_{11}(0) = r_x + \frac{r_y}{\tan^2 z} + \frac{\bar{y}_p^2}{\sin^4 z} r_s \quad (8)$$

However, in the present case, velocity estimation from first two samples would create large variance due to the large measurement uncertainty. This may be reduced by using prior knowledge about the target motion and as in [8] the initial velocity estimation is selected as $\hat{x}_2(0) = 0$ and associated variance as $P_{22}(0) = 1$. The off diagonal terms $P_{12}(0)$ and $P_{21}(0)$ are taken as zero.

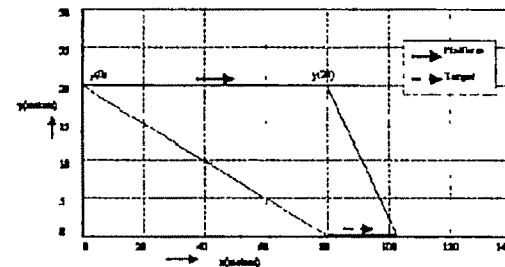


Fig.1 Tracking platform Kinematics

III. EXTENDED KALMAN FILTER

Extended Kalman filter is the linearised Kalman filter algorithm and may be found out in many standard books and literature so we are avoiding the algorithm details.

IV. GAUSS HERMITE FILTER

A. Introduction

In this section we describe the Gauss-Hermite Filter (GHF) algorithm, which is based on the Gaussian filter and Gauss-Hermite quadrature rule.

Consider the nonlinear plant described by the state and measurement equations with additive noise as follows

$$x_{k+1} = f(x_k) + w_k \quad (9)$$

$$y_k = g(x_k) + v_k \quad (10)$$

Dimensionally, $w_k \in R^n$, $v_k \in R^p$, $x_k \in R^n$ and $y_k \in R^p$ of which x_k denotes the state of the system and y_k is the measurement at the instance k . $f(x_k)$ and $g(x_k)$ are general nonlinear functions of x_k and k . It is assumed that the process and measurement noise and the random variable signifying initial values of the variable are uncorrelated to each other. It may be noted that filtering algorithm presented in this section need not constrain the model to have only additive noise.

B. Filter Algorithm

We consider the Gauss-Hermite filter is based on the Gaussian-Hermite quadrature rule is given by

$$\int_{R^n} F(x) \frac{1}{(2\pi)^{n/2}} e^{-\frac{1}{2}x^T x} dx \approx \sum_{i=1}^N w_i F(q_i) \quad (11)$$

Where $q_i = \frac{x_i}{\sqrt{3}}$, $1 \leq i \leq m$, x_i and w_i are the quadrature points and corresponding weights respectively.

Let \hat{x}_0 and P_0 be the starting values for the mean and covariance of the random variable $x(0)$.

Filter initialization

Set $P_{0|0} = P_0$ and $x_{0|0} = \hat{x}_0$

Predictor step

Compute the factorization: $P_{k|k} = S^T S$

Generation of quadrature points:

The quadrature points x_i and weights w_i are generated using the methods discussed in [12]

Compute: $x_i = S^T q_i + x_{k|k}$

Compute the mean and covariance:

$$x_{k+1|k} = \sum_{i=1}^N f(x_i) w_i \quad (12)$$

$$P_{k+1|k} = Q + \sum_{i=1}^N (f(x_i) - x_{k+1|k})(f(x_i) - x_{k+1|k})^T w_i \quad (13)$$

Corrector step

Compute the factorization: $P_{k+1|k} = \tilde{S}^T \tilde{S}$

Compute: $x_i = \tilde{S}^T q_i + x_{k+1|k}$

Compute:

$$x_{k|k} = \hat{x}_{k+1|k} + L_k (y(k) - Z_{k+1}) \quad (14)$$

$$P_{k|k} = P_{k+1|k} - L_k P_{zz}^T \quad (15)$$

Where

$$Z_{k+1} = \sum_{i=1}^N g(x_i) w_i \quad (16)$$

$$P_{zz} = \sum_{i=1}^N (x_i - x_{k+1|k})(g(x_i) - Z_{k+1})^T w_i \quad (17)$$

$$P_{zz} = \sum_{i=1}^N (g(x_i) - Z_k)(g(x_i) - Z_{k+1})^T w_i \quad (18)$$

$$L_{k+1} = P_{zz} (R + P_{zz})^{-1} \quad (19)$$

Recursion

Estimates for the subsequent steps may be computed by repeating the predictor and corrector steps above.

One of the advantage of this quadrature based filter is that we are not required to have the derivative of f and g .

V. CENTRAL DIFFERENCE FILTER

Here we present the filter algorithm based on the central difference approximation. System dynamic and measurement model same as described in section IV.

Let \hat{x}_0 and P_0 be the starting values for the mean and covariance of the random variable $x(0)$.

Filter initialization

Set $P_{0|0} = P_0$ and $x_{0|0} = \hat{x}_0$

Predictor step

Compute the factorization: $P_{k|k} = S^T S$

Choose a suitable scalar h and compute

$$a_i = \frac{f(x_{k|k} + hS^T e_i) - f(x_{k|k} - hS^T e_i)}{2h}, \text{ and}$$

$$H_{i,i} = \frac{f(x_{k|k} + hS^T e_i) - 2f(x_{k|k}) + f(x_{k|k} - hS^T e_i)}{h^2}$$

Where e_i is the unit vector in the i^{th} direction and $1 \leq i \leq n$.

Compute the mean and covariance as

$$\hat{x}_{k+1|k} = f(x_{k|k}) + \sum_{i=1}^n \frac{1}{2} H_{i,i}, \text{ and} \quad (20)$$

$$P_{k+1|k} = Q + \sum_{i=1}^n a_i a_i^T + \sum_{i=1}^n \frac{1}{2} H_{i,i} H_{i,i}^T \quad (21)$$

Corrector step

Compute the factorization: $P_{k+1|k} = \tilde{S}^T \tilde{S}$

Compute the central difference approximation as

$$b_i = \frac{g(x_{k+1|k} + h\tilde{S}^T e_i) - g(x_{k+1|k} - h\tilde{S}^T e_i)}{2h} \text{ and}$$

$$G_{i,i} = \frac{g(x_{k+1|k} + h\tilde{S}^T e_i) - 2g(x_{k+1|k}) + g(x_{k+1|k} - h\tilde{S}^T e_i)}{h^2}$$

, where $1 \leq i \leq n$

Compute:

$$x_{k|k} = \hat{x}_{k+1|k} + L_k (y(k) - Z_{k+1}) \quad (22)$$

$$P_{k|k} = P_{k+1|k} - L_k P_{zz}^T \quad (23)$$

Where

$$Z_{k+1} = \sum_{i=1}^N g(x_i) w_i \quad (24)$$

$$P_{zz} = \sum_{i=1}^N (x_i - x_{k+1|k})(g(x_i) - Z_{k+1})^T w_i \quad (25)$$

$$P_{zz} = \sum_{i=1}^N (g(x_i) - Z_k)(g(x_i) - Z_{k+1})^T w_i \quad (26)$$

$$L_{k+1} = P_{zz} (R + P_{zz})^{-1} \quad (27)$$

Recursion:

Estimates for the subsequent steps may be computed by repeating the predictor and corrector steps above.

VI. RESULTS AND COMPARISON

We use the average root mean square error for our comparison of the methods [12]. Monte Carlo batch consisting of 10,000 runs. For each run, random number generator was re-seeded with the clock. For robustness studies, 10 such batches were used. We defined a *track-loss run* whenever the absolute position error after the last (20s) time step failed to settle below a specified value X_{limi} . In order to arrive at a suitable value of X_{limi} , the approximate frequency of failure in EKF was first determined manually by inspecting the error settling trends for the cases with large initial measurement error (>170 m) [15]. Using MC runs in EKF, the value of X_{limi} was gradually decreased from 80 m till the number of failures approximately matched the value obtained by and the variance of the frequency value from different batches were sufficiently low. By this iterative procedure, the value of X_{limi} was set to 15m [15]. Identical $\hat{x}(0)$, $P(0)$, $Q(k)$ and $R(k)$ as described in Section II were used in batches of 10,000 Monte Carlo runs.

The CDF was run using the step size $h = \sqrt{3}$ and for the GHF the quadrature points and the normalized weights are calculated as in section IV. The frequency of track loss with nominal parameters for all the filters and relative computational time are shown in Table I. The performance (RMS error) for small batches (100) Monte Carlo runs was found to be nearly identical to that of Lin *et al* [12], with allowances made for the randomness of small populations. RMS error settling for a batch of 10,000 MC runs

Technique Used	Mean Track loss frequency	SD Frequency(over 10 sets of 10,000 MC runs)	Computational time(sec)
EKF	27.1	5.78	33.45
CDF	1.8	1.23	96.5
GHF	1.5	0.85	222.45

Table I: Frequency of Track-Loss (Per 10000 MC Runs)

using EKF with the track loss cases removed are shown in Fig. 2 (a)&(b). Ignoring the track loss cases, the rms error in position and velocity for about 10,000 Monte Carlo run is shown in Fig. 2 (a) & (b). The decay of position error of the CDF is initially slower than the EKF but is the same as EKF after 10 sec. Figure shows a comparative plot of the position errors of EKF, CDF and GHF in a representative case when there is a large initial mismatch. In case of GHF the cases of track loss (as shown in Table I) are far less compared to EKF, but slightly better estimates than CDF. But computation time is required for the GHF is high than the EKF and CDF.

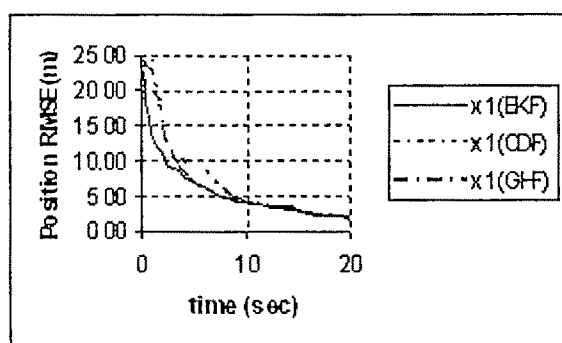


Figure 2 (a) RMS Position error setting for EKF, CDF, & GHF

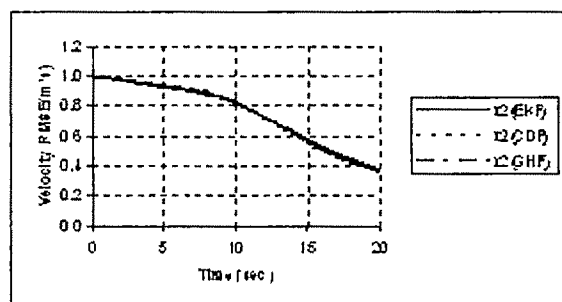


Figure 2 (b) RMS Velocity error setting for EKF, CDF, & GHF

VII. CONCLUSION

The failure rate (0.271%) observed in the present work for EKF has been higher than that obtained (0.165%) by Lin et al., [8]. This may be attributed to different failure criteria being used. However, as we use the same criteria to assess all the filters, this should be adequate for a comparative analysis.

The present study we have applied three filters namely EKF, CDF and GHF for bearing only tracking problem. The RMSE of position and velocity is compared. The EKF implementation, as expected, reduced computation time but did not have any impact on the error settling performance. Same features are observed for CDF and GHF also. Using the criteria for track loss, CDF and GHF are found to be superior in terms of robustness i.e. lower incidence of track loss.

ACKNOWLEDGMENT

The authors are grateful to TEQIP for financial support and Haldia Institute of Technology for encouragement in research activities. They also thank Dr. Smita Sadhu of Deptt of Electrical Engg, Jadavpur University for her encouragement and support.

REFERENCES

- [1] Hwang & Brown, "Introduction to Random Signals and Applied Kalman filtering", 2nd edition, John Wiley & Sons, Inc. 1992.
- [2] Mohinder S. Grewal & Angus P. Andrews, "Kalman Filtering Theory & Practice" Prentice Hall, 1993.
- [3] Zarchen & Musoff, "Fundamentals of Kalman Filtering: A Practical Approach", American Institute of Aeronautics & Astronautics, 2000.
- [4] Anderson & Moore, "Optimal filtering", Prentice Hall, 1971.

- [5] Bar Shalom, Li and Kirubarajan, "Estimation with applications to Tracking and Navigation", John Wiley & Sons, Inc, 2001.
- [6] Andrew H. Jazwinski, "Stochastic process and filtering theory", Academic press, 1970
- [7] Press, Teukolsky, Vetterling, Flannery, "Numerical Recipes in C", Cambridge University Press, 1992..
- [8] Lin X, Kirubarajan T, Bar-Shalom Y, Maskell S. Comparison of EKF, "Pseudomeasurement and Particle Filters for a Bearing-only Target Tracking Problem", *Proc. SPIE Conference of Signal and Data Processing of small Targets*, Orlando, FL, 2002.
- [9] LaViola, J. A. "Comparison of Unscented and Extended Kalman Filtering for Estimating Quaternion Motion", *Proc. of the 2003 American Control Conf.* IEEE Press, 2435-2440, June 2003.
- [10] R.E. Kalman, "A new approach to linear filtering and prediction problem", *Trans ASME, J. Basic engineering for D* vol 83, Dec 1961 pp 95-107
- [11] Simon J. Julier, Jeffrey K. Uhlmann, "A New Extension of the Kalman Filter to nonlinear Systems", 11th internal synopsis on *Aerospace/ Defense sensing, simulation & Control*, 1997.
- [12] Kazufumi Ito and Kaiqi Xiong, "Gaussian Filters for Nonlinear Filtering Problems", *IEEE Transactions on Automatic*, Vol. 45, No. 5, May 2000.
- [14] M. Sanjeev, Arulampalam, Simon Maskell, Neil Gordon, and Tim Clapp, "A Tutorial on Particle Filters for Online Nonlinear/Non-Gaussian Bayesian Tracking", *IEEE Transactions on Signal Processing*, Vol. 50, No. 2, February 2002
- [15] S. Sadhu, M. Srinivasan, S. Mondal and T.K. Ghoshal, "Bearing only Tracking using Square Root Sigma Point Kalman Filter", *IEEE Indian Annual Conference 2004*, Indicon 2004.
- [16] Greg Welch and Gary Bishop, "An Introduction to the Kalman Filter", *UNC -Chapel Hill*, TR95-041, April 5, 2004.
- [17] Ian B. Rhodes, "A Tutorial Introduction to Estimation and Filtering", *IEEE Transactions on Automatic Control*, Vol. AC-16, No. 6, Dec 1971.
- [18] Jayesh H. Kotecha and Petar M. Djuric, "Gaussian Particle Filtering", *IEEE Transactions on Automatic Control*, Vol. 51, NO. 10, OCTOBER 2003.
- [19] Kazufumi Ito, "Gaussian Filter for Nonlinear Filtering Problems", *Proceedings of the 39a IEEE Conference on Decision and Control* Sydney, Australia December, 2000.
- [20] Simon J. Julier, Jeffrey K. Uhlmann, "Unscented Filtering and Nonlinear Estimation", *Proceedings of the IEEE*, Vol. 92, No. 3, March 2004.

Robust Control of Inverted Pendulum System by Convex Optimization: An LMI Approach

Sharmistha Mandal¹, A. Sutradhar²

¹ Electrical Engineering Department, JIS College of Engineering, W.B., India, e-mail: sharmi_mandal@yahoo.co.in

² Electrical Engineering Department, Bengal Engineering & Science University, W.B., India, e-mail: aseel@rediffmail.com

Abstract—In this paper, the concept of Linear Matrix Inequality (LMI) regions has been used for designing a robust controller for an inverted pendulum along with driving servo-system. The system is a parameter-dependent system and state-feedback controller is designed in order to satisfy a number of specifications. The closed-loop time domain specifications settling time and maximum overshoot have been taken into account. The designed controller turns out to be robust with respect to the uncertainties in the plant and gives satisfactory closed-loop system.

Key words: Inverted Pendulum, Linear Fractional Representation, Linear Matrix Inequalities, Robust Control.

I. INTRODUCTION

MODEL uncertainty and robustness have been a control theme in the development of the field of automatic control system. Improper modeling of the system, variations, perturbations in specific physical parameters of real systems lead to uncertainties in the model. A great variety of uncertainty in modeling can be handled easily by *linear matrix inequalities (LMIs) and LMI techniques* [1]-[5]. LMI is very powerful design tool in system and control theory. Multi-objective control problem can be tackled with LMI techniques, due to its ability to include convex constraints such as pole-placement, H_2 performance and H_∞ performance [2], [4], [6].

This paper addresses the design of a robust controller for an inverted pendulum and its driver servo system. The output feedback control design method using LMI of an inverted pendulum system has been discussed in [5], [7]. The LMI framework is particularly well suited to multi-objective state-feedback synthesis [1], [4]. In the present paper, we address the design problem of the closed loop servo driven inverted pendulum system by both state-feedback and output feedback methods using LMI approach to get robust performance.

A good controller should provide a fast and well-damped time response. Satisfactory transient response can be obtained by confining the closed-loop poles within a suitable region of the left-half of the complex plane [2], [6], [8], [9]. This class of regions is the set of convex regions symmetric with respect to the real axis. These regions include relevant regions such as disks, half-planes, conic sectors etc., and any intersection of the above.

Once the design specifications are expressed as a convex optimization problem involving LMI, can be solved numerically very efficiently using interior-point optimization algorithm [1], [10].

This paper is organized as follows. Section II gives the description of the servo-driven inverted pendulum system. Section III gives the linear fractional models of uncertainty. Section IV gives the concept of linear matrix inequality, LMI regions, and state-feedback synthesis with quadratic stability via LMIs. In section V, the performance characteristics of a laboratory type servo-driven inverted pendulum system using present design method have been presented.

The notations we use are as follows: \square and \mathbb{C} denote the sets of real and complex numbers respectively. For a real matrix P , $P > 0$ (resp. $P \geq 0$) means P is symmetric and positive-definite (resp. positive semi-definite); $\|x\|$ denotes the Euclidean norm of vector x .

II. THE INVERTED PENDULUM CONTROL PROBLEM

The inverted pendulum control system consists of a cart driven by a D.C. motor, and a pendulum attached to the cart (see Fig.1). Here our goal is to move the cart from one position to another along the track with the pendulum rod at the upright position and also to control the pendulum so that it remains in vertical position in any disturbance along with parameter variations. For the inverted pendulum system, x is the position of the cart, θ is the angular position of the pendulum rod with the vertical axis, and u is control voltage applied to the servo-motor driving the cart. The mass of the cart, M ; mass of the pendulum bob, m ; the length of pendulum rod, l and the effective moment of inertia on the drive motor, J_m are the parameters of the system. We consider m and J_m as the constant but uncertain parameters.

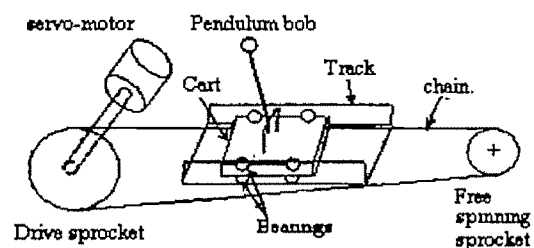


Fig1: Inverted pendulum with its driver servo system

The linearized dynamic equations of the inverted pendulum are:

$$\begin{aligned} (M+m)\ddot{x} + ml\ddot{\theta} &= u \\ ml\ddot{\theta} + m\ddot{x} &= mg\theta \end{aligned} \quad (1)$$

where g is the gravity constant, θ is the angular position of rod and x is the linear position of the cart.

The state-space model of the inverted pendulum along with the driving motor (assuming armature inductance of the D.C. motor equal to zero) is

$$\begin{bmatrix} \dot{x}_1 \\ \dot{x}_2 \\ \dot{x}_3 \\ \dot{x}_4 \end{bmatrix} = \begin{bmatrix} 0 & 1 & 0 & 0 \\ \frac{r^2 mg}{l(J_m + M^2)} + \frac{g}{l} & 0 & 0 & \frac{R_a B_m + K_t K_b}{R_a(J_m + M^2)} \\ 0 & 0 & 0 & 1 \\ -\frac{r^2 mg}{J_m + M^2} & 0 & 0 & \frac{R_a B_m + K_t K_b}{R_a(J_m + M^2)} \end{bmatrix} \begin{bmatrix} x_1 \\ x_2 \\ x_3 \\ x_4 \end{bmatrix} + \begin{bmatrix} 0 \\ \frac{K_t r}{R_a(J_m + M^2)} \\ 0 \\ \frac{K_t r}{R_a(J_m + M^2)} \end{bmatrix} v_a \quad (2)$$

where,

R_a = armature resistance; J_m = moment of inertia of motor

B_m = viscous friction coefficient; v_a = armature voltage;

K_b = back-emf constant; K_t = motor torque constant

r = radius of the driving gear.

In this case the state vector is

$$X = [\theta \quad \dot{\theta} \quad x \quad \dot{x}]^T = [x_1 \quad x_2 \quad x_3 \quad x_4]^T$$

Here we assume that the mass m and moment of inertia J_m are uncertain but bounded: $m \in [m_0 - \Delta m, m_0 + \Delta m]$ and $J_m \in [J_{m0} - \Delta J_m, J_{m0} + \Delta J_m]$ where m_0 , J_{m0} are the nominal values and Δm , ΔJ_m are the uncertainties. Here, the system is the affine parameter-dependent system and depends on the uncertain parameters m and J_m . We accept the other parameters of the system as constant for the present study.

III. LINEAR FRACTIONAL MODELS OF UNCERTAINTY

Linear-fractional model is widely used in mathematical representation of uncertainty (see Fig.2). In this model, $P(s)$ represents a nominal linear time-invariant system, which consists of the transfer function for the plant plus the system weighting functions, and Δ is a diagonal matrix containing the uncertain parameters of the system in lumped form [13], [14]. Δ is unknown, but bounded. Vectors $q(t)$ and $p(t)$ are the fictitious (not accessible) perturbation inputs and outputs.

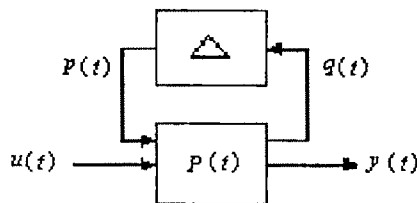


Fig. 2: Linear-Fractional Model

The above multivariable system can be described by the state-space equations:

$$\begin{aligned} \dot{x}(t) &= Ax(t) + B_u u(t) + B_p p(t) \\ y(t) &= C_x x(t) + D_{yu} u(t) + D_{yp} p(t) \\ q(t) &= C_q x(t) + D_{qp} p(t) + D_{qu} u(t) \\ p(t) &= \Delta(t)q(t); \quad \|\Delta(t)\| \leq 1 \end{aligned} \quad (3)$$

where $x \in \mathcal{R}^n$ is the state vector, $u \in \mathcal{R}^{n_u}$ is the control input and $y \in \mathcal{R}^{n_y}$ is the measured output.

IV. LMI FRAMEWORK

A. Definition of LMI

A linear matrix inequality has the form

$$F(x) = F_0 + \sum_{i=1}^m x_i F_i > 0 \quad (4)$$

where $x \in \mathcal{R}^m$ is the variable, and $F_i = F_i^T \in \mathcal{R}^{n \times n}$, $i=0, 1, \dots, m$ are given. The inequality symbol in (4) means that $F(x)$ is positive definite, i.e., $u^T F(x)u > 0$ for all non-zero $u \in \mathcal{R}^n$. An LMI is a set of n polynomial inequalities in x .

Multiple LMIs $F_1(x) > 0, \dots, F_n(x) > 0$ can be expressed as the single LMI $\text{diag}((F_1(x), \dots, F_n(x))) > 0$. An LMI problem is an optimization problem over LMI constraints.

B. LMI Regions

In order to stabilize a system and to get satisfactory time response, the closed-loop poles should be confined within a suitable sub-region of the left-half of the s -plane, called LMI region. The concept of LMI regions has been used to formulate the pole-placement objectives in LMI terms. An LMI region is any convex subset \mathcal{D} of the complex plane that can be defined as

$$\mathcal{D} = \{z \in \mathbb{C} : L + zH + \bar{z}H^T < 0\}$$

where H and $L = L^T$ are real matrices. The matrix-valued function

$f_{\mathcal{D}}(z) = L + zH + \bar{z}H^T$ is called the characteristic function of \mathcal{D} .

The useful LMI regions include half-planes, vertical/horizontal strips, conic sectors, disks etc. The characteristic functions of these LMI regions are given in [2], [6], [11]. Advantage of LMI regions is the availability of *Lyapunov stability characteristics* for such regions as described in [15].

In practical applications, LMI regions are often specified as the intersection of the elementary regions, such as conic sectors, disks or vertical half-planes. Given LMI regions $\mathcal{D}_1, \mathcal{D}_2, \dots, \mathcal{D}_N$ and their associated characteristic functions $f_{\mathcal{D}_1}(z), f_{\mathcal{D}_2}(z), \dots, f_{\mathcal{D}_N}(z)$, the intersection $\mathcal{D} = \mathcal{D}_1 \cap \dots \cap \mathcal{D}_N$ is also an LMI region with function:

$$f_D(z) = \text{diag}_{i=1}^N f_{D_i}(z)$$

C. State-feedback synthesis with quadratic stability via LMIs

The system can be stabilized quadratically via state-feedback $u(t) = KX(t)$. For this the closed-loop poles are required to lie in some LMI region \mathcal{D} contained in the left-half plane. In this section, we consider the state-feedback synthesis problem i.e., the problem of finding a state-feedback gain K that places the closed-loop poles in some LMI region \mathcal{D} . With $u = KX$, the uncertain system (3) is quadratically stable if and only if [1]

$$\begin{bmatrix} (AQ + QA^T + \mu B_p B_p^T) & \mu B_p D_{qp}^T \\ + B_u KQ + QK^T B_u^T & + Q(C_q + D_{qu}K)^T \\ \mu D_{qp} B_p^T + (C_q + D_{qu}K)Q & -\mu(I - D_{qp} D_{qp}^T) \end{bmatrix} < 0$$

If there exist $Q > 0, \mu > 0$ [1].

With $Y = KQ$, the closed-loop system is quadratically stable if there exist $Q > 0, \mu > 0, Q > 0, \mu > 0$ and Y such that

$$\begin{bmatrix} (AQ + QA^T + \mu B_p B_p^T) & \mu B_p D_{qp}^T + QC_q^T + Y^T D_{qu}^T \\ + B_u Y + Y^T B_u^T & \\ \mu D_{qp} B_p^T + C_q Q + D_{qu} Y & -\mu(I - D_{qp} D_{qp}^T) \end{bmatrix} < 0$$

The closed-loop system is robustly \mathcal{D} -stable if the eigen values of the closed-loop system lie in \mathcal{D} for all admissible uncertainties Δ . The robust stability, quadratic stability and relation between robust, quadratic stability are discussed in [16], [17].

V. NUMERICAL RESULTS

We have used the data from the servo-driven inverted pendulum system developed in the laboratory [18] using chain-sprocket drive assembly for the cart. The numerical data for the parameters and constants are listed below in Table 1.

Table 1: Numerical values of different parameters

Parameters and Constants	Symbols	Value
Pendulum rod length	l	0.32 m
Acceleration due to gravity	g	9.81 m/s ²
Mass of the pendulum bob	m	0.11 kg
Mass of the cart	M	1.094 kg
Armature resistance	R_a	2.8 Ω
Armature inductance	L_a	0 H
Back-emf constant	K_b	0.23 V/rad/s
Torque constant	K_t	0.23 N-m/A
Moment of inertia of motor	J_m	0.00325 kg-m ²
Coefficient of viscous friction	B_m	0.013 N-m/rad/s
Radius of driving gear	r	0.025 m

Here we have considered parameter perturbation of $\pm 50\%$ of both m and J_m over their nominal values. For this case in order to balance the inverted pendulum on the cart one regulator problem and another tracking have been considered separately. For the regulator problem, we have designed a state-feedback controller to keep the pendulum in vertical position and for the tracking system, we have used output feedback along with state feedback. The closed-loop specifications for the system are:

- The settling time is about 5s with minimal overshoot and zero steady-state error for the nominal plant $P(\Delta=0)$ for the cart movement in a step fashion.
- The time-domain specifications must be met and the closed-loop system is internally stable for all perturbations Δm and ΔJ_m .

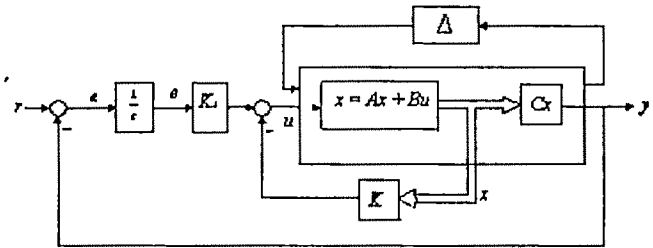


Fig. 3 Synthesis structure of the servo-driven inverted pendulum system

The feedback structure of the tracking problem is shown in Fig.3. Here, r denotes the reference cart position; e and u are respectively the tracking error and control input. The control input is $u = -KX + K_i e$.

The closed-loop specifications are achieved assigning in the intersection of the half-plane $x < -\alpha = -0$, where $\alpha = 0.25$ and the conic sector with apex at $x=0$ and angle $\theta = 1.5$ rad. The LMI region is shown in Fig.4.

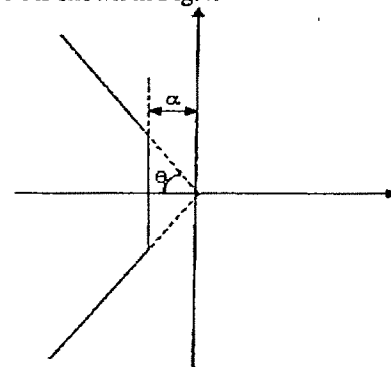


Fig. 4 LMI region

We have tried the LMI techniques for both the regulator and tracking problems using fixed parameter as well as a nominal plant design with $\pm 50\%$ perturbations in m and J_m .

For the regulator problem, we obtain the gain matrices:

Fixed parameter plant design:

$$K = [68.1102 \quad 8.6576 \quad 4.7770 \quad 22.3556]$$

Nominal plant design:

$$K = [59.5810 \quad 7.5682 \quad 4.1759 \quad 21.4967]$$

For the tracking problem, we obtain:

- Fixed parameter plant design:
Gain matrix: $K=[109.1843 \ 15.9263 \ 20.3670 \ 34.0421]$
and forward path gain for tracking error $K_I = -8.8477$
- Nominal plant design:
Gain matrix: $K=[99.4339 \ 14.4974 \ 18.5396 \ 32.3812]$
and forward path gain for tracking error $K_I = -8.0539$.

The responses for the regulator system for initial conditions of 0.2 rad in pendulum position θ and -0.1m cart position from equilibrium condition are given in Fig. 5 and 6. Fig five shows the performance with fixed parameter LMI design. Fig. 6 shows the performance for two extreme parameter variations with nominal plant design.

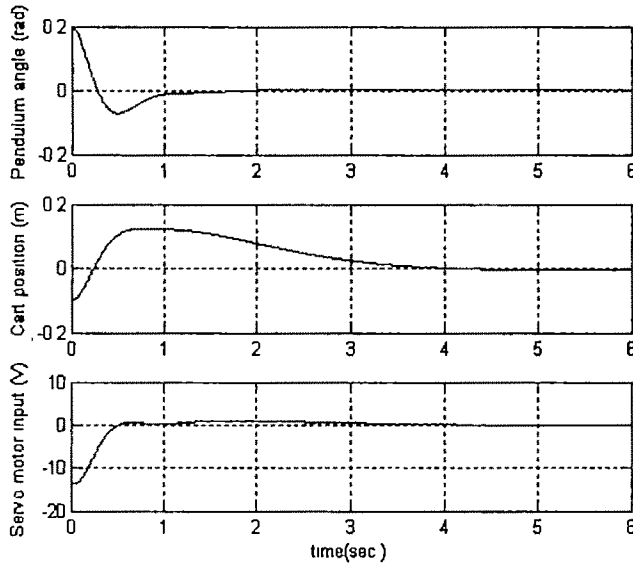


Fig. 5. Regulator performance with fixed parameter design.

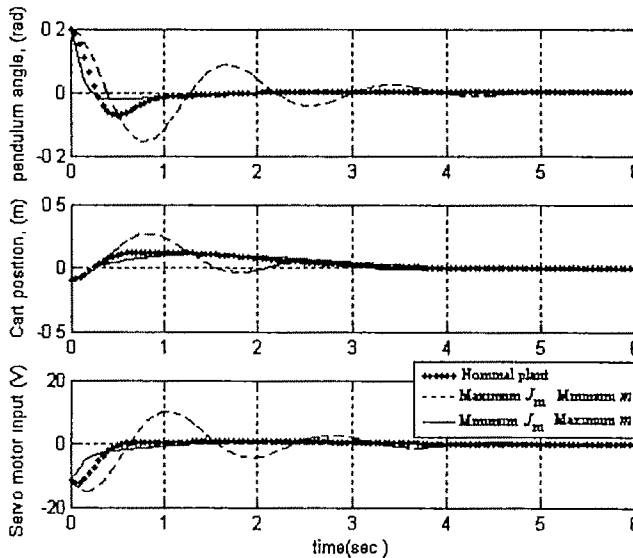


Fig. 6 Regulator performance with nominal plant design.

For the tracking problem,, 4.69sec. settling-time and zero steady-state error are obtained. Fig. 7 shows the response with fixed parameter design and Fig. 8 shows the performance with nominal plant design with extreme but bounded variation of the parameters. The robust performance in each case shows that the parameter perturbation is well tolerated in the closed loop system in nominal plant design both in tracking as well as regulator problem. Note also that the stability, decay rate are robust within bounded variations in m and J_m .

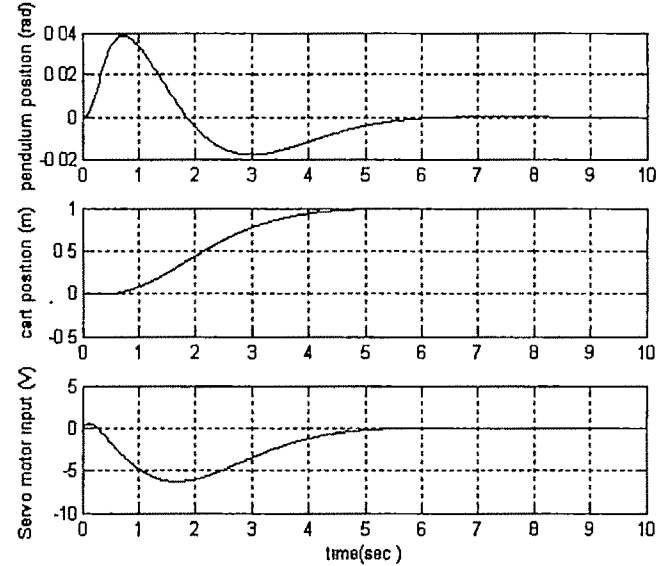


Fig. 7. Tracking performance with fixed parameter design.

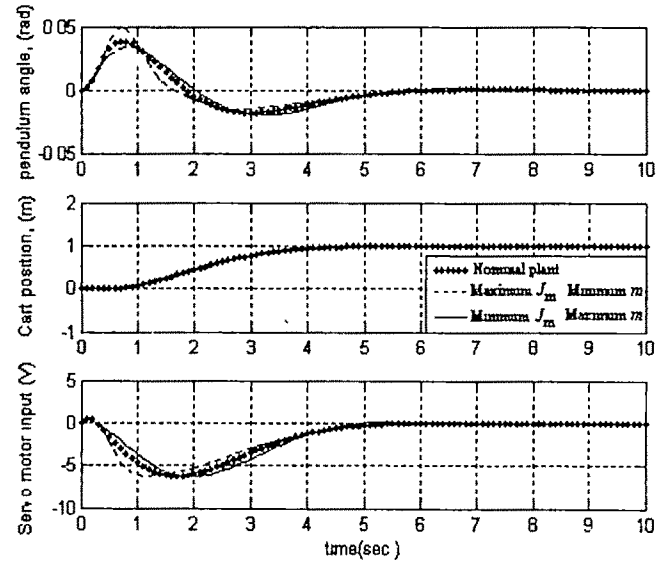


Fig. 8. Tracking performance with fixed parameter design.

VI. CONCLUSION

In this paper tractable analysis and synthesis techniques have been discussed for robust pole placement in LMI region for inverted pendulum system. We provide a solution to the

dynamic instability in the inverted pendulum system for parametric variation and uncertainties. The state feedback and output feedback design in a typical LMI region yielded robust performance of the controller for such an inherently unstable system. The linearized model of the mechanical system has been considered for the system design. The time domain performance exactly matched the desired specifications for a wide range of uncertainties in the parameters m and J_m for both the regulator and tracking system applications. The norms of output and input showed that minimum control effort required for acceptable disturbance rejection. The detailed friction model may be the area of further study for this design approach.

ACKNOWLEDGMENT

The authors express their sincerest gratitude to the Heads of the Departments of Electrical Engineering of JIS College of Engineering, Kalyani and Bengal Engineering & Science University, Shibpur for extending their laboratory and other infra-structural facilities to carry out the research work. Thanks are also due the contributors whose works have been referred to here.

REFERENCES

- [1] S. Boyd, L. El Ghaoui, E. Feron, and V. Balakrishnan, "Linear Matrix Inequalities in system and control theory", vol. 15. Philadelphia SIAM, 1994.
- [2] M. Chilali, P. Gahinet, "H₂ design with pole placement constraints: An LMI approach", IEEE Int. Trans. Automat. Contr., vol. 41, no. 3, pp. 358-367, March 1996.
- [3] A. Jadbabaie, C.T. Abadallah, D. Famularo, P. Dorato, "Robust, non-fragile and optimal controller design via Linear Matrix Inequalities", Proc. American Contr. Conf. Philadelphia, Pennsylvania, June 1998.
- [4] J. P. Polcher, L. El. Ghaoui, "State-feedback design via Linear Matrix Inequalities: Application to a benchmark problem", Proc. 3rd IEEE Conf. on Control Applications, pp. 1217-1222, August 1994.
- [5] S. Dussy, L. El. Ghaoui, "Robust gain-scheduled control of a class of nonlinear parameter-dependent systems: Application to an uncertain Inverted Pendulum", Proc. IEEE Int. Conf. on Control Applications Dearborn, MI, pp. 516-521, September 1996.
- [6] M. Chilali, P. Gahinet, P. Apkarian, "Robust pole placement in LMI regions", IEEE Trans. Automat. Contr., vol. 44, no. 12, December 1999.
- [7] S. Dussy, L. El. Ghaoui, "Measurement scheduled control for the RTAC problem: An LMI Approach", Int. J. Robust Nonlinear Control 8, pp. 377-400, 1998.
- [8] G. Garcia, J. Daafouz, J. Bernussou, "Output feedback disk pole assignment for systems with positive real uncertainty", IEEE Trans. Automat. Contr., vol. 41, no.9, pp. 1385-1391, 1996.
- [9] D. Peaucelle, D. Arzelier, "Robust disk pole assignment by state and output feedback for generalized uncertainty models", Proc. 37th IEEE Conf. on Decision & Control Tampa, Florida USA, pp. 1728-1733, December 1998.
- [10] S. Boyd, L. Vandenberghe, "Convex optimization", Cambridge University Press, 2004.
- [11] P. Gahinet, A. Nemirovski, A. Laub, M. Chilali, "The LMI control toolbox", The Mathworks, Inc., 1995.
- [12] K. Ogata, "Modern control engineering", Pearson Education, Fourth Edition, 2002.
- [13] S. Lall, C. Beck, "Model reduction of complex systems in the linear-fractional framework", Proc. IEEE Int. Symposium on Computer Aided Control System Design, Hawaii, USA, pp.22-27, August 1999.
- [14] C. Beck, R. D'Andrea, "Minimality, controllability and observability for uncertain systems", Proc. American Contr. Conf., New Mexico, June 1997.
- [15] S. Gutman, E. I. Jury, "A general theory for matrix root clustering in subregions of the complex plan", IEEE Trans. Automat. Contr., vol. AC-26, pp. 853-863, 1981.
- [16] P. P. Khargonekar, I. R. Petersen, K. Zhou, "Robust stabilization of uncertain linear systems: Quadratic stabilizability and H₂ control theory", IEEE Trans. Automat. Contr., vol. 35, no. 3, March 1990.
- [17] M. A. Rotea, M. Corless, D. Da, I. R. Petersen, "Systems with structured uncertainty: Relations between quadratic and robust stability", IEEE Trans. Automat. Contr., vol.38, no.5, May 1993.
- [18] K. Sahu, "Design and analysis of controller for inverted pendulum system", M.E. thesis, Dept. Electrical Engg., Bengal Engineering and Science Univ., W.B., India, June 2007.

Microprocessor Based Identification of Sampled Data System with/without Hold Device using a Set of Sample-and-Hold and Dirac Delta Functions

Anindita Sengupta¹, Anish deb², Sudipta Mandal³

¹Departments of Electrical Engineering, BESU, Shibpur, India, e-mail: aninsen2002@yahoo.com

²Department of Applied Physics, University of Calcutta, Kolkata, India, e-mail: anishdeb2000@yahoo.co.in

³Departments of Electrical Engineering, BWSU, Shibpur, India, e-mail: sudiptae@yahoo.co.in.

Abstract— In this work, a sample-and-hold function (SHF) set and Dirac delta function (DF) set are employed for microprocessor-based identification of sample-and-hold systems as well as discrete time systems. The method is applicable for identification of control systems with known input and output sequences, in absence of measurement noise. It uses different operational transfer functions defined in SHF and DF domains to identify first order open loop as well as closed loop systems. The results of identification match nicely with exact solutions derived via conventional z-transform analysis. Supporting experiments have also been carried out to establish the method.

Key words— Dirac delta function, Identification, Orthogonal functions, Operational matrices, Sample-and-hold function.

I. INTRODUCTION

PIECEWISE constant basis functions (PCBF) have a very rich history [1] starting from the year 1910. With progress in research in the area of such kind of orthogonal functions, it was found that the block pulse function (BPF) set was the simplest as well as the most efficient [2] amongst its sister functions. The BPF set encouraged many researchers to invent similar sets for different applications. One such work by Deb et al [3] introduced the sample-and-hold function (SHF) set for solving problems related to sample-and-hold systems and they also used Dirac delta functions as a set [4] to solve discrete control system problems using operational technique. In the present work, Dirac delta function set and sample-and-hold function set are used for microprocessor-based

identification of discrete time as well as sample-and-hold systems. A first order open loop system and a closed loop sampled data system – with/without hold device have been identified and the results obtained are compared with exact solutions. Experimental support for the above method has also been carried out.

II. DIRAC DELTA FUNCTION (DF) SET AND SAMPLE-AND-HOLD FUNCTION (SHF) SET RELATED OPERATIONAL MATRICES AND OPERATIONAL TRANSFER FUNCTIONS

In a packet-switched network, a feedback-based congestion control mechanism is essential to provide data transfer services efficiently. Its main objective is to prevent packet losses in the network, and to utilize network resources effectively. The Random Early Detection (RED) algorithm is simply a congestion avoidance technique. It monitors network traffic loads in an effort to anticipate and avoid congestion at common network bottlenecks i.e. the scheme kicks in before any congestion actually occurs.

A. Dirac-delta function (DF)

For a linear SISO control system, with the usual notation, we can write,

$$C(s) = G(s)R(s) \quad (1)$$

We can express the sampled version of the input $r(t)$ and the output $c(t)$ in terms of an m -set delta functions [4] as

$$r^*(t) = R \underline{\Delta}_m(t)$$

$$c^*(t) = C \underline{\Delta}_m(t) \quad (2)$$

where, R and C are the coefficient matrices for input and output expressed in DF domain.

Let us take a first order plant as,

$$G(s) = (s+a)^{-1} = a^{-1}(as^{-1} - a^2s^{-2} + a^3s^{-3} - \dots + \infty) \quad (3)$$

The respective DOTF [4] may be obtained as

$$\text{DOTF} = \begin{bmatrix} 1 & \exp(-ah) & \exp(-2ah) & \exp(-3ah) & \exp(-4ah) & \dots \\ \exp(-m-1)ah \end{bmatrix}_{m \times n} \quad (4)$$

$$\text{where, } \begin{bmatrix} a & b & c \\ 0 & a & b \\ 0 & 0 & a \end{bmatrix} = \begin{bmatrix} a & b & c \\ 0 & a & b \\ 0 & 0 & a \end{bmatrix}$$

Using DOTF in equation (1), we can write

$$C = R \text{ DOTF} \quad (5)$$

This is the key equation for delta domain analysis of SISO control system.

B. Sample and Hold Function (SHF)

Though the art of sample-and-hold technique is quite old in the literature, Deb et al [3] was the first to define a set of piecewise constant basis functions (PCBF) which used the property of sample-and-hold in a very special manner.

SHOTF for the plant $G(s) = (s+a)^{-1}$ can be derived by expanding $G(s)$ binomially and replacing integrators of different orders by their SHF operational equivalents. Thus,

$$\text{SHOTF} = \frac{(1 - \exp(-ah))}{a} \begin{bmatrix} 1 & \exp(-ah) & \exp(-2ah) & \dots & \exp(-m-1)ah \end{bmatrix}_{m \times m} \quad (6)$$

Hence from (1), we can write in SHF domain,

$$C = R \text{ SHOTF} \quad (7)$$

where, C =output vector of the system in SHF domain, R =input vector to the system in SHF domain.

III. IDENTIFICATION OF FIRST ORDER SISO CONTROL SYSTEM USING DELTA FUNCTION

We know, from equations (2) and (4)

$$R = [r_0 \ r_1 \ r_2 \ \dots \ r_{m-1}] \quad (8)$$

$$C = [c_0 \ c_1 \ c_2 \ \dots \ c_{m-1}] \quad (9)$$

$$\text{DOTF} = \begin{bmatrix} g_0 & g_1 & g_2 & \dots & g_{m-1} \end{bmatrix}_{m \times m} \quad (10)$$

Putting equations (8), (9) and (10) in equation (5) we get,

$$g_0 = c_0 / r_0, \text{ and} \quad (11)$$

$$g_i = c_i / r_0 - \sum_{p=1}^i [(r_p / r_0)] g_{i-p}$$

where $i = 1, 2, 3, 4, \dots (m-1)$

Equation (11) will now be used to find out the time domain component of the sampled data SISO control system as shown in Fig.1 and 2.

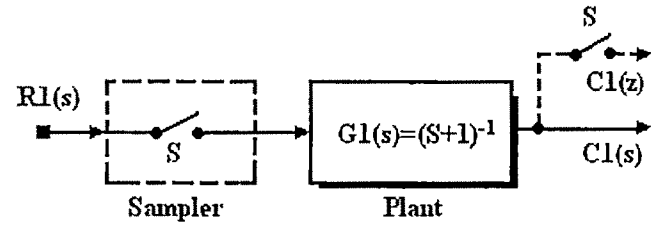


Fig.1 Open loop discrete control system having first-order transfer function.

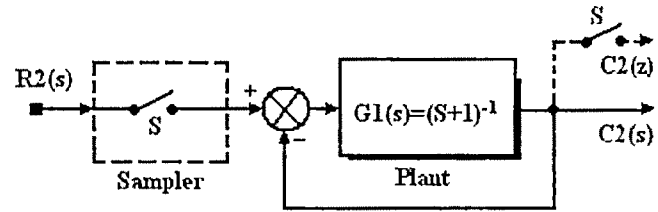


Fig.2 Simple feedback control system with sampler at the input

Observation

The following curve shows a comparison of the exact solution of $G(z)$ using z-transform analysis with DF domain analysis for the sampled data system without any hold device.

1 Plant Transfer function $G(s) = 1/(s+1)$ with step input. ($m=16$, $h=1/16$ s)

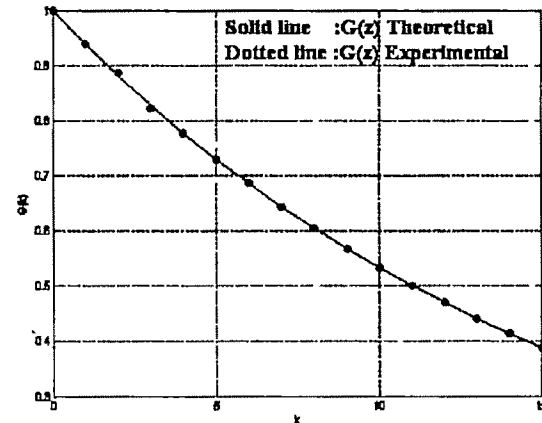


Fig.3 Coefficients of $G(z)$ computed via DF domain compared with the result obtained via z- transform analysis

2. Plant Transfer function $G(s) = 1/(s+2)$ with step input, ($m=16, h=1/16s$)

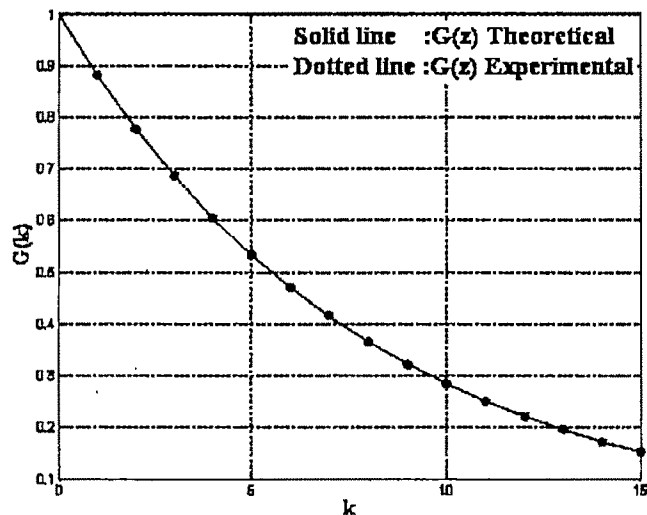


Fig 4 Coefficients of $G(z)$ computed via DF domain compared with the result obtained via z- transform analysis.

IV. IDENTIFICATION OF FIRST ORDER SISO CONTROL SYSTEM USING SAMPLE-AND-HOLD FUNCTIONS

R, C and SHOTF in equation (7), can be expressed as follows:

$$R = [r_0 \ r_1 \ r_2 \ r_3 \dots r_{m-1}] \quad (12)$$

$$C = [c_0 \ c_1 \ c_2 \ c_3 \dots c_{m-1}] \quad (13)$$

$$\text{SHOTF} = [(1-g_1)/a], [[0 \ g_0 \ g_1 \ \dots g_{m-2}]] \quad (14)$$

$$\begin{aligned} \text{Hence, } [c_0 \ c_1 \ c_2 \ c_3 \dots c_{m-1}] \\ = [r_0 \ r_1 \ r_2 \ r_3 \dots r_{m-1}] \cdot ((1-g_1)/a) \cdot [0 \ g_0 \ g_1 \ g_2 \ g_3 \dots g_{m-2}] \end{aligned} \quad (15)$$

For a first order system, like an RC network, the 0th element of the plant in z-transform analysis is unity. Hence, we have from equation (15)

$$\begin{aligned} g_0 &= 1 \\ g_1 &= c_2/c_1 - r_1/r_0 \\ &\quad \vdots \\ \text{So, } g_i &= (c_{i+1}/c_1 - r_i/r_0) - \sum_{p=1}^{i-p} (r_p/r_0) g_{i-p} \end{aligned} \quad (16)$$

where $i = 2, 3, 4 \dots (m-2)$.

Observation

The following curves show the comparison of exact solution of $G(z)$ using z transform analysis with SHF domain analysis for sampled data systems with hold device.

V. MICROPROCESSOR BASED IDENTIFICATION OF LINEAR SINGLE INPUT SINGLE OUTPUT (SISO) SAMPLED DATA SYSTEM VIA SHF APPROACH

The basic philosophy of microprocessor-based simulation of a linear SISO sampled data system is to configure the system impulse response with the help of a program. This is done in such a fashion that when samples of the input signal and the output signal are accessed by the

1. Plant transfer function $G(s) = 1/(s+1)$ (with unit step input and $m=16, h=1/16s$)

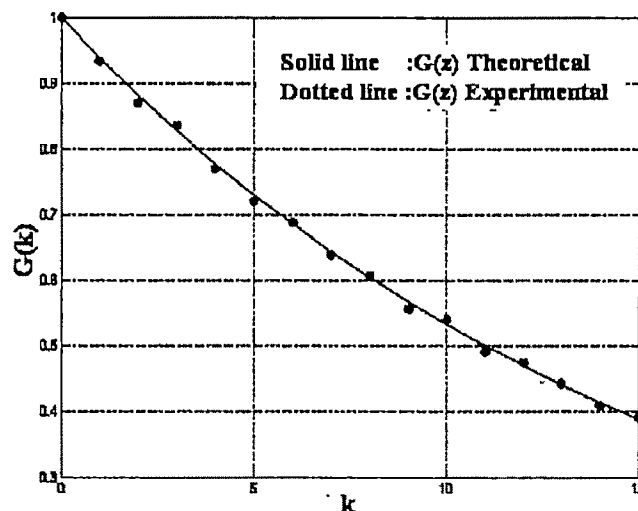


Fig.5 Coefficients of $G(z)$ obtained via SHF domain approach compared with the results obtained via z-transform analysis.

2. Plant transfer function $G(s) = 1/(s+2)$ (with unit step input and $m=16, h=1/16s$)

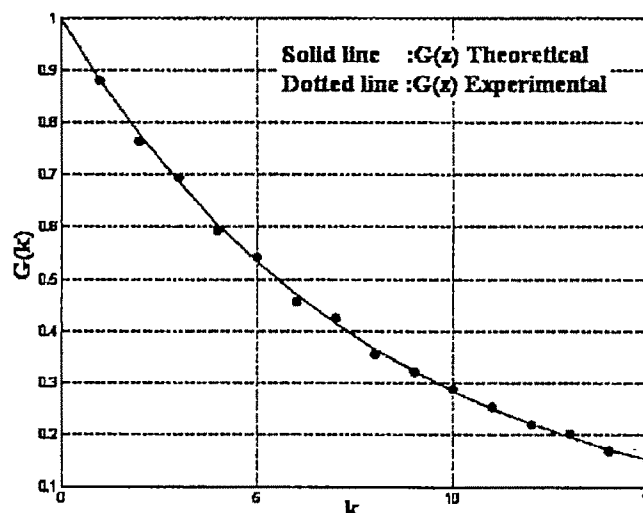


Fig 6 Coefficients of $G(z)$ obtained via SHF domain approach compared with the results obtained via z-transform analysis.

microprocessor, the program accepts those samples values and come up with samples of the system function ($g(t)$) in time domain, giving the impulse response.

Inclusion of a zero order hold (Z_{OH}) in the system having a transfer function $G(s)$ introduces an additional transfer function

$G_{ho}(s)=[1-\exp(-hs)]/s$ where h is the sampling period. Using equation (15), for a step input (in this case 1.5v), for the plant $G(s)=1/(s+a)$,

$$g_i = 1/c_1(c_{i+1}-c_i) \quad (17)$$

where, $i = 0, 1, 2, 3, 4, \dots, (m-2)$

Hence, knowing the samples of the system output i.e. c_i , the coefficients of $G(z)$ can be computed.

A. Brief description of the experiment

Parameters of the system are

$$0 \quad \text{when } t=0$$

$$r(t) = 1.5v =$$

$$1 \quad \text{when } t \geq 0$$

$$R=1M\Omega, C=1\mu F \text{ and } G(s) = 1/(s+1).$$

Results obtained from the experiment is shown in Table I

Table I

t in sec	C (output)
0	0
0.2	0.229
0.4	0.432
0.6	0.613
0.8	0.762
1.0	0.887
1.2	0.987
1.4	1.072
1.6	1.14
1.8	1.201
2.0	1.256
2.2	1.301
2.4	1.342

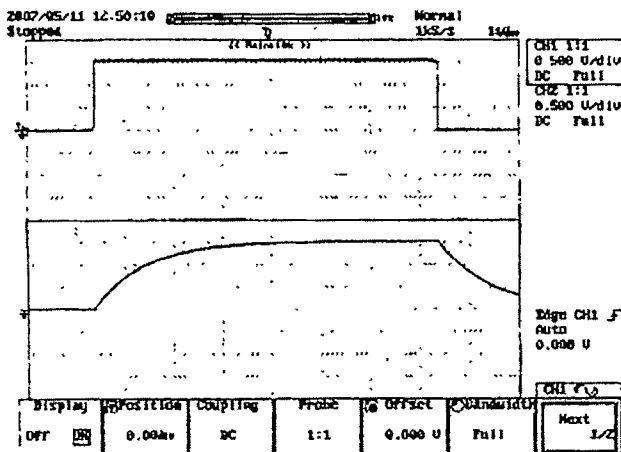


Fig.7 Input and output of the system obtained from digital storage oscilloscope (DSO)

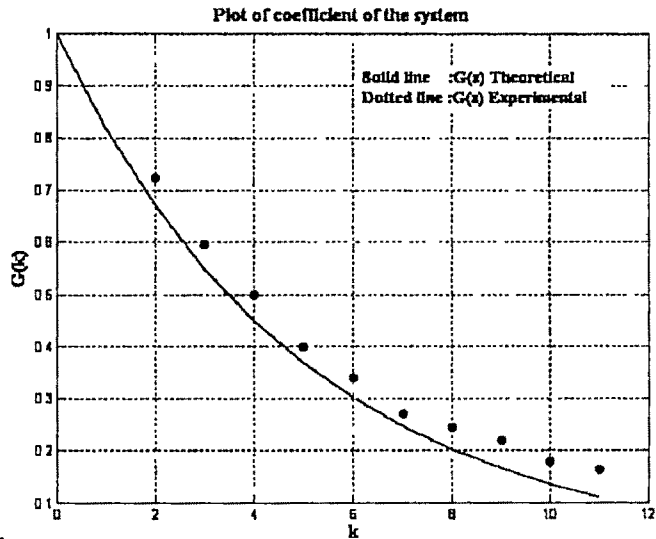


Fig.8 Coefficients of $G(z)$: theoretical as well as experimental, obtained via SHF domain.

B. Algorithm for the microprocessor program

1. Take m number of samples of the system output.
2. Multiply the samples by 1000 (decimal) for reducing error in base conversion.
3. After multiplication, round off the fractional part.
4. Store the sample values in consecutive memory locations of the microprocessor.
5. Subtract c_i from c_{i+1} to get the i^{th} sample value (g_i) of the system.
6. Multiply the result by $1/c_1$.
7. Repeat the process for $(m-1)$ times.

Obviously the final results are to be scaled by $1/1000$ to get the actual results, which match the computed output of the system nicely.

VI. CONCLUSION

The present work identified successfully the time description of a sampled-data system, having a pulse transfer function $G(z)$, via Dirac delta function approach. Since impulse sampling is not possible in practice, the work used theoretical time samples of input-output data and computed the coefficients of $G(z)$ by employing a microprocessor. This has been done for two systems having transfer functions $(s+1)^{-1}$ and $(s+1)^{-2}$ and the results were compared with those determined via conventional z-transform technique.

Similar studies have been done with the same systems with sample-and-hold via SHF domain approach. Theoretical values of input-output samples were used and a microprocessor was employed to compute the coefficients of the pulse transfer functions. Again, the results were found to be in concurrence with those obtained via z-transform analysis.

Finally, a plant having a transfer function $G(s)=(s+1)^{-1}$ was designed using appropriate circuit elements and an experimental set up was used to identify the plant $G(z)$ by employing a microprocessor. The results of such experimental study were compared with the theoretical results and figure 8 shows that they conform reasonably.

VII. ACKNOWLEDGEMENT

The authors acknowledge the active support of Mr. Raktim Maity, Technical Assistant of Electrical Engineering Department, BESUS, in performing experiments related to this work. The help provided by Mr. K. L. Naidu is also acknowledged.

VIII. REFERENCES

- [1] K.G.Beauchamp, *Application of Walsh and related functions with an introduction to sequence theory*, Academic Press, London, 1984.
- [2] A. Deb, G. Sarkar and S K. Sen, "Block pulse functions, the most fundamental of all piecewise constant basis functions," *Int. J. Syst. Sci.*, vol. 25, no. 2, pp. 351-363, 1994
- [3] A. Deb, G. Sarkar, M. Bhattacharjee, and S. K. Sen, "A new set of Piecewise constant Orthogonal functions for the analysis of linear SISO systems with sample-and-hold," *J. Franklin Institute*, vol. 335B, no. 2, pp. 333-358, 1998.
- [4] A. Deb, G. Sarkar, M. Bhattacharjee, and S. K. Sen, "Analysis of linear discrete SISO control systems via a set of delta functions," *IEE Proc.-Control Theory and Applications*, vol. 143, no. 6, pp. 514-518, 1996.
- [5] G. Sarkar, A. Dasgupta and A. Deb "Microprocessor-based simulation of sampled data systems with/without a hold device using a set of sample-and-hold functions and Dirac delta functions," *J. Franklin Institute*, vol. 342, no. 1, pp 85-95, 2005.
- [6] A. Deb, G. Sarkar, and A. Sengupta *Triangular orthogonal functions for the analysis of continuous time systems*, Elsevier India, New Delhi, 2007.

Robust Control of Stochastic Systems via Lyapunov Approach and Linear Matrix Inequalities (LMIs)

S. Ben Attia¹, S.Salhi², and M.Ksouri³

¹ National Institute of engineers, Tunis e-mail: benattiaselma@yahoo.fr.

² National Institute of engineers, Tunis e-mail: salhis@lycos.com

³ National Institute of engineers, Tunis, e-mail: mekki ksouri@mrstd.gov.tn

Abstract—This paper addresses the problem of robust stabilization of uncertain Markovian jump linear systems. The uncertain markovian jump system under consideration involves parameter uncertainties in the mode transition rate matrix. The results given are expressed in terms of linear matrix inequalities (LMIs) in order to formulate the synthesis problem of a robust feedback controller. Finally, numerical simulations are tested to prove the developed theory.

Key words— jump linear system, polytopic uncertainty, linear matrix inequality, robust control.

I. INTRODUCTION

A great deal of attention has been given nowadays to a class of stochastic linear systems subject to abrupt variations in their structures, namely, Markovian Jump Linear systems (MJLS's). This family of systems is regarded as a particular class of stochastic systems modeling by a set of linear systems with the transitions between the models determined by a markov chain taking values in a finite set[3][4].

MJLS also belong to the category of hybrid systems: to the usual continuous state variable, one appends a discrete variable called the mode that describes sudden changes.

This class of systems was initially studied by Krasovskii and Lidskii[5] and more recently received a renewed attention, motivated by various applications from different physical systems like manufacturing systems, maneuvered target tracking, speech recognition, production systems, telecommunication systems, economic problems...[6]

The aim of this paper consists of given the sufficient conditions, which guarantee the stability robustness of the

parameters.

The paper is organized as follows: in section 2, we give a general formulation of problem statement. In section 3, we consider the class of uncertain Markovian jump linear system with a mode transition rate matrix witch varies into a fix polytope. The analysis problem can be tackled in terms of the solvability of a set of coupled LMIs, we obtain sufficient conditions ensuring mean-square stabilisability. A Numerical example is also given.

II. PRELIMINAIRES

We consider a linear Markovian jump system defined by the following equations [2]:

$$\begin{cases} \dot{x}(t) = A(r_t)x(t) + B(r_t)u(t) \\ y(t) = C(r_t)x(t) + D(r_t)u(t) \\ x(t_0) = x_0, \quad r_0 = r_0 \end{cases} \quad (1)$$

Let $(x(t), r(t))$, represents the state of this class of systems. The parts $x(t)$ is called the continuous state of the system. The parts $r(t)$ is called the mode of the system and it describes the stochastic aspect.

$x(t) \in \mathbb{R}^n, y(t) \in \mathbb{R}^p, u(t) \in \mathbb{R}^m, x_0 \in \mathbb{R}^n$ and r_0 are

respectively the state vector, the output vector, the control vector, the state and the initial mode at time t_0 of the system.

$A(r_t), B(r_t), C(r_t)$ and $D(r_t)$ are constant real matrices of appropriate dimensions representing the nominal system

matrices at time t and correspond to the different modes, function of a random process $\{r_t, t \geq t_0\}$ corresponding to the discrete state of the system. This discrete state is governed by a continuous-time Markov process r_t , called mode, taking values in a finite set $S = \{1, 2, \dots, s\} \subset \mathbb{N}$. For each possible value of $r(t) \in S$, we have

$$A(r(t)) = A_i, B(r(t)) = B_i \text{ when } r(t)=i$$

The mode transition rate matrix is defined by:

$$\Pi = \begin{bmatrix} \pi_{11} & \dots & \pi_{1s} \\ \vdots & \ddots & \vdots \\ \pi_{s1} & \dots & \pi_{ss} \end{bmatrix}$$

The π_{ij} 's are transition probability rates from the i -th mode to the j -th mode described by the following relations:

$$P_r\{r_{t+dt} = j | r_t = i\} = \begin{cases} \pi_{ij} dt + o(dt) & \text{if } i \neq j \\ 1 + \pi_{ii} dt + o(dt) & \text{else} \end{cases}$$

Where $\frac{o(dt)}{dt} \rightarrow 0$ when $dt \rightarrow 0$ and verify:

$$\begin{cases} \pi_{ij} \geq 0 & \forall j \neq i \\ \pi_{ii} = -\pi_{i\cdot} = -\sum_{j=1}^s \pi_{ij} \end{cases}$$

Moreover, the probability vector $P_t = [p_t^1, \dots, p_t^s]$ with

$p_t^i := P_r(r_t = i), i \in S$ verifying the following equation:

$$\begin{cases} \frac{dP_t}{dt} = P_t \Pi, \quad t \geq 0 \\ P_0 = (p_0^1, \dots, p_0^s) \end{cases}$$

When P_0 is the initial probability vector of the process $\{r_t, t \geq t_0\}$ at time t_0 and have the solution:

$$P_t = P_0 e^{\Pi t}, \quad t \geq 0$$

Then, going from an initial given condition $x(t_0) = x_0, r_{t_0} = i \in S$, the system evolves respecting to the dynamic described by the equation (1) arriving to the first jump $r_{T_1} = j \in S$ at the time T_1 , governed by the exponential law with a rate π_{ij} and a distribution law $P_r\{T_1 > t\} = F(t)$ defined by:

$$F(t) = \begin{cases} e^{-\pi_{ij}(t-t_0)}, & \text{pour } t < T_1 \\ 0, & \text{pour } t \geq T_1 \end{cases}$$

We have the following definitions and propositions throughout

the paper.

Definition 1 [1] the nominal Markovian jump system (1) (with $u(t)=0$) is said to be mean square stable if

$$\lim_{t \rightarrow \infty} E\{\|x(t, x_0, r_0)\|^2\} = 0$$

For any initial conditions $x_0 \in \mathbb{R}^n$ and $r_0 \in S$.

Proposition 1.1[1] the nominal Markovian jump system (1) (with $u(t)=0$) is mean square stable if and only if the coupled LMIs

$$A_i^T M_i + M_i A_i + \sum_{j=1}^s \pi_{ij} M_j < 0 \text{ for all } i \in S$$

Are feasible for a set of matrices $\{M_i : M_i \in S^{n \times n}, i \in S\}$

Proposition 1.2[1] the MJLS is stabilizable in the mean square sense if there exist matrices Y_i and real, symmetric matrices Q_i such that

$$A_i Q_i + Q_i A_i^T + B_i Y_i + Y_i^T B_i^T + \sum_{j=1}^s \pi_{ij} Q_j < 0$$

Holds for all $i \in S$.

A stabilizing control law is then given by $u(t) = K(r(t))x(t) = K_i x(t)$, with $K(r(t)) = Y_i Q_i^{-1}$ when $r(t)=i$.

III. ROBUST STABILIZATION OF THE MJLS WITH POLYTOPIC UNCERTAINTY IN THE MODE TRANSITION RATE MATRIX

The problem of analysis and synthesis studied on robust control of MJLS are supposed that the transition probabilities are known precisely a priori.

In applications, however, values of mode transition rates are only estimated.

So, real physical systems can be described by means of an uncertain model and robust control theory has taken in consideration the influence of this uncertainty in the stability and performance control systems.

We consider the following MJLS defined by:

$$\dot{x}(t) = A(\hat{r}(t))x(t) + B(\hat{r}(t))u(t) \quad (2)$$

The mode transition probabilities

$$P_r\{\hat{r}_{t+dt} = j | \hat{r}_t = i\} = \begin{cases} \hat{\pi}_{ij} dt + o(dt) & \text{if } i \neq j \\ 1 + \hat{\pi}_{ii} dt + o(dt) & \text{else} \end{cases}$$

The mode transition, rate matrix $\hat{\Pi} = \hat{\Pi}_{ij}$ are not precisely known a priori but belong to a fix polytope P :

$$P = \left\{ \hat{\Pi} = \sum_{k=1}^L \lambda_k \Pi^k \mid \lambda_k \geq 0, k = 1 \dots L, \sum_{k=1}^L \lambda_k = 1 \right\}$$

The number of vertex matrices is:

$$L = 2^{r(r-1)}$$

And $\Pi^k = (\pi_{ij}^k)_{1 \leq i, j \leq r}, k=1 \dots L$ are given transition probability matrices.

The aim of this part is to stabilize in the mean square sense the closed-loop system via a state feedback controller[1]:

$$u(t) = K(r(t))x(t) = K_i x(t) \text{ when } r(t)=i \quad (3)$$

Theorem 3[]: there exist a control of the form (3) such that the closed -loop system (2) is mean square stable for every $\hat{\Pi}(t) \in P$ if the LMIs

$$Q_i > 0, A_i Q_i + Q_i A_i^T + B_i Y_i + Y_i^T B_i^T + \sum_{j=1}^n \pi_{ij}^k Q_j < 0, i \in S, k=1, \dots, L$$

Hold for some Q_1, \dots, Q_L and Y_1, \dots, Y_L . A stabilizing control

law is then given by (3), with $K(r(t)) = Y_i Q_i^{-1}$ when $r(t)=i$.

The problem of robust stabilization via a state feedback with a polytopic uncertainty in the mode transition rate matrix is therefore equivalent to the check the solvability of $(L+1)sn \times (L+1)sn$ linear matrix inequality with respect to $(n(n+1)/2)s$ scalar variables.

Numerical example:

We consider a MJLS described by three modes with a

transition rate matrix uncertain $\hat{\Pi} = \delta \Pi^0$

Where Π^0 is a given nominal transition probability matrix and δ is an unknown-but-bounded parameter: $\delta \in [0.1 \ 2]$

The dynamic of the system is described by:

$$A_1 = \begin{bmatrix} 0 & 0 & 1 & 0 \\ 0 & 0 & 0 & 1 \\ -1 & 1 & 0 & 0 \\ 1 & -1 & 0 & 0 \end{bmatrix}, A_2 = \begin{bmatrix} 0 & 0 & 1 & 0 \\ 0 & 0 & 0 & 1 \\ -1.3 & 1.3 & 0 & 0 \\ 1.2 & -1.2 & 0 & 0 \end{bmatrix}$$

$$A_3 = \begin{bmatrix} 0 & 0 & 1 & 0 \\ 0 & 0 & 0 & 1 \\ -1.7 & 1.7 & 0 & 0 \\ -1.5 & 1.5 & 0 & 0 \end{bmatrix},$$

$$B_1 = \begin{pmatrix} 0 \\ 0 \\ 1 \\ 0 \end{pmatrix}, B_2 = \begin{pmatrix} 0 \\ 0 \\ 1.3 \\ 0 \end{pmatrix}, B_3 = \begin{pmatrix} 0 \\ 0 \\ 1.7 \\ 0 \end{pmatrix},$$

$$\Pi^0 = \begin{bmatrix} -2.24 & 1.792 & 0.448 \\ 3.36 & -5.04 & 1.68 \\ 2.24 & 1.96 & -4.2 \end{bmatrix}$$

According to the proposition (1), we conclude that the system studied is not stable in the mean square sense.

The objective of this first part is to find a state feedback controller of the form (3):

$$u(t) = K_i x(t) = K(r(t))x(t) = \begin{cases} K_1 x(t) & \text{si } r(t)=1 \\ K_2 x(t) & \text{si } r(t)=2 \\ K_3 x(t) & \text{si } r(t)=3 \end{cases}$$

Assuring the stabilization in the mean square sense of the nominal system.

Therefore, the problem designs the stabilization of MJLS with the nominal rate transition matrix Π^0 .

The synthesis problem can be tackled in terms of the solvability of a set of coupled LMIs using the proposition 1.2.

We obtain the following three controllers:

$$\begin{cases} K_1 = [-28.6264 & 10.5550 & -13.2130 & -29.4331] \\ K_2 = [-9.5542 & 2.5682 & -3.7899 & -10.0681] \\ K_3 = [-16.7728 & 14.6507 & -4.3485 & 5.9250] \end{cases}$$

Such that the resulting closed -loop system:

$$\dot{x}(t) = A_{cl}(r(t))x(t)$$

is mean square stable.

$$\text{Where: } A_{cl}(r(t)) = \begin{cases} A_1 + B_1 K_1 & \text{si } r(t)=1 \\ A_2 + B_2 K_2 & \text{si } r(t)=2 \\ A_3 + B_3 K_3 & \text{si } r(t)=3 \end{cases}$$

In order to check the robustness of the nominal state feedback control law $u(t)$, we vary the parameter $\delta \in [0.1 \ 2]$.

Solving a LMI feasibility problem that gives necessary and sufficient conditions which guarantee the mean square stability of the system, we remark that the closed -loop system with a

transition rate matrix uncertain $\hat{\Pi} = \delta \Pi^0$ is instable. This is proved that the nominal state-feedback control law is not robust.

In this second part, we will apply the theorem 3 which takes in consideration the polytopic uncertainty affecting the rate transition matrix and procures a sufficient condition for the robust stabilization of the system via LMI.

We obtain the three robust controllers above:

$$\begin{cases} \tilde{K}_1 = 10^3 \times [-2.0647 & 1.8046 & -0.1717 & -1.9330] \\ \tilde{K}_2 = [-223.3543 & 206.8172 & -19.8567 & -109.8256] \\ \tilde{K}_3 = [-141.3400 & 146.0244 & -14.0323 & 42.2542] \end{cases}$$

The state feedback control law:

$$\tilde{u}(t) = \begin{cases} \tilde{K}_1 x(t) & \text{si } r(t) = 1 \\ \tilde{K}_2 x(t) & \text{si } r(t) = 2 \\ \tilde{K}_3 x(t) & \text{si } r(t) = 3 \end{cases}$$

And the closed -loop system: $\dot{x}(t) = \tilde{A}_{cl}(r(t))x(t)$

$$\text{Where } \tilde{A}_{cl}(r(t)) = \begin{cases} A_1 + B_1 \tilde{K}_1 & \text{si } r(t) = 1 \\ A_2 + B_2 \tilde{K}_2 & \text{si } r(t) = 2 \\ A_3 + B_3 \tilde{K}_3 & \text{si } r(t) = 3 \end{cases}$$

With this control law, the system is stable for any value of the transition probability matrix $\hat{\Pi} = \delta \Pi^0$, with $\delta \in [0.1 \ 2]$.

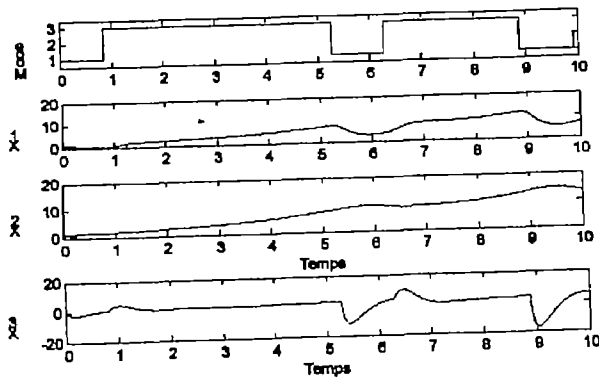


Fig.1. Closed-loop system with nominal state feedback control law for $\delta = 0.9$

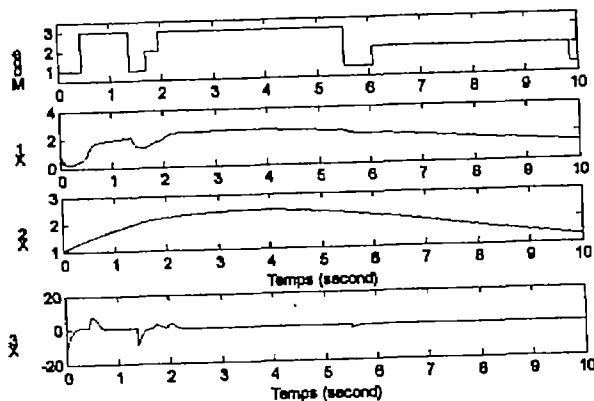


Fig.2. Closed-loop system with robust state feedback control law for $\delta = 0.9$

IV. CONCLUSION

A wide variety of problems arising in systems and control theory can be reduced to a handful of standard convex optimization problems that involve matrix inequalities.

In this paper, we tackle the problem of stabilization of jump linear system via state feedback. Necessary and sufficient conditions are given when the rate transition matrix is exactly known. A robust state feedback control law is determined in the case of an uncertain Markovian jump linear system with a mode transition rate matrix which varies into a fix polytope, our stabilization conditions are sufficient.

REFERENCES

- [1] L El Ghaoui and M Ait Rami "Robust state-feedback stabilization of jump linear systems via LMIs", submitted to Int Jour. Robust&Nonlinear control, 1996.
- [2] M.Benbrahim et K.Benjelloun, "La commande robuste sous contraintes des systèmes linéaires à sauts Markoviens", Dans la 6^{ème} conférence francophone de modélisation et simulation- MOSIM'06
- [3] S Allam , P.Bertrand.,F.Dufour., I.Dann, M.Mariton and C.Yang, " Les systèmes à sauts: théorie et Applications", traitement du signal-volume 15-n°6-spécial, 1998.
- [4] J Bertram and E.Sarachik "Stability Of Circuits With Randomly Time Varying Parameters", Trans IRE, Vol PGIT-5, pp. 260-270, 1959.
- [5] N.Karasovski and E.Lidskii "Analytical Design Of Controllers In Systems With Random Attributes", Automatic And Remote Control, Parts I-III, No 22, pp.1021-1025, 1961.
- [6] M.Mariton "Jump Linear Systems in Automatic Control",Marcel Dekker,New York and Basel, 1990.

New Approach for Static Output Feedback Problem

N. Bédioui¹, S. Salhi², M. Ksouri³

¹ ACS Research Unity, National School of Engineers, Tunisia e-mail: beioui_ncila_enit@yahoo.fr

² ACS Research Unity, National School of Engineers, Tunisia e-mail: ssalhi@lycos.com

³ ACS Research Unity, National School of Engineers, Tunisia e-mail: mekki.ksouri@insat.mu.tn

Abstract—In this paper, we propose a new sufficient condition of stability via static output feedback for discrete linear time-invariant systems. It is based on the application of the singular value decomposition to some variable matrices. This new approach is also extended to polytopic uncertain systems. Numerical examples are provided to illustrate the relevance of the new condition.

Key words—LMI, Lyapunov theories, polytopic uncertainty Stability, Static output feedback.

I. INTRODUCTION

On control theory, the first goal is to assure the stability of a system. Many approaches and methods are developed in the context.

They treated essentially the stability problem by static state feedback [11], dynamical output feedback [4].

The static output feedback (SOF) problem has been also investigated. It is still considered an open topic. In fact, the principal problem appeared on SOF synthesis is the non-convexity. It is principally due to the bilinear terms, which appeared on the problem formulation like the BMI when we use the LMI formulation. In this case, the BMI are highly non-convex optimization and solving them was shown to be NP-hard [12].

Divers searches are developed in the aim to find a better solution to this SOF synthesis.

We distinguish methods using BMI formulation [8], we have also methods based on Riccati equation [5]-[10] or on algebraic Riccati inequality [6], min-max algorithm formulated by LMI [7], approaches using an iterative LMI algorithm [1], or others LMI formulation called substitutive [3] and convex approaches based on LMI formulation [2]-[9] which present a sufficient condition to SOF synthesis.

In our research, we investigate a new approach based on LMI formulation. In fact, this approach provides a new

sufficient stability condition which does not depend only on the Lyapunov matrix but also on additional matrix variable. This new approach can be applied to certain and uncertain systems with polytopic uncertainty.

The paper is organized as follows: first we present in section II the static output feedback (SOF) problem formulation.

Second, in section III we propose a new sufficient robust quadratic stability condition for SOF synthesis. In this section we consider the discrete linear time systems certain case.

We show also that it is possible to extend the idea of our contribution to the uncertain systems case with polytopic uncertainty. In this case, LMI conditions based on parameter dependent Lyapunov functions are given. This part is developed in section IV. We finish this paper by numerical examples in section V to illustrate our results and to provide a comparison with existing methods.

For conciseness reasons, some abbreviations are used. $co\{A^1, \dots, A^N\}$ is the convex hull of the polytope defined by

its vertices. $sym(A) = A + A^T$ and $\begin{bmatrix} A & B \\ (*) & C \end{bmatrix} = \begin{bmatrix} A & B \\ B^T & C \end{bmatrix}$.

II. PROBLEM FORMULATION AND PRELIMINARIES

We consider the discrete linear time-invariant system described by the following state space representation (1):

$$\begin{cases} x_{k+1} = Ax_k + Bu_k \\ y_k = C_y x_k \end{cases} \quad (1)$$

where $x_k \in \mathbb{R}^n$ is the state vector, $u_k \in \mathbb{R}^m$ is the control input and $y_k \in \mathbb{R}^p$ is the measured output. A, B, C_y are constant matrices of appropriate dimensions.

The following assumptions are made:

- The pairs (A, B) and (A, C_y) are stabilisable and detectable respectively. We can suppose also that the matrix C_y is full column rank.

In this paper, we treat the static output feedback problem (SOF). It consists essentially to find a stabilisable SOF gain verifying the following control law:

$$u_k = Ky_k \quad (2)$$

In this case, the closed loop system is:

$$\begin{cases} x_{i+1} = A_{cl}x_i \\ y_i = C_yx_i \end{cases} \quad (3)$$

where $A_{cl} = A + BKC_y$.

In the next section, we introduce the new robust stability approach via SOF which represents a sufficient condition.

III. IMPROVED LMI CONDITIONS FOR STATIC OUTPUT FEEDBACK STABILIZATION

We represent in this section a new sufficient condition which represents the main contribution of this paper. We consider in this section the certain case.

Let us consider the discrete linear time invariant described by (3).

Theorem 1:

System (3) is asymptotically stable by static output feedback if there exist a matrix $(P > 0) \in \mathbb{R}^{n \times n}$, a general matrices $G_1 \in \mathbb{R}^{p \times p}$, $G_2 \in \mathbb{R}^{(n-p) \times (n-p)}$ and a matrix $R \in \mathbb{R}^{m \times p}$ such that the LMI (4) is feasible:

$$\begin{bmatrix} P & A(V_1G_1V_1^T + V_2G_2V_2^T) + BRC_y \\ (*) & \text{sym}(V_1G_1V_1^T + V_2G_2V_2^T) - P \end{bmatrix} > 0 \quad (4)$$

A quadratically stabilizing SOF gain is then given by

$$K = RUC_0G_1^{-1}C_0^{-1}U^T \quad (5)$$

Proof:

It is shown in [11] that the general system (3) is asymptotically stable if and only if there exist a matrix $(P > 0) \in \mathbb{R}^{n \times n}$, and a general matrix $G \in \mathbb{R}^{n \times n}$ such that the LMI (6) is feasible:

$$\begin{bmatrix} P & A_{cl}G \\ (*) & \text{sym}(G) - P \end{bmatrix} > 0 \quad (6)$$

In the case of output feedback problem SOF synthesis, replacing A_{cl} by its expression, the matrix inequality (6) becomes:

$$\begin{bmatrix} P & AG + BKC_yG \\ (*) & \text{sym}(G) - P \end{bmatrix} > 0 \quad (7)$$

This new inequality admits a BMI term given by KC_yG and cannot be solved by the LMI toolbox.

For this reason, we introduce some transformations to (7):

- Giving a specific structure to the matrix G .
- Simplifying KC_yG by using the singular value decomposition (SVD) of the matrix C_y such that:

$$C_y = U[C_0 \ 0]V \quad (8)$$

where $U \in \mathbb{R}^{p \times p}$, $V \in \mathbb{R}^{n \times n}$ are both unitary matrices and $C_0 \in \mathbb{R}^{p \times p}$.

We suppose that the matrix G has the following structure:

$$G = V \begin{bmatrix} G_1 & 0 \\ 0 & G_2 \end{bmatrix} V^T \quad (9)$$

where $G_1 \in \mathbb{R}^{p \times p}$, $G_2 \in \mathbb{R}^{(n-p) \times (n-p)}$ and $V \in \mathbb{R}^{n \times n}$ is the matrix obtained by (SVD) of the matrix C_y .

We suppose, also, that the matrix V can be writing as follows:

$$V = [V_1 \ V_2] \quad (10)$$

where $V_1 \in \mathbb{R}^{n \times p}$ et $V_2 \in \mathbb{R}^{n \times (n-p)}$.

Consequently, by mixing (9) and (10), the matrix G has the following expression:

$$G = V_1G_1V_1^T + V_2G_2V_2^T \quad (11)$$

In the other side, let us simplify the KC_yG term of the inequality (10) by using (8) and (9) as follows:

$$KC_yG = KU[C_0 \ 0]V^T V \begin{bmatrix} G_1 & 0 \\ 0 & G_2 \end{bmatrix} V^T \quad (12)$$

Simplify (12), we have:

$$KC_yG = KU[C_0G_1 \ 0]V^T \quad (13)$$

The equality (13) can be also written as follows:

$$KC_yG = KUC_0G_1C_0^{-1}U^{-1}U[C_0 \ 0]V^T \quad (14)$$

Therefore, we introduce the matrix $R \in \mathbb{R}^{m \times p}$ such that:

$$R = KUC_0G_1C_0^{-1}U^{-1} \quad (15)$$

So, the equality (14) is given by:

$$KC_yG = RU[C_0 \ 0]V^T \quad (16)$$

Finally (16) is equal to:

$$KC_yG = RC_y \quad (17)$$

The inequality (7) is simplified as follows by replacing G by (11) and KC_yG by (17):

$$\begin{bmatrix} P & AV_1G_1V_1^T + AV_2G_2V_2^T + BRC_y \\ (*) & \text{sym}(V_1G_1V_1^T + V_2G_2V_2^T) - P \end{bmatrix} > 0 \quad (18)$$

If the LMI (18) is feasible, the static output feedback controller is given by:

$$K = RUC_0G_1^{-1}C_0^{-1}U^T \quad (19)$$

Remark 1:

The approach of robust stabilization for SOF proposed in this section is based on sufficient condition which is restrictive. And this is due to the imposed structure introduced to the matrix G (9).

IV. IMPROVED LMI CONDITIONS BY SOF FOR UNCERTAIN SYSTEMS

The main advantage of the new approach of SOF given in the previous section is that it allows to decouple the computation of the SOF gain and the computation of Lyapunov matrix. This result allows us to derive a new sufficient condition of robust SOF based on parameter Lyapunov functions.

We will consider the following discrete linear time-invariant system:

$$\begin{cases} x_{k+1} = Ax_k + Bu_k \\ y_k = C_yx_k \end{cases} \quad (20)$$

In this section, we assume that the matrices that characterize the system (20) are uncertain.

We define the matrix M such that:

$$M = \begin{bmatrix} A & B \end{bmatrix} \in \Omega = \text{co} \left\{ \begin{bmatrix} A^1 & B^1 \end{bmatrix}, \dots, \begin{bmatrix} A^N & B^N \end{bmatrix} \right\} \quad (21)$$

Hence, Ω is a convex polytope of matrices for which each element may be expressed as a convex combination of the N vertices of Ω :

$$M(\xi) = \begin{bmatrix} A(\xi) & B(\xi) \end{bmatrix} = \sum_{i=1}^N \xi_i \begin{bmatrix} A^i & B^i \end{bmatrix} \quad (22)$$

$$\text{where } \xi \in \Xi = \left\{ \xi = \sum_{i=1}^N \xi_i = 1 \quad \xi_i \geq 0 \right\} \quad (23)$$

The uncertain vector of parameters ξ is supposed to be time-invariant so that the realization of the model (22) is not time-varying. When necessary, the notation $\begin{bmatrix} A(\xi) & B(\xi) \end{bmatrix}, \forall \xi \in \Xi$ instead of $\begin{bmatrix} A & B \end{bmatrix} \in \Omega$ will be used in the sequel.

The problem imposed in this paper is to find a stabilizing static output feedback control law $u_k = Ky_k$ for the model (21) i.e. to find a single gain $K \in \mathbb{R}^{m \times p}$ such that every member of the polytope $\Omega_d = \text{co} \{A_d^1, \dots, A_d^N\}$ maintains eigenvalue location in the unitary circle and where $A_d^i = A^i + B^i KC_y$ for all $i = 1, \dots, N$.

Theorem 2:

Ω is said to be quadratically stabilizable via static output feedback if there exist a common matrix $(P > 0) \in \mathbb{R}^{n \times n}$, generals common matrices $G_1 \in \mathbb{R}^{m \times p}, G_2 \in \mathbb{R}^{(n-p) \times (n-p)}$ and a common matrix $R \in \mathbb{R}^{m \times p}$ such that the LMI (24) is feasible for all $i = 1, \dots, N$:

$$\begin{bmatrix} P & A^i(V_1G_1V_1^T + V_2G_2V_2^T) + B^iRC_y \\ (*) & \text{sym}(V_1G_1V_1^T + V_2G_2V_2^T) - P \end{bmatrix} > 0 \quad (24)$$

A quadratically stabilizing SOF gain is then given by

$$K = RUC_0G_1^{-1}C_0^{-1}U^T \quad (25)$$

Proof:

Let us consider the following general discrete linear time-invariant system:

$$\begin{cases} x_{k+1} = A_d x_k \\ y_k = C_y x_k \end{cases} \quad (26)$$

Where $A_d \in \Omega = \text{co} \{A_d^1, \dots, A_d^N\}$

According to [13] and [11], it is proved that the system (26) is robustly stable in the uncertain domain (21) if and only if there exist a symmetric matrix $(P(\xi) > 0) \in \mathbb{R}^{n \times n}$ and a general matrix $G \in \mathbb{R}^{n \times n}$ such that:

$$\begin{bmatrix} P(\xi) & A_d(\xi)G \\ (*) & \text{sym}(G) - P(\xi) \end{bmatrix} > 0 \quad (27)$$

where $P(\xi) = \sum_{i=1}^N \xi_i P_i$, $\sum_{i=1}^N \xi_i = 1$ represent an arbitrary parameter dependent Lyapunov functions. In this way we choose a common P , such that $P(\xi) = P$ used at all vertices of the polyhedron (21).

Consequently, the system (20) is robustly stable in the uncertain domain (26) if and only if there exist a symmetric common matrix $(P > 0) \in \mathcal{R}^{n \times n}$ and a general common matrix $G \in \mathcal{R}^{m \times n}$ such that:

$$\begin{bmatrix} P & A'_d G \\ (*) & \text{sym}(G) - P \end{bmatrix} > 0 \quad (28)$$

holds for $i = 1, \dots, N$.

In the case of output feedback problem SOF synthesis, we replace the matrix A'_d by its correspondent expression. We obtain the developed form of (28) as follows:

$$\begin{bmatrix} P & A'G + B'KC_y G \\ (*) & \text{sym}(G) - P \end{bmatrix} > 0 \quad (29)$$

This new inequality admits a BMI term given by $KC_y G$ for all the polytope. To solve this problem, the same procedure can be applied as in the proof of section III, for every member of the polytope $\Omega = \text{co}\{[A^1 \ B^1], \dots, [A^N \ B^N]\}$, to convert the inequality (28) into the inequality (24) in theorem 2.

V. NUMERICAL EXAMPLES

In this section, we present the results of our experiments to show the performance and the improvement contributed by our approach. Our experiments are represented by numerical evolution of our method presented in section 3, in comparison to [2] and [9].

To compare our approach of robust stabilization by SOF as presented in section 3 with approaches developed in [2], and [9]. We defined a two class of systems. The first and the second one are composed by 100 systems choosing aleatory and verifying hypothesis. Each system of the first class has $n=3$, $m=1$ and $p=2$ and for the second class it has $n=5$, $m=2$ and $p=3$.

The purpose of this comparison is to find the percentage of systems in each class which could be stabilizable by SOF using the different methods.

The results are illustrated in Fig.1 and Fig.2.

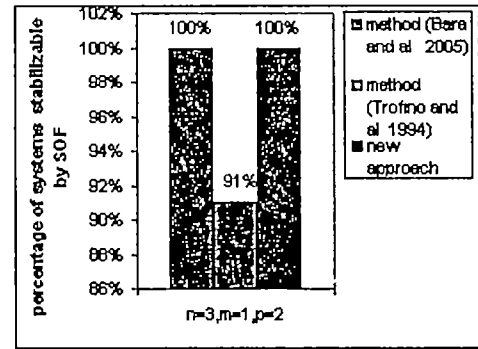


Fig. 1: The percentage of first class systems stabilizable by different methods

For the first class of 100 systems, the methods [2] and our approach given by the Theorem 1 allowed to stabilize 100% of these systems while the method [9] worked successfully for 91% of them.

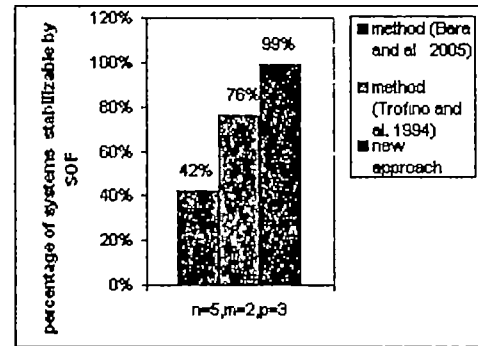


Fig.2: The percentage of second class systems stabilizable by different methods

However, for the second class of 100 systems, the methods [2] and [9] allowed to stabilize a 42% and 76% of these systems by SOF respectively while our approach given by the Theorem 1 worked successfully for 99% of them.

Our approach presents a better performance than the others methods.

VI. CONCLUSION

In this paper, we proposed a new sufficient condition quadratic stability by static output feedback (SOF) for discrete linear time invariant systems. This condition is elaborated by using Lyapunov theory and formulated by LMI constraints. The proposed approach is also extended to uncertain systems with polytopic uncertainty. Numerical comparisons with existent method in the literature are given to illustrate the improvement contributed by our approaches.

This new improved sufficient condition can be extended to other performances in relation with SOF problem like H_2 and H_∞ synthesis by SOF.

REFERENCES

- [1] Yong He and Qing-Geo Wang, "An improved ILMI Method For Static Output Feedback Control With Application to Multivariable PID control", *IEEE Transactions on Automatic Control*, vol. 51, no. 10, pp. 1678-1683, 2006.
- [2] G. IULIA BARA and M.BOUTAYEB, "Static Output Feedback Stabilization With H_∞ Performance for Linear Discrete-Time Systems", *IEEE Transactions on Automatic Control*, vol. 50, no. 2, pp. 250-254, 2005.
- [3] Atsushi Fujimori, "Optimization of Static Output Feedback Using Substitutive LMI Formulation", *IEEE Transactions on Automatic Control*, vol. 49, no. 6, pp. 995-999, 2004.
- [4] C.SCHERER, P.GAHINET, and M.CHILALI, "Multiobjective Output feedback Control Via LMI Optimization", *IEEE Transactions on Automatic Control*, vol. 42, no. 7, pp. 896-911, 1997.
- [5] A.TORFINO and V.KUCERA, "Stabilization Via Static output Feedback", *IEEE Transactions on Automatic Control*, vol. 38, no. 5, pp. 764-765, 1993.
- [6] E.ROBERT BENTON, Jr. and DIRK Smith, "Static Output Feedback Stabilization with prescribed Degree of Statbility", *IEEE Transactions on Automatic Control*, vol. 43, no. 10, pp. 1493-1496, 1998.
- [7] J.C Geromel, C.C.De Souza and R.E.Skelton, "LMI Numerical solution for output feedback stabilization", in *Proc.Amer.control. Conf.*, Maryland, Jun 1994, pp. 40-44.
- [8] M. G. SAFONOV, K. C. GOH, and H. LY, "Control System Via Bilinear Matrix Inequalities", in *Proc.Amer. Control Conf.*, pp. 45-49, 1994.
- [9] César A. R. CRUSIUS and Alexandre TROFINO, "Sufficient LMI conditions for Output Feedback Control Problems", *IEEE Transactions on Automatic Control*, vol. 44, no. 5, pp. 1053-1057, 1999.
- [10] G. GARCIA, B. PRADIN and F. ZENG "Stabilization of Discrete Time Linear Systems by Static Output Feedback", *IEEE Transactions on Automatic Control*, vol. 46, no. 12, pp. 1954-1958, 2001.
- [11] M.C. DE OLIVEIRA, J.C.GEROMEL and J.BERNUSOU, "Extended H_2 and H_∞ norm characterization and controller parameterization for discrete time systems", *INT.J control.*, vol. 75, no. 9, pp. 666-679, 2002.
- [12] O. TOKER and H.Osby, "On the NP-hardness of solving bilinear matrix inequalities and simultaneous stabilization with static output feed back", in *Proc.Amer.control. Conf.*, Seattle,WA, Jun 1995, pp. 2525-2526.
- [13] M.C. DE OLIVEIRA and J.C.GEROMEL, "A class of robust stability conditions where linear parameter dependence of the Lyapunov function is a necessary condition for arbitrary parameter dependence", *INT.J control.*, vol. 75, no. 9, pp. 666-679, 2002.

A Parameter Plane Design Methodology for Two-Loop Lateral Missile Autopilot

Mousiki Kar(Deb)¹, Kalyankumar Datta², and Shyamal Kumar Goswami³

¹ ECE Department, Haldia Institute of Technology, Haldia, India, e-mail: mousiki@rediffmail.com

² Electrical Engineering Department, Jadavpur University, Kolkata, India, e-mail: kalyandatta@debesh.wb.nic.in

³ Electrical Engineering Department, Jadavpur University, Kolkata, India, e-mail: goswami_shyamal@yahoo.com

Abstract— A parameter plane methodology has been proposed for designing the control gains of a two-loop lateral missile autopilot. This design approach allows the designer to obtain admissible set of control gains satisfying certain frequency domain specifications. It also enables to find out maximum attainable autopilot gain crossover frequency and the corresponding set of control gains. In the proposed methodology, the designer gets a graphical view of the range of values of control gains to choose from in order to satisfy a certain design specification. As the critical gain margin, critical phase margin and stability margin can be easily visualized in the parameter plane, gain scheduling becomes easier, thus avoiding complex analytical evaluation of critical loop. The design methodology for the proposed algorithm has been given in details and illustrated with numerical examples using four different types of missile data.

Key words—Autopilot, Critical phase margin, Critical gain margin, Parameter plane.

NOTATIONS

K_r	: Lateral autopilot control gain outer loop
K_f	: Fin servo gain [sec]
q	: Missile body rate in pitch [rad/s]
T_r	: Incidence lag of airframe [sec]
K_b	: Airframe aerodynamic gain [sec ⁻¹]
ω_a	: Natural frequency of oscillation of actuator [rad/s]
ω_b	: Weathercock frequency [rad/s]
σ	: a quantity whose inverse determines the location of non-minimum phase zero in s-plane
ζ_a	: damping ratio of actuator

ω_r	: Lateral autopilot control gain
m_r	: Mass of the missile [kg]
U	: Missile velocity in X-direction [m/s]
η	: Elevator deflection [rad]
γ	: Flight path rate [rad/s]
γ_d	: Demanded flight path rate [rad/s]
GM	: Gain Margin [dB]
PM	: Phase Margin [degrees]
GCF	: Gain Crossover Frequency [rad/s]
PCF	: Phase Crossover Frequency [rad/s]

I. INTRODUCTION

IN guided missiles, lateral autopilots are used to deliver lateral acceleration based on the demand from the guidance computer. The autopilot responds to the guidance system demands by deflecting the control surfaces of the missile for aerodynamically controlled missiles. The deflection in control surfaces, produce change in the resultant lift force acting on the missile. This changes the angle of attack of the missile consequently generating the lateral acceleration required to steer the missile in the desired path.

In the past few decades several attempts have been made to design missile autopilots. Lateral autopilots may be classified based on the feedback sensors used to feedback missile information. Two configurations are:

- Two-loop autopilot
- Three-loop autopilot

Lateral autopilot configuration with one accelerometer and one rate gyro feedback, which are more common in high performance command and homing missiles has been suggested in [1]. Based on this basic configuration G. Das et al. [2] has suggested a two loop lateral autopilot configuration which is a simplified version of the conventional configuration suggested in [1]. In [2] G. Das et al. has suggested a systematic design methodology to design the control gains of

two-loop lateral autopilot based on frequency domain performance specifications.

In this paper, a PI controller design methodology for a two-loop lateral missile autopilot has been proposed. The methodology is based on the parameter plane method as suggested in [6]. It is a simple and straightforward controller design method that can achieve a solution carpet of all the admissible controller gains in the parameter plane, given a specified gain and phase margin. The proposed design enables to find out the maximum attainable gain crossover frequency and the corresponding set of control gains, graphically. Here graphical analysis also helps to visualize the effect of variation of the controller gains on the frequency domain performance specifications of the autopilot. In multi-loop systems it is necessary to identify the loop which when opened provides the critical stability margins. The proposed graphical approach provides a way to visualize and identify pictorially the critical loop to be opened to guarantee the specified stability margins.

II. DESIGN PROBLEM

A. Given missile parameters

Actuator : Natural frequency ω_a , Damping ratio ζ_a .

Airframe & environment : $T_r, m_\eta, \sigma, \omega_b$.

B. Desired specification

Critical gain-margin \geq GM (a specified value).

Critical phase-margin \geq PM (a specified value).

Illustrative examples are used for understanding of the design methodology. The methodology has been tested for four sets of missile data and the results have been presented. All the simulations have been done using MATLAB 6.1 application software.

III. PLANT TRANSFER FUNCTION

The two-loop lateral missile autopilot configuration has been presented in [1]. Das et al [2,3] used modified two-loop autopilot configuration with unity feedback gains. In this paper, this basic configuration has been used and has been modified slightly to obtain the configuration of FIG. 1 by placing an integrator in the outer loop of the autopilot.

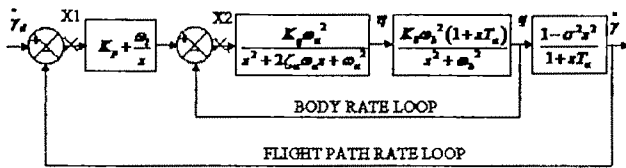


FIG.1.

IV. PARAMETER PLANE ANALYSIS

A function known as the Gain-Phase Margin Tester Function is used for interpreting frequency domain performance specifications in the parameter-plane [6].

For an open loop transfer function,

$$G_o(s) = \frac{N(s)}{D(s)} \quad (1)$$

the gain-phase margin tester function can be described as,

$$F(j\omega) = D(j\omega) + Ae^{j\theta} N(j\omega) = 0 \quad (2)$$

where

$D(j\omega)$ = denominator of the open loop transfer function in frequency domain.

$N(j\omega)$ = numerator of the open loop transfer function in frequency domain.

$Ae^{j\theta}$ is known as gain-phase margin tester where

$$A = \frac{1}{|G_o(j\omega)|} \quad \text{and} \quad \theta = \angle G_o(j\omega) + 180^\circ$$

$F(j\omega)$ is a complex function of A , θ and ω and the desirable control parameters. If $A=1$ is selected then the chosen value of θ will represent the desired phase-margin and the chosen value of ω will be the gain-crossover frequency. Similarly, if $\theta=0$ is selected, then the chosen value of A will represent the value of gain margin for a particular chosen value of phase-crossover frequency ω . If, the value of A is chosen as 1 and $\theta=0$, then for various values of ω a locus which contains the stability boundary of the system may be plotted in the ω versus K_p plane, for any constant K_q .

V. FREQUENCY DOMAIN ANALYSIS

Frequency domain analysis of the autopilot has been carried out by opening the loops at two critical points X1, X2, as shown in FIG.1.

1. Loop opened at X1:

By opening the autopilot loop at point X1, the open loop transfer function of the autopilot system is,

$$GX1(s) = \frac{K_p K_q \omega_a^2 \omega_b^2 (-K_p \sigma^2 s^2 - \sigma^2 \omega_b^2 s + K_p s + \omega_b^2)}{s^2 + 2\zeta_a \omega_a s + (\omega_a^2 + \omega_b^2) s^2 + (2\zeta_a \omega_a \omega_b^2 + K_p K_q \omega_a^2 \omega_b^2 T_r) s^2 + (\omega_a^2 \omega_b^2 + K_p K_q \omega_a^2 \omega_b^2) s} \quad (3)$$

Employing gain-phase margin tester function, as described in the earlier section, the control gains K_p and ω_i can be written in terms of A , θ and ω as, in (4) and (5).

$$K_p = \frac{C_{11} \cdot D_{12} - C_{12} \cdot D_{11}}{B_{11} \cdot C_{12} - B_{12} \cdot C_{11}} \quad (4)$$

and

$$\omega_l = \frac{B_{12} \cdot D_{11} - B_{11} \cdot D_{12}}{B_{11} \cdot C_{12} - B_{12} \cdot C_{11}} \quad (5)$$

Where

$$B_{11} = A_1 \sin(\theta_1) \cdot \frac{\omega_l}{T_a} \omega_a^2 \omega (1 + \sigma^2 \omega^2)$$

$$C_{11} = A_1 \cos(\theta_1) \cdot \frac{\omega_l}{T_a} \omega_a^2 \omega (1 + \sigma^2 \omega^2)$$

$$D_{11} = 2\zeta_a \omega_a \omega^4 - (2\zeta_a \omega_a \omega_b^2 + \omega_c \omega_a^2) \omega^2$$

$$B_{12} = A_1 \cos(\theta_1) \cdot \frac{\omega_l}{T_a} \omega_a^2 \omega (1 + \sigma^2 \omega^2)$$

$$C_{12} = -A_1 \sin(\theta_1) \cdot \frac{\omega_l}{T_a} \omega_a^2 \omega (1 + \sigma^2 \omega^2)$$

$$D_{12} = \omega^5 - (\omega_a^2 + \omega_b^2) \omega^3 + \left(\omega_a^2 \omega_b^2 + \frac{\omega_c}{T_a} \omega_a^2 \right) \omega$$

$$A_1 = \frac{1}{|GX_1(j\omega)|} \quad \& \quad \theta_1 = \angle GX_1(j\omega) + 180^\circ$$

2. Loop opened at X2:

By opening the autopilot loop at point X2 the open loop transfer function can be written as,

$$GX2(s) = \frac{\frac{\omega_l}{T_a} \omega_a^2 [-K_p \sigma^2 s^3 + (T_a - \sigma^2 \omega_l) s^2 + (1 + K_p) s + \omega_l]}{s^5 + 2\zeta_a \omega_a s^4 + (\omega_a^2 + \omega_b^2) s^3 + 2\zeta_a \omega_a \omega_b^2 s^2 + \omega_a^2 \omega_b^2 s} \quad (6)$$

Employing gain-phase margin tester function, the control gains K_p and ω_l can be written in terms of A_2 , θ_2 and ω as,

$$K_p = \frac{C_{21} \cdot D_{22} - C_{22} \cdot D_{21}}{B_{21} \cdot C_{22} - B_{22} \cdot C_{21}} \quad (7)$$

$$\omega_l = \frac{B_{22} \cdot D_{21} - B_{21} \cdot D_{22}}{B_{21} \cdot C_{22} - B_{22} \cdot C_{21}} \quad (8)$$

Where

$$B_{21} = A_2 \sin(\theta_2) \cdot \frac{\omega_l}{T_a} \omega_a^2 \omega (1 + \sigma^2 \omega^2)$$

$$C_{21} = A_2 \cos(\theta_2) \cdot \frac{\omega_l}{T_a} \omega_a^2 \omega (1 + \sigma^2 \omega^2)$$

$$D_{21} = 2\zeta_a \omega_a \omega^4 - 2\zeta_a \omega_a \omega_b^2 \omega^2 - A_2 \cos(\theta_2) \cdot \frac{\omega_l}{T_a} \omega_a^2 \omega (T_a \omega^2) + A_2 \sin(\theta_2) \cdot \frac{\omega_l}{T_a} \omega_a^2 \omega$$

$$B_{22} = A_2 \cos(\theta_2) \cdot \frac{\omega_l}{T_a} \omega_a^2 \omega (1 + \sigma^2 \omega^2)$$

$$C_{22} = -A_2 \sin(\theta_2) \cdot \frac{\omega_l}{T_a} \omega_a^2 \omega (1 + \sigma^2 \omega^2)$$

$$D_{22} = \omega^5 - (\omega_a^2 + \omega_b^2) \omega^3 + \omega_a^2 \omega_b^2 \omega + A_2 \cos(\theta_2) \cdot \frac{\omega_l}{T_a} \omega_a^2 \omega + A_2 \sin(\theta_2) \omega_a \omega_b^2 \omega^2$$

$$A_2 = \frac{1}{|GX_2(j\omega)|} \quad \& \quad \theta_2 = \angle GX_2(j\omega) + 180^\circ$$

VI. DESIGN STEPS

Step 1: A suitable value of K_p is chosen.

Step 2: K_p versus ω_l curves are plotted by setting

- $A1=1$ and $\theta1=0$ in (4) and (5),

- $A2=1$ and $\theta2=0$ in (7) and (8)

to obtain the stability boundary for loop open at X1 and X2 respectively.

Step 3: K_p versus ω_l curves are plotted by setting

- $A1=$ specified gain margin (GM) and $\theta1=0$ in (4) and (5)

- $A2=$ specified gain margin (GM) and $\theta2=0$ in (7) and (8)

to obtain the constant gain margin curve for loop open at X1 and X2 respectively

Step 4: K_p versus ω_l curves are plotted by setting

- $A1=1$ and $\theta1=$ specified phase-margin (PM) in (4) and (5)

- $A1=2$ and $\theta2=$ specified phase-margin (PM) in (7) and (8)

to obtain the constant phase margin curve for loop open at X1 and X2 respectively.

Step 5: The K_p - ω_l parameter plane area which satisfies both PM and GM specification and gives a stable system is obtained by finding the common area under the curves plotted in Step 2, Step 3 and Step 4.

Step6: A set of constant G.C.F curves are obtained by setting $A1=1$, $\omega=$ required GCF and $\theta1$ is varied such $0 \leq \theta_1 \leq \pi$ in (4) and (5). The point of intersection of the maximum constant G.C.F. line with the common area obtained in Step5 will give the required (K_p, ω_l) pair.

VII. ILLUSTRATIVE EXAMPLE

The autopilot design has been carried out for four representative sets of missile data as presented in TABLE 1. The four missile data sets are given as Case-1, Case-2, Case-3 and Case-4.

Case	T_a, s	σ, s^{-1}	ω_a, s^{-1}	ω_b, s^{-1}	$\omega_c, rad \cdot s^{-1}$	ζ_a	K_p, s^2	$\omega_l, rad \cdot s^{-1}$
Case-1	0.36	11.77	0.00029	53	180	0.6	-9.91	470
Case-2	2.65	5.6	0.00142	12.84	180	0.6	-0.1437	3000
Case-3	3.58	3.6	0.0067	15.39	180	0.6	0.3317	500
Case-4	1.37	8.59	0.00206	128	157	0.6	1.265	200

TABLE 1.

The design objective is to obtain the maximum GCF of the

missile autopilot under the following stability conditions:

The critical gain-margin ≥ 2 (6 dB).

The critical phase-margin $\geq 40^\circ$

DESIGN FOR CASE-2

The design for Case-2 has been detailed out below.

The value of K_q is chosen to be -1.4 from [8]

Design of control gains K_p and ω_i :

The constant phase-margin plots for loop opened at X1, X2 are shown in Fig.2 in green and blue solid line plots respectively.

The constant gain-margin plots with loops opened at X1, X2 are shown in Fig.2 in magenta and red solid line plots respectively.

The stability boundary is obtained for loops opened at X1, X2 and is shown in Fig.2 in dotted black and solid black line plots respectively.

The common parameter area is the parameter area (area containing parameter values) which satisfies both critical phase margin and gain margin criterion. The area is shown in hashed region of Fig.2.

Now in order to find the maximum attainable GCF, the constant GCF curves are plotted for $\omega=11, 12, 13$ rad/s as shown in Fig.2 in dotted magenta, red and blue plots respectively.

It can be concluded that the maximum obtainable GCF here is approximately 12 rad/s as the 12 rad/s constant GCF plot is the maximum value of GCF that intersects the hashed region and the corresponding (K_p, ω_i) pair is (30.5, 19.3).

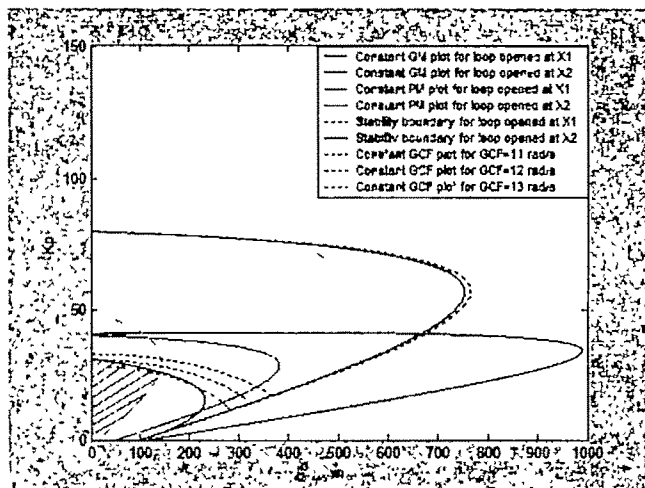


FIG.2.

The autopilot frequency response for loops opened at X1 and X2 are shown in FIG.3, FIG.4 respectively. The time response of the autopilot system is shown in FIG.5.

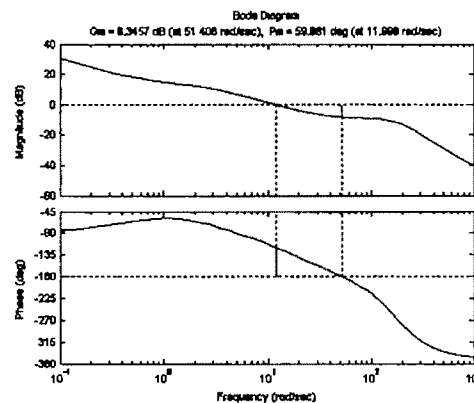


FIG.3.

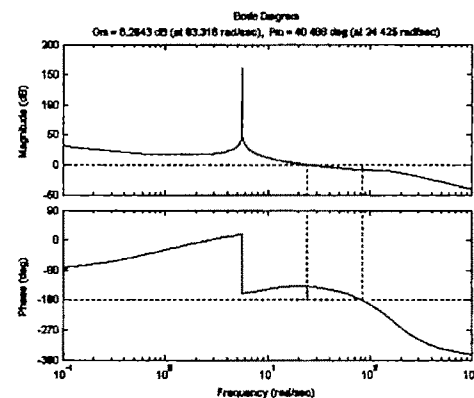


FIG.4.

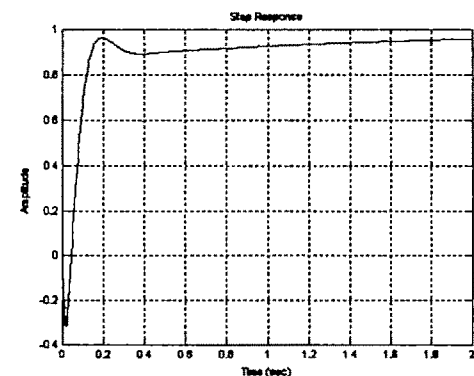


FIG.5.

The frequency domain performance, of autopilots, for all the four cases have been presented in TABLE 2. The representative time response parameters have been provided in TABLE 3.

Case	Control Gain			Loop opened at X1				Loop opened at X2			
	K_p	K_v	ω_c	GM (dB)	PCF (rad/s)	ϕ_M (deg)	GCF (rad/s)	GM (dB)	PCF (rad/s)	ϕ_M (deg)	GCF (rad/s)
Case-1	6.8	-0.05	4	11.114	61.28	76.3	17.25*	11.71*	118.77	41.72*	34.12
Case-2	30.52	-1.4	19.3	8.345	51.4	69.08	12*	8.26*	93.32	40.45*	24.42
Case-3	20.1	0.8	10	7.8	25.43	69.56	6.56*	7.8*	57.08	40.45*	13.16
Case-4	11.25	-0.12	8	8.71	44.89	61.34	10*	8.81*	73.75	41.61*	22.82

* indicates critical value of the corresponding quantity

TABLE 2.

Case	K_p	K_v	ω_c	Over-shoot %	Under-shoot	Rise Time (s)	Settling time(s)	Steady State Value
Case-1	6.8	-0.05	4	0	0	2.67	5.85	1
Case-2	30.52	-1.4	19.3	0	-0.314	0.0942	2.82	1
Case-3	20.1	-0.8	10	0	-0.425	0.19	4.78	1
Case-4	11.25	-0.12	8	0	-0.27	4.17	8.42	1

TABLE 3.

In the present work K_q has been chosen based on the results obtained in [8]. However for each value of K_q a different set of value of K_p, ω_c will be obtained. Thus K_q can be chosen according to the designer's performance requirements in an iterative fashion.

VIII. CONCLUSION

It can be concluded from the results that unity steady state value of the flight path rate response has been obtained. There is no overshoot. Also the undershoot, of the flight path rate response is reduced compared to proportionally controlled two loop lateral missile autopilot in [8]. The prime advantage of the method is that the designer gets a graphical view of which loop is critical at a given frequency of operation. Also in case of design tradeoff, the designer knows the allowable range of values to choose from. The procedure provides K_p, ω_c control gain pair admissible zone and helps in determining the control gain pair K_p, ω_c for obtaining the maximum GCF of the autopilot.

The analysis and design does not take into account the effects of various types of non-linearity. Thus design may be extended, by taking system non-linearity into consideration. Also implementation of the design procedures in the digital domain may be done.

REFERENCES

- [1] P. Garnell and D. J. East, Guided Weapon Control System, Pergamon Press, 1977.
- [2] G. Das, K. Datta, T. K. Ghoshal, S. K. Goswami, Structured Designed Methodology of Missile Autopilot, Journal of the Institution of Engineers (India), pt As, Vol. 76, March 1996, pp 49- 59.
- [3] G. Das, K. Datta, T. K. Ghoshal, S. K. Goswami, Structured Designed Methodology of Missile Autopilot - II, Journal of the Institution of Engineers (India), pt El, Vol. 79, May 1998, pp 28-34.
- [4] G. Das, Structured Methodology for Aerospace FCS System, Ph D (Engineering) Thesis, 1998.
- [5] G. Das, K. Datta, T. K. Ghoshal, S. K. Goswami, Structured Linear Design Methodology for Three-Loop Lateral Missile Autopilot, Journal

of the Institution of Engineers (India), pt El, Vol.85, March 2005, pp 231-238.

- [6] Y.J. Huang and Y.J. Wang, Robust PID controller design for non-minimum phase time – delay system, ISA Transaction, Vol. 40, July 2000, pp 31-39.
- [7] Mousiki Deb, Design Methodology of Two-Loop Lateral Missile Autopilot with P and PI Controllers, Master in Control Systems Engineering thesis, Jadavpur University, 2005.
- [8] M. Kar, K. Datta, S. K. Goswami, A Simple Design Methodology for Two-Loop Lateral Missile Autopilot, Paper communicated to Journal of the Institution of Engineers (India), pt El, dated 25th June, 2007.

Technical Session 3C

Induction Machines

Eigen-Frequency Improvement of Induction Machine Using PI Controller

S. Ekram¹, A. K. Sen² and B. Sarkar³

¹ CG Global R&D Center, Crompton Greaves Ltd., Kanjurmarg (East), Mumbai -400042, India, e-mail: samsul.ekram@cgl.co.in

² St. Francis Institute of Technology, SVP Road, Borivali (W), Mumbai - 400103, India, e-mail: asim_sen@linuxmail.com

³ Dept of Electrical Engineering, SGS Institute of Tech & Science, 23 Park Road, Indore - 452003, India, e-mail: b.sarkar@usa.net

Abstract—This paper presents the analysis of induction machine dynamics through eigen-structure variation in closed loop and open loop condition. Such an eigen-structure-based analysis shows the dynamic inter-dependence of q -axis and d -axis flux linkages of both stator and rotor of the induction machine. The support of arbitrary reference frame of rotating magnetic field gives the eigen-structures of stator and rotor in a clear and distinct manner. Also, for inter-dependency of the variables, the reference frame is synchronized with the stator frame. The dynamic inter-dependency of the variables is shown through eigen-loci that begin at the time of starting and stopping at steady state condition. The analysis shows the existence of two pair of complex conjugate eigen-values, which suggest the existence of two-damped oscillator. The reduction in the imaginary part of eigen-value due to proportional plus integral (PI) closed loop application shows the reduction of oscillation that is the reduction of the transient of the induction machine. Further the imaginary part of one pair of eigen-value is settling to zero, indicates the speed settlement of the machine to rated speed. Hence, the work shows the improvement of stability, eigen-frequency, transient of the induction machine due to the PI closed-loop control.

Key words—Arbitrary Reference, PI Closed Loop Control, Eigen-Value, Eigen-Frequency, and Signal Flow Graph.

I. INTRODUCTION

THE dynamic model of induction machine is highly nonlinear and complex. The established theory of d - q axis transformation [2], [4] has shown the cross coupling between the dynamic equations. A well representation of a.c. machine dynamics by complex signal flow graphs is described earlier [2]. Also the discussion on rotating reference frame and winding dynamics has been well explained. In particular it was stated [2] that two phase windings q and d being orthogonal in space do represent two independent energy storage elements but these are not coupled and hence these cannot exchange energy. Thus, the concept of reference frame

that may be arbitrarily rotating has entered so that it forms an observation platform. With the help of this arbitrary rotating frame it was shown that total magnetic energy appears rotating. This has lead to the concept of single complex eigen-value that is associated with the first order system that represents say stator winding dynamics. The author in [2] has elegantly explained the induction machine dynamics by using complex state variable approach [3]. In this work [3] the arbitrary rotating reference frame is taken to be stationary and root locus plot is drawn. At the same time, when the reference frame is synchronized with the rotor, the root locus plot is shown to dislocate.

The closed loop stability is an important point for a system designer. The present trends of work on induction machine are mainly in the direction of feedback control. Hence for the feedback control method through adaptation, observation, estimation, etc. gives rise to the stability in question. In this regards, study of eigen-structure becomes all the important in that of a certain feedback control law may be designed say the eigen-frequency of the overall closed loop system.

The present work considers the problem of analyzing the induction machine dynamics through eigen-structure variation. At first the induction machine dynamics is being considered using d - q axis transformation and arbitrary reference frame theory [1]-[4] & [5]. The complete state space dynamics is written based on arbitrary reference frame rotating at speed ω_b . To study the eigen-structure variation in open loop and closed loop, the speed of reference frame is set to the stator synchronous speed ω_b . Such a study of eigen-structure variation of an induction machine helps in designing the adaptive control laws.

II. DYNAMICS OF AN INDUCTION MACHINE

To analyze the dynamics of any electrical machine the two-axis theory is conveniently used. The two axes are d -axis as main field and q -axis as the axis at which dynamic emf is induced. The two axes being orthogonal to each other rotate at synchronous speed. Thus if two voltages are impressed at these

axes then the resultant field due to these voltages shall be created that will also rotate at uniform synchronous speed in space. The derivation of the dynamics of the induction machine may be found elsewhere [4], [5]. The dynamic of the induction machine may be modelled by defining,

$$x_1 = \omega_r, \quad x_2 = \psi_{qs}, \quad x_3 = \psi_{ds}, \quad x_4 = \psi_{qr}, \quad x_5 = \psi_{dr}, \quad u_1 = V_{qs}, \\ u_2 = V_{ds}, \quad v = m_l,$$

as,

$$\left. \begin{aligned} \dot{x}_1 &= -\frac{f}{J}x_1 + \left(\frac{3}{2}\right)\left(\frac{PX_M}{2D\omega_b}\right)(x_2x_5 - x_3x_4) - \frac{1}{J}v \\ \dot{x}_2 &= -(r_s X_{rr}'\omega_b x_2)/D - \omega_a x_3 + (r_s X_{M}\omega_b x_4)/D + \omega_b u_1 \\ \dot{x}_3 &= \omega_a x_2 - (r_s X_{rr}'\omega_b x_3)/D + (\omega_b X_{M}r_s x_5)/D + \omega_b u_2 \\ \dot{x}_4 &= (r_r X_{M}\omega_b x_2)/D - (r_r X_{rr}'\omega_b x_4)/D - (\omega_a - x_1)x_5 \\ \dot{x}_5 &= (r_r X_{M}\omega_b x_3)/D + (\omega_a - x_1)x_4 - (r_r X_{rr}'\omega_b x_5)/D \end{aligned} \right\} \quad (1)$$

where:-

$$D = X_{ss}X_{rr}' - X_M^2$$

The parameter r & X stand respectively as resistance and reactance. The subscript s & r respectively denote stator and rotor windings. The prime (') is meant for referring the rotor parameter to the stator. The variables ω_a , ω_b and ω_r mean respectively as arbitrary speed of the rotating field, base speed of rotating field (60 Hz) and rotor speed in radians per second. The flux linkage is represented by ψ and the d - q axis stator input voltages are v_{qs} and v_{ds} . J gives the moment of inertia of the rotor and the load while f and P represent the friction and the total number of poles of the machine respectively.

The above state space description is the exact dynamics of the induction machine with reference to arbitrary reference frame. Let,

$$\left. \begin{aligned} K_s &= \frac{X_M}{X_{ss}}, \quad K_r' = \frac{X_M}{X_{rr}'}, \quad \sigma = \frac{D}{X_{ss}X_{rr}'}, \\ \tau &= \omega_b t, \quad \tau_s' = \frac{D}{r_s X_{rr}'}, \quad \tau_r' = \frac{D}{r_r X_{ss}} \end{aligned} \right\} \quad (1a)$$

where:-

ω_b = base angular speed of the system

ω_a = speed of arbitrary reference frame

ω_r = actual mechanical speed of the rotor

$\omega_m = \frac{\omega_r}{\omega_b}$ = normalized rotor speed and

$\omega_{an} = \frac{\omega_a}{\omega_b}$ = normalized speed of the arbitrary reference frame.

Then with these definitions,

$$\frac{d\psi}{dt} = \omega_b \frac{d\psi}{d\tau}$$

The state dynamics of flux linkages using the equation (1) and (1a) can be rewritten as,

$$\left. \begin{aligned} \tau_s' \frac{d\psi_{qs}}{d\tau} + \psi_{qs} &= -\omega_{an} \tau_s' \psi_{ds} + k_r' \psi_{qr}' + \tau_s' u_{qs} \\ \tau_s' \frac{d\psi_{ds}}{d\tau} + \psi_{ds} &= \omega_{an} \tau_s' \psi_{qs} + k_r' \psi_{dr}' + \tau_s' u_{ds} \\ \tau_r' \frac{d\psi_{qr}}{d\tau} + \psi_{qr}' &= -(\omega_{an} - \omega_m) \tau_r' \psi_{dr}' + K_s \psi_{qs} \\ \tau_r' \frac{d\psi_{dr}}{d\tau} + \psi_{dr}' &= (\omega_{an} - \omega_m) \tau_r' \psi_{qr}' + K_s \psi_{ds} \end{aligned} \right\} \quad (2)$$

Note that the description (1) and (2) are the same. The equations (2) together with developed electromagnetic torque expression have been represented through signal flow graph shown in Fig. 1. These equations have also been obtained in [3].

III. DESIGN OF PI CONTROLLER LAWS

The first step to design a proportional plus integral (PI) controller is the speed error calculation. Accordingly the speed error of the machine is defined as,

$$e_\omega = \omega_{ref} - a_\omega \hat{\omega}_r \quad (3)$$

$$\text{where } a_\omega = \frac{1}{\text{rated } \omega_r} \quad (3a)$$

Then the control law may be expressed as follows,

$$v_s = K \left(e_\omega + \frac{1}{\tau_i} \int e_\omega dt \right) \quad (4)$$

$$f_s = \frac{v_s}{2\pi\psi_s} \quad (5)$$

where v_s = stator voltage, ψ_s = stator flux linkage (constant), and f_s = stator frequency. This applied voltage is transformed to d - q axis through the transformation matrix K_s [4] as given in

$$\text{equation (6) below.} \\ K_s = \frac{2}{3} \begin{bmatrix} \cos \theta & \cos \left(\theta - \frac{2\pi}{3} \right) & \cos \left(\theta + \frac{2\pi}{3} \right) \\ \sin \theta & \sin \left(\theta - \frac{2\pi}{3} \right) & \sin \left(\theta + \frac{2\pi}{3} \right) \\ 1/2 & 1/2 & 1/2 \end{bmatrix} \quad (6)$$

Where, $\theta = 0$ so that $v_{qs} \neq 0$ but $v_{ds} = 0$.

IV. ROOT LOCUS OF ELECTROMAGNETIC SUB-SYSTEMS

The signal flow diagram (Fig. 1) visualizes the properties of the dynamics of induction machine. It shows the interaction of different components (stator and rotor) of flux with respective input and output. The method to visualize the properties of the dynamics of induction machine is the root locus plot. The main variables in the root locus plot are the eigen-value. In this method of solution the expression $(\lambda I - A)$, (where, ' I ' is the identity $(n \times n)$ matrix) is known as characteristic polynomial and the roots of $(\lambda I - A) = 0$ are known as eigen-values of the

system. The root locus plot of the electromagnetic subsystem of 250hp-induction machine is shown in Fig. 2 considering arbitrary reference frame synchronized with stator frame. The root-loci remain unaffected by the choice of the model. Such independence has been tested through the simulation by using C++ programming.

With reference to equation (1) the machine dynamics is complete. In order to study the variation in eigen-values of electromagnetic subsystems with reference frame be fixed with stator, the eigen-values of the whole system are calculated. The electromagnetic subsystem described by (1) shall have four eigen-values.

V. RESULTS AND DISCUSSIONS

The entire work presented in this paper has been simulated in C++ and MATLAB. A 3-phase, 250 hp, 2300 V, 4-pole, 60 Hz, induction machine is considered for the present simulation. However, the required parameters of the 3-phase 250hp-induction machine are presented here for convenience as:

$$r_s = 0.681\Omega, r_r' = 0.401\Omega, X_s = 88.331\Omega, X_r' = 88.331\Omega$$

$$\text{as: } X_m = 85.88\Omega, J = 6.918 \text{ Kg m}^2$$

with negligible friction.

The complex electromagnetic subsystem of induction machine contains two pairs of conjugate complex eigen-values that lead to the existence of two oscillatory systems. These oscillatory systems are one for stator and one for rotor. Each oscillatory system when factored shall have one complex root each that will have no conjugate part. This is due to the effect of introducing arbitrary reference frame. In these pair of conjugate complex eigen-values, the real part represents the damping of the associated oscillator and the imaginary part represents the eigen-frequency. If the arbitrary reference frame is rotating synchronously with the stator, then the eigen-values get displaced to different locations than when the reference frame is stationary. As pointed out in [3] such a result indeed proves out the motion of these complex roots when the machine starts and reaches the steady state. This concludes that the eigen-frequency is not an inherent property of the induction machine.

The root locus plots of the four eigen-values are shown in Fig. 2 for open loop and Fig.3 for closed-loop. Fig. 3 shows that the imaginary part of the eigen-values has reduced compare to Fig. 2. It also shows that the imaginary parts of one pair of eigen-value are tending to zero. Hence the eigen-frequency has improved due to PI closed-loop control. Also the speed of the induction machine has settled to rated speed (reference speed) due to PI closed loop control. It is to note that when load is applied to the machine there is some change in the eigen-value being observed. However such changes are not prominent in the root-loci plot.

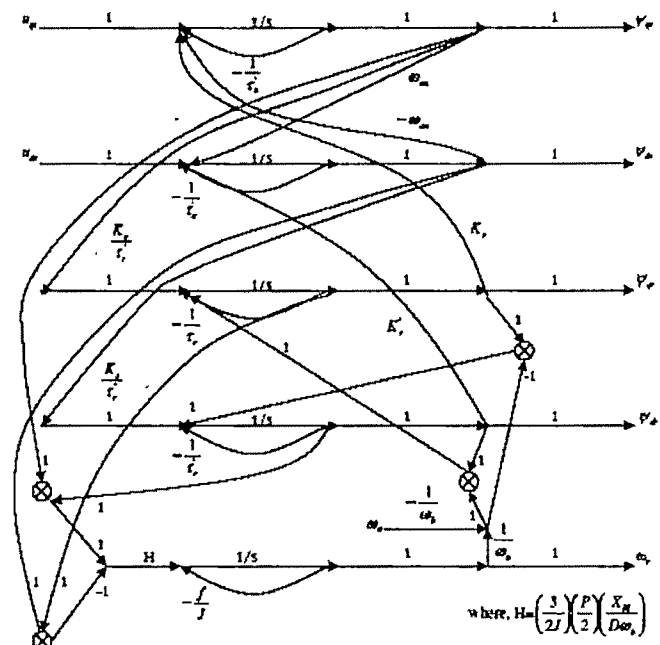


Fig.1- Signal flow graph of induction machine dynamics

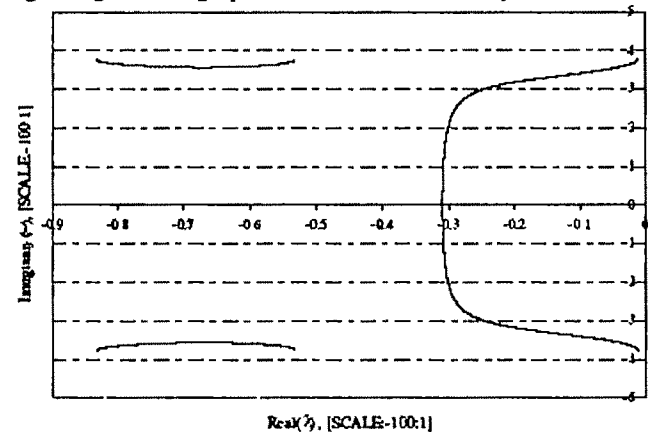


Fig. 2- Root locus plot of electromagnetic subsystem for 250hp induction machine

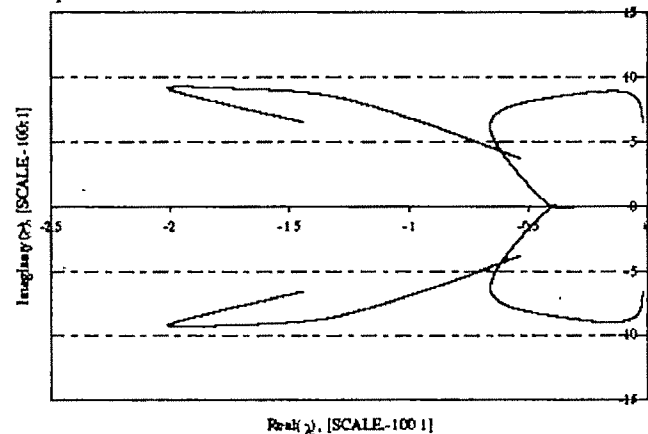


Fig. 3 - Root locus plot of electromagnetic subsystem for 250hp induction machine using PI control

VI. CONCLUSION

The work has presented induction machine dynamics through real state variables. The calculation of eigen-values indicates that these are time dependent. The imaginary parts of eigen-values represent the eigen-frequency. However, the loci of complex eigen-values get displaced to different locations when the arbitrary reference frame is synchronized with the stator. The variable in the eigen-value remains unaffected by the choice of the dynamic model. The signal flow graph obtained from the dynamics shows the interdependence between the direct and quadrature axes flux linkages of both stator and rotor. Such a study of the eigen-structure of the machine may led to intricate design of adaptive control laws.

REFERENCES

- [1] D.W Novotny, J.H Wouterse: Induction machine transfer functions and dynamic response by means of complex time variable, *IEEE-Trans on Power Apparatus & System*, Vol.PAS-95, no.4, 1976, pp.1325-1333.
- [2] J. Holtz: The representation of ac machine dynamics by complex signal flow graph, *IEEE-Trans. on Industrial. Electronics*, Vol.A2, no.3, 1995, pp. 263-271.
- [3] J Holtz: On the spatial propagation of transient magnetic field in ac machine, *IEEE-Trans. on Industrial. Applications*, Vol.IA-32, no.4, 1996, pp. 927-937.
- [4] P C. Krause: Analysis of electric machinery, Mc Graw-Hill International Edition, 1987.
- [5] R. Krishnan: Electrical motor drives – Modelling, analysis, and control, Prentice-Hall of India Pvt. Ltd., New Delhi-110001, 2002.
- [6] W Leonhard: Control of electrical drives, Springer-Verlag, Berlin, 1985.

A New Integrated Motor Starter for Induction Motor

J.P.Tewari¹, R.K.Singh², Naveen Nischal Chava³

¹ Department of Electrical Engineering, Institute of Technology, BHU, India, email: jptewari@bhu.ac.in

² Department of Electrical Engineering, Institute of Technology, BHU, India email: iksingh@yahoo.com

³ Department of Electrical Engineering, Institute of Technology, BHU, India, email: chava.naveen@gmail.com

Abstract—The present paper deals with the design of a solid state starter for the induction motor together with a protection circuit. Protection circuit provides the over load and short circuit protection to the solid state starter and is developed with the help of topologies of solid state circuit breaker[7]. The size of the total starter is very compact in size and can be embedded in the motor terminal box. The circuit breaker normally used in front of the starter for the protection can be removed. The circuit breaker normally used in front of the starter takes a time of 3 cycles which is approximately (60msec). With the proposed scheme the fault level of 65 kA prospective current can be cleared by the protection circuit in the time range of less than 100µsec. The soft start and soft stop capability can be adapted to the present system. Results with a fault level of 65 kA prospective current are simulated using the Saber (simulation tool).

Key words— fault current, protection circuit, thyristor.

I. INTRODUCTION

THE efficiency of a lightly loaded induction motor can be very substantially improved by controlling the voltage applied to it. In addition, controlling the voltage also improves the power factor at which the motor operates [1]. The power factor is improved by loss minimization. The loss minimization is based on the principle that a lightly loaded motor operates most efficiently with the magnetic flux so reduced that an optimal tradeoff between the copper and iron losses is achieved[2]. The reduced voltage type can include solid state starters, adjustable frequency drives, and auto-transformers [3]. Solid state starters use power semiconductors to control the power to the motor. Most designs use a pair of reverse-blocking thyristors, or thyristors, in each phase of the motor supply, although diode-thyristor pairs and even bi-

directional thyristors (triacs) are sometimes used. The ability to phase control all three power lines gives the solid state starter a performance advantage over electromechanical systems [4]. It is possible to control the motor voltage over a wide range. In a full voltage solid state starter, the thyristors are turned-on, usually using a zero-crossing switching circuit, and apply full voltage to the motor. Clearly, the thyristors must be sized to handle the motor's locked rotor current. In this application, thyristors are used to replace mechanical contacts, and if suitably sized can provide highly repetitive motor starts without deterioration.. Generally a safety circuit breaker [5] is placed in front of the starter to protect the starter from the fault current. Safety circuit breaker will take three cycles of supply to clear the fault. The time period is approximately 60 msec. An anti-parallel thyristor module [6] is selected for this application considering that it occupies very small area pre phase. The surge on state current that can flow through it is 2000 A for 10 m sec. The thyristor can not with stand if a fault current more than this flow for more time. To reduce the total starter size a protection circuit is essential. The protection circuit should clear the fault very fast and it should occupy small area so that total size of the starter is very compact.

II. SYSTEM DESCRIPTION

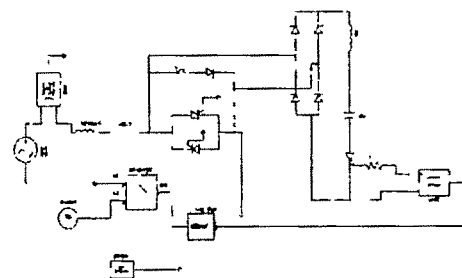


Fig. 1 single phase of the starter

The fig.1 represents a single phase of the starter. Protection circuit is connected parallel to the anti parallel thyristor module. Main components of the protection circuit are 500 V ac capacitor, an auxiliary thyristor, and a control circuit for trip logic greater than 500 A. The control circuit consists of a current transformer continuously monitoring line current; its secondary is connected to the comparator. When the control circuit detects the line current more than the 500 A comparator produces a triggering pulse to the auxiliary thyristor which is in forward bias. The capacitor which is pre charged to the 500V in the reverse direction starts discharging. Through auxiliary thyristor Ta, diode D3 to the load. The capacitor voltage which is greater than the supply voltage keeps the main thyristor in the reverse bias .This is the forced commutation of the thyristor where the thyristor is reverse biased and current through it is made as zero by providing the commutating current which is greater than the current carried by the main thyristor by pre charged capacitor. In this method of turning-off the main thyristor at zero current through it, fault current follows the path of D1- inductor -capacitor-Ta and to the load .when the capacitor is charged in the reverse direction the current through the auxiliary thyristor will become zero and it stops conducting so fault current is stopped .The fault current flows to the load even after the main thyristor is opened but as the capacitor is charging in the reverse direction quickly it allows the fault current to flow for very less time. For every operation of the protection circuit the capacitor has to be re-charged for 500V. Charging circuit for the capacitor is to be placed adjacent to it and it should charge the capacitor for every operation of the Halt circuit. For charging the capacitor a step up transformer is of rating 5KVA, 440/600 Volts transformer should be placed. The protection circuit can clear the fault in the time less than the 100 μ sec. It can protect the main thyristor bridge from the over load and short circuit currents. This protection circuit is derived from the fast acting solid state circuit breakers where a mechanical contactor is placed and it is opened at zero current through it. Solid state circuit breakers provide arc less fast operation.

III. SYSTEM OPERATION

Fault impedance is calculated for 65 kA prospective current. The operation of the protection circuit is simulated at a 65 kA prospective current. Fig.2 shows the fault current through line and fault current through main thyristor. Even the fault current through the main thyristor is cleared it passes to the load for some time. When the capacitor of the halt circuit fully charges to the reverse direction the fault current to the load becomes zero. The time deference between the fault current clearing in main thyristor and load can be seen in below fig.2.

The line current taken by the motor is 20Amp and for the induction motor the starting current is high .normally it takes 7times the rated current. Considering the safety factor and taking it as 15 times that will be 300 A and it peak value is 424 A. So the maximum fault current can flow through the line is 500 A. If the value goes smaller than this, protection circuit may act at the starting of the motor and motor may stop at the

starting it self. Capacitance value is directly proportional to holding time. Simulations are run

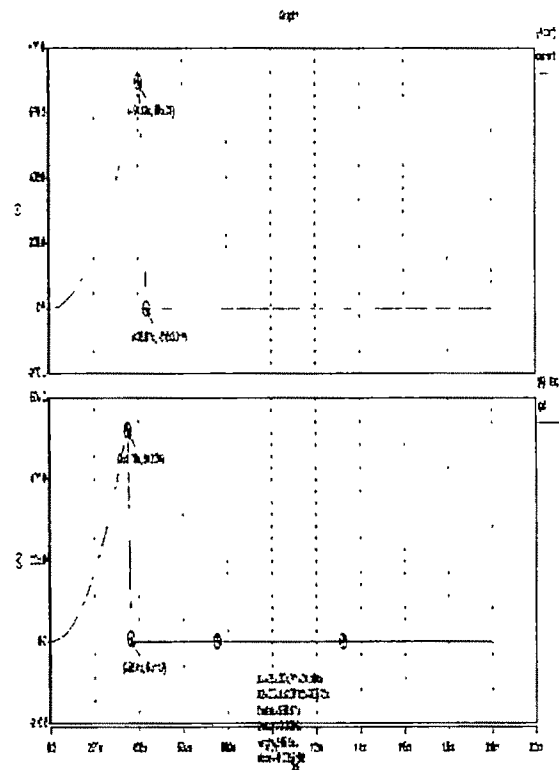


Fig.2 Fault current through line and main thyristor with different capacitance values available in the market to get the optimized circuit components. A 47 μ f is able to clear the 65kA prospective current. When 47 μ f capacitor is replaced with the 30 μ f capacitor, holding time of the capacitor is reduced so that it is unable bring the anode current of the thyristor below holding current. Fault current conducts through thyristor and thyristor may get burn. It can be observed in fig 4. When control circuit detects the fault current firing pulse is given to auxiliary thyristor at the same time pulses to the main thyristor should be stopped.

If the pulses to the main thyristor continue fault current can not be cleared because when the anode current through the main thyristor reduces below the holding current it comes to the forward blocking state. When thyristor is in forward blocking state and a gate pulse is applied. Thyristor comes from forward blocking state to forward conducting state. The gate pulse to main thyristor should be stopped at very instant we fire the commutation thyristor. It can be observed in fig.5. so an intelligence circuit should be placed to stop the pulses to the main thyristor.

IV. CONCLUSION

This paper is devoted to design of a solid state starter and a protection circuit. The size of the starter reduces ten times and gives noise less operation. Soft start and soft stop capability can be embodied to it.

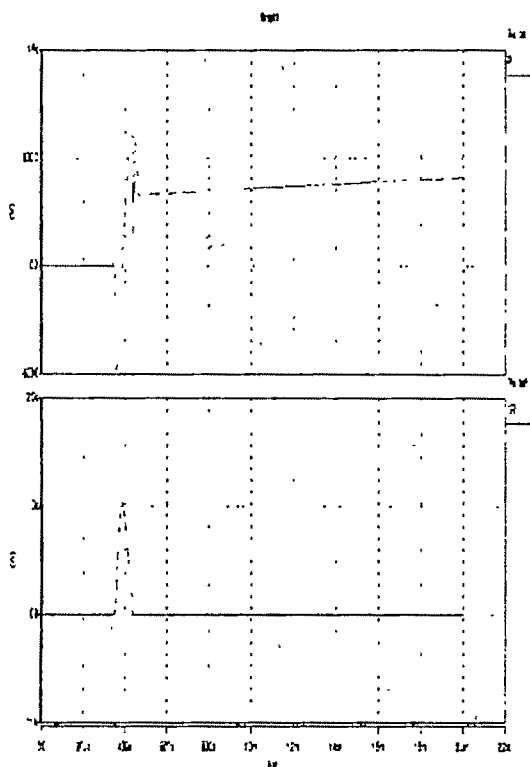


Fig. 3 : Capacitor voltage and commutating current

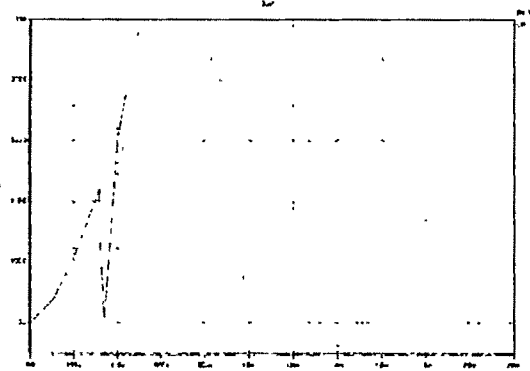


Fig 4.protection circuit operation for 47μf and 30μf

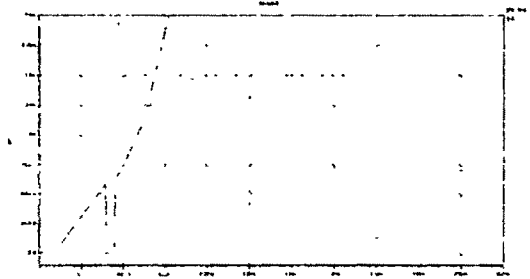


Fig. 5 with 47μf and continuous pulse to main Thyristor

REFERENCES

- [1] N.Mohan, "Improvement in energy Efficiency of Induction Motor by Means of Voltage, Control". IEEE Trans. PAS-9NO.4, 1980, pp. 1466-1471
- [2] Prede Blaaberg, John K. Pedersen, Soren Rise, Hans- Henrik Hansen and Andrzej M.Trynadlowski, "Can Soft- Starters Help Save Energy?" IEEE Industry Applications Magazine, pp. 56-66, September/ October 1997. A review of reduced voltage ac motor Starters. John P. C. Allen, Firing Circuits.
- [3] John Larabee Member IEEE, Brian Pellegrino Member IEEE Benjamin Flick "Induction motor starting methods and Issues" Copyright Material IEEE Paper No. ECIC-2005-24.
- [4] D. W. Novotny and T.A. Lipo. "Induction Machine Efficiency Improvement by Means of Voltage Control" Proc. of U.S. Japan Seminar on Power Electronics, Nov 1981, pp. 199-206.
- [5] LCadirci, M.Ermig, E. Nalgaci, B.Ertan and M.Rahman "A Solid State Direct On Line Starter for Medium Voltage Induction Motors with Minimized Current and Torque Pulsations" IEEE Transactions on Energy Conversion, Vol. 14, No. 3, September 1999..
- [6] <http://www.semikron.com>.
- [7] C. Meyer, S. Schroeder, and R. W. De Doncker, "Solid-State circuit breakers and Current limiters for medium-voltagesystems having distributed power systems," IEEE Trans. Power Electron. vol. 19, no 5, pp. 1333-1340, Sep. 2004.

Current and Vibration Analysis of Induction Motor for Detection of Broken Rotor bar

B. K. Kundu¹, P. P. Pal², P. Chattopadhyay³, and G. Bandyopadhyay³

¹ Academy of Technology, Hoogly, WB, India, e-mail : barnali_aec@rediffmail.com.

² BHEL, India, e-mail : paijatprasun@gmail.com

³ Electrical Engineering Department, BESU, Shibpur, e-mail : paramita_chattopadhyay@yahoo.com

⁴ Electrical Engineering Department, BESU, Shibpur, e-mail : gb@ee.becs.ac.in

Abstract— Condition monitoring has become a very important technology in the field of electrical equipment maintenance and has attracted more and more attention world wide. Keeping this in mind a broken rotor bar detection scheme of three phase induction motor has been attempted. In the present study advanced signal processing techniques like continuous wavelet transform (CWT) are used to analyse the motor stator current, shaft and frame vibrations during start-up. The encouraging results obtained from CWT analysis is hoped to set up a base of condition monitoring technique of induction motor which will be simple, fast and overcome the limitations of traditional FFT techniques.

Key words— Condition Monitoring, induction Motor, Broken Bars, Continuous Wavelet Transform

I. INTRODUCTION

CONDITION monitoring is a maintenance practice where a comprehensive program of data collection and analysis provide early detection of a problem and identify the need for maintenance based on the condition of the monitored equipment. Thus it allows maintenance to be performed in a planned and systematic manner before equipment fails. Since induction motors are extensively used in various industries, the condition based maintenance, on-line monitoring, fault detection and diagnosis of these motors are of utmost importance in order to avoid catastrophic failures. The faults that commonly occur in induction motors are stator winding faults generally caused by insulation breakdown, broken rotor bars due to pulsating loads or direct online starting, bearing problems, and air-gap eccentricities [2].

As the induction motor is highly symmetrical, the presence

of any kind of fault in it affect its symmetry. This leads to a corresponding change in the interaction of flux between stator and rotor, resulting in changes to the stator currents, voltages, magnetic field and machine vibration.

Vibration monitoring is one of the oldest condition monitoring techniques and is widely used to detect mechanical faults in the machine[7, 8]. On the other hand stator current contains frequency components which can be related to a variety of faults such as mechanical asymmetries, broken rotor bars and shorted turns in the stator winding. Motor Current Signature Analysis (MCSA)[12], recently used motor faults detection technique, offers the facilities like remote operation and non-invasion compared to the traditional and most common technique of vibration analysis [1].

The analysis of the motor current or vibration signal for determining the harmonic components is essentially done with the help of Fast Fourier Transform (FFT) as introduced in several works [4]-[6]. But FFT is, however, not appropriate to analyze signals that have a transitory characteristic. Analysis is greatly depended on the load to the machine and a very high resolution of frequency scale is needed for correct identification of very closed fault frequency components[9]. The advantages of using Wavelet techniques for fault monitoring and diagnosis of induction motors are increasing because these techniques help to perform stator current or vibration signal analysis during transients. The wavelet technique can be used for a localized analysis in the time-frequency or time-scale domain. Some recent works have explored these advantages of using wavelet analysis [9]-[11]. Keeping these view points in mind the investigation aims to design and develop an on-line monitoring and incipient fault detection scheme of induction motors by assessing the signature of the motor line current (I_{line}) as well as motor frame (g_{frame}) and motor shaft vibrations (g_{shaft}). Among various motor faults, proposed investigation has been restricted to *broken rotor bar* fault only.

II. PROPOSED METHOD

The schematic representation of the work is shown in fig. 1. The scheme consists of three major parts, namely (i) simulation of different induction motor faults and (ii) data acquisition and (iii) signal processing. For identifying the faults, motor line current (I_{line}) as well as motor frame (g_{frame}) and shaft (g_{shaft}) Vibrations signals are monitored and results are compared in each cases. Photograph of the experimental setup is presented in fig. 2.

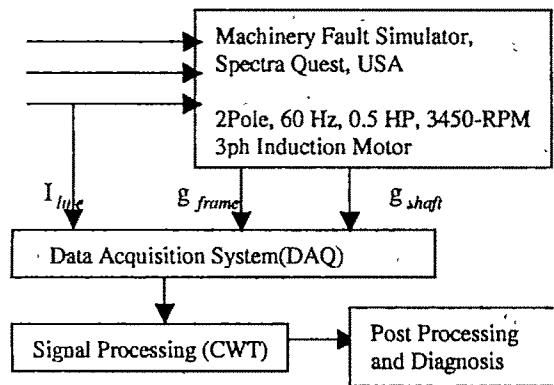


Fig. 1(a): Schematic diagram of the work

A. Simulation of faults

Machinery Fault Simulator (MFS)[16], a tool for simulating various types of induction motor faults initially fitted with a healthy motor and a motor with three broken rotor bars of same specification have been used for the fault simulation.

B. Data acquisition

The generated data corresponding to that fault are collected using clip-on Hall effect current and accelerometer probes, recorded and stored using a computer with four channel Data Acquisition system (DAQ). The collection is done for both the healthy motor and the faulted motor with three rotor bars broken under the same running conditions.

C. Signal processing:

Signal processing part of the scheme has used Continuous Wavelet Transform (CWT) for analyzing start-up current and vibration signals. Mathematically, the process of Fourier analysis is represented by the Fourier transform:

$$F(w) = \int_{-\infty}^{+\infty} f(t) e^{-j\omega t} dt \quad (1)$$

Which is the sum over all time of the signal $f(t)$ multiplied by a complex exponential. The results of the transform are the

Fourier coefficients $F(w)$, which when multiplied by a sinusoid of frequency w yield the constituent sinusoidal components of the original signal.

Similarly, the continuous wavelet transform (CWT) is defined as the sum over all time of the signal multiplied by scaled, shifted versions of the wavelet function Ψ

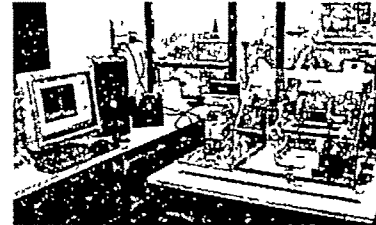


Fig. 2: Photograph of the experimental Set-up

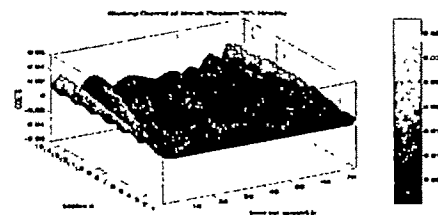


Fig. 3(a) CWT of startup current (I_{line}) of healthy motor at No-Load

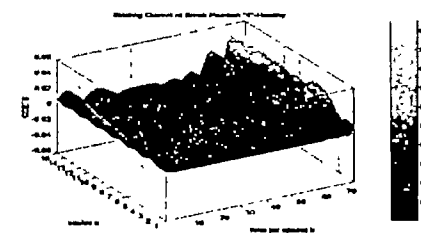


Fig. 4(a) CWT of startup current (I_{line}) of healthy motor at Full-Load

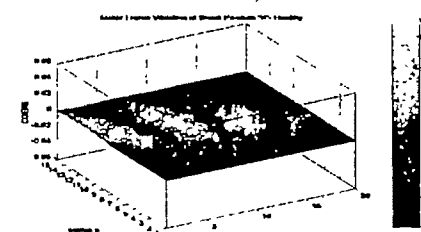


Fig. 5(a) CWT of startup frame vibration (g_{frame}) of healthy motor at No-Load

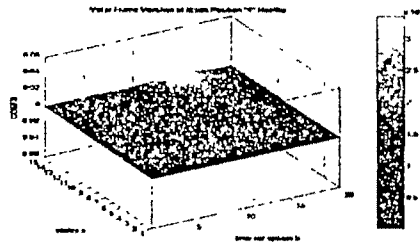


Fig. 6(a) CWT of startup frame vibration (g_{frame}) of healthy motor at Full-Load

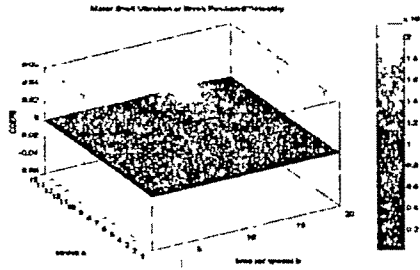


Fig. 7(a) CWT of startup shaft vibration (g_{shaft}) of healthy motor at No-Load

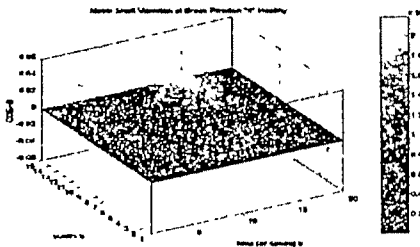


Fig. 8(a) CWT of startup shaft vibration (g_{shaft}) of healthy motor at Full-Load

$$L_{\psi} f(s, \tau) = \int f(t) \psi_{s, \tau}^*(t) dt \quad (2)$$

$f(t)$ is decomposed into a set of basis function $\psi_{s, \tau}(t)$, called wavelets generated from a single basic wavelet $\psi(t)$, the so called mother wavelet, by scaling and translation:

$$\psi_{s, \tau}(t) = \frac{1}{\sqrt{|s|}} \psi\left(\frac{t - \tau}{s}\right) \quad (3)$$

s is a scale factor, τ is the translation and the factor $|s|^{-1/2}$ is for energy normalization across the different scale. Scaling a wavelet simply means stretching (or compressing) it.

III. RESULTS AND ANALYSIS

The stator current, frame and shaft vibrations of the healthy and the faulty motors at the time of starting were collected through DAQ at the frequency resolution of 0.5 Hz/line. The operations were carried out under different loading and frequency conditions. The recorded data are decomposed using CWT. In this investigation Daubechies 8 (db8) mother

wavelet has been used for all CWT operations and implemented in the MATLAB[14] environment. The following 3D images fig. 3-8 showing the wavelet coefficients in Z axis, scale(s) in Y axis and translation(τ) in X axis, are representation of current and vibration signals of the healthy and the motor with three broken bars at no-load & close to full load conditions respectively at a supply frequency of 50 Hz. R.M.S value of the wavelet coefficients are compared and furnished in Table -I. By Examining the results, the wavelet coefficients for faulty motors are found to be much much higher as compared to the healthy one. These observations are valid for both current and vibration signals and may be flagged as defective.

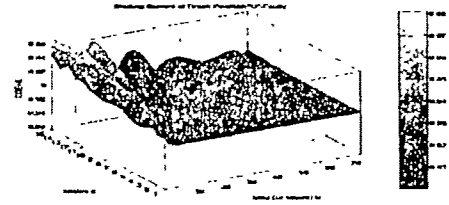


Fig. 3(b) CWT of startup current (I_{line}) of motor with broken rotor bars at No-load

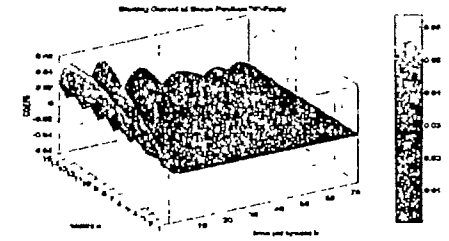


Fig. 4(b) CWT of startup current (I_{line}) of motor with broken rotor bars at Full-Load

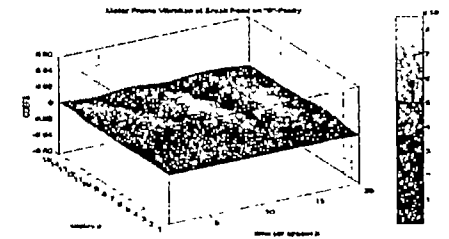


Fig. 5(b) CWT of startup frame vibration (g_{frame}) of motor with broken rotor bars at No-Load

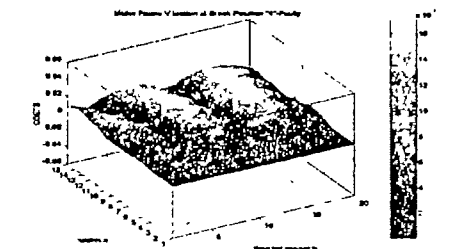


Fig. 6(b) CWT of startup frame vibration (g_{frame}) of motor with broken rotor bars at Full-Load

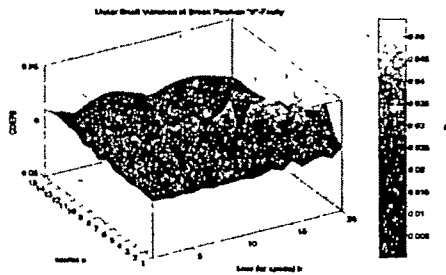


Fig. 7(b) CWT of startup shaft vibration (g_{shaft}) of motor with broken rotor bars at No-Load

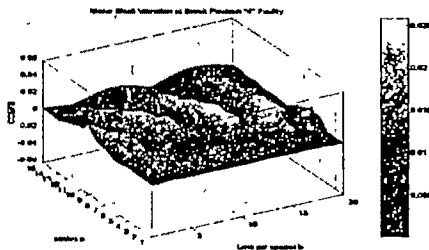


Fig. 8(b) CWT of startup shaft vibration (g_{shaft}) of motor With broken rotor bars at Full-Load

Table-I: Comparison of wavelet Coefficients

Analyzed Signals	No- Load (Break Position 0°)		Closed to full Load (Break Position "4")	
	Healthy	Faulty	Healthy	Faulty
Stator Current	4.77×10^{-4}	11.33×10^{-4}	3.26×10^{-4}	16.22×10^{-4}
Motor Frame Vibration	0.47×10^{-4}	4.77×10^{-4}	1.13×10^{-4}	3.13×10^{-4}
Motor Shaft Vibration	0.86×10^{-4}	4.17×10^{-4}	0.62×10^{-4}	2.61×10^{-4}

IV. CONCLUSION

The results obtained from the application of Continuous Wavelet Transform on the startup stator current, motor frame and shaft vibrations shows very encouraging results which definitely can be used as characteristics feature to diagnose the faults due to broken rotor bars or defective bearing in a motor. These techniques have the capability of analyzing transient signals which can exploit more characteristics features of fault conditions. There are certain advantages of this technique which is prevalent in the foregoing tests.

- The capability of analyzing signals during transient conditions, hence capturing more characteristics features of fault conditions.
- Like FFT technique, very high resolution of recorded data is not required since the method is itself capable of analyzing with increasing resolution.
- Time required for sampling and recording is very short.

- The results are almost same in different loading conditions. So the method is not greatly dependent on loading.

In the present study advance signal processing techniques like CWT have been used to develop a diagnosis scheme for broken rotor bar and bearing defects in an induction motor. The result obtained is hoped to setup a base of condition monitoring technique which will be simple, fast and will overcome the limitations of traditional techniques.

ACKNOWLEDGMENT

The authors are thankful to AICTE and TEQIP(BESU, Shibpur unit), Govt. of India for their financial support toward the project without which it would have not been possible to carry out the work.

REFERENCES

- [1] G. Kliman and R. Koegl, "Noninvasive detection of broken bars in operating induction motors," *IEEE Trans. on Energy Conversion*, vol. 3, no 4, pp. 874-879, 1988.
- [2] P. J. Tavner and J. Penman, *Condition Monitoring of Electrical Machines*. Research Studies Press, Ltd., 1987.
- [3] W. T. Thomson and R. J. Gilmore, "Motor current signature analysis to detect faults in induction motor drives - fundamentals, data interpretation, and industrial case histories," *Proceedings of the thirty-second turbomachinery symposium*, pp. 145-156, 2003.
- [4] C. Hargis, B. G. Gaydon, and K. Kamash, "The detection of rotor defects in induction motors", *IEE International Conference on Electrical Machines design and application*, pp. 216-220, 1982.
- [5] G. B. Kliman and J. Stein, "Methods of motor current signature analysis," *Electric machines and power systems*, pp. 463-474, 1992.
- [6] R. R. Schoen, T. G. Habetlar, and F. Kamran, "Motor bearing damage detection using stator current monitoring," *IEEE Trans. Ind. Appl.*, vol. 31, pp. 1280-1286, 1995.
- [7] C.M. Railey, B.K. Lin, T.G. Habetlar and G.B. Kliman, "Stator Current Harmonics and their Casual Vibrations: A Preliminary Investigation of Sensorless Vibration Monitoring Applications," *IEEE Trans. On Ind. Appl.*, vol. 35, no.1, Jan/Feb. 1999, pp.94-99.
- [8] W.R. Finley, M.M. Hodowance and W.G. Holter, "An Analytical approach to Solving Motor Vibration Problems," *IEEE Trans. On Ind. Appl.*, vol. 36, no. 5, Sep/Oct. 2000, pp.1467-1480.
- [9] K. Abbaszadeh, J. Milimonfared, M. Haji, and H. A. Toliat, "Broken bar detection in induction motor via wavelet transformation," *The 27th Annual Conference of the IEEE Industrial Electronics Society*, pp. 95-99, 2001.
- [10] H. Douglas, P. Pillay, and A. Ziarani, "Detection of broken rotor bars in induction motors using wavelet analysis," *IEEE International Electric Machines and Drives Conference*, vol. 2, pp. 923-928, 2003.
- [11] L. Eren, and M. J. Devaney, "Bearing damage detection via wavelet packet decomposition of the stator current", *IEEE Trans. On Instrumentation and Measurement*, vol. 53, no. 2, 2004.
- [12] M. E. H. Benbouzid, "A review of induction motors signature analysis as a medium for faults detection," *IEEE Transactions on Industrial Electronics*, vol. 47, no. 5, pp. 984-993, October 2000.
- [13] J. A. Antonino, M. Reira, J. Roger-Folch, and V. Climente. (2006) Study of the startup transient for the diagnosis of broken bars in induction motors: A review. [Online]. Available: http://www.aedle.org/9CHLIE-paper-send/318_Antonino.pdf
- [14] M. Misiti, Y. Misiti, G. Oppenheim, and J.-M. Misiti, (2001) Wavelet Toolbox User's Guide [Online], Available: <http://www.mathworks.com>.
- [15] J. S. Walker, *A Primer on Wavelets and their Scientific Applications*, Chapman & Hall/CRC, 1999.
- [16] User's Manual, Machinery Fault Simulator, *Spectra Quest Inc*, USA, 2005.

Decoupled Control of Linear Induction Motor

S. N. Mahendra¹, K. Chaudhary¹, Akshay K. Rathore² and Pankaj Chaudhary¹

¹Dept of Elect. Engg Institute of Technology, Banaras Hindu University, Varanasi – 221005, (U.P.) India. mahendra20@gmail.com

²Dept of Elect & Comm Engg., University of Victoria, Canada. akshay@uvic.ca

Abstract- Paper presents a methodology for decoupled control of linear induction motor. With decoupled control the attraction and propulsion forces of LIM can be controlled independently. d-q model of LIM has been solved through Matlab/simulink. Ratio of attraction and propulsion force has been compared for uncontrolled and decoupled controlled operation of LIM.

Keywords-linear induction motor, decoupled control

Symbols

τ_p = Pole pitch of LIM in meters

λ = flux in wb

V = voltage in volts

I = current in amperes

l_p = Primary length in meters

P = No. of poles

R_s = Primary resistance per phase in Ω

L_s = Primary leakage inductance per phase in H

R_r = Secondary resistance per phase in Ω

L_r = Secondary leakage inductance per phase in H

R_m = Primary resistance per phase in Ω

L_m = Magnetizing leakage inductance per phase in H

p = first derivative operator

M = Total mass of the system in Kg

B = Viscous friction co-efficient in N-sec/m

v = Linear speed in m/sec

σ = Leakage factor

T_r = Secondary time constant

F_p = Propulsion force or thrust in Newton

F_a = Attraction force or normal force in Newton

Suffix

d – d-axis

q – q-axis

s – Primary member

r – Secondary member

I. INTRODUCTION

Effective speed control of electric motor is the prime requirement in transportation system. For this reason the use of induction machine in traction was delayed due to non-availability of a cost

effective and reliable vvvf controller. Advances in inverter technology in early eighties have led to the adoption of 3-phase rotary as well as linear induction motors in traction applications. Now the LIM based traction is operating in a cost-effective manner and performance-experience of user-countries like Japan indicate that it has:

- Low noise and vibration
- Ability to negotiate steeper gradient and sharper turns
- Reliable with negligible maintenance even at high speed operation

Speed of an LIM based system is controlled by conventional controller by controlling the propulsion force produced in the LIM. In this process the force of attraction between the moving-primary-member iron and the reaction-rail backing-iron also increases/decreases with the force of propulsion because the same flux decides both the forces [1,2,3]. However it is desirable that the ratio of attraction-to-propulsion force should be less at starting (to reduce the effective weight on wheel) whereas this ratio should be higher to increase the effective-weight on the wheel for better-stability at higher speed of operation and better-adhesion during braking. This requirement calls for design of a controller capable of controlling the forces of propulsion and attraction independently to meet the specific requirement at different operating conditions. The desired control can be achieved by employing decoupled control of LIM [6,7]. Decoupled/vector control of LIM can be achieved by splitting I_s in two parts I_{sd} and I_{sq} . The controlling signal I_{sd}^* and I_{sq}^* are generated by three PI controllers. LIM equivalent circuit in d-q is simulated in Matlab/simulink.

II. MATHEMATICAL MODELING OF LIM

LIM q-axis equivalent circuit is identical to that of a rotary induction motor (RIM) as the parameters do not vary with the end-effects. On the other hand in an LIM the d-axis entry secondary-currents affect the air-gap flux and hence λ_{dr} . Therefore, the d-axis equivalent circuit of LIM (incorporating end-effects) differs from that of RIM. Fig. 1(a) shows the d-axis equivalent circuit, in which magnetization branch is different from the RIM model. The Q factor associated with the length of the primary member quantifies the end effects as a function of the velocity. Fig. 1(b) shows the q-axis equivalent circuit which is similar to that of the RIM model.

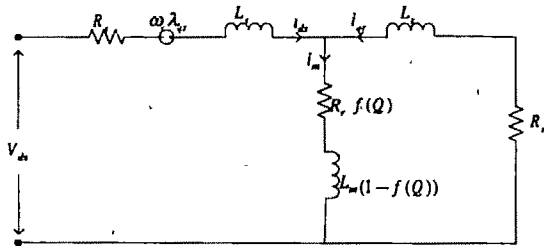


Fig (a) d-axis equivalent circuit

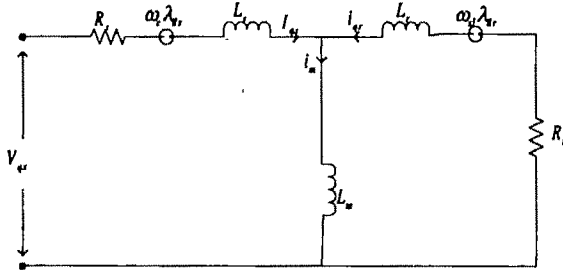


Fig (b) q-axis equivalent circuit

Fig. 1 d-q equivalent circuits of LIM

The primary and secondary voltage equations (using a synchronous reference system) for linear induction motor are as follows:

$$pI_d = -\left(\frac{R_s}{\sigma L_s} + \frac{1-\sigma}{\sigma T_r}\right)I_d + \frac{L_m}{\sigma L_s L_r T_r} \lambda_{dr} + \frac{L_m \pi}{\sigma L_s L_r \tau_p} v \lambda_{qr} + \frac{1}{\sigma L_s} V_d \quad (1)$$

$$pI_q = -\left(\frac{R_s}{\sigma L_s} + \frac{1-\sigma}{\sigma T_r}\right)I_q + \frac{L_m}{\sigma L_s L_r T_r} \lambda_{qr} - \frac{L_m \pi}{\sigma L_s L_r \tau_p} v \lambda_{dr} + \frac{1}{\sigma L_s} V_q \quad (2)$$

$$p\lambda_{dr} = \frac{L_m}{T_r} I_{ds} - \frac{1}{T_r} \lambda_{dr} - \frac{\pi}{\tau_p} v \lambda_{qr} \quad (3)$$

$$p\lambda_{qr} = \frac{L_m}{T_r} I_{qs} - \frac{1}{T_r} \lambda_{qr} + \frac{\pi}{\tau_p} v \lambda_{dr} \quad (4)$$

The propulsion and attraction forces respectively are given as follows [7]:

$$F_t = \frac{3}{2} \frac{P}{2} \frac{\pi}{\tau_p} \frac{L_m}{L_r} (\lambda_{dr} I_{qs} - \lambda_{qr} I_{ds}) \quad (5)$$

$$F_a = \frac{3}{4} \frac{P}{2} \frac{L_m}{L_r} \frac{1}{g_e} (\lambda_{dr} I_{dr} + \lambda_{qr} I_{qs}) \quad (6)$$

Using equations 1-6 a Simulink model of LIM has been modeled as shown in Fig. 2

III. DECOUPLED CONTROL OF LIM

As mentioned earlier in decoupled control the primary current is split into two components, one is known as direct axis current component $I_{d\phi}$ and another is the quadrature axis component $I_{q\phi}$ [3]. The direct axis component $I_{d\phi}$ is responsible for production of flux and is called magnetizing current component. The quadrature axis component $I_{q\phi}$ is responsible for the production of thrust or propulsion force. These two components act as control signals. In the proposed control scheme, the control signal $I_{d\phi}$ is generated from the secondary flux-controller and the control signal $I_{q\phi}$ is generated from the successive outputs of the speed and the thrust controllers. The independent control of these two current components serves the objective of achieving the desired decoupling, which is obtained by the optimum setting of the parameters of the three PI controllers.

Fig. 3 shows the implemented block diagram of a decoupled controlled linear induction motor and Fig. 4 shows the Simulink diagram for decoupled control for decoupled control of LIM. The starred variables represent the reference value of these variables and G is a high gain proportional controller. The reference values of the primary voltages are defined [2]

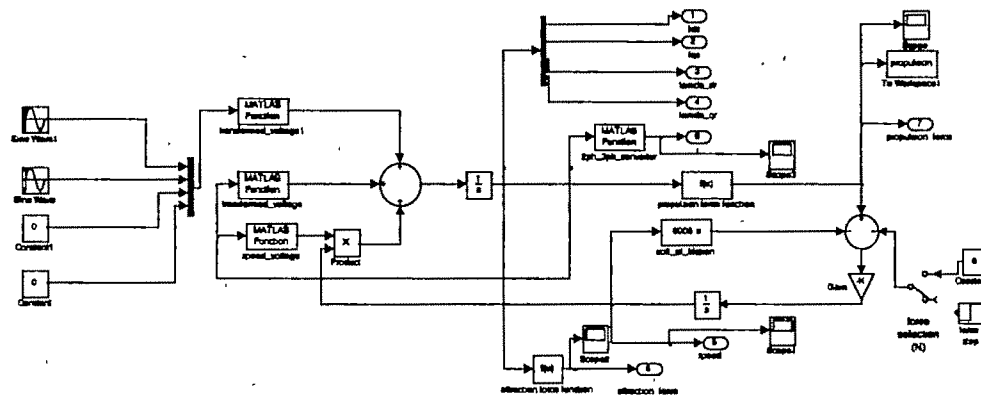


Fig 2 Implementation of d-q model of Linear Induction Motor in Simulink

IV SIMULATION RESULTS AND DISCUSSION

Simulink model of uncontrolled LIM is shown in Fig. 2. Specifications of LIM used in this study are given in Table I.

Table I. IT-BHU Varanasi Centre LIM Specifications

Dimensions	Value
Pole pitch	0.1209 m
No. of Pole	8
Primary resistance	6.36 Ohm
Secondary resistance	3.84 Ohm
Primary leakage inductance	0.06 H
Secondary leakage inductance	0.055 H
Magnetizing inductance	0.168 H
Frequency	50 Hz
Power	20 kW
Voltage	220 volts
Current	18 Amp

Table II gives details of studies conducted on uncontrolled LIM to see the effect of transverse-effect. Figs.5-8 give the variation of F_a and F_t w.r.t. time with 20N load at 0.6 sec. and the results are tabulated in Table III. It is seen that due to transverse edge effect the F_a/F_t ratio increases. From Fig. 5-6 it is also seen that the settling time reduces when the transverse edge effect is considered.

Table II Cases studied for uncontrolled LIM

Force	Without transverse edge effect	With transverse edge effect
F_t	Fig5	Fig6
F_a	Fig7	Fig8

Table III : Ratio of F_a/F_t for uncontrolled LIM

Without transverse edge effect	With transverse edge effect
0.395	0.40

Table IV gives details of studies conducted on decoupled controlled LIM. Fig 9-14 give the variation of F_a and F_t w.r.t. time with 20N load for two different flux-commands and Table V presents value of F_a/F_t ratio for

two different reference fluxes. From the Table it can be concluded that the ratio F_a/F_t and hence F_a can be controlled with a decoupled controller by controlling the reference flux command and the propulsion force by controlling the reference speed command.

Table IV: Cases studied for decoupled controlled LIM

Ref speed		Ref flux		F_t	F_a
12m/s	10m/s	0.5wb	2.0wb		
√	----	√	----	Fig. 9	Fig. 11
√	----	----	√	Fig. 10	Fig. 12
----	√	√	----	Fig. 13	Fig. 14

Table V: Ratio of F_a/F_t for different reference fluxes at starting for decoupled controlled LIM

Reference flux (wb)	F_a/F_t
0.5	0.122
2.0	0.91

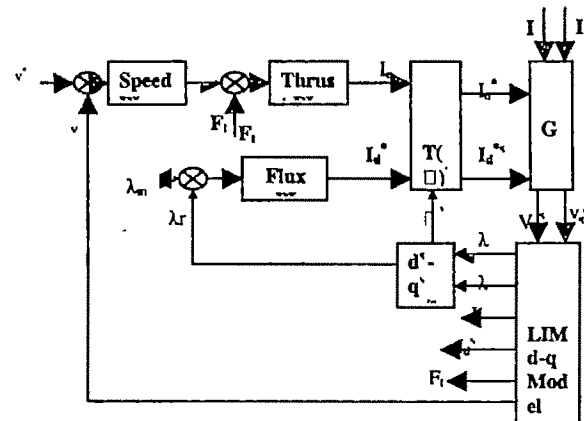


Fig 3 Block diagram of Decoupled control of LIM

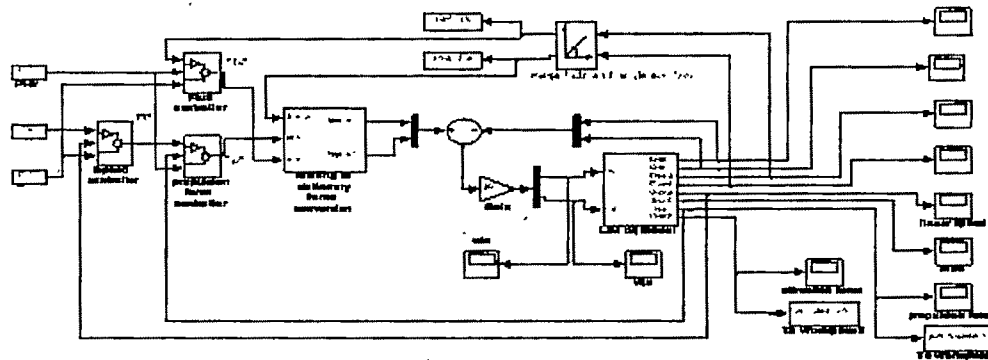


Fig 4 Implementation of decoupled control of LIM

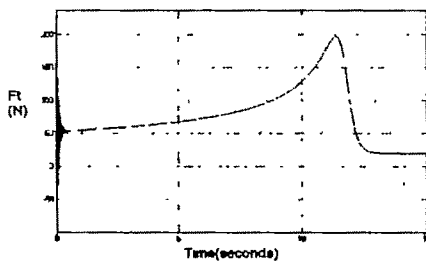


Fig 5 propulsion (N) vs time (sec) characteristics of uncontrolled LIM with load 20N at 0.6 sec. without transverse edge effect

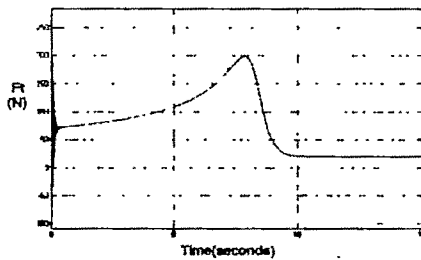


Fig 6 Propulsion (N) vs time (sec) characteristics of uncontrolled LIM with load 20N at 0.6 sec. with transverse edge effect

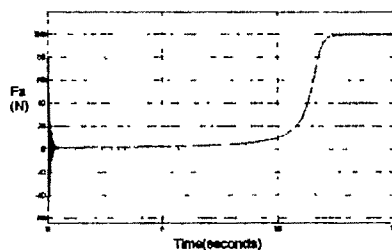


Fig 7 Attraction (N) vs time (sec) characteristics of uncontrolled LIM with load 20N at 0.6 sec. without transverse edge effect

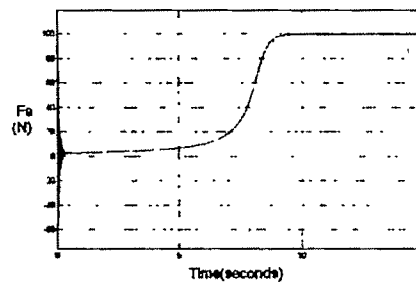


Fig 8 Attraction (N) vs time (sec) characteristics of uncontrolled LIM with load 20N at 0.6 sec. with transverse edge effect

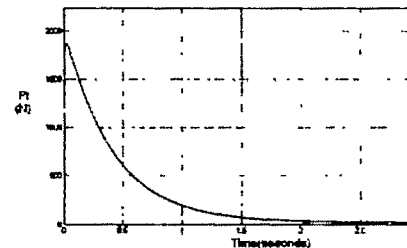


Fig 9 Propulsion force (N) vs time (sec) characteristics of decoupled control of LIM with Ref. speed command 12m/s & Ref. flux command 0.5 wb with transverse edge effect

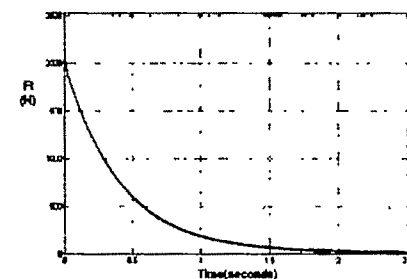


Fig 10 Propulsion force (N) vs time (sec) characteristics of decoupled control of LIM with Ref. speed command 12m/s & Ref. flux command 2 wb with transverse edge effect

V CONCLUSIONS

An equivalent circuit model has been developed for the decoupled control of a linear induction motor. Simulation results show that with decoupled control the ratio of F_a/F_t at starting is reduced in comparison to the uncontrolled LIM. With a decoupled control of LIM the forces of attraction and propulsion can be controlled independently.

REFERENCES

- [1]. A.K. Rathore and S. N. Mahendra, "Modelling and Simulation of Linear Induction Motor Transients Using MATLAB/SIMULINK," International Conference on Electrical Engineering (ICEE) Proceeding, July 2003.
- [2]. M. A. Ouhrouche, "Simulation of Direct Field Oriented Controller for an Induction Motor Using MATLAB/SIMULINK Software Package," Proceedings of the IASTED International Conference, May 15-17, 2000, Pittsburgh, Pennsylvania, USA
- [3]. I. Takahashi and Y. Ide, "Decoupling Control of Thrust and Attractive Forces of an LIM Using a Space Vector Control Inverter," IEEE Transactions on Industry Applications, Vol. 29, pp. 161-167, January/February 1993.
- [4]. S. N. Mahendra, "On Design, Analysis and Fabrication of LIM for ITBHU Malaviya Center for Development & Evaluation of Low Cost LIM Propelled Rail Metro System", Department of Electrical Engineering, Banaras Hindu University, Varanasi, India, 1997.
- [5]. S. N. Mahendra, " LIM Based Traction: Philosophy, Selection, Design Aspects and Application to Transport Sector," International Workshop on LIM Propelled Rail Metro System, Banaras Hindu University, Varanasi, India
- [6]. A.K. Rathore and S. N. Mahendra, "Direct Secondary Flux Oriented Control of Linear Induction Motor Drive", IEEE International Conference On Industrial Technology ICIT Dec 2006, pp1586-90. IIT Mumbai
- [7]. P. Choudhry, "Decoupled control of Linear Induction Motor", M.Tech. dissertation submitted in Dept. of Elect. Engg IT-BHU. Supervisor Dr. S. N. Mahendra. 2007

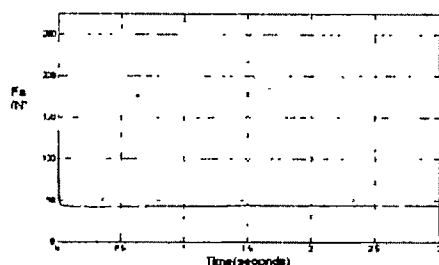


Fig 11 Attraction force (N) vs time (sec) characteristics of decoupled control of LIM with Ref. speed command 12m/s & Ref. flux command 0.5 wb with transverse edge effect

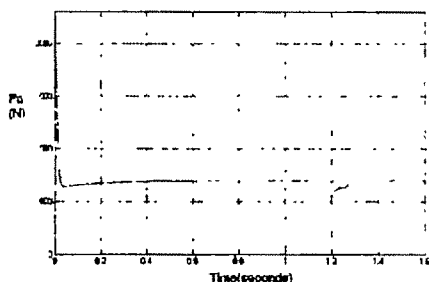


Fig 12 Attraction force (N) vs time (sec) characteristics of decoupled control of LIM with Ref. speed command 12m/s & Ref. flux command 2 wb with transverse edge effect

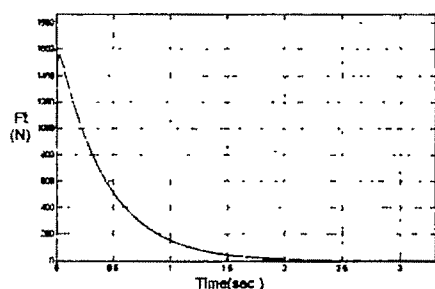


Fig 13 Propulsion force (N) vs time (sec) characteristics of decoupled control of LIM with Ref. speed command 10m/s & Ref. flux command 0.5 wb with transverse edge effect

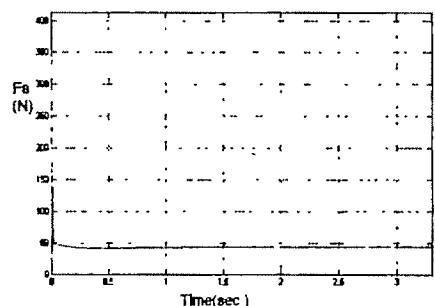


Fig 14 Attraction force (N) vs time (sec) characteristics of decoupled control of LIM with Ref speed command 10m/s & Ref flux command 0.5 wb with transverse edge effect

Fault identification of An Induction Motor by Fractal Analysis Technique

Dilip Dey¹, P. B. Duttagupta², S. Sengupta³

¹Dept of Instrumentation Engineering, Haldia Institute Of Technology, Haldia, Purba Medinipur, West Bengal, (e-mail: dilip_de@rediffmail.com / dilip_de@indiatimes.com)

² Dept of Instrumentation Engineering, Haldia Institute of Technology, Haldia, Purba Medinipur, West Bengal.

³Dept of Applied Physics, University College of Technology, Kolkata, West Bengal (e-mail: samarsgp@vsnl.net)

Abstract— Phase current and vibration of any type induction motor change when fault occur. This paper presents the application of the concept of fractal geometry to analyze chaotic properties fault. Root-mean- square value of current and instantaneous values of vibration is used to characterization of temporal system behavior; this result in relatively short time-series available for analysis. An algorithm is presented for pattern recognition and detection if faults; it is based on techniques suited for analysis. It is based on techniques suited for analysis of relatively small data sets. This paper also presents an approach for quantization of power system behavior which lies between strict fractal dimension calculation algorithms and statistical estimation of randomness of change of variables in the system.

Key words— Induction motor, current signal, vibration signal, rotor unbalance fault, fractals.

I INTRODUCTION

MOTORS today use two thirds of the total electricity consumed in the industry. The industry is becoming increasingly concerned about the ability of motors to ride through power system disturbances [1-2]. The majority of motors in the field are induction motor and there are many method pertinent to fault identification. The induction motor faults are generally classified as either mechanical or insulation system faults. Common mechanical faults include rotor bar breakage, rotor end ring cracking, static and/or dynamic air-gap irregularities, stator winding faults, bent shaft, rotor unbalance, bearing gearbox failures etc. Statistical data [3] shows that mechanical faults are responsible for more than 95% of all failures.

There are different methods for detection of mechanical faults. Typical examples as related to this may include detection of air-gap eccentricity, shaft and bearing faults by monitoring the vibration signal [4], acoustic noise, radio

frequency emission monitoring, partial discharge measurement, motor current signature analysis etc.

Different concepts of fractal geometry have been employed in recent years for quantization of chaotic behavior of nonlinear systems [5]. Fractal dimensions, Lyapunov exponents, entropies, attractors etc. have been used with different rate of success for distinction between random noise in the system and chaos determined by some underlying physical process [6].

In the field of Engineering and Science different tools are used to studies the time varying signals. If there is a series of large no of data sets, estimation of fractal dimensions can be performed quite reliable. In recent years, estimation of fractal dimension has been sought for small data sets as well with their length in the range of several hundred data points.

This paper presents an approach for quantization of the behavior of faulty motor which lies between strict fractal dimension calculation algorithms and statistical estimation of randomness of change of vibration in the system. This compromise allows adjustment of sensitivity of the algorithm to changes of input values on different time scales, from fraction of second to multiple minutes.

II. FAULT DATA FROM THE MOTOR

Vibration monitoring is a reliable tool for detecting bearing failures, rotor unbalance failures. Vibration data typically contain fault signatures and salient fault features because of direct measurement of the critical signal and placement of the vibration sensor. However, placing a sensing device on the motor might not be possible or practical in many applications, especially for a facility that employs a large number of electrical machines. For vibration measurement electromechanical systems are often equipped with mechanical sensors, primarily vibration sensors based on proximity probes. These are too expensive for industrial systems, and can cause heavy loss to the customer. This is why, in spite of the existence of vibration methods, it has been suggested that stator current monitoring can provide the same information without requiring access to the motor body. On the other hand, stator current is readily available in many applications, and is usually measured for motor protection. Many papers have been

published presenting methods for indication of these faults by use of stator current measurement.

In the present paper, some experiments and fractal analysis are presented using motor vibration signal.

III. FRACTAL ANALYSIS

A. Theoretical Background:

The fractal dimension (FD) of a waveform represents a powerful tool for transient detection. The term "fractal dimension" refers to a non-linear or fractional dimension of any object. Calculating the FD of waveforms is useful for transient detection with the additional advantage of fast computation. It consist of estimating the dimension of a time varying signal (waveform) directly in time domain, which allows significant saving in program run-time [7]. Given the S set of N data points $\{R_i\}$ in a metric space, a capacity fractal dimension can be found, using box counting technique [8]

$$d_B = \lim_{\epsilon \rightarrow 0} \frac{\log N_B(\epsilon)}{\log(1/\epsilon)} \quad \dots\dots\dots(1)$$

where $N_B(\epsilon)$ is a minimal number of boxes (squares of two dimensional sets) neede to cover the set, and ϵ is the linear size of box.

Information dimension d_I is similar to the capacity of dimension , except that N_B is subtituted with the average information entropy function:

$$I(\epsilon) = \sum_{k=1}^{N(\epsilon)} -P(\epsilon, k) \log(P(\epsilon, k)) \quad \dots\dots(2)$$

where $P(\epsilon, k)$ is the probability of the event that the k-th box of size ϵ contains point of set S.

One of the most popular measures is the spatial correlation dimension [8]

$$d_c = \lim_{r \rightarrow 0} \frac{\log C(r)}{\log r} \quad (3)$$

where the correlation integral, $C(r)$ is given by

$$C(r) = \lim_{N \rightarrow \infty} \frac{1}{N^2} \sum_{i=1}^N \sum_{j=1, j \neq i}^N H(r - \|R_i - R_j\|) \quad \dots\dots(4)$$

where H is the Heaviside function, and norm is Euclidian.

The relationship between these three dimensions is defined by the inequality:

$$d_c \leq d_I \leq d_B \quad \dots\dots\dots(5)$$

Although this inequality is theoretically strict, calculated values of fractal dimensions of different objects do not always conform to it, which may serve as indicator of poor estimation of the fractal dimensions.

B. Calculation of fractal dimensions

The fractal dimension value is obtained according to how the fractal itself is built. Fractals are constructed through a process of repetition where a shape is replaced with another shape, that is more complex but similar to the original. Fractals " arise from the iterated application of simple rule,"[9.10]. All fractal shapes are built using the replacement rule.

The temporal dynamics of vibration signal of induction motor is low-dimensional, with values of fractal dimension varying between 1 and 2. It is confirmed by calculation of fractal for

time series-data sets for both normal and faulted conditions and can be for detection and discrimination of faults. Here fractal characteristics of chaotic behavior caused faulty condition are different from normal operation values, the direct use of fractal dimensions for pattern recognition purposes seems to be unreasonable.

Fractal dimensions are calculated for the data set shown in the fig. 1. The absolute theoretical minimum number of data points needed for estimation of fractal is 10d, and another sometimes recommended estimate of minimum number of data point is 24d.

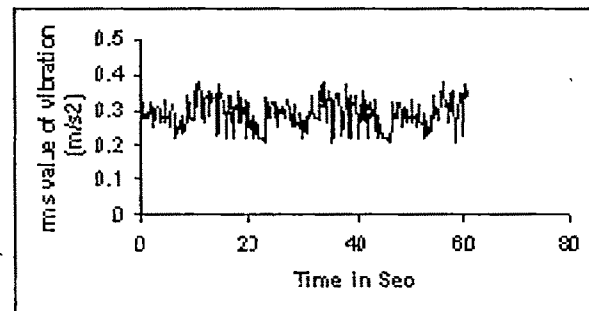


Fig. 1 variation of rms value of vibration with time

The traditional box-counting technique used for estimation of fractal dimension involves monotone increase of the size of the time-vibration rectangles (boxes).Here procedure of increasing the size if the boxes quantizes chaotic temporal variations on different time scales. A somewhat similar, but more flexible concept of combined use of fractal number a classical smoothing function described latter.

Chaos is generally misconstrued as incomprehensible disorder. To start with, chaos is defined as a function with sensitive dependence on initial conditions. A chaotic system is a class of motions in deterministic physical and mathematical systems whose time history has a sensitive dependence on initial conditions.

As an aside, it should be noted here that more precise estimation of fractal dimension of vibration signals could be achieved by using larger set of instantaneous value of vibration signal. However the computational time t_c required for calculation of fractal dimension by the algorithm increases significantly with the number of data points N_B in the subset

$$t_c = f(d_B) N_B \log N_B \quad \dots\dots\dots(6)$$

Where $f(d_B)$ is a slowly varying function which depends on hardware and software used. This time increase hinders the possibility of real-time on-line fault identification. Only RMS values have been used in this paper. Nevertheless, use of more effective algorithms for estimation of fractal dimension could lead to the use of instantaneous vibration value.

IV. DESCRIPTION OF THE ALGORITHM

Here the detection of the algorithm has been designed to insensitive to the amplitude changes of the vibration signal, unless their chaotic temporal behavior changes with the

amplitude as well. This is achieved by the normalization of the values in each subset so that they are in the range of (0,1). A sliding time window is used for calculation of various parameters described below.

A. Fractal Number:

The fractal number F of the m -th data set S_m , which contains N data points is defined as

$$F = \left| 1 - \frac{\sum_{j=1}^{N-1} R_{j+k} - R_j}{\sum_{j=1}^{N-1} R_{j+l} - R_j} \right| 100 \quad \dots\dots\dots(7)$$

where k and l are small integers, which define the interval between neighboring data points, $l > k$. Different norms can be assumed, however, a conventional Euclidean norm has been chosen. From the above equation it is seen that the ratio of metric lengths of the same time sequence is found using two different sampling rates. The algorithm was found to be more effective when the ratio l/k was not an integer. In this case, not all data points from the l -step sampled subset belong to the k -sampled subset, which sometimes causes the fractal number to be less than zero. The minimum sampling frequency required for this algorithm is defined by the smallest common divisor of l and k .

B. Heaviside Function:

The heaviside function $H(s)$ of a parameter s is normally defined as:

$$H(s) = 1 \text{ if } s \geq 0 \quad \dots\dots\dots(8)$$

$$H(s) = 0 \text{ if } s < 0 \quad \dots\dots\dots(9)$$

Once the fractal number, F , is found for the subset of length N , its value is compared with a predetermined threshold value T . If the chaotic variations of the time series are relatively low, and no spike are present in the subset, the fractal number F is lower than the threshold value T , and the Heaviside function is set to 0. If the Heaviside function is higher than the threshold value, it is set to 1 as per the flow-chart.

The period between changes of the Heaviside function is N times as long as the sampling period. The procedure is similar to increasing the box size in the box-counting algorithm.

C. Smoothing Function:

Chaotic variations of the fractal number are not always above the threshold level during the fault, and neither are they always below it during the fault and neither are they always below it during normal conditions. However, they are generally higher during the fault. The decision-making mechanism requires transition from flickering value of the Heaviside function to the state of accumulated confidence that the rotor unbalance fault indeed has happened, and it has not self cleared. This is achieved by using the smoothing technique.

Smoothing function $SM(t)$ for the time-changing Heaviside function $H(s(t))$ at the time t_0 is defined as

$$SM(t_0) = 0 \text{ if } \int_{t_0-\omega/2}^{t_0+\omega/2} H(s(t))dt < 0.5 \quad \dots\dots\dots(10)$$

where ω is the width of the smoothing window. For better performance, the smoothing has been performed twice by putting $SM(t)$ under the integral the integral instead of $H(s(t))$ of the above equation.

D. Fault Identification:

The final decision for identification of the fault. An intrinsic delay of $n\omega/2$ in the decision making process exists where n is the number of runs of a smoothing function. The shaded rectangles of the Figs..... show the width of the sliding window which contains information necessary for the output of the fault identification function .

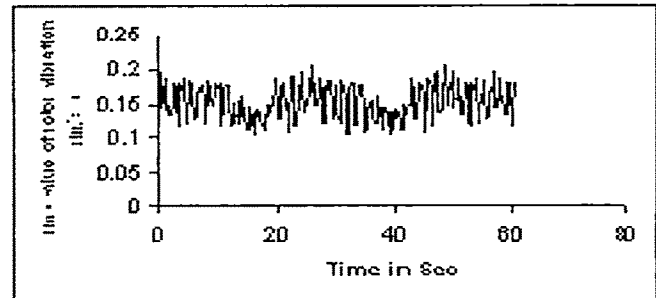


Fig 2.1 (a) RMS value of the vibration at the normal condition

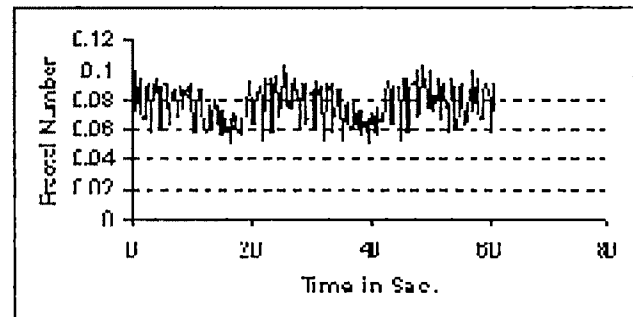


Fig. 2.1 (b) Fractal number variation with time at the normal condition

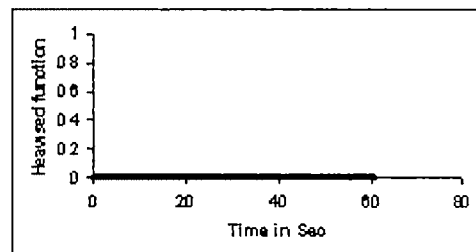


Fig. 2.1 (c) Heaviside function with time at the normal condition

Fig.2.1(a) and 2.2 (a) shows the RMS value of the vibration signal at the normal and faulty condition respectively. The problem encountered with existing algorithms is that not only fault but also different transients are sometimes detected, and distinguishing between transients and faults is hard to perform automatically. Sharp transients probably are caused

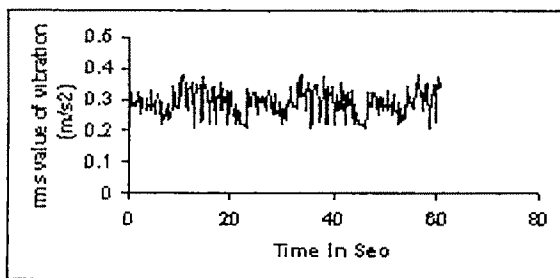


Fig. 2.2 (a) RMS value of the vibration faulty condition

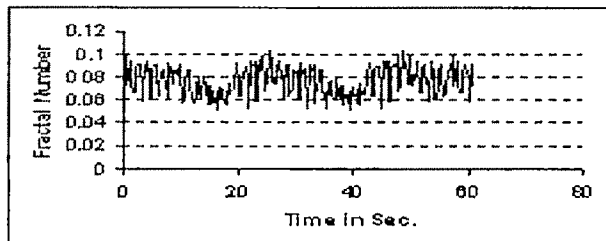


Fig. 2.2(b) Fractal number variation with time at the faulty condition

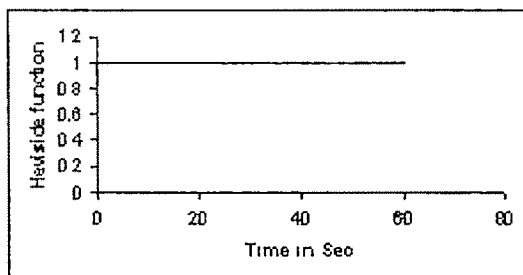


Fig. 2.2 (c) Heaviside function with time at the faulty condition

by unsuccessful starting of a large electric motor; the Heaviside function is virtually unaffected by them because the values of the fractal number remain low. One random spike, still of a fairly low value is picked up by the Heaviside function but eliminated in the smoothing step.

V. CONCLUSIONS

This is a new method for induction motor mechanical faults are obtained by Fractal analysis of the vibration signal. Faults can be detected in the time series of changing RMS values of the vibration signals using concept of fractal analysis. This can be used for the purpose of online noninvasive detection diagnosis of mechanical faults. One major advantage is that the described algorithm allows distinction between switching transients in the system and faults. Sensitivity to different aspects of chaotic changes in time series can be adjusted by changing several key parameters of the algorithm

ACKNOWLEDGMENT

The authors are grateful to TEQIP for financial support and Haldia Institute of Technology for encouragement.

REFERENCES

- [1] J. S. Hsu, and B. P. Scogging, "Field Test of motor efficiency and load changes through air gap torque," IEEE Trans. Energy Conv. Vol.10, no 3, pp.471-477, Sept 1995.
- [2] A. H. Bonnet, "An update on AC induction motor efficiency," IEEE Trans. Industry Application, Vol.30, no. 5, sept/oct.1994.
- [3] Zhongming Ye, Bin Wu and Alireza sadeghian, "Current signature analysis of Induction Motor Mechanical Faults by Wavelet Packet Decomposition," IEEE Trans.on Industrial Electronics Vol.50, No.6, December 2003.
- [4] D. Dorrell, W. Thomson and S. Roach, "Analysis of air gap flux, current and vibration signals as function of the combination of static and dynamic air gap eccentricity in 3-phase induction motors," IEEE Trans. Ind Application, vol 33, pp.24-34, Jan/Feb.1996
- [5] A. Namajunas and A. Tamasevicius, "A Technique for measuring Fractal Dimensions from Time Series on a Real-time Scale," Physica D. Nonlinear Phenomena, Vol 58, No.1-4, 1992, pp 482-488
- [6] J. B. Ramsey and H. J. Yuan, "The Statistical Properties of Dimension Calculations Using Small Data Sets," Nonlinearity, Vol.3 No. 1, 1990, pp 155-176.
- [7] R. Esteller, G. Vachtsevanos, J. Echauz, B. Litt, "A Comparison of Fractal Dimension Algorithms Using Synthetic And Experimental Data," IEEE ,1999(0-7803-5471-0/99/\$10.00) pp 11-199-202
- [8] A. V. Mamishev, B. D. Russell, Carl L. Benner, "Analysis of High Impedance Faults Using Fractal Technique" IEEE Trans on power system Vol 11, No. 1, February 1996
- [9] L. Lazareck, G. Verch, J. K. Peters, "Fractals in Circuits," pp 0589 -0594
- [10] McGuire, Michel "An Eye For Fractals, A Graphic & Photographic Essay," New York: Addison-Wesley Publishing Company, 1991.

Multi-Class Fault Identification of Induction Motor by Using Support Vector Machine

Dilip Dey¹, P. B. Duttagupta², S. Sengupta³

¹Dept of Instrumentation Engineering, Haldia Institute Of Technology, Haldia, India,
e-mail: dilip_de@rediffmail.com

²Dept of Instrumentation Engineering, Haldia Institute of Technology, India.

³Dept of Applied Physics, University of Calcutta, Kolkata, India, e-mail. samarsgp@vsnl.net)

Abstract— Mechanical vibrations become a serious concern in drive applications when they adversely affect the dynamic performances of these applications and may end with physical deterioration of their structures. Support Vector Machine (SVM) is used to classify different faults of the induction motor based on motor vibration or motor current. Here support vector training can be practically implemented, kernel mapping technique which is used to construct SVM solutions, it has large VC dimension for homogeneous polynomial and Gaussian radial basis function kernels. A SVM based classification routine is applied to the PSD estimates to perform the fault classification of an induction motor and there exist several fault in addition to healthy operation.

Key words—Electrical Machines, Vibration Monitoring, Fault Classification, Data Fusion, Support Vector Machine, Power spectra Density. VC dimension, Pattern recognition.

I. INTRODUCTION

All electric machines have complex mechanical structures that oscillate and coupled parts of machines generate noise and vibration, and the analysis of the produced noise and vibration can be used to provide information on the condition of the machine, including some of its parts. Noise and vibration in electrical machines are mainly caused by forces which are magnetic, mechanical aerodynamic origin. The largest sources of vibration in electrical machines are the radial forces due to the air-gap field. Since the air gap flux density distribution is the product of the resultant m.m.f. wave and the total permeance wave. The resultant m.m.f. also contain the effects of possible stator or rotor asymmetries. The permeance wave depends on the variations of the air-gap as well the resulting magnetic forces. Vibration will also depends on these asymmetries [1,2].

Vibration can also arise due to vibration transmitted from the supporting structure to motor or due to asymmetries in the power supply, or unbalances in the driven load. Even small amplitude of vibrations can cause large amount of damage in different parts of the machine. When a mechanical part of the motor either wears or breaks up, a frequency component in the spectrum will change. Thus it is important to monitor the vibration signals [2].

Vibration monitoring system requires storing of a large amount of data. Vibration in electrical machines can be monitored by use of vibration transducer (e.g. piezoelectric accelerometers are most widely used transducers for this purpose) mounted on different parts of the machine. For each machine there are typically several vibration signals and the detected vibration signals contain vital information for being analyzed in addition to some static parameters like load [1-3]. The examination of data can be tedious and sensitive to errors. Also, fault related machine vibration is usually corrupted with structural machine vibration and noise from interfering machinery. Further, depending on the sensor position, large deviations on noise may occur in measurements.

Due to these problems intelligent compression of the multi-channel measurement data may aid in data management for fault diagnostics purpose. Independent component analysis (ICA) can be used to find a structure in large amount of multivariate data. ICA may be used to compress measurements from several channels into a smaller amount of channel combinations – statistically independent components of the measurements – that could clearly indicate faults in the machine.

In this article, independent component analysis (ICA) is studied to provide a robust and reliable fault diagnostics routine for a cage induction motor. In our study, resulting independent components are further processed with Power Spectrum Density (PSD) estimation and support vector machine (SVM) [8] – [9] based classification to obtain the knowledge of the motor condition.

II. CLASSIFICATION WITH SUPPORT VECTOR MACHINES:

SVM based classification is a relatively new machine learning method based on statistical learning theory [6]. In SVM, an optimal hyperplane is determined to maximize the generalization ability of the classifier by mapping the original input space into a high dimensional dot product space called feature space.

A. Brief overview of some multi-class SVM methods

a. one-against-all method:

For k-class problem, the one-against-all method constructs k SVM models. The *i*th SVM is trained with all of the training

examples in the i th class with positive level and all other examples with negative labels [18]. The final output of the one-against-all method is the class that corresponds to the SVM with the highest output value. Given l training examples $(x_1, y_1), (x_2, y_2), \dots, (x_l, y_l)$, where $x_j \in R$, $j = 1, \dots, l$ and $y_j \in \{1, 2, \dots, k\}$ is the class of x_j , the i th SVM solves the following optimization problem:

$$\min \frac{1}{2} \|w^i\|^2 + C \sum_{j=1}^l \xi_j' \quad \dots \dots \dots (1)$$

subject to

$$\langle \phi(x_j), w^i \rangle + b^i \geq 1 - \xi_j', \text{ if } y_j = i,$$

$$\langle \phi(x_j), w^i \rangle + b^i \geq -1 + \xi_j', \text{ if } y_j \neq i,$$

$$\xi_j' \geq 0, \quad j = 1, \dots, l.$$

The decision function of the i th SVM is

$$f_i(x) = \langle \Phi(x), w^i \rangle + b^i \quad \dots \dots (2)$$

A point x is in the class that corresponds to the largest value of the decision function:

$$\text{The class of } x = \arg \max_{i=1, \dots, k} (\langle \Phi(x), w^i \rangle + b^i).$$

b. All-together method:

Vapnik proposed an approach for multi-class problems that constructed a single optimisation problem by considering all classes at once [18]. It is similar to the above method. It calculates k decision functions where the m th decision function

$\langle \Phi(x), w^m \rangle + b^m$ separates the training examples of the class m from the other examples. In the one-against-all method there are k different optimisation problems whereas in this method all are obtained by solving one optimisation problem. The formulation is as follows:

$$\min \frac{1}{2} \sum_{j=1}^l \|w^m\|^2 = C \sum_{j=1}^l \sum_{m \neq y_j} \xi_j^m \quad \dots \dots (3)$$

$$\text{subject to } \langle \Phi(x_j), w^m \rangle + b^m \geq \langle \Phi(x_j), w^m \rangle + b^m + 2 - \xi_j^m$$

$$\xi_j^m \geq 0, \quad j = 1, \dots, l.$$

$$m \in \{1, \dots, k\} \setminus y_j$$

A point x is in the class that corresponds to the largest value of the decision functions:

$$\text{The class of } x = \arg \max_{m=1, \dots, k} (\langle \Phi(x), w^m \rangle + b^m).$$

Which is same as one against all method.

B. The Vapnik-Chervonenkis (VC) Dimension :

The VC dimension is a property of a set of functions $\{f(\alpha)\}$ (again, we use α as a generic set of parameters: a choice of α specifies a particular function), and can be defined for various classes of function f . Here we will only consider functions that correspond to the two-class pattern recognition case, so that $f(x, \alpha) \in \{-1, +1\}$. Now if a given set of l points can be labeled in all possible 2^l ways, and for each labeling, a member of the set $\{f(\alpha)\}$ can be

found which correctly assigns those labels, we say that that set of points is shattered by that set of functions. The VC dimension for the set of functions $\{f(\alpha)\}$ is defined as the maximum number of training points that can be shattered by $\{f(\alpha)\}$. Note that, if the VC dimension is h , then there exists at least one set of h points that can be shattered, but in general it will not be true that every set of h points can be shattered [11]. VC dimension of the set of a hyper plane is equal to $n+1$ (Where n is the dimension of the space).

C. Δ -Margin separating hyper-plane :

Let $x_j = x \in R^n$, be a sample of $x \in R^n$ and belong to Class I or Class II. For linearly separable data, it is possible to determine a hyperplane that separates the data leaving one class on one side of the hyperplane, the other on the other side. This plane can be describe by the equation:

$$f(x) = w^T x + b = \sum_{j=1}^l w_j x_j + b = 0 \quad \dots (4)$$

where $w \in R^n$ is a weight vector and b is a scalar. The vector w and the scalar b determine the position of the separating hyperplane.

Let us define the label y_i associated to x_i as $y_i = 1$ if x_i belongs to Class I, $y_i = -1$ if x_i belongs to Class II. A

separating hyperplane satisfies the constraints $f(x_i) \geq 0$, if $y_i = 1$, and $f(x_i) < 0$, $y_i = -1$. A separating hyperplane is called a Δ -margin separating hyperplane, if it satisfies $\|w\| = 1$ and

$$y = 1, \text{ if } w^T x + b \geq \Delta \quad \dots \dots \dots (4)$$

$$y = -1, \text{ if } w^T x + b \leq -\Delta \quad \dots \dots \dots (5)$$

However, Vapnik has shown that, if $x \in R^n$ belong to sphere of radius R , the VC dimension of Δ -margin separating hyperplanes is bounded by the following:

$$d \leq \left\lceil \left[\frac{R^2}{\Delta^2} \right] \cdot n \right\rceil + 1 \quad \dots \dots \dots (6)$$

D. Maximal margin classification:

When formulating SVMs [11], Δ -margin separating hyper planes are considered with aim to maximize the margin and setting $\Delta = \frac{1}{\|w\|}$, so that $f(x_i) \geq +1$, if $y_i = +1$ and $f(x_i) \leq$

-1 , if $y_i = -1$. The inequalities can be combined with equation (3.2.1) so that:

$$y_i f(x_i) = y_i (w^T x_i + b) \geq 1, \quad \text{for } i=1, 2, \dots, M \quad \dots (7)$$

The margin can also be calculated through the geometrical margin γ , which is defined as half of the sum of the distance between arbitrary separating hyperplane the nearest negative and positive datum (x^- and x^+):

$$\gamma = \frac{1}{2} \left(\left(\frac{-w^T (x^0 - x^+)}{\|w\|_2} \right) - \left(\frac{-w^T (x^0 - x^-)}{\|w\|_2} \right) \right)$$

$$= \frac{1}{2\|w\|_2} ((w^T x^+) - (w^T x^-))$$

..... (8)

Where x^0 is a point on a hyperplane. The separating hyperplane that maximizes the margin is called the optimal separating hyperplane. An example of optimal separating hyperplane of two datasets is in the fig 2.3.

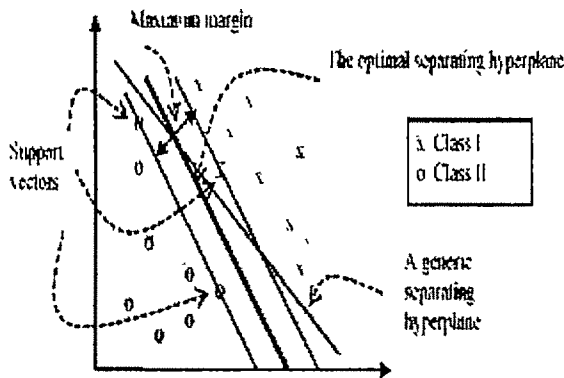


Fig. 1 Optimal Hyperplane

The optimal separating hyperplane can be searched among so-called canonical hyperplanes, which fulfil $w^T x^+ + b = 1$ and $w^T x^- + b = -1$, leading to the following simplified expression for the geometrical margin:

$$\gamma = \frac{1}{\|w\|_2} \quad \dots\dots\dots (9)$$

Since the optimal hyperplane maximizes the margin, it can be found by solving the following convex quadratic optimisation problem:

$$\text{minimize } \frac{1}{2} \|w\|^2$$

subject to $y_i (w^T x_i + b) \geq 1 \quad \dots\dots\dots (10)$

If the number of attributes of data examples is large, the calculations can be considerably simplified by converting the problem to the equivalent Lagrange dual problem. The Lagrange function for equation (4) is:

$$L(w, b, \alpha) = \frac{1}{2} (w^T w) - \sum_i \alpha_i [y_i ((w^T x_i) + b) - 1] \quad \dots\dots (11)$$

where $\alpha = (\alpha_1, \alpha_2, \alpha_3, \dots, \alpha_M)^T$ is the Lagrange multiplier. The dual problem is :

maximize $L(w, b, \alpha)$

subject to $\alpha_j \geq 0, j=1, 2, \dots, M \quad \dots\dots (12)$

By differentiating equation (11) with respect to w and b and imposing stationary, we get:

$$\frac{\partial L}{\partial w} (w, b, \alpha) = w - \sum_{i=1}^M y_i \alpha_i x_i = 0 \quad \dots\dots (13)$$

$$\frac{\partial L}{\partial b} (w, b, \alpha) = \sum_{i=1}^M y_i \alpha_i = 0$$

From equation (11) & (13) the dual representation of the optimization problem is achieved:

$$\text{maximize } W(\alpha) = \sum_{i=1}^M \alpha_i - \frac{1}{2} \sum_{i,j=1}^M \alpha_i \alpha_j y_i y_j x_i^T x_j$$

subject to $\sum_{i=1}^M y_i \alpha_i = 0$

$\alpha_i \geq 0, i = 1, 2, \dots, M$

... (14)

where α is the Lagrange multiplier vector. Let us assume that optimal solution for the dual problem is α^* and b^* . According to the Karush-Khun-Tucker theorem, the equality condition holds for training input-output pair. In this case, the training example x_i is called a support vector (SV), i.e. the SVs are such training samples that are on the margin of two datasets. As shown in the fig.

These samples give the name to this learning machine, because they show to be very important in the classification both computationally and concerning the generalization.

E. The Non-Separable Case :

For non-separable data, will find no feasible solution: this will be evidenced by the objective function (i.e. the dual Lagrangian) growing arbitrarily large. Here it is done by introducing positive slack variables $\xi_i, i=1, 2, \dots, l$ in the constraints (Cortes and Vapnik, 1995), which then become:

$$x_i \cdot w + b \geq +1 - \xi_i, \text{ for } y_i = +1 \quad \dots\dots\dots (15)$$

$$x_i \cdot w + b \geq -1 + \xi_i, \text{ for } y_i = -1 \quad \dots\dots\dots (16)$$

Thus, for an error to occur, the corresponding ξ_i must exceed unity, so $\sum \xi_i$ is an upper bound on the number of training errors. Hence a natural way to assign an extra cost for errors is

to change the objective function be minimized from $\|w\|^2 / 2$ to $\|w\|^2 / 2 + C(\sum_i \xi_i)^k$, where C is a parameter to be chosen by the user, a larger C corresponding to assigning a higher penalty to errors. As it stands, this is a convex programming problem for any positive integer k ; for $k=2$ and $k=1$ it is also a quadratic programming problem, and the choice $k=1$ has the further advantage that neither the ξ_i , nor their Lagrange multipliers, appear in the Wolfe dual problem, which becomes: Maximize:

$$L_D = \sum_i \alpha_i - \frac{1}{2} \sum_{i,j} \alpha_i \alpha_j y_i y_j x_i^T x_j \quad \dots\dots (17)$$

subject to :

$$0 \leq \alpha_i \leq C \quad \dots\dots\dots (18)$$

$$\sum_i y_i \alpha_i = 0 \quad \dots\dots\dots (19)$$

The solution is again given by

$$w = \sum_{i=1}^N \alpha_i y_i x_i \quad \dots\dots\dots (20)$$

Thus the only difference from the optimal hyperplane case is that the α_i now have an upper bound of C. The situation is summarized schematically in Figure 2.4.

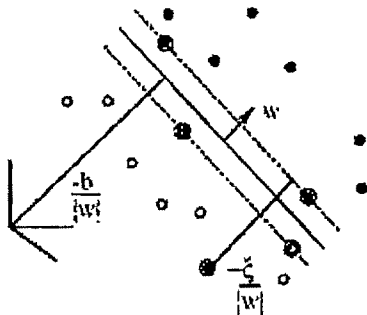


Figure:2 Linear separating hyperplanes for the non-separable case

We will need the Karush-Kuhn-Tucker conditions for the primal problem. The primal Lagrangian is

$$L_p = \frac{1}{2} \|w\|^2 + C \sum_i \xi_i - \sum_i \alpha_i \{y_i(x_i \cdot w + b) - 1 + \xi_i\} - \sum_i \mu_i \xi_i \quad \dots\dots\dots (21)$$

where the μ_i are the Lagrange multipliers introduced to enforce positivity of the ξ_i , The

KKT conditions for the primal problem are therefore

$$\frac{\partial L}{\partial w}(w, b, \alpha) = w - \sum_{i=1}^M y_i \alpha_i x_i = 0 \quad \dots\dots\dots (22)$$

$$\frac{\partial L}{\partial b}(w, b, \alpha) = \sum_{i=1}^M y_i \alpha_i = 0 \quad \dots\dots\dots (23)$$

$$\frac{\partial L}{\partial \xi_i} = C - \alpha_i - \mu_i = 0 \quad \dots\dots\dots (24)$$

$$y_i(x_i \cdot w + b) - 1 + \xi_i \geq 0 \quad \dots\dots\dots (25)$$

$$\xi_i \geq 0 \quad \dots\dots\dots (26)$$

$$\alpha_i \geq 0 \quad \dots\dots\dots (27)$$

$$\mu_i \geq 0 \quad \dots\dots\dots (28)$$

$$\alpha_i \{y_i(x_i \cdot w + b) - 1 + \xi_i\} = 0 \quad \dots\dots\dots (29)$$

$$\mu_i \xi_i = 0 \quad \dots\dots\dots (30)$$

As before, we can use the KKT complementarity conditions, Eq. (2.4.13) and (2.4.14), to determine the threshold b.

III. MULTI-CLASS SVM CLASSIFICATION ALGORITHM:

SVM was originally designed for binary classification. Multi-class (K- class, $k > 2$) classification can be obtained of binary classification. There is a relationship between the binary classification and multi-classification.

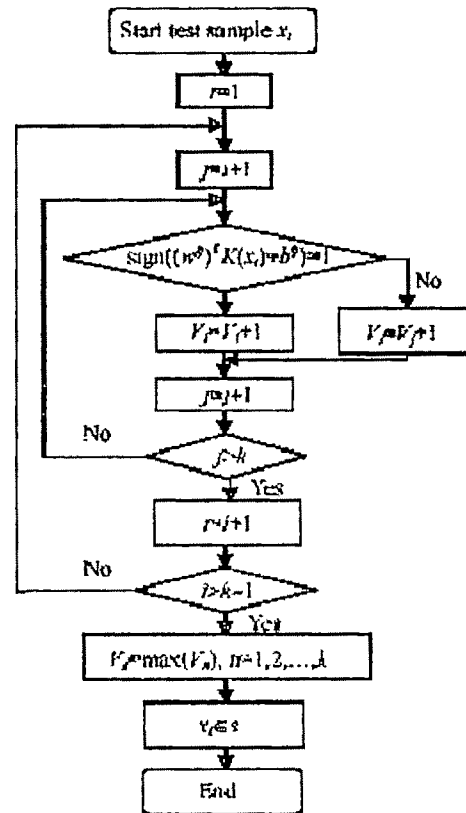


Fig. 3 Flow-chart for SVM classification algorithm
Suppose we have classable K-class problem; then it must be separated from each other by binary classification; On the contrary, in a K-class event, it must be K- class classable if any two classes of it is separable. Two method "one-against-one" and one-against-all" two methods are discussed above. We see that for both the case class of 'x' should be same, each classifier is trained with all the data. In case that two classes have identical votes and both are the maximum, how we can make the decision? In this it may not be good strategy. To deal with this problem we simply we select one with the small index. So it is necessary to number the important or more often appearing fault with small index.

IV. RESULT:

ROTOR UNBALANCE FAULT:

In fig 4.1 presented current and vibrations in a healthy situation with no load.

Training data is formed by calculating PSD estimates from different parts of vibration signal in healthy and rotor unbalance situations [1].

V. CONCLUSION

This system is applied to multi-channel vibration measurements of an induction motor to fuse the measurement information of several channels, and provide robust and reliable rotor unbalance fault detection. All components were found from the measurement set and their PSD estimates were calculated with Welch's method. A SVM based

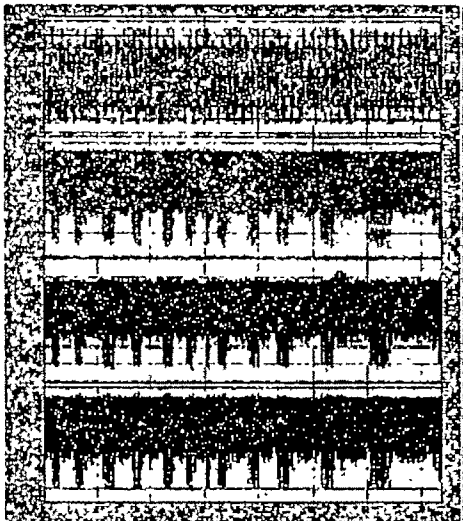


Fig 4.1 : current and vibration measurements (m/s²) in healthy motor

In fig 4.2 presented vibrations when the rotor unbalance fault occur with no load.

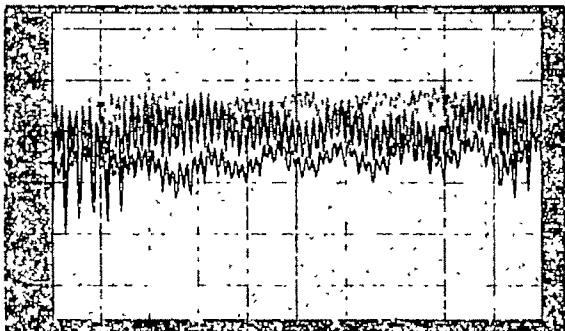


Fig 4.2 : vibration measurements (m/s²) in rotor unbalance situation.

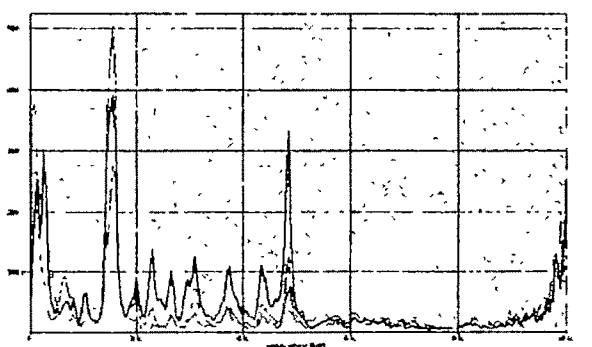


Fig 4.3 : PSD estimation of the Vibration in rotor Unbalance situation.

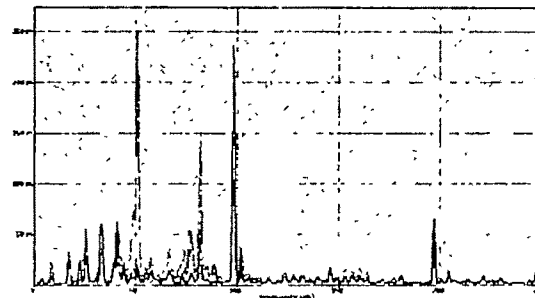


Fig 4. 4: PSD estimation of the Vibration in healthy situation

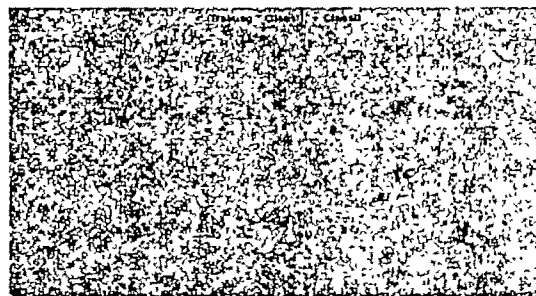


Fig:4.5 Training point for Classification

classification routine was applied to the PSD samples to perform the fault diagnosis which is basically artificial intelligent technique for fault diagnosis.

ACKNOWLEDGMENT

The authors are grateful to TEQIP for financial support and Haldia Institute of Technology for encouragement

REFERENCES

- [1] Sana Poyhonen, Pedro Jover, Heikki Hyotyniemi, " Independent Component Analysis Of Vibrations For Fault Diagnosis of An Induction Motor" Proc. Of the IASTED International Conference, CIRCUITS, SIGNALS, AND SYSTEMS, May 19-21, 2003, Cancun, Mexico.
- [2] Peter Vas , " Artificial- Intelligent- Based Electrical Machines And Drives", OXFORD SCIENCE PUBLICATIONS
- [3] G. Betta, C. Liguori, A. Paolillo, A. Pietrosanto, A., A DSP-based FFT analyzer for the fault diagnosis of rotating machine based on vibration analysis, Proc. IEEE Conf. on Instrumentation and Measurement Technology, Budapest, Hungary, 2001, 572-577.
- [4] R.F.M. Marcal, M. Negreiros, A.A. Susin, J.L. Kovalski, Detecting faults in rotating machines, IEEE Instrumentation & Measurement Magazine, 3(4), 2000, 24-26.
- [5] P.A. Laggan, Vibration monitoring., Proc. IEE Colloquium on Understanding your Condition Monitoring, 1999, 1-11.
- [6] A. Ypma, P. Pajunen, P. Rotating machine vibration analysis with second-order independent component analysis, Proc. of the Workshop on ICA and Signal Separation , Aussois, France, 1999, 37-42.
- [7] A. Ypma, D.M.J. Tax, R.P.W. Duun, Robust machine fault detection with independent component analysis and support vector data description, Proc IEEE Signal Processing Society Workshop on Neural Networks for Signal Processing, Madison, Wisconsin, USA, 1999, 67- 76.
- [8] N. Cristianini, J. Shawe-Taylor, Support vector machines and other kernel-based learning methods (Cambridge University Press, 2000).

- [9] Sanna Poyhonen, " Support Vector Machine Based Classification in Condition Monitoring of Induction Motors", PhD Thesis Technische University Helsinki
- [10] Kristin P. BColin Campbell, " Support Vector Machine Hype or Hallelujah?" SGKDD Explorations December-2000, vol 2, Issue2- page1-4
- [11] Christopher J C. Burges, " A Tutorial On Support Vectro Machine for Pattern Recognition", Data Mining and Knowledge Discovery, 2, 1998 pp 121 – 167
- [12] A Ypma, A Leshem, Blind separation of machine vibration with bilinear forms, Proc. 2nd Int Workshop on ICA and Signal Separation, Helsinki, Finland, 2000, 405- 410.
- [13] A Ypma, A , Leshem, R.P.W. Duin, Blind separation of rotating machine sources bilinear forms and convolutive mixtures, Neurocomputing - Special Issue on ICA/BSS, 49(1-4), 2002, 349-368.
- [14] G. Gelle, M Colas, C Serviere, Blind source separation: A tool for rotating machine monitoring by vibration analysis, Journal of Sound and Vibration, 248(5), 2001, 865-885.
- [15] A. Hyvarinen, J. Karhunen, E. Oja, Independent component analysis (John Wiley & Sons, Inc , NY 2001)
- [16] A. Hyvarinen, Fast and robust fixed-point algorithms for independent component analysis, IEEE Trans on Neural Networks, 10(3), 1999, 626-634.
- [17] J A K Suykens, T Van Gestel, J De Brabanter, B De Moor, J Vandewalle, Least squares support vector machines, (World Scientific, Singapore, 2002).
- [18] R. Debnath Æ N. Takahide Æ H. Takahashi, "A decision based one-against-one method for multi-class support vector machine" Pattern Anal Applic (2004) 7 pp. 164–175

Diagnosis of Fault Due to Unbalanced Rotor of an Induction Motor by Analysis of Vibration and Motor Current Signatures

Subrata Karimakar¹, S.K. Ahamed², M.Mitra³ and S. Sengupta⁴

^{1,3,4} Department of Applied Physics, University of Calcutta, Kolkata.

² Govt. College of Engineering & Textile Technology, Serampur, West Bengal

e-mail: ^{1,2,3,4} (subkarim, ska123_ahamed, madhuchhanda94, samarsgp)@rediffmail.com

Abstract—This paper presents a technique for diagnosis of rotor mass unbalance of an induction motor using analysis of motor vibration and Motor Current Signatures. The signatures of both motor current and vibration for a known faulty motor are first captured and analyzed through FFT to detect diagnostic harmonics for the specific fault. This developed technique has been tested in the laboratory on a machine fault simulator having an unknown motor and seen to show results in conformity with the developed technique. This paper first discusses unbalanced rotor fault of an induction motor and then gives a brief overview of the change in different harmonics present in the stator current and the rotor vibration in the Z-direction in comparison to those present in the healthy motor.

Key words—Data acquisition, Fault diagnosis, FFT, Induction motor, MCSA, Unbalanced rotor fault.

I. INTRODUCTION

Induction motor drives are the most widely used electrical drives due to motor robustness, simple construction, low cost, high efficiency, simple starting arrangement, reliable operation and easy maintenance. About 50% of the total energy used in an industry is consumed by induction motor drives. Hence it is an important issue to avoid any kind of failure of induction motor to avoid any loss in production time or money. Because in many applications the failure in induction motor can shut down, even, the entire industrial process. Operators of electrical motors are under continual pressure to reduce maintenance cost and prevent unscheduled downtime of motors. This necessitate the on-line monitoring of the health of the drive system which gives birth to the condition based maintenance (CBM). In CBM technique, generally, vibration signature analysis is used to diagnose

motor faults which may be electrical or mechanical or any other fault either internal or external.

One of the most inconvenient fault in the induction motor is the unbalanced rotor. There are a lot of causes for rotor unbalance. On review of the recent research works it is seen that many techniques have been proposed for motor fault detection and diagnosis. These techniques include MCSA to detect broken rotor bars [1], [3], [6], [7]; to detect bearing defects [5], [10]; to detect stator short circuit fault [6]; vibration monitoring to detect eccentricity defect [8]; coupling misalignment [11]; acoustic diagnosis technique to detect machine insulation fault [9]. But very little work has been done on mass-unbalance-rotor fault. In this paper, the target is fixed on mass unbalance of the rotor. To diagnose the mass unbalance, besides the vibration signature analysis, Motor Current Signature Analysis (MCSA) is also simultaneously done.

Rotor unbalance is unequal distribution of weight around the center of rotation of rotor due to which the centre of gravity of the rotor does not coincide with the center of rotation causing excessive vibration. Unbalance may happen due to :

- Manufacturing problems,
- Nonsymmetrical mass addition or reduction due to wear, corrosion or erosion etc.,
- Internal misalignment or shaft bending due to thermal expansion or contraction.

Different type of unbalance are :

1. Static unbalance- where rotational axis and weight distribution axis of rotor are parallel but offset.
2. Couple unbalance- here rotational axis and weight distribution axis of rotor intersect at the center of rotor.
3. Dynamic unbalance- here rotational axis and weight distribution axis of rotor do not coincide. It is a combination of static and couple unbalance. It is the most common type of unbalance.

It is known that in a cage winding induction motor rotor current produces an effective 3 phase magnetic field with the

same number of poles as the stator field but rotates at slip frequency $f_1 = s.f$ with respect to the rotating rotor where f is supply frequency and s is slip. With a symmetrical cage winding, only a forward rotating magnetic field exists. If rotor asymmetry occurs then there will also be a resultant backward rotating field at slip frequency with respect to the forward rotating rotor [1]. This implies that unbalance rotor faults can be detected by analyzing the change in current spectrum. The main focus of the paper is to prepare a data bank containing vibration signature and motor current signature at rated speed of a mass-unbalanced-rotor induction motor in comparison to a healthy induction motor and to study their FFT to make a diagnostic to locate this fault in a motor. The same analysis has been applied to an unknown motor in the laboratory in which it is seen that the developed diagnostic gives a good indication of the health of the motor.

II. THEORY

It has been observed that individual faults are sensitive to particular number of harmonics and the amplitude of harmonics changes for different faults. Also if amplitude of these harmonics is over 50dB smaller than the fundamental frequency component amplitude, then the faulty motor can't be differentiated from the healthy one [2].

In case of unbalance rotor of induction motor, air gap flux changes during the run of the motor. As a result induced voltage in the rotor changes which changes the stator voltage and hence stator current also changes. This change in stator current depends on the amount of variation of the air gap flux. It is proportional to the flux density squared waveform in the induction motor [3]. Thus the motor current should give a reflection of the mechanical fault in motor.

Moreover it is well known that mechanical fault in a motor is generally detected by mechanical vibration spectrum analysis. In some cases the vibration analysis alone or MCSA alone may not give sufficient information about the fault in a motor. Hence in this attempt both the signatures are captured and analyzed for detection of the fault.

III. EXPERIMENTAL SETUP

Experiment was carried out by test-set-up built by Spectraquest, USA, having a high speed data acquisition system. Rating of the induction motor is 3ph, 1/3HP, 380V, 50Hz, 2980rpm. An induction motor of same rating with unbalanced rotor is used as faulty motor. Motor is loaded mechanically and is supplied through power supply converter as shown in Fig.1. For current signature Hall Probe (LEM PR30 ACV 600V CATHI 30Ampac/3Vac) and for vibration signature Piezo-electric transducer (IMI 604B31 ICP 9.6Mv/(mm/sec²)) are used. Data for current signature for all the three phases and for vibration signature in X,Y,Z directions are collected.

Vibration Sensor Optical Mech.
Induction Motor speedometer Load

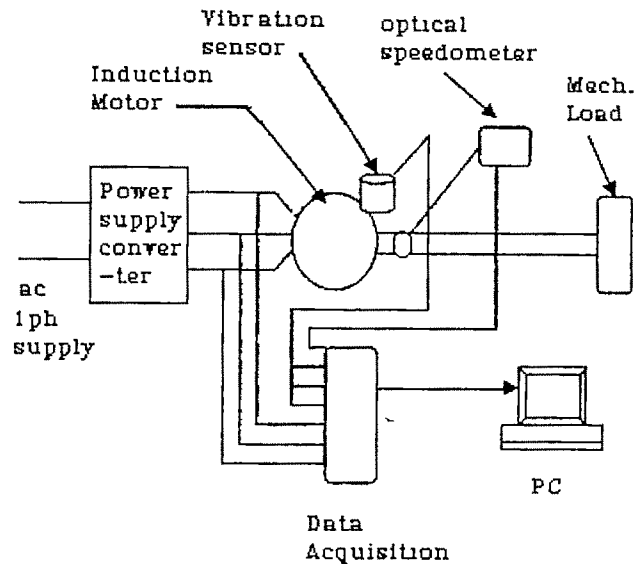


Fig. 1a Block diagram of the Measurement Configuration

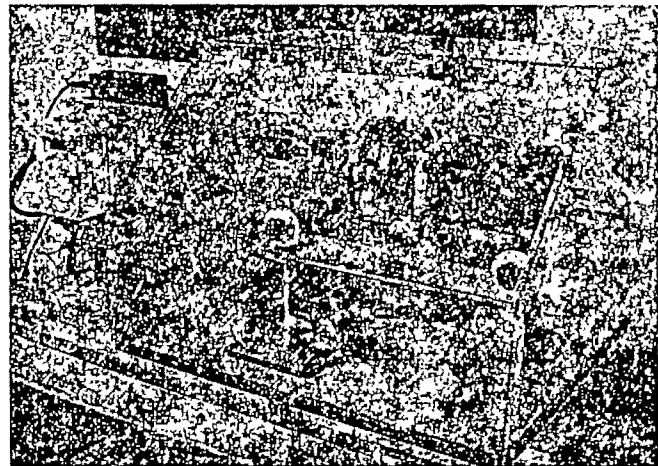


Fig. 1b Experimental Setup

IV. RESULTS AND DISCUSSION

A. Analysis of Current Data: Current data for all the three phases are collected, but being similar for all the phases here only Y phase has been presented. In the following Table 1 the amplitudes of the predominant harmonics are given for the Y phase only, both for healthy and faulty motors of same rating and their graphs are shown in Figs.2, 3, 4. Figs.2a, 3a, 4a for healthy motor and Figs.2b, 3b, 4b for unbalance rotor motor.

Table 1
Data of healthy and faulty motor for MCSA

Spectral Freq (Hz)	harmonic	Amplitude in mV					
		Healthy motor			Unbalanced rotor		
		At No Load	Single Mass Load	double Mass load	At No Load	Single Mass Load	double Mass load

50	1 st	125.6	125	126.6	118.6	118.8	121
100	2 nd	2.615	2.544	2.7	3.442	2.7	2.7
150	3 rd	3.636	3.701	3.782	2.935	3.03	2.8
200	4 th	1.12	1.125	1.153	1.232	1.174	1.2
250	5 th	1.778	1.809	1.83	1.754	1.566	1.743
350	7 th	1.356	1.494	1.586	1.407	1.41	1.65

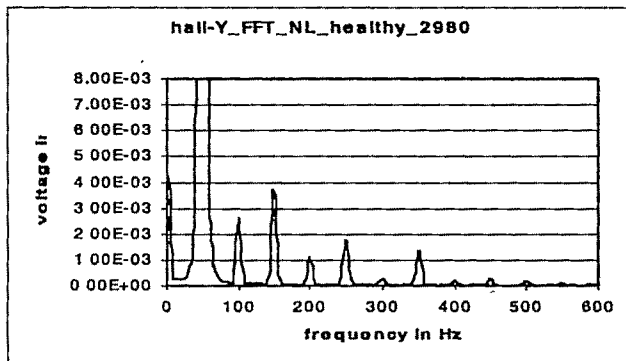


Fig. 2a Hall Probe output of Y phase of healthy motor at 2980rpm under no-load condition

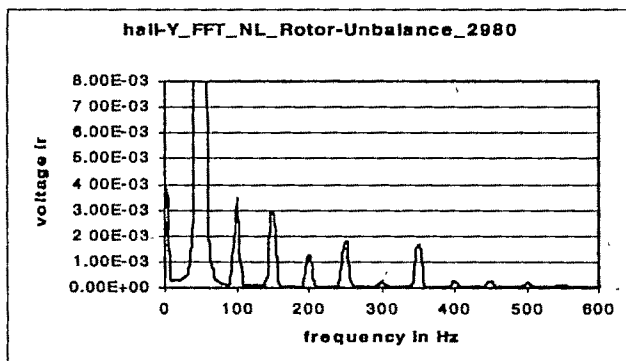


Fig. 2b Hall Probe output of Y phase of faulty motor at 2980rpm under no-load condition

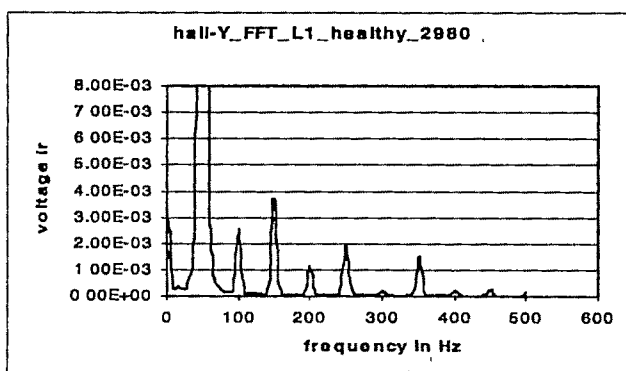


Fig. 3a Hall Probe output of Y phase of healthy motor at 2980rpm with single-mass load condition

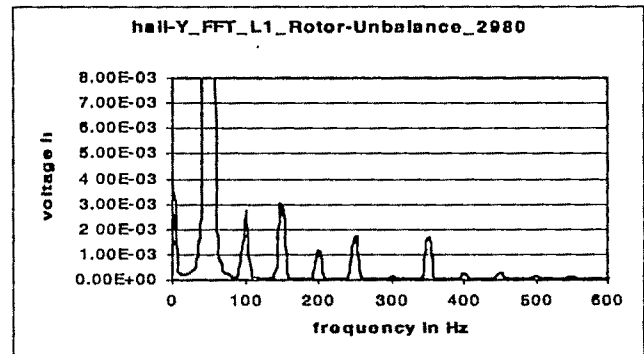


Fig. 3b Hall Probe output of Y phase of faulty motor at 2980rpm with single-mass load condition

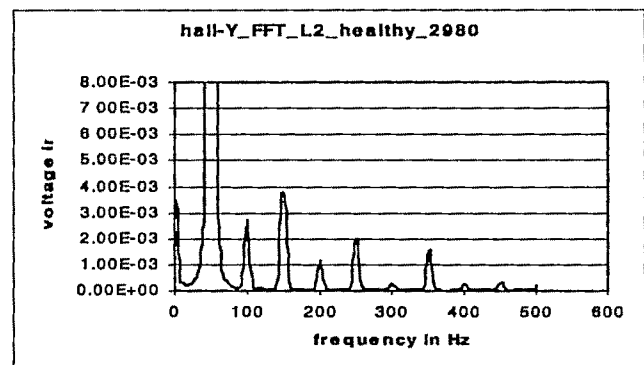


Fig. 4a Hall Probe output of Y phase of healthy motor at 2980rpm with double-mass load condition

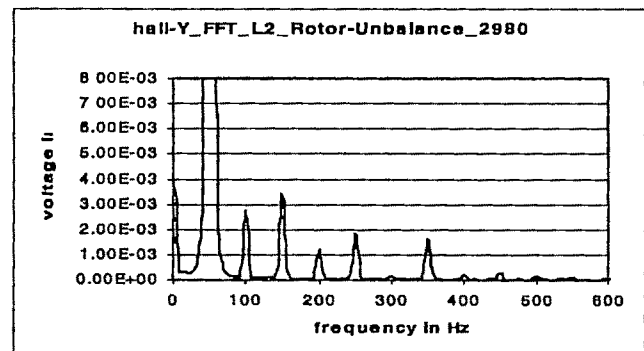


Fig. 4b Hall Probe output of Y phase of faulty motor at 2980rpm with double-mass load condition

Table 2 Ratio of amplitudes of 2 nd and 3 rd harmonics						
Ph	Healthy Motor			Unbalanced rotor Motor		
	At No Load	single mass load	double mass load	At No Load	single mass load	double mass load
Y	0.7192	0.6873	0.7139	1.1723	0.9643	0.9643

B. Analysis of Vibration Data: Data for all the three directions, X, Y, Z, are collected but vibration in the Z-

direction being more prominent in Figs. 5, 6 and 7 the FFT of vibration spectrum in the Z-direction at different loads are shown. Figs. 5a, 6a and 7a are for healthy motor and Figs. 5b, 6b and 7b are for mass-unbalance-rotor motor.

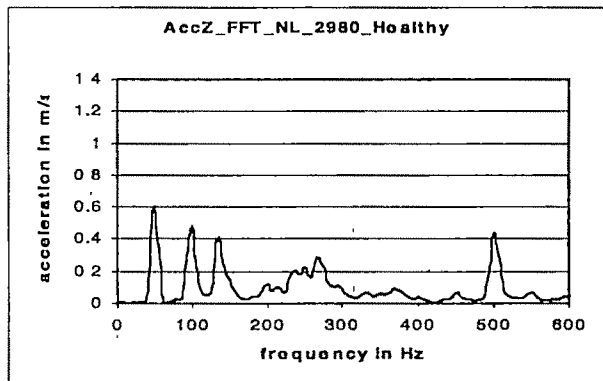


Fig. 5a Vibration of healthy motor at 2980rpm at No Load

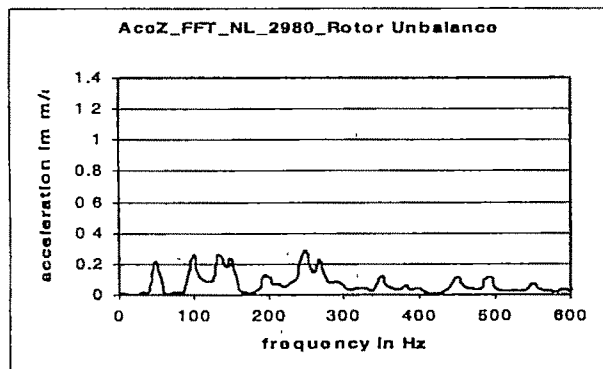


Fig. 5b Vibration of mass-unbalance-rotor motor at 2980rpm at No Load

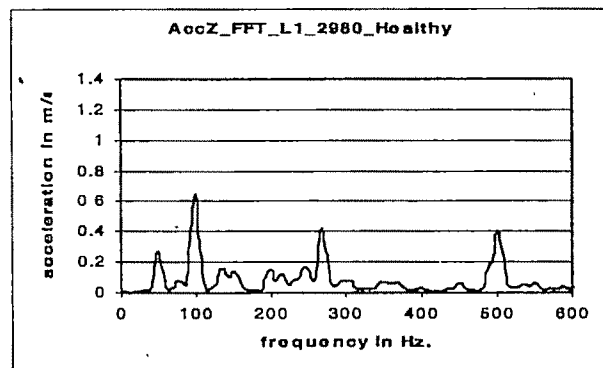


Fig. 6a Vibration of healthy motor at 2980rpm with single mass Load

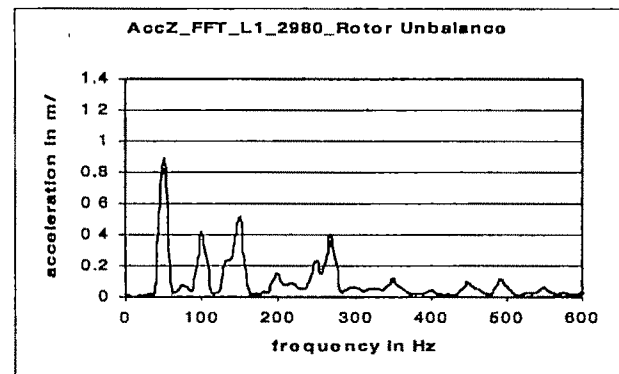


Fig. 6b Vibration of mass-unbalance-rotor motor at 2980rpm with single mass Load

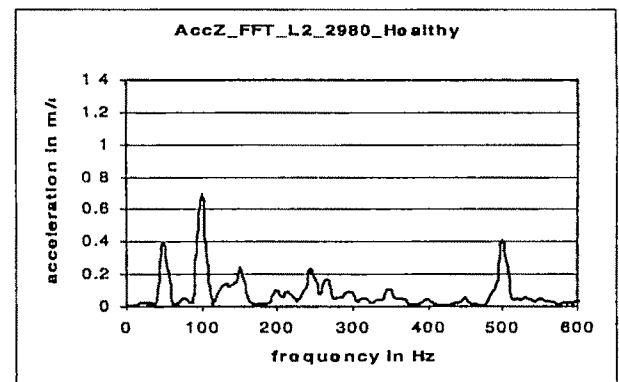


Fig. 7a Vibration of healthy motor at 2980rpm with double mass Load

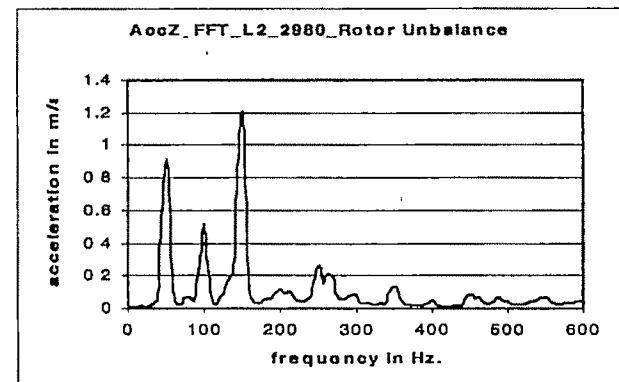


Fig. 7b Vibration of mass-unbalance-rotor motor at 2980rpm with double mass Load

Table 3
Data of healthy and faulty motor for Vibration analysis

Harmonics	Healthy Motor			Faulty Motor		
	Amplitude in m/sq.sec.			Amplitude in m/sq.sec.		
	At No Load	single Mass load	doubl mass load	At No Load	Single Mass load	Double Mass load
1 st	0.604	0.267	0.392	0.218	0.888	0.914
2 nd	0.481	0.644	0.692	0.259	0.421	0.517
3 rd	0.159	0.141	0.246	0.229	0.509	1.198
(1 st +3 rd)/2 nd	1.5846	0.6348	0.9225	1.7296	3.3175	4.0851

C. Discussions

From the table of current signature data, variations, though very small, in the amplitudes of different harmonics are observed. This is due to small unbalance in a very small motor. The variations in the 3rd harmonic being prominent, in Table 2, the ratio of the magnitudes of 2nd and 3rd for Y phase at different load is shown. It is seen that in case of mass-unbalance-rotor motor the ratio is more than that of healthy motor. From the FFT curves, acceleration vs. frequency, in no-load or loaded condition distinct variations, in compare to the healthy motor, are observed in case of the rotor-unbalance motor. To get a relation between healthy and faulty motors one column depicting the ratio of amplitudes of (1st + 3rd) and 2nd harmonics is introduced in Table 3, which shows that in case of mass-unbalance-rotor motor the ratio is more than that of healthy motor.

V CONCLUSION

Though vibration sensors are delicate and expensive, analysis of Vibration signature for motor health determination is a well-known fact. On the other hand, in many applications, stator current is readily available, as is usually measured for motor protection. This stator current can provide same indications regarding motor health [5]. For these reasons stator current monitoring are preferred presently. In this present paper, both current signature and vibration signature are analyzed by FFT. From analysis it is seen that for the mass-unbalance-rotor motor (here called faulty motor), both current signature and vibration signature analysis can provide concrete conclusion to identify the faulty motor from that of healthy one. Hence it can be concluded that for condition maintenance, prior to the fault occurrence, both vibration and current signature analysis are required, for zero down-time operation of the motor. Here the experiment was carried out on a small motor. Tests for large and medium sized motor on higher loads are to be carried out for validity of the conclusion made in this paper.

. ACKNOWLEDGMENT

The authors acknowledge the support provided by Department of Applied Physics, University of Calcutta to carry out this research work in the TEQIP funded Virtual Instrumentation Laboratory.

REFERENCES

- [1] Mark Fenger, William T. Thomson, *Development of a Tool to detect Fault in Induction motors via current Signature Analysis*. In: Rotating Machine Conference, June 2002, San Antonio, TX.
- [2] Jordi Cusido, Javier Rosero, Emiliano Aldabas, Juan Antonio Ortega, Luis Romeral, *New Fault detection techniques for Induction Motors* Electrical Power Quality and Utilisation, Magazine Vol II, No.1, 2006
- [3] Mohamed El Hachemi Benbouaid, "A Review of Induction motors Signature Analysis as a medium for Fault Detection", IEEE Transactions on Industrial Electronics, Vol.47, No 5, October 2000.
- [4] C. Hargis, B. G. Gaydon and K. Kamish, "The Detection of Rotor Defect in Induction Motors", Proc. IEE EMDA Conference, London, 1982, pp 216-220.
- [5] Izzet Y Onel, K. Burak Dalci and Ibrahim Senol, "Detection of Bearing defects in three phase Induction Motor using Park's Transform and radial basis function neural networks", Sadhana Vol 31, Part 3, June 2006, pp 235-244.
- [6] Aderiano M da Silva, Richard J Povinelli, Nabeel A O Demerdash, "Induction Machines Broken bar and Stator short-circuit Fault diagnostics based on three phase stator current envelopes"
- [7] Arezki Menacer et al, "Stator current analysis of Incipient Fault into Asynchronous motor rotor bars using Fourier Fast Transform" *Journal of Electrical Engineering*, Vol.55, No 5-6, 2004, 122-130.
- [8] Don-Ha Hwang, Ki-Chang Lee, Joo-Hoon Lee, Dong-Sik Kang et al, "Analysis of a three phase Induction motor under eccentricity condition", *IEEE Trans.* 2005.
- [9] Y.S Lee, J K. Nelson et al, "An acoustic diagnostic technique for use with electric machine insulation", *IEEE Trans on Dielectrics and Electrical Insulation*, vol. 1, no.6, pp. 1186-1193, 1994
- [10] Randy R. Schoen, Thomas G Habetler, Farrukh Kamran and Robert G Bartheld, "Motor Bearing Damage Detection Using Stator Current Monitoring", IEEE Transactions on Industry Applications, vol.31, no 6, pp.1274 - 1279, Nov./Dec., 1995.
- [11] Sekhar, A.S, and Prabhu, B.S., 1995, "Effects of Coupling Misalignment on Vibrations of Rotating Machinery," *Journal of Sound and Vibration*, Vol. 185(4), pp. 655-671.

Technical Session 3D

General Applications-I

The Motion of Spherical Shock Waves in Self-gravitating Heat Conducting Medium

R.P. Yadav¹, Ratnesh Kumar² and Virendra K. Gangwar³
 Deptt. of Physics, Govt P.G. College, Bisalpur (Pilibhit)-262201 (U.P.) INDIA
 e-mail: rpyadav93physics@yahoo.co.in

Abstract – The motion of weak spherical shock in non-uniform atmosphere has been investigated by Chester-Chesnell-Whitham model. This model often used to study the freely propagation of shock waves in uniform and non-uniform media. Though the effect of overtaking disturbances plays an important role, for the sake of simplicity, its effect on the shock has been ignored here. The analytical relations for shock velocity and shock strength have been discussed with the help of figures/tables. These results obtained are also compared with those obtained elsewhere.

Keywords - Shock Waves, Fluid Mechanics

I. INTRODUCTION

HOMOTHERMAL flows have been discussed by Sedov (1959), Koroboinikov (1956), Riazanov, Zababakhin and Simonenko (1965) have considered the structure of a converging shock, taking into account the radiant heat exchange and have found that a shock wave becomes nearly isothermal as it approaches its faces. Laumbach and Probststein (1970) have discussed the point explosion for radiating flow in an exponential atmosphere and in another paper, they have studied the isothermal flow in the case of an ascending shock in an atmosphere which behave as a continuum. Nath (1989) studied the theoretical model of cylindrical MHD shock wave under the action of monochromatic radiation in non-uniform stellar atmosphere with a constant intensity on unit area, assuming the gas to be grae and opaque as well as the shock to be transparant.

Sachdev and Ashraf explained the converging spherical and cylindrical shocks with zero temperature gradient in the rare flow fluid. Verma and Singh (1980) extended the problem of self-similar strong shocks in magnetoradiative gas. Ashok Ganguly and Mrinal Jana (2002) discussed the propagation of cylindrical of MHD shock with veyring energy in a non-uniform medium. In this present paper we have extended C.C.W. method for the problem of the motion of spherical shock waves in self-gravitating heat conducting medium and analysed the flow of shock propagation like shock velocity U , praticle velocity u , shock strength U/a_0 and pressure p/p_0 .

II. EQUATIONS OF MOTION AND BOUNDARY CONDITIONS:

The basic equations of motion in cylindrical symmetry are

$$\frac{\partial p}{\partial t} + u \frac{\partial p}{\partial r} + \frac{\rho u}{r} = 0 \quad --(1)$$

$$\frac{\partial u}{\partial t} + u \frac{\partial u}{\partial r} + \frac{1}{\rho} \frac{\partial p}{\partial r} + \frac{h}{\rho} \frac{\partial h}{\partial r} + \frac{Gm}{r} - \frac{v^2}{r} = 0 \quad --(2)$$

$$\frac{\partial h}{\partial t} + u \frac{\partial h}{\partial r} + \frac{h}{r} \frac{\partial}{\partial r}(ur) = 0 \quad --(3)$$

$$\frac{\partial}{\partial t}(vr) = 0 \quad --(4)$$

$$\frac{\partial \epsilon}{\partial t} + u \frac{\partial \epsilon}{\partial r} - \frac{p}{\rho^2} \left[\frac{\partial \rho}{\partial t} + u \frac{\partial \rho}{\partial r} \right] + \frac{1}{\rho r} \frac{\partial}{\partial r}(jr) = 0 \quad --(5)$$

$$\frac{\partial m}{\partial t} = 2\pi\rho r \quad --(6)$$

$$\frac{\partial i}{\partial t} = k_j \quad --(7)$$

The strong shock conditions are given by:

$$u = \frac{2U}{(\gamma-1)}, v = \frac{2U}{(\gamma+1)}, \rho = \rho_0 \frac{(\gamma+1)}{(\gamma-1)}, p = \frac{2\rho_0 U^2}{(\gamma+1)} \quad --(8)$$

$$c = \frac{2U^2}{(\gamma+1)^2}, h = h_0 \frac{(\gamma+1)}{(\gamma-1)}, m_1 = m_0 = \frac{2\pi b r^{2+\beta}}{(2+\beta)}$$

III SOLUTION

The characteristic equation is-

$$dp + \rho adu + \frac{ah}{u+a} dh + \frac{ap}{u+a} \left[\frac{e(\gamma-1)^2}{ap} \frac{\partial}{\partial r}(jr) + Gm - v^2 + \infty \right] \frac{dr}{r} = 0 \quad --(9)$$

when medium has density distribution $\rho \propto r^\omega$, where ω is constant, from equation (8)

$$du = \frac{2dU}{(\gamma+1)}$$

$$dh = \frac{\alpha r^{\alpha-1}(\gamma+1)}{(\gamma-1)} dr$$

$$G = \frac{\left[(1-r)\rho^{2\omega} r^2 + \frac{4rC^{2\omega}}{(\gamma-1)^2} - 2A(2+\beta)(1+\beta) \right]}{4\rho^{2\omega} r^{2\omega} [1+(1-r)(1+\beta)]}$$

putting those values in equation (9) and solving we get

$$\begin{aligned} \frac{dU}{dr} = & [2\omega r^{\omega-1}(\gamma-1)U^2 + [2U-a(\gamma+1)](1+2\gamma)(\gamma+1)\frac{c^2 r}{a} \\ & + (5\gamma-1)(1-9\gamma)[2U-a(\gamma+1)]\left(\frac{64NU^8}{R^4 a}\right) \\ & + (1+\beta)(1+\gamma)(1+2\gamma)[2U-a(\gamma+1)][1-(1-r)(1+\beta)] \\ & \left(\frac{a}{4U^2 r}\right) [(1-r)r^{\omega} 4U^2(1-2\gamma) + 2UC^2 r^2(1+2\gamma) - A(1+2\gamma)(1-2\gamma)] \\ & + r^{\omega} - 1a[2U-a(\gamma+1)] + \left(\frac{r^{\omega-1}}{a}\right)[a(\gamma+1)-2U] \Big/ \\ & [4r^{\omega} U(1-\gamma) - 2r^{\omega} a(1+\gamma)] \end{aligned}$$

after integrating above expression. The expression for shock velocity U , shock strength U/a_0 , particle velocity u and pressure p/p_0 are computed.

IV. RESULTS AND DISCUSSION

Results are obtained in the following forms:

$$\begin{aligned} U = & \int [2\omega r^{\omega-1}(\gamma-1)U^2 + [2U-a(\gamma+1)](1+2\gamma)(\gamma+1)\frac{c^2 r}{a} \\ & + (5\gamma-1)(1-9\gamma)[2U-a(\gamma+1)]\left(\frac{64NU^8}{R^4 a}\right) \\ & + (1+\beta)(1+\gamma)(1+2\gamma)[2U-a(\gamma+1)][1-(1-r)(1+\beta)] \\ & \left(\frac{a}{4U^2 r}\right) [(1-r)r^{\omega} 4U^2(1-2\gamma) + 2UC^2 r^2(1+2\gamma) - A(1+2\gamma)(1-2\gamma)] \\ & + r^{\omega} - 1a[2U-a(\gamma+1)] + \left(\frac{r^{\omega-1}}{a}\right)[a(\gamma+1)-2U] \Big/ \\ & [4r^{\omega} U(1-\gamma) - 2r^{\omega} a(1+\gamma)] \end{aligned}$$

$$\begin{aligned} \frac{U}{a_0} = & \int [2\omega r^{\omega-1}(\gamma-1)U^2 + [2U-a(\gamma+1)](1+2\gamma)(\gamma+1)\frac{c^2 r}{a} \\ & + (5\gamma-1)(1-9\gamma)[2U-a(\gamma+1)]\left(\frac{64NU^8}{R^4 a}\right) \\ & + (1+\beta)(1+\gamma)(1+2\gamma)[2U-a(\gamma+1)][1-(1-r)(1+\beta)] \\ & \left(\frac{a}{4U^2 r}\right) [(1-r)r^{\omega} 4U^2(1-2\gamma) + 2UC^2 r^2(1+2\gamma) - A(1+2\gamma)(1-2\gamma)] \\ & + r^{\omega} - 1a[2U-a(\gamma+1)] + \left(\frac{r^{\omega-1}}{a}\right)[a(\gamma+1)-2U] \Big/ \\ & [4r^{\omega} U(1-\gamma) - 2r^{\omega} a(1+\gamma)] a_0 \end{aligned}$$

$$u = \frac{2U}{\gamma+1}$$

$$\frac{p}{p_0} = \frac{2\gamma U^2}{a_0^2 (\gamma+1)}$$

Initially taking $\beta=1$, $\omega=1$ and $U=1500$ at $r=10$, the nature of flow variable are illustrated through tables 1 and 2. In the table 1, it is observed that the shock velocity U , shock strength U/a_0 , particle velocity u and pressure p/p_0 decreases as the distance increases from the shock source. Similar results are obtained in the table-2 as the propagation distance from the shock source increases.

Table 1

r	U	U/a ₀	u	p/p ₀
10.1	1470.44	4.20	1262.18	20.15
10.2	1441.75	4.11	1237.55	19.37
10.3	1413.89	4.03	1213.63	18.62
10.4	1386.83	3.96	1190.41	17.92
10.5	1360.54	3.88	1167.84	17.25
10.6	1334.99	3.81	1145.91	16.60
10.7	1310.15	3.74	1124.59	15.99
10.8	1286.00	3.67	1103.80	15.41
10.9	1262.51	3.60	1083.69	14.85
11	1239.66	3.54	1064.08	14.32

Table 2

r	U	U/a ₀	u	p/p ₀
11.1	1217.43	3.47	1045.00	13.81
11.2	1195.79	3.41	1026.42	13.32
11.3	1174.72	3.35	1008.34	12.85
11.4	1154.20	3.29	990.72	12.41
11.5	1134.21	3.24	973.57	11.98
11.6	1114.74	3.18	956.85	11.58
11.7	1095.77	3.13	940.57	11.18
11.8	1077.27	3.07	924.69	10.80
11.9	1059.24	3.02	909.21	10.41
12	1041.66	2.97	894.12	10.11

V. REFERENCES

- [1] V.P. Korobrinikow, Strong point explosion in a gas when the temperature Gradient is zero Dokl. Akad. Nauk, SSSR. 109, 271 (1956).
- [2] L.I. Sedov S. and D method in Mechanics (State publishing house, MOSCOW 1959).
- [3] E.I. Zababa Khin and V.A. Simonenko, convergent shock wave in a heat conducting Gas, P.M.M. 29,375 (1965)
- [4] D.D. Laumbach and R.F. Probst, A point explosion in a cold exponential atmosphere part 2. Radiating flow. J. Fluid mech. Vol. 40, 833-858, (1970)
- [5] P.L. Sachdev and S. Ashraf. Jour. of Applied Mathematics and Physics (ZAMP) Vol. 22, (1971).
- [6] Lerche, Astrophysics and space science 50, 323-342 (1977)
- [7] B.G. Verma and J.B. Singh (Jour, Math, Phys. Sci Vol. 14, No. 6, 1980).
- [8] Nath, Onkar, Astrophysics space sci 155-763, (1989).
- [9] Ashok Ganguly and Marinal Jana (Proc. Nat. Acad. India, 72(A), 1, (2002).

Sizing and Optimization of Hybrid Renewable Power System

S.C.Gupta, Dr. Y Kumar, and Dr.Gayatri Agnihotri

Maulana Azad National Institute of Technology, Bhopal
biral_50@yahoo.com, ykmact@yahoo.co.in, gayatri1@rediffmail.com

Abstract— This paper presents the development of a computational model for simulating the sizing and techno-economical optimization of hybrid photovoltaic-wind power system (HPWS). The performance of PV and wind system has been evaluated through more accurate and practical mathematical models, combining with hourly measured meteorological input data and load data. Design of HPWS is based on Concept of Loss of Power Supply Probability (LPSP) as key system parameter for reliability and minimization of the life cycle cost of the system. Methodology used in this model, allows quick identification of optimal configuration based on user's desired reliability level and economical (life cycle cost) performance of system. Applicability of model has been illustrated with a case study. Program has been developed in MATLAB 7.0 environment using energy balance calculation method.

Key words—Economic evaluation, PV/wind hybrid system, Loss of power supply probability, Optimum configuration.

I. INTRODUCTION

Renewable energy resources, such as solar and wind power are inexhaustible within the time horizon of humanity. Unlike the fossil fuels, they are very well distributed all over the world. The main hurdle associated with them is their diluted nature, due to which high cost equipments are needed to convert them in to usable form. Economic considerations, quality of supply, and type of necessary energy need plays an important role in the selection of such technology. In this context, the photovoltaic and wind turbine technology are most promising.

Many studies have been carried out in the area of hybrid renewable power system [2]-[8]. Most of these works

reported so far use the single diode model of photovoltaic (PV) module to evaluate solar power, and a simple mathematical model based on mean wind speed of site and the speed characteristics of wind turbine, for wind power prediction.

This paper addresses a computer program for simulation of hybrid power system. The program includes, an improved mathematical model for PV module, considering the second order effects, such as the influence of the irradiance in the open circuit voltage, the non-linearity due to low irradiance and a wind turbine model derived by fitting the practical output characteristics curve, using least square method for accurate prediction of available solar and wind power. In order to have fitting guarantee, three binomial expressions are used in wind model. Program selects the optimal wind turbine on the basis of calculation of optimum wind speed using weinbull scale parameter and shape parameter.

Loss of power supply probability (LPSP) technique is used as performance measure to assess the system reliability. For a fix capacity of wind turbine generators, the whole year's LPSP values of PV-Wind hybrid systems with different no of photovoltaic module and battery combinations are calculated first and then, all possible combinations satisfying the desired reliability level are extracted from them for life cycle cost calculation. The developed program allows quick identification of optimal configuration based on user's desired reliability level and economical (life cycle cost) performance of system.

II. HYBRID SYSTEM CONFIGURATION

The block diagram for a typical standalone PV-wind hybrid system is shown in Fig. 1. The system consists of PV array, wind turbine, battery storage, charge controller, ac load and a dump load. The generating system components are selected,

for the load to be supplied on the basis of optimum wind speed of wind turbine and the cost of photovoltaic module. However, this is not a requirement, and the model can be used to estimate the total generating capacity (PV+wind+battery) and its cost for a particular application.

When the generated power by PV and wind system is more than the required load power, the storage batteries are charged until a specific upper limit of battery charge is reached. At this point the excess power is diverted to the dump load. The purpose of incorporating the dump load (a controlled resistor) is to maintain the stability of the system frequency and voltage. If the excess energy can not be consumed by the load, then it must be disposed as heat by controlled resistor [9]. Storage batteries will discharge, supplying power to the load, when load demand exceeds the generated power. They will continuously be supplying power to the load until specified lower limit for battery charge is reached. At that point, the battery will stop supplying power to the load.

III. COMPONENT MODELING

A. PV Array Model

The photo-voltaic (PV) module is modeled, by equivalent circuit shown in Fig.2. The module equivalent circuit current I can be expressed as function of the module voltage V by [10]:

$$I = I_{sc} \left[1 - \exp \left(\frac{V - V_{oc} + IR_s}{V_t} \right) \right] \quad (1)$$

$$R_s = \frac{V_{oc}^* - V_{oc} + V_t \ln \left(1 - \frac{I_{sc}^*}{I_{sc}} \right)}{I_{sc}^*} \quad (2)$$

Where I_{sc} , V_{oc} , R_s , V_t are short circuit current, open circuit voltage, series resistance, thermal voltage respectively.

The voltage V_t equals 25mV at 300 K for a typical crystalline silicon solar cell. This expression is inconvenient to use in the sense that I is implicit, theoretically making it necessary to solve it iteratively. However, for voltage close to maximum power point, a reasonably accurate solution can be obtained with only one iteration by setting $I=0.9I_{sc}$ in the second term.

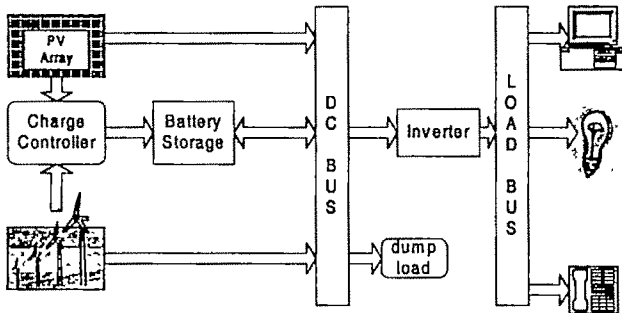


Fig.1.Hybrid System Configuration

The model represented by (1) is based on standard and

widely use information, which is an undeniable advantage. Furthermore, it is simple to use. However, such simplicity is at the cost neglecting the second order effects. These second order effects can be taken in to account by, using the modified values of short circuit current and open circuit voltage in the expression (1) as under [10]:

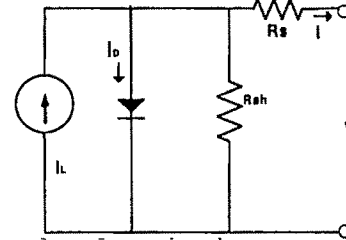


Fig.2 Equivalent circuit of a module

$$I_{sc} = I_{sc}^* \cdot \frac{G}{G^*} \left[1 + \frac{dI_{sc}}{dT_c} (T_c - T_c^*) \right] \quad (3)$$

$$T_c = T_a + C_i G_{eff} \quad (4)$$

$$C_i = \frac{NOCT(^{\circ}C) - 20}{800W/m^2} \quad (5)$$

$$V_{oc} = \left[V_{oc}^* + \frac{dV_{oc}}{dT_c} (T_c - T_c^*) \right] \left[1 + \sigma_{oc} \ln \left(\frac{G_{eff}}{G^*} \right) \ln \left(\frac{G_{eff}}{G^*} \right) \right] \quad (6)$$

where, the parameters in above equation are:

NOCT=normal operating cell temperature of module

STC=standard test conditions of module

I_{sc}^* = Short circuit current of module at STC

V_{oc}^* = Open circuit voltage of module at STC

I_M^* = Maximum current of module at STC

V_M^* = Maximum voltage of module at STC

G^* = Irradiance at STC

T_c^* = Temperature of module at STC

T_a = Ambient temperature

T_c = Operating temperature of module above ambient

G_{eff} = Effective irradiance, related to incidence angle

dI_{sc}/dT_c = Temperature coefficient of current

dV_{oc}/dT_c = Temperature coefficient of voltage

σ_{oc} = Empirically adjusted parameter = -0.04

G_{oc} = Empirically adjusted parameter = G^*

The power generated by solar system is calculated as:

$$P_v(t) = N_{pv} \cdot V_m(t) \cdot I_m(t) \quad (7)$$

Where $P_v(t)$ is power generated by solar system, N_{pv} is the number of modules used in solar system, $V_m(t)$ and $I_m(t)$ are the values of maximum voltage and current of module at time t , respectively, assuming that solar system has a tracking system and a maximum power point tracker.

B. Wind Turbine Model

The hourly output of wind turbine is determined by average hourly wind speed at the hub height and output characteristic of wind generator. Therefore, when

calculating the output of wind generator, the measured data of average hourly wind speed must be converted to the corresponding values at the hub height using following relation [3].

$$V = V_0 (h/h_0)^{\alpha} \quad (8)$$

Where V is wind speed at projected height, h ; V_0 is wind speed at the reference height, h_0 ; α is the ground surface friction coefficient, in this paper, the one-seventh-power law ratio is used. It has been observed that, even if different types of wind generators with the same rated power are used at the same site, they can generate different amount of power output because of difference in their output characteristics. The hourly power output of any wind generator can be calculated accurately only by using the performance characteristic of its own. In this paper, the characteristic equation of wind generator is obtained by fitting the practical output characteristic curve using a least square minimization technique. In order to guarantee the fitting accuracy three quadratic functions are used. The curve fitting equation of the output characteristic of wind generator can be expressed as:

$$P_w(t) = \begin{cases} 0 & (v < v_{in}) \\ a_1 v^2 + b_1 v + c_1 & (v_{in} \leq v < v_1) \\ a_2 v^2 + b_2 v + c_2 & (v_1 \leq v < v_2) \\ a_3 v^2 + b_3 v + c_3 & (v_2 \leq v \leq v_{out}) \\ 0 & (v > v_{out}) \end{cases} \quad (9)$$

Where $P_w(t)$ is the hourly output power of wind generator at wind speed, v ; v is wind speed at projected height at time t ; v_{in} and v_{out} are cut-in and cut-off wind speed of the wind generator, respectively.

C. Storage Battery Model

A model for the storage battery is needed to predict the rate at which the battery is charged (discharged), when the generated power is more (less) than demand. When generated power exceeds load demand, battery bank will be in charging state. On the other hand, the battery bank will be in discharging state. The output signal representing the health of battery is the battery state of charge (SOC), which will vary as a function of power flow into or out of battery. The SOC of battery storage at any hour t can be obtained by monitoring the charge/discharge energy to/from the battery as given by following expressions:

$$Eb(t) = Eb(t-1) - E_{b,dis}(t) + E_{b,ch}(t) \quad (10)$$

$$E_{b,ch}(t) = \min[\text{Charge Lim}, (El(t)/\eta_{inv} - Eg(t))\eta_{batt}] \quad (11)$$

$$E_{b,dis}(t) = \min[\text{Charge Lim}, (Eg(t) - El(t)/\eta_{inv})\eta_{batt}] \quad (12)$$

where $Eb(t)$ and $Eb(t-1)$ are the state of charge (SOC) of battery at the time t and $(t-1)$ respectively; $E_{b,dis}(t)$ and $E_{b,ch}(t)$ are the charge and discharge quantities of battery storage; $El(t)$ is load demand; $Eg(t)$ is the total energy

produced by photovoltaic and wind systems at time t ; η_{inv} and η_{batt} are the efficiency of inverter and charge/discharge efficiency of battery storage respectively; Charge Lim is the maximum allowable charge/discharge energy to/from the battery, assumed to be equal to 10% of total battery storage capacity. In this paper, the charge/discharge efficiency of battery is assumed to be the same and equal to the round trip efficiency of battery storage.

At any time t , the charge/discharge energy of battery bank is subject to the following constraints:

$$E_{b,dis}(t) = E_{b,ch}(t) \leq 0.10Cb \quad (13)$$

$$Ebmin \leq Eb(t) \leq Ebmax \quad (14)$$

$$Eb(t)_{min} \geq 0.90Ebmax \quad (15)$$

Here, maximum charge quantity of battery bank $Ebmax$ takes the value of 100% capacity of battery storage Cb in beginning of simulation, and the minimum charge quantity of battery storage $Ebmin$ is calculated by maximum depth of discharge (DOD): $Ebmin = (1 - DOD)Cb$. According to the specifications of battery, the lifetime of battery can be prolonged drastically if DOD of the battery is selected within the range 30-60%. In order for the system with battery to be sustained over a long period of time, the battery SOC at the end of simulated period must be greater than a given percentage (say, 90%) of its $Ebmax$ as shown in equation (15). The inverter used with the battery storage should be rated in terms of the peak load demand. Though the efficiency of inverter is a function of the ratio of the actual load to the inverter rating but here we used a constant value of inverter efficiency based on the average load demand.

IV. DESIGN METHODOLOGY

Total power generated by photovoltaic and wind system during each hour is calculated first as follows:

$$Pg(t) = NwtPw(t) + NpvPv(t), \quad (16)$$

where $Pw(t)$, $Pv(t)$, and $Pg(t)$ are the power generated by wind system, solar system and total power generated by wind and solar system at time t , respectively. All these powers are equivalent to energy generated at time t , since one hour time step is chosen for simulation. Nwt and Npv are the number of wind turbines and number of PV modules used with the system. Performance data of wind turbine, photovoltaic module, and the parameters of different components used in hybrid system are given in table 1.

Energy balance calculation method is used here to design optimal hybrid system. Concept of loss of power supply probability (LPSP) is applied as a numerical measure of hybrid system reliability. The LPSP, for a considered period of time T is the ratio of total power deficit to the sum of load demand. This can be expressed as:

$$LPSP = \frac{\sum_{t=1}^T LPS(t)}{\sum_{t=1}^T El(t)} \quad (17)$$

$$LPS(t) = El(t) - (Eg(t) + Eb(t-1) - Ebmin)\eta_{inv} \quad (18)$$

There may be number of configurations, which can satisfy a desired reliability level of the whole year in terms of loss of power supply probability.. In this paper, a computer program has been developed to size hybrid system components in order to meet the load demand ,at certain desired reliability level, while minimizing an objective function representing life cycle cost of hybrid system (Lcc). Lcc is the sum of the present values of all installation, operation, and maintenance cost including salvage values treated as negative costs[11]. Hence, objective function to determine the optimal configuration of hybrid system can be defined as[5]:

$$\text{Minimize: } Lcc = \sum_{j=1}^3 (I_j - S_{dj}) X_j + \sum_j OM_{dj} \cdot E_j \quad (19)$$

where the index X_j is made to account for wind, solar, battery storage. I_j is the summation of discounted capital cost of generating unit j , S_{dj} is the discounted salvage value of generating unit j , X_j is decision variable representing number of generating units j , and OM_{dj} is the discounted operation and maintenance costs, E_j is the decision variable, indicating energy output from unit j . The objective function Lcc is constrained to:

$$(Eg(t) + x \cdot Cb + LPS(t)) \eta_{inv} \geq El(t) \quad (20)$$

$$1 - LPSP \geq R \quad (21)$$

Where, $Eg(t)$ is the total solar and wind energy generated, t is the period, x is the fraction of battery capacity expected to discharge in each period, Cb is the capacity of battery storage, LPS is the amount of power deficit, El is total load demand, and R is the certain/desired reliability level .The stepwise iterative procedure adapted in the program is as follows:

1. Collect program input data : solar radiation , wind speed, load demand ,commercially available wind turbine ,PV module, batteries, and their performance parameters.
2. Select the optimal type of wind turbine suitable for the site, based on optimum wind speed V_{opt} of turbine[48] as

$$V_{opt} = c \left(\frac{k+2}{k} \right)^{1/k} \text{ m/s} \quad (22)$$

where, c and k are the weinbull parameters.

3. Calculate energy produced by solar and wind using (7)-(9).
4. Calculate the battery storage level using (10)-(12)
5. Calculate LPSP and hence reliability values for all possible combinations of number of batteries and PV modules, keeping constant capacity of wind turbine.
6. Choose the desired reliability level.

7. Find all configurations satisfying the desired reliability level.
8. Calculate the hybrid system life cycle costs for all configurations found in step 7, using component parameters given in the table. I and (18).
9. Find the configuration with minimum cost.

V. CASE STUDY

To illustrate the applicability of iterative optimization procedure used in the developed computer program, resource and load data of a sight located in remote area in South-Central Montana have been taken.[3]. Hourly average wind speed and solar insolation data over 3-year period, which was collected in a remote location in Montana, are shown in Fig.3 The annual average hourly load profile for a house situated in this region is shown in Fig 4. Wind speed data were taken at a height of four meters, whereas the turbine hub height was 30 meters.

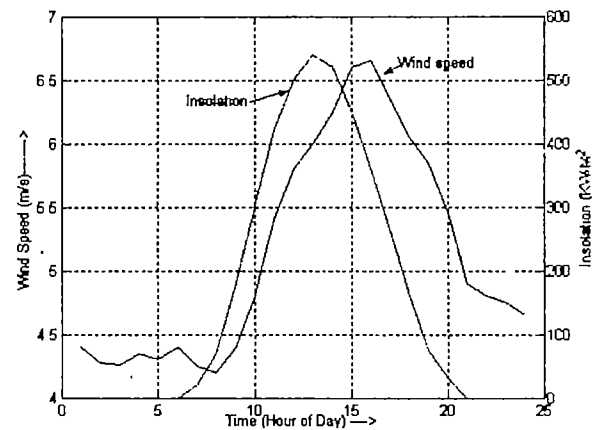


Fig.3 Average hourly wind and insolation profile

Generation and load are assumed to remain constant in each hour interval .System components size ,costs and other parameters used in sizing and optimization are taken from[3]and are shown in Table.I. Cost analysis is performed after the unit-sizing program has been run.the life time of the system is taken 20 years. All the discounted costs of system appearing in(19) have been calculated by dividing their annual values by capital recovery factor (CRF).The CRF is defined as[11]:

$$CRF = [i_r (1+i_r)^{ny}] / [(1+i_r)^{ny} - 1] \quad (23)$$

Where i_r is the annual interest rate(6% taken for this case)and ny is the life time of the component. These details are used to validate the program described in the former section. The optimization results are shown in Table.II.

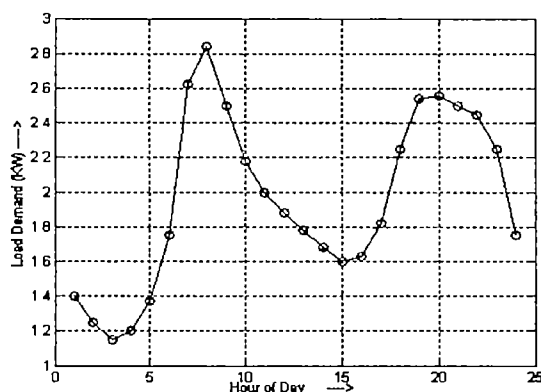


Fig.4 Hourly average demand of a typical residence

TABLE II.
COMPARISON OF OPTIMIZATION RESULTS

	WT	PV	Battery	COE	Reliability
Montana HPWS	10 (KW)	72	11	\$0.38	100%
Designed HPWS	10 (KW)	70	10	\$0.37	100%

As shown in Table II. Optimal Configuration found from the developed program is almost identical with the hybrid system of Montana for 100% reliability. However, some difference in number of PV modules and battery is observed which is due to more accurate photovoltaic and wind model used in this study. Applicability of energy balance method for optimum configuration with 100% reliability is clearly shown in Fig. 5. It should be noted that while calculating cost of energy/Kwh (COE), tax rebate available for use of renewable energy has not been considered in both cases for the comparison of results.

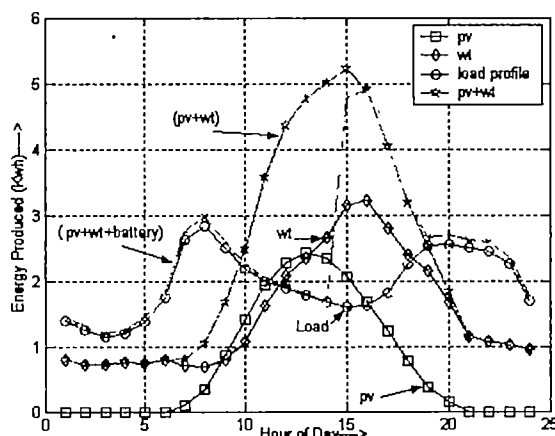


Fig. 5 Showing energy balance for 100%reliability level

VI. CONCLUSION

A complete set of energy balance calculation method for the optimum design of renewable hybrid (PV/wind) power system is introduced. In this paper, more accurate mathematical models for evaluating the performance of solar and wind system are used. A program is developed which utilizes these models to find a cost effective and reliable

configuration to generate the electricity for stand alone applications. It is observed that reliability level plays a very important role in such designs. The cost of the hybrid system reduces drastically, if reliability level is sacrificed little a bit.

TABLE I.
SYSTEM COMPONENT RATING AND OTHER PARAMETERS

Component	Rating/performance/cost Parameters
Wind Turbine (BWC XL1)	1 KW
Capital cost	\$ 2500 including BOS
Annual O&M cost(\$)	\$ 1.63
Turbine hub height/ Life	30 meters/20 years
PV Module	53 W
Capital cost	\$ 525 including BOS cost
Annual O&M cost	\$ 0.047
Life	20 years
Battery(Deep cycle) 12V	2.1 KWh
Annual Capital cost/ O&M cost	\$170/0.00
Life/ Efficiency/DOD	4 year / 80% / 80%
Inverter	3KW
Efficiency/Life	98% /20 years
Life of project/interest rate	20years/ 6%

REFERENCES

- [1] J. Jayadev. "Harnessing the wind,"IEEE Spectr vol 32,no11,pp78-83,Nov 1995 (N)
- [2] Jose L. Bernal-Agustin, Rodolfo Dofo-Lopez, and David M Rivas-Ascaso, "Design of isolated hybrid system minimizing costs and pollutant emissions "Renewable Energy 31, pp 2227-2244 , 2006
- [3] W D Kellogg, M.H Nehrir, G.Venkataramanan, and V.Gerz,"Generation unit sizing and cost analysis for stand- alone wind, PV, and hybrid wind/PV system, IEEE Trans Energy conversion, vol3, no.1, pp.70-75, Mar.1998.
- [4] C. Protopoulos, B J. Brinkworth, and R. H. Marshall, "Sizing and techno-economical optimization for hybrid solar PV wind power systems with battery storage, " Int. J. Energy Res., vol .21,no6,pp.465-479,1997
- [5] R. Chedid and Y. Saliba, "Optimization and control of autonomous renewable energy systems. "Int. J. Energy Res., vol. 20,no 7, pp 609-624, 1996.
- [6] M. H. Nehrir, Brock J La Meres and Giri Venkataramanan,,"An approach to evaluate the general performance of stand alone wind/photovoltaic generating systems" IEEE Trans Energy conversion, vol 15, no 4, Dec.2000.
- [7] Tomonobu Senjyu, Daisuke Hayashi, Naomitsu Urasaki, and Toshitsugu Funabashi, "Optimum configuration for renewable generating system in residence using genetic algorithm" IEEE Trans. Energy conversion, vol. 21, no. 2, June 2006.
- [8] R. chadid and S.Rahman, "Unit sizing and control of hybrid wind-solar power system."IEEE Trans. Energy conversion, vol.12, no.1, pp.79-84, March.1997.
- [9] R. Hunter, and G Elliot, Wind-Diesel System, Press Syndicate of the University of Cambridge, 1994
- [10] Antonio Luque. "Hand Book of photovoltaic science and engineering", Wiley publication, pp 951-955. 2003
- [11] HOMER pro,Ver.1.58,National Renewable Energy Laboratory, Golden Co,4 April 2 002

Performance Comparison of a PV Powered Water-Pumping System with and without Maximum Power Point Tracker

Abu Tariq¹ and M.S. Jamil Asghar²

Department of Electrical Engineering, Aligarh Muslim University, Aligarh 202002, India.

¹qariabutariq@rediffmail.com, ²msjasghar@gmail.com

Abstract—Water pumping systems powered by a photovoltaic (PV) source normally use permanent magnet dc motors, directly coupled to the PV source. As the characteristics of a PV source is nonlinear and highly dependant on the weather condition, it is impossible to match the characteristics of motor with that of the PV source under changing weather conditions. As a result the PV source remains under utilized most of the times. This paper suggests use of a simple and cheap analog maximum power point tracker (MPPT) for this application. The proposed scheme is simulated and realized. The performance of the proposed scheme is compared with that of directly coupled system. The proposed scheme significantly enhances the performance of water pumping system, especially under poor insolation condition.

Key words—PV panel, maximum power point tracker, permanent magnet dc motor, water pumping system.

I. INTRODUCTION

APPLICATION of PV generators for water pumping applications in remote locations has received much attention. Since the output of a PV generator is essentially dc in nature, a dc motor is an obvious choice for the prime mover of the pump. This avoids the use of an inverter, which will be required to drive the induction motor in case the conventional water pumping systems is chosen. The dc motor option gives better overall efficiency for low power applications (less than 1 kW). Therefore, for low power applications dc motors are preferred in spite of maintenance problem.

The i - v characteristic of a solar cell is highly nonlinear. The characteristic varies drastically with the solar insolation (light intensity) and the temperature. Fig. 1 shows the i - v characteristics of a cell for various insolation levels and temperatures [1]. The cell characteristic at a particular ambient condition consists of a constant voltage segment and a constant current segment. The cell generates maximum power at the knee of the characteristic, where the two segments meet. The operating point at which the PV cell generates maximum power is referred as maximum power point (MPP). The MPP changes with the change in ambient condition. For efficient utilization of a photovoltaic (PV) panel, that consists of a large number of series and parallel connected solar cells, maximum available power should be drawn from it. In other words, the PV panel should be forced to operate at its maximum power point under varying ambient conditions

In order to match the characteristic of a dc motor with that of the PV source, the motor-pump system is judiciously chosen. In [2] operations of shunt, series, and separately excited motor driving different types of mechanical loads are

discussed. It has been concluded that a separately excited motor driving a centrifugal load is most compatible with the PV array. Matching of the motor-pump system with the solar array further improves by the use of a dc compound motor [3].

As a separately excited motor requires a separate PV source to energize the field winding, permanent magnet dc (PMDC) motor, is the most popular choice for water pumping using a PV source. Moreover, it avoids the losses of field excitation, thus efficiency improves. However, even with PMDC motors, perfect matching with the PV source is possible only at a unique ambient condition. Normally close matching takes place when insolation is high. High insolation condition occurs for a short period of time only, therefore, sun tracking (a mechanical method) is employed which somehow improves the matching condition at low insolation. Normally, sun tracking PV panel panels are designed to manually change the orientation of PV panels three times a day to maximize the incident solar energy. By manual sun tracking 20% more output can be obtained as compared to fixed tilted PV panel [4]. An alternative method of improving the matching is to use different series-parallel array configurations for different ambient conditions [5].

The methods described above give only approximate matching of the mot-pump system with the PV source. For more accurate matching an analog or digital circuit, known as maximum power point tracker (MPPT), is interfaced between the PV panel and the load. This paper suggests use of a simple and cheap analog MPPT for this application. The proposed scheme is simulated and realized. The performance of the proposed scheme is compared with that of directly coupled water pumping system.

II. MAXIMUM POWER POINT TRACKING TECHNIQUES

In a very simple MPP tracking technique [6], the PV panel voltage is compared with a constant reference voltage that corresponds to the MPP voltage under specific ambient condition. The error signal is used to change the duty cycle of a dc-dc converter, interfaced between the PV panel and the load, so as to make the PV panel voltage equal to the MPP voltage. This method is very simple to implement, but it is not accurate. There is substantial power wastage, as it does not take into account the effects of changes in solar insolation and temperature.

The maximum power point voltage (MPPV) method [7 -11], is based on the observation that MPP voltage (V_{mp}) has

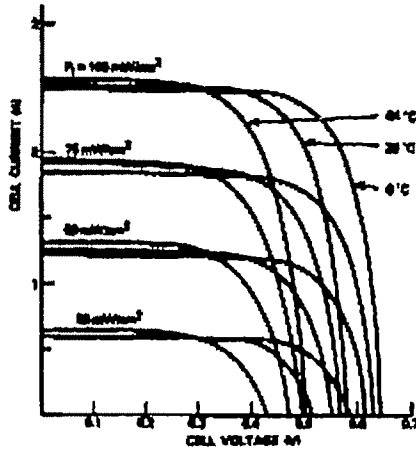


Fig. 1 The I - v characteristic of a solar cell.

almost a linear relation with open-circuit voltage (V_{oc}) of the PV panel.

$$V_{mp} = M_v V_{oc} \quad (1)$$

where M_v is called the voltage factor and has different values for different solar panels. The PV panel is locked at the reference voltage given by (1). The open-circuit voltage required to determine the MPP voltage can be measured by disconnecting load from the PV panel after regular intervals. The measured value of V_{oc} is stored and used for determination of V_{mp} . The open-circuit voltage can also be sensed using an unloaded pilot PV panel installed along with the main PV panel.

In perturb and observation (PAO) method [12, 13], the current drawn from the PV panel is perturbed and the resulting output power is observed. If an increased current results in higher power, it is further increased till the output power begins to decline. On the other hand, if an increase in current results in less power than before, then current is decreased until output power stops increasing and begins to go down.

The incremental conductance method [14] compares the incremental conductance of the PV panel with its instantaneous conductance and changes the duty ratio of the dc-dc converter such that their sum is zero. This method is based on the fact that the slope of power-voltage curve of the PV panel is zero at the MPP. The method is accurate and can be used for rapidly changing ambient condition. However, the method is complicated and needs a complex control circuit.

III. PROPOSED SCHEME

The block-diagram of the proposed system is shown in Fig. 2. To track the MPP, MPPV tracking technique is employed. An unloaded pilot PV panel is used to obtain the V_{oc} . The control unit generates a PWM output to drive the MOSFET of a step-down dc-dc converter. The duty cycle of the converter changes till the PV panel voltage becomes equal to the MPP voltage.

IV. SYSTEM DESCRIPTION

The water pumping system consists of permanent magnet dc motor coupled to a centrifugal pump. The system used for theoretical study has the following parameters [4]:

Electrical parameters:

Rated voltage = 60 V.

Rated current = 16.5 A.

Rated speed = 272.3 rad/s.

Armature resistance; $R_a = 0.8 \Omega$

Armature inductance; $L_a = 0.04 H$.

Motor constant; $K = 0.175 V/(rad/sec)$.

Mechanical parameters:

Coulomb friction torque of motor; $\tau_{fM} = 0.08 Nm$.

Coulomb friction torque of load (i.e. pump);

$$\tau_{fL} = 0.15 Nm$$

Viscous friction constant of motor and load;

$$B_M + B_L = 0.001 Nm/(rad/sec)$$

Coefficient of ω^2 term of load torque;

$$D = 1.6532 \times 10^{-5} Nm/(rad/sec)^2$$

Moment of inertia of the system; $J = 0.024 kg-m^2$

For experimental verification, PV panel (Model No. SW 900), manufactured by Central Electronics Limited, Sahibabad, India, is used. The panel consists of 24 PV modules each of 37.5 W_p (nominal), with aggregate capacity of 900 W_p. The modules are made up of suitable number of single crystalline silicon solar cells, connected in series and hermetically sealed between a highly transparent toughened glass and encapsulating material.

V. SIMULATION OF THE PROPOSED SYSTEM

The MATLAB Simulink is used for transient analysis of the system. Fig. 3 shows the simulation model of the PV powered water pumping system. The PV panel is simulated based on experimental data for I - v characteristic

The voltage equation of the motor can be written as

$$v_a = e_b + i_a R_a + L_a \frac{di_a}{dt} \quad (2)$$

where i_a is the armature current. The back emf, e_b , is given by

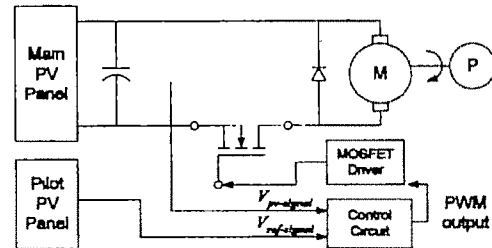


Fig. 2 The block-diagram of the proposed system

$$\omega = \frac{1}{J} \int (\tau_e - \tau_L - \tau_M) dt \quad (8)$$

The model implements the equations of the system described above using various functional blocks. Details of motor-pump system block are shown in Fig. 3 b.

The simulation was carried out for the directly coupled system and the proposed scheme using Simulink software. The PV panel is simulated using actual data of I - V characteristics of the panel. The insolation is changed by using data for higher insolation at $t = 20$ sec. For simulation of directly coupled system, the output of the PV panel block was directly connected to the input of the motor-pump system block.

VI. RESULTS

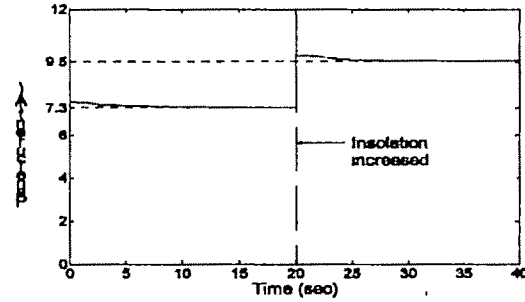
Simulation for directly coupled system was carried out for 40 seconds. Initially the motor is started with low insolation condition ($\lambda=638 \text{ W/m}^2$). At $t = 20$ sec, insolation is increased by using data for higher insolation condition ($\lambda=850 \text{ W/m}^2$). The simulation results are shown in Fig. 4.

Initially, the PV panel is virtually short-circuited by the low armature resistance of the motor. Therefore, the panel current rises close to its short-circuit current of 7.65 A (Fig. 4a) and the panel voltage drops to about 8 volts (Fig. 4b). Therefore the starting current of the motor is limited to the short-circuit current of the PV panel. The motor accelerates to the steady-state speed of 223 rpm (Fig 4d). Under the steady-state condition, the panel voltage and current settle to 45 volts and 7.3 amperes, respectively. The power output of the PV panel is 327 W as shown in Fig. 4c.

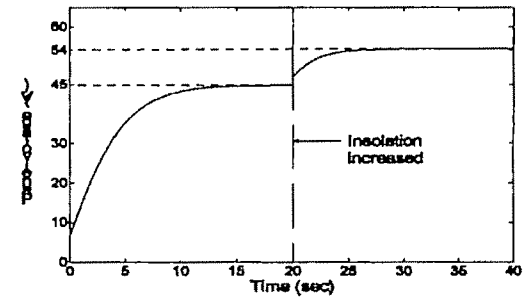
At $t = 20$ sec, insolation is increased by using data for higher insolation condition. The current overshoots and then settles to the new steady-state value of 9.5 amperes and the panel voltage rises to 54 volts. As the voltage increases the motor speed also increases to 266 rad/sec. The panel output power increases to 520 watts.

The simulation results motor-pump system with MPPT are shown in Fig. 5. It can be observed that the panel current rises to near its short-circuit value after the motor is switched on at $t = 1$ sec. and then settles to its MPP value in less than 0.1 seconds (Fig. 5a). The current rises and settles to its new MPP value after the insolation is increased at $t = 20$ s. The panel voltage drops from its no-load value to about 10 volts just after the motor is switched on (Fig. 5b). This is due to the low resistance armature winding which virtually short-circuits the panel. As the motor gains speed, the panel voltage rises and settles to its MPP value in less than 0.1 seconds. When insolation increases at $t = 20$ s, the panel voltage settles to new MPP value in 0.04 seconds.

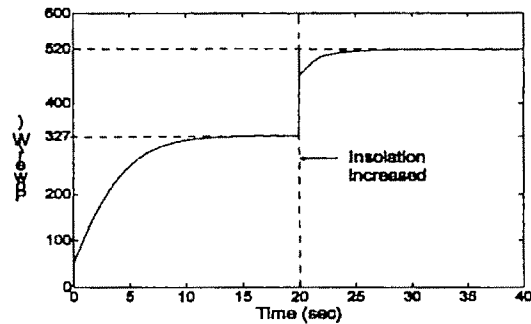
The steady-state power drawn from the PV panel is 400 W for $\lambda = 638 \text{ W/m}^2$ and 529 W for $\lambda = 850 \text{ W/m}^2$. These values are very close to the respective maximum available power of 402 W and 537 W in these ambient conditions. The corresponding values for a directly coupled system were 327 W and 520 W respectively.



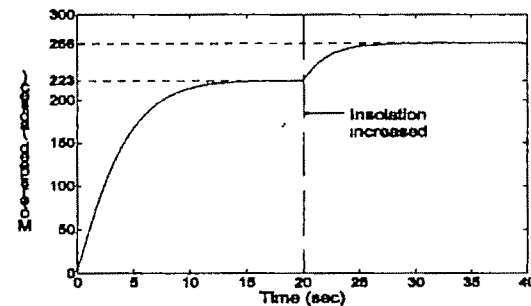
(a)



(b)



(c)



(d)

Fig 4 Simulation results of directly coupled water-pumping system: (a) Panel current, (b) Panel voltage, (c) Output power, (d) Motor speed,

The motor reaches the steady-state speed of 239 rad/sec in about 10 seconds (Fig. 5c). This settling period is less than the time taken by the motor to reach steady-state (about 15 seconds) when connected directly to the PV panel, as shown in Fig. 4c. Also, the motor reaches to attains the new steady state speed within 5 seconds, when insolation changes. Again, it is

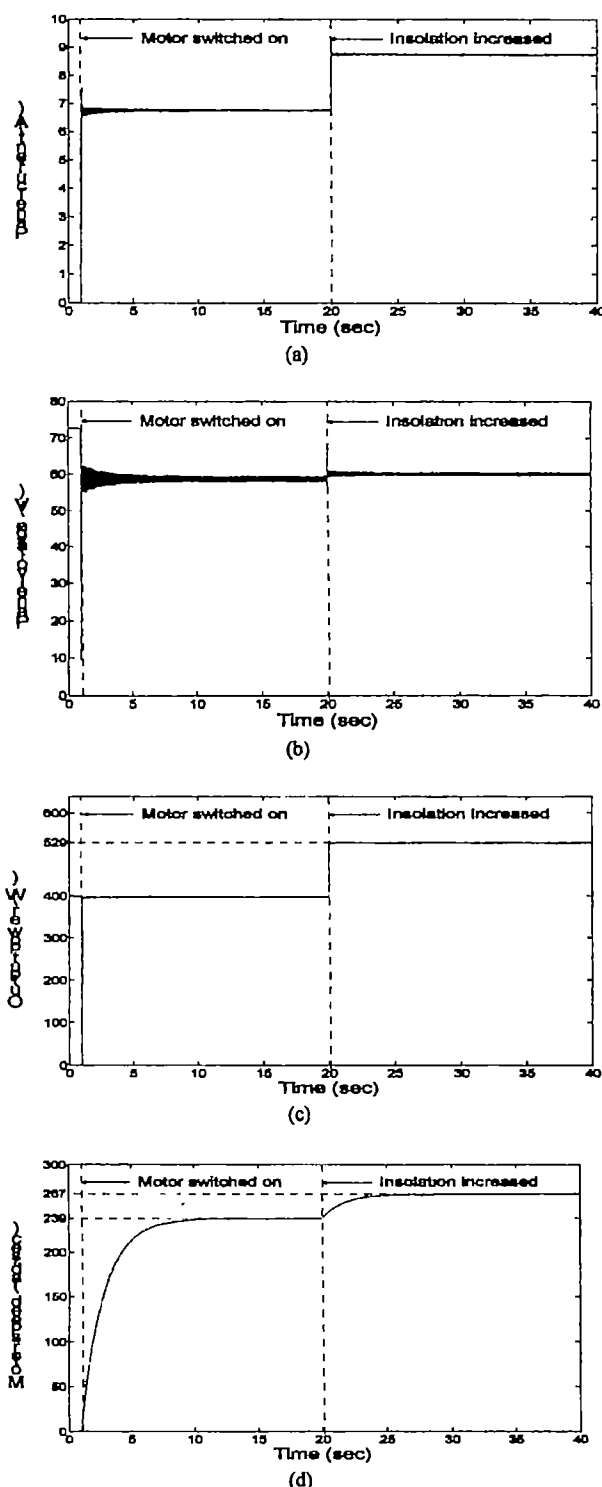


Fig. 5 Simulation waveform of panel voltage of water-pumping system with MPPT (a) Panel current, (b) Panel voltage, (c) Output power, (d) Motor speed

less than the time taken (10 seconds) in case of the directly coupled motor-pump system. Thus, it is evident that the use of MPPT not only increases the power output of the PV panel

almost throughout the day but also improves the transient response of the system. Thus the MPPT increases the power output during the transient condition which is very useful for passing clouds and when the ambient condition changes frequently.

The proposed scheme was realized in the laboratory and a significant increase in the discharge rate of the pump was observed especially at low insolation levels. It was also observed that the system with MPPT operates successfully at very low insolation level of 200 W/m^2 . The directly coupled system does not operate at this insolation level.

VII. CONCLUSION

With the use of proposed MPPT, the PV panel operates very close to its maximum power point. Moreover, the MPPT tracks the MPP very quickly (within a few tens of ms) under varying ambient conditions. The system with MPPT starts quickly and has better transient response as compared to directly coupled system.

REFERENCES

- [1] Ned Mohan, Tore M. Undeland, William P. Robbins, Power Electronics- Converters, applications, and design, 3rd Edition. John Wiley & sons (Asia) pte. Ltd, Singapore, 2005.
- [2] K. Khouzam and L. Khouzam, "Optimum matching of direct-coupled electromechanical loads to a photovoltaic generator," *IEEE Trans. on Energy Conversion*, vol. 8, no. 3, pp. 343-349, 1993.
- [3] M. M. Saleh, "The available matching of solar arrays to dc motors having both constant and series excited field components," *IEEE Trans. on Energy Conversion*, vol. 17, no. 3, Sept. 2002.
- [4] M. Kolhe, J.C. Joshi, and D.P. Kothari, "Performance analysis of a directly coupled photovoltaic water-pumping system," *IEEE Trans. on Energy Conversion*, vol. 19, no. 3, pp. 613-618, Sep. 2004.
- [5] Z. M. Salameh, Z.M. and F. Dagher, "The effect of electrical array reconfiguration on the performance of a PV-powered volumetric water pump," *IEEE Trans. on Energy Conversion*, vol. 5, no. 4, pp. 653-658, Dec. 1990.
- [6] D. Maheshappa, J. Nagaraju, and M.V. Krishna Murthy, "An improved maximum power point tracker using step-up converter with current locked loop," *Renewable Energy Conversion and Management*, vol. 13, no. 2, pp. 195-201, 1998.
- [7] John H.R. Enslin, Mario S. Wolf, Deniel B. Snyman, and Wernher Swiegers, "Integrated Photovoltaic maximum power point tracking converter," *IEEE Trans. on Industrial Electronics*, vol. 44, no. 6, Dec. 1997.
- [8] Abu Tariq and M.S. Jamil Asghar, "Development of an Analog Maximum Power Point Tracker for Photovoltaic Panel," *Proc. of the sixth IEEE Int. Conf. on Power Electronics and Drive Systems*, vol. 1, pp. 542 - 547, Kuala Lumpur, Malaysia, Nov. 28-Dec. 1, 2005.
- [9] M.A.S. Masoum, Hooman Dehboni, and E.F. Fuchs, "Theoretical and experimental analysis of photovoltaic systems with voltage and current based maximum power point tracking," *IEEE Trans on Energy Conversion*, vol. 17, no. 4, Dec. 2002.
- [10] M.A.S. Masoum, S.M. Mosavi, and E.F. Fuchs, "A Microprocessor-controlled new class of optimal battery chargers for photovoltaic applications," *IEEE Trans. on Energy Conversion*, vol. 19, no. 3, Sep. 2004.
- [11] M.S. Jamil Asghar, "Development of maximum power controller for PV based power generation," *UGC Major Research project Report*, March 2002.
- [12] Efthios Koutroulis, Kostas Kalkaitzakis, and Nicholas C. Voulgaris, "Development of a Microcontroller-based Photovoltaic maximum power point tracking control system," *IEEE Trans. on Power Electronics*, vol. 16, no.1, Jan. 2001.
- [13] Nicola Femia, Giovanni Petrone, Giovanni Spagnuolo, Massimo Vitelli, "Optimization of Perturb and Observe Maximum power point tracking method," *IEEE Trans. on Power Electronics*, vol. 20, no. 4, pp. 963-973, Jul. 2005.
- [14] K.H. Hussein, I. Muta, T. Hoshino, and M. Osakada, "Maximum photovoltaic power tracking: an algorithm for rapidly changing atmospheric conditions," *IEE Proc. Gener. Transm. Distrib.*, vol.142, no. 1, pp. 59 - 64, Jan. 1995.

Modeling and Analysis of Particle Movement in a Common Enclosure Gas Insulated Bus Duct Under Unbalanced Voltages

G.V.Nagesh Kumar¹, J.Amarnath², and B.P.Singh³

¹ Vignan's Institute of Information Technology, Andhra Pradesh, INDIA e-mail: gundavarapu_kumar@yahoo.com

² Jawaharlal Nehru Technological University, Hyderabad, INDIA e-mail: amarnathjinka@yahoo.com

³ BHEL Corporate (R & D), Vikas Nagar, Hyderabad, INDIA

Abstract— Sulphur Hexafluoride (SF_6) is generally found to be very sensitive to field perturbations such as those caused by conductor surface imperfections and by conducting particle contaminants. A study of CIGRE group suggests that 20% of failures in Gas Insulated Substations (GIS) is due to the existence of various metallic contaminations in the form of loose particles. The presence of contamination can therefore be a problem with gas-insulated substations operating at high fields. If the effects of these particles could be eliminated, then this would improve the reliability of compressed gas insulated substation. It would also offer the possibility of operating at higher fields to affect a potential reduction in the GIS size with subsequent savings in the cost of manufacture and installation. The purpose of this paper is to develop techniques, which will formulate the basic equations that will govern the movement of metallic particles like aluminium and copper in a bus duct. Simulation is carried out on particle movement with balanced and unbalanced voltages and the results have been presented and analyzed.

Key words— Metallic particles, Electric field effects, Gas Insulated Substations.

I. INTRODUCTION

DEMAND for electrical power has become one of the major challenges faced by the developing countries. Considering the relatively low per capita power consumption, there is a constant need for power capacity addition and technological upgradation whereas non-conventional energy systems have proved to be good alternative sources for energy. In developing countries like India most of the additional power has been met by conventional electrical sources. Hence, the emphasis has shifted towards improving the reliability of transmission and distribution systems and ensuring that the innovations are not harmful to the environment.

Rapid urbanization and overgrowing population is making the task of expanding transmission network very difficult due

to right of way problem and limited space availability. In addition, conventional air insulated substations have many problems such as pollution by salt or dust, meteorological difficulties, safety etc. Hence, there is a need to replace the conventional transmission lines and substations with underground cable and Gas Insulated Substation (GIS) to overcome the above problems. Due to its many advantages, most of the utilities and industrial units are opting for Gas Insulated Substation [1]. In this context, Gas Insulated Substation (GIS) have found a broad range of applications in power systems for more than two decades because of their high reliability, easy maintenance and small ground space requirement etc.

In a Gas Insulated Bus duct (GIB), all live parts are enclosed in compressed Sulphur Hexafluoride gas chambers, which are divided into a number of compartments or bays according to the layout or configuration of its several components. Basic components of the GIS bay are circuit breakers, disconnectors, earthing switches, bus ducts, current and voltage transformers, etc. The inner live parts of GIS are supported by insulators called spacers, which are made of alumina filled epoxy material. The GIS enclosure forms an electrically integrated, grounded enclosure for the entire substation. Even though SF_6 exhibits very high dielectric strength, the withstand voltage of SF_6 within the GIS is drastically reduced due to the presence of particles or defects like:

1. Free particles on the inner surface of the enclosure,
2. Protrusion on the high voltage (HV) bus,
3. Protrusion on the inner surface of the enclosure and
4. Narrow gaps between the spacer and the electrode due to imperfect casting and or imperfect mechanical strength, which may lead to high electrical stress and thus micro discharges.

Free conducting particles are most dangerous to GIS. These free conducting particles may have any shape or size, may be spherical or filamentary (wire like) or in the form of fine dust.

Particles may be free to move or may be fixed on to the surfaces. They may be of conducting material or of insulating material. Particles of insulating materials are not so harmful as they have little effect on the insulating properties of gases. So wire like particles made of conducting material are more harmful and their effects are more pronounced at higher gas pressures. The origin of these particles may be from the manufacturing process, from mechanical vibrations or from moving parts of the system like breakers or disconnectors etc.

Several authors conducted experiments on insulating particles [1-3]. However the presence of atmospheric dust containing conducting particles, especially on the cathode, reduces the breakdown voltage. Conducting particles placed in a uniform ac field lift-off at a certain voltage. As the voltage is raised, the particles assume a bouncing state reaching a height determined by the applied voltage. With a further increase in voltage, the bounce height and the corona current increase until break down occurs. The lift off voltage is independent of the pressure of gas. After the onset of bouncing, the offset voltage is approximately 30% lower than the lift-off voltage. Some of the methods of conducting particle control and de-activation are:

- Electrostatic trapping
- Use of adhesive coatings to immobilize the particles
- Discharging of conducting particles through radiation, and
- Coating conducting particles with insulating films

The work reported in this paper deals with the movement of metallic particle in 3-phase common enclosure Gas Insulated busduct in a common enclosure with balanced and unbalanced voltages. In order to determine the axial and radial movement in an enclosure, Monte-Carlo technique has been adopted in conjunction with motion equation. The specific work reported deals with the charge acquired by the particle due to macroscopic field at the tip of the particle, the force exerted by the field i.e., electric field on the particle, drag due to viscosity of the gas and random behavior during the movement. Wire like particles of aluminum and copper of a fixed geometry in a 3-phase bus duct have been considered. The movement pattern for higher voltages class has been also obtained [4-5]. In Monte-Carlo technique it has been assumed that at every time step the particle can have a maximum movement in a solid angle of 1^0 to 4^0 from vertical.

II. MODELING TECHNIQUE

A typical horizontal three-phase bus duct shown in Figure 1 has been considered for the analysis.

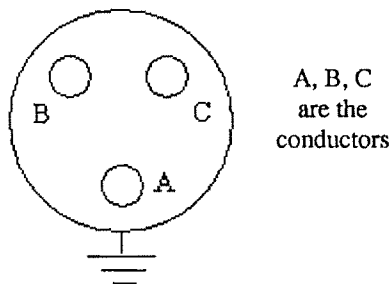


Fig 1 A typical 3-phase common enclosure Gas insulated bus duct

Understanding the dynamics of a metallic particle in a coaxial electrode system is of vital importance for determining the effect of metallic contamination in a Gas Insulated System (GIS). If the motion pattern of a metallic particle is known, the probability of particle crossing a coaxial gap and causing a flashover can be estimated. The lift-off field for a particle on the surface of an electrode can be estimated by solving the motion equation.

A conducting particle in motion in an external electric field will be subjected to a collective influence of several forces. The forces may be divided into:

- Electrostatic force (F_e)
- Gravitational force (mg)
- Drag force (F_d)

The motion equation is given by

$$\frac{m d^2 y}{dt^2} = F_e - mg - F_d \quad (1)$$

where m = mass of the particle

y = displacement in vertical direction

F_e = Electrostatic force

g = gravitational constant

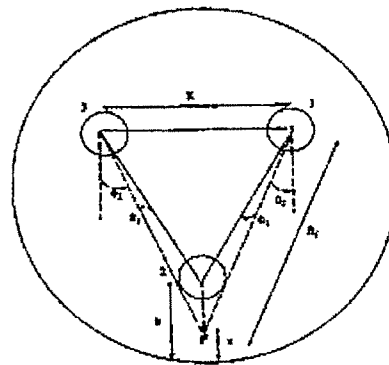


Fig 2. Schematic Diagram of 3-phase common enclosure GIS

Figure 2 shows a horizontal three phase bus duct comprising of inner conductors spaced equilaterally in a metal enclosure. The enclosure is filled with SF_6 gas at a high pressure (0.3 MPa). A particle is assumed to be at rest at the enclosure surface, just beneath the bus bar 2, until a voltage sufficient enough to lift the particle and move in the field is applied.

After acquiring an appropriate charge in the field, the particle lifts and begins to move in the direction of field having overcome the forces due to its own weight and drag. The simulation considers several parameters e.g. the macroscopic field at the surface of the particle, its weight, Reynold's number, coefficient of restitution on its impact to both enclosures and viscosity of the gas. During return flight, a new charge on the particle is assigned based on the instantaneous electric field.

The direction of drag force is always opposed to the direction of motion. The expression for drag Force and Electrostatic force given in equation (2) and equation (3).

$$F_d = \dot{y} \pi \left(6\mu K_d (\dot{y}) + 2.656 \left[\mu \rho_g l \dot{y} \right]^{0.5} \right) \quad (2)$$

where

\dot{y} is the velocity of the particle

μ is the viscosity of the fluid

r is the particle radius

ρ_g is the gas density

l is the particle length

$K_d (\dot{y})$ is the drag coefficient

The Electrostatic Force is given by

$$F_e = \frac{\pi \epsilon_0 l^2 E(t_0)}{\ln\left(\frac{2l}{r}\right) - 1} \times 48.64 \times 10^3 \left[\left(\frac{1}{0.125 - x} \right) - \left(\frac{\cos \theta_2}{R_1} \right) \right] \sin \omega t \quad (3)$$

The above forces are substituted in equation (1) and it becomes a second order non – linear differential equation. To solve the motion equation Runge-Kutta 4th order method is adopted.

III. SIMULATION OF PARTICLE MOTION

The study of the motion of moving metallic particles in GIS requires a good knowledge of the charge of the particle. Simulation of the motion of metallic particles were carried out on GIB of 64 mm inner diameter for each enclosure and 500 mm outer diameter with 400 kV applied to inner conductors with 120° phase difference. Aluminum and copper wire like particles were considered to be present on enclosure surface. Simulation have also been carried out on the same enclosure with unbalanced voltages with phase differences of 0°, 150°, 210°.

In order to determine the random behavior of moving particles, the calculation of movement in axial and radial directions was carried at every time step using rectangular random numbers. The above simulation yields the particle movement in the radial direction only. However, the configuration at the tip of the particle is generally not sufficiently smooth enough to enable the movement unidirectional. This decides the movement of particle in axial direction. The randomness of movement can be adequately simulated by Monte-Carlo method. In order to determine the randomness; it is assumed that the particle emanates from its original site at any angle less than ϕ , where $\phi/2$ is half of the solid angle subtended with the vertical axis. At every step of movement, a new rectangular random number is generated between 0 and 1 and modified to ϕ . The angle thus assigned, fixes the position of particle at the end of every time step, and in turn determines the axial and radial positions. The position in the next step is computed on the basis of equation of motion with new random angles as described above.

IV. RESULTS AND DISCUSSIONS

Table 1 and Table 2 show the radial and axial movement of the particle in a 3- Phase Gas Insulated Bus duct with balanced and unbalanced voltages. The results have been presented by using Monte-Carlo Technique also shown in Table 1 and Table 2. Figure 3 to Figure 20 shows the movement patterns of copper and aluminum particles with balanced voltages and with Monte Carlo Technique for different applied voltages. The radius of the particles in all cases is considered as 0.1 mm and length of the particle as 10 mm.

During its movement it makes several impacts with the enclosure. As the applied voltage increases the maximum radial movement also increases as given in Table 1. Further calculations may reveal the limiting voltage to enable the particle to reach the high voltage conductor. A graphical representation of radial movement in relation to axial movement is given by Monte-Carlo technique as shown in Figure 4. The movements are also calculated for other voltages.

The movement of copper particle with balanced and unbalanced voltages is also given in Table 1 and Table 2. It is noticed that the movement of copper particle is far less than aluminum particle of identical size. This is expected due to higher density of copper particle. The axial and radial movement of aluminum and copper particles are calculated using Monte-Carlo technique with a solid angle of 1°. The movement of aluminum and copper particles with unbalanced voltages is shown in Figures 15 to 20.

Table I. Axial and radial movement of aluminum and copper particles with balanced voltages using Monte-Carlo technique.

Voltage	Type	Max. Radial Movement (mm)	Monte – Carlo (1°)	
			Axial (mm)	Radial (mm)
500 kV	Al	55.69	661.12	55.69
	Cu	13.85	255.70	13.85
600 kV	Al	80.57	1886.6	80.57
	Cu	23.49	457.77	23.49
700 kV	Al	108.23	915.43	108.23
	Cu	32.03	492.1	32.03

Table II. Axial and radial movement of aluminum and copper particles with unbalanced voltages using Monte-Carlo technique.

Voltage	Type	Max. Radial Movement (mm)	Monte – Carlo (1°)	
			Axial (mm)	Radial (mm)
500 kV	Al	9.428	78.82	9.428
	Cu	N.M	N.M	N.M
600 kV	Al	13.56	172.95	13.56
	Cu	N.M	N.M	N.M
700 kV	Al	18.57	307.96	18.57
	Cu	N.M	N.M	N.M

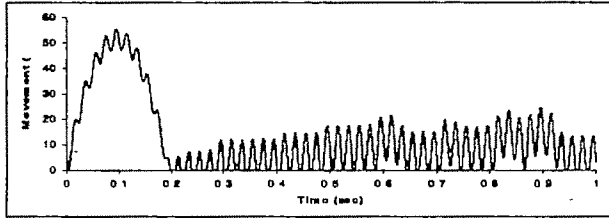


Fig. 3 Particle movement with balanced voltages in a 3-Phase GIB for 500 KV/ Al/ 10mm / 0.1radius

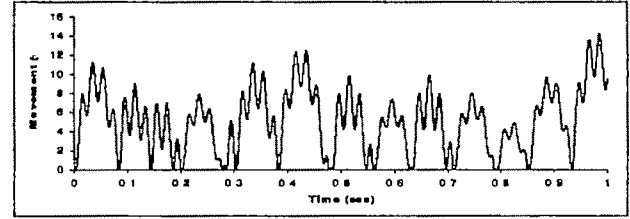


Fig. 9. Particle movement with balanced voltages in a 3-Phase GIB for 500 KV/ Cu/ 10mm / 0.1radius

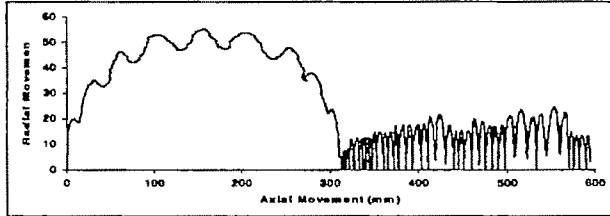


Fig. 4 Axial & Radial movement with balanced voltages in a 3-Phase GIB for 500 KV/ Al/ 10mm / 0.1radius

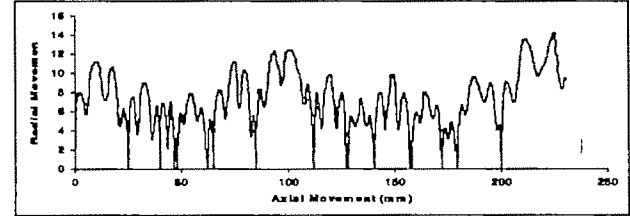


Fig. 10. Axial & Radial movement with balanced voltages in a 3-Phase in a GIB for 500 KV/ Cu/ 10mm / 0.1radius

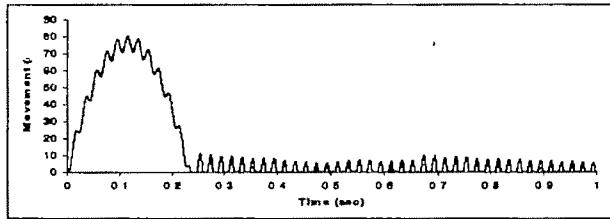


Fig. 5 Particle Movement with balanced voltages in a 3-Phase GIB for Al / 600kV / 10mm / 0.1mm radius

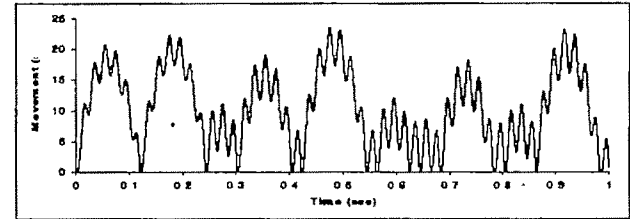


Fig. 11 Particle Movement with balanced voltages in a 3-Phase GIB for CU / 600kV / 10mm / 0.1mm radius

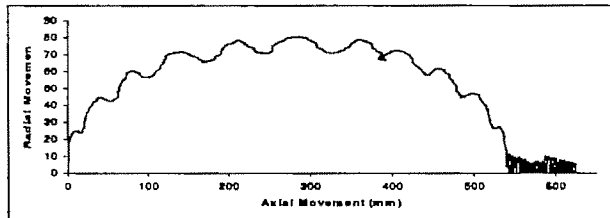


Fig. 6 Axial and Radial Movement with balanced voltages in a 3-Phase GIB for Al / 600kV / 10mm / 0.1mm radius

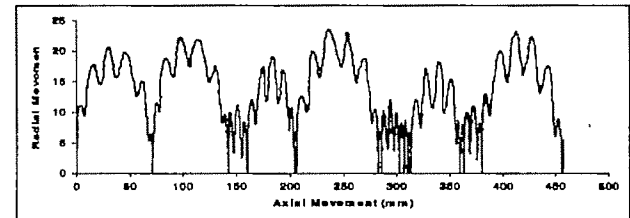


Fig. 12 Axial and Radial Movement with balanced voltages in a 3-Phase GIB for CU / 600kV / 10mm / 0.1mm radius

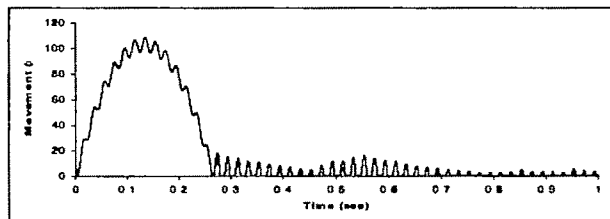


Fig. 7 Particle Movement with balanced voltages in a 3-Phase GIB for Al / 700kV / 10mm / 0.1mm radius

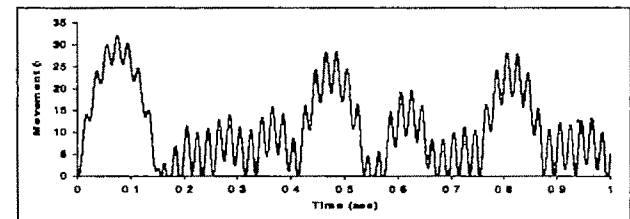


Fig. 13 Particle Movement with balanced voltages in a 3-Phase GIB for CU / 700kV / 10mm / 0.1mm radius

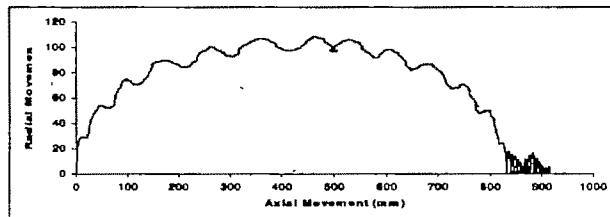


Fig. 8 Axial and Radial Movement with balanced voltages in a 3-Phase GIB for Al / 700kV / 10mm / 0.1mm radius

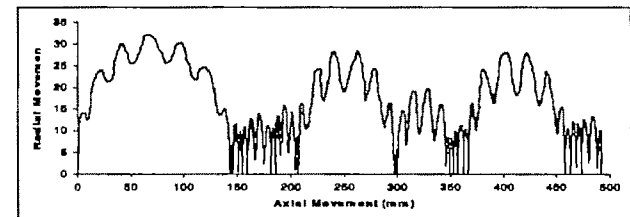


Fig. 14 Axial and Radial Movement with balanced voltages in a 3-Phase GIB for CU / 700kV / 10mm / 0.1mm radius

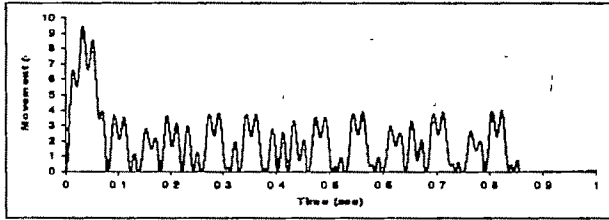


Fig. 15 Particle Movement with unbalanced voltages in a 3- Phase GIB for Al / 500kV / 10mm / 0.1mm radius

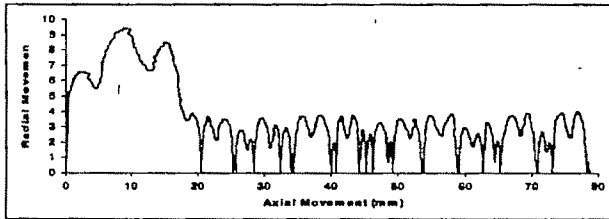


Fig. 16 Axial and Radial Movement with unbalanced voltages in a 3- Phase GIB for Al / 500kV / 10mm / 0.1mm radius

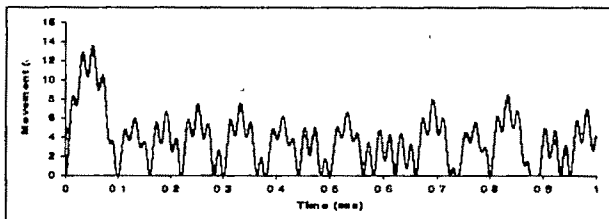


Fig. 17 Particle Movement with unbalanced voltages in a 3- Phase GIB for Al / 600kV / 10mm / 0.1mm radius

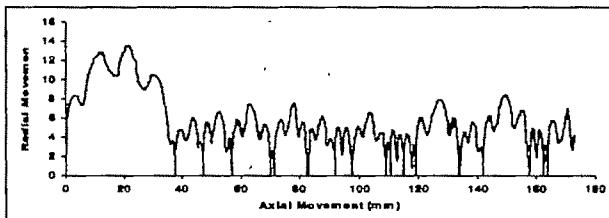


Fig. 18 Axial and Radial Movement with unbalanced voltages in a 3- Phase GIB for Al / 600kV / 10mm / 0.1mm radius

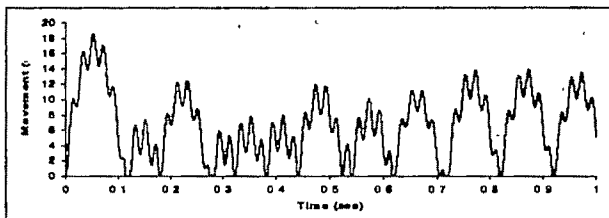


Fig. 19 Particle Movement with unbalanced voltages in a 3- Phase GIB for Al / 700kV / 10mm / 0.1mm radius

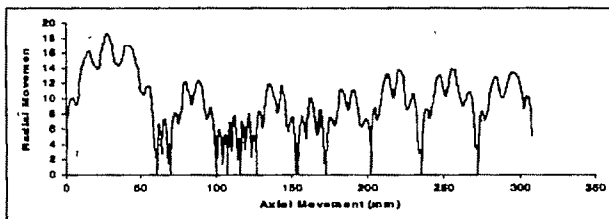


Fig. 20 Axial and Radial Movement with unbalanced voltages in a 3- Phase GIB for Al / 700kV / 10mm / 0.1mm radius

V. CONCLUSION

A model has been formulated to simulate the movement of wire like particle in 3-phase common enclosure GIB on bare electrode. When electrostatic force exceeds the gravitational and drag forces the particle lifts from its position. A further increase in the applied voltage makes the particle move into the inter electrode gap in the direction of applied field. This increases the probability of a flashover.

The influence of increased voltage level on the motion of the particles is also investigated and observed that the particle will lift higher from the surface and the time between bounces will increase. It is also observed that aluminum particles are more influenced by the voltage than copper or silver particles due to their lighter mass. This results in the aluminum particle acquiring greater charge-to-mass ratio.

Generally the system always will not be in balanced condition. So it is required to estimate the particle movement under unbalanced voltage conditions also. In this paper, unbalanced load conditions have been studied and results were presented and analyzed. It has been observed that under these conditions the movement will be less compared to balanced load conditions. This is expected due to resultant electric field under unbalanced conditions is very much reduced so that movement is also decreased.

Monte-Carlo simulation is also adopted to determine axial as well as radial movements of particle in the bus duct. All the above investigations have been carried out for balanced and unbalanced voltages under power frequency.

ACKNOWLEDGMENT

The authors are thankful to the managements of JNT University, Hyderabad and Vignan's Institute of Information Technology, Visakhapatnam for providing facilities and to publish this work.

REFERENCES

- [1] L. G. Christophorou, J. K. Olthoff, R. J. Van Brunt, "SF₆ and the Electric Power Industry", IEEE Electrical Insulation Magazine, DEIS, 1997, pp. 20-24.
- [2] K.S. Prakash, K.D. Srivastava, M.M. Morcos, "Movement of Particles in Compressed SF₆ GIS with Dielectric Coated Enclosure", IEEE Trans. DEI, Vol. 4 pp. 344-347, 1997, No. 600.
- [3] J. Amarnath "Determination of Particle Trajectories in Gas Insulated Bus duct by Monte-Carlo Technique" – Presented at CEIDP-99 Austin (Texas), USA sponsored by IEEE during October 17-21, 1999, Austin, USA.
- [4] H Anis and K.D. Srivastava, "Breakdown Characteristics of Dielectric Coated Electrodes in Sulphur Hexafluoride Gas with Particle Contamination", Sixth Intern Sympos High Voltage Engineering, Paper No. 32.06, New Orleans, LA, USA. 1989.
- [5] G.V.Nagesh Kumar, J. Amarnath, B.P. Singh and K.D. Srivastava, "Electric Field Effect on Metallic Particle Contamination in a Common Enclosure Gas Insulated Bus duct", IEEE Transactions in Dielectrics and Electrical Insulation, April 2007, PP. 334-340.

Maximum Power Point Tracking Using Perturb and Observe Algorithm

Vineta Agarwal¹, Alok Kumar Vishwakarma², B.K. Pandey³

¹Electrical Engineering Department MNNIT Allahabad, India, e-mail: vineta_agarwal123@rediffmail.com

²NCPS DADRI, NTPC Ltd., India, e-mail: alok_ec@yahoo.com

³NCPS DADRI, NTPC Ltd., India, e-mail: brajeshkumarpandey@ntpc.co.in

Abstract—Modeling of solar cell has been done based on single diode model. A MATLAB script file has been written to obtain the various characteristics with changing atmospheric condition. It is seen that there exists a maximum power point, which changes with varying atmospheric condition. To track the maximum power point, Perturb and Observe based algorithm has been implemented. Simulation results demonstrate the fast and effective response.

Key Words— Insolation, Maximum power point, Photovoltaic, Perturbation & Observation

I INTRODUCTION

PHOTOVOLTAIC (PV) generation is becoming increasingly important as a renewable source since it offers many advantages such as incurring no fuel costs, not being polluting, requiring little maintenance, and emitting no noise, among others [1]. Due to their nonlinear and temperature-dependent voltage– current and power-voltage characteristics, these modules have relatively high fabrication cost and low conversion efficiency. These drawbacks can be overcome by improving the manufacturing processes of solar arrays with respect to materials and manufacturing of PV arrays [2]. Controlling the insolation input to PV arrays, the input solar energy is maximized using sun-tracking solar collectors or rearranging the solar-cell configurations of PV arrays with respect to changes in environmental conditions [3].

The main reasons for low electrical efficiency are the nonlinear variations of output voltage and current with solar radiation levels, operating temperature. The amount of power generated by a PV depends on the operating voltage of the array. A PV's maximum power point (MPP) varies with solar insolation and temperature. Its V-I and V-P characteristic curves specify a unique operating point at which maximum possible power is delivered. At the MPP, the PV operates at its highest efficiency. Therefore, many methods have been developed to determine MPP. In Look-up table based methods [4], the nonlinear and time-varying nature of solar cells and their great dependency on

radiation and temperature levels as well as degradation (aging, dirt) effects, make it difficult to record and store all possible system conditions. Perturbation and observation (P&O) method [5] employs the measured cell characteristics (current, voltage, power) along with an online search algorithm to compute the corresponding maximum power point independent of insolation, temperature, or degradation levels. In Computational methods [6], the non-linear V-I characteristics of solar panel are modeled using mathematical equations or numerical approximations. Based on the modeled V-I characteristics, the corresponding maximum power points are computed for different load conditions as a function of cell open-circuit voltages or cell short-circuit currents. All these methods vary in complexity, sensors requirement, convergence speed, cost, and range of effectiveness, hardware implementation, and popularity. It is difficult to adequately determine which method is most appropriate for a given PV system.

In this paper an attempt has been made to implement Perturbation and observation (P&O) based algorithm to track the maximum power point. For this purpose a model of solar cell is developed in MATLAB and used to obtain the various characteristics with changing atmospheric condition.

II. PV SYSTEM MODULE

Fig. 1 shows the block diagram of a photovoltaic drive system. It consists of a power source, which is basically a solar cell array and a power conditioner unit (PCU), which may be a dc/dc converter (step up/step down), acts as an interface between the load and the module. It serves the purpose of transferring maximum power from the solar PV module to the load.

The photovoltaic modules are made up of silicon solar cell consisting of a p-n junction fabricated in a thin wafer or layer of semiconductor. It converts sunlight into electricity. The simplest equivalent circuit of a solar cell is a current source in parallel with a shunt diode and a series

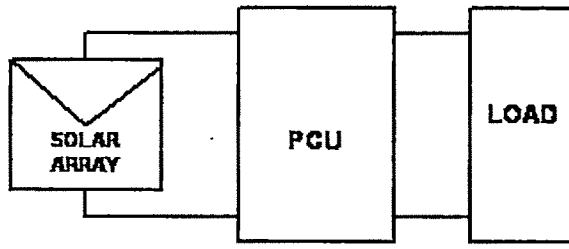


Fig. 1 Block diagram of grid connected PV system

resistance R_S as shown in Figure 2. This model is a simplified version of the two diode model presented by Gow and Manning [9].

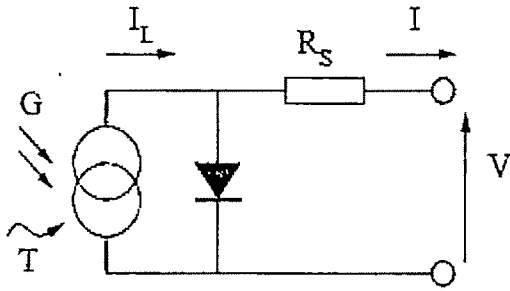


Fig. 2 Circuit diagram of the PV model

The output of the current source is directly proportional to the light falling on the cell. The I-V output characteristic of a solar cell has an exponential characteristic similar to that of a diode and given by (1)

$$I = I_L - I_o \left[e^{\frac{q}{\eta KT}(v + iR_s)} - 1 \right] \quad (1)$$

Where, I_L = light generated current
 I_o = reverse saturation current

Fig. 3 shows the I-V characteristics of the solar cell. It can be noted that the characteristics is highly non linear. In general, the output current of a solar array is the function of the insolation and temperature. The various important parameters of the cell are the short circuit current I_{SC} , which is almost equal to I_L . It can be noted that the cell is safe with a short circuit. The magnitude of this current depends on the area of cell and is directly proportional to solar insolation. V_{OC} is the open circuit voltage and it varies logarithmically with solar insolation, hence does not vary very much. It is sensitive to temperature. In general, a silicon solar cell, gives an output voltage of around 0.7V under open circuit condition. When many such cells are connected in series a solar PV module is obtained. Normally in a module there are 36 cells which amount for

a open circuit voltage of about 20V. For obtaining higher power output the solar PV modules are connected in series and parallel combinations forming solar PV arrays [10].

The nonlinear V-I characteristics of M parallel strings with N series cells per string is given by (2)

$$V_{PV} = \frac{N}{\lambda} \ln \left(\frac{I_{SC} - I_{PV} + MI_O}{MI_O} \right) - \frac{N}{m} \times R_S \times I_{PV} \quad (2)$$

Here λ is a constant co-efficient and depends on the cell material.

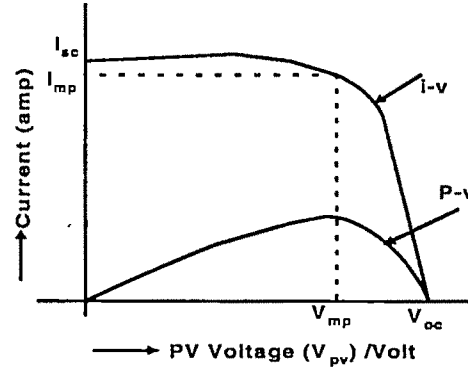


Fig. 3 V-I and P-V Characteristics of Solar Cell

Fig. 3 also shows the power-voltage characteristic curve for a PV array. It can be noted that maximum power is available at a certain voltage V_{mp} and current I_{mp} only. So in order to obtain the maximum efficiency of PV cell, it is necessary to find automatically the voltage V_{mp} or current I_{mp} at which a PV array should operate to obtain the maximum power output P_{mp} under a given temperature and irradiance. It is noted that under partial shading conditions, in some cases it is possible to have multiple local maxima, but overall there is still only one true maximum power point.

III. MAXIMUM POWER TRACKING

To ensure that the array keeps on operating at the maximum power point, a perturb and observe method is used where at regular intervals (one every few seconds) the amount of current drawn is perturbed and the resulting power output is observed. If an increased current results in a higher power, it is further increased until power output begins to decline. On the other hand, if an increase in current results in less power than before, then the current is decreased until the power output stops increasing and begins to go down.

A suitable dc/dc converter with a proper duty cycle can be introduced between the load and the solar PV module as shown in Fig. 1. The duty cycle, D, of the converter is changed till the peak power point is obtained.

Fig. 4 shows the flow chart of the algorithm for tracking maximum power. The algorithm reads the value of current and voltage from the solar PV module and power is calculated from those measured voltage and current. The value of voltage and power at k th instant are stored. Then next values at $(k+1)$ th instant are measured again and power is calculated from the measured values. The power and voltage at $(k+1)$ th instant are subtracted with the values from k th instant. It has been observed from the power voltage curve of the solar PV module that in the right hand side curve where the voltage is almost constant the slope of power voltage is negative ($dP/dV < 0$) where as in the left hand side the slope is positive ($dP/dV > 0$). The right side curve is for the lower duty cycle (nearer to zero) where as the left side curve is for the higher duty cycle (nearer to unity). Depending on the sign of $dP = (P(k+1) - P(k))$ and $dV = (V(k+1) - V(k))$ after subtraction the algorithm decides whether to increase the duty cycle or to reduce the duty cycle.

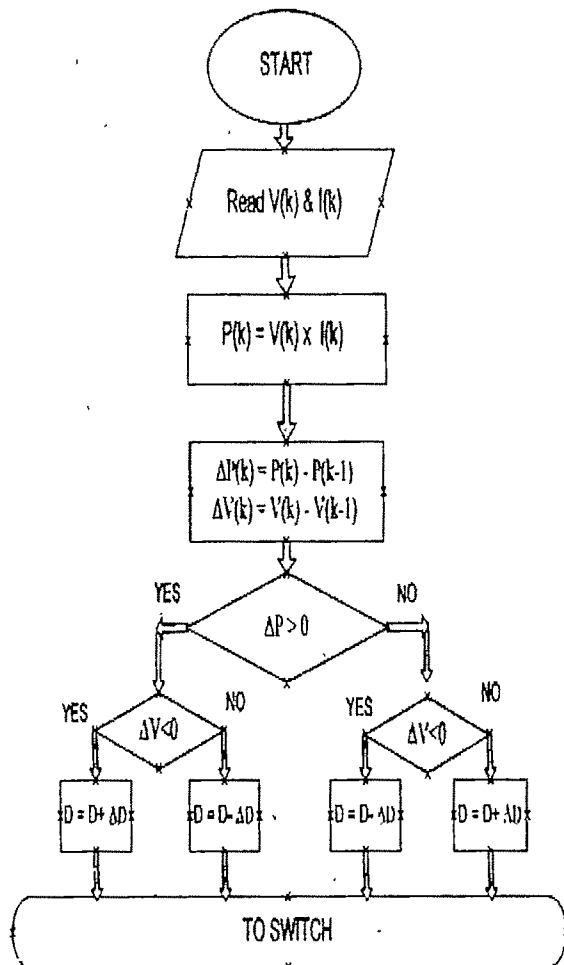
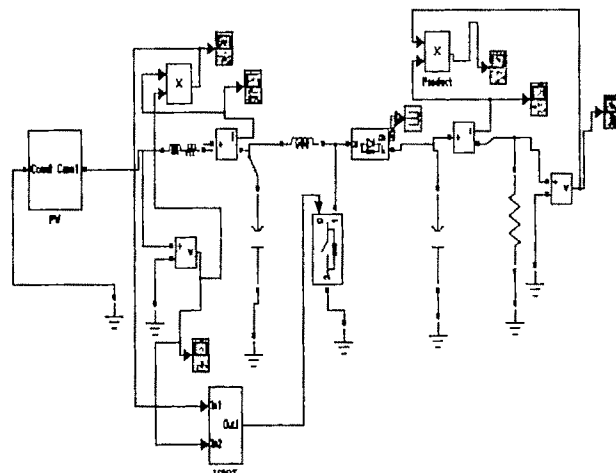


Fig 4 Perturb & Observe MPPT Algorithm

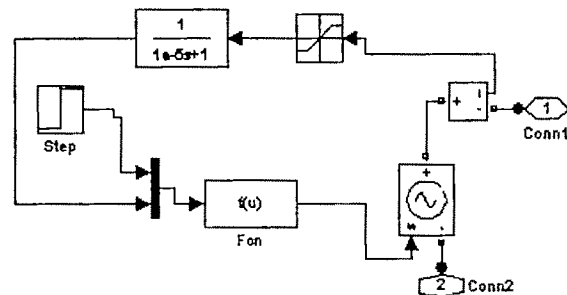
IV. MATLAB SIMULATION

SUMILINK software and its facilities has been used to model a resistive- load solar system with a P&O tracker as shown in Fig. 5(a). For the solar cell equivalent circuit, a block has been created called "PV source" which simulates the nonlinear $V-I$ characteristics of one PV panel employing the cell short circuit (I_{sc}) as a measure of insolation level as shown in Fig. 5(b). A delay function has been introduced to limit the fast current response of the "controlled voltage source" and to improve the convergence of solution.

Fig. 6 shows the relationship between the output voltage and current of a PV panel in MATLAB environment with changing solar insolation and temperature. The short circuit current is influenced mostly by solar irradiation reaching the panel. Higher is irradiation higher is the current. The open-circuit voltage is affected with the temperature of the panel. Higher temperature results lower voltage.

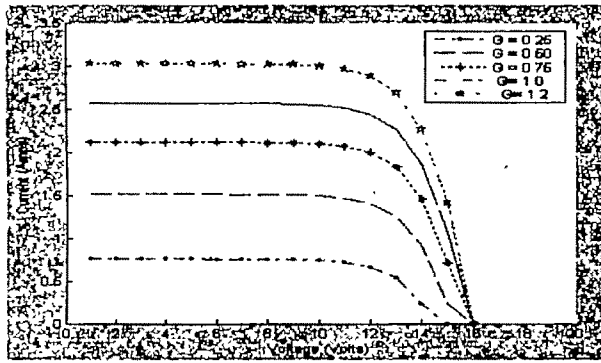


(a) Circuit Diagram

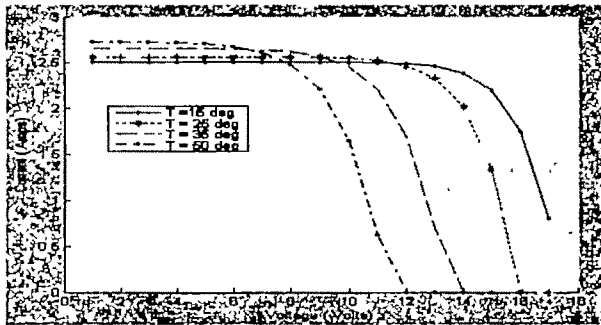


(b) Subsystem PV source

Fig. 5 Simulation Diagram



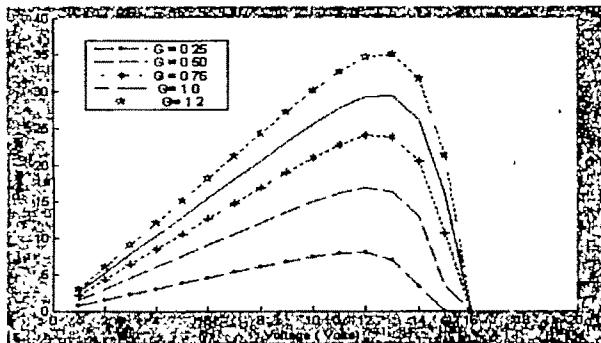
(a) With changing solar insolation



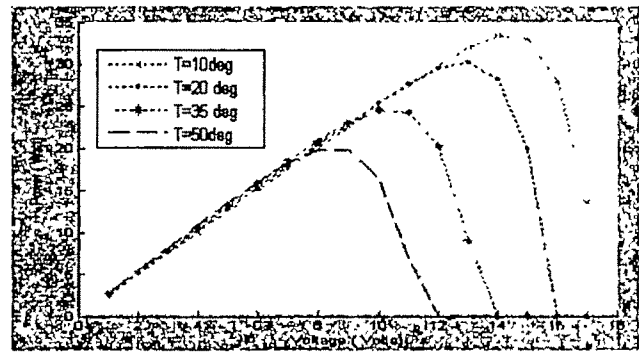
(b) With temperature variation

Fig. 6. I-V characteristics of PV cell

Fig. 7 shows the power vs. voltage (P-V) characteristics with temperature variation and solar insolation. As seen in the PV curve of the module there is a single maxima of Power. That is there exists a peak power corresponding to a particular voltage and current. Since the efficiency of the solar PV module is low about 13%, it is desirable to operate the module at the peak power point so that the maximum power can be delivered to the load under varying temperature and insolation conditions.



(a) with changing solar insolation



(b) with temperature variation

Fig 7 P-V characteristics

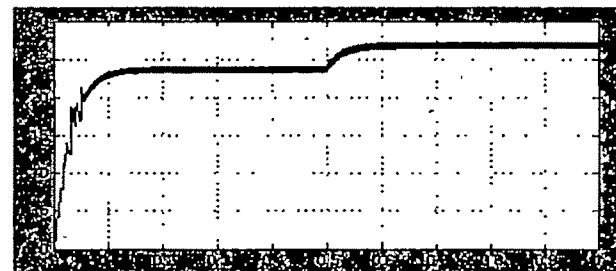
Tracking performance has been demonstrated for different changes in solar insolation level. Fig. 8 and 9 show the various plots for PV power, load power, and load voltage, when solar insolation level change from 800 W/m² to 1000 W/m² at $t = 0.5$ s as shown in Fig. 8 and from 900 W/m² to 800 W/m² at $t = 0.5$ s as shown in Fig. 9.



(a) PV power



(b) Load Power



(c) Load Voltage

Fig. 8 Simulation results when solar insolation level change from 800 W/m² to 1000 W/m²

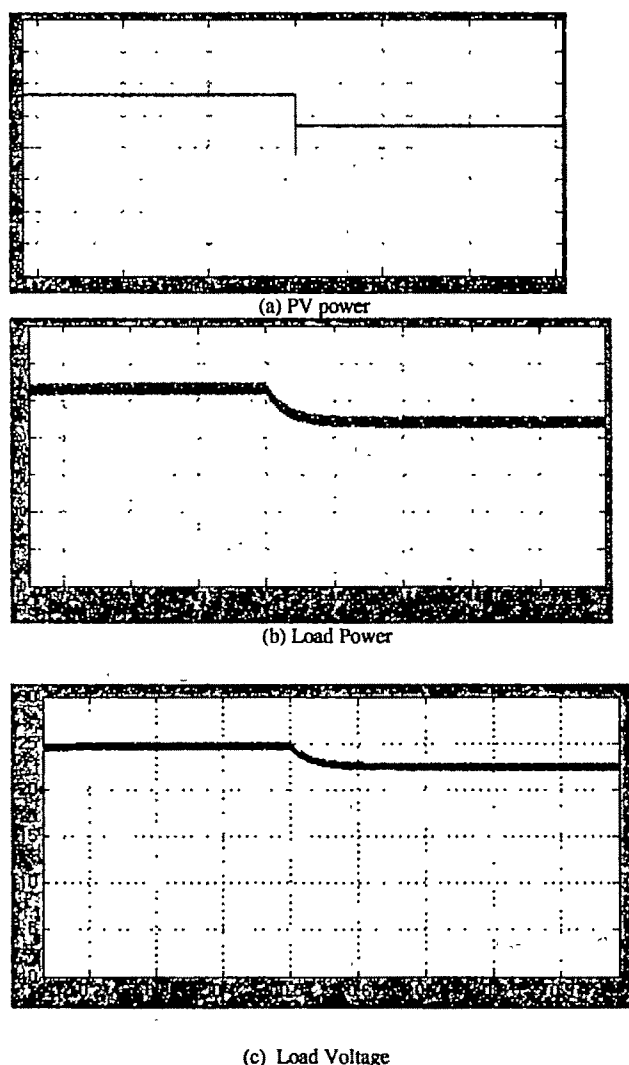


Fig.9 Simulation results when solar insolation level from 900 W/m² to 800 W/m² at $t = 0.5$ s

It can be seen from the curves that power tracked by MPPT is constant for a specified solar insolation. When the insolation is changed the power generated by PV cell also changes proportionally and remains constant. Thus, it shows the new maximum power point. The simulation results show the fast and effective tracking of the new maximum power point by P&O algorithm.

VI. CONCLUSIONS

Modeling of solar cell has been done using based on single diode model. Various characteristics of PV cell with changing atmospheric condition has been obtained and It is seen that there exists a maximum point point, which changes with changing atmospheric condition. To track the maximum power point, Perturb & observe based MPPT algorithm has been implemented. Simulation results demonstrate the fast and effective response under changing atmospheric condition.

REFERENCES

- [1] C. Hua, C. Shen, "Comparative study of Peak Power Tracking Techniques for Solar Storage Systems," IEEE Applied Power Electronics Conference and Exposition Proceedings, Vol. 2, Feb. 1998.
- [2] [1] Z. Zinger and A Brawnstem, "Optimum operation of a combined system of solar cell array and a DC motor", IEEE Transactions on Power System apparatus and systems, vol. PAS-100, pp. 1193-1197, 1983
- [2] C. Hua and C. Shen, "Study of Maximum Power Tracking Techniques and Control of DC/DC Converters for Photovoltaic Power System," 29th Annual IEEE PESC, IEEE Computer Soc. Press, New York, USA, 1998
- [3] G. Walker, "Evaluating MPPT converter topologies using a MATLAB PV model," Journal of Electrical & Electronics Engineering, Australia, vol. 21, 2001
- [4] H. Sugimoto and H. Dong, "A new scheme for maximum photovoltaic power tracking control," in Proceedings of the Power Conversion Conference, 1997
- [5] H. S.-H.Chung, K. K. Tse, S. Y. R. Hui, C. M. Mok, and M. T. Ho, "A novel maximum power point tracking technique for solar panels using a SEPIC or Cuk converter," IEEE Transactions on Power Electronics, vol. 18, pp. 717-724, May 2003.
- [6] C. Hua, C. Shen, "Comparative study of Peak Power Tracking Techniques for Solar Storage Systems," IEEE Applied Power Electronics Conference and Exposition Proceedings, Vol. 2, Feb. 1998.
- [7] Nicola Femla, Giovanni Spagnuolo, "Optimization of Perturb and Observe maximum Power Point Tracking Method", IEEE transactions on Power Electronics, Vol. 20, No. 4, July 2005.
- [8] Sachin Jain, Vivek Agrawal, "A new algorithm for rapid tracking of approximate maximum power point in photovoltaic system," IEEE Power Electronics Letters, Vol. 2, No. 1, March 2004
- [9] J.A. Gow, C.D. Manning, "Development of a photovoltaic array model for use in power electronics simulation studies," IEE Proceedings on Electric Power Applications, Vol. 146, no. 2, March 1999
- [10] H. H. Lim and D. C. Hamill, "Simple maximum power point tracker for photovoltaic arrays," Electronics Letters, vol. 36, pp. 997-999, May 2000.
- [11] J. A. M. Bleijs and A. Gow, "Fast maximum power point control of current-fed DC-DC converter for photovoltaic arrays," Electronics Letters, vol. 37, pp. 5-6, Jan. 2001.
- [12] S. Yuvarajan and S. Xu, "Photo-voltaic power converter with a simple maximum-power-point-tracker," in Proceedings of the 2003 International Symposium on Circuits and Systems, 2003.
- [13] V. Arcidiacono, S. Corsi, and L. Lambri, "Maximum power point tracker for photovoltaic plants," in Proceedings of the IEEE Photovoltaic Specialists Conference, 1982.

Open Circuit VMPPT with current compensation for low power photovoltaic cell

Vineeta Agarwal¹, Alok Kumar Vishwakarma², B.K. Pandey³

¹Electrical Engineering Department MNNIT Allahabad, India, e-mail: vineeta_agarwal123@rediffmail.com

²NCPS DADRI, (U.P) NTPC Ltd., e-mail: alok_ee@yahoo.com

³NCPS DADRI, (U.P) NTPC Ltd., e-mail: brajeshkumarpandey@ntpc.co.in

Abstract- A Photovoltaic cell has been modeled for small-scaled low power application where a boost converter with current compensation has been used to track maximum power point. The method samples the open circuit voltage of PV module to get the reference voltage including current compensation during one sampling period. It has been found that proposed MPPT technique with current compensation increases power transferred to the load approximately 6%. Since it doesn't require digital signal processor (DSP), so its having the merits of both a cost efficiency and a simple control circuit design. The validity of proposed MPPT technique is verified through simulation in MATLAB/SIMULINK.

Keywords- Photovoltaic, open circuit voltage, maximum power point tracking (MPPT), DSP, Voltage factor

I. INTRODUCTION

PHOTOVOLTAIC (PV) generation is becoming increasingly important as a renewable source since it offers many advantages such as incurring no fuel costs, not being polluting, requiring little maintenance, and emitting no noise, among others [1]. But these modules have relatively low conversion efficiency. Therefore, controlling maximum power point tracking (MPPT) for the solar array becomes essential in a PV system. The amount of power generated by a PV depends on the operating voltage of the array. A PV's maximum power point (MPP) varies with solar insolation and temperature [2]. Its I-V and P-V characteristic curves specify a unique operating point at which maximum possible power is delivered. At the MPP, the PV operates at its highest efficiency. Many methods have been developed to determine MPPT. The electric power supplied by a photovoltaic power generation system depends on the solar radiation and temperature. Designing efficient PV systems heavily emphasizes to track the maximum power operating point. In fact, so many methods have been developed that it has become difficult to adequately determine which method, newly proposed or existing, is most appropriate for a given PV system.

Some MPPT methods may require digital signal processor (DSP) and some systems may be without using DSP. MPPT systems based on DSP include the hill-climbing Methods [3] and the MPPT method using short circuit current of PV-module [4]. Between the hill-climbing methods, P&O method [5] tracks MPP of PV-module by

repeatedly increasing or decreasing the output voltage at MPP of PV module. This method not only has relatively simple control algorithm but also tracks MPP of PV-module well. However, when atmospheric conditions are constant or slowly changed, P&O method is oscillated close to MPP. Especially, when those are rapidly changed, this method fails to track MPP.

The incremental conductance method developed to improve these problems of P&O method tracks MPP of PV-module by comparing incremental conductance with instantaneous one. As a result, under rapidly changing atmospheric conditions, this method tracks MPP very well, but the response speed of finding MPP is declined because the calculation time of DSP is increased by relatively complicated control algorithm. Although the MPPT methods based on DSP, above mentioned, are applicable to above 1KW large scaled PV systems, to use DSP loses cost efficiency in small-scaled PV-applications. Therefore, the MPPT methods without using DSP in small-scaled PV-system have also been developed [6]. Among them, the MPPT method using open circuit voltage of PV-module uses the fact that the operating voltage at MPP of PV-module is near linearly proportional to open circuit voltage at MPP of PV-module [7]. This method has a cost efficiency as well as a very simple control circuit because it does not use the DSP. However, in this method, the reference voltage is not changed until the next sampling occurs. As a result, in this method the considerable error power occurs because the output voltage of PV module only follows the unchanged reference voltage during one sampling period.

In this paper an improved MPP tracking method with current compensation has been proposed so that the output current of PV-module always follows the continuously changing reference current during one sampling period under changing atmospheric conditions. The validity of the proposed method is verified through simulation in MATLAB/SIMULINK.

II. PV SYSTEM MODULE

Fig. 1 shows the block diagram of a photovoltaic drive system. It consists of a power source, which is basically a solar cell array and a power conditioner unit (PCU) that may be a dc/dc converter (boost converter) which acts as an interface between the load and the module. It serves the purpose of transferring maximum power from the solar PV

module to the load. By changing the duty cycle the load impedance as seen by the source is varied and matched at the point of the peak power with the source so as to transfer the maximum power.

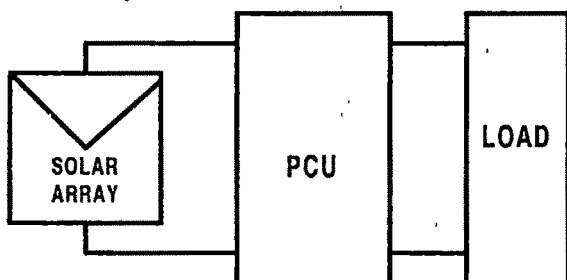


Fig. 1 Block diagram of grid connected PV system

Solar cells consist of a p-n junction fabricated in a thin wafer or layer of semiconductor. In the dark, the I-V output characteristic of a solar cell has an exponential characteristic similar to that of a diode.

When exposed to light, photons with energy greater than the band-gap energy of the semiconductor are absorbed and create an electron-hole pair. These carriers are swept apart under the influence of the internal electric fields of the p-n junction and create a current proportional to the incident radiation. When the cell is short circuited, this current flows in the external circuit; when open circuited, this current is shunted internally by the intrinsic p-n junction diode. The characteristic of this diode therefore sets the open circuit voltage characteristics of the cell.

Thus the simplest equivalent circuit of a solar cell is a current source in parallel with a diode [8]. The output of the current source is directly proportional to the light falling on the cell. The diode determines the I-V characteristics of the cell [9].

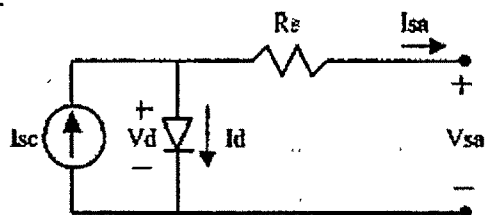


Fig. 2 Circuit diagram of PV model

Using the equivalent circuit of solar cells (Fig.1), the nonlinear V-I characteristics of M parallel strings with N series cells per string is given as,

$$V_{PV} = \frac{N}{\lambda} \ln \left(\frac{I_{SC} - I_{PV} + M I_0}{M I_0} \right) - \frac{N}{m} \times R_S \times I_{PV} \quad (1)$$

Where I_{SC} is the short circuit current (representing insolation level), I_0 is the reverse saturation current, R_S is the series resistance and λ is a constant co-efficient and depends on the cell material.

Figures 3, 4, 5 and 6 show the I-V and P-V characteristic curves of PV-module for different value of irradiation and temperature.

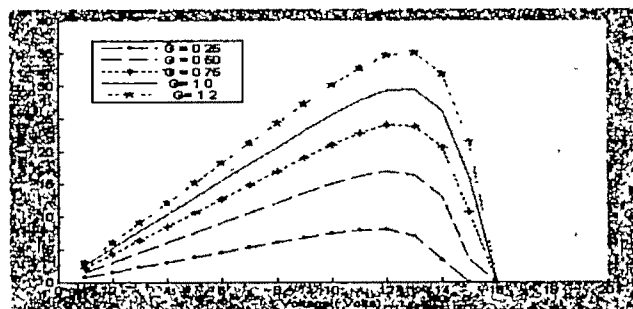


Fig 3: P-V chars for various insolation levels

From Fig. 3, it can be seen that the output characteristics of PV-module are nonlinear and each curve only has one MPP. Additionally, the output current of PV module is mainly affected by irradiation variation, whereas the output voltage of PV-module is mainly affected by temperature variation. Therefore, to efficiently use PV module, in case the atmospheric conditions are varied, the MPP tracking of PV-module should be implemented.

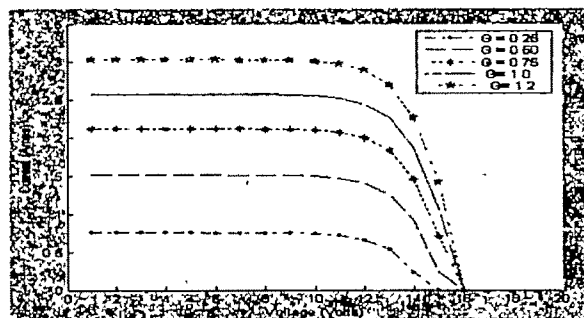


Fig 4: I-V chars for various insolation level

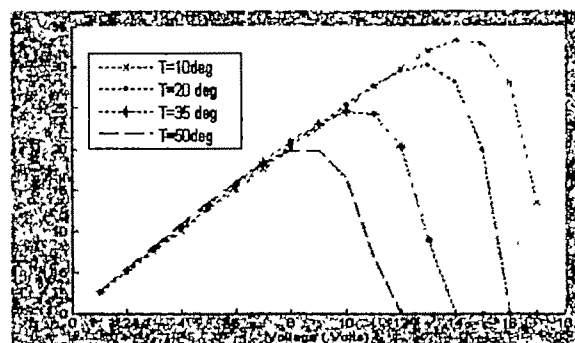


Fig 5: P-V characteristics for different values of temperatures

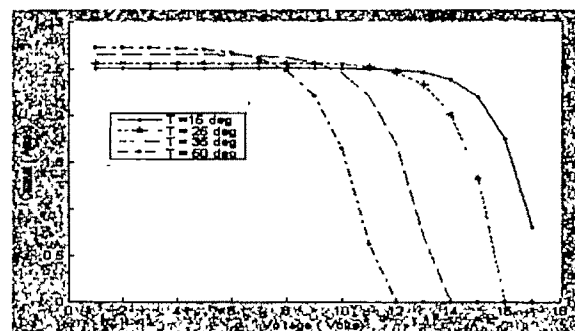


Fig 6: I-V characteristics for different values of temperatures

III MAXIMUM POWER POINT TRACKING

a. Conventional Method

Fig. 7 shows the conventional MPPT converter using open circuit voltage of PV-module in small-scaled PV-power system. This method uses the fact that the operating voltage at MPP of PV-module is nearly linear proportional to open circuit voltage (V_{oc}) of PV-module.

$$V_{mp} = M_v \times V_{PV} \quad (2)$$

The proportional constant (M_v) generally lies in between 0.68 - 0.8. The open circuit voltage is sampled and the reference voltage corresponding to MPP is calculated by (2). The reference voltage is kept constant by a hold circuit during one sampling period. This method achieves MPP tracking of PV module by giving the switching signal acquired through voltage control loop to the switch of boost converter.

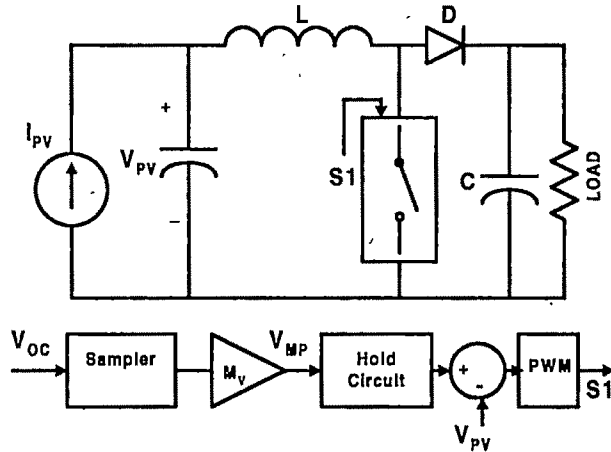


Fig. 7 Conventional MPPT converter based on open circuit voltage

Though the method tracks the MPP well, but the reference voltage is not changed until the next sampling occurs. As a result, always there occurs the considerable error power because the output voltage of PV module only follows the unchanged reference voltage during one sampling period.

b. Proposed MPP tracking with current compensation

Fig. 8 shows the block diagram of the proposed MPP tracking system.

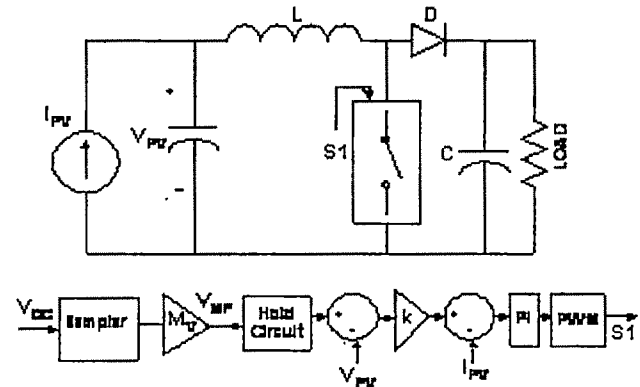


Fig.8 Proposed technique with current compensation

To determine the operating point corresponding to maximum power for different insolation levels, (1) is used to compute the partial derivative of power. At the point of maximum power, it is zero.

In order to improve the tracking performance, the proposed method includes the current compensation so that current control loops continuously helps in reducing the error during the sampling period of V_{oc} . The sampler samples the open circuit voltage of the PV module. The sampling time is $100\mu s$. The sampled voltage multiplied with voltage factor (M_v) is kept in hold circuit as a reference voltage for the voltage control loop during the sampling period. The output of voltage control loop produces reference signal for current control loop continuously during one sampling period. As a result, the proposed tracking method has less power error in tracking as compared to conventional method of tracking using open circuit voltage of PV module without compensation. So, the utilization efficiency of PV module increases.

IV. SIMULATION

To verify the validity of the proposed MPP tracking method, which is mostly suitable for small-scaled PV systems, and to compare the proposed method with the conventional method, the simulations were implemented under same conditions in MATLAB/SIMULINK.

For the solar cell equivalent circuit, a block "PV source" has been created as shown in Fig. 9, which simulates the nonlinear V-I characteristics of a 30 W solar panel, employing the short circuit current as a measure of insolation level. A delay function has been introduced to limit the fast response of the "controlled voltage source" and to improve the convergence of the solution.

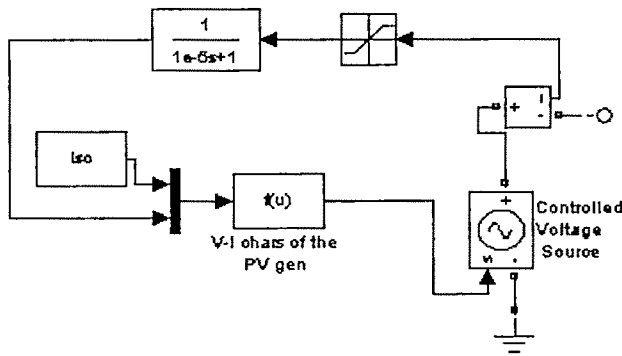


Fig. 9 PV Source

To represent the changing environment conditions I_{SC} is varied as shown in Fig. 10.

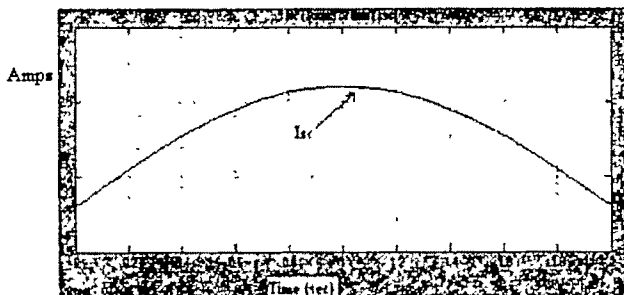


Fig. 10 I_{sc} variation to represent variation in solar intensity

Fig. 11 and Fig. 12 shows the waveforms of the ideal and the tracked output power of the conventional and the proposed MPP tracking method, respectively.

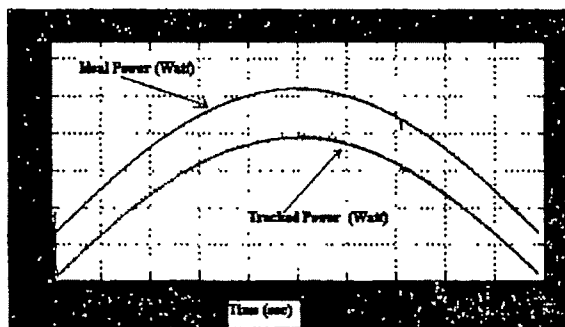


Fig.11 Tracked power with conventional method

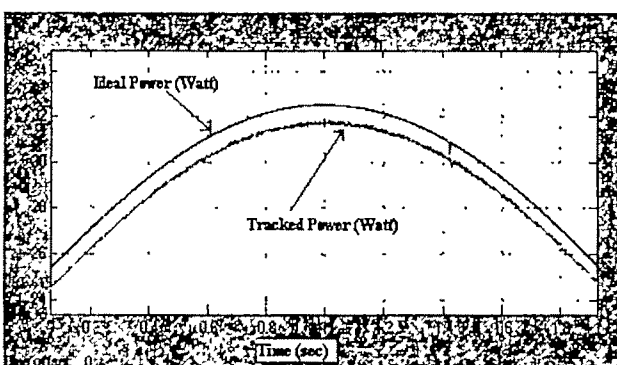


Fig.12 Tracked power with current compensation

It can be seen from Fig 11 and Fig 12 that in the proposed method with current compensation the tracked power increases by more than 6%.

V. CONCLUSION

A maximum power point tracking technique based on open circuit voltage of PV module with current compensation was presented in this paper.

The concept of proposed technique was explained and simulation was performed in MATLAB/SIMULINK. The proposed MPPT tracking method increases output power more than 6% as compared to the conventional method. So, the utilization efficiency of the PV module will be increased. This method has the merits such as simple control circuit and doesn't require DSP leading to cost advantage. Therefore, this method is suitable for low power, low cost Photovoltaic applications.

VI. REFERENCES

- [1]. Chihchiang Hua and Chihming Shen, "Study of maximum power tracking techniques and control of DC/DC converters for photovoltaic power system", *IEEE-PESC. Conf. Rec.*, vol. 1, pp. 86-93, 1998
- [2]. Mohamad A. S. Masoum, Seyed Mahdi Mousavi Badejani, and Ewald F. Fuchs, "Theoretical and experimental analyses of photovoltaic systems with Voltage- and Current- Based maximum power point tracking" *IEEE TRANSACTIONS ON ENERGY CONVERSION*, VOL. 17, NO. 4, DECEMBER 2002
- [3]. K.H.Hussein, I.Muta, T.Hoshino and M.Osakada., "Maximum photovoltaic power tracking: an algorithm for rapidly changing atmospheric conditions", *IEE Proceeding. Generation, Transmission and Distribution*, vol. 142, Jan. 1995.
- [4]. T. Noguchi, S.Togashi and R.Nakamoto., "Short-current pulse-based maximum-power-point tracking method for multiple photovoltaic-and-converter module system", *IEEE Trans. Ind. Electronics*, vol. 49, pp. 217-223, Feb. 2002.
- [5]. E. Koutroulis, K.Kalaitzakis and N.C.Voulgaris., "Development of a microcontroller-based, photovoltaic maximum power point tracking control system", *IEEE Trans. Power Electronics*, vol. 16, pp. 46-54, Jan. 2001.
- [6]. Vitor Fernao Pires, and Jose Fernando, "Teaching Nonlinear modeling, simulation, and control of electronic power converters using MATLAB/SIMULINK" *IEEE TRANSACTIONS ON EDUCATION*, Vol 45, No.3, AUGUST 2002.
- [7]. D. B. Snyman and J.H.R.Enslin., "Simplified maximum power point controller for PV installations", *IEEE Photovoltaic Specialists Conf. Rec.*, pp. 1240-1245, 1993
- [8]. G. Walker, "Evaluating MPPT converter topologies using a MATLAB PV model," *Journal of Electrical & Electronics Engineering, Australia*, vol. 21, 2001
- [9]. J. H.R. Enslin, M.S.Wolf, D.B.Snyman and W.Swiegers., "Integrated photovoltaic maximum power point tracking converter", *IEEE Trans Ind. Electronics*, vol. 44, pp. 769-773, Dec. 1997

An Approach for Attribute Data Measurement from a Network of Electrical Equipments as an Application of GIS

Epsita Das¹, Susmita Kundu², J.N. Bera³, R.Bramhachari³

¹Meghnad Saha Institute of Technology, Kolkata, India, e-mail:epsita_das@rediffmail.com

²Meghnad Saha Institute of Technology, Kolkata, India, e-mail:susmita_kundu7 @rediffmail.com

³Department of Applied Physics, University of Calcutta, Kolkata, India, e-mail:jitendrabera@rediffmail.com

Abstract:- In this era of technological advancements particularly in the field of wireless multimedia communications, embedded controller, etc. a centralized control system is now being demanded from each and every corner of our civilization. Apart from a single end user like a person, industries are also in demand for a centralized control system.

The centralized monitor and control systems of electrical power systems can also be improved with the adoption of the latest multimedia wireless and embedded technology. This motivates the authors to take such a work of 'An Approach for Attribute Data Measurement from a Network of Electrical Equipments as an Application of GIS'.

In this paper, the measurement and continuous monitoring technique of voltage and current of different electrical equipments placed at different locations in an area are presented.

Key words- Asynchronous Serial Communication, Network, RS-232 Standard, RS-485 Standard.

I. INTRODUCTION

SCADA is an acronym that stands for Supervisory Control and Data Acquisition.. SCADA refers to a system that collects data from various sensors at a factory, plant or in other remote control locations and then sends this data to a central computer which then sends this data to a central computer which then manages and controls the data [1].

Geographic Information System (GIS) is a powerful analytical tool used for capturing, storing, analyzing and managing data and associated attributes, which are spatially referenced to the earth. The power of GIS comes from the ability to relate different information in a spatial context and to reach a conclusion about this relationship. Different kinds of data in map form can be entered into GIS. A GIS can also convert existing digital information, which may not be in map form, into forms it can recognize and use [2].

Fundamentally, SCADA systems are designed with a purposely-sized database, very high-speed data event

processing, high reliability and rather simple graphical display functionality. The data volume associated with GIS systems is substantially higher than that of typical SCADA systems and the spatial data display requirements are considerably different to the rather basic single line diagrams SCADA systems are designed to display. Still today, SCADA systems struggle to provide a powerful and responsive geographical data display environment [3-4]. Whereas, GIS data represents real world object. Additional non-spatial data can also be stored besides the spatial data. For example, the position of any equipment at a substation is a spatial data for GIS, but the type of parameter like voltage, current, power-factor, temperature, speed etc are the additional information and can be treated as non-spatial attribute data. This paper proposes to measure different parameters from different equipments and to display them as an approach for GIS related non-spatial data.

II. DATA COMMUNICATIONS

The capturing of data is done by using 8-bit microcontroller based card and these data are fed to a PC. Asynchronous serial communication between PC and card is established by using a transmitter, a receiver and a wire. It is the simplest of serial communication protocols, and the least expensive to implement. As the name implies, asynchronous communication is performed between two (or more) devices, which operate on independent clocks [5]. In this paper, full duplex transmission has been established between the master node (PC) and the slave nodes (cards). Asynchronous serial data communication is widely used for character-oriented transmission, while block-oriented data transfers use the synchronous method. In the asynchronous method, each character is placed in between start and stop bits. This is called framing. The start bit is always one bit but the stop bit can be one or two bits. The start bit is always a 0 (low) and the stop bit(s) is 1 (high). When there is no transfer, the signal is 1 (high) is known as mark. The 0 (low) is referred to as space[6]. Serial communication requires following four parameters[7]:

(i) the baud rate of the transmission

- (ii) the number of data bits encoding a character
- (iii) the sense of the optional parity bit
- (iv) the number of stop bits

Here the baud rate is set to 9600 bps and a total of 10 bits per character. Therefore, the duration of the start bit and each subsequent bit is about 0.104 ms. The entire character frame of ten bits would be transmitted in about 1.04 ms. So, the transmission rate is $9600/10 = 960$ character per second.

Network is required to provide co-ordination between processes running on different nodes and also to accommodate remote I/O devices [8]. For a network, topology refers to a physical link or connection between different network elements. For a microcontroller network, the topologies having more reliable operation are daisy chain and common bus [9]. In this paper common bus topology is adopted because of its simplicity and cost effectiveness. In polling type of protocol, a centrally assigned master periodically polls (by sending a polling message) the slave nodes, giving them explicit permission to transmit on the network [10]. Here the assigned master is the PC that sends message to the slave nodes i.e cards.

The communication between nodes is made by using RS-485 standard of serial communication that specifies full-duplex, bi-directional data transfer. It is the only EIA standard that allows communication between multiple drivers and receivers in bus configuration. The standard has the advantage that it can treat the node as any device, which has asynchronous serial communication capabilities [9-12]. The data that travel by RS-485 network do it in form of differential electrical signals. The differential system transmits their data like a signal of voltage through a pair of conductors.

RS-232 standard is also used to link up the signals leaving or entering the PC port with the signals entering or leaving the nodes. The RS-232 standard specifies that the voltage on the wire for sending a logic 0 are from +5V to +15V and the voltage for sending a 1 are from -5V to -15V [13,14].

III. FABRICATION OF CIRCUITS

A network can be formed by a number of equipments but the observer should identify each every equipment. To make them distinct each of them must have a unique address along with a tag number. The tag number will use by the user and the address will require during communications. For example, Machine 1 (tag number) can have address of 0000H.

To start the procedure, first, the user has to specify the electrical equipment number that he/she wants to monitor and then the type of parameter(s) (voltage/current/both) through PC. This instruction is sent to each card serially. An arrangement of the cards in the network is shown in Fig 1. All of the information passes through card 1 because along with measuring parameters it is also forming the transmit (Tx Bus) and receive buses (Rx Bus) to allow data transfer. The circuit diagram of the whole experimental setup is shown in Fig 2.

When user asks for a certain parameter of a particular machine, the information is sent from the serial port of PC towards the bus. At the exit of serial port the signals are at

RS-232 standard. RS-232 signal is represented by voltage with respect to system common. It will send logic 0 for voltage between +5 V to +15 V and a logic 1 for voltage between -5 V to -15V on wire.

Most microcontrollers run on a single supply voltage of +5 V. In rough terms, logical 1 on these devices indicates that +5V is the voltage on the output pin. Logical 0 specifies that 0V is on the line. So, to connect a microcontroller serial port to a true RS-232 device, one need to convert the TTL voltages 0V and +5V into voltages about -10V and +10V [12].

Therefore, a RS-232 to TTL level converter is implemented at card 1. The voltages output of the converter are used to generate the RS-232 compliant signals [12]. It can also convert the RS-232 level signals from serial port of PC to TTL output levels. The RS-232 specification allows data transmission among only one transmitter and receiver. Therefore, a RS-485 network is established which allows multiple receivers and drivers in bus configuration. In this system all the elements that confirm it have the capacity to transmit; nevertheless a single one can do it simultaneously. Here centrally assigned master periodically polls (by sending a polling message) the slave nodes, giving them explicit permission to transmit on the network.

That called node by the user measure the asked parameter and fed it to microcontroller through ADC. From microcontroller information is sent to bus. As the bus is working at differential voltage level therefore two transceivers are implemented, one is acting as transmitter and another is acting as receiver. The transmitter is converting the information from TTL voltage level (coming from microcontroller) to RS-485 standard and sending it to bus. The receiver is doing the vice-versa. From the bus the PC retrieves the information through card 1, which forms interconnection between PC and the bus. In this way card 1 is serving the dual purpose. Card 2 and Card 3 have equal ranking and they are identical in configuration. They are only measuring electrical parameters. Continuous data is displayed at PC end and can be stored also. Front-end is designed with Visual Basic 6.0 language. Here forms are created using drag and drop techniques. A tool is used to place controls (e.g., text boxes, buttons, etc.) on the form (window). Controls have attributes and event handlers associated with them.

High level language Visual Basics 6.0 is used for developing the PC based acquisition software applicable to the GIS format. Universal Microprocessor Programming and Simulation (UMPS) software is used for assembly language programming for microcontroller 8051 firmware. The steps of the algorithm of the whole process formulated are given below:

1. Initialization of Serial Port.
2. Choose Machine Number (M/C 1 or M/C 2 or M/C 3).
3. Choose Machine Parameter (Voltage and/or Current, Temperature etc.)
4. Instruction to Start the Specified Data Acquisition.
5. Data Collection and Display.
6. Save the Data as per the GIS Format

7. For Other Machine Number and/or Machine Parameter Go to Step 2.
8. Instruction to Stop Data Acquisition.
9. Exit.

IV. CIRCUIT DIAGRAM

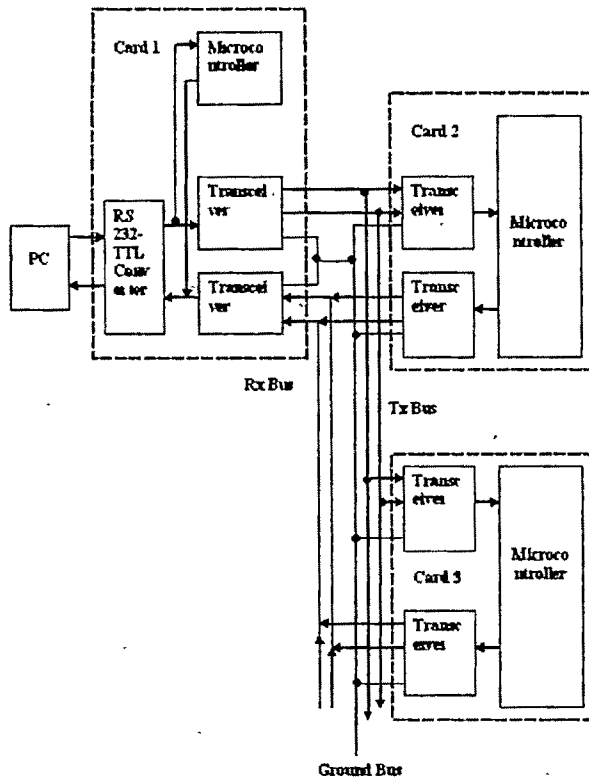


Fig. 1 Arrangements of Interconnected Cards

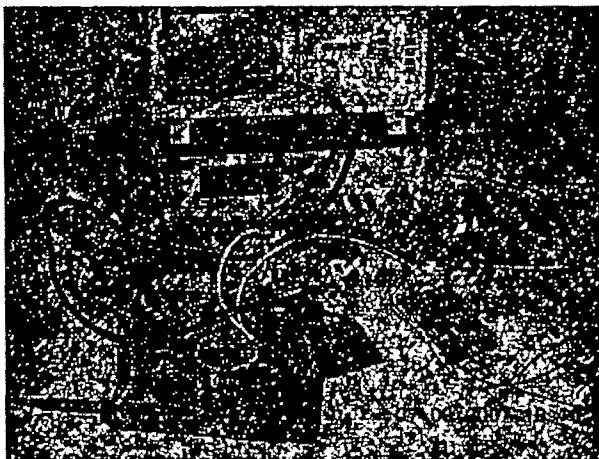


Fig. 2 Experimental Setup of Interconnected Cards

V. RESULT ANALYSIS

The following figure shows the voltage data for machine number 2. The next figure shows measured voltage and current for machine number 1.

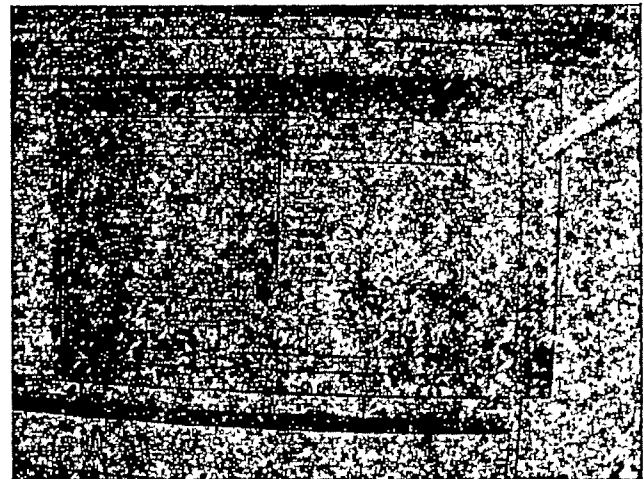


Fig. 3. Voltage Data of Machine 2

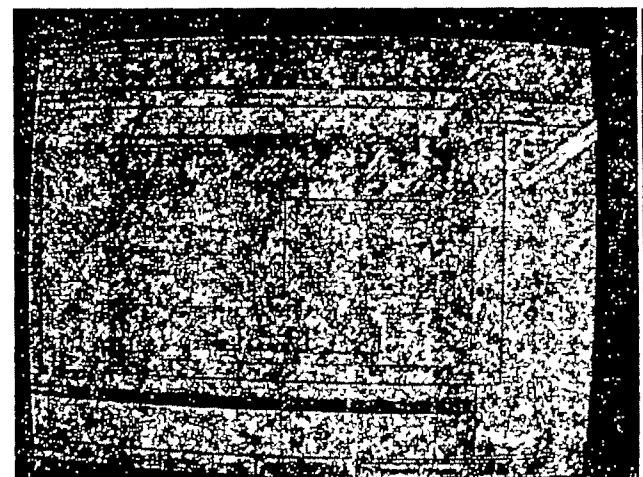


Fig. 4. Voltage and Current Data of Machine 1

The measured values of the parameters are accurate up to 99%. The deviation is due to the presence of ripples of the power supply for which the ADC produces some error in its conversion. Introducing proper filtering in the power supply can eliminate this.

VI. CONCLUSION

This paper introduces the technique to measure and monitor continuously the data of different equipments situated at different locations in an area. Three microcontroller based measuring cards, each responsible for one equipment, have been placed into a network. From the whole setup, required parameters can be monitored continuously, and can be stored for future analysis. Last stored value in the buffer of previous data acquisition is being sent as the first value. It can be resolved by refreshing the buffer through firmware programming at the instant of data acquisition. The methodology proposed in this paper is suitable for measuring the parameters like voltage, current, temperature, speed, power-factor etc. Some suitable techniques should also be introduced to establish wireless communications between

measuring cards. The system can be upgraded to control the parameters along with its monitoring facility so that a centralized GIS based electrical monitoring and control can be developed.

REFERENCES

- [1] Courtesy: <http://www.tech-faq.com/scada.shtml>
- [2] Courtesy: http://erg.usgs.gov/isb/pubs/gis_poster/
- [3] Courtesy: <http://www.gisdevelopment.net/proceedings/gita/2000/os/os003pf.htm>
- [4] Courtesy: <http://www.logicacmg.com/t/400003973/page/400003496>
- [5] Courtesy: <http://www.quatech.com/support/comm-over-asyncserial.php>
- [6] K.J. Ayala, "The 8051 Microcontroller Architecture, Programming and Applications", 2nd Edition, 1997, pp. 76-82.
- [7] Courtesy: <http://cnx.org/content/m12293/latest/>
- [8] Courtesy: http://users.ictp.it/~radionet/1998_school/networking_presentation/page2.html
- [9] F. C. Montiel, S. F. H. Machuca, D. H. Ventura, "Microcontrollers Hybrid Network for Distributed Instrumentation", *Journal of Applied Research and Technology*, August 2004, vol. 2, pp. 179-188.
- [10] B.P. Upender, P.J. Koopman Jr., "Communication Protocols for Embedded Systems", *Embedded Systems Programming*, 7(11), November 1994, pp. 46-58.
- [11] Mathew S. Gast, "802.11 Wireless Networks- the Definite Guide", O'Reilly- Shroff Publishers & Distributors Pvt Ltd, 1st edition
- [12] Courtesy: http://www.maximc.com/appnotes.cfm/appnote_number/736/
- [13] Courtesy: <http://www.seattlerobotics.org/encoder/aug97/cable.html>
- [14] "Control systems for Live Entertainment" by John Huntington, Focal Press publication, 1st edition, pp 27-37.

Author Index

- A. A. A. Jeddi, 238
 A. Aram, 247
 A. B. Chowdhury, 6
 A. Chakrabarti, 33
 A. Das, 570
 A. De, 33
 A. Gupta, 805
 A. Haddouk, 755
 A. Jaya Lakshmi, 552
 A. K. Chakrabarty, 163
 A. K. Dhakar, 746
 A. K. Dhara, 269
 A. K. Jain, 805
 A. K. M. Nurul Amin, 129
 A. K. Mukhopadhyay, 570
 A. K. Pal, 678
 A. K. Sen, 373
 A. Kazemi, 556
 A. Lekshmi, 528
 A. Mirdehghan, 717
 A. Mondal, 669
 A. Rahmati, 456,461
 A. Rastgo, 124
 A. Rastgoo, 238,247,717
 A. Sarada Devi, 43
 A. Sutradhar, 349
 A. Tadjer, 229
 Abdullah Abasiun, 726
 Abhijit Chakroborti, 6
 Abhik Mukherjee, 488
 Abu Tariq, 412
 Ajay K. Yagati, 471
 Ajoy K Chakraborty, 589
 Akashdeep Agrawal, 167
 Akshay K Rathore, 384
 Alakananda Bhattacharya, 656
 Alireza Rezazade, 110
 Alok Kumar Vishwakarma, 422,427
 Amit Konar, 656
 Amitava Das, 746
 Amrit Ghosh, 782
 Anayet U Patwari, 129
 Anil Ahlawat, 115
 Anil Kumar Bag, 297
 Anindita Senguptaa, 354
 Anish Deb, 265,354
 Ankush Ghosh, 775
 Anushree Roy, 585
 Arghya Sarkar, 561
 Arindam Ghosh, 628
 Arun JB, 699
 Ashim Kumar Dey, 637
 Asim Datta, 664
 Atif Iqbal, 521
 Awadhesh Kumar Singh, 778
 B. B. Chaudhuri, 219,224,883
 B. Basavaraja, 538
 B. Bouhafs, 229
 B. J. J Raju, 43
 B. K. Pandey, 422,427
 B. Kundu, 380
 B. M. Mohan, 293
 B. Mahdian, 556
 B. P. Singh, 417,616
 B. R. Das, 542
 B. S. Sathyanarayana, 712
 B. Sarkar, 373
 B. Chakraborty, 332
 Barwal Shwetla, 449
 Bhargab B. Bhattacharya, 646
 Bijoy K. Mukherjee, 56
 Bijoy Kumar Upadhyaya, 651
 Bipan Tudu, 297,479
 Bishakha Nandi, 605
 C Ghanshyam, 320
 C. Christofer Asir Rajan, 133
 C. Das, 669
 C. Ghennai, 533
 C. K. Chanda, 6
 C. K. Roy, 589
 C. RoyChaudhuri, 324
 CG Nandakumar, 498
 CH. Siva Kumar, 566
 Ch.Prasanth Babu, 552
 Chandhal Dey, 307
 Christian Berger-Vachon, 882
 D Sanyal, 873
 D. Das, 143
 D. Devaraj, 683
 D. Roy Choudhury, 251
 D. S. Karanjkar, 47
 D. V. S. S. Siva Sarma, 538
 David. J, 201
 Debajit Bharali, 471
 Debashis Das, 479
 Debasis Mitra, 646
 Debasis Samanta, 775
 Debasish Mondal, 339
 Deepika Masand, 147
 Devmalya Banerjee, 782
 Dibyendu Bhattacharyya, 297
 Dilip De, 282
 Dilip Dey, 389,393
 Dilip Kumar Mitra, 440
 Dipak Kumar Basu, 206,771
 Dipanwita Gangopadhyay, 80
 Durjoy Majumder, 488
 Enrique Acha, 864
 Epsita Das, 431
 F. Haghjoo, 621
 F. Shamila, 16,731
 Fazilatunnessa, 277
 G Pavan Kumar, 317
 G. B. Gharehpetian, 610
 G. Bandyopadhyay, 380
 G. Jumatova, 822
 G. Prakash, 775
 G. Sarkar, 751
 G. Tulasi Ram Das, 552
 G. Uma, 712
 G. V. Nagesh Kumar, 417
 G. V. Nagesh Kumar, 616
 Gautam Sarkar, 265,673
 Gayatri Agnihotri, 147,407
 H. Askarian, 610
 H. Baudrand, 819
 H. Belhaneche, 255
 H. Heydari, 456,461,741
 H. Mechergui, 755
 H. R. Karimi, 238
 H. R. Toodeji, 610
 H. Saha, 324
 H. Sohanian, 247
 Harsha. A., 201
 IDER Zahir, 688
 Indrajeet Boiragi, 320
 Ishtiyag M. Hossain, 129
 J.N. Bera, 269,751
 J. Amarnath, 417,616
 J. C. Singh, 775
 J. Dheeba, 796
 J. K. Das, 580,637
 J. N. Bera, 431,669
 J. N. Sharma, 722
 J. P. Tewari, 377
 J. Pal Choudhury, 282
 J. R. P. Gupta, 251
 J. Ramanjaneya Reddy, 566
 J. Sil, 302
 Jayadev Bhat, 273

Jayashri Vajpai, 699
 Jitendra Nath Bera, 585
 Jun-ichi Inoue, 786
 Jyothiraj V. P., 192,483
 K. A. Muraleedharan, 16,731
 K. Baskaran, 503
 K. C. Pradhan, 104
 K. Chaudhary, 384
 K. D. Srivatsava, 616
 K. Das (Bhattacharya), 580
 K. Gomathy, 16,731
 K. K. Mazumdar, 561
 K. S. Sherpa, 832
 K. S. Sumam, 52
 K. Selvajyothi, 80
 K. Thippeswamy, 11
 K. Vaisakh, 21,153
 K. K Garg, 449
 Kabir Chakraborty,
 1,605,832
 Kalyankumar Datta, 368
 Kaushik Mukherjee, 736
 Kavita Khare, 642
 KP Mohandas, 547
 L. Dekkiche, 840
 L. R. Srinivas, 153
 M A Sheikh, 312
 M. Abedi, 610
 M. Ahmadi, 456,461
 M. G. Wani, 453
 M. H. Banna, 277
 M. K. Saini, 805
 M. Kadjoudj, 533
 M. Malki, 255
 M. Mitra, 219,224,399,669
 M. N. Gupta791
 M. R. Shakarmai, 556
 M. Raju Hossain, 277
 M. Rizwan Khan, 521
 M. S. Bhowmick, 61,66
 M. S. Jamil Asghar, 412
 M. Shiva Kumar, 476
 M. Siva Kumar, 43
 M. Sukumar, 476
 M. Sushama, 552
 M. Umapathy, 712
 M. V. Aware, 85,517
 M. V. Ramesh, 28,435
 M. Vijaya Kumar, 99
 M. E. Benbouzid, 533
 M. Ksouri, 359
 Madhuchhanda Mitra, 38,216
 Mahantapas Kundu, 206,771
 Mallikarjun S. Holi, 187
 Mallikarjuna Swamy M. S,
 187
 Manas Kumar Bera, 344
 Manash Chanda, 782
 Manjunatha M, 187
 Manoj Pandey, 115
 Masato Okada, 786
 Md. Anwar Hussain, 814
 Mendil Boubekeur, 688
 Mita Nasipuri, 206,771
 Mohammad Hassan
 Rahimian, 726
 Mohandas K P, 211
 Mohsen Modarres, 110
 Monisha Chakraborty, 479
 Mousiki Kar (Deb), 368
 Mukhtar Ahmad, 521
 Muraleedharan CV, 498
 N. Albert Singh,
 16,683,731,796
 N. Farokhnia, 610
 N. Futane, 324
 N. Herald Anantha Rufus,
 796
 N. K. Singh, 177,182
 N. Kumaravel, 710
 N. Mandal, 329,332
 N. Ramezani, 598
 N. Sajikumar, 52
 N. Sreenivasulu, 594
 Nabanita Nath Chowdhury,
 265
 Nabarun Bhattacharyya, 297
 Narendra Nath Sinha, 637
 Naveen Kumar KU, 498
 Naveen Nischal Chava, 377
 Neeraj Verma, 94
 Neila Bédoui, 363
 Nibaran Das, 771
 Nikhil Mondal, 736
 Nilay Khare, 642
 Nitai Pal, 440,444
 Nivedita Sharma, 722
 O. V. Raghava Reddy, 99
 P A Saheeda, 768
 P. A. Janakiraman, 80,836
 P. Aruna Jeyanthi, 683
 P. B. Dutttagupta,
 389,393,589
 P. Bera, 143
 P. Chattopadhyayd, 380
 P. Das, 243
 P. K. Chattopadhyay, 163
 P. K. Chaturvedi, 104
 P. K. Gujarathi, 85
 P. Kanta Rao, 21
 P. L. MuthuKaarthik, 694
 P. Naga Manasa, 43
 P. Nagabhushan, 809
 P. P. Pal, 380
 P. R. Venkateswaran,
 273,712
 P. Ram Mohan, 99
 P. S. Rawat, 704
 P. S. Venkataramu, 694
 P. Sumathi, 836
 P. V. Prasad, 594
 P. Venkateswaran, 651
 Palash Kundu, 673
 Pankaj Chaudhary, 384
 Parikshit Yadav, 75
 Paul Forsyth, 877
 Pijush Biswas, 782
 Piyali Chatterjee, 206
 Prabal Deb, 89
 Pradip Kumar Sadhu,
 440,444
 Prasenjit Basak, 633
 Pratap Chandra Karfa, 580
 Probir Kumar Dhar, 488
 R. A. Gupta, 75,507,512
 R. Agrawal, 805
 R. Arulmozhiyal, 503
 R. Bramhachari, 431
 R. D. Kharadkar, 453
 R. Gupta, 669
 R. K. Pandey, 167,177,182
 R. K. Singh, 377
 R. Kaviani, 124
 R. Nandi, 651
 R. Naoum, 840
 R. P. Yadav, 404,704
 R. Ramchandani, 805
 R. S. Bbajpai, 466
 R. Sankaran, 528
 R. Sarkar, 332
 R. Seetharaman, 710
 Rabindranath Bera, 859
 Rahul Sharma, 119
 Rajani K. Mudi, 307
 Rajesh Babu Kollipara, 104
 Rajesh Gupta, 466,628
 Rajesh Kumar, 75,507,512
 Rajesh Tyagi, 115
 Rajeshwari S, 187
 Rajib Bandhopadhyaya, 297
 Ram Sarkar, 771
 Rambabu. Ch, 158
 Rameshkumar P, 211
 Ramtin Hadidi Ahad Kazemi,
 172

Ranjit Roy, 575	S. Sengupta,	Susmita Dey (Chaudhuri),
Ratnesh Kumar, 404	269,389,393,399,561, 637,	585
Reena M Roy, 768	664,832	Susmita Kundu, 431
Rick Kuffel, 877	S. Shabu, 493	Susmita Sur-Kolay, 646
Roshna. R, 493	S. SivaNagaraju, 594	Swanirbhar Majumder,
Rupaban Subadar, 138	S. Tripath, 805	138,216,814
Rupendranath Chakrabarti,	S. Ushakumari, 528	Swapnadip De, 782
440	S. V. Bhangale, 507,512	T. Ananthapadmanabha, 694
Rupendranath Chakrabarti,	Sahana D. Gowda, 809	T. Benabdesselam, 229
444	Saheeda P. A., 764	T. Datta, 775
Rusakov M. A., 761	Salah Salhi, 359,363	T. K. Basu, 143
S Ashok, 547	M.Ksouri, 363	T. K. Chatterjee, 444
S. Banerjee, 542	Samarjit Sengupta, 38	T. K. Mitra, 669,849
S. Basu, 805	Samir Zaki Mohamed	T. K. Sengupta, 570
S. C. Bera,	Mehrez, 234	T. R. Rangaswamy, 288
61,66,70,329,332,336	Sandeep Bharti, 704	Tanima Bhattacharya, 605
S. C. Gupta, 407	Sandeep K. Dey, 646	U. Chakraborty, 70
S. C. Kar, 269	Sandhya Rao, 187	U. Kar, 302
S. Chakraborty, 336	Sangita Das Biswas, 1,605	Umalakshmi A, 187
S. Chattopadhyay, 70,660	Satyendra Nath Mandal, 282	V. K. Keshavan, 11
S. Chattopadhyay, 844	Satyendra Prakash, 704	V. K. Sharma, 453
S. Chowdhuri, 269,751	Saurabh Goyal, 75	V. Mukherjee, 56
S. Chowdhury, 633	Saurabh Pal, 216,344	V. S. Dixit, 800
S. Ekram, 373	Selma Ben Attia, 359	Vertika Singh, 293
S. G. Hingmire, 47	Shailendra Jain, 147	Vinceta Agarwal, 94,422,427
S. G. Karad, 47	Sharmistha Mandal, 349	Vinod Chandra, 317
S. G. Thampi, 52	Sheeba O, 196	Virendra K. Gangwar,
S. H. Fathi, 610	Shilpa G. S, 187	404,704
S. Halder nee Dey, 33	Shilpi Bhattacharya, 89	Virendra P. Vishwakarma,
S. Jagadish Kumar, 566	Shveta Kundra Bhatia, 800	791
S. K. Ahamed, 399	Shyamal Kumar Goswami,	Vishnu Vardhan, 646
S. K. Basak, 542	368	Y. Kumar, 407
S. K. Mondal, 542	Sohini Roy, 471	Yang Chunyan, 260
S. K. Mukherjee, 282	Soumya Ray, 736	Yogesh V. Hote, 251
S. K. Sanyal, 651,660,844	SrinivasaRao. Gorantla,	Yohei Saika, 786
S. K. Sen, 542	28,435	Z. Mekkioui, 819
S. K. Srivastava829	Subhadip Basu, 206,771	
S. L. Mahmood, 277	Subir Kumar Sarkar, 775,855	
S. Larbi, 255	Subrata Karmakar, 399	
S. M. Ale Emran, 610	Subrata Majumdar, 163	
S. M. Pedramrazi, 741	Sucharita Mitra, 219,224	
S. M. Shahrtash, 598,621	Sudha Balagopalan, 547	
S. Meenatchisundaram, 273	Sudipta Mandal, 354	
S. Meenatchisundaram, 712	Sujata Pandey, 115,791	
S. N. Mahendra, 384	Sujesh Sreedharan, 498	
S. P. Bhattacharyya, 119	Sujit K. Biswas, 89,736,851	
S. P. Chowdhury, 633	Sujoy K. Guha, 471	
S. P. Ghoshal, 56,575	Sukesh Kumar A, 192,	
S. P. Muley, 517	201,483,196	
S. Pal, 70	Suman Saha, 6	
S. Paruya, 824	Sumana Chowdhuri, 585	
S. Phoujdar, 751	Sunil Kumar, 471	
S. Saha, 302	Sunita Mishra, 320	
S. Sao, 28,435	Surajit Chattopadhyay, 38	